ORNL/SR-2016/424
ORNL/TM-2016/424

FY 2016 Status Report: Documentation of All CIRFT Data including Hydride Reorientation Tests

Fuel Cycle Research & Development

Prepared for
US Department of Energy
Used Fuel Disposition Campaign

J.-A. Wang, H. Wang, H. Jiang, Y. Yan
B. B. Bevard, J. M. Scaglione
Oak Ridge National Laboratory

September 14, 2016
M2FT-16OR080202031

ORNL/SR-2016/424
ORNL/TM-2016/424

Materials Science and Technology Division

FY 2016 Status Report: Documentation of All CIRFT Data including Hydride Reorientation Tests

Jy-An John Wang, Hong Wang, Hao Jiang, Yong Yan

Program Manager
Bruce Bevard and John Scaglione

Date Published: September 14, 2016

Prepared by
OAK RIDGE NATIONAL LABORATORY
Oak Ridge, TN 37831-6283
managed by
UT-BATTELLE, LLC
for the
US DEPARTMENT OF ENERGY
under contract DE-AC05-00OR22725

This page intentionally left blank.

SUMMARY

The first portion of this report provides a detailed description of fiscal year (FY) 2015 test result corrections and analysis updates based on FY 2016 updates to the Cyclic Integrated Reversible-Bending Fatigue Tester (CIRFT) program methodology, which is used to evaluate the vibration integrity of spent nuclear fuel (SNF) under normal conditions of transport (NCT). The CIRFT consists of a U-frame test setup and a real-time curvature measurement method. The three-component U-frame setup of the CIRFT has two rigid arms and linkages connecting to a universal testing machine. The curvature SNF rod bending is obtained through a three-point deflection measurement method. Three linear variable differential transformers (LVDTs) are clamped to the side connecting plates of the U-frame and used to capture deformation of the rod.

The CIRFT contact-based measurements, a three LVDT-based curvature measurement system, on SNF rods has been proven reliable in testing. However, how the LVDT head contacts the SNF rod may have a significant effect on the curvature measurement, depending on the magnitude and direction of rod curvature. It has been demonstrated that the contact issues can be corrected by using a correction to the sensor spacing. The sensor spacing defines the separation of the three LVDT probes and is critical to calculating rod curvature after deflections are obtained.

The sensor spacing correction can be determined using chisel-type probes. The method has been critically examined this FY and has proven difficult to execute in a hot cell environment. Thus, this correction cannot be implemented effectively. A correction based on the proposed equivalent gauge length has the required flexibility and accuracy and can be appropriately used as a correction factor.

The correction method based on the equivalent gauge length has been successfully used in CIRFT data analysis for the dynamic tests conducted on Limerick Nuclear Power Station (LMK) (17 tests), North Anna Power Station (6 tests), and Catawba Nuclear Station mixed oxide (MOX) (10 tests) SNF samples. These CIRFT tests were completed in FY 2014 and FY 2015. The data sets obtained from static measurements and dynamic online monitoring were processed and analyzed, and the fatigue life of rods was characterized in terms of moment, curvature, and equivalent stress and strain.

The second portion of this report provides the latest CIRFT data, including data for the hydride reorientation test. The variations in fatigue life are provided in terms of moment, equivalent stress, curvature, and equivalent strain for the tested SNFs. The equivalent stress plot collapsed the data points from all of the SNF samples into a single zone. A detailed examination revealed that, at the same stress level, fatigue lives display a descending order as follows: H. B. Robinson Nuclear Power Station (HBR), LMK, and MOX. Just looking at the strain, LMK fuel has a slightly longer fatigue life than HBR fuel, but the difference is subtle.

A discontinuity, or knee point, for the endurance limit in the curve of moment and curvature or equivalent quantities is more clearly defined for LMK and HBR fuels.

The test results appear to indicate that impacts and radial hydride treatment (RHT) have a negative effect on fatigue life. The effect of thermal annealing on MOX fuel rods was smaller at higher amplitudes, but the intensity increased at lower amplitudes of moment. Thermal annealing tended to extend the fatigue life of MOX fuel rod specimens. However, for HR4 specimens, the thermal annealing treatment showed a negative impact on the fatigue life compared to the HBR rod.

The third portion of this report provides finite element analysis (FEA) dynamic deformation simulation of SNF assemblies . In a horizontal layout under NCT, the fuel assembly's skeleton, which is formed by guide tubes and spacer grids, is the primary load bearing apparatus carrying and transferring vibration loads within an SNF assembly. These vibration loads include interaction forces between the SNF assembly and the canister basket walls. Therefore, the integrity of the guide tubes and spacer grids

critically affects the vibration intensity of the fuel assembly during transport and must be considered when developing the multipurpose canister (MPC) design for safe SNF transport.

Random vibration registered at the SNF transport cask, which is excited from the railcar bed, provides the external loading driver to vibrate the SNF assembly. In addition to this external vibration driver, the fuel assembly also registers internal transient shocks resulting from the dynamic contact interactions among the fuel assembly components inside the cask. These components include the skeleton, fuel rods, and canister basket walls. Their dynamic interactions can significantly increase the high-rate impact loading intensity within fuel assembly components during NCT.

This research also investigates SNF assembly deformation dynamics during normal vibration modes, and during the cask's internal transient shock mode during NCT. The finite element method was used to develop vibration simulation modeling for the targeted SNF subassembly. Dynamics analyses were performed in the frequency domain to study the modal characteristics of the fuel assembly system and in time domain to simulate the transient dynamic response of the fuel assembly. FEA simulation results were used to determine the stress and strain states of submodel components, such as fuel rods, guide tubes, spacer grids, nozzles, and the basket wall, under vibration loading during normal vibration conditions and transient shocks during NCT. The resulting stress/strain data can be used further in fuel assembly component failure analyses. The contact interactions between system components during transient dynamic simulation have also been investigated.

To further evaluate the intensity of contact interaction induced by the local contacts' impact loading at the spacer grid, detailed models of the spring and dimples of the spacer grids were created. The impacts between the fuel rod and springs and dimples were simulated with a 20 g transient shock load. The associated contact interaction intensities in terms of reaction forces were estimated from the FEA results. The corresponding bending moment that generates the same resultant stress on the cladding registered a 20 g acceleration transient shock was also determined to define the same intensity pure bending loading to be used in CIRFT vibration testing. To estimate the damage potential of this transient shock to the SNF vibration lifetime, drop tests were performed on the CIRFT specimens. The combined drop-impact and CIRFT cyclic test results show reduced fatigue strength from SNF specimens. FEA was used to investigate the contact reaction for CIRFT samples during impact loading induced by drop tests, and the result was compared with that from a 20 g acceleration transient shock load. This report also provides CIRFT system dynamic simulation to predict the system's dynamic performance and to verify the system's efficiency under different vibration frequencies.

ACKNOWLEDGMENTS

This research was sponsored by the US Department of Energy (DOE) Used Fuel Disposition Campaign under DOE contract DE-AC05-00OR22725 with UT-Battelle, LLC. The authors thank ORNL program managers Bruce Bevard and John Scaglione for their support and guidance during the project, Chuck Baldwin for post-irradiation examination, Dale Caquelin and Bob Morris for providing logistic support, Josh Schmidlin for fuel rod cutting and dimension measurement, Bryan Woody and Scott Thurman for hot cell operation support, Brian Sparks and Randy Parten for drawing and machining support, Lianshan Lin, Rose Montgomery, and Emily Huckabay for reviewing the report.

This page intentionally left blank.

CONTENTS

This page intentionally left blank.

LIST OF FIGURES

LIST OF TABLES

This page intentionally left blank.

ACRONYMS

BWR	boiling water reactor
CIRFT	Cyclic Integrated Reversible-Bending Fatigue Tester
DOE	US Department of Energy
FEA	finite element analysis
FY	fiscal year
HBR	H. B. Robinson Nuclear Power Station
HBU	high-burnup
HR	Hydride Reorientation
ID	inner diameter
LMK	Limerick Nuclear Power Station
LVDT	linear variable differential transformer
MOX	Catawba mixed uranium-plutonium oxide
MPC	multipurpose canister
NA	North Anna Power Station
NCT	normal conditions of transport
NRC	US Nuclear Regulatory Commission
NUREG	Nuclear Regulatory Commission technical report
NUREG/CR	NUREG contractor report
OD	outer diameter
ORNL	Oak Ridge National Laboratory
PCI	peripheral component interconnect
PIE	post-irradiation examination
PNNL	Pacific Northwest National Laboratory
PPI	pellet-to-pellet interface
PWR	pressurized water reactor
RHT	radial hydride treatment
SNF	spent nuclear fuel
SS	stainless steel

This page intentionally left blank.

USED FUEL DISPOSITION CAMPAIGN

FY 2016 Status Report: Documentation of All CIRFT Data including Hydride Reorientation Tests

1. INTRODUCTION

The objective of this research is to collect experimental data on spent nuclear fuel (SNF) from pressurized water reactors (PWRs), including the H. B. Robinson Nuclear Power Station (HBR) and North Anna Power Station (NA), and the Limerick Nuclear Power Station (LMK) boiling water reactor (BWR) under simulated transportation environments using the Cyclic Integrated Reversible-Bending Fatigue Tester (CIRFT) [1–5], an enabling hot-cell testing technology developed at Oak Ridge National Laboratory (ORNL). This data will be used to support ongoing spent fuel modeling activities and to address regulatory issues associated with SNF transport.

Testing of SNF rods from PWRs—HBR and NA Zircaloy-4 cladding and Catawba M5 cladding [6–8]—demonstrated that the cyclic fatigue lifetime of SNF rods generally depends on the amplitude of the applied moment when a 5 Hz waveform is used. It was also demonstrated that the lifetime of SNF is related to the degree of damage to cladding and fuel pellets resulting from irradiation after long-term service inside a reactor. Lifetime is also affected by the loading amplitude and loading rate of the applied moment caused by different fatigue damage mechanisms triggered by the intensity of pellet-cladding mechanical interaction. Detailed high-burnup (HBU) HBR CIRFT results are published in Nuclear Regulatory Commission technical report (NUREG)/CR-7198 [9]. The CIRFT program also extended the vibration data collected to include Zircaloy-2 data from a BWR environment [10]. A stress-failure frequency (S-N) trend similar to the PWR data was also observed in the BWR data. Furthermore, the accumulated damage from the combination of low-amplitude CIRFT cyclic bending plus transient shocks (high-amplitude bending load) indicates an accelerated aging effect compared with low-amplitude cyclic loading alone.

CIRFT enables examination of the underlying mechanisms of SNF system dynamic performance. Major findings from CIRFT evaluations on HBU SNF include:

- SNF system interface bonding plays an important role in SNF vibration performance.
- Fuel structure contributes to the SNF system stiffness.
- There are significant variations in the stress and curvature of SNF systems during vibration cycles, which results from the interaction of pellets and cladding.
- SNF failure initiates at the pellet-pellet interface region and appears to be spontaneous.

Due to the inhomogeneous composite structure of the SNF system, finite element analyses (FEA) are needed to translate the global moment-curvature measurement into local stress-strain profiles for further investigation. Furthermore, the detailed mechanisms of the pellet-pellet and pellet-cladding interactions and the stress concentration effects at the pellet-pellet interface cannot be readily obtained from a CIRFT system measurement. Therefore, detailed FEA will be necessary to further understand the global test response.

In addition to continuing CIRFT data collection, the other primary focus in fiscal year (FY) 2016 was to develop the theoretical basis to improve CIRFT curvature measurements and to verify testing protocols needed to validate this approach. The effort was extended to cover all the Department of Energy (DOE)-sponsored CIRFT data, excluding HBR data sponsored by the US Nuclear Regulatory Commission (NRC) [9].

The FEA protocols developed for this activity provide powerful tools to quantify the CIRFT system biases and the associated uncertainties of HBU SNF during CIRFT examinations. In FY 2016, efforts were also extended to loading intensity investigations and evaluation w.r.t. SNF vibration under normal condition of transport (NCT). These efforts served as additional benchmarks for quantifying and justifying the CIRFT test loading intensity ranges.

1.1 Cyclic Integrated Reversible-Bending Fatigue Tester

The CIRFT, which was developed by ORNL [1–5, 10–14], consists of a U-frame (Fig. 1). The U-frame includes two rigid arms, connecting plates, and universal testing machine links. A rod specimen is coupled to the arms with two specially designed grips. The U-frame is oriented in a horizontal plane and is driven by electromagnetic force–based Bose dual linear motors. With assistance from the coupling, linear motions applied at the loading points of the rigid arms are converted into bending moments. The dual linear motor (model LM2) test bench has a maximum load capacity of ±3,000 N and a maximum stroke of ±25.6 mm. Bending is imposed through the U-frame's dual driving points and a 101.60 mm loading arm. Under a pair of outward-facing forces, or displacements, the rigid arms are opened, and bending moments force the rod to deflect away from the operator. The rigid arms are closed by a pair of facing forces, forcing the rod to deflect inward. The CIRFT can deliver dynamic loading to a rod specimen in the load-control mode at 5 to 10 Hz. The current configuration enables the system to test a rod 9.70 mm to 11.74 mm in diameter, 152.40 mm (6 in.) in length, and 50.80 mm (2 in.) in gauge section. Three linear variable differential transformers (LVDTs) measure rod deflections at three adjacent points within the gauge section to determine rod curvature, which is then correlated to the applied moment to characterize the mechanical properties of the bending rod. Online monitoring captures the mechanical property changes during testing, revealing fatigue behavior.

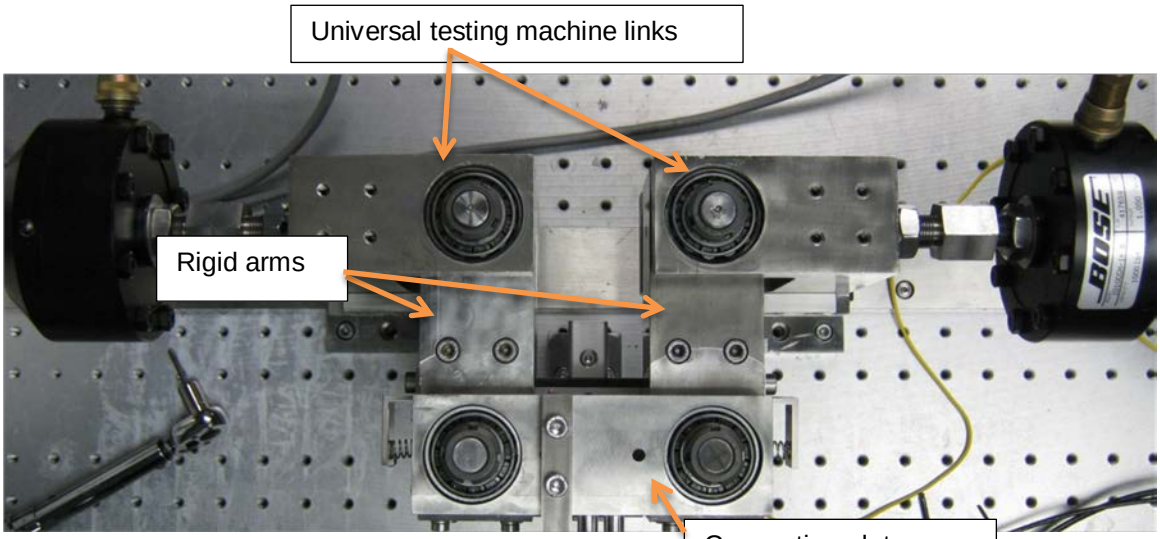

(a)

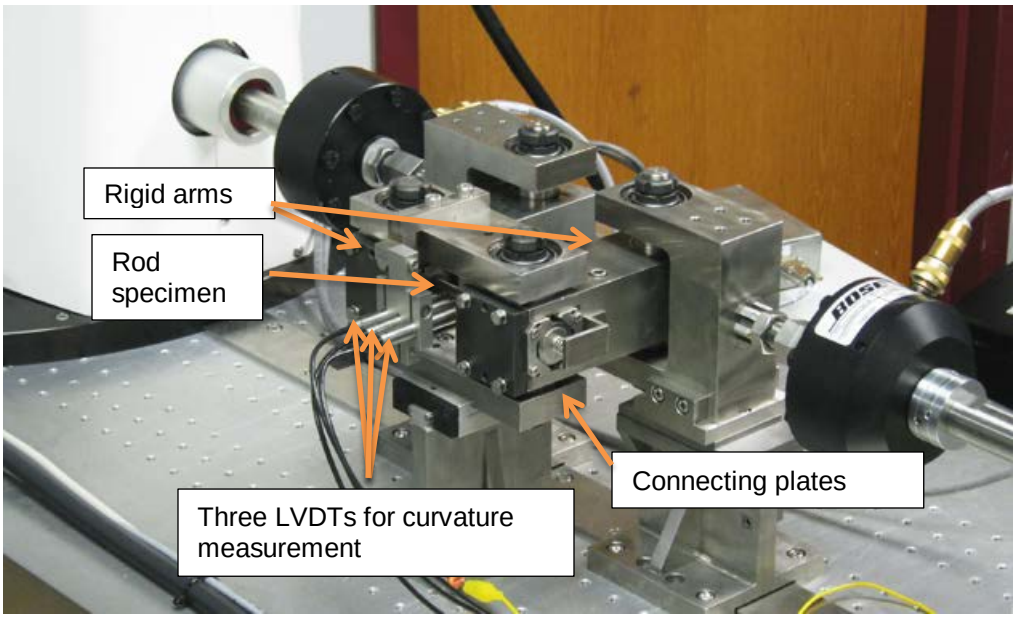

(b)

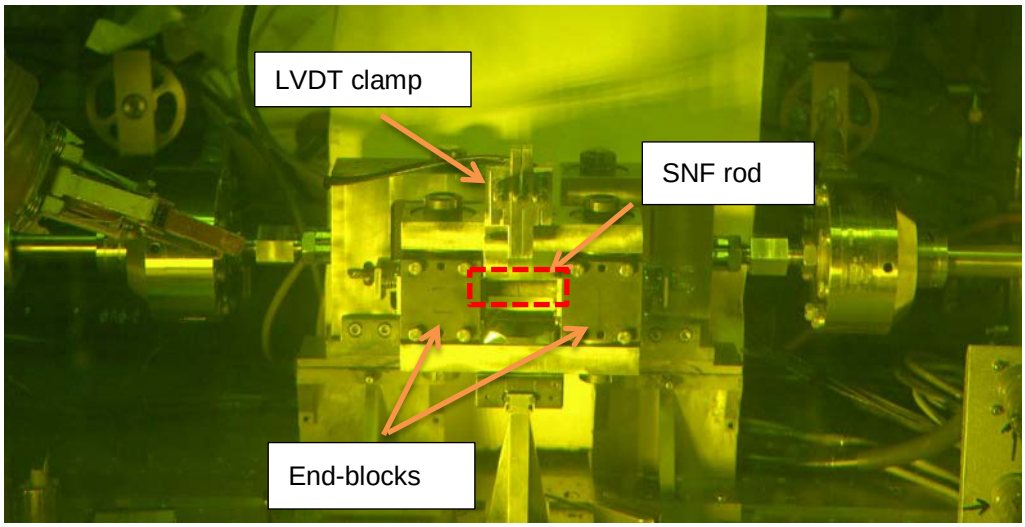

(c)

Fig. 1. Three views of the CIRFT at ORNL: (a) Horizontal layout of the U-frame setup, (b) a rod specimen undergoing testing with three LVDTs in place for curvature measurements (the operator is facing the LVDTs), and (c) a front view of the CIRFT installed in a hot cell.

1.2 Moment and Curvature Calculations

Measurement data are converted into the applied moment and curvature based on the load channel (load1 and load2) information, the loading arm length (101.60 mm), and LVDT data (LVDT1, 2, and 3).

The moment was estimated by

$$M = F \times L \quad , \tag{1}$$

where F is the averaged value of applied loads (load1 and load2) from the Bose dual motors, and L is the loading arm length, 101.60 mm.

Theoretically, the bending radius and maximum strain of a rod can be estimated based on the traveling displacement at the loading points of the rigid arm. However, the displacement measured contains the contribution of the compliant layers and the level of loading.

To address this issue, direct measurement of specimen displacement at three adjacent points along the rod method was adopted [15] and has been implemented to evaluate the curvature of a bending rod in this study [1, 11].

Given any curve C and a point P on it, there is a unique circle or line that most closely approximates the curve near P, the osculating circle at P. The curvature of C at P is then defined as the curvature of that circle or line. The radius of the curvature is defined as the reciprocal of the curvature. Given the deflections from three LVDTs—d_1, d_2, and d_3 (Fig. 2)—the curvature κ of the bending rod was determined using the following equation:

$$\kappa = [(x_0 - d_2)^2 + y_0^2]^{-1/2} \quad , \tag{2}$$

where

$$x_0 = \frac{-2m_a m_b h - m_a(d_2 + d_3) + m_b(d_1 + d_2)}{2(m_b - m_a)} \quad ,$$

$$y_0 = -\frac{1}{m_a}\left(x_0 - \frac{d_1 + d_2}{2}\right) - \frac{h}{2} \quad ,$$

and

$$m_a = \frac{h}{d_2 - d_1} \quad ,$$

$$m_b = \frac{h}{d_3 - d_2} \quad .$$

The sensor distance is h (12 mm).

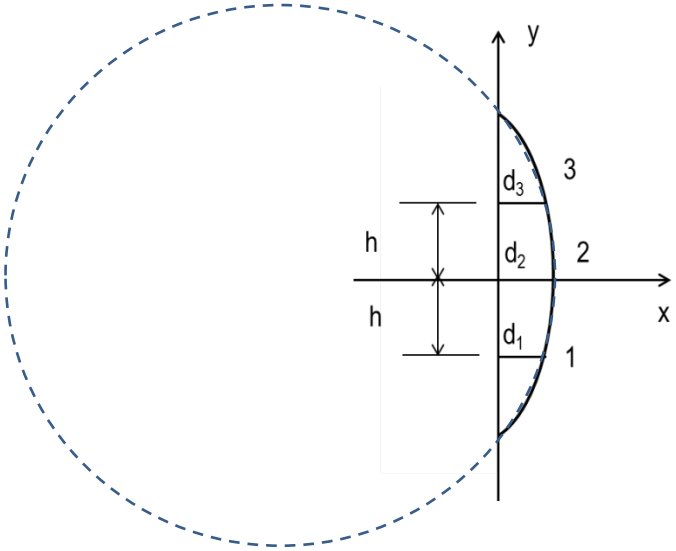

Fig. 2. Determination of the bending curvature of the rod based on deflections measured at three points.

The arrangement of the three LVDTs and their position in the setup can be seen in Fig. 3. An equivalent strain-stress curve (Eq. 3) can be obtained by assuming the SNF rod can be idealized as a linear, elastic, homogeneous material without considering the effects of pellet-cladding interaction. The equivalent stress was calculated using

$$\sigma = M \times y_{max}/I, \tag{3}$$

where I is the moment of inertia, $I = I_c + I_p$. I_c and I_p are moments of inertia of the cladding and pellet, respectively, and y_{max} is the maximum distance to the neutral axis of the test rod for the section and is measured by the radius of the cladding. The calculation of stress disregards the difference in elastic moduli between cladding and pellets.

The equivalent strain is determined using

$$\varepsilon = \kappa \times y_{max}. \tag{4}$$

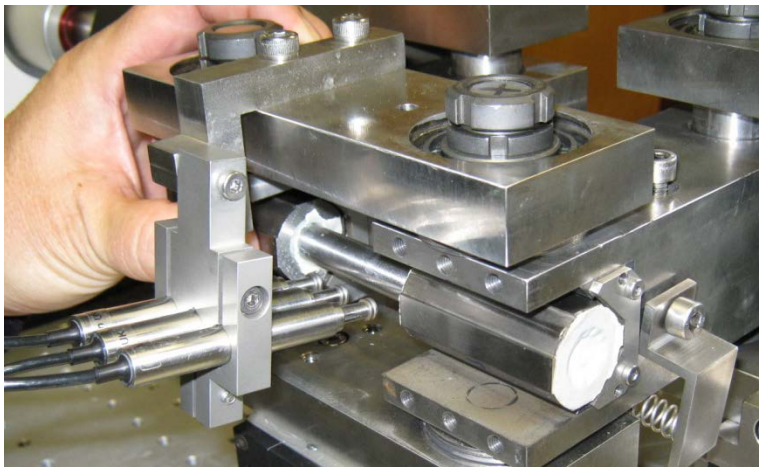

Fig. 3. Grip design of CIRFT with one end-block removed.

1.3 Sensor Spacing Correction for Curvature Measurements

The contact of the LVDT probe with the rod being tested depends on the bending direction and induced curvature, especially when contact is made by a disk with a flat head. This contact caused the sensor spacing to deviate from the ideal condition (Fig. 4).

For a positive curvature, when tensile load was applied to U-frame, actual sensor spacing h_2 is,

$$h_2 = h + \Delta h, \tag{5}$$

and for negative curvature, when compressive load was applied to U-frame, actual sensor spacing h_1 is

$$h_1 = h - \Delta h. \tag{6}$$

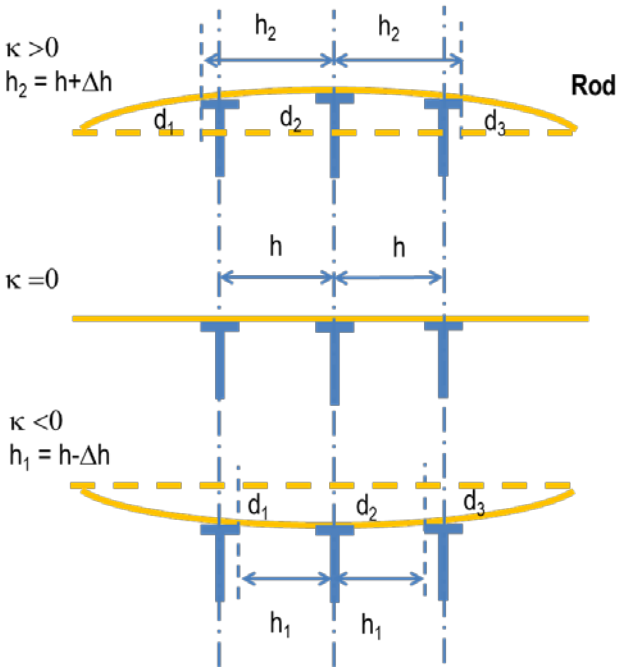

Fig. 4. Deflections measured by LVDTs may be at different points from initial positions, and sensor spacing *h* needs to be corrected.

A polycarbonate rod (0.4375 in. diameter and 6 in. length), specimen PC01, was tested under -6 mm and +6 mm rigid arm end displacements with disk-head LVDTs. The curvatures in positive and negative direction appeared to be quite different (Fig. 5).

The same specimen (PC01) was tested with the same level of applied displacement, but curvatures were based on chisel-head LVDTs. The curvatures in both directions were close to 2 m^{-1}. The repeatable results indicated that PC01 behaved elastically, and the effect of chisel-head LVDTs on the curvature was negligible.

Analysis revealed the following:

- For a positive curvature induced by tension on the U-frame, a sensor adjustment of 2.90 mm is needed to have the disk-based measurement match the chisel-based measurement.
- For a negative curvature induced by compression on the U-frame, a sensor adjustment of 2.40 mm is needed for the disk-based measurement to match the chisel-based measurement.

The obtained sensor spacing adjustments for both conditions will be used in the data analysis in Section 2.

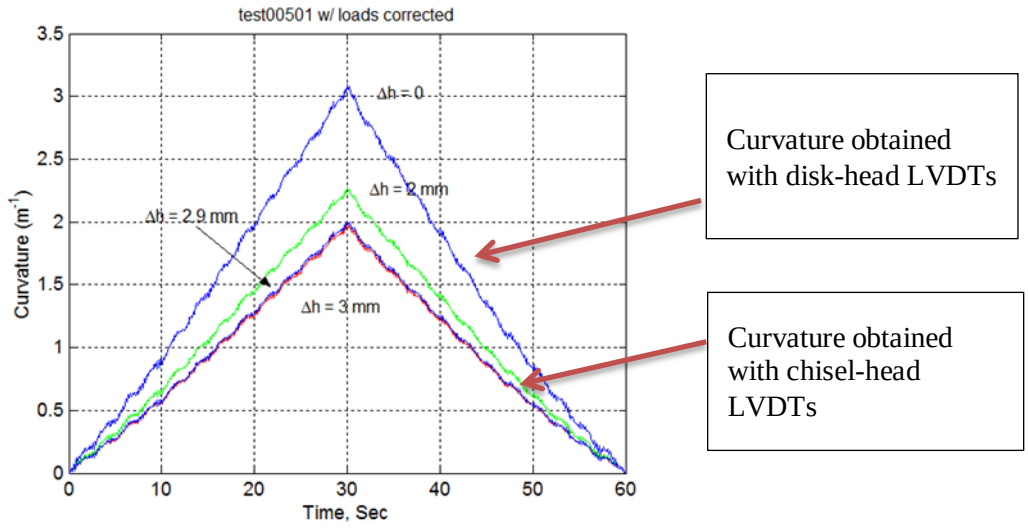

(a)

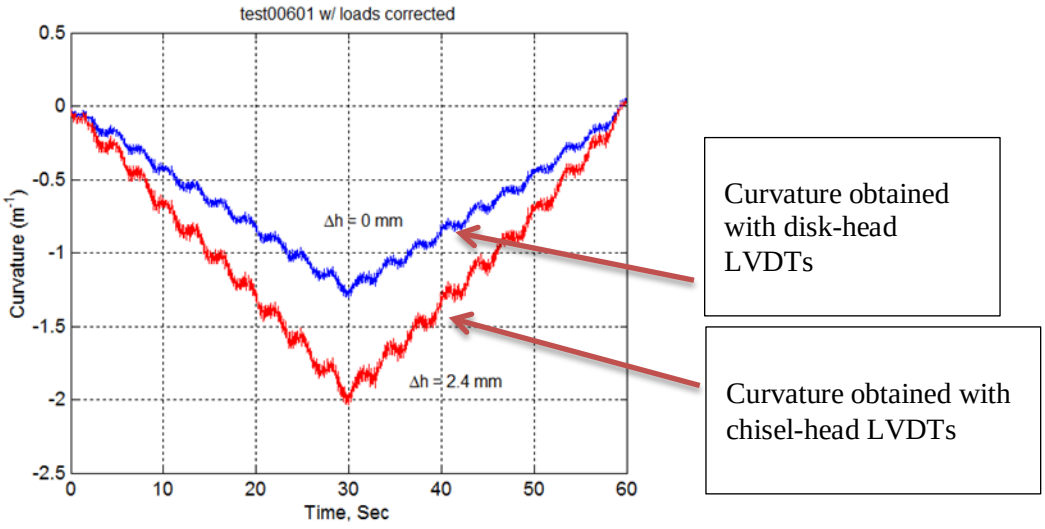

(b)

Fig. 5. (a) For a positive curvature induced by tension on U-frame, a sensor adjustment of 2.9 mm is needed to have the disk-based measurement matched with the chisel-based measurement. (b) For the negative curvature induced by compression on U-frame, a sensor adjustment of 2.4 mm is needed for the disk-based measurement to match the chisel-based measurement.

2. DEVELOPMENT OF REFINEMENT TECHNIQUES FOR CIRFT CURVATURE DATA MEASUREMENT

2.1 Technical Issues

Known technical issues with CRIFT curvature measurements include:

1) Can the curvature measured by the three LVDTs be evaluated?
2) How close is the corrected curvature to the actual curvature?
3) Is the correction method applicable to all levels of curvature?
4) Is the correction method applicable to both static and dynamic cases?

Consequently, these questions represent the core activities of the CIRFT data update initiative.

2.2 Technical Approach

ORNL proposed using strain gauge measurements on surrogate rods to further benchmark the three LVDT curvature measurement method. This is based on the following rationale:

1) When using a homogenous bending rod, the maximum strain at the extreme fiber can be evaluated because the estimate of that strain has been theoretically established. For the calculation to be effective, the deformation of the rod is limited to the elastic region of the material.
2) The three LVDT-based curvatures in step one can be converted into the strain at the extreme fiber.
3) The strain at the extreme fiber can be measured with a strain gauge.
4) To verify the curvature measurement in step one, the gauge-based strain in step three can be compared with the three LVDT-based strains.

2.3 Experimental Results

During FY 2016, ORNL accomplished the following:

1) Purchased a four-channel strain gauge signal conditioning amplifier (Vishay Micro-Measurements 2310B).
2) Integrated the conditioning amplifier 2310B into the control box of PCI-82 in the Bose testing machine (L218, 4515).
3) Studied strain gauges for surrogate rods for out-cell verification tests for both small and large deformation cases.
4) Performed CIRFT evaluations on a surrogate rod made of 304 cladding only (no pellets involved) for small deformation.
5) Performed CIRFT evaluations on a surrogate rod made of polycarbonate for large deformation.
6) Analyzed the hot cell CIRFT data on MOX SNF and other SNF tested under DOE sponsorship (Sect. 3).

The 4-channel 2310B amplifier (Vishay Micro-Measurements, Raleigh, NC, Fig. 6) has following features:

- Fully adjustable calibrated gain from 1 to 11,000.
- Accepts all strain gauge inputs (foil or piezoresistive), potentiometers, direct current differential transformers (DCDTs), etc.

- Bridge excitation from 0.7 to 15 Vdc (11 steps), plus 0.2 to 7 V continuously variable
- Input impedance above 100 megohms
- Two simultaneous buffered outputs: ±10 V, ±1.4 V (for tape recorders)
- Wide band operation exceeding 60 kHz, −0.5 dB at all gains and output levels
- Four-frequency active 6-pole filter (10 to 10,000 Hz)
- Dual-range (±5000 and ±25000 με) automatic bridge balance with keep-alive power to preserve balance for months without external power
- Dual-polarity two-step double-shunt calibration

Fig. 6. Strain gauge signal conditioning amplifier 2310B, Micro-Measurements.

Two types of strain gauges (Vishay Micro-Measurements, Raleigh, NC) were identified for this study, and the gauge factors are given in Table 1. The setups of surrogate rods with the strain gauge mounted are shown in Fig. 7 and Fig. 8.

Table 1. Strain gauges used in out-cell verification tests

Surrogate rod	Strain gauge designation	Gauge factor
SS304 surrogate rod	EA-06-250BF-350	2.055 ± 0.5%
Polycarbonate rod	CEA-06-125UW-350	2.095 ± 0.5%

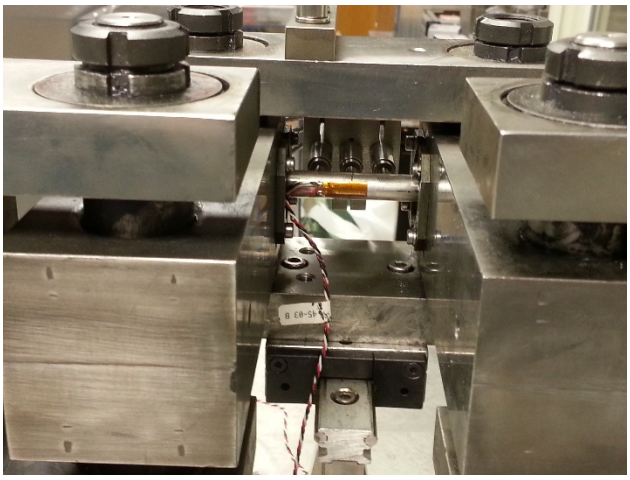

Fig. 7. Setup of SS304 surrogate rod with strain gauge mounted in CIRFT.

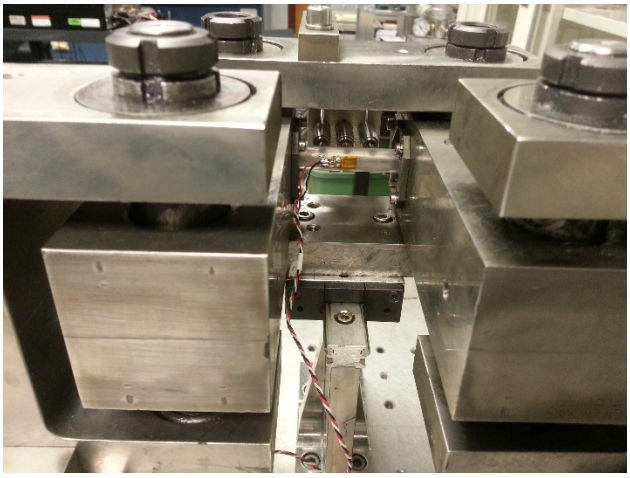

Fig. 8. Setup of polycarbonate surrogate rod with strain gauge mounted in CIRFT.

2.3.1 SS304 Surrogate Rod CIRFT Evaluation and Data Analysis

The proposed curvature correction was tested against several established methods, including curvature measurements using a chisel-type probe and a strain gauge.

2.3.1.1 Base Considerations for Data Analysis

The following information was used in the data analysis:

1) The LVDT-based strain calculation was based on the discussion in Section 1.1.

2) The correction was based on the assumption that the gauge length is equal in both the peak and valley of one data block (two cycles of a sine wave). The half gauge length (Lg/2) was calculated using the following equation:

$$Lg/2 = \sqrt{2d_2/\kappa}\,, \tag{7}$$

where d_2 is the middle LVDT reading in m and κ is the calculated curvature in m^{-1}.

3) The gauge-based strain was obtained with the following equation:

$$\varepsilon = 10^6/(0.25*V_{BR}*A*S_g) , \quad (8)$$

where ε is micro strain or με, V_{BR} is the bridge voltage, A is the amplification, and S_g is the gauge factor.

4) The strain can be estimated according to the condition of the rod by

$$\varepsilon = (M / EI) y_{max} , \quad (9)$$

where M is the applied moment amplitude, EI is estimated 42.8 Nm^2, y_{max} = 4.78 mm.

2.3.1.2 Chisel-Type Probe as Calibration Method

Testing on surrogate rod SS30402 was conducted in 0.05 Hz and 5 Hz to simulate static and dynamic loading (Table 2).

Table 2. Testing condition of surrogate rod SS30402 with disk- and chisel-probes

No.	pk1 (mm, N)	pk2 (mm, N)	Frequency	Cycles	Sum	LVDT type
44	−0.4	0.4	0.05	3		Flat disk, D6
45	−0.6	0.6	0.05	3		Flat disk, D6
46	−0.8	0.8	0.05	3		Flat disk, D6
47	75	75	5	500	500	Flat disk, D6
48	−0.4	0.4	0.05	3		Flat disk, D6
49	−0.6	0.6	0.05	3		Flat disk, D6
50	−0.8	0.8	0.05	3		Flat disk, D6
51	−100	100	5	500	1,000	Flat disk, D6
52	−0.4	0.4	0.05	3		Flat disk, D6
53	−0.6	0.6	0.05	3		Flat disk, D6
54	−0.8	0.8	0.05	3		Flat disk, D6
55	−125	125	5	500	1,500	Flat disk, D6
56	−0.4	0.4	0.05	3		Chisel, D6
57	−0.6	0.6	0.05	3		Chisel, D6
58	−0.8	0.8	0.05	3	0	Chisel, D6
59	−75	75	5	500	500	Chisel, D6
60	−0.4	0.4	0.05	3		Chisel, D6
61	−0.6	0.6	0.05	3		Chisel, D6
62	−0.8	0.8	0.05	3		Chisel, D6
63	−100	100	5	500	1,000	Chisel, D6
64	−0.4	0.4	0.05	3		Chisel, D6
65	−0.6	0.6	0.05	3		Chisel, D6
66	−0.8	0.8	0.05	3		Chisel, D6
67	−125	125	5	500	1,500	Chisel, D6

The curvature values based on the disk-type probe and the corrected curvature are presented in Fig. 9 through Fig. 12, along with those based on flexural rigidity (EI) and the chisel-type probe. Major curvature observations included the following:

1) Measurement with the chisel-type probe showed uncertainty in curvature measurments; no defined trend was seen in the measured curvatures as compared to those taken with the disk-type probe.
2) The tests with the chisel- and disk-type probes were not conducted concurrently. The probe contact condition was changed when the probe was changed, and the three LVDTs were remounted; the sensor spacing was sensitive to the change of contact condition.
3) The corrected curvature was shown to be close to the EI-based curvature.
4) The spacing correction (Δh) exhibited a trend to increase with the level of displacement input (disp1 on the side of motor 1). However, a large variance of correction was seen near small displacements.
5) The level of correction was also far less than those based on the calibration of chisel-type probe (2.40 or 2.90 mm).

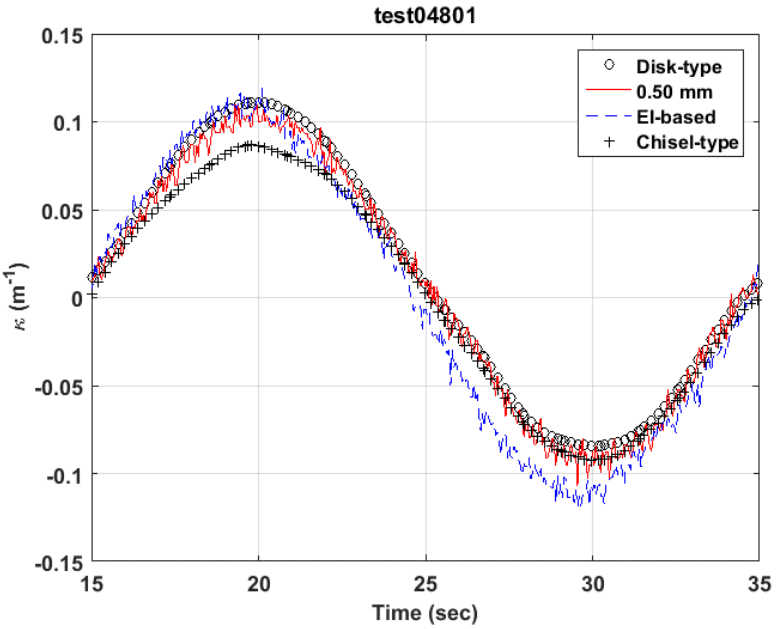

(a) 0.4 mm

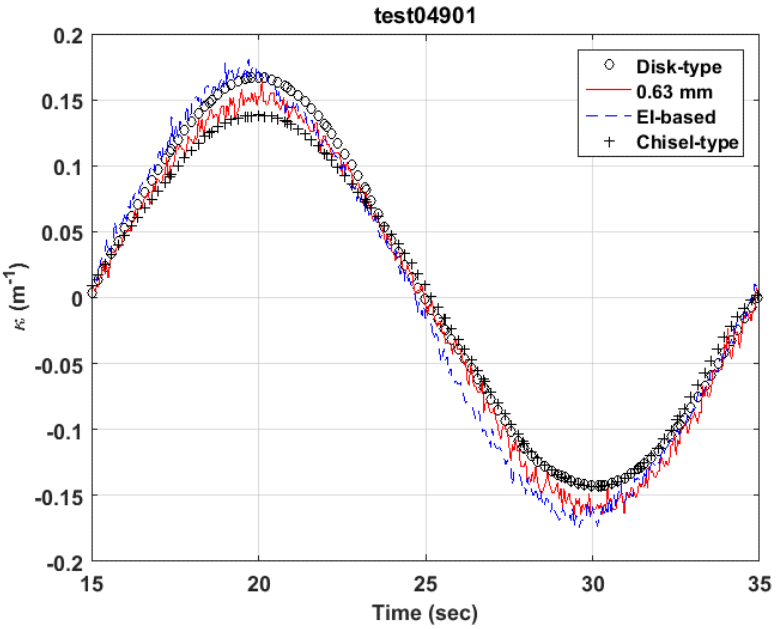

(b) 0.6 mm

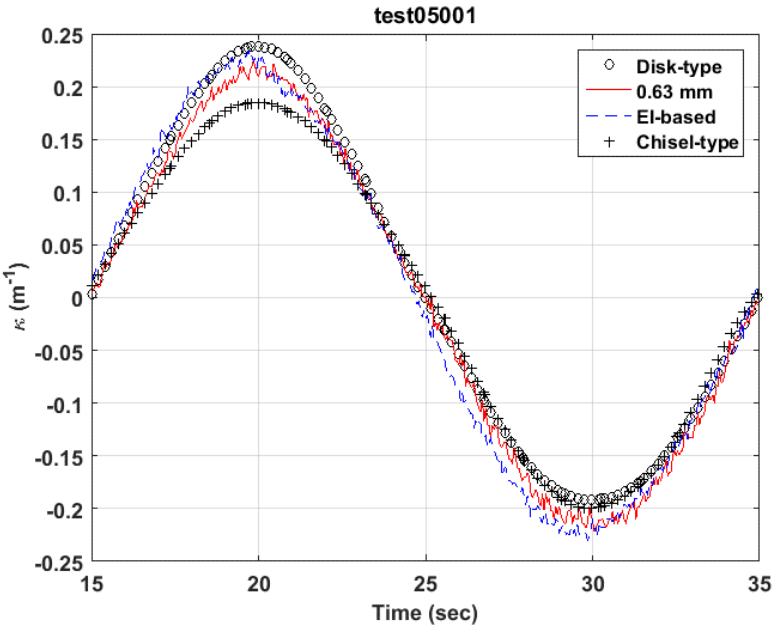

(c) 0.8 mm

Fig. 9. Curvatures based on disk-type probe, corrected, EI-based, and chisel-type probe, for 0.05 Hz displacement at loading point of U-frame arm: (a) 0.4 mm, (b) 0.6 mm, and (c) 0.8 mm. EI = 42.8 Nm^2.

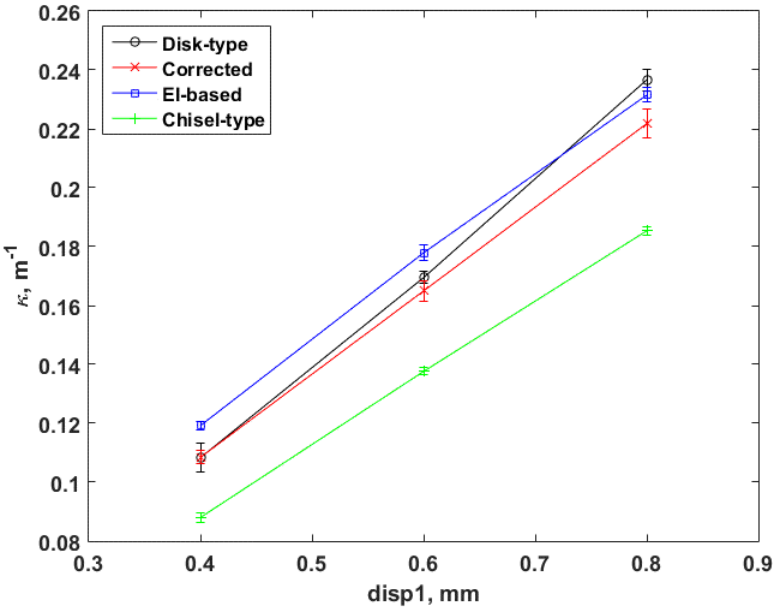

(a) Peak

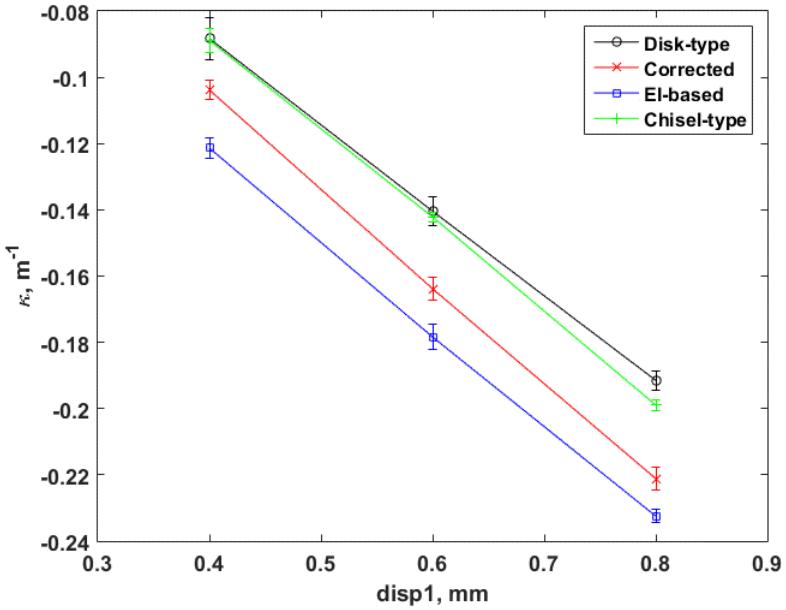

(b) Valley

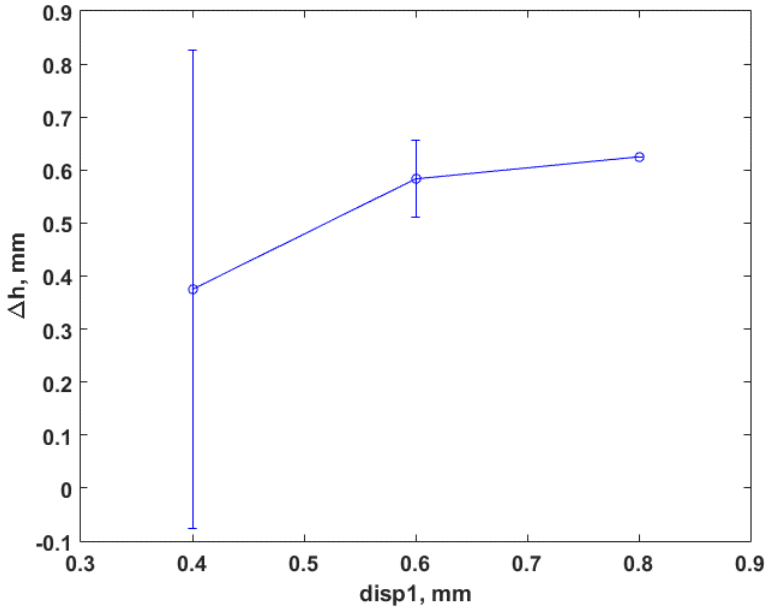

(c) Spacing correction

Fig. 10. (a) Peak and (b) valley responses of curvature waveforms and (c) spacing corrections under various disp1 amplitudes at 0.05 Hz.

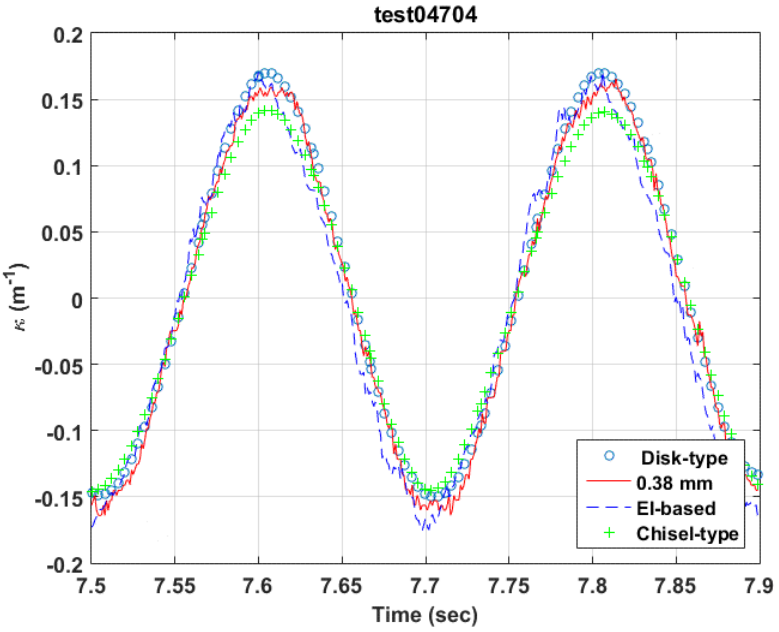

(a) 75 N

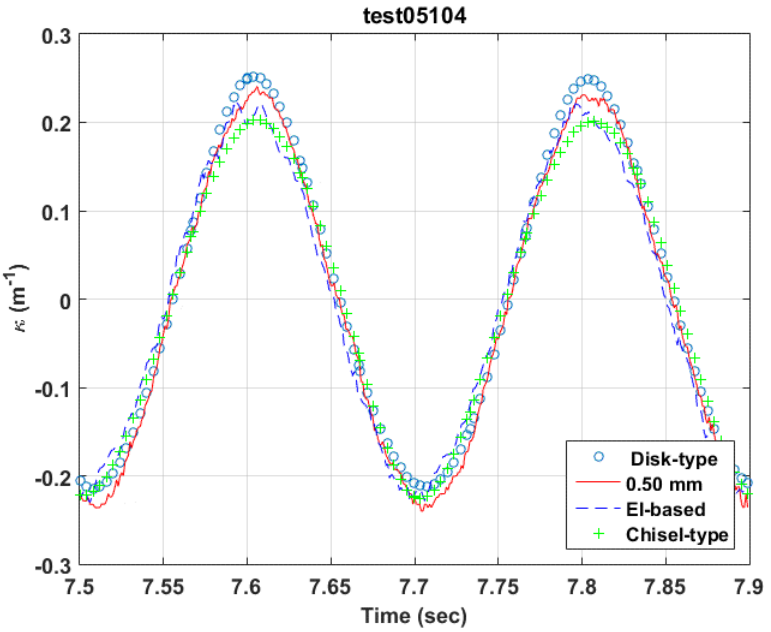

(b) 100 N

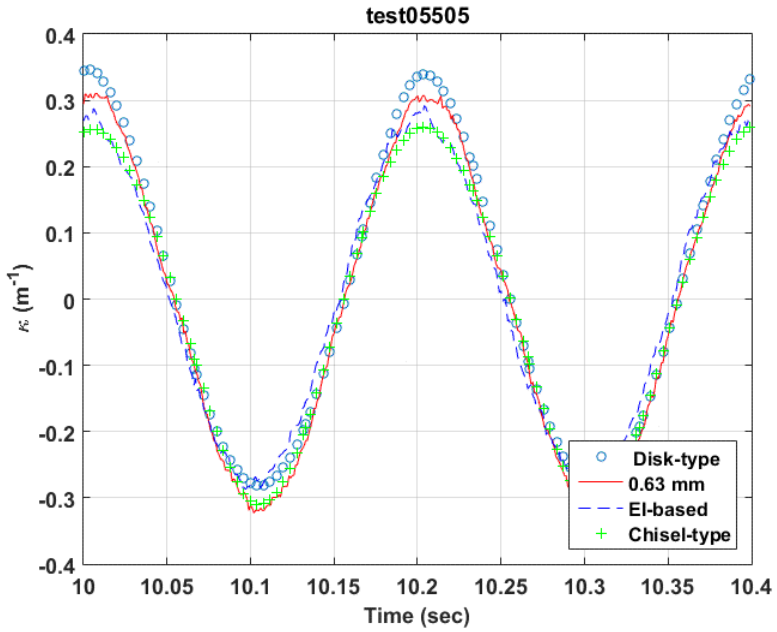

(c) 125 N

Fig. 11. Curvatures based on disk-type probe, corrected, EI-based, and chisel-type probe for 5 Hz load at a loading point of the U-frame arm: (a) 75 N, (b) 100 N, and (c) 125 N. EI = 42.8 Nm^2.

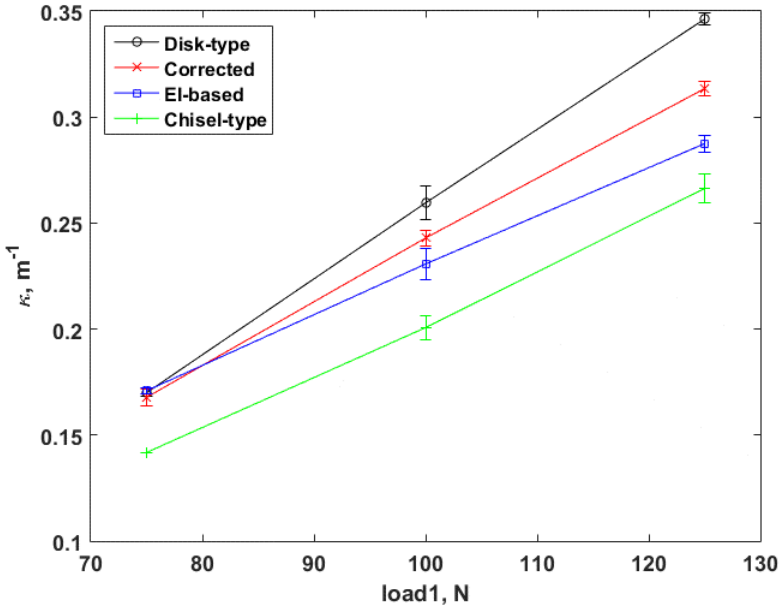

(a) Peak

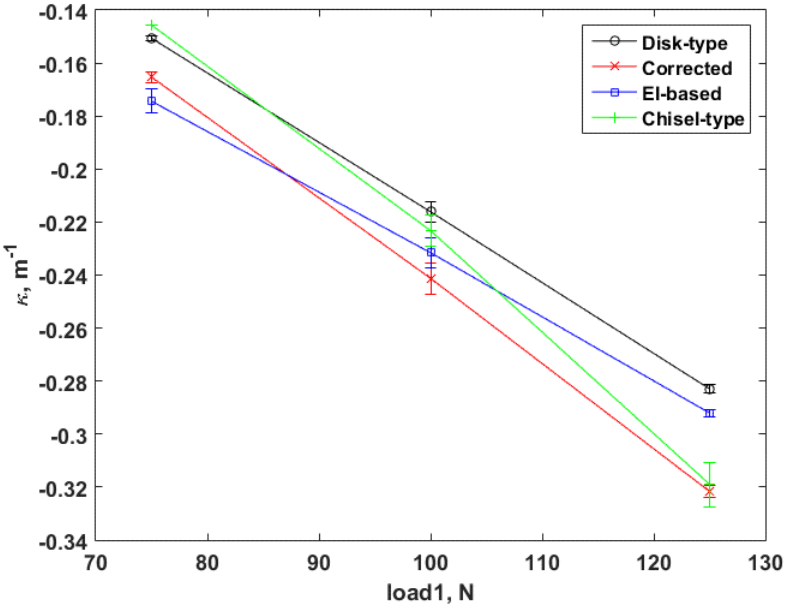

(b) Valley

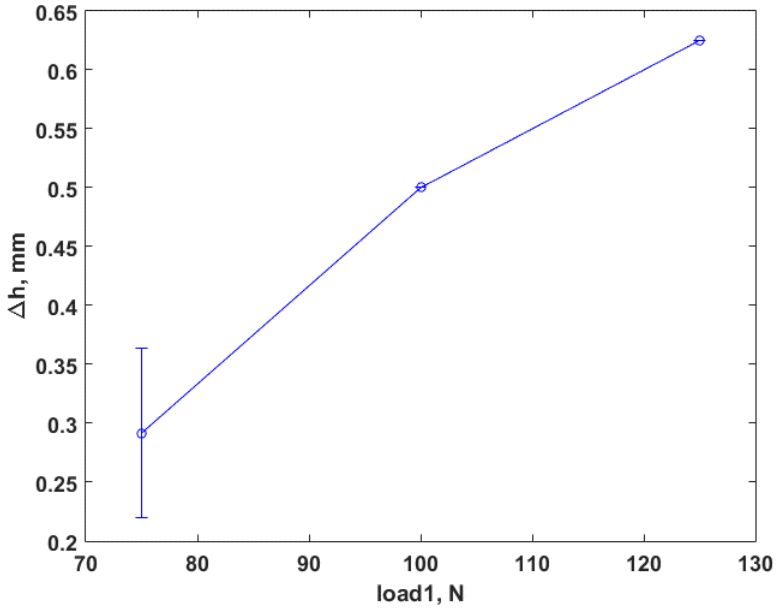

(c) Spacing correction

Fig. 12. (a) Peak and (b) valley responses of curvature waveforms, and (c) spacing corrections under various load1 amplitudes at 5 Hz.

2.3.1.3 Strain Gauge as Calibration Method

The strain gauge was installed on the surface of the bending rod opposite the three LVDTs (Fig. 7). The test conditions using 0.05 Hz sine wave with varying amplitudes are given in Table 3. For numbers 71–73, the strains were acquired using a P3 strain indicator and recorder (Vishay Micro-Measurements, Raleigh, NC). For numbers 81–84, strains were acquired using a 2310B strain signal conditioning amplifier (Vishay Micro-Measurements, Raleigh, NC).

Table 3. Test condition with strain gauge installed

No.	pk1 (mm, N)	pk2 (mm, N)	Frequency	Cycles	LVDT type
71	−0.4	0.4	0.05	3	Flat disk, D5
72	−0.6	0.6	0.05	3	Flat disk, D5
73	−0.8	0.8	0.05	3	Flat disk, D5
81	−0.4	0.4	0.05	3	Flat disk, D5
82	−0.6	0.6	0.05	3	Flat disk, D5
83	−0.8	0.8	0.05	3	Flat disk, D5
84	−100	100	5	500	Flat disk, D5

The curvatures measured using three LVDTs were converted into the maximum strain at the outer fiber of the bending rod. The results of tests 71–73 are illustrated in Fig. 13 and Fig. 14.

1) Overall, the strain gauge has a synchronized response with curvature-based strain, although the curvature-based strain at 0.6 mm lagged in the first half of period.
2) The peak/valley response of the curvature-based strain with the correction applied matched the strain gauge measurement.

3) Once again, the spacing correction (Δh) demonstrated an increasing trend with the input displacements. However, the correction, especially at small displacement inputs, showed a lower level than in the previous test session (Fig. 10).

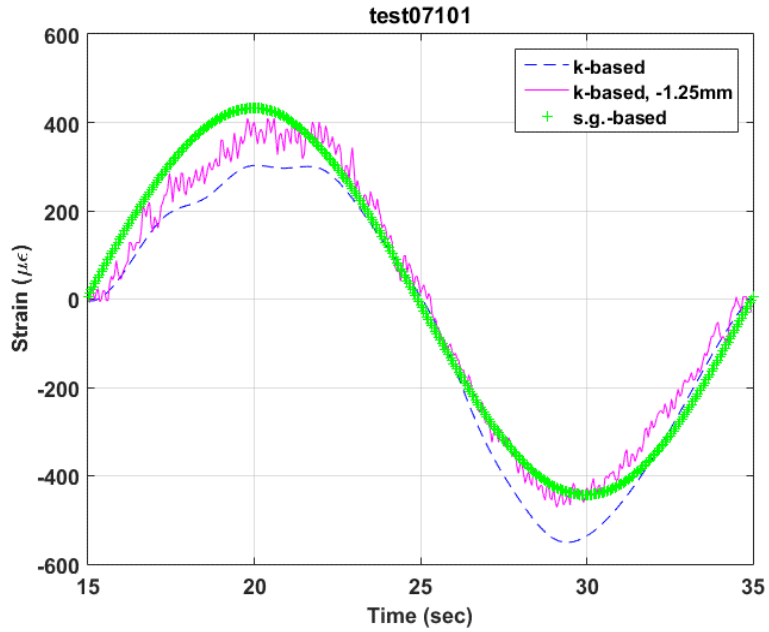

0.4 mm

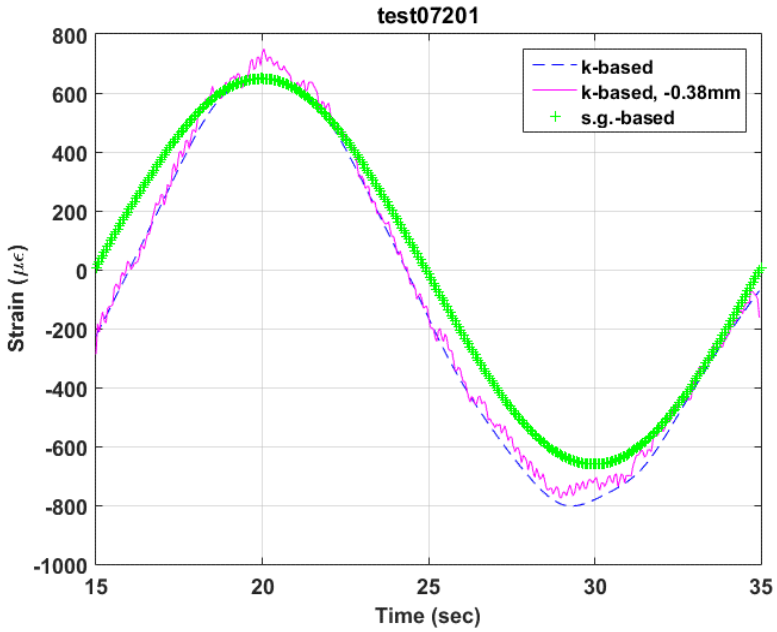

0.6 mm

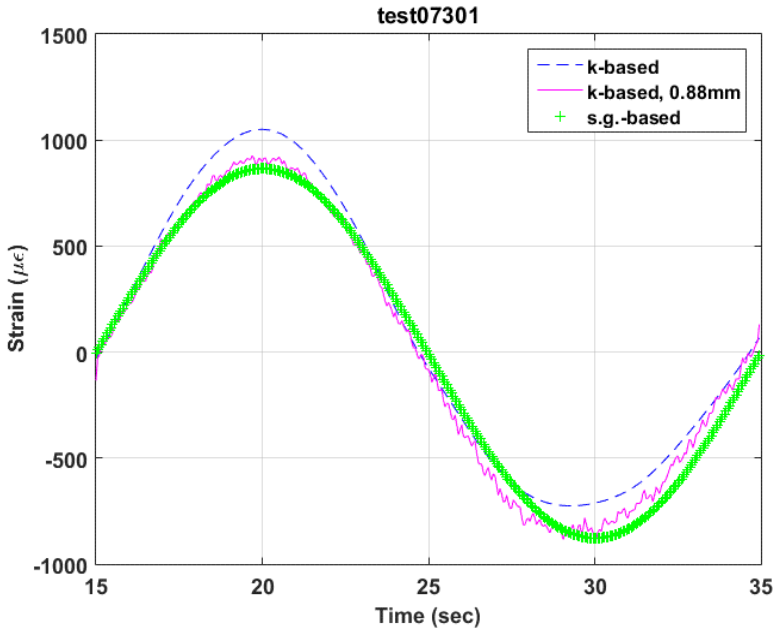

0.8 mm

Fig. 13. Strain curves based on original disk-type curvature, corrected curvature, and strain gauge for 0.05 Hz displacement at the loading point of U-frame arm: (a) 0.4 mm, (b) 0.6 mm, and (c) 0.8 mm.

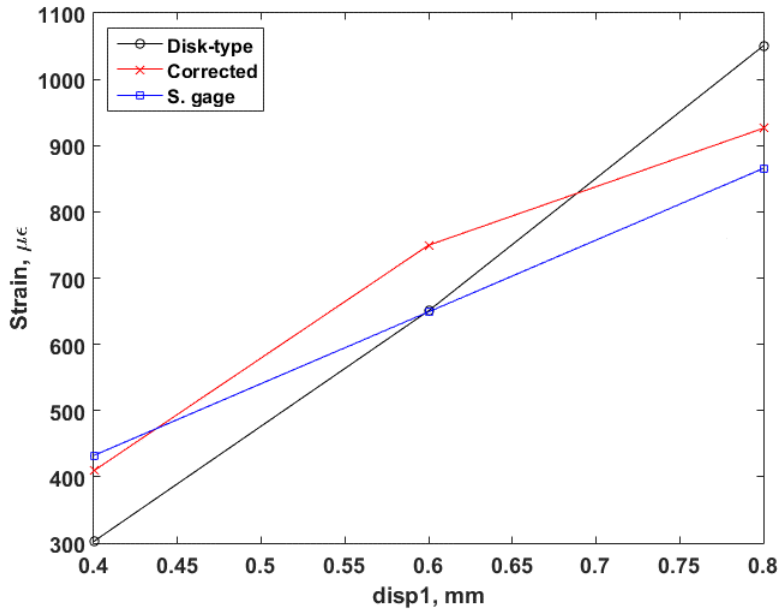

(a) Peak

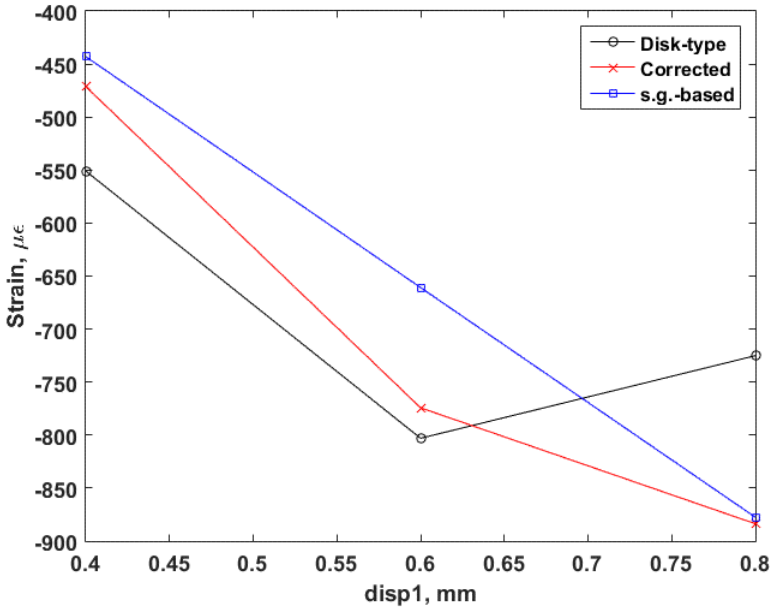

(b) Valley

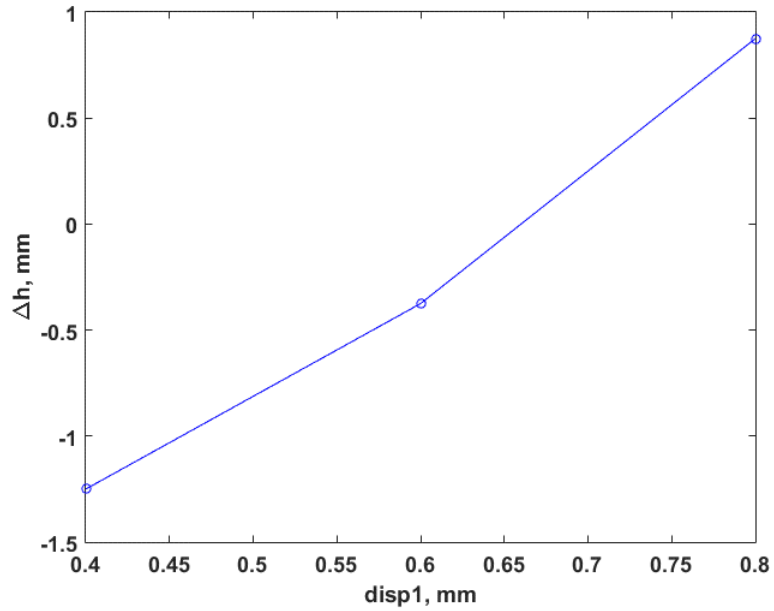

(c) Spacing correction

Fig. 14. (a) Peak and (b) valley responses of a strain waveform, and (c) spacing corrections under various disp1 amplitudes at 0.05 Hz.

The results of tests 81–84 are given in Fig. 15 for 0.05 Hz and in Fig. 16 for 5 Hz. The following observations were made:

1) The strain gauge showed a lower level of strain than the curvature-based strain.
2) The spacing correction (Δh) and its variation with displacements were smaller than previous tests (Fig. 10 and Fig. 14). The degree of correction for κ-based strain was smaller as well.
3) The corrected curvature-based strains were close to EI-based strains.

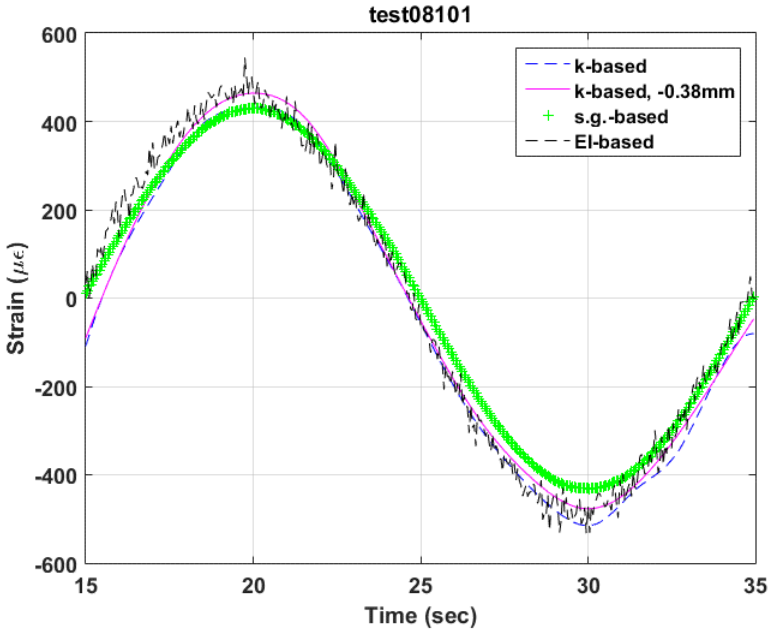

(a) Displacement amplitude 0.4 mm

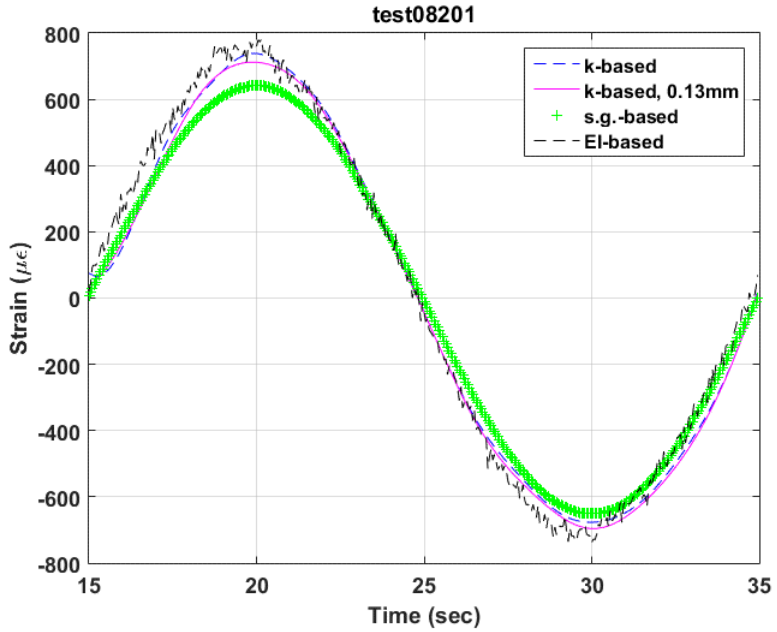

(b) Displacement amplitude 0.6 mm

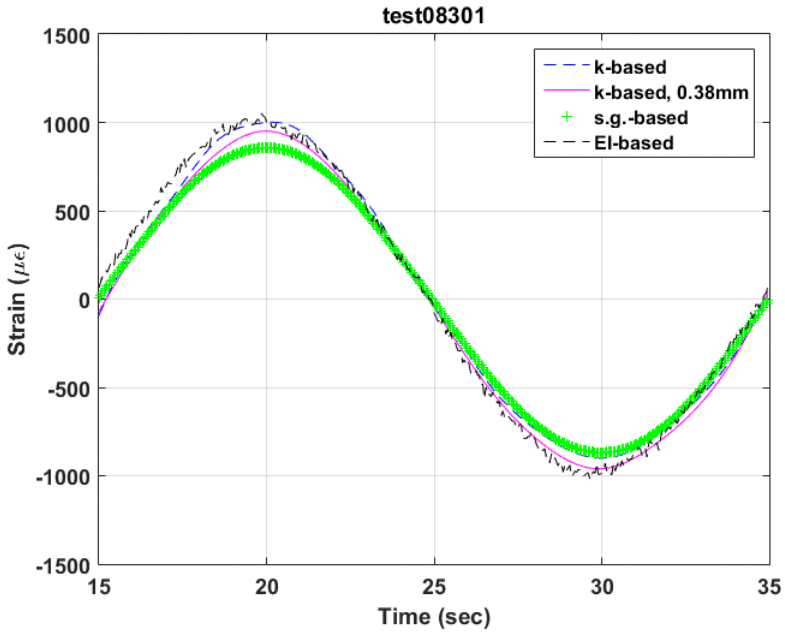

(c) Displacement amplitude 0.8 mm

Fig. 15. Strain results based on original curvature, corrected curvature, strain gauge, and flexural rigidity (EI) for 0.05 Hz tests under three displacement amplitudes.

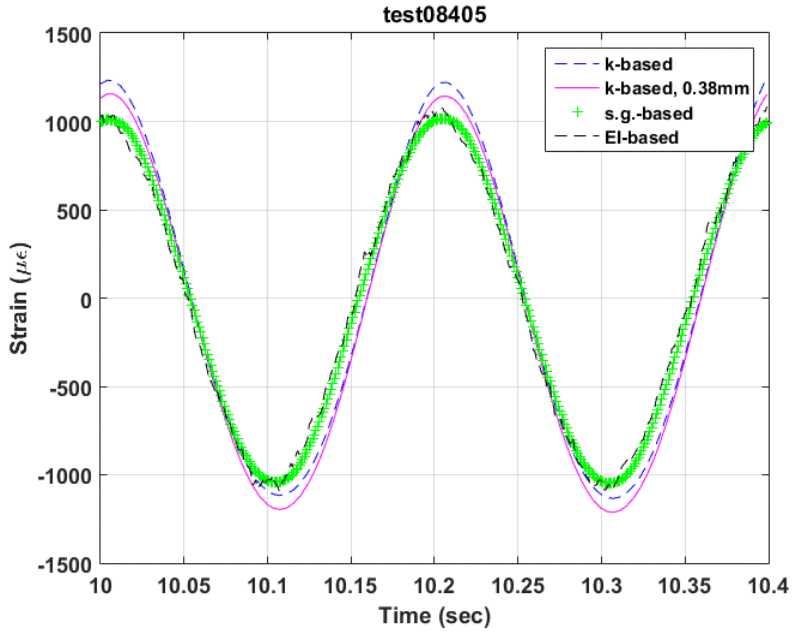

(a) Data block 5

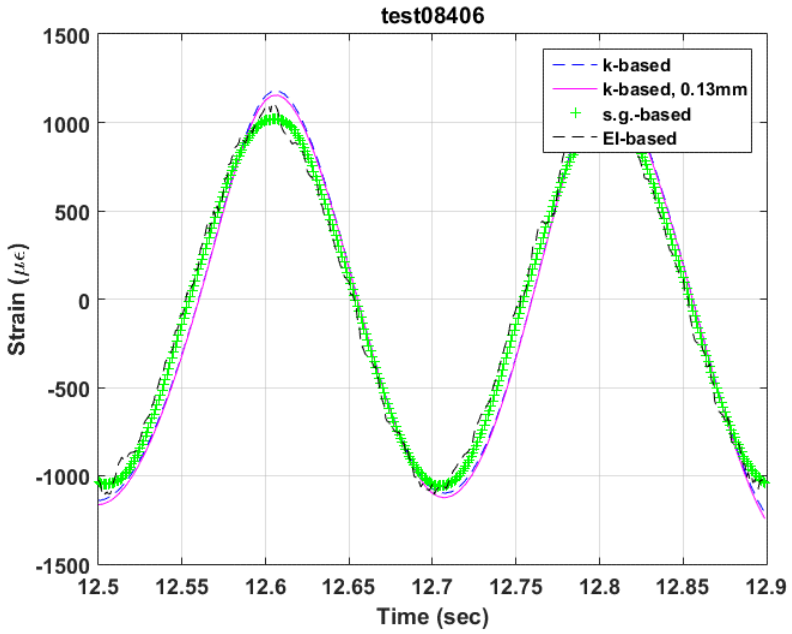

(b) Data block 6

Fig. 16. Strain results based on original curvature, corrected curvature, strain gauge, and flexural rigidity (EI) for 5 Hz tests under amplitude 100 N.

2.3.1.4 Summary

The use of a SS304 surrogate rod for out-cell verification tests provided the opportunity to examine the small curvature measurement currently used in CIRFT evaluations. Major observations included the following:

1) The corrected curvature was close to the EI-based curvature, and the corrected curvature-based strain was also close to the strain gauge measurement.
2) The spacing correction (Δh) was smaller than those based on the large curvature measurement. The degree of correction for curvature-based strain was also smaller.
3) The spacing correction increased with the level of displacement input, but it also showed a large variance at the small displacements.
4) The level of spacing correction in specified displacement inputs varied among test sessions. A change in the contact condition between the probe and the surface of the rod is believed to cause the variation. A systematic correction scheme was developed accordingly.

2.3.2 CIRFT Evaluations of Polycarbonate Surrogate Rod Material

The test conditions for a polycarbonate rod (PC01) consisted of two load waveforms: ramp and sine.

2.3.2.1 Ramp Waveform Test

The displacement at each loading point of the U-frame was ramped up to a designated level and then down to zero; one loading cycle was used. The bending in ramp was unidirectional with a single wave pulse pointed in either a positive or negative direction.

Two types of LVDT probes were tested, a flat disk-type probe and a chisel-type probe. Test conditions are outlined in Table 4.

Table 4. Test condition using ramp process

No.	pk1 (mm)	pk2 (mm)	rate(mm/s)	Cycles	LVDT
1	0	6	0.2	1	flat disk, D5
2	0	−6	0.2	1	flat disk, D5
7	0	6	0.2	1	chisel, D5
8	0	−6	0.2	1	chisel, D5

The data sets for a specified probe were compiled to obtain a complete waveform for reversed bending. The three LVDT-based curvatures obtained with both disk-type and chisel-type probes are presented with the corrected curvature in Fig. 17, in which EI = 1.8 Nm^2 was used for the EI-based estimate.

1) The correction procedure suggests that a sensor spacing correction of 2.50 mm was needed. With the suggested procedure, only one correction was needed. The previous procedure required two corrections: one in a positive direction (2.90 mm) and one in a negative direction (2.40 mm).

2) The corrected curvature corresponds with the chisel-type probe measurement and the EI-based estimate.

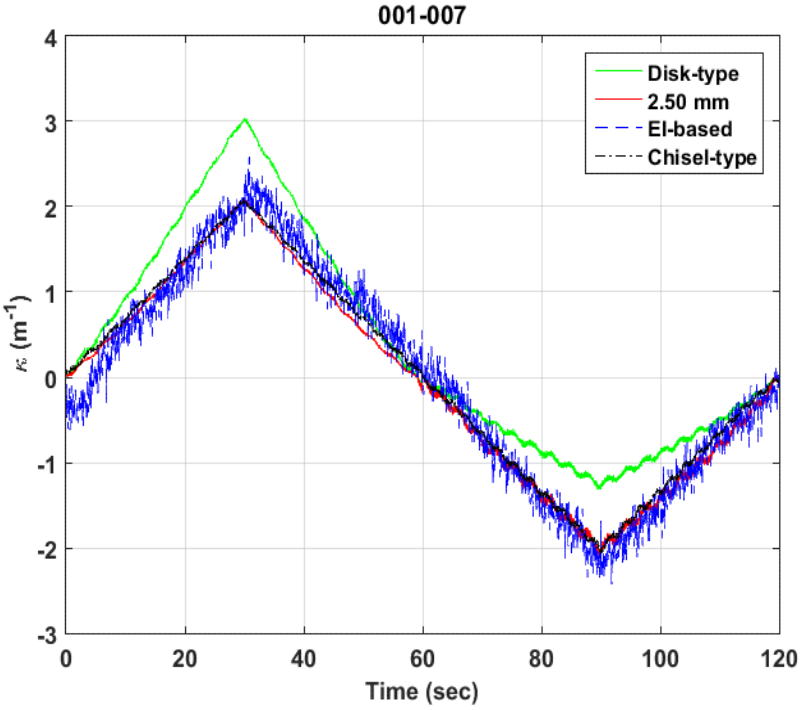

Fig. 17. Curvature measurements for a polycarbonate surrogate rod using disk- and chisel-type probes, a 2.50 mm sensor spacing correction, and an EI-based estimate.

2.3.2.2 Sine Waveform Test

Reverse bending was conducted using a 0.05 Hz sine wave. A total of 12 amplitudes were tested with one LVDT disk-type probe. Strain gauge measurements were enabled, and strains were acquired using a P3 strain indicator and recorder. The test conditions are outlined in Table 5.

Table 5. Test conditions using a sine wave

No.	pk1 (mm)	pk2 (mm)	F(Hz)	Cycles	LVDT
35	0.5	−0.5	0.05	3	flat disk, D5
36	1	−1	0.05	3	flat disk, D5
37	1.5	−1.5	0.05	3	flat disk, D5
38	2	−2	0.05	3	flat disk, D5
39	2.5	−2.5	0.05	3	flat disk, D5
40	0.3	−0.3	0.05	3	flat disk, D5
41	0.3	−0.3	0.05	3	flat disk, D5
42	0.3	−0.3	0.05	3	flat disk, D5
43	0.5	−0.5	0.05	3	flat disk, D5
44	0.5	−0.5	0.05	3	flat disk, D5
45	0.5	−0.5	0.05	3	flat disk, D5
46	1	−1	0.05	3	flat disk, D5
47	1	−1	0.05	3	flat disk, D5
48	1.5	−1.5	0.05	3	flat disk, D5

Table 5. (continued)

No.	pk1 mm	pk2 (mm)	F(Hz)	Cycles	LVDT
49	1.5	−1.5	0.05	3	flat disk, D5
50	2	−2	0.05	3	flat disk, D5
51	2	−2	0.05	3	flat disk, D5
52	2.5	−2.5	0.05	3	flat disk, D5
53	2.5	−2.5	0.05	3	flat disk, D5
54	3	−3	0.05	3	flat disk, D5
55	3	−3	0.05	3	flat disk, D5
56	3	−3	0.05	3	flat disk, D5
57	3.5	−3.5	0.05	3	flat disk, D5
58	3.5	−3.5	0.05	3	flat disk, D5
59	3.5	−3.5	0.05	3	flat disk, D5
60	4	−4	0.05	3	flat disk, D5
61	4	−4	0.05	3	flat disk, D5
62	4	−4	0.05	3	flat disk, D5
63	4.5	−4.5	0.05	3	flat disk, D5
64	4.5	−4.5	0.05	3	flat disk, D5
65	4.5	−4.5	0.05	3	flat disk, D5
66	5	−5	0.05	3	flat disk, D5
67	5	−5	0.05	3	flat disk, D5
68	5	−5	0.05	3	flat disk, D5
69	5.5	−5.5	0.05	3	flat disk, D5
70	5.5	−5.5	0.05	3	flat disk, D5
71	5.5	−5.5	0.05	3	flat disk, D5
72	6	−6	0.05	3	flat disk, D5
73	6	−6	0.05	3	flat disk, D5
74	6	−6	0.05	3	flat disk, D5
75	6	−6	0.05	3	flat disk, D5

The typical results from tests using a 0.05 Hz sine wave are given in Fig. 18. The peak and valley values of the strain waveforms obtained for various cases are shown in Fig. 19, including strains based on original curvature (disk-type probe), corrected curvature, and strain gauge. The variation for spacing correction as a function of displacement input is also presented.

1) The strains measured with the strain gauge usually corresponded with those based on the corrected curvatures, but they deviated from the corrected curvature-based strain at high levels.
2) The spacing correction (Δh) exhibited a defined trend to increase with displacement input and a larger variance with the small displacements.
3) The spacing corrections were again lower than those obtained in ramping.
4) The corrected ultimate curvatures obtained in ramp and sine waveforms were the same (around 2 m^{-1} at 6.00 mm disp1). Because tests were completed in different project periods, there may have been a significant change in the contact condition between the probe and the surface of the rod.

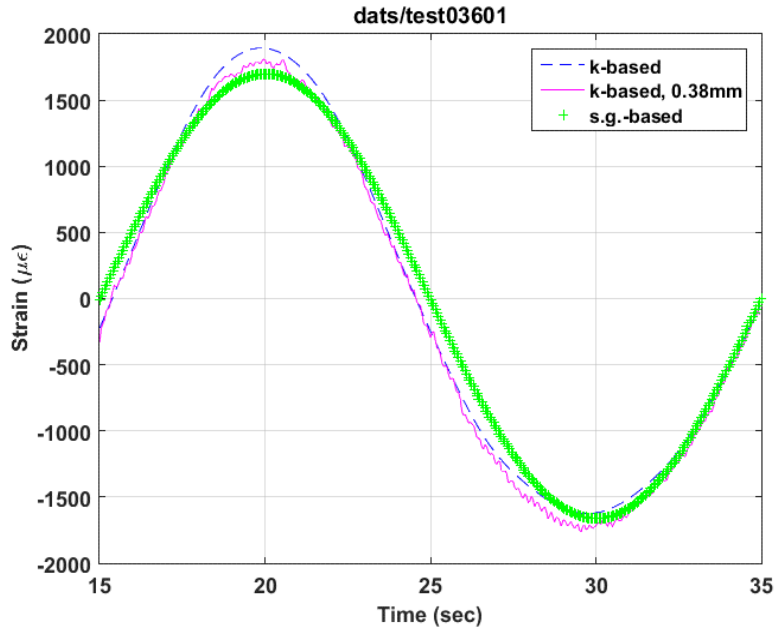

(a)

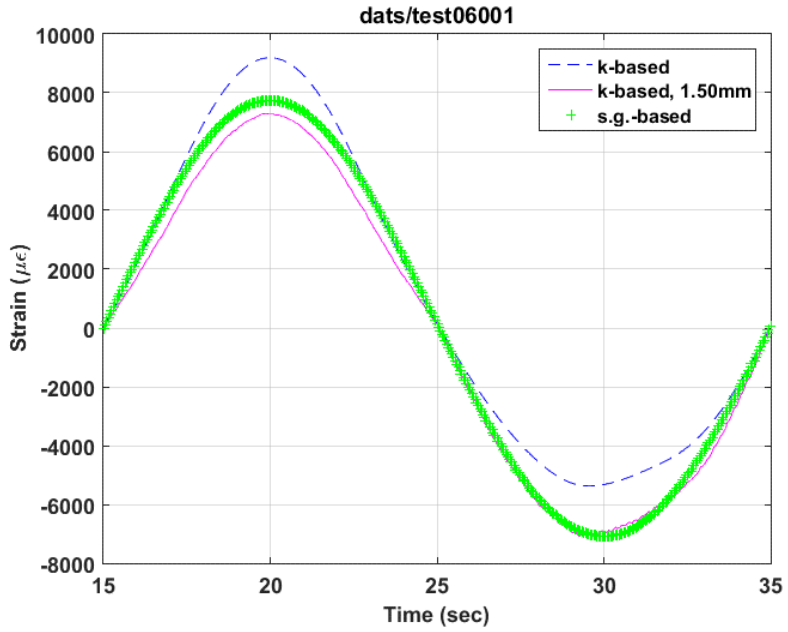

(b)

Fig. 18. Strain waveforms obtained from original curvature, corrected curvature, and strain gauge: (a) displacement amplitude at 1.00 mm and (b) 4.00 mm.

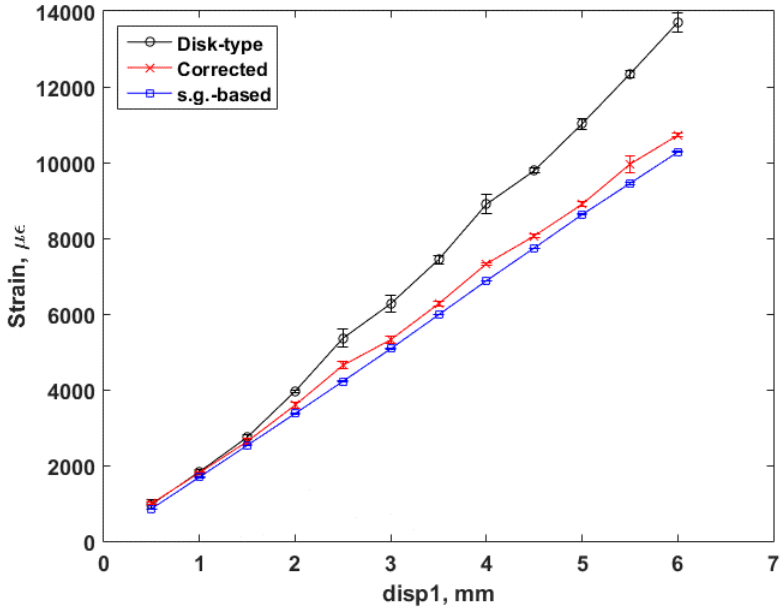

(a) Peak

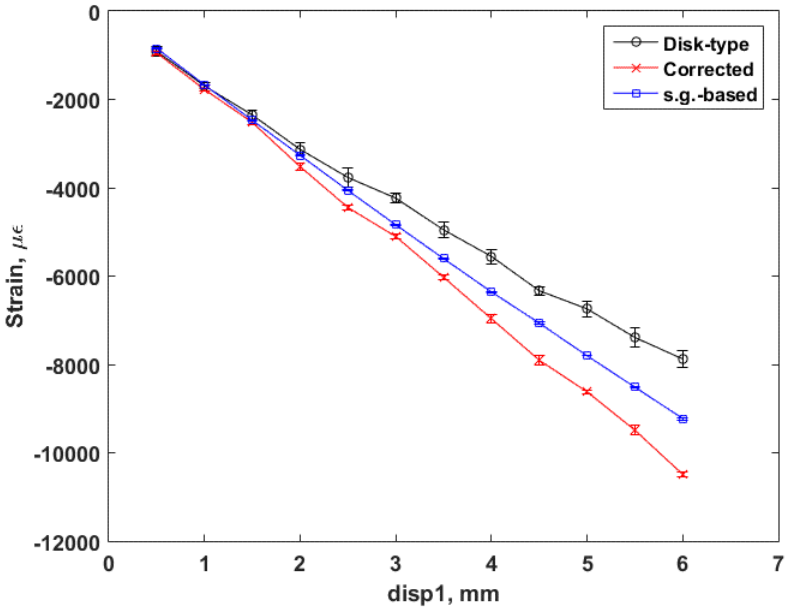

(b) Valley

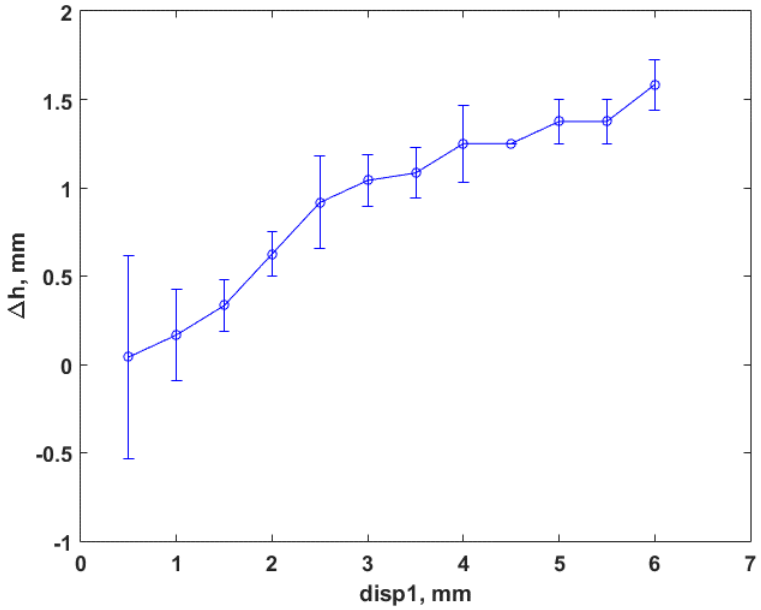

(c) Spacing correction

Fig. 19. (a) Peak and (b) valley responses of a strain waveform, and (c) spacing corrections under various disp1 amplitudes at 0.05 Hz.

2.3.2.3 Summary

Based on the tests of the polycarbonate rod, the following conclusions can be made about the disk-type curvature measurement and correction:

1) The corrected curvature measurements closely corresponded to the chisel-type probe measurements and the EI-based estimate. The corrected curvature-based strain strongly correlates to the strain gauge measurement, particularly near small-to-intermediate levels of displacement input.

2) The spacing correction (Δh) again exhibited a defined trend to increase with the displacement input and exhibited a larger variance at small displacements.

3) The correction procedure recommended a spacing correction of 2.50 mm (at 6.00 mm disp1) aside from dual corrections reported in ramping (2.40 mm in negative curvature and 2.90 mm in positive curvature). However, corrected curvatures obtained from ramping tests and sine waveforms were the same (approximately 2 m^{-1} at 6.00 mm disp1).

4) The change in contact conditions between the probe and surface of the rod in different test sessions may be responsible for the variation in spacing corrections observed.

2.4 Recommendation

Sensor spacing correction depends on the level of imposed displacement. The corrected curvature based on disk-type probes agrees to a varying extent with the EI-based estimate for both small and large curvature measurements and for chisel-type probe measurements in large curvature cases. The corrected curvature-based strain also corresponds with the strain gauge measurement, particularly at small-to-intermediate levels of displacement input.

There is some uncertainty about the contact of the probe against the rod during reversible-bending tests. However, the proposed dynamic correction method using LVDT probes is independent of the contact spacing correction described earlier. The identification of sensor spacing corrections dynamically accounts for the changes and evolution of contacts. This effect is still a work in progress and will be reported in the next performance period.

The proposed correction procedure will be applied to the analysis of all CIRFT data. The analysis results for LMK, NA, and MOX fuels are presented below.

3. ANALYSIS OF CIRFT EVALUATIONS OF LMK BWR SNF

3.1 Overview of CIRFT Evaluations of LMK Fuel Rods

A total of 16 specimens—LM1–LM4 and LM5–LM17—were tested in a hot cell. LM1 was used in the tuning and static test. The remaining 15 specimens were used in dynamic tests. The dynamic tests were conducted with a range of moment amplitudes from 7.11 to 30.48 Nm. A total of 13 specimens failed with fatigue lives from 10^4 to 4.7×10^6 cycles. LM12 and LM17 were cycled to more than 3.4×10^6 cycles without failure. LM12 was stopped at 7.6×10^6 cycles. LM17 was tested continuously at an increased amplitude of 30.48 Nm and failed at 1.3×10^4 cycles.

3.2 Data Analysis Results for Dynamic Tests

The data sets for each of the dynamic tests, including measurement data and online monitoring data, were processed following the procedure described in Section 2.

Results for each test are provided in Appendix A. For each test

1) The variations of curvature range, moment range, flexural rigidity, curvature peak/valley, and moment peak/valley are presented whenever they are available.
2) The curvature and moment plots are given for the beginning data block of a test session when the load reaches the designated level. The results for two test sessions are presented, namely, the first (tested to 1,000 cycles) and last sessions.
3) Finally, the data based on online monitoring are presented, including the variations of curvature range, moment range, flexural rigidity, curvature peak/valley, and moment peak/valley as a function of number of cycles or the cycles to failure.

For each cyclic test, several sets of measurements were obtained between test sessions. These measurements were made with small displacement amplitudes at 0.05 Hz. With this input, both moment and curvature varied or decreased with the accumulated number of cycles. The obtained rigidities were generally higher than those from monitoring data, and the degree of change was similar to the monitoring data.

The corrected curvature depends on the spacing correction applied. Generally, the correction observed for the curvature is not significant because of the small input. However, the signal-to-noise ratio is reduced at lower input levels. The amplitude of de-noised curvature was lower compared with the original noisy data, which can be seen from the pots of specimen LM12 in Fig. A.40.

Major results for the dynamic tests are summarized in Table 6. The table is self-explanatory and includes the following columns:

1) TN—test number
2) Spec—Specimen ID
3) ID—inner diameter of cladding
4) OD—outer diameter of cladding
5) Dia—diameter of pellet
6) Load—load amplitude at the loading point of U-frame
7) N—number of cycles accumulated or the cycles to failure
8) Fail—1 as failure, and 0 as no failure
9) ma—mean of moment amplitude ($\Delta M/2$) based on de-noised monitoring data

10) ma_std—standard deviation of moment amplitude (4 in. or 101.60 mm loading arm) based on de-noised monitoring data
11) ka—mean of curvature amplitude ($\Delta\kappa/2$) based on corrected and de-noised monitoring data
12) ka_std—standard deviation of curvature amplitude based on corrected and de-noised monitoring data
13) km—mean of curvature extreme values based on corrected and de-noised monitoring data, km = $\max\{|\kappa_p|,|\kappa_v|\}$, where κ_p and κ_v are peak/valley values
14) km_std—standard deviation of curvature extremes based on corrected and de-noised monitoring data
15) R—mean of flexural rigidity
16) R_std—standard deviation of flexural rigidity
17) sa—mean of equivalent stress amplitude ($\Delta\sigma/2$) based on de-noised monitoring data
18) sa_st—d – standard deviation of equivalent stress amplitude based on de-noised monitoring data
19) ea—mean of equivalent strain amplitude ($\Delta\varepsilon/2$) based on corrected and de-noised monitoring data
20) ea_std—standard deviation of equivalent strain amplitude based on corrected and de-noised monitoring data
21) em—mean of strain extreme values based on corrected and de-noised monitoring data, em = $\max\{|\varepsilon_p|,|\varepsilon_v|\}$
22) em_std—standard deviation of strain extremes based on corrected and de-noised monitoring data
23) Lg2—mean of half gauge length, Lg/2
24) Lg2_std—standard deviation of half gauge length
25) dh—mean of sensor spacing correction, Δh
26) dh_std—standard deviation of sensor spacing correction

The plots based on the mean values of major quantities can be found in Fig. 20(a)–(d), where the circles represent the tests with failure and the circles with arrows designate the tests no failure. The results obtained from the follow-up tests for LM1 and LM17 are also included.

As expected, the fatigue life increased with decreasing amplitude, but the variation was not continuous. A discontinuity, or knee point, was observed near 7 Nm and 0.2 m^{-1} in the moment–N and curvature–N curves. For this SNF, these parameters correspond to 50 MPa of equivalent stress and 0.1% of equivalent strain. At the same time, curvature extreme values were generally higher than curvature amplitudes as expected, but the difference was small.

The flexural rigidity was mostly shown to be either quite flat or featuring a decreasing trend with the number of cycles. Several tests also suggested a tendency to increase with number of cycles, including LMK2, 8, and 14. Overall, the degree of variation of rigidity is limited. Meanwhile, no relation of rigidity to the number of cycles to failure can be seen.

The effective half-gauge length was found to be limited with a range between 38 and 50 mm and to increase with increased amplitude of moment. On the other hand, the sensor spacing correction did not suggest any relation to the moment amplitude.

Table 6a. Dynamic test results for LMK SNF rods

TN	Spec	Load N	N cycles	Fail	ma Nm	ma_std Nm	ka m^1	ka_std m^−1	km m^−1	km_std m^−1
1	LM1	250.000	9.40E + 03	1	23.426	0.087	0.901	0.027	1.007	0.027
2	LM2	125.000	1.71E + 05	1	11.468	0.090	0.266	0.006	0.275	0.008
3	LM3	100.000	4.92E + 05	1	9.016	0.081	0.243	0.008	0.258	0.011
5	LM5	85.000	2.49E + 05	1	7.570	0.074	0.165	0.008	0.205	0.013
6	LM6	75.000	1.79E + 06	1	6.488	0.071	0.154	0.008	0.201	0.008
7	LM7	150.000	1.22E + 05	1	13.930	0.085	0.347	0.005	0.362	0.009
8	LM8	75.000	4.70E + 06	1	6.601	0.077	0.128	0.007	0.192	0.007
9	LM9	100.000	7.31E + 05	1	9.058	0.077	0.216	0.004	0.226	0.007
10	LM10	200.000	5.20E + 04	1	18.903	0.089	0.490	0.004	0.496	0.005
11	LM11	85.000	3.55E + 05	1	7.657	0.111	0.162	0.007	0.194	0.010
12	LM12	70.000	7.58E + 06	0	6.141	0.087	0.206	0.014	0.226	0.021
13	LM13	250.000	2.10E + 04	1	21.396	2.415	0.533	0.071	0.553	0.073
14	LM14	100.000	3.90E + 05	1	9.048	0.082	0.198	0.008	0.228	0.010
15	LM15	100.000	4.41E + 05	1	8.997	0.073	0.225	0.007	0.230	0.007
16	LM16	300.000	1.36E + 04	1	28.560	0.168	0.654	0.008	0.679	0.014
17	LM17	85.000	3.37E + 06	0	7.459	0.374	0.204	0.011	0.212	0.013
18	LM17	300.000	1.31E + 04	1	28.063	0.131	0.853	0.006	0.863	0.011

Table 6b. Dynamic test results for LMK SNF rods

TN	Spec	R Nm^2	R_std Nm^2	sa MPa	sa_std MPa	ea %	ea_std %	em %	em_std %	Lg2 mm	Lg2_std mm	dh mm	dh_std mm
1	LM1	26.017	0.809	179.649	0.667	0.515	0.015	0.575	0.015	43.766	0.767	0.279	0.182
2	LM2	43.120	0.891	88.227	0.691	0.151	0.004	0.156	0.005	44.250	0.634	−0.084	0.347
3	LM3	37.187	1.025	69.286	0.623	0.138	0.004	0.147	0.007	44.455	0.738	0.325	0.298
5	LM5	45.948	2.117	58.177	0.566	0.094	0.005	0.117	0.007	41.932	0.756	−1.436	0.577
6	LM6	42.226	2.287	49.862	0.548	0.088	0.005	0.114	0.005	40.157	0.749	−1.723	0.312
7	LM7	40.176	0.586	107.050	0.656	0.197	0.003	0.206	0.005	45.455	0.565	−0.426	0.190
8	LM8	51.567	2.504	50.733	0.590	0.073	0.004	0.109	0.004	42.342	0.890	2.568	0.338
9	LM9	41.880	0.736	69.615	0.590	0.123	0.003	0.129	0.004	43.120	0.698	0.206	0.215
10	LM10	38.563	0.336	145.272	0.684	0.279	0.002	0.282	0.003	46.986	0.528	0.355	0.173
11	LM11	47.437	2.009	58.848	0.856	0.092	0.004	0.110	0.006	41.396	0.757	−1.864	0.362
12	LM12	29.879	1.859	47.196	0.665	0.117	0.008	0.129	0.012	38.475	0.965	0.732	0.683
13	LM13	40.225	0.903	164.428	18.563	0.303	0.040	0.315	0.042	47.411	0.705	−0.138	0.143
14	LM14	45.659	1.768	69.535	0.632	0.113	0.005	0.130	0.006	44.092	0.781	−1.307	0.387
15	LM15	40.008	1.219	69.141	0.561	0.128	0.004	0.131	0.004	44.196	0.698	−0.148	0.585
16	LM16	43.672	0.480	219.490	1.295	0.372	0.005	0.386	0.008	50.296	0.440	−0.435	0.153
17	LM17	36.630	1.138	57.325	2.872	0.116	0.006	0.121	0.007	44.656	0.919	−0.849	0.338
18	LM17	32.913	0.252	215.671	1.004	0.485	0.003	0.491	0.006	47.420	0.331	1.211	0.092

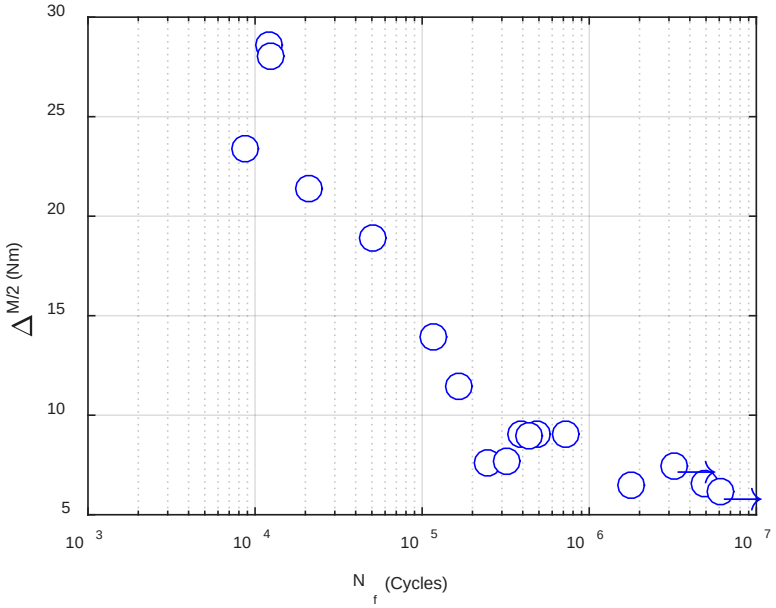
30
25
20
15
10
5
ΔM/2 (Nm)
10 3
10 4
10 5
10 6
10 7
N f (Cycles)

(a)

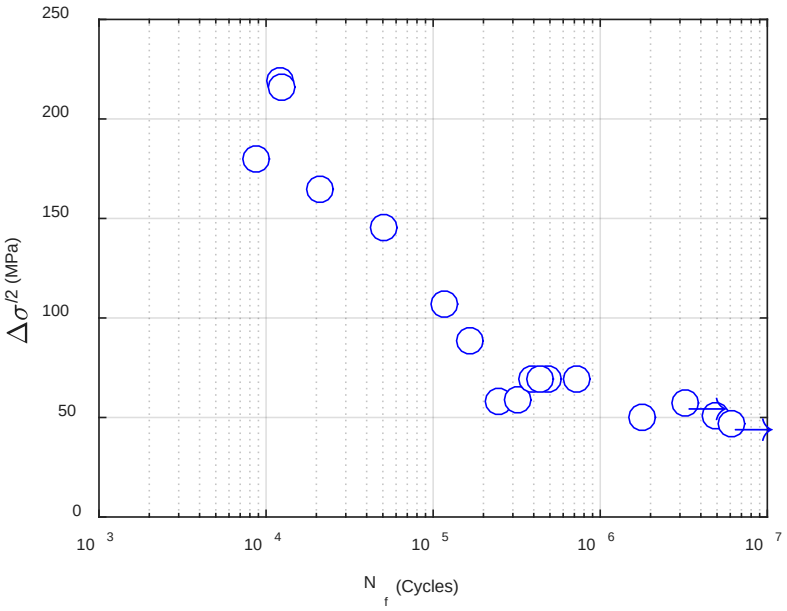
250
200
150
100
50
0
Δσ/2 (MPa)
10 3
10 4
10 5
10 6
10 7
N f (Cycles)

(b)

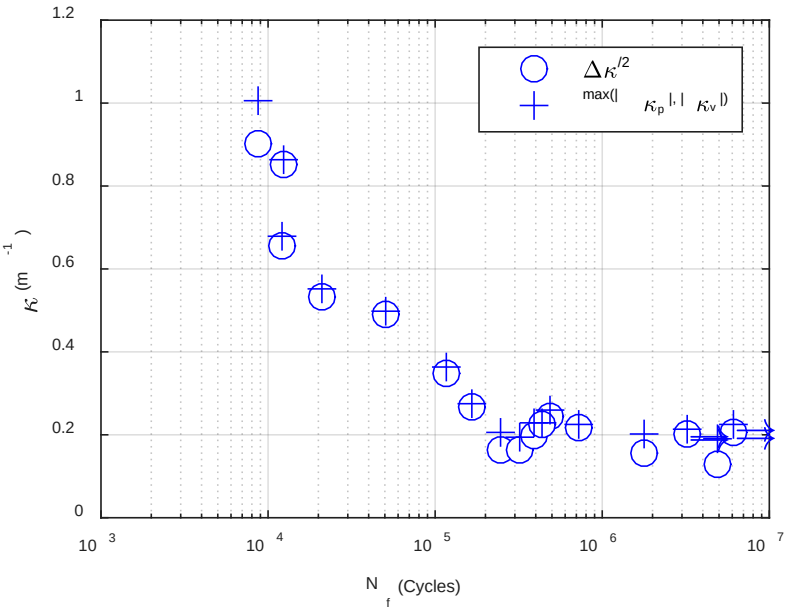

(c)

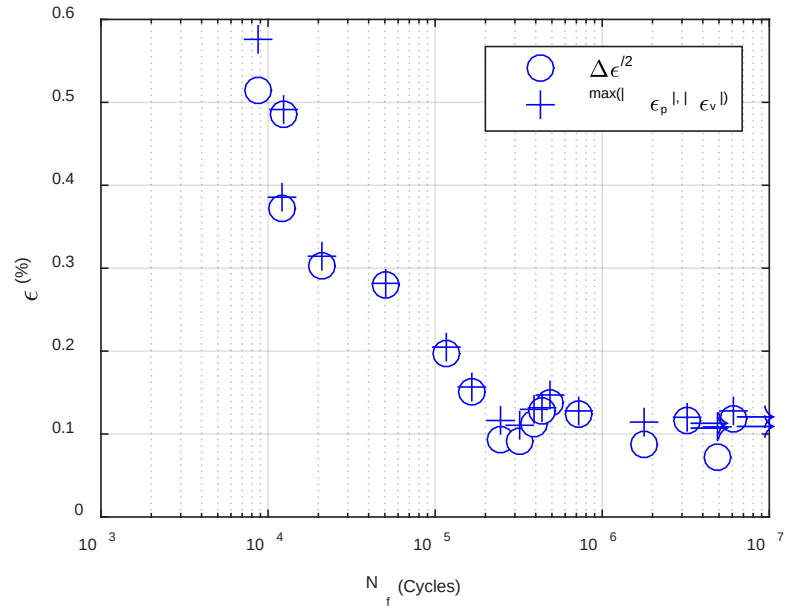

(d)

Fig. 20. (a) Moment amplitude, (b) stress amplitude, (c) curvature amplitude/ maximum, and (d) strain amplitude/maximum as a function of cycles or cycles to failure.

4. DATA ANALYSIS OF CIRFT EVALUATIONS OF NA FUEL

4.1 Overview

Six dynamic tests were conducted with applied amplitudes from 5.08 to 15.24 Nm; five specimens failed, and the fatigue life ranged from 1.26×10^4 to 4.27×10^5 cycles. One specimen (NA5) was cycled to 5.11×10^6 cycles without failure and stopped.

4.2 Data Analysis Results for Dynamic Tests

The results for each test are given in Appendix B. For each test, plots similar to those of LMK fuels are presented for NA fuel, including variations for curvature range, moment range, flexural rigidity, curvature peak/valley, and moment peak/valley values.

The results of the dynamic tests are summarized in Table 7. The column headings are the same as those for LMK fuels in Section 3.2.

The plots based on the mean values of quantities can be found in Fig. 21(a)–(d). There are knee points near 4 Nm and 0.05 m^{-1} in the moment, N_f, and curvature, N_f curve. However, the knee was not well defined because of the limited data points.

The rigidity variation was generally limited for a specified cyclic test, but abrupt variations were observed in several tests. However, the effective half-gauge length was limited to a range between 40 and 49 mm, increasing with the amplitude of moment.

Table 7. Dynamic test results for NA SNF rods

TN	Spec	Load N	N cycles	Fail	ma Nm	ma_std Nm	ka m^1	ka_std m^−1	km m^−1	km_std m^−1
1	NA1	125.000	1.57E + 04	1	11.001	0.053	0.512	0.007	0.536	0.013
2	NA2	100.000	2.20E + 04	1	8.802	0.082	0.391	0.013	0.412	0.017
4	NA4	75.000	6.10E + 04	1	6.331	0.083	0.221	0.009	0.255	0.010
5	NA5	50.000	5.11E + 06	0	3.982	0.068	0.143	0.014	0.161	0.014
6	NA6	50.000	4.27E + 05	1	3.986	0.090	0.121	0.010	0.163	0.009
7	NA7	150.000	1.26E + 04	1	13.540	0.542	0.610	0.039	0.629	0.026

Table 8. Dynamic test results for NA SNF rods

TN	Spec	R Nm^2	R_std Nm^2	sa Mpa	sa_std MPa	ea %	ea_std %	em %	em_std %	Lg2 mm	Lg2_std mm	dh mm	dh_std mm
1	NA1	21.494	0.268	135.887	0.650	0.246	0.003	0.258	0.006	46.055	0.469	−0.359	0.247
2	NA2	22.561	0.695	108.926	1.017	0.187	0.006	0.197	0.008	45.473	0.670	1.271	0.371
4	NA4	28.676	0.888	78.196	1.023	0.106	0.004	0.123	0.005	45.209	0.775	1.248	0.353
5	NA5	28.084	2.764	49.186	0.842	0.069	0.007	0.078	0.007	40.101	1.533	−0.148	0.770
6	NA6	33.140	2.801	49.237	1.113	0.058	0.005	0.078	0.004	43.153	0.968	1.745	0.404
7	NA7	22.261	1.174	167.085	6.690	0.295	0.019	0.303	0.013	49.444	1.317	0.163	0.345

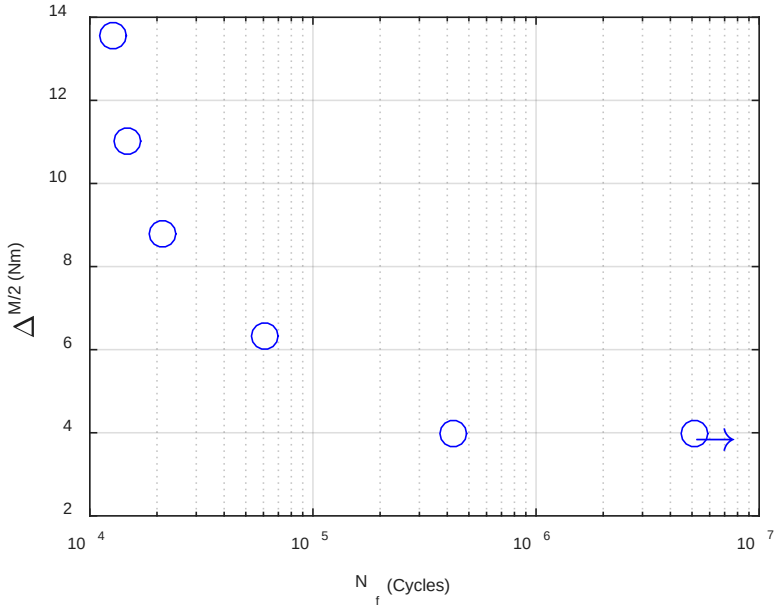
14
12
10
8
6
4
2
ΔM/2 (Nm)
10 4
10 5
10 6
10 7
N f (Cycles)

(a)

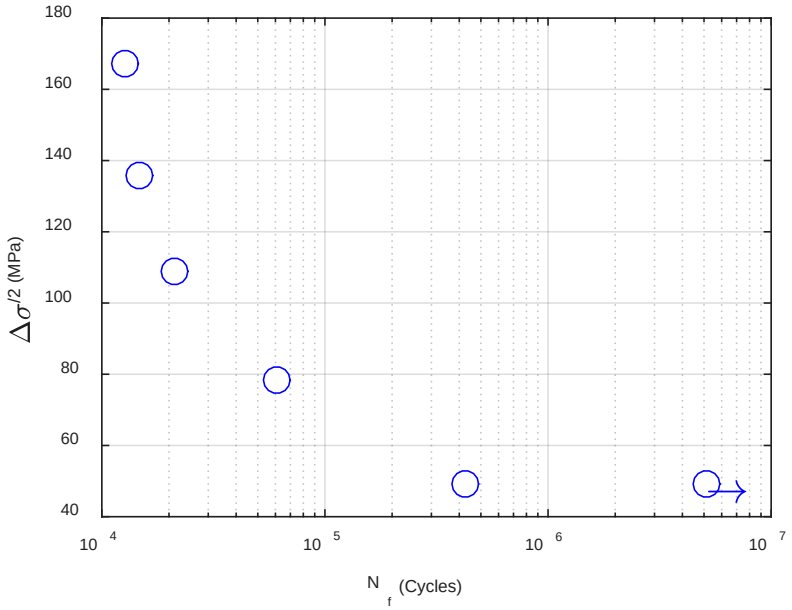
180
160
140
120
100
80
60
40
Δσ/2 (MPa)
10 4
10 5
10 6
10 7
N f (Cycles)

(b)

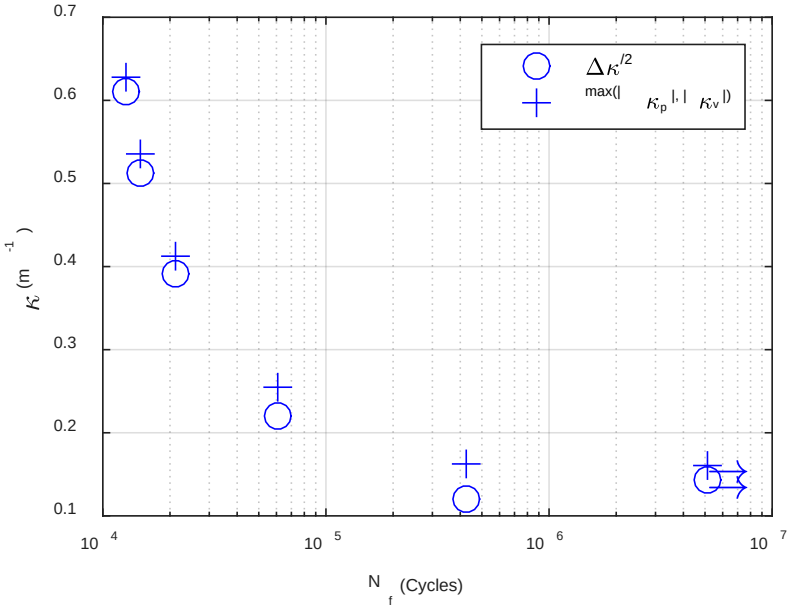

(c)

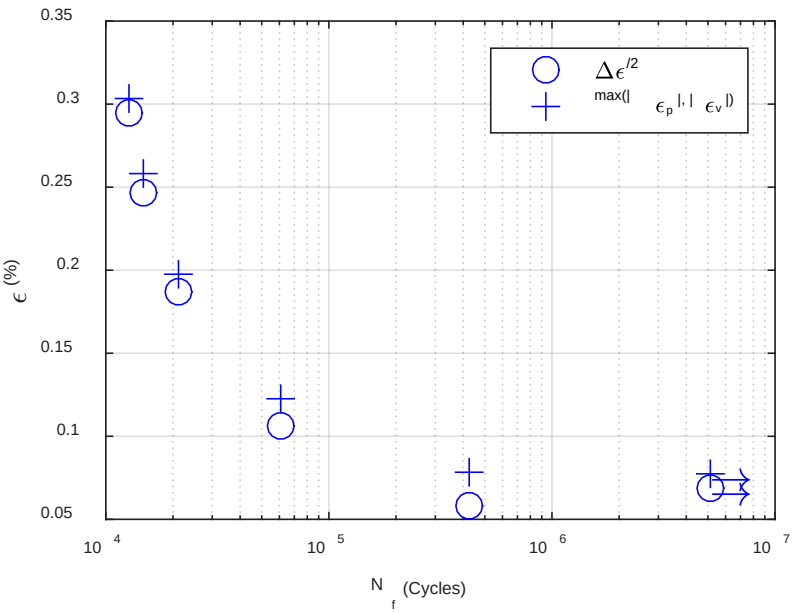

(d)

Fig. 21. (a) Moment amplitude, (b) stress amplitude, (c) curvature amplitude/maximum, and (d) strain amplitude/maximum as a function of cycles or cycles to failure.

5. DATA ANALYSIS OF CIRFT EVALUATIONS OF MOX FUEL

5.1 Overview

Ten dynamic tests were completed with the applied amplitudes from 5.08 to 15.24 Nm, and all specimens failed. The fatigue life ranged from 1.29×10^4 and 2.15×10^6 cycles.

5.2 Data Analysis Results for Dynamic Tests

The results for each test are given in Appendix C. Plots similar to those for LMK fuels are presented for MOX fuel and include variations for curvature range, moment range, flexural rigidity, curvature peak/valley, and moment peak/valley values.

The results for the dynamic tests of MOX fuel are summarized in Table 9. The column headings are the same as those for LMK fuels (Sect. 3.2).

The plots are based on the mean values of quantities can be found in Fig. 22(a)–(d). In the moment–N_f curve, there is knee point near 4 Nm. However, the variation of fatigue life in curvature–N appeared to be continuous within the tested amplitude range.

The fatigue rigidity response depended on the moment amplitudes applied. At high levels (e.g., >10.2 Nm), the rigidity was either relatively stable, or it decreased with the accumulated number of cycles. At low levels, the rigidity increased during cyclic tests, but the fatigue life of MOX fuel increased with the increasing initial rigidity.

Conversely, the effective half-gauge length limited to a range between 40 and 52 mm, increasing with increased amplitude of moment.

Table 9a. Dynamic test results for MOX SNF rods

TN	Spec	Load N	N cycles	Fail	ma Nm	ma_std Nm	ka m^1	ka_std m^-1	km m^-1	km_std m^-1
2	MOX2	100.000	3.70E + 04	1	8.480	0.103	0.425	0.010	0.437	0.012
4	MOX4	50.000	2.15E + 06	1	3.900	0.075	0.132	0.016	0.148	0.017
5	MOX5	60.000	4.49E + 05	1	4.794	0.061	0.179	0.009	0.186	0.010
6	MOX6	50.000	5.42E + 05	1	3.830	0.054	0.169	0.008	0.174	0.010
7	MOX7	150.000	1.55E + 04	1	13.857	0.127	0.629	0.008	0.640	0.009
8	MOX8	125.000	1.29E + 04	1	11.036	0.104	0.542	0.009	0.587	0.013
9	MOX9	75.000	8.98E + 04	1	6.294	0.084	0.319	0.009	0.353	0.015
10	MOX10	100.000	3.85E + 04	1	8.729	0.068	0.378	0.016	0.397	0.017
11	MOX11	100.000	4.23E + 04	1	8.662	0.047	0.375	0.008	0.415	0.011
12	MOX12	100.000	4.23E + 04	1	8.711	0.067	0.415	0.005	0.439	0.010

Table 9b. Dynamic test results for MOX SNF rods

TN	Spec	R	R_std	sa	sa_std	ea	ea_std	em	em_std	Lg2	Lg2_std	dh	dh_std
		Nm^2	Nm^2	Mpa	MPa	%	%	%	%	mm	mm	mm	mm
2	MOX2	19.955	0.533	104.839	1.274	0.204	0.005	0.210	0.006	43.811	0.621	1.243	0.291
4	MOX4	29.939	3.703	48.216	0.932	0.063	0.008	0.071	0.008	40.575	2.133	−1.512	0.927
5	MOX5	26.797	1.235	59.265	0.758	0.086	0.004	0.089	0.005	43.766	1.027	−1.178	0.684
6	MOX6	22.744	1.021	47.347	0.662	0.081	0.004	0.084	0.005	43.751	0.867	0.059	0.395
7	MOX7	22.042	0.316	171.317	1.569	0.302	0.004	0.307	0.004	48.523	0.454	0.409	0.129
8	MOX8	20.377	0.282	136.440	1.282	0.260	0.004	0.282	0.006	49.223	0.484	0.441	0.144
9	MOX9	19.716	0.470	77.823	1.041	0.153	0.004	0.169	0.007	45.835	0.536	−0.505	0.190
10	MOX10	23.127	0.855	107.918	0.840	0.181	0.008	0.190	0.008	49.626	1.075	−0.428	0.276
11	MOX11	23.098	0.534	107.096	0.585	0.180	0.004	0.199	0.005	52.390	0.622	−1.036	0.260
12	MOX12	20.979	0.242	107.694	0.825	0.199	0.002	0.211	0.005	48.820	0.550	−0.678	0.182

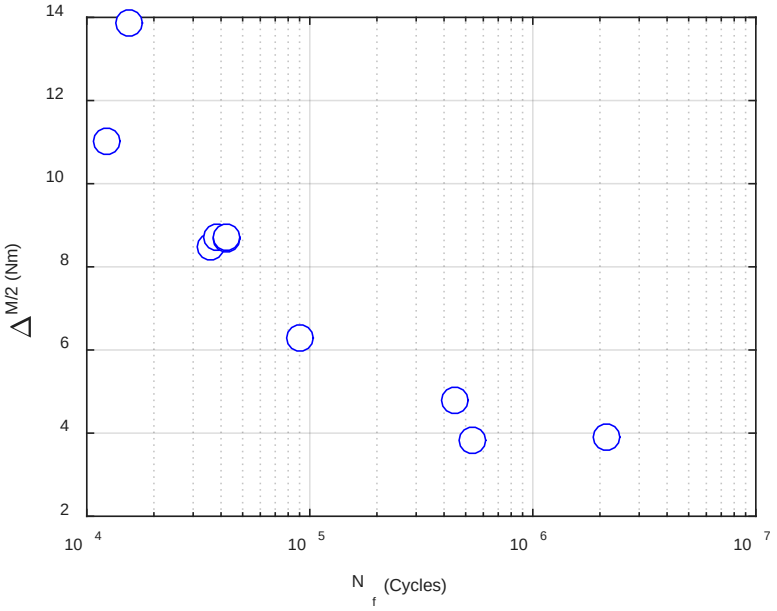

(a)

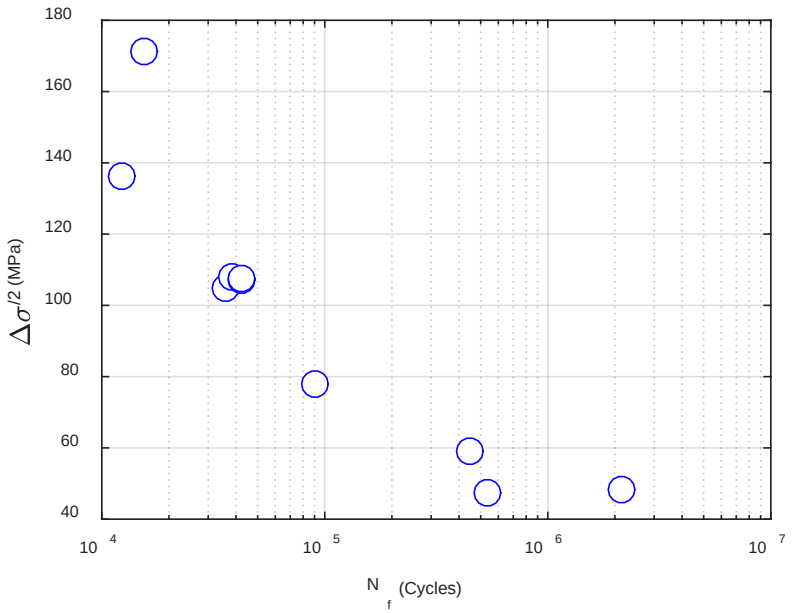
180
160
140
120
100
80
60
40
$\Delta\sigma^{/2}$ (MPa)
10 4
10 5
10 6
10 7
N f (Cycles)

(b)

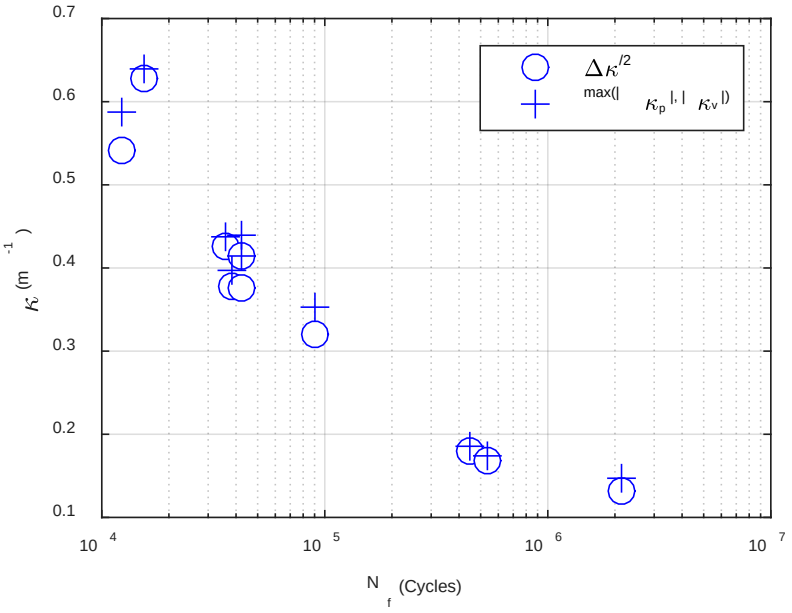
0.7
0.6
0.5
0.4
0.3
0.2
0.1
κ (m -1)
$\Delta\kappa^{/2}$
max(| κ_p |, | κ_v |)
10 4
10 5
10 6
10 7
N f (Cycles)

(c)

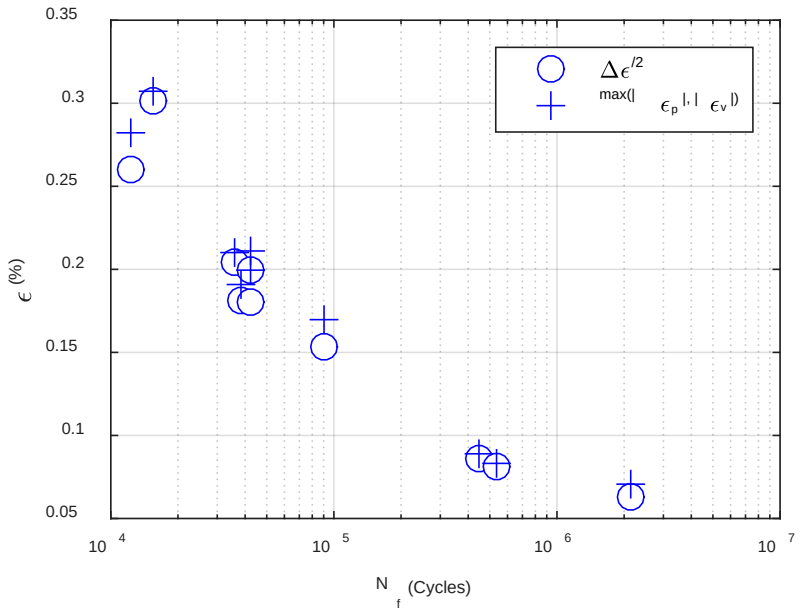

(d)

Fig. 22. (a) Moment amplitude, (b) stress amplitude, (c) curvature amplitude/ maximum, and (d) strain amplitude/maximum as a function of cycles or cycles to failure.

6. DISCUSSION

6.1 SNF Fatigue Life

The variations of fatigue life are given in Fig. 23 in terms of moment, equivalent stress, curvature, and equivalent strain for the tested SNFs.

The equivalent stress collapsed the data points from all sources of SNF into a single zone. A detailed examination revealed, at same stress level, the LMK fuel showed a longer fatigue life than the other two SNFs between 10^4 and 10^6 cycles. The strain–N curve shows that the LMK fuel has a longer fatigue life in a wider range from 10^4 to 10^7 cycles.

The knee point in the curve of moment and curvature or equivalent quantities is more clearly defined for LMK fuel than for the other two fuels.

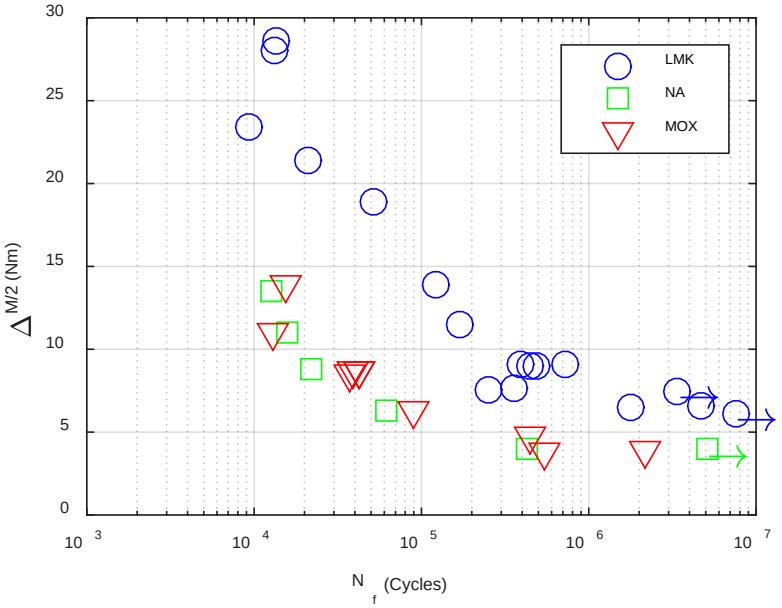

(a)

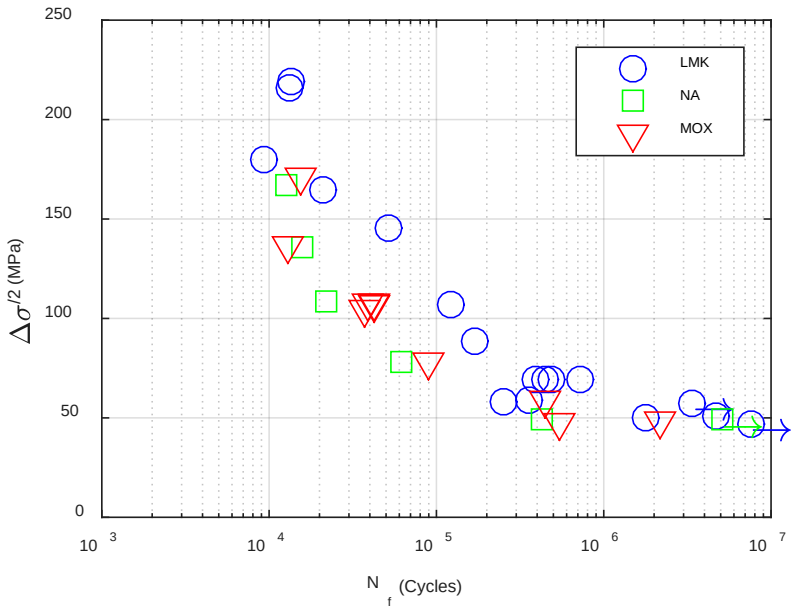
LMK
NA
MOX
250
200
150
100
50
0
$\Delta\sigma^{1/2}$ (MPa)
10^3
10^4
10^5
10^6
10^7
N_f (Cycles)

(b)

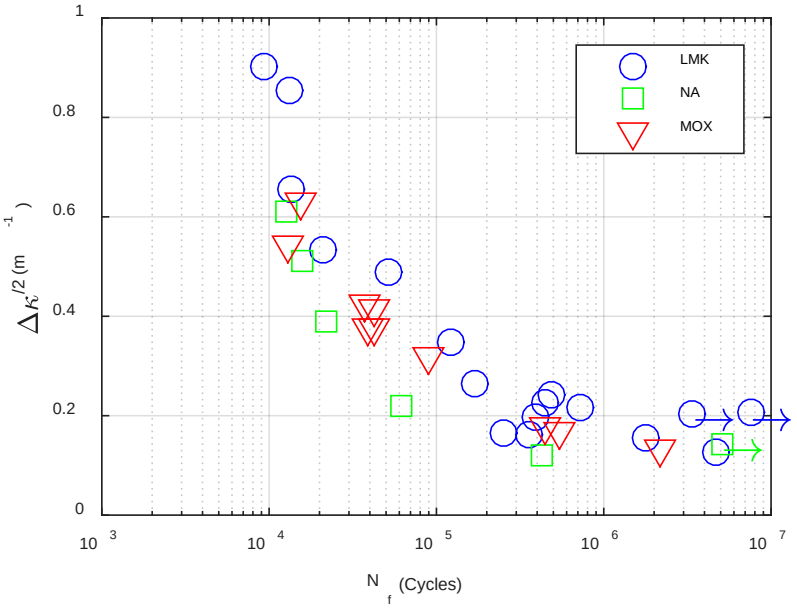
LMK
NA
MOX
1
0.8
0.6
0.4
0.2
0
$\Delta\kappa^{1/2}$ (m^{-1})
10^3
10^4
10^5
10^6
10^7
N_f (Cycles)

(c)

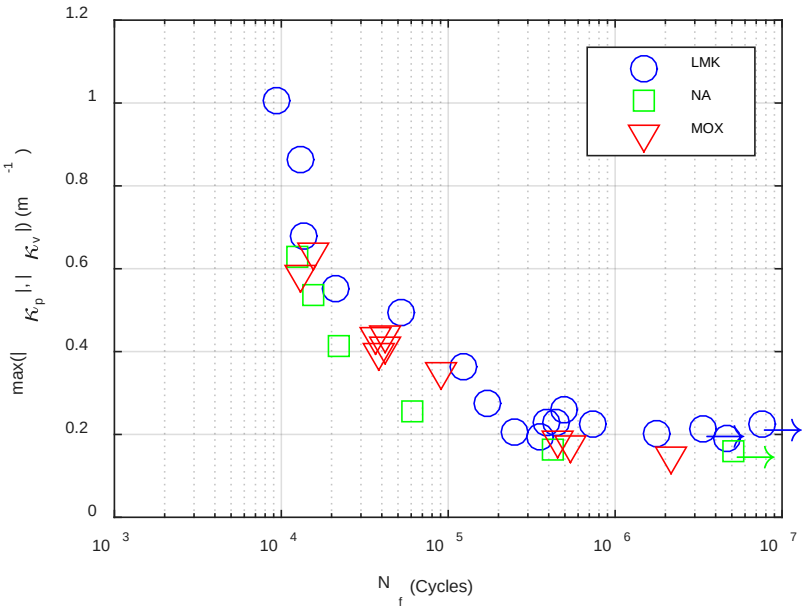
LMK
NA
MOX
max(| κ_p |, | κ_v |) (m^{-1})
N_f (Cycles)

(d)

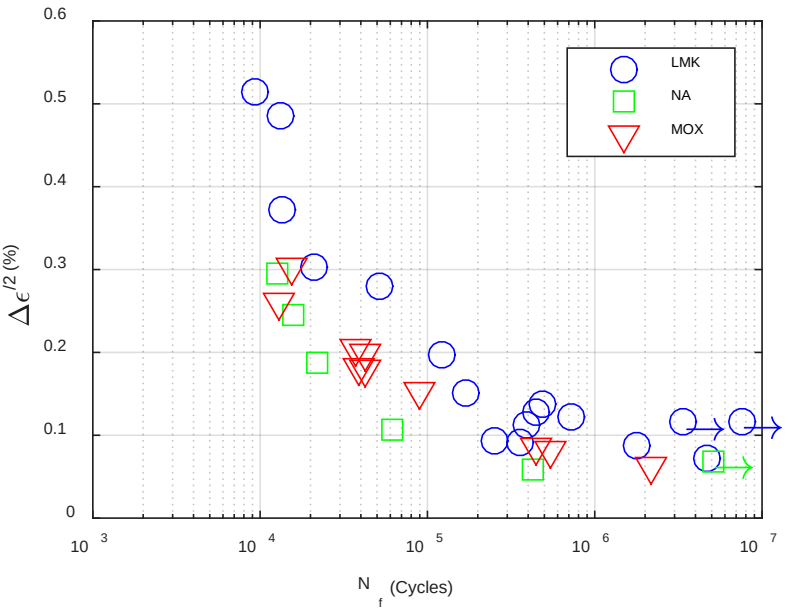
LMK
NA
MOX
$\Delta\epsilon^{/2}$ (%)
N_f (Cycles)

(e)

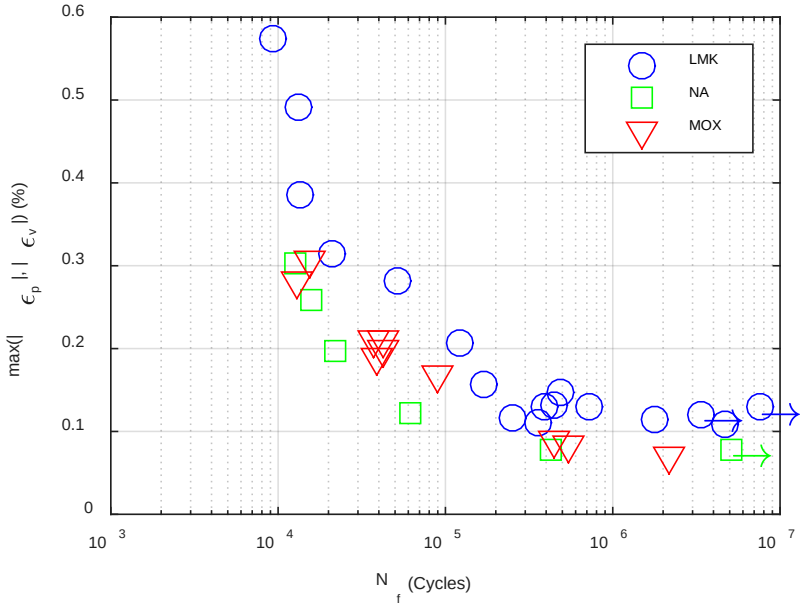

(f)

Fig. 23. (a) Moment amplitude, (b) stress amplitude, (c) curvature amplitude, (d) curvature maximum, (e) strain amplitude, and (f) strain maximum as a function of cycles or cycles to failure.

7. CIRFT EVALUATIONS OF LMK BWR SNF

7.1 Overview of CIRFT Evaluations of LMK Fuel Rods

A specified number of LMK rod segments, each measuring 6 in. in length, were prepared from four parent LMK rods [10]. Endcaps were added to the rod segments using the vise mold designed for the larger outer diameter (OD) of the SNF rods. The endcap labels and segment IDs are provided in Table 10.

Table 10. CIRFT number and segment labels of Limerick spent fuel rod

Spec	Endcap A*	Endcap B*	Segment ID	Note
LM01	LM1A	LM1B	574D-A	
LM02	LM2A	LM2B	575D-A	
LM03	LM3A	LM3B	575B-A	
LM04	LM4A	LM4B	575B-C	Endcaps misaligned. No test on this specimen.
LM05	LM5A	LM5B	574D-B	
LM06	LM6A	LM6B	574D-E	
LM07	LM7A	LM7B	575C-A	
LM08	LM8A	LM8B	575B-D	
LM09	LM9A	LM9B	574D-D	
LM10	LM10A	LM10B	575B-E	
LM11	LM11A	LM11B	575B-D	
LM12	LM12A	LM12B	575B-A	
LM13	LM13A	LM13B	575C-D	FY 2016
LM14	LM14A	LM14B	575C-B	FY 2016
LM15	LM15A	LM15B	575C-C	FY 2016
LM16	LM16A	LM16B	575D-E	FY 2016
LM17	LM17A	LM17B	575C-E	FY 2016

*Rod specimen was loaded into the testing machine so that endcaps A and B were on the same sides as motor 2 and motor 1, respectively.

Eleven specimens (LM1 to LM4, LM5 to LM12) were tested in FY 2015, and the data were analyzed using the procedure described in Section 1.3. Major results are provided in

Table 11. The column headings are the same as Table 6.

Table 11a. Dynamic test results for LMK SNF rods, FY 2015

TN	Spec	Load N	N cycles	Fail	ma Nm	ma_std Nm	ka m^1	ka_std m^1	km m^1	km_std m^1
1	LM1	250	9.40E + 03	1	23.426	0.087	0.901	0.027	1.007	0.027
2	LM2	125	1.71E + 05	1	11.468	0.090	0.266	0.006	0.275	0.008
3	LM3	100	4.92E + 05	1	9.016	0.081	0.243	0.008	0.258	0.011
5	LM5	85.	2.49E + 05	1	7.570	0.074	0.165	0.008	0.205	0.013
6	LM6	75	1.79E + 06	1	6.488	0.071	0.154	0.008	0.201	0.008
7	LM7	150	1.22E + 05	1	13.930	0.085	0.347	0.005	0.362	0.009
8	LM8	75	4.70E + 06	1	6.601	0.077	0.128	0.007	0.192	0.007
9	LM9	100	7.31E + 05	1	9.058	0.077	0.216	0.004	0.226	0.007
10	LM10	200	5.20E + 04	1	18.903	0.089	0.490	0.004	0.496	0.005
11	LM11	85	3.55E + 05	1	7.657	0.111	0.162	0.007	0.194	0.010
12	LM12	70	7.58E + 06	0	6.141	0.087	0.206	0.014	0.226	0.021

Table 11b. Dynamic test results for LMK SNF rods, FY 2015

TN	Spec	R Nm^2	R_std Nm^2	sa MPa	sa_std MPa	ea %	ea_std %	em %	em_std %	Lg2 mm	Lg2_std mm	Dh mm	dh_std mm
1	LM1	26.017	0.809	179.649	0.667	0.515	0.015	0.575	0.015	43.766	0.767	0.279	0.182
2	LM2	43.120	0.891	88.227	0.691	0.151	0.004	0.156	0.005	44.250	0.634	−0.084	0.347
3	LM3	37.187	1.025	69.286	0.623	0.138	0.004	0.147	0.007	44.455	0.738	0.325	0.298
5	LM5	45.948	2.117	58.177	0.566	0.094	0.005	0.117	0.007	41.932	0.756	−1.436	0.577
6	LM6	42.226	2.287	49.862	0.548	0.088	0.005	0.114	0.005	40.157	0.749	−1.723	0.312
7	LM7	40.176	0.586	107.050	0.656	0.197	0.003	0.206	0.005	45.455	0.565	−0.426	0.190
8	LM8	51.567	2.504	50.733	0.590	0.073	0.004	0.109	0.004	42.342	0.890	2.568	0.338
9	LM9	41.880	0.736	69.615	0.590	0.123	0.003	0.129	0.004	43.120	0.698	0.206	0.215
10	LM10	38.563	0.336	145.272	0.684	0.279	0.002	0.282	0.003	46.986	0.528	0.355	0.173
11	LM11	47.437	2.009	58.848	0.856	0.092	0.004	0.110	0.006	41.396	0.757	−1.864	0.362
12	LM12	29.879	1.859	47.196	0.665	0.117	0.008	0.129	0.012	38.475	0.965	0.732	0.683

7.2 FY 2016 Tests and Results (Appendix D)

Five tests were conducted on specimens LM13 to LM17 during the reporting period. As in FY 2015, specimens were tested in as-received condition. The load amplitude range was also the same (from 8.64 to 30.48 Nm). The test at 8.64 Nm ran more than 3.37×10^6 cycles, and the specimen did not fail. That test was then stopped, and a new test was started at an increased amplitude.

7.2.1 Measurements and Monitoring Data

The data sets for each of the dynamic tests, including measurement data and online monitoring data, were processed using the procedure suggested in Section 2.

1) For each test, the following results are provided in Appendix E:When available, variations for curvature range, moment range, flexural rigidity, curvature peak/valley, and moment peak/valley are included.

2) The curvature and moment plots are given for the beginning data block of a test session when the load reaches the designated level. The results for the first (tested to 1,000 cycles) and last sessions are included.

3) Finally, the online monitoring data is presented, including curvature range variations, moment range, flexural rigidity, curvature peak/valley, and moment peak/valley as a function of the number of cycles or the cycles to failure.

For each cyclic test, two sets of measurements were obtained between test sessions. These measurements were made with small displacement amplitudes at 0.05 Hz. With this input, both moment and curvature varied or decreased with the accumulated number of cycles. The rigidity measurements were generally higher than those from the monitoring data, and the degree of change was similar to that of the monitoring data.

The flexural rigidity during the cyclic either remained flat or decreased as the number of cycles increased. The rigidity of the LM4 specimen displayed a rise-and-fall variation pattern, but the degree of variation was limited. Meanwhile, there was no clear relationship between rigidity and the number of cycles to failure. The correction observed for the curvature was not significant because of the low input, and the signal-to-noise ratio was reduced at lower input levels. The amplitude of the de-noised curvature was generally lower compared with the original data, as expected.

7.2.2 Fatigue Life

The major results of the dynamic tests are summarized in Table 12. The definitions given for the columns in Table 11 also apply to this table. Overall, the trends observed from FY 2015 tests were consistent with the FY 2016 data. For instance, fatigue life increased as the input level decreased; the effective half-gauge length was limited to a range between 38 and 50 mm and increased as the amplitude of moment increased.

Plots based on the mean values of relevant quantities are shown in Fig. 24(a)–(d), where the circles represent the tests with failure, and the circles with arrows designate the tests with no failure. The results from FY 2015 and FY 2016 (Tables 11 and Table 12) are presented to obtain a comprehensive picture of SNF responses. The variation in fatigue life with amplitude was not continuous. A discontinuity, or knee, was observed near 7 Nm and 0.2 m^{-1} in the moment–N and curvature–N plots, respectively. For the SNF, these parameters correspond to 50 MPa of equivalent stress and 0.1% of equivalent strain. At the same time, curvature extreme values were generally higher than curvature amplitudes as expected, but the difference was small.

All of the failures of the specimens tested were observed to have occurred within the gauge section, as illustrated in Fig. 25.

Table 12a. Dynamic test results for LMK SNF rods, FY 2016

TN	Spec	Load N	N cycles	Fail	ma Nm	ma_std Nm	ka m^1	ka_std m^1	km m^1	km_std m^1
13	LM13	250	2.10E + 04	1	21.396	2.415	0.533	0.071	0.553	0.073
14	LM14	100	3.90E + 05	1	9.048	0.082	0.198	0.008	0.228	0.010
15	LM15	100	4.41E + 05	1	8.997	0.073	0.225	0.007	0.230	0.007
16	LM16	300	1.36E + 04	1	28.560	0.168	0.654	0.008	0.679	0.014
17	LM17	85	3.37E + 06	0	7.459	0.374	0.204	0.011	0.212	0.013
18	LM17	300	1.31E + 04	1	28.063	0.131	0.853	0.006	0.863	0.011

Table 12b. Dynamic test results for LMK SNF rods, FY 2016

TN	Spec	R Nm^2	R_std Nm^2	sa MPa	sa_std MPa	Ea %	ea_std %	em %	em_std %	Lg2 mm	Lg2_std mm	dh mm	dh_std mm
13	LM13	40.225	0.903	164.428	18.563	0.303	0.040	0.315	0.042	47.411	0.705	−0.138	0.143
14	LM14	45.659	1.768	69.535	0.632	0.113	0.005	0.130	0.006	44.092	0.781	−1.307	0.387
15	LM15	40.008	1.219	69.141	0.561	0.128	0.004	0.131	0.004	44.196	0.698	−0.148	0.585
16	LM16	43.672	0.480	219.490	1.295	0.372	0.005	0.386	0.008	50.296	0.440	−0.435	0.153
17	LM17	36.630	1.138	57.325	2.872	0.116	0.006	0.121	0.007	44.656	0.919	−0.849	0.338
18	LM17	32.913	0.252	215.671	1.004	0.485	0.003	0.491	0.006	47.420	0.331	1.211	0.092

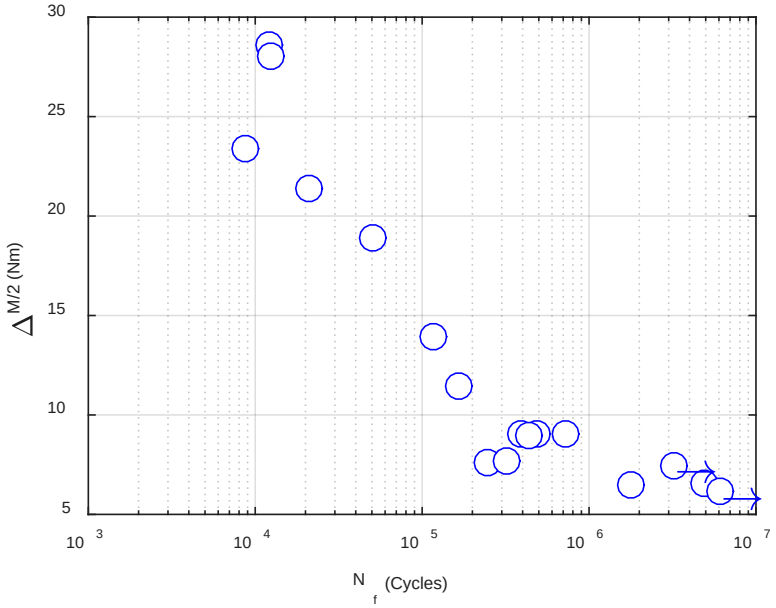
30
25
20
15
10
5
ΔM/2 (Nm)
10 3
10 4
10 5
10 6
10 7
N f (Cycles)

(a)

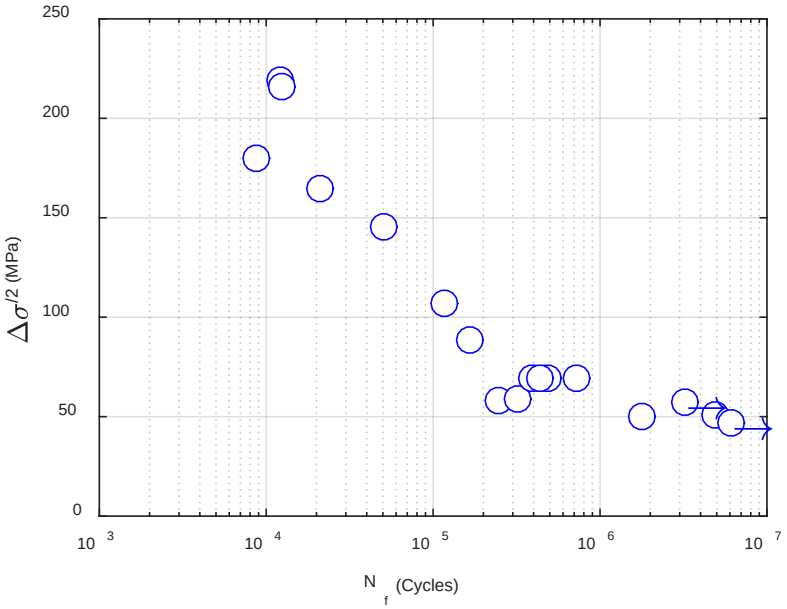
250
200
150
100
50
0
Δσ'/2 (MPa)
10 3
10 4
10 5
10 6
10 7
N f (Cycles)

(b)

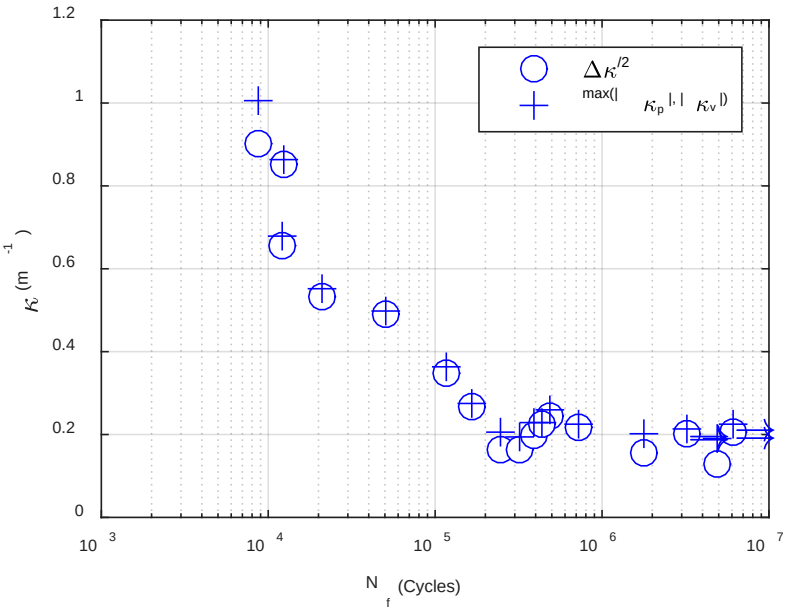

(c)

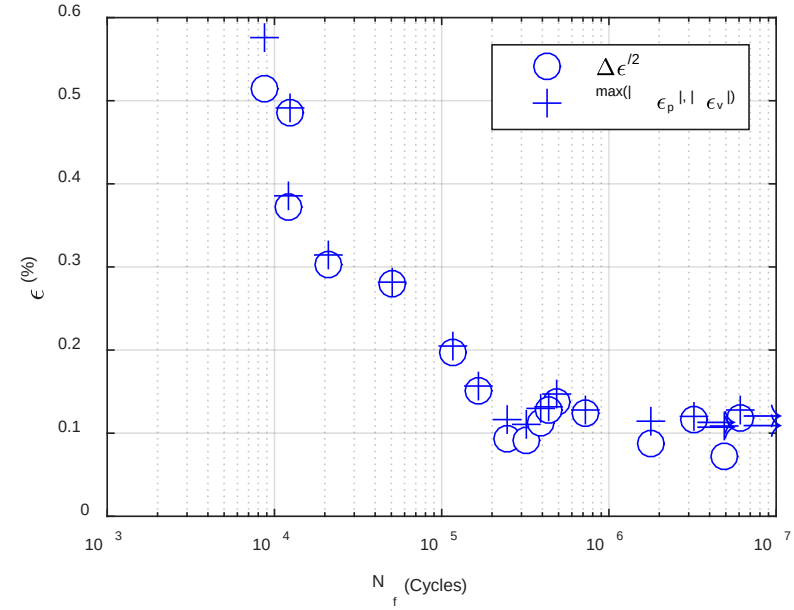

(d)

Fig. 24. (a) Moment amplitude, (b) stress amplitude, (c) curvature amplitude/ maximum, and (d) strain amplitude/ maximum as a function of cycles or cycles to failure.

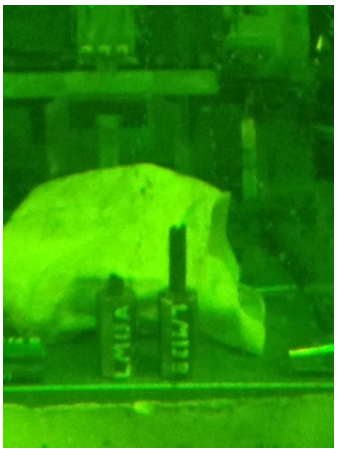

(a)

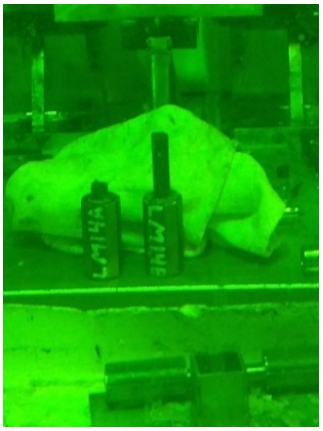

(b)

(c)

(d)

(e)

Fig. 25. Images showing failure modes or failure positions for specimens (a) LM13, (b) LM14, (c) LM15, (d) LM16, and (e) LM17.

8. CIRFT EVALUATIONS OF MOX FUEL

8.1 Overview of CIRFT Evaluations of MOX Fuel Rods

The segment ID and CIRFT labels for MOX fuel specimens are given in Table 13. Twelve tests were completed in FY 2014 and FY 2015. Of these, 10 dynamic tests were conducted with amplitudes from 5.08 to 15.24 Nm; all of the specimens failed, and the fatigue life ranged from 1.29×10^4 and 2.15×10^6 cycles. The measurement and monitoring data sets for these tests were processed using the procedure previously described, and the results are provided in Table 14.

Table 13. Specimen labels used for MOX SNF

CIRFT label	Endcap A	Endcap B	Segment ID	Note
MOX1	MOX-1A	MOX-1B	MOX-A-11	
MOX2	MOX-2A	MOX-2B	MOX-A-12	
MOX3	MOX-3A	MOX-3B	MOX-A-13	
MOX4	MOX-4A	MOX-4B	MOX-B-05	
MOX5	MOX-5A	MOX-5B	MOX-B-06	
MOX6	MOX-6A	MOX-6B	MOX-B-07	
MOX7	MOX-7A	MOX-7B	MOX-C-06	
MOX8	MOX-8A	MOX-8B	MOX-C-07	
MOX9	MOX-9A	MOX-9B	MOX-C-08	
MOX10	MOX-10A	MOX-10B	MOX-K-09	
MOX11	MOX-11A	MOX-11B	MOX-K-10	
MOX12	MOX-12A	MOX-12B	MOX-K-11	
MOX13	MOX-13A	MOX-13B	MOX-K-08	FY 2016
MOX14	MOX-14A	MOX-14B	MOX-C-09	FY 2016
MOX15	MOX-15A	MOX-15B	MOX-B-02	FY 2016
MOX16	MOX-16A	MOX-16B	MOX-K-16	FY 2016
MOX17	MOX-17A	MOX-17B	MOX-B-08	FY 2016
TH1	TH1-A	TH1-B	MOX-A-17	FY 2016
TH2	TH2-A	TH2-B	MOX-A-18	FY 2016
TH3	TH3-A	TH3-B	MOX-A-16	FY 2016
TH4	TH4-A	TH4-B	MOX-C-12	FY 2016
TH5	TH5-A	TH5-B	MOX-C-11	FY 2016
TH6	TH6-A	TH6-B	MOX-C-10	FY2016

Table 14a. Dynamic test results for MOX SNF rods, FY 2014 and FY 2015

TN	Spec	Load N	N cycles	Fail	ma Nm	ma_std Nm	ka m^1	ka_std m^1	Km m^1	km_std m^1
2	MOX2	100	3.70E + 04	1	8.480	0.103	0.425	0.010	0.437	0.012
4	MOX4	50	2.15E + 06	1	3.900	0.075	0.132	0.016	0.148	0.017
5	MOX5	60	4.49E + 05	1	4.794	0.061	0.179	0.009	0.186	0.010
6	MOX6	50	5.42E + 05	1	3.830	0.054	0.169	0.008	0.174	0.010
7	MOX7	150	1.55E + 04	1	13.857	0.127	0.629	0.008	0.640	0.009
8	MOX8	125	1.29E + 04	1	11.036	0.104	0.542	0.009	0.587	0.013
9	MOX9	75	8.98E + 04	1	6.294	0.084	0.319	0.009	0.353	0.015
10	MOX10	100	3.85E + 04	1	8.729	0.068	0.378	0.016	0.397	0.017
11	MOX11	100	4.23E + 04	1	8.662	0.047	0.375	0.008	0.415	0.011
12	MOX12	100	4.23E + 04	1	8.711	0.067	0.415	0.005	0.439	0.010

Table 14b. Dynamic test results for MOX SNF rods, FY 2014 and FY 2015

TN	Spec	R Nm^2	R_std Nm^2	sa Mpa	sa_std Mpa	ea %	ea_std %	em %	em_std %	Lg2 mm	Lg2_std mm	Dh mm	dh_std mm
2	MOX2	19.955	0.533	104.839	1.274	0.204	0.005	0.210	0.006	43.811	0.621	1.243	0.291
4	MOX4	29.939	3.703	48.216	0.932	0.063	0.008	0.071	0.008	40.575	2.133	−1.512	0.927
5	MOX5	26.797	1.235	59.265	0.758	0.086	0.004	0.089	0.005	43.766	1.027	−1.178	0.684
6	MOX6	22.744	1.021	47.347	0.662	0.081	0.004	0.084	0.005	43.751	0.867	0.059	0.395
7	MOX7	22.042	0.316	171.317	1.569	0.302	0.004	0.307	0.004	48.523	0.454	0.409	0.129
8	MOX8	20.377	0.282	136.440	1.282	0.260	0.004	0.282	0.006	49.223	0.484	0.441	0.144
9	MOX9	19.716	0.470	77.823	1.041	0.153	0.004	0.169	0.007	45.835	0.536	−0.505	0.190
10	MOX10	23.127	0.855	107.918	0.840	0.181	0.008	0.190	0.008	49.626	1.075	−0.428	0.276
11	MOX11	23.098	0.534	107.096	0.585	0.180	0.004	0.199	0.005	52.390	0.622	−1.036	0.260
12	MOX12	20.979	0.242	107.694	0.825	0.199	0.002	0.211	0.005	48.820	0.550	−0.678	0.182

8.2 FY 2016 Tests and Results (Appendix E)

Thirteen CIRFT evaluations were completed on MOX specimens in FY 2016. Six tests were conducted on the specimens that had been pretreated by dropping them from a height of 12 in. with specimen laid horizontally, and the remaining seven tests used specimens that had been subjected to two cycles of thermal treatment for 10 h at 400°C. The tests were performed under amplitudes ranging from 7.62 to 12.70 Nm.

8.2.1 Measurement and Monitoring Data

The results for each test are given in Appendix E. The plots of the MOX fuels are similar to those of LMK fuels, including the variations in curvature range, moment range, flexural rigidity, curvature peak/valley, and moment peak/valley values.

The flexural rigidity of the rod specimens that were either dropped or annealed was lower than the as-received specimens. In most cases, the online monitoring generally demonstrated a steady or continuous variation in curvature during cyclic testing, depending on the moment amplitude and material condition. MOX14 was the exception, where a discontinuous rigidity variation was observed. Such a discontinuous response was associated with the asymmetrical curvature increase of the specimen, and an abrupt increase was seen near 10^4 cycles, as the specimen was approaching failure. For MOX15, a substantial negative shift in κ and a reduction in the κ range were observed after a test restart around 3.3×10^6 cycles.

8.2.2 Fatigue Life

The results for the dynamic tests of MOX fuel in FY 2016 are summarized in Table 15. Definitions for the column heads are same as those given for LMK fuels in Table 11.

Plots based on the mean values of quantities are given in Fig. 26(a)–(d), where MOX1 represents the as-received specimens, MOX2 represents those subjected to 12 in. height drop, and MOX3 represents those that were thermal annealed. Fatigue life was shown to be affected by the condition of specimens. The 12 in. height drop seemingly reduces the fatigue life of SNF rods. Conversely, thermal annealing extends fatigue life, which can be seen clearly from the two tests under 7.62 Nm as shown in Fig. 26(a).

Several images of the failed specimens that were pretreated with the 12 in. drop are shown in Fig. 27, and specimens that had been thermally annealed are given in Fig. 28. Although a couple of specimens failed near the edge of endcaps, the failures were taking place in the gauge section of these specimens.

Table 15a. Dynamic test results for MOX SNF rods, FY 2016

TN	Spec	Load N	N cycles	Fail	Ma Nm	ma_std Nm	ka m^1	ka_std m^−1	km m^−1	km_std m^−1
13	MOX13	100	2.70E + 04	1	8.725	0.059	0.450	0.007	0.466	0.011
14	MOX14	75	8.72E + 04	1	6.190	0.091	0.668	0.172	1.456	1.160
15	MOX15	50	4.65E + 06	0	3.842	0.074	0.184	0.028	0.216	0.011
16	MOX16	150	3.66E + 03	1	13.209	1.656	0.986	0.273	1.007	0.345
17	MOX17	125	1.16E + 04	1	11.104	0.951	0.700	0.663	0.768	0.960
18	MOX15	100	1.95E + 04	1	8.474	0.065	0.439	0.005	0.445	0.008
19	TH1	100	5.70E + 04	1	8.770	0.065	0.538	0.007	0.564	0.009
20	TH2	75	3.75E + 06	0	6.234	0.107	0.353	0.009	0.380	0.013
21	TH3	125	1.51E + 04	1	10.573	0.289	0.696	0.029	0.732	0.033
22	TH4	75	2.51E + 06	1	6.284	0.150	0.399	0.025	0.438	0.027
23	TH5	125	2.76E + 04	1	11.190	0.069	0.821	0.008	0.829	0.011
24	TH6	150	1.25E + 04	1	13.391	0.157	0.812	0.014	0.832	0.018
25	TH2	125	5.73E + 04	1	11.029	0.135	0.671	0.012	0.678	0.013

Table 15b. Dynamic test results for MOX SNF rods, FY 2016

TN	Spec	R Nm^2	R_std Nm^2	sa MPa	sa_std MPa	Ea %	ea_std %	Em %	em_std %	Lg2 mm	Lg2_std mm	dh mm	dh_std mm
13	MOX13	19.380	0.268	107.870	0.734	0.216	0.003	0.224	0.005	47.339	0.524	−0.040	0.190
14	MOX14	9.844	2.432	76.530	1.122	0.321	0.083	0.699	0.557	27.459	7.996	1.240	2.671
15	MOX15	21.440	3.764	47.501	0.917	0.088	0.013	0.104	0.005	43.138	3.120	0.741	1.512
15	MOX15	19.081	0.547	47.442	0.999	0.097	0.004	0.103	0.006	41.513	0.755	0.275	0.315
16	MOX16	13.822	1.700	163.310	20.479	0.473	0.131	0.483	0.165	48.167	0.841	0.188	0.275
17	MOX17	17.668	2.371	137.285	11.752	0.336	0.318	0.369	0.461	46.586	2.074	0.081	0.390
18	MOX15	19.310	0.165	104.774	0.804	0.211	0.002	0.214	0.004	47.594	0.516	0.170	0.192
19	TH1	16.292	0.186	108.425	0.800	0.258	0.004	0.271	0.004	49.023	0.443	0.738	0.145
20	TH2	17.656	0.350	77.071	1.322	0.170	0.004	0.182	0.006	48.349	0.802	−0.743	0.224
21	TH3	15.214	0.713	130.719	3.569	0.334	0.014	0.351	0.016	47.431	0.867	0.337	0.247
22	TH4	15.809	0.862	77.695	1.856	0.191	0.012	0.210	0.013	48.093	0.793	−0.217	0.790
23	TH5	13.638	0.151	138.354	0.847	0.394	0.004	0.398	0.005	47.979	0.372	0.297	0.136
24	TH6	16.504	0.394	165.556	1.942	0.390	0.007	0.399	0.008	49.765	0.385	−0.563	0.134
25	TH2	16.450	0.137	136.353	1.674	0.322	0.006	0.325	0.006	50.304	0.464	−0.366	0.109

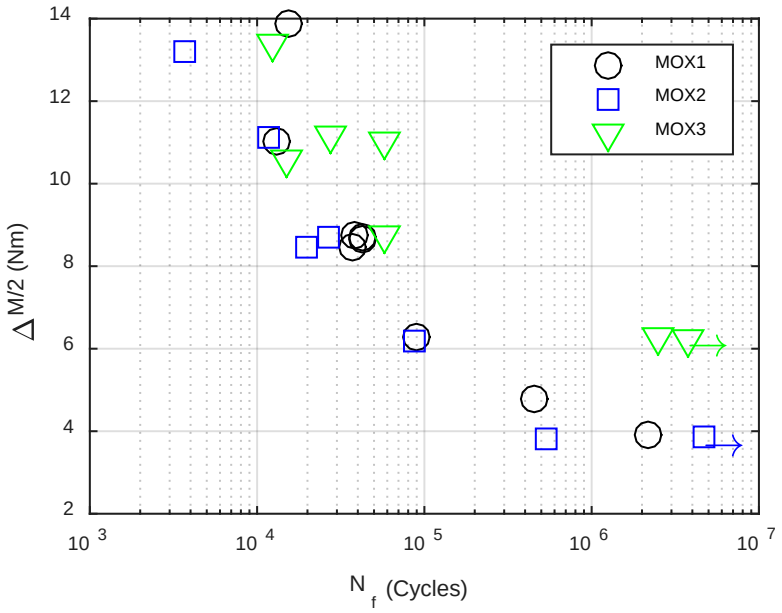
MOX1
MOX2
MOX3
Δ M/2 (Nm)
N f (Cycles)
14
12
10
8
6
4
2
10 3
10 4
10 5
10 6
10 7

(a)

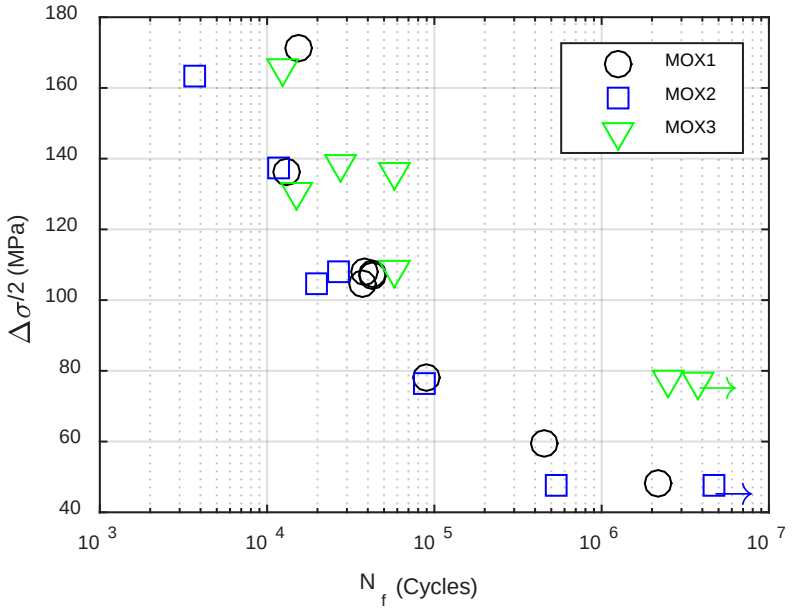
MOX1
MOX2
MOX3
Δσ/2 (MPa)
N f (Cycles)
180
160
140
120
100
80
60
40
10 3
10 4
10 5
10 6
10 7

(b)

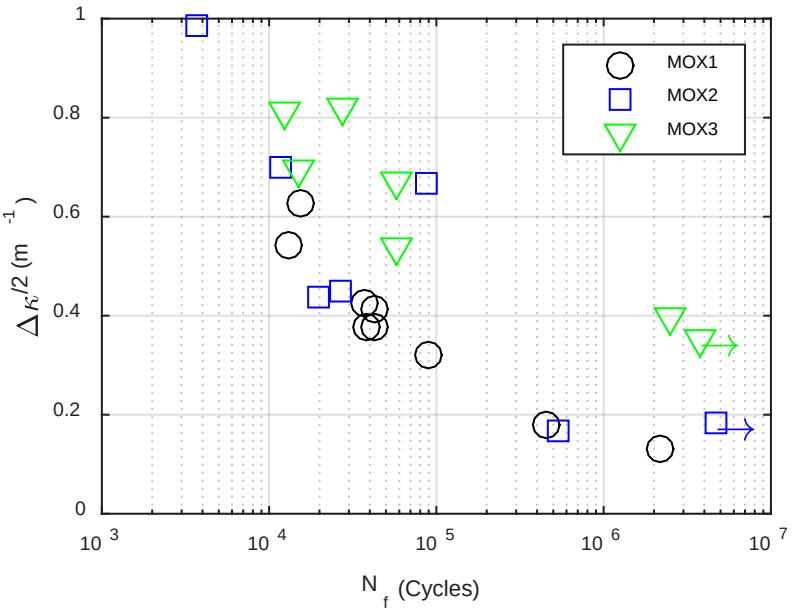

(c)

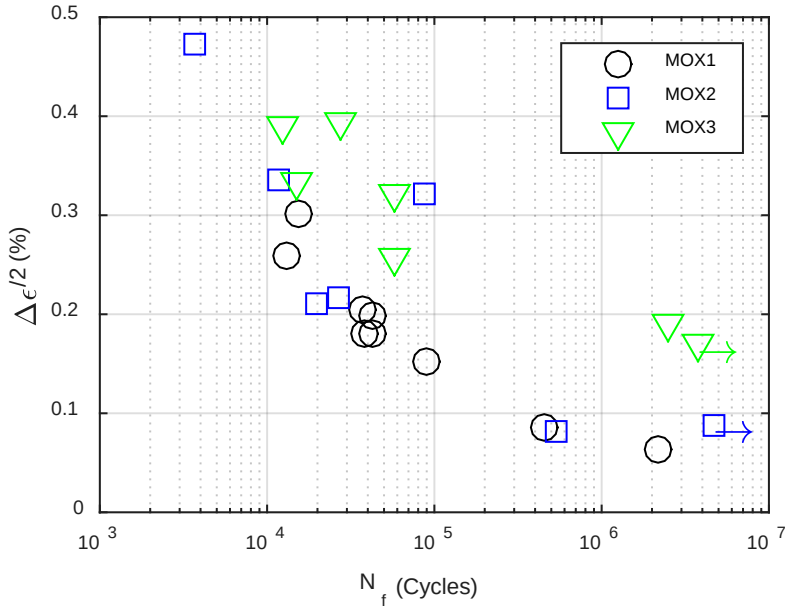

(d)

Fig. 26. (a) Moment amplitude, (b) stress amplitude, (c) curvature amplitude/maximum, and (d) strain amplitude/maximum as a function of cycles or cycles to failure. MOX1—as-received; MOX2—12 in. drop; MOX3—thermal annealed.

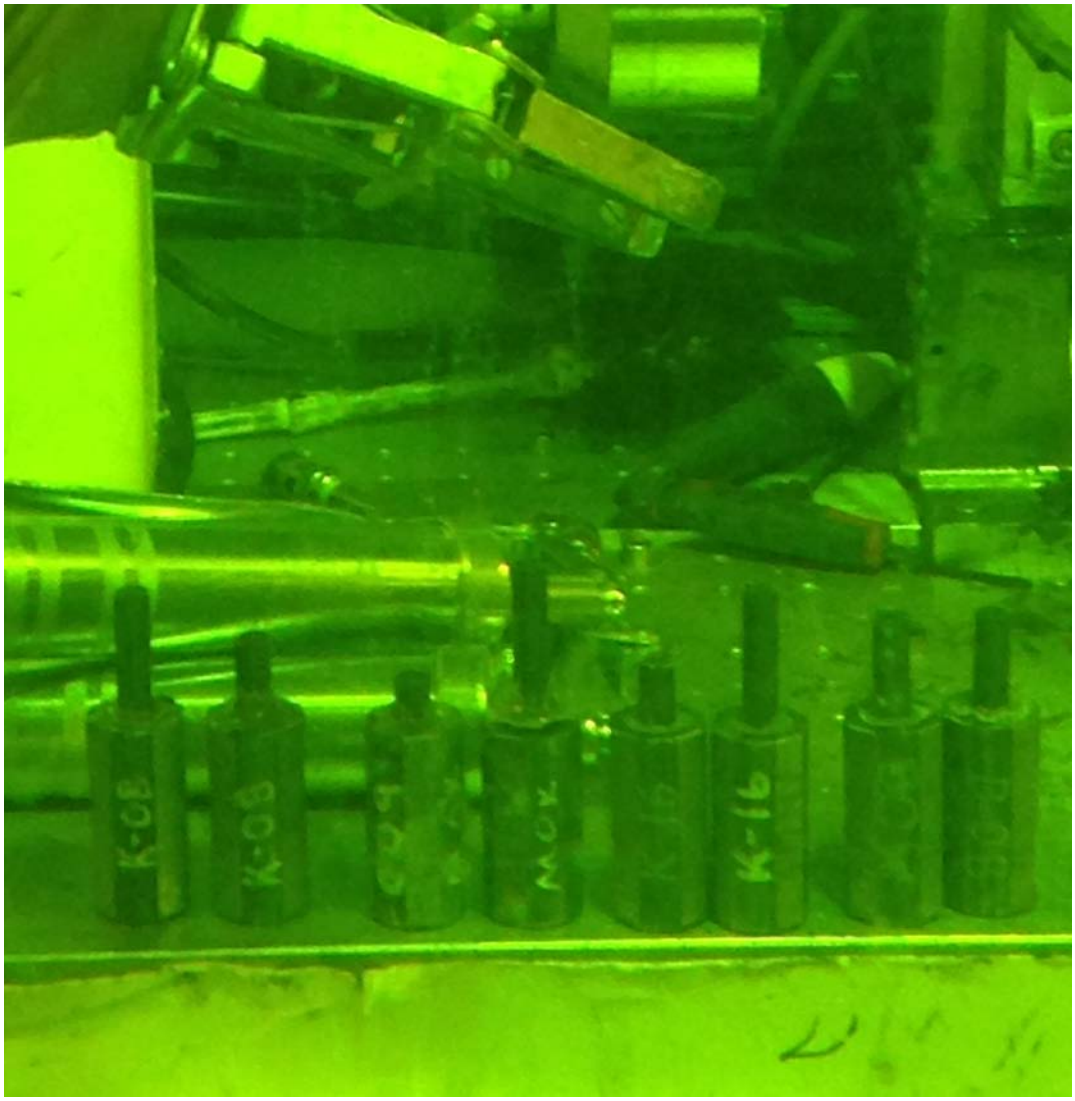

Fig. 27. Images of MOX fractured samples with 12 in. drop, MOX13 (K-08), MOX14 (C-09), MOX15 (B-02), and MOX16 (K-16).

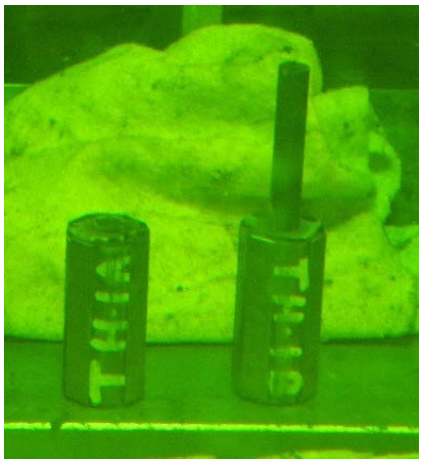

(a)

(b)

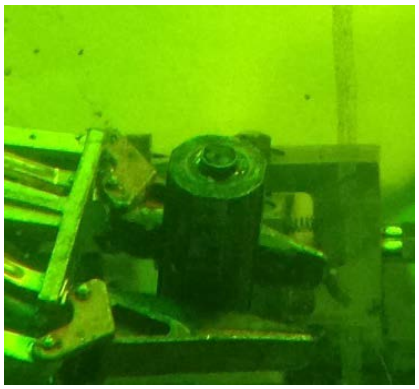

(c)

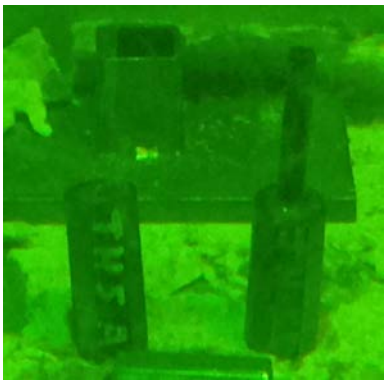

(d)

(e)

(f)

Fig. 28. Images showing the failure positions of (a) TH1, (b) TH2, (c) TH3, (d) TH4, (e) TH5, and (f) TH6.

9. CIRFT EVALUATIONS OF HBR FUEL FOR HYDRIDE REORIENTATION STUDY

9.1 Overview of CIRFT Evaluations and Results for HBR Fuel Rods

Rod segments, measuring 6 in. long, for CIRFT evaluations were prepared from five HBU HBR SNF rods. Specimen labels and corresponding segment IDs are given in Table 16.

ORNL completed 24 tests in FY 2013 and FY 2014. Fifteen tests were dedicated to dynamic testing conditions with amplitudes ranging between 5.08 and 35.56 Nm. Several tests were run at amplitudes below 8.89 Nm over tens of millions of cycles, and the specimens did not show any sign of failure, so these tests were stopped.

Table 16. Specimen labels used for HBR SNF

Spec ID	Endcap A	Endcap B	Seg. ID	Note
Demo1	Demo1-A	Demo1-B	606B2	
S3	S3-A	S3-B	605D1F	
S1	S1-A	S1-B	606C3C	
S2	S2-A	S2-B	605D1E	
Dcal	Dcal-A	Dcal-B	609C5	
DL1	DL1-A	DL1-B	607C4B	
DL2	DL2-A	DL2-B	608C4B	
DL3	DL3-A	DL3-B	605C10A	
DM2	DM2-A	DM2-B	605D1B	
DM1	DM1-A	DM1-B	605D1C	
DH1	DH1-A	DH1-B	609C4	
DH2	DH2-A	DH2-B	609C3	
DM3	DM3-A	DM3-B	606C3E	
DH3	DH3-A	DH3-B	609C7	
S5	S5-A	S5-B	606C3A	
R1	R1-A	R1-B	607C4A	
R2	R2-A	R2-B	608C4A	
R3	R3-A	R3-B	606B3E	
R4	R4-A	R4-B	606B3D	
R5	R5-A	R5-B	606B3C	
HR1	HR1-A	HR1-B	607D4C	FY 2016
HR2	HR2-A	HR2-B	607D4A	FY 2016
HR3	HR3-A	HR3-B	608D4A	FY 2016
HR4	HR4-A	HR4-B	608D4C	FY 2016

9.2 FY 2016 Test Results (Appendix F)

Four CIRFT evaluations were completed on the HBR specimens with radial hydride treatment (RHT), 120 MPa hoop stress, 170 to 400°C, five cycles) in FY 2016. Amplitudes ranging from 10.16 and 16.26 Nm were tested. One of the HBR RHT specimens (HR2) was tested under the following static conditions before dynamic testing: (1) six cycles of unidirectional bending with relative peak displacement 12 mm at U-frame loading points and (2) four cycles of fully reversed bending with relative peak/valley displacement ±12 mm. This specimen survived the static loading without failure and was then tested under dynamic loading, as will be discussed. Due to a welded endcap leak, only thermal heat treatment was applied to the HR4 sample.

The sample preparation for the hydride reorientation (HR) project is detailed below [10].

- The HBU HBR fuels under simulated drying operation conditions of the SNF were used for the HR testing study. Based on out-of-cell benchmark HR tests with hydrided HBR cladding, four in-cell HR tests were conducted with HBU HBR fuel samples at approximately 145 MPa at 400°C.
- The HBR fuel samples for HR tests were prepared in the irradiation fuel examination laboratory. After the samples were sectioned into 6 in.-long pieces, the surface oxide layer and fuels were removed from both ends to a depth of approximately 0.5 in. Endcaps were welded at both ends, and the HBR fuel specimens were then pressurized with argon gas at a maximum hoop stress level of 145 MPa and a target hold temperature (T = 400°C). Thermal cycling was performed to increase the radial hydrides. After fabrication, the specimens were placed in a holder within the furnace for heating to a target temperature of 400°C, held for 3 h, cooled at 1°C/min to 170°C, and then heated at 1°C/min to a target hold temperature of 400°C again for five cycles. The samples were furnace cooled from 170°C to room temperature for the last cycle. All in-cell tests had the same temperature profiles. Fig. 29 shows the temperature history of the first in-cell HR test, HR1, with a HBU HBR sample.

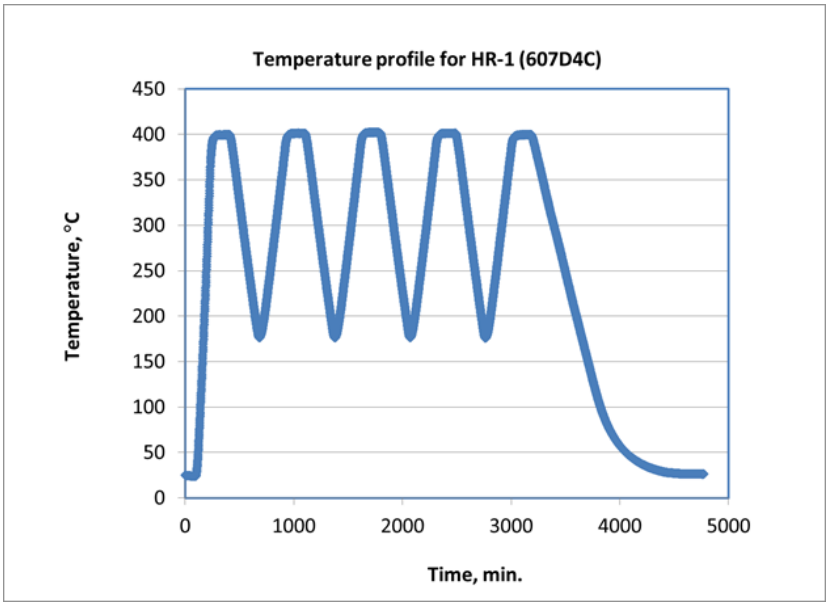

Fig. 29. Sample temperature as a function of time for in-cell HR test HR-1.

- The hydride-reoriented samples were sent to Work Station 12, where the CIRFT exams were performed at RT to evaluate the materials performance after the HR tests. After the tests were completed in the CIRFT, the specimens were sent to work station three, where the post-hydride-reoriented sample was examined to verify the radial hydrides had been generated. Fig. 30 shows

the hydride morphology of hydride-reoriented sample HR1. The hydrogen concentration of this sample was about 360–400 wppm. The MET mount specimen was sectioned at the midplane of a 6 in.-long sample. Although the in-cell HR test conditions were the same as the out-of-cell test HR-HBR#2 and the hydrogen concentration of these two samples were compatible, the morphology of HBU sample HR1 was different from hydrided sample HR-HBR#2. For the unirradiated sample, the circumferential hydrides were uniformly distributed across the wall, and the maximum length of its radial hydrides was about 50–60 μm. For HBU samples, the radial hydrides were mainly distributed near the inner surface, and the circumferential hydrides are mostly seen near the outer surface. The length of the radial hydride of the HBU sample, Fig. 30(a), was also much longer than the unirradiated sample, Fig. 30(b).

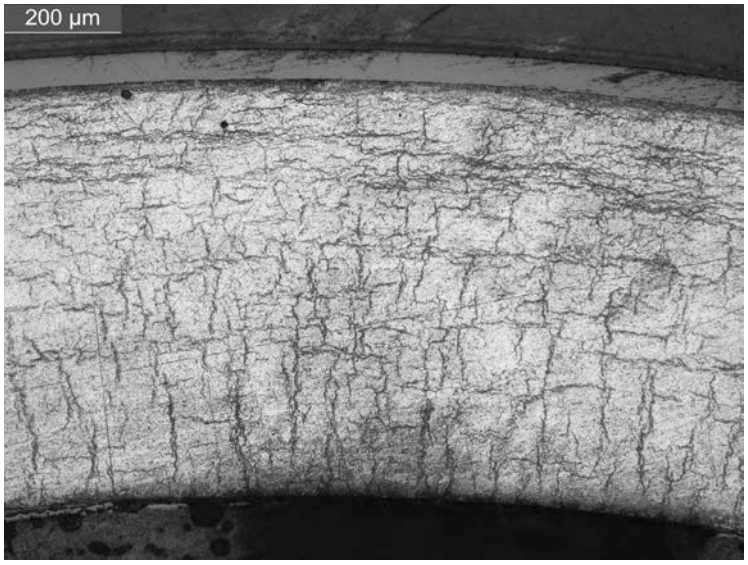

(a)

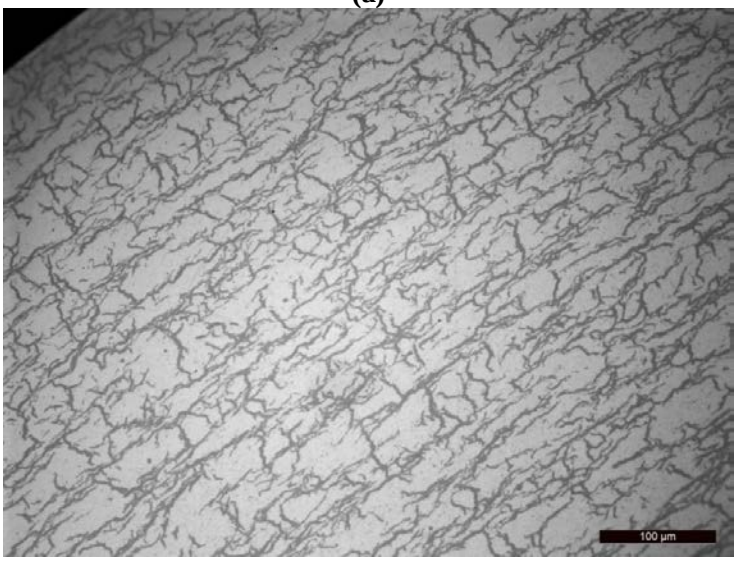

(b)

Fig. 30. (a) High magnification micrograph showing radial hydrides of Sample HR-1 (H ≈ 360–400 ppm). The HBU HBR specimen was pressurized to 145 MPa at 400°C with five thermal cycles. (b) High magnification micrograph showing radial hydrides of Sample HR-HBR#2 (H ≈ 286 ppm). The specimen was sectioned at the midplane of a 6 in.-long sample.

9.2.1 Measurements and Monitoring Data

The results for each test are given in Appendix F. The plots of HBR fuels are similar to those of LMK fuels, including the variations of curvature range, moment range, flexural rigidity, curvature peak/valley, and moment peak/valley values.

The flexural rigidity of the rod specimens treated by hydride reorientation was shown to be much lower than as-received specimens under equivalent amplitude. For example, under the same amplitude of 100 N, the rigidity of the RHT specimen (HR3) was only about 57% of the as-received specimen (DL3). The variation of rigidity during a cyclic test was continuous. In HR3, a sudden drop was observed before failure.

9.2.2 Fatigue Life

The results for the dynamic tests of HBR fuel in FY 2016 are summarized in Table 17. Again, definitions of the column heads are same as those for LMK fuels in Table 10.

The plots based on the mean values of quantities are given in Fig. 31(a)–(d), where HBR1 represents the as-received specimen, and HBR2 represents the specimen after radial hydride treatment (RHT). Note the data of as-received HBR specimens were based on the original analysis method; (i.e., no correction was applied). It has been shown that the RHT reduces the fatigue life of SNF rods, which can be seen from the tests around 15 Nm. It was further observed for HR2, as indicated by the arrow, there was an additional fatigue life reduction. Such reduction obviously resulted from the large-deformation static loading before the dynamic cyclic loading.

Several images of the failed specimens that were pretreated with thermal annealing are provided in Fig. 32. The failures of these specimens were in the gauge section, and in two of them, the failure was taking place at a pellet-to-pellet interface.

Table 17a. Dynamic test results for HBR SNF rods, FY 2016

TN	Spec	Load in.	N cycles	Fail	ma Nm	ma_std Nm	ka m^1	ka_std m^−1	km m^−1	km_std m^−1
25	HR1	150	4.19E + 04	1	15.152	0.549	0.517	0.016	0.527	0.019
26	HR2	160	9.47E + 03	1	14.702	0.806	0.478	0.121	0.511	0.205
27	HR3	100	2.44E + 05	1	8.982	0.066	0.267	0.005	0.291	0.009
28	HR4	160	5.47E + 04	1	14.759	0.089	0.394	0.008	0.421	0.009

Table 17b. Dynamic test results for HBR SNF rods, FY 2016

TN	Spec	R Nm^2	R_std Nm^2	Sa MPa	sa_std MPa	ea %	ea_std %	em %	em_std %	Lg2 mm	Lg2_std mm	dh mm	dh_std mm
25	HR1	29.329	0.775	128.788	4.666	0.278	0.009	0.284	0.010	44.733	0.565	1.329	0.197
26	HR2	31.567	3.256	124.964	6.848	0.257	0.065	0.275	0.110	50.657	1.593	-0.174	0.372
27	HR3	33.659	0.602	76.342	0.560	0.144	0.003	0.157	0.005	43.368	0.643	-1.649	0.252
28	HR4	37.497	0.593	125.449	0.755	0.212	0.004	0.227	0.005	45.977	0.578	1.206	0.201

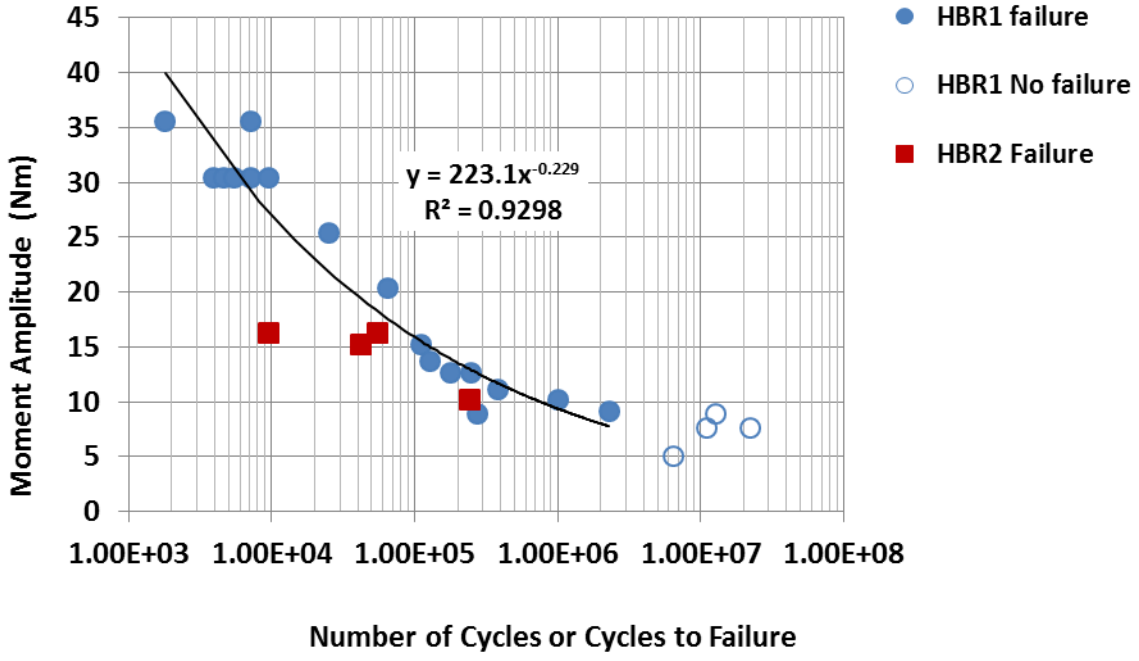
45
40
35
30
25
20
15
10
5
0
Moment Amplitude (Nm)
y = 223.1x-0.229
R² = 0.9298
1.00E+03
1.00E+04
1.00E+05
1.00E+06
1.00E+07
1.00E+08
Number of Cycles or Cycles to Failure
HBR1 failure
HBR1 No failure
HBR2 Failure

(a)

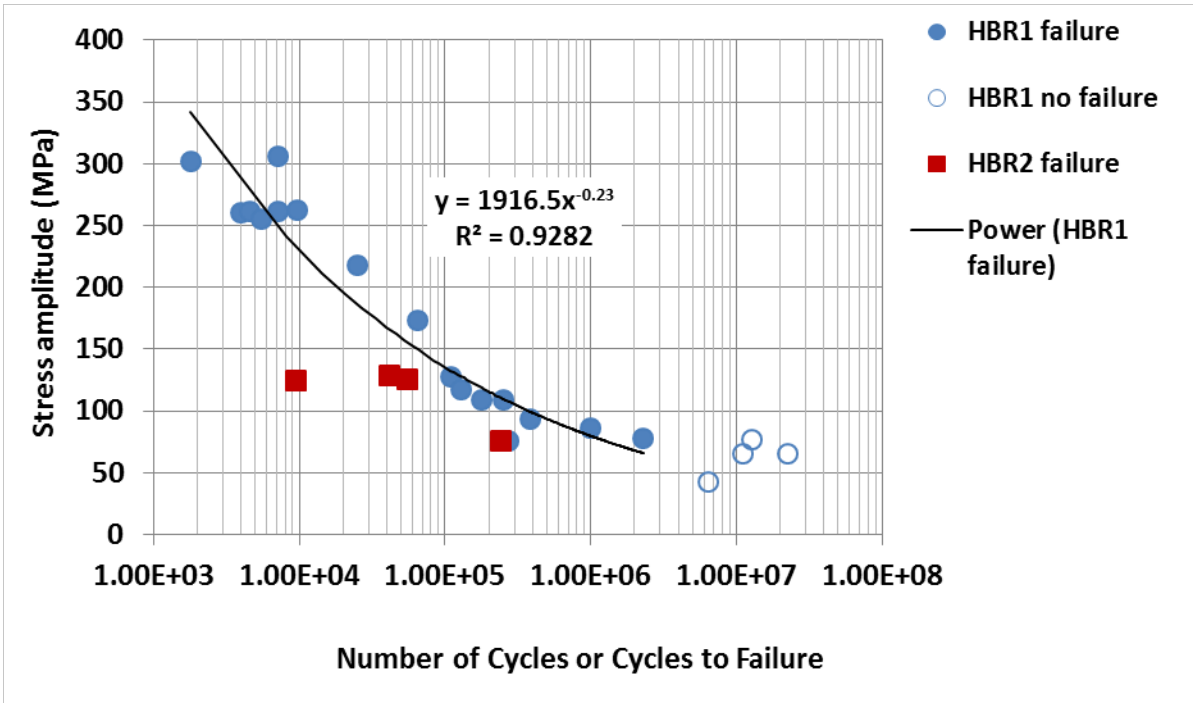
400
350
300
250
200
150
100
50
0
Stress amplitude (MPa)
y = 1916.5x-0.23
R² = 0.9282
1.00E+03
1.00E+04
1.00E+05
1.00E+06
1.00E+07
1.00E+08
Number of Cycles or Cycles to Failure
HBR1 failure
HBR1 no failure
HBR2 failure
Power (HBR1 failure)

(b)

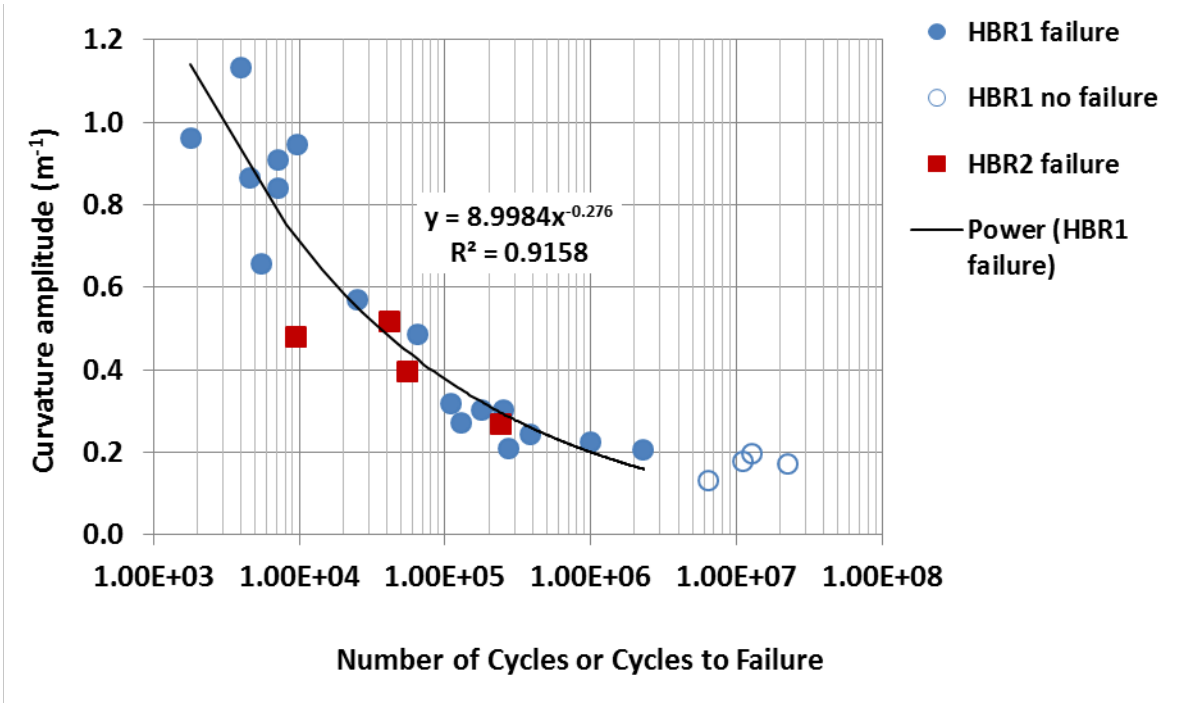

(c)

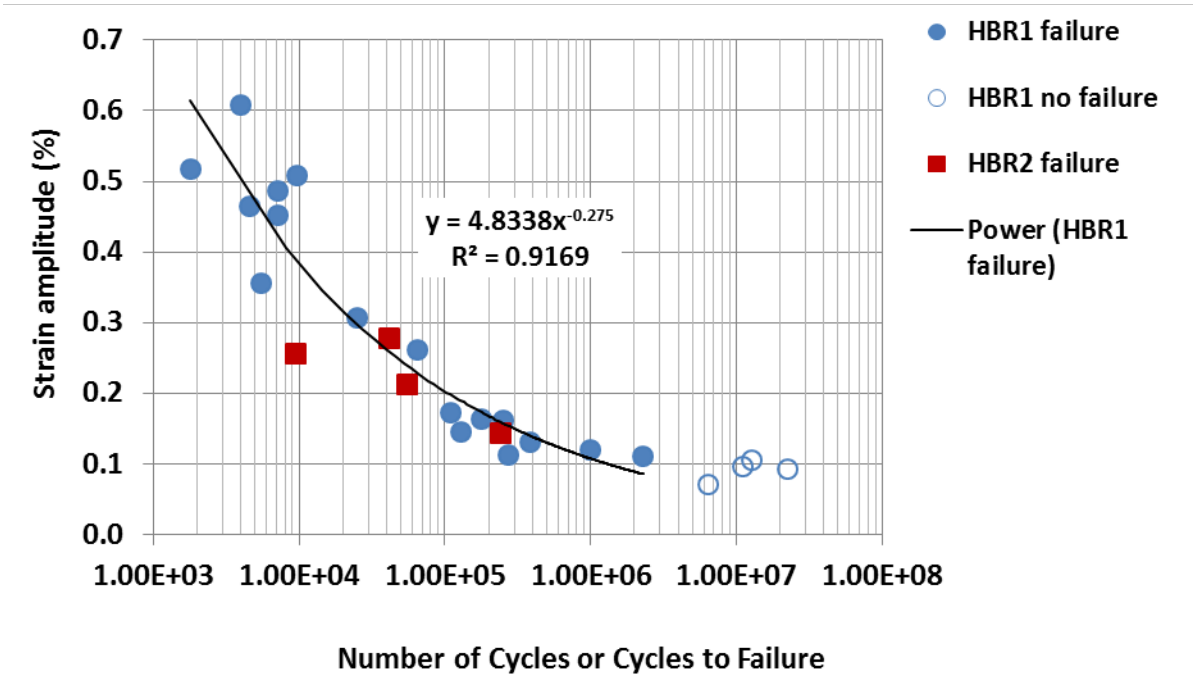

(d)

Fig. 31. (a) Moment amplitude, (b) stress amplitude, (c) curvature amplitude, and (d) strain amplitude rigidity as a function of cycles or cycles to failure.

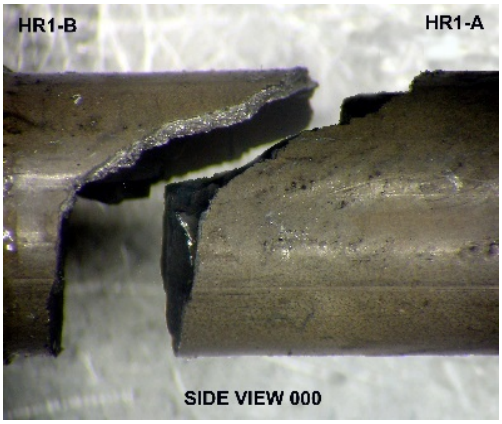
HR1-B
HR1-A
SIDE VIEW 000

(a)

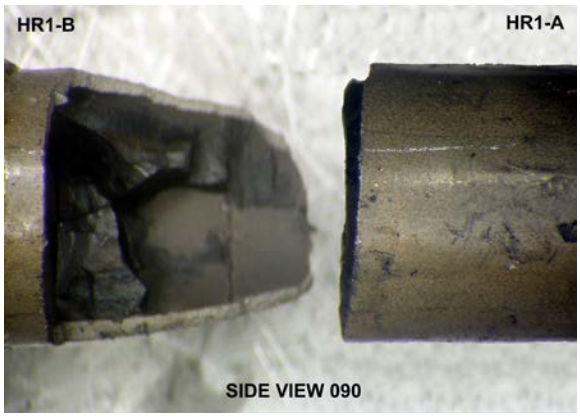
HR1-B
HR1-A
SIDE VIEW 090

(b)

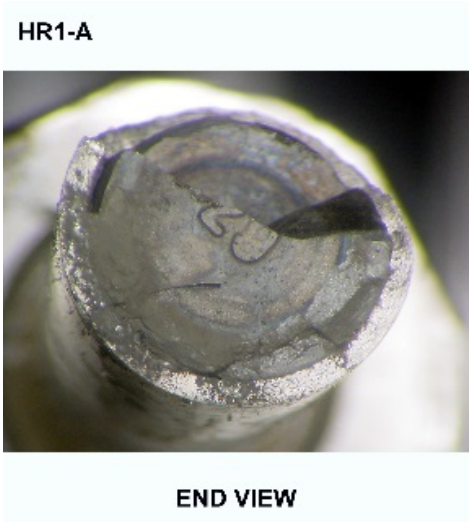
HR1-A
END VIEW

(c)

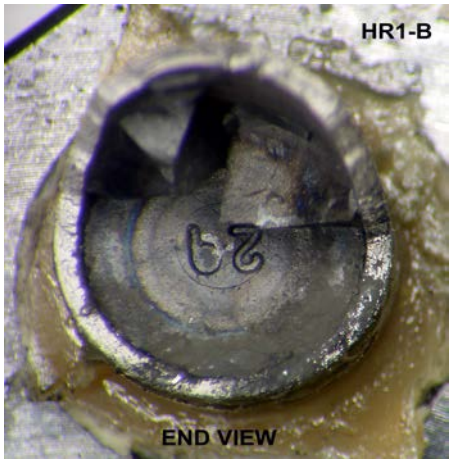
HR1-B
END VIEW

(d)

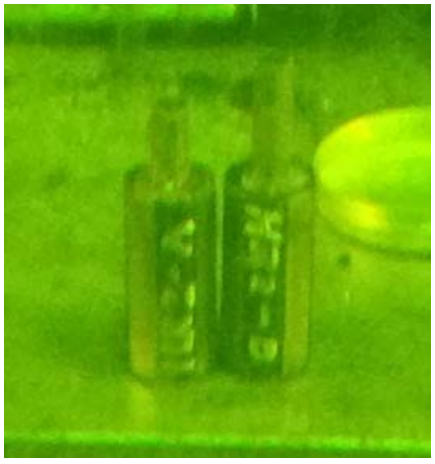

(e)

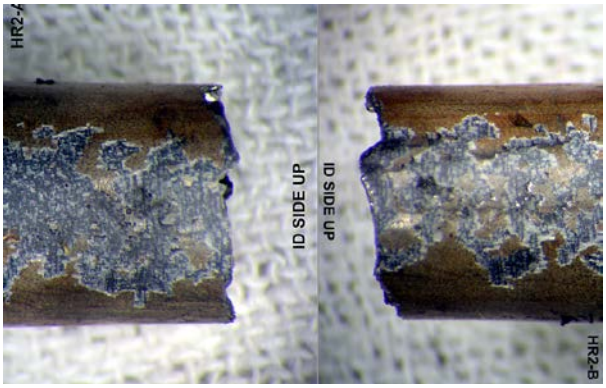
ID SIDE UP
ID SIDE UP
HR2-B

(f)

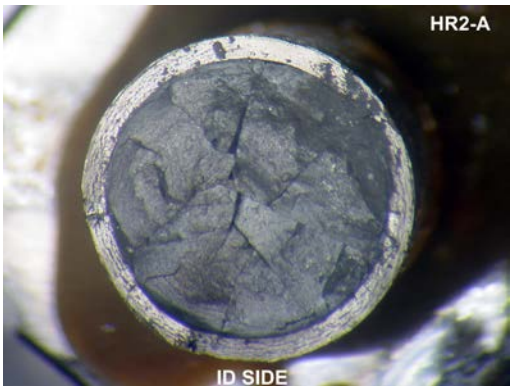
HR2-A
ID SIDE

(g)

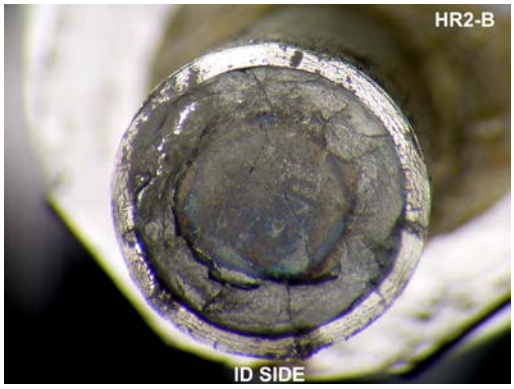
HR2-B
ID SIDE

(h)

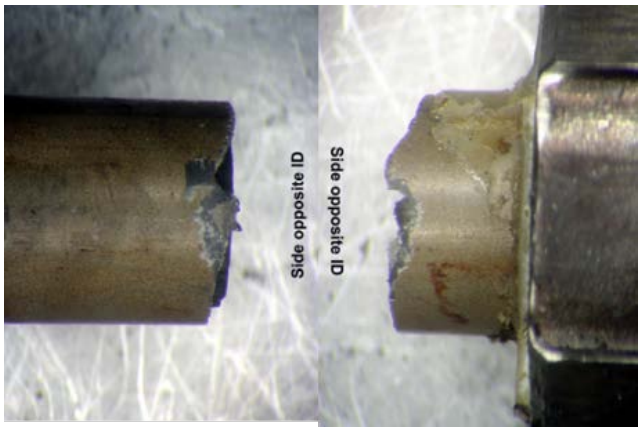
Side opposite ID
Side opposite ID

(i)

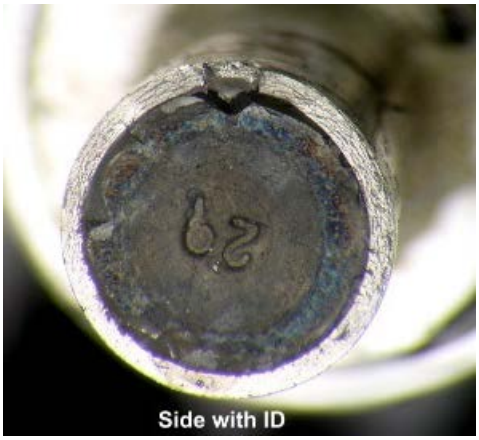
Side with ID

(j)


HR-4A
B-4YK

(k)

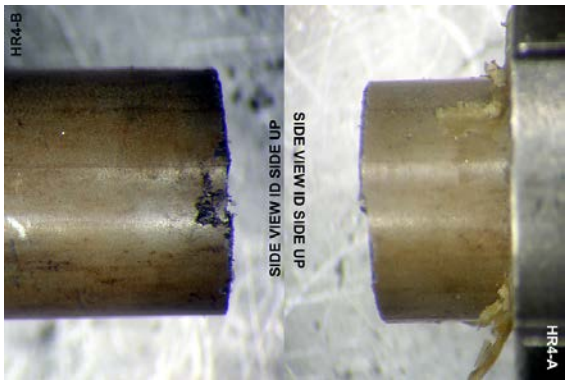
HR4-B
SIDE VIEW ID SIDE UP
SIDE VIEW ID SIDE UP
HR4-A

(l)

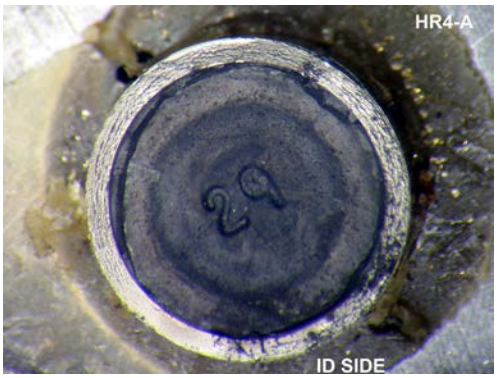

(m)

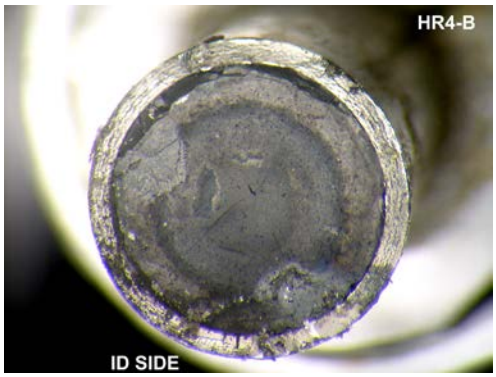

(n)

Fig. 32. Images showing the failure modes for (a) (b) (c) (d) HR1, (e) (f) (g) (h) HR2, (i) (j) HR3, and (k) (l) (m) (n) HR4.

10. DISCUSSION AND REMAINING ISSUES

10.1 SNF Fatigue Life

The variations in fatigue life are given in Fig. 33, including moment, equivalent stress, curvature, and equivalent strain for the tested SNFs. The following designations are used:

1) LMK—as-received
2) MOX1—as-received
3) MOX2—12 in. height drop treatment
4) MOX3—thermal annealing treatment
5) HBR1—as-received
6) HBR2—RHT

The equivalent stress collapsed the data points of all of the SNFs into a single zone. A detailed examination revealed that, at same stress level, fatigue lives display a descending order as follows: HBR, LMK, and MOX. Looking at the strain, LMK fuel has a slightly longer fatigue life than HBR, but the difference is subtle.

The apparent knee point of endurance limit in the curve of moment and curvature or equivalent quantities is more clearly defined for LMK and HBR fuels.

The test results appear to indicate that impacts and RHT have a negative effect on fatigue life. The effect of thermal annealing on MOX fuel rods was smaller at higher amplitudes but increased in intensity at lower amplitudes of moment. Thermal annealing tended to extend the fatigue life of MOX fuel rod specimens. However, for HR4 testing, thermal annealing had a negative effect on fatigue life compared to the HBR rod.

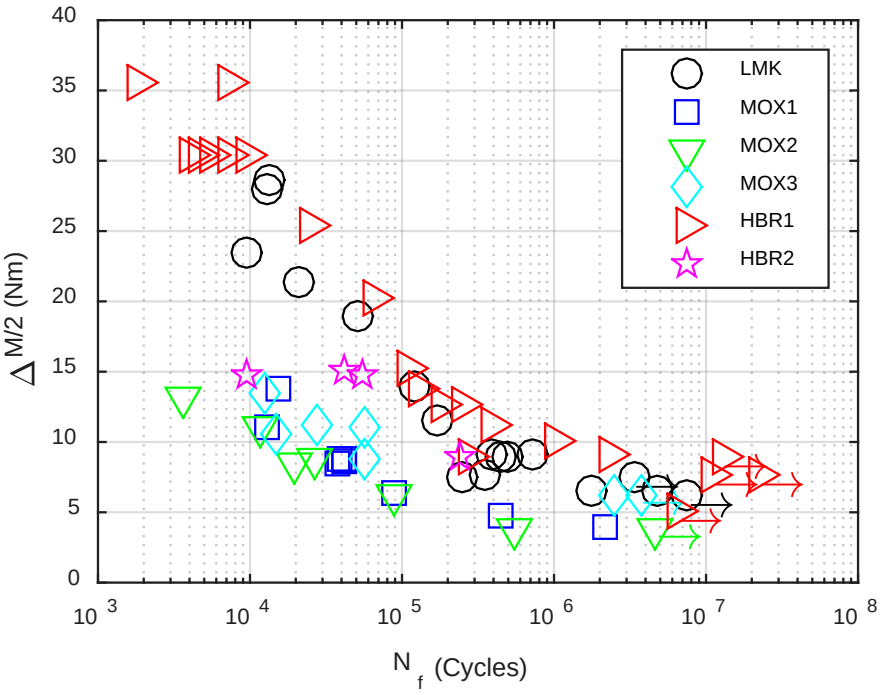
LMK
MOX1
MOX2
MOX3
HBR1
HBR2
ΔM/2 (Nm)
N f (Cycles)

(a)

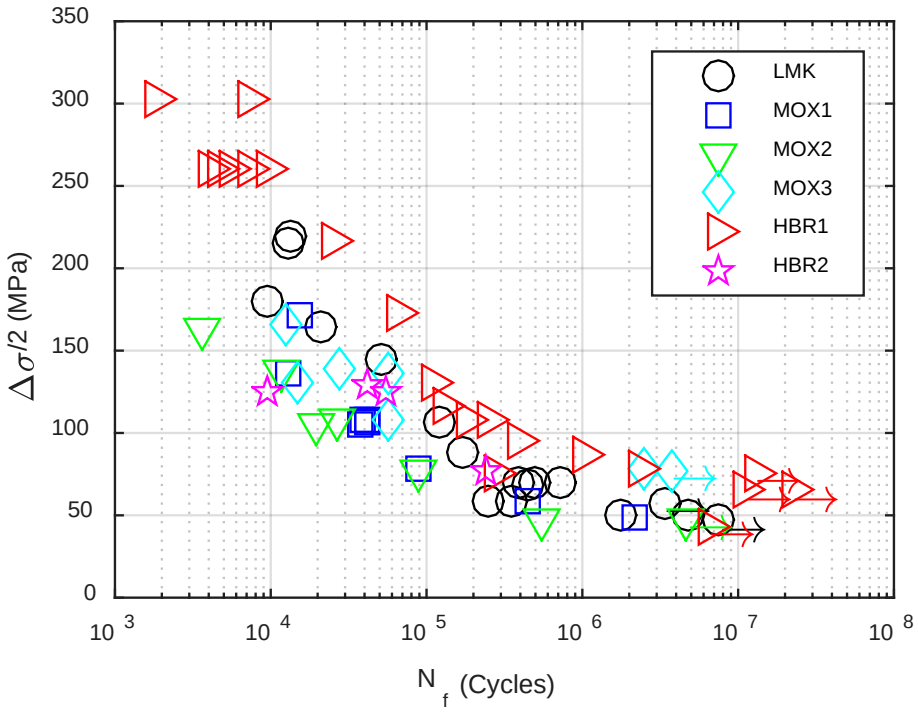
LMK
MOX1
MOX2
MOX3
HBR1
HBR2
Δσ/2 (MPa)
N f (Cycles)

(b)

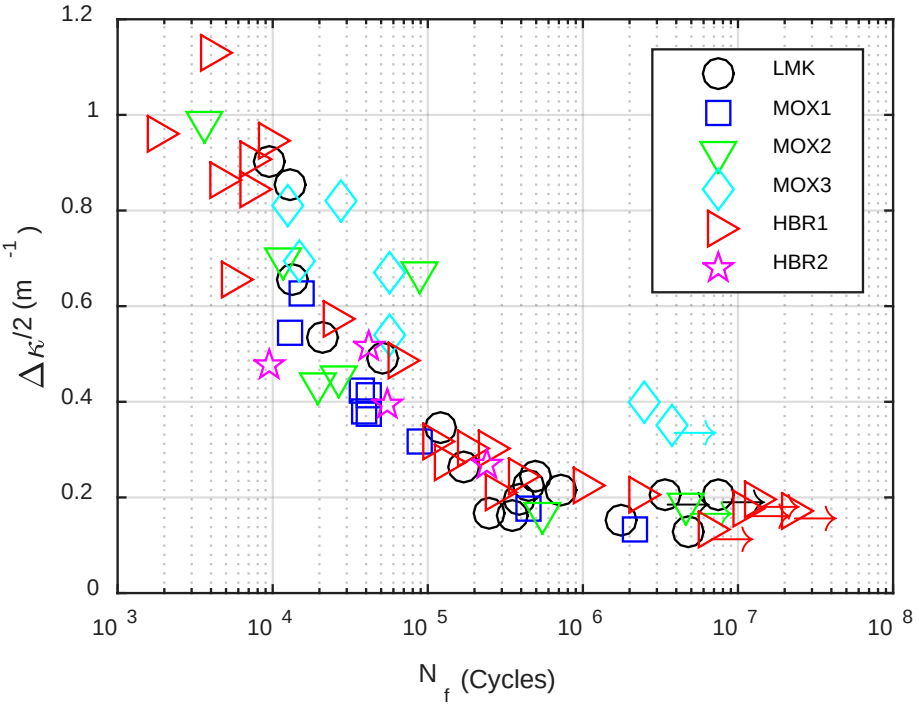
1.2
1
0.8
0.6
0.4
0.2
0
$\Delta\kappa^{1/2}$ (m $^{-1}$)
10^3
10^4
10^5
10^6
10^7
10^8
N_f (Cycles)
LMK
MOX1
MOX2
MOX3
HBR1
HBR2

(c)

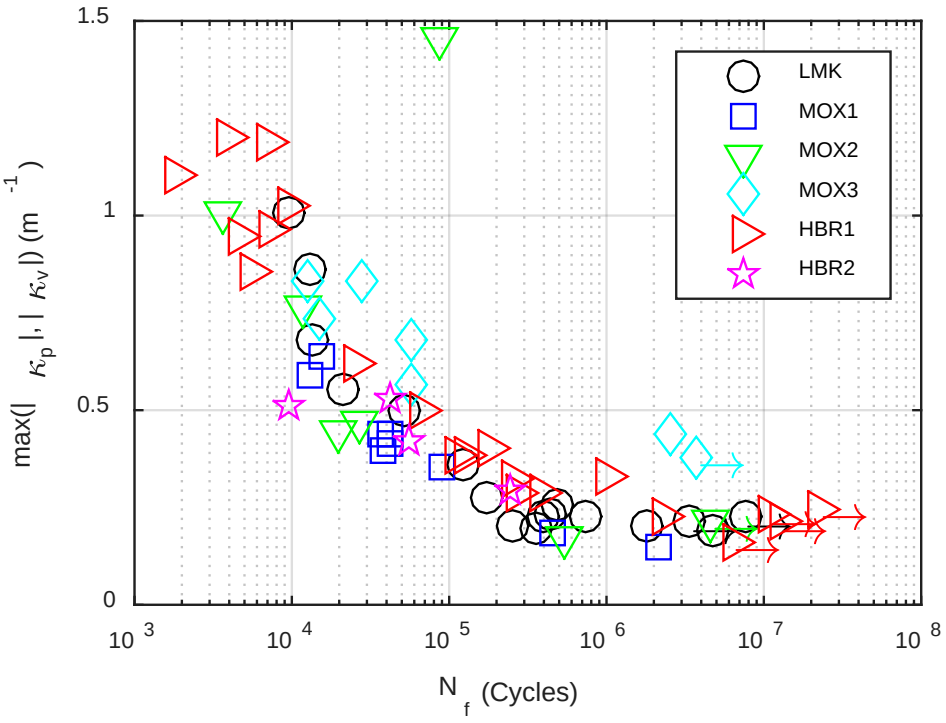
1.5
1
0.5
0
max(| κ_p |, | κ_v |) (m $^{-1}$)
10^3
10^4
10^5
10^6
10^7
10^8
N_f (Cycles)
LMK
MOX1
MOX2
MOX3
HBR1
HBR2

(d)

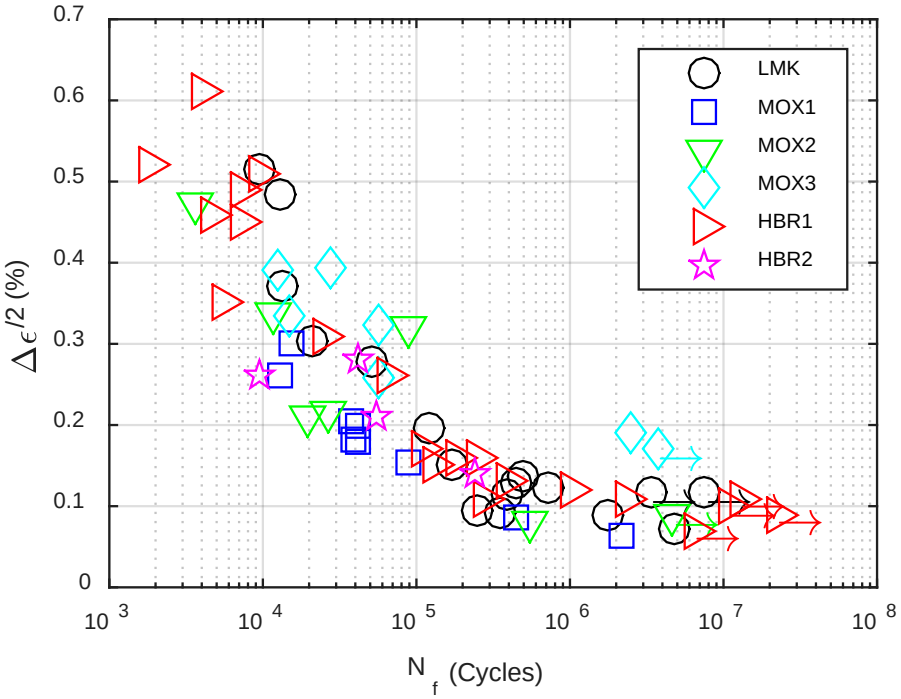

(e)

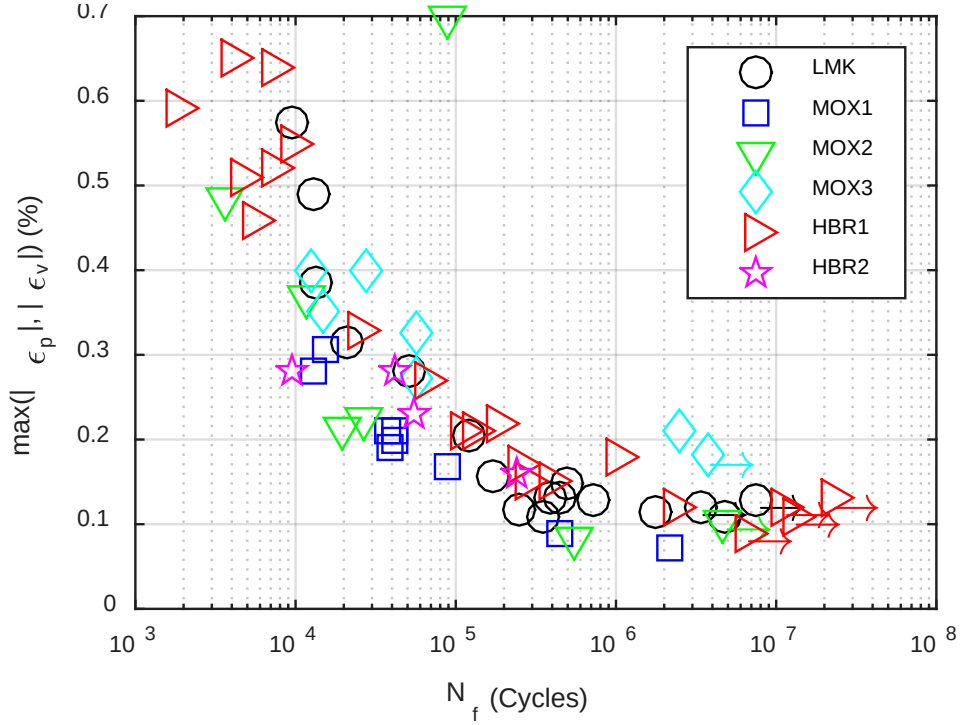

(f)

Fig. 33. (a) Moment amplitude, (b) stress amplitude, (c) curvature amplitude, (d) curvature maximum, (e) strain amplitude, and (f) strain maximum as a function of cycles or cycles to failure

11. DYNAMIC DEFORMATION SIMULATION OF SNF SYSTEM

The PWR fuel assembly skeleton (Fig. 34), is formed by guide tubes and spacer grids, which are designed to constrain fuel rods during reactor operation. In a vertical setup, the skeleton was subjected to vibration loads induced by fluid dynamics, and during reactor operation, the rods' dead weight was transmitted though the spacer grids to the guide tubes. When the SNF assembly was in a horizontal position under NCT, the skeleton became the primary load-bearing system that carried and transferred the vibration loads within the SNF assembly, including the interaction of forces between the assembly and the canister basket walls. Therefore, the integrity of guide tubes and spacer grids critically affects the vibration intensity of the fuel assembly during transport and, consequently, affects the multipurpose canister (MPC) design development to ensure safe SNF transport.

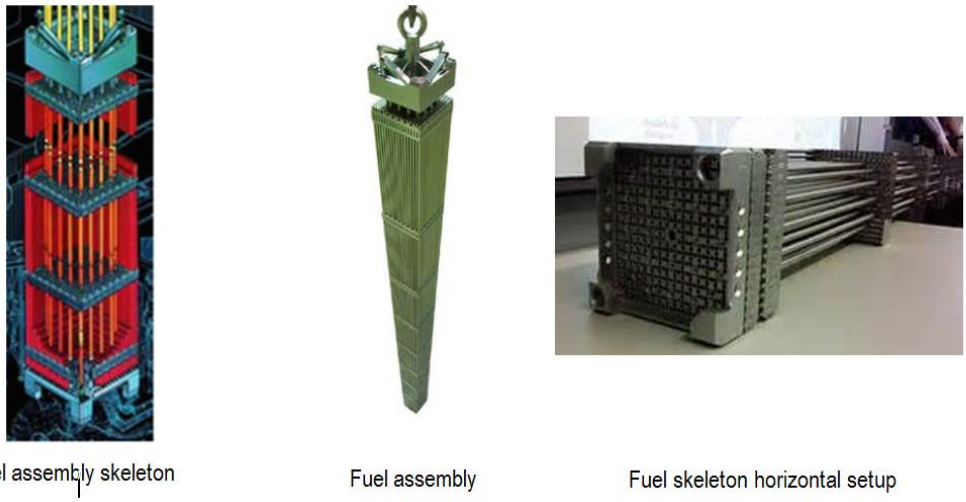

Fig. 34. SNF assembly schematic.

Random vibration registered in the SNF transport cask, which can be excited from railcar beds, provides the external loading driver to vibrate the SNF assembly. In addition to this external vibration driver, the fuel assembly also registers internal transient shocks from the dynamic interactions among the fuel assembly components inside the cask. These components include the skeleton, fuel rods, and canister basket walls. Their dynamic interactions can significantly increase the high-rate impact loading intensity within fuel assembly components during NCT.

An aging or fatigued skeleton system can increase contact impact loading intensity between fuel rods, and it can enhance the probability of SNF resonance vibration deformation. The contact interactions between fuel rods, spacer grids, and the basket wall can also increase fuel rod transient shock load frequencies. Consequently, external cask vibration needs to be mitigated, along with internal amplification from fuel assembly system vibration and related transient shocks. System damping may need to be increased to reduce vibration intensity, and such mitigations will eventually influence canister system design.

This research also investigated SNF assembly deformation dynamics during normal vibration modes and the cask's internal transient shock mode during NCT. FEA was used to develop vibration simulation modeling for a targeted SNF subassembly. Dynamics analyses were performed in the frequency domain to study frequency characteristics of the fuel assembly system and in the time domain to simulate the transient dynamic response of the fuel assembly. FEA simulation results were used to determine the stress and strain states of submodel components, such as fuel rods, the guide tube, spacer grids, nozzles, and the basket wall, under vibration loading during normal vibration conditions and transient shocks from NCT. The resulting stress/strain data can be used in future fuel assembly component failure analyses. The

contact interactions among system components during transient dynamic simulation have also been investigated.

To further evaluate the intensity of contact interaction induced by the local contacts' impact loading at the spacer grid, detailed models of the spring and dimples of the spacer grids were created. The impacts between fuel rod and springs and dimples were simulated with a 20 g transient shock load. The associated contact interaction intensities in terms of reaction forces were estimated from the FEA results. The corresponding bending moment generated the same resultant stress on the cladding registered a 20 g acceleration transient shock and was determined to define the same intensity as the pure bending loading from CIRFT vibration evaluations. To estimate the damage potential of transient shocks to the SNF vibration lifetime, drop tests were performed on the CIRFT specimens. The combined drop-impact and CIRFT results show reduced fatigue strength for SNF CIRFT specimens. FEA was used to investigate the contact reaction in CIRFT samples during impact loading induced by drop tests, and the result was compared with those from a 20 g acceleration transient shock load.

The CIRFT system dynamic simulation was also used to predict the system's dynamic performance and to verify the system's efficiency under different vibration frequencies. The CIRFT deformation sensor's dynamic stability was studied in detail. Adjustment factors for correcting CIRFT deformation probe geometry stability were developed for static and dynamic testing based on SNF CIRFT results.

12. SNF ASSEMBLY DYNAMIC SIMULATION

The FEA modeling effort focused on the SNF assembly during transportation in a horizontal setup. Fig. 35 shows a fuel assembly consisting of fuel rods, the bottom nozzle, the top nozzle, guide tubes, and spacer grids.

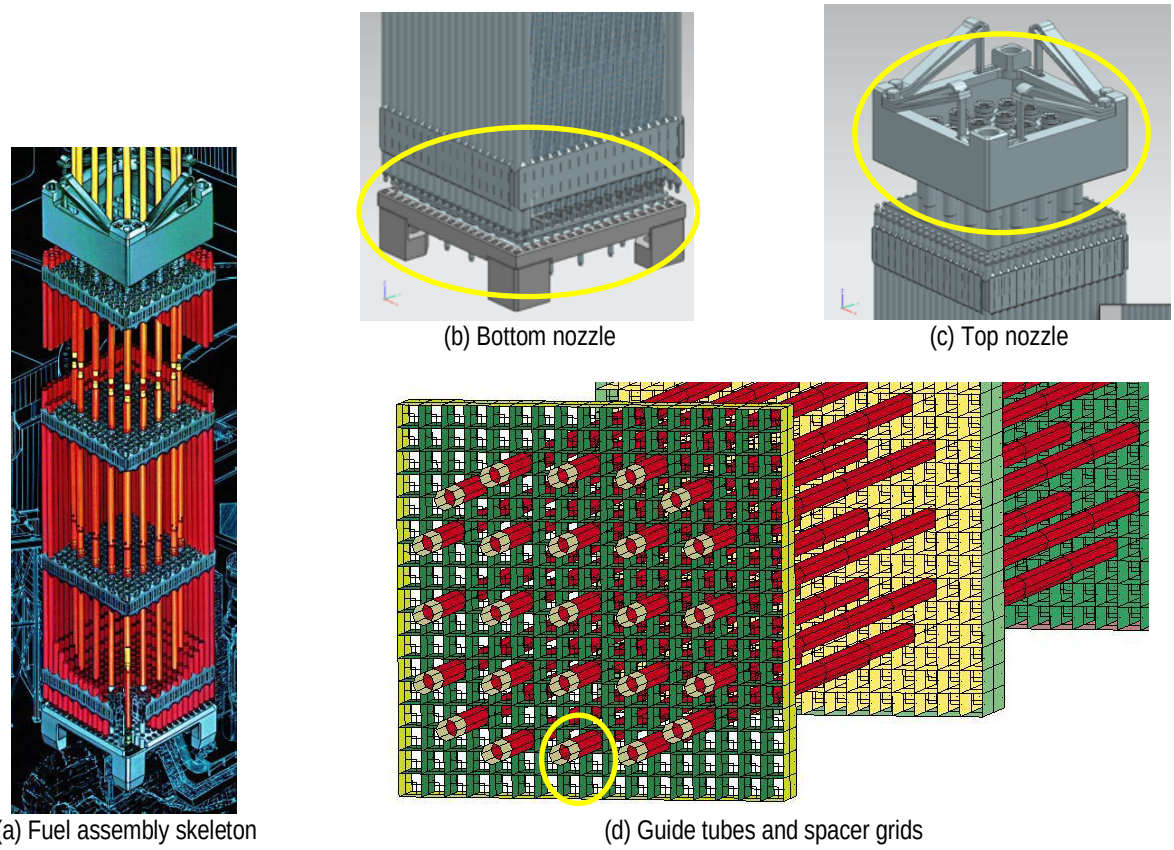

(a) Fuel assembly skeleton

(b) Bottom nozzle

(c) Top nozzle

(d) Guide tubes and spacer grids

Fig. 35. 17 × 17 PWR fuel assembly.

The targeted SNF assembly model was a 3-D ABAQUS-explicit transient FEM of a simplified single fuel assembly. The fuel rod in the simplified geometry was 144 in. long. To simulate the contacts of fuel pellets, two hundred and forty 0.6 in. fuel pellets were used in the model. Fig. 36 shows the modeled 240 fuel pellets in a 144 in. long fuel rod, where pellets contacted each other at the ends. In one fuel rod, there were 239 contact pairs among the fuel pellets. To have a meaningful, practical investigation of the SNF rod's dynamic response and the SNF system components' interactions during NCT, the SNF assembly was simplified as a horizontal submodel (Fig. 37). The skeleton of the SNF assembly consisted of guide tubes and spacers, which are the primary structural components that carry the vibration loading originally excited from railcar bed. The following key assumptions and primary simplifications were made in the targeted submodel development:

- Two fuel rods with a guide tube, as highlighted in Fig. 35(d), at the bottom edge of the full fuel assembly were modeled. The guide tube is on top of two fuel rods(Fig. 37). Each fuel rod contained 240 fuel pellets and a 144 in. long cladding.
- The guide tube and two fuel rods were connected with eight spacers, including top and bottom Inconel spacers, as well as six intermediate Zircoloy-4 spacers (Fig. 37 and Fig. 38).
- The spacer grids were modeled as simplified box structures, and the spacer grid leaf springs/dimples were modeled as translational springs.

- The fuel rods were connected to spacer grids through the springs/dimples (Fig. 39).
- The guide tube was firmly connected to the spacer grids with tie constraints in ABAQUS.
- To eliminate unnecessary geometric details, the top and bottom nozzles were simplified as two plates.
- A long rectangular plate was modeled to represent the basket floor and was assumed to be part of the basket enclosure that interacts with the fuel rod assembly from below (Fig. 37).
- The guide tube was connected to the nozzles by ties, and the nozzles were tied to the basket to properly transfer the dynamic loading (Fig. 40).

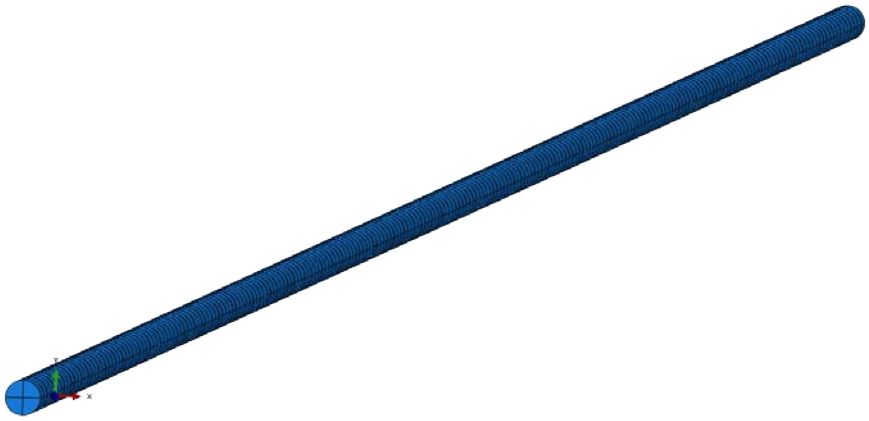

Fig. 36. The modeled 240 fuel pellets in one fuel rod.

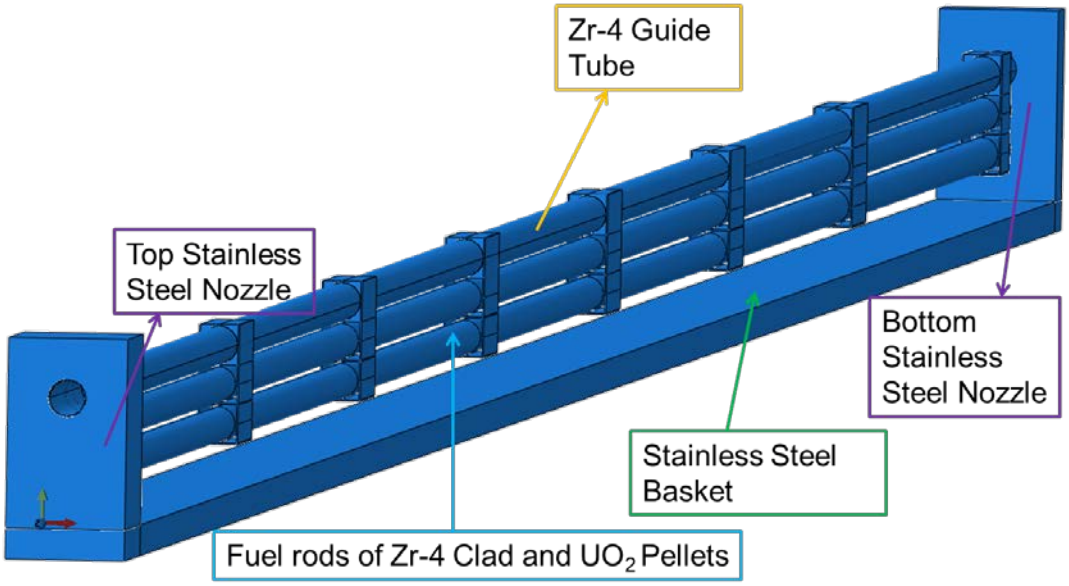

Fig. 37. SNF assembly submodel for normal transportation evaluation.

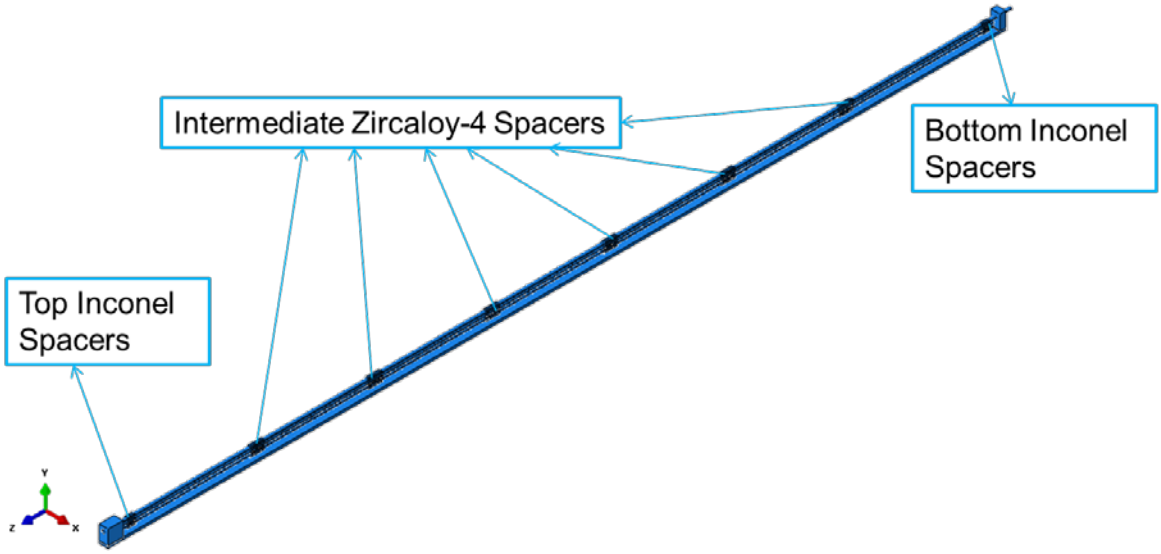

Fig. 38. SNF assembly submodel with spacers.

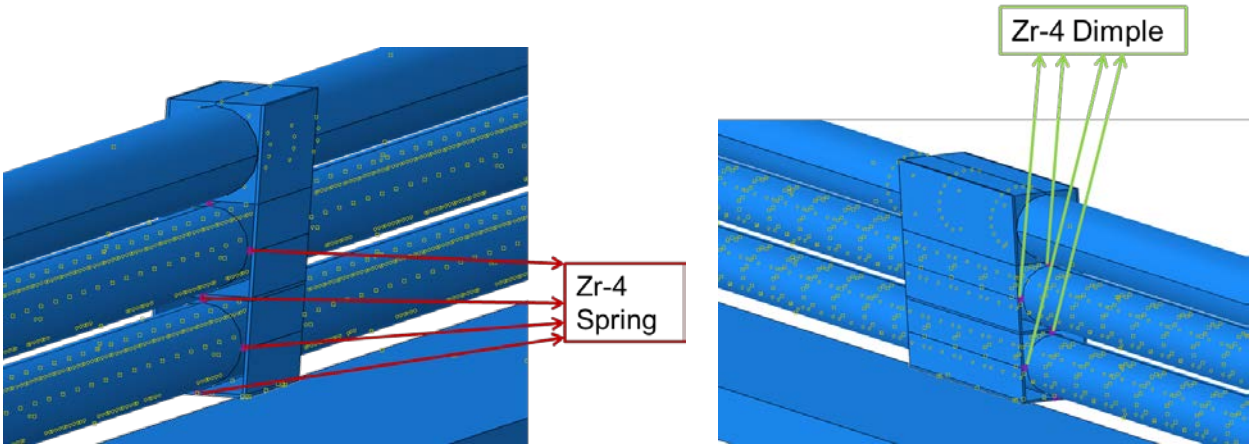

Fig. 39. Spacer grid leaf spring/dimples modeled as translational springs.

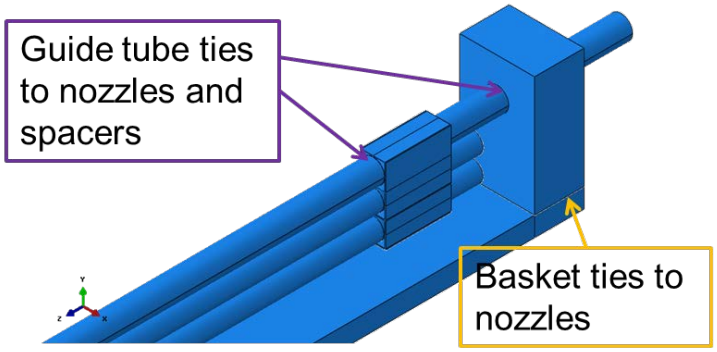

Fig. 40. Tie constraint to transfer dynamic loading.

The geometry of the fuel assembly submodel was derived from dimensions provided in DOE's *Used Nuclear Fuel Loading and Structural Performance Under Normal Conditions of Transport—Demonstration of Approach and Results of Used Fuel Performance Characterization* [17] and

summarized in Table 18. This fuel assembly submodel retains the proper mass and inertial properties for dynamic simulation.

Table 18. Dimensions for fuel rods and fuel assembly

Dimension	**Value (in.)**
Fuel pellet length	0.6
Fuel pellet diameter	0.382
Fuel cladding length	144
Fuel cladding outer diameter (OD)	0.36
Guide tube OD	0.474
Guide tube inner diameter	0.45
Guide tube length	150
Intermediate spacer axial length	2.25
Intermediate spacer shell thickness	0.018
Intermediate spacer width	0.51
Top and bottom spacer axial length	1.322
Top and bottom spacer shell thickness	0.018
Top and bottom spacer width	0.51
Bottom nozzle plate thickness	1
Bottom nozzle width	1.51
Bottom nozzle height	2.4077
Top nozzle plate thickness	2.5
Top nozzle width	1.51
Top nozzle height	2.4077
Basket floor plate thickness	0.3937
Basket floor plate length	148.5
Basket floor plate width	1.51
Distance form base of bottom nozzle to:	**Value (in.)**
Top of 1st spacer grid	3.5
Top of 2nd spacer grid	27.08
Top of 3rd spacer grid	45.66
Top of 4th spacer grid	66.02
Top of 5th spacer grid	85.49
Top of 6th spacer grid	104.96
Top of 7th spacer grid	124.43
Top of 8th spacer grid	144.82

Fig. 41 shows the mesh of the SNF fuel assembly submodel. All components were modeled with 8-node linear hexahedral brick elements. The mesh was coarsened to optimize the solution time without losing accuracy. The fuel rods were supported by two sets of translational springs in every slot: one set of leaf springs and one set of dimples. ABAQUS explicitly requires the incremental time between calculation steps to be smaller than the shortest duration of stress wave propagation through an element. This was accomplished with the Courant-Friedrichs-Levy stability criterion. Special care was taken to stabilize the dynamic calculation, including mesh distortion control, severe distorted element deletion, reduced integration, and hourglass control. However, a long solution time for dynamic simulation was still anticipated because a very small increment (on the order of 1.0E-8 s) was required to converge the solution. Furthermore, the model consisted of roughly 130,000 nodes and 80,000 elements, which also resulted in a long solution time.

Contact was implemented throughout the fuel assembly between interacting components. The most time consuming and tedious work was defining the 239 surface-to-surface contact pairs between the 240 fuel pellets. Surface-to-surface contacts between the guide tube and fuel rod, between spacer grids and the basket floor, and between fuel rod and basket floor were defined when they touch each other. As mentioned, the guide tube was rigidly attached to spacer grids and nozzles with tie constraints, and the

fuel rods were supported by translational springs on the spacer grids. The friction coefficient was reasonably assumed to be 0.3 at contact surfaces.

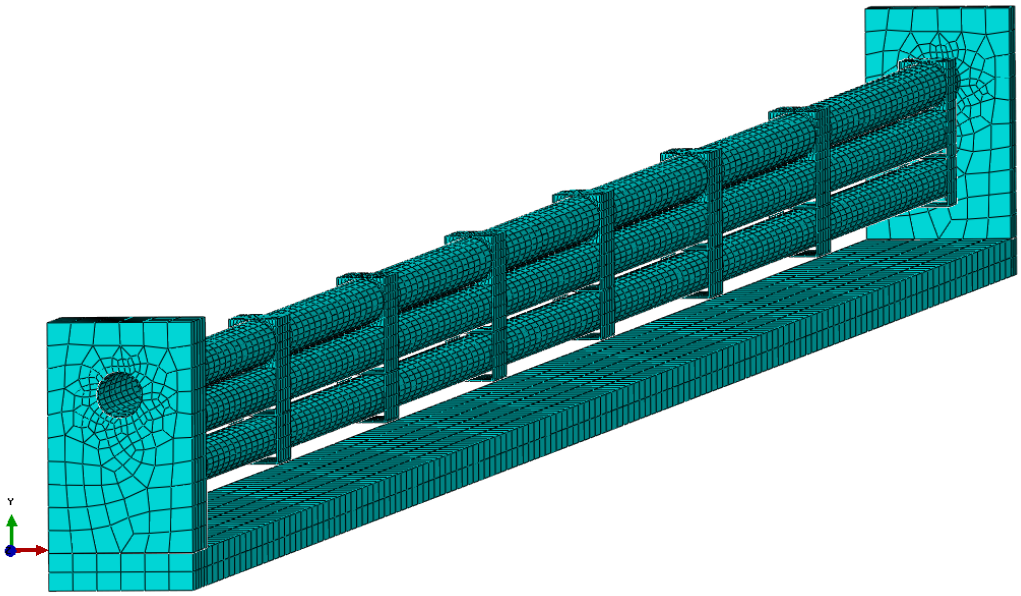

Fig. 41. Mesh of the fuel assembly submodel.

As shown in Fig. 37 and Fig. 38, fuel pellets were made of UO_2; however, the fuel cladding, the intermediate spacer grids, and the guide tube were made of Zircaloy-4. The top and bottom spacer grids were made of Inconel, and the top and bottom nozzles and basket were made of stainless steel. The material properties of the fuel assembly's components are outlined in Table 19. The leaf spring and dimple spring material was Zircaloy-4. The spring stiffness value for Zircaloy-4 leaf spring is 280 lbf/in., and the value for Zircaloy-4 dimple was 719.5 lbf/in. [17].

Table 19. Mechanical properties of the fuel assembly

	Material	Young's modulus (psi)	Poisson's ratio	Yield strength (psi)	Density (lb/in^3)
Pellet	UO_2 [3]	2.92e7	0.32	3.11e5	0.396
Clad, intermediate spacer grids, guide tube	Zircaloy-4 [3]	1.32e7	0.33	1.31e5	0.237
Top and bottom spacer grids	Inconel [18]	3.06e7	0.284	1.432e5	0.296
Basket, nozzles	Stainless steel [3]	2.8e7	0.3	4.206e4	0.2901

12.1 Modal Analysis

Dynamics analysis of a vibrating system is often performed in the frequency domain because the dynamic response of structures depends on the frequency characteristics of the system, specifically natural frequencies and mode shapes. When the excitation frequency loaded on the structure is near its natural frequency, resonance occurs, which significantly amplifies the system's dynamic response to the extent

that causes structure failure. Modal analysis was used to determine the natural frequencies of the SNF assembly submodel and the dominant modes. The results provided a better understanding of the frequency characteristics of fuel assembly systems.

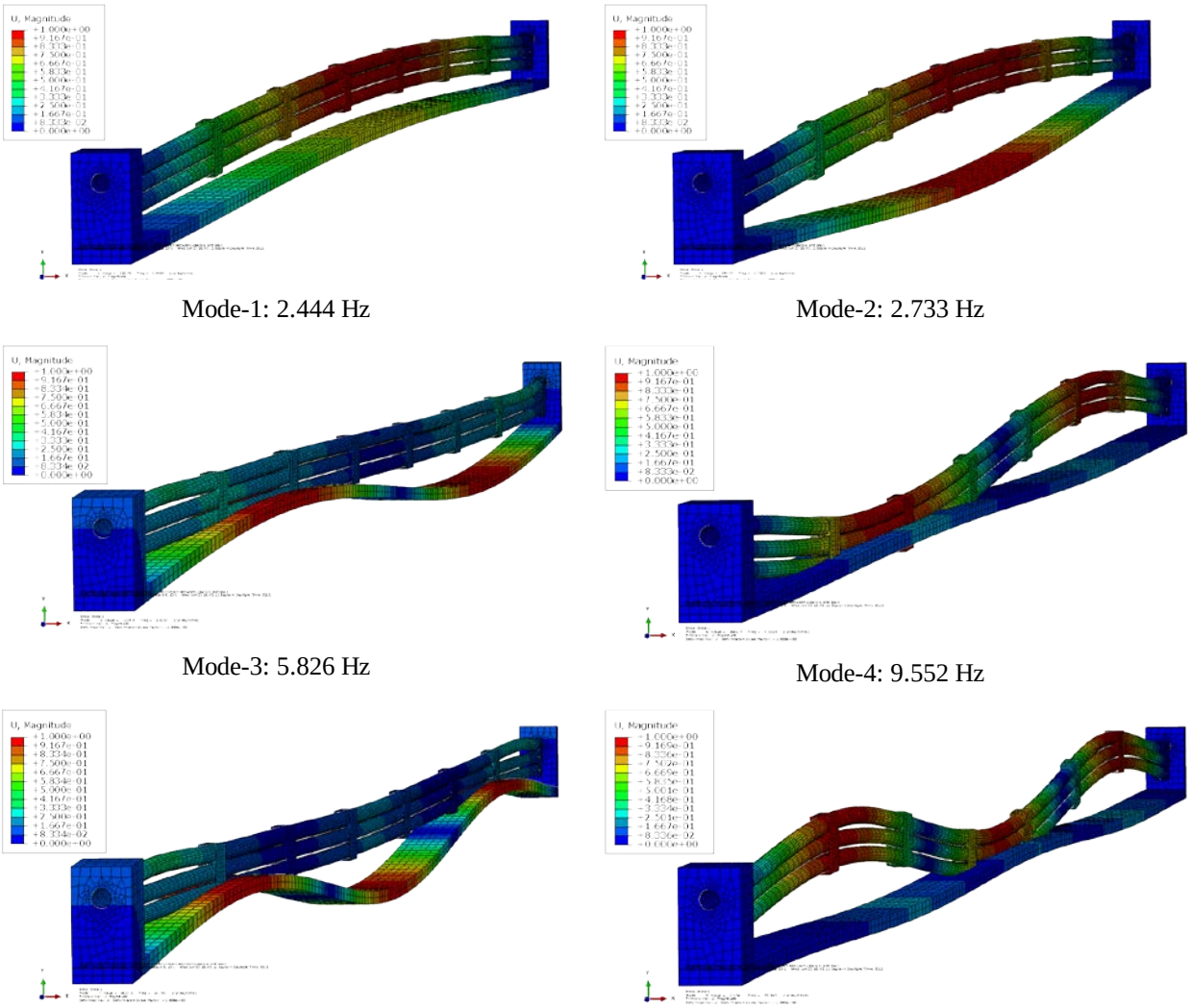

Mode-1: 2.444 Hz

Mode-2: 2.733 Hz

Mode-3: 5.826 Hz

Mode-4: 9.552 Hz

Mode-5: 14.792 Hz

Mode-6: 20.845 Hz

Fig. 42a. The first six modes, and the associated natural frequencies of the fuel assembly submodel.

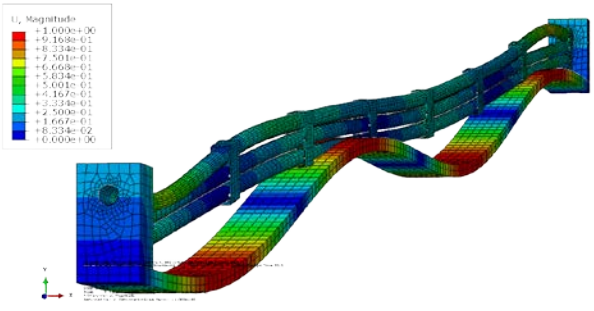

Mode-7: 22.665 Hz

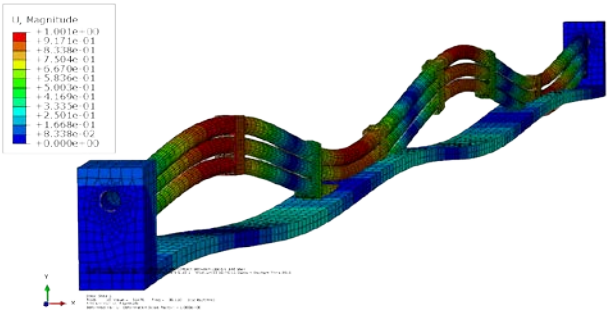

Mode-8: 36.11 Hz

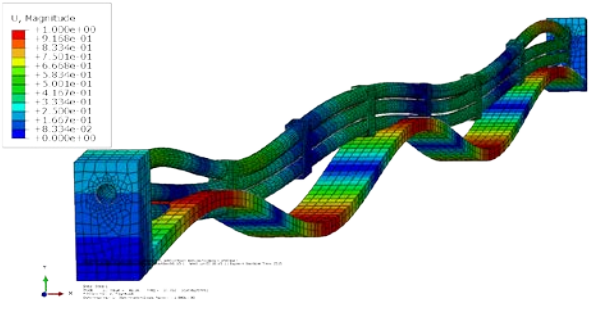

Mode-9: 37.702 Hz

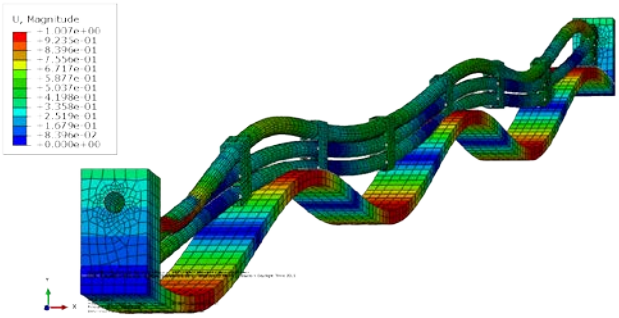

Mode-10: 50.287 Hz

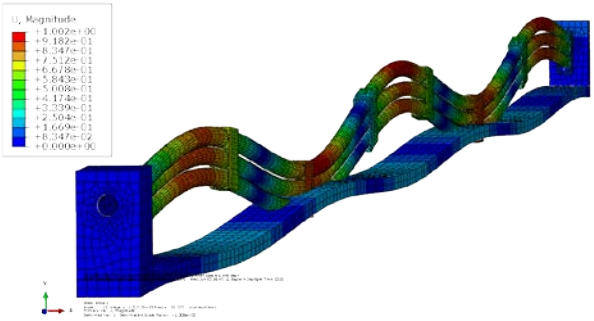

Mode-11: 55.525 Hz

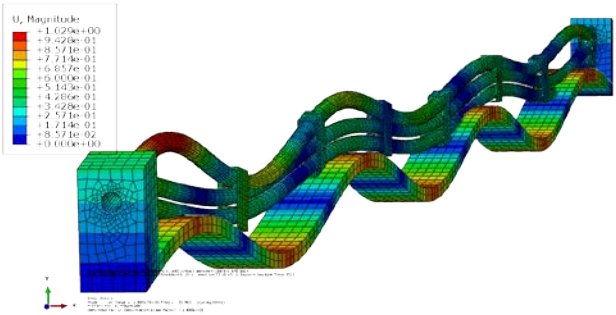

Mode-12: 70.983 Hz

Fig. 42b. The second six modes, and the associated natural frequencies of the fuel assembly submodel.

A modal analysis of the SNF assembly submodel was conducted using ABAQUS linear perturbation-frequency code, in which the system was modeled with a simply supported structure. The first 12 mode shapes and associated natural frequencies are shown in Fig. 42. The fundamental mode of this submodel has a natural frequency of 2 Hz, which is considerably lower than cradle/cask system models with fuel assembly weights [19]. In the first 12 modes shown in Fig. 42, the guide tube and fuel rods were mostly synchronized (i.e., within the same phase), but the basket floor vibrates during a difference phase. When higher vibration modes occur, as shown in Fig. 43, system components such as the guide tube and fuel rods were no longer in the same phase. Local vibration motions were involved with different components, and in some modes (e.g., modes 16–18), the fuel rod vibrations dominate.

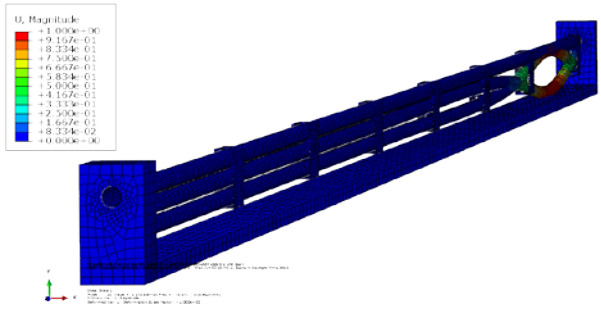

Mode-13: 75.871 Hz

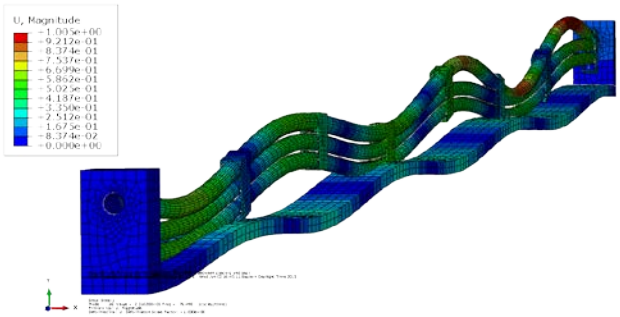

Mode-14: 76.498 Hz

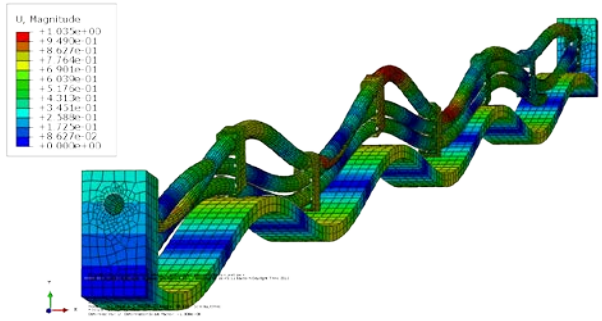

Mode-15: 90.103 Hz

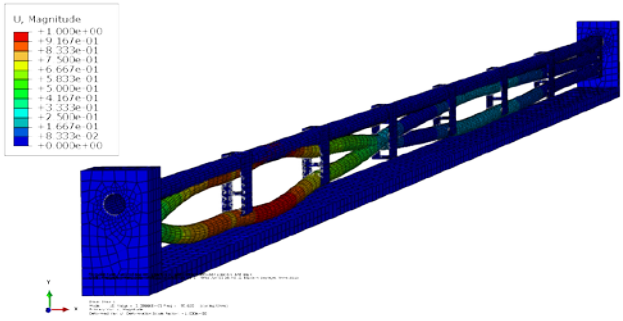

Mode-16: 92.62 Hz

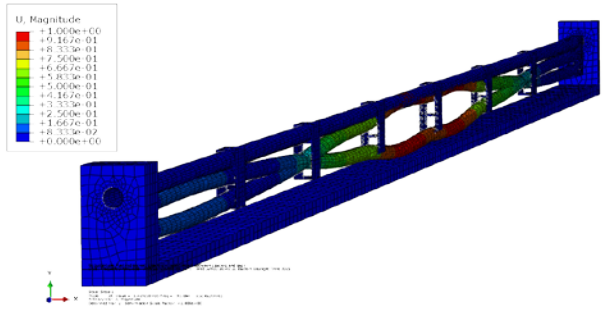

Mode-17: 93.064 Hz

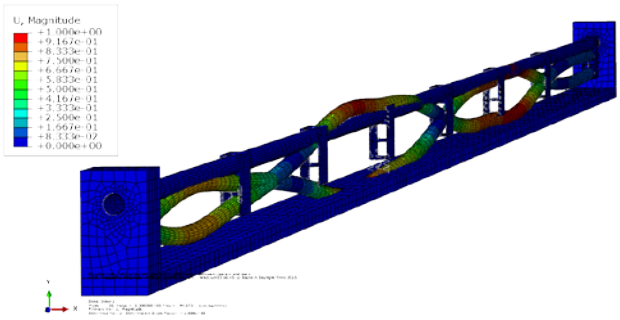

Mode-18: 94.273 Hz

Fig. 43. Higher modes and associated natural frequencies of the fuel assembly submodel.

Modal analysis results of the SNF fuel assembly submodel are summarized in Table 20. The natural frequencies for the mode are listed up to mode 51, and the associated participation factor and effective mass were evaluated accordingly. The relative strength of each mode was ranked by participation factors, which were normalized and listed as ratio values. The participation factor with the strongest mode was assigned a value of 1.0, and the other participation factors were normalized to that value. The participation of effective mass in the deformation of the mode shape is another way to indicate the strength of modes. Larger mass indicates a stronger mode. The participation factor and effective mass correspond to each other. Table 20 shows the strongest mode is the first mode's frequency of 2.444 Hz. The modes containing odd numbers of half sine wave had higher participation factor ratios (Fig. 42). For example, mode 5's frequency of 14.792 Hz and mode 6's frequency of 20.845 Hz have three half sine wave shapes in the basket floor, the guide tube, and the fuel rods, respectively, where the participation factor ratio is in the second and third place. A modal analysis was performed for a realistic cradle/cask system model and a concrete block model of equivalent mass. The results showed the strongest mode for the cradle/cask system is a frequency of 52.4 Hz. In the case of the concrete block model, the strongest

mode was 318.1 Hz, which was as high as the frequency of mode 49 for the fuel assembly submodel. The modal analysis indicated that system models with different structure level setups and different associated boundary conditions reveal significantly different natural frequency characteristics.

Table 20. Modal analysis of SNF assembly submodel

Mode number	Frequency	Participation factor ratio	Effective mass (lbf s^2/in)
1	2.444	1.000	8.195E-02
2	2.734	0.162	2.870E-03
3	5.826	0.004	1.246E-06
4	9.552	0.004	6.399E-07
5	14.792	0.381	1.079E-02
6	20.845	0.236	2.525E-03
7	22.665	0.011	1.037E-05
8	36.11	0.076	2.857E-04
9	37.702	0.221	3.965E-03
10	50.287	0.026	5.776E-05
11	55.525	0.182	1.419E-03
12	70.983	0.163	1.865E-03
13	75.871	0.001	6.431E-09
14	76.498	0.063	8.095E-05
15	90.103	0.026	4.378E-05
16	92.62	0.000	4.972E-10
17	93.064	0.000	4.257E-11
18	94.273	0.000	4.901E-10
…			
49	318.29	0.001	6.104E-09
51	345.44	0.014	6.133E-07

12.2 Transient Dynamic Analysis

The objective of the transient dynamic analysis of the fuel assembly submodel was to determine the stress and strain states of submodel components in response to vibration loading from transient shocks under NCT. Components included the fuel rods, guide tube, spacer grids, nozzles, and the basket wall. The resulting stress/strain can be used in further component failure analyses. The contact interactions between fuel assembly system components during transient dynamic simulation were studied. The fuel assembly submodel contained numerous contact conditions and represented itself as a highly nonlinear system. The performed transient dynamic analysis used ABAQUS-explicit code in the time domain for nonlinear system evaluation.

Fig. 35(d) shows that there are 25 guide tubes in a 17 × 17 fuel assembly. Thus, there were 264 fuel rods in the spacer grid slots. It was assumed that the guide tube modeled at the edge of the full SNF assembly roughly carried the gravity load for the neighboring 10 fuel rods. A gravitational acceleration loading of 386 in/s^2 was applied to all components. The gravitation loads from the remaining eight fuel rods were applied as the concentrated loads evenly distributed to eight spacer grids(Fig. 44). The dynamic simulation protocol consisted of two stages. During the first stage, the basket wall was constrained, while the assembly (mainly the intermediate spacer grids) sagged because of the gravity load and came to rest on the basket floor. During the second stage, the acceleration with a sine waveform or impulse signal was

used to represent the normal vibration excitation or transient shock excitation that was applied to the basket and nozzles for transient dynamic analysis. In the second transient excitation stage, the constraint at the basket floor was removed, but the gravity loads were maintained for both stages of simulations. Therefore, the procedure for the subassembly model included an initialization stage to establish contacts caused by gravity followed by a transient dynamic loading stage [17].

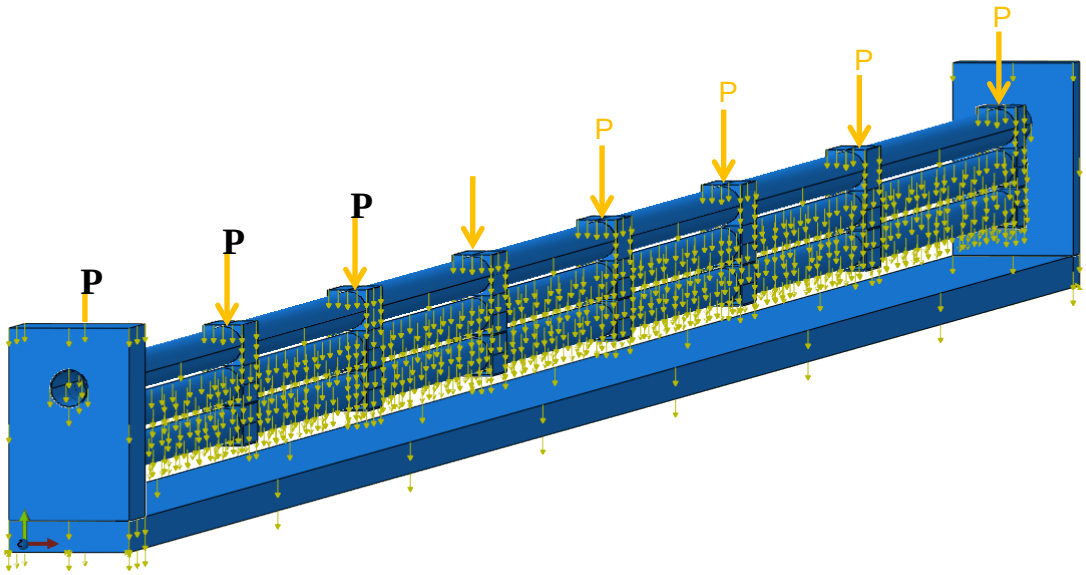

Fig. 44. Gravity loads for the initial stage of transient dynamic simulation of the fuel assembly submodel.

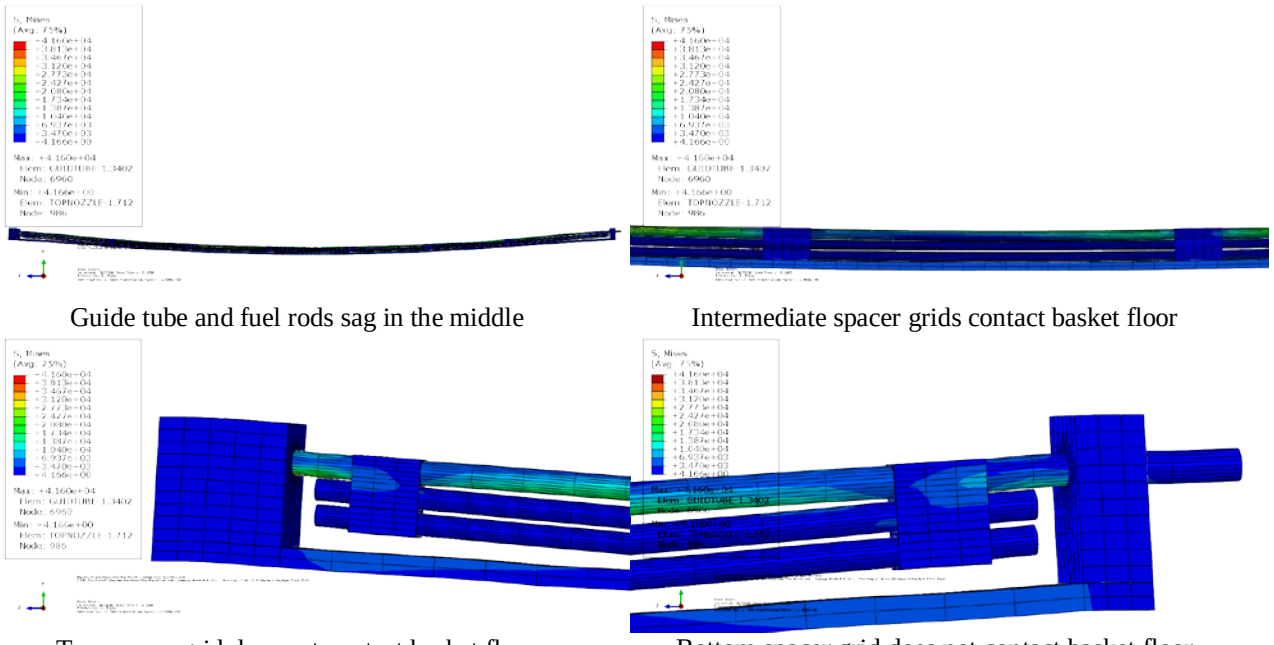

Guide tube and fuel rods sag in the middle

Intermediate spacer grids contact basket floor

Top spacer grid does not contact basket floor

Bottom spacer grid does not contact basket floor

Fig. 45. Dynamic response of the fuel assembly submodel for the initialization stage.

Fig. 45 shows the stress distribution and deformation of the SNF assembly submodel after the initialization stage. During the initialization stage, only gravity loading was applied to the system, and the basket floor was assumed to be simply supported by the cask. Maximum stress of 41.6 ksi occurred at the

guide tube. The maximum stress level was below all the material yield strengths listed in Table 19, so no yielding was observed in the system. The guide tube and fuel rods sagged in the middle sections as a result of dead weight loads. Close-up views show that intermediate spacer grids rested on the basket floor after submodel assembly sagging stabilized. The top and bottom spacer grids did not contact the basket floor. Maximum contact pressure occurred at an intermediate spacer grid touching the basket wall (Fig. 46). Contact pressure level was relatively low because the fuel assembly gradually sagged to reach the basket floor, and the loading process was assigned as a ramp-up in conjunction with the quasistatic state loading condition during each loading interval.

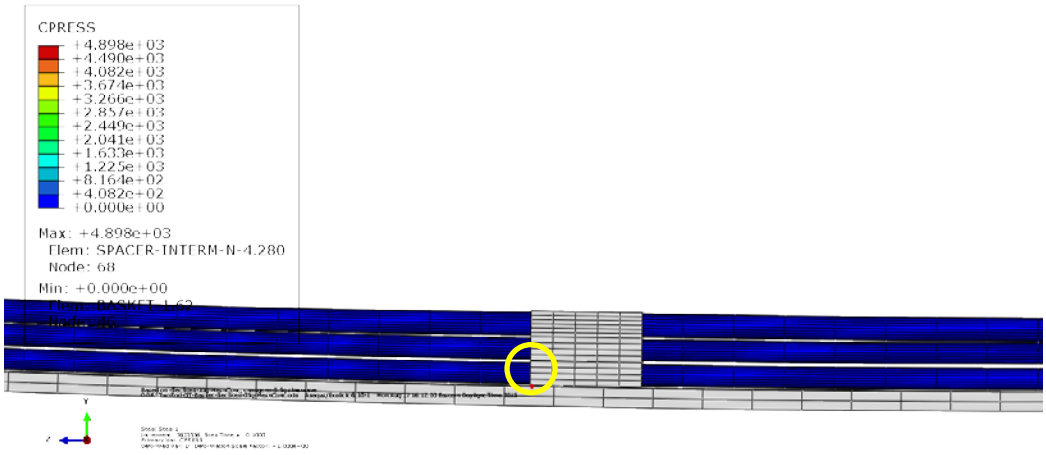

Fig. 46. Maximum contact stress resided at region where the spacer grid was in contact with the basket floor during the initialization stage.

The typical load-time history [10] registered by an accelerometer on a transport cask is shown in Fig. 47, which illustrates transient shock signals superimposed on continuous vibration signals of NCT. This random vibration from the cask provided the external loading to the SNF assembly. Inside the cask, another form of transient shock comes from the dynamic impact induced by dynamic contact interactions between the fuel assembly components during NCT. These components include the canister basket wall, guide tube, fuel rods, and spacer grids.

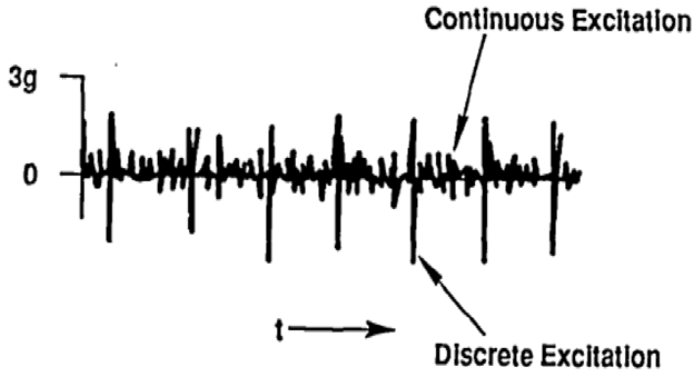

Fig. 47. Typical acceleration time history of a transport cask.

During the second stage (Fig. 48), the gravity load remained, and the constraint on the basket wall was removed. The typical vibration load as acceleration-time history was applied to the basket and the top and bottom nozzles, exciting the SNF assembly submodel under normal vibrations or transient shocks of

NCT. The first case of transient dynamics analysis was to simulate normal vibrations during NCT. A 0.5 g sine wave acceleration excitation was applied to the basket wall and the top and bottom nozzles of the fuel assembly submodel (Fig. 49). The sine wave had a frequency of 5 Hz.

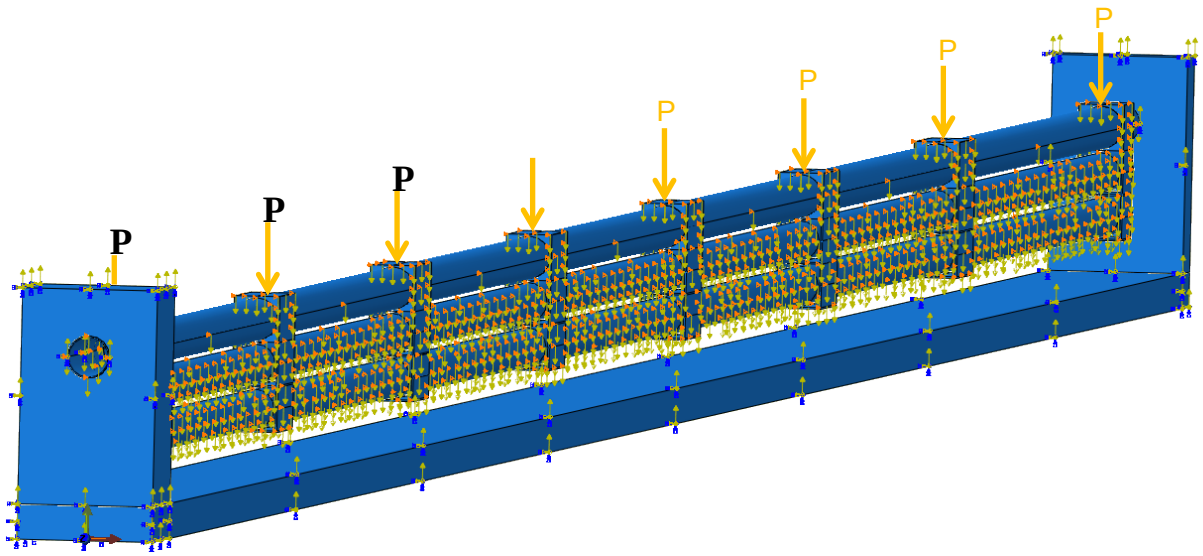

Fig. 48. Vibration boundary conditions and gravity system loads for the second stage of transient dynamic simulation of the fuel assembly submodel.

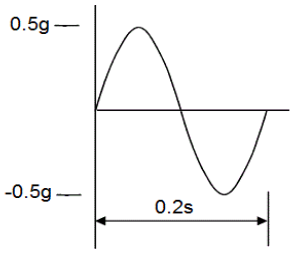

Fig. 49. A 0.5 g sine wave acceleration excitation used to simulate the normal vibration of NCT.

Fig. 50 shows the dynamic responses of the fuel assembly submodel under a vibration of 0.5 g acceleration amplitude. The stress level was higher than in the initial stage. After 0.5 g normal vibration excitation, the fuel rod, guide tube, spacer grids and basket wall deformed nonuniformly compared to deformation during the initialization stage. Some intermediate spacer grids lost contact with the basket wall. According to the von Mises stress distribution, besides the fuel pellets, the maximum stress occurred at the bottom Inconel spacer grid section where the material yielded.

(a) Fuel assembly (b) Bottom Inconel spacer

Fig. 50. The dynamic response of the fuel assembly submodel under 0.5 g sine wave acceleration excitation.

Due to the horizontal orientation of the fuel assembly during SNF transport, guide tubes and spacer grids become load bearing to carry the dead weight and transmit the dynamic loads in the fuel assembly system. Therefore, spacer grids and guide tubes are responsible for load transferring within the fuel assembly during transport. The stress distributions in the guide tube are shown in Top nozzle location Bottom nozzle location

Fig. 51 51. The maximum stress in the guide tube reached the yield strength. Guide tube yielding occurred at both the top and bottom nozzles. FEA results indicated the guide tube and spacer grids are at a high risk of failure. The failure of the skeleton will increase the random vibration contact frequencies among the fuel rods, and it will increase their vibration intensity. Therefore, the integrity of the guide tube and spacer grids will critically affect the vibration modes and the vibration intensity of fuel assembly during transport.

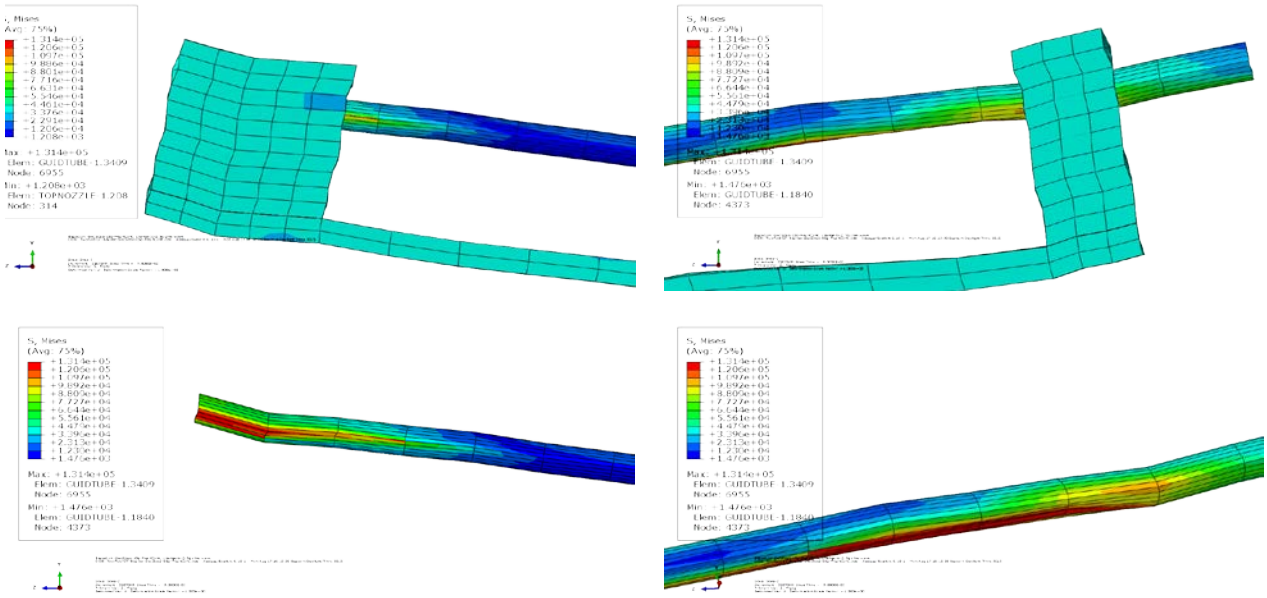

Top nozzle location Bottom nozzle location

Fig. 51. The dynamic response of guide tube under 0.5 g sine wave acceleration excitation.

Fig. 52 shows the stress distribution and deformation of other system components in the fuel assembly submodel (including the fuel cladding, the basket floor, and the top and bottom nozzles) with reference to the dynamic response of vibration under 0.5 g sine wave acceleration excitation. Under a 0.5 g simulated normal vibration load, the maximum stress of claddings is below the material yield strength, so the claddings remain intact. However, the basket wall and the top and bottom nozzles yielded, possibly due to the transient shocks and/or the impact load induced by the contact interaction among the spacer grids, guide tube, and fuel rods.

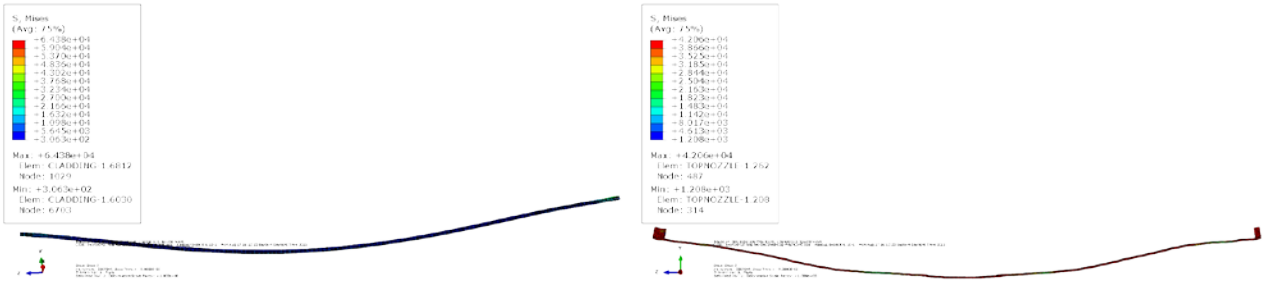

Claddings Basket wall, top and bottom nozzles

Fig. 52. The dynamic response of cladding, basket floor, top and bottom nozzles under 0.5 g sine wave acceleration excitation.

Fig. 53 shows that the maximum contact pressure of the SNF assembly submodel under 0.5 g sine wave acceleration excitation was located at the contact point of the spacer grid and the basket floor. Compared to the contact point in the initialization stage, the maximum contact pressure level was almost one order of magnitude higher. However, the maximum contact pressure was still under the material yield strength.

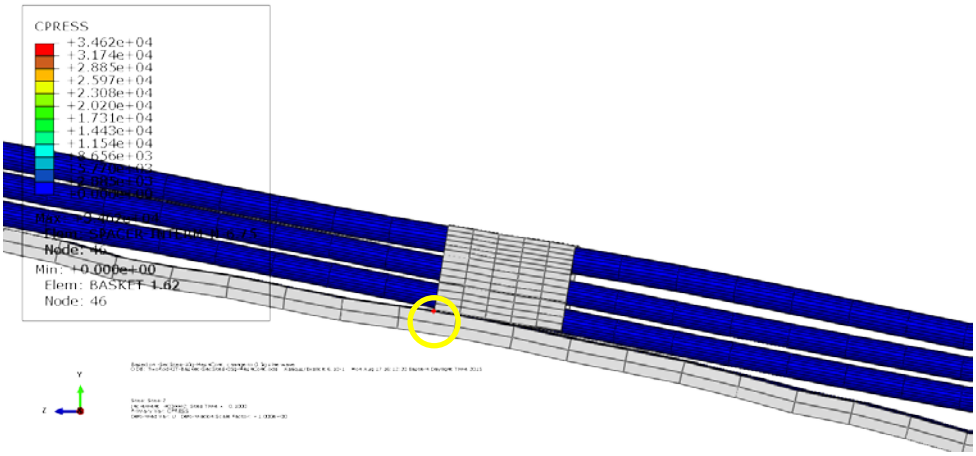

Fig. 53. Maximum contact pressure under 0.5 g sine wave acceleration excitation resides at the contact point of the spacer grid and the basket floor (indicated by the yellow circle).

The second phase of transient dynamics analysis studied the dynamic response of the SNF assembly submodel under transient shock loading during NCT. According to Fig. 47, a 3 g periodic impulse acceleration excitation was simulated as transient shock during transportation (Fig. 54). It is assigned a peak value of three times gravity and a duration period of 1 s. The resulting system dynamic responses

within this loading cycle period are shown in Fig. 55. Similar to the dynamic response of 0.5 g sine wave acceleration excitation, yielding occurs at bottom Inconel spacers during 3 g transient shock excitation (Fig. 55). Fig. 56 reveals that the guide tube also yields at the top and bottom nozzle locations during 3 g transient shock loading. Therefore, the integrity of the spacer grids and guide tube are the concern under such transient shock loading during NCT.

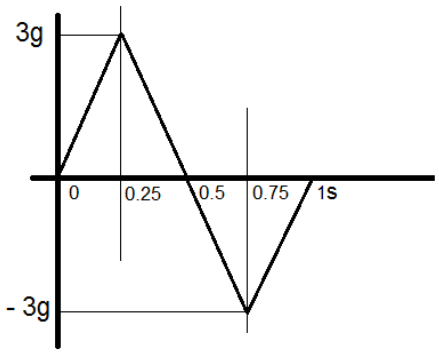

Fig. 54. A 3 g impulse acceleration excitation time-history representing the transient shock of NCT.

Fuel assembly

Bottom Inconel spacer

Fig. 55. The dynamic response of the fuel assembly submodel under 3 g transient shock excitation.

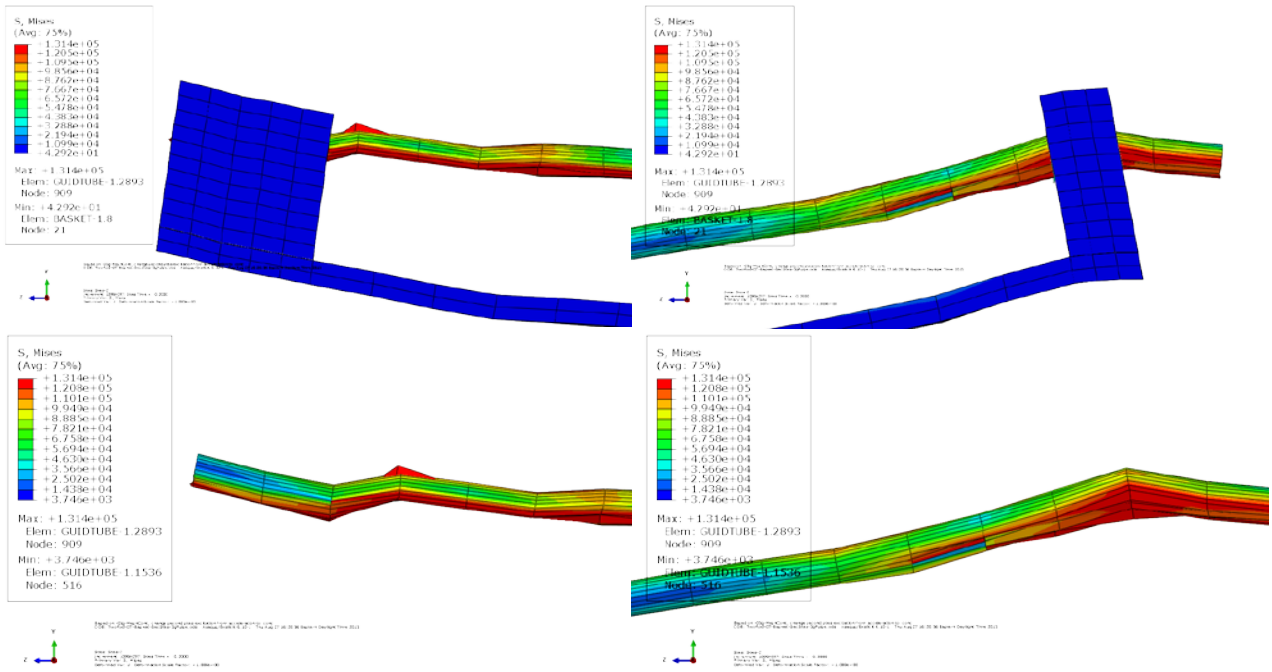

Top nozzle location Bottom nozzle location

Fig. 56. The dynamic response of guide tube under 3 g transient shock excitation.

The dynamic response of claddings under 3 g transient shock excitation is shown in Fig. 57. The FEA result indicates that the maximum stress level was twice the 0.5 g sine wave acceleration excitation and was near the yield strength. The basket wall and the top and bottom nozzles also have regions that reached their associated yield strengths.

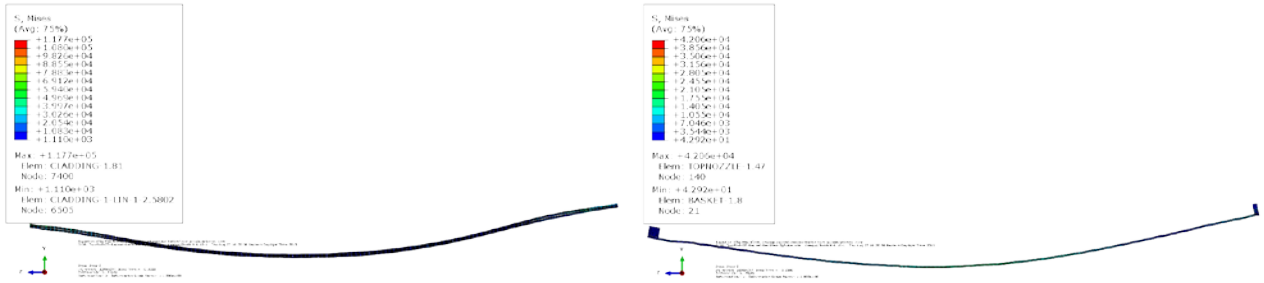

Claddings Basket, top and bottom nozzles

Fig. 57. The dynamic response of the cladding, basket wall, and top and bottom nozzles under 3 g transient shock excitation.

In the transient shock excitation case, the maximum contact pressure occurred at the location where the guide tube was in contact with the top fuel rod (Fig. 58). The FEA result indicated the maximum contact pressure level is relatively high at this point. This type of dynamic contact interaction will inevitably form another pattern of transient shock loading within the fuel assembly system. Therefore, the contact interaction in the fuel assembly system, that can introduce transient shock loadings and impact SNF vibration integrity, needs more thorough investigation.

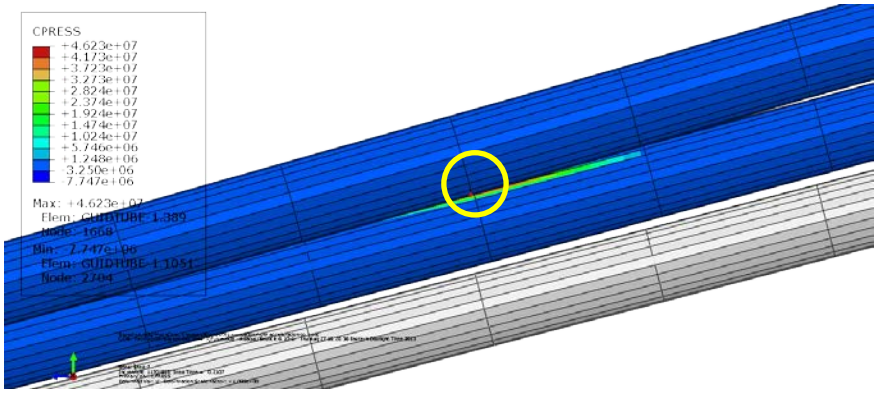

Fig. 58. Maximum contact pressure of 3 g transient shock excitation is located at the contact point of guide tube and top fuel rod (indicated by the yellow circle).

13. EVALUATION OF CONTACT INTERACTIONS BETWEEN FUEL RODS AND SPACER GRIDS INDUCED BY IMPACT LOADING

The primary focus of this section is to estimate the interaction intensity at contact points between a fuel rod and spacer grids induced by dynamic impact loading. Due to the complex design of the fuel assembly system, a simplified scheme was needed to enable a practical solution for FEA efforts; for example, in FEA modeling, the leaf springs and dimples of a spacer grid were modeled as translational springs in earlier dynamic simulations. Fuel rods were connected to the spacer grid with the modeled translational springs. The SNF assembly submodel simplified the spacer grid structure and ignored the contact interaction between the fuel rods and the spacer grids. However, a 3-D section model of the leaf springs and dimples was built to evaluate contact interaction between the fuel rod and spacer grids induced by the impact loading from cask vibration during NCT.

Fig. 59 and Fig. 60 provide a detailed view of the 3-D model of the fuel rod section with the dimples and leaf spring structures at the spacer grids. The fuel rod length is equivalent to a quarter of the length between the spacer grids. According to the targeted spacer grid design, there are two dimples on one side of a slot and one spring on the opposite side of the slot. Each dimple and spring is an elongated component that arches from the associated grid strap to inside the associated slot. Two dimples are modeled as arch-shaped structures, where the flat section of the dimple is aligned and in contact with the fuel rod's surface contour. The two dimples are 0.021 m from each other on the fuel rod axial. The leaf spring is modeled as an arch-shaped component and is oriented at a 45° angle to the fuel rod axial. The surface profile of the spacer grid region was obtained from a precision electronic scanning instrument. The sketch was imported in ABAQUA CAE to build the spring/dimple structure geometry. The spring and dimple are made of Zircaloy-4 with a thickness of 0.47 mm. The fuel rod dimensions are provided in

Table 18 and possess the same material properties that were used in transient dynamics simulations. SI units are used for all simulations, calculations, and results in this section, as seen in Table 21.

The general contact algorithm was assigned at interfaces between the cladding's bottom surface and the top surfaces of the dimples and spring. The ABAQUS dynamic explicit code was used in this impact response analysis. The approach was to simulate the impact load induced by the fuel rod's inertia onto the dimples and spring within the spacer grids at a target impact velocity. Upon dynamic contact of the fuel rod and the dimples/spring, the contact stress and deformation of the interacting components (cladding, dimples, and spring) evolved progressively. Reaction forces at the contact surfaces were then estimated to evaluate the loading intensity of the target impact event.

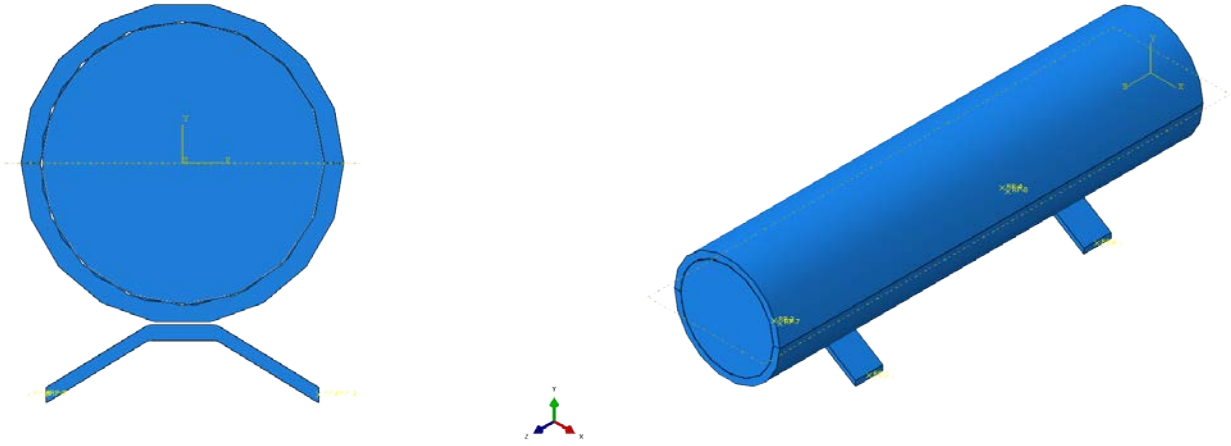

Fig. 59. Cross section view of the fuel rod with two dimples, modeled within the spacer grid region.

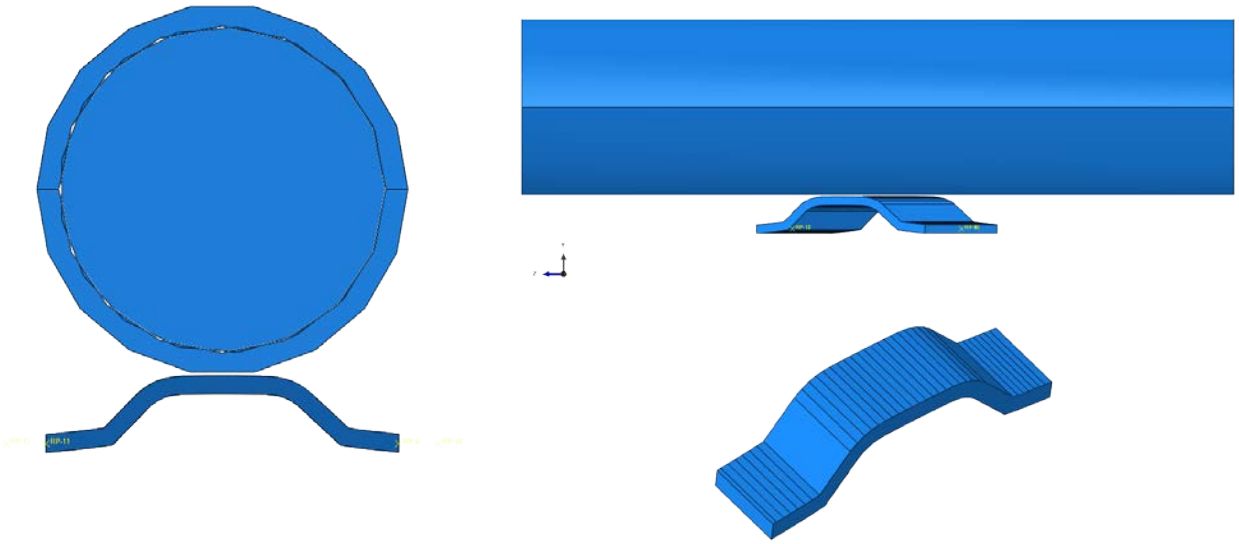

Fig. 60. Cross section view of the fuel rod with the leaf spring modeled at the spacer grid region.

Table 21. Mechanical properties of the fuel rod (SI)

	Material	Young's modulus (GPa)	Poisson's ratio	Yield strength (MPa)	Density (kg/m^3)
Pellet	UO_2 [3]	201	0.32	2,146	10,970
Cladding, spring/dimple	Zircaloy-4 [3]	91	0.33	906	6,560
Block	Stainless steel [20]	79.3	0.30	138	8,030

During a truck transportation test performed at Sandia National Laboratory, the vibration load transferred from the cask to the fuel assembly was approximately 20 g peak vertical vibration acceleration at the second spacer grid from the A7 accelerometer reading (Fig. 61). The FEA simulation protocol was developed and implemented to generate a quantitative estimate of the loading intensity experienced by an SNF rod under transient shock loading events. Practical assumptions were made based on the conservation of momentum and the system components' constraints to represent 20 g transient shock vibration periods for a new fuel assembly and an aging fuel assembly, including their associated initial contact velocities at the interface of the spacer grid and the fuel rod. In

Fig. 62, for a newer fuel assembly skeleton system, the vibration time period was 0.04 s, and the initial contact impact velocity of the fuel rod onto the spacer grid at 20 g acceleration was estimated at 0.98 m/s. For an aging skeleton system, the vibration time period was 0.2 s, and the estimated initial contact impact velocity was 4.9 m/s. The impact response time period was strongly dependent on the structural system stiffness and was the key factor to dictate the initial contact velocity during the transient shock of NCT.

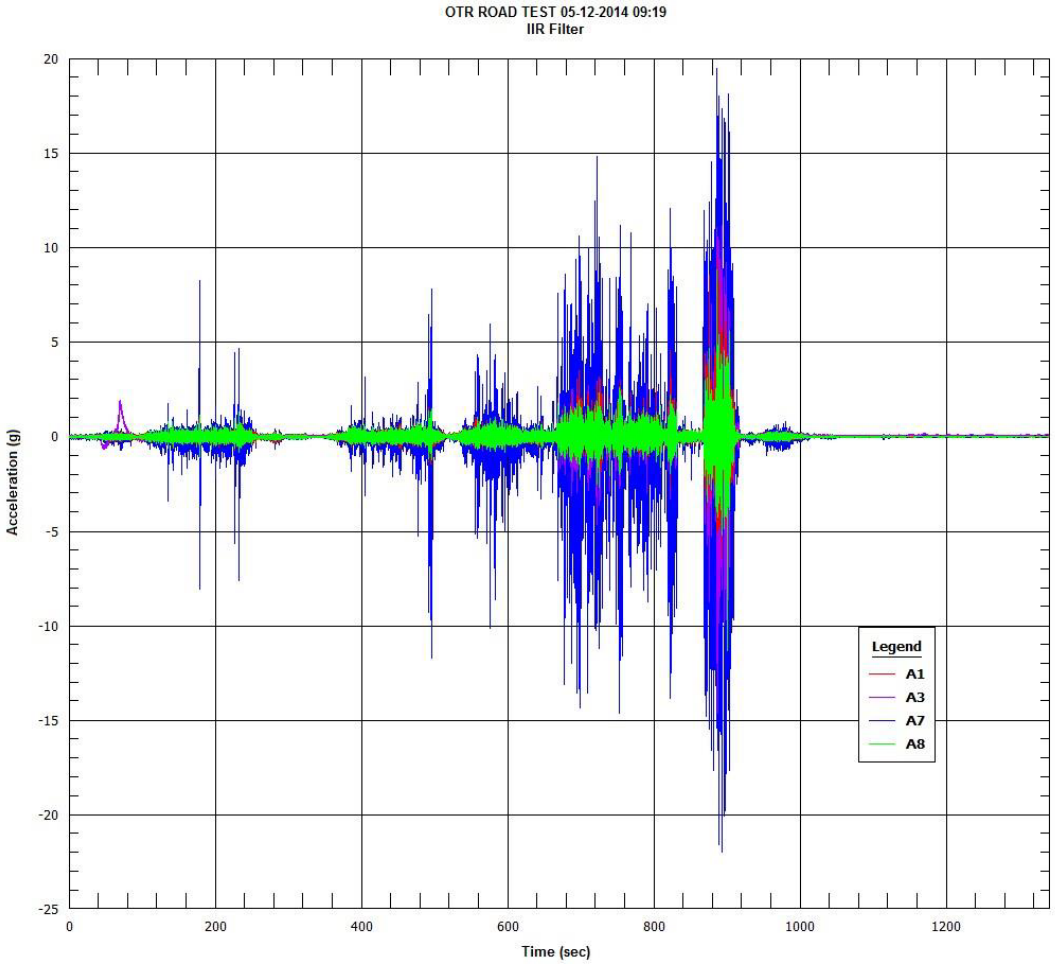

Fig. 61. Segment 1 accelerometer time-histories [21].

Momentum = Mass * Velocity = $\int F * dt$, F=mass*acceleration

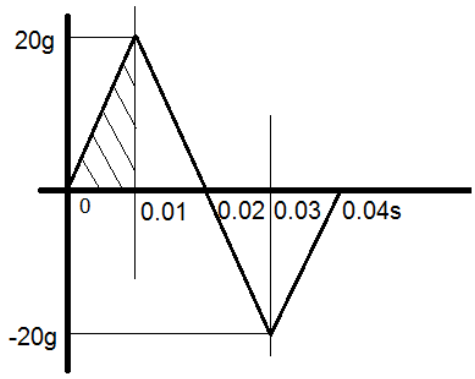

(a) Fresh fuel assembly system with good constraints among the fuel assembly skeleton system

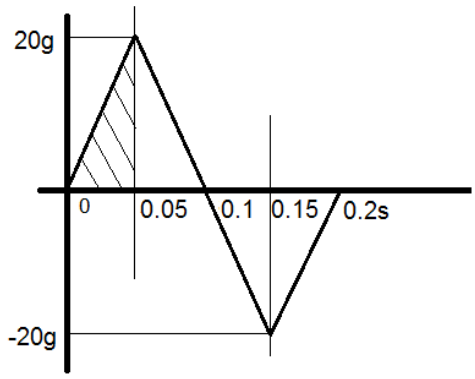

(b) Aging fuel assembly with less constraint functionality due to gaps' density increased among the fuel assembly components

Fig. 62. Schematics of 20 g acceleration transient shock periods for newer and aging fuel assemblies, showing an increased vibration cycle period assigned for loss of system constraints.

For instance, an aging fuel assembly structure would typically have lower system stiffness when compared with its virgin state because of the increased gaps in the assembly's skeleton system. This leads to an increase in the impact loading reaction cycle period. To further investigate the contact interaction upon impact, the fuel rod and spacer grid's interaction was simulated with the dimples and leaf spring at a targeted initial contact velocity of 0.98 m/s for a newer fuel assembly and at a velocity of 4.9 m/s for an older fuel assembly. Resulting contact stress profiles were compared to evaluate the transient shock impact effects under different scenarios.

Fig. 63 illustrates the progressive fuel rod impact on dimples at the initial velocity of 0.98 m/s. The impact mass of the fuel rod is limited within the 2 in. spacer grid section. The fuel rod traveled at the relative velocity of 0.98 m/s to the spacer grid dimple. A fuel rod approximately 1.04×10^{-3} s came into contact with dimples. The velocity of the fuel rod changed during progressive contact interaction. Due to the rod's initial momentum, it moved forward continuously against the dimples until its momentum reached zero at 1.11×10^{-3} s. At this point, the maximum stress of the dimple reached 752.8 MPa. Because of the dimple material's elastic recovery, the fuel rod started to bounce back. At 1.19×10^{-3} s, the contact stress level was reduced to the initial contact at 1.04×10^{-3} s. At 1.26×10^{-3} s, the fuel rod lost contact with the dimples, and the system's stress level further decreased. Residual stresses at the end of the impact event were low, indicating that under a transient shock load cycle, the fuel rod and dimples largely remained intact with a slight increase in the dimple's permanent deformation (i.e., a slight gap increase between the fuel rod and the spacer grid).

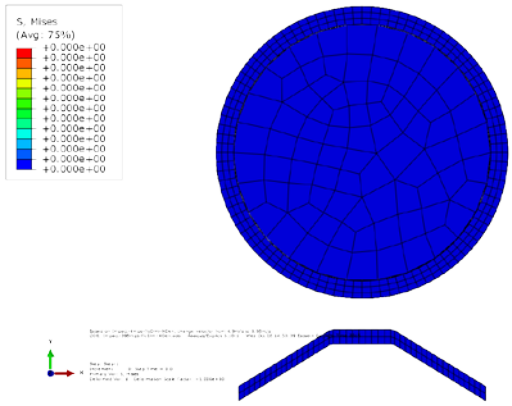

Original position

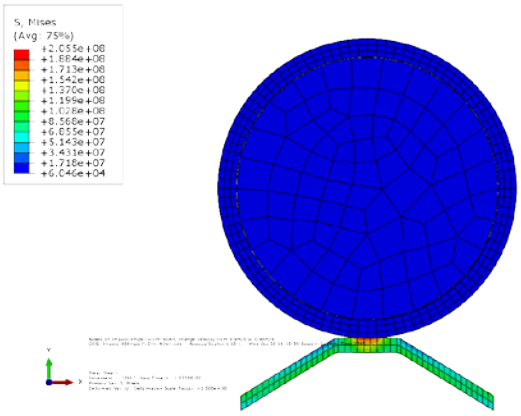

Impact at 1.04e-3 s

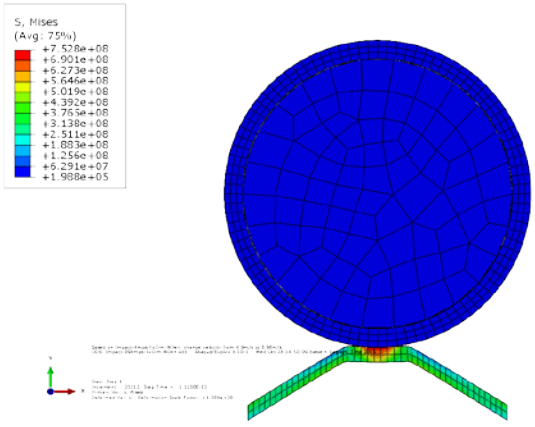

Impact at 1.11e-3 s

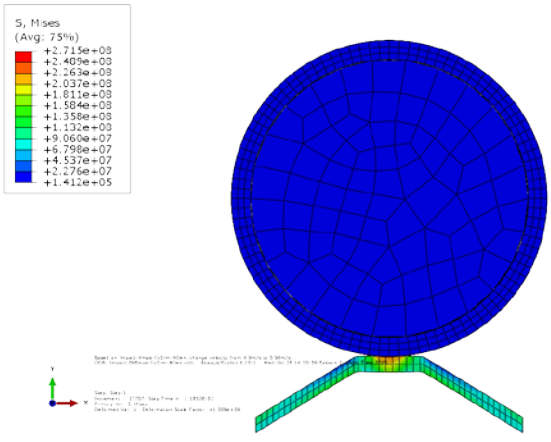

Impact at 1.19e-3 s

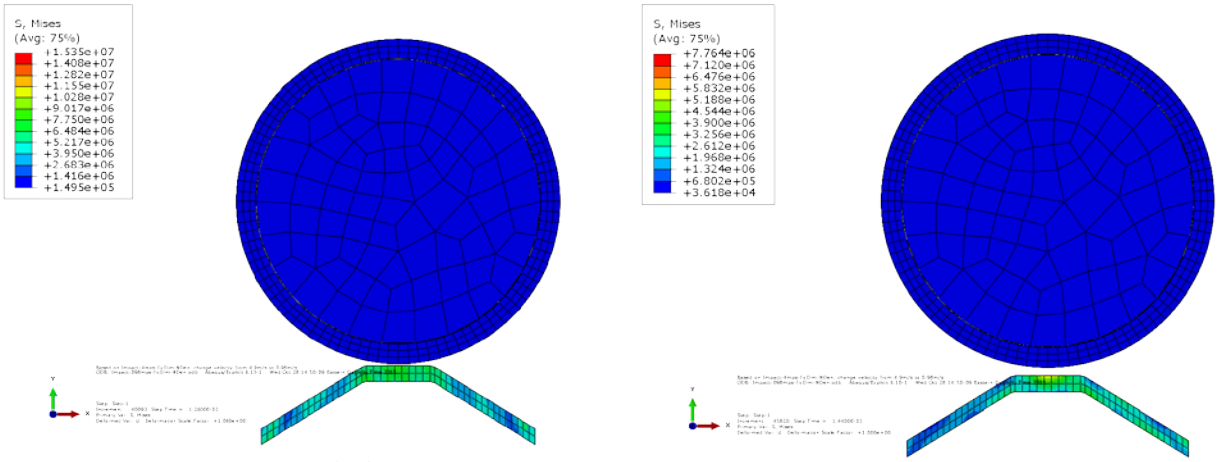

Impact at 1.26e-3 s

Impact at 1.44e-3 s

Fig. 63. The progressive evolution of a fuel rod impact onto dimples at the velocity of 0.98 m/s.

Fig. 64 reveals that dimples experience maximum stress during high speed impact. Dimples reached a maximum stress of 752.8 MPa, which is less than the yield stress. Both the fuel rod and the dimples did not yield. Under the cladding wall that is in contact with the dimples, a maximum stress of 254.5 MPa was reached on the inner surface of the cladding wall because impact loading induced flexural bending tension stress on the inner wall of the cladding.

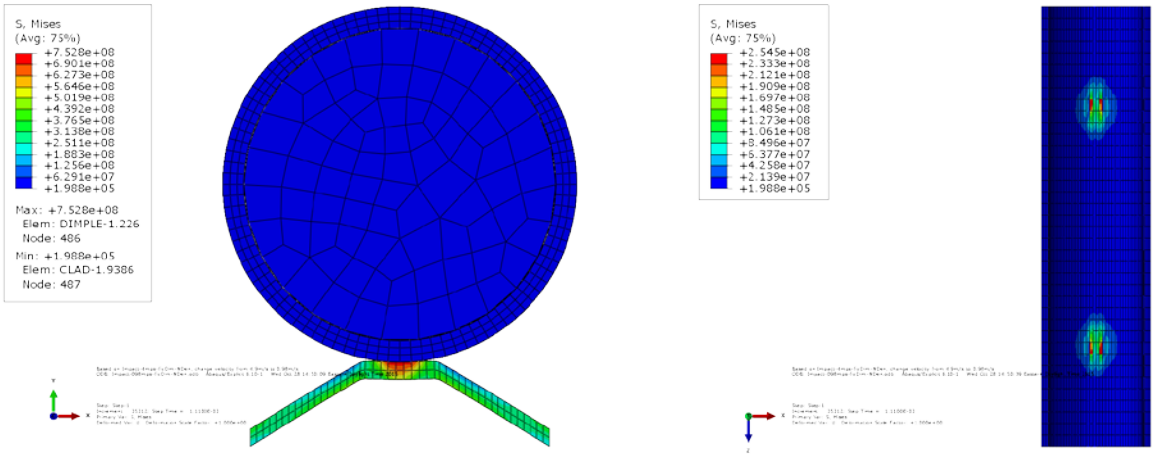

Fig. 64. Stress distribution of dimples and cladding during the fuel rod impact onto the dimples at an initial velocity of 0.98 m/s.

Fig. 65 shows the highest contact pressure occurred on the contact surfaces of dimples and cladding during impact. The highest impact contact pressure occurred at 1.11×10^{-3} s. Contact pressure on the dimples and cladding, both of which are under material yield stresses, are 270.8 MPa and 323 MPa, respectively. The reaction force was calculated by integrating contact pressures over the associated contact areas on the dimples. The reaction force applied on one dimple is 291 N.

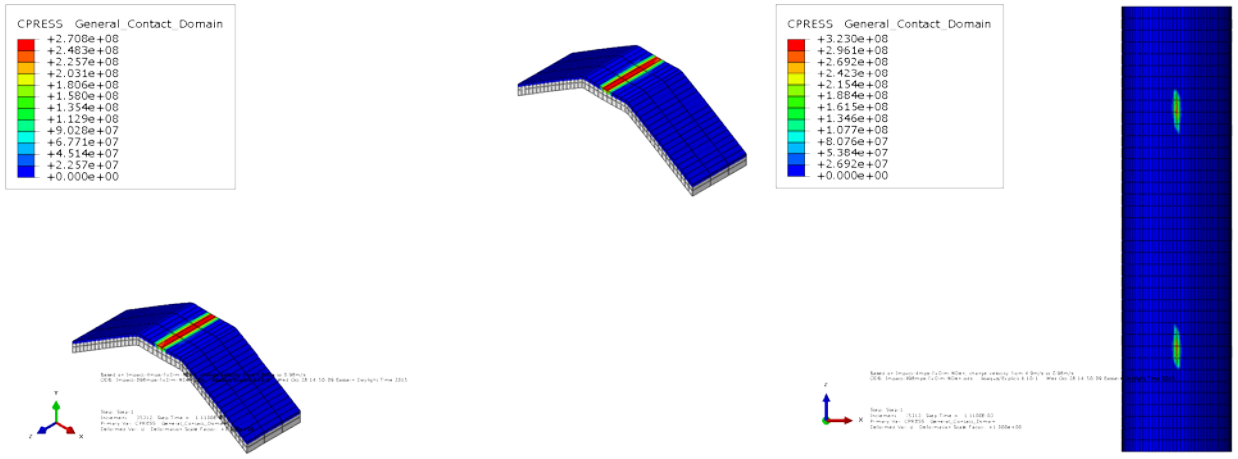

Fig. 65. Contact pressure on dimples and cladding during a fuel rod impact on dimples at the initial velocity of 0.98 m/s.

The fuel rod's impact on the dimple with an initial contact velocity at 4.9 m/s was also investigated (Fig. 66 and Fig. 67). The resulting contact stress profiles are much higher than an impact velocity at 0.98 m/s, and the dimple experienced local yielding under impact loading. The maximum stress on the cladding reached 386 MPa, so the cladding did not yield. Maximum stress also occurred on the inner surface of the cladding wall because of impact-induced bending. The contact pressure levels on the dimples and cladding are higher than the impact at the velocity of 0.98 m/s, but the contact pressure profiles of the system are still below material yield strength. The contact force estimated on one dimple is 371 N, which is 27% higher than a lower speed impact at 0.98 m/s.

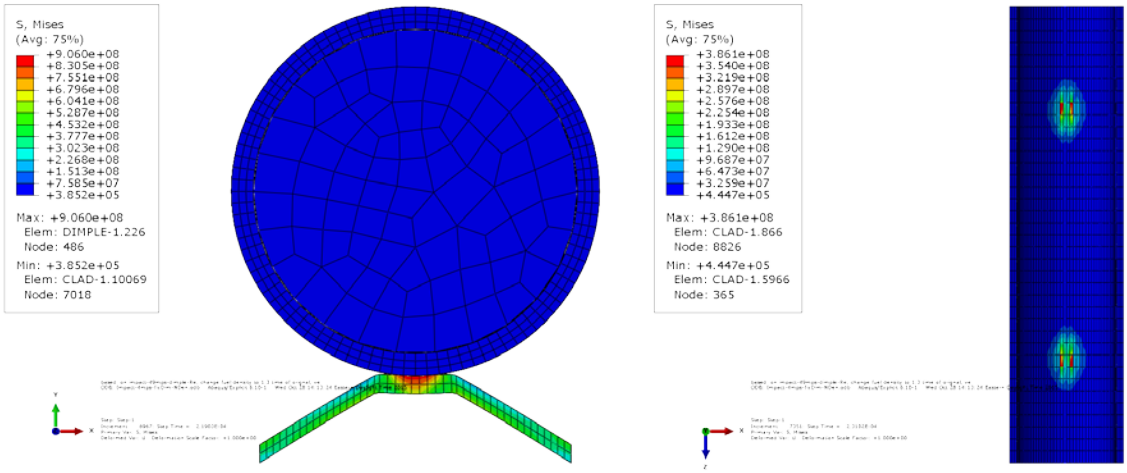

Fig. 66. Stress distribution profiles of dimples and cladding during the fuel rod impact on dimples at the initial velocity of 4.9 m/s.

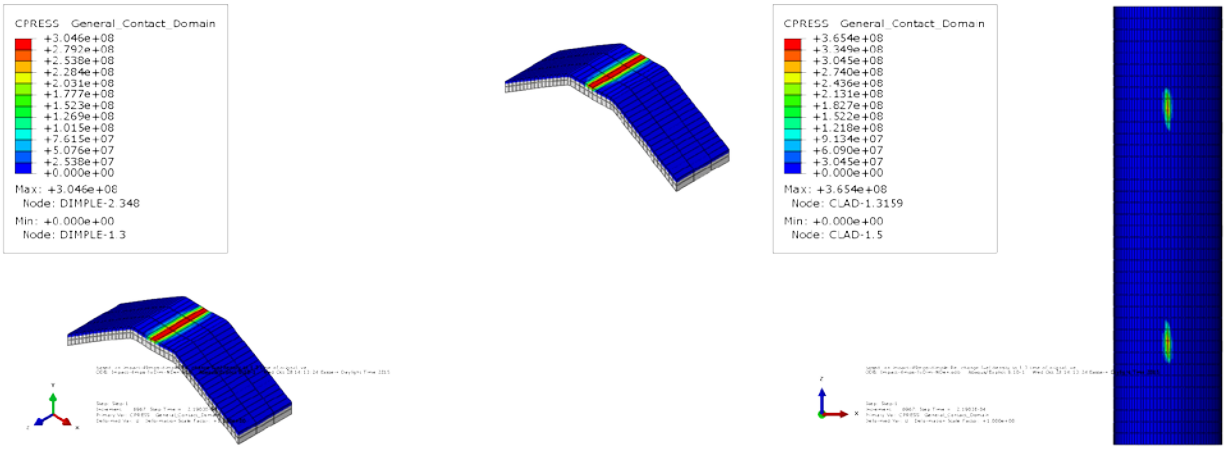

Fig. 67. Contact pressure on dimples and cladding during the fuel rod's impact on dimples at the initial velocity of 4.9 m/s.

Fig. 68 and Fig. 69 show the results for the fuel rod's impact onto the spring at the initial velocity of 0.98 m/s. The maximum stresses are 702 MPa at the spring and 151 MPa at the clad, where both the spring and the cladding did not yield. Compared to the stress of the fuel rod's impact onto the dimples at the same velocity, the stress level of the spring is relatively lower. This is because the spring is less stiff than the dimples. Contact pressure of 231 MPa on the spring is higher than that on the cladding at 140 MPa. In general, the spring's contact pressure is lower than the dimples' at the same initial contact velocity. The estimated contact force on the springs is 357 N, which is higher than the contact force on one dimple at 291 N for the same velocity impact. However, the contact force on the spring is less than the total contact force of two dimples at 582 N. The contact pressure on the spring is also higher than the contact pressure on the dimples, but the reaction force on the spring is lower than the reaction force from both dimples.

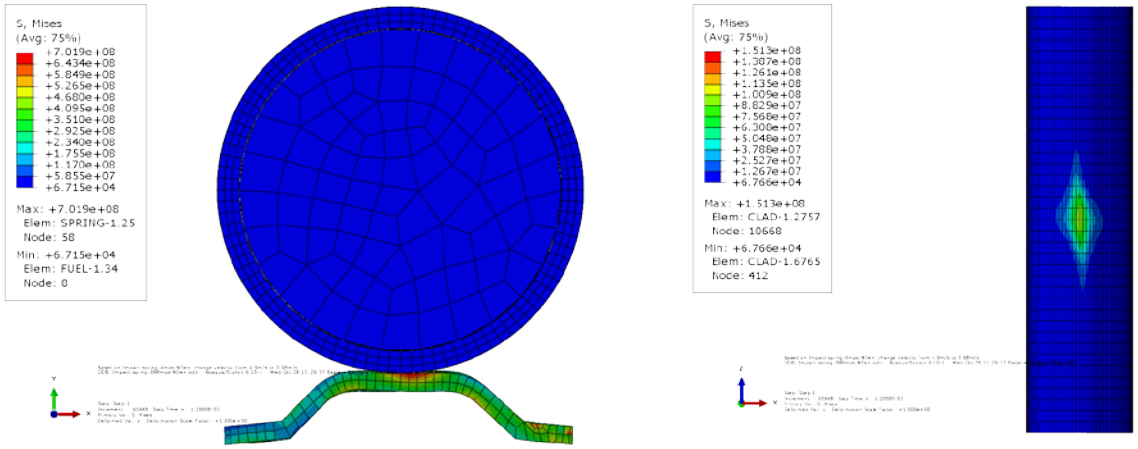

Fig. 68. Stress distribution of the spring and cladding during the fuel rod's impact on the spring at a velocity of 0.98 m/s.

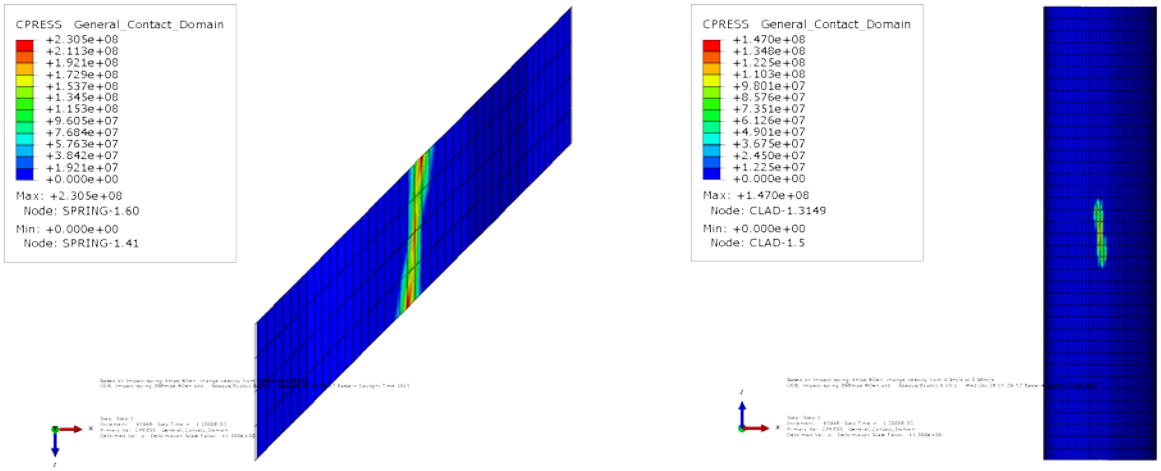

Fig. 69. Contact pressure on the spring and cladding during the fuel rod's impact on the spring at a velocity of 0.98 m/s.

Fig. 70 and Fig. 71 show FEA simulation results for the fuel rod's impact on the spring at a velocity of 4.9 m/s. Like the fuel rod's impact on the dimples at the same velocity, the spring yielded locally during impact. The maximum stress was 190 MPa on the cladding, which is lower than the cladding yield but higher than the lower impact velocity test. This maximum cladding stress of 190 MPa was only half of that in the fuel rod and dimple impact case at the same impact velocity. The trends of the resultant spring contact pressure were similar for the two impact velocity cases. The maximum contact pressures on the spring and the cladding were 298 MPa and 191 MPa, respectively, and both were below the material yield stresses. The estimated contact force on the spring for this impact was 505 N, which is 40% higher than at a lower speed impact at 0.98 m/s.

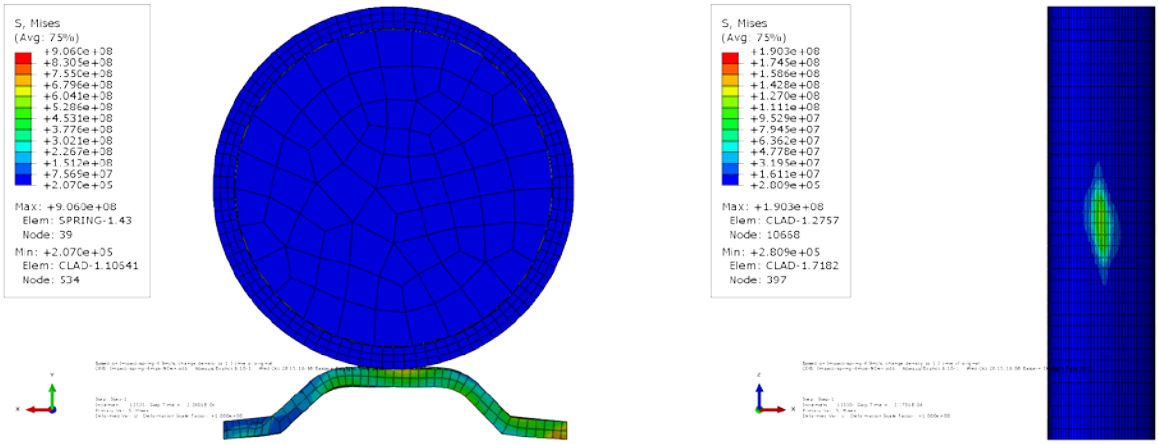

Fig. 70. Stress distribution of the spring and cladding during the fuel rod's impact on the spring at the initial velocity of 4.9 m/s.

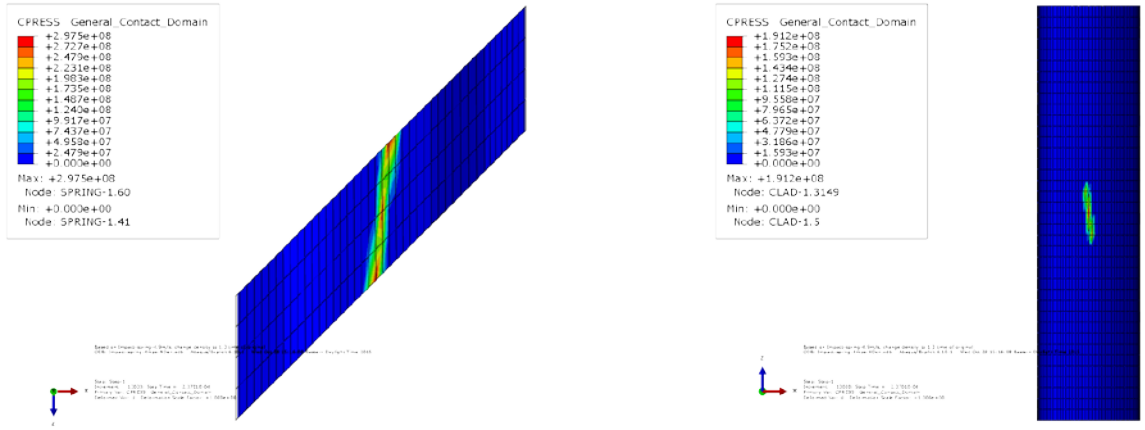

Fig. 71. Contact pressure on the spring and cladding during the fuel rod's impact on the spring at the initial velocity of 4.9 m/s

14. COMPARISON OF STRESS INTENSITY BETWEEN TRANSIENT SHOCK LOAD AND CIRFT BENDING LOADING LEVELS

A bridge between the transient shock loading intensity and CIRFT evaluations must be established to incorporate transient shock loads into the CIRFT program to determine the integrated bending fatigue load with the periodic transient shock load from NCT. This capability will be used to provide an overall accumulated damage estimate or an effective SNF vibration lifetime estimate.

Fig. 72 shows the CIRFT static bending test results and compares CIRFT data on the HBR fuel rod with the Pacific Northwest National Laboratory (PNNL) moment-curvature curve converted from PNNL cladding stress-strain data. The moment-curvature data from PNNL does not take fuel pellet support into consideration. For cladding tubing without fuel support, the cladding's bending moment resistance capacity is much less than the SNF rod without defueling. To relate the transient shock stress level to a CIRFT bending test, the maximumcladding stress of HBR SNF rod under the targeted 20 g transient shock load was estimated from the same FEA simulation procedure used above, with an initial velocity of 4.9 m/s for the aging fuel assembly under consideration.

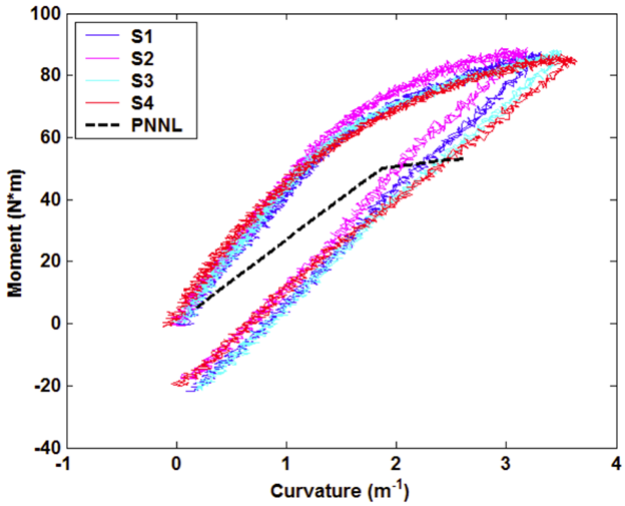

Fig. 72. Comparison of static CIRFT data with PNNL moment-curvature curve converted from PNNL cladding stress-strain data (without fuel).

The HBR fuel rod dimension is the same as that provided in Table 18. The classic flexure normal stress formula presented in Eq. (1) is rearranged as shown in Eq. (2):

$$\sigma = \frac{My}{I}, \tag{1}$$

and

$$M = \frac{\sigma I}{y} \tag{2}$$

where M is the bending moment, σ is the stress on the clad, I is the area moment of inertia (6.666E−10 m^4), and y is the cladding radius (5.398E−3 m)

Equation (2) was used to determine the corresponding bending moment on the SNF rod that experienced the same stress intensity as the same SNF rod under 20 g transient shock impact loading. Here the average contact stress concentration on an HBR rod from the target 20 g transient shock impact load is 341 MPa, and the estimated corresponding bending moment is 42 Nm. This moment is below the static bending moment capacity of HBR CIRFT data (~90 N-m), and 42 N-m is still at the linear range portion of the

HBR static CIRFT data trend. Therefore, the bending moment that has maximum bending stress matched that of a 20 g transient shock loading and can be effectively estimated and used to carry out high-rate CIRFT vibration testing for the equivalent transient shock impact load.

To estimate the damage potential of transient shocks to the SNF vibration reliability, a pilot study was carried out on Catawba MOX and LMK SNF. CIRFT specimens were dropped twice from heights ranging from 0.305 m (1 ft) to 0.610 m (2 ft) to simulate the transient shock before carrying out the bending cycling test at a frequency of 5 Hz under the target loading amplitudes. The accelerated aging of the tested MOX and LMK CIRFT samples that were dropped are shown in Fig. 73. LMK CIRFT rods that were dropped from 0.305 m and then subjected to the cyclic load at 10 N-m showed a 50% reduction in fatigue life. MOX CIRFT rods that were dropped 0.610 m at 5 N-m load showed a 73% reduction in fatigue life. The reduction in the lifetime of CIRFT-tested SNF samples was observed by combining the harmonic vibration loading and the drop-induced transient shock load [10].

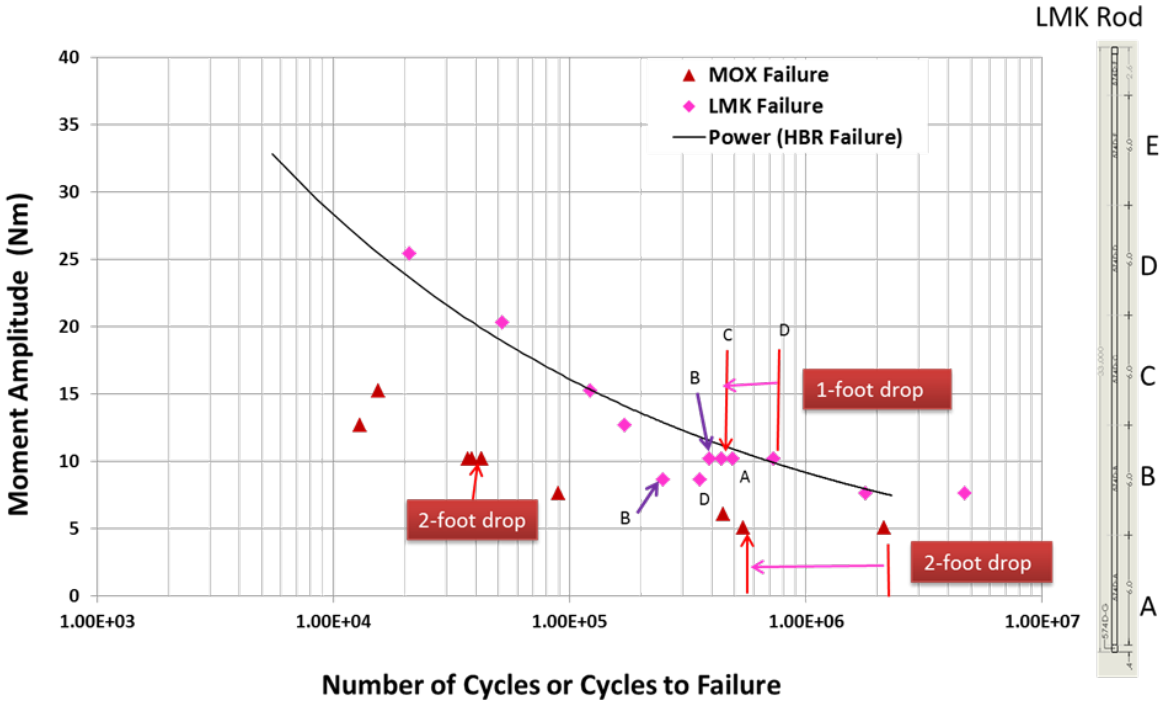

Fig. 73. Pilot transient shocks simulation study on MOX and LMK SNF [10].

This pilot test showed that drop-induced transient shock load impacts the performance of SNF CIRFT samples. To understand the drop intensity, FEA simulation was conducted to investigate the contact reaction for the CIRFT sample during drop impact loading events. Fig. 74 shows a surrogate CIRFT sample with a 0.0508 m gauge section and two rigid gripping sections on both ends.

Fig. 74. Surrogate CIRFT sample.

In the FEA, a similar SNF Zicaloy-4 rod with a 0.0508 m radius was used (Fig. 75). The total weight of the simulated test sample, including the 2 in. gauge section and the two end grip sections, is 310 g. The SNF CIRFT samples were dropped from heights of 1–2 ft onto a stainless steel hollow square block stand (0.0127 m × 0.0254 m) with a wall thickness of 0.0038 m, as indicated by the red square in Fig. 75.

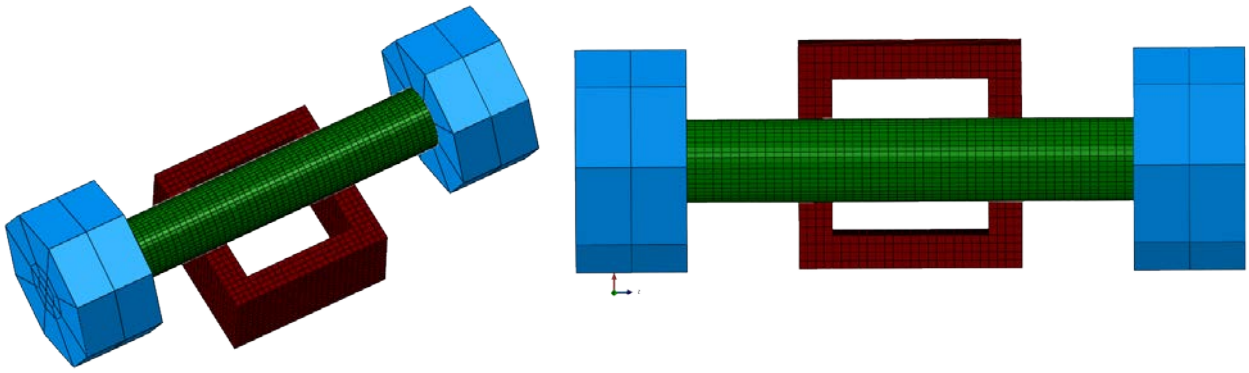

Fig. 75. FEA simulation of a SNF CIRFT sample drop onto a stainless steel block.

For the free fall, the velocity of the falling object's impact with the object on the ground is calculated using

$$v = \sqrt{2gh}\ , \tag{3}$$

Where g is gravity (9.8 m/s^2) and h is the drop distance between the drop starting point to the top surface of the stainless block.

When the sample was dropped from 0.305 m (1 ft), it hit the stainless steel block at a speed of 2.444 m/s at the initial contact impact. The ABAQUS impact simulation procedure was applied to investigate the contact reaction of the fuel rod under the impact induced by the drop. Fig. 76 shows the stress profiles in the fuel rod where the maximum stress on the cladding at contact locations is 525 MPa. As in the previous impact study, the maximum stress occurs on the inner surface of the cladding wall due to impact-induced bending. This maximum stress is less than the material yield strength of 906 MPa. Nevertheless, residual stress contours remain in the cladding after the impact event and will eventually reduce the fatigue life of the sample, as validated by the CIRFT evaluations illustrated in Fig. 73.

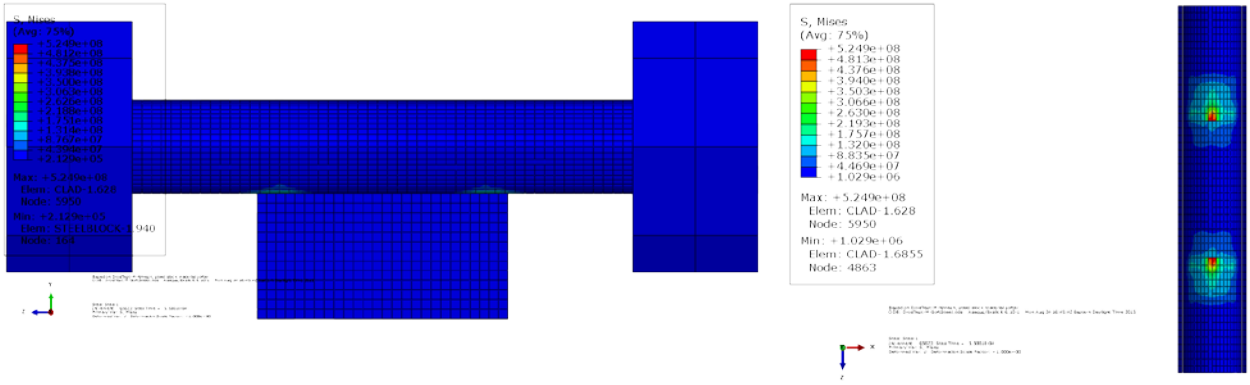

Fig. 76. Resulting stress on the stainless steel block and the fuel rod under the impact induced by the 1 ft CIRFT sample drop.

Fig. 77 shows that the highest contact pressure occurred during the CIRFT rod's impact with the stainless steel block stand. The maximum contact pressure of 356 MPa, which is under the material yield strength, was evaluated. The reaction force estimated from the contact pressure profiles is 641 N.

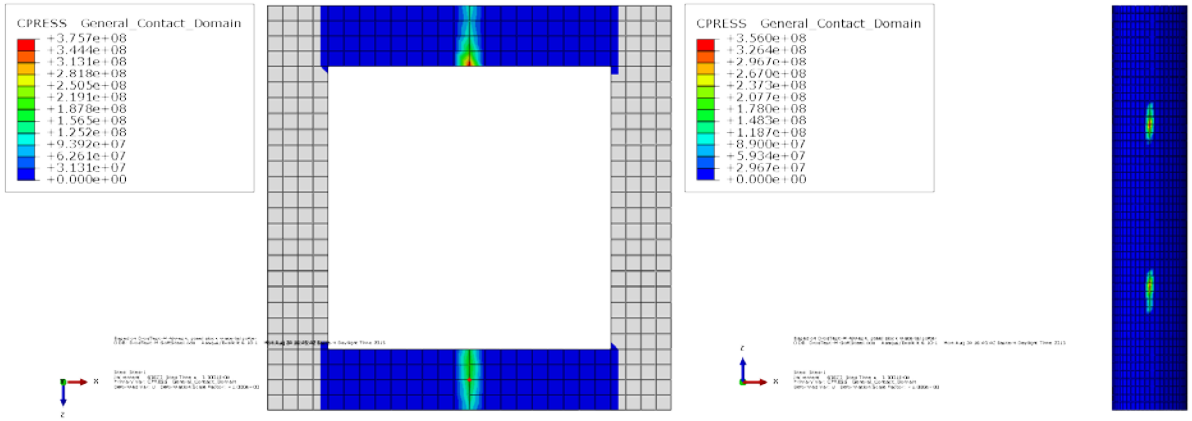

Fig. 77. Contact pressure on the stainless steel block stand and the fuel rod upon impact induced by a 1 ft drop of the CIRFT sample.

15. CIRFT DYNAMICS PERFORMANCE VERIFICATION

The CIRFT [1–12, 22–24] was designed to evaluate dynamic response of SNF rods under NCT. A U-frame testing setup (Fig. 80) is used to impose bending loads on the fuel rod specimen. The bending loads are considered due to the moment of inertia from vibration during NCT. The U-frame setup consists of two rigid arms, side plates connected to the rigid arms, and links to a universal testing machine.

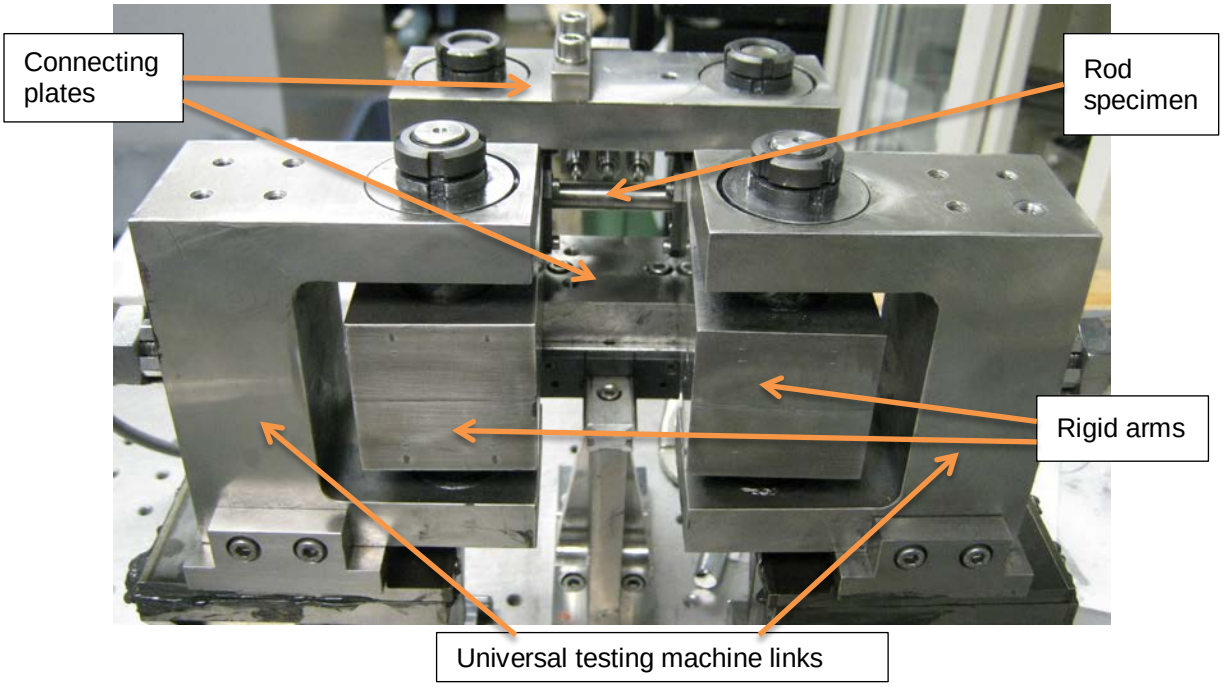

Fig. 78. Horizontal layout of ORNL CIRFT.

The rod specimen is coupled to the rigid arms with two specially designed grips. The U-frame is oriented horizontally and driven by electromagnetic force–based Bose dual linear motors (Fig. 80).

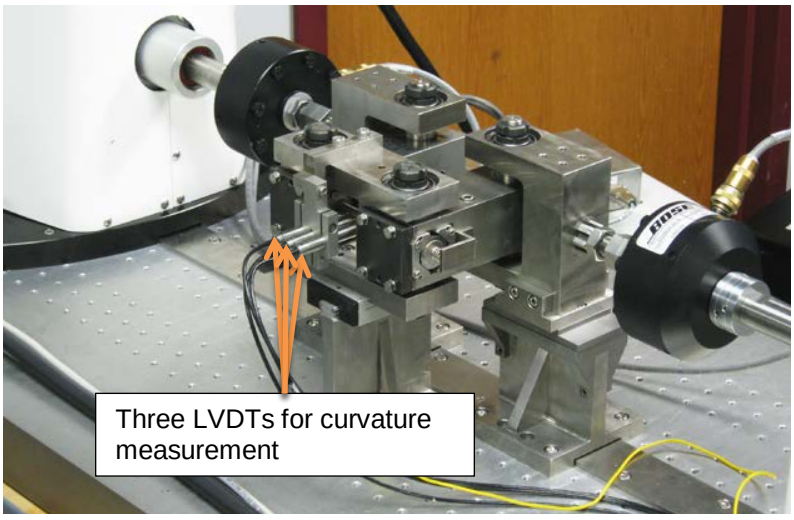

Fig. 79. Three linear variable differential transformers (LVDTs) for curvature measurement and Bose dual linear motors.

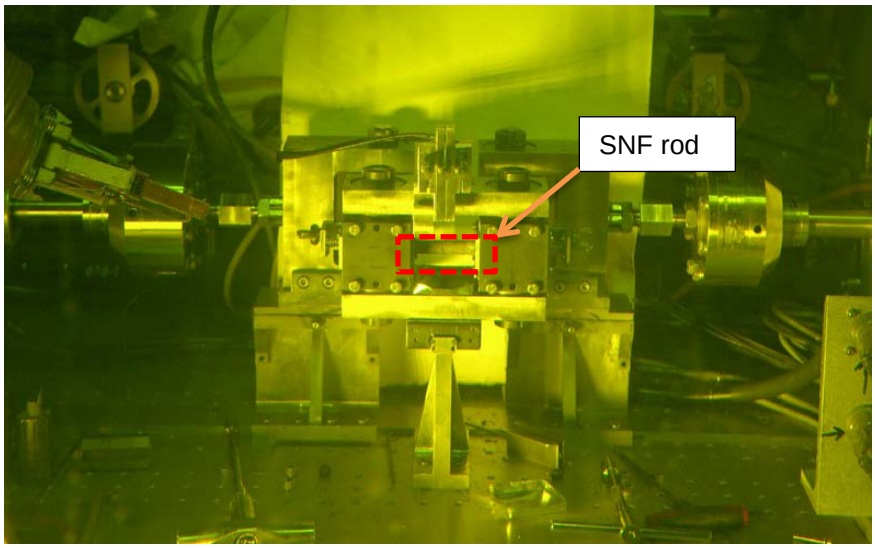

Fig. 80. Front view of CIRFT installed in ORNL hot cell.

During CIRFT system development, a series of finite element analyses were conducted using ABAQUS code to evaluate the testing system dynamic performances and to optimize system design [1–3]. For the final design, an FEA model was established to verify the system dynamic response and efficiency(Fig. 81).

The major components shown in Fig. 80 were modeled as the real geometries. The ball bearings were simplified as pivot pins to eliminate unnecessary geometric details, and the connecting parts can rotate through the simplified ball bearings. The rigid arms featured a cross section 2 in. × 2 in. (50.8 mm × 50.8 mm) and 6.2 in. (157.5 mm) in length. There was a hole in the arms for the fuel rod, which was located 1.2 in. (30.48 mm) away from the inside ends of the arms (Fig. 81).

The connectors had a width of 2 in. (50.8 mm), a thickness of 0.7 in., (17.8 mm) and a length of 6 in. (152.4 mm). The pivot pins at the connecting plates had a diameter of 0.8 in. (20.3 mm), and the pivot pins at the links had a diameter of 1 in. (25.4 mm). A 6 in. (152.4 mm) long fuel rod was oriented horizontally with a gauge section of 2 in. (50.8 mm). The cladding had an ID of 0.372 in. (9.449 mm) and an OD of 0.436 in. (11.074 mm).

The inside fuel pellets were modeled as a single equivalent rod with the same diameter and length as the ID and length of the cladding. The compliant layers were used between the fuel rod and the wall of specimen holes to control and eliminate contact damage. The links were U-shaped and measured 2 in. (50.8 mm) × 4 in. (101.6 mm) × 4.4 in. (111.8 mm).

A harmonic sine wave translational force or displacement in Z-direction was applied in the middle of each side of each universal testing machine link to simulate the loading from the Bose dual-linear motors. From the driving point to the fuel rod location, there was a 4 in. (101.6 mm) effective loading length in each rigid arm.

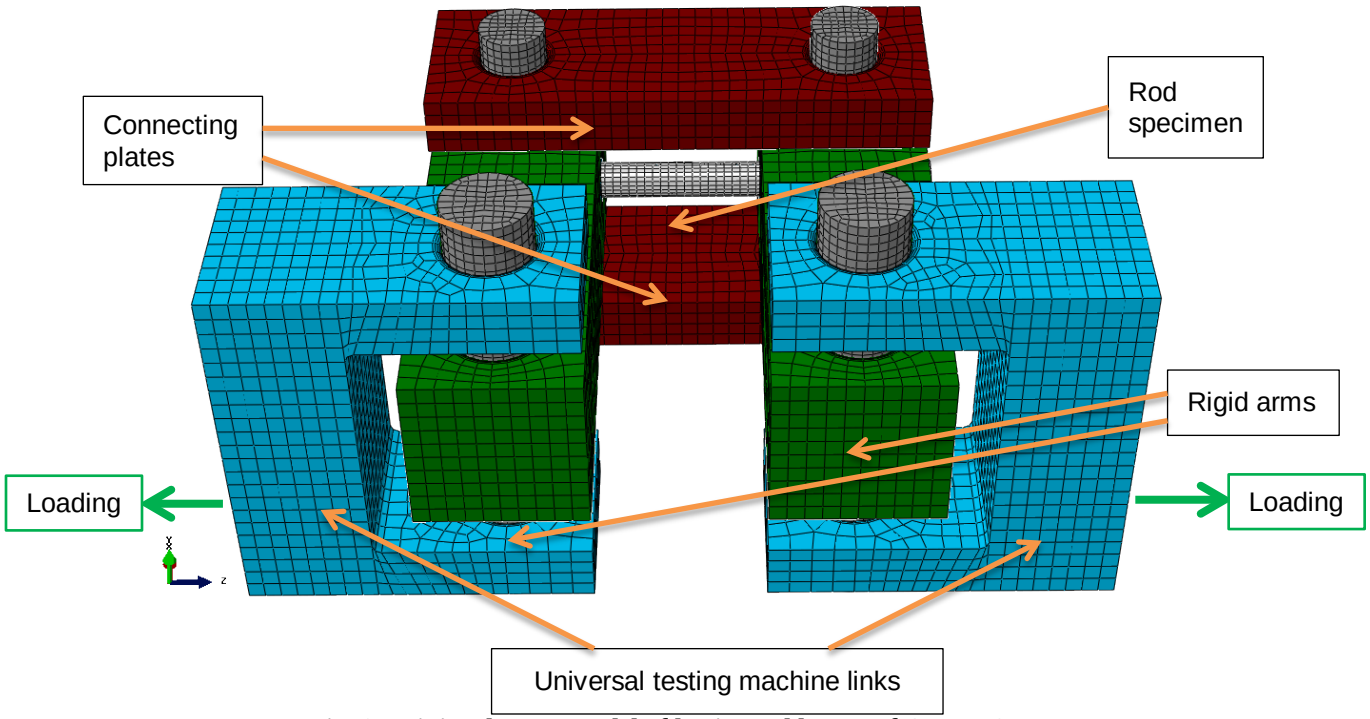

Fig. 81. Finite element model of horizontal layout of ORNL CIRFT.

Two loading cases were studied to verify the system's dynamic response and efficiency. The harmonic sine wave force of 22.5 lbf (100 N) with 5 Hz or 10 Hz frequency was imposed on the testing links as shown in Fig. 81. The dynamic deformation responses of the CIRFT system in terms of stress distribution are illustrated in Fig. 82. The CIRFT system transferred the translational linear motion of universal testing machine links into the bending of the fuel rod through the loading arms' closing and opening actions. The maximum von Mises stress of 12.12 ksi was observed at the fuel rod (pellets and cladding assembly) in the CIRFT system operation, which indicates that CIRFT system efficiently transferred dynamic loading energy into the flexural bending mode of the fuel rod. This also ensured maximum stress occurred in the 2 in. gauge section. At the fuel rod, the von Mises stress profiles show symmetry distributions across the rod neutral axis. This represents a pure bending behavior of the deformed rod, as expected.

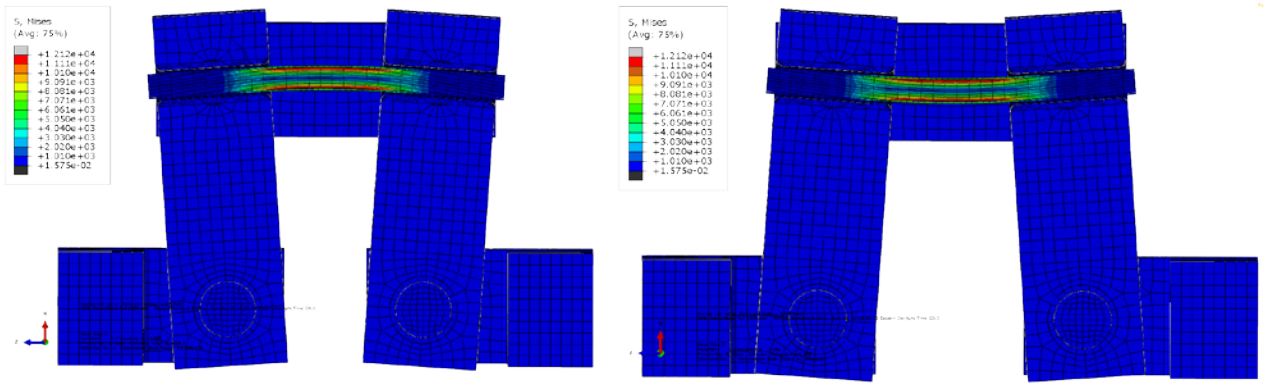

(a) arms close (b) arms open

Fig. 82. Von Mises stress distribution in CIRFT system under 100 N harmonic sine wave of 5 Hz.

The efficiency and stability of the CIRFT system needs additional confirmation to verify the system design, specifically for transferring or transmitting translation forces into the bending moment of the fuel rod at different vibration frequencies. This was performed with FEA simulations on the CIRFT system, including the linking surrogate rod, under two targeted loads at vibration frequencies of 5 and 10 Hz for comparison. If the evaluated transmitted bending moment on the surrogate rod is similar to that anticipated, this will further confirm the CIRFT system can efficiently overcome energy dissipations from system inertia and system damping to accurately project the targeted bending loading onto the linking surrogate rod.Fig. 83 shows the resultant longitudinal stress profiles induced by bending for both 5 Hz and 10 Hz with 100 N force loading cases. Results indicate that a pure bending state was achieved. By integrating longitudinal stresses over the rod's cross section areas, the resultant bending moments on the fuel rod can be estimated. For the sine wave force of 22.5 lbf with 5 Hz and 10 Hz loading cases, the FEA estimated bending moment is 91.6 lbf-in and 95.7 lbf-in., respectively. In theory, the input bending moment on the rod can be directly calculated as 22.5 lbf load force multiplied by the 4 in. loading arm, which is equal to 90 lbf-in. A 1.78% error was observed between projected results and the CIRFT FEA simulation results for the dynamic frequency of 5 Hz case. The FEA results further verify the efficiency of the CIRFT system design.

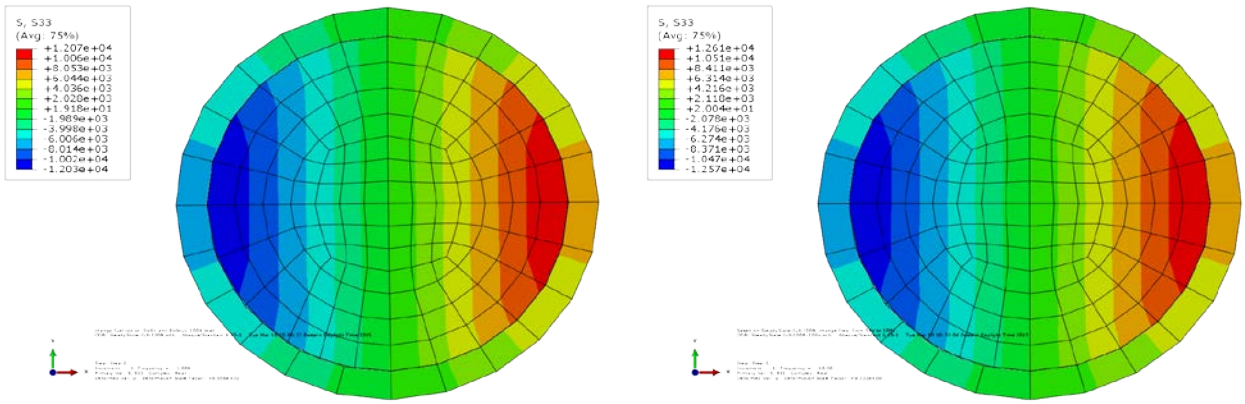

(a) 100N, 5 Hz (b) 100N, 10 Hz

Fig. 83. Longitudinal stress at the middle of fuel rod induced by bending.

16. EFFECT OF CIRFT DRIVING FREQUENCY

A variation was observed after the modification of the first CIRFT had been made for hot-cell delivery. SSAP047 tested under ±250N at 10 Hz failed at a cycle number very different from those under ±250N 5 Hz(1.3×10^3 versus $0.8 - 2.0 \times 10^4$).

The inertia may have an effect during the cycle test, such as the Honeywell and Bose load cells have different weights. A verification test using two surrogate rods made of SS304 showed that (1) the load cells behaved normally under monotonic or quasi-static testing, as validated by the measured Young's modulus, and (2) there is a certain frequency dependence of rod response over the tested range of 1 to 10 Hz. The related results and analysis are presented and discussed in Section 16.1.

16.1 Frequency Response of Test Setup

The resistance of system components to driving duallinear motors is a major concern, especially when needed for small amplitude cyclic testing in hot cells.

16.1.1 Surrogate Rod and Testing Condition

The surrogate rod SS30402 was made of a SS304 tube with an ID of 7.874 mm, an OD of 9.563 mm, and an E = 193 GPa. Because the specimen is a tube-only rod, its flexural rigidity can be estimated according to the given geometrical size and Young's modulus of the materials, and flexural rigidity (EI) = 42.8 Nm^2. Tests were conducted under ±100 N, 1–10 Hz to evaluate the system's response. The load amplitude was selected so the stress of the tube was within the elastic region of the material, and no yielding was involved.

16.1.2 Results of SS30402 Specimen

Two runs of the tests were carried out to examine the repeatability of data. One set of input-output is shown in Fig. 84, and part of the data were smoothed and used in the evaluation. The correction of sensor spacing was not applied in this case because, as demonstrated in the previous stage, the effect of disk contact in the dynamic loading was not significant.

The curvature response of the rod was monitored, and data were acquired periodically. One data set was obtained for curvature and moment ranges for each frequency tested. The moment (input)–curvature range (output) plots as a response of the rod are given in Fig. 85 for all frequencies tested. Whereas the moment range was narrowed between 18.2 and 19.2 Nm, the curvature range systematically increased with the applied frequency.

Because the rigidity of rod EI is given, the curvature can be converted into the moment applied to the rod. Therefore, the moment applied to the rod as output and that applied to the U-frame as input can be correlated. The gain defined as a ratio of output moment to input moment is given in Fig. 86 as a function of frequency. It can be seen that the data are quite repeatable, and the gain is about 5 Hz, which is being used in the hot-cell cyclic test. A thorough understanding of the system is needed to confirm these observations.

16.2 Summary

The SS304 tube-only surrogate rod was tested as a calibration rod under a defined load amplitude of 1, 5, and 10 Hz frequencies. The frequency response of the rod was observed in the tested range, and the data are repeatable. It has been shown that the gain of the system was around one at 5 Hz, which is being used in the hot-cell CIRFT evaluations.

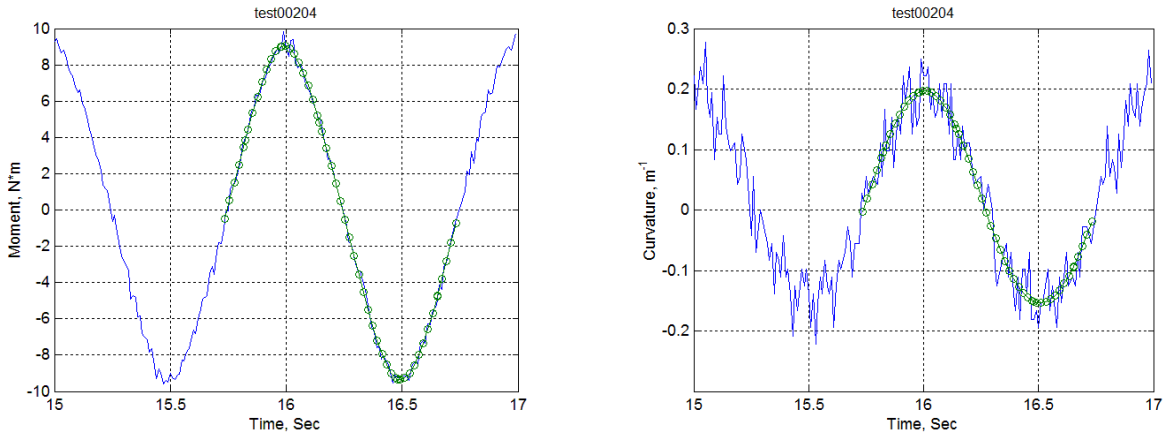

(a) (b)

Fig. 84. (a) Applied moment (b) and curvature based on tests at 1 Hz, SS30402. (Smoothing was applied to both signals; one-period data block was used in characterization.)

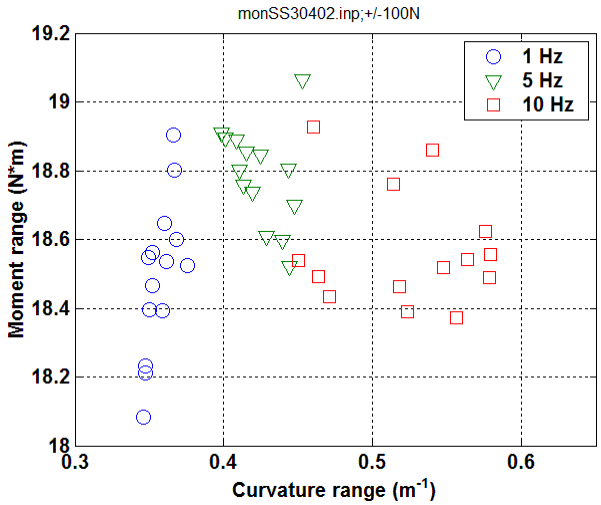

Fig. 85. Scatter plot of the moment range and curvature range based on the first run (SS30402).

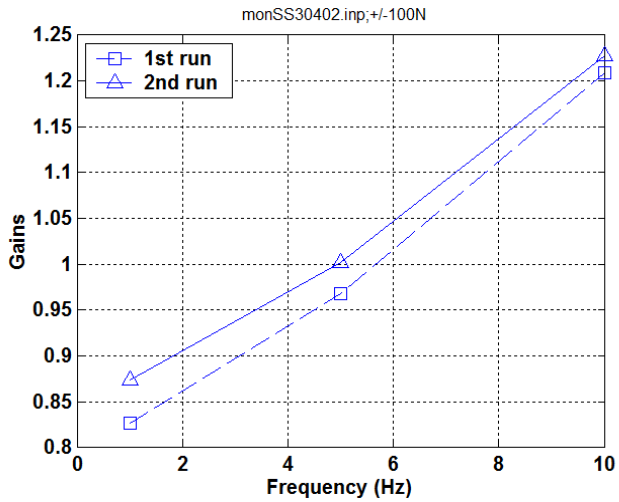

Fig. 86. Gain as a function of frequency based on results of SS30402.

17. CONCLUSION

General observations from CIRFT evaluations include

- The fuel pellet provided strength (flexural rigidity) to the fuel/claddingsystem
- When the fuel is fatigued to failure, the failure occurs or initiates primarily at the pellet-pellet interface
- In dynamic CIRFT evaluations, fuel pellets retain their shape (dishing and chamfering is evident) and do not become fragmented—very little residue is released from rods that are broken into two pieces
- Considering the complexity and nonuniformity of the HBU fuel cladding system, it was significant to find the strain or equivalent stress-to-failure data for the SNF was characterized by a curve expected of standard uniform materials
- It was significant to find that the HBU HBR exhibited an endurance limit, if an endurance limit is defined by survival of $>10^7$ cycles
- Pellet-clad-interaction includes pellet-clad interface bonding efficiency
- Hydrogen concentration does affect SNF system strength
- The SNF rod system has significant stress concentrations and residual stress distributions
- Transient shocks of NCT-induced accumulated damage can significantly reduce the SNF fatigue lifetime
- In addition to the fatigue strength data, fracture toughness data of the SNF system is also essential for the SNF vibration reliability study, especially in a high-rate loading (NCT transient shocks) arena

The more specific findings from this report are stated below.

17.1 CIRFT Data Trends and Curvature Data Adjustments

The lessons learned from CIRFT data and curvature data adjustments are outlined below.

1) The equivalent stress collapsed the data points from all of the SNFs into a single zone. A detailed examination, based on the mean trend curves of the corresponding subgroups, revealed, at same stress level, fatigue lives display a descending order as follows: HBR, LMK, MOX. Focusing on the strain, LMK fuel has a slightly longer fatigue life than HBR, but the difference is subtle.
2) The apparent knee point in the curve of moment and curvature or equivalent quantities is more clearly defined for LMK and HBR fuels.
3) Both the 12 in. drop and RHT appears it could have a negative impact on the fatigue life of CIRFT specimens.
4) The effect of the thermal heating treatment on MOX fuel rod was relatively smaller at the higher amplitude, but it became more significant at the low amplitude of moment. Thermal heating treatment extends the fatigue life of MOX specimens. However, for HR4 CIRFT testing of the HBR rod, thermal heating treatments have a negative impact on the fatigue life of the HBR rod. This may indicate that the effect of thermal heat treatment on SNF rods is likely to be material dependent.

5) There is an effect from the contact of the probe on the curvature measurement for current CIRFT evaluations. The effect of the contact can be mitigated by using the sensor spacing correction that is defined between LVDT probes used for curvature measurements.

6) The sensor spacing correction can be determined by using a chisel-type probe. However, this method is limited in its application and cannot be implemented effectively.

7) The sensor spacing correction based on equivalent gauge length has the required flexibility and can meet the demands of application.

8) The correction method based on the equivalent gauge length has been demonstrated in this report in CIRFT data analysis for the dynamic tests on LMK (17), NA (6), and MOX (10) fuel rods.

9) Some important issues, such as the effects of large amplitude curvature, transverse movement of probes, etc., remain to be investigated.

17.2 SNF Dynamic Deformation Simulation Assessments

Modal analysis was performed on the SNF assembly submodel in the frequency domain. The results provided a better understanding of the frequency characteristics of the fuel assembly submodel. The fundamental mode of the submodel has a natural frequency of 2.44 Hz, which is also the dominant mode with the highest participation factor ratio. Modes containing odd numbers of half sine waves have higher participation factor ratios than those with even numbers. The modal analysis results for a cradle/cask system model and a concrete block of equivalent mass with the basket/assembly weight model [19] show that the strongest modes are at frequencies 52.4 Hz and 318.1 Hz, respectively. Those are much higher than 2.44 Hz, which is the strongest mode of the fuel assembly submodel. Thus, system models with different structural detail levels have significantly different natural frequency characteristics.

In the time domain, the transient dynamic simulation consists of two stages: (1) an initialization stage to establish contact due to gravity, and (2) the second stage for transient dynamic loading. During the second stage, the acceleration as a sine waveform or impulse signal was used to represent normal transportation excitation or shock excitation for transient dynamic analysis. The dynamic response of the fuel assembly submodel in the initialization stage shows that intermediate spacer grids rest on the basket floor after sagging due to gravity, but the top and bottom spacer grids do not. The maximum stress of 41.6 ksi occurs at the guide tube, but there is no yielding in the system. Maximum contact pressure occurs at the location where the intermediate spacer touches the basket, and the pressure level is low.

A 0.5 g sine wave acceleration excitation represents normal transportation vibration. The dynamic responses of fuel assembly submodel under the vibration of 0.5 g sine wave acceleration shows system stress level is higher than in the initial stage. After normal transportation vibration, the fuel rod, guide tube, spacer grids and basket did not deform as uniformly as in the initialization stage. Some intermediate spacer grids lost contact with the basket wall. According to the von Mises stress distribution, besides the fuel pellets, the max. stress occurs at the bottom Inconel spacer, where the material yields. The maximum stress in the guide tube reached the yield strength. Yielding on the guide tube occurs at both top and bottom nozzle locations. Results show that the guide tube and spacer grids are at the greatest risk of failure. Due to the horizontal orientation needed for transport, the guide tubes and spacer grids become the major gravity-bearing components, supporting the dynamic loads of the fuel assembly. The integrity of the guide tube and spacer grids critically affects the vibration modes and the vibration intensity of fuel assembly during transport.

Under vibrations of 0.5 g sine wave acceleration, the maximum stress of the claddings is under material yield strength. The basket wall, top, and bottom nozzles yield, and maximum contact pressure occurs at the location where the spacer grid touches the basket floor. The maximum contact pressure level is almost one order magnitude higher than it was in the initialization stage, but it is still low.

A 3 g impulse acceleration excitation represents transient shock during transportation. As in the dynamic response under 0.5 g sine wave acceleration excitation, yielding occurs at the bottom Inconel spacers. The guide tube also yielded at the top and bottom nozzle locations during 3 g transient shock excitation. Thus there were concerns for the integrity of the spacer grids and the guide tube under transient shock loading during NCT. The maximum stress level on the cladding was twice of that under 0.5 g sine wave acceleration excitation near yield strength. The basket, top, and bottom nozzles had reached yield strength. The maximum contact pressure occurred at the location where the guide tube contacts the top clad. The maximum contact pressure level is high at this contacting moment. An issue of concern is that this dynamic contact interaction might form another transient shock loading to the fuel assembly.

To further evaluate the contact's interaction intensity between the fuel rod and the spacer grids induced by impact loading, a 3-D finite element (FE) section model of the detailed leaf spring/dimples has been developed to simulate the impact between the fuel rod and the spacer grids as induced by the cask vibration during transportation. Under the assumed 20 g transient shock, the spring/dimples severely yielded, and the cladding yielded locally during the high speed impact. The outer surface of the cladding wall contacted the dimples. The yield points are on the inner surface of the cladding wall because the bending induced by the impact caused tension there. The contact forces on the spring/dimples estimated from the FEA were high enough to cause significant plastic deformation. The bending moment estimated from the resultant stress on the cladding under 20 g transient shock can be used to define the loading in CIRFT vibration testing for the equivalent condition.

As indicated by the pilot drop test of the SNF CIRFT showed that the impact induced by the drop affected the integrity of the samples. An FEA was conducted to investigate the contact intensity of the test sample during impact. Results from the simulated 1 ft drop of the CIRFT sample revealed that the maximum stress on the cladding at contact locations was 525 MPa, which is more than half of the material yield strength of 906 MPa. The cladding did not yield. However, the residual stress in the cladding affected the fatigue lifetime of SNF testing samples. The contact force was much lower than that estimated on spacer grids under impact induced by 20 g transient shock. Therefore, the CIRFT sample 1 ft drop-induced impact did not reach the intensity of a 20 g transient shock.

The CIRFT system was developed at ORNL to support the SNF transport vibration reliability study. A simulation was conducted to predict the system's dynamic performance. The results show that the CIRFT system efficiently transferred the translational forces into the bending moment on the fuel rod. The von Mises stress distributed symmetrically across the fuel rod's neutral axis represented the rod's pure bending behavior, as expected. Dynamic responses verified the efficiency of the CIRFT system design. The SS304 tube-only surrogate rod was tested as a calibration rod under defined load amplitude at 1, 5, and 10 Hz frequencies. The rod's frequency response was observed to be in the tested range, and the data are repeatable. It has been shown that the gain of the system was approximately one at 5 Hz, which is being used in the hot cell testing.

18. FUTURE WORK

18.1 Remaining Issues with Curvature Measurement Refinement

18.1.1 Small Amplitude Curvature

In CIRFT evaluations, small curvatures usually occur in dynamic tests. The following questions about small curvature measurments still remain:

1) How close are the contact conditions of SS cladding-only surrogate rods to SNF rods?
This question is critical because the contact dictates the sensor spacing used in the curvature calculation. This is mainly because the cladding material, especially the surface conditions of SNF rods, varies from the surface of surrogate rods. The initial engagement and the subsequent contact of LVDT probes with the rod will be affected by these factors.

2) How are curvature measurements impacted by the transverse motions of LVDT probes?
There is a clearance between the measurement probe and the LVDT cylinders, which is designed to ensure a smooth longitudinal motion of the probe within the cylinder. This clearance causes the probe to move in an unavoidable transverse motion, which affects the initial engagement of probe with the rod and the subsequent translational movement of the probe during measurements.

3) What is the effect of driving frequency on curvature measurements?
There is a frequency effect on the response of the bending rod. This effect occurs because the contact of probe against the rod is influenced by the dynamics of system. How this frequency impacts the curvature measurement needs to be addressed.

18.1.2 Large Amplitude Curvature

The following questions about large curvature measurements still remain:

1) How will the pellet-cladding mechanical interaction impact the curvature measurement when the deformation becomes large?
This is obvious because the local plastic deformation can be substantial because of local buckling in compressive side, for instance. This alters the surface condition, which in turn alters the contact of the probe against the rod.

2) How will the transverse motion of the probe be changed with large deformation?
Transverse motions are associated with clearance of LVDT measurement. Large deformation of the rod may close the gap between the measurement rod and the cylinder on one side and open it on other side.

3) How is the correction applicable to the real SNF rods?
The spacing correction relation was developed using a flexible rod made of materials like polycarbonate. This provides a useful approach to investigate the response of the rod system in large deformation cases, but it needs to be justified before being used for CIRFT data analysis.

18.2 SNF Dynamic Deformation Assessment

To continue supporting the study of SNF transport vibration reliability, the following SNF assembly dynamic simulations studies are recommended:

(1) The FEA model can be refined from the geometry and boundary. The SNF assembly sub-mode can be further expanded to apply to a 17 × 17 full fuel assembly with anticipated computational cost. A full-scale model of the targeted fuel assembly will provide more realistic fuel assembly system interactions and their associated boundary conditions, resulting in a more reliable dynamic response prediction outcome. Refining the model can also provide more insight on the transient shock loading effect to the SNF's vibration reliability with increased confidence.

(2) A future FEA effort can also include investigation of the SNF transport cask design to ensure the low vibration intensity transmitted from the cask to the fuel assembly. The effort would analyze optimization of the casks' dimension, cask-fuel assembly system interaction and dynamic stability, and development of an effective train bed-cask-fuel assembly configuration system to mitigate the vibration load intensity transmitted from the rail track bed to the fuel assembly under NCT.

(3) The CIRFT testing protocol can be used to study systematic parameters on the targeted rod systems and to quantify the interface bonding efficiency, as well as the gap effect to the surrogate rod's mechanical properties and surrogate system performance. This would include the flexural deformation amplitude and frequency of the targeted surrogate rod system, as well as the use of FEA to evaluate/project the strain-stress profile of the selected system at the target loading amplitude of NCT. It would also be used to estimate the response of the localized rod system deformation and the intensity level of the stress concentration.

REFERENCES

1. Wang, J.-A. J, H. Wang, T. Cox, and Y. Yan. (2012). *Progress Letter Report on U-Frame Test Setup and Bending Fatigue Test for Vibration Integrity Study (Out-of-Cell Fatigue Testing Development–Task 2.3)*. Oak Ridge, TN: Oak Ridge National Laboratory. Report No. ORNL/TM-2012/417.
2. Wang, J.-A. J, H. Wang, and T. Tan, inventors; Oak Ridge National Lab, assignee. Reversal Bending Fatigue Testing. (2014). United States patent US 8,863,585 B2. Oct. 21, 2014.
3. Wang, H., J.-A. J. Wang, T. Tan, H. Jiang, T. S. Cox, R. L. Howard, B. B. Bevard, and M. E. Flanagan. (2013) "Development of U-frame Bending System for Studying the Vibration Integrity of Spent Nuclear Fuel," *Journal of Nuclear Materials*, 440, 201–13.
4. Wang, J.-A. J., H. Wang, T. Cox, and C. Baldwin. (2013). *Progress Letter Report on Bending Fatigue Test System Development for Spent Nuclear Fuel Vibration Integrity Study (Out-of-Cell Fatigue Testing Development–Task 2.4).* Oak Ridge, TN: Oak Ridge National Laboratory. Report No. ORNL/TM-2013/225.
5. Wang, J.-A. J., H. Wang, B. B. Bevard, R. L. Howard, and M. E. Flanagan. (2013). "Reversible Bending Fatigue Test System for Investigating Vibration Integrity of Spent Nuclear Fuel During Transportation." Paper presented at the International Symposium on the Packaging and Transportation of Radioactive Materials, San Francisco, CA, August 18–23, 2013.
6. Wang, J.-A. J., and H. Wang. (2014). *The Development of Reversible Bending Fatigue Tester and Its Application to High Burn-up Spent Nuclear Fuel Integrity Study under Normal Transportation Vibration*. Oak Ridge, TN: Oak Ridge National Laboratory. Report No. ORNL/TM-2013/573. http://info.ornl.gov/sites/publications/Files/Pub47469.pdf.
7. Wang, J.-A. J., and H. Wang. (2014). *Semi-Annual Progress Letter Report on Used Nuclear Fuel Integrity Study in Transportation Environments*. Report No. ORNL/TM-2014/63. http://info.ornl.gov/sites/publications/Files/Pub48652.pdf.
8. Wang, J.-A. J., H. Wang, and H. Jiang. (2014). *FY14 Status Report: CIRFT Testing Results on High Burnup UNF*. Oak Ridge, TN: Oak Ridge National Laboratory. Report No. ORNL/LTR-2014/310. http://info.ornl.gov/sites/publications/Files/Pub51054.pdf.
9. Wang, J.-A. J., and H. Wang. (2015). *Mechanical Fatigue Testing of High-Burnup Fuel for Transportation Applications.* Oak Ridge, TN: Oak Ridge National Laboratory. Report Nos. ORNL/TM-2014/214 and NUREG/CR-7198.
10. Wang, J.-A. J., H. Wang, H. Jiang, Y. Yan, and B. B. Bevard. (2015). *CIRFT Testing of High-Burnup Used Nuclear Fuel Rods from Pressurized Water Reactor and Boiling Water Reactor Environments*. Oak Ridge, TN: Oak Ridge National Laboratory. Report Nos. ORNL/SPR-2015/313 and M2-FCRD-UFD-2015-000101.
11. Wang, J.-A. J., H. Wang, Y. Yan, R. Howard, and B. B. Bevard. (2011). *High Burn-up Spent Fuel Vibration Integrity Study Progress Letter Report (Out-of-Cell Fatigue Testing Development–Task 2.1)*. Oak Ridge, TN: Oak Ridge National Laboratory. Report No. ORNL/TM-2010/288.
12. Wang, J.-A. J., H. Wang, T. Tan, H. Jiang, T. Cox, and Y. Yan. (2012). *Progress Letter Report on U Frame Test Setup and Bending Fatigue Test for Vibration Integrity Study (Out-of-Cell Fatigue Testing Development–Task 2.2).* Oak Ridge, TN: Oak Ridge National Laboratory. Report No. ORNL/TM-2011/531.
13. Wang, J.-A. J., H. Wang, and T. Tan. (2011). *An Innovative Dynamic Reversal Bending Fatigue Testing System for Evaluating Spent Nuclear Fuel Rod Vibration Integrity or Other Materials Fatigue Aging Performance*. Oak Ridge, TN: Oak Ridge National Laboratory. ORNL Invention Disclosure No. 201102593. DOE Report No. DOE S 124,149.
14. Wang, J.-A. J., H. Wang, B. B. Bevard, R. L. Howard, and M. E. Flanagan. (2013). "SNF Test System for Bending Stiffness and Vibration Integrity." Paper presented at the *International High-Level Radioactive Waste Management Conference*, Albuquerque, NM, April 28–May 2, 2013.

15. Wang, J.-A. J., H. Wang, T. Cox, and C. Baldwin. (2013). *Progress Letter Report on Bending Fatigue Test System Development for Spent Nuclear Fuel Vibration Integrity Study (Out-of-Cell Fatigue Testing Development–Task 2.4)*. Oak Ridge, TN: Oak Ridge National Laboratory. Report No. ORNL/TM-2013/225.
16. Bjorkman, G. (2011). "High Burnup Spent Fuel Testing Program Objectives." Paper presented at the NRC Program Review Meeting, Oak Ridge National Laboratory, Oak Ridge, TN, August 8, 2011.
17. Adkins, H. E., et.al. "Used Nuclear Fuel Loading and Structural Performance Under Normal Conditions of Transport—Demonstration of Approach and Results of Used Fuel Performance Characterization." FCRD-UFD-2013-000325, September 30, 2013.
18. "Special Metals INCONEL Alloy 718," *Matweb* website, accessed November 13, 2015, http://www.matweb.com/search/.
19. Ross, S., N. Klymyshyn, P. Jensen, R. Best, S. Maheras, P. McConnell, and J. Orchard. (2015). "Rail Shock and Vibration Pre-Test Modeling of a Used Nuclear Fuel Assembly." Paper presented at the International High-Level Radioactive Waste Management meeting, Charleston, SC, April 12–16, 2015.
20. "Special Metals T300 Series Stainless Steel," *Matweb* website, accessed November 13, 2015, http://www.matweb.com/search/.
21. McConnell, P., R. Wauneka, S. Saltzstein, and K. Sorenson. (2014). "Normal Conditions of Transport Truck Test of a Surrogate Fuel Assembly." Report No. FCRD-UFD-2014-000066, Sandia National Laboratories, August 29, 2014
22. J.-A. J., Wang, H. Wang, Y. Yan, R. Howard, and B. B. Bevard. (2011). *High Burn-up Spent Fuel Vibration Integrity Study Progress Letter Report (Out-of-Cell Fatigue Testing Development–Task 2.1)*. Oak Ridge, TN: Oak Ridge National Laboratory. Report No. ORNL/TM-2010/288.
23. J.-A. J., Wang, H. Wang, and T. Tan. (2012). *An Innovative Dynamic Reversal Bending Fatigue Testing System for Evaluating Spent Nuclear Fuel Rod Vibration Integrity or Other Materials Fatigue Aging Performance*. Oak Ridge, TN: Oak Ridge National Laboratory. ORNL Invention Disclosure 201102593. DOE Report No. DOE S 124,149. United States patent review no. 13/396,413.
24. Wang, J.-A. J., H. Wang, B. B. Bevard, R. L. Howard, and M. E. Flanagan. (2013). "SNF Test System for Bending Stiffness and Vibration Integrity." Paper presented at the International High-Level Radioactive Waste Management meeting, Albuquerque, NM, April 28–May 2, 2013.

APPENDIX A CIRFT RESULTS FOR LMK BWR SNF

TABLE OF CONTENTS

Measurement and monitoring rigidity curves for LMK BWR SNF

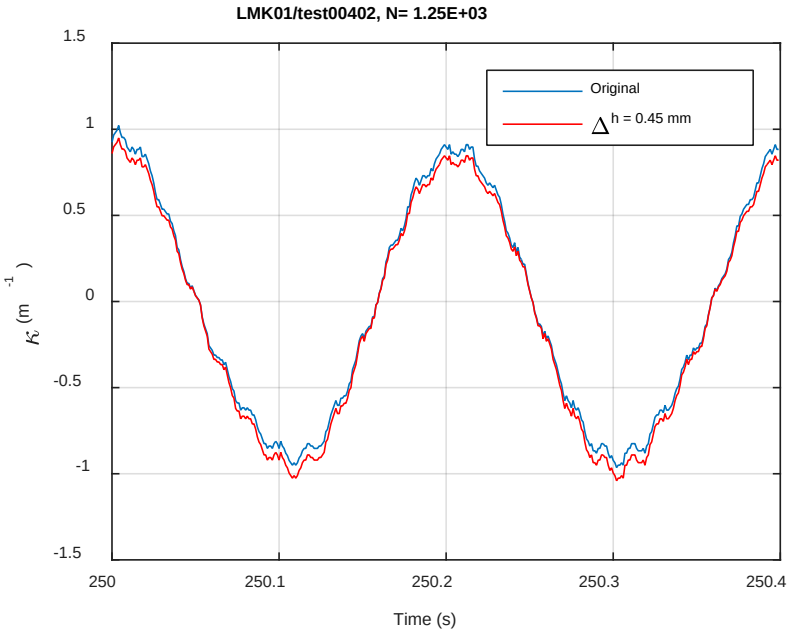
LMK01/test00402, N= 1.25E+03
Original
Δh = 0.45 mm
κ (m-1)
Time (s)
1.5
1
0.5
0
-0.5
-1
-1.5
250
250.1
250.2
250.3
250.4

(a)

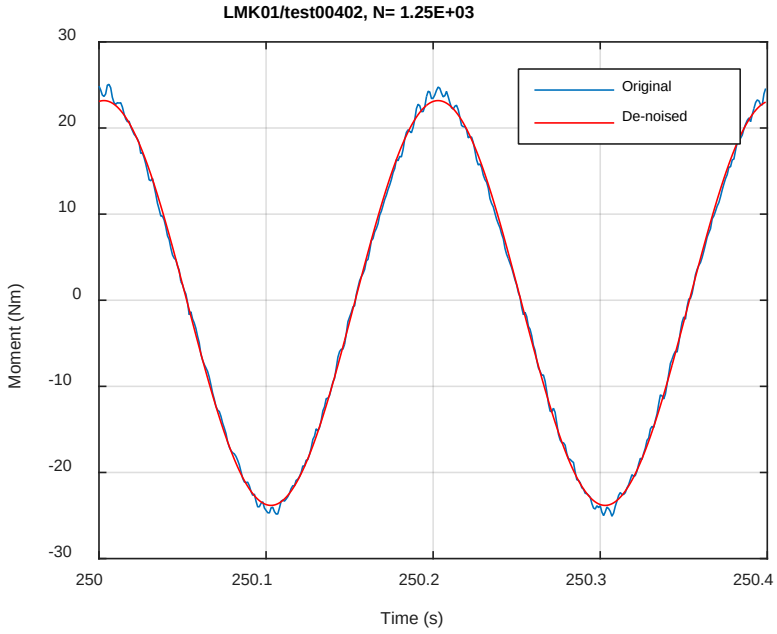
LMK01/test00402, N= 1.25E+03
Original
De-noised
Moment (Nm)
Time (s)
30
20
10
0
-10
-20
-30
250
250.1
250.2
250.3
250.4

(b)

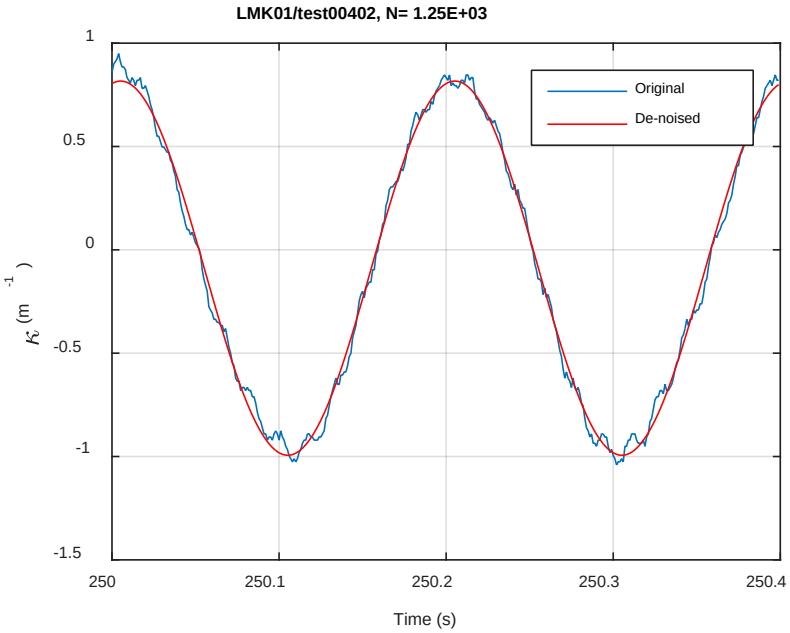

(c)

Fig. A.1. Monitoring-based responses: (a) curvature, (b) moment, (c) curvature, LMK01, 25.40 Nm, Ns = 1.25E+03 cycles.

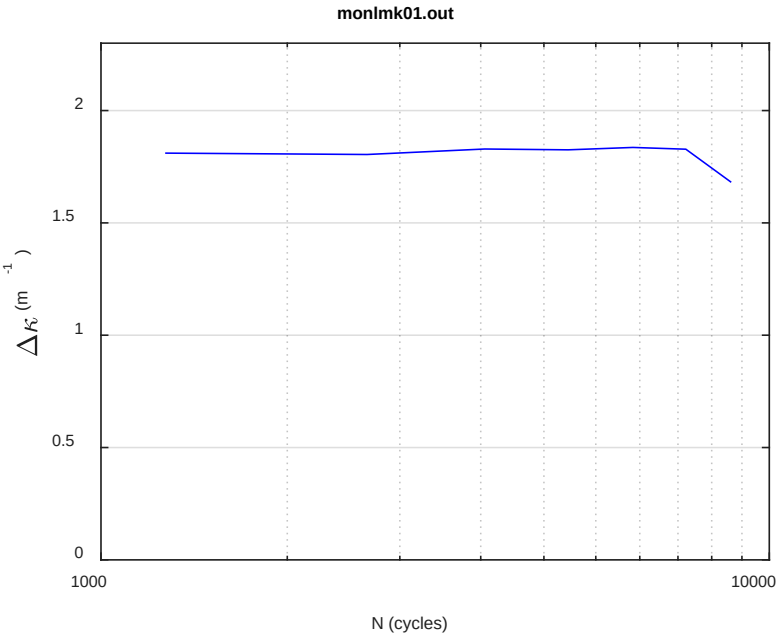
monlmk01.out
2
1.5
1
0.5
0
Δκ (m-1)
1000
10000
N (cycles)

(a)

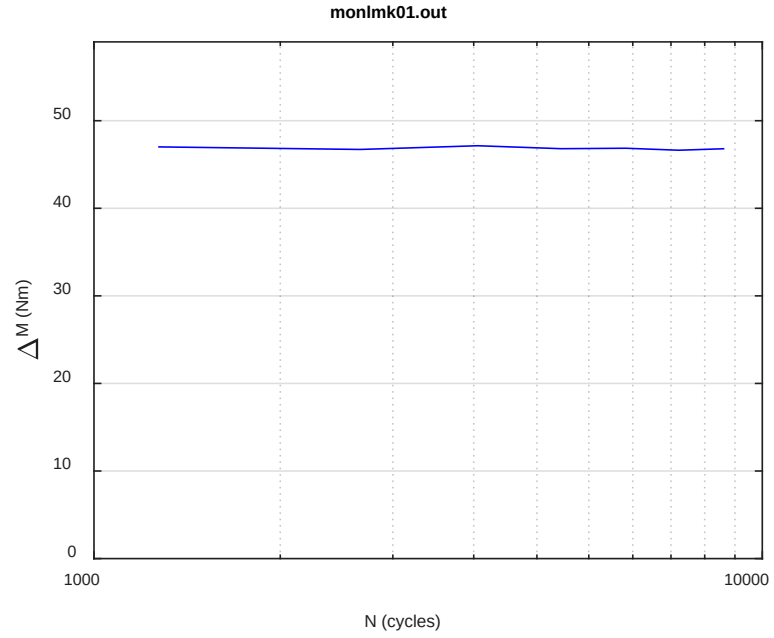
monlmk01.out
50
40
30
20
10
0
Δ M (Nm)
1000
10000
N (cycles)

(b)

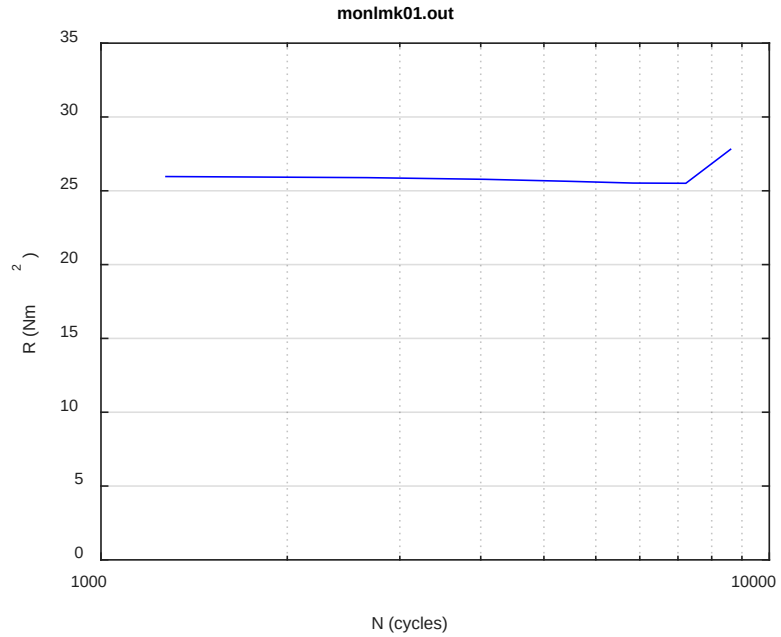
monlmk01.out
35
30
25
20
15
10
5
0
R (Nm 2)
1000
10000
N (cycles)

(c)

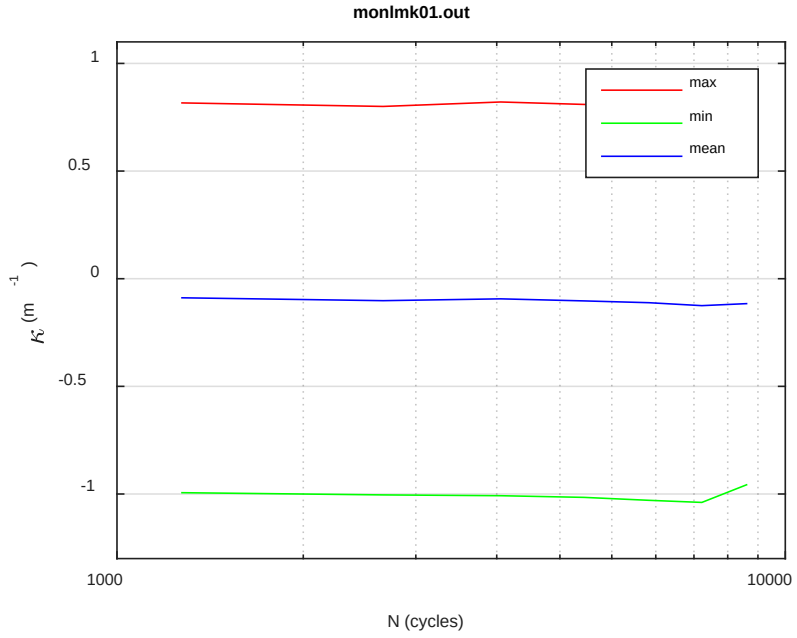
monlmk01.out
1
0.5
0
-0.5
-1
κ (m -1)
max
min
mean
1000
10000
N (cycles)

(d)

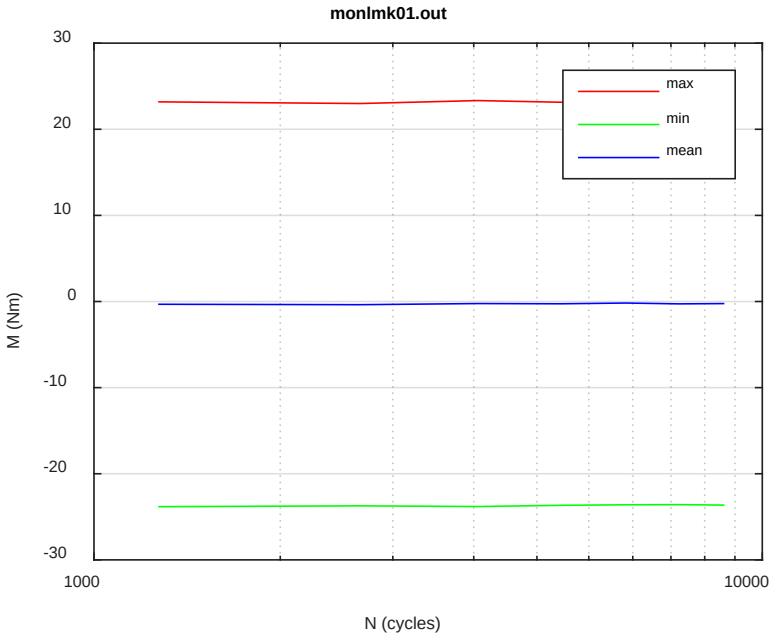

(e)

Fig. A.2. Monitoring-based responses: (a) curvature range, (b) moment range, (c) rigidity, (d) curvature peak/valley, (e) moment peak/valley, LMK01, 25.40 Nm, Nf = 9.40E+03 cycles.

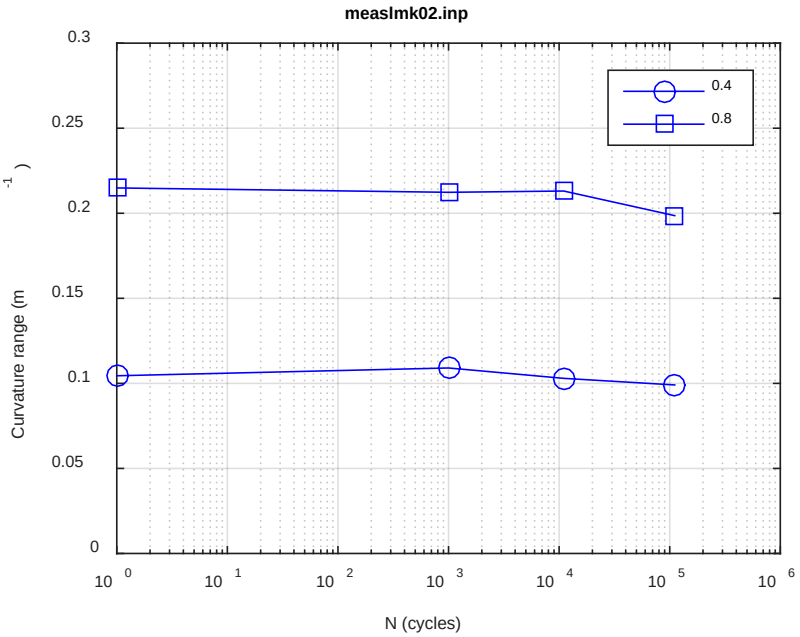
measlmk02.inp
Curvature range (m-1)
N (cycles)
0.4
0.8
0.3
0.25
0.2
0.15
0.1
0.05
0
10 0
10 1
10 2
10 3
10 4
10 5
10 6

(a)

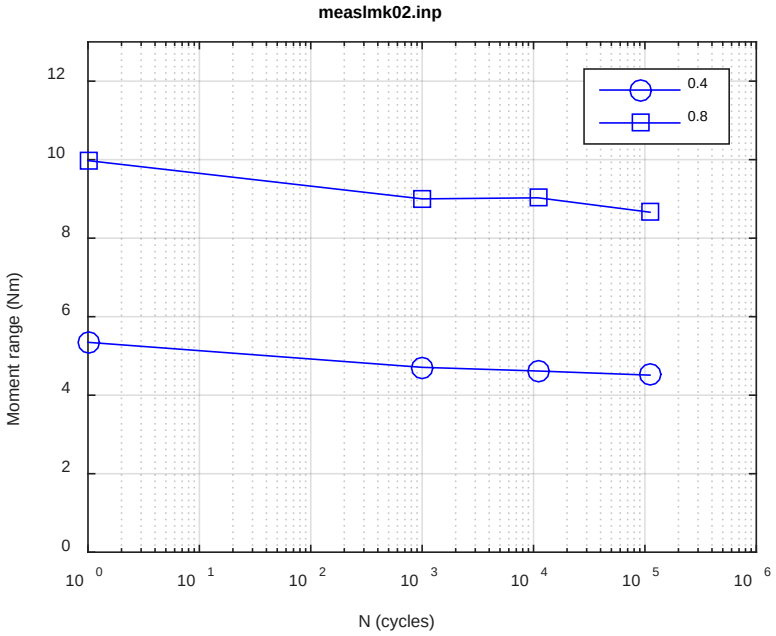
measlmk02.inp
Moment range (Nm)
N (cycles)
0.4
0.8
12
10
8
6
4
2
0
10 0
10 1
10 2
10 3
10 4
10 5
10 6

(b)

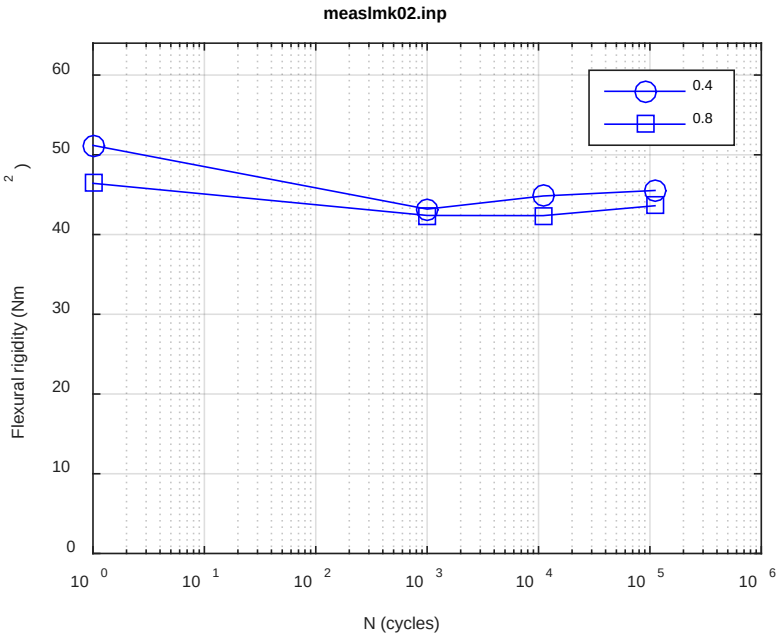
measlmk02.inp
0.4
0.8
Flexural rigidity (Nm^2)
N (cycles)
0
10
20
30
40
50
60
10^0
10^1
10^2
10^3
10^4
10^5
10^6

(c)

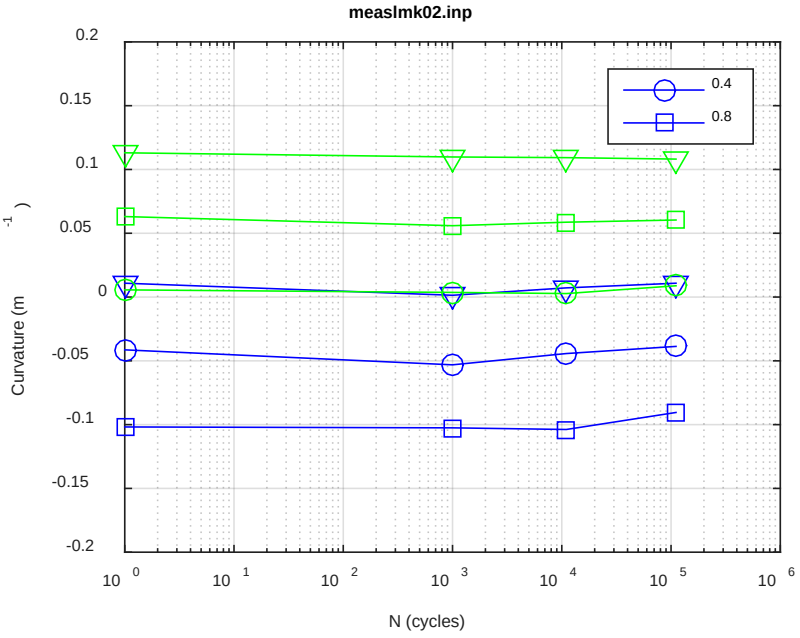
measlmk02.inp
0.4
0.8
Curvature (m^-1)
N (cycles)
0.2
0.15
0.1
0.05
0
-0.05
-0.1
-0.15
-0.2
10^0
10^1
10^2
10^3
10^4
10^5
10^6

(d)

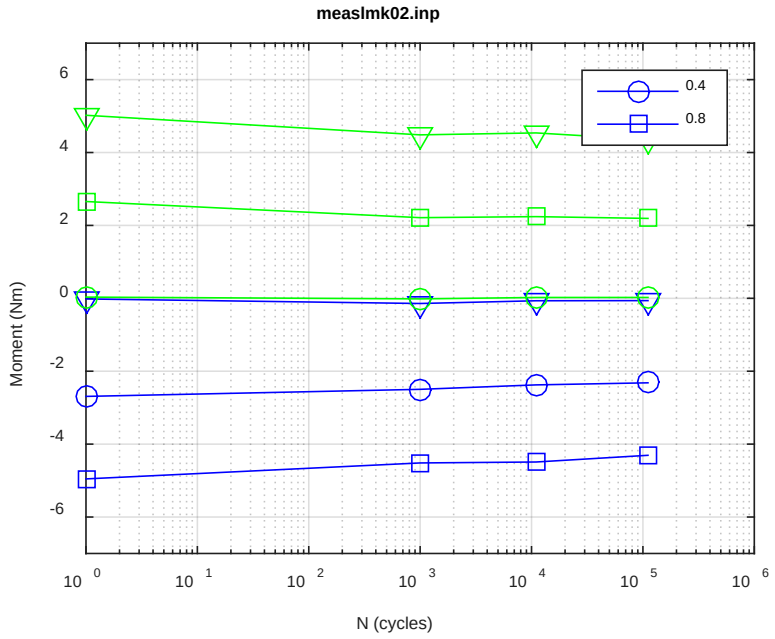

(e)

Fig. A.3. Measurement-based responses: (a) curvature range, (b) moment range, (c) rigidity, (d) curvature peak/valley, (e) moment peak/valley, LMK02, 12.70 Nm.

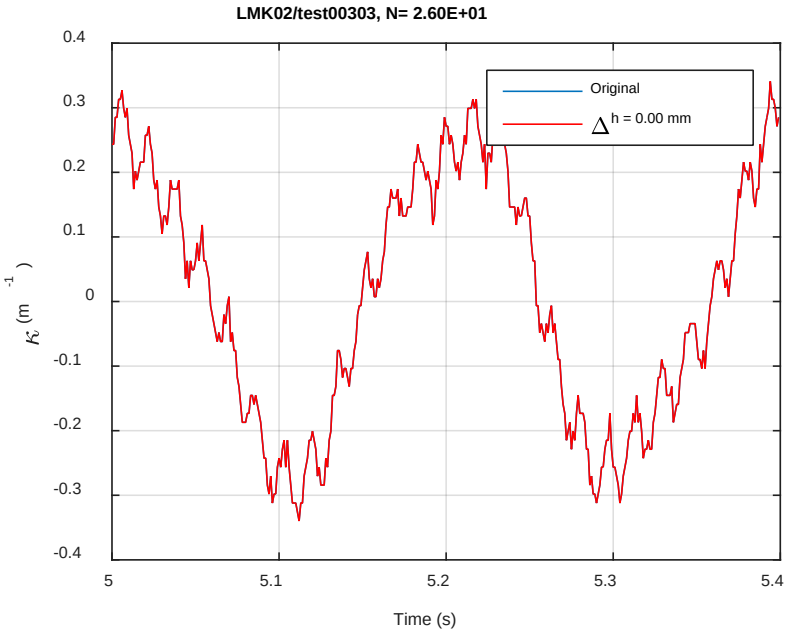
LMK02/test00303, N= 2.60E+01
Original
Δh = 0.00 mm
κ (m-1)
Time (s)

(a)

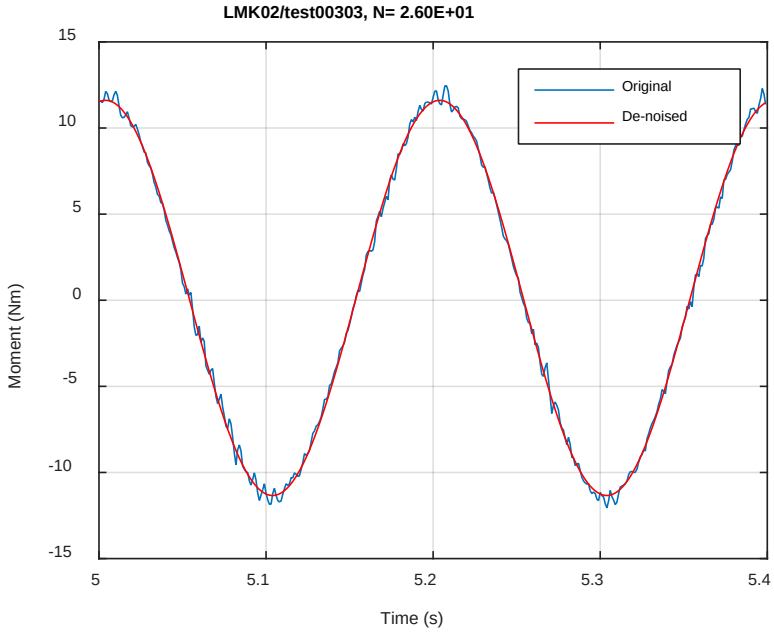
LMK02/test00303, N= 2.60E+01
Original
De-noised
Moment (Nm)
Time (s)

(b)

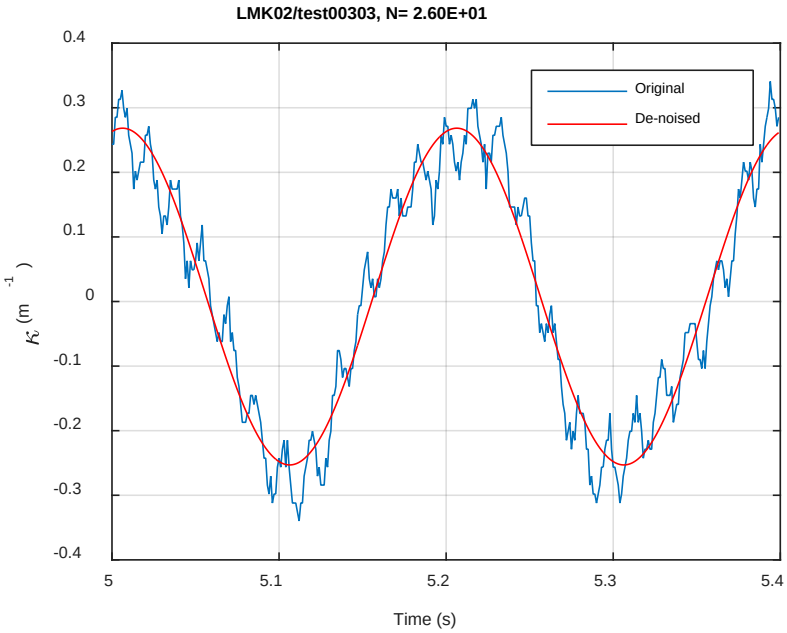

(c)

Fig. A.4. Monitoring-based responses: (a) curvature, (b) moment, (c) curvature, LMK02, 12.70 Nm, Ns = 2.60E+01 cycles.

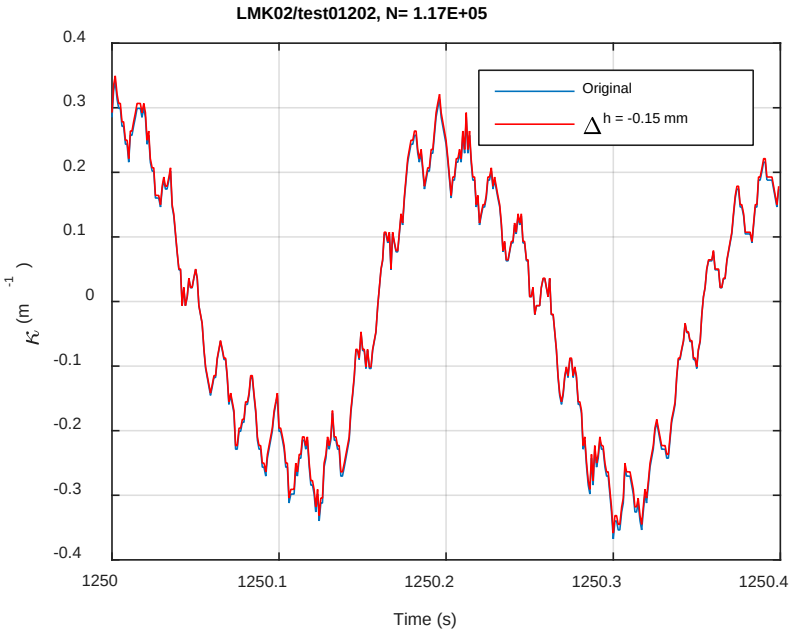
LMK02/test01202, N= 1.17E+05
Original
Δh = -0.15 mm
κ (m-1)
Time (s)
0.4
0.3
0.2
0.1
0
-0.1
-0.2
-0.3
-0.4
1250
1250.1
1250.2
1250.3
1250.4

(a)

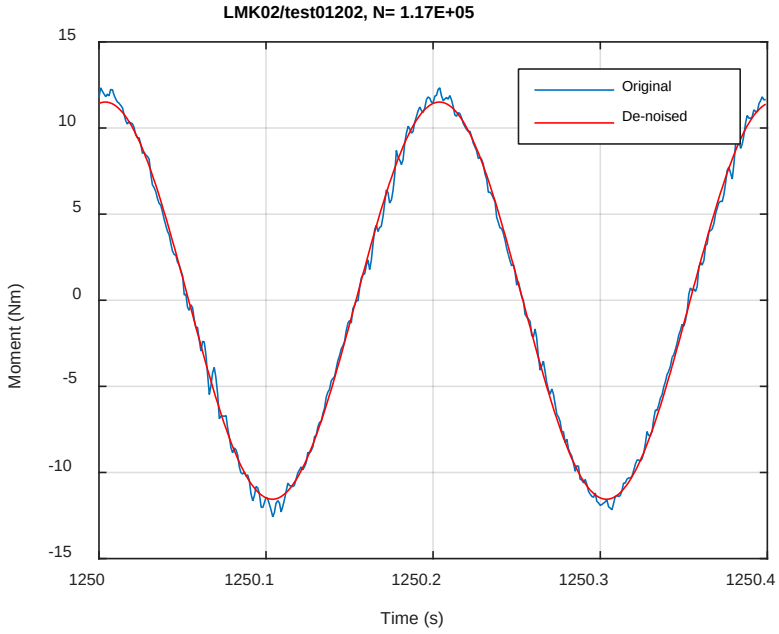
LMK02/test01202, N= 1.17E+05
Original
De-noised
Moment (Nm)
Time (s)
15
10
5
0
-5
-10
-15
1250
1250.1
1250.2
1250.3
1250.4

(b)

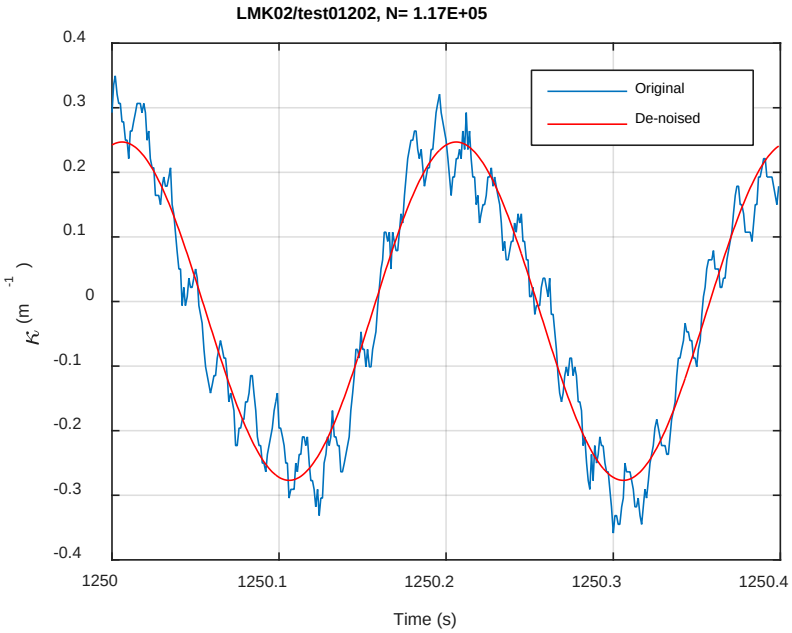

(c)

Fig. A.5. Monitoring-based responses: (a) curvature, (b) moment, (c) curvature, LMK02, 12.70 Nm, Ns = 1.17E+05 cycles.

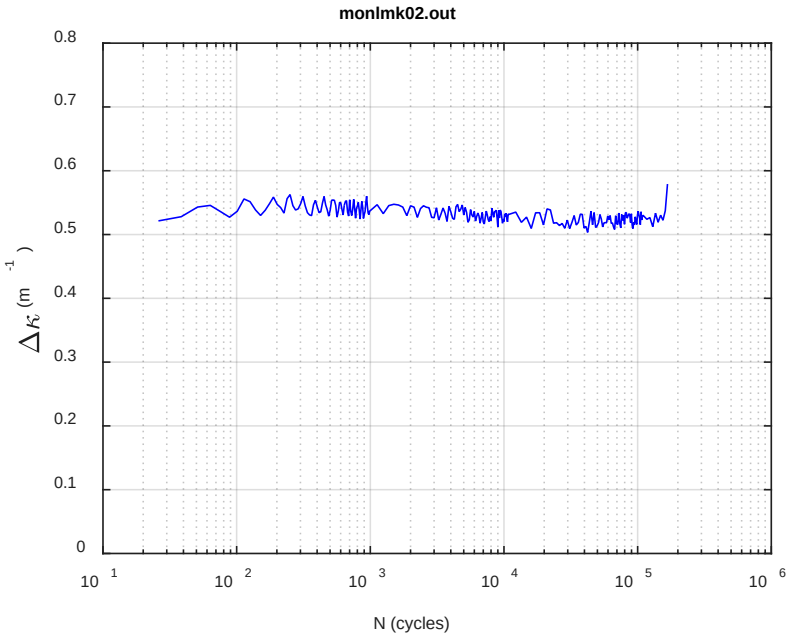
monlmk02.out
0.8
0.7
0.6
0.5
0.4
0.3
0.2
0.1
0
$\Delta\kappa$ (m^{-1})
10 1
10 2
10 3
10 4
10 5
10 6
N (cycles)

(a)

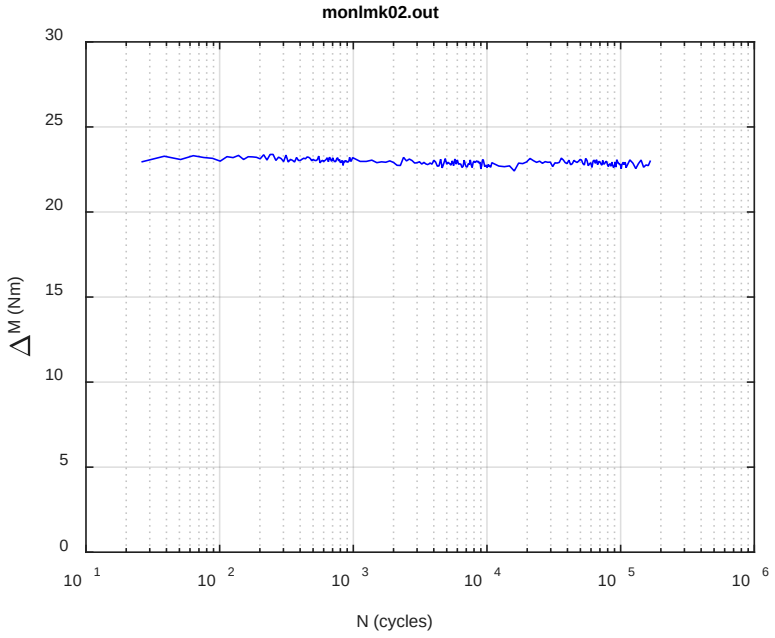
monlmk02.out
30
25
20
15
10
5
0
Δ M (Nm)
10 1
10 2
10 3
10 4
10 5
10 6
N (cycles)

(b)

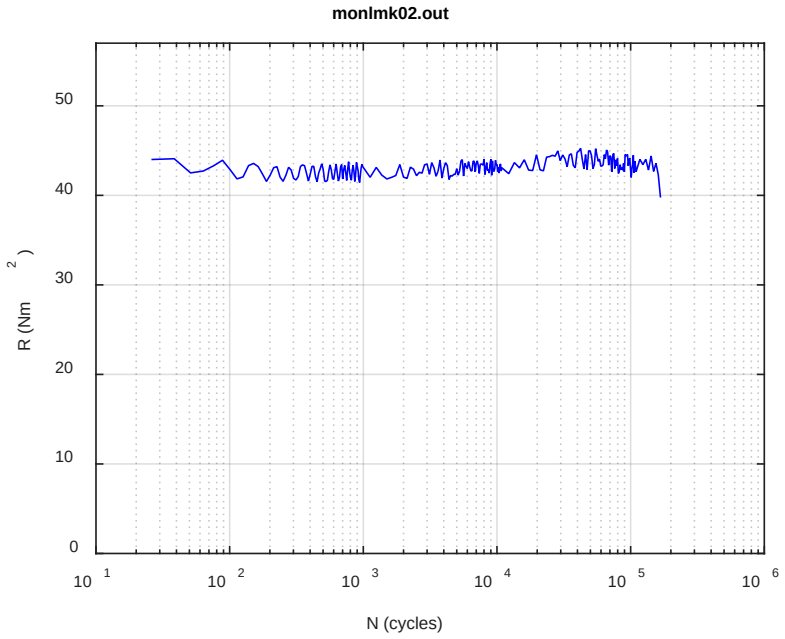
monlmk02.out
R (Nm 2)
N (cycles)

(c)

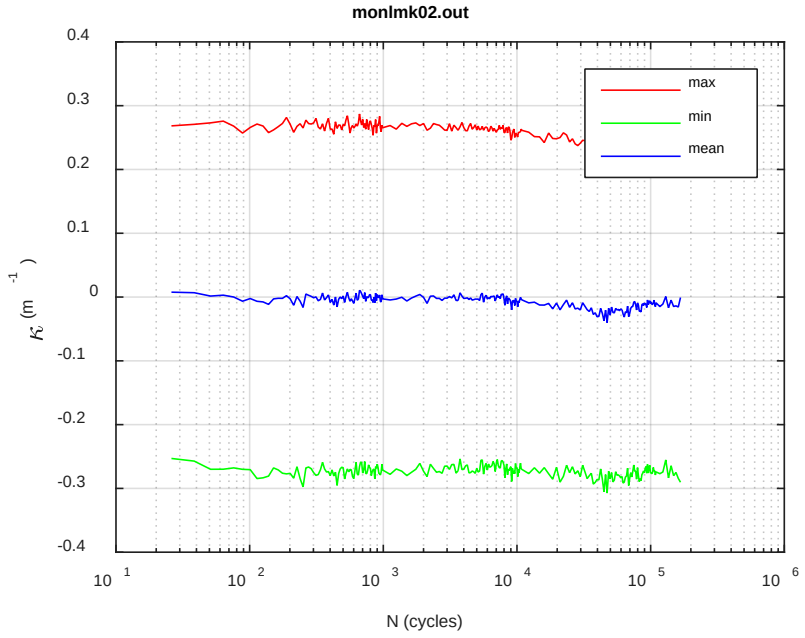
monlmk02.out
max
min
mean
κ (m -1)
N (cycles)

(d)

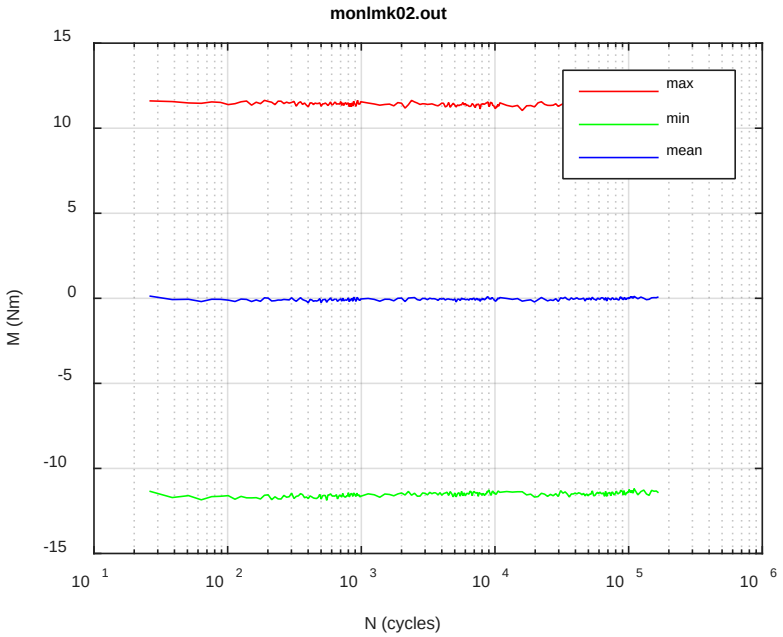

(e)

Fig. A.6. Monitoring-based responses: (a) curvature range, (b) moment range, (c) rigidity, (d) curvature peak/valley, (e) moment peak/valley, LMK02, 12.70 Nm, Nf = 1.71E+05 cycles.

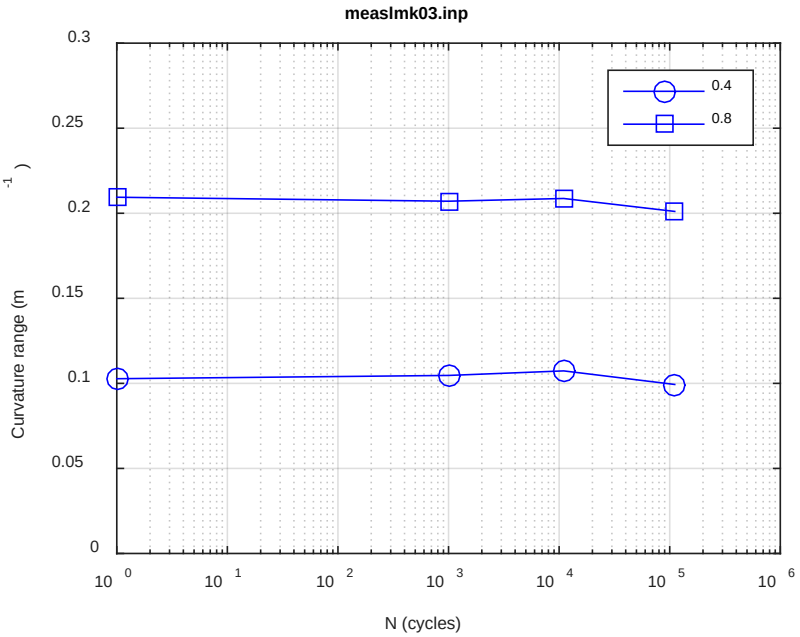
measlmk03.inp
0.3
0.25
0.2
0.15
0.1
0.05
0
Curvature range (m-1)
0.4
0.8
10 0
10 1
10 2
10 3
10 4
10 5
10 6
N (cycles)

(a)

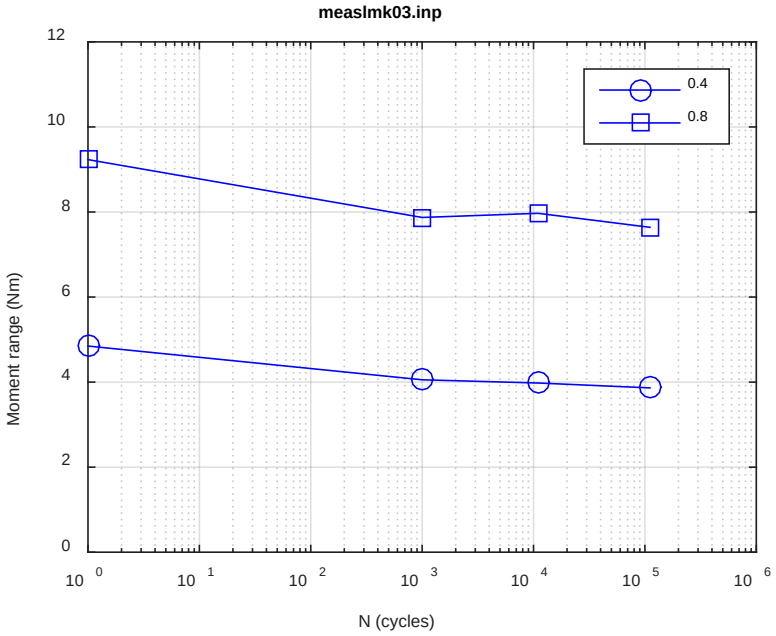
measlmk03.inp
12
10
8
6
4
2
0
Moment range (Nm)
0.4
0.8
10 0
10 1
10 2
10 3
10 4
10 5
10 6
N (cycles)

(b)

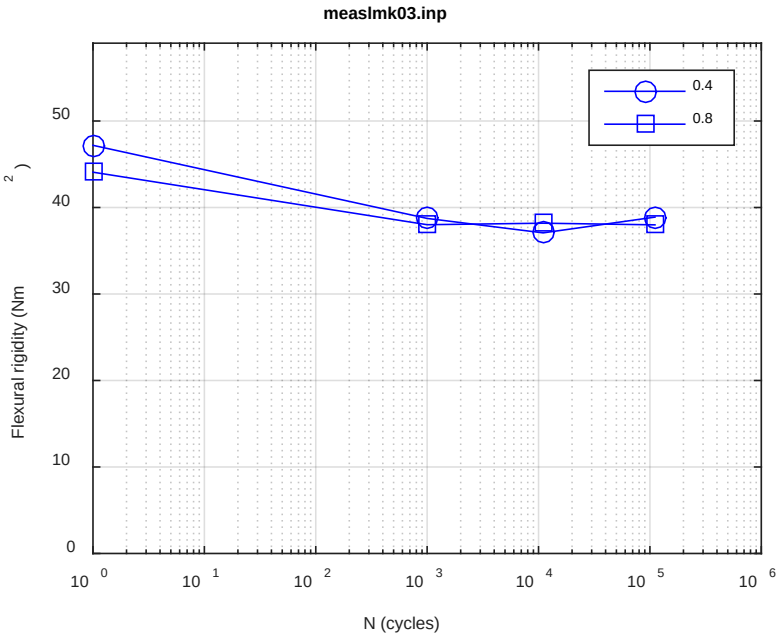
measlmk03.inp
0.4
0.8
Flexural rigidity (Nm 2)
N (cycles)

(c)

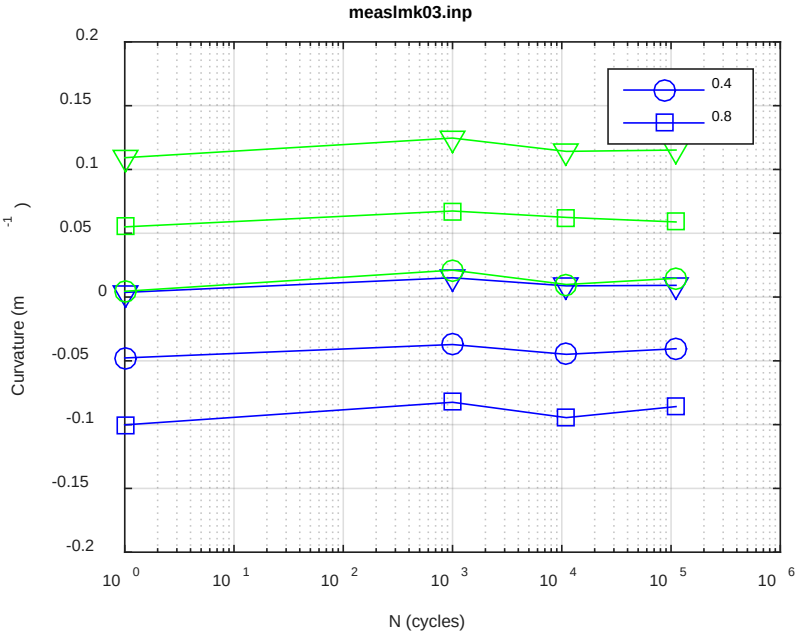
measlmk03.inp
0.4
0.8
Curvature (m -1)
N (cycles)

(d)

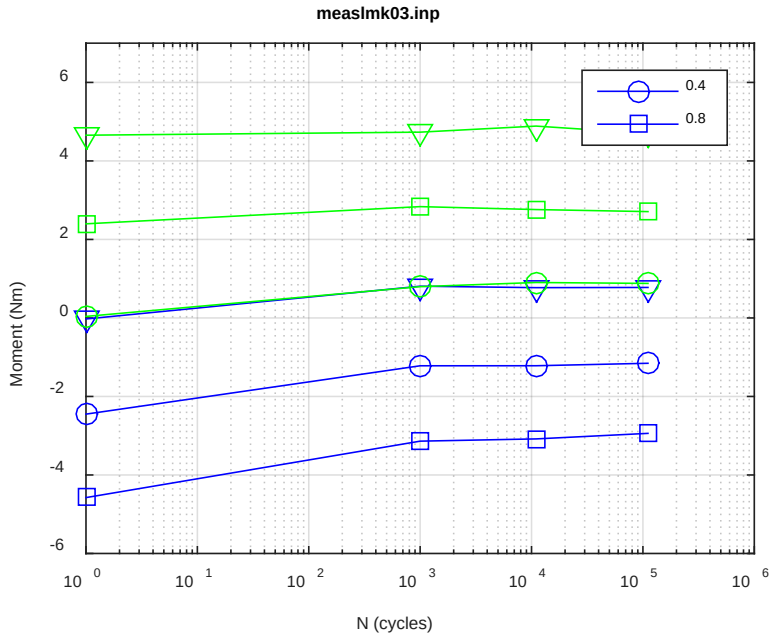

(e)

Fig. A.7. Measurement-based responses: (a) curvature range, (b) moment range, (c) rigidity, (d) curvature peak/valley, (e) moment peak/valley, LMK03, 10.16 Nm.

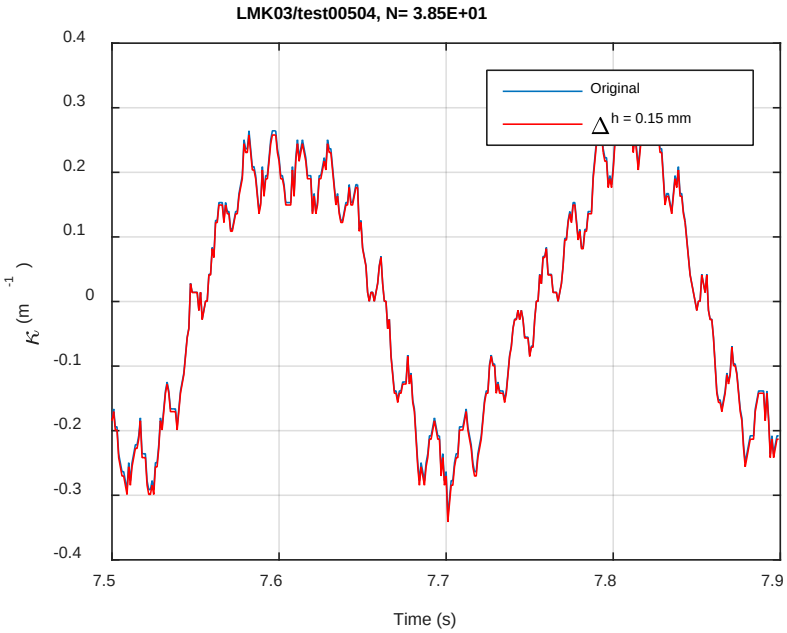
LMK03/test00504, N= 3.85E+01
Original
Δh = 0.15 mm
κ (m-1)
Time (s)

(a)

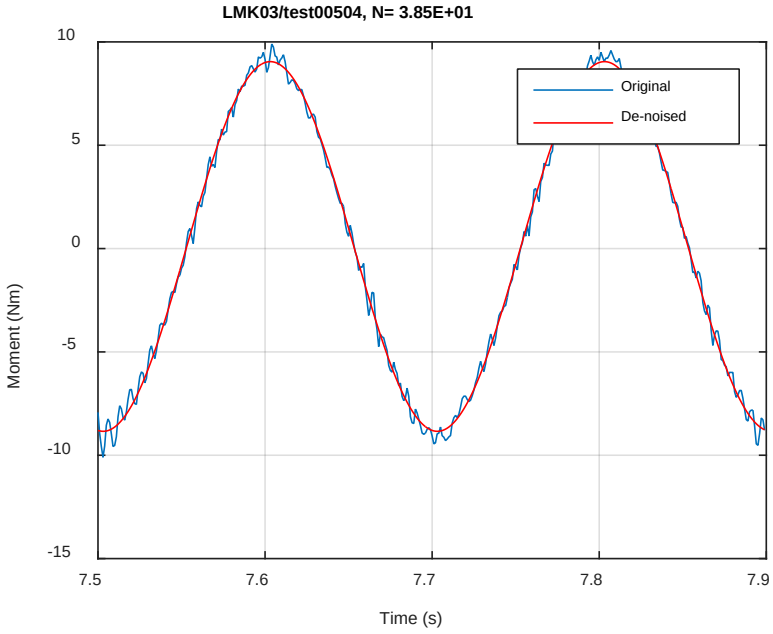
LMK03/test00504, N= 3.85E+01
Original
De-noised
Moment (Nm)
Time (s)

(b)

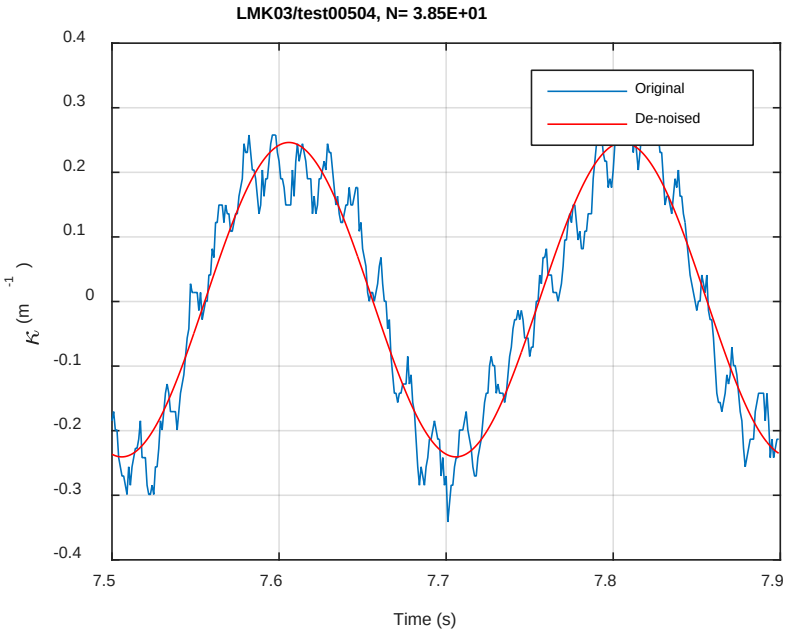

(c)

Fig. A.8. Monitoring-based responses: (a) curvature, (b) moment, (c) curvature, LMK03, 10.16 Nm, Ns = 3.85E+01 cycles.

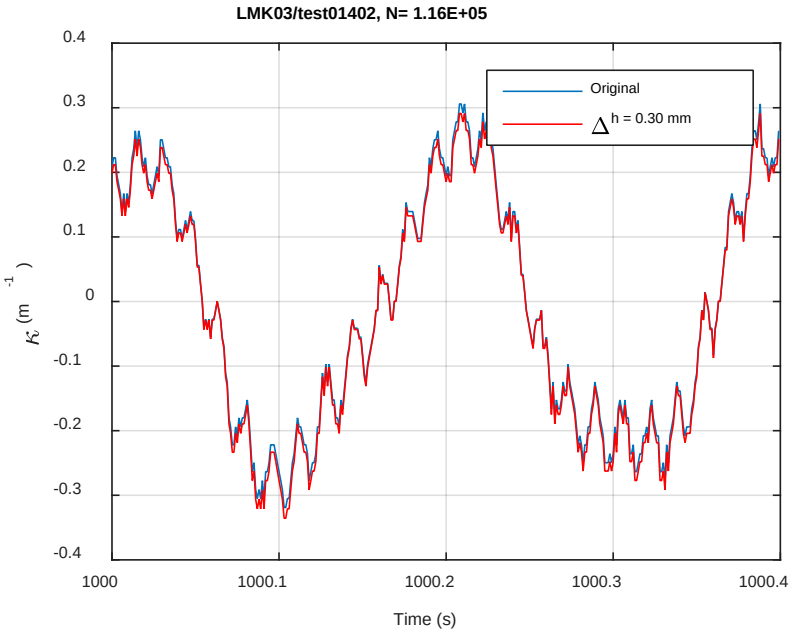
LMK03/test01402, N= 1.16E+05
Original
Δh = 0.30 mm
κ (m-1)
Time (s)
0.4
0.3
0.2
0.1
0
-0.1
-0.2
-0.3
-0.4
1000
1000.1
1000.2
1000.3
1000.4

(a)

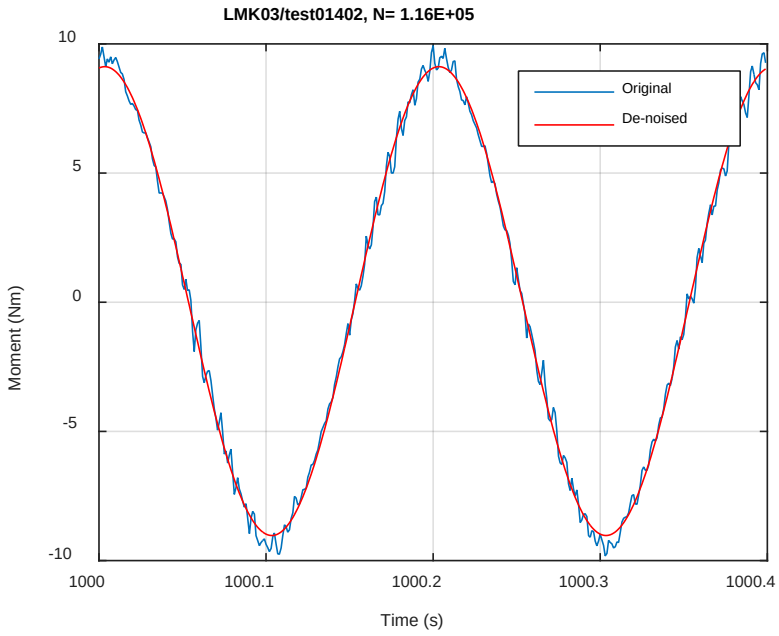
LMK03/test01402, N= 1.16E+05
Original
De-noised
Moment (Nm)
Time (s)
10
5
0
-5
-10
1000
1000.1
1000.2
1000.3
1000.4

(b)

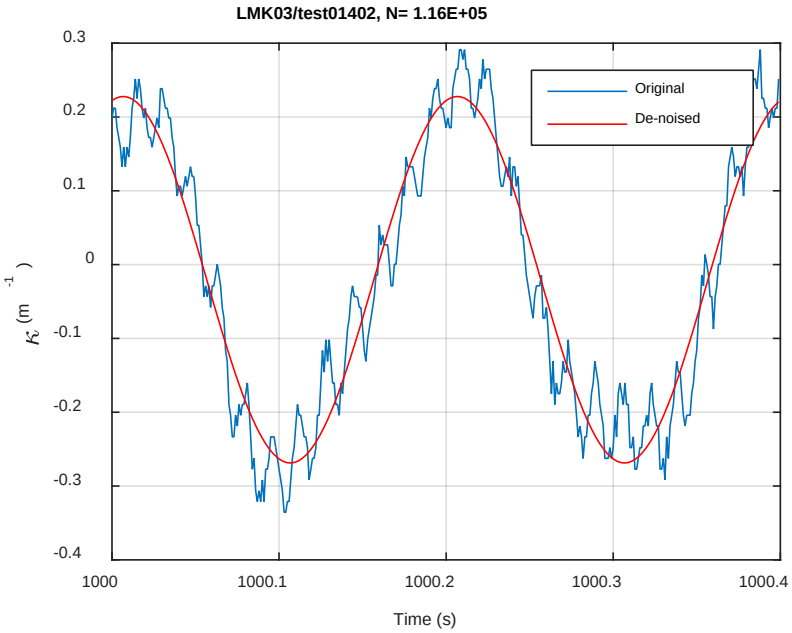

(c)

Fig. A.9. Monitoring-based responses: (a) curvature, (b) moment, (c) curvature, LMK03, 10.16 Nm, Ns = 1.16E+05 cycles.

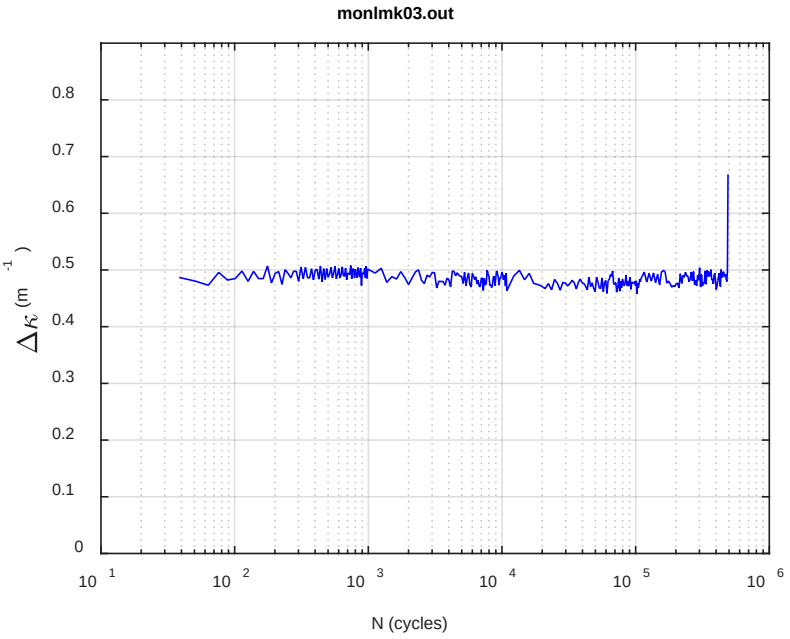
monlmk03.out
0.8
0.7
0.6
0.5
0.4
0.3
0.2
0.1
0
Δκ (m-1)
10 1
10 2
10 3
10 4
10 5
10 6
N (cycles)

(a)

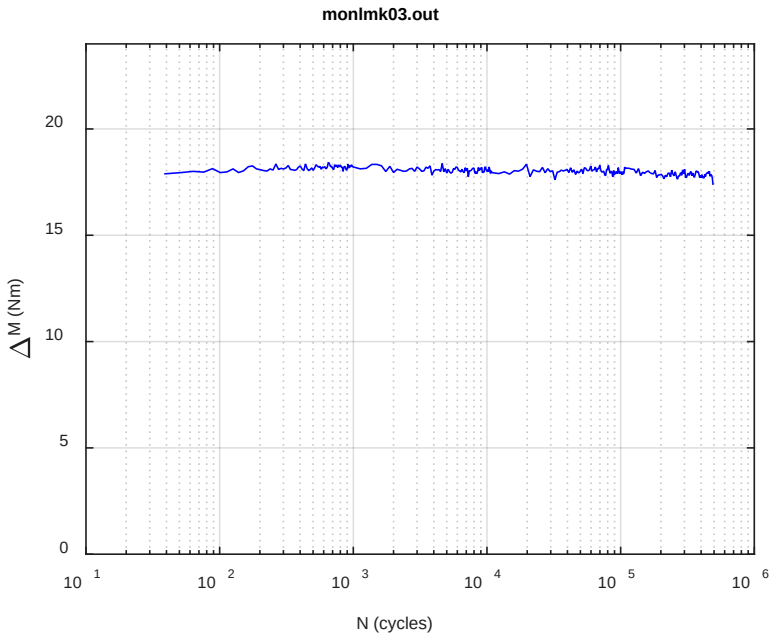
monlmk03.out
20
15
10
5
0
ΔM (Nm)
10 1
10 2
10 3
10 4
10 5
10 6
N (cycles)

(b)

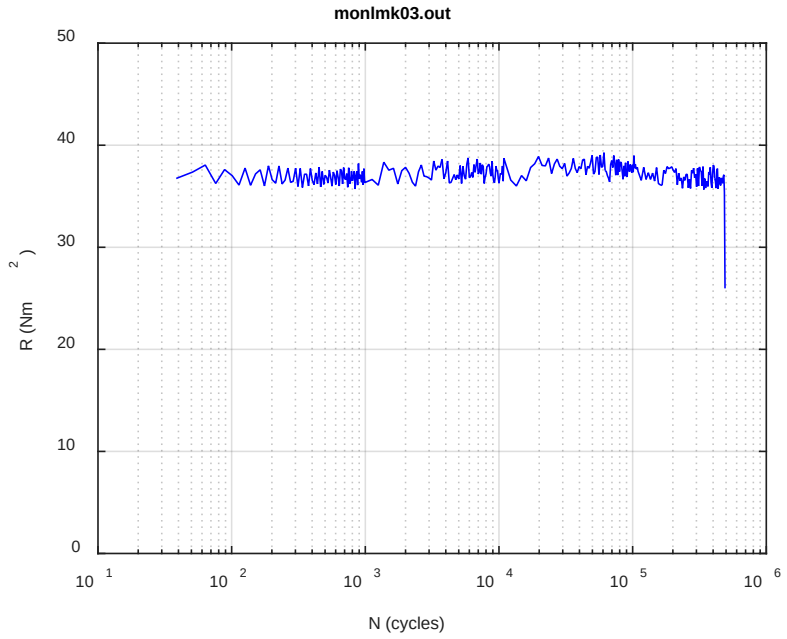
monlmk03.out
R (Nm^2)
N (cycles)

(c)

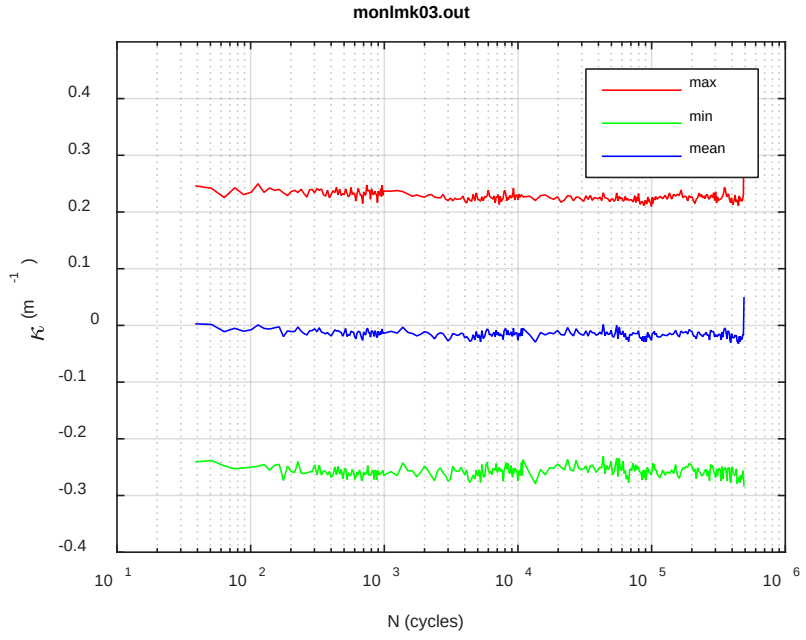
monlmk03.out
max
min
mean
κ (m^-1)
N (cycles)

(d)

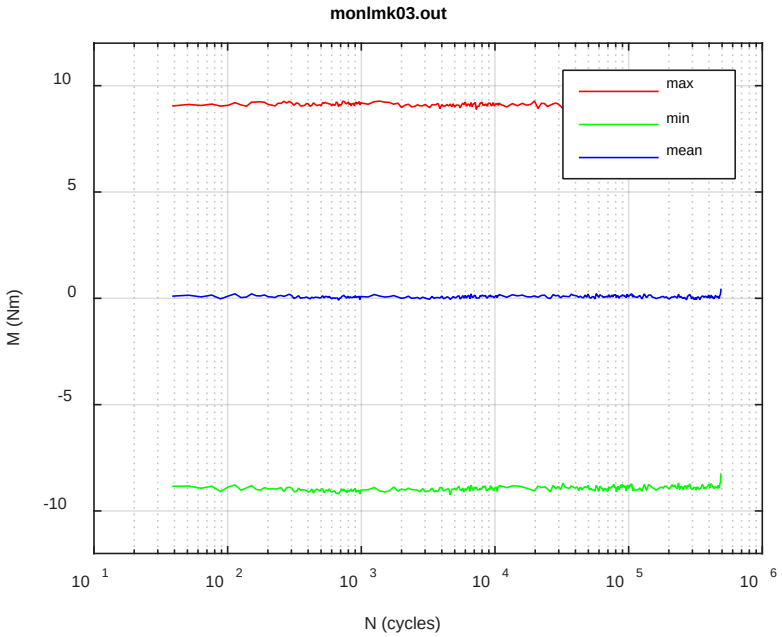

(e)

Fig. A.10. Monitoring-based responses: (a) curvature range, (b) moment range, (c) rigidity, (d) curvature peak/valley, (e) moment peak/valley, LMK03, 10.16 Nm, Nf = 4.92E+05 cycles.

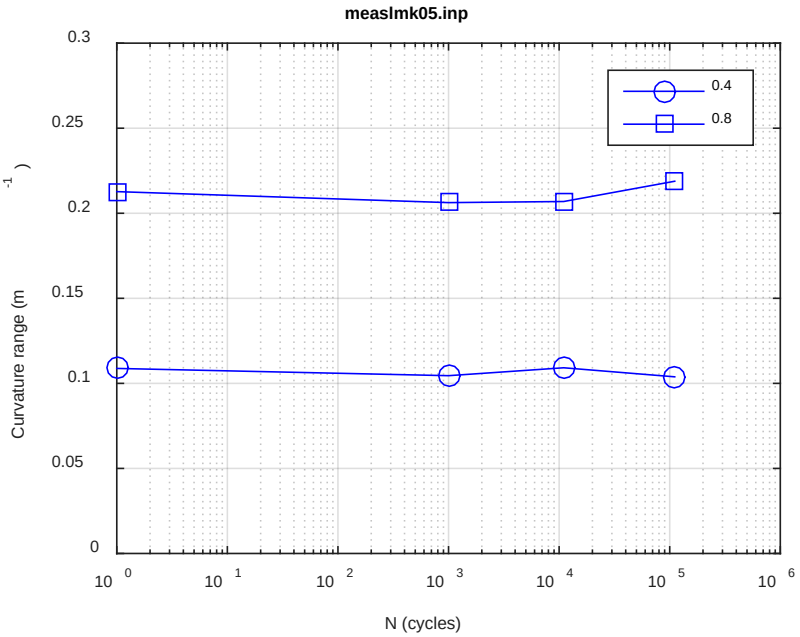
measlmk05.inp
0.3
0.25
0.2
0.15
0.1
0.05
0
Curvature range (m -1)
0.4
0.8
10 0
10 1
10 2
10 3
10 4
10 5
10 6
N (cycles)

(a)

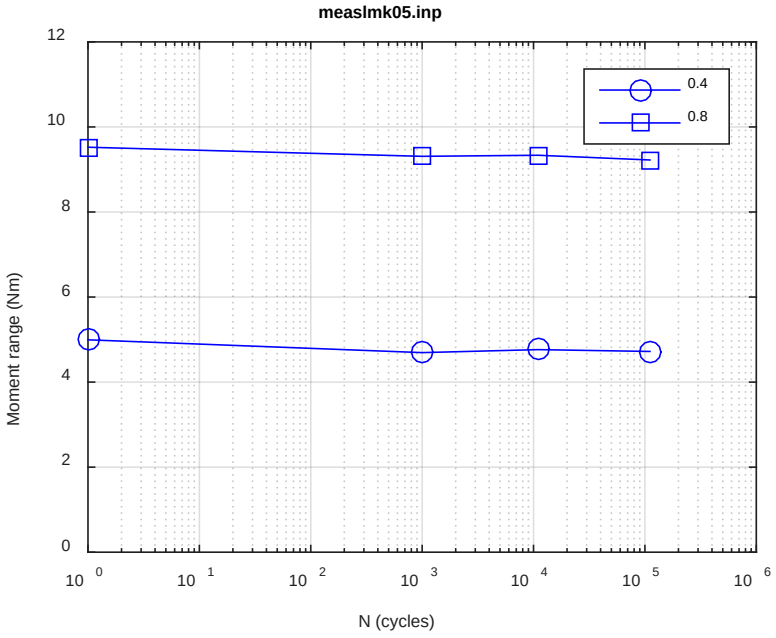
measlmk05.inp
12
10
8
6
4
2
0
Moment range (Nm)
0.4
0.8
10 0
10 1
10 2
10 3
10 4
10 5
10 6
N (cycles)

(b)

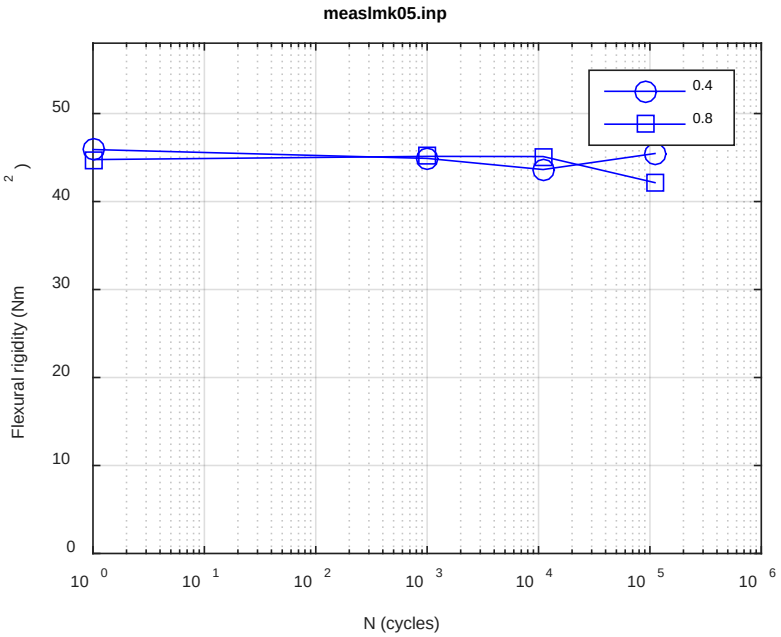
measlmk05.inp
0.4
0.8
Flexural rigidity (Nm 2)
N (cycles)

(c)

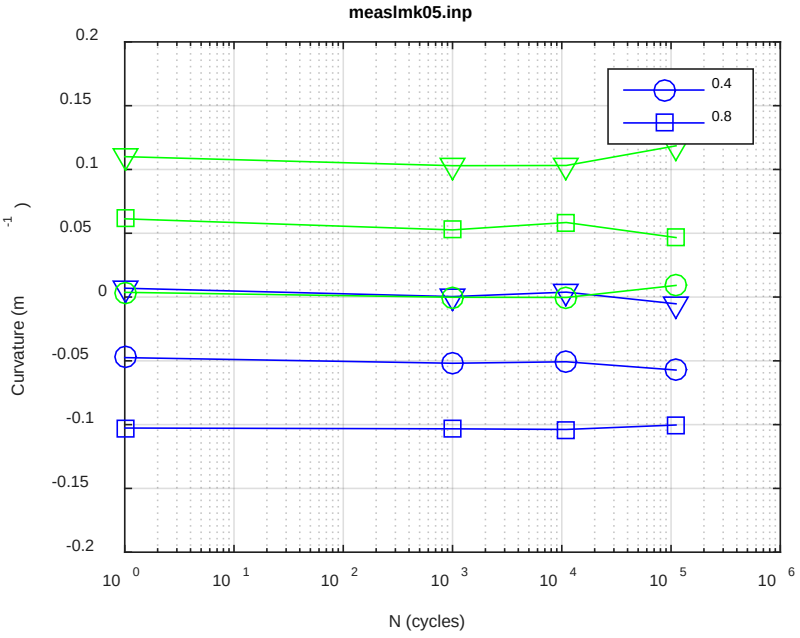
measlmk05.inp
0.4
0.8
Curvature (m -1)
N (cycles)

(d)

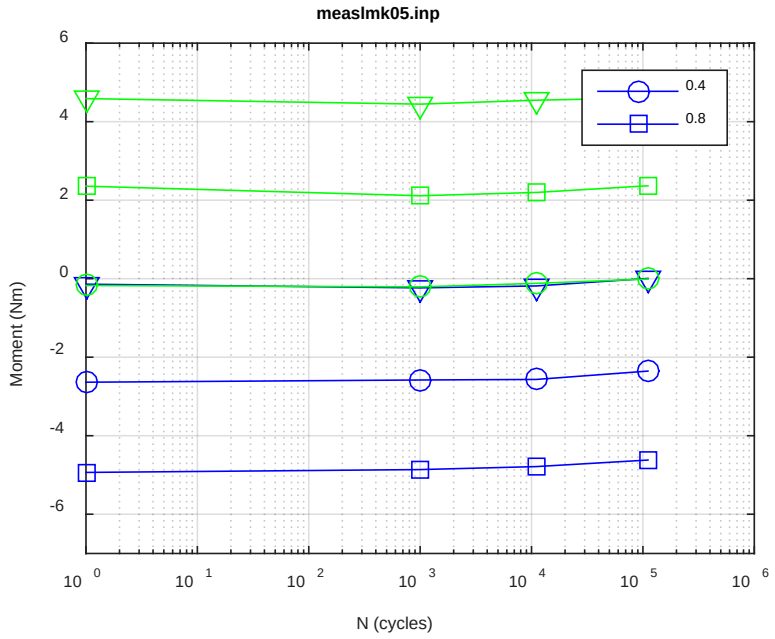

(e)

Fig. A.11. Measurement-based responses: (a) curvature range, (b) moment range, (c) rigidity, (d) curvature peak/valley, (e) moment peak/valley, LMK05, 8.64 Nm.

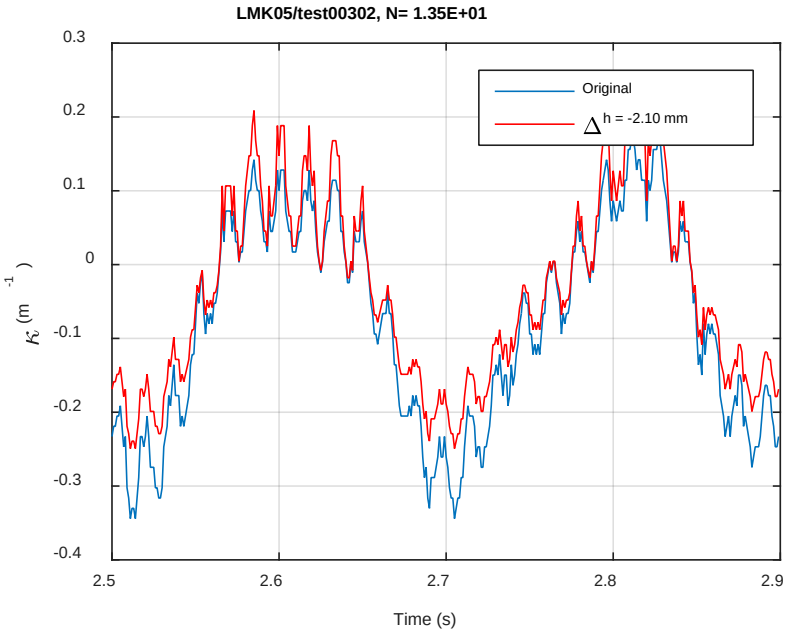
LMK05/test00302, N= 1.35E+01
Original
Δh = -2.10 mm
κ (m-1)
Time (s)

(a)

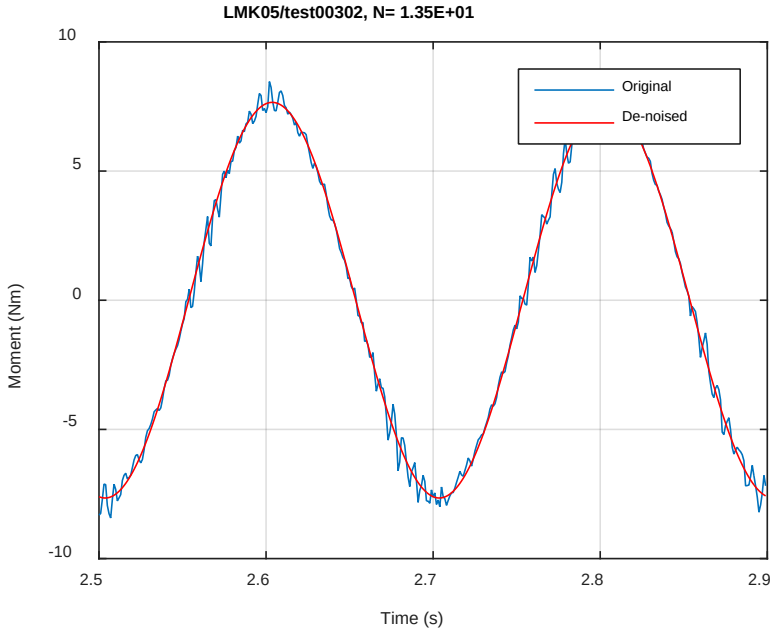
LMK05/test00302, N= 1.35E+01
Original
De-noised
Moment (Nm)
Time (s)

(b)

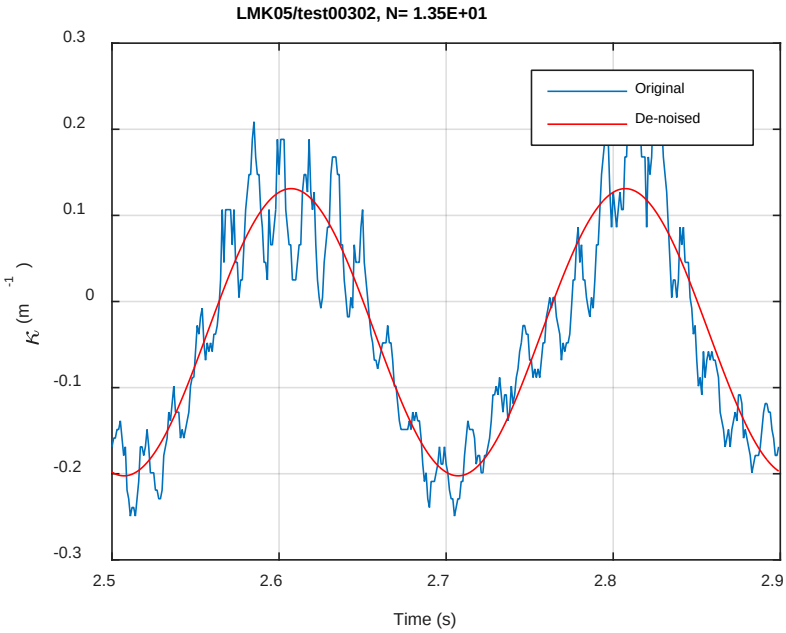

(c)

Fig. A.12. Monitoring-based responses: (a) curvature, (b) moment, (c) curvature, LMK05, 8.64 Nm, Ns = 1.35E+01 cycles.

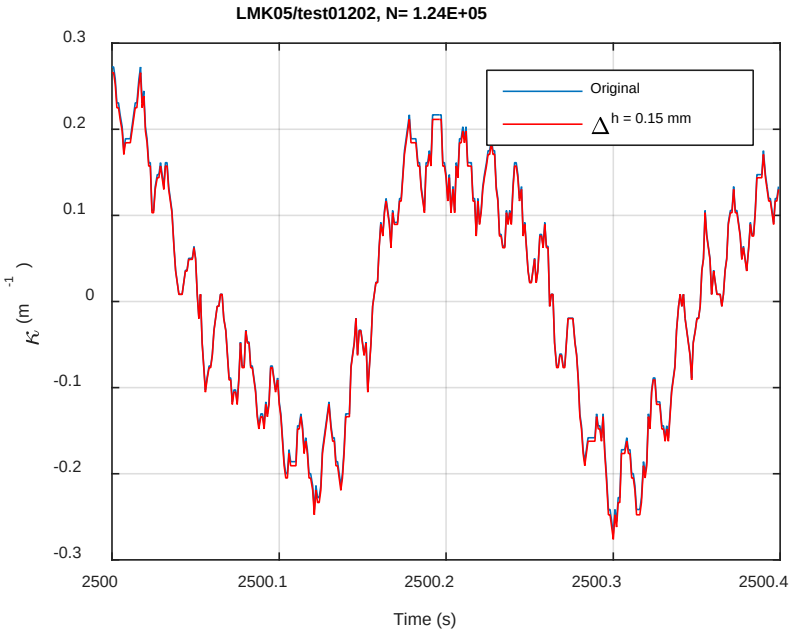
LMK05/test01202, N= 1.24E+05
Original
Δh = 0.15 mm
κ (m-1)
Time (s)
0.3
0.2
0.1
0
-0.1
-0.2
-0.3
2500
2500.1
2500.2
2500.3
2500.4

(a)

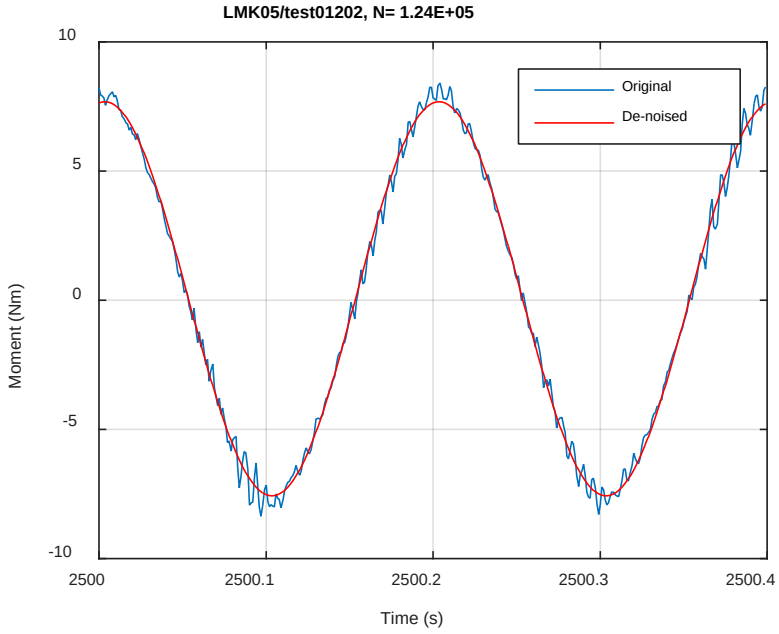
LMK05/test01202, N= 1.24E+05
Original
De-noised
Moment (Nm)
Time (s)
10
5
0
-5
-10
2500
2500.1
2500.2
2500.3
2500.4

(b)

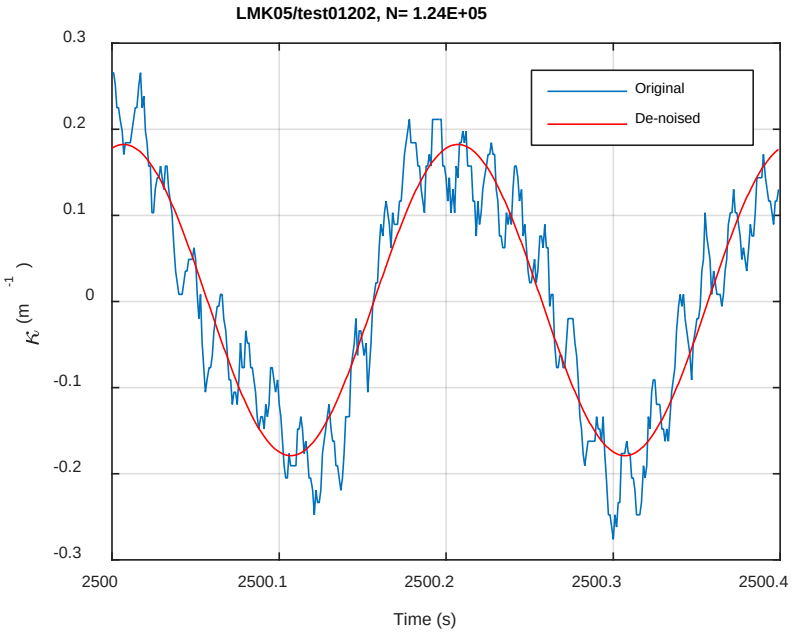

(c)

Fig. A.13. Monitoring-based responses: (a) curvature, (b) moment, (c) curvature, LMK05, 8.64 Nm, Ns = 1.24E+05 cycles.

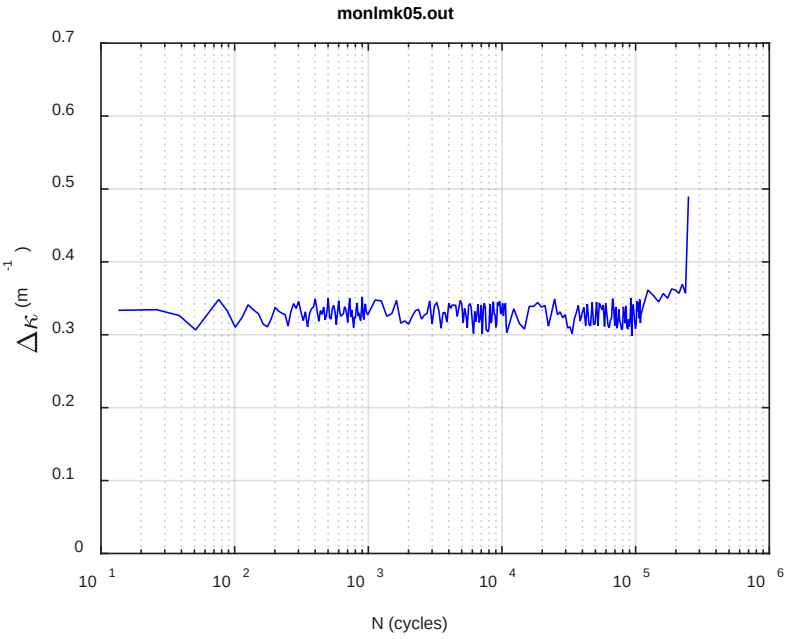
monlmk05.out
0.7
0.6
0.5
0.4
0.3
0.2
0.1
0
$\Delta\kappa$ (m^{-1})
10 1
10 2
10 3
10 4
10 5
10 6
N (cycles)

(a)

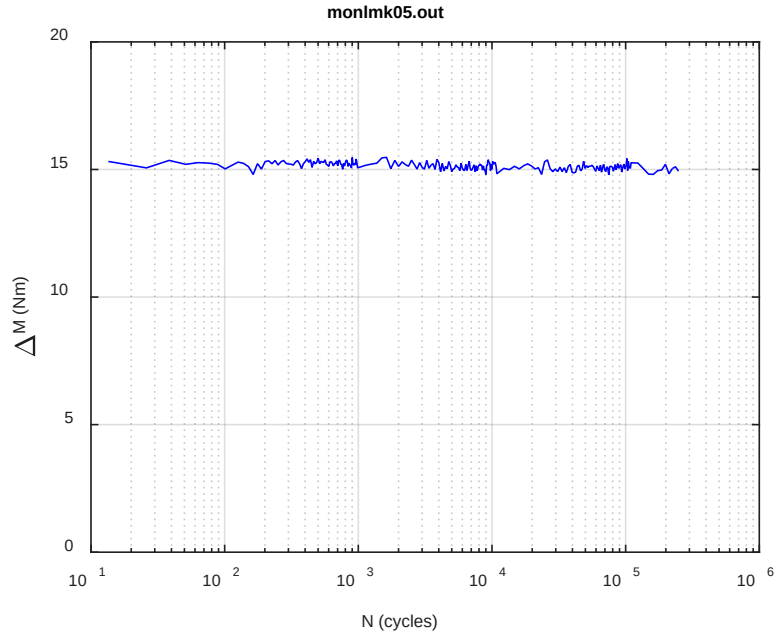
monlmk05.out
20
15
10
5
0
Δ M (Nm)
10 1
10 2
10 3
10 4
10 5
10 6
N (cycles)

(b)

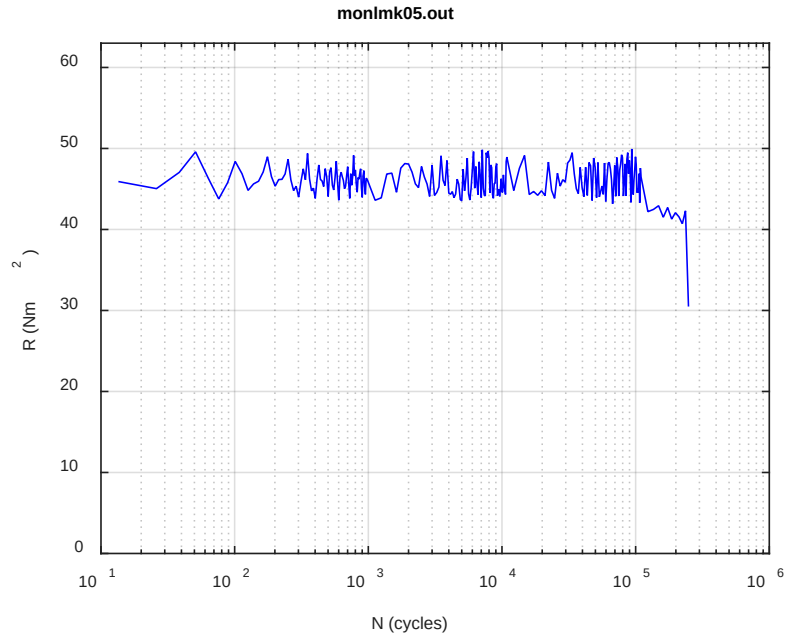
monlmk05.out
R (Nm^{2})
N (cycles)
60
50
40
30
20
10
0
10^{1}
10^{2}
10^{3}
10^{4}
10^{5}
10^{6}

(c)

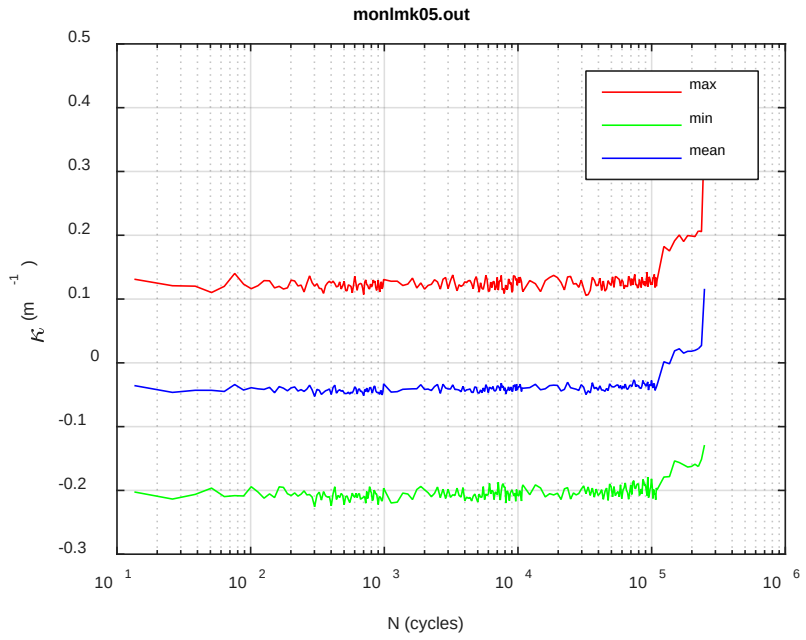
monlmk05.out
max
min
mean
κ (m^{-1})
N (cycles)
0.5
0.4
0.3
0.2
0.1
0
-0.1
-0.2
-0.3
10^{1}
10^{2}
10^{3}
10^{4}
10^{5}
10^{6}

(d)

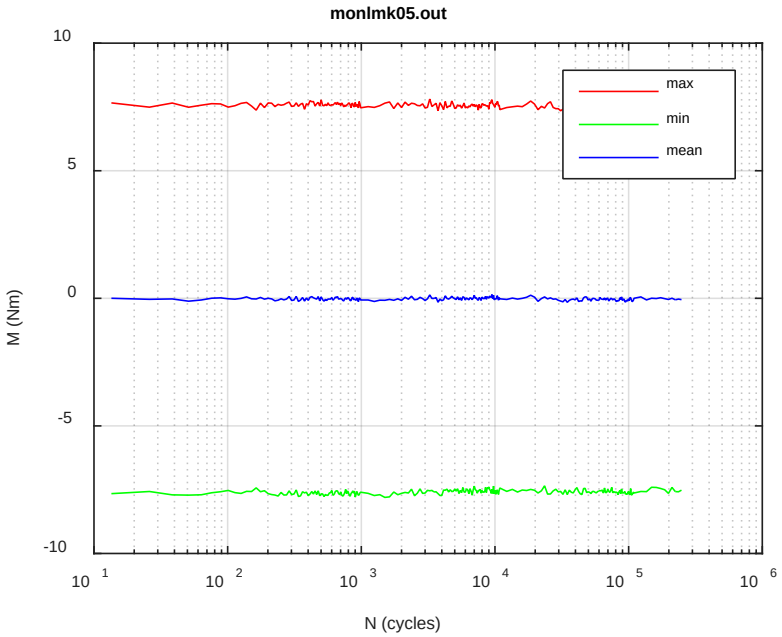

(e)

Fig. A.14. Monitoring-based responses: (a) curvature range, (b) moment range, (c) rigidity, (d) curvature peak/valley, (e) moment peak/valley, LMK05, 8.64 Nm, Nf = 2.49E+05 cycles.

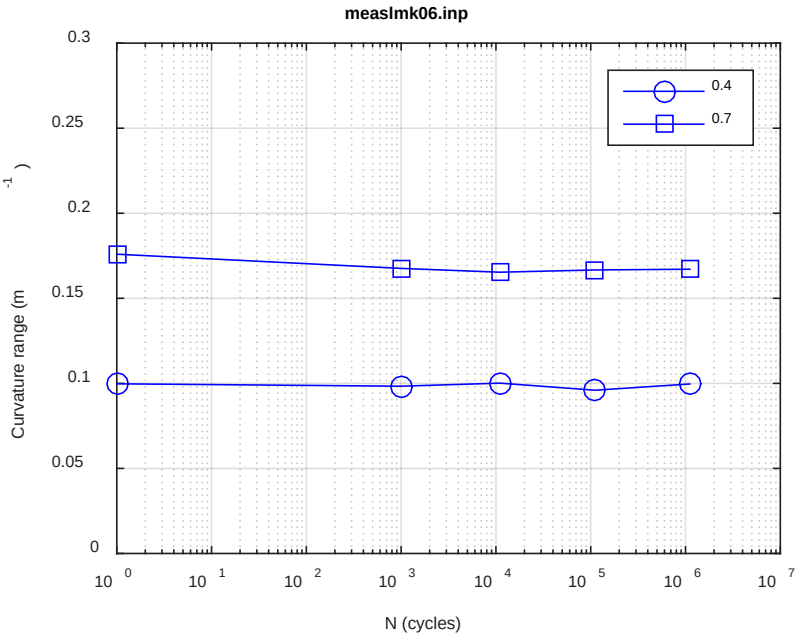
measlmk06.inp
0.3
0.25
0.2
0.15
0.1
0.05
0
Curvature range (m-1)
0.4
0.7
10 0
10 1
10 2
10 3
10 4
10 5
10 6
10 7
N (cycles)

(a)

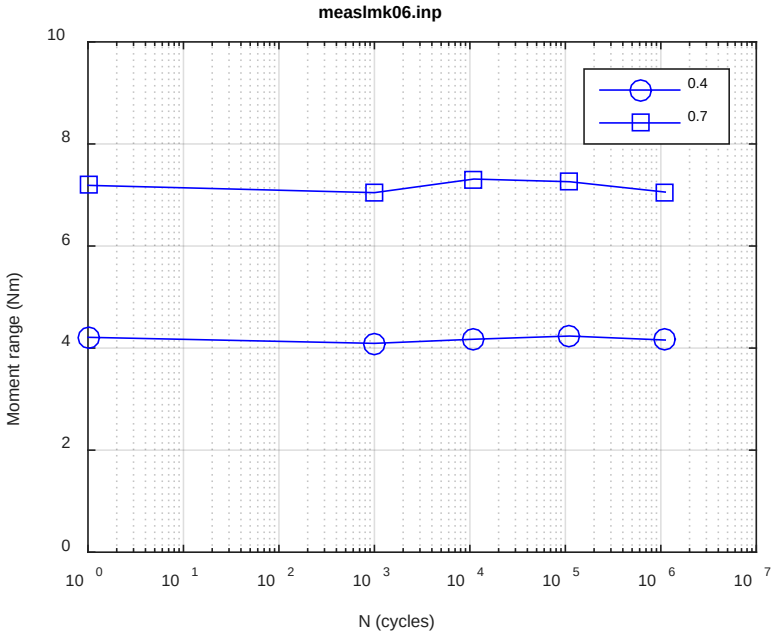
measlmk06.inp
10
8
6
4
2
0
Moment range (Nm)
0.4
0.7
10 0
10 1
10 2
10 3
10 4
10 5
10 6
10 7
N (cycles)

(b)

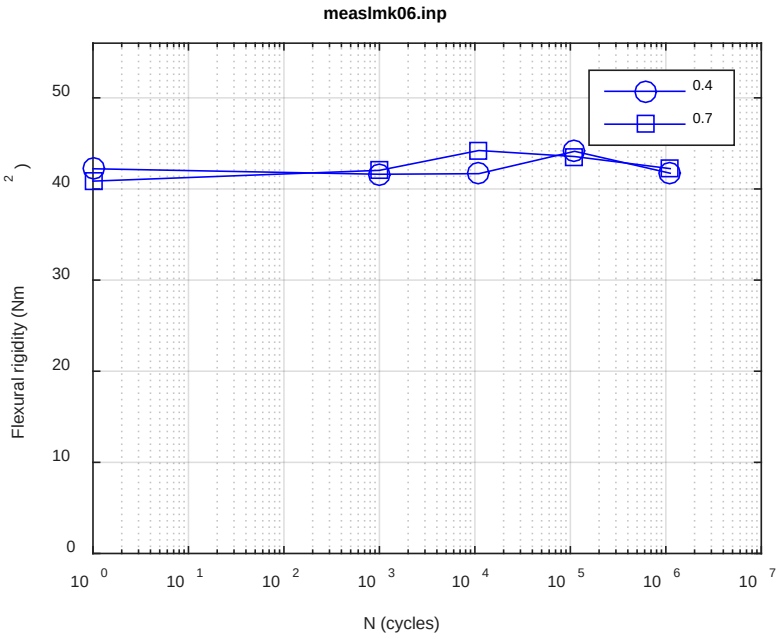
measlmk06.inp
0.4
0.7
Flexural rigidity (Nm 2)
N (cycles)

(c)

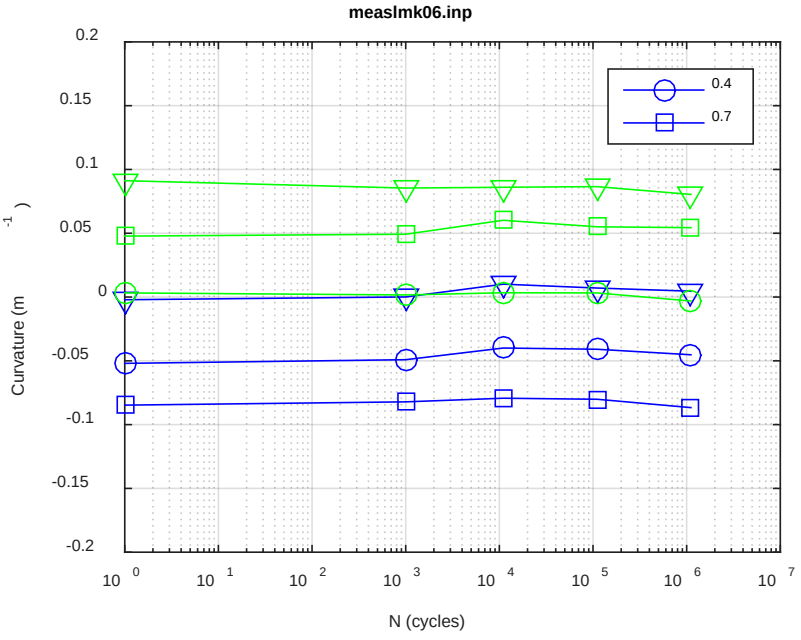
measlmk06.inp
0.4
0.7
Curvature (m -1)
N (cycles)

(d)

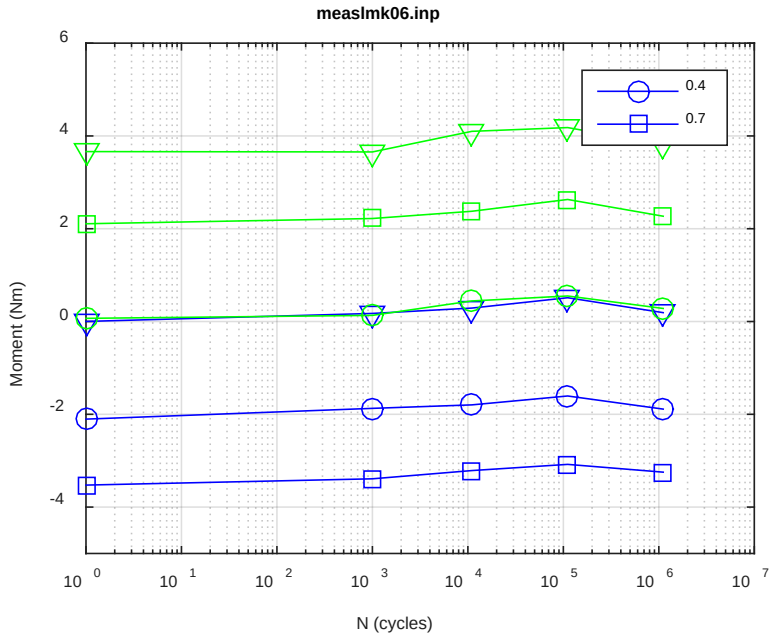

(e)

Fig. A.15. Measurement-based responses: (a) curvature range, (b) moment range, (c) rigidity, (d) curvature peak/valley, (e) moment peak/valley, LMK06, 7.62 Nm.

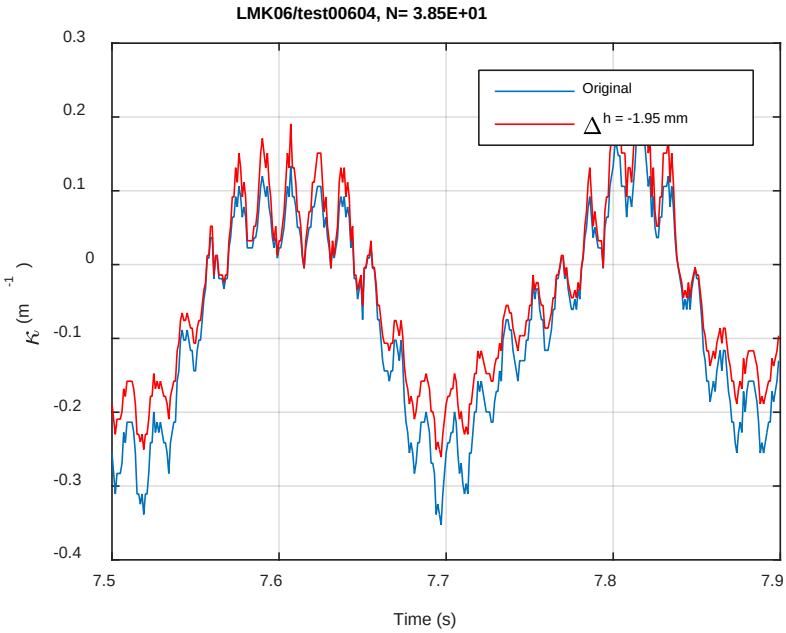
LMK06/test00604, N= 3.85E+01
Original
Δh = -1.95 mm
κ (m-1)
Time (s)

(a)

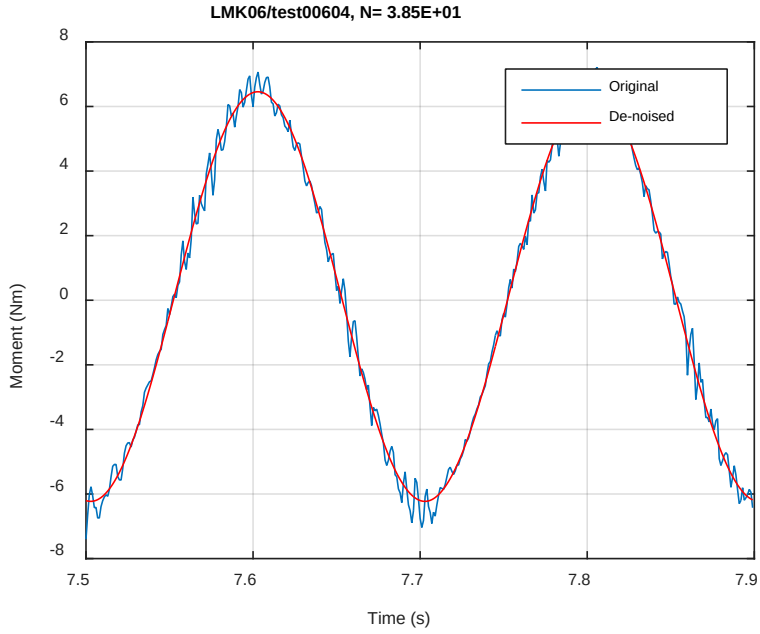
LMK06/test00604, N= 3.85E+01
Original
De-noised
Moment (Nm)
Time (s)

(b)

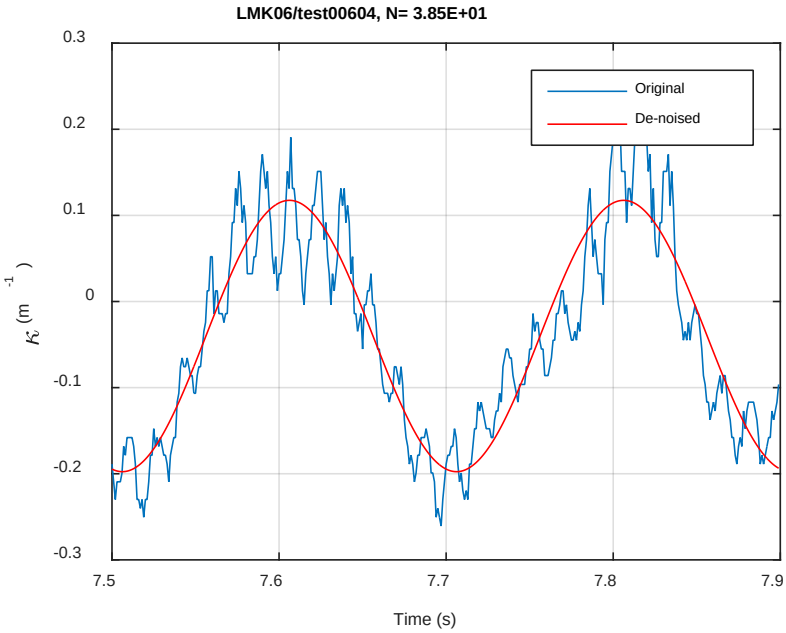

(c)

Fig. A.16. Monitoring-based responses: (a) curvature, (b) moment, (c) curvature, LMK06, 7.62 Nm, Ns = 3.85E+01 cycles.

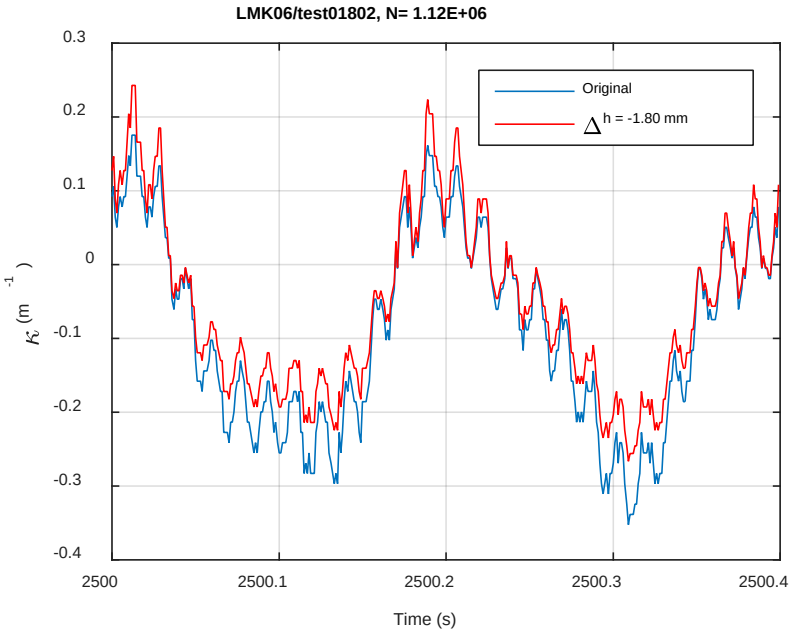
LMK06/test01802, N= 1.12E+06
Original
Δh = -1.80 mm
κ (m-1)
Time (s)
0.3
0.2
0.1
0
-0.1
-0.2
-0.3
-0.4
2500
2500.1
2500.2
2500.3
2500.4

(a)

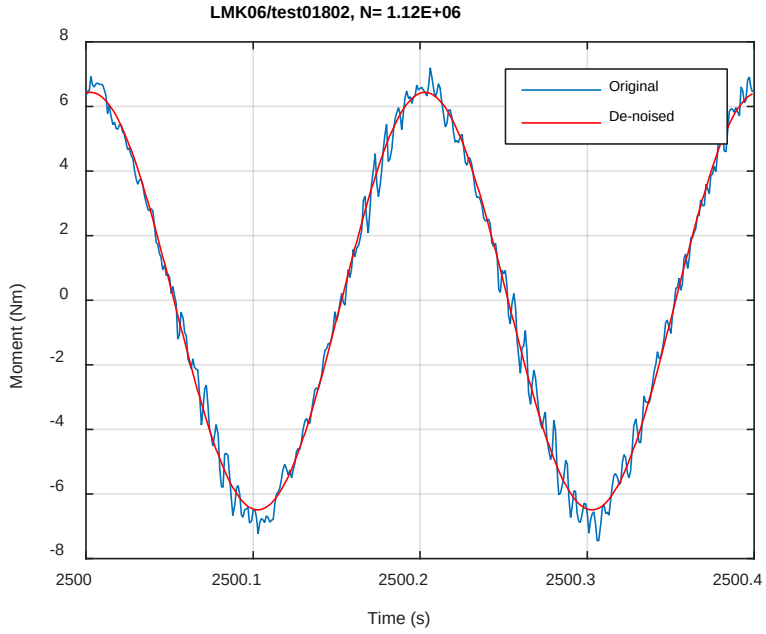
LMK06/test01802, N= 1.12E+06
Original
De-noised
Moment (Nm)
Time (s)
8
6
4
2
0
-2
-4
-6
-8
2500
2500.1
2500.2
2500.3
2500.4

(b)

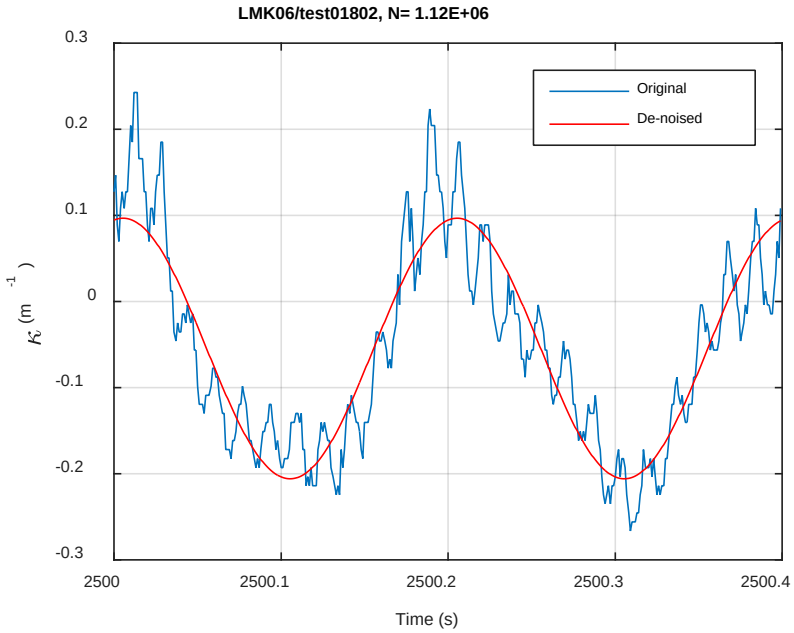

(c)

Fig. A.17. Monitoring-based responses: (a) curvature, (b) moment, (c) curvature, LMK06, 7.62 Nm, Ns = 1.12E+06 cycles.

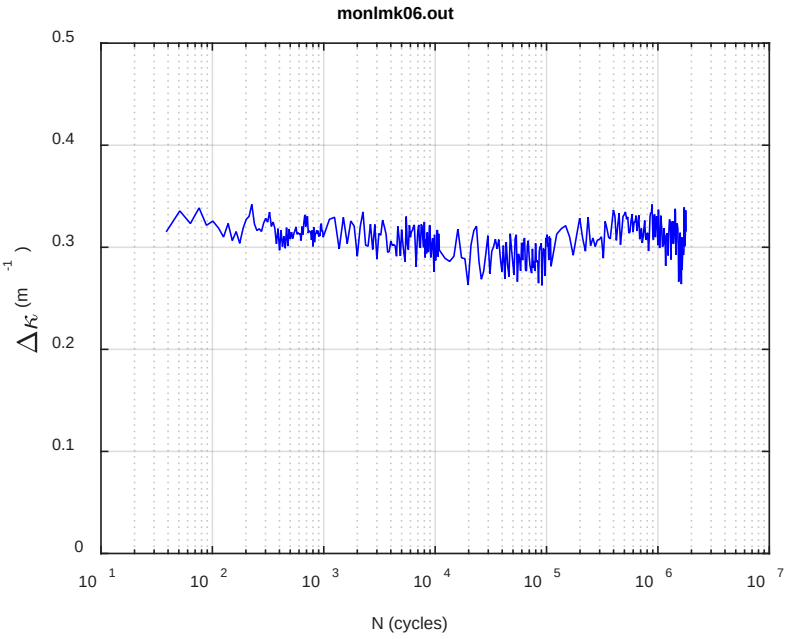
monlmk06.out
0.5
0.4
0.3
0.2
0.1
0
Δκ (m -1)
10 1
10 2
10 3
10 4
10 5
10 6
10 7
N (cycles)

(a)

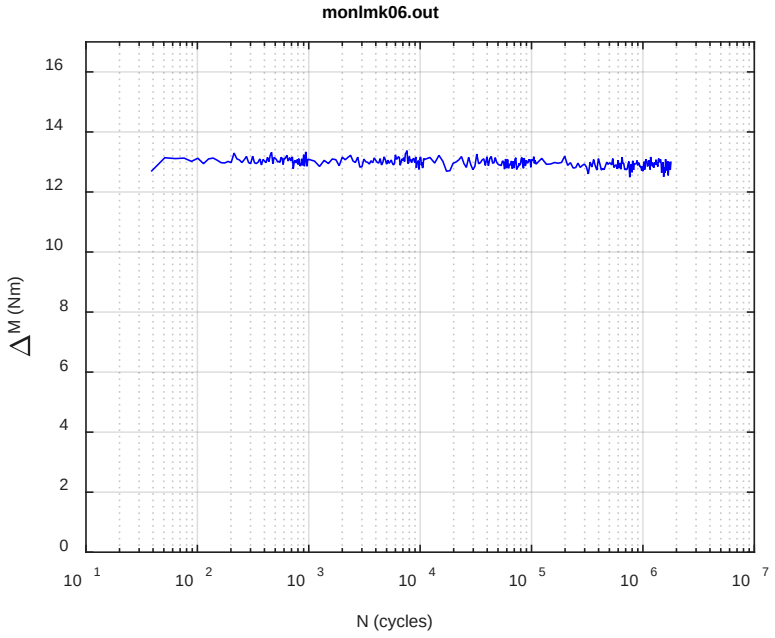
monlmk06.out
16
14
12
10
8
6
4
2
0
Δ M (Nm)
10 1
10 2
10 3
10 4
10 5
10 6
10 7
N (cycles)

(b)

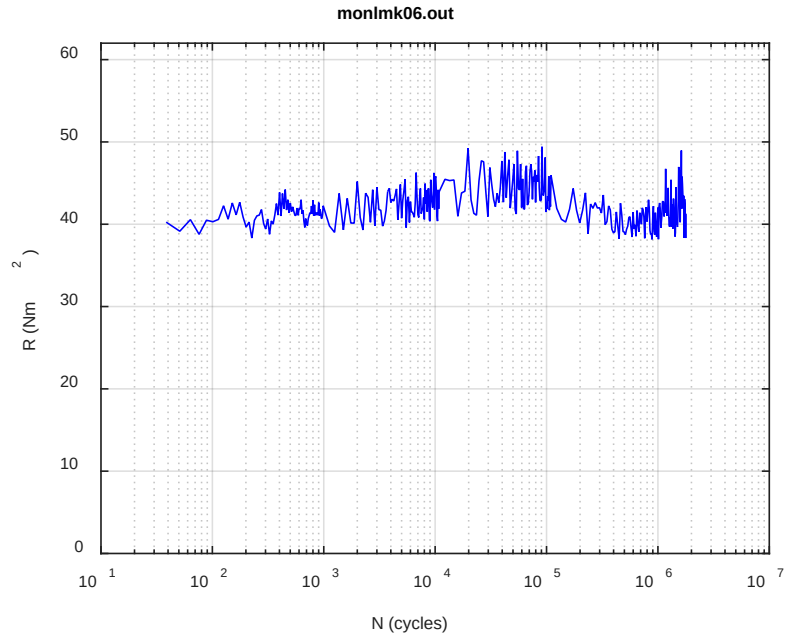
monlmk06.out
R (Nm 2)
N (cycles)

(c)

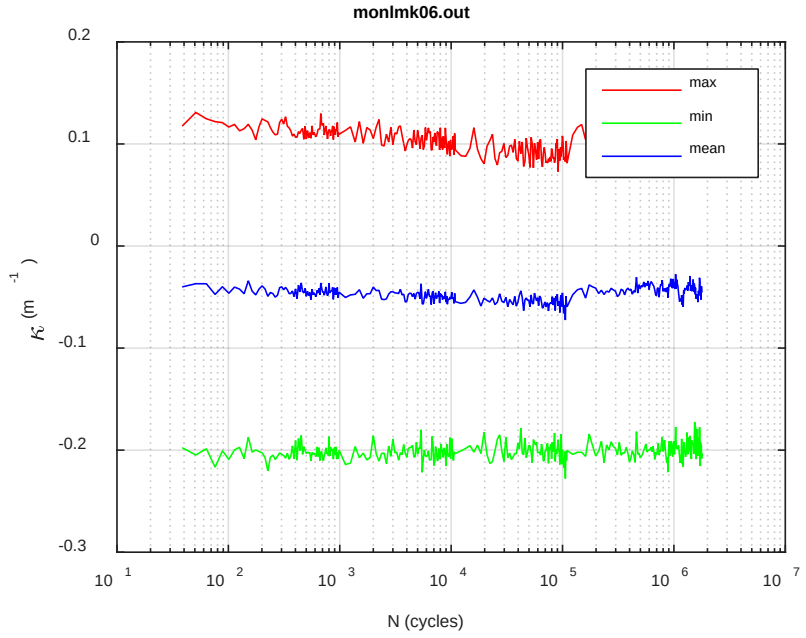
monlmk06.out
max
min
mean
κ (m -1)
N (cycles)

(d)

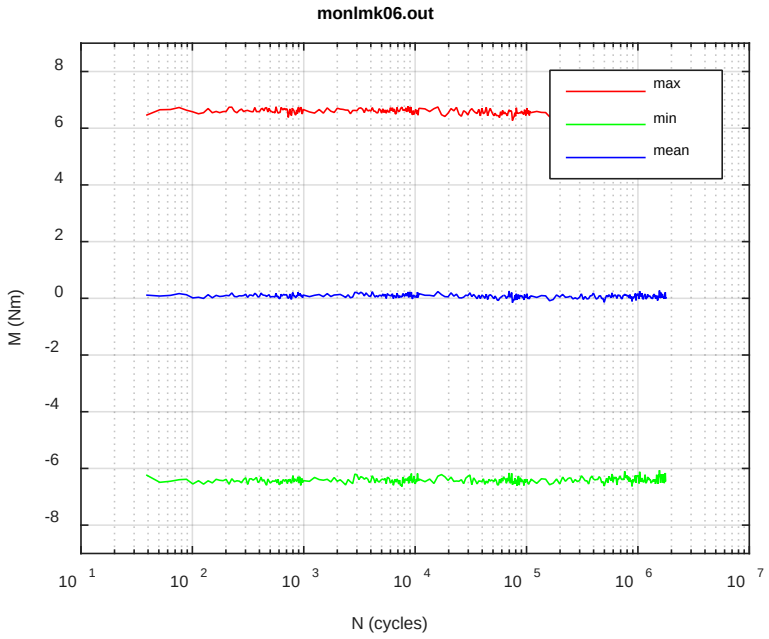

(e)

Fig. A.18. Monitoring-based responses: (a) curvature range, (b) moment range, (c) rigidity, (d) curvature peak/valley, (e) moment peak/valley, LMK06, 7.62 Nm, Nf = 1.79E+06 cycles.

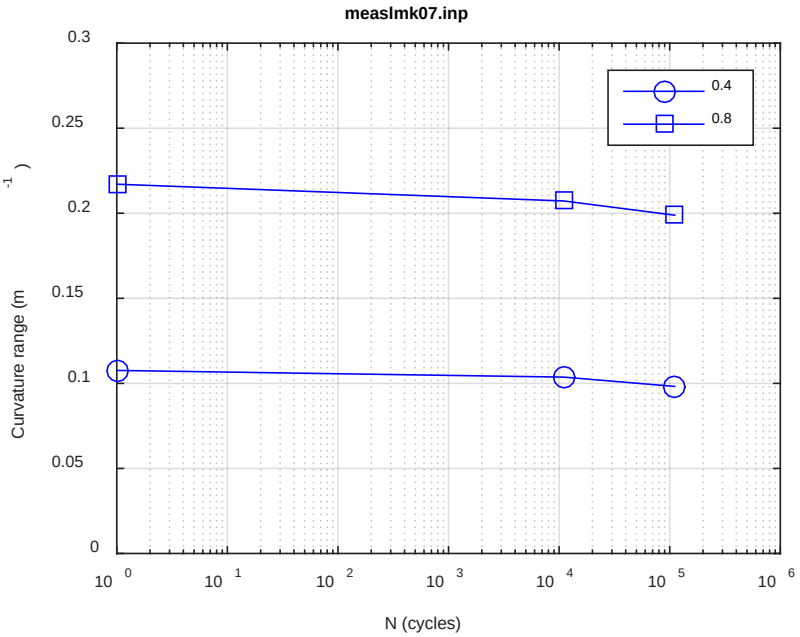
measlmk07.inp
0.3
0.25
0.2
0.15
0.1
0.05
0
Curvature range (m-1)
0.4
0.8
10 0
10 1
10 2
10 3
10 4
10 5
10 6
N (cycles)

(a)

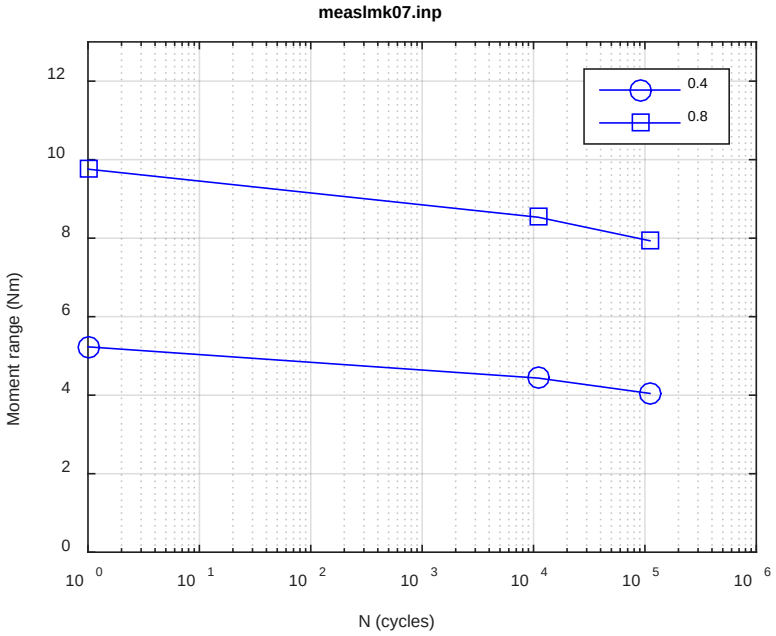
measlmk07.inp
12
10
8
6
4
2
0
Moment range (Nm)
0.4
0.8
10 0
10 1
10 2
10 3
10 4
10 5
10 6
N (cycles)

(b)

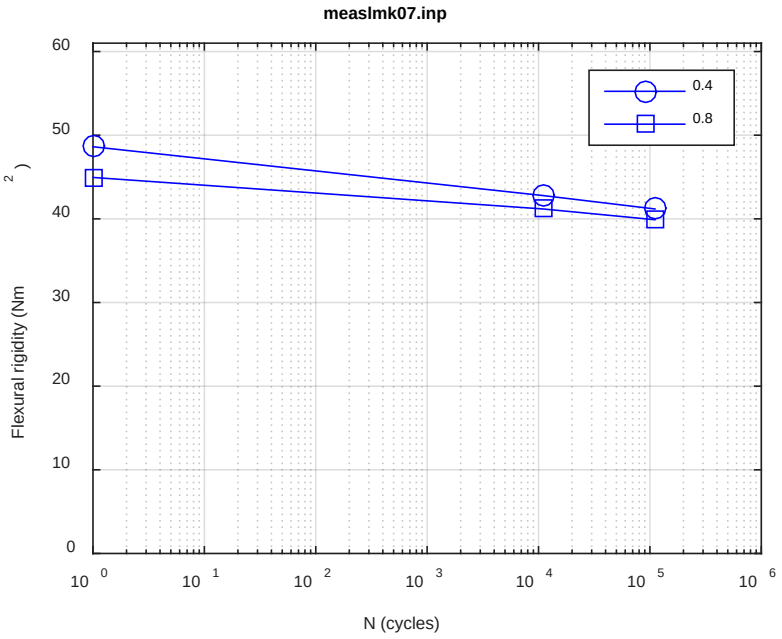
measlmk07.inp
0.4
0.8
Flexural rigidity (Nm 2)
N (cycles)

(c)

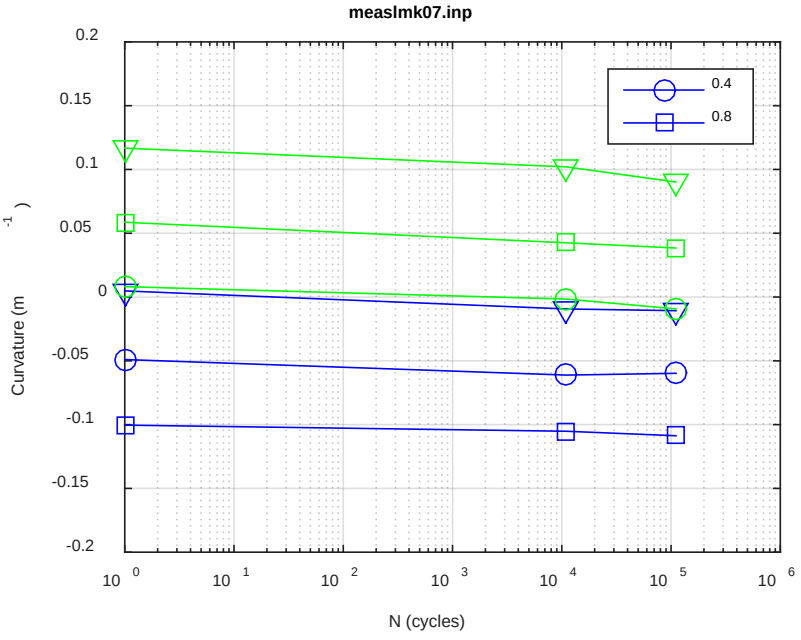
measlmk07.inp
0.4
0.8
Curvature (m -1)
N (cycles)

(d)

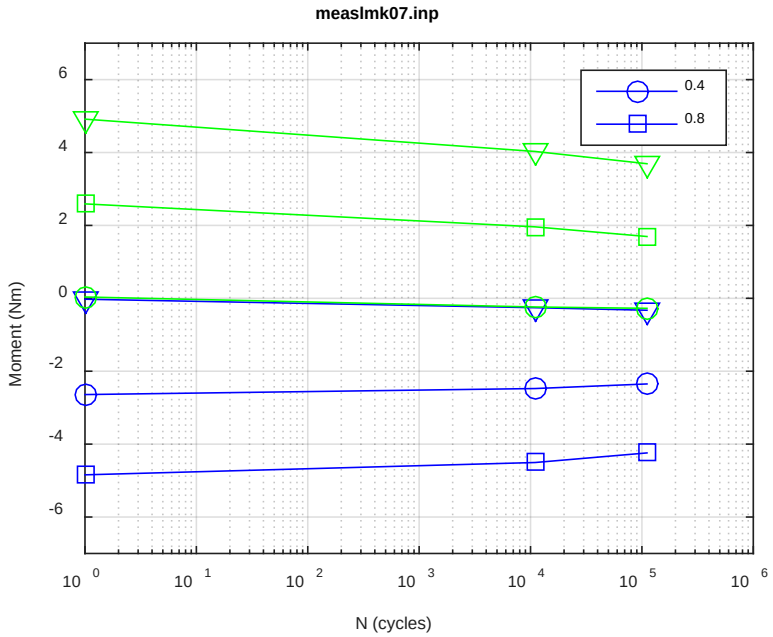

(e)

Fig. A.19. Measurement-based responses: (a) curvature range, (b) moment range, (c) rigidity, (d) curvature peak/valley, (e) moment peak/valley, LMK07, 15.24 Nm.

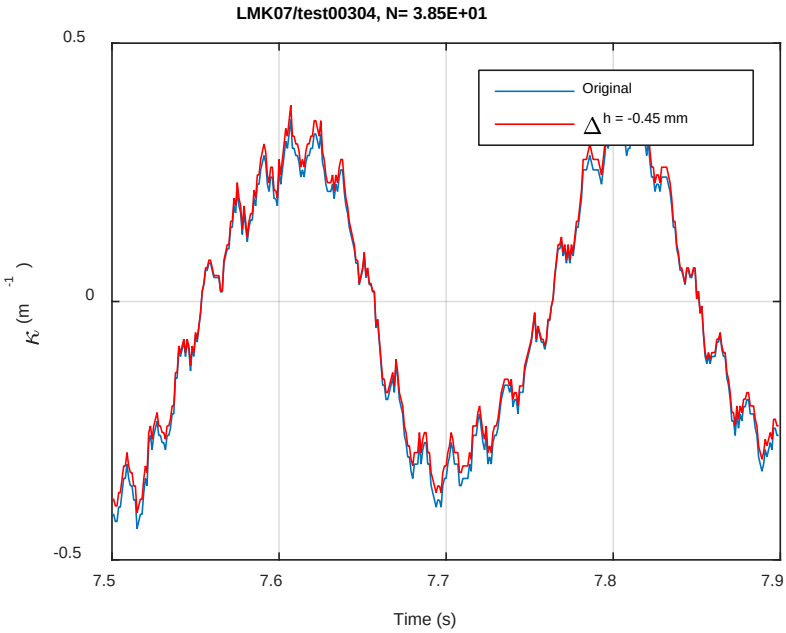
LMK07/test00304, N= 3.85E+01
Original
Δh = -0.45 mm
κ (m-1)
Time (s)
0.5
0
-0.5
7.5
7.6
7.7
7.8
7.9

(a)

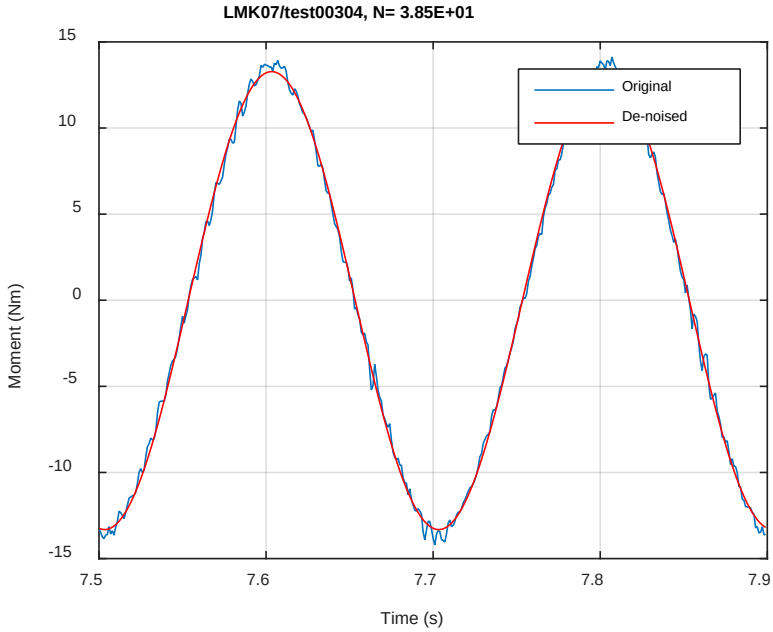
LMK07/test00304, N= 3.85E+01
Original
De-noised
Moment (Nm)
Time (s)
15
10
5
0
-5
-10
-15
7.5
7.6
7.7
7.8
7.9

(b)

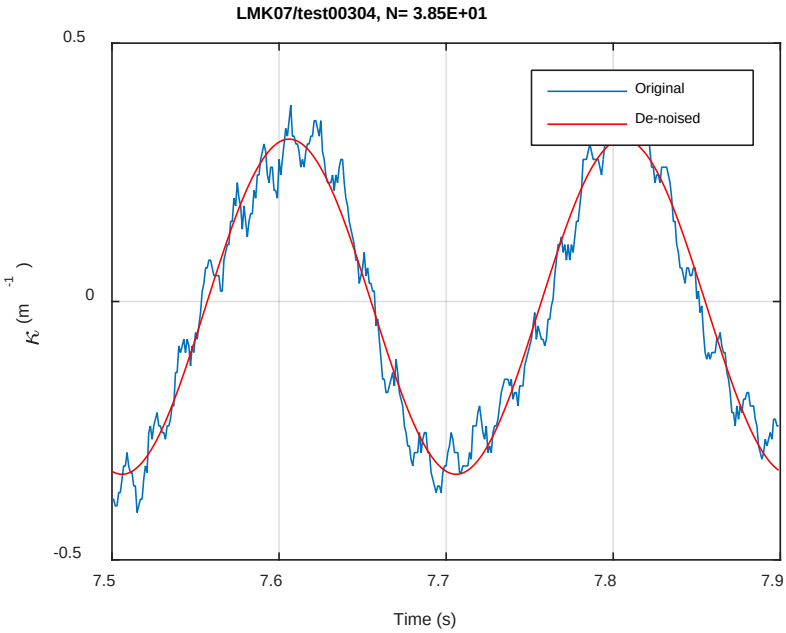

(c)

Fig. A.20. Monitoring-based responses: (a) curvature, (b) moment, (c) curvature, LMK07, 15.24 Nm, Ns = 3.85E+01 cycles.

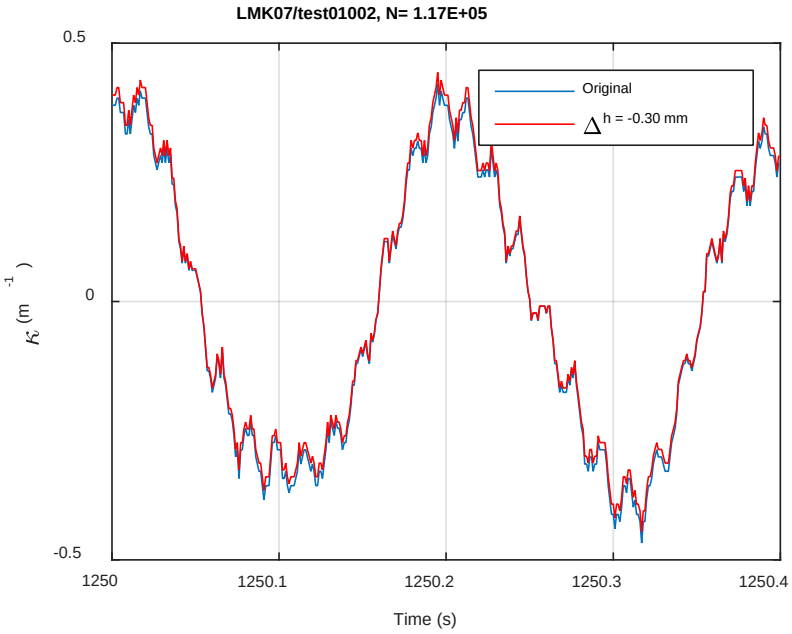
LMK07/test01002, N= 1.17E+05
Original
Δh = -0.30 mm
κ (m-1)
0.5
0
-0.5
1250
1250.1
1250.2
1250.3
1250.4
Time (s)

(a)

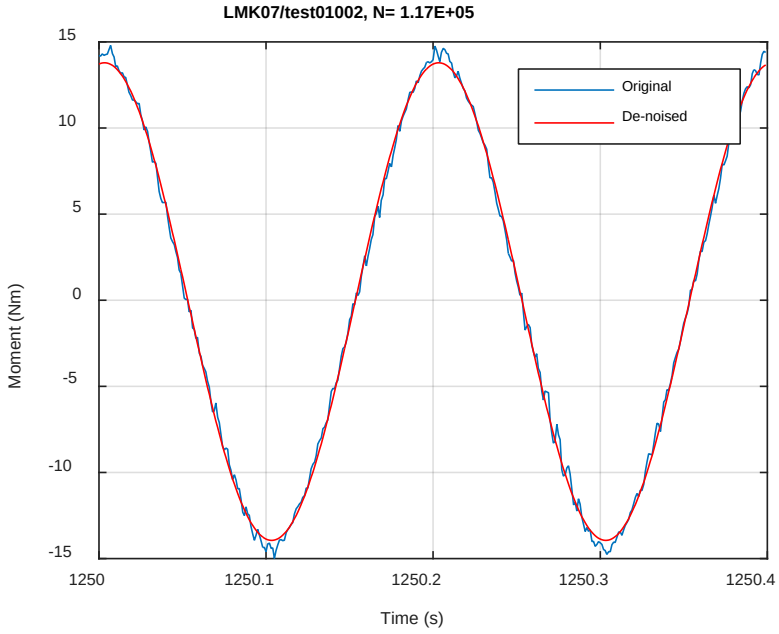
LMK07/test01002, N= 1.17E+05
Original
De-noised
Moment (Nm)
15
10
5
0
-5
-10
-15
1250
1250.1
1250.2
1250.3
1250.4
Time (s)

(b)

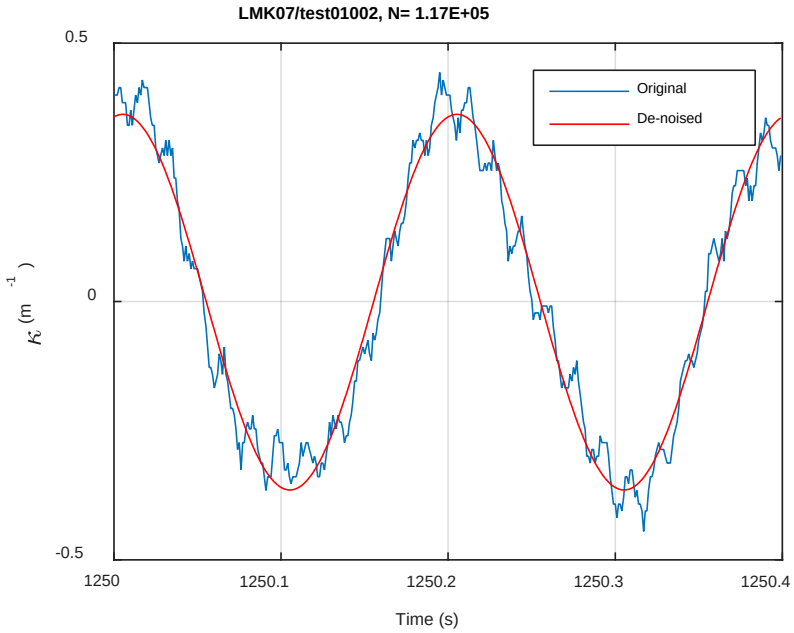

(c)

Fig. A.21. Monitoring-based responses: (a) curvature, (b) moment, (c) curvature, LMK07, 15.24 Nm, Ns = 1.17E+05 cycles.

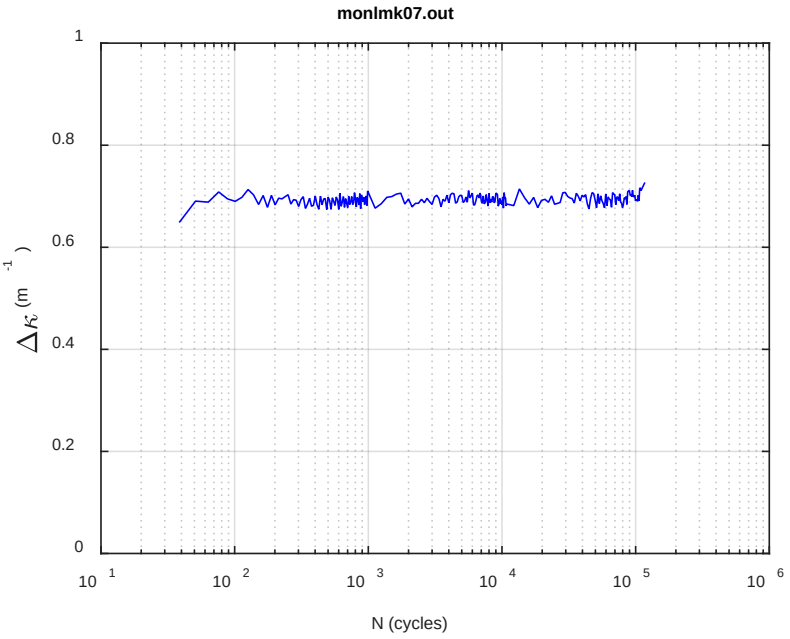
monlmk07.out
1
0.8
0.6
0.4
0.2
0
Δκ (m -1)
10 1
10 2
10 3
10 4
10 5
10 6
N (cycles)

(a)

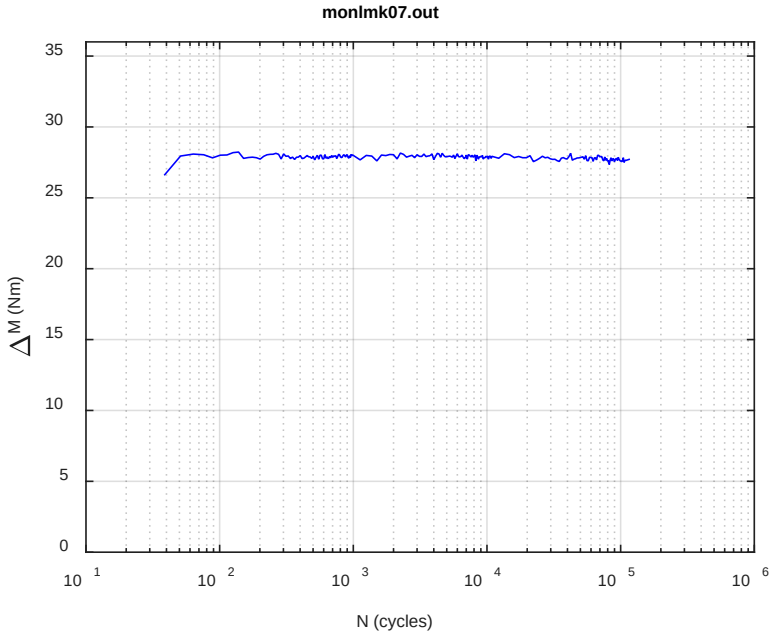
monlmk07.out
35
30
25
20
15
10
5
0
ΔM (Nm)
10 1
10 2
10 3
10 4
10 5
10 6
N (cycles)

(b)

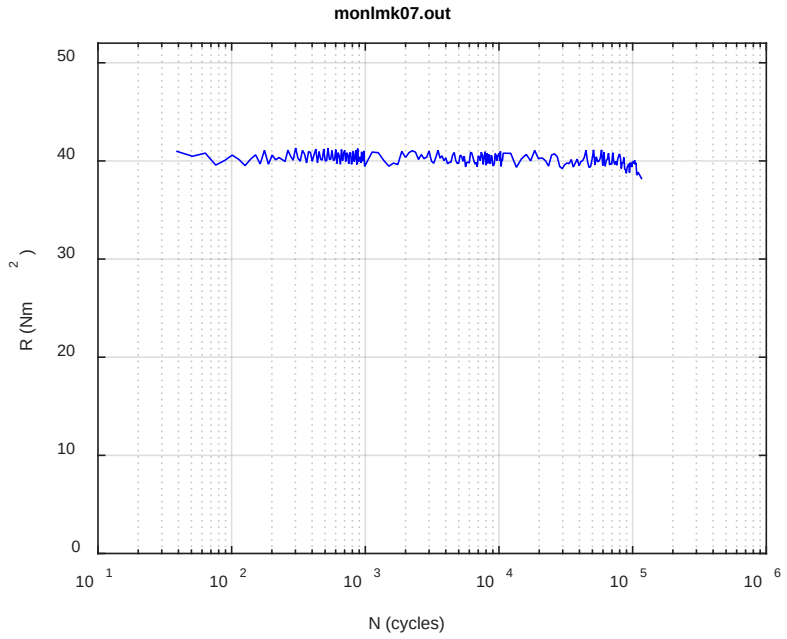
monlmk07.out
50
40
30
20
10
0
R (Nm 2)
10 1
10 2
10 3
10 4
10 5
10 6
N (cycles)

(c)

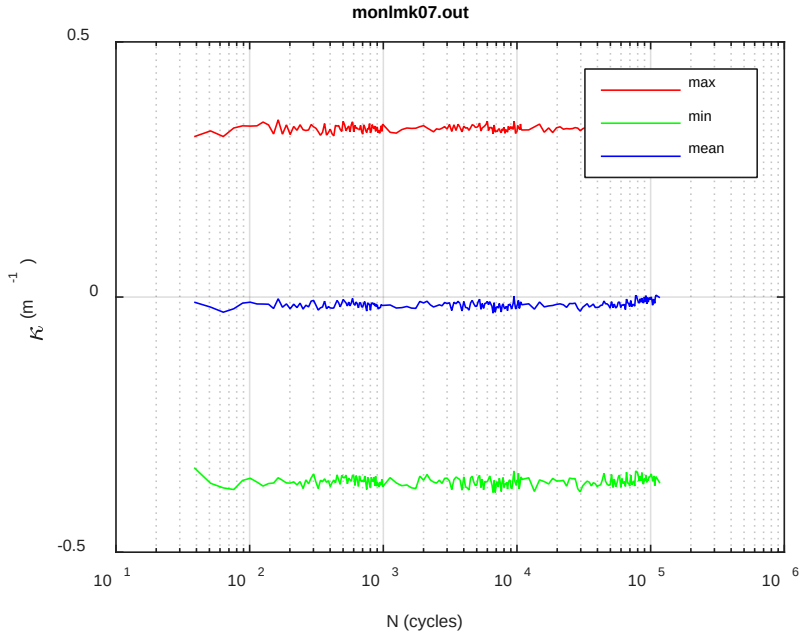
monlmk07.out
0.5
0
-0.5
κ (m -1)
max
min
mean
10 1
10 2
10 3
10 4
10 5
10 6
N (cycles)

(d)

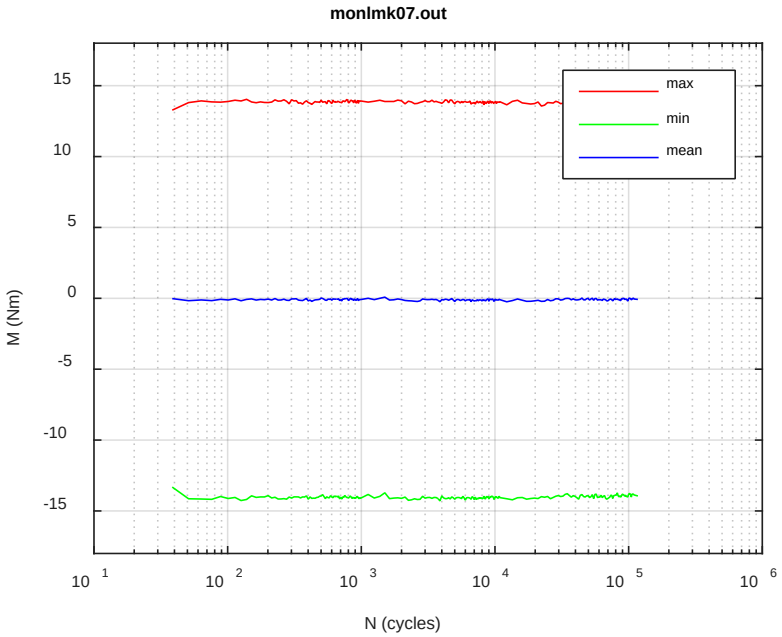

(e)

Fig. A.22. Monitoring-based responses: (a) curvature range, (b) moment range, (c) rigidity, (d) curvature peak/valley, (e) moment peak/valley, LMK07, 15.24 Nm, Nf = 1.22E+05 cycles.

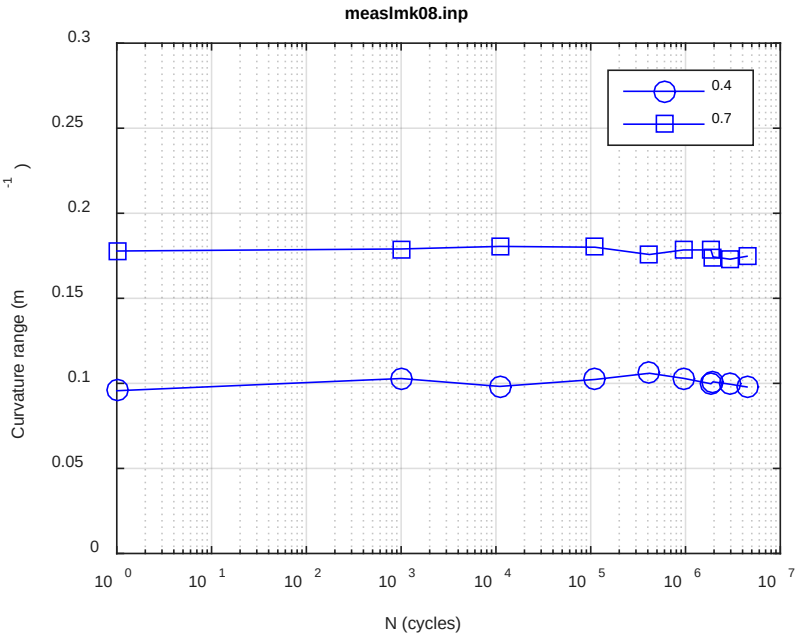
measlmk08.inp
0.3
0.25
0.2
0.15
0.1
0.05
0
Curvature range (m-1)
0.4
0.7
10 0
10 1
10 2
10 3
10 4
10 5
10 6
10 7
N (cycles)

(a)

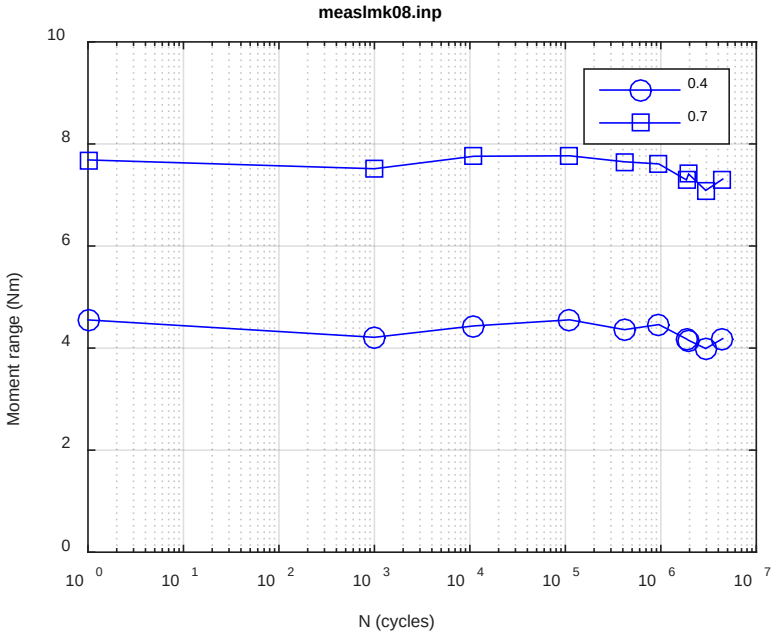
measlmk08.inp
10
8
6
4
2
0
Moment range (Nm)
0.4
0.7
10 0
10 1
10 2
10 3
10 4
10 5
10 6
10 7
N (cycles)

(b)

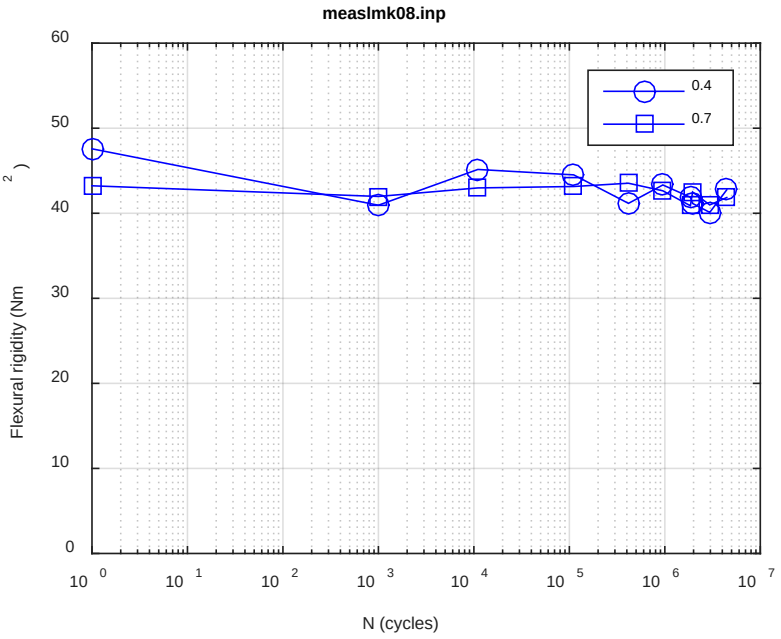
measlmk08.inp
0.4
0.7
Flexural rigidity (Nm 2)
N (cycles)

(c)

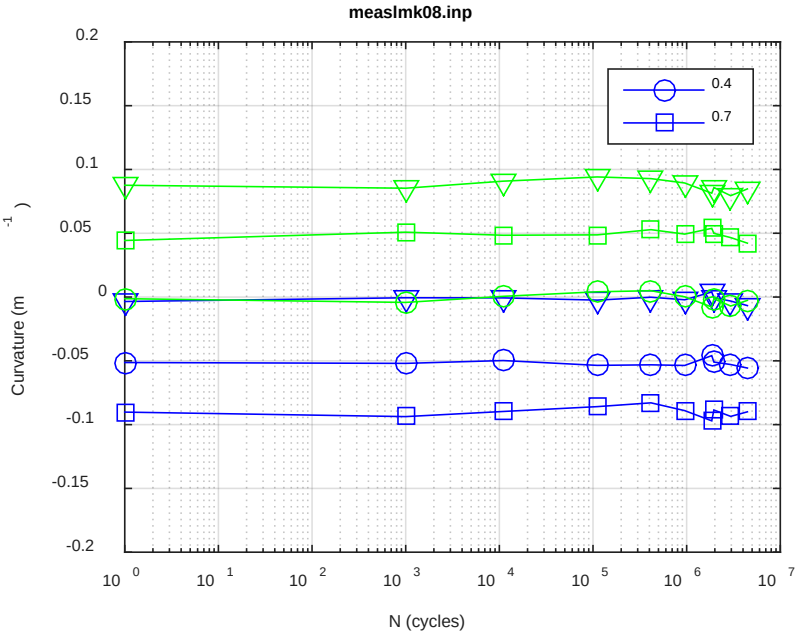
measlmk08.inp
0.4
0.7
Curvature (m -1)
N (cycles)

(d)

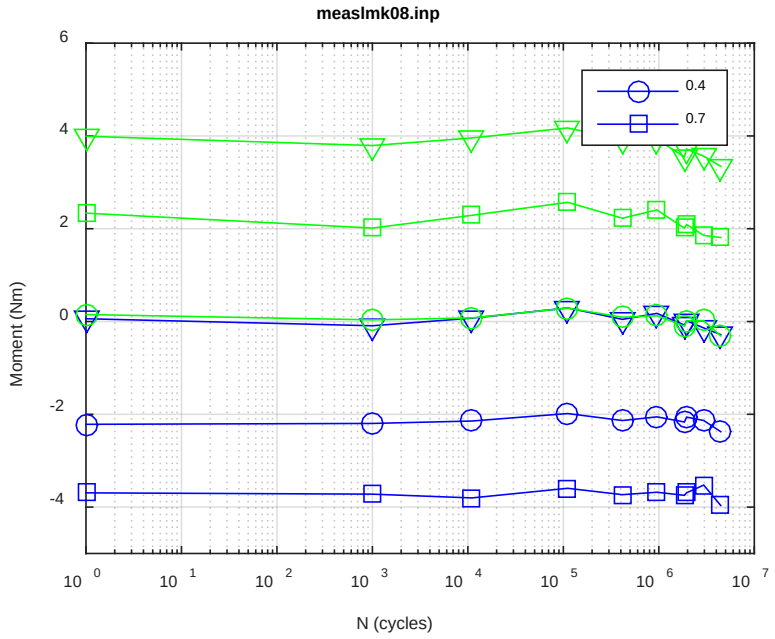

(e)

Fig. A.23. Measurement-based responses: (a) curvature range, (b) moment range, (c) rigidity, (d) curvature peak/valley, (e) moment peak/valley, LMK08, 7.62 Nm.

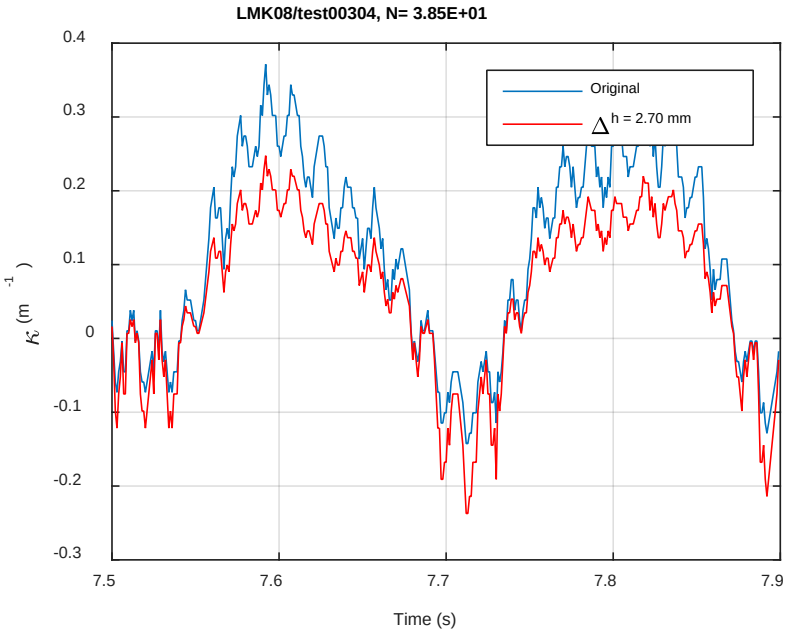
LMK08/test00304, N= 3.85E+01
Original
Δh = 2.70 mm
κ (m-1)
Time (s)

(a)

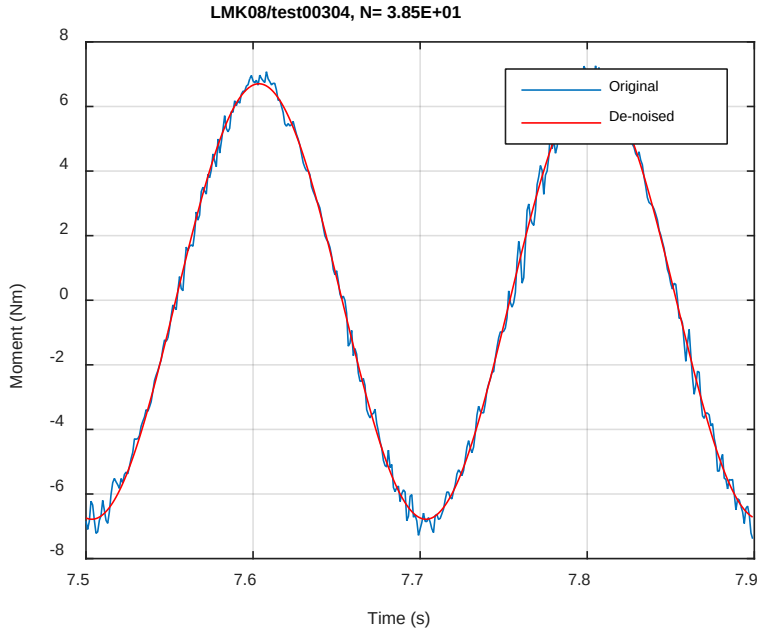
LMK08/test00304, N= 3.85E+01
Original
De-noised
Moment (Nm)
Time (s)

(b)

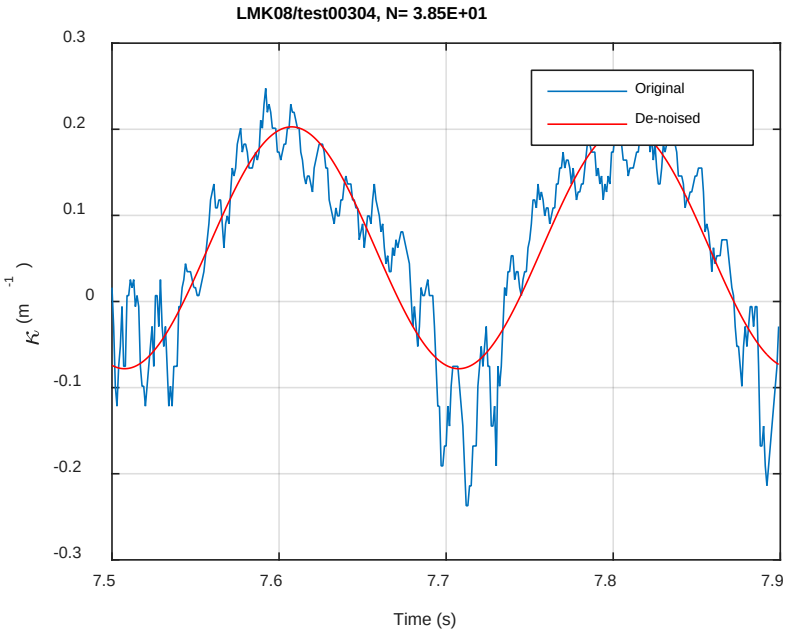

(c)

Fig. A.24. Monitoring-based responses: (a) curvature, (b) moment, (c) curvature, LMK08, 7.62 Nm, Ns = 3.85E+01 cycles.

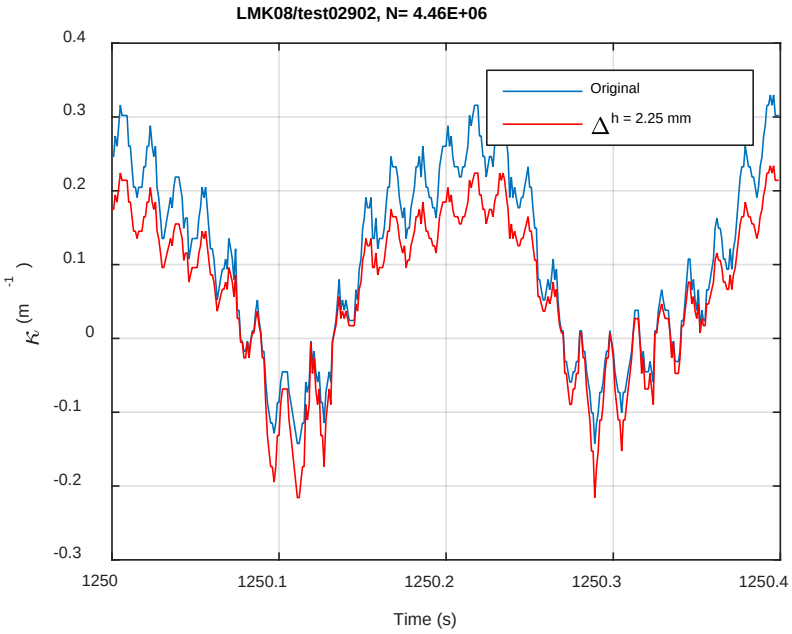
LMK08/test02902, N= 4.46E+06
Original
Δh = 2.25 mm
κ (m-1)
Time (s)
0.4
0.3
0.2
0.1
0
-0.1
-0.2
-0.3
1250
1250.1
1250.2
1250.3
1250.4

(a)

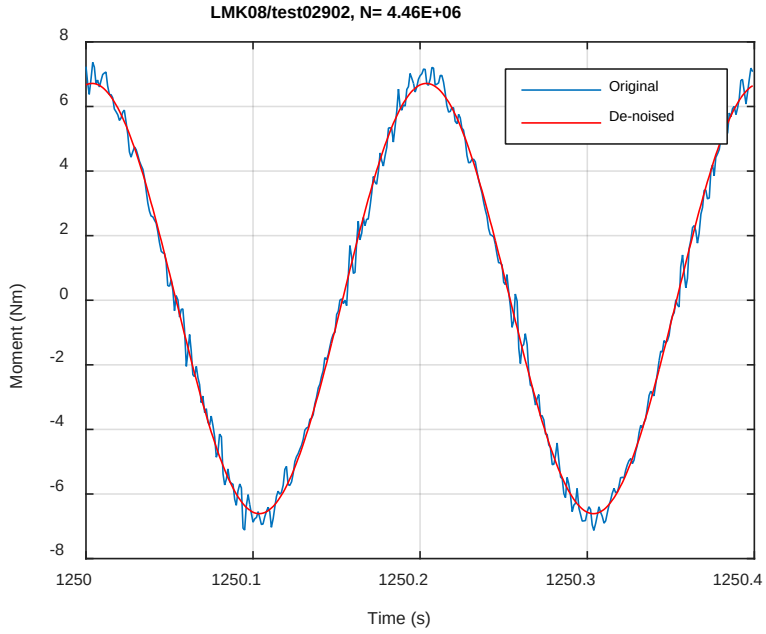
LMK08/test02902, N= 4.46E+06
Original
De-noised
Moment (Nm)
Time (s)
8
6
4
2
0
-2
-4
-6
-8
1250
1250.1
1250.2
1250.3
1250.4

(b)

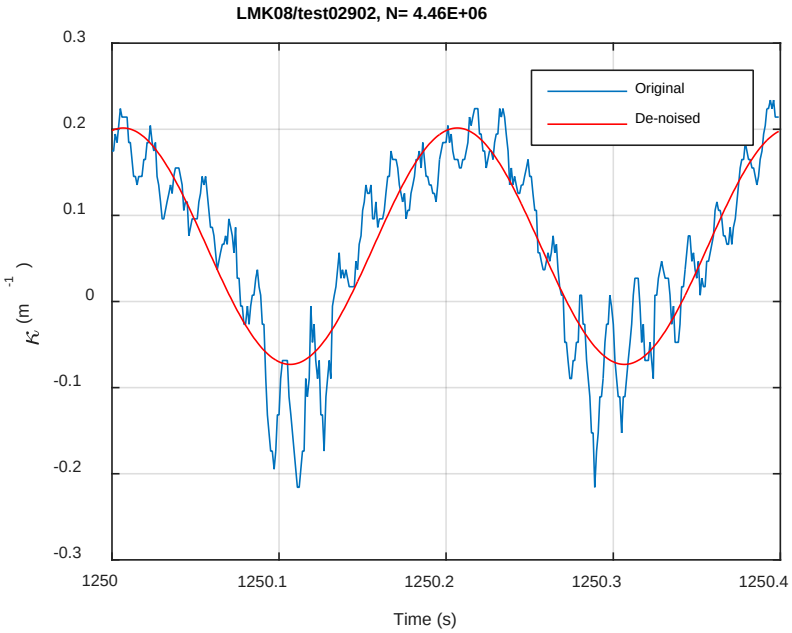

(c)

Fig. A.25. Monitoring-based responses: (a) curvature, (b) moment, (c) curvature, LMK08, 7.62 Nm, Ns = 4.46E+06 cycles.

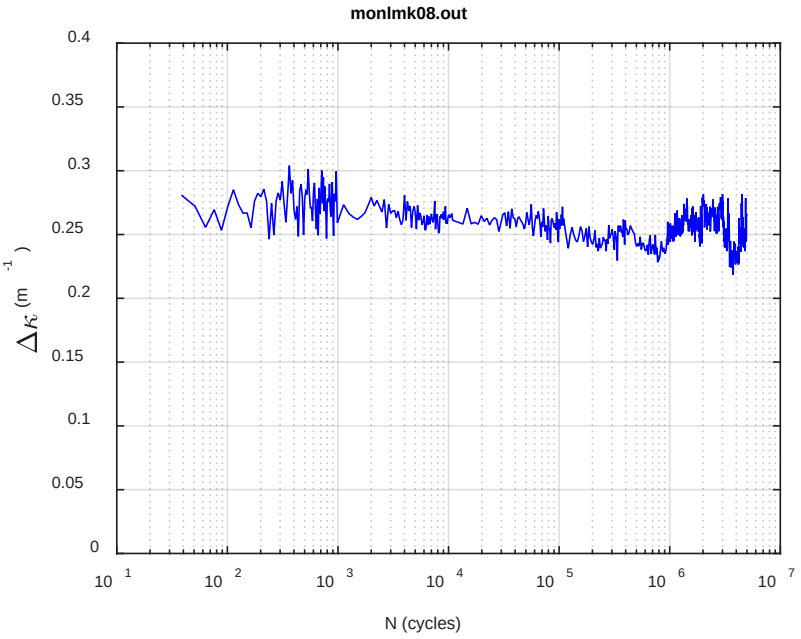
monlmk08.out
0.4
0.35
0.3
0.25
0.2
0.15
0.1
0.05
0
Δκ (m -1)
10 1
10 2
10 3
10 4
10 5
10 6
10 7
N (cycles)

(a)

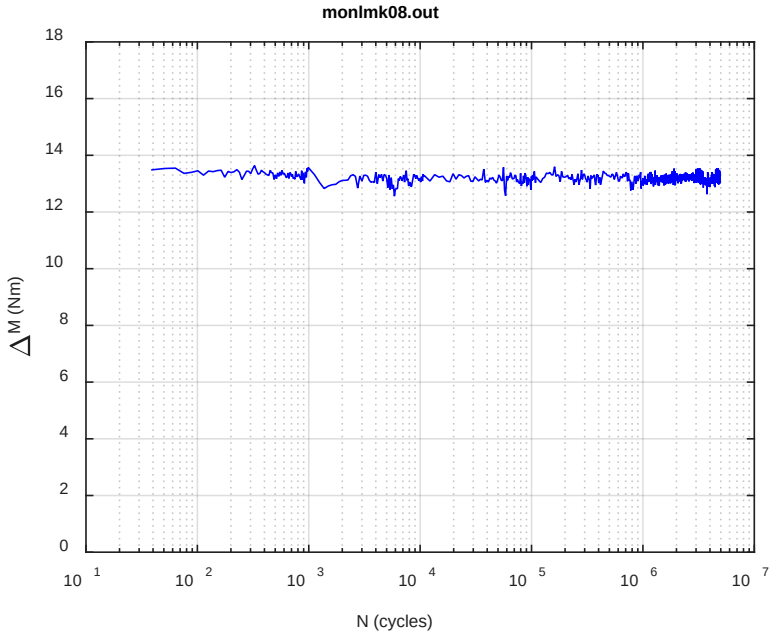
monlmk08.out
18
16
14
12
10
8
6
4
2
0
Δ M (Nm)
10 1
10 2
10 3
10 4
10 5
10 6
10 7
N (cycles)

(b)

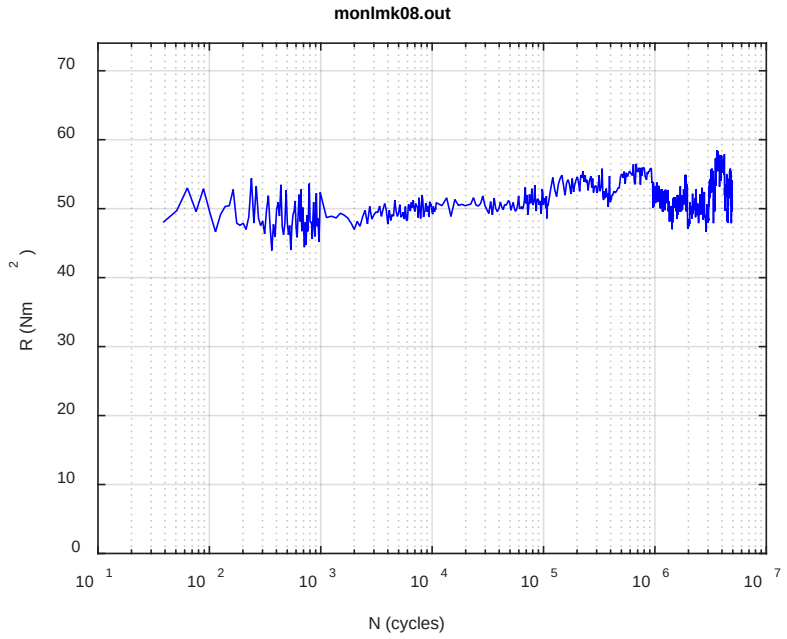
monlmk08.out
R (Nm 2)
N (cycles)

(c)

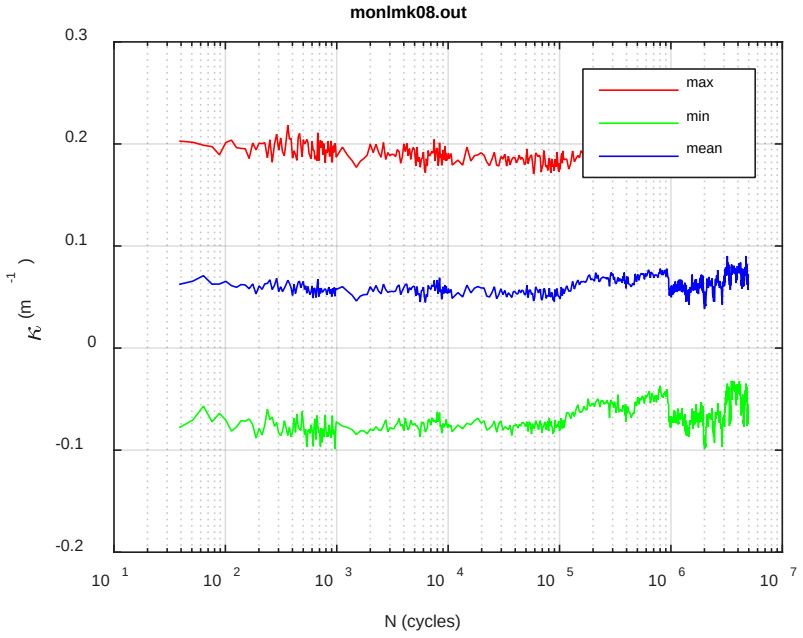
monlmk08.out
max
min
mean
κ (m -1)
N (cycles)

(d)

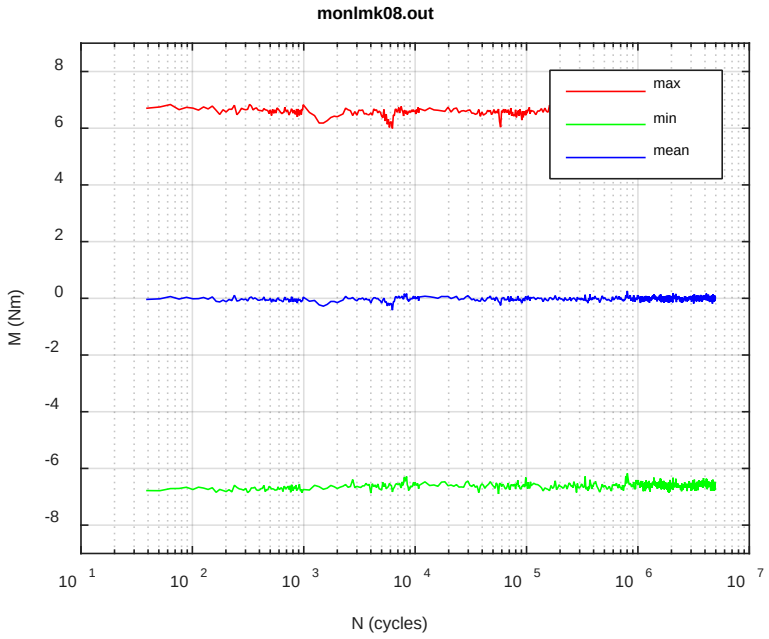

(e)

Fig. A.26. Monitoring-based responses: (a) curvature range, (b) moment range, (c) rigidity, (d) curvature peak/valley, (e) moment peak/valley, LMK08, 7.62 Nm, Nf = 4.70E+06 cycles.

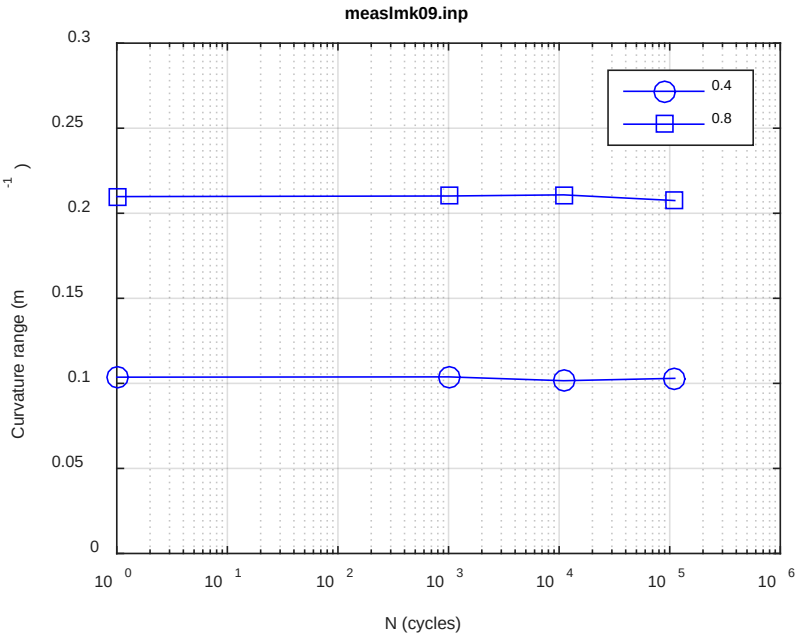
measlmk09.inp
Curvature range (m-1)
N (cycles)
0.4
0.8
0.3
0.25
0.2
0.15
0.1
0.05
0
10 0
10 1
10 2
10 3
10 4
10 5
10 6

(a)

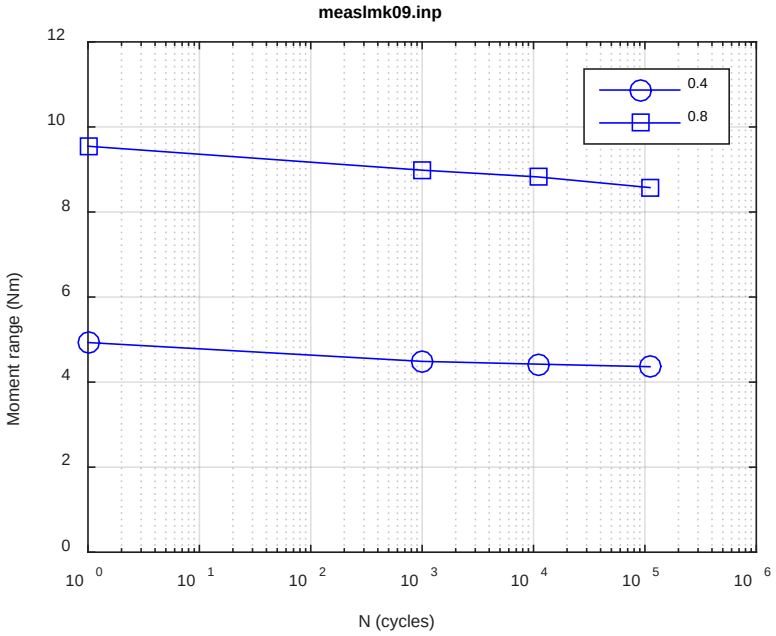
measlmk09.inp
Moment range (Nm)
N (cycles)
0.4
0.8
12
10
8
6
4
2
0
10 0
10 1
10 2
10 3
10 4
10 5
10 6

(b)

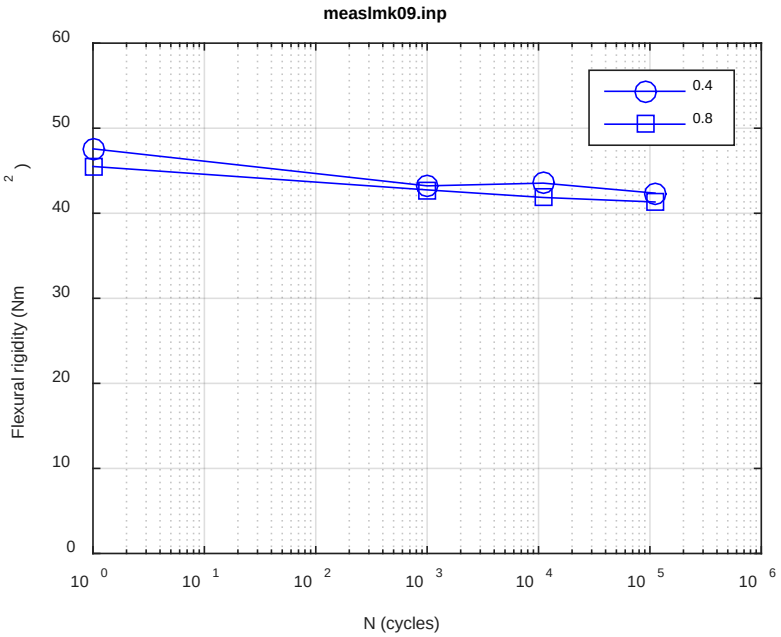
measlmk09.inp
Flexural rigidity (Nm 2)
N (cycles)
0.4
0.8
60
50
40
30
20
10
0
10 0
10 1
10 2
10 3
10 4
10 5
10 6

(c)

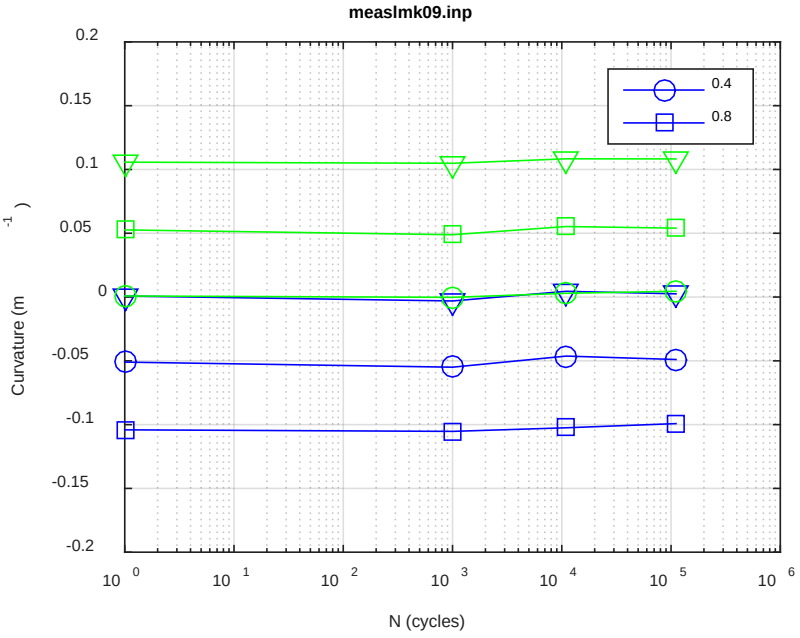
measlmk09.inp
Curvature (m -1)
N (cycles)
0.4
0.8
0.2
0.15
0.1
0.05
0
-0.05
-0.1
-0.15
-0.2
10 0
10 1
10 2
10 3
10 4
10 5
10 6

(d)

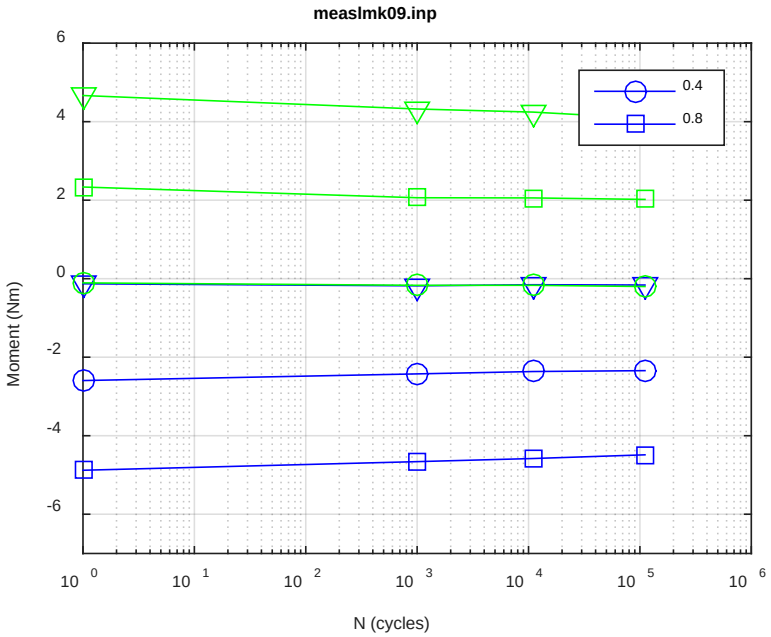

(e)

Fig. A.27. Measurement-based responses: (a) curvature range, (b) moment range, (c) rigidity, (d) curvature peak/valley, (e) moment peak/valley, LMK09, 10.16 Nm.

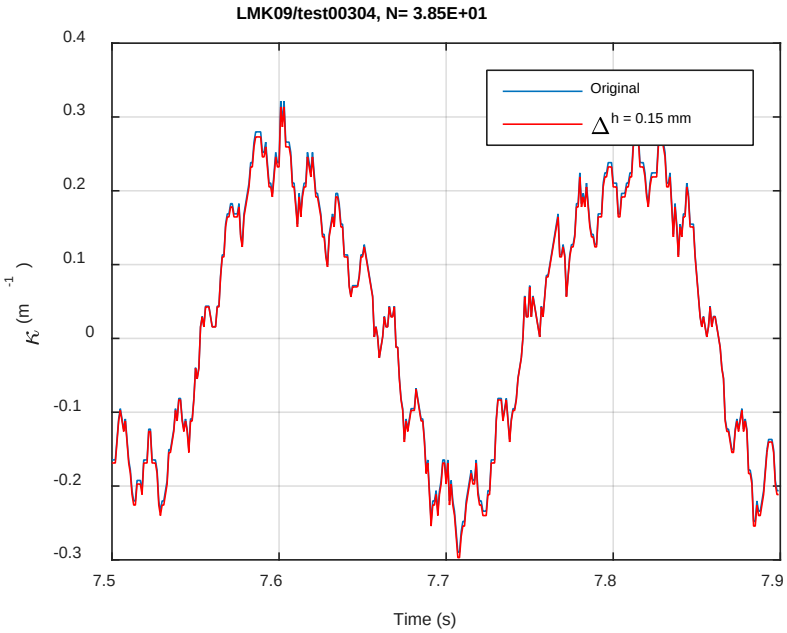
LMK09/test00304, N= 3.85E+01
Original
Δh = 0.15 mm
κ (m-1)
Time (s)
0.4
0.3
0.2
0.1
0
-0.1
-0.2
-0.3
7.5
7.6
7.7
7.8
7.9

(a)

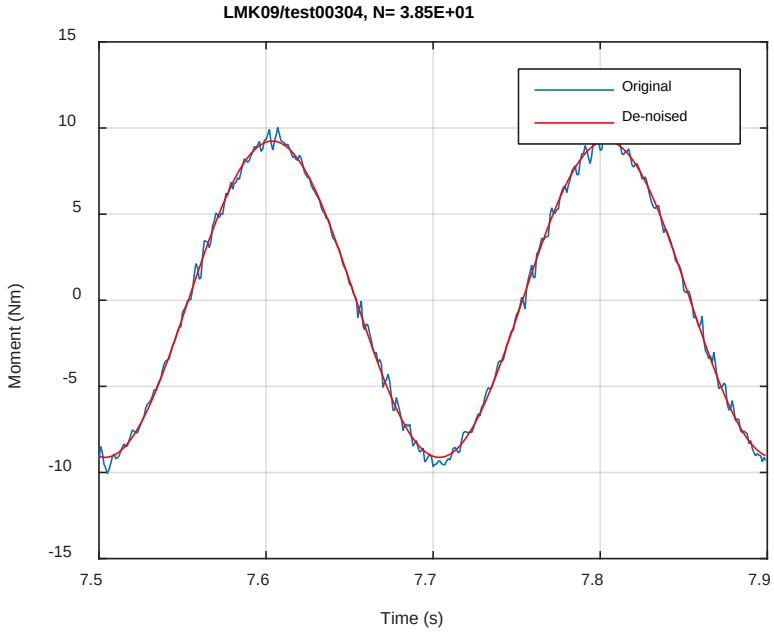
LMK09/test00304, N= 3.85E+01
Original
De-noised
Moment (Nm)
Time (s)
15
10
5
0
-5
-10
-15
7.5
7.6
7.7
7.8
7.9

(b)

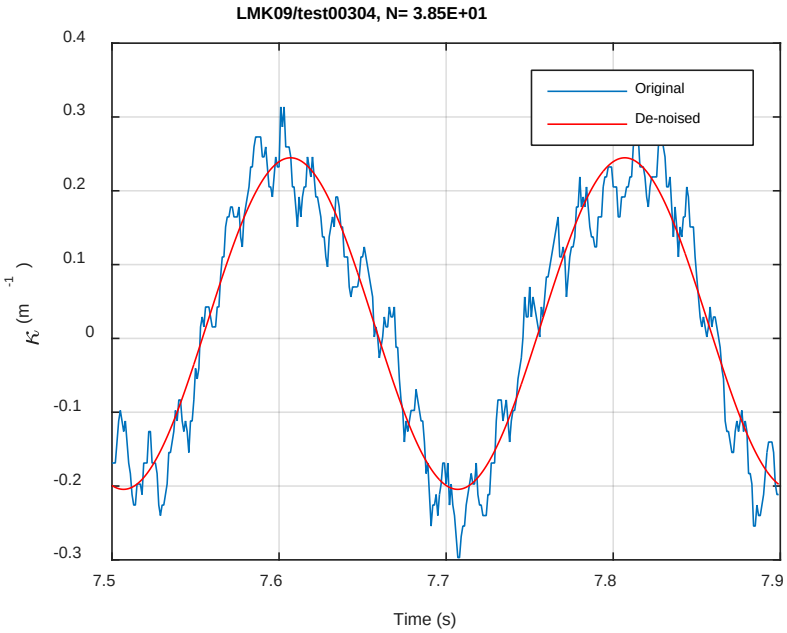

(c)

Fig. A.28. Monitoring-based responses: (a) curvature, (b) moment, (c) curvature, LMK09, 10.16 Nm, Ns = 3.85E+01 cycles.

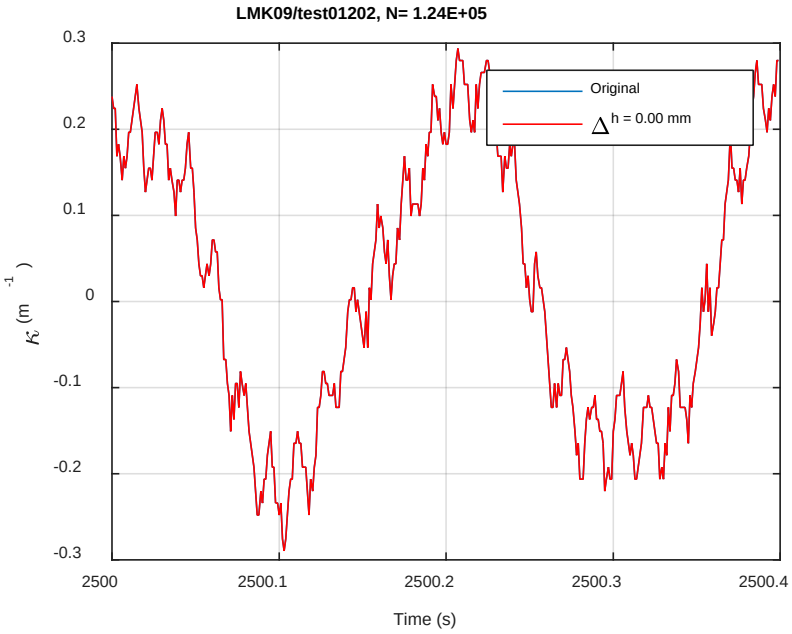
LMK09/test01202, N= 1.24E+05
Original
Δh = 0.00 mm
κ (m-1)
Time (s)
0.3
0.2
0.1
0
-0.1
-0.2
-0.3
2500
2500.1
2500.2
2500.3
2500.4

(a)

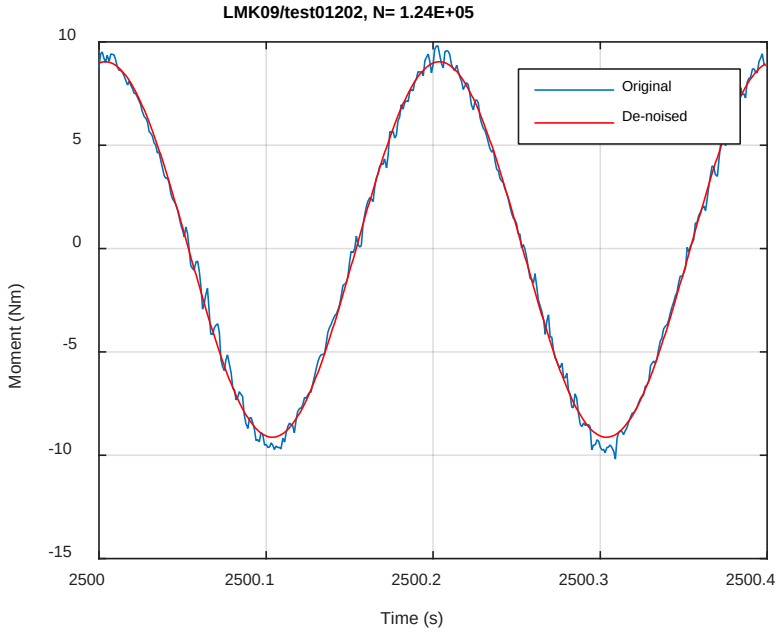
LMK09/test01202, N= 1.24E+05
Original
De-noised
Moment (Nm)
Time (s)
10
5
0
-5
-10
-15
2500
2500.1
2500.2
2500.3
2500.4

(b)

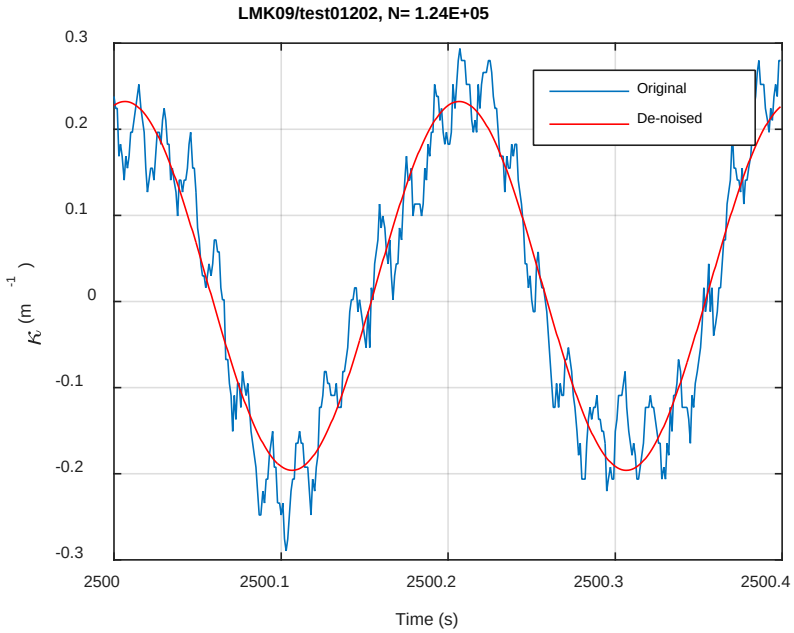

(c)

Fig. A.29. Monitoring-based responses: (a) curvature, (b) moment, (c) curvature, LMK09, 10.16 Nm, Ns = 1.24E+05 cycles.

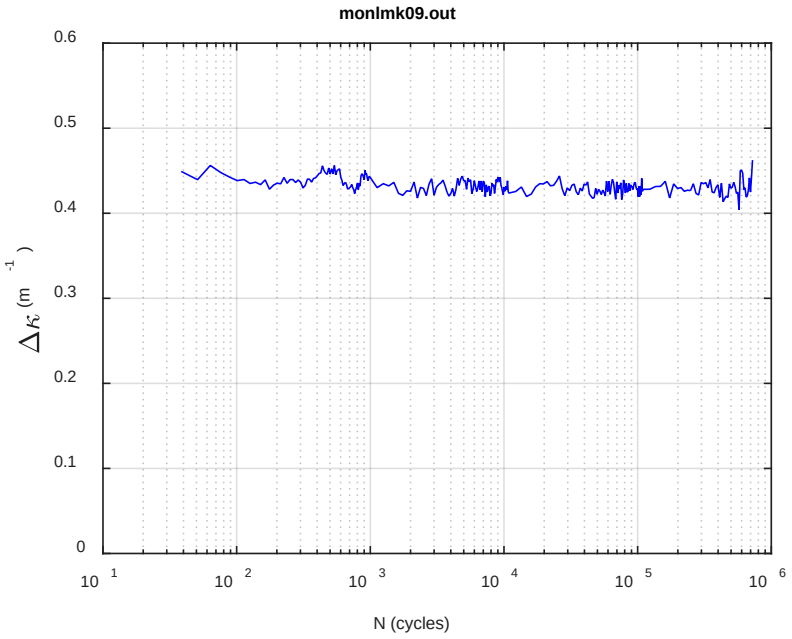
monlmk09.out
0.6
0.5
0.4
0.3
0.2
0.1
0
$\Delta\kappa$ (m^{-1})
10^1
10^2
10^3
10^4
10^5
10^6
N (cycles)

(a)

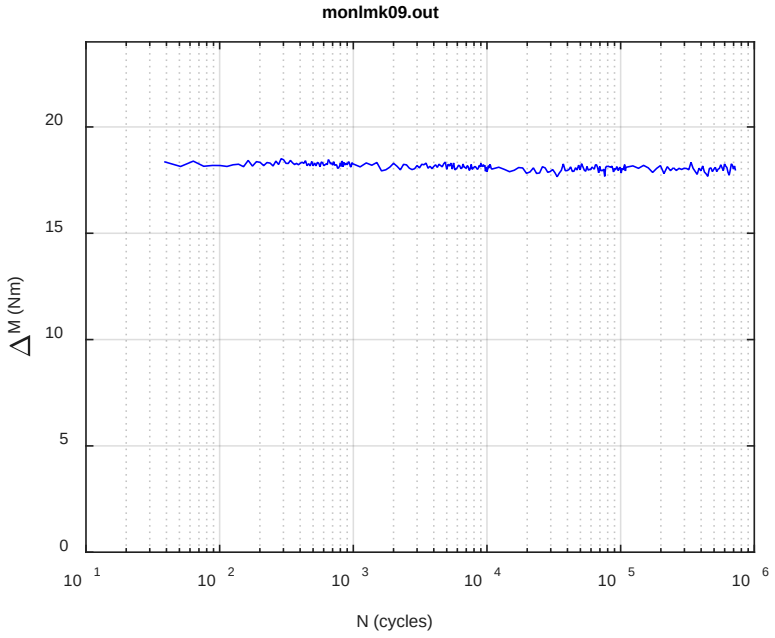
monlmk09.out
20
15
10
5
0
Δ M (Nm)
10^1
10^2
10^3
10^4
10^5
10^6
N (cycles)

(b)

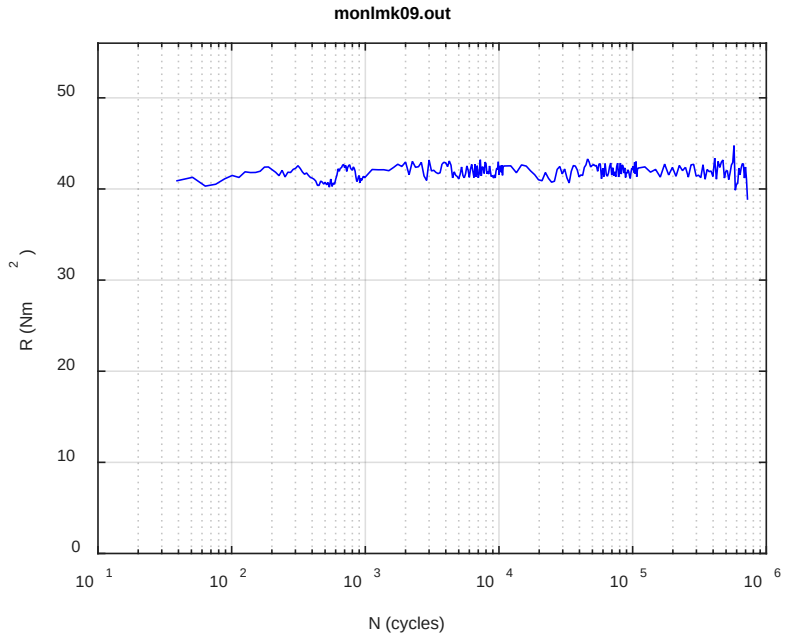
monlmk09.out
R (Nm 2)
N (cycles)

(c)

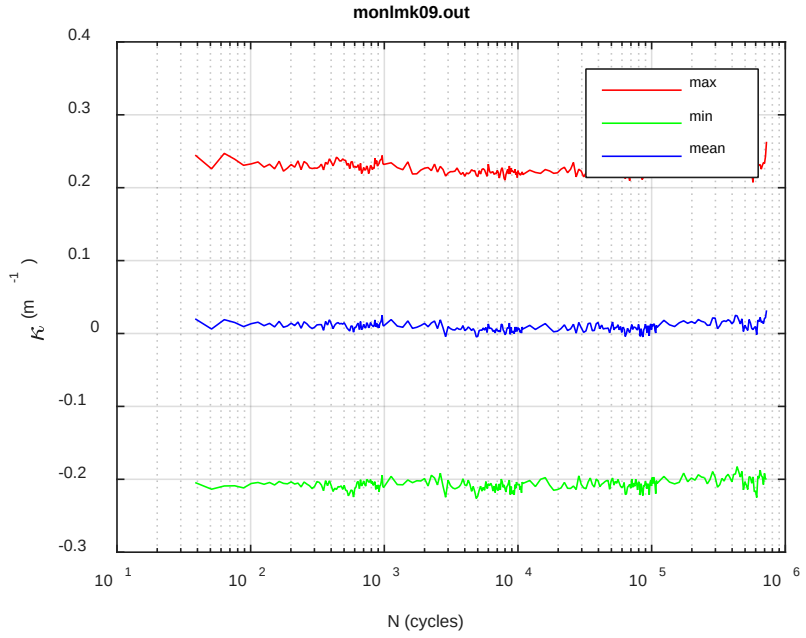
monlmk09.out
max
min
mean
κ (m -1)
N (cycles)

(d)

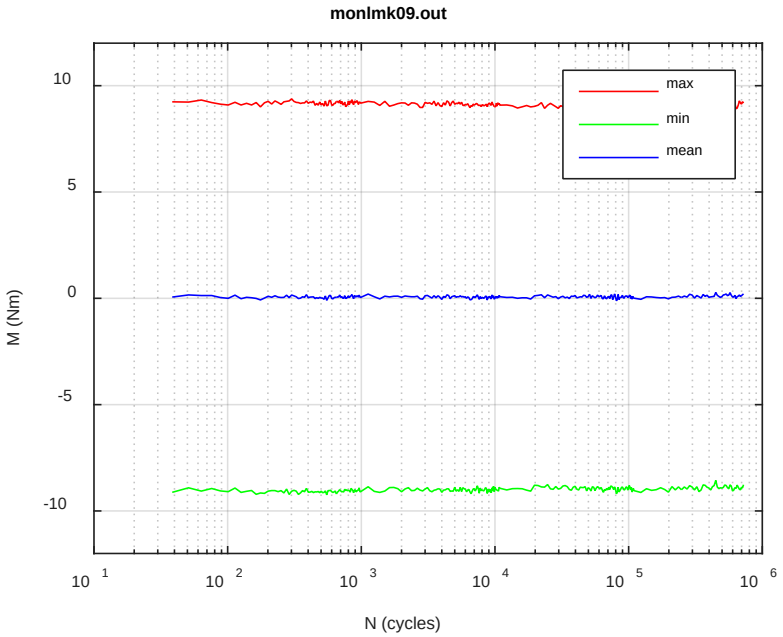

(e)

Fig. A.30. Monitoring-based responses: (a) curvature range, (b) moment range, (c) rigidity, (d) curvature peak/valley, (e) moment peak/valley, LMK09, 10.16 Nm, Nf = 7.31E+05 cycles.

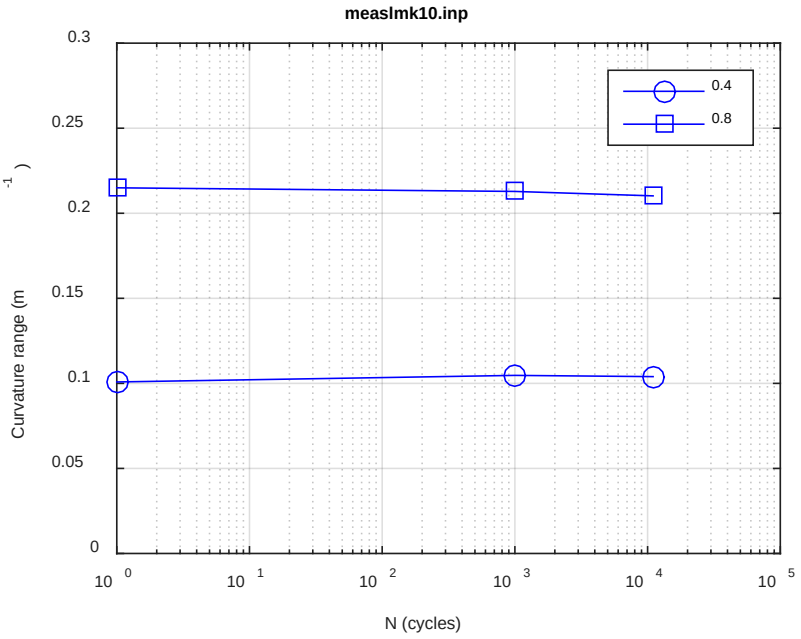
measlmk10.inp
0.3
0.25
0.2
0.15
0.1
0.05
0
Curvature range (m -1)
0.4
0.8
10 0
10 1
10 2
10 3
10 4
10 5
N (cycles)

(a)

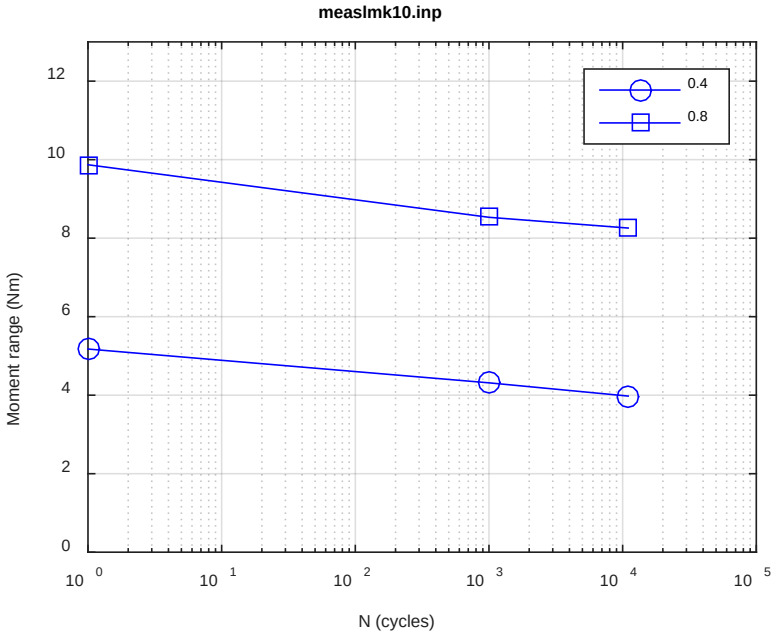
measlmk10.inp
12
10
8
6
4
2
0
Moment range (Nm)
0.4
0.8
10 0
10 1
10 2
10 3
10 4
10 5
N (cycles)

(b)

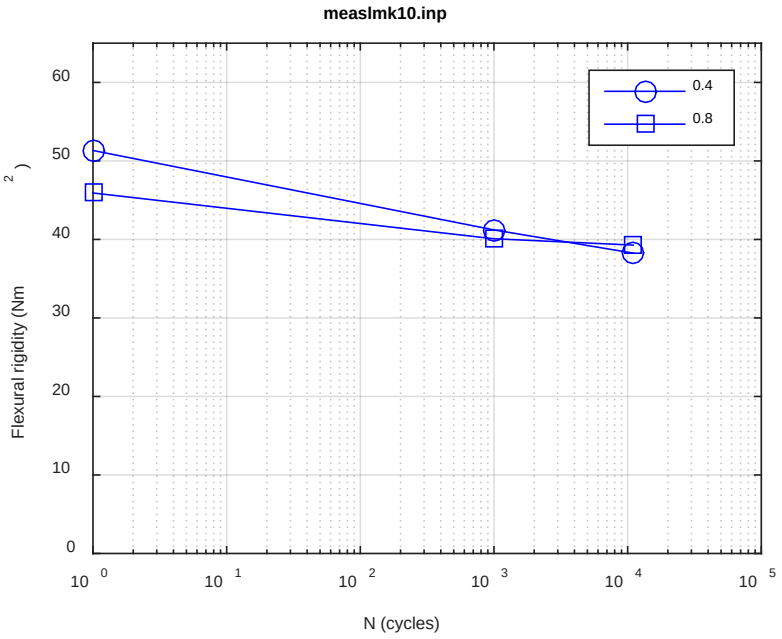
measlmk10.inp
0.4
0.8
Flexural rigidity (Nm 2)
N (cycles)
0
10
20
30
40
50
60
10 0
10 1
10 2
10 3
10 4
10 5

(c)

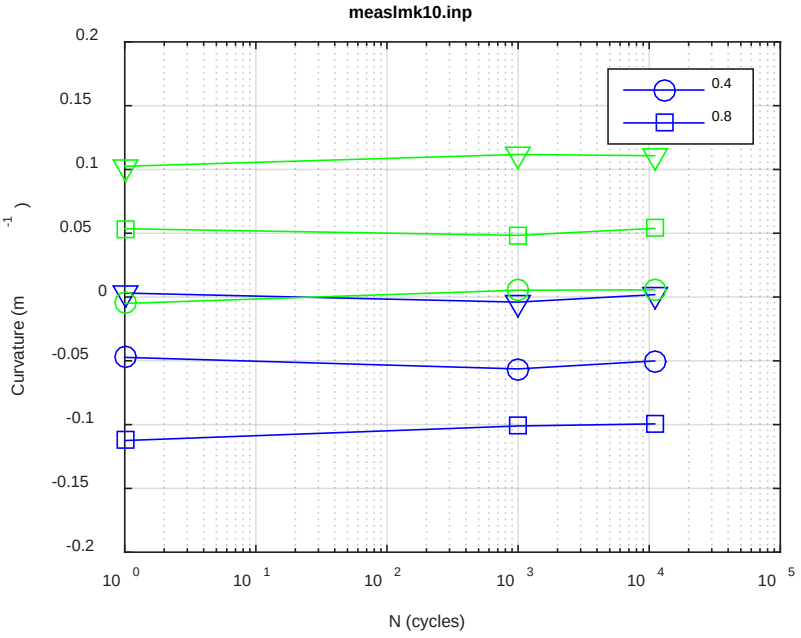
measlmk10.inp
0.4
0.8
Curvature (m -1)
N (cycles)
0.2
0.15
0.1
0.05
0
-0.05
-0.1
-0.15
-0.2
10 0
10 1
10 2
10 3
10 4
10 5

(d)

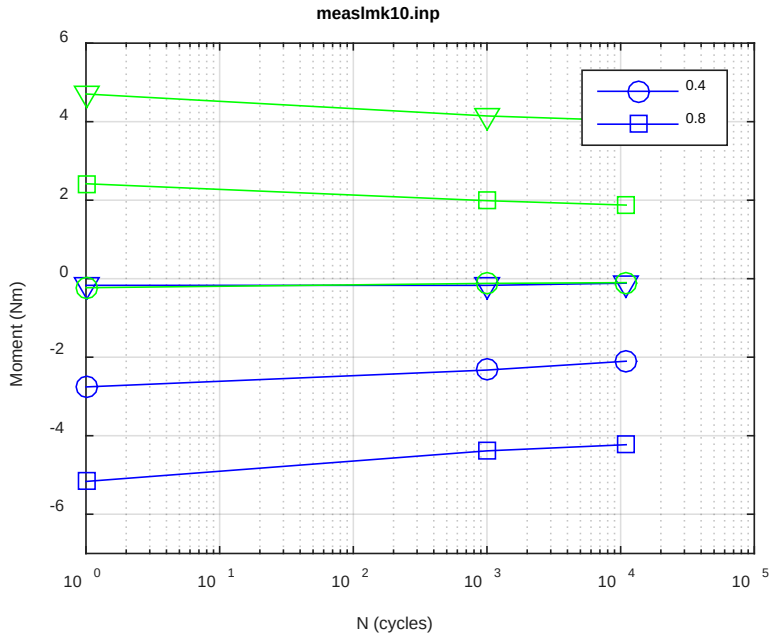

(e)

Fig. A.31. Measurement-based responses: (a) curvature range, (b) moment range, (c) rigidity, (d) curvature peak/valley, (e) moment peak/valley, LMK10, 20.32 Nm.

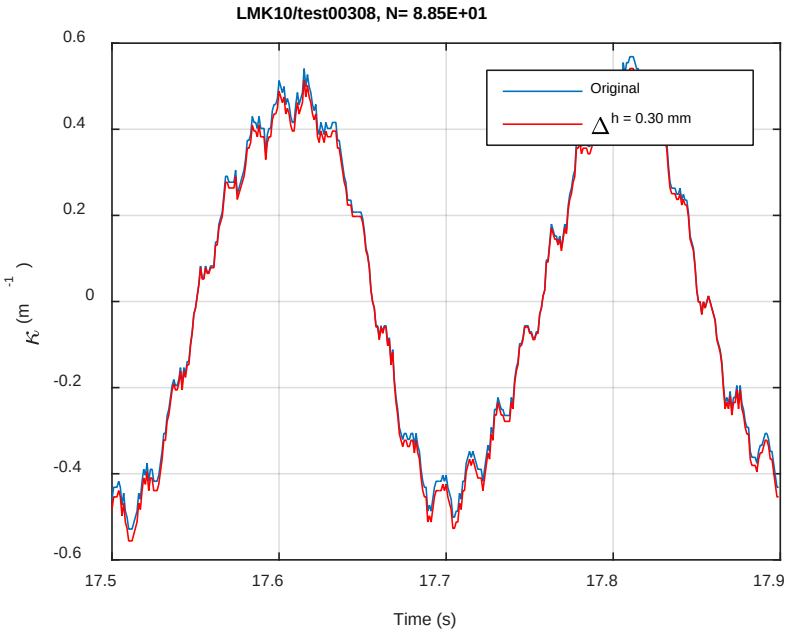
LMK10/test00308, N= 8.85E+01
Original
Δh = 0.30 mm
κ (m-1)
Time (s)
0.6
0.4
0.2
0
-0.2
-0.4
-0.6
17.5
17.6
17.7
17.8
17.9

(a)

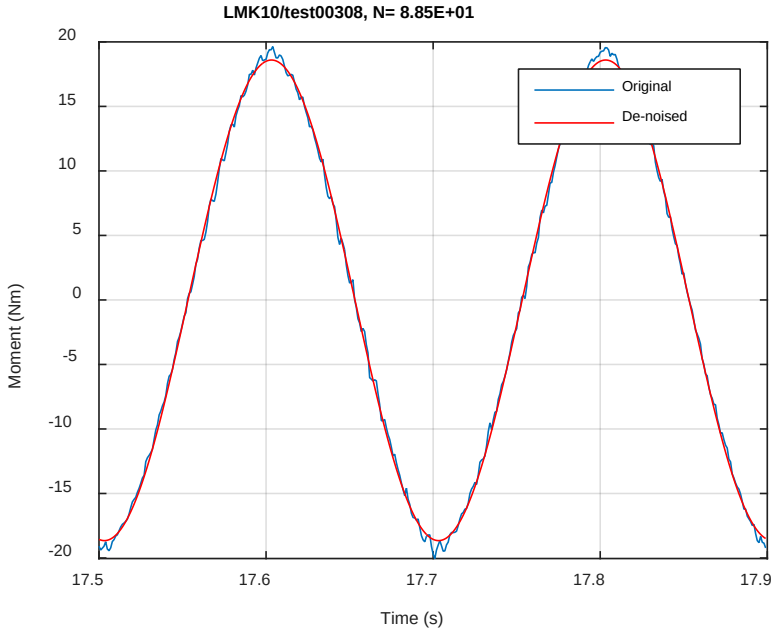
LMK10/test00308, N= 8.85E+01
Original
De-noised
Moment (Nm)
Time (s)
20
15
10
5
0
-5
-10
-15
-20
17.5
17.6
17.7
17.8
17.9

(b)

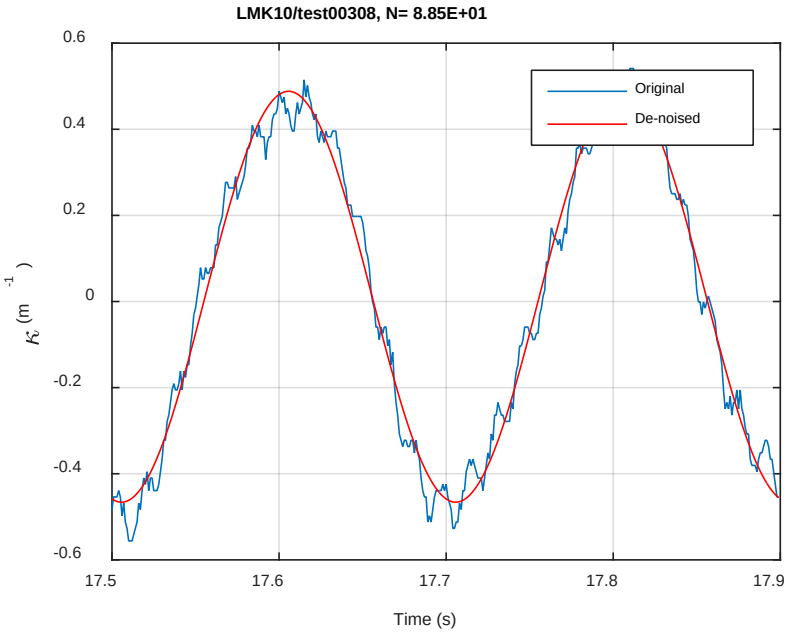

(c)

Fig. A.32. Monitoring-based responses: (a) curvature, (b) moment, (c) curvature, LMK10, 20.32 Nm, Ns = 8.85E+01 cycles.

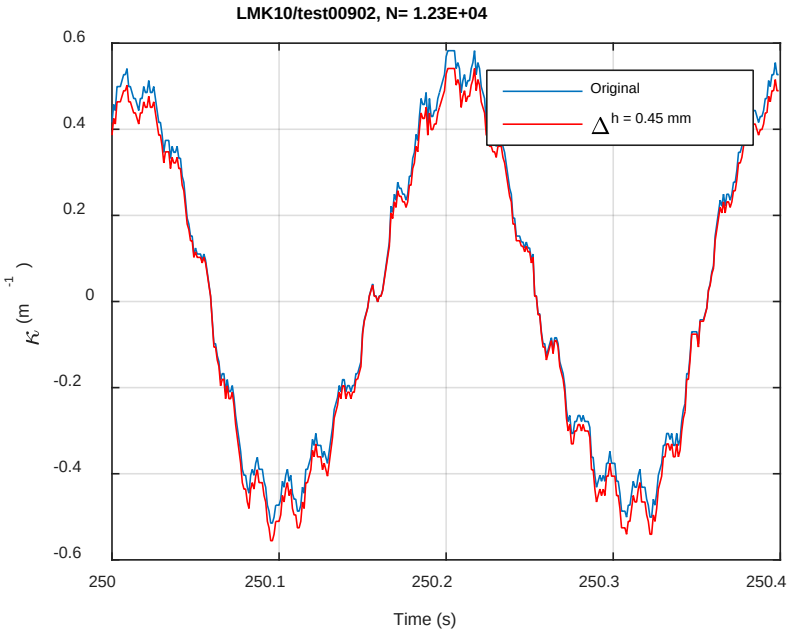
LMK10/test00902, N= 1.23E+04
Original
Δh = 0.45 mm
κ (m-1)
Time (s)
0.6
0.4
0.2
0
-0.2
-0.4
-0.6
250
250.1
250.2
250.3
250.4

(a)

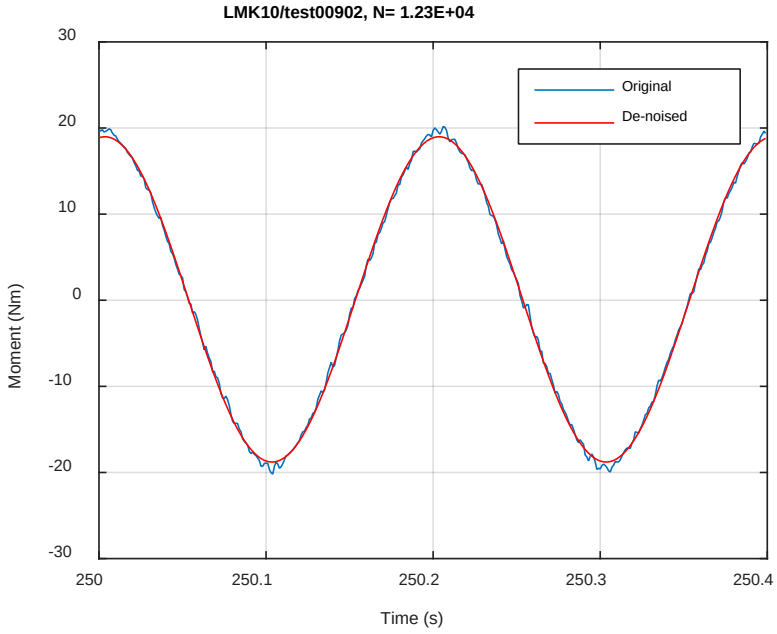
LMK10/test00902, N= 1.23E+04
Original
De-noised
Moment (Nm)
Time (s)
30
20
10
0
-10
-20
-30
250
250.1
250.2
250.3
250.4

(b)

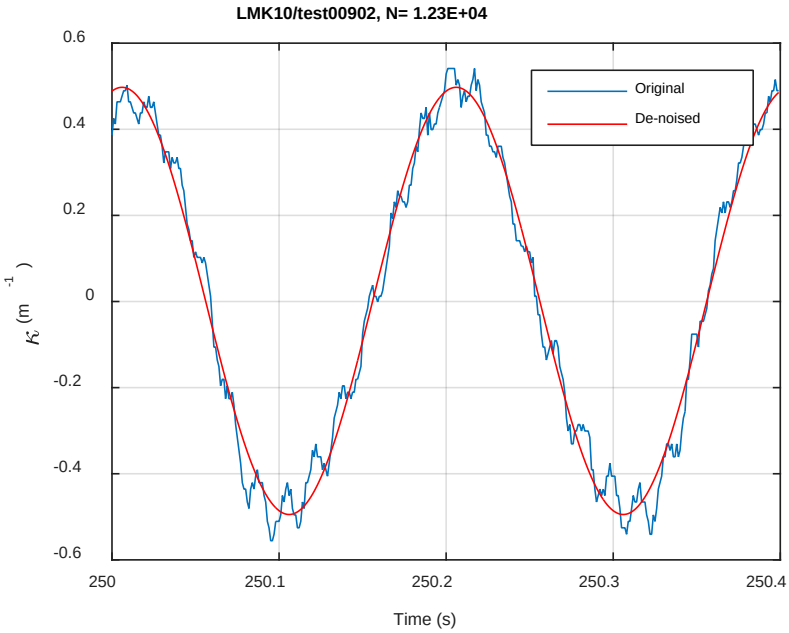

(c)

Fig. A.33. Monitoring-based responses: (a) curvature, (b) moment, (c) curvature, LMK10, 20.32 Nm, Ns = 1.23E+04 cycles.

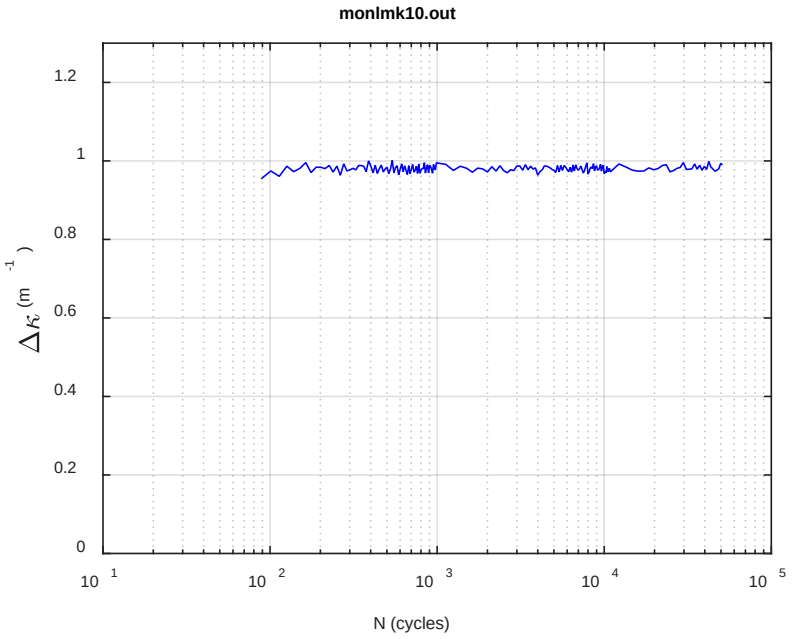
monlmk10.out
1.2
1
0.8
0.6
0.4
0.2
0
$\Delta\kappa$ (m^{-1})
10^1
10^2
10^3
10^4
10^5
N (cycles)

(a)

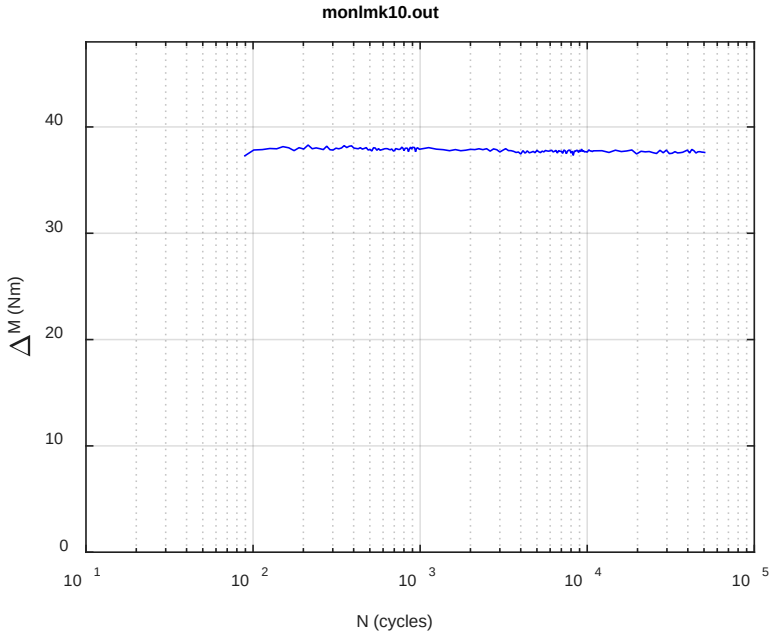
monlmk10.out
40
30
20
10
0
Δ M (Nm)
10^1
10^2
10^3
10^4
10^5
N (cycles)

(b)

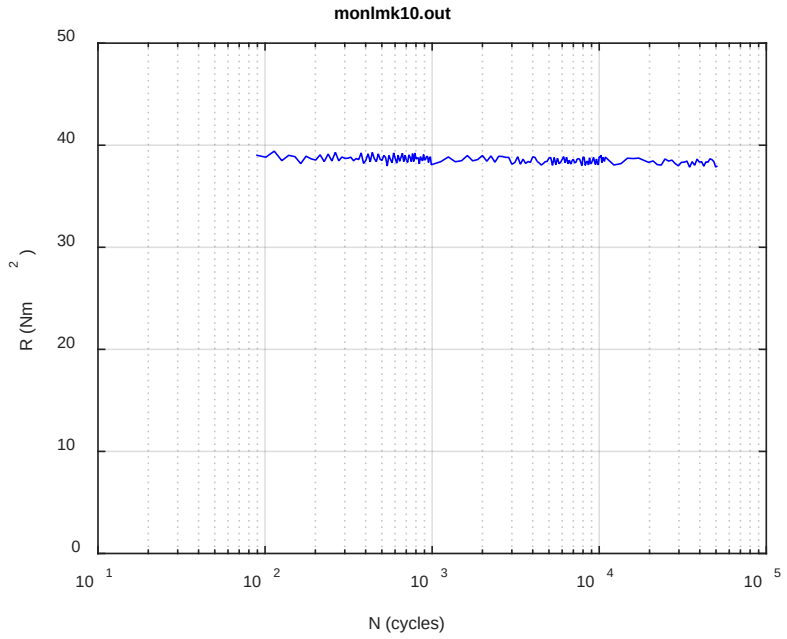
monlmk10.out
R (Nm 2)
N (cycles)

(c)

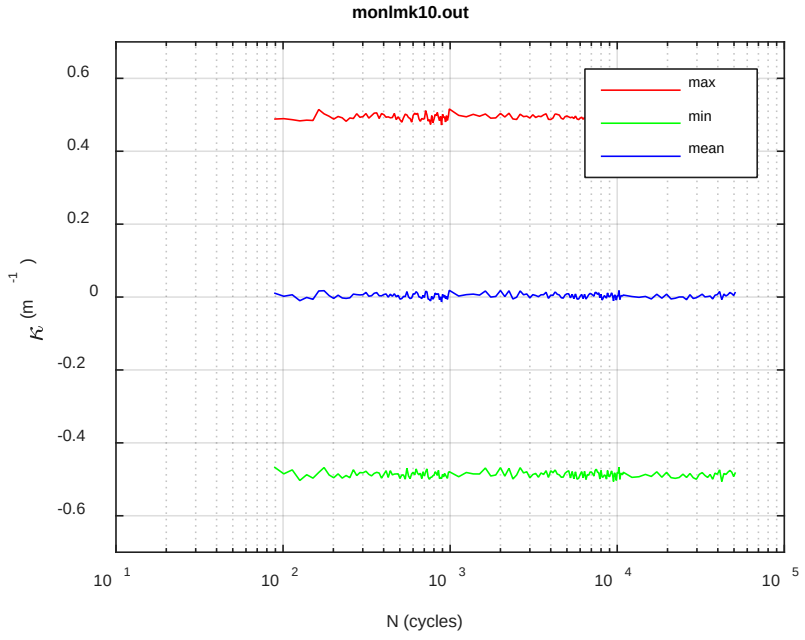
monlmk10.out
max
min
mean
κ (m -1)
N (cycles)

(d)

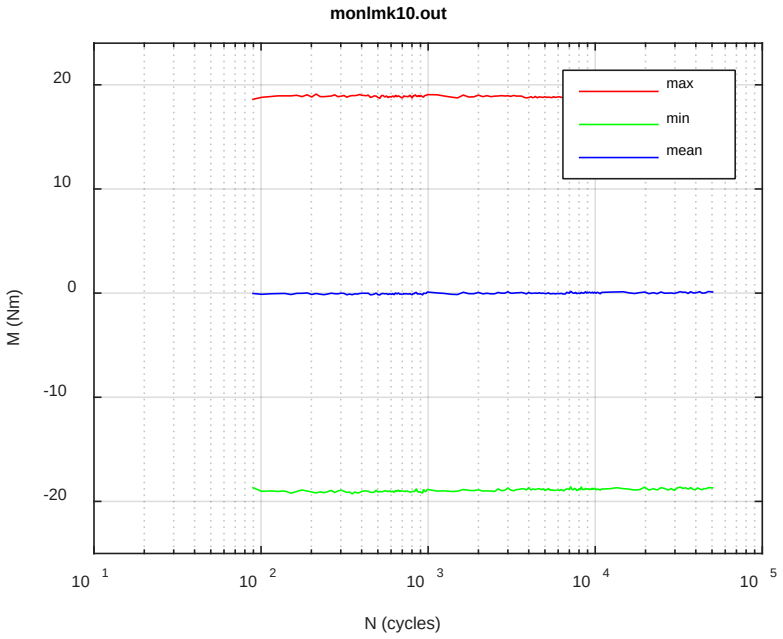

(e)

Fig. A.34. Monitoring-based responses: (a) curvature range, (b) moment range, (c) rigidity, (d) curvature peak/valley, (e) moment peak/valley, LMK10, 20.32 Nm, Nf = 5.20E+04 cycles.

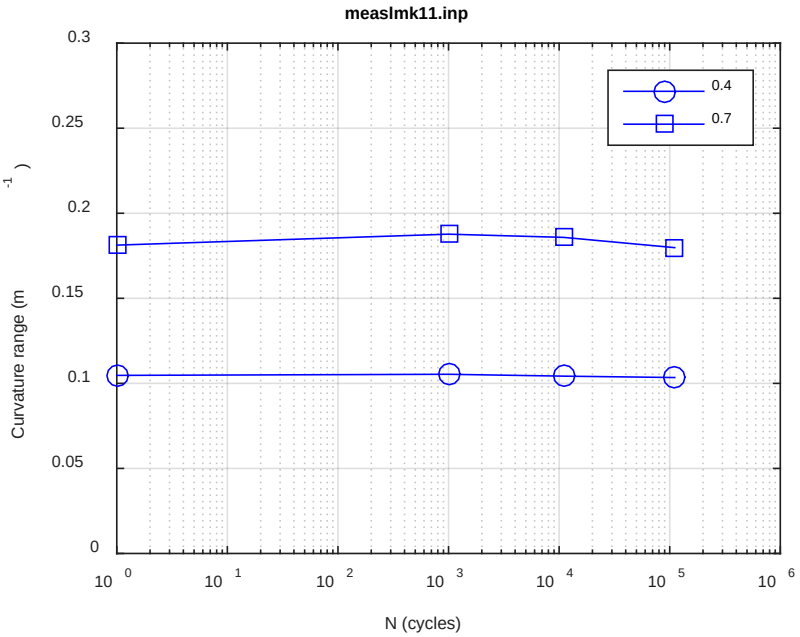
measlmk11.inp
0.3
0.25
0.2
0.15
0.1
0.05
0
Curvature range (m-1)
0.4
0.7
10 0
10 1
10 2
10 3
10 4
10 5
10 6
N (cycles)

(a)

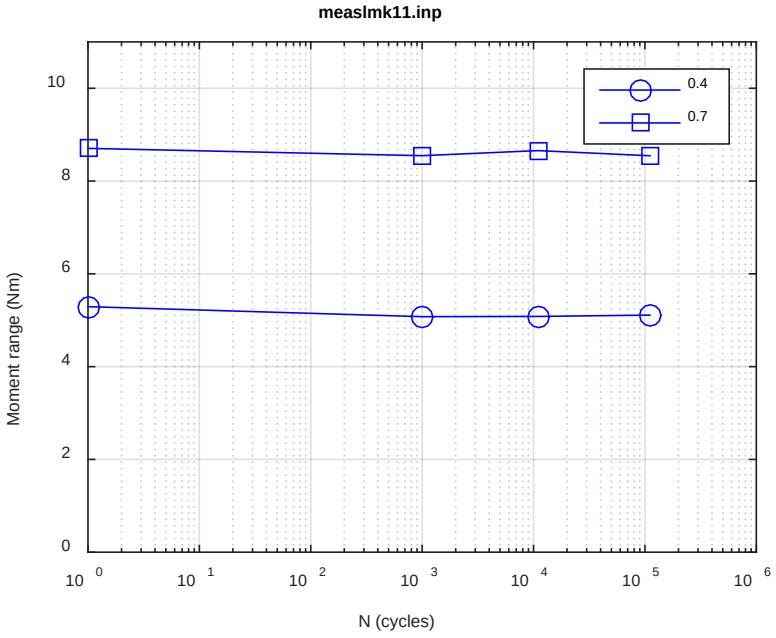
measlmk11.inp
10
8
6
4
2
0
Moment range (Nm)
0.4
0.7
10 0
10 1
10 2
10 3
10 4
10 5
10 6
N (cycles)

(b)

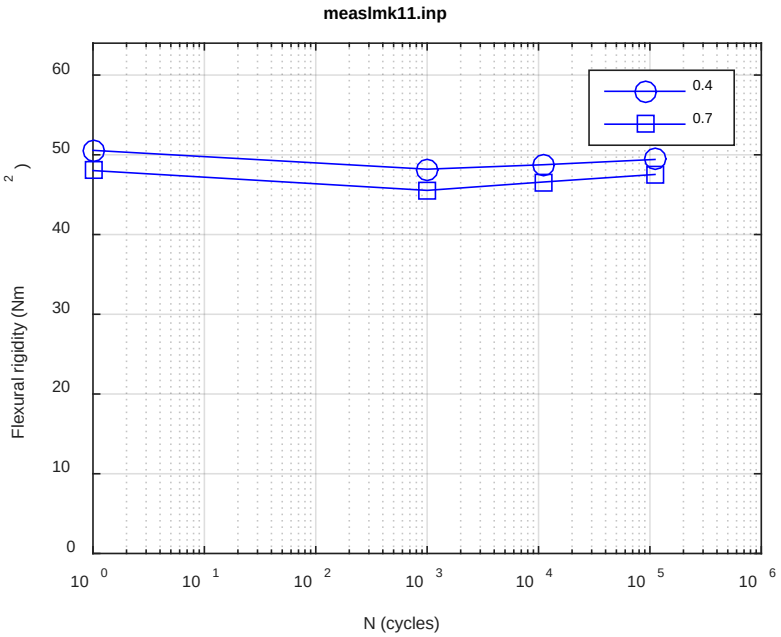
measlmk11.inp
0.4
0.7
Flexural rigidity (Nm 2)
N (cycles)

(c)

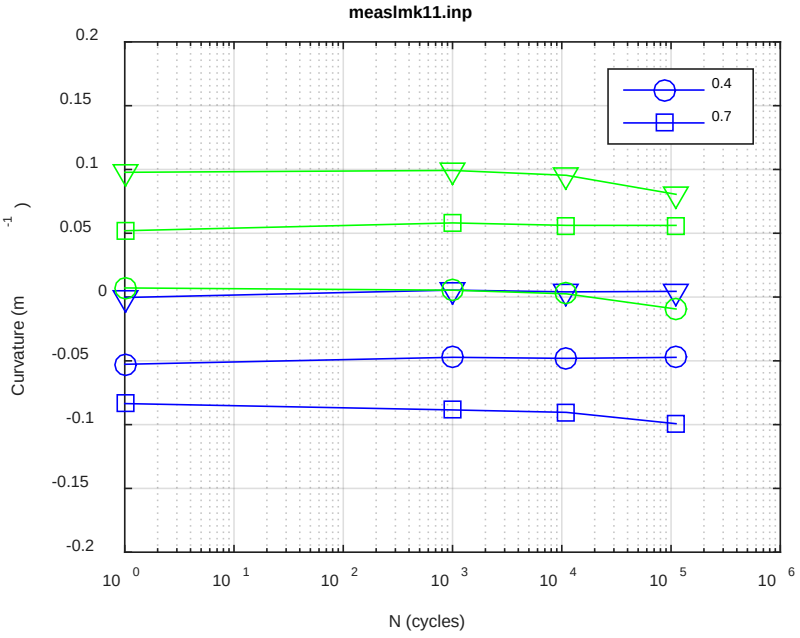
measlmk11.inp
0.4
0.7
Curvature (m -1)
N (cycles)

(d)

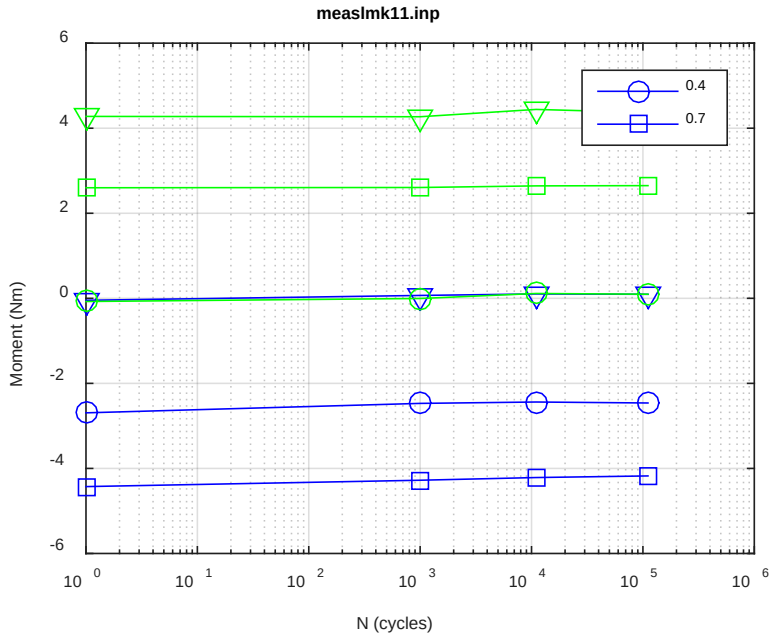

(e)

Fig. A.35. Measurement-based responses: (a) curvature range, (b) moment range, (c) rigidity, (d) curvature peak/valley, (e) moment peak/valley, LMK11, 8.64 Nm.

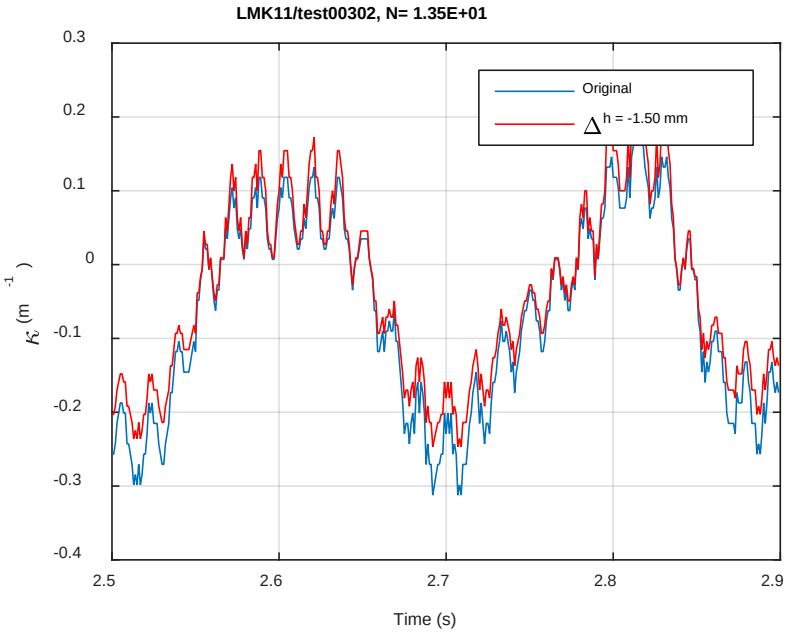
LMK11/test00302, N= 1.35E+01
Original
Δh = -1.50 mm
κ (m-1)
Time (s)
0.3
0.2
0.1
0
-0.1
-0.2
-0.3
-0.4
2.5
2.6
2.7
2.8
2.9

(a)

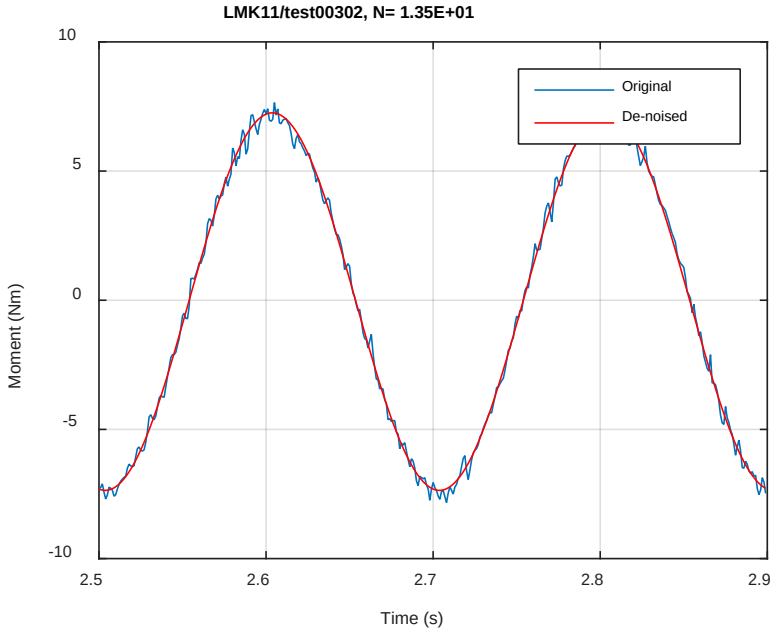
LMK11/test00302, N= 1.35E+01
Original
De-noised
Moment (Nm)
Time (s)
10
5
0
-5
-10
2.5
2.6
2.7
2.8
2.9

(b)

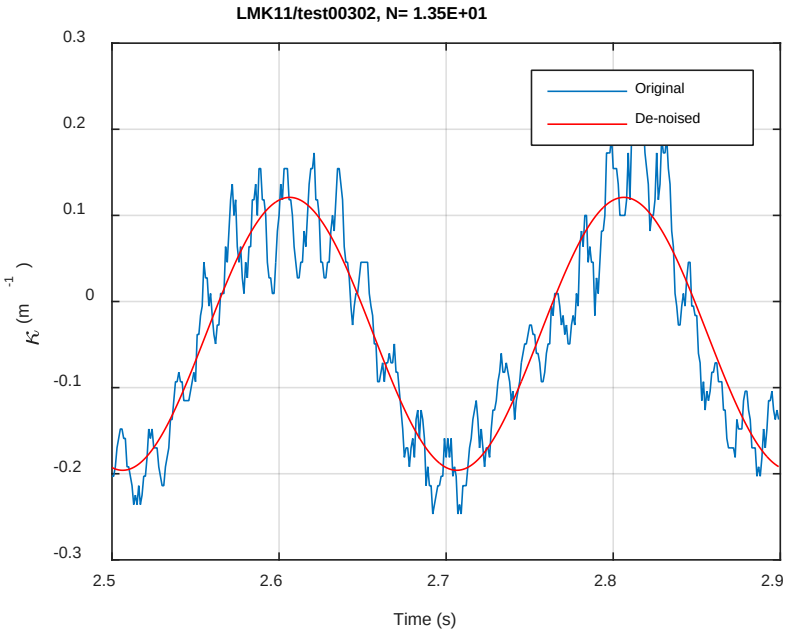

(c)

Fig. A.36. Monitoring-based responses: (a) curvature, (b) moment, (c) curvature, LMK11, 8.64 Nm, Ns = 1.35E+01 cycles.

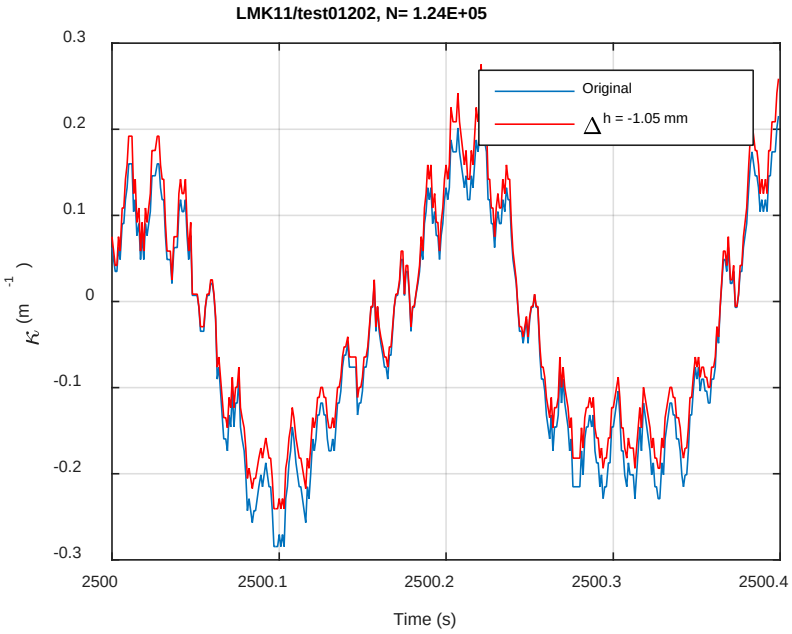
LMK11/test01202, N= 1.24E+05
Original
Δh = -1.05 mm
κ (m-1)
Time (s)
0.3
0.2
0.1
0
-0.1
-0.2
-0.3
2500
2500.1
2500.2
2500.3
2500.4

(a)

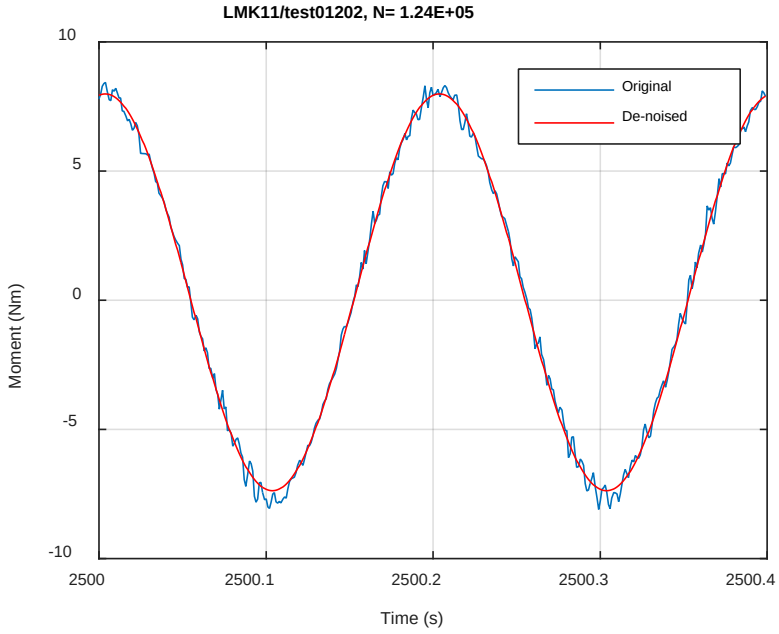
LMK11/test01202, N= 1.24E+05
Original
De-noised
Moment (Nm)
Time (s)
10
5
0
-5
-10
2500
2500.1
2500.2
2500.3
2500.4

(b)

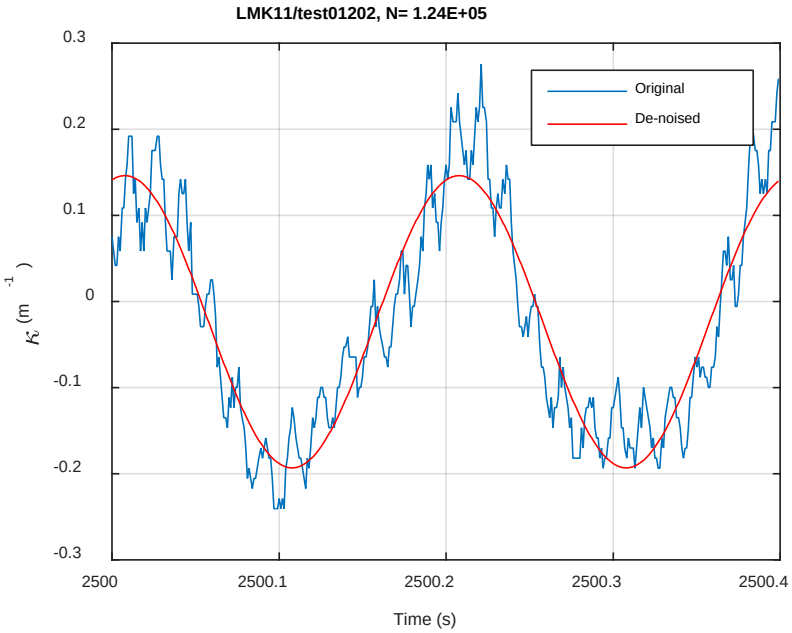

(c)

Fig. A.37. Monitoring-based responses: (a) curvature, (b) moment, (c) curvature, LMK11, 8.64 Nm, Ns = 1.24E+05 cycles.

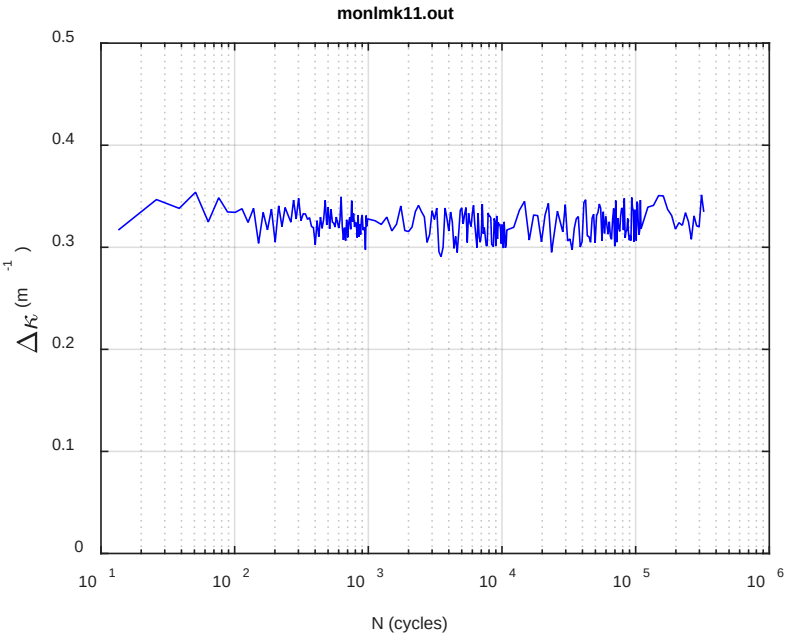
monlmk11.out
0.5
0.4
0.3
0.2
0.1
0
Δκ (m-1)
10 1
10 2
10 3
10 4
10 5
10 6
N (cycles)

(a)

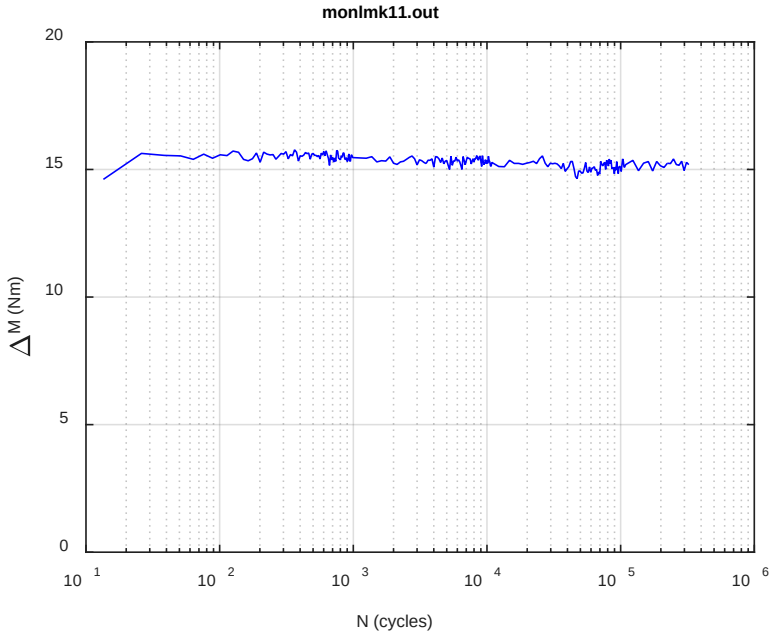
monlmk11.out
20
15
10
5
0
Δ M (Nm)
10 1
10 2
10 3
10 4
10 5
10 6
N (cycles)

(b)

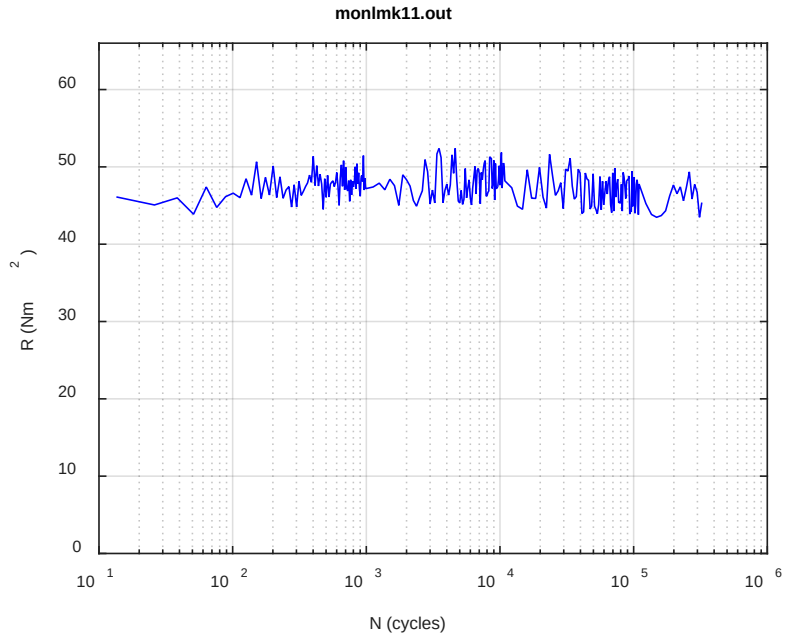
monlmk11.out
R (Nm 2)
N (cycles)

(c)

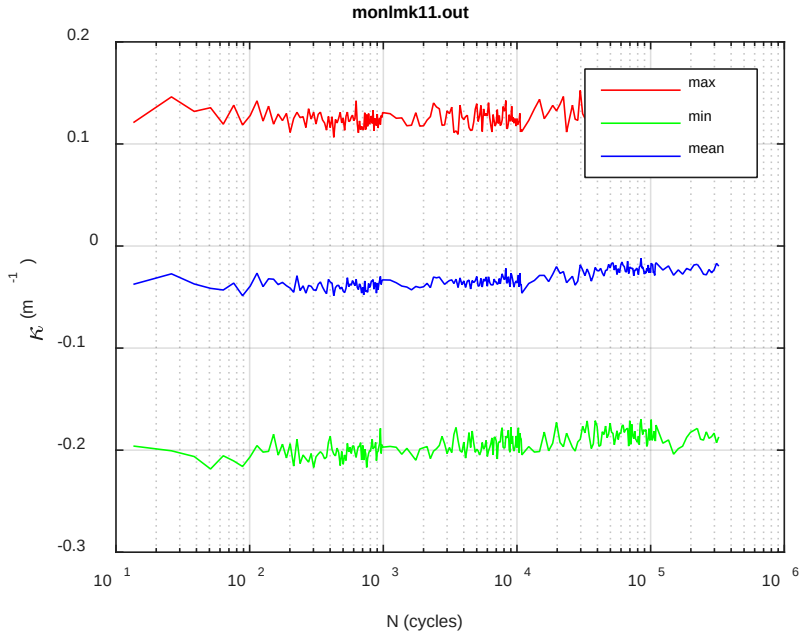
monlmk11.out
max
min
mean
κ (m -1)
N (cycles)

(d)

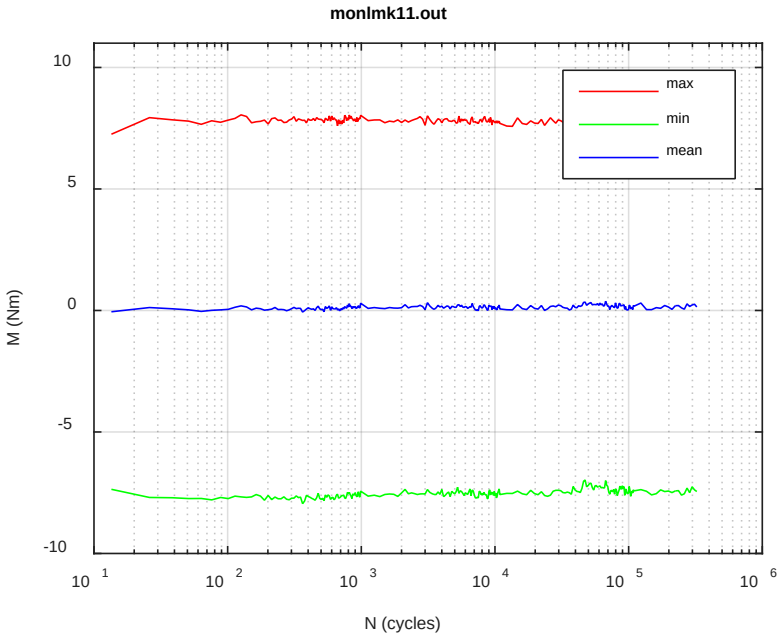

(e)

Fig. A.38. Monitoring-based responses: (a) curvature range, (b) moment range, (c) rigidity, (d) curvature peak/valley, (e) moment peak/valley, LMK11, 8.64 Nm, Nf = 3.55E+05 cycles.

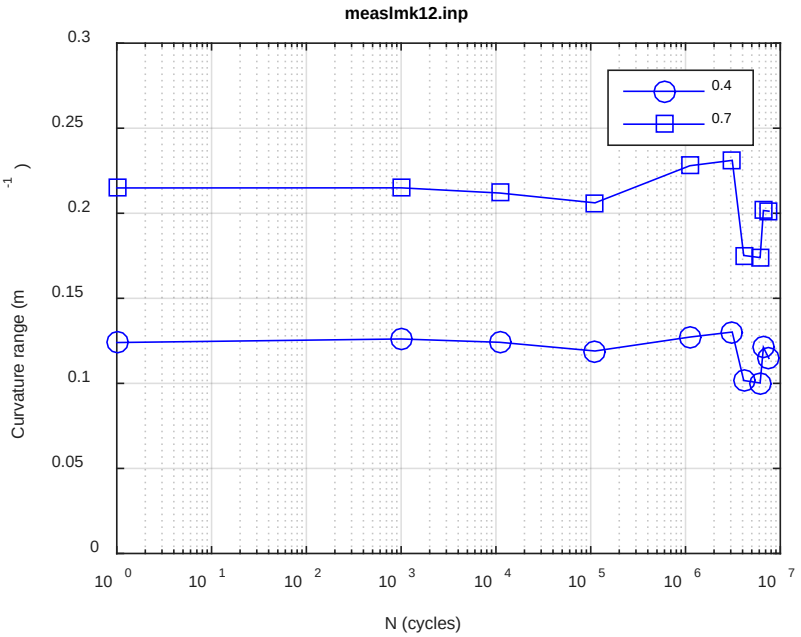
measlmk12.inp
0.4
0.7
Curvature range (m-1)
N (cycles)

(a)

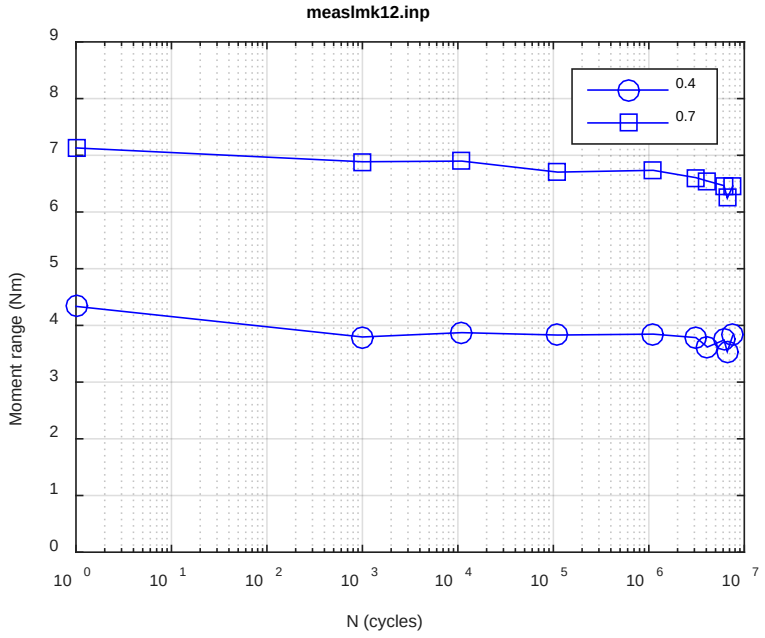
measlmk12.inp
0.4
0.7
Moment range (Nm)
N (cycles)

(b)

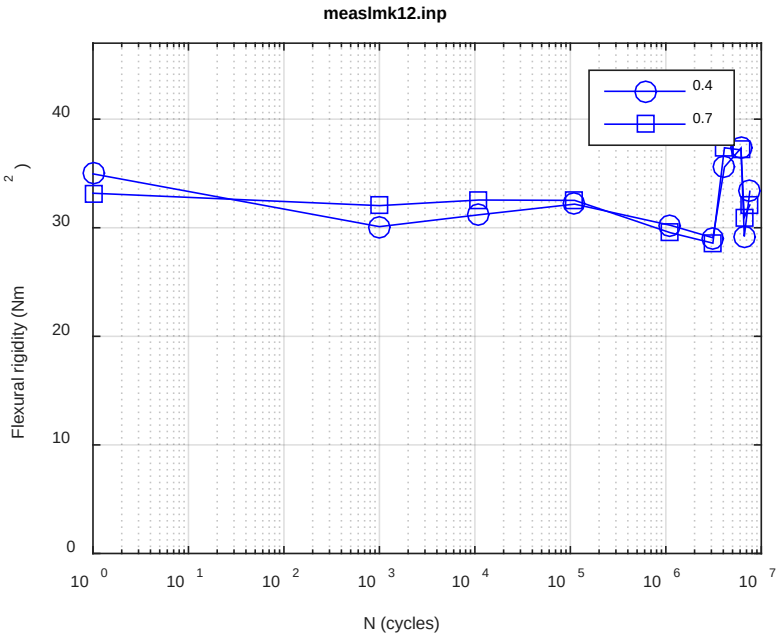
measlmk12.inp
0.4
0.7
Flexural rigidity (Nm 2)
N (cycles)

(c)

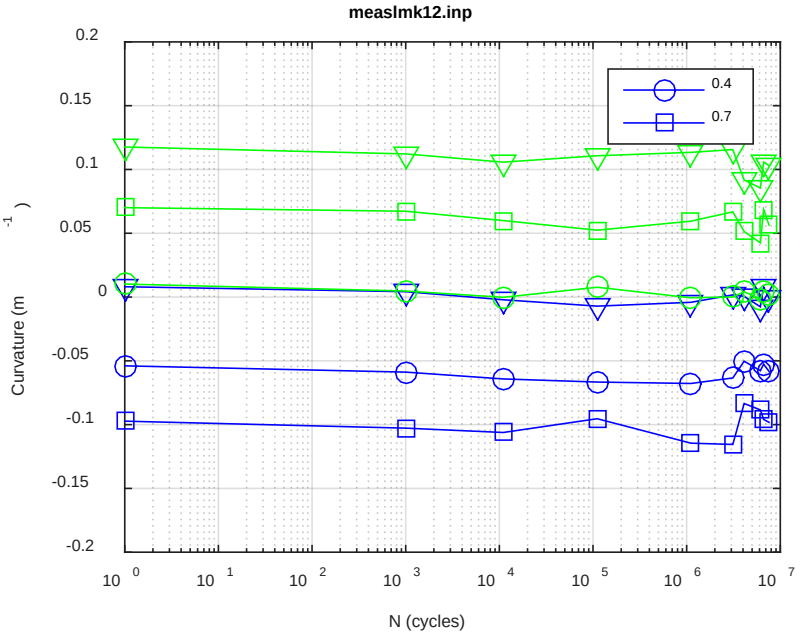
measlmk12.inp
0.4
0.7
Curvature (m -1)
N (cycles)

(d)

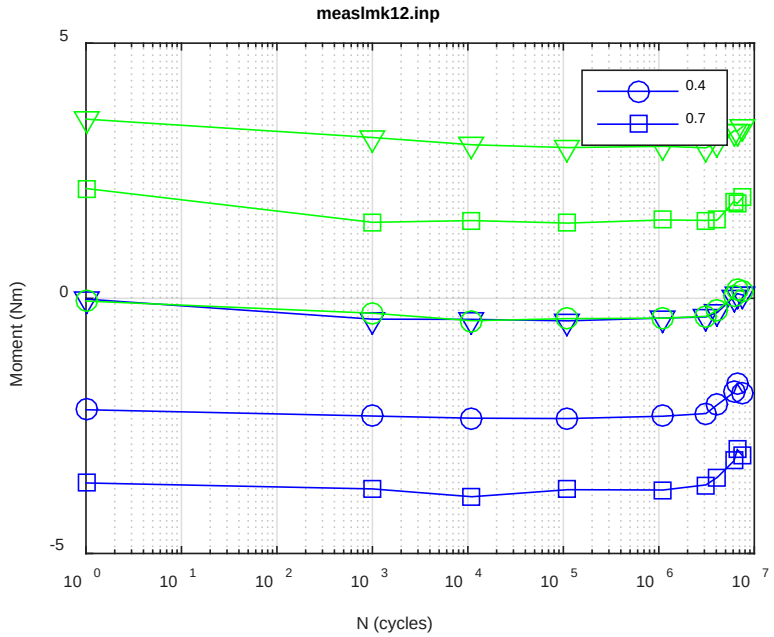

(e)

Fig. A.39. Measurement-based responses: (a) curvature range, (b) moment range, (c) rigidity, (d) curvature peak/valley, (e) moment peak/valley, LMK12, 7.11 Nm.

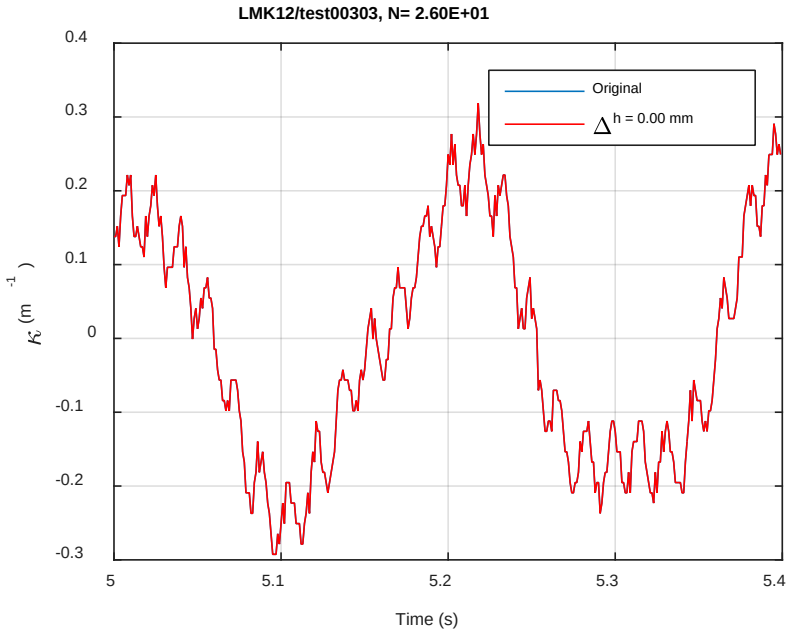
LMK12/test00303, N= 2.60E+01
Original
Δh = 0.00 mm
κ (m-1)
Time (s)

(a)

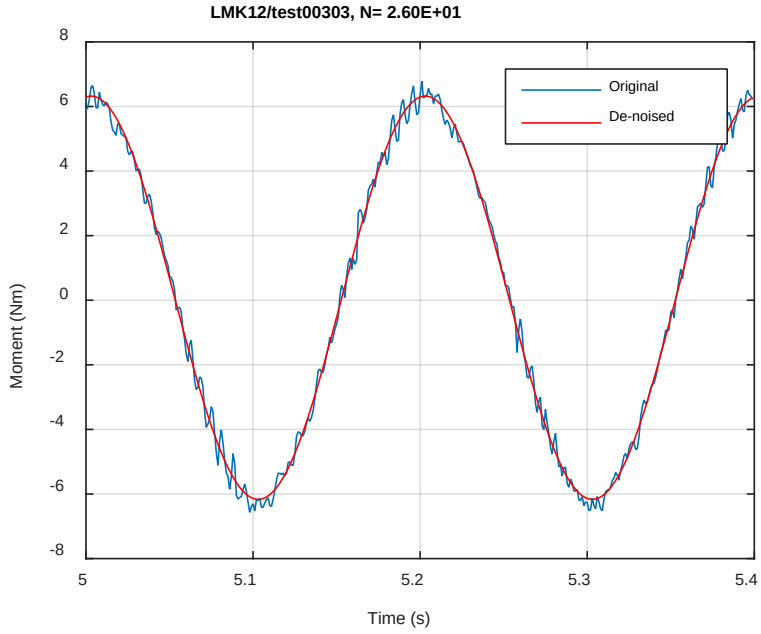
LMK12/test00303, N= 2.60E+01
Original
De-noised
Moment (Nm)
Time (s)

(b)

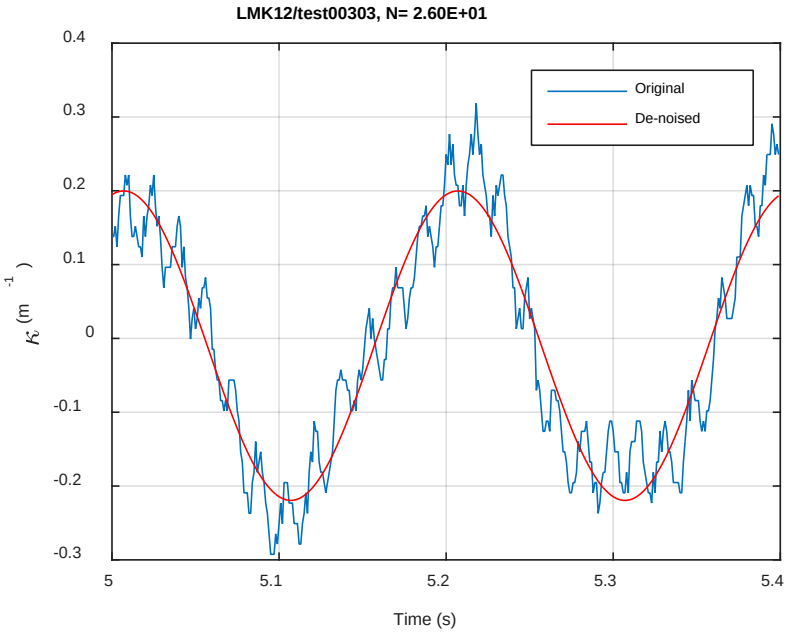

(c)

Fig. A.40. Monitoring-based responses: (a) curvature, (b) moment, (c) curvature, LMK12, 7.11 Nm, Ns = 2.60E+01 cycles.

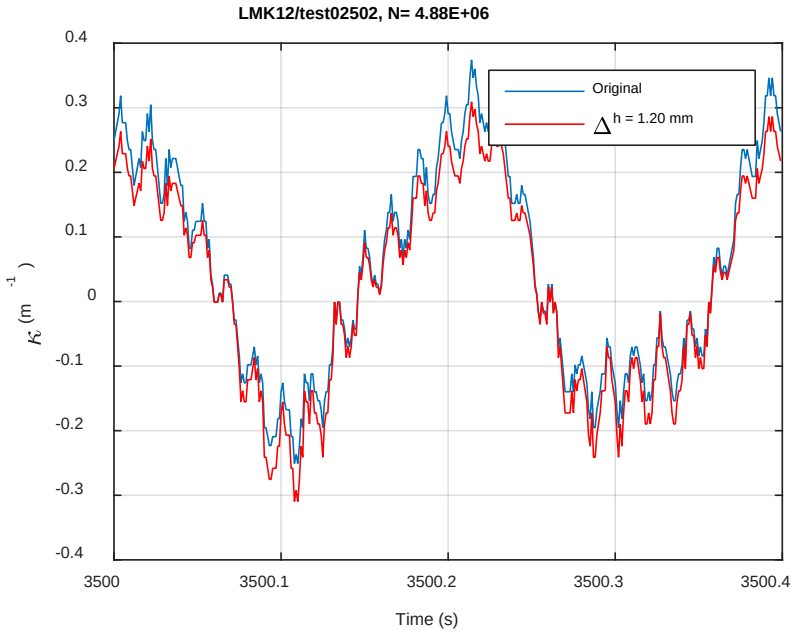
LMK12/test02502, N= 4.88E+06
Original
Δh = 1.20 mm
κ (m-1)
Time (s)
0.4
0.3
0.2
0.1
0
-0.1
-0.2
-0.3
-0.4
3500
3500.1
3500.2
3500.3
3500.4

(a)

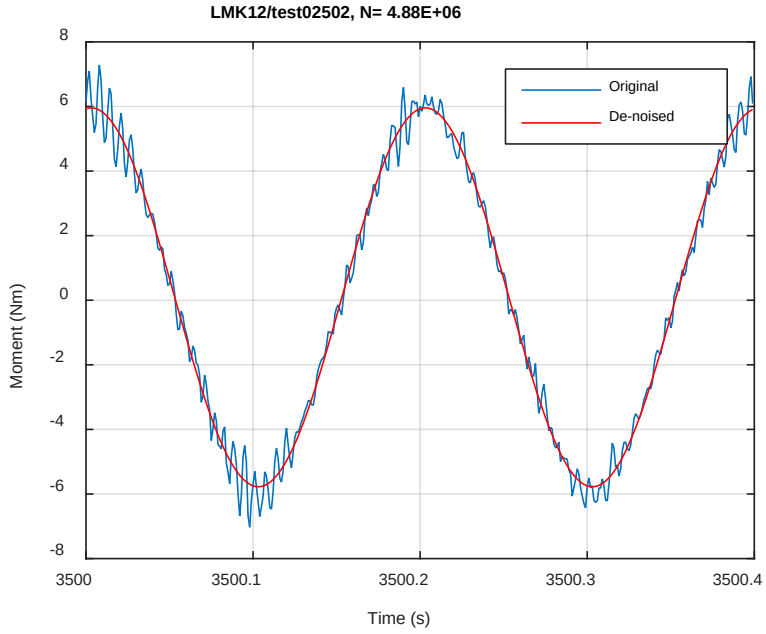
LMK12/test02502, N= 4.88E+06
Original
De-noised
Moment (Nm)
Time (s)
8
6
4
2
0
-2
-4
-6
-8
3500
3500.1
3500.2
3500.3
3500.4

(b)

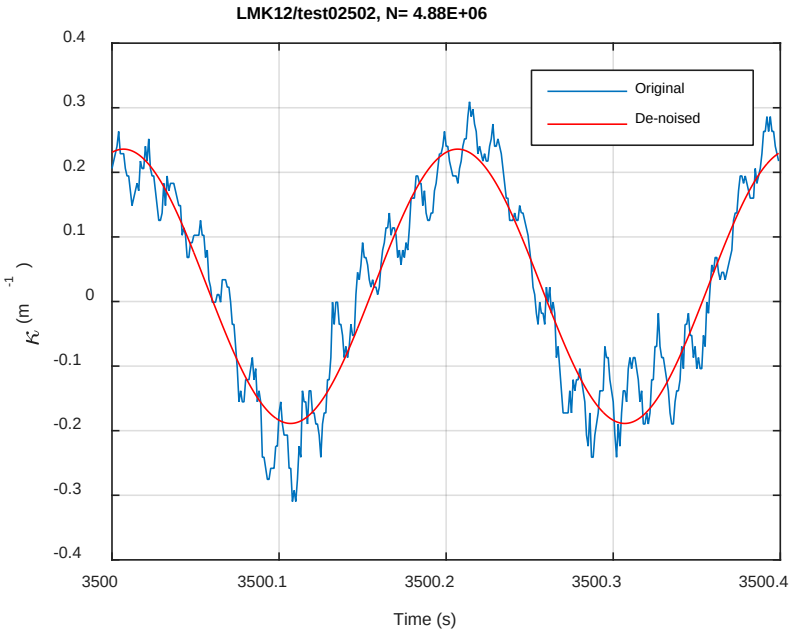

(c)

Fig. A.41. Monitoring-based responses: (a) curvature, (b) moment, (c) curvature, LMK12, 7.11 Nm, Ns = 4.88E+06 cycles.

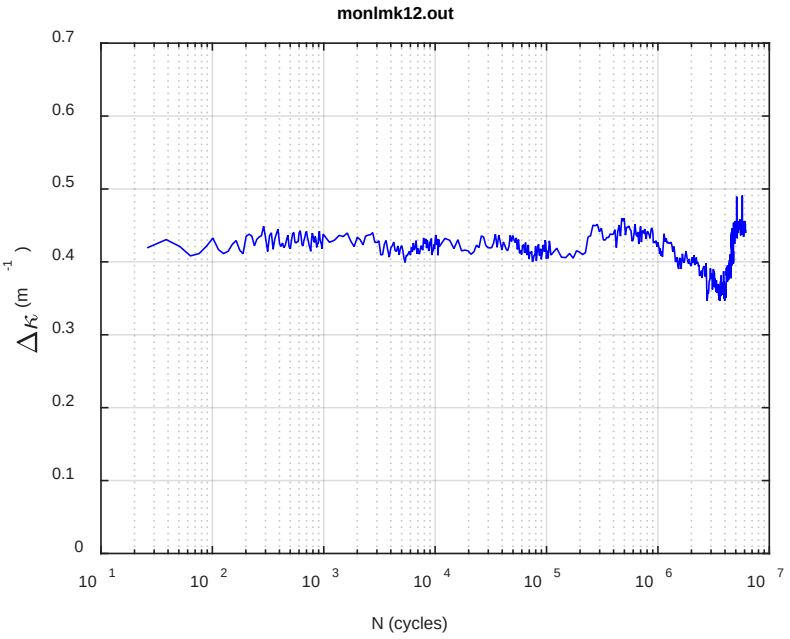
monlmk12.out
0.7
0.6
0.5
0.4
0.3
0.2
0.1
0
Δκ (m -1)
10 1
10 2
10 3
10 4
10 5
10 6
10 7
N (cycles)

(a)

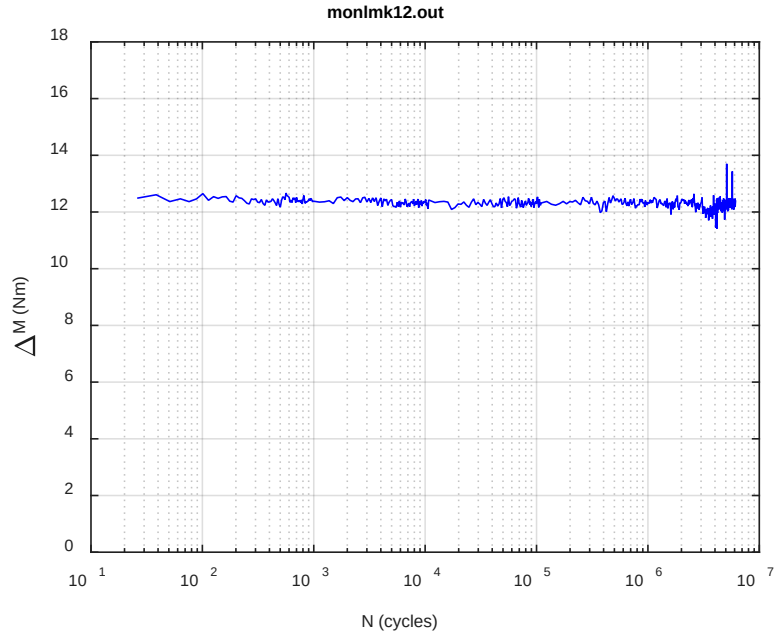
monlmk12.out
18
16
14
12
10
8
6
4
2
0
Δ M (Nm)
10 1
10 2
10 3
10 4
10 5
10 6
10 7
N (cycles)

(b)

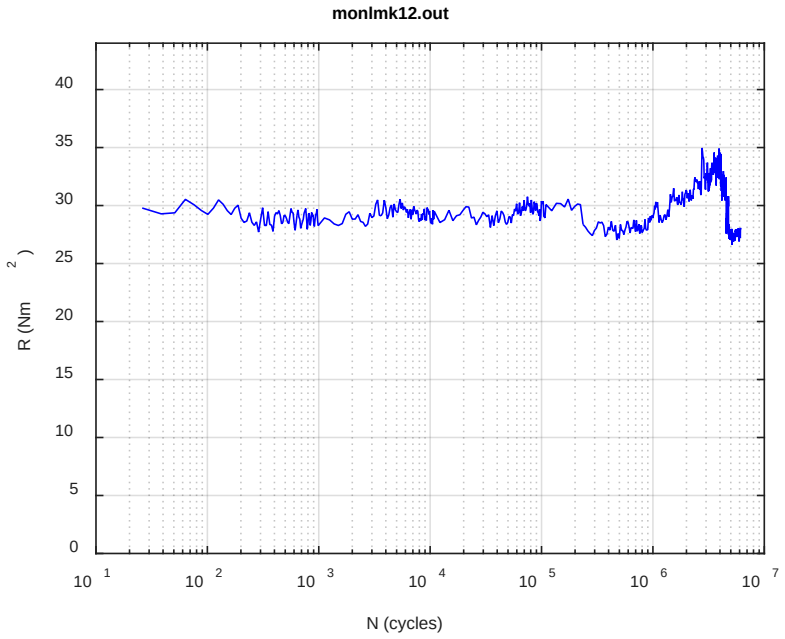
monlmk12.out
R (Nm 2)
N (cycles)

(c)

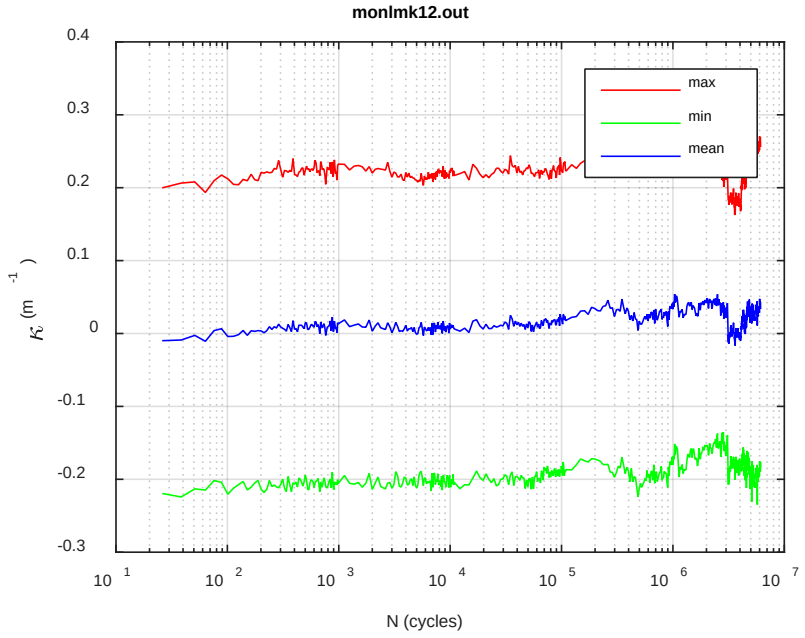
monlmk12.out
max
min
mean
κ (m -1)
N (cycles)

(d)

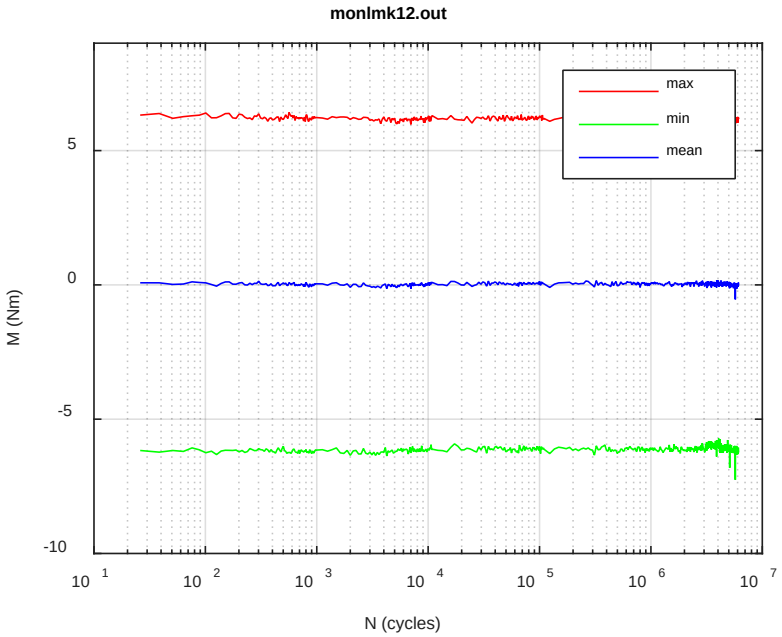

(e)

Fig. A.42. Monitoring-based responses: (a) curvature range, (b) moment range, (c) rigidity, (d) curvature peak/valley, (e) moment peak/valley, LMK12, 7.11 Nm, Nf = 7.58E+06 cycles.

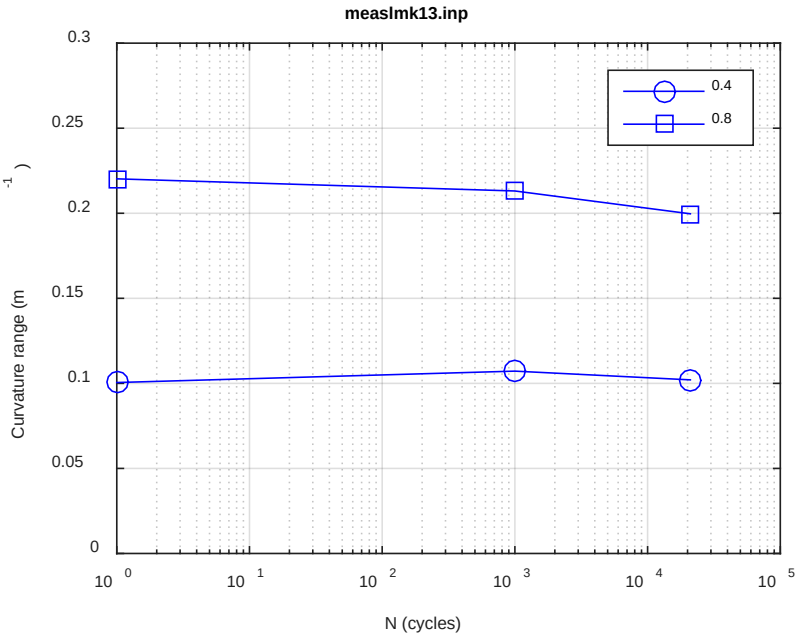
measlmk13.inp
0.3
0.25
0.2
0.15
0.1
0.05
0
Curvature range (m -1)
0.4
0.8
10 0
10 1
10 2
10 3
10 4
10 5
N (cycles)

(a)

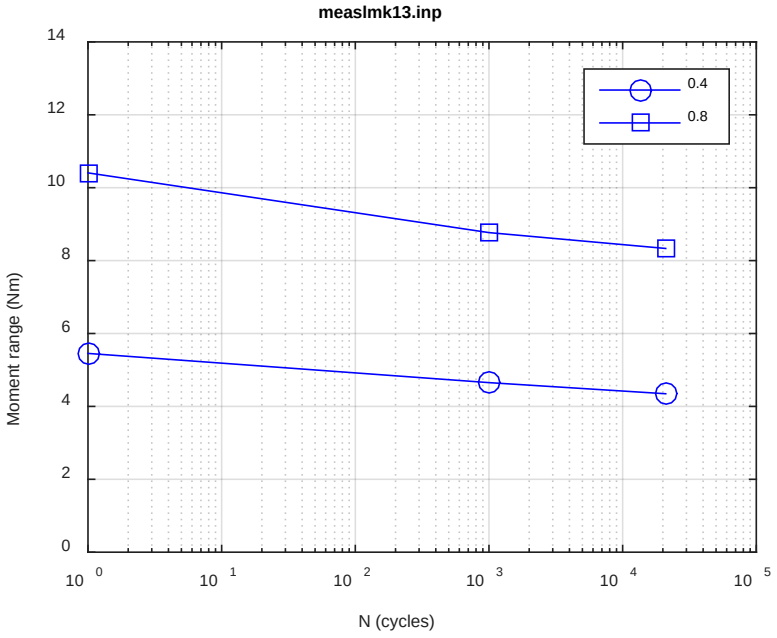
measlmk13.inp
14
12
10
8
6
4
2
0
Moment range (Nm)
0.4
0.8
10 0
10 1
10 2
10 3
10 4
10 5
N (cycles)

(b)

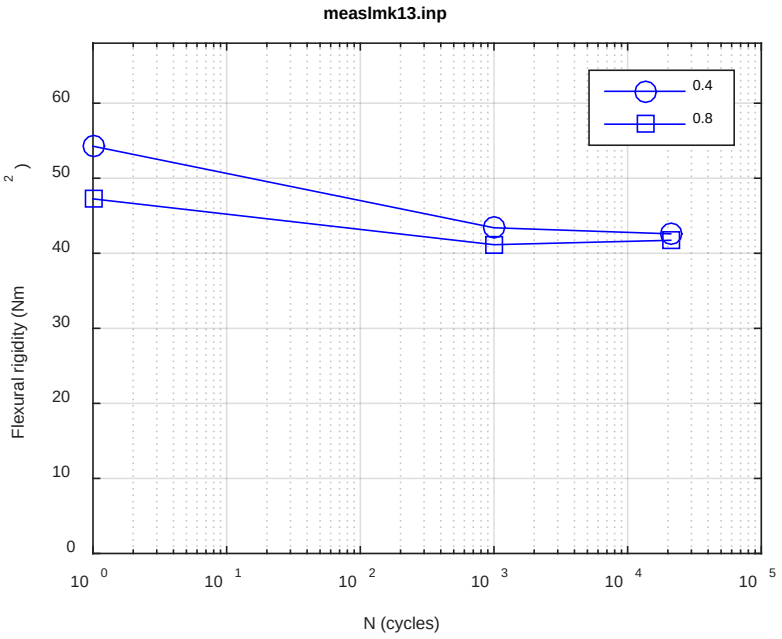
measlmk13.inp
0.4
0.8
Flexural rigidity (Nm 2)
N (cycles)

(c)

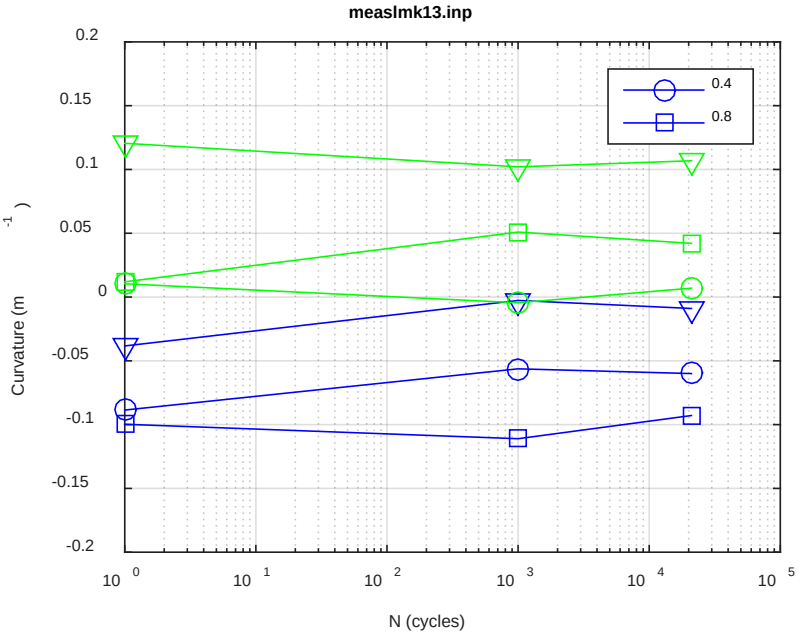
measlmk13.inp
0.4
0.8
Curvature (m -1)
N (cycles)

(d)

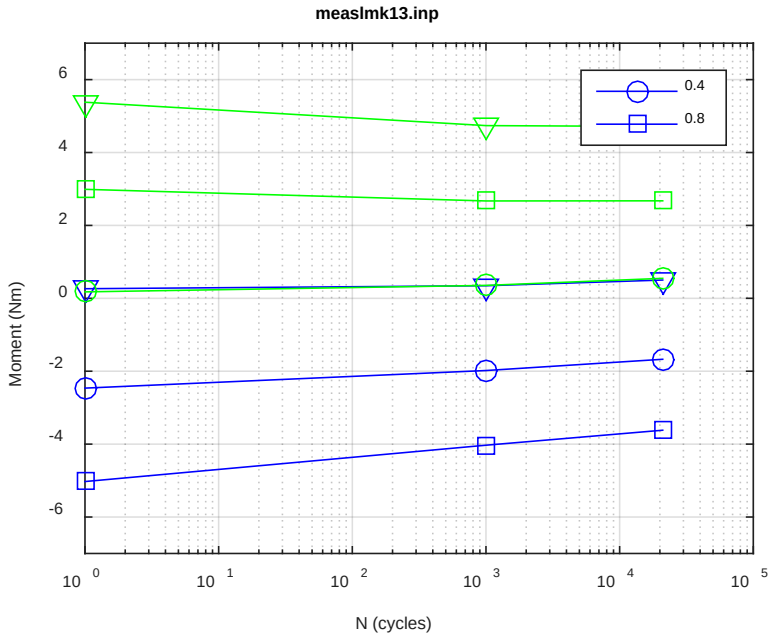

(e)

Fig. A.43. Measurement-based responses: (a) curvature range, (b) moment range, (c) rigidity, (d) curvature peak/valley, (e) moment peak/valley, LMK13, 25.40 Nm.

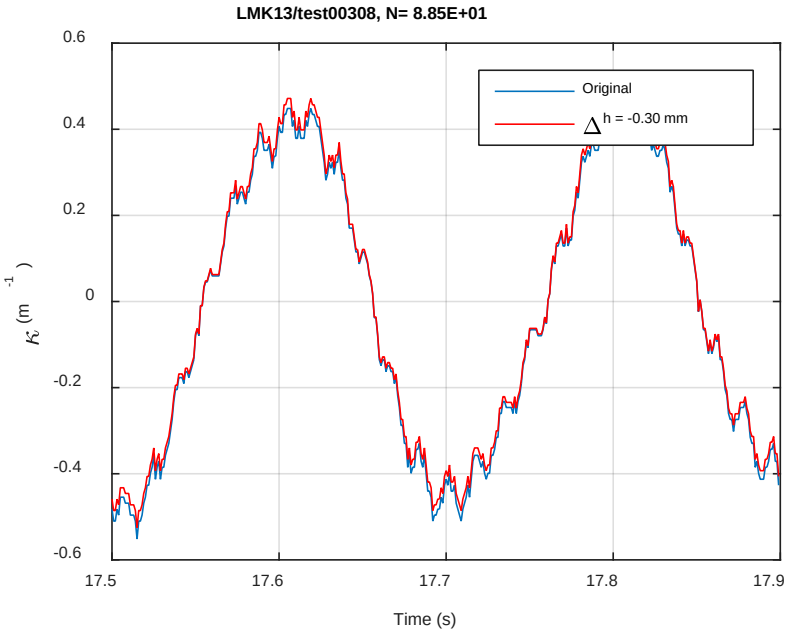
LMK13/test00308, N= 8.85E+01
Original
Δh = -0.30 mm
κ (m-1)
Time (s)
0.6
0.4
0.2
0
-0.2
-0.4
-0.6
17.5
17.6
17.7
17.8
17.9

(a)

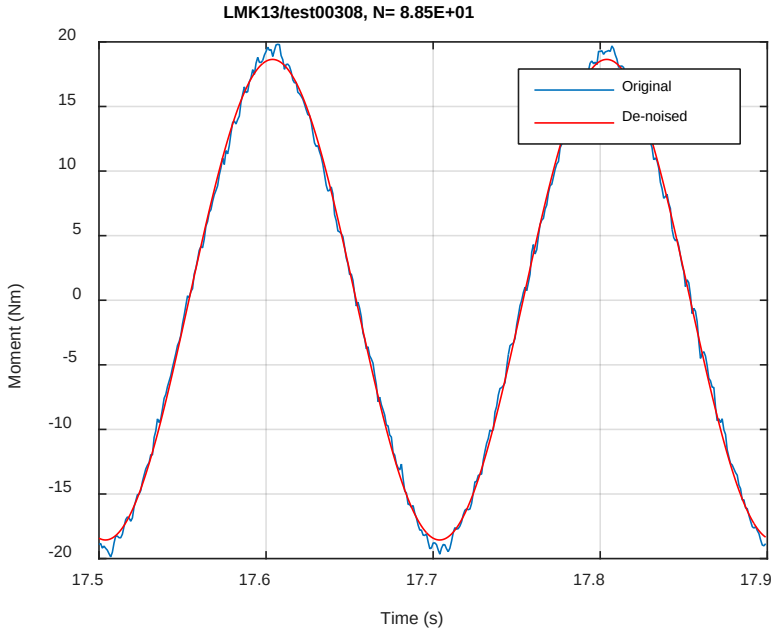
LMK13/test00308, N= 8.85E+01
Original
De-noised
Moment (Nm)
Time (s)
20
15
10
5
0
-5
-10
-15
-20
17.5
17.6
17.7
17.8
17.9

(b)

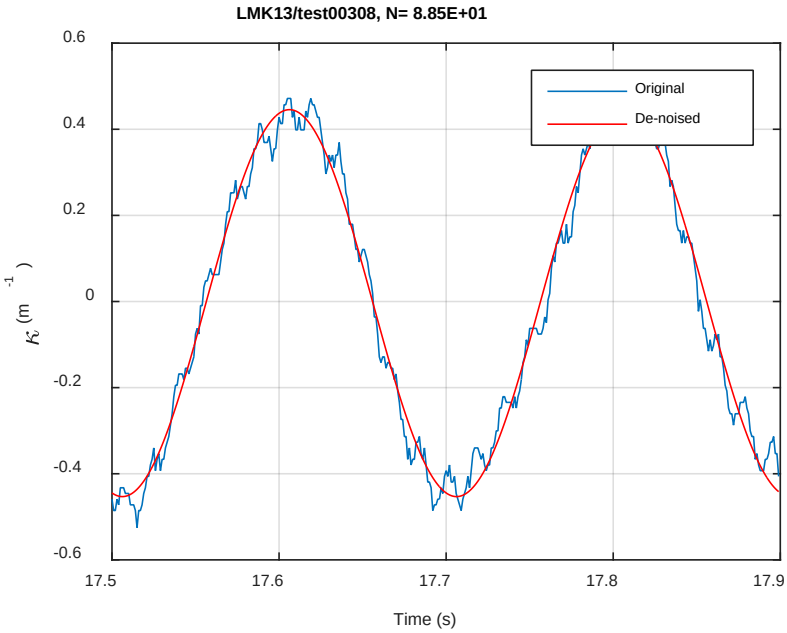

(c)

Fig. A.44. Monitoring-based responses: (a) curvature, (b) moment, (c) curvature, LMK13, 25.40 Nm, Ns = 8.85E+01 cycles.

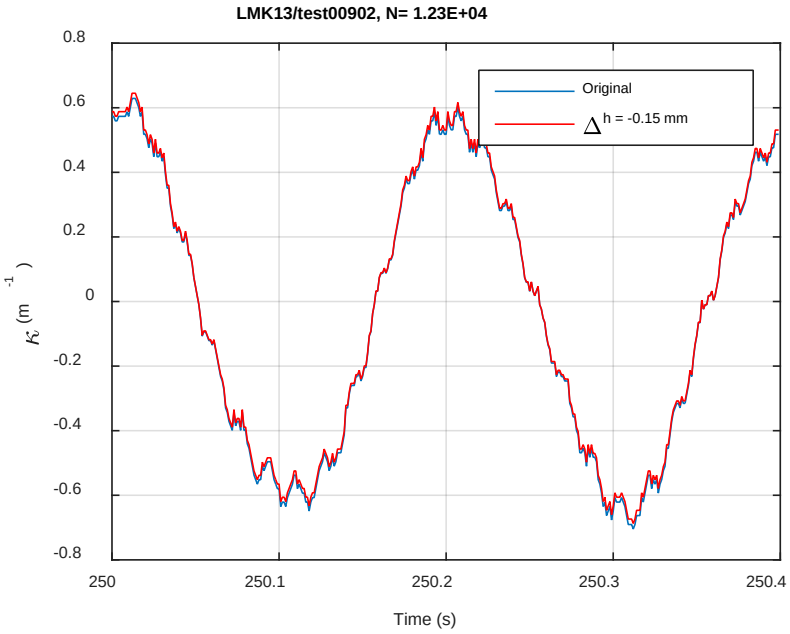
LMK13/test00902, N= 1.23E+04
Original
Δh = -0.15 mm
κ (m-1)
Time (s)
0.8
0.6
0.4
0.2
0
-0.2
-0.4
-0.6
-0.8
250
250.1
250.2
250.3
250.4

(a)

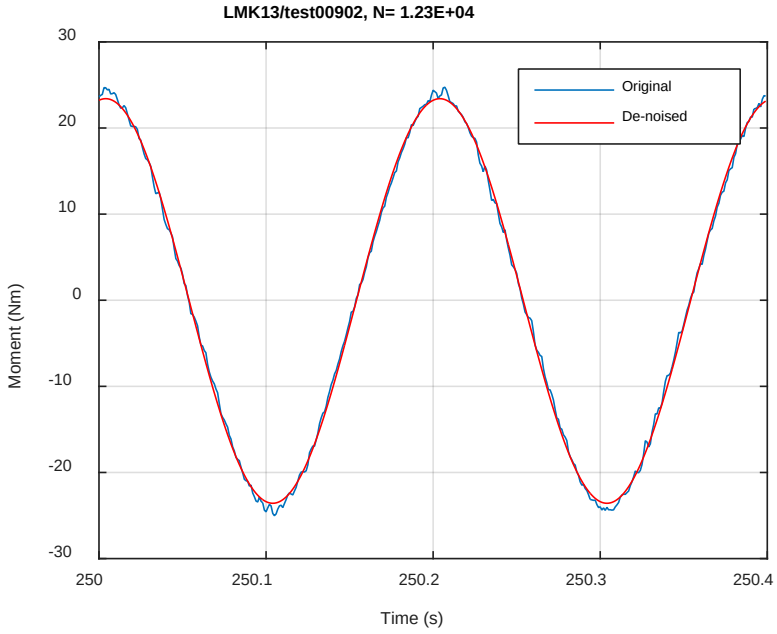
LMK13/test00902, N= 1.23E+04
Original
De-noised
Moment (Nm)
Time (s)
30
20
10
0
-10
-20
-30
250
250.1
250.2
250.3
250.4

(b)

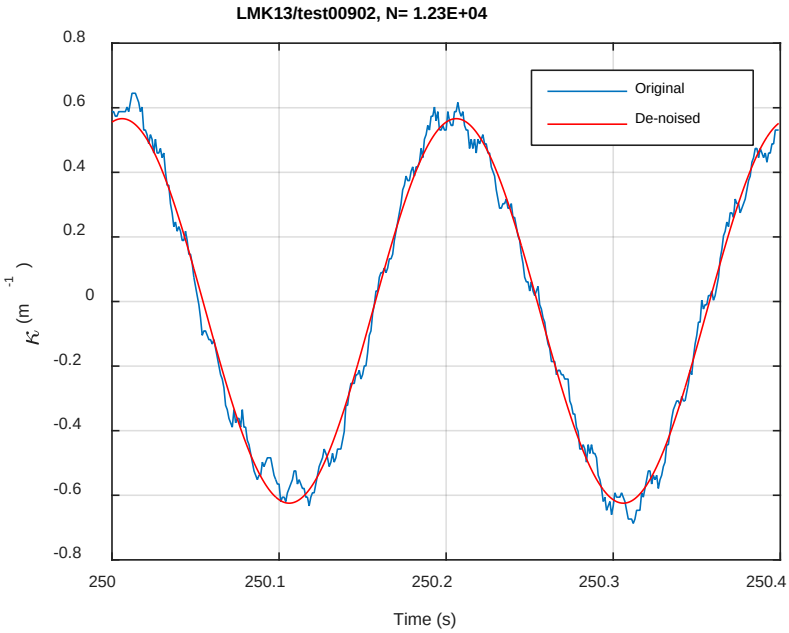

(c)

Fig. A.45. Monitoring-based responses: (a) curvature, (b) moment, (c) curvature, LMK13, 25.40 Nm, Ns = 1.23E+04 cycles.

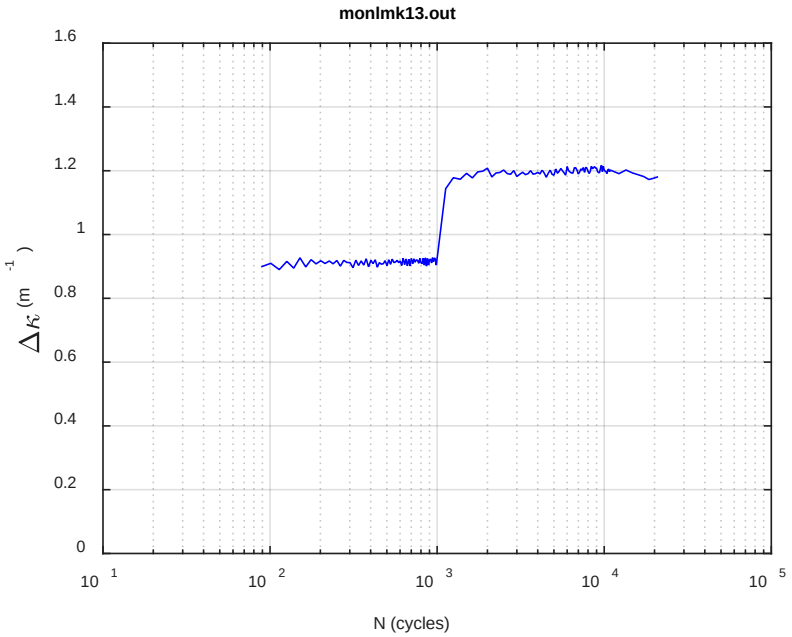
monlmk13.out
1.6
1.4
1.2
1
0.8
0.6
0.4
0.2
0
$\Delta\kappa$ (m^{-1})
10^1
10^2
10^3
10^4
10^5
N (cycles)

(a)

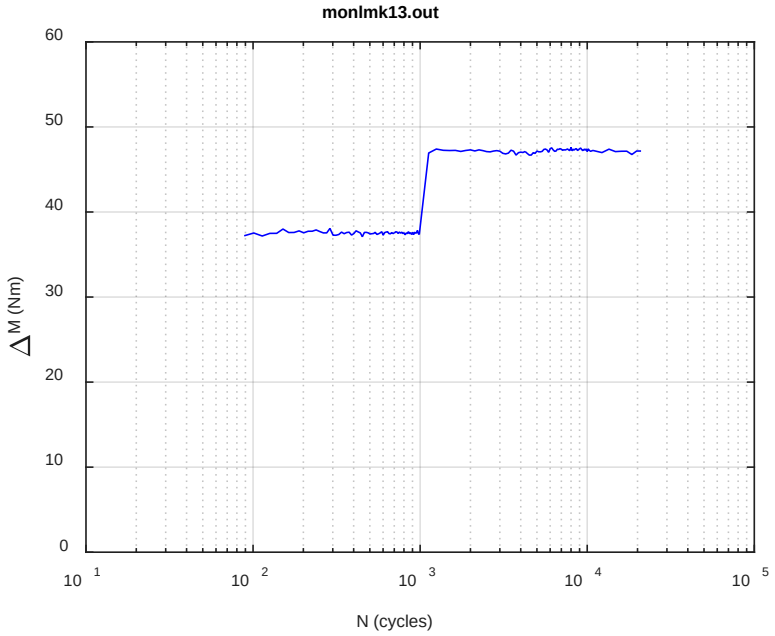
monlmk13.out
60
50
40
30
20
10
0
Δ M (Nm)
10^1
10^2
10^3
10^4
10^5
N (cycles)

(b)

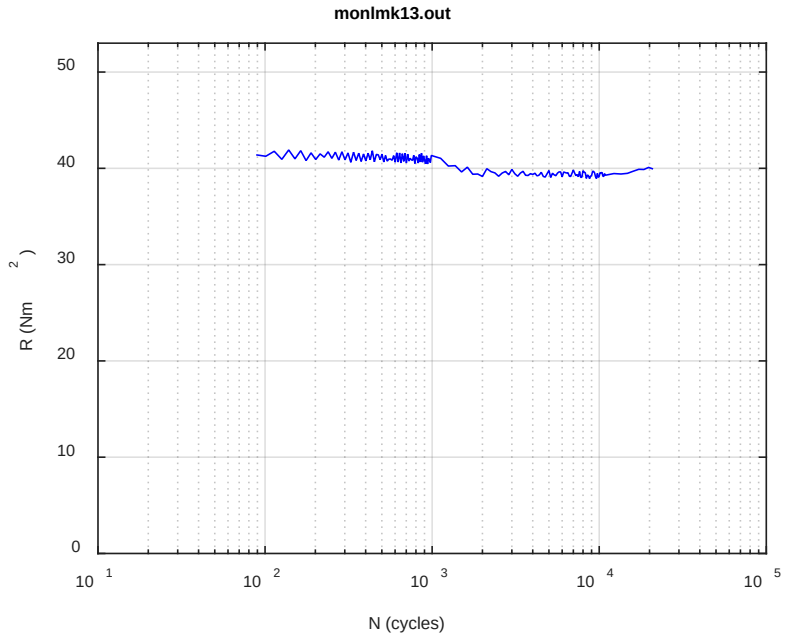
monlmk13.out
R (Nm 2)
N (cycles)

(c)

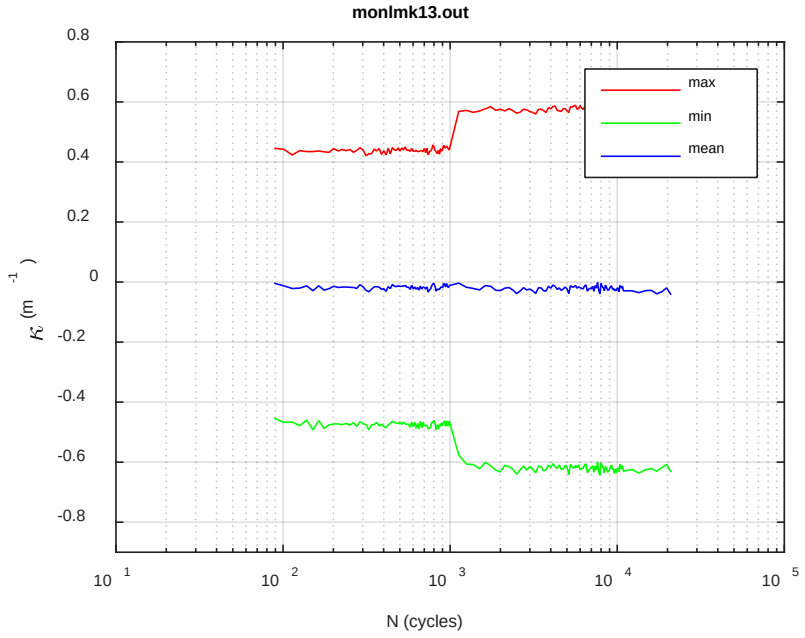
monlmk13.out
max
min
mean
κ (m -1)
N (cycles)

(d)

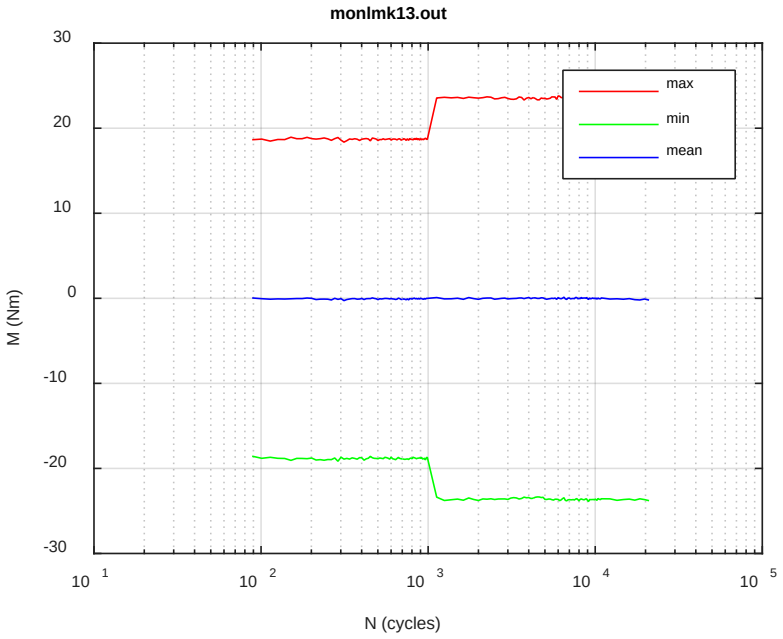

(e)

Fig. A.46. Monitoring-based responses: (a) curvature range, (b) moment range, (c) rigidity, (d) curvature peak/valley, (e) moment peak/valley, LMK13, 25.40 Nm, Nf = 2.10E+04 cycles.

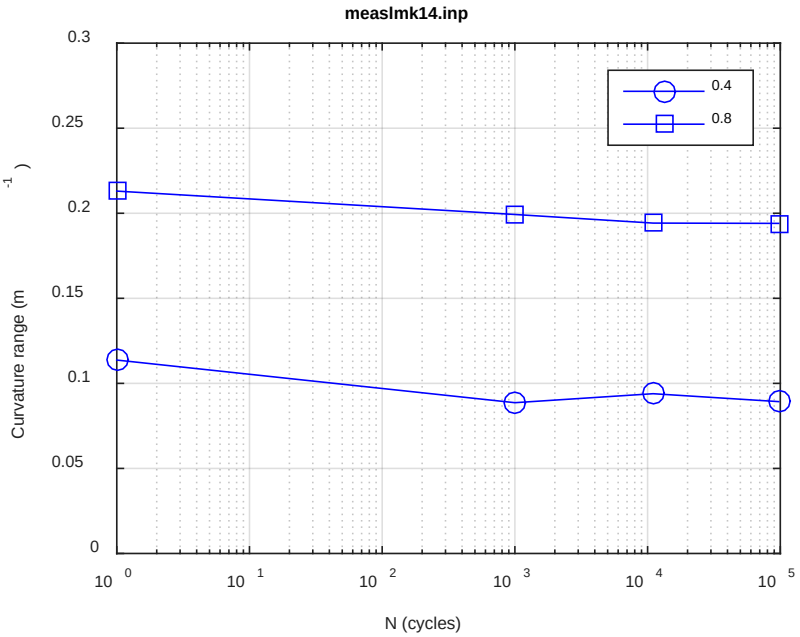
measlmk14.inp
0.3
0.25
0.2
0.15
0.1
0.05
0
Curvature range (m -1)
0.4
0.8
10 0
10 1
10 2
10 3
10 4
10 5
N (cycles)

(a)

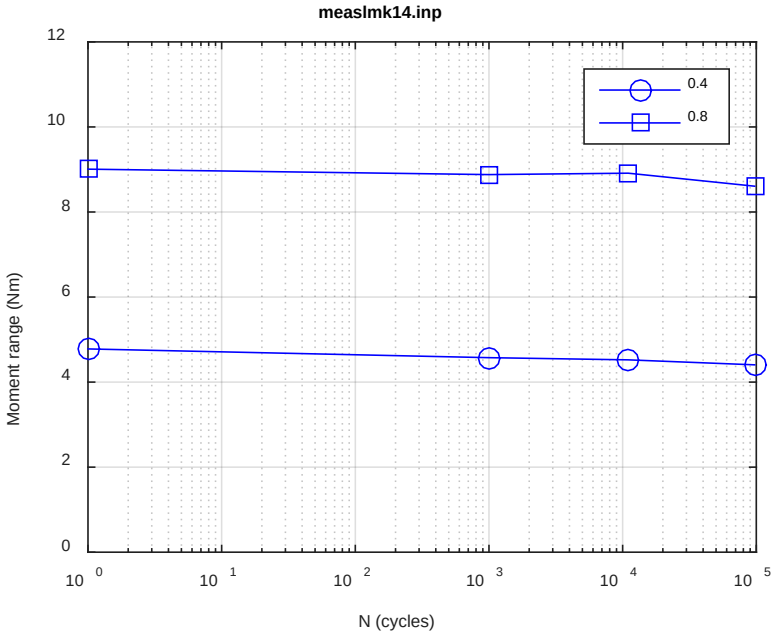
measlmk14.inp
12
10
8
6
4
2
0
Moment range (Nm)
0.4
0.8
10 0
10 1
10 2
10 3
10 4
10 5
N (cycles)

(b)

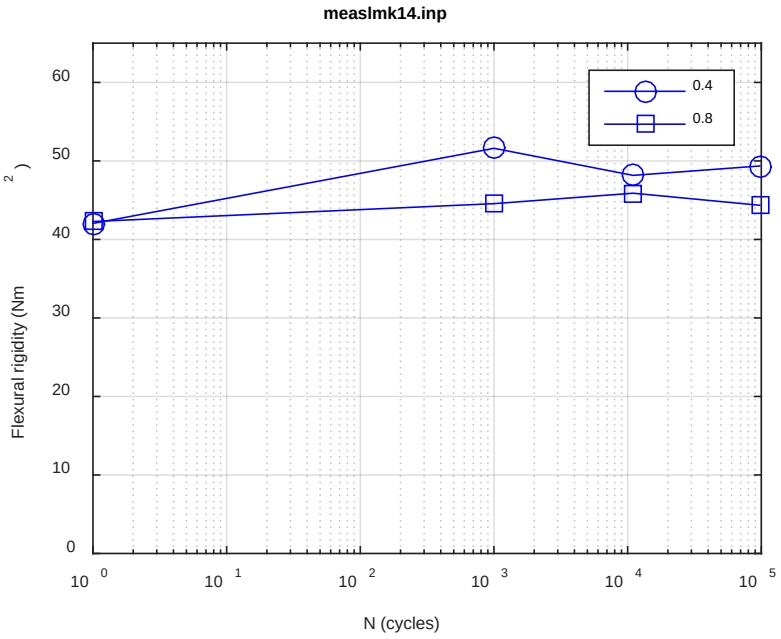
measlmk14.inp
0.4
0.8
Flexural rigidity (Nm 2)
N (cycles)
0
10
20
30
40
50
60
10 0
10 1
10 2
10 3
10 4
10 5

(c)

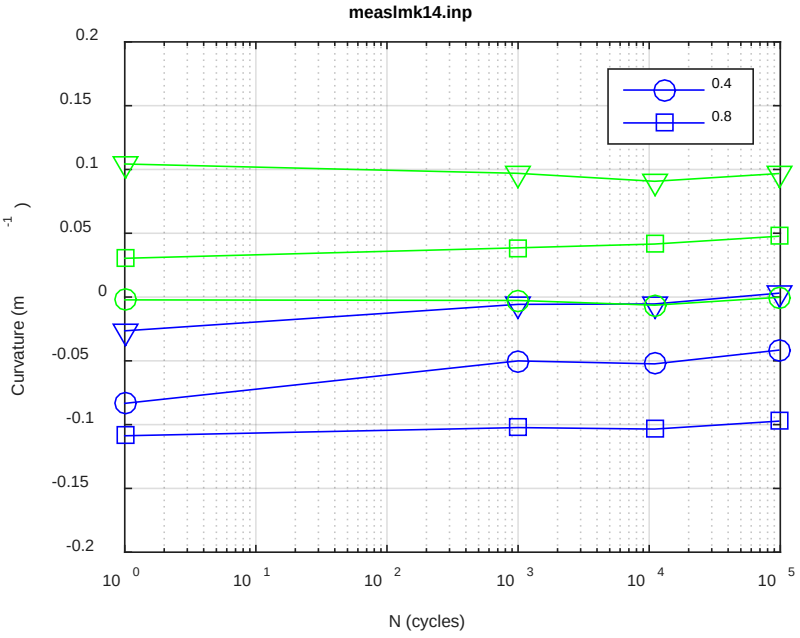
measlmk14.inp
0.4
0.8
Curvature (m -1)
N (cycles)
0.2
0.15
0.1
0.05
0
-0.05
-0.1
-0.15
-0.2
10 0
10 1
10 2
10 3
10 4
10 5

(d)

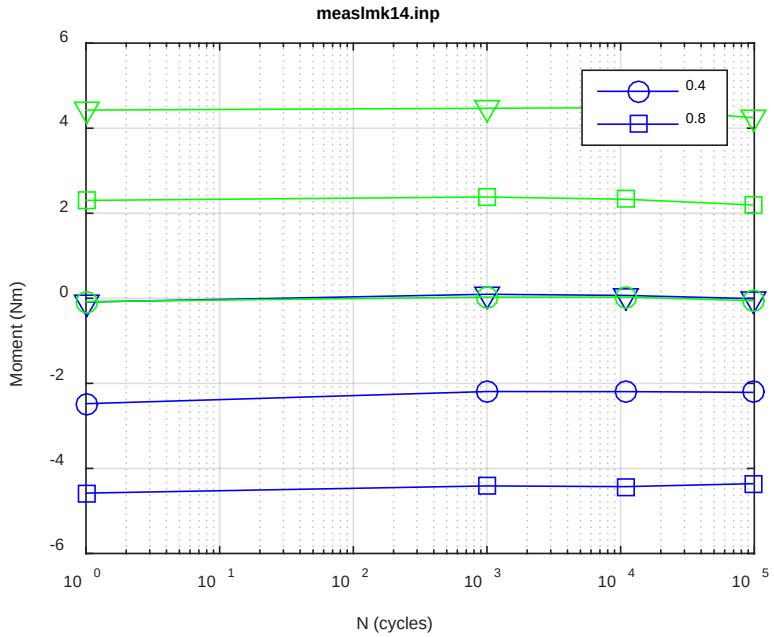

(e)

Fig. A.47. Measurement-based responses: (a) curvature range, (b) moment range, (c) rigidity, (d) curvature peak/valley, (e) moment peak/valley, LMK14, 10.16 Nm.

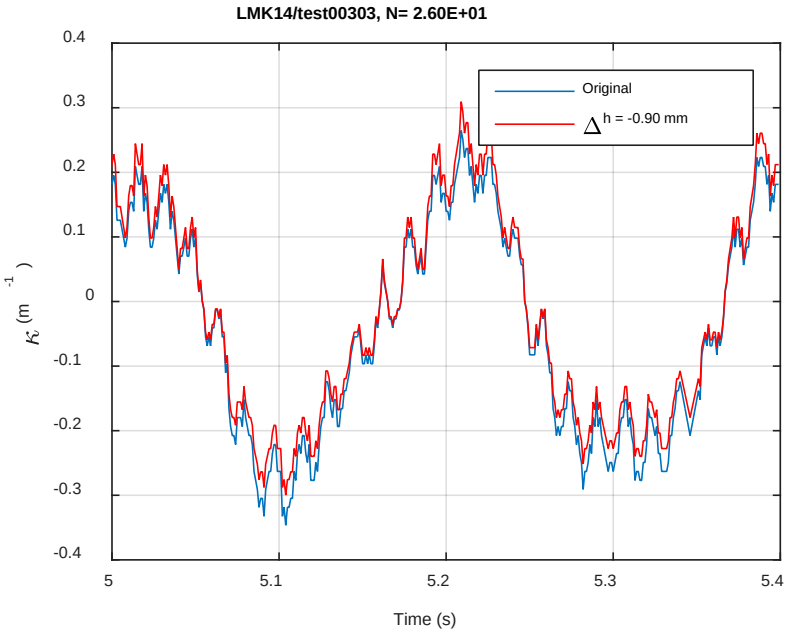
LMK14/test00303, N= 2.60E+01
Original
Δh = -0.90 mm
κ (m-1)
Time (s)

(a)

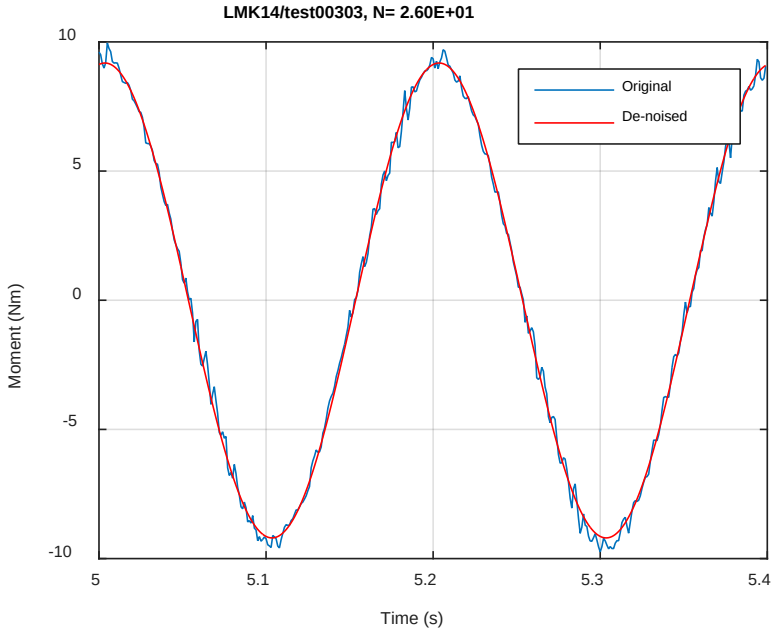
LMK14/test00303, N= 2.60E+01
Original
De-noised
Moment (Nm)
Time (s)

(b)

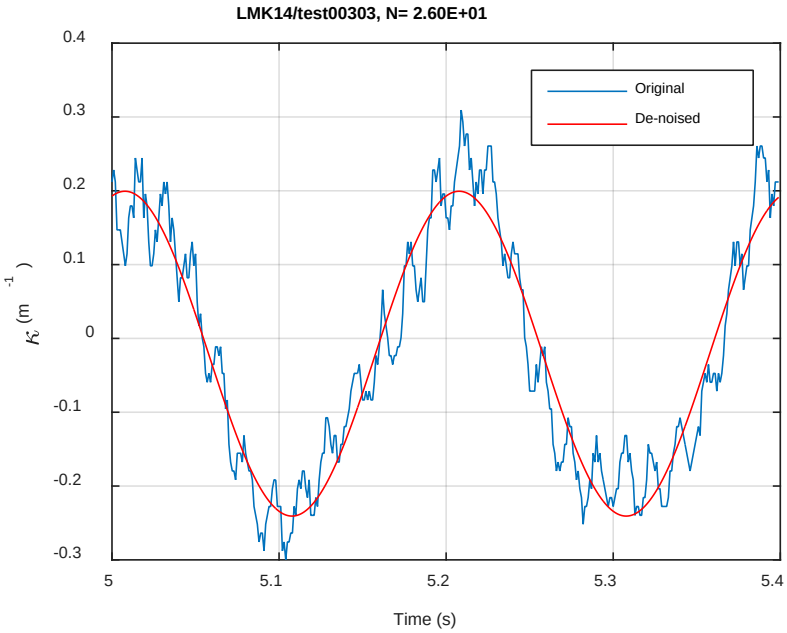

(c)

Fig. A.48. Monitoring-based responses: (a) curvature, (b) moment, (c) curvature, LMK14, 10.16 Nm, Ns = 2.60E+01 cycles.

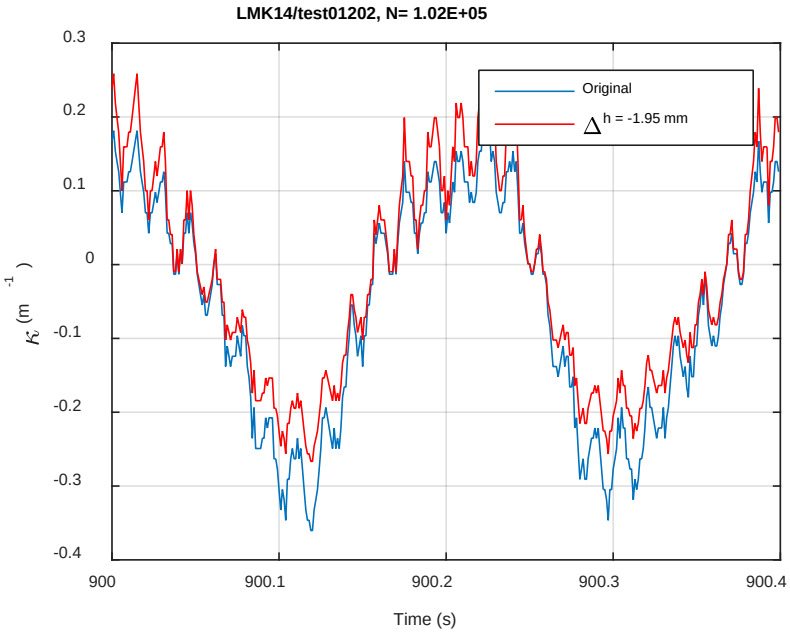
LMK14/test01202, N= 1.02E+05
Original
Δh = -1.95 mm
κ (m-1)
Time (s)
0.3
0.2
0.1
0
-0.1
-0.2
-0.3
-0.4
900
900.1
900.2
900.3
900.4

(a)

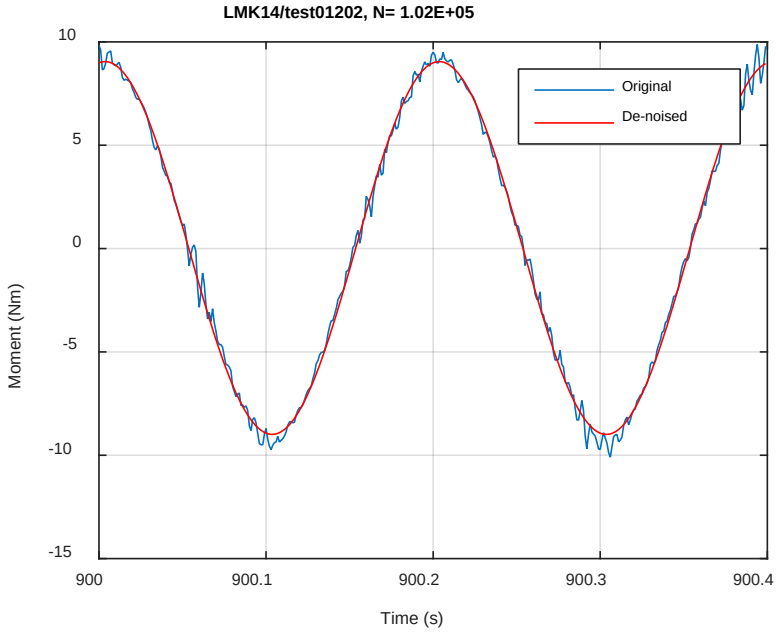
LMK14/test01202, N= 1.02E+05
Original
De-noised
Moment (Nm)
Time (s)
10
5
0
-5
-10
-15
900
900.1
900.2
900.3
900.4

(b)

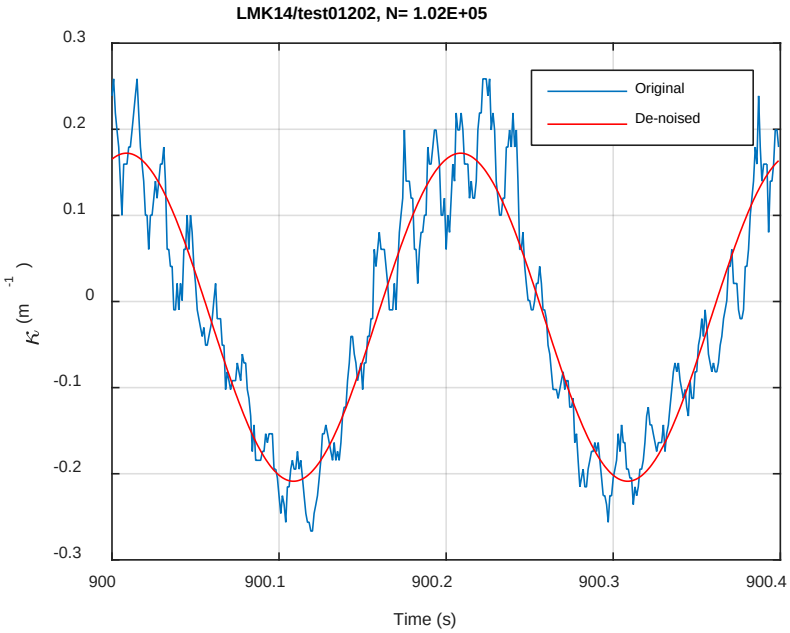

(c)

Fig. A.49. Monitoring-based responses: (a) curvature, (b) moment, (c) curvature, LMK14, 10.16 Nm, Ns = 1.02E+05 cycles.

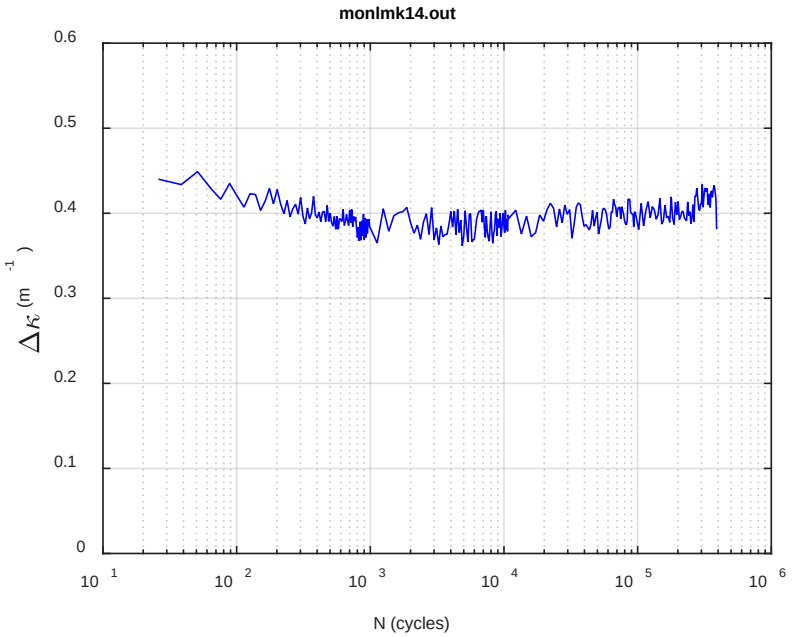
monlmk14.out
0.6
0.5
0.4
0.3
0.2
0.1
0
Δκ (m -1)
10 1
10 2
10 3
10 4
10 5
10 6
N (cycles)

(a)

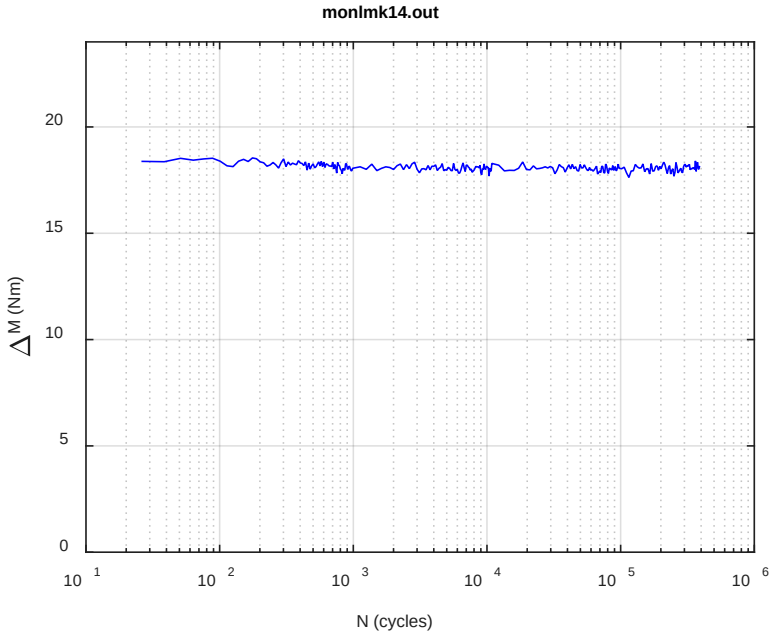
monlmk14.out
20
15
10
5
0
Δ M (Nm)
10 1
10 2
10 3
10 4
10 5
10 6
N (cycles)

(b)

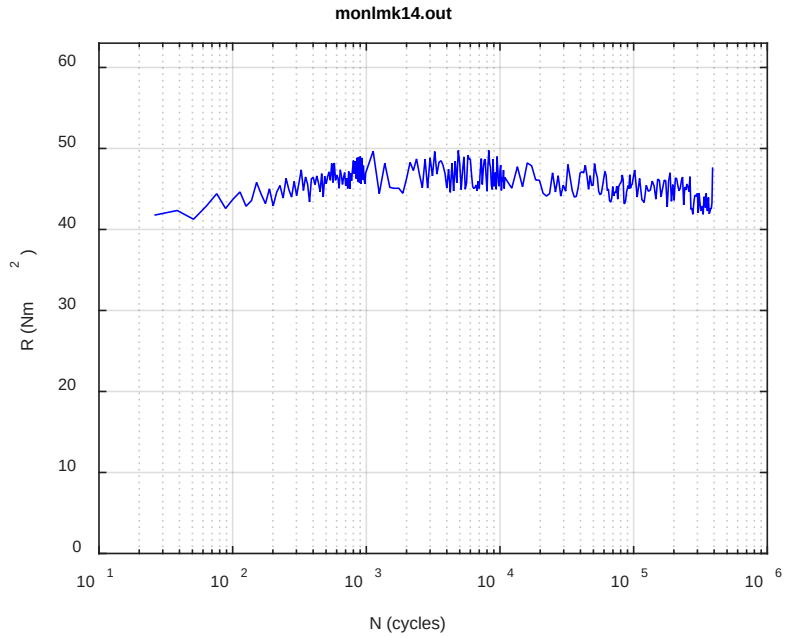
monlmk14.out
R (Nm 2)
N (cycles)

(c)

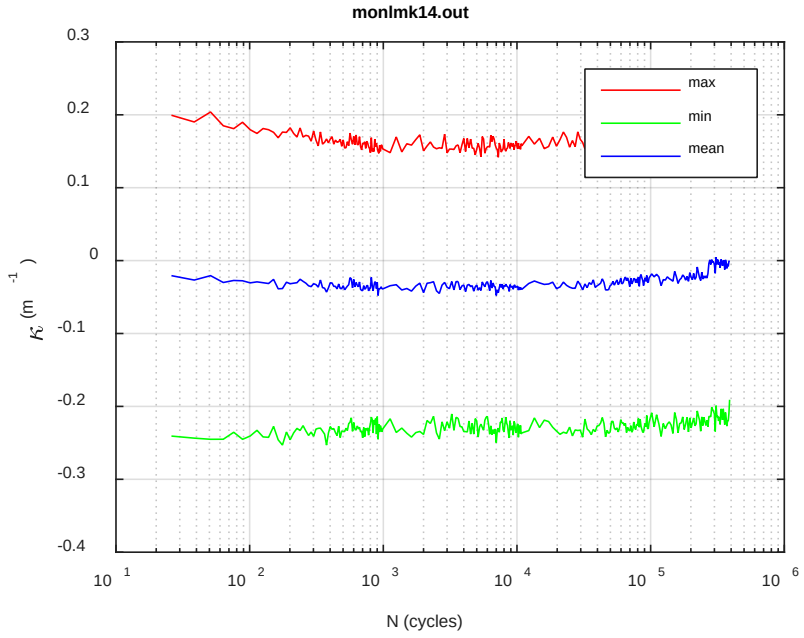
monlmk14.out
max
min
mean
κ (m -1)
N (cycles)

(d)

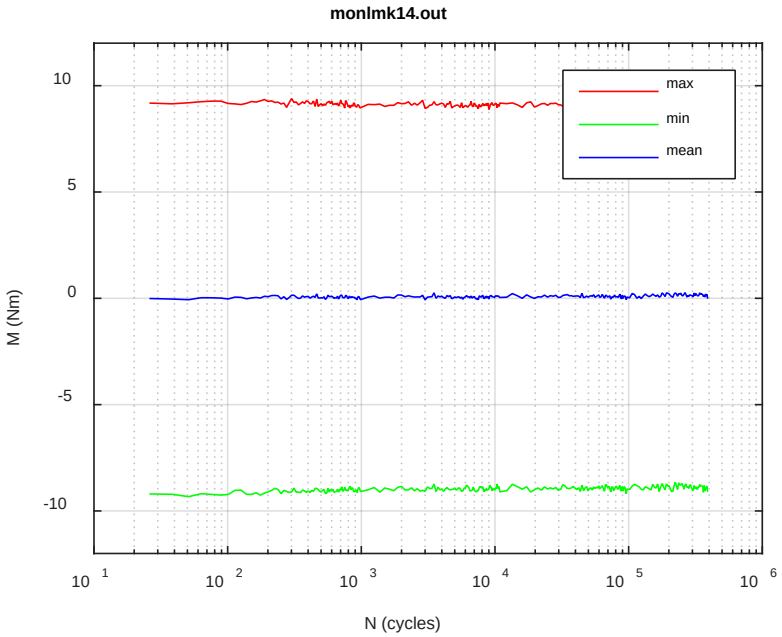

(e)

Fig. A.50. Monitoring-based responses: (a) curvature range, (b) moment range, (c) rigidity, (d) curvature peak/valley, (e) moment peak/valley, LMK14, 10.16 Nm, Nf = 3.90E+05 cycles.

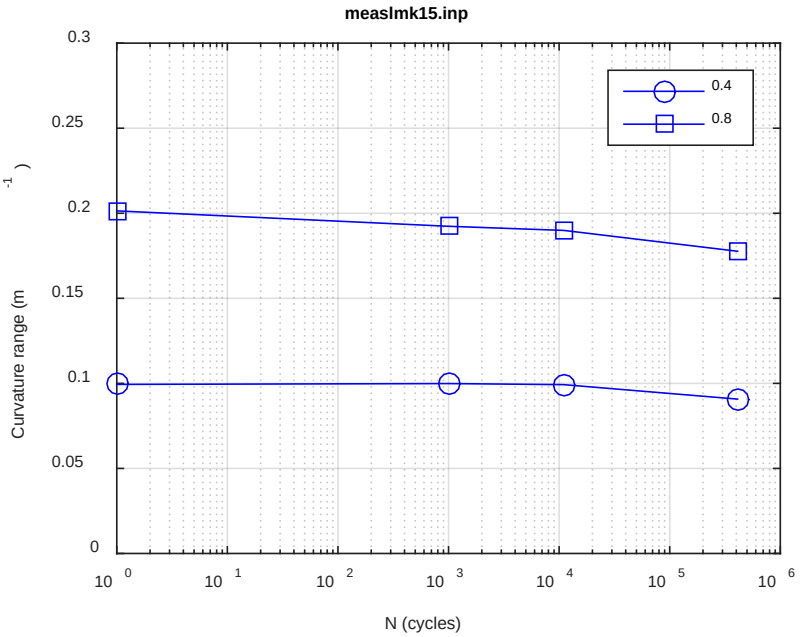
measlmk15.inp
0.3
0.25
0.2
0.15
0.1
0.05
0
Curvature range (m -1)
0.4
0.8
10 0
10 1
10 2
10 3
10 4
10 5
10 6
N (cycles)

(a)

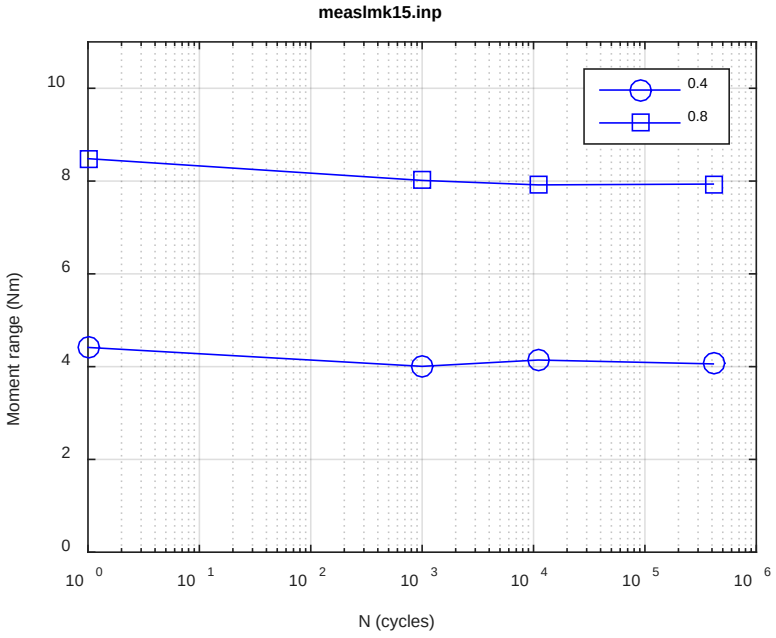
measlmk15.inp
10
8
6
4
2
0
Moment range (Nm)
0.4
0.8
10 0
10 1
10 2
10 3
10 4
10 5
10 6
N (cycles)

(b)

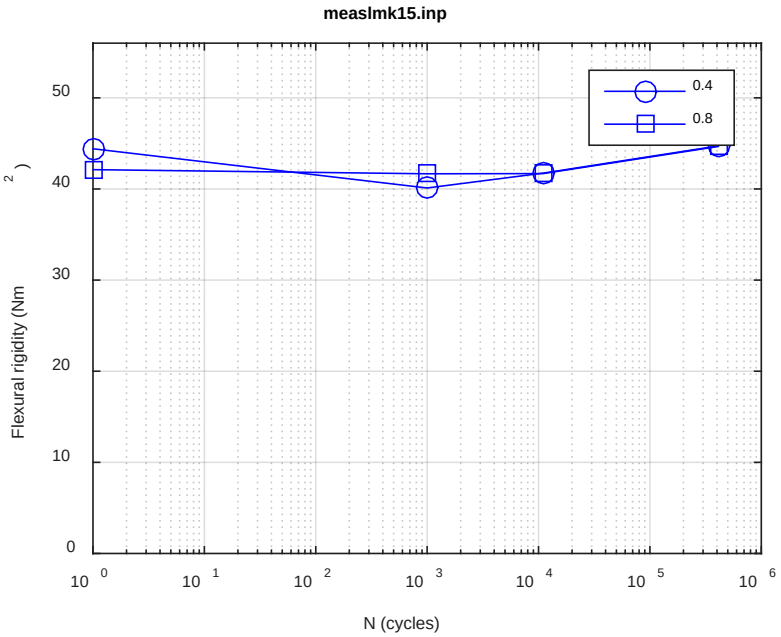
measlmk15.inp
0.4
0.8
Flexural rigidity (Nm^2)
N (cycles)
0
10
20
30
40
50
10^0
10^1
10^2
10^3
10^4
10^5
10^6

(c)

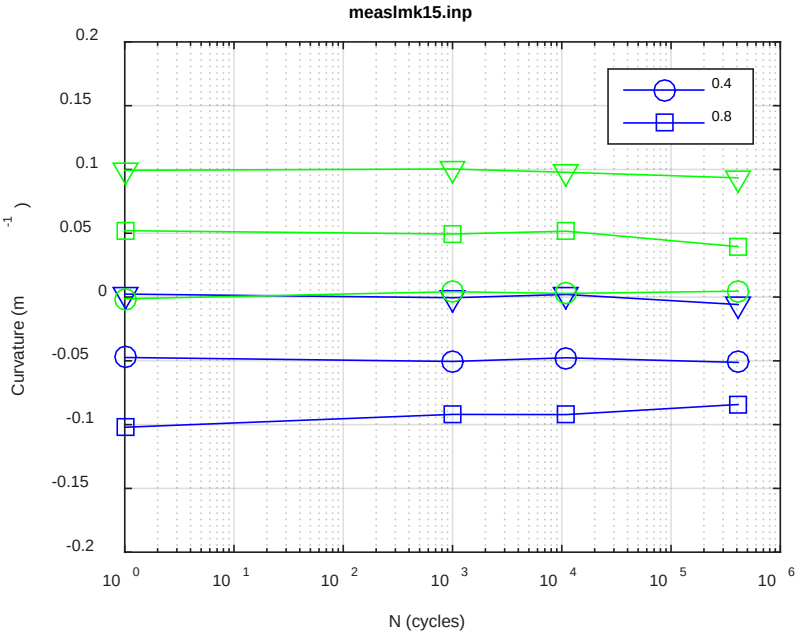
measlmk15.inp
0.4
0.8
Curvature (m^{-1})
N (cycles)
0.2
0.15
0.1
0.05
0
-0.05
-0.1
-0.15
-0.2
10^0
10^1
10^2
10^3
10^4
10^5
10^6

(d)

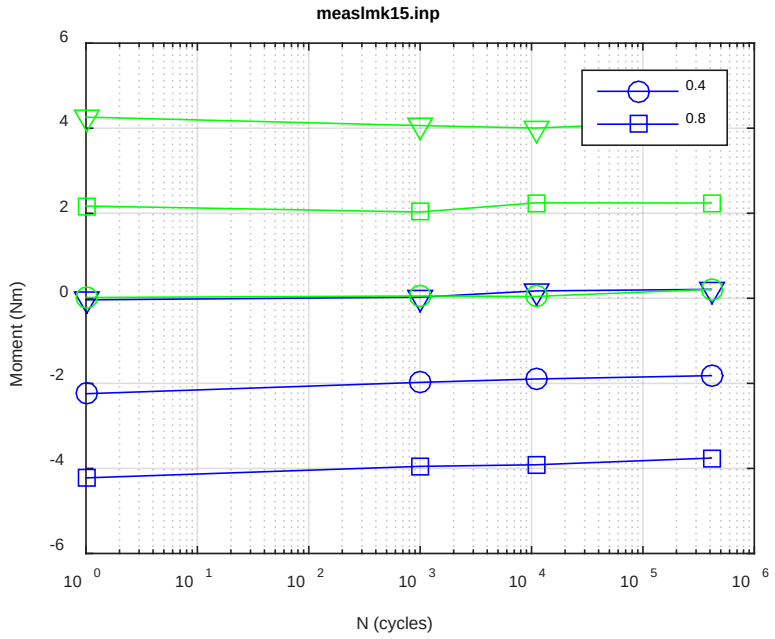

(e)

Fig. A.51. Measurement-based responses: (a) curvature range, (b) moment range, (c) rigidity, (d) curvature peak/valley, (e) moment peak/valley, LMK15, 10.16 Nm.

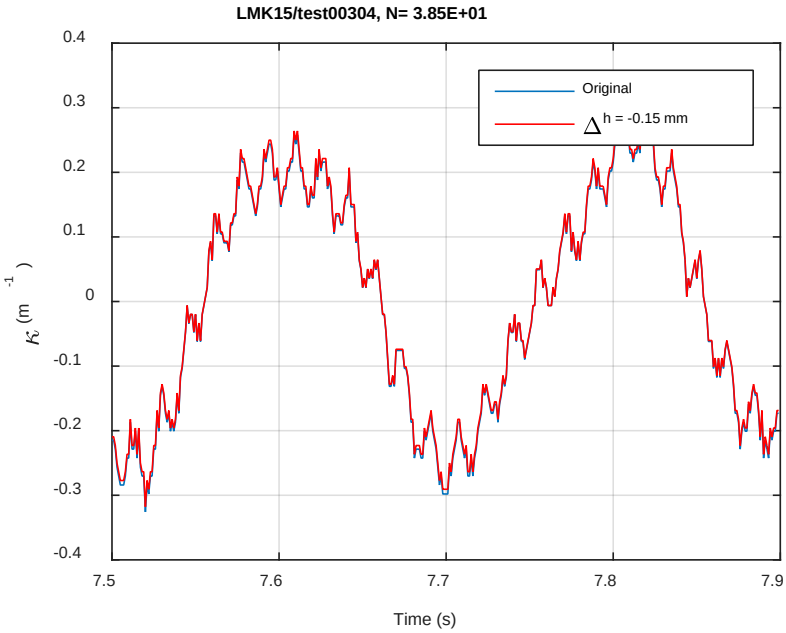
LMK15/test00304, N= 3.85E+01
Original
Δh = -0.15 mm
κ (m-1)
Time (s)
0.4
0.3
0.2
0.1
0
-0.1
-0.2
-0.3
-0.4
7.5
7.6
7.7
7.8
7.9

(a)

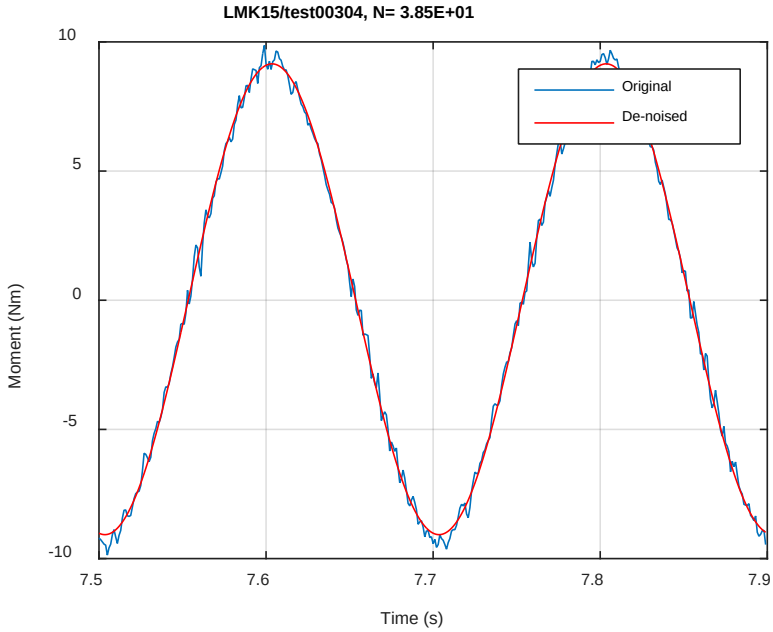
LMK15/test00304, N= 3.85E+01
Original
De-noised
Moment (Nm)
Time (s)
10
5
0
-5
-10
7.5
7.6
7.7
7.8
7.9

(b)

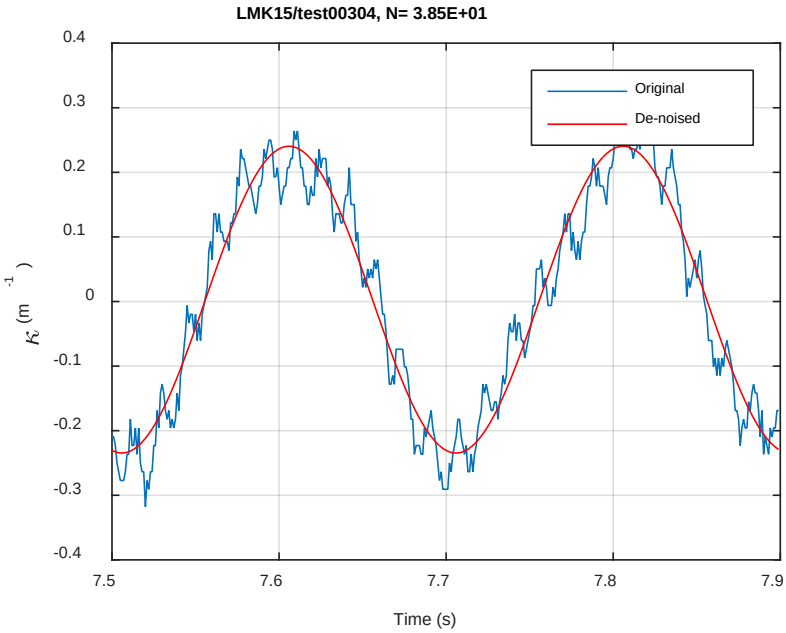

(c)

Fig. A.52. Monitoring-based responses: (a) curvature, (b) moment, (c) curvature, LMK15, 10.16 Nm, Ns = 3.85E+01 cycles.

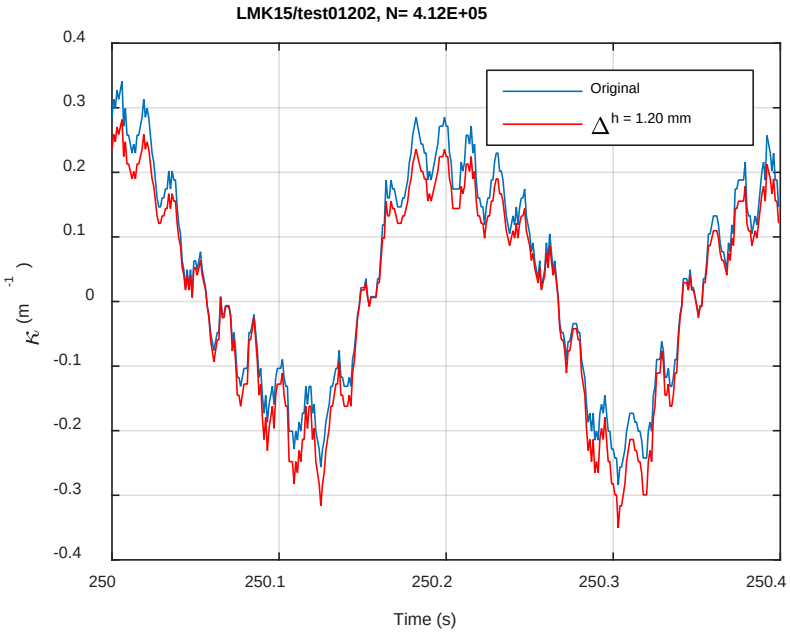
LMK15/test01202, N= 4.12E+05
Original
Δh = 1.20 mm
κ (m-1)
Time (s)
0.4
0.3
0.2
0.1
0
-0.1
-0.2
-0.3
-0.4
250
250.1
250.2
250.3
250.4

(a)

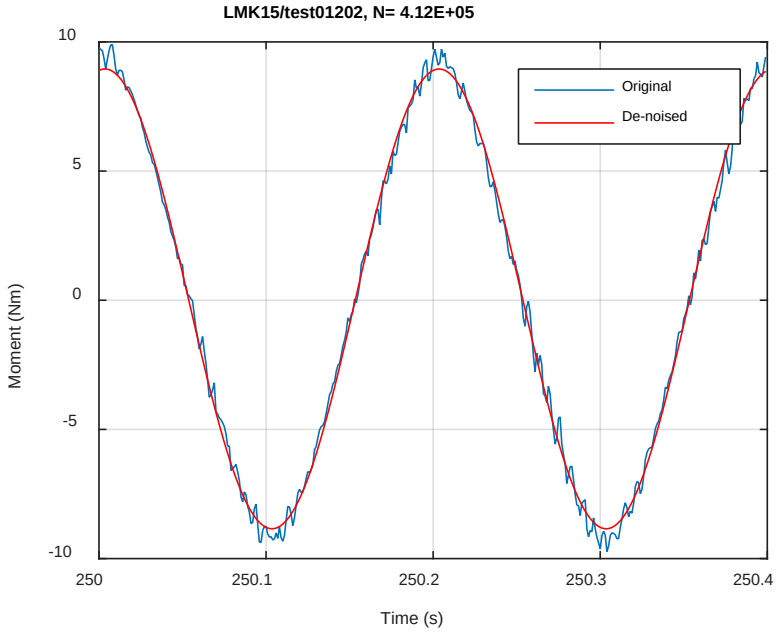
LMK15/test01202, N= 4.12E+05
Original
De-noised
Moment (Nm)
Time (s)
10
5
0
-5
-10
250
250.1
250.2
250.3
250.4

(b)

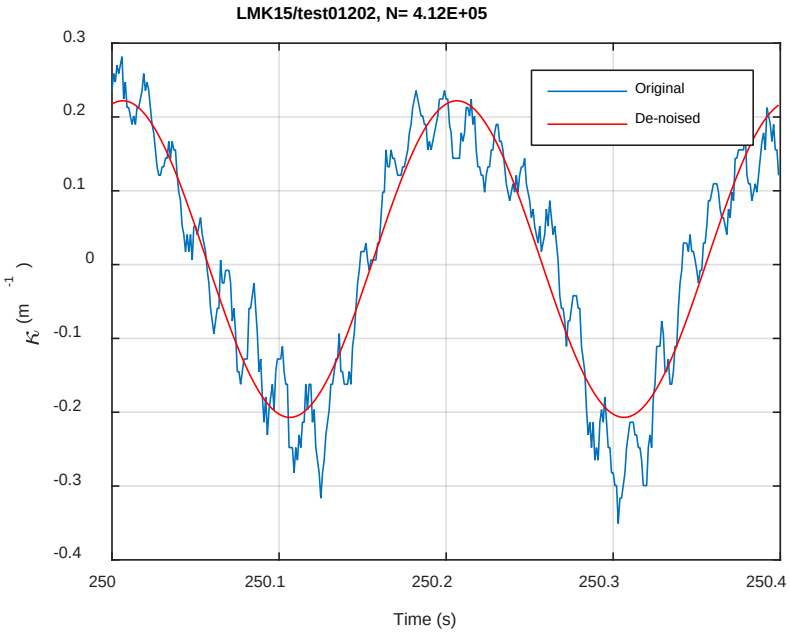

(c)

Fig. A.53. Monitoring-based responses: (a) curvature, (b) moment, (c) curvature, LMK15, 10.16 Nm, Ns = 4.12E+05 cycles.

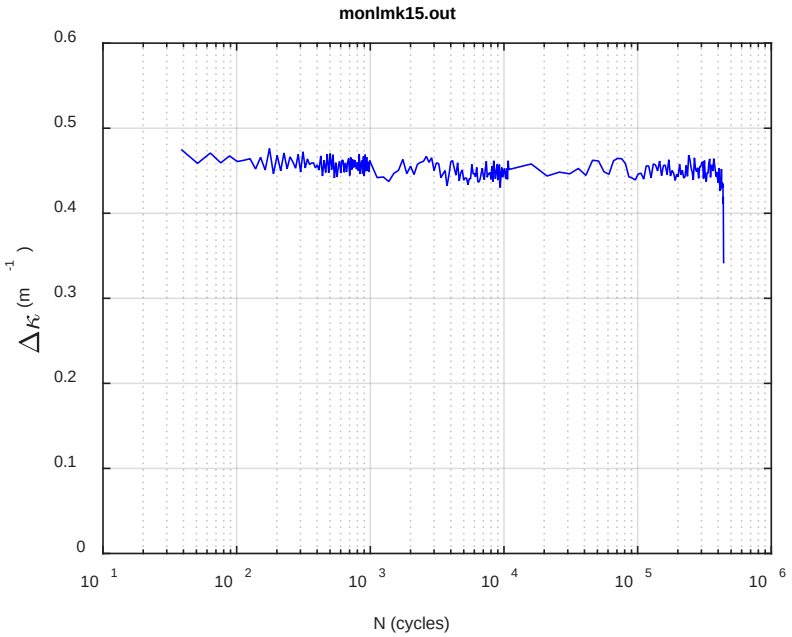
monlmk15.out
0.6
0.5
0.4
0.3
0.2
0.1
0
Δκ (m -1)
10 1
10 2
10 3
10 4
10 5
10 6
N (cycles)

(a)

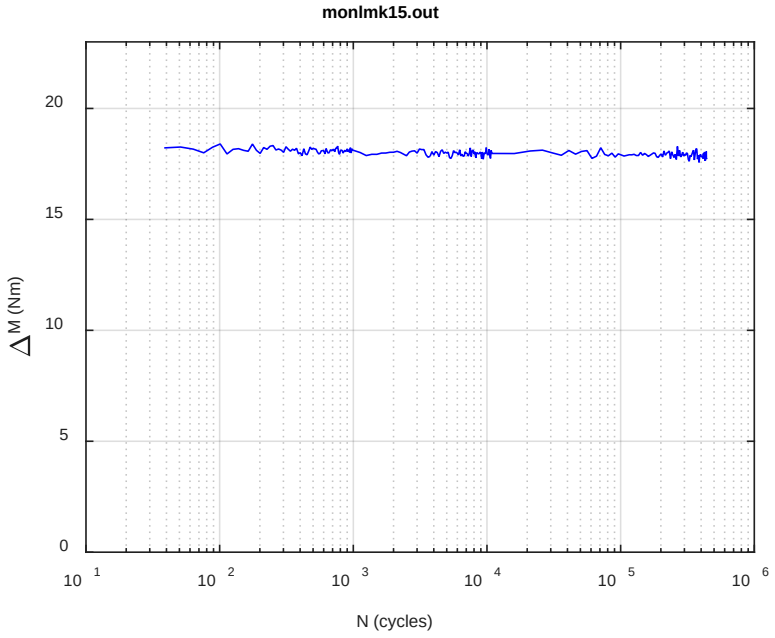
monlmk15.out
20
15
10
5
0
Δ M (Nm)
10 1
10 2
10 3
10 4
10 5
10 6
N (cycles)

(b)

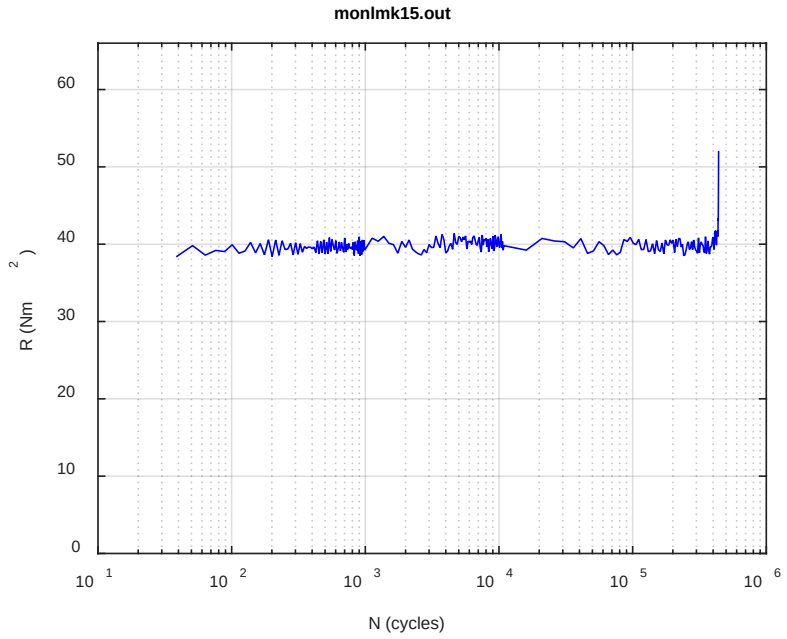
monlmk15.out
R (Nm 2)
N (cycles)

(c)

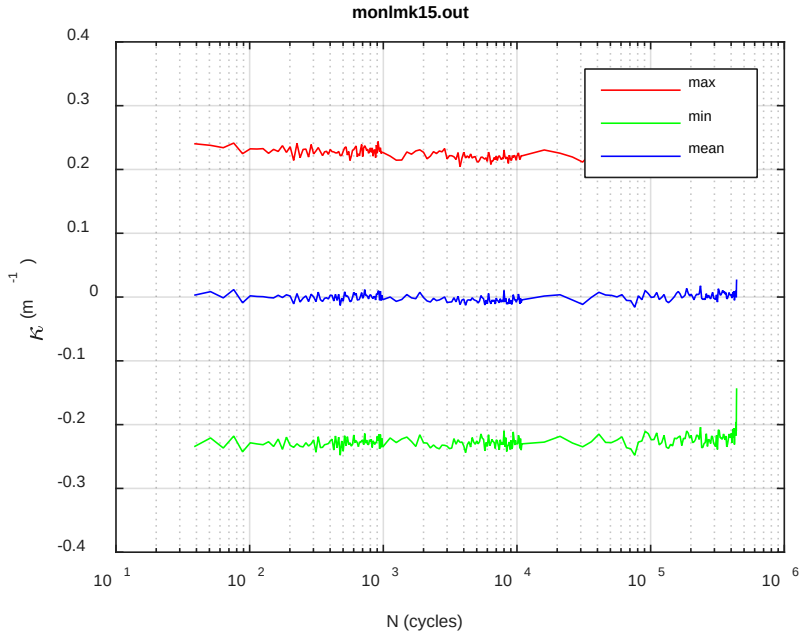
monlmk15.out
max
min
mean
κ (m -1)
N (cycles)

(d)

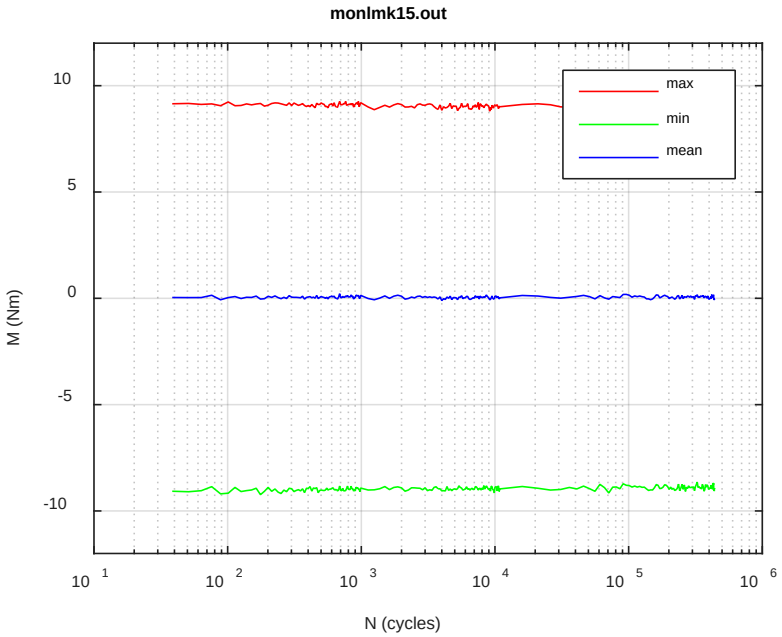

(e)

Fig. A.54. Monitoring-based responses: (a) curvature range, (b) moment range, (c) rigidity, (d) curvature peak/valley, (e) moment peak/valley, LMK15, 10.16 Nm, Nf = 4.41E+05 cycles.

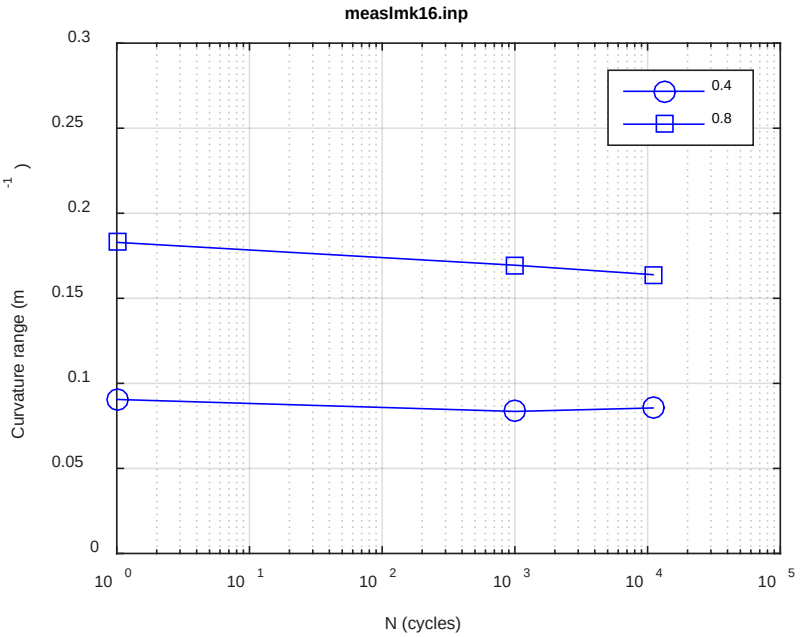
measlmk16.inp
0.3
0.25
0.2
0.15
0.1
0.05
0
Curvature range (m -1)
0.4
0.8
10 0
10 1
10 2
10 3
10 4
10 5
N (cycles)

(a)

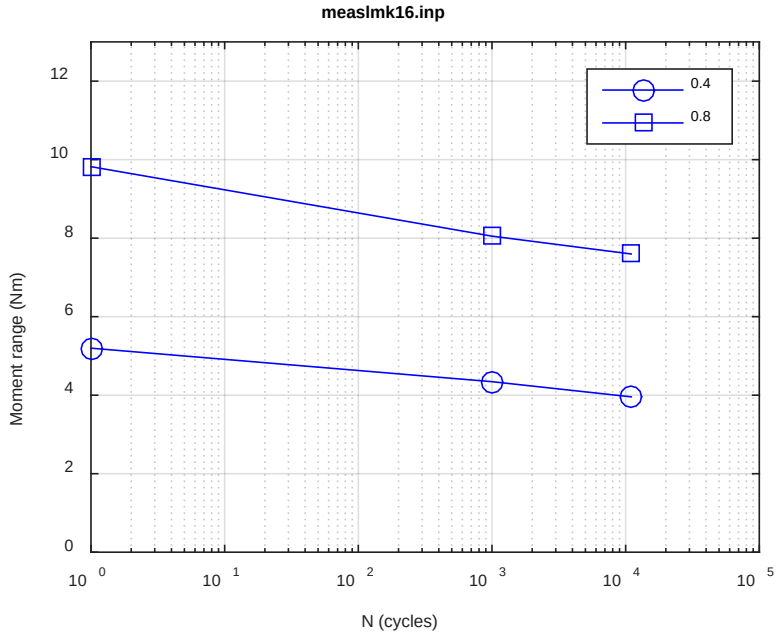
measlmk16.inp
12
10
8
6
4
2
0
Moment range (Nm)
0.4
0.8
10 0
10 1
10 2
10 3
10 4
10 5
N (cycles)

(b)

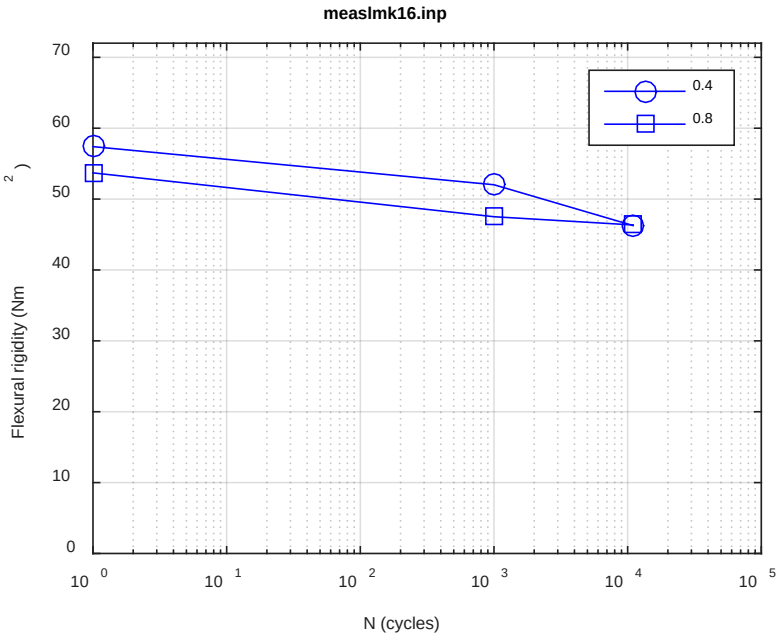
measlmk16.inp
Flexural rigidity (Nm 2)
N (cycles)
0.4
0.8
70
60
50
40
30
20
10
0
10 0
10 1
10 2
10 3
10 4
10 5

(c)

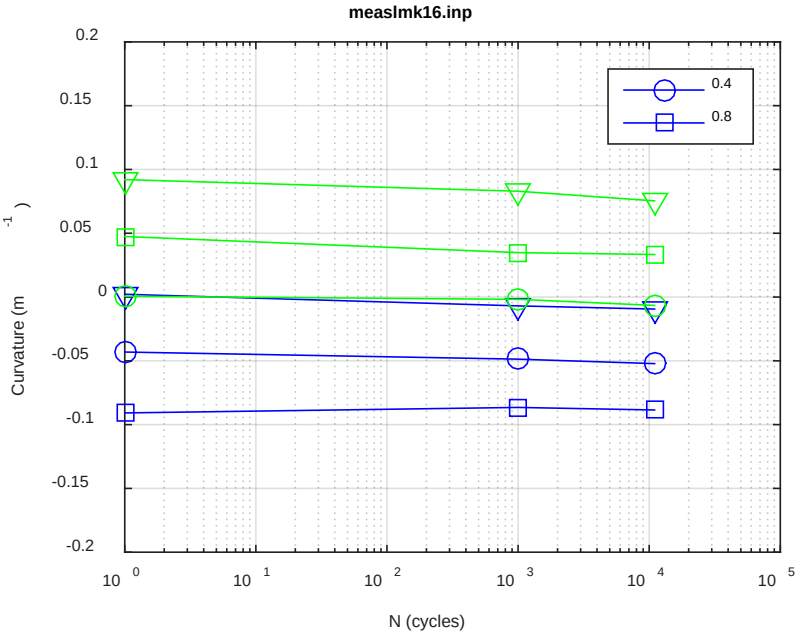
measlmk16.inp
Curvature (m -1)
N (cycles)
0.4
0.8
0.2
0.15
0.1
0.05
0
-0.05
-0.1
-0.15
-0.2
10 0
10 1
10 2
10 3
10 4
10 5

(d)

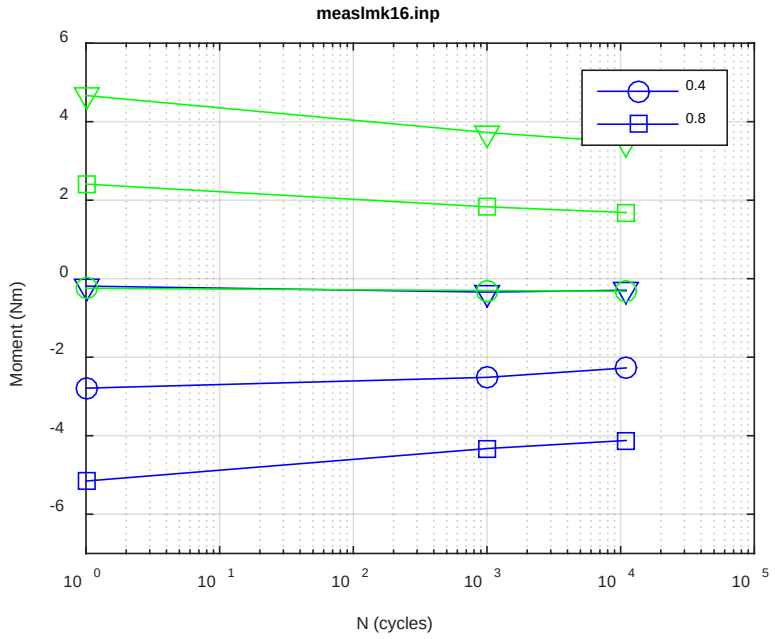

(e)

Fig. A.55. Measurement-based responses: (a) curvature range, (b) moment range, (c) rigidity, (d) curvature peak/valley, (e) moment peak/valley, LMK16, 30.48 Nm.

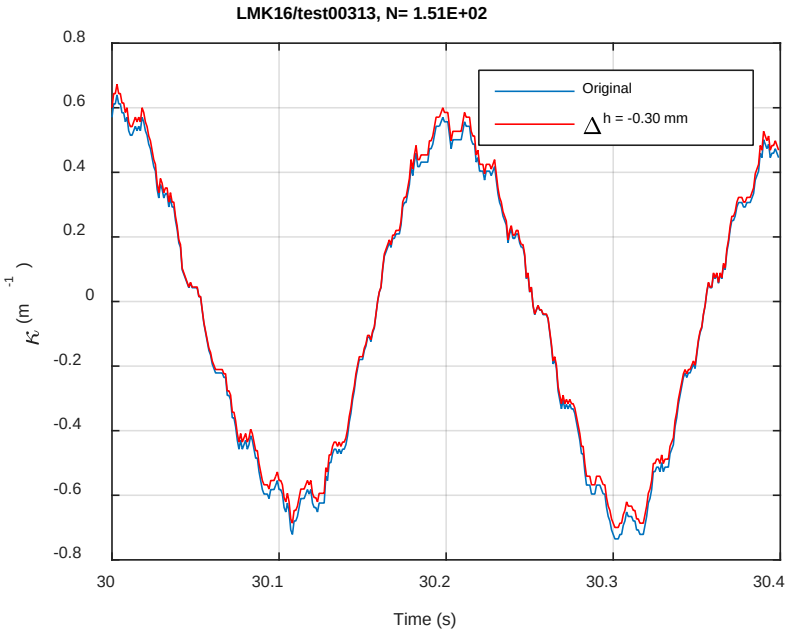
LMK16/test00313, N= 1.51E+02
Original
Δh = -0.30 mm
κ (m-1)
Time (s)
0.8
0.6
0.4
0.2
0
-0.2
-0.4
-0.6
-0.8
30
30.1
30.2
30.3
30.4

(a)

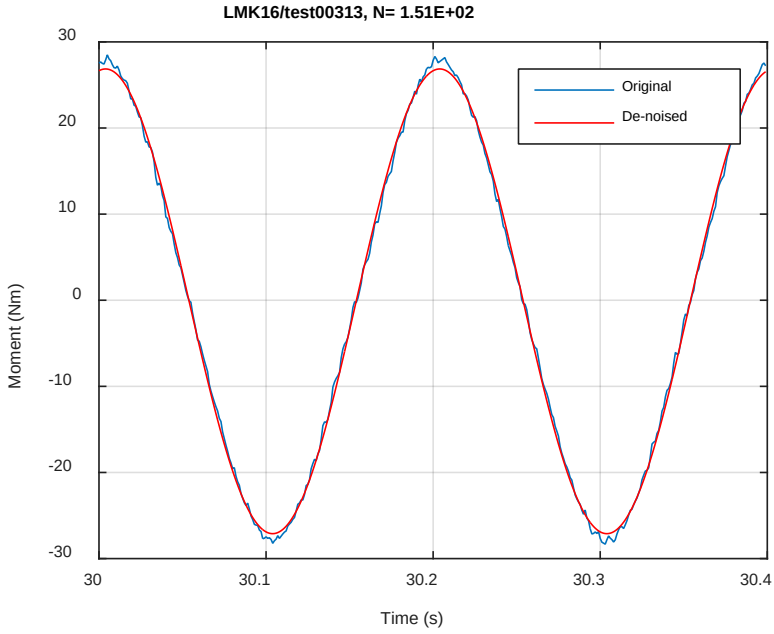
LMK16/test00313, N= 1.51E+02
Original
De-noised
Moment (Nm)
Time (s)
30
20
10
0
-10
-20
-30
30
30.1
30.2
30.3
30.4

(b)

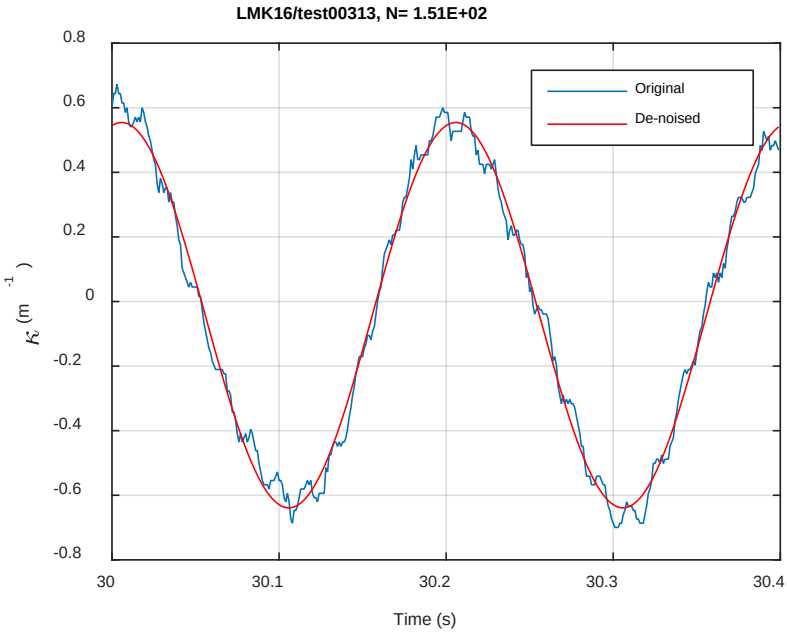

(c)

Fig. A.56. Monitoring-based responses: (a) curvature, (b) moment, (c) curvature, LMK16, 30.48 Nm, Ns = 1.51E+02 cycles.

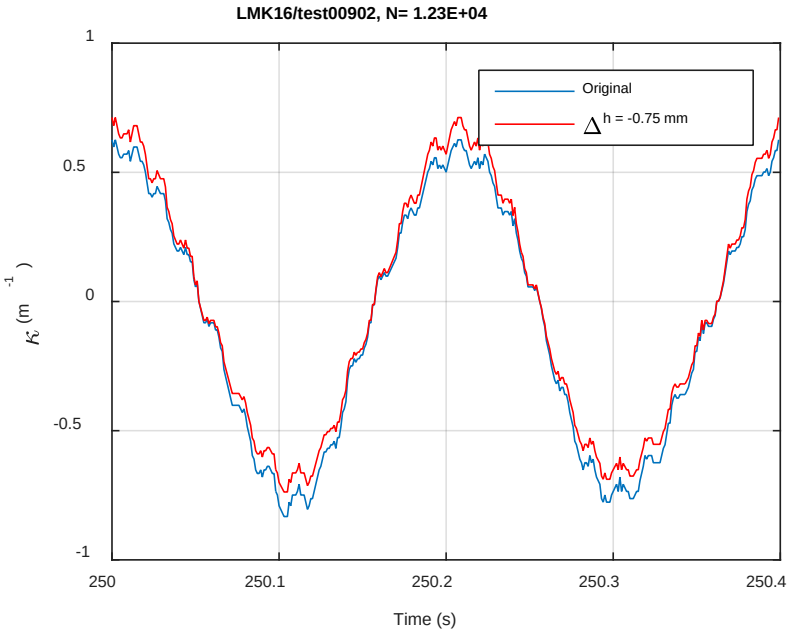
LMK16/test00902, N= 1.23E+04
Original
Δh = -0.75 mm
κ (m-1)
Time (s)
1
0.5
0
-0.5
-1
250
250.1
250.2
250.3
250.4

(a)

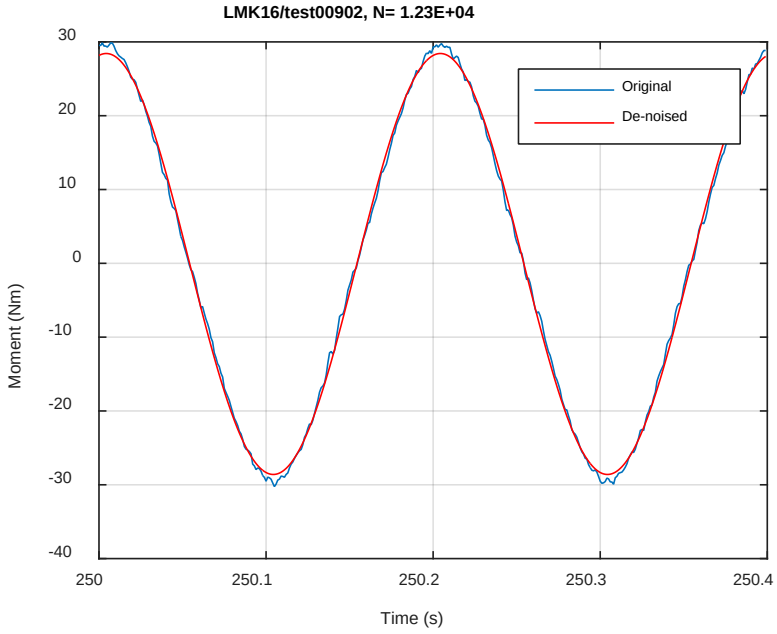
LMK16/test00902, N= 1.23E+04
Original
De-noised
Moment (Nm)
Time (s)
30
20
10
0
-10
-20
-30
-40
250
250.1
250.2
250.3
250.4

(b)

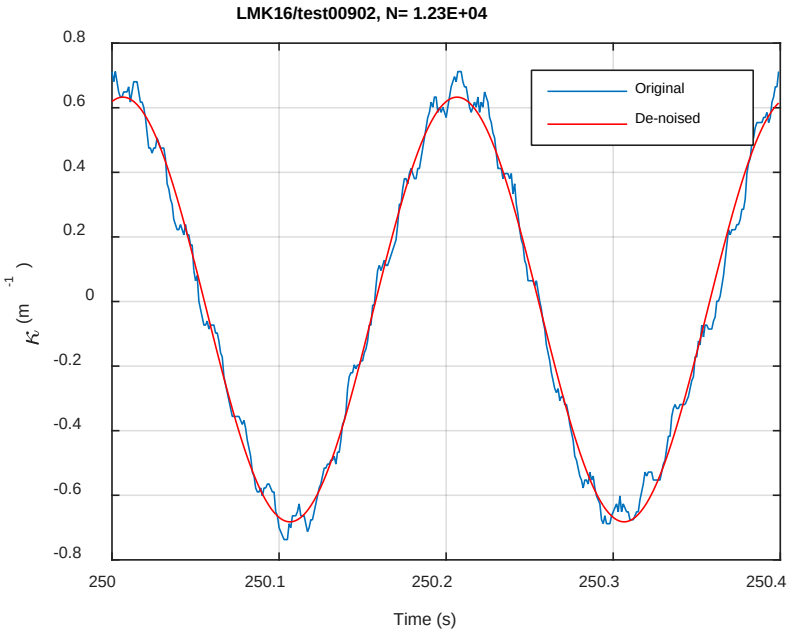

(c)

Fig. A.57. Monitoring-based responses: (a) curvature, (b) moment, (c) curvature, LMK16, 30.48 Nm, Ns = 1.23E+04 cycles.

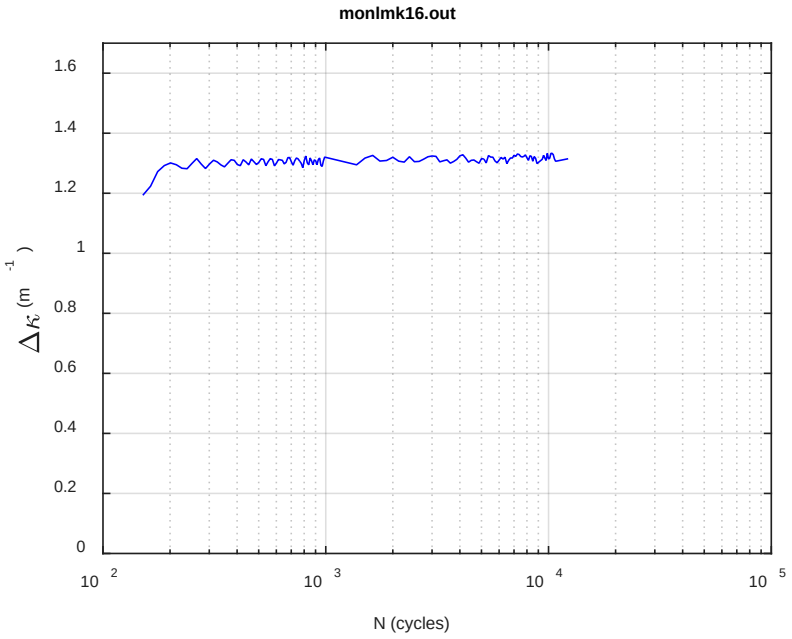
monlmk16.out
1.6
1.4
1.2
1
0.8
0.6
0.4
0.2
0
$\Delta\kappa$ (m^{-1})
10 2
10 3
10 4
10 5
N (cycles)

(a)

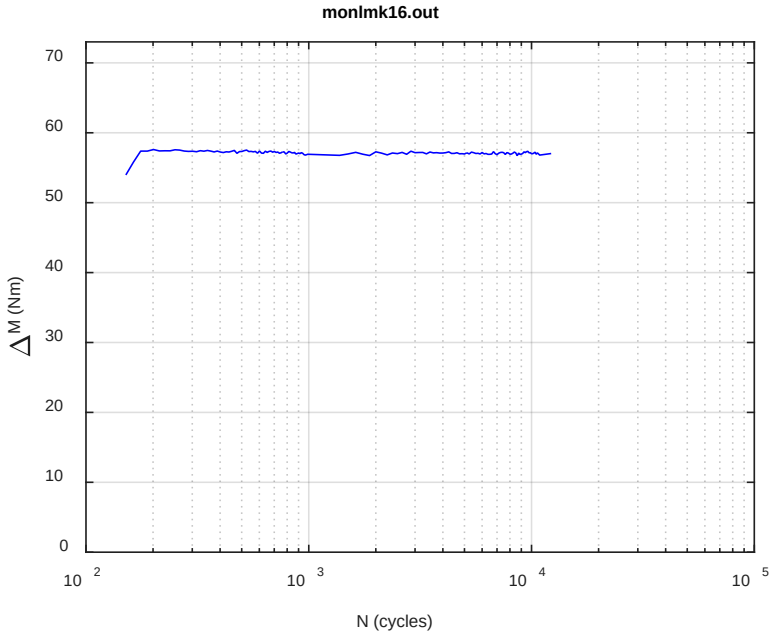
monlmk16.out
70
60
50
40
30
20
10
0
Δ M (Nm)
10 2
10 3
10 4
10 5
N (cycles)

(b)

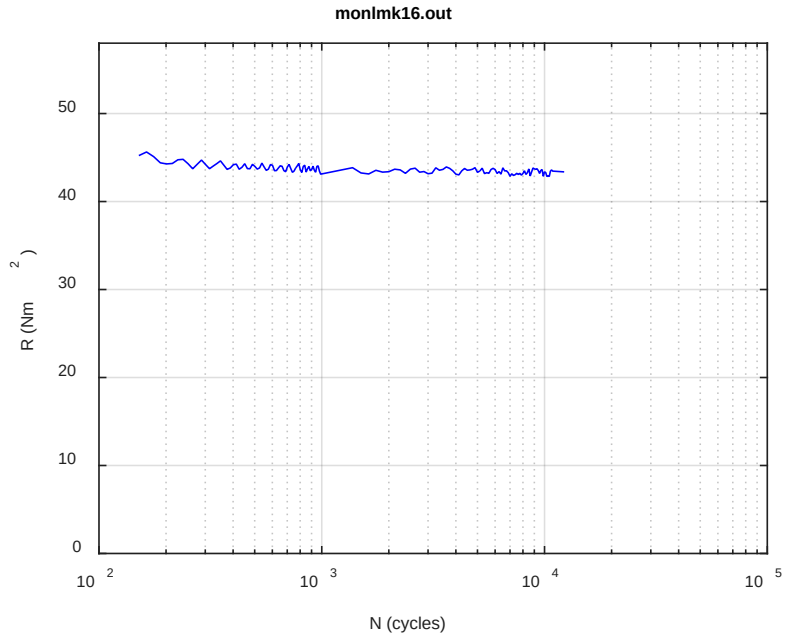
monlmk16.out
R (Nm^-2)
N (cycles)
0
10
20
30
40
50
10^2
10^3
10^4
10^5

(c)

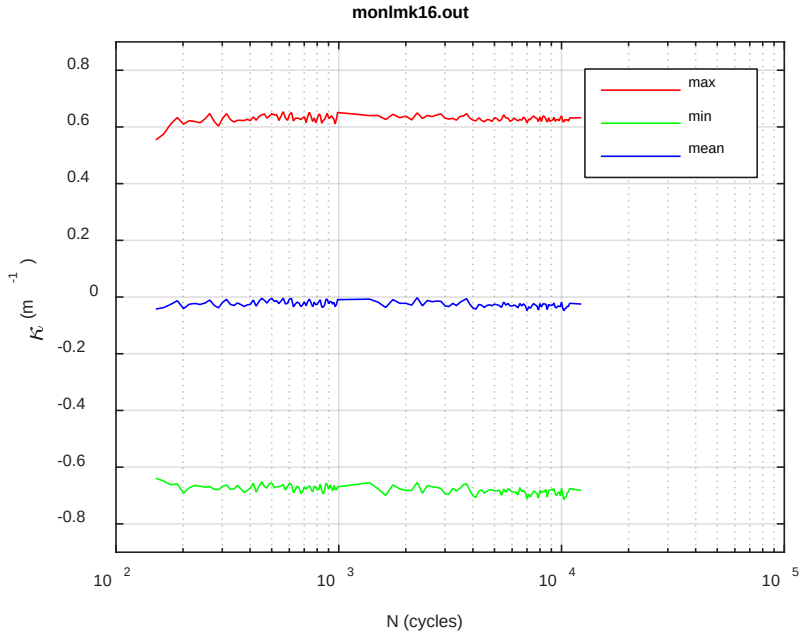
monlmk16.out
max
min
mean
κ (m^-1)
N (cycles)
0.8
0.6
0.4
0.2
0
-0.2
-0.4
-0.6
-0.8
10^2
10^3
10^4
10^5

(d)

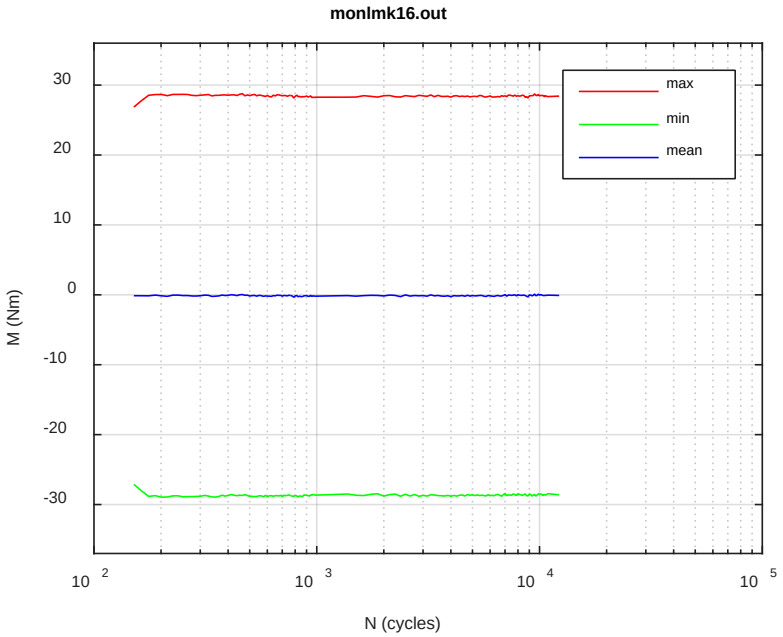

(e)

Fig. A.58. Monitoring-based responses: (a) curvature range, (b) moment range, (c) rigidity, (d) curvature peak/valley, (e) moment peak/valley, LMK16, 30.48 Nm, Nf = 1.36E+04 cycles.

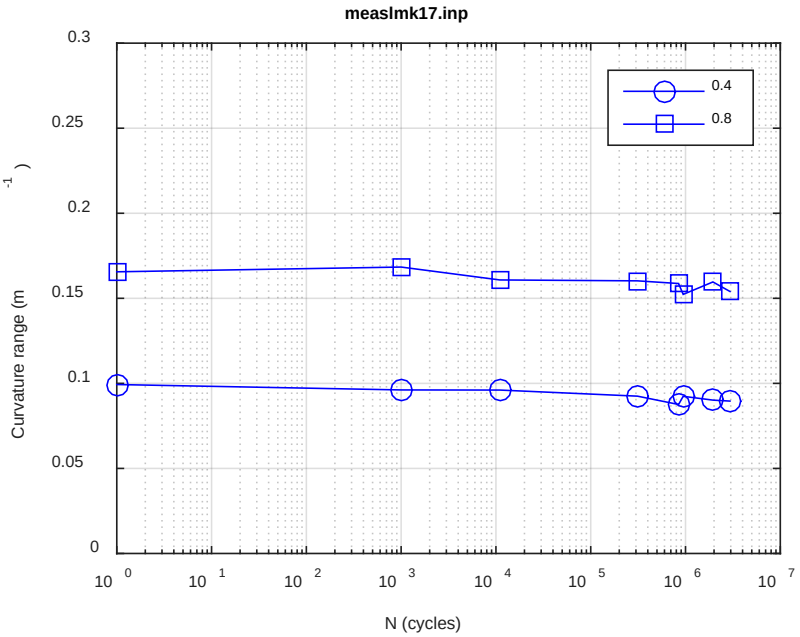
measlmk17.inp
0.3
0.25
0.2
0.15
0.1
0.05
0
Curvature range (m-1)
0.4
0.8
10 0
10 1
10 2
10 3
10 4
10 5
10 6
10 7
N (cycles)

(a)

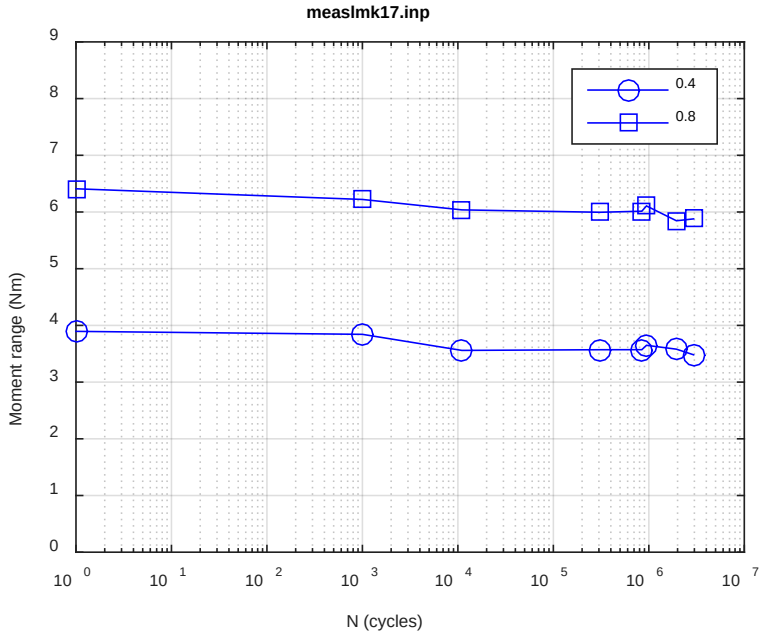
measlmk17.inp
9
8
7
6
5
4
3
2
1
0
Moment range (Nm)
0.4
0.8
10 0
10 1
10 2
10 3
10 4
10 5
10 6
10 7
N (cycles)

(b)

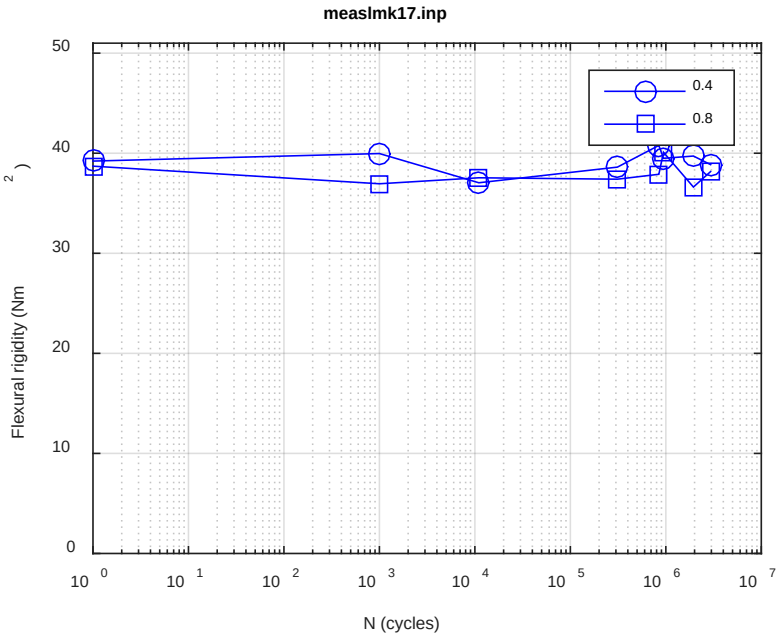
measlmk17.inp
0.4
0.8
Flexural rigidity (Nm 2)
N (cycles)

(c)

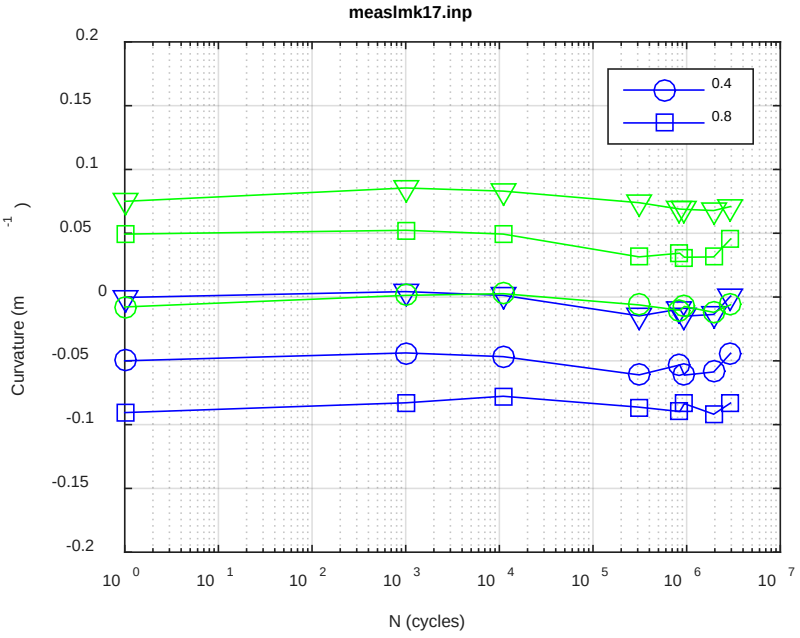
measlmk17.inp
0.4
0.8
Curvature (m -1)
N (cycles)

(d)

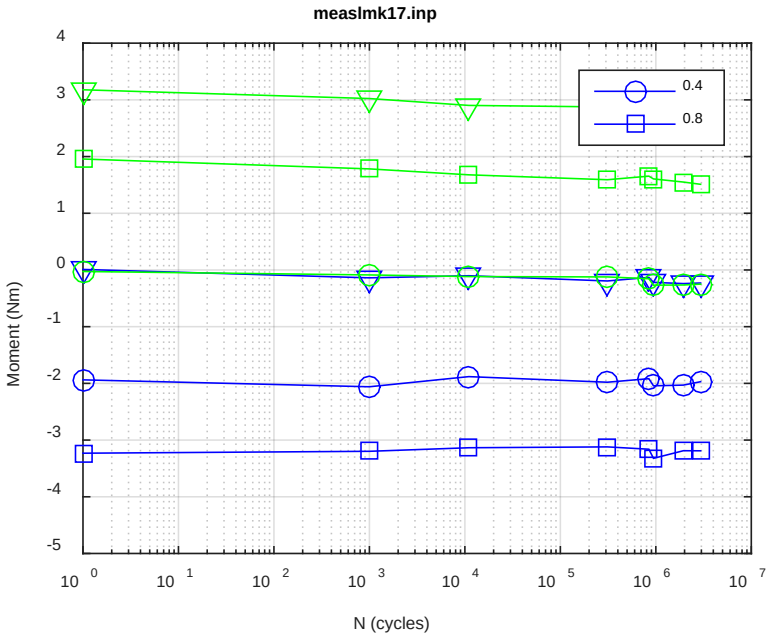

(e)

Fig. A.59. Measurement-based responses: (a) curvature range, (b) moment range, (c) rigidity, (d) curvature peak/valley, (e) moment peak/valley, LMK17, 8.64 Nm.

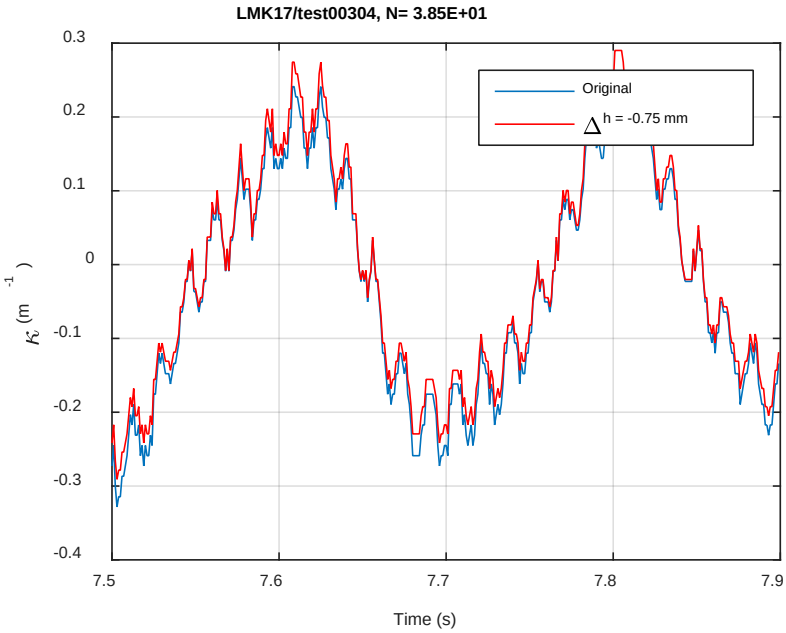
LMK17/test00304, N= 3.85E+01
Original
Δh = -0.75 mm
κ (m-1)
Time (s)
0.3
0.2
0.1
0
-0.1
-0.2
-0.3
-0.4
7.5
7.6
7.7
7.8
7.9

(a)

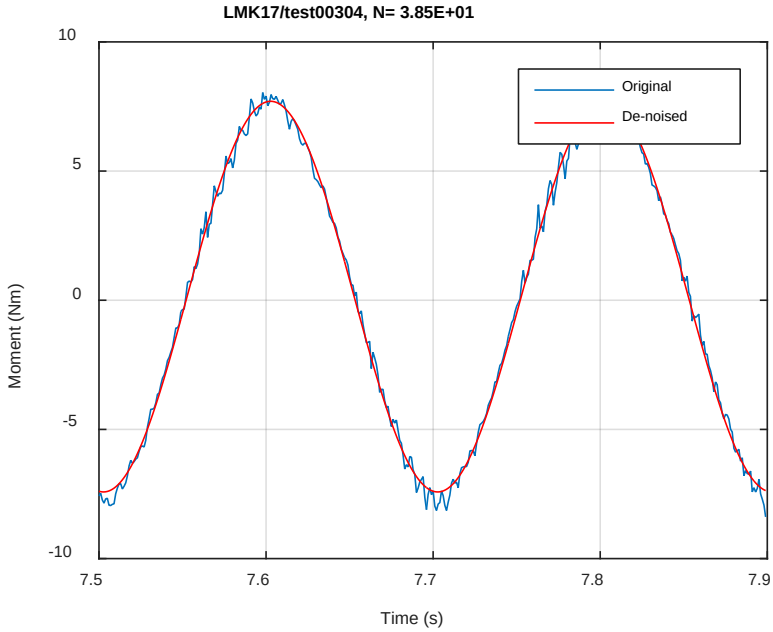
LMK17/test00304, N= 3.85E+01
Original
De-noised
Moment (Nm)
Time (s)
10
5
0
-5
-10
7.5
7.6
7.7
7.8
7.9

(b)

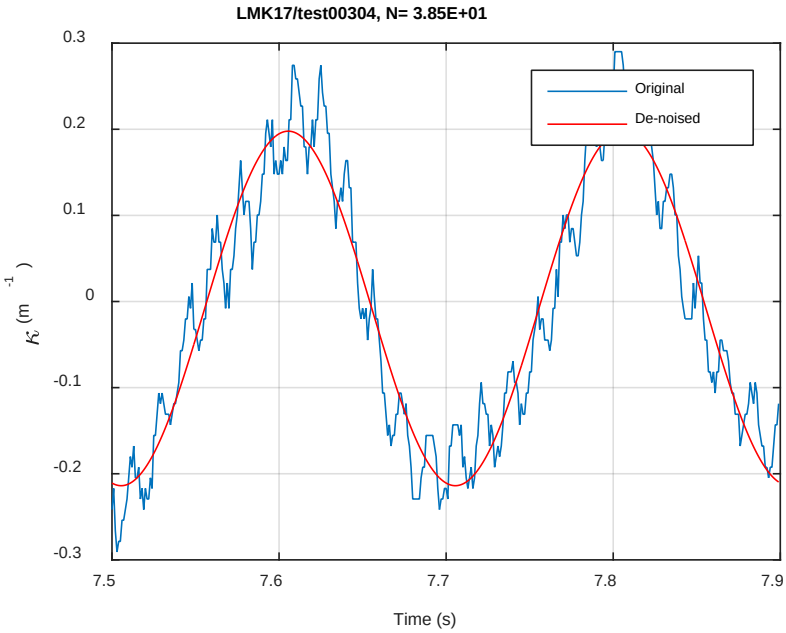

(c)

Fig. A.60. Monitoring-based responses: (a) curvature, (b) moment, (c) curvature, LMK17, 8.64 Nm, Ns = 3.85E+01 cycles.

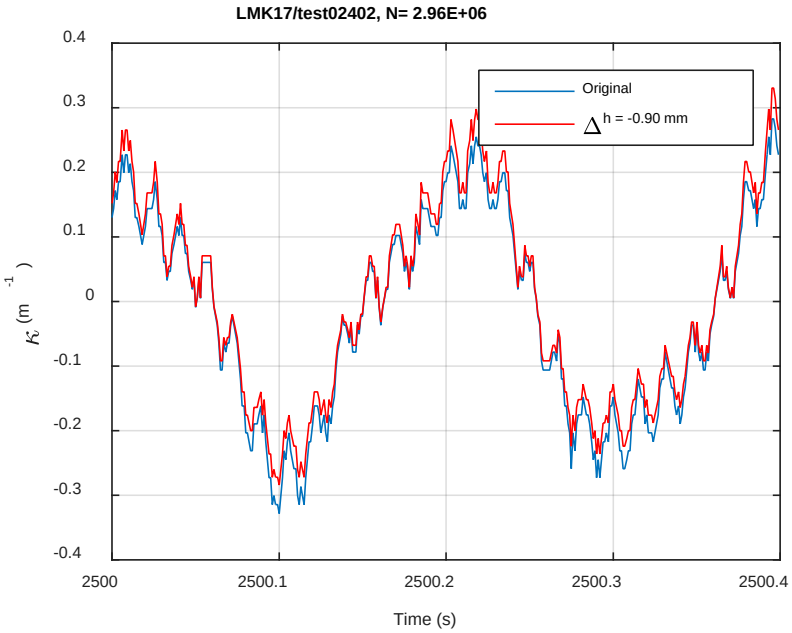
LMK17/test02402, N= 2.96E+06
Original
Δh = -0.90 mm
κ (m-1)
Time (s)
0.4
0.3
0.2
0.1
0
-0.1
-0.2
-0.3
-0.4
2500
2500.1
2500.2
2500.3
2500.4

(a)

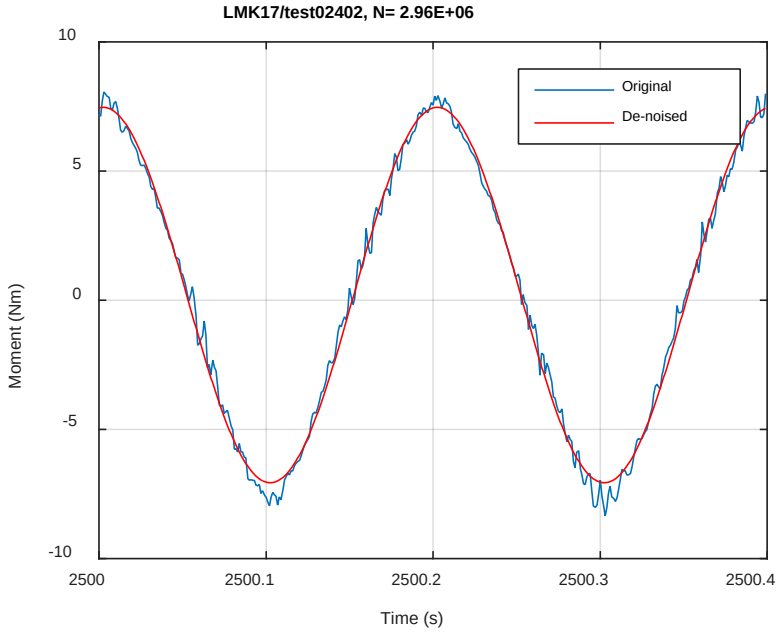
LMK17/test02402, N= 2.96E+06
Original
De-noised
Moment (Nm)
Time (s)
10
5
0
-5
-10
2500
2500.1
2500.2
2500.3
2500.4

(b)

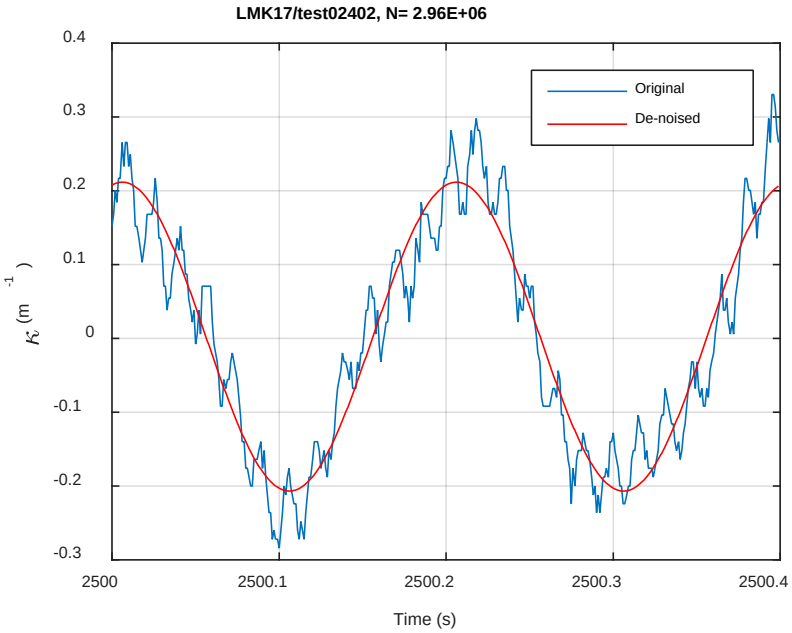

(c)

Fig. A.61. Monitoring-based responses: (a) curvature, (b) moment, (c) curvature, LMK17, 8.64 Nm, Ns = 2.96E+06 cycles.

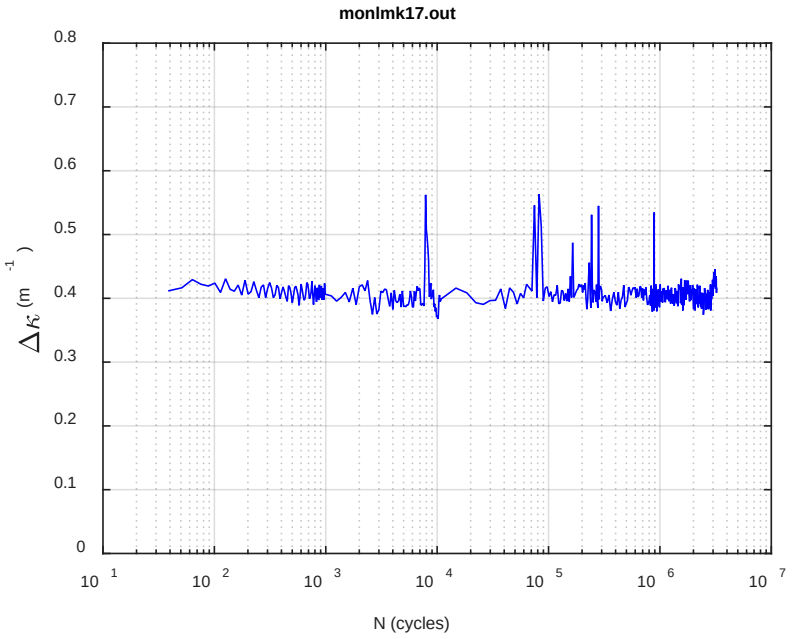
monlmk17.out
0.8
0.7
0.6
0.5
0.4
0.3
0.2
0.1
0
Δκ (m -1)
10 1
10 2
10 3
10 4
10 5
10 6
10 7
N (cycles)

(a)

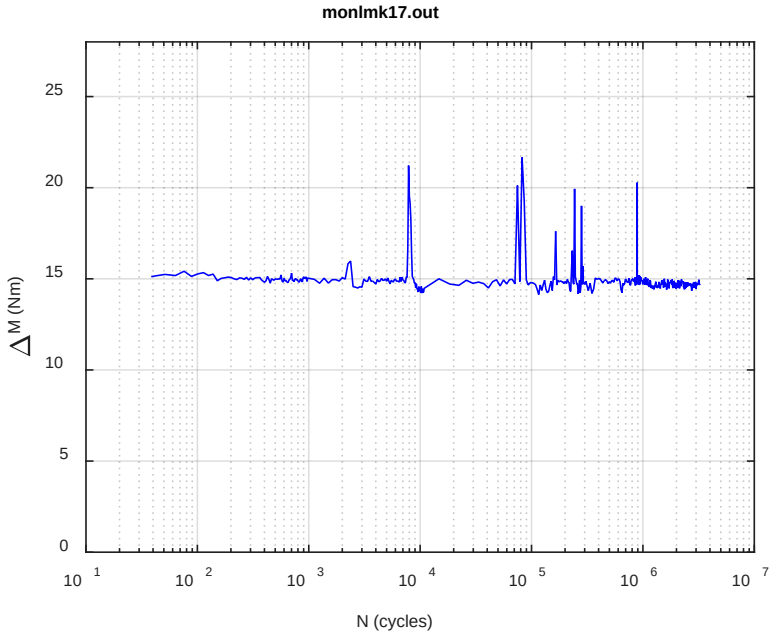
monlmk17.out
25
20
15
10
5
0
Δ M (Nm)
10 1
10 2
10 3
10 4
10 5
10 6
10 7
N (cycles)

(b)

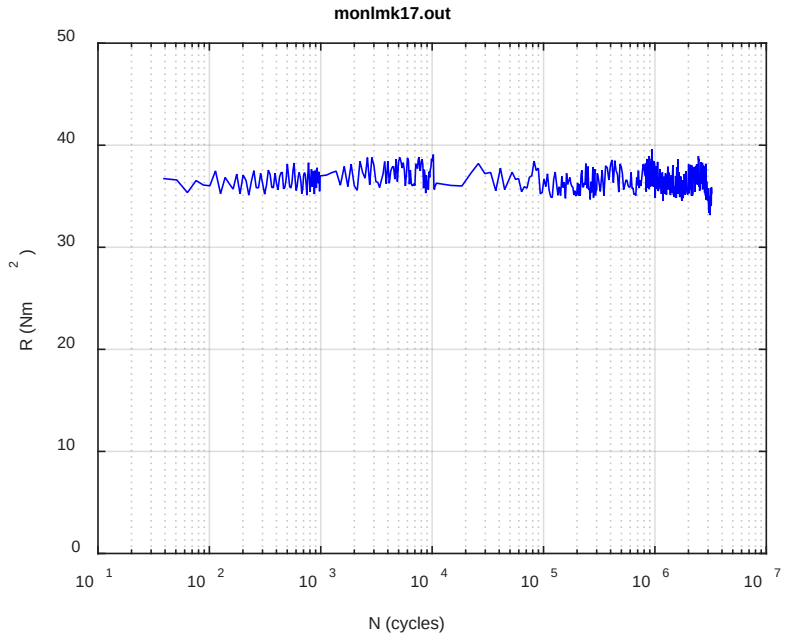
monlmk17.out
R (Nm 2)
N (cycles)

(c)

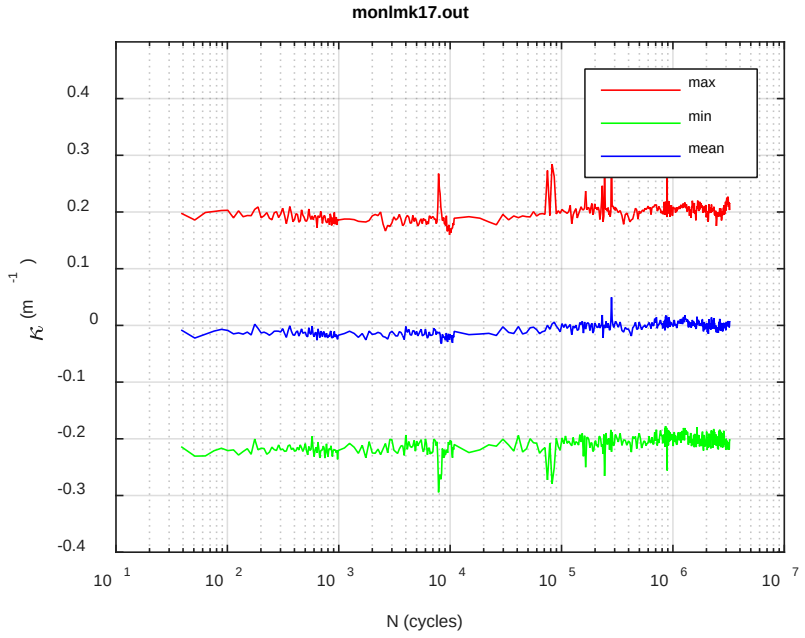
monlmk17.out
max
min
mean
κ (m -1)
N (cycles)

(d)

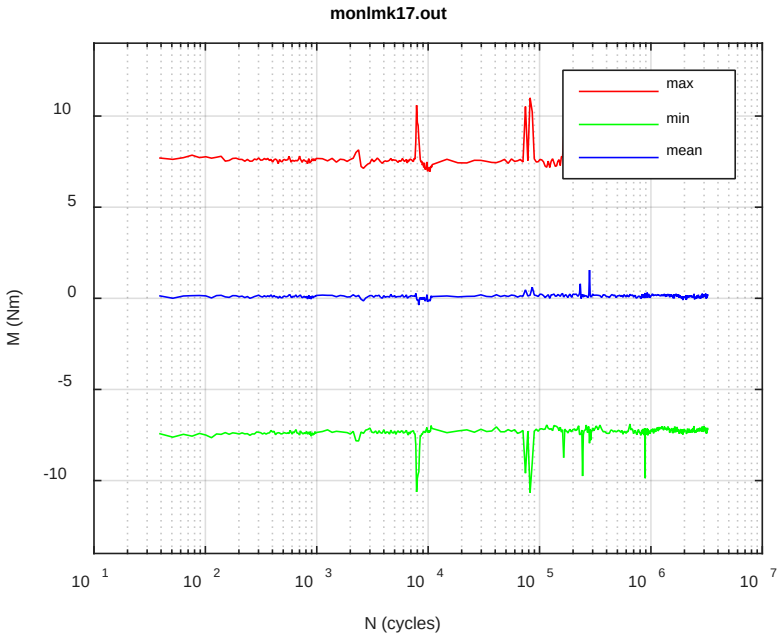

(e)

Fig. A.62. Monitoring-based responses: (a) curvature range, (b) moment range, (c) rigidity, (d) curvature peak/valley, (e) moment peak/valley, LMK17, 8.64 Nm, Nf = 3.37E+06 cycles.

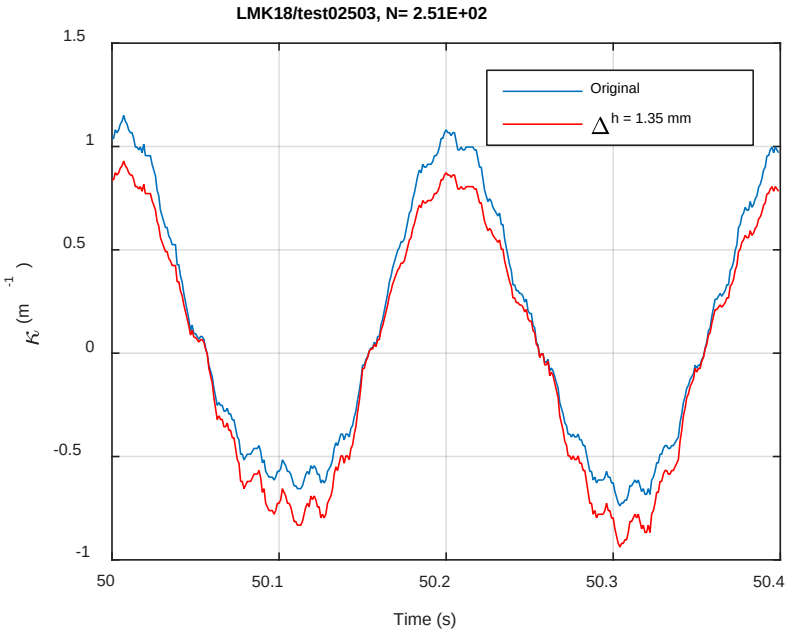
LMK18/test02503, N= 2.51E+02
Original
Δh = 1.35 mm
κ (m-1)
Time (s)
1.5
1
0.5
0
-0.5
-1
50
50.1
50.2
50.3
50.4

(a)

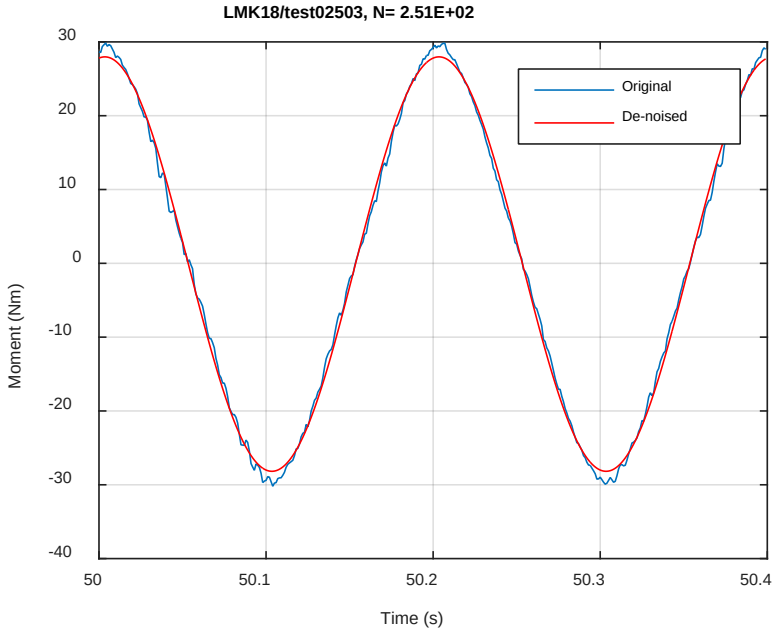
LMK18/test02503, N= 2.51E+02
Original
De-noised
Moment (Nm)
Time (s)
30
20
10
0
-10
-20
-30
-40
50
50.1
50.2
50.3
50.4

(b)

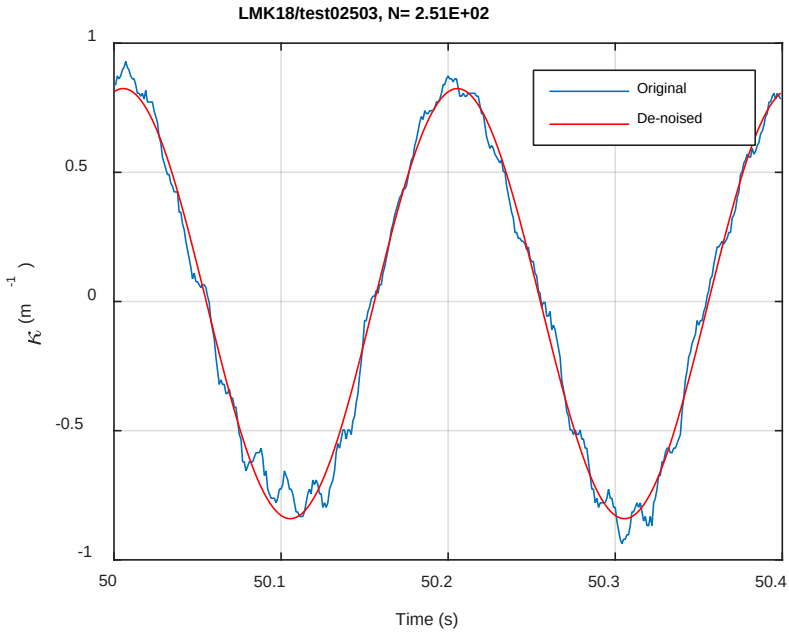

(c)

Fig. A.63. Monitoring-based responses: (a) curvature, (b) moment, (c) curvature, LMK18, 30.48 Nm, Ns = 2.51E+02 cycles.

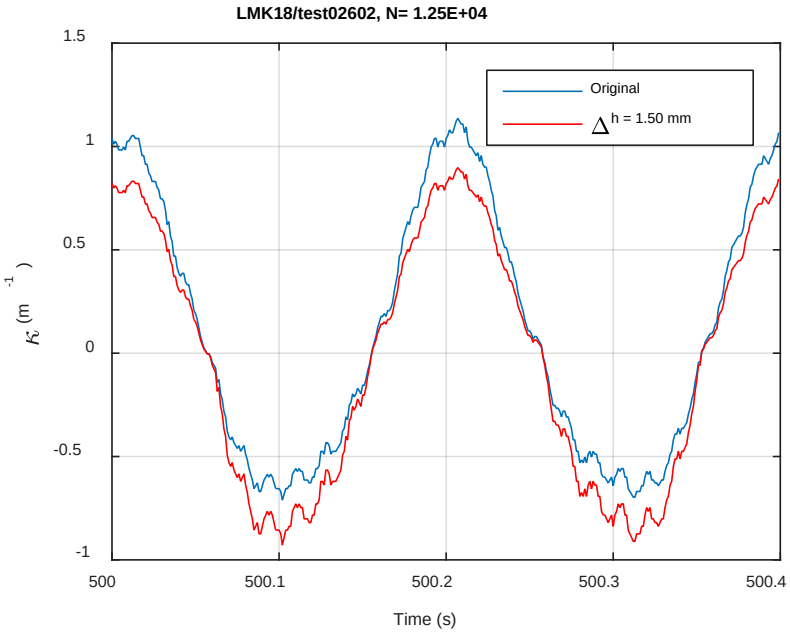
LMK18/test02602, N= 1.25E+04
Original
Δh = 1.50 mm
κ (m-1)
Time (s)
1.5
1
0.5
0
-0.5
-1
500
500.1
500.2
500.3
500.4

(a)

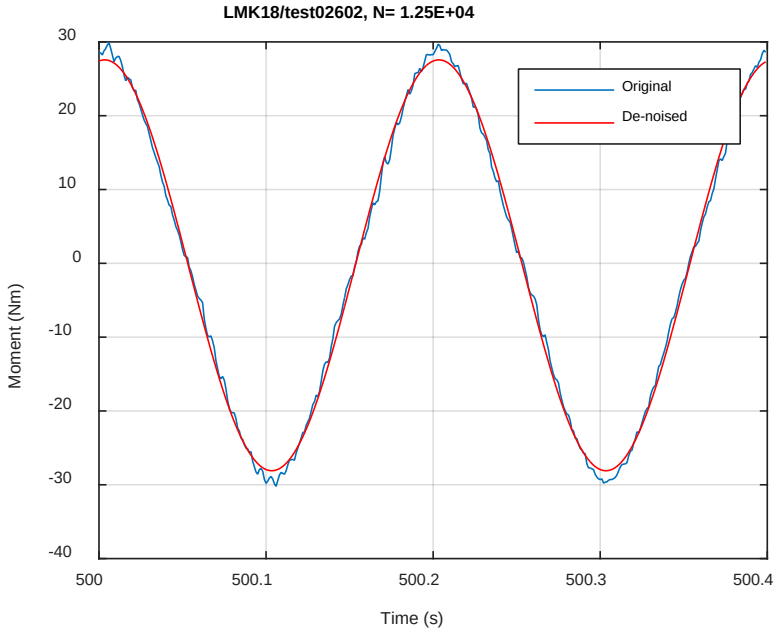
LMK18/test02602, N= 1.25E+04
Original
De-noised
Moment (Nm)
Time (s)
30
20
10
0
-10
-20
-30
-40
500
500.1
500.2
500.3
500.4

(b)

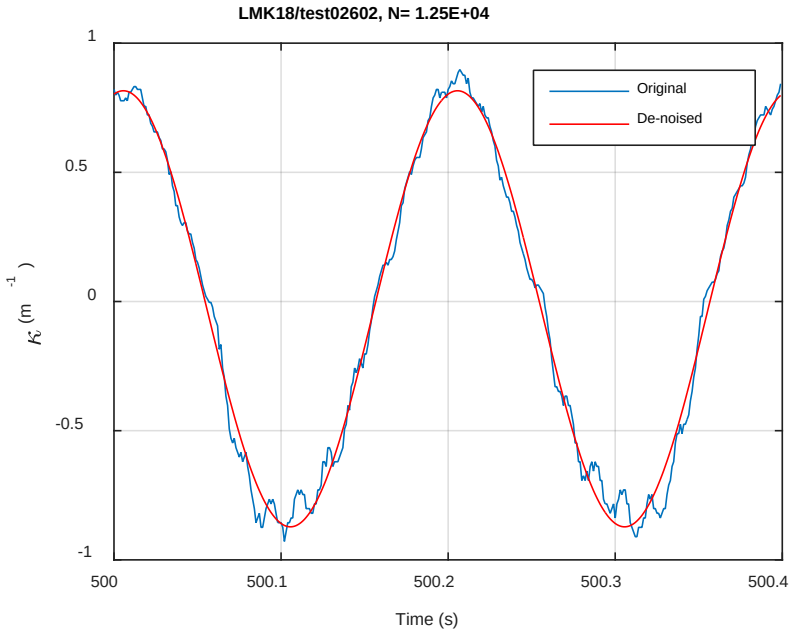

(c)

Fig. A.64. Monitoring-based responses: (a) curvature, (b) moment, (c) curvature, LMK18, 30.48 Nm, Ns = 1.25E+04 cycles.

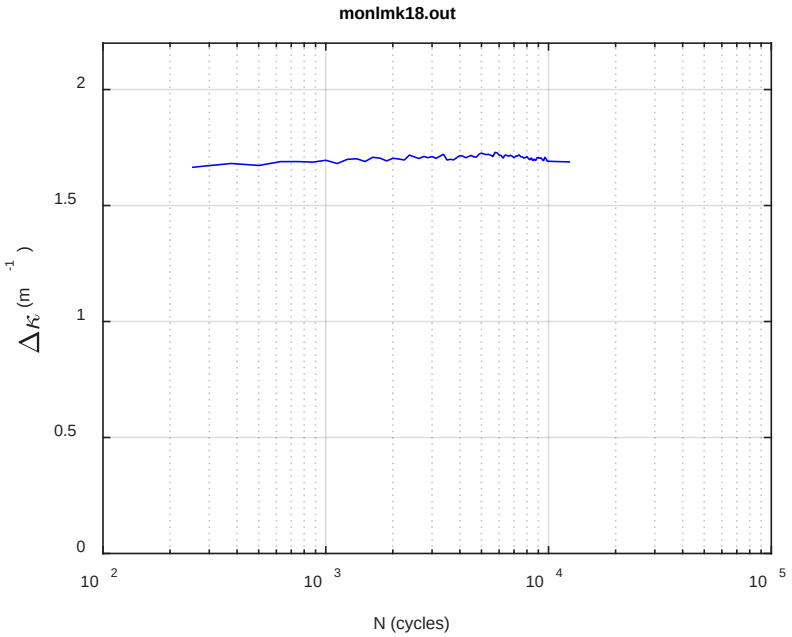
monlmk18.out
2
1.5
1
0.5
0
$\Delta\kappa$ (m^{-1})
10 2
10 3
10 4
10 5
N (cycles)

(a)

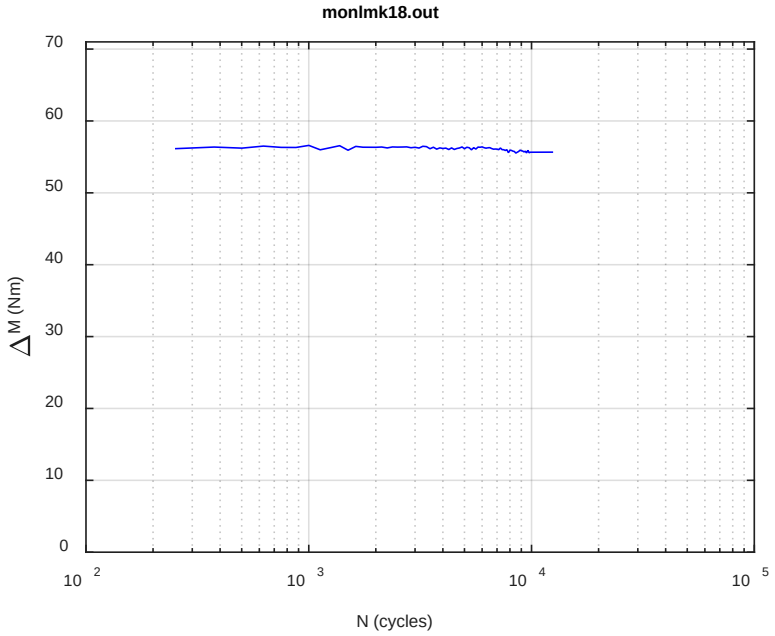
monlmk18.out
70
60
50
40
30
20
10
0
ΔM (Nm)
10 2
10 3
10 4
10 5
N (cycles)

(b)

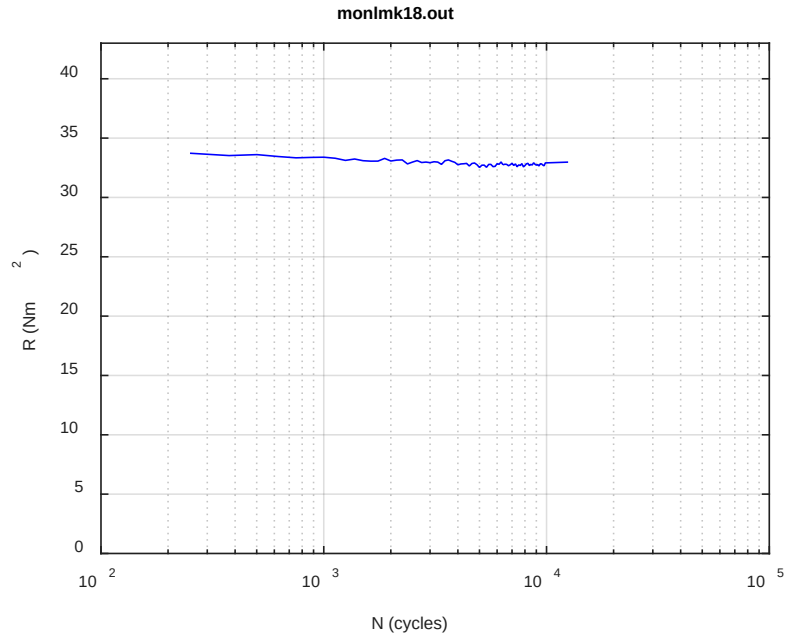
monlmk18.out
R (Nm 2)
N (cycles)
40
35
30
25
20
15
10
5
0
10 2
10 3
10 4
10 5

(c)

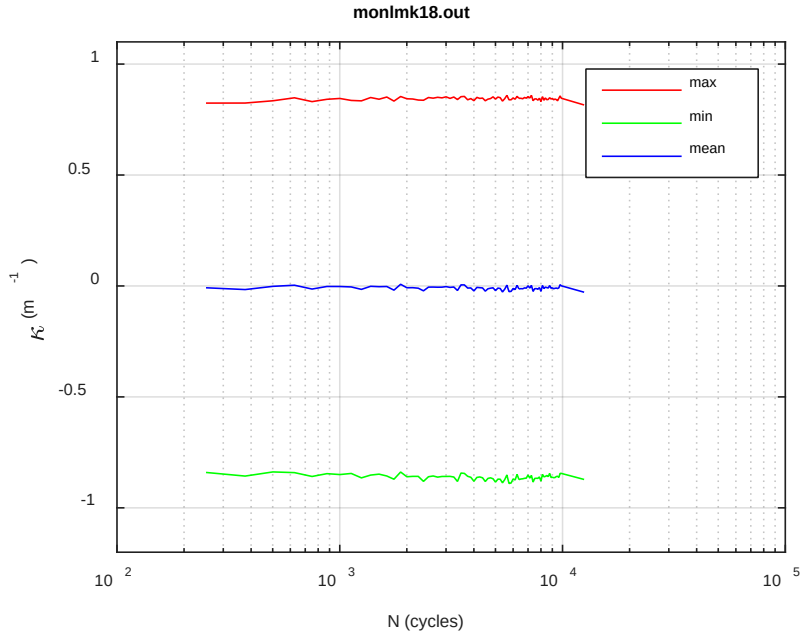
monlmk18.out
max
min
mean
κ (m -1)
N (cycles)
1
0.5
0
-0.5
-1
10 2
10 3
10 4
10 5

(d)

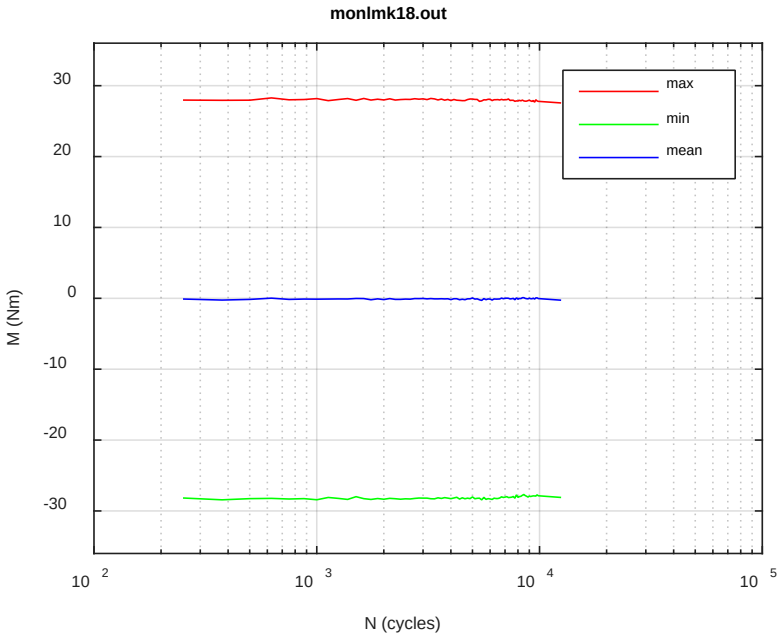

(e)

Fig. A.65. Monitoring-based responses: (a) curvature range, (b) moment range, (c) rigidity, (d) curvature peak/valley, (e) moment peak/valley, LMK18, 30.48 Nm, Nf = 1.31E+04 cycles.

This page intentionally left blank.

APPENDIX B CIRFT RESULTS OF NA SNF

TABLE OF CONTENTS

Measurement and monitoring rigidity curves of NA SNF

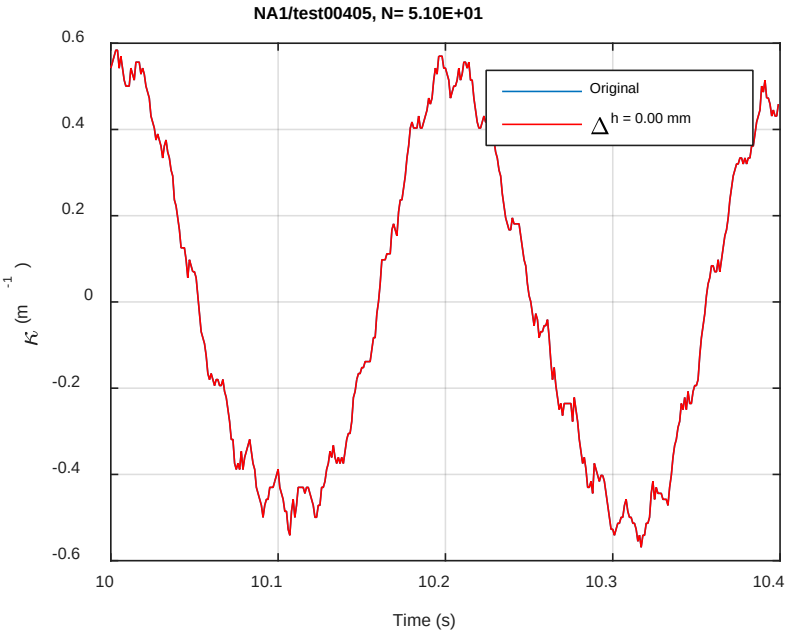
NA1/test00405, N= 5.10E+01
Original
Δh = 0.00 mm
κ (m-1)
Time (s)

(a)

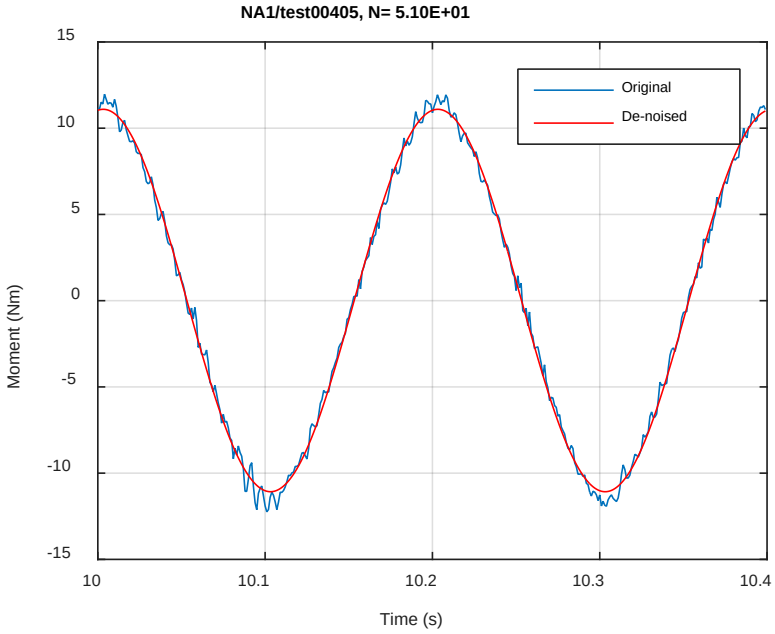
NA1/test00405, N= 5.10E+01
Original
De-noised
Moment (Nm)
Time (s)

(b)

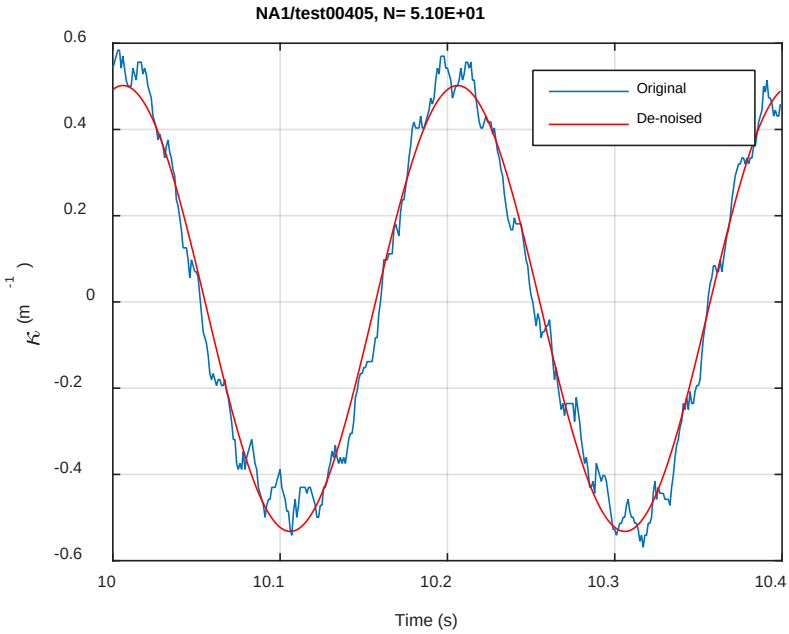

(c)

Fig. B.1. Monitoring-based responses: (a) curvature, (b) moment, (c) curvature, NA1, 12.70 Nm, Ns = 5.10E+01 cycles.

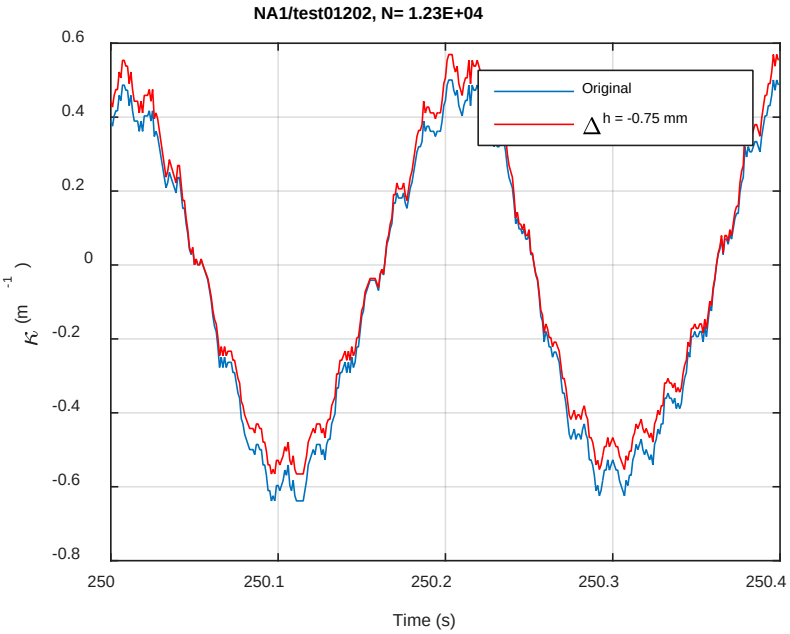
NA1/test01202, N= 1.23E+04
Original
Δh = -0.75 mm
κ (m-1)
Time (s)
0.6
0.4
0.2
0
-0.2
-0.4
-0.6
-0.8
250
250.1
250.2
250.3
250.4

(a)

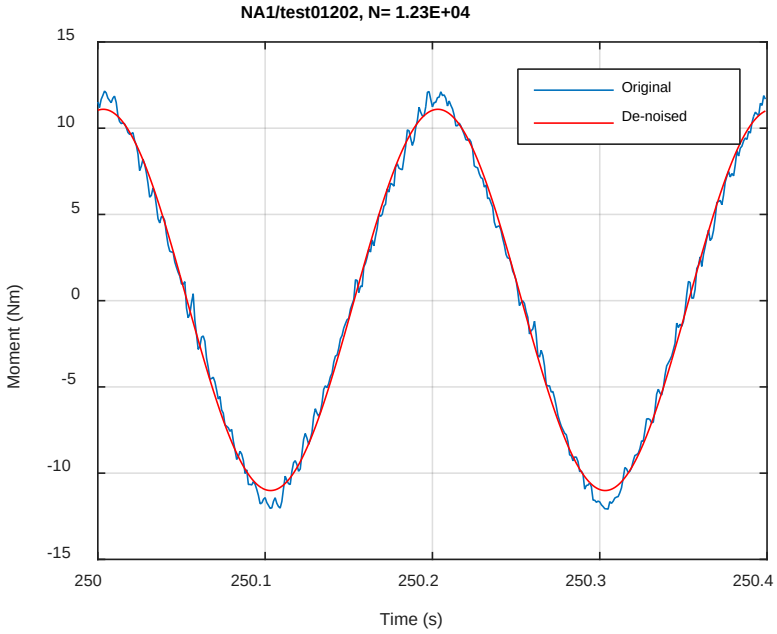
NA1/test01202, N= 1.23E+04
Original
De-noised
Moment (Nm)
Time (s)
15
10
5
0
-5
-10
-15
250
250.1
250.2
250.3
250.4

(b)

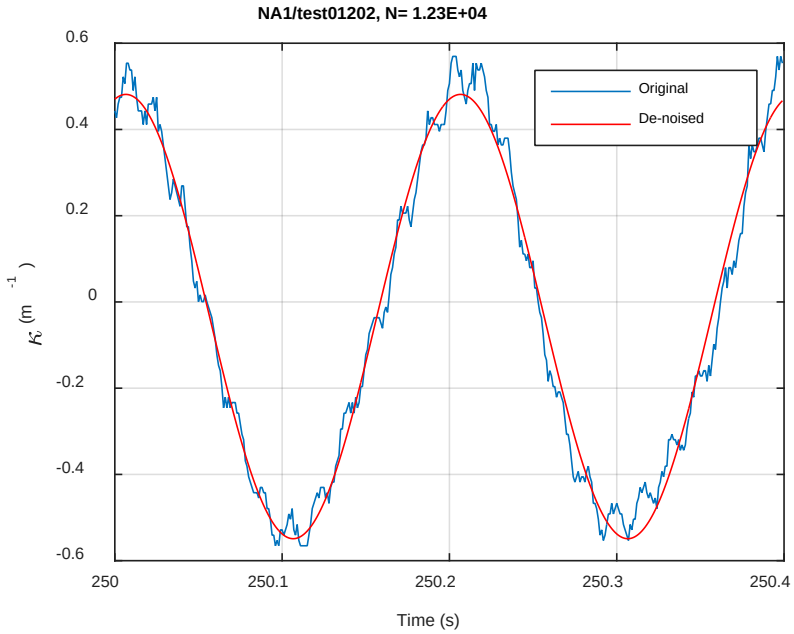

(c)

Fig. B.2. Monitoring-based responses: (a) curvature, (b) moment, (c) curvature, NA1, 12.70 Nm, Ns = 1.23E+04 cycles.

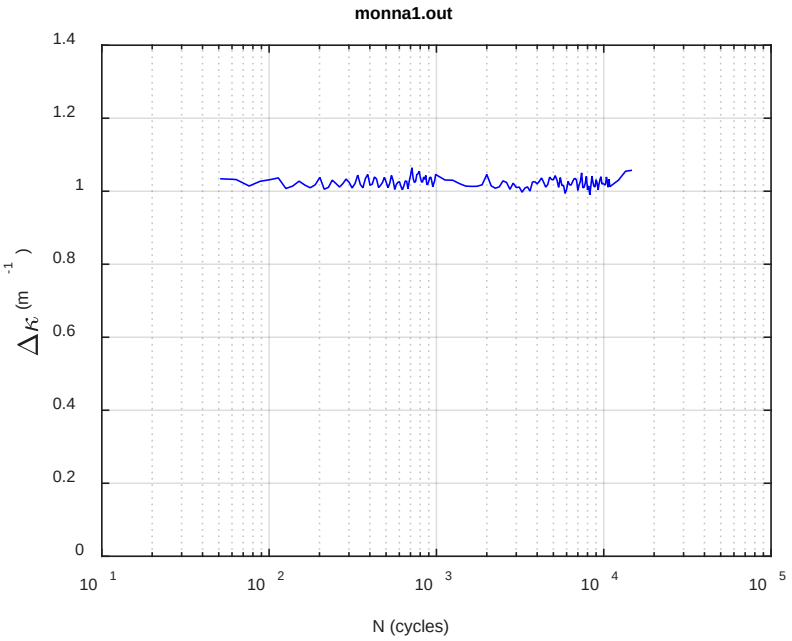
monna1.out
1.4
1.2
1
0.8
0.6
0.4
0.2
0
Δκ (m-1)
10 1
10 2
10 3
10 4
10 5
N (cycles)

(a)

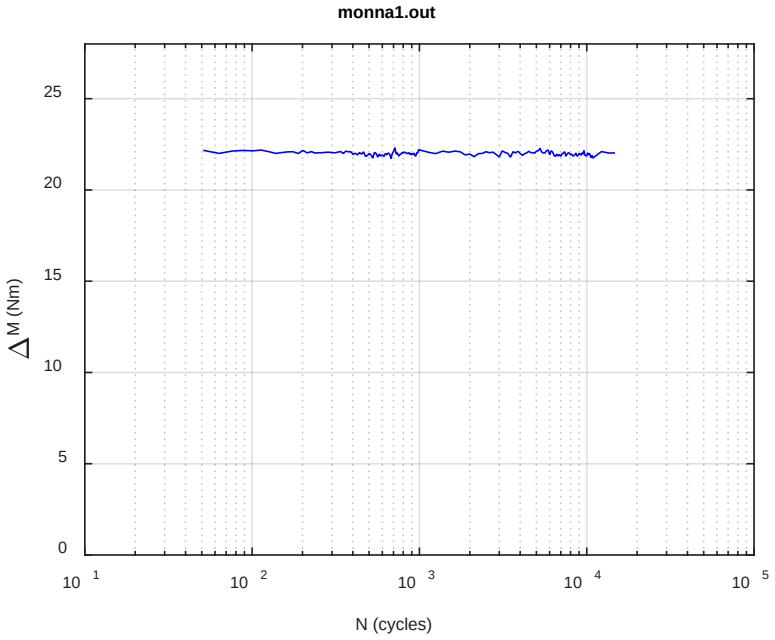
monna1.out
25
20
15
10
5
0
ΔM (Nm)
10 1
10 2
10 3
10 4
10 5
N (cycles)

(b)

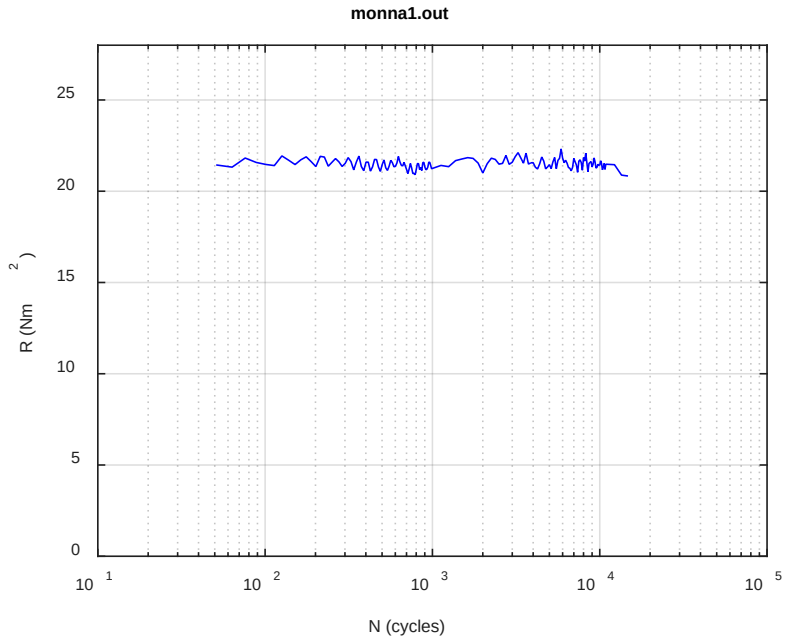
monna1.out
25
20
15
10
5
0
R (Nm 2)
10 1
10 2
10 3
10 4
10 5
N (cycles)

(c)

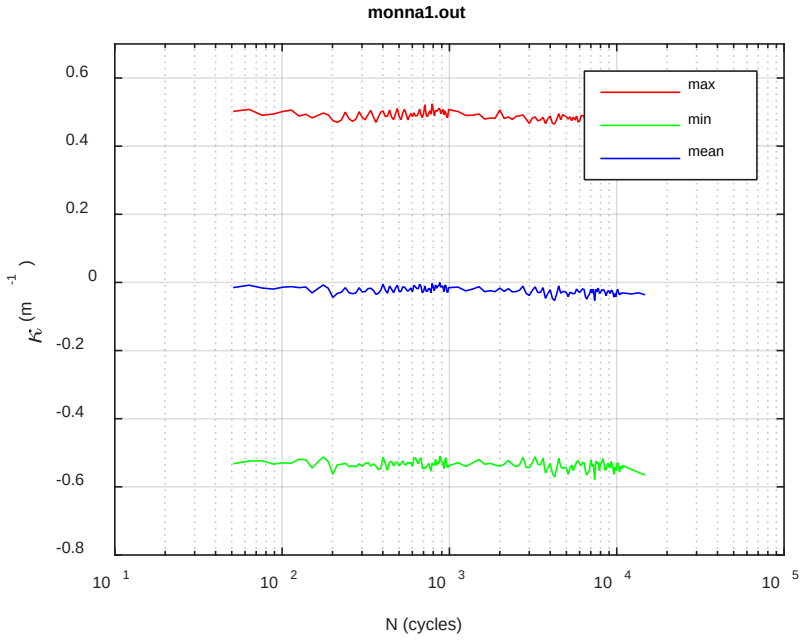
monna1.out
max
min
mean
0.6
0.4
0.2
0
-0.2
-0.4
-0.6
-0.8
κ (m -1)
10 1
10 2
10 3
10 4
10 5
N (cycles)

(d)

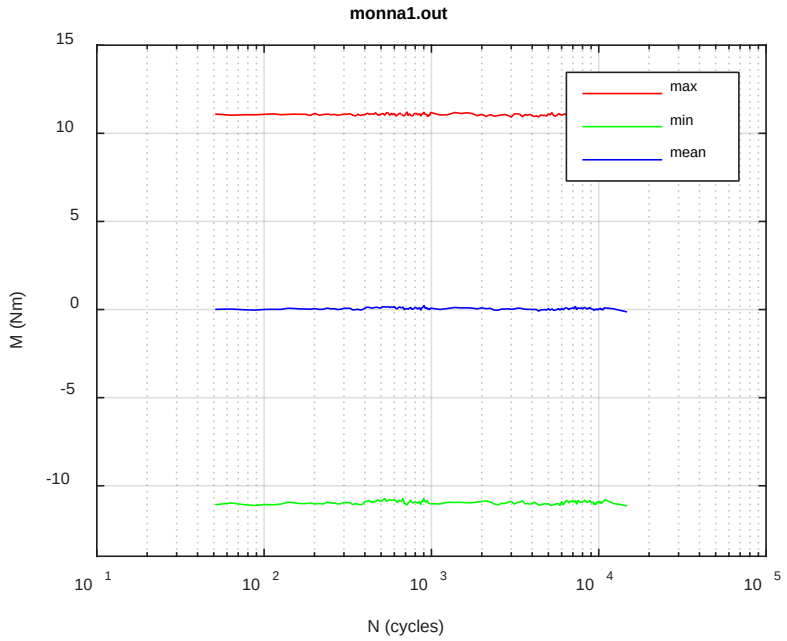

(e)

Fig. B.3. Monitoring-based responses: (a) curvature range, (b) moment range, (c) rigidity, (d) curvature peak/valley, (e) moment peak/valley, NA1, 12.70 Nm, Nf = 1.57E+04 cycles.

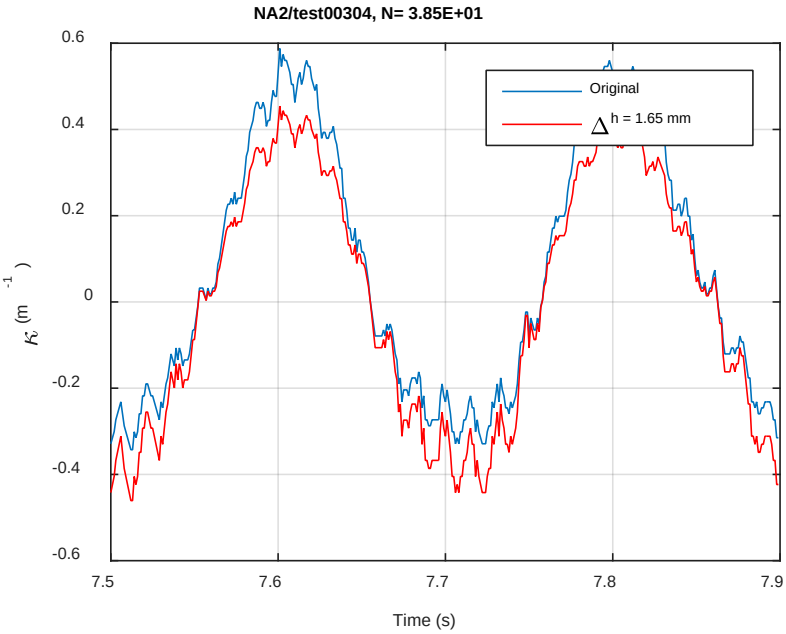
NA2/test00304, N= 3.85E+01
Original
Δh = 1.65 mm
κ (m-1)
Time (s)

(a)

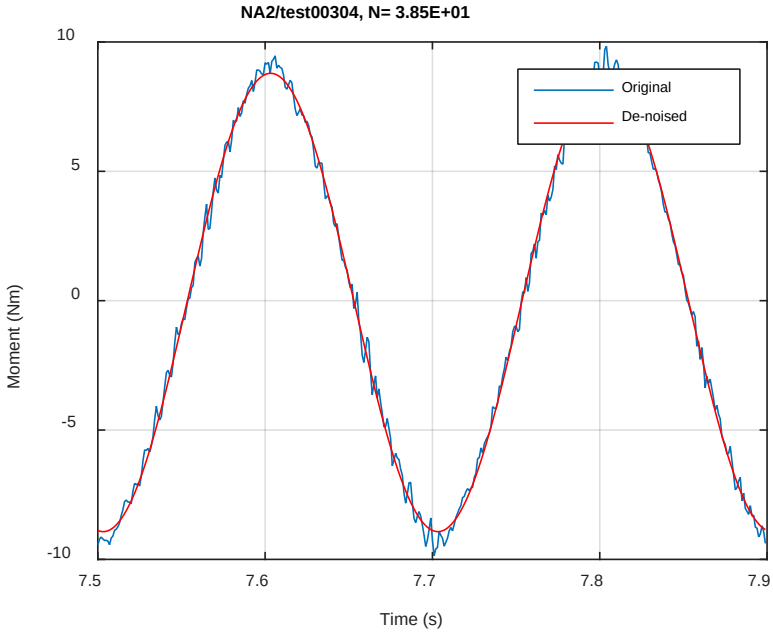
NA2/test00304, N= 3.85E+01
Original
De-noised
Moment (Nm)
Time (s)

(b)

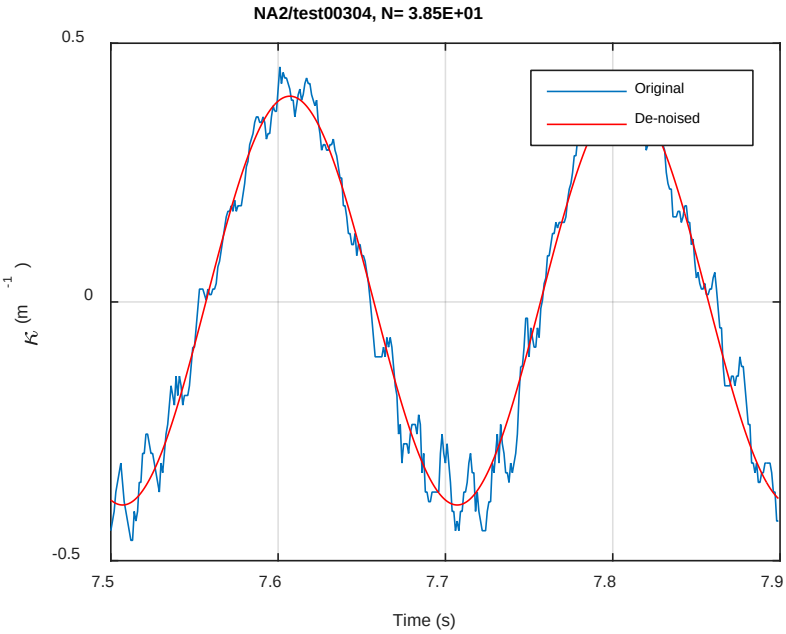

(c)

Fig. B.4. Monitoring-based responses: (a) curvature, (b) moment, (c) curvature, NA2, 10.16 Nm, Ns = 3.85E+01 cycles.

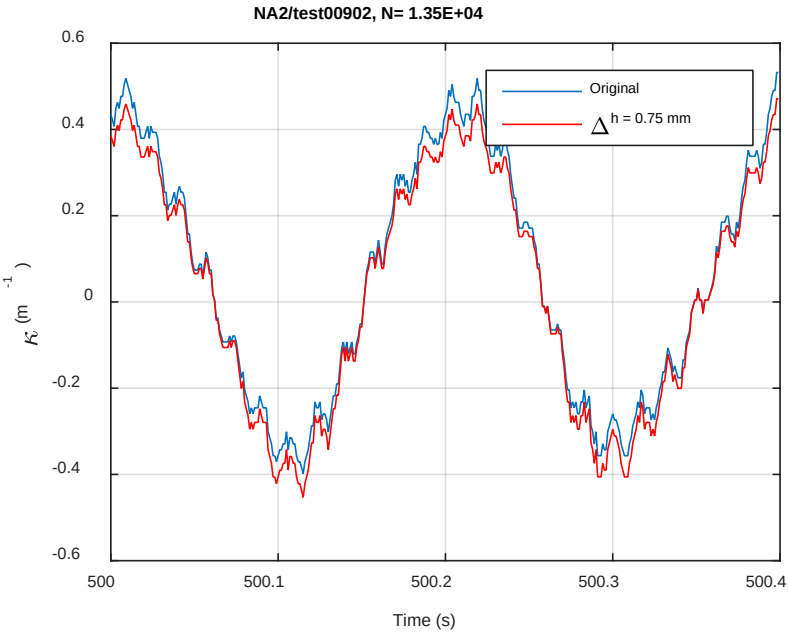
NA2/test00902, N= 1.35E+04
Original
Δh = 0.75 mm
κ (m-1)
Time (s)

(a)

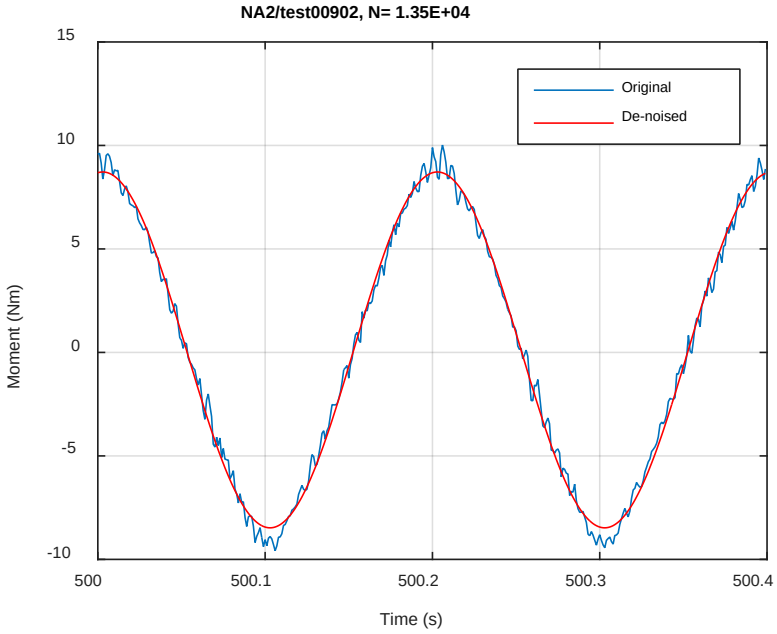
NA2/test00902, N= 1.35E+04
Original
De-noised
Moment (Nm)
Time (s)

(b)

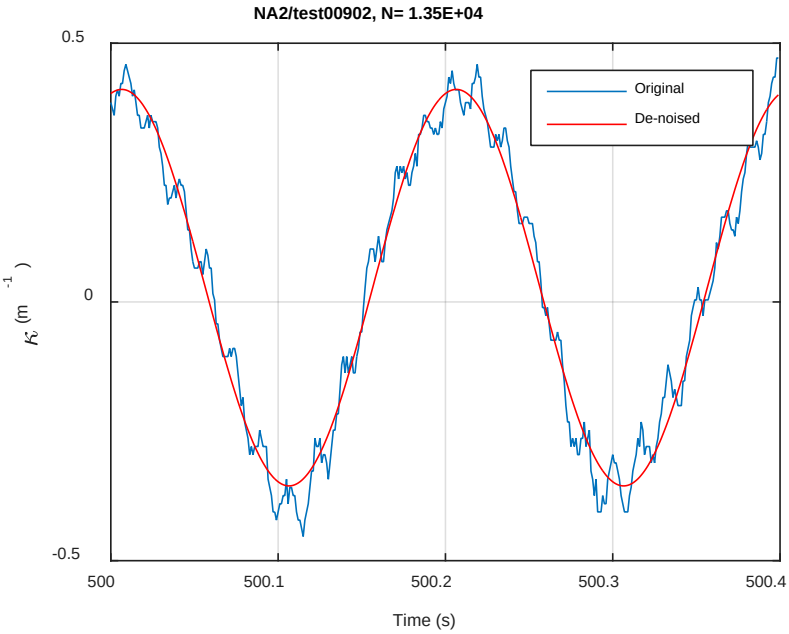

(c)

Fig. B.5. Monitoring-based responses: (a) curvature, (b) moment, (c) curvature, NA2, 10.16 Nm, Ns = 1.35E+04 cycles.

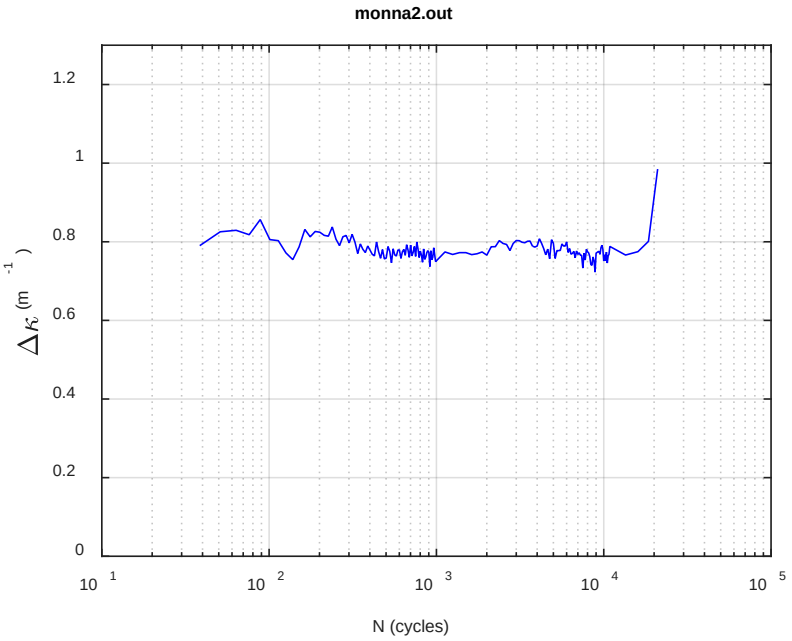
monna2.out
1.2
1
0.8
0.6
0.4
0.2
0
Δκ (m-1)
10 1
10 2
10 3
10 4
10 5
N (cycles)

(a)

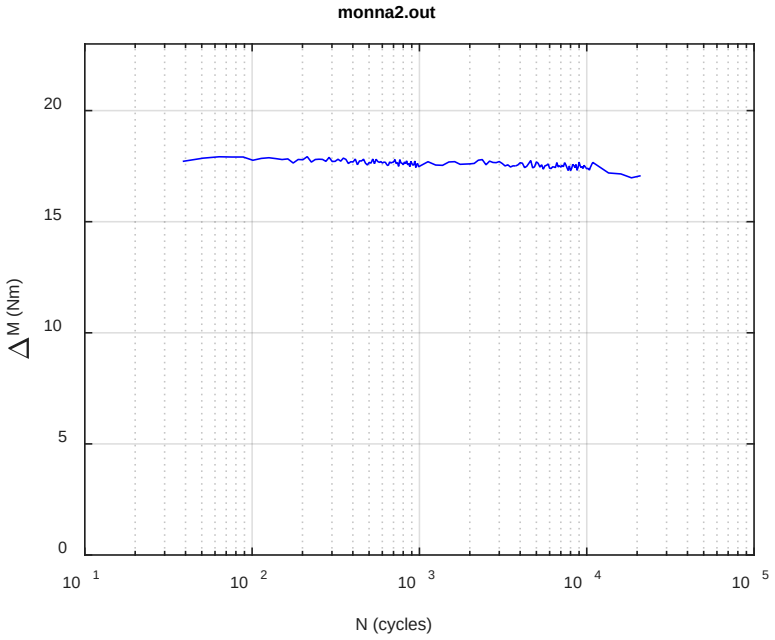
monna2.out
20
15
10
5
0
ΔM (Nm)
10 1
10 2
10 3
10 4
10 5
N (cycles)

(b)

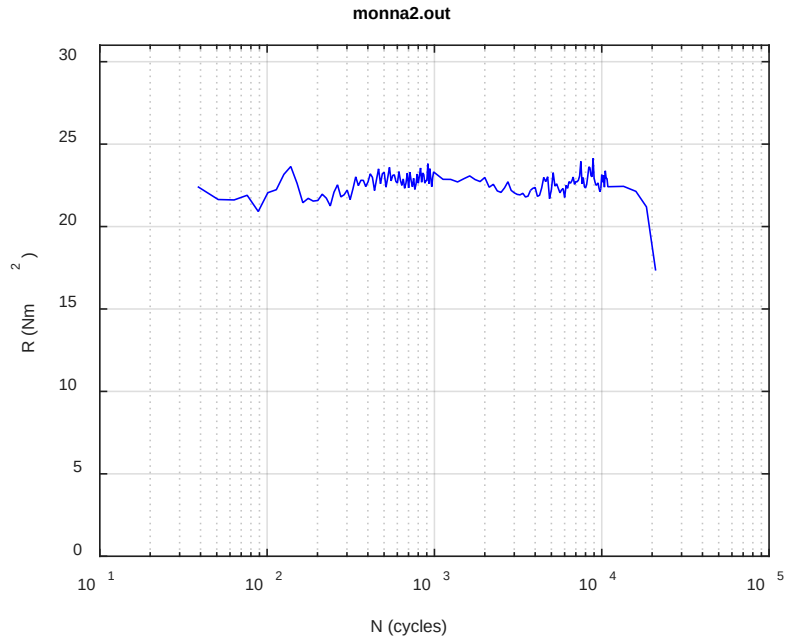

(c)

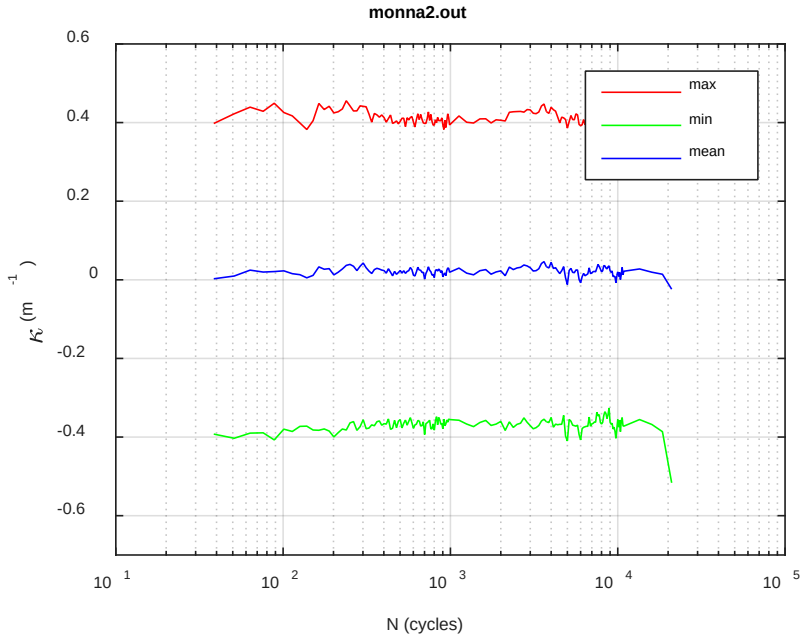

(d)

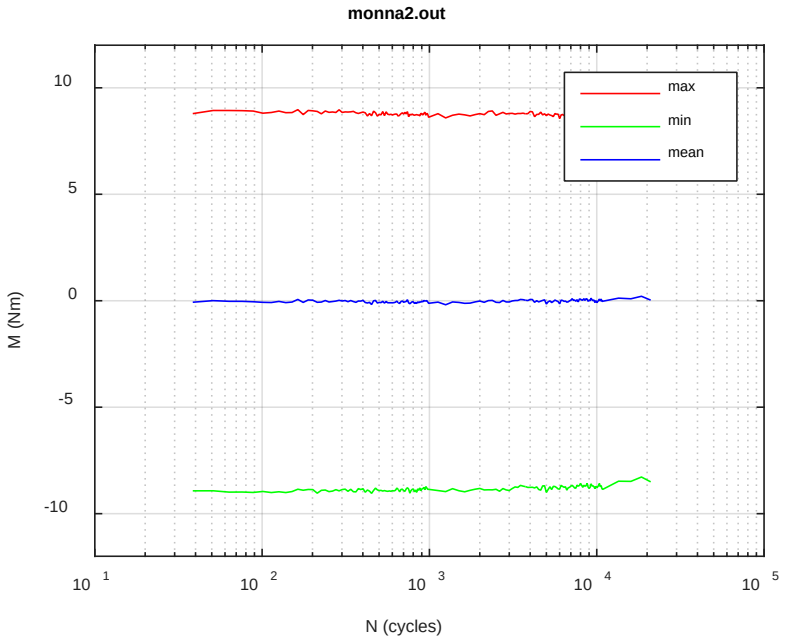

(e)

Fig. B.6. Monitoring-based responses: (a) curvature range, (b) moment range, (c) rigidity, (d) curvature peak/valley, (e) moment peak/valley, NA2, 10.16 Nm, Nf = 2.20E+04 cycles.

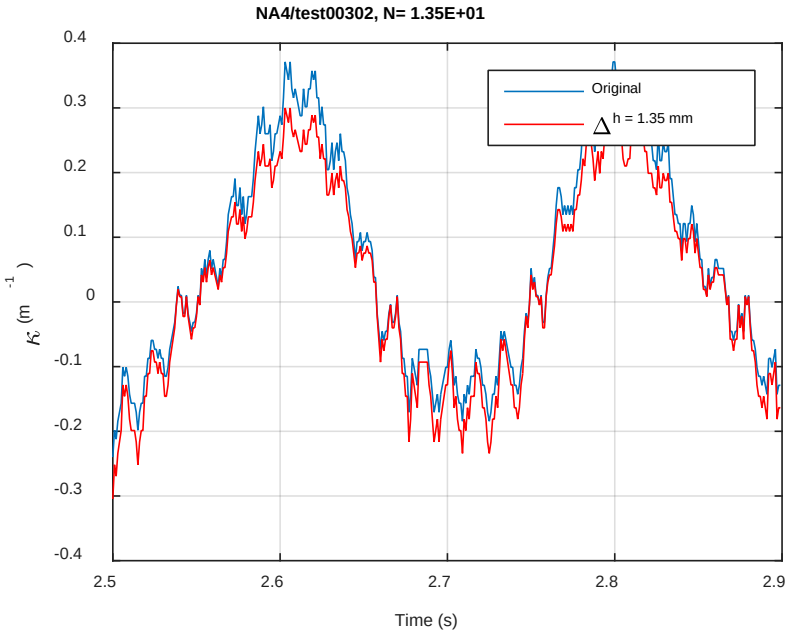
NA4/test00302, N= 1.35E+01
Original
Δh = 1.35 mm
κ (m-1)
Time (s)

(a)

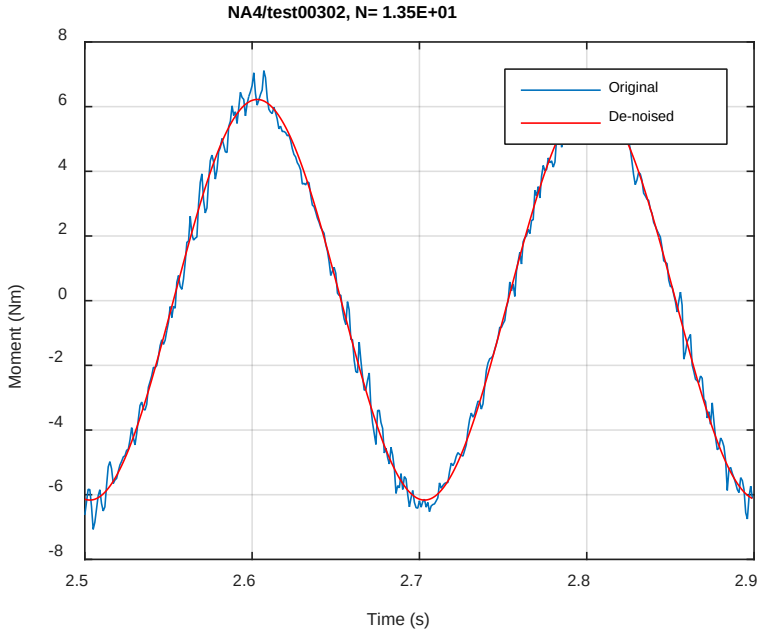
NA4/test00302, N= 1.35E+01
Original
De-noised
Moment (Nm)
Time (s)

(b)

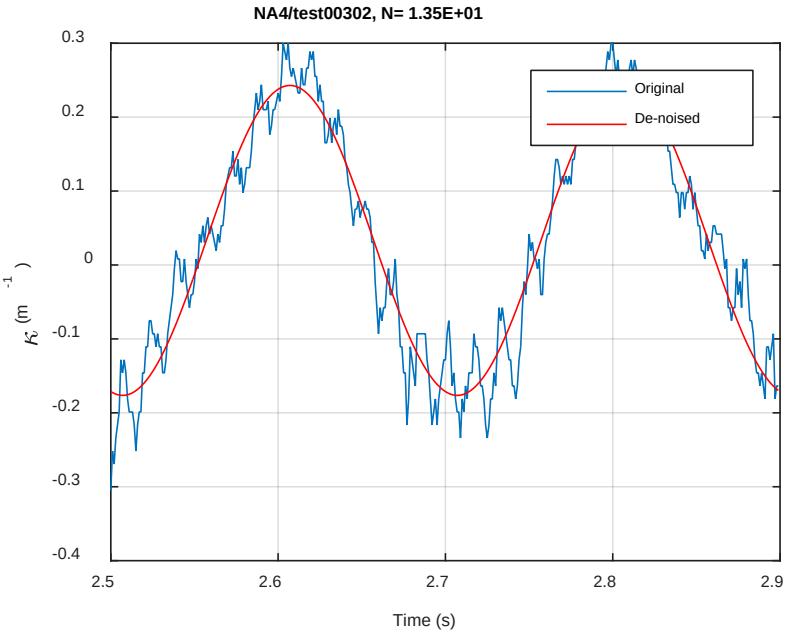

(c)

Fig. B.7. Monitoring-based responses: (a) curvature, (b) moment, (c) curvature, NA4, 7.62 Nm, Ns = 1.35E+01 cycles.

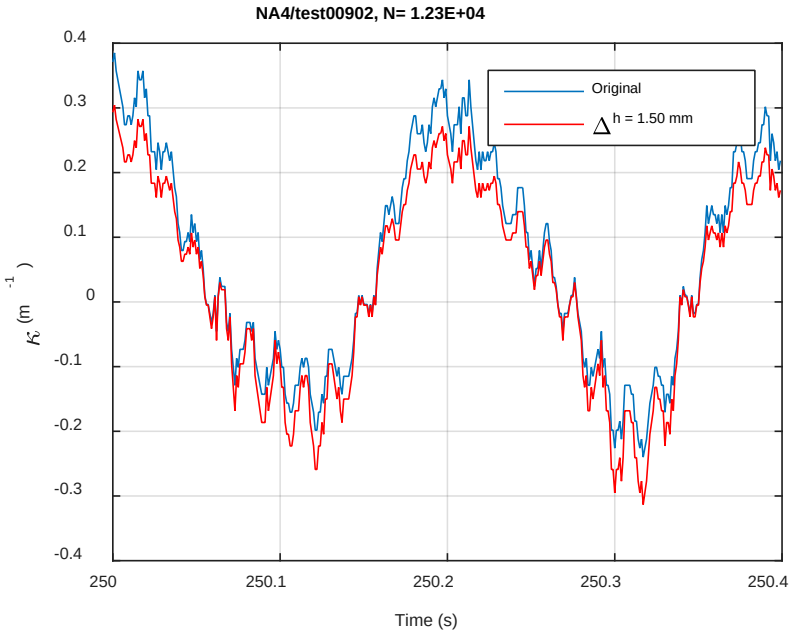
NA4/test00902, N= 1.23E+04
Original
Δh = 1.50 mm
κ (m-1)
Time (s)

(a)

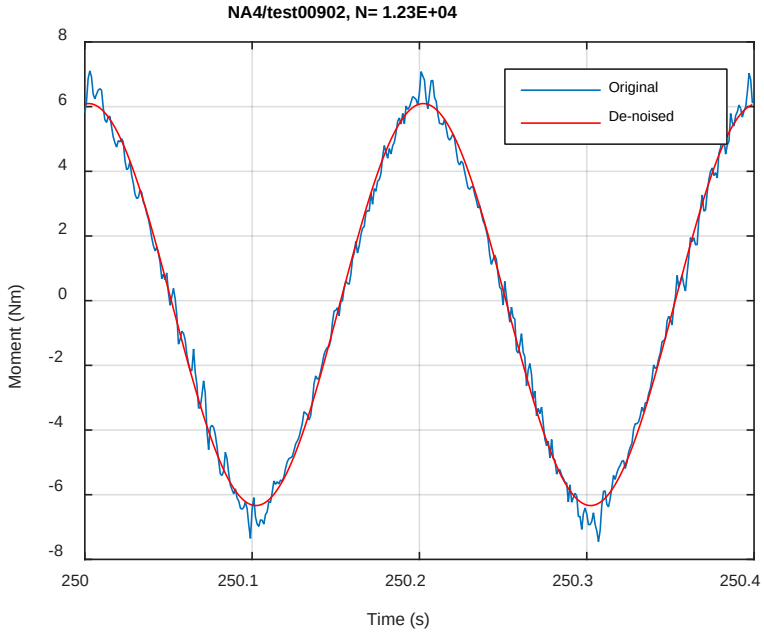
NA4/test00902, N= 1.23E+04
Original
De-noised
Moment (Nm)
Time (s)

(b)

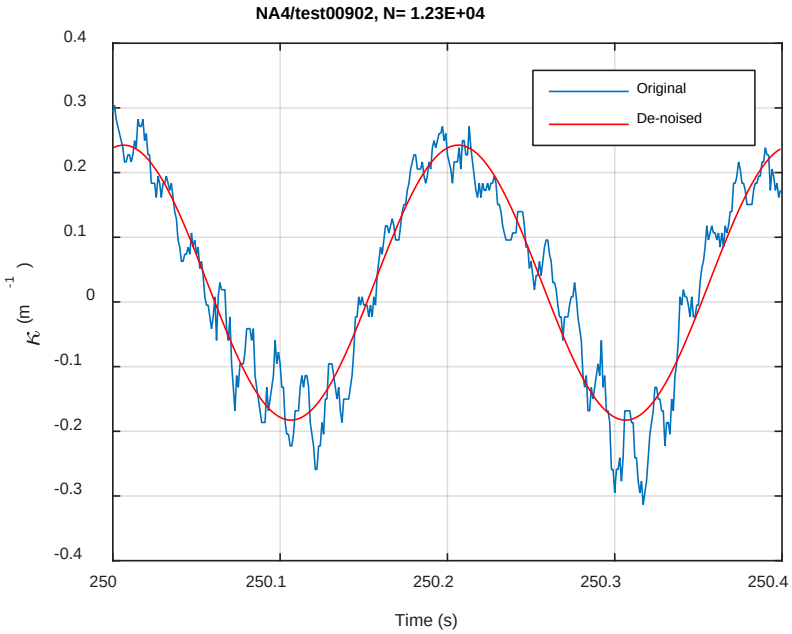

(c)

Fig. B.8. Monitoring-based responses: (a) curvature, (b) moment, (c) curvature, NA4, 7.62 Nm, Ns = 1.23E+04 cycles.

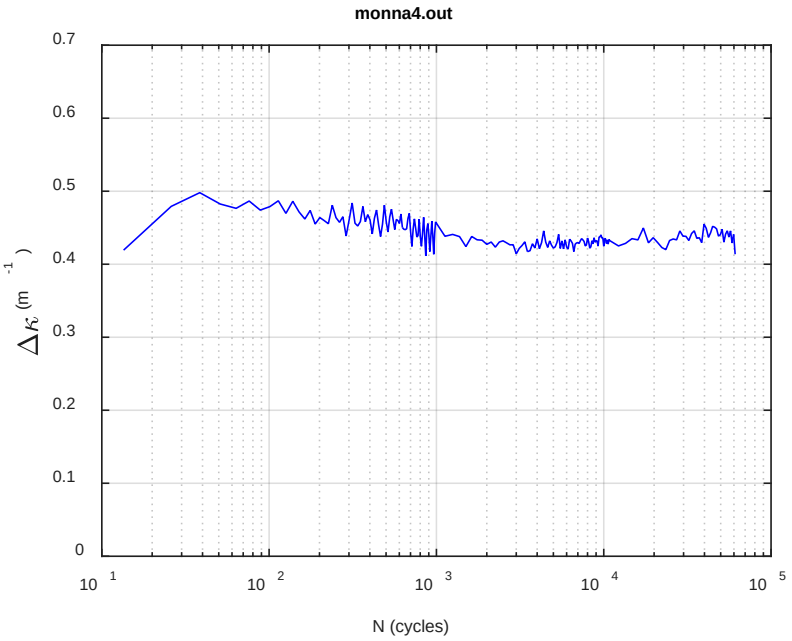
monna4.out
0.7
0.6
0.5
0.4
0.3
0.2
0.1
0
Δκ (m-1)
10 1
10 2
10 3
10 4
10 5
N (cycles)

(a)

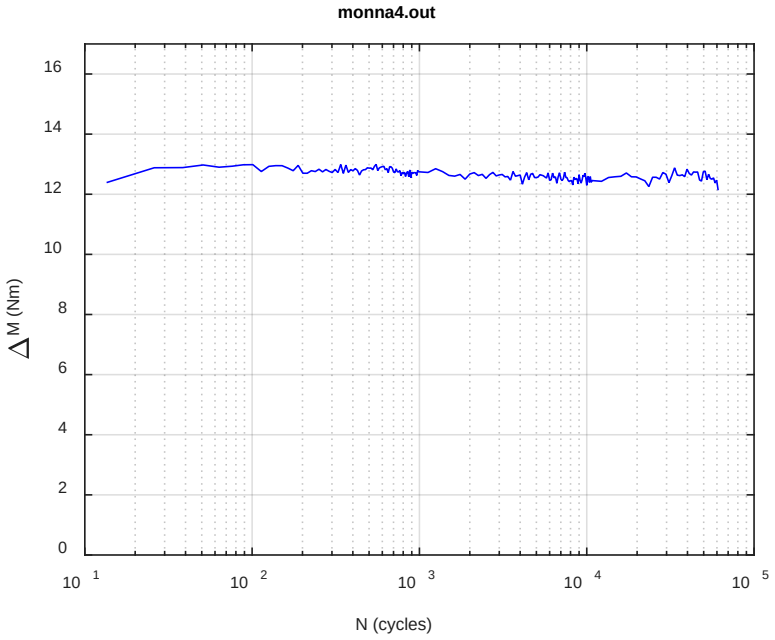
monna4.out
16
14
12
10
8
6
4
2
0
Δ M (Nm)
10 1
10 2
10 3
10 4
10 5
N (cycles)

(b)

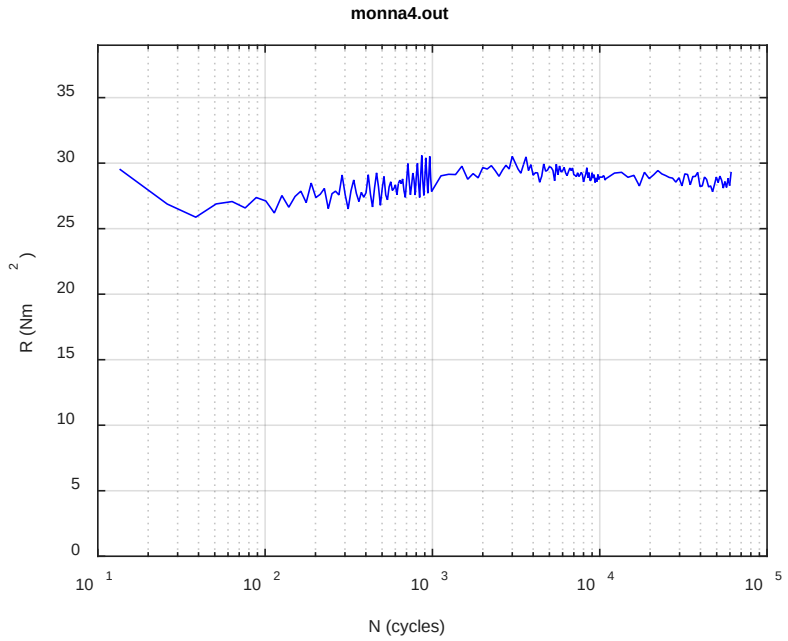

(c)

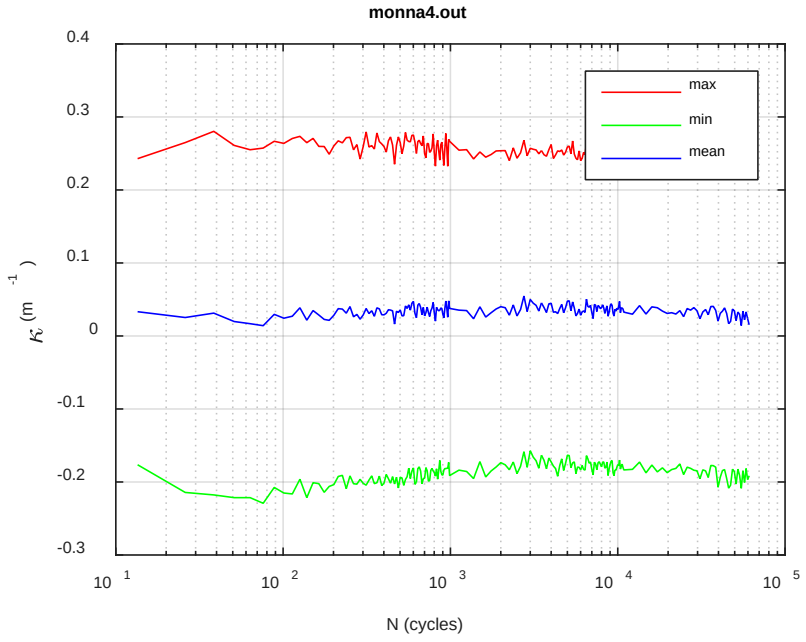

(d)

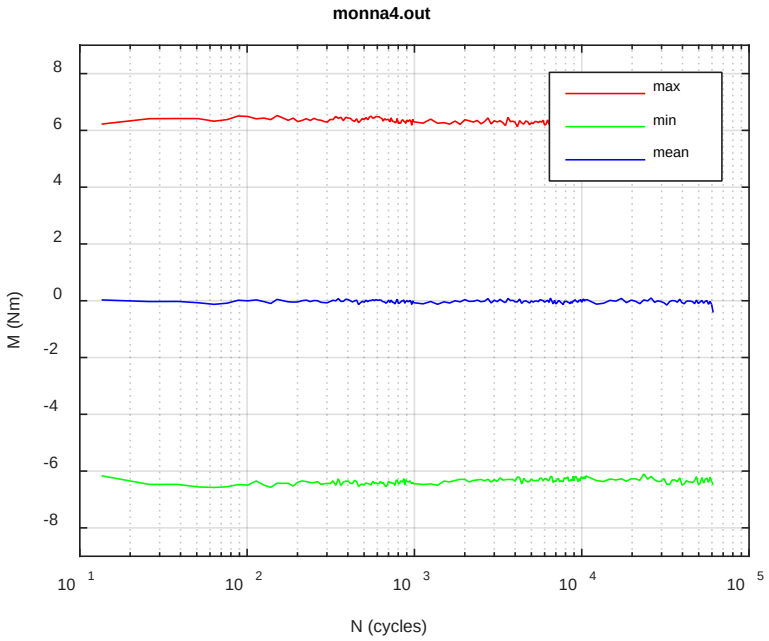

(e)

Fig. B.9. Monitoring-based responses: (a) curvature range, (b) moment range, (c) rigidity, (d) curvature peak/valley, (e) moment peak/valley, NA4, 7.62 Nm, Nf = 6.10E+04 cycles.

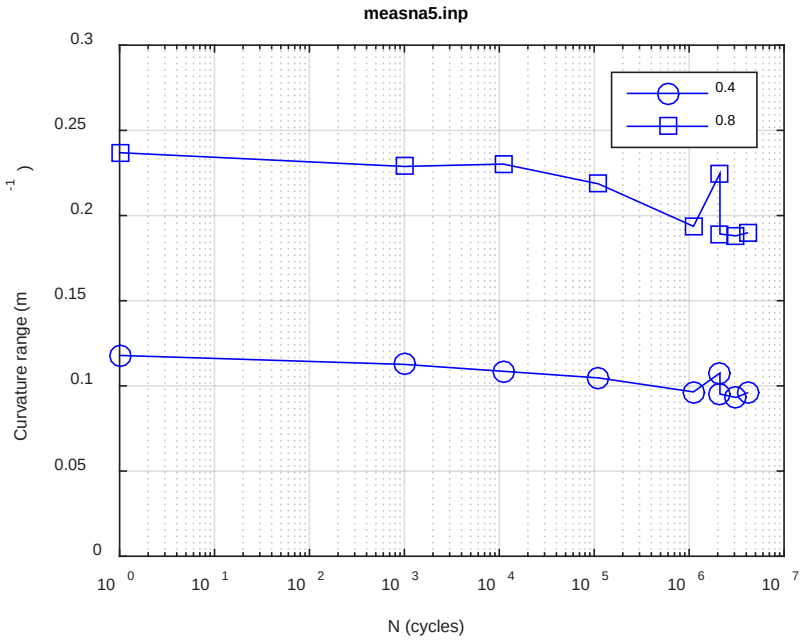
measna5.inp
0.4
0.8
Curvature range (m -1)
N (cycles)

(a)

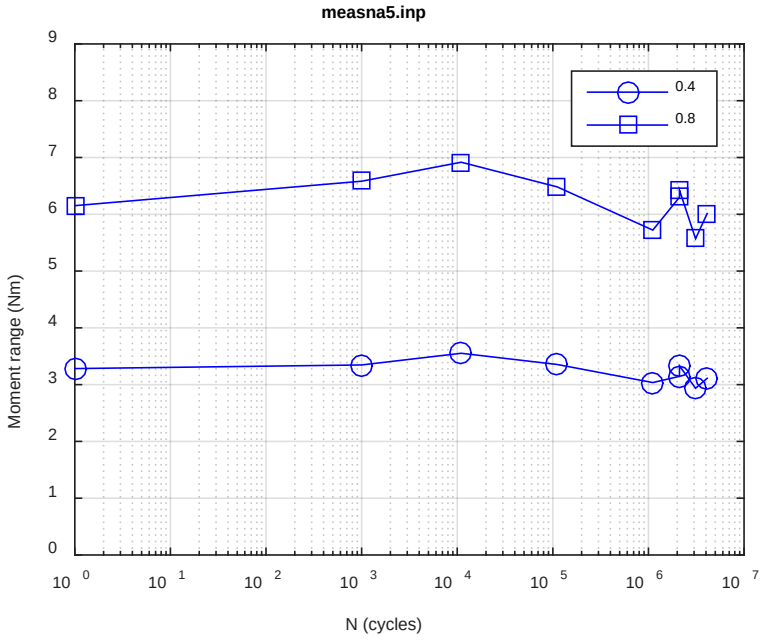
measna5.inp
0.4
0.8
Moment range (Nm)
N (cycles)

(b)

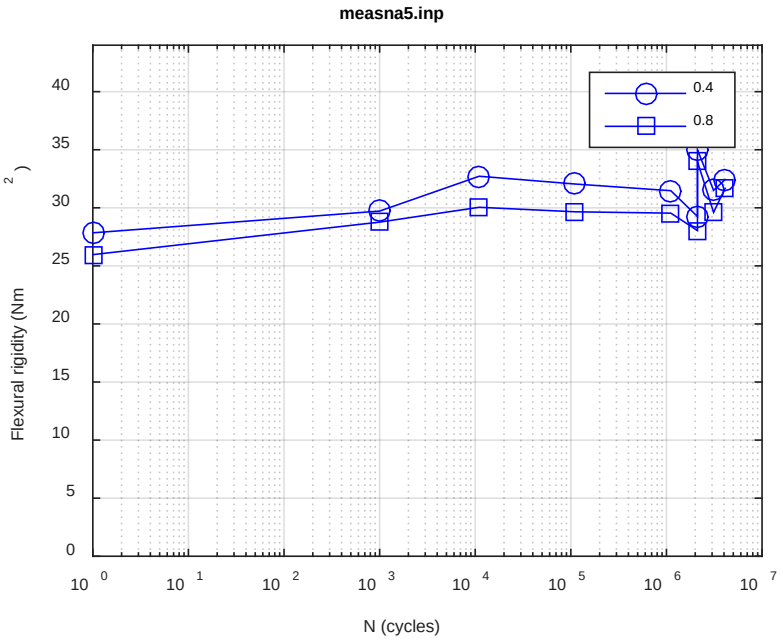
measna5.inp
0.4
0.8
Flexural rigidity (Nm 2)
N (cycles)

(c)

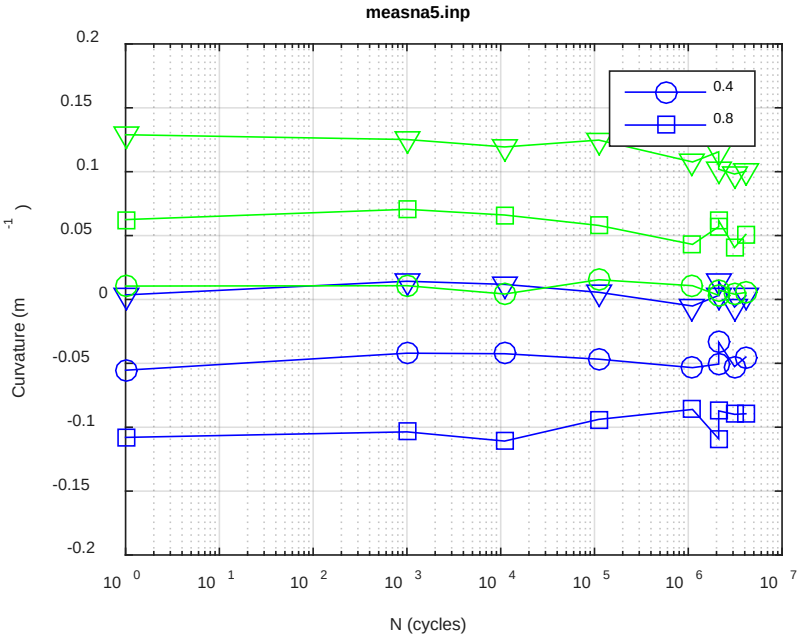
measna5.inp
0.4
0.8
Curvature (m -1)
N (cycles)

(d)

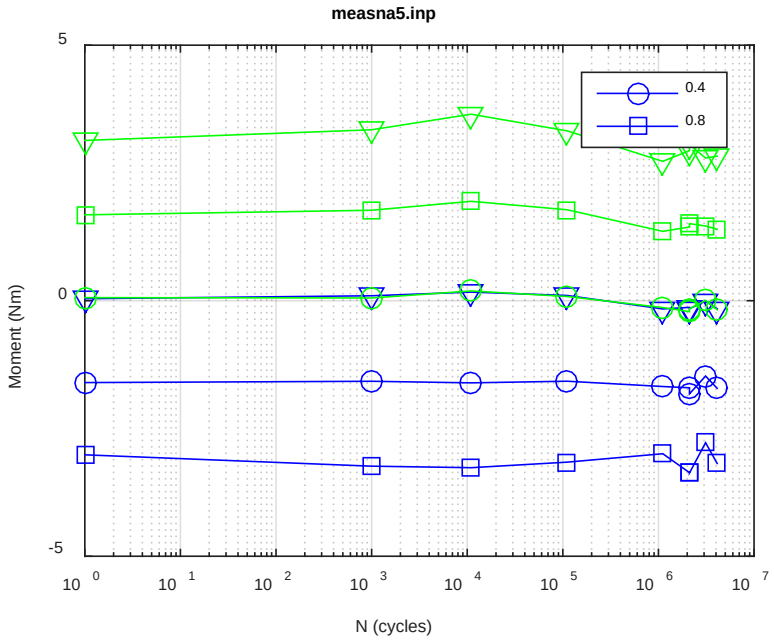

(e)

Fig. B.10. Measurement-based responses: (a) curvature range, (b) moment range, (c) rigidity, (d) curvature peak/valley, (e) moment peak/valley, NA5, 5.08 Nm.

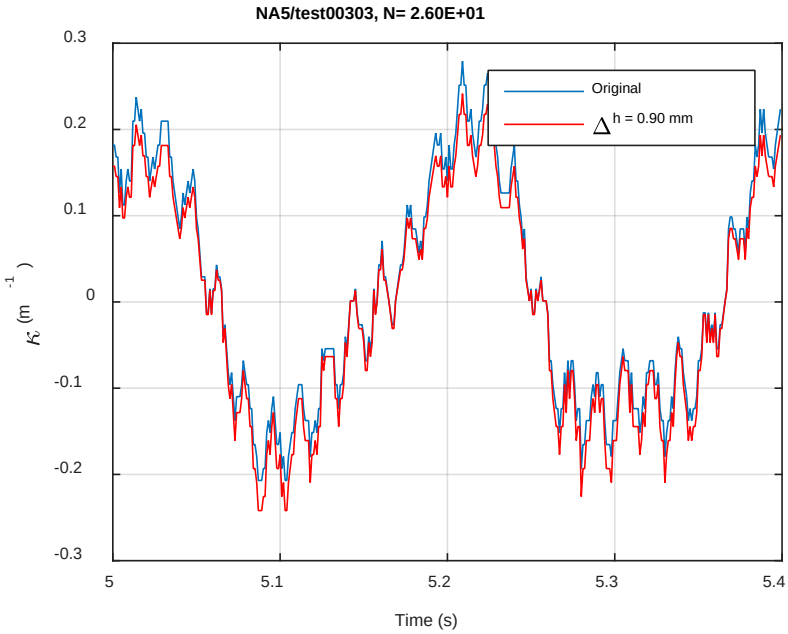
NA5/test00303, N= 2.60E+01
Original
Δh = 0.90 mm
κ (m-1)
Time (s)

(a)

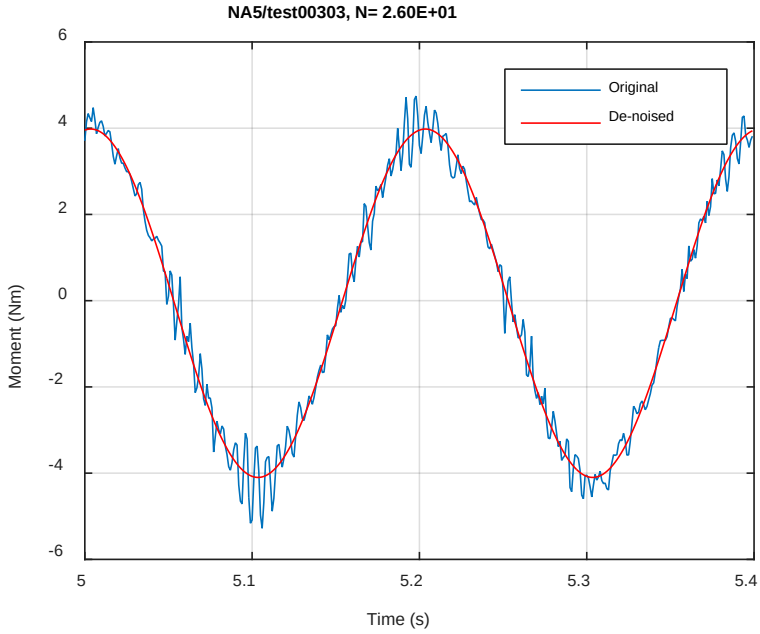
NA5/test00303, N= 2.60E+01
Original
De-noised
Moment (Nm)
Time (s)

(b)

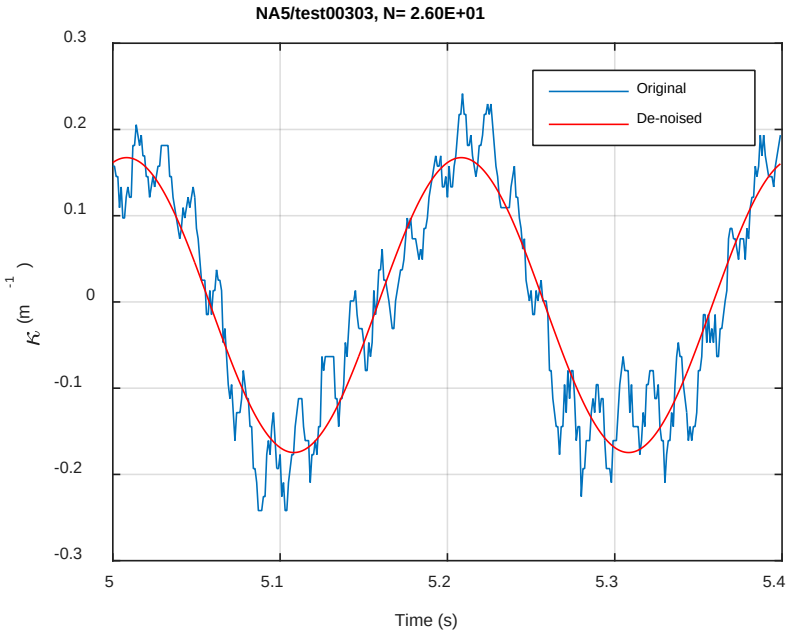

(c)

Fig. B.11. Monitoring-based responses: (a) curvature, (b) moment, (c) curvature, NA5, 5.08 Nm, Ns = 2.60E+01 cycles.

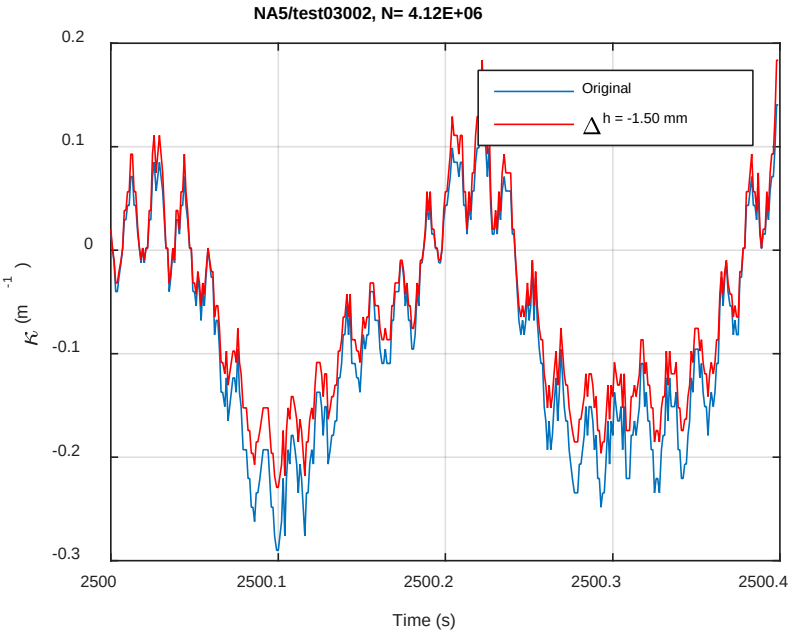
NA5/test03002, N= 4.12E+06
Original
Δh = -1.50 mm
κ (m-1)
Time (s)
0.2
0.1
0
-0.1
-0.2
-0.3
2500
2500.1
2500.2
2500.3
2500.4

(a)

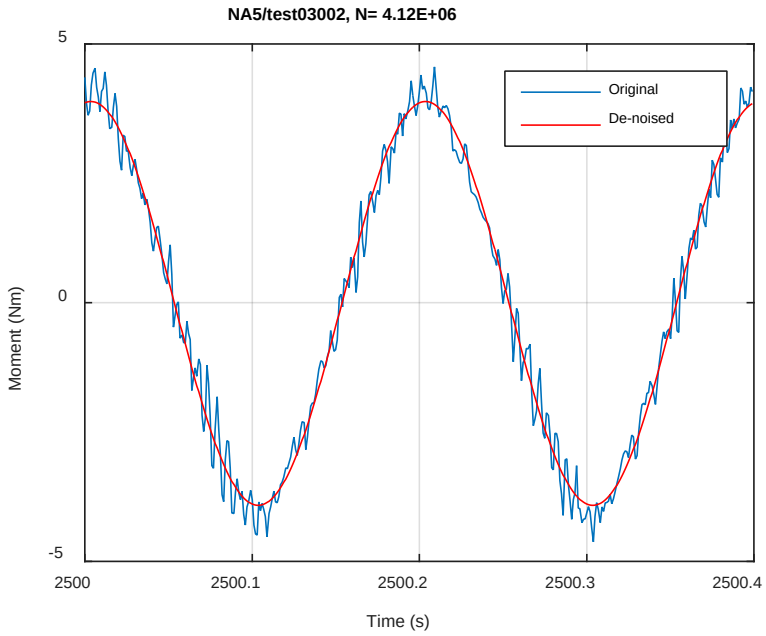
NA5/test03002, N= 4.12E+06
Original
De-noised
Moment (Nm)
Time (s)
5
0
-5
2500
2500.1
2500.2
2500.3
2500.4

(b)

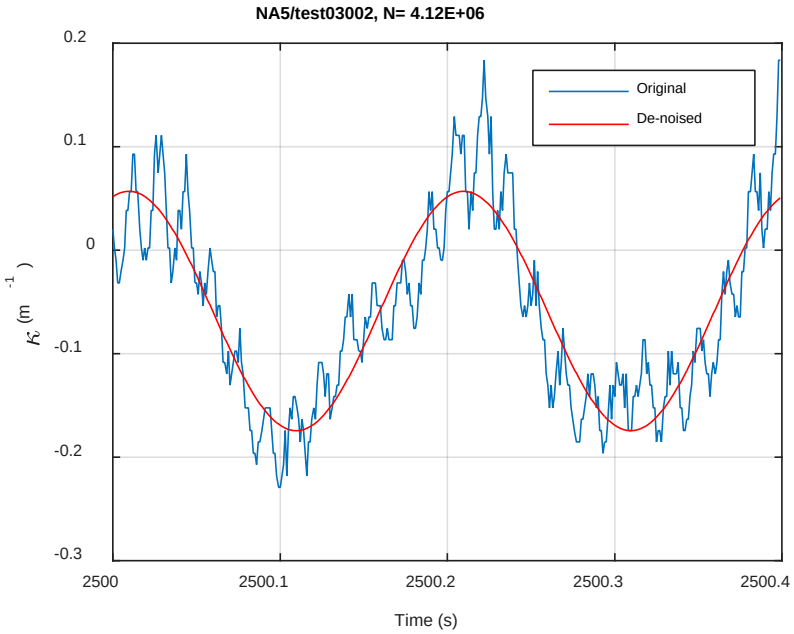

(c)

Fig. B.12. Monitoring-based responses: (a) curvature, (b) moment, (c) curvature, NA5, 5.08 Nm, Ns = 4.12E+06 cycles.

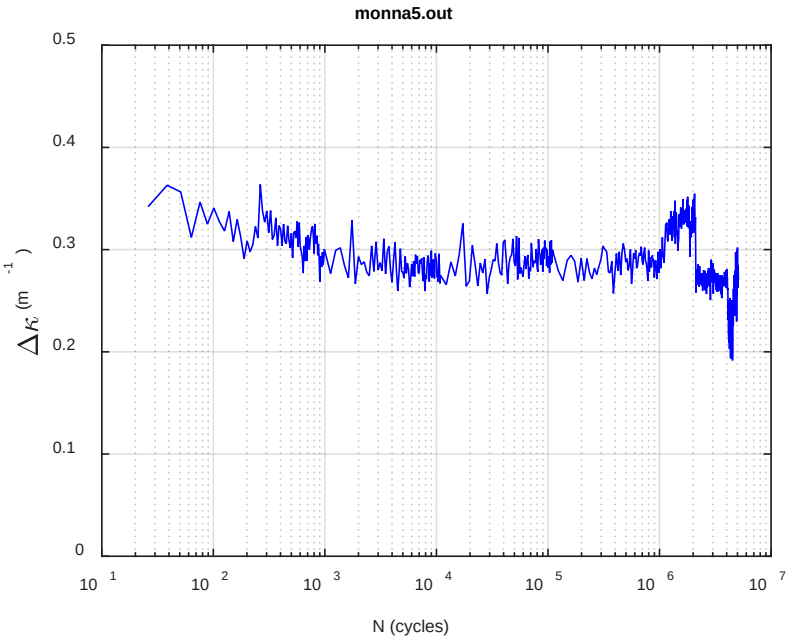
monna5.out
0.5
0.4
0.3
0.2
0.1
0
Δκ (m -1)
10 1
10 2
10 3
10 4
10 5
10 6
10 7
N (cycles)

(a)

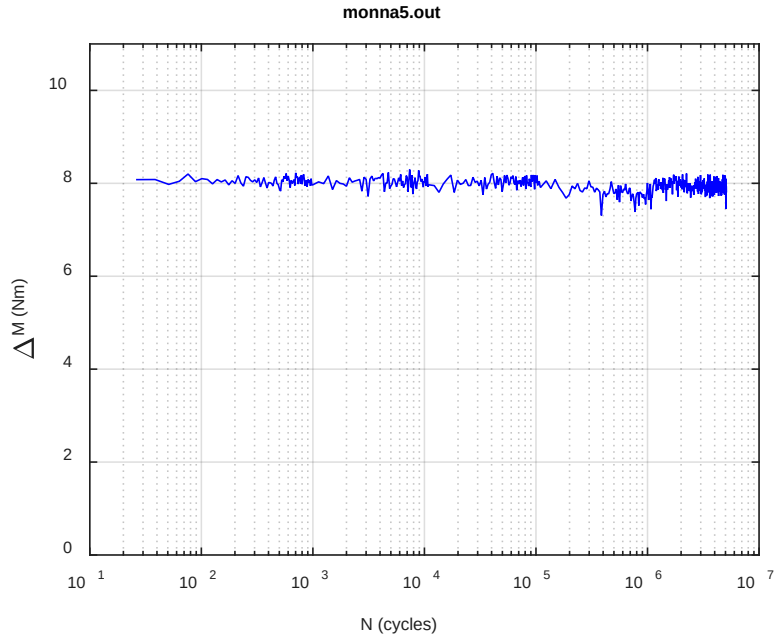
monna5.out
10
8
6
4
2
0
Δ M (Nm)
10 1
10 2
10 3
10 4
10 5
10 6
10 7
N (cycles)

(b)

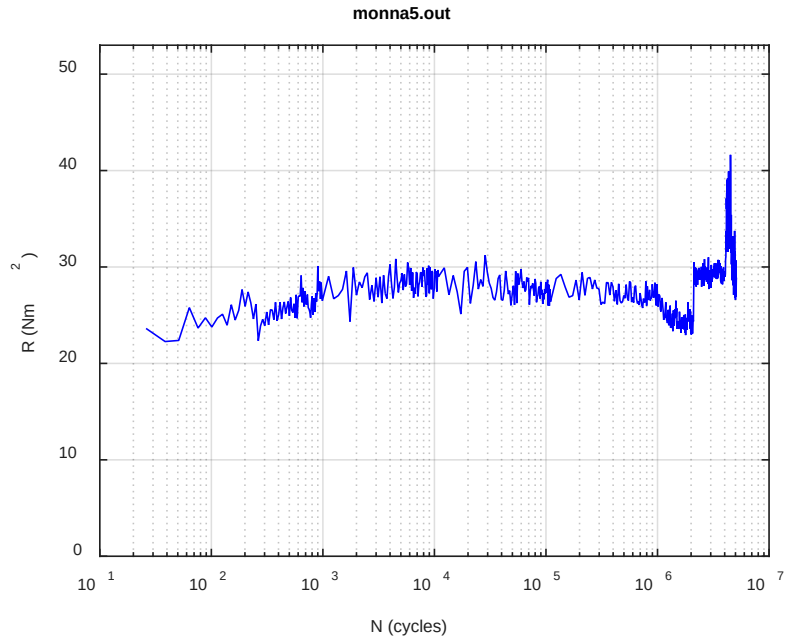
monna5.out
R (Nm^2)
N (cycles)
0
10
20
30
40
50
10^1
10^2
10^3
10^4
10^5
10^6
10^7

(c)

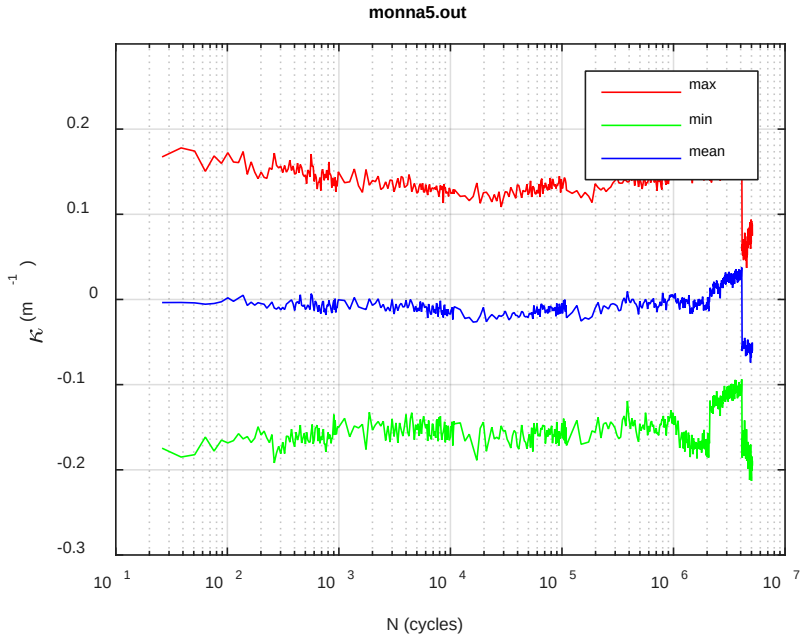
monna5.out
max
min
mean
κ (m^-1)
N (cycles)
0.2
0.1
0
-0.1
-0.2
-0.3
10^1
10^2
10^3
10^4
10^5
10^6
10^7

(d)

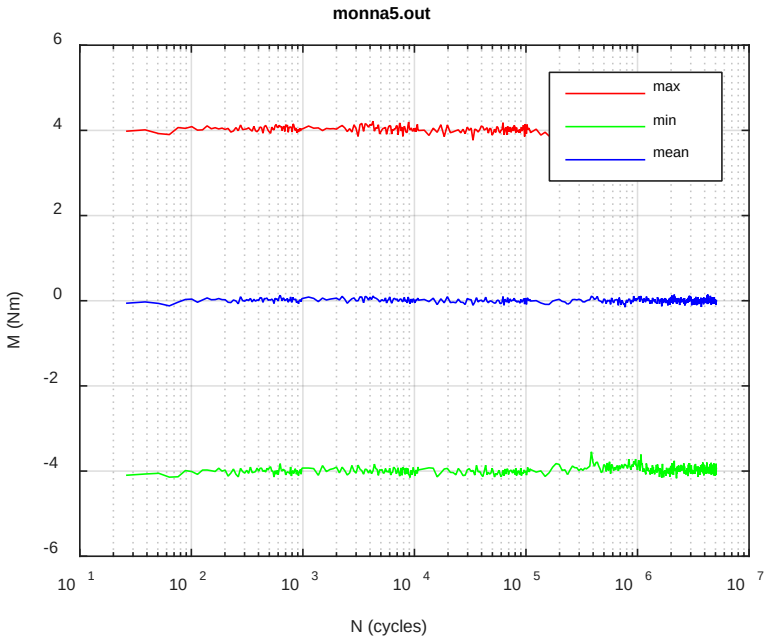

(e)

Fig. B.13. Monitoring-based responses: (a) curvature range, (b) moment range, (c) rigidity, (d) curvature peak/valley, (e) moment peak/valley, NA5, 5.08 Nm, Nf = 5.11E+06 cycles.

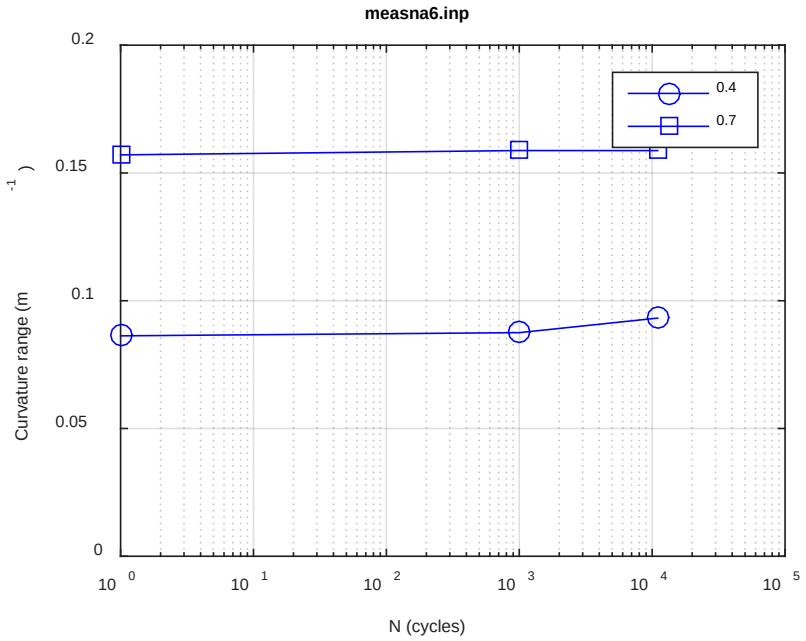
measna6.inp
0.2
0.15
0.1
0.05
0
Curvature range (m -1)
0.4
0.7
10 0
10 1
10 2
10 3
10 4
10 5
N (cycles)

(a)

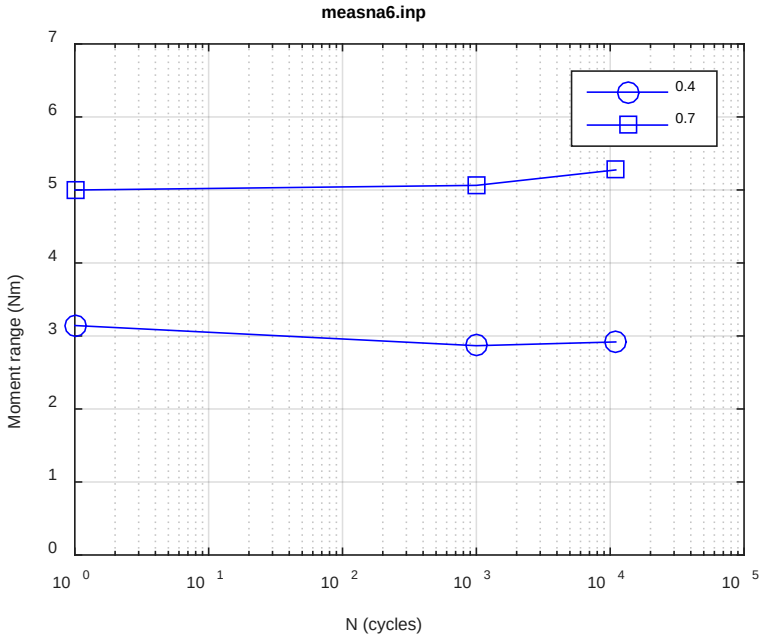
measna6.inp
7
6
5
4
3
2
1
0
Moment range (Nm)
0.4
0.7
10 0
10 1
10 2
10 3
10 4
10 5
N (cycles)

(b)

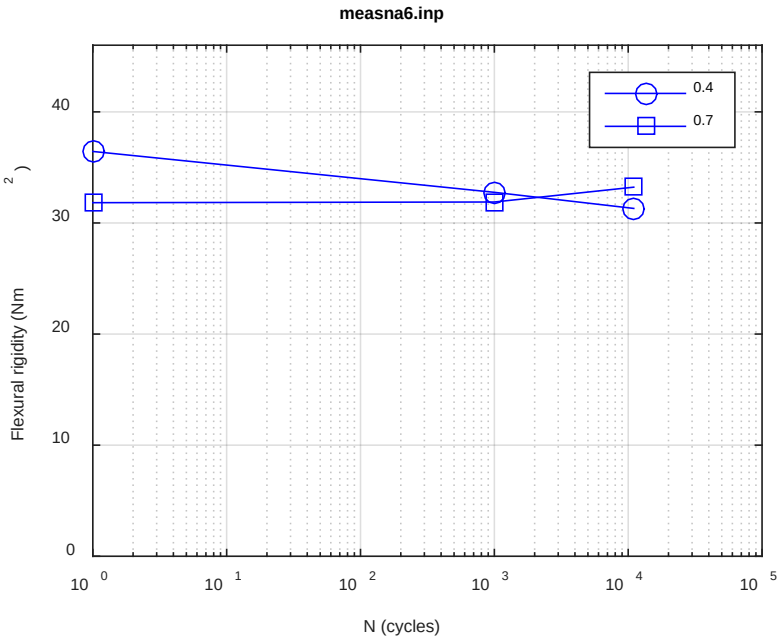
measna6.inp
0.4
0.7
Flexural rigidity (Nm 2)
40
30
20
10
0
10 0
10 1
10 2
10 3
10 4
10 5
N (cycles)

(c)

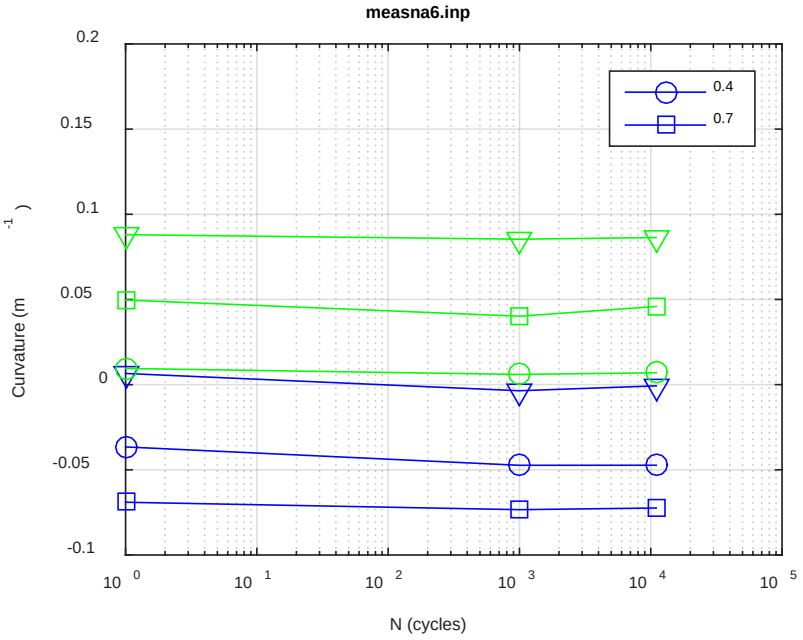
measna6.inp
0.4
0.7
Curvature (m -1)
0.2
0.15
0.1
0.05
0
-0.05
-0.1
10 0
10 1
10 2
10 3
10 4
10 5
N (cycles)

(d)

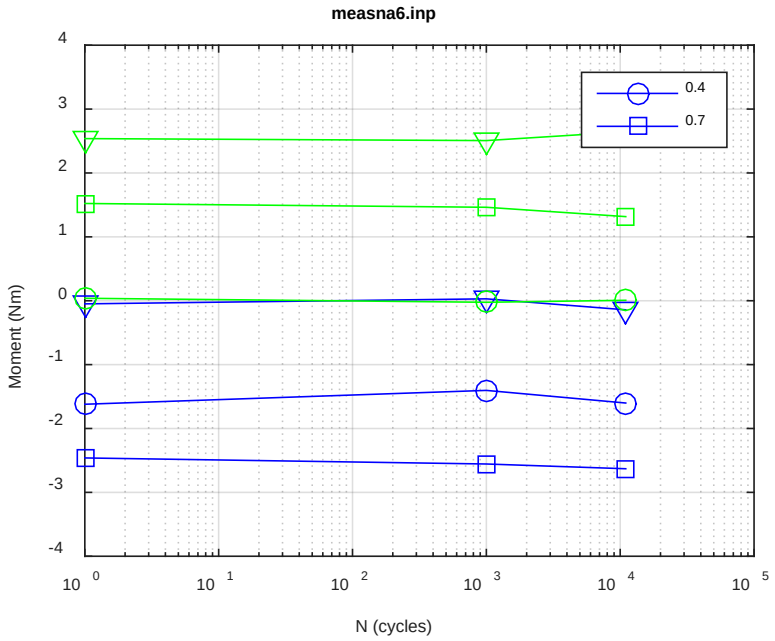

(e)

Fig. B.14. Measurement-based responses: (a) curvature range, (b) moment range, (c) rigidity, (d) curvature peak/valley, (e) moment peak/valley, NA6, 5.08 Nm.

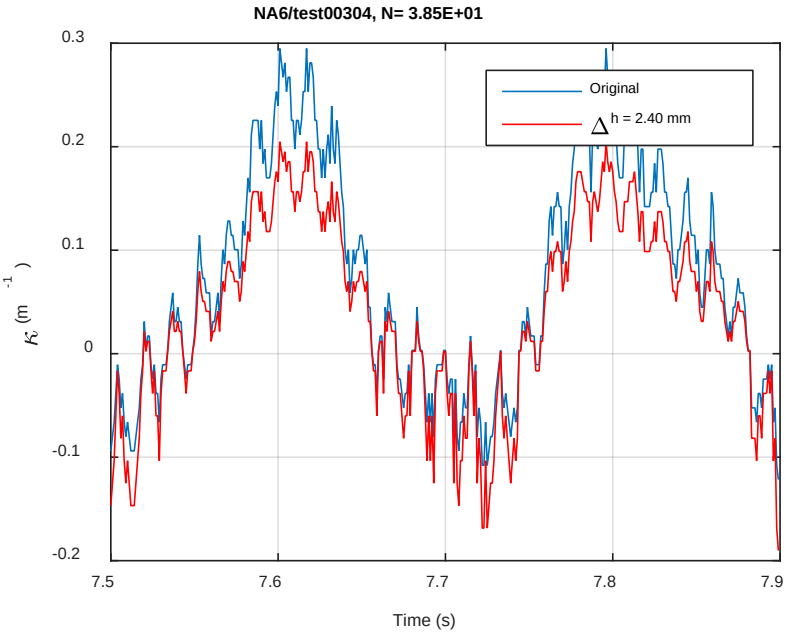
NA6/test00304, N= 3.85E+01
Original
Δh = 2.40 mm
κ (m-1)
Time (s)

(a)

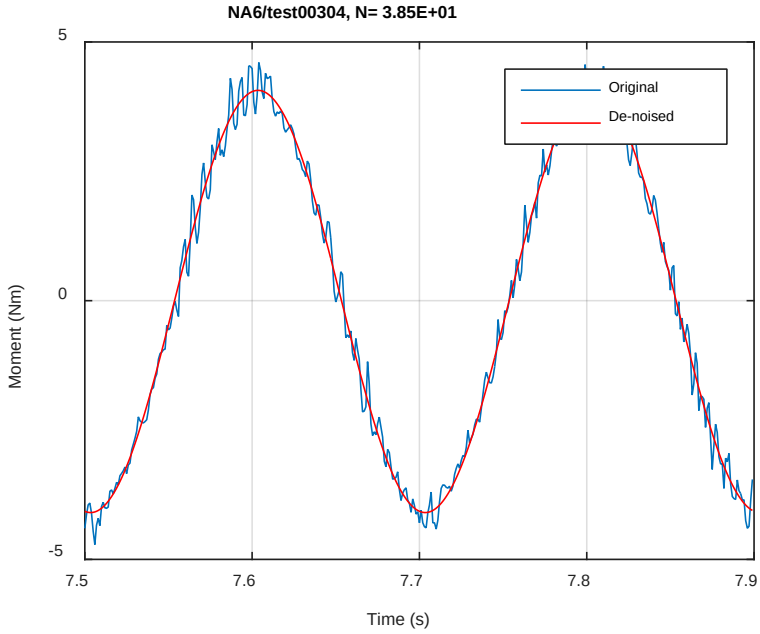
NA6/test00304, N= 3.85E+01
Original
De-noised
Moment (Nm)
Time (s)

(b)

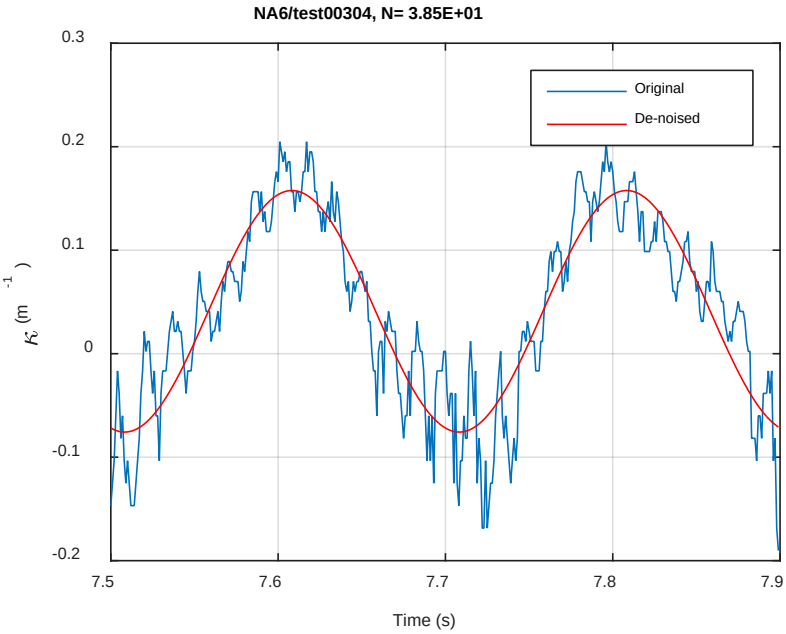

(c)

Fig. B.15. Monitoring-based responses: (a) curvature, (b) moment, (c) curvature, NA6, 5.08 Nm, Ns = 3.85E+01 cycles.

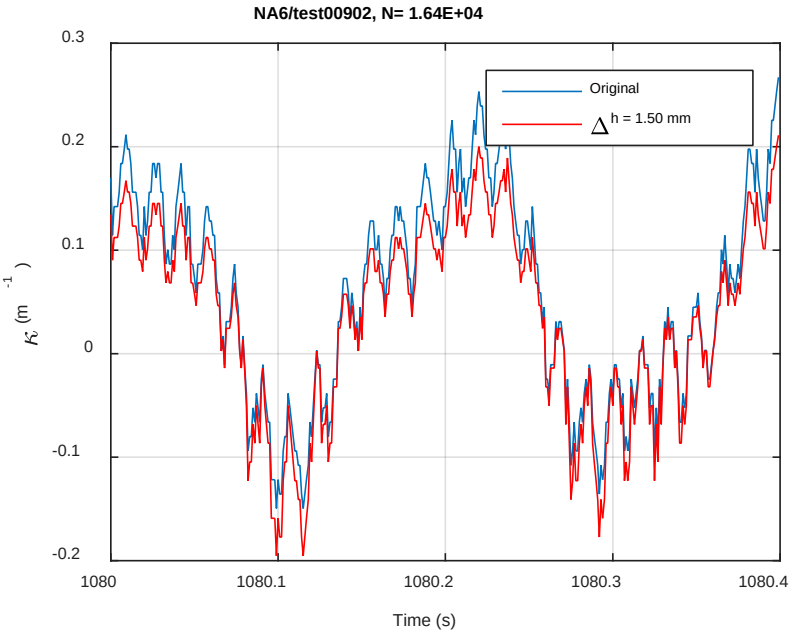
NA6/test00902, N= 1.64E+04
Original
Δh = 1.50 mm
κ (m-1)
Time (s)
0.3
0.2
0.1
0
-0.1
-0.2
1080
1080.1
1080.2
1080.3
1080.4

(a)

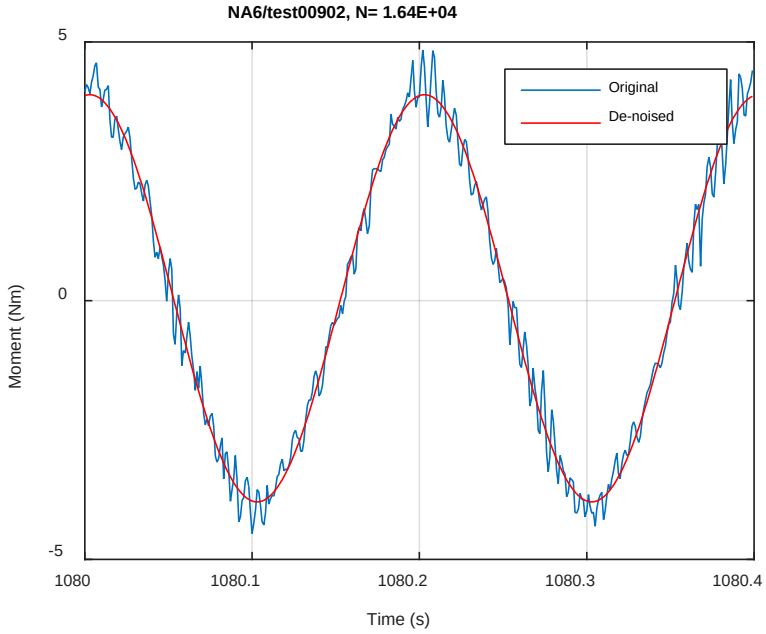
NA6/test00902, N= 1.64E+04
Original
De-noised
Moment (Nm)
Time (s)
5
0
-5
1080
1080.1
1080.2
1080.3
1080.4

(b)

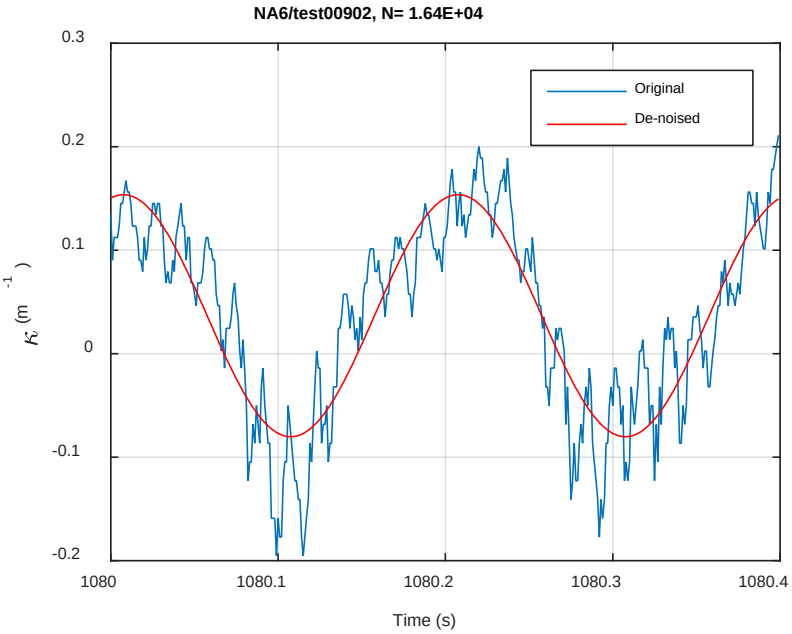

(c)

Fig. B.16. Monitoring-based responses: (a) curvature, (b) moment, (c) curvature, NA6, 5.08 Nm, Ns = 1.64E+04 cycles.

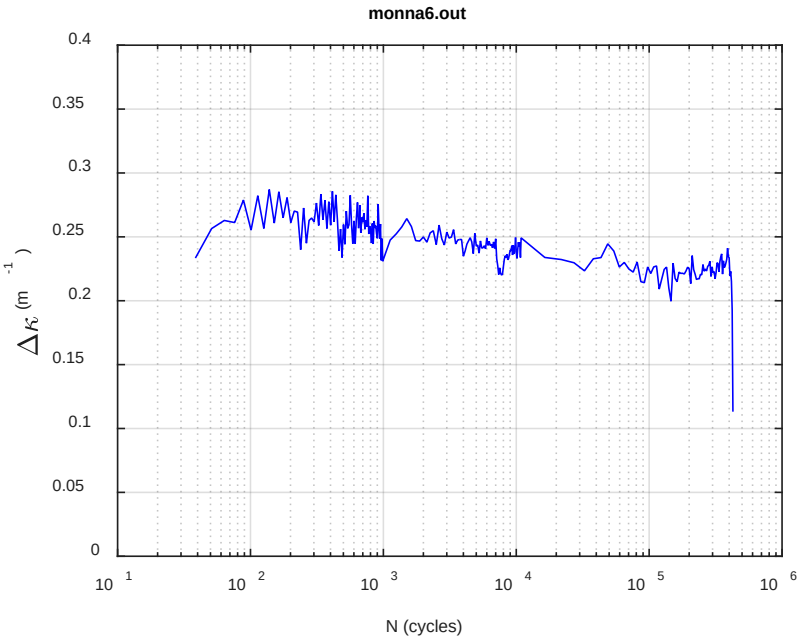
monna6.out
0.4
0.35
0.3
0.25
0.2
0.15
0.1
0.05
0
Δκ (m -1)
10 1
10 2
10 3
10 4
10 5
10 6
N (cycles)

(a)

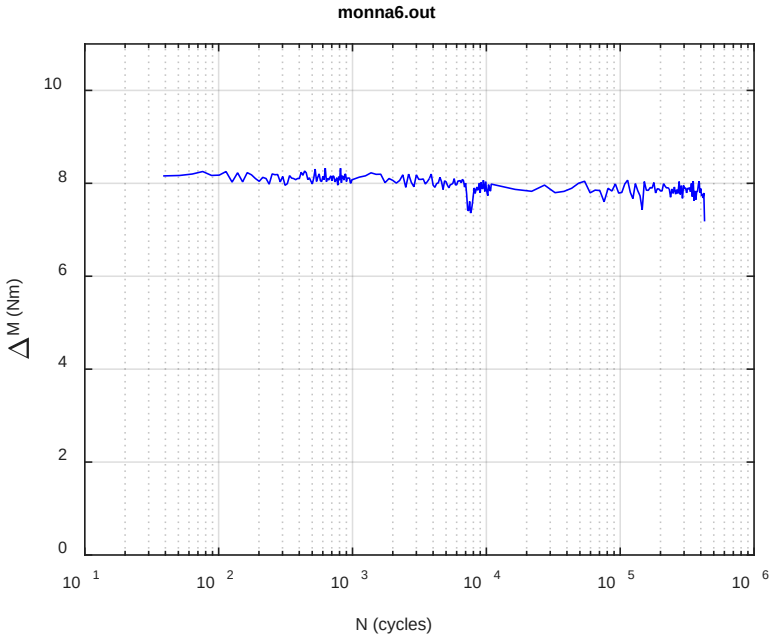
monna6.out
10
8
6
4
2
0
Δ M (Nm)
10 1
10 2
10 3
10 4
10 5
10 6
N (cycles)

(b)

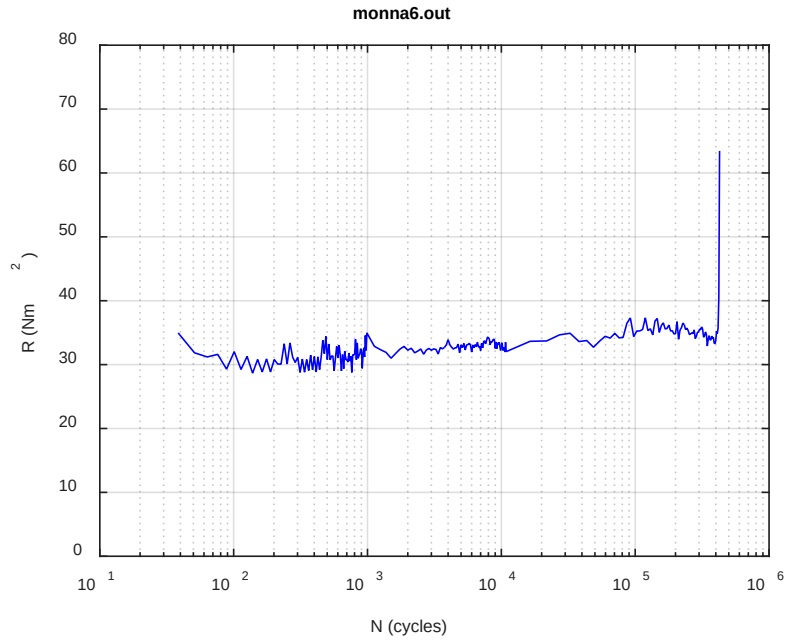

(c)

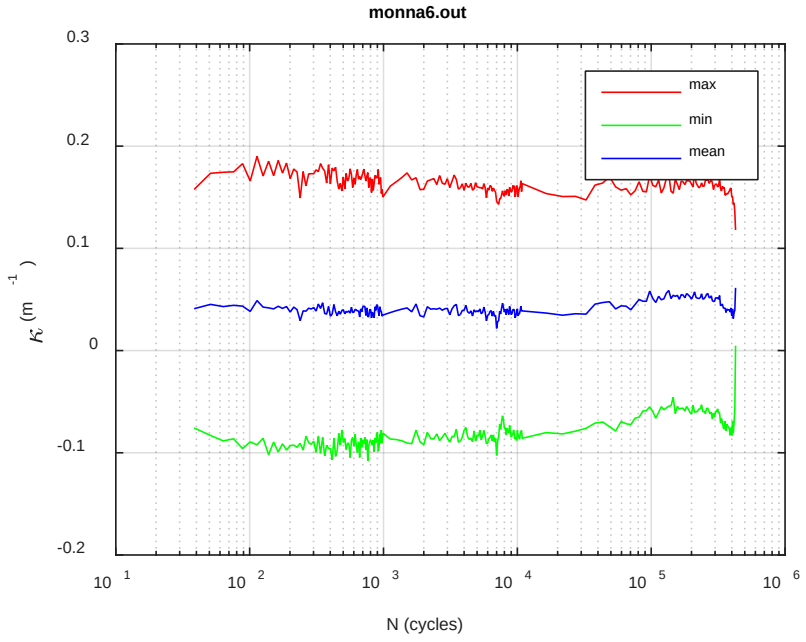

(d)

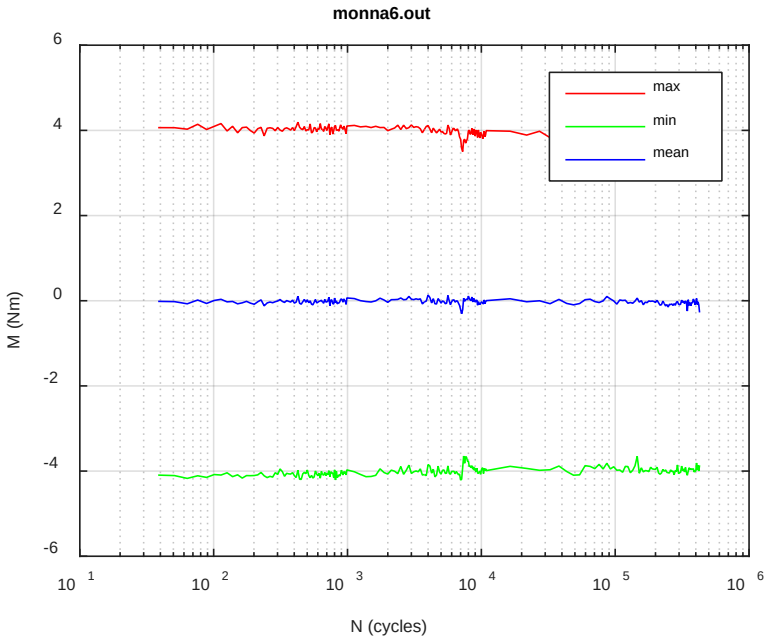

(e)

Fig. B.17. Monitoring-based responses: (a) curvature range, (b) moment range, (c) rigidity, (d) curvature peak/valley, (e) moment peak/valley, NA6, 5.08 Nm, Nf = 4.27E+05 cycles.

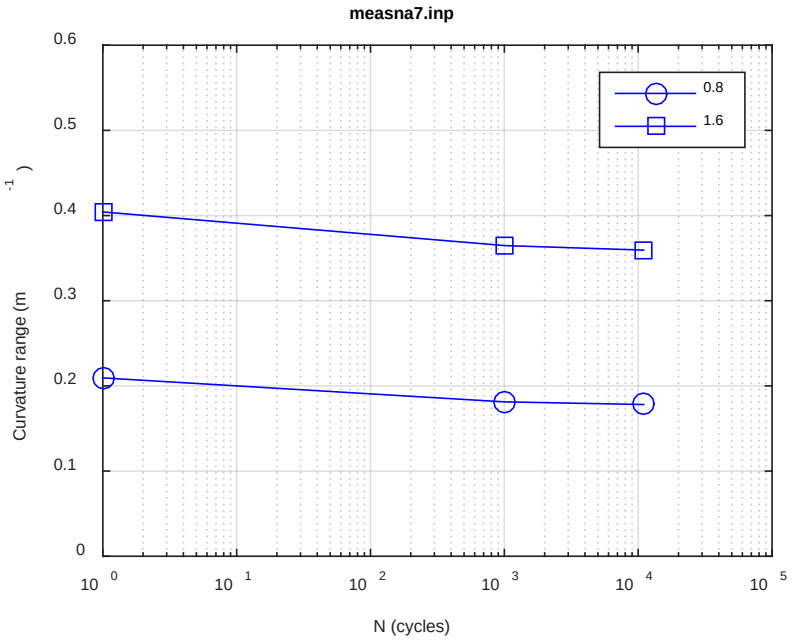
measna7.inp
Curvature range (m-1)
N (cycles)
0.8
1.6
0
0.1
0.2
0.3
0.4
0.5
0.6
10 0
10 1
10 2
10 3
10 4
10 5

(a)

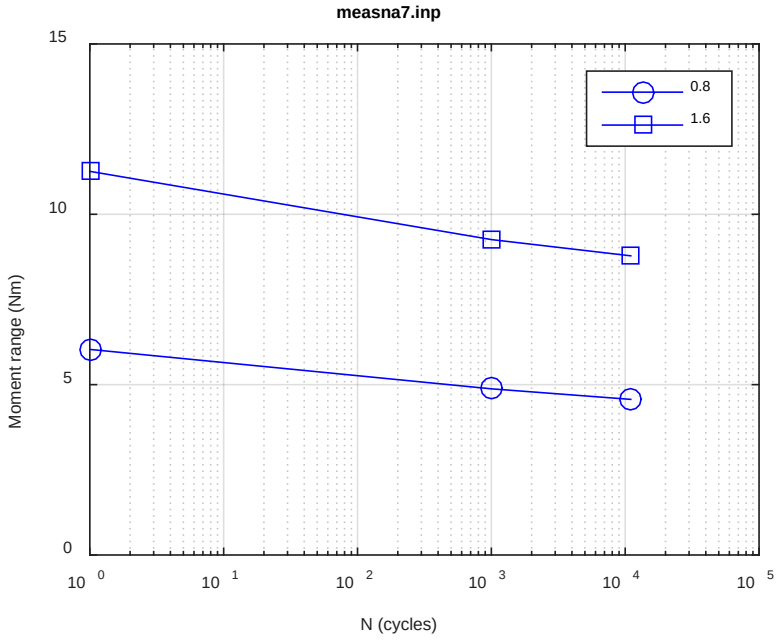
measna7.inp
Moment range (Nm)
N (cycles)
0.8
1.6
0
5
10
15
10 0
10 1
10 2
10 3
10 4
10 5

(b)

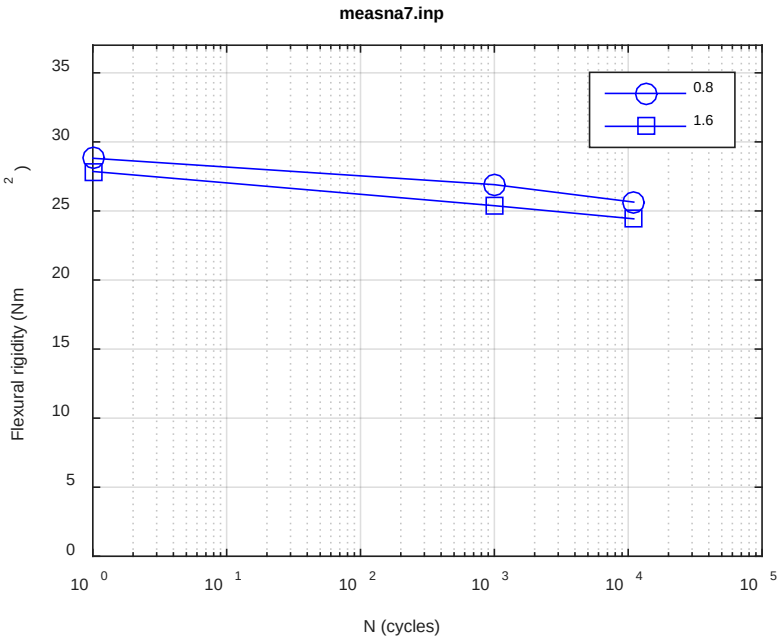
measna7.inp
0.8
1.6
Flexural rigidity (Nm 2)
N (cycles)

(c)

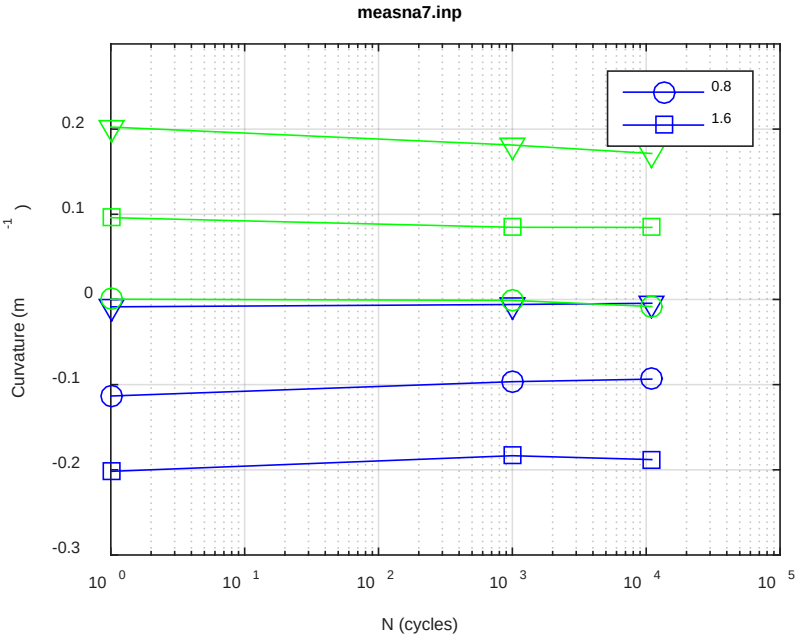
measna7.inp
0.8
1.6
Curvature (m -1)
N (cycles)

(d)

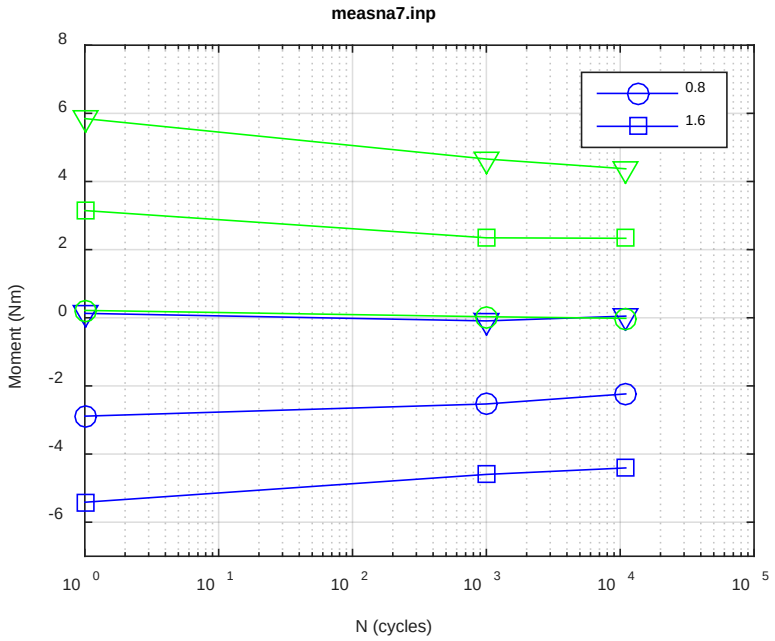

(e)

Fig. B.18. Measurement-based responses: (a) curvature range, (b) moment range, (c) rigidity, (d) curvature peak/valley, (e) moment peak/valley, NA7, 15.24 Nm.

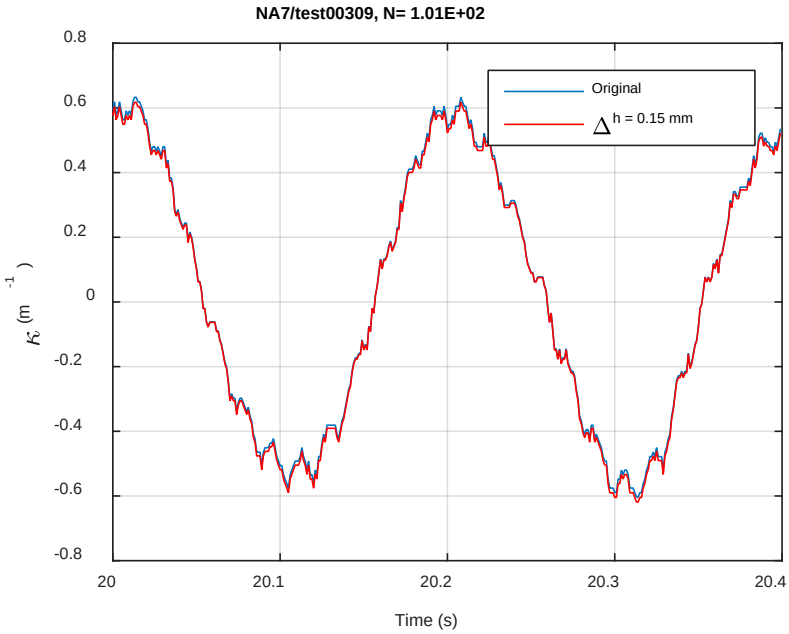
NA7/test00309, N= 1.01E+02
Original
Δh = 0.15 mm
κ (m-1)
Time (s)

(a)

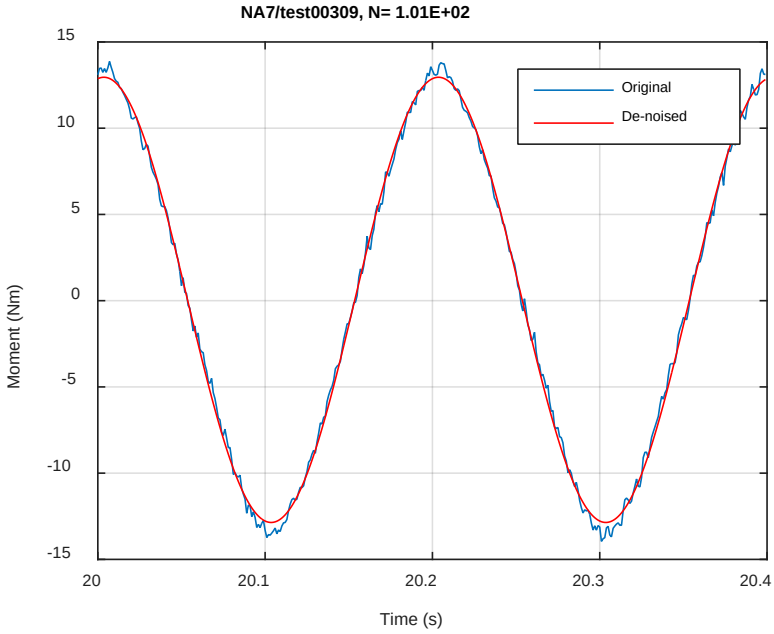
NA7/test00309, N= 1.01E+02
Original
De-noised
Moment (Nm)
Time (s)

(b)

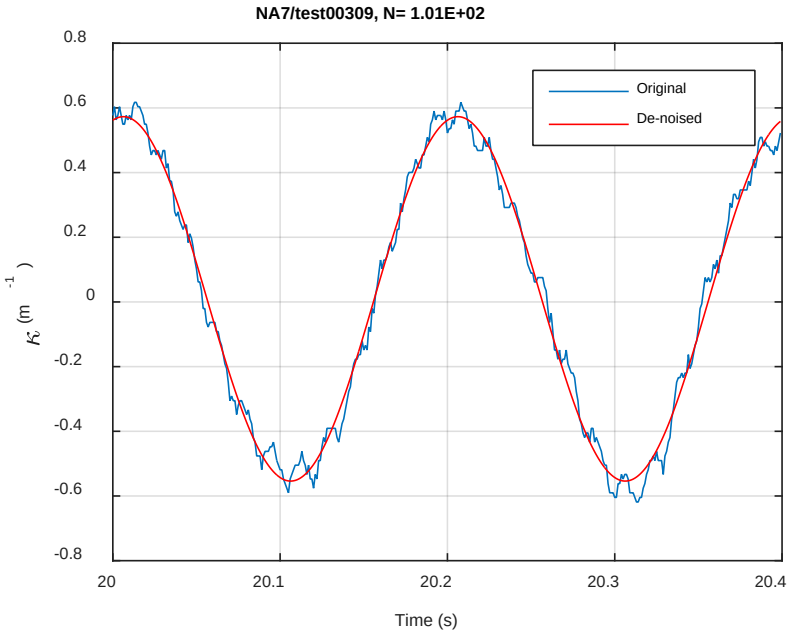

(c)

Fig. B.19. Monitoring-based responses: (a) curvature, (b) moment, (c) curvature, NA7, 15.24 Nm, Ns = 1.01E+02 cycles.

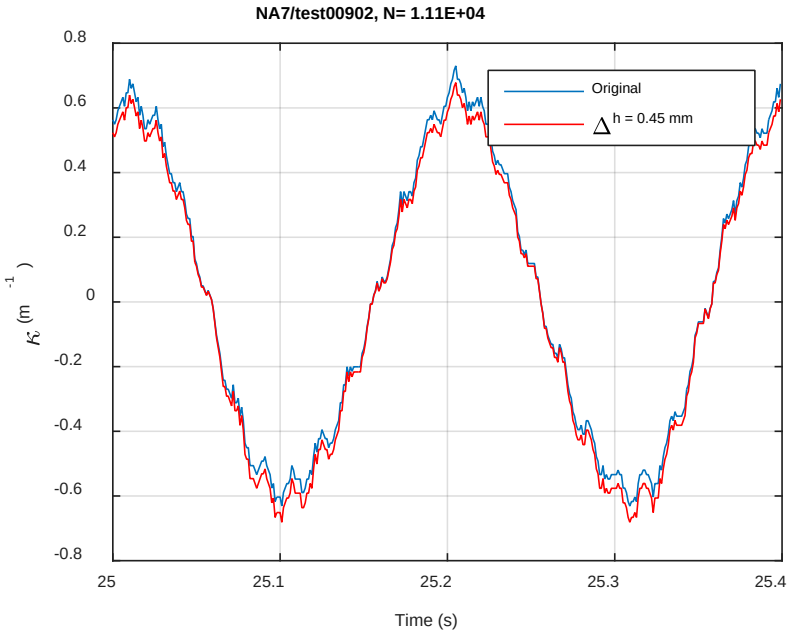
NA7/test00902, N= 1.11E+04
Original
Δh = 0.45 mm
κ (m-1)
Time (s)

(a)

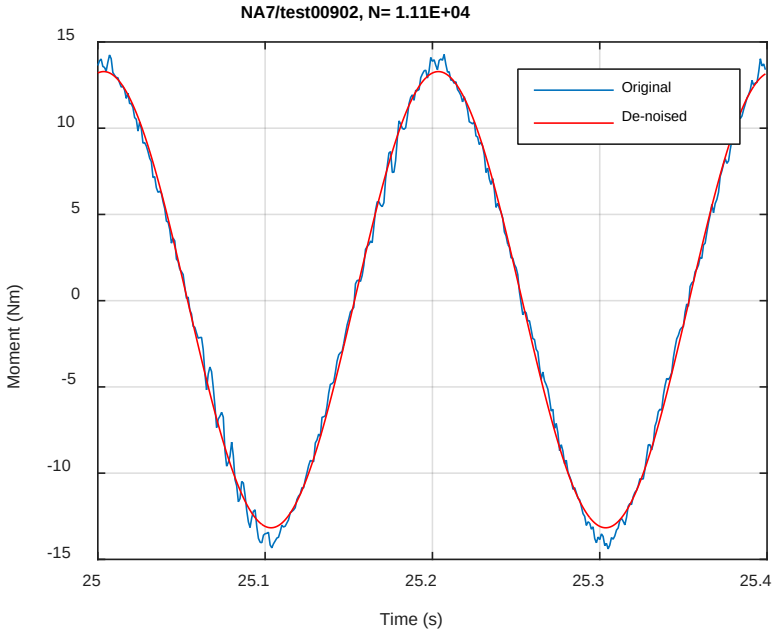
NA7/test00902, N= 1.11E+04
Original
De-noised
Moment (Nm)
Time (s)

(b)

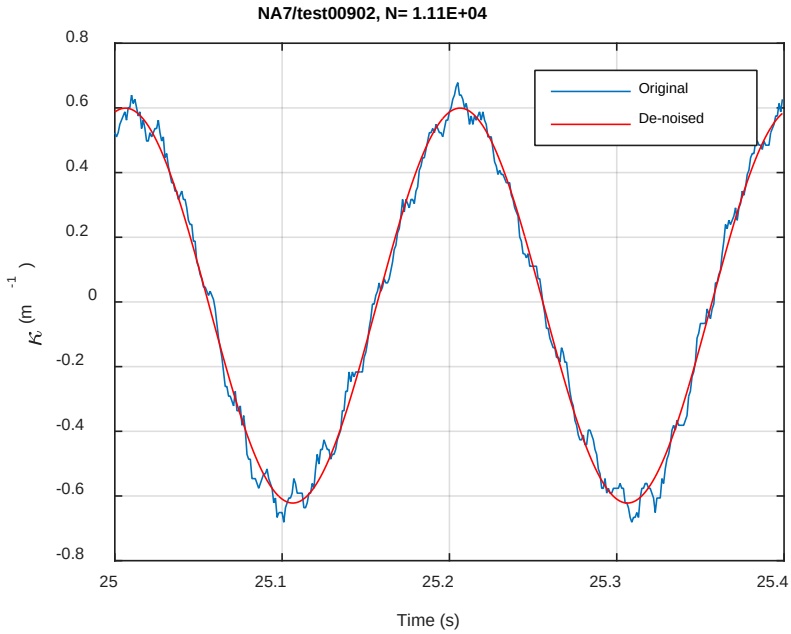

(c)

Fig. B.20. Monitoring-based responses: (a) curvature, (b) moment, (c) curvature, NA7, 15.24 Nm, Ns = 1.11E+04 cycles.

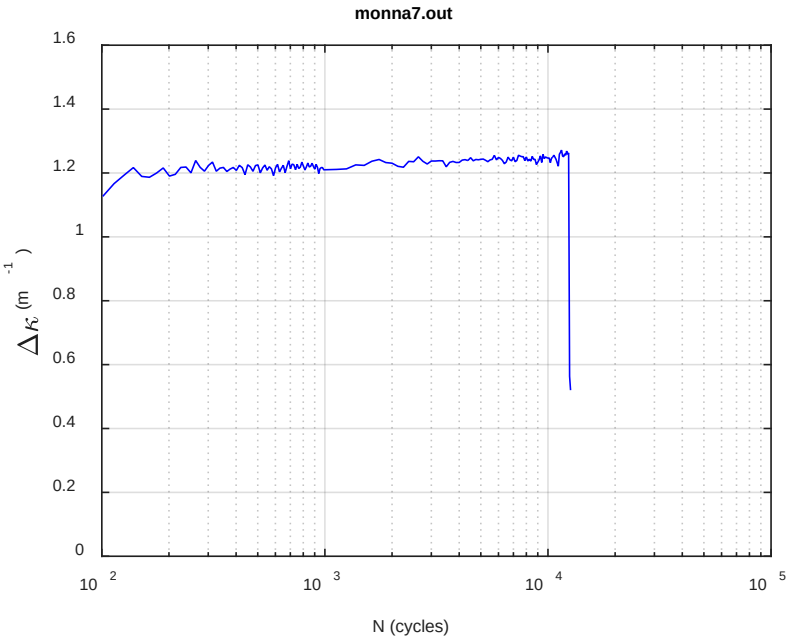
monna7.out
1.6
1.4
1.2
1
0.8
0.6
0.4
0.2
0
Δκ (m -1)
10 2
10 3
10 4
10 5
N (cycles)

(a)

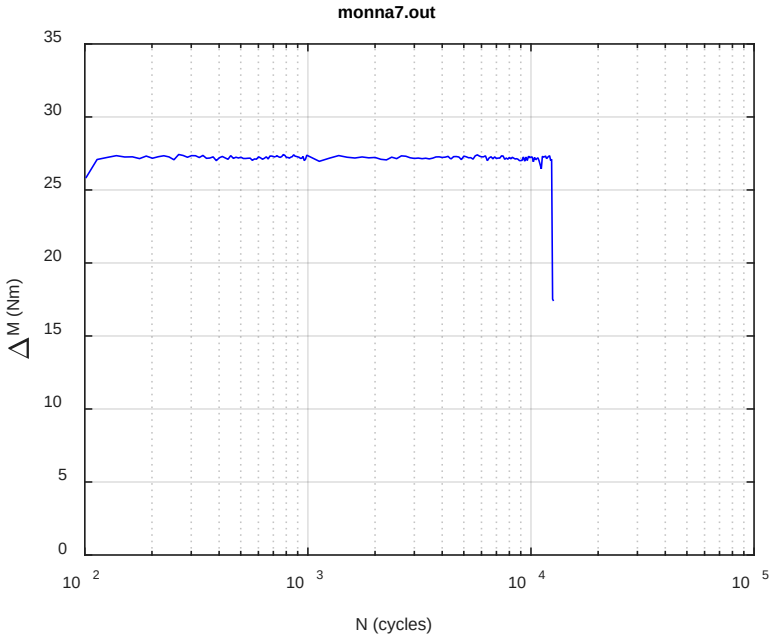
monna7.out
35
30
25
20
15
10
5
0
ΔM (Nm)
10 2
10 3
10 4
10 5
N (cycles)

(b)

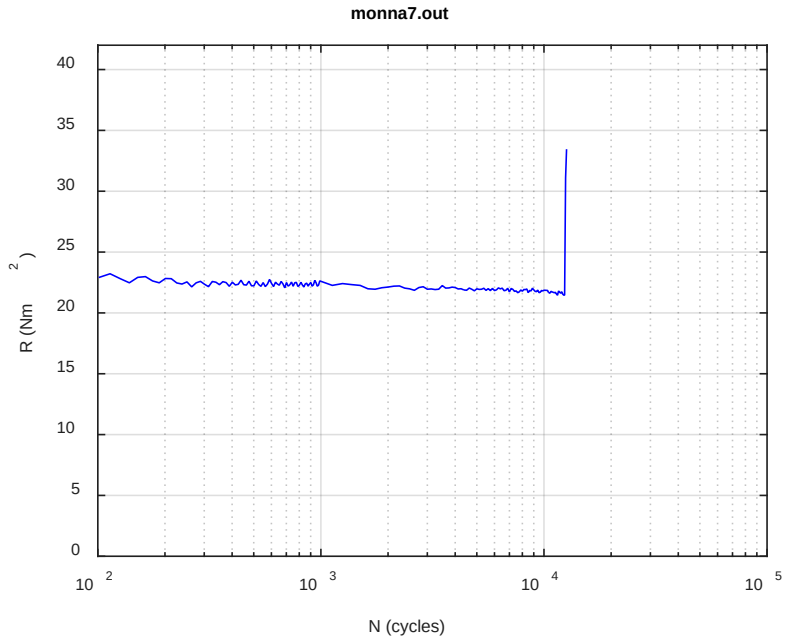
monna7.out
R (Nm^2)
N (cycles)
0
5
10
15
20
25
30
35
40
10^2
10^3
10^4
10^5

(c)

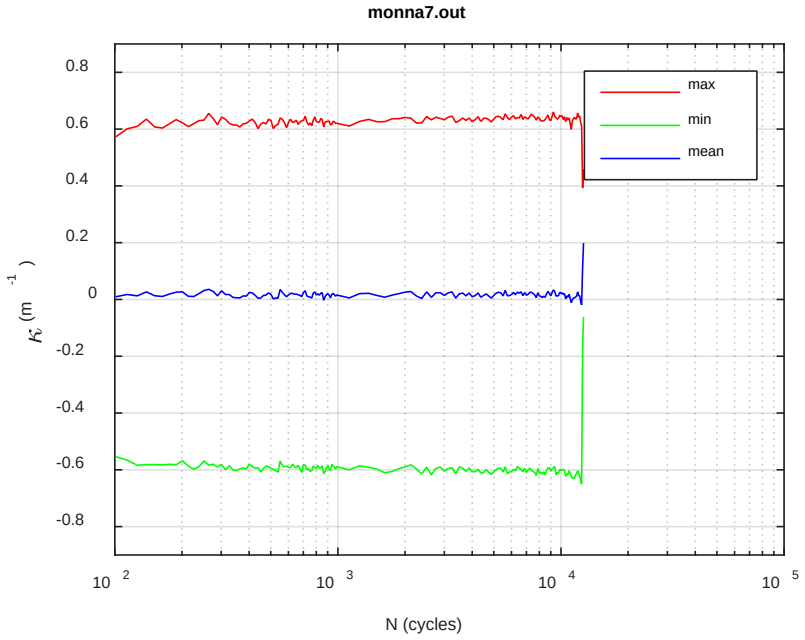
monna7.out
κ (m^-1)
N (cycles)
max
min
mean
0.8
0.6
0.4
0.2
0
-0.2
-0.4
-0.6
-0.8
10^2
10^3
10^4
10^5

(d)

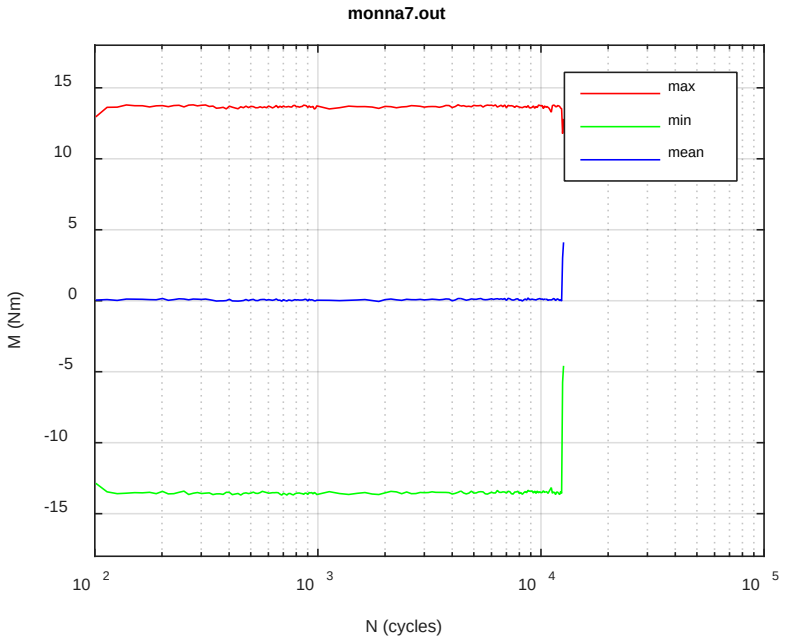

(e)

Fig. B.21. Monitoring-based responses: (a) curvature range, (b) moment range, (c) rigidity, (d) curvature peak/valley, (e) moment peak/valley, NA7, 15.24 Nm, Nf = 1.26E+04 cycles.

APPENDIX C CIRFT RESULTS OF MOX SNF

TABLE OF CONTENTS

Measurement and monitoring rigidity curves of MOX SNF

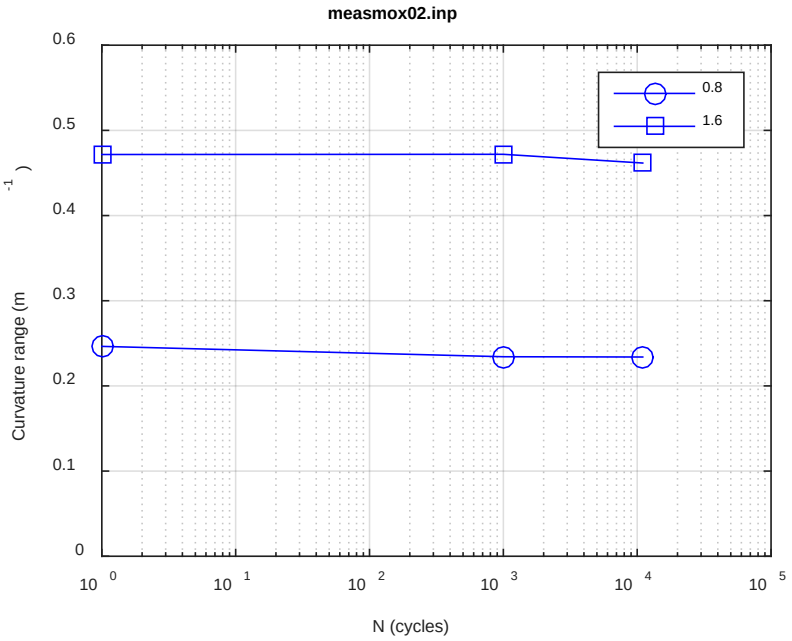
measmox02.inp
0.6
0.5
0.4
0.3
0.2
0.1
0
Curvature range (m -1)
0.8
1.6
10 0
10 1
10 2
10 3
10 4
10 5
N (cycles)

(a)

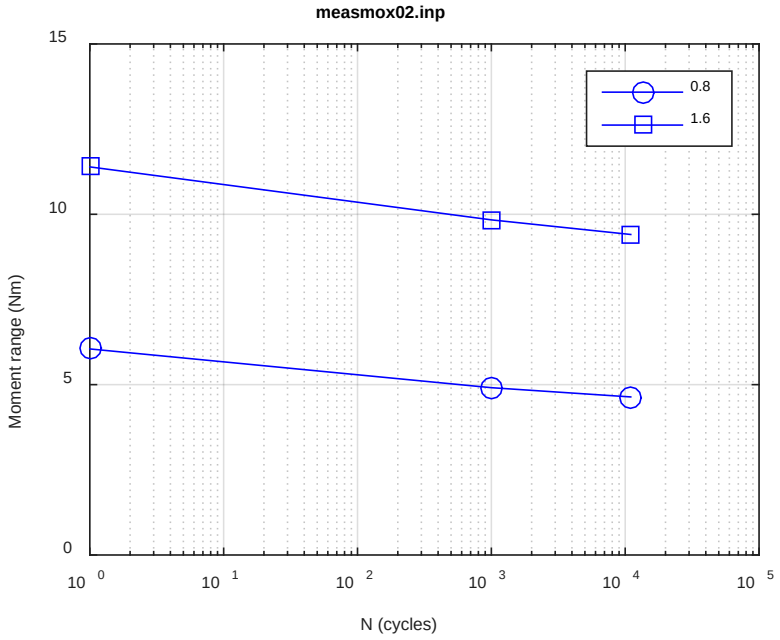
measmox02.inp
15
10
5
0
Moment range (Nm)
0.8
1.6
10 0
10 1
10 2
10 3
10 4
10 5
N (cycles)

(b)

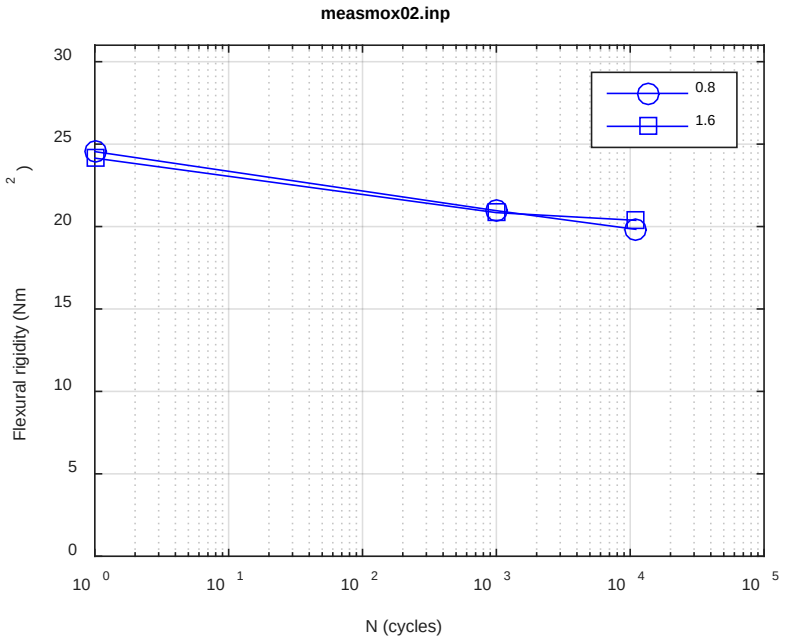
measmox02.inp
0.8
1.6
Flexural rigidity (Nm 2)
N (cycles)
30
25
20
15
10
5
0
10 0
10 1
10 2
10 3
10 4
10 5

(c)

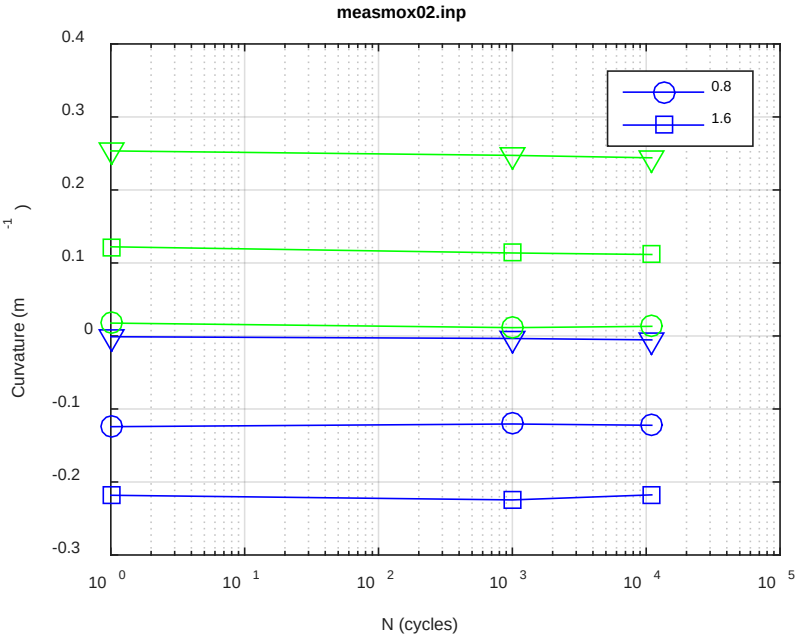
measmox02.inp
0.8
1.6
Curvature (m -1)
N (cycles)
0.4
0.3
0.2
0.1
0
-0.1
-0.2
-0.3
10 0
10 1
10 2
10 3
10 4
10 5

(d)

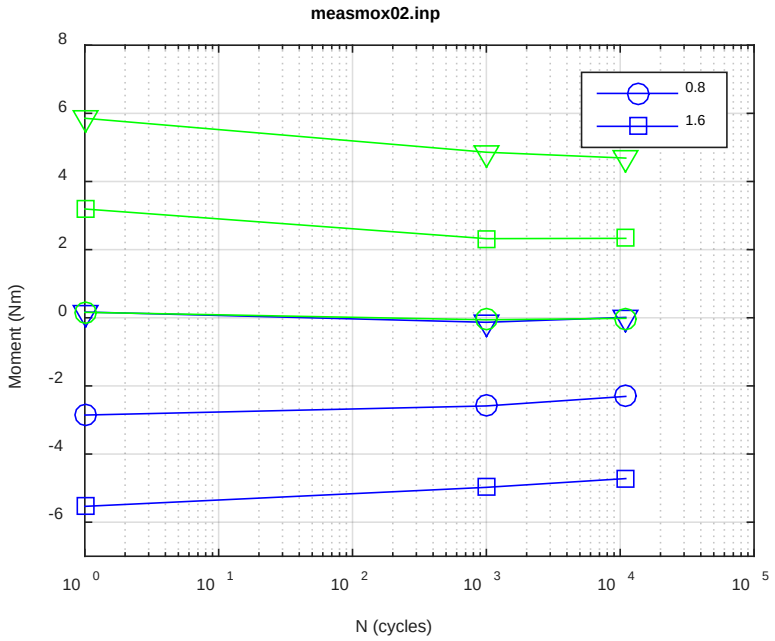

(e)

Fig. C.1. Measurement-based responses: (a) curvature range, (b) moment range, (c) rigidity, (d) curvature peak/valley, (e) moment peak/valley, MOX02, 10.16 Nm.

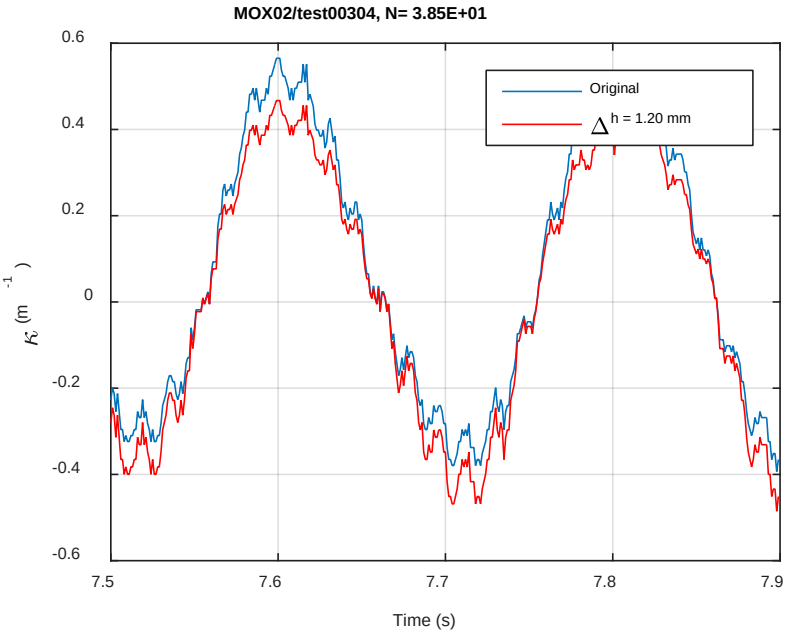
MOX02/test00304, N= 3.85E+01
Original
Δh = 1.20 mm
κ (m-1)
Time (s)

(a)

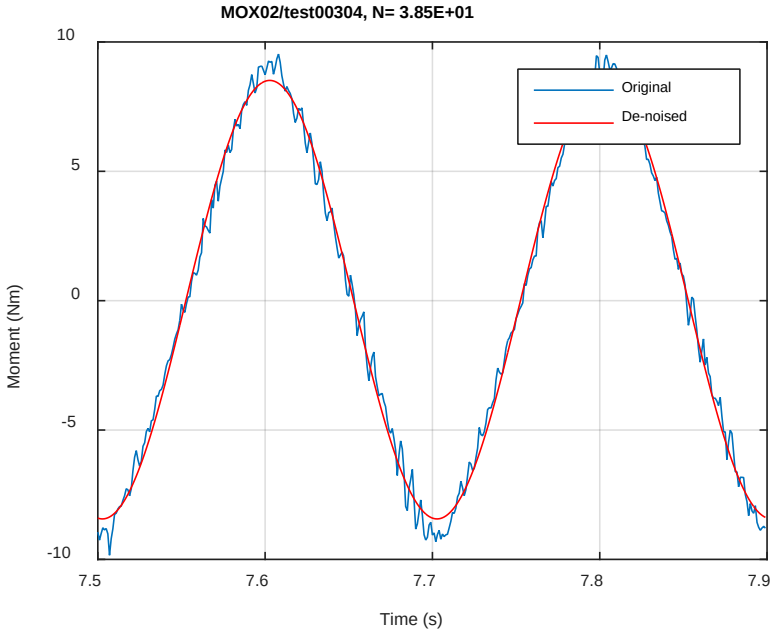
MOX02/test00304, N= 3.85E+01
Original
De-noised
Moment (Nm)
Time (s)

(b)

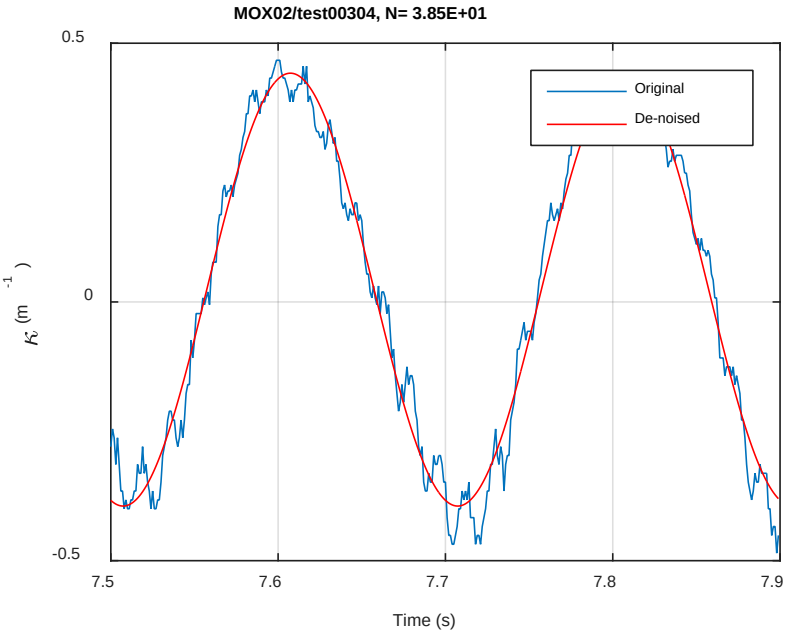

(c)

Fig. C.2. Monitoring-based responses: (a) curvature, (b) moment, (c) curvature, MOX02, 10.16 Nm, Ns = 3.85E+01 cycles.

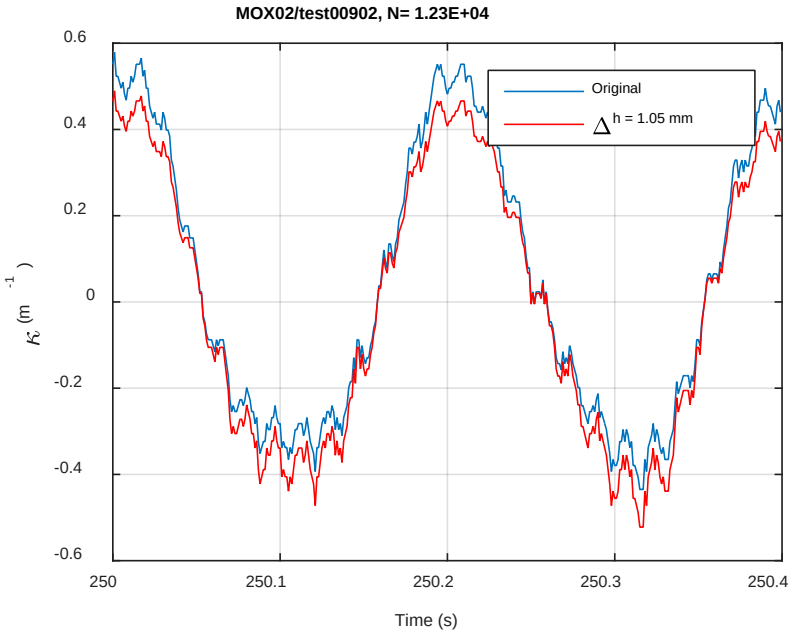
MOX02/test00902, N= 1.23E+04
Original
Δh = 1.05 mm
κ (m-1)
Time (s)
0.6
0.4
0.2
0
-0.2
-0.4
-0.6
250
250.1
250.2
250.3
250.4

(a)

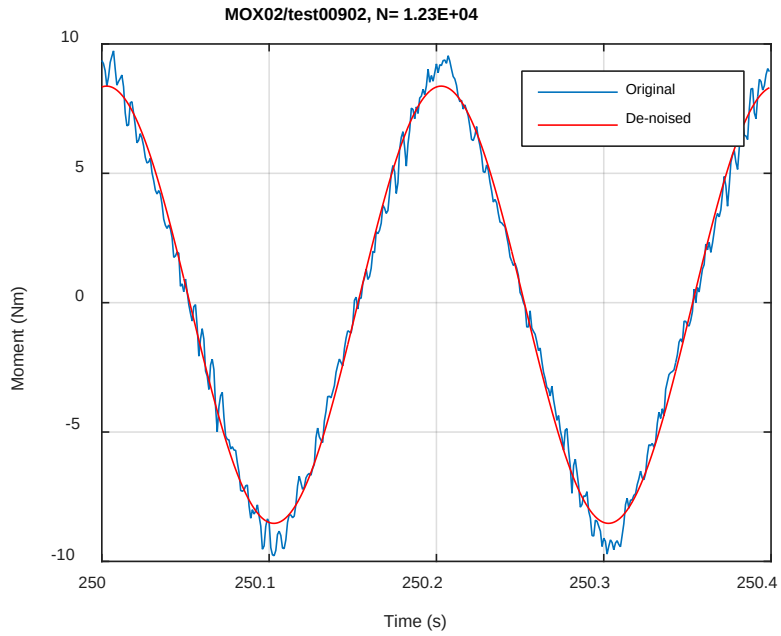
MOX02/test00902, N= 1.23E+04
Original
De-noised
Moment (Nm)
Time (s)
10
5
0
-5
-10
250
250.1
250.2
250.3
250.4

(b)

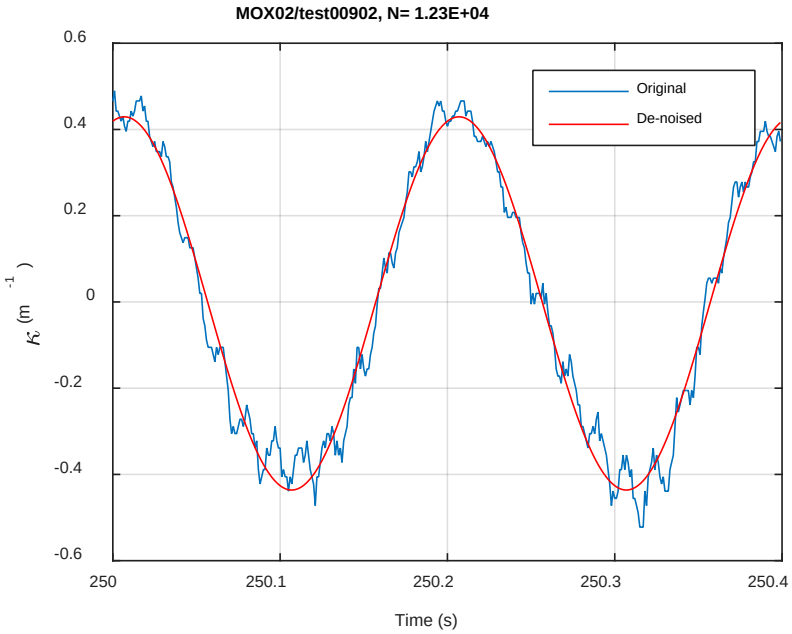

(c)

Fig. C.3. Monitoring-based responses: (a) curvature, (b) moment, (c) curvature, MOX02, 10.16 Nm, Ns = 1.23E+04 cycles.

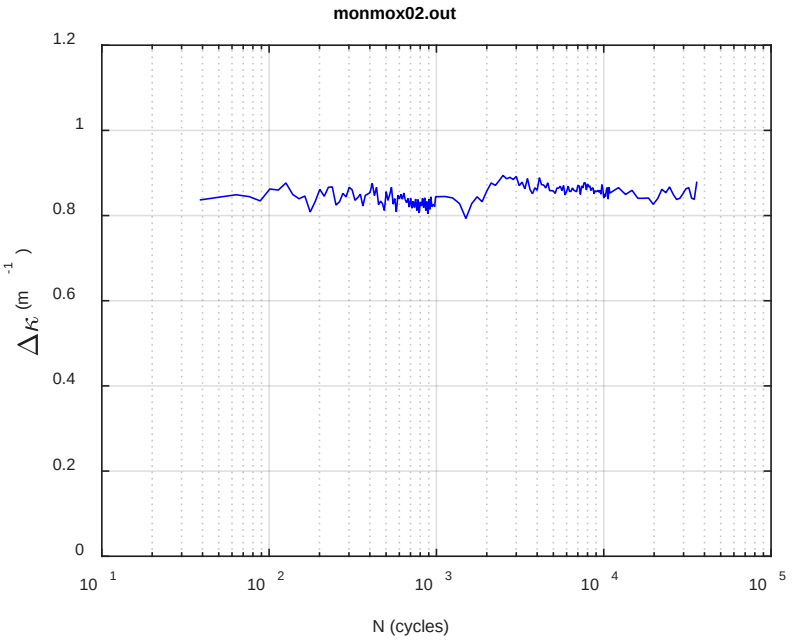
monmox02.out
1.2
1
0.8
0.6
0.4
0.2
0
Δκ (m-1)
10 1
10 2
10 3
10 4
10 5
N (cycles)

(a)

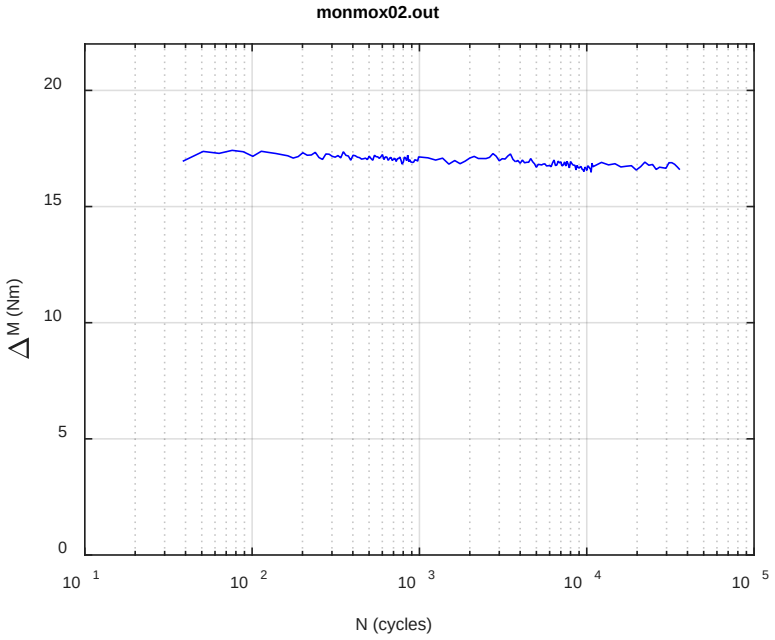
monmox02.out
20
15
10
5
0
ΔM (Nm)
10 1
10 2
10 3
10 4
10 5
N (cycles)

(b)

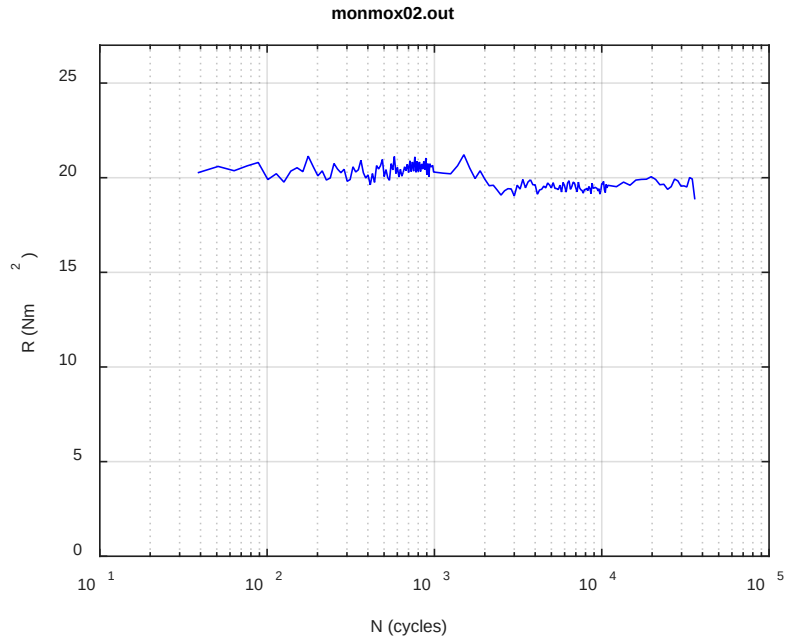
monmox02.out
R (Nm 2)
N (cycles)

(c)

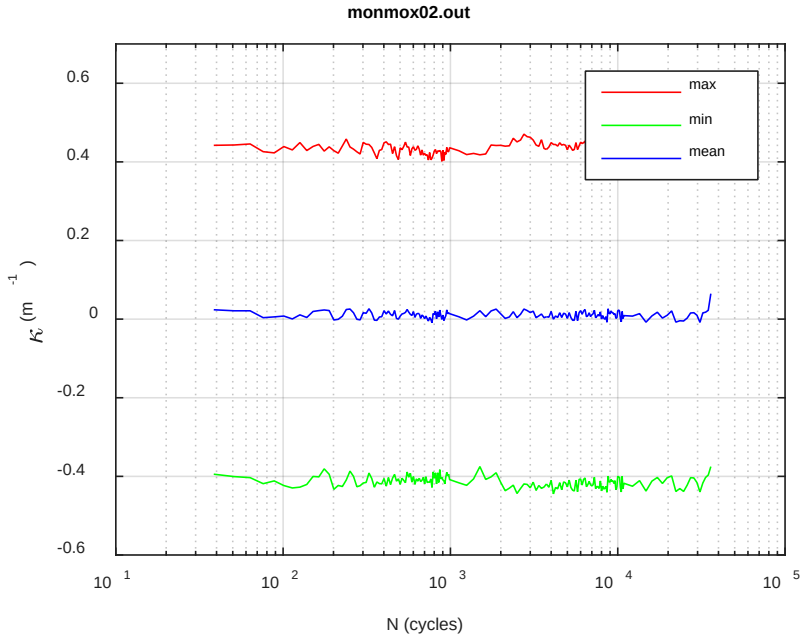
monmox02.out
max
min
mean
κ (m -1)
N (cycles)

(d)

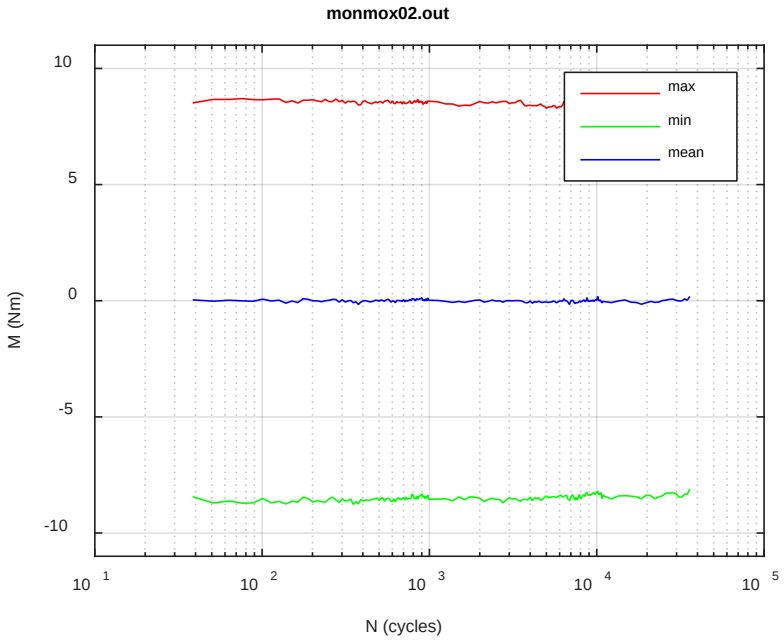

(e)

Fig. C.4. Monitoring-based responses: (a) curvature range, (b) moment range, (c) rigidity, (d) curvature peak/valley, (e) moment peak/valley, MOX02, 10.16 Nm, Nf = 3.70E+04 cycles.

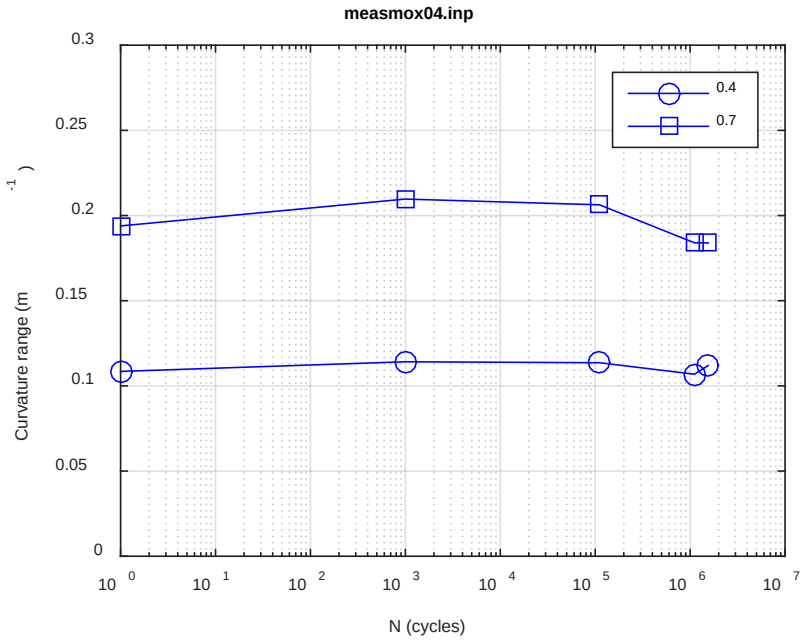
measmox04.inp
Curvature range (m -1)
N (cycles)
0.4
0.7
0.3
0.25
0.2
0.15
0.1
0.05
0
10 0
10 1
10 2
10 3
10 4
10 5
10 6
10 7

(a)

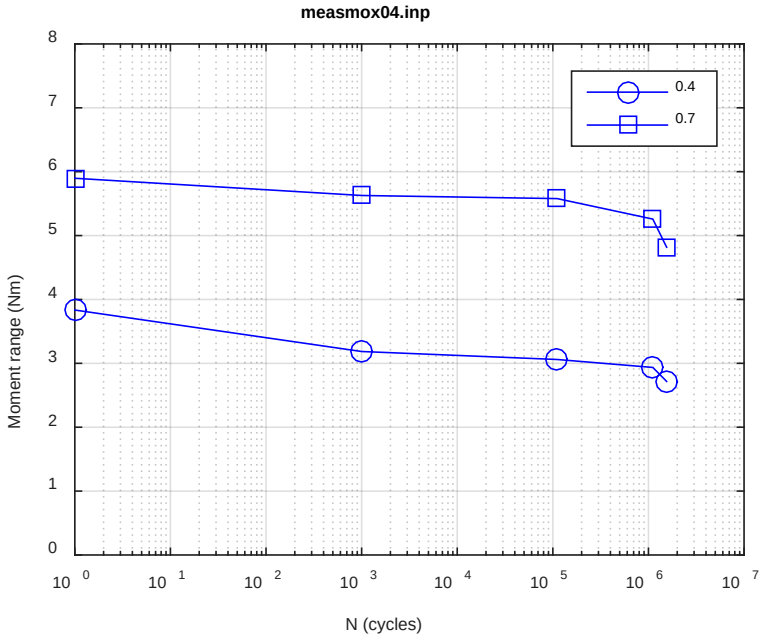
measmox04.inp
Moment range (Nm)
N (cycles)
0.4
0.7
8
7
6
5
4
3
2
1
0
10 0
10 1
10 2
10 3
10 4
10 5
10 6
10 7

(b)

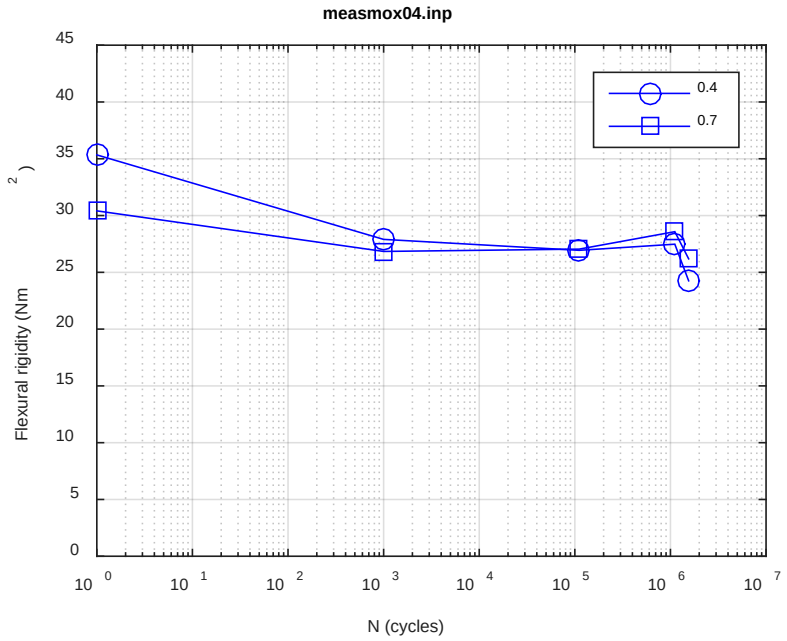
measmox04.inp
Flexural rigidity (Nm 2)
N (cycles)
0.4
0.7

(c)

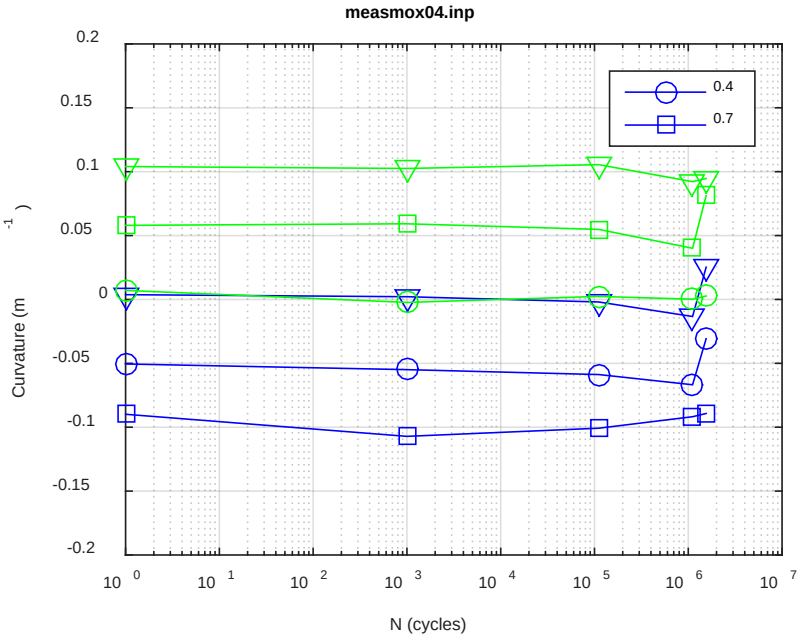
measmox04.inp
Curvature (m -1)
N (cycles)
0.4
0.7

(d)

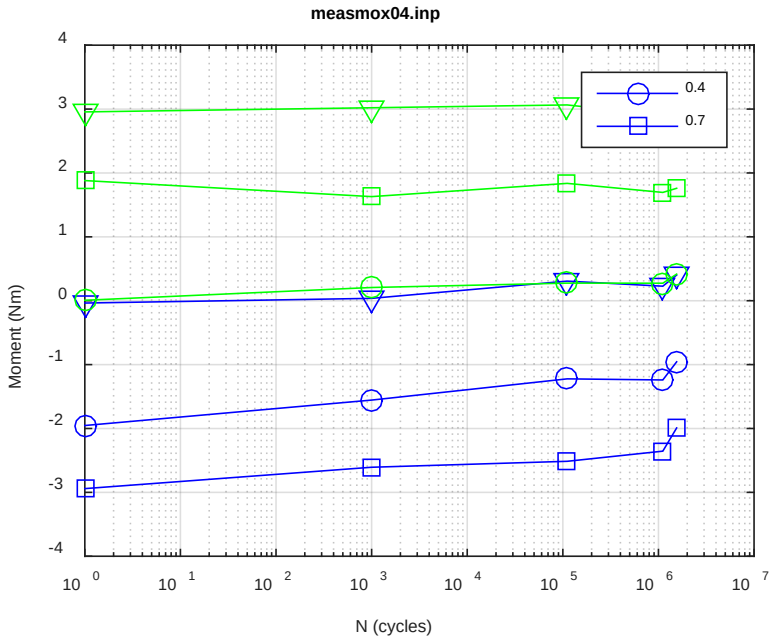

(e)

Fig. C.5. Measurement-based responses: (a) curvature range, (b) moment range, (c) rigidity, (d) curvature peak/valley, (e) moment peak/valley, MOX04, 5.08 Nm.

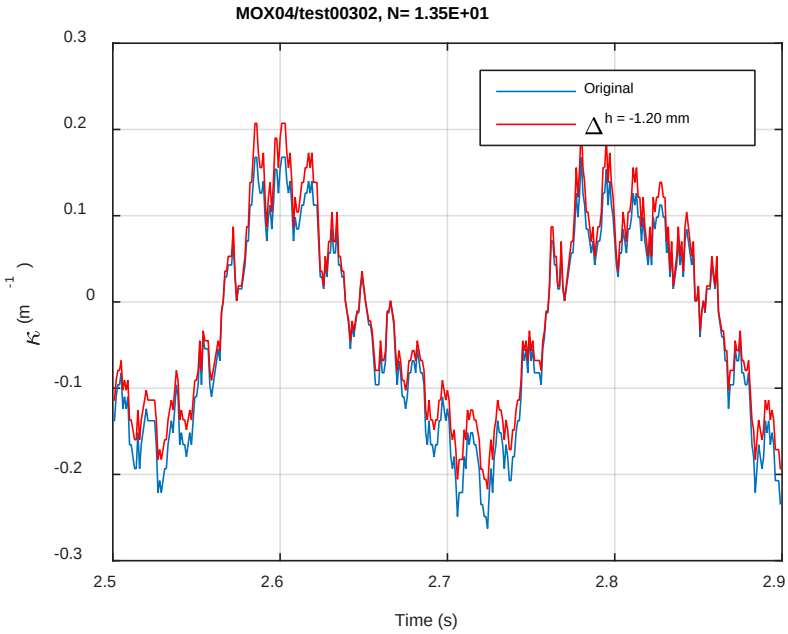
MOX04/test00302, N= 1.35E+01
Original
Δh = -1.20 mm
κ (m-1)
Time (s)

(a)

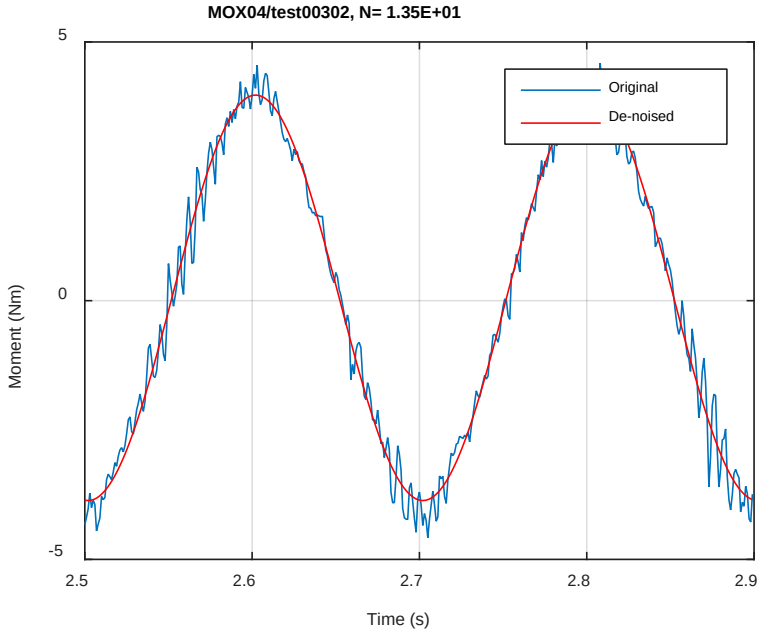
MOX04/test00302, N= 1.35E+01
Original
De-noised
Moment (Nm)
Time (s)

(b)

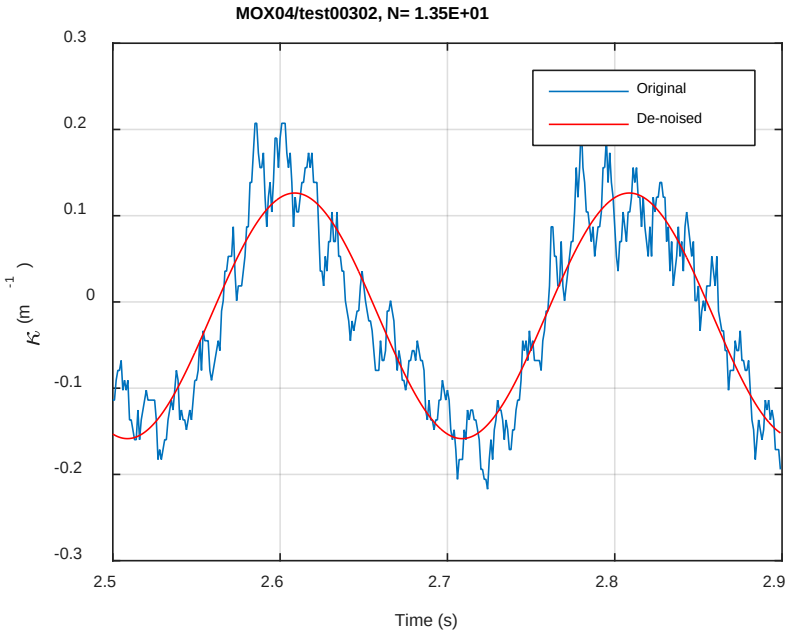

(c)

Fig. C.6. Monitoring-based responses: (a) curvature, (b) moment, (c) curvature, MOX04, 5.08 Nm, Ns = 1.35E+01 cycles.

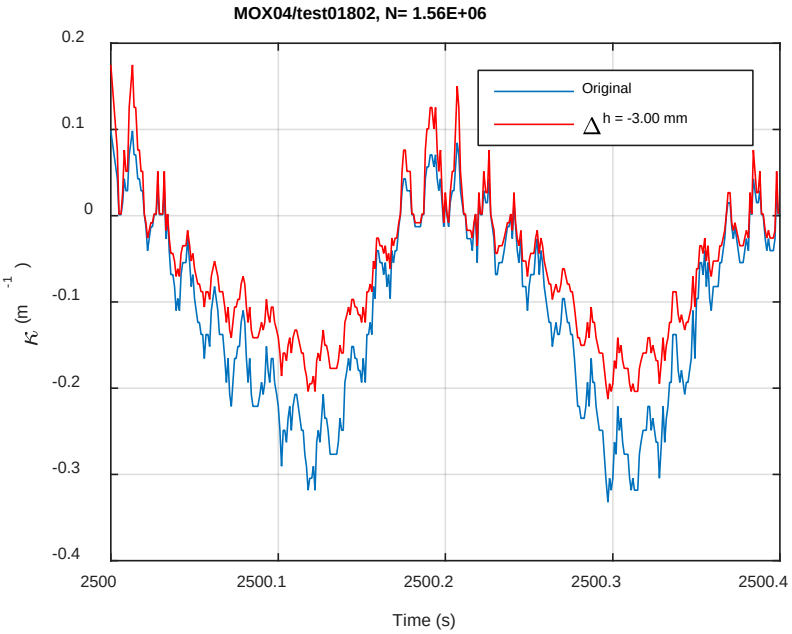
MOX04/test01802, N= 1.56E+06
Original
Δh = -3.00 mm
κ (m-1)
Time (s)
0.2
0.1
0
-0.1
-0.2
-0.3
-0.4
2500
2500.1
2500.2
2500.3
2500.4

(a)

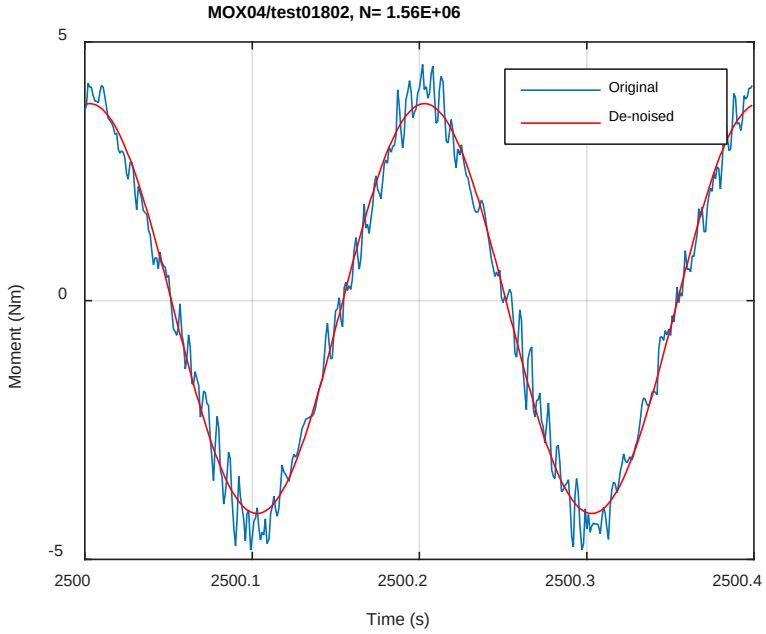
MOX04/test01802, N= 1.56E+06
Original
De-noised
Moment (Nm)
Time (s)
5
0
-5
2500
2500.1
2500.2
2500.3
2500.4

(b)

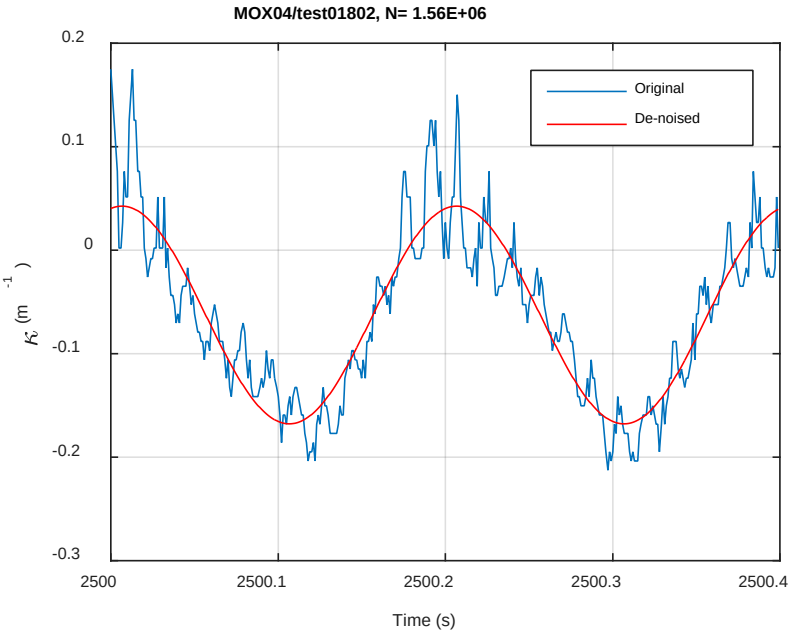

(c)

Fig. C.7. Monitoring-based responses: (a) curvature, (b) moment, (c) curvature, MOX04, 5.08 Nm, Ns = 1.56E+06 cycles.

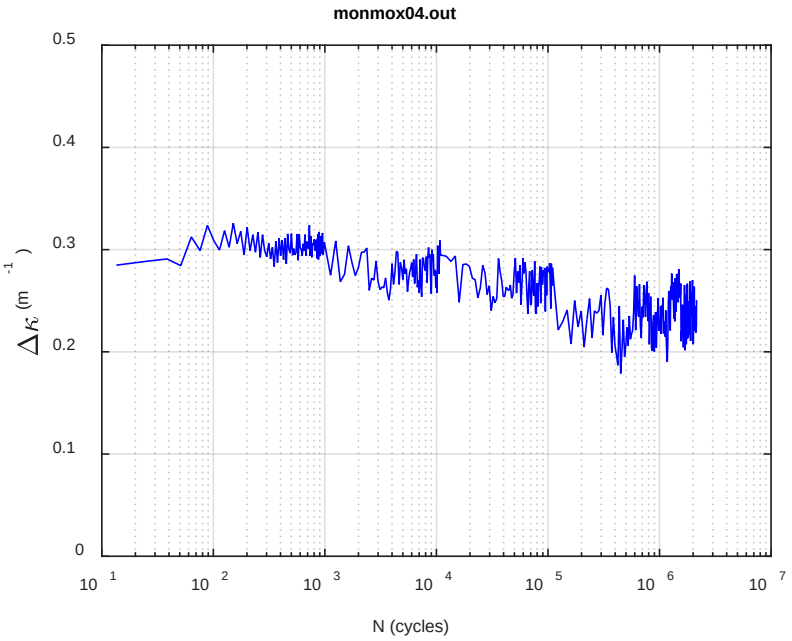
monmox04.out
0.5
0.4
0.3
0.2
0.1
0
Δκ (m-1)
10 1
10 2
10 3
10 4
10 5
10 6
10 7
N (cycles)

(a)

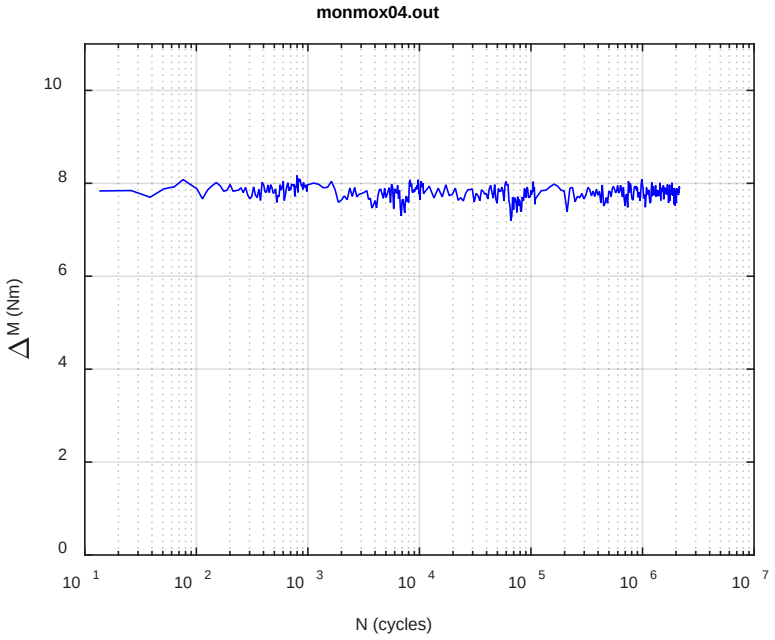
monmox04.out
10
8
6
4
2
0
Δ M (Nm)
10 1
10 2
10 3
10 4
10 5
10 6
10 7
N (cycles)

(b)

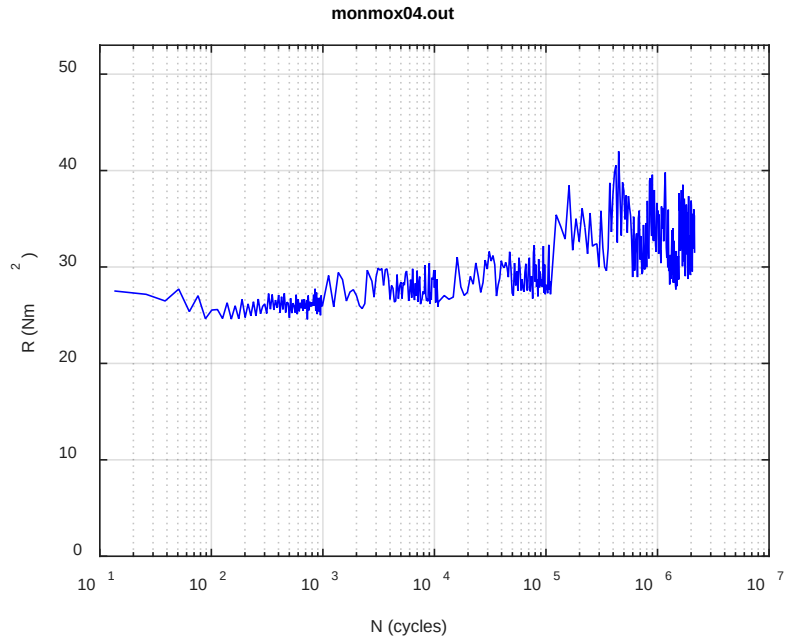
monmox04.out
R (Nm 2)
N (cycles)

(c)

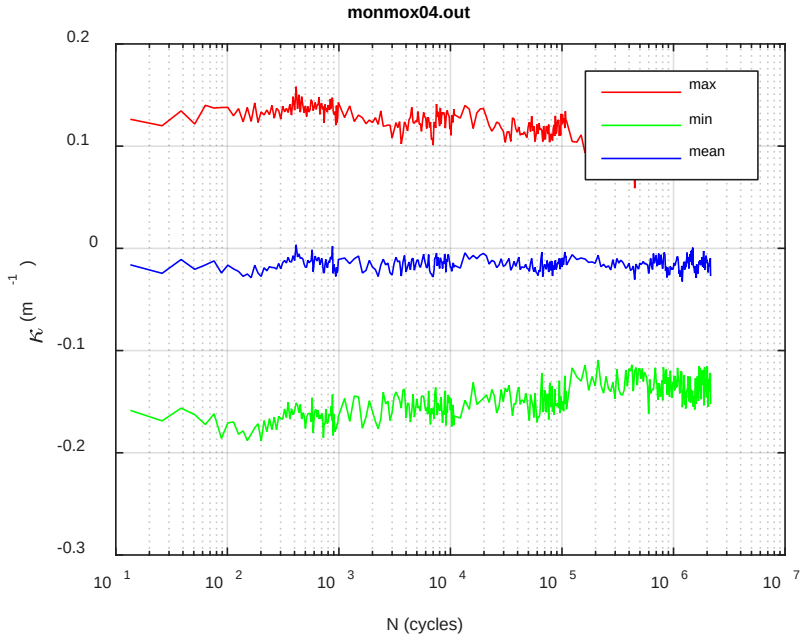
monmox04.out
max
min
mean
κ (m -1)
N (cycles)

(d)

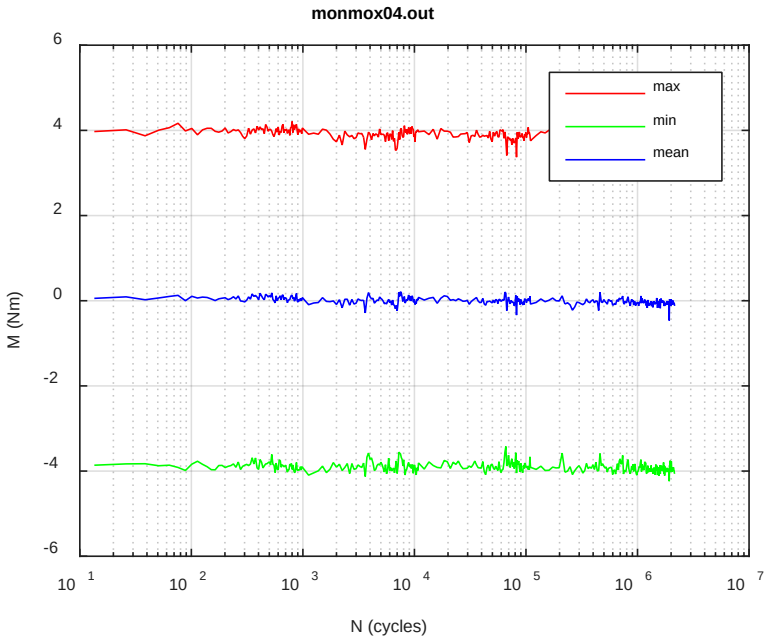

(e)

Fig. C.8. Monitoring-based responses: (a) curvature range, (b) moment range, (c) rigidity, (d) curvature peak/valley, (e) moment peak/valley, MOX04, 5.08 Nm, Nf = 2.15E+06 cycles.

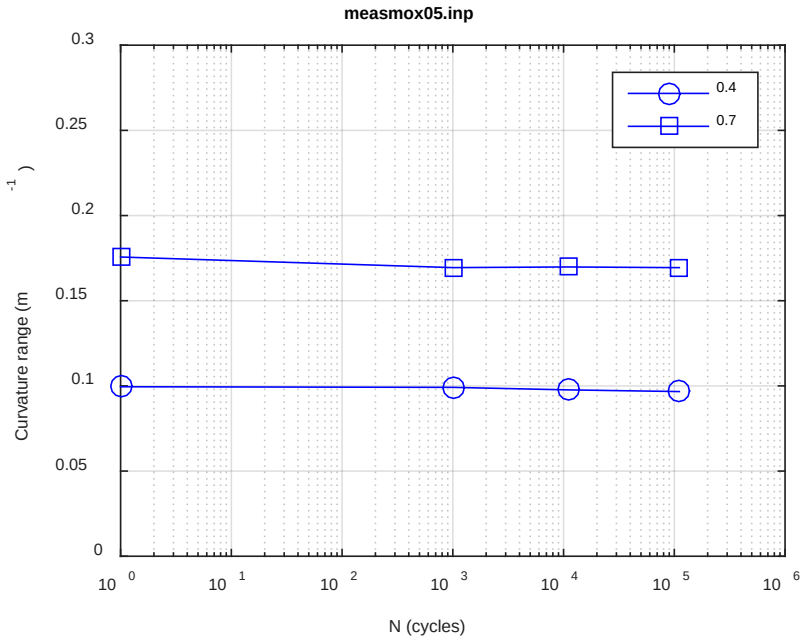
measmox05.inp
0.4
0.7
Curvature range (m -1)
N (cycles)
0
0.05
0.1
0.15
0.2
0.25
0.3
10 0
10 1
10 2
10 3
10 4
10 5
10 6

(a)

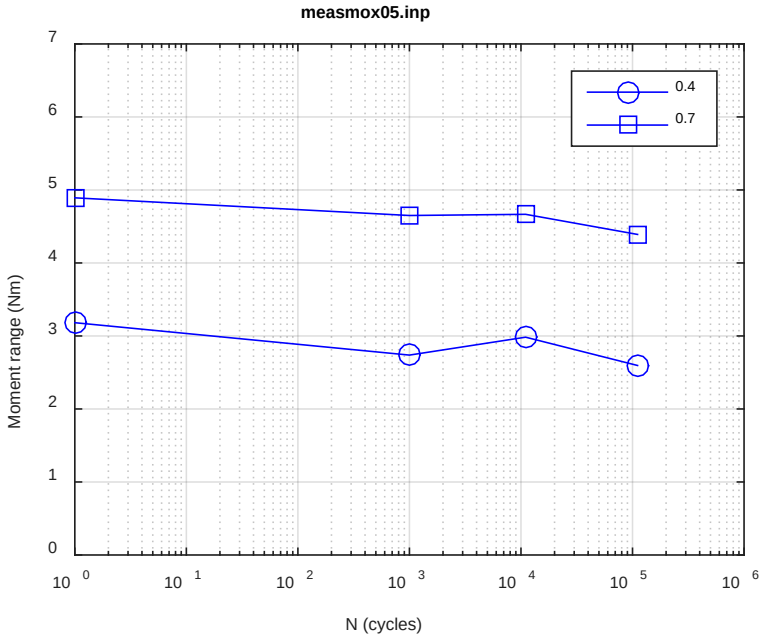
measmox05.inp
0.4
0.7
Moment range (Nm)
N (cycles)
0
1
2
3
4
5
6
7
10 0
10 1
10 2
10 3
10 4
10 5
10 6

(b)

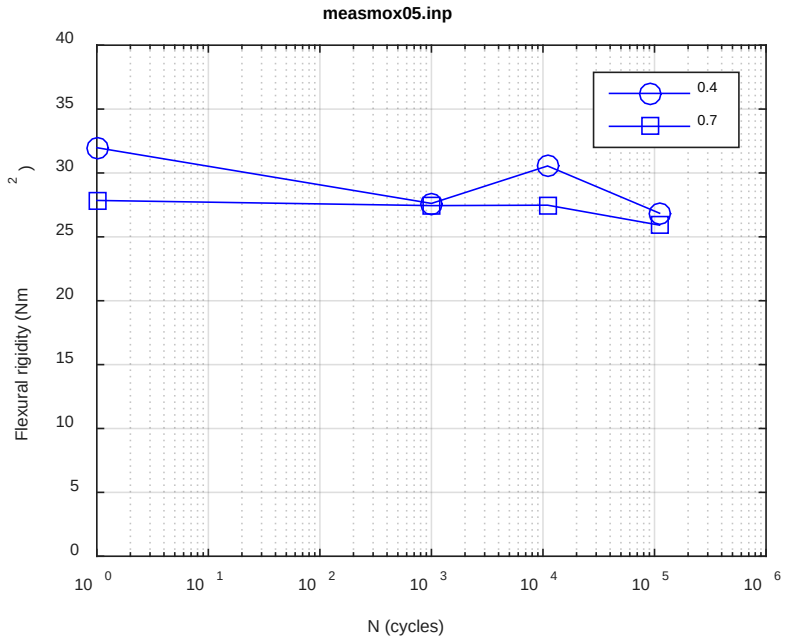
measmox05.inp
Flexural rigidity (Nm^2)
N (cycles)
0.4
0.7

(c)

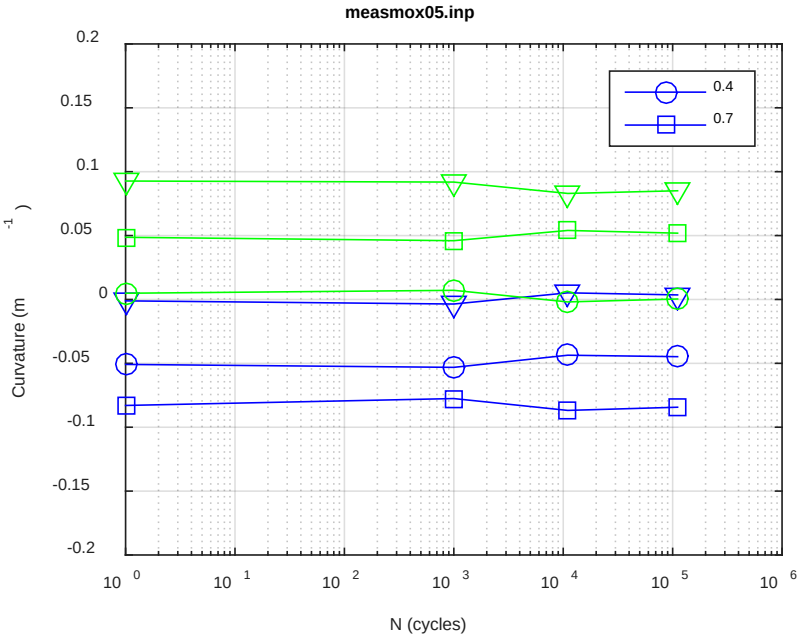
measmox05.inp
Curvature (m^-1)
N (cycles)
0.4
0.7

(d)

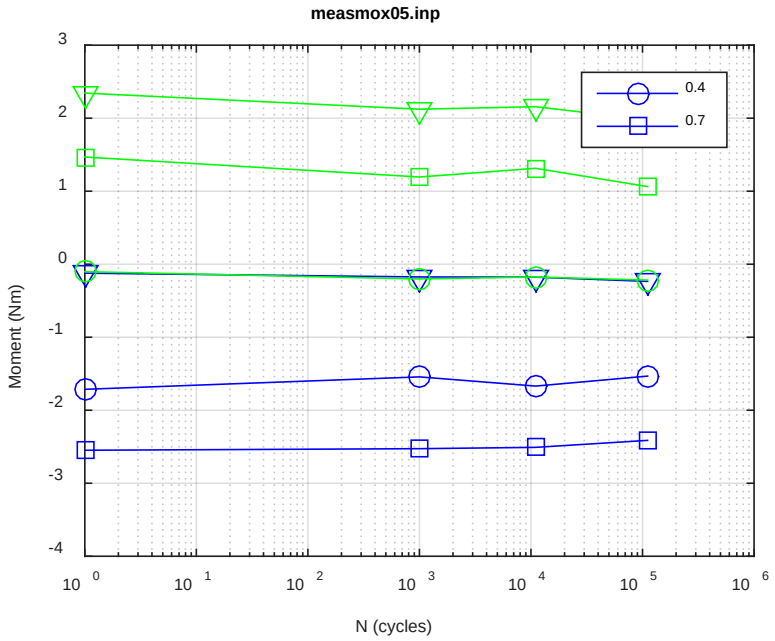

(e)

Fig. C.9. Measurement-based responses: (a) curvature range, (b) moment range, (c) rigidity, (d) curvature peak/valley, (e) moment peak/valley, MOX05, 6.10 Nm.

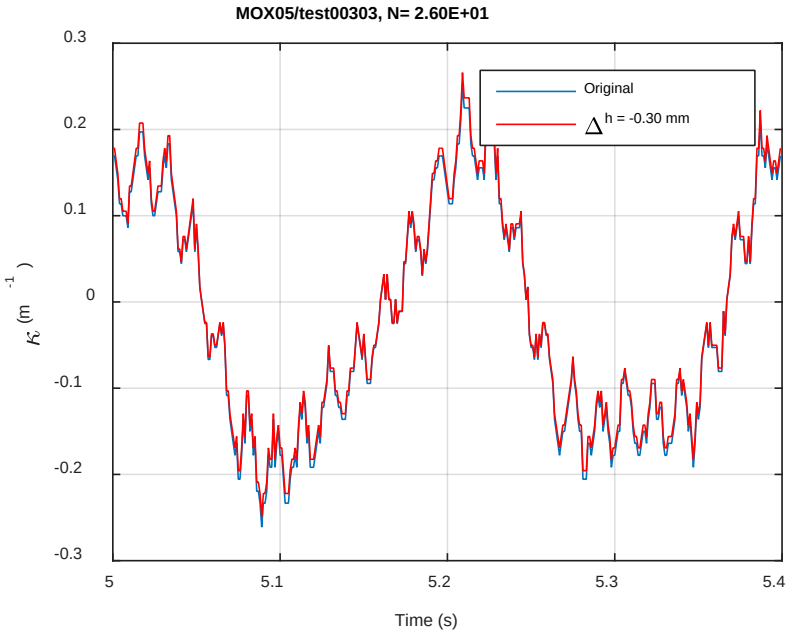
MOX05/test00303, N= 2.60E+01
Original
Δh = -0.30 mm
κ (m-1)
Time (s)

(a)

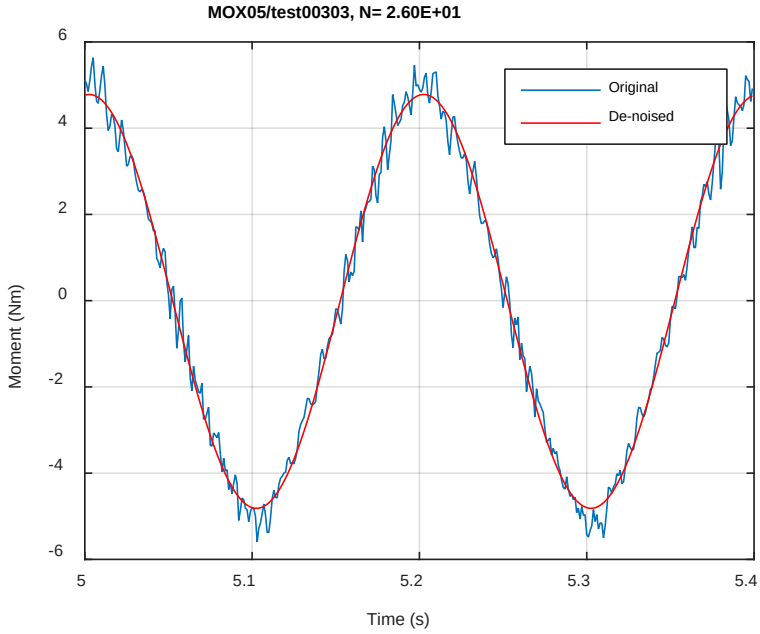
MOX05/test00303, N= 2.60E+01
Original
De-noised
Moment (Nm)
Time (s)

(b)

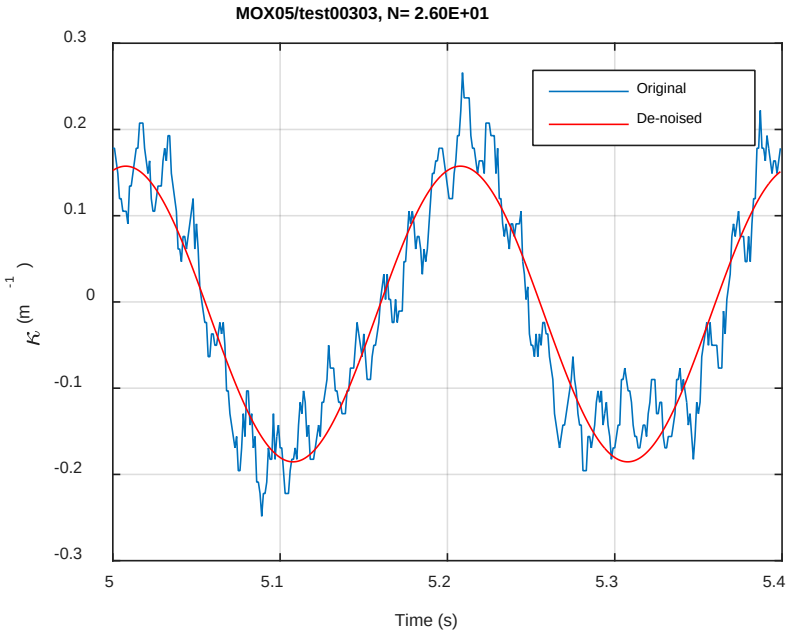

(c)

Fig. C.10. Monitoring-based responses: (a) curvature, (b) moment, (c) curvature, MOX05, 6.10 Nm, Ns = 2.60E+01 cycles.

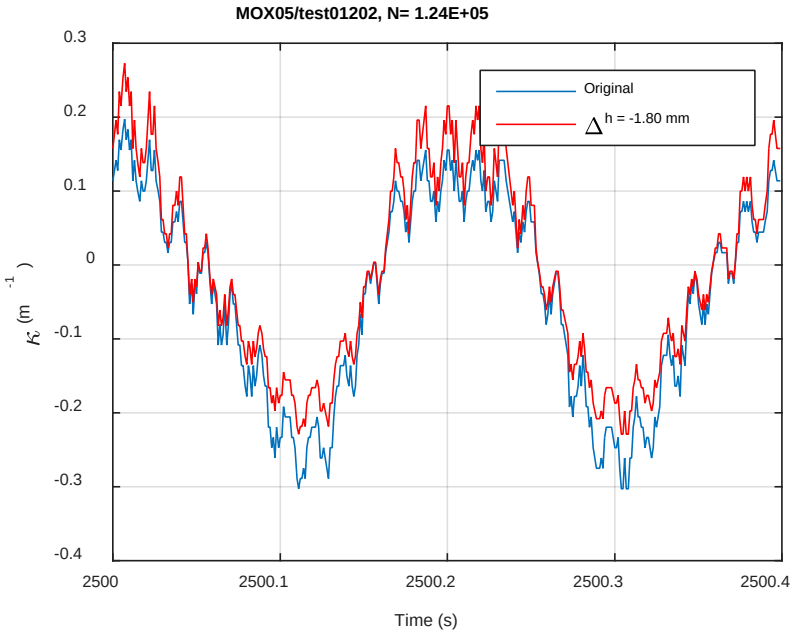
MOX05/test01202, N= 1.24E+05
Original
Δh = -1.80 mm
κ (m-1)
Time (s)
0.3
0.2
0.1
0
-0.1
-0.2
-0.3
-0.4
2500
2500.1
2500.2
2500.3
2500.4

(a)

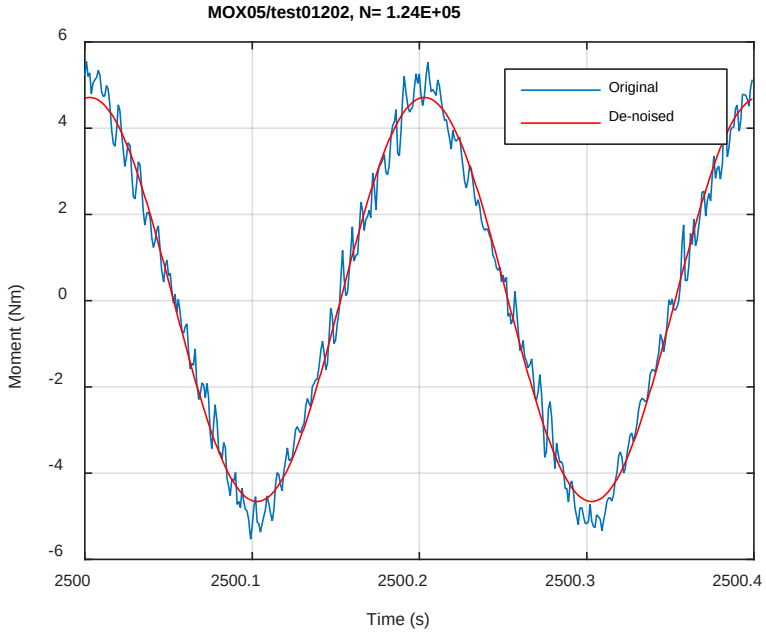
MOX05/test01202, N= 1.24E+05
Original
De-noised
Moment (Nm)
Time (s)
6
4
2
0
-2
-4
-6
2500
2500.1
2500.2
2500.3
2500.4

(b)

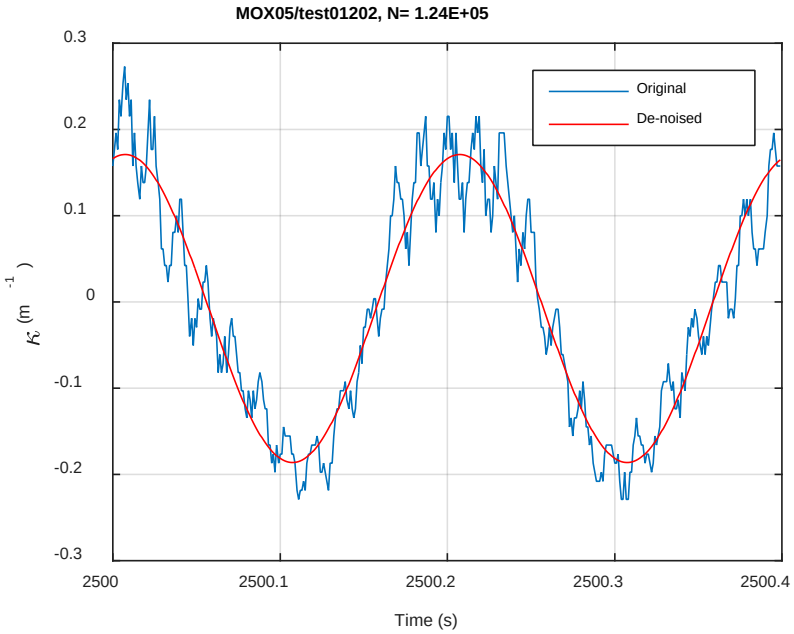

(c)

Fig. C.11. Monitoring-based responses: (a) curvature, (b) moment, (c) curvature, MOX05, 6.10 Nm, Ns = 1.24E+05 cycles.

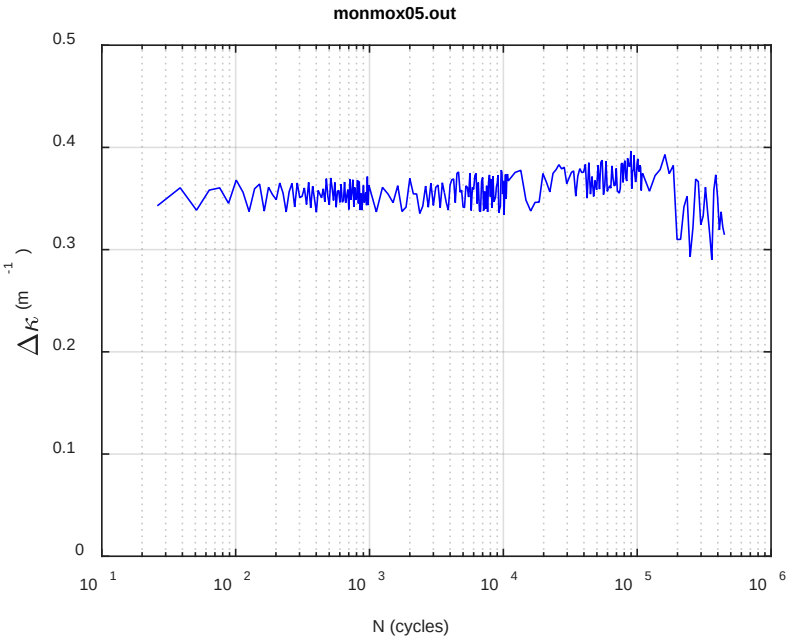
monmox05.out
0.5
0.4
0.3
0.2
0.1
0
Δκ (m -1)
10 1
10 2
10 3
10 4
10 5
10 6
N (cycles)

(a)

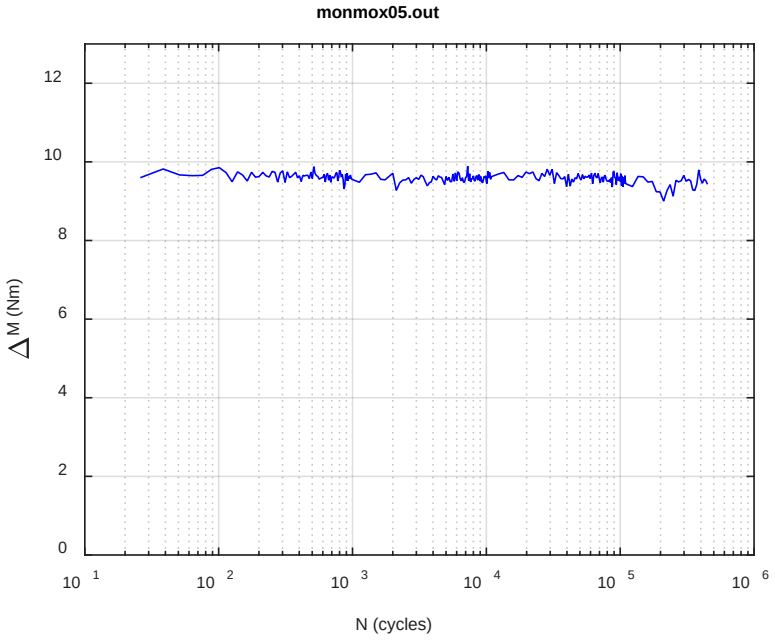
monmox05.out
12
10
8
6
4
2
0
Δ M (Nm)
10 1
10 2
10 3
10 4
10 5
10 6
N (cycles)

(b)

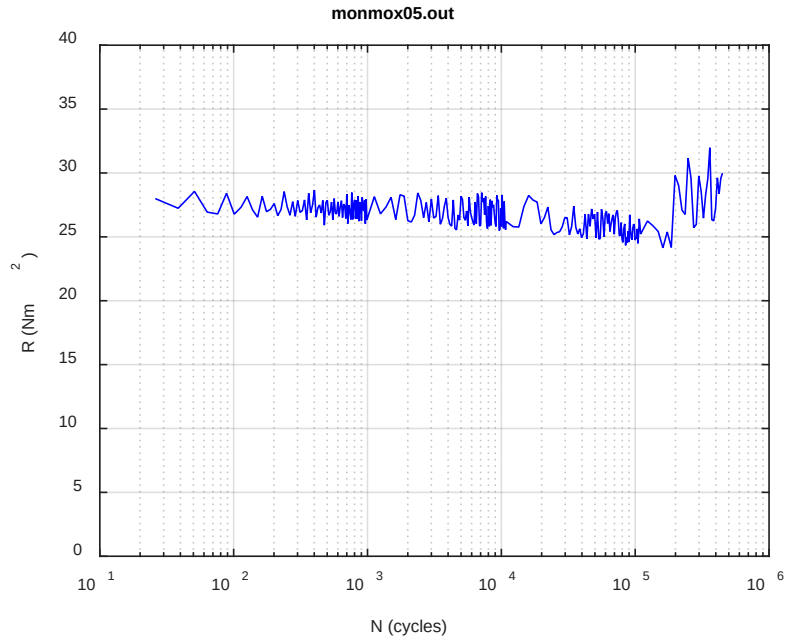
monmox05.out
R (Nm 2)
N (cycles)

(c)

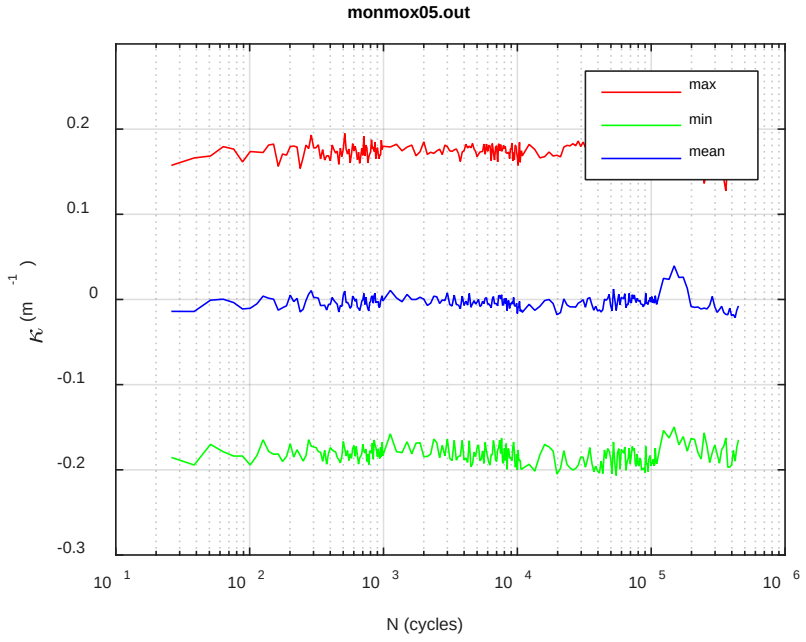
monmox05.out
max
min
mean
κ (m -1)
N (cycles)

(d)

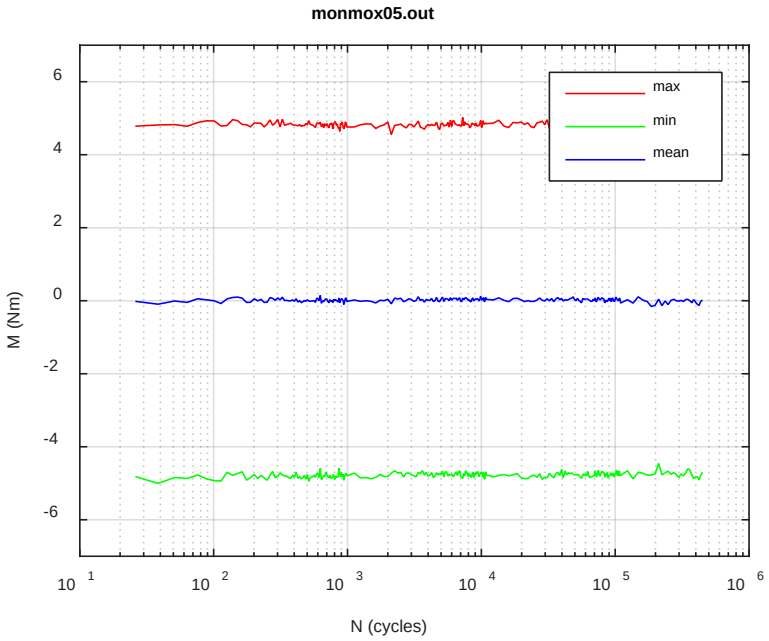

(e)

Fig. C.12. Monitoring-based responses: (a) curvature range, (b) moment range, (c) rigidity, (d) curvature peak/valley, (e) moment peak/valley, MOX05, 6.10 Nm, Nf = 4.49E+05 cycles.

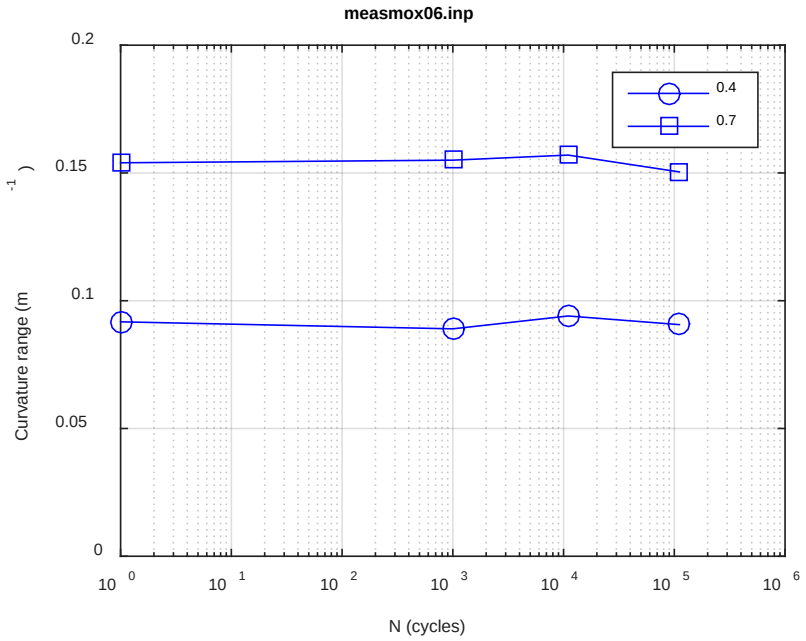
measmox06.inp
0.2
0.15
0.1
0.05
0
Curvature range (m -1)
0.4
0.7
10 0
10 1
10 2
10 3
10 4
10 5
10 6
N (cycles)

(a)

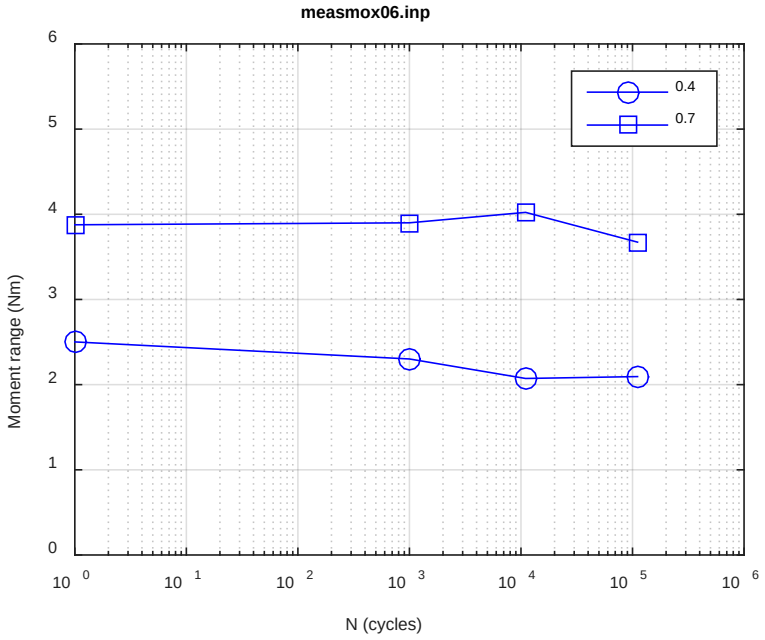
measmox06.inp
6
5
4
3
2
1
0
Moment range (Nm)
0.4
0.7
10 0
10 1
10 2
10 3
10 4
10 5
10 6
N (cycles)

(b)

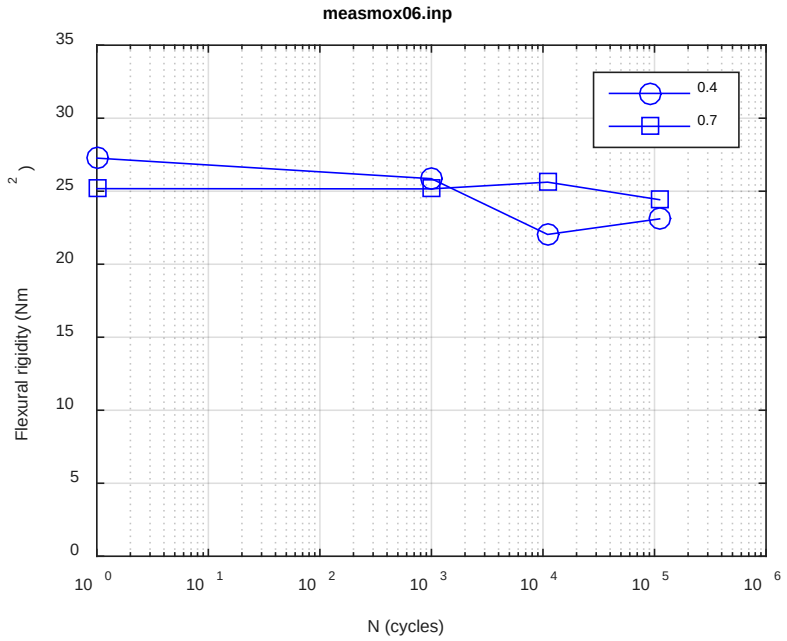
measmox06.inp
Flexural rigidity (Nm 2)
N (cycles)
0.4
0.7
35
30
25
20
15
10
5
0
10 0
10 1
10 2
10 3
10 4
10 5
10 6

(c)

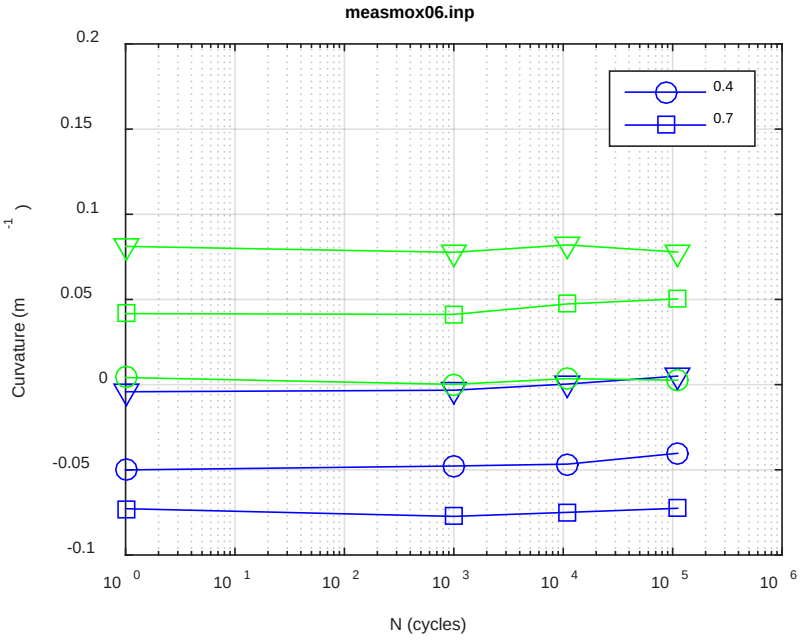
measmox06.inp
Curvature (m -1)
N (cycles)
0.4
0.7
0.2
0.15
0.1
0.05
0
-0.05
-0.1
10 0
10 1
10 2
10 3
10 4
10 5
10 6

(d)

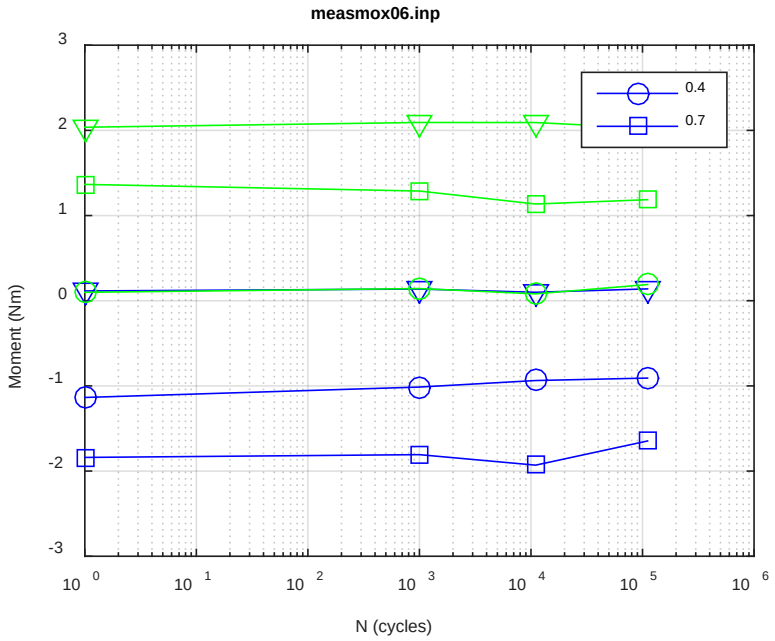

(e)

Fig. C.13. Measurement-based responses: (a) curvature range, (b) moment range, (c) rigidity, (d) curvature peak/valley, (e) moment peak/valley, MOX06, 5.08 Nm.

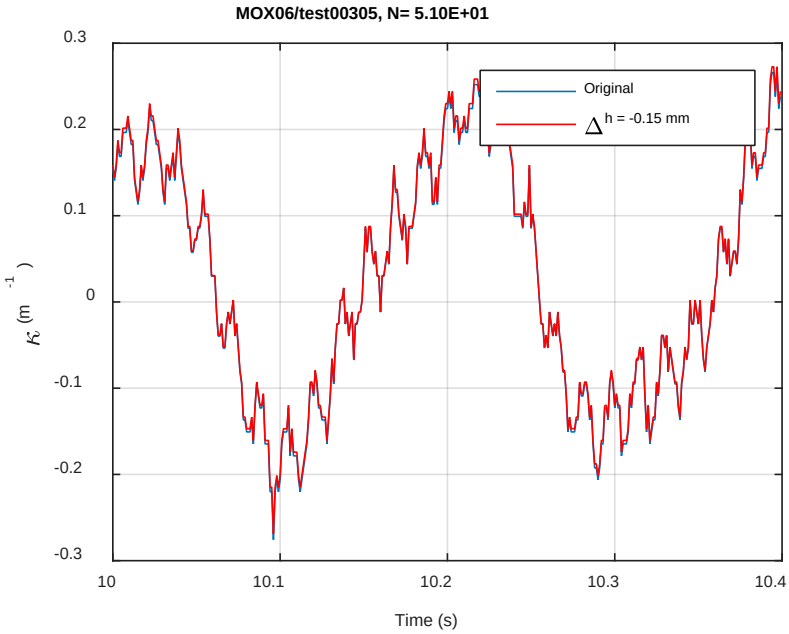
MOX06/test00305, N= 5.10E+01
Original
Δh = -0.15 mm
κ (m-1)
Time (s)

(a)

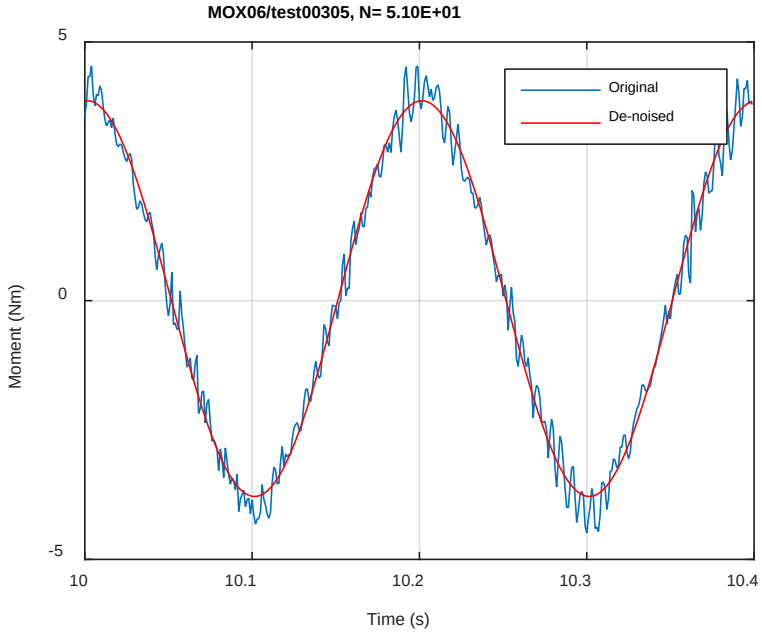
MOX06/test00305, N= 5.10E+01
Original
De-noised
Moment (Nm)
Time (s)

(b)

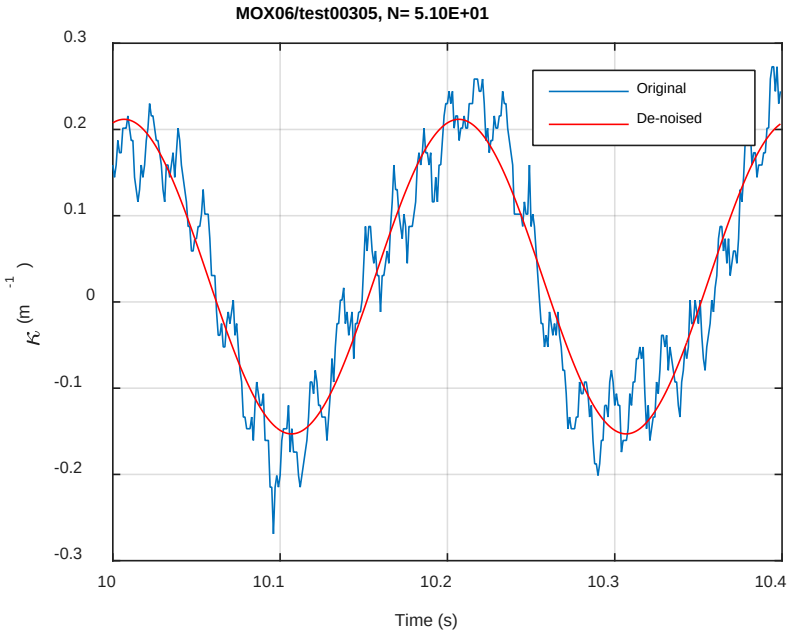

(c)

Fig. C.14. Monitoring-based responses: (a) curvature, (b) moment, (c) curvature, MOX06, 5.08 Nm, Ns = 5.10E+01 cycles.

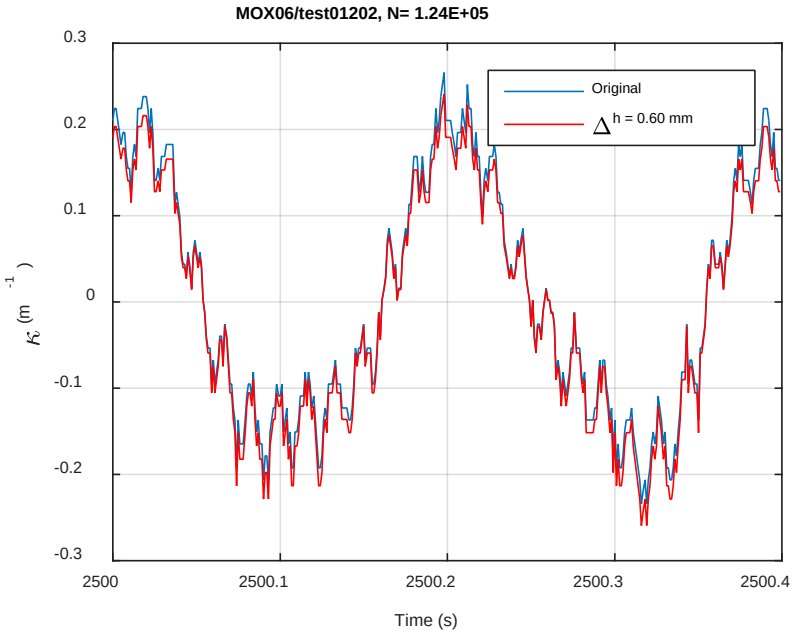
MOX06/test01202, N= 1.24E+05
Original
Δh = 0.60 mm
κ (m-1)
Time (s)

(a)

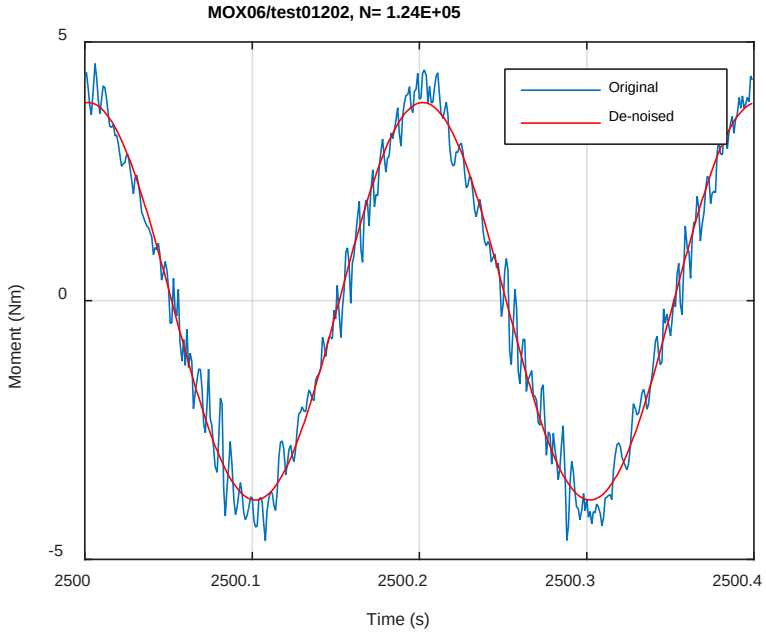
MOX06/test01202, N= 1.24E+05
Original
De-noised
Moment (Nm)
Time (s)

(b)

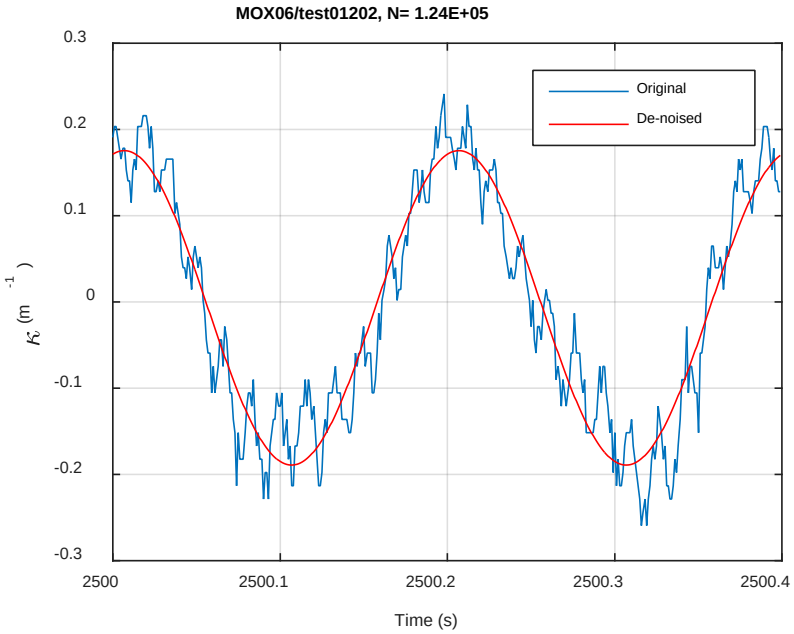

(c)

Fig. C.15. Monitoring-based responses: (a) curvature, (b) moment, (c) curvature, MOX06, 5.08 Nm, Ns = 1.24E+05 cycles.

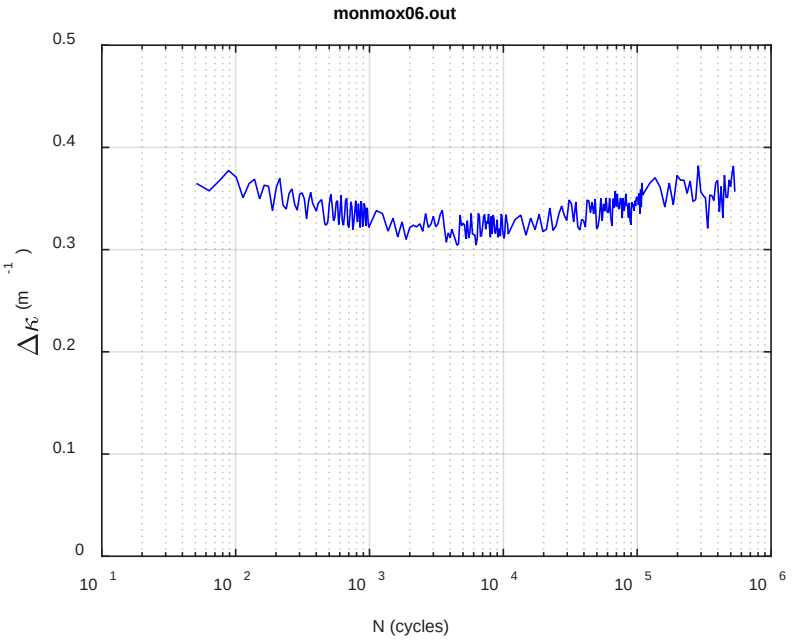
monmox06.out
0.5
0.4
0.3
0.2
0.1
0
Δκ (m-1)
10 1
10 2
10 3
10 4
10 5
10 6
N (cycles)

(a)

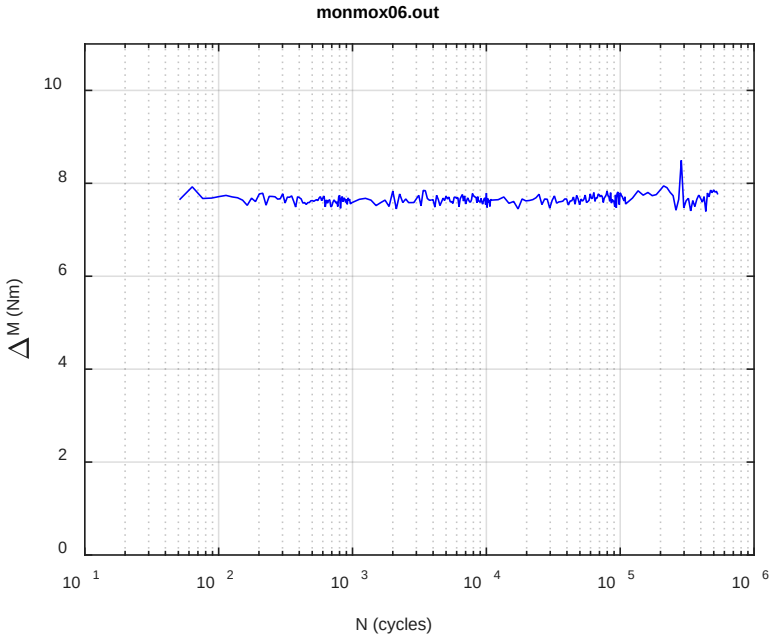
monmox06.out
10
8
6
4
2
0
Δ M (Nm)
10 1
10 2
10 3
10 4
10 5
10 6
N (cycles)

(b)

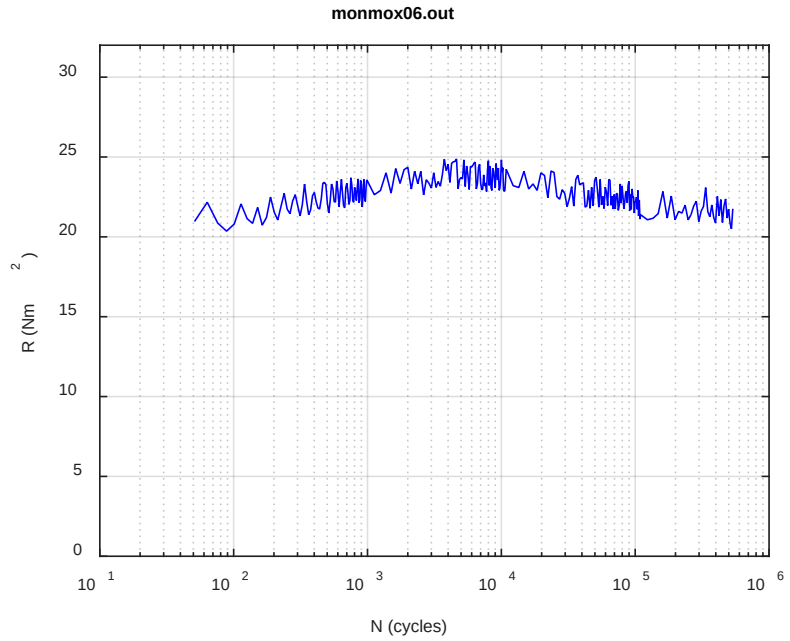
monmox06.out
R (Nm^2)
N (cycles)

(c)

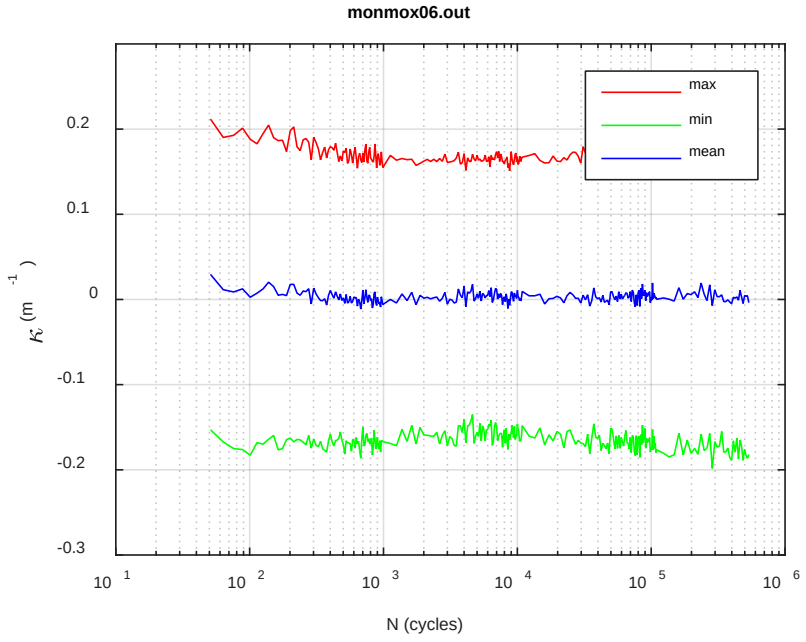
monmox06.out
max
min
mean
κ (m^-1)
N (cycles)

(d)

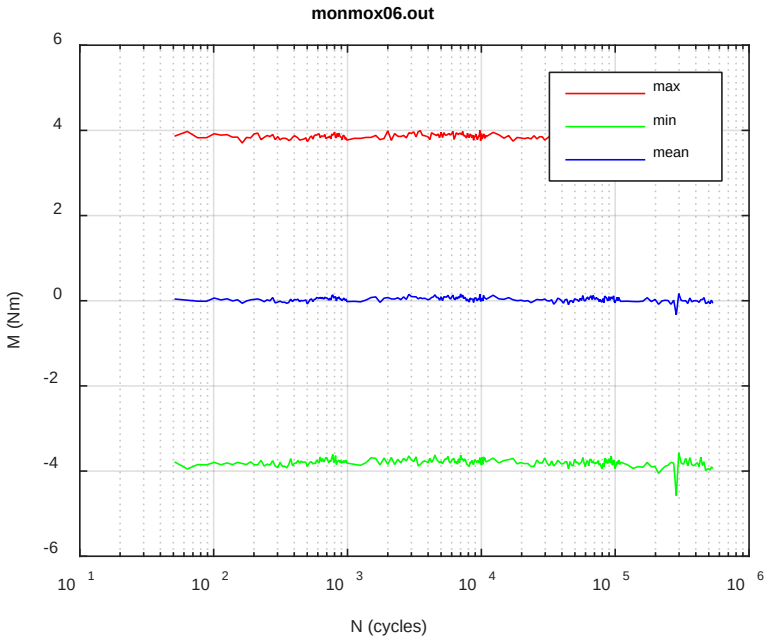

(e)

Fig. C.16. Monitoring-based responses: (a) curvature range, (b) moment range, (c) rigidity, (d) curvature peak/valley, (e) moment peak/valley, MOX06, 5.08 Nm, Nf = 5.42E+05 cycles.

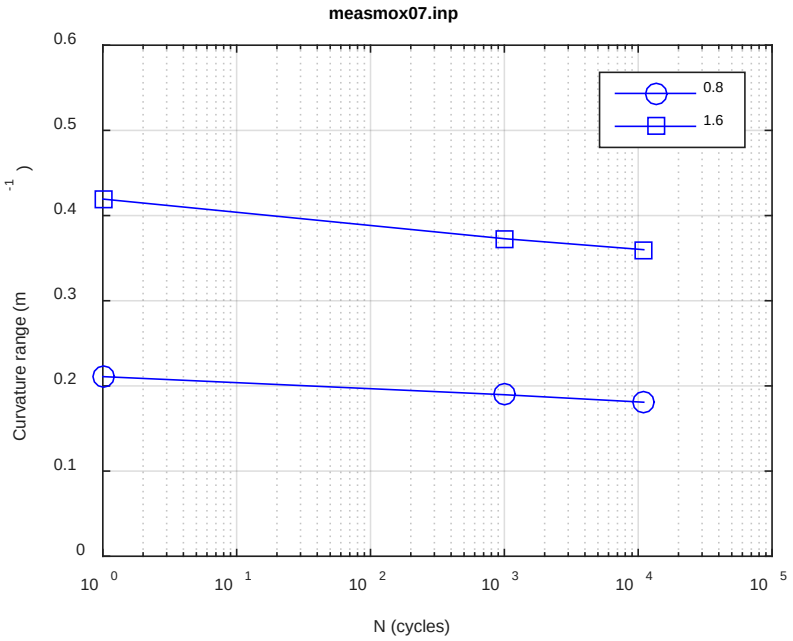
measmox07.inp
0.8
1.6
Curvature range (m -1)
N (cycles)
0
0.1
0.2
0.3
0.4
0.5
0.6
10 0
10 1
10 2
10 3
10 4
10 5

(a)

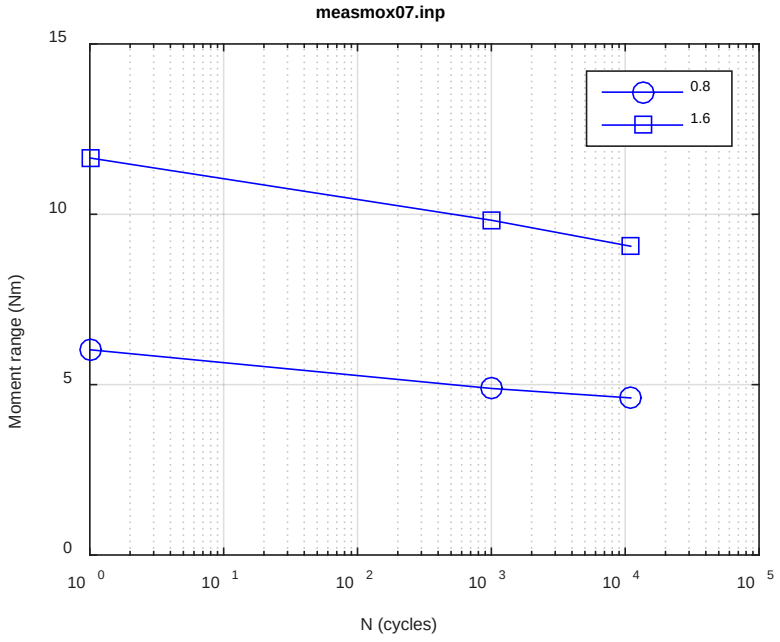
measmox07.inp
0.8
1.6
Moment range (Nm)
N (cycles)
0
5
10
15
10 0
10 1
10 2
10 3
10 4
10 5

(b)

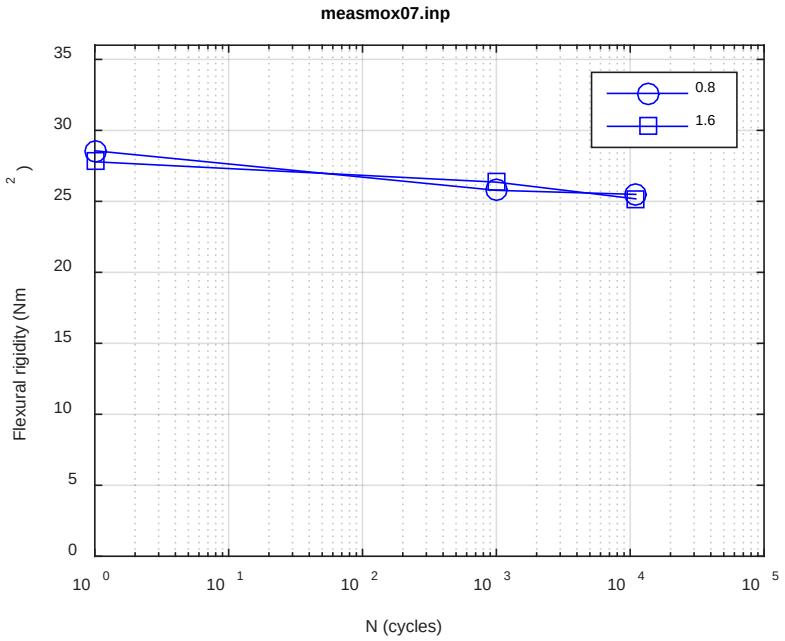
measmox07.inp
Flexural rigidity (Nm 2)
N (cycles)
0.8
1.6
35
30
25
20
15
10
5
0
10 0
10 1
10 2
10 3
10 4
10 5

(c)

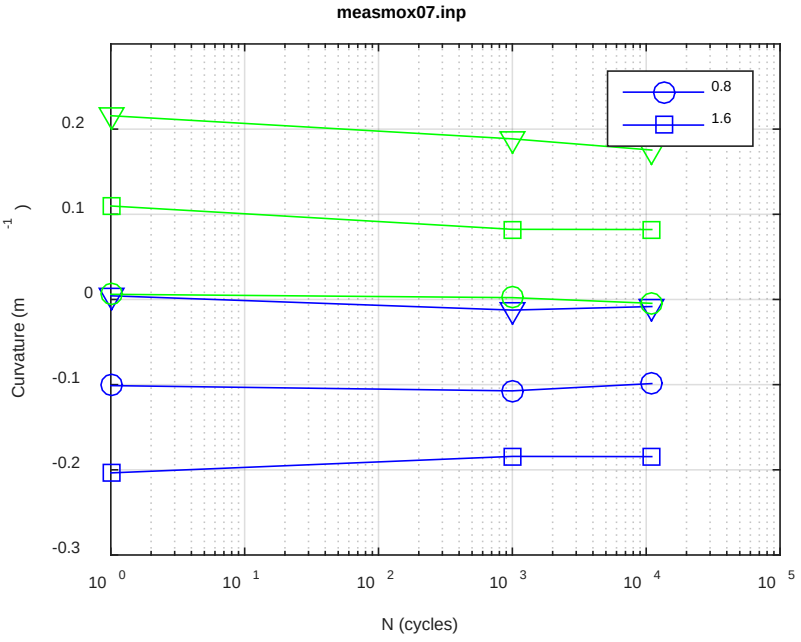
measmox07.inp
Curvature (m -1)
N (cycles)
0.8
1.6
0.2
0.1
0
-0.1
-0.2
-0.3
10 0
10 1
10 2
10 3
10 4
10 5

(d)

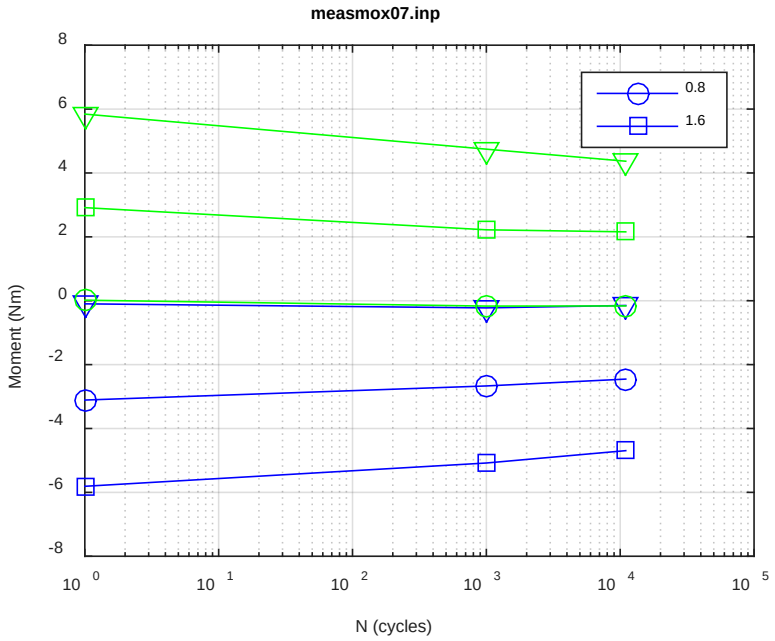

(e)

Fig. C.17. Measurement-based responses: (a) curvature range, (b) moment range, (c) rigidity, (d) curvature peak/valley, (e) moment peak/valley, MOX07, 15.24 Nm.

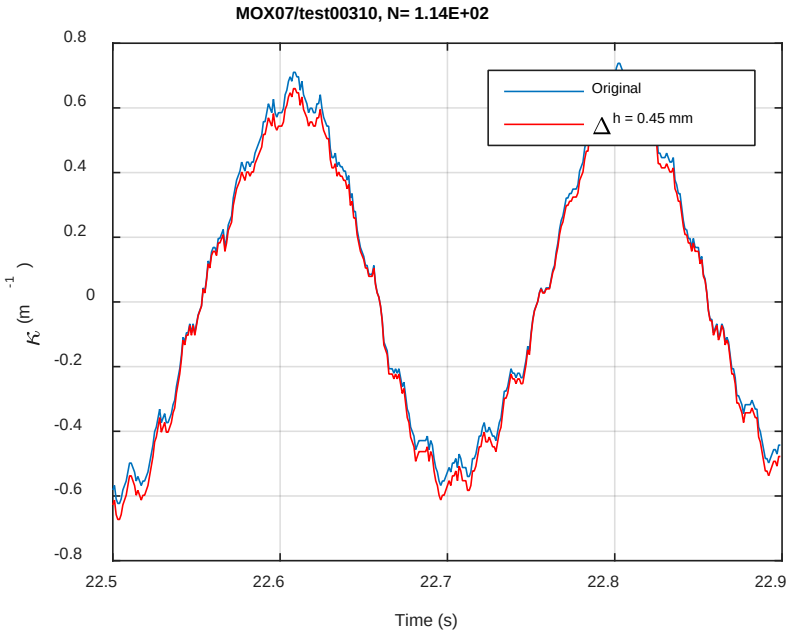
MOX07/test00310, N= 1.14E+02
Original
Δh = 0.45 mm
κ (m-1)
Time (s)

(a)

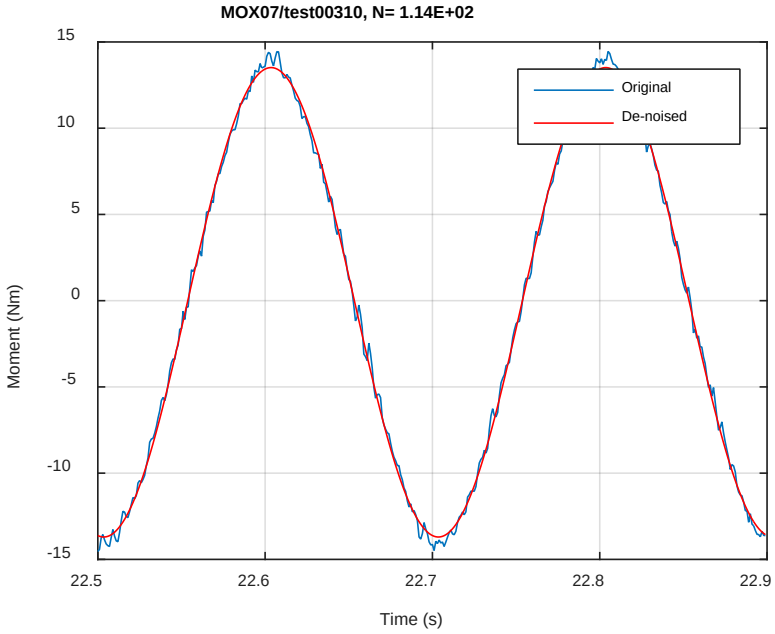
MOX07/test00310, N= 1.14E+02
Original
De-noised
Moment (Nm)
Time (s)

(b)

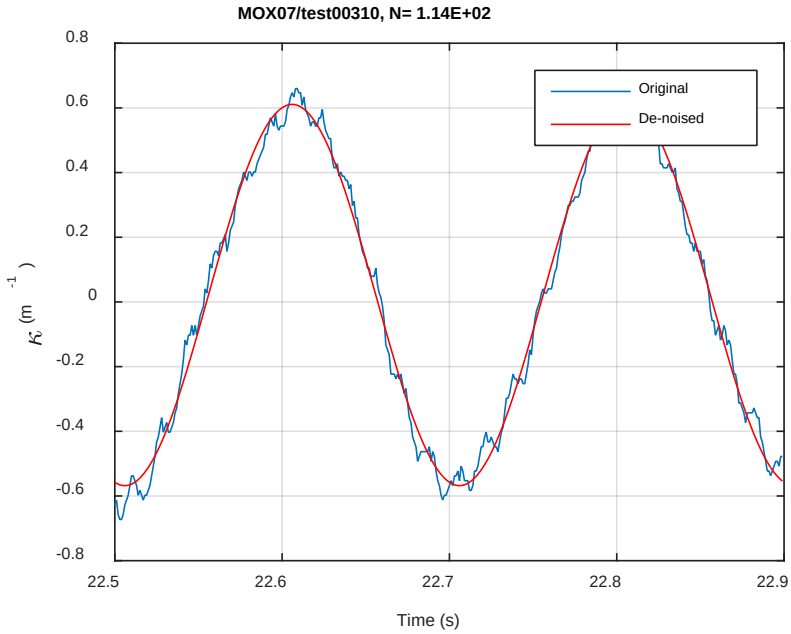

(c)

Fig. C.18. Monitoring-based responses: (a) curvature, (b) moment, (c) curvature, MOX07, 15.24 Nm, Ns = 1.14E+02 cycles.

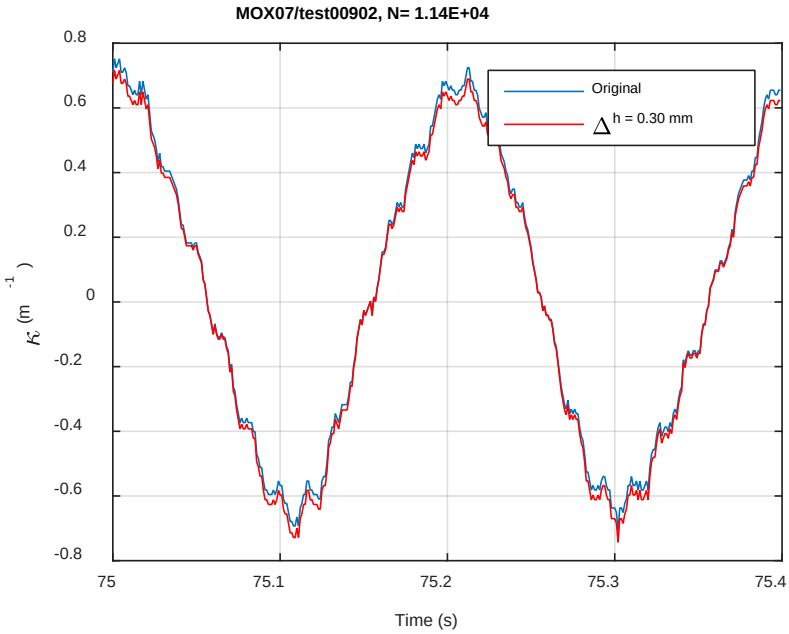
MOX07/test00902, N= 1.14E+04
Original
Δh = 0.30 mm
κ (m-1)
Time (s)

(a)

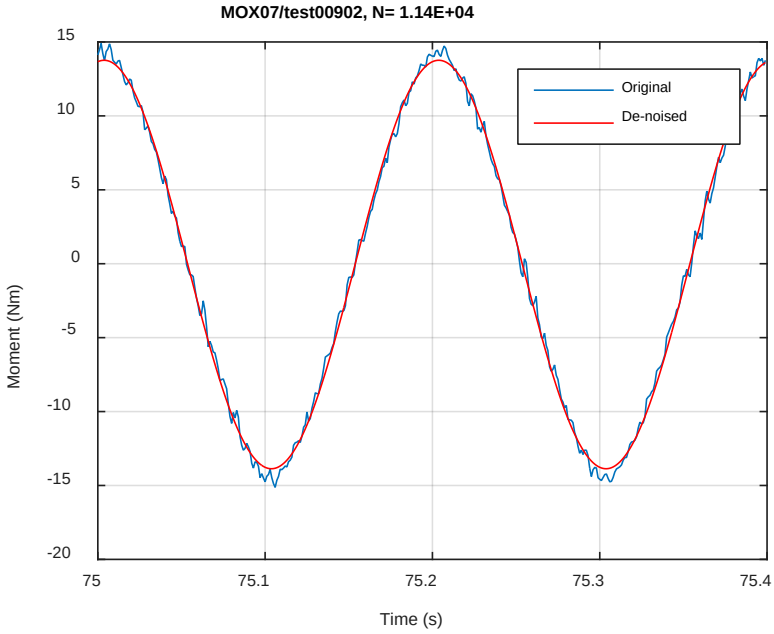
MOX07/test00902, N= 1.14E+04
Original
De-noised
Moment (Nm)
Time (s)

(b)

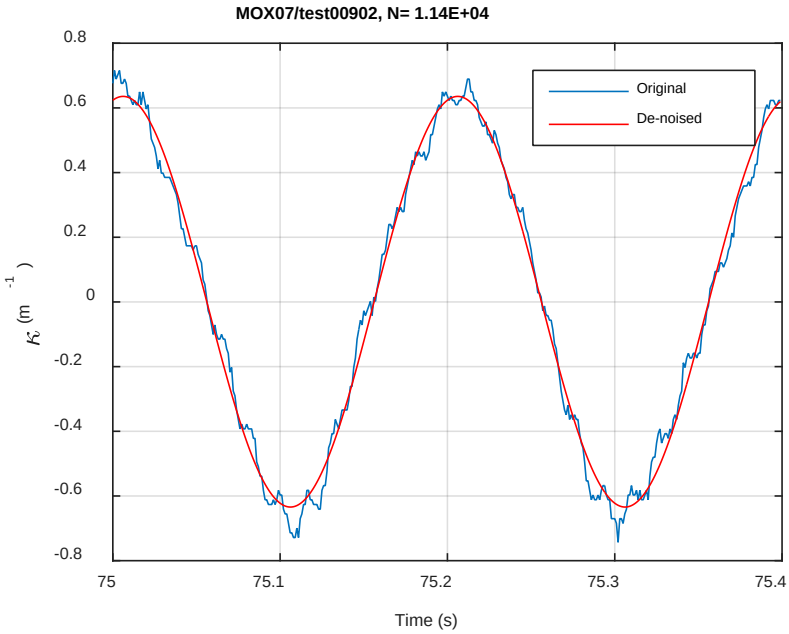

(c)

Fig. C.19. Monitoring-based responses: (a) curvature, (b) moment, (c) curvature, MOX07, 15.24 Nm, Ns = 1.14E+04 cycles.

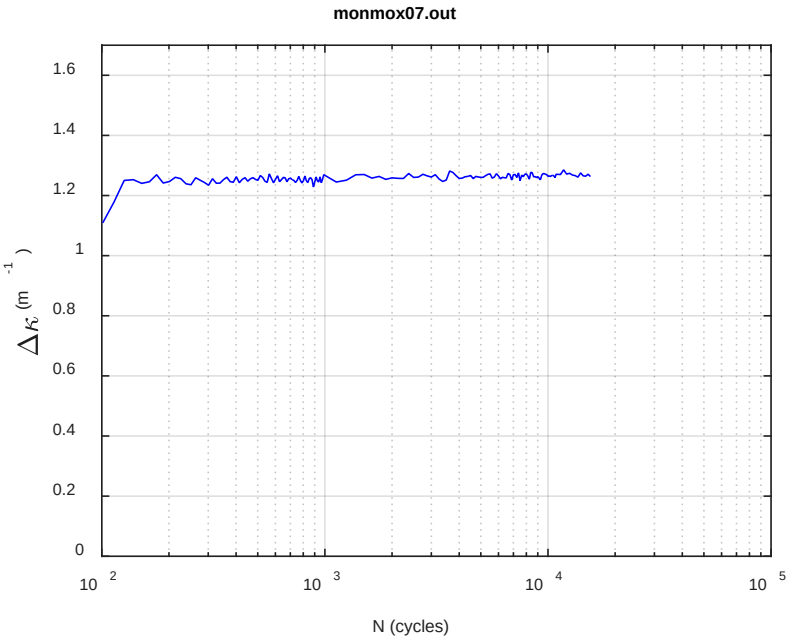
monmox07.out
1.6
1.4
1.2
1
0.8
0.6
0.4
0.2
0
Δκ (m-1)
10 2
10 3
10 4
10 5
N (cycles)

(a)

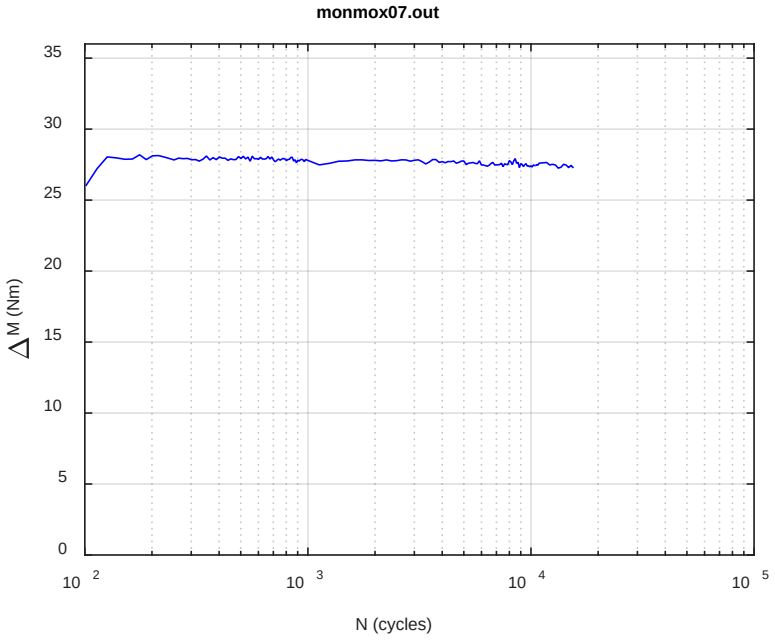
monmox07.out
35
30
25
20
15
10
5
0
ΔM (Nm)
10 2
10 3
10 4
10 5
N (cycles)

(b)

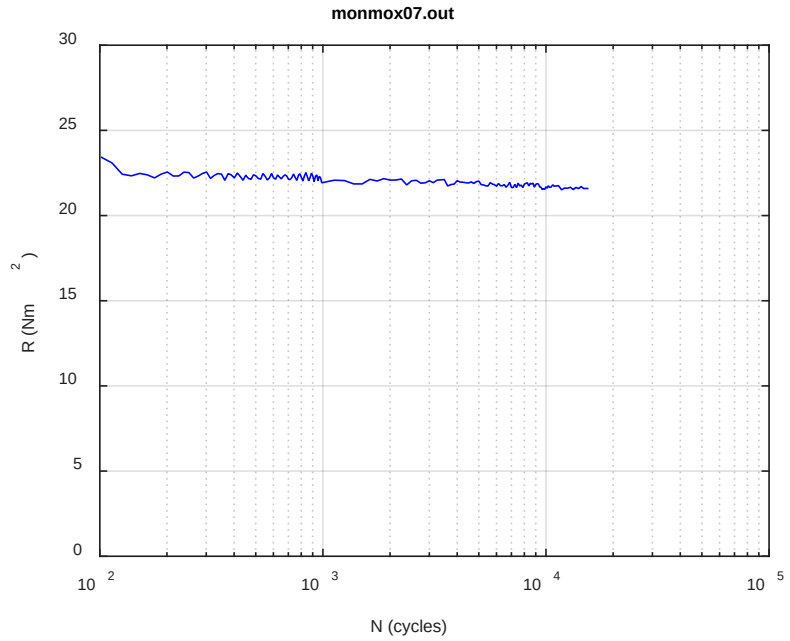
monmox07.out
R (Nm 2)
N (cycles)
30
25
20
15
10
5
0
10 2
10 3
10 4
10 5

(c)

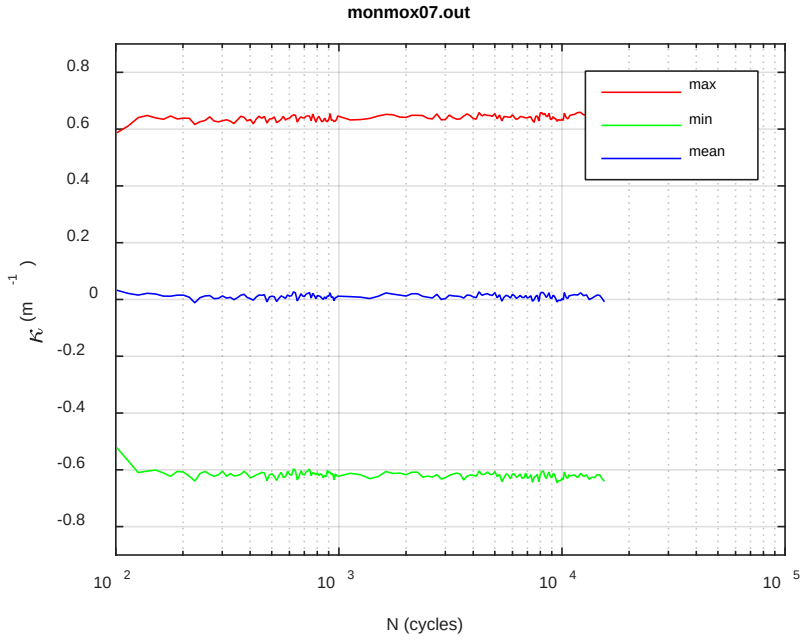
monmox07.out
κ (m -1)
N (cycles)
max
min
mean
0.8
0.6
0.4
0.2
0
-0.2
-0.4
-0.6
-0.8
10 2
10 3
10 4
10 5

(d)

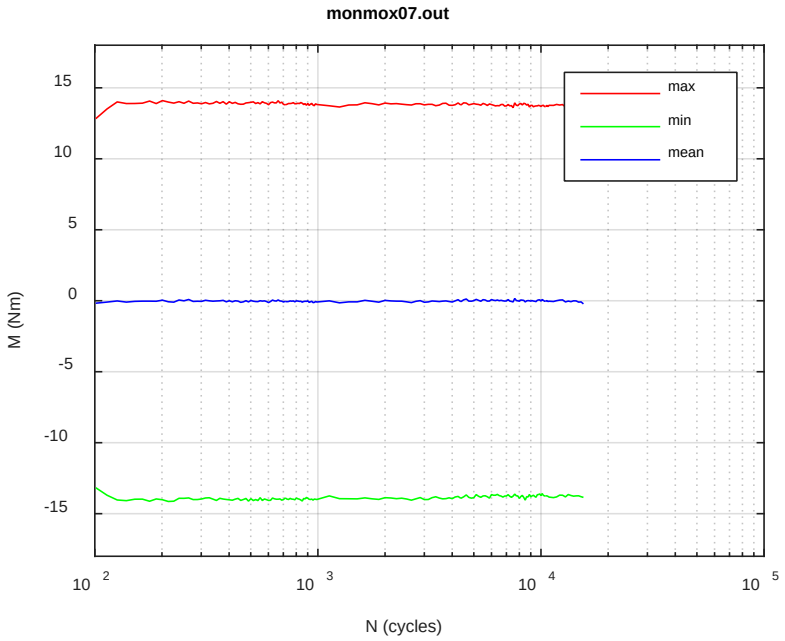

(e)

Fig. C.20. Monitoring-based responses: (a) curvature range, (b) moment range, (c) rigidity, (d) curvature peak/valley, (e) moment peak/valley, MOX07, 15.24 Nm, Nf = 1.55E+04 cycles.

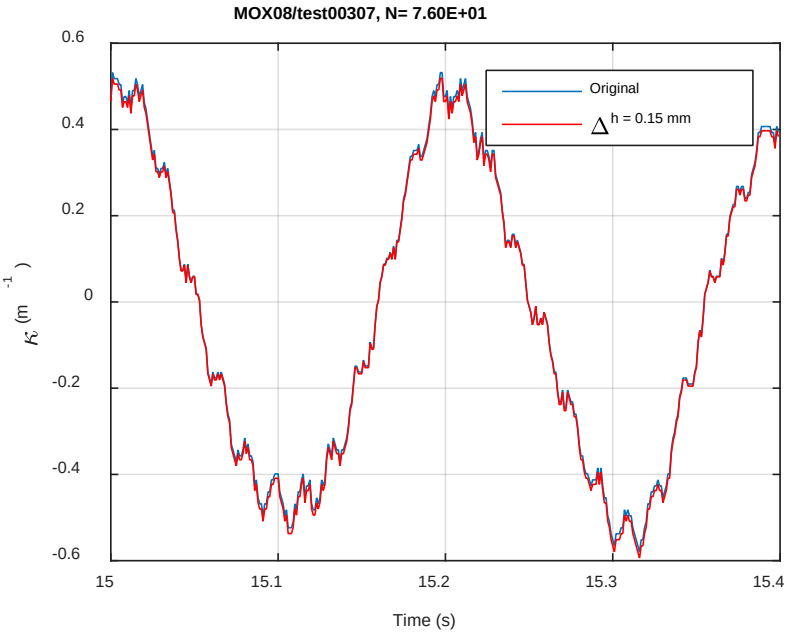
MOX08/test00307, N= 7.60E+01
Original
Δh = 0.15 mm
κ (m-1)
Time (s)

(a)

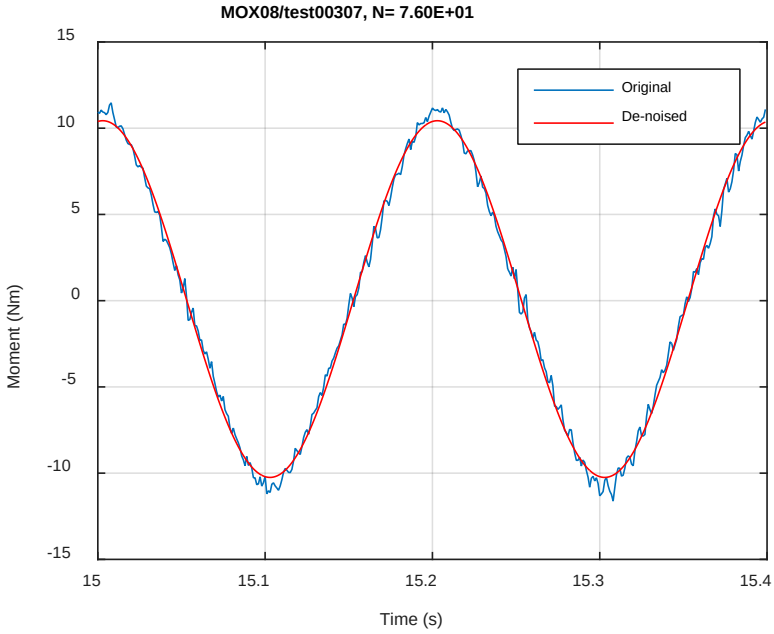
MOX08/test00307, N= 7.60E+01
Original
De-noised
Moment (Nm)
Time (s)

(b)

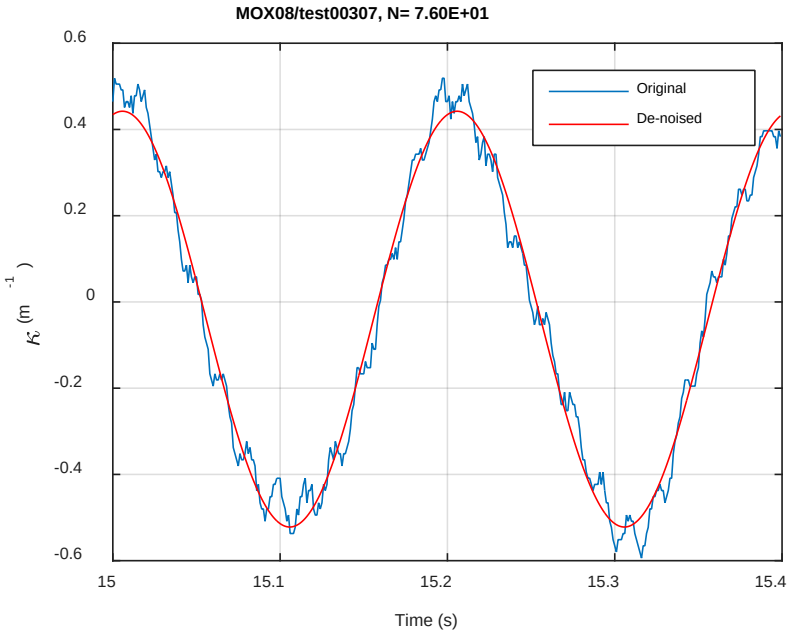

(c)

Fig. C.21. Monitoring-based responses: (a) curvature, (b) moment, (c) curvature, MOX08, 12.70 Nm, Ns = 7.60E+01 cycles.

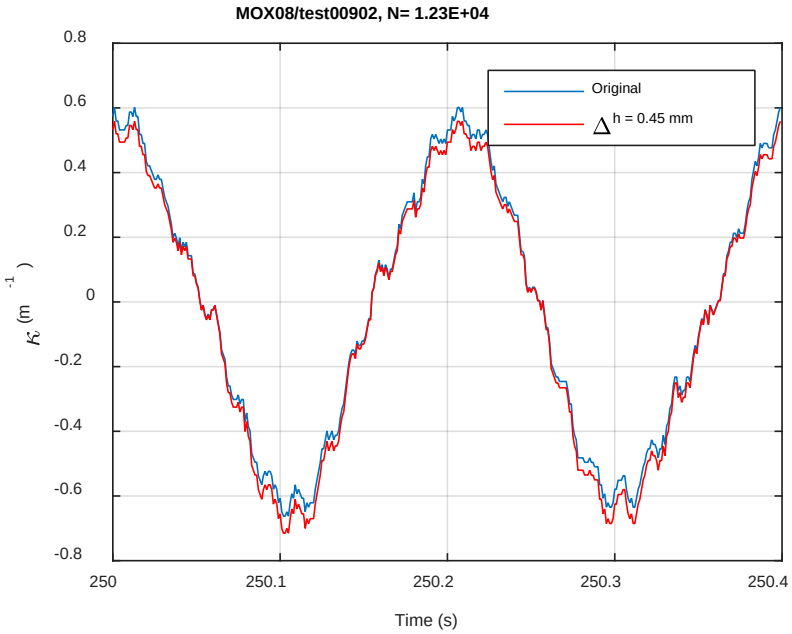
MOX08/test00902, N= 1.23E+04
Original
Δh = 0.45 mm
κ (m-1)
Time (s)
0.8
0.6
0.4
0.2
0
-0.2
-0.4
-0.6
-0.8
250
250.1
250.2
250.3
250.4

(a)

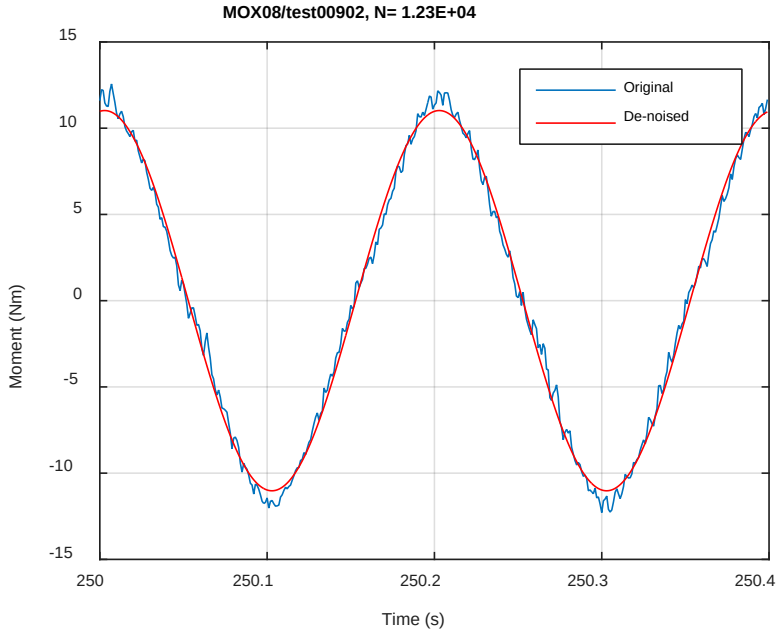
MOX08/test00902, N= 1.23E+04
Original
De-noised
Moment (Nm)
Time (s)
15
10
5
0
-5
-10
-15
250
250.1
250.2
250.3
250.4

(b)

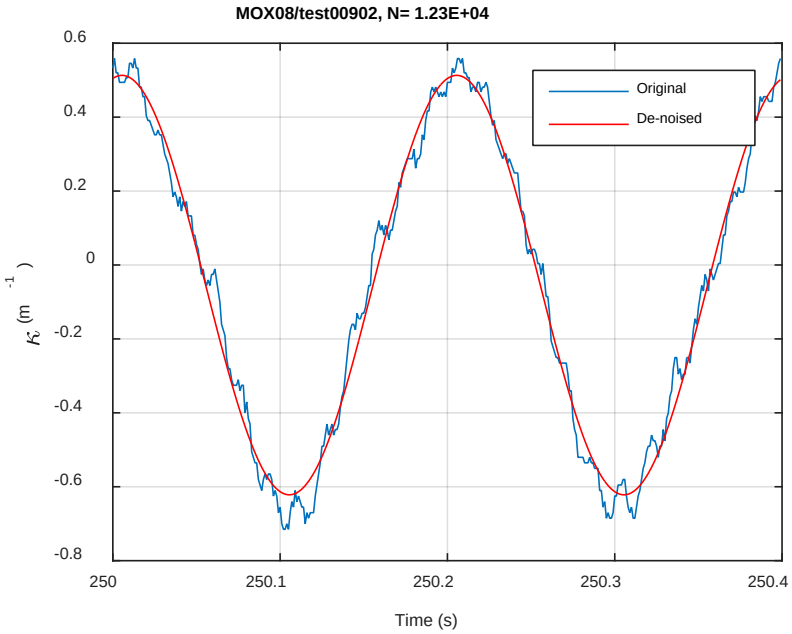

(c)

Fig. C.22. Monitoring-based responses: (a) curvature, (b) moment, (c) curvature, MOX08, 12.70 Nm, Ns = 1.23E+04 cycles.

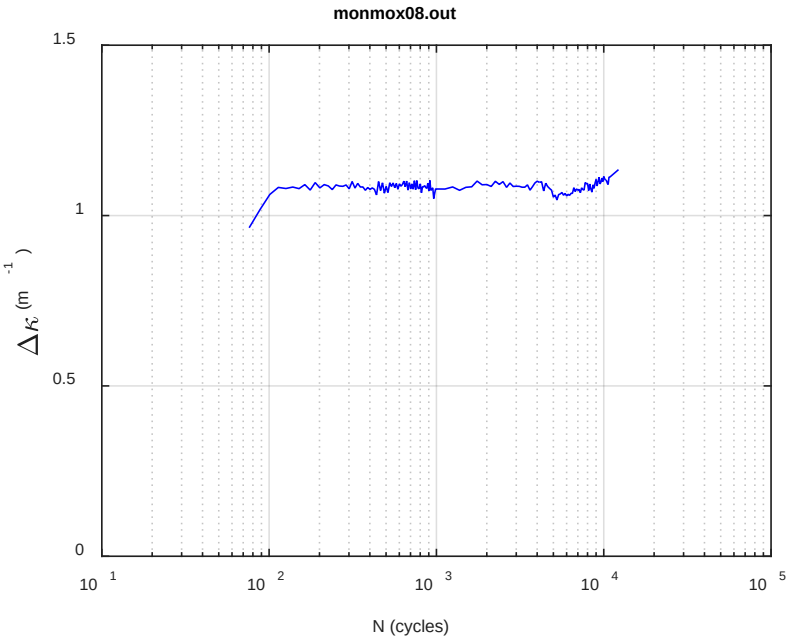
monmox08.out
1.5
1
0.5
0
Δκ (m-1)
10 1
10 2
10 3
10 4
10 5
N (cycles)

(a)

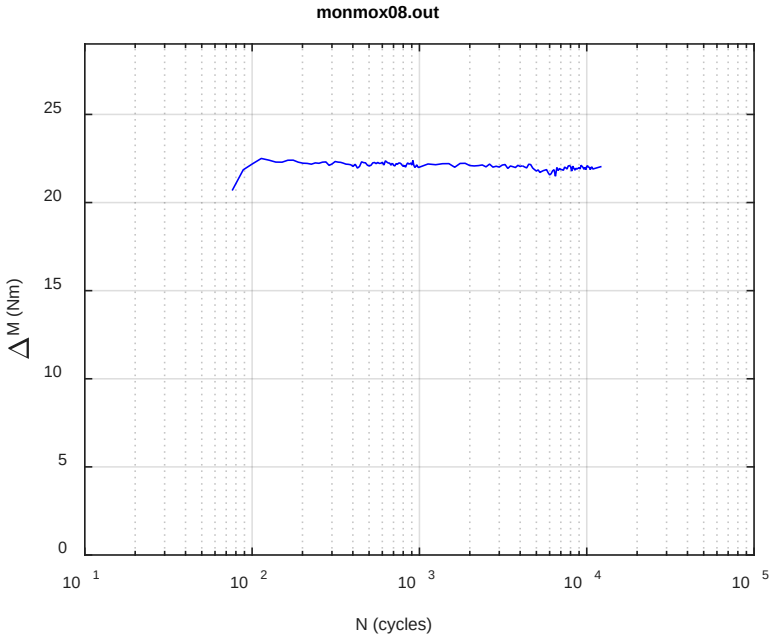
monmox08.out
25
20
15
10
5
0
Δ M (Nm)
10 1
10 2
10 3
10 4
10 5
N (cycles)

(b)

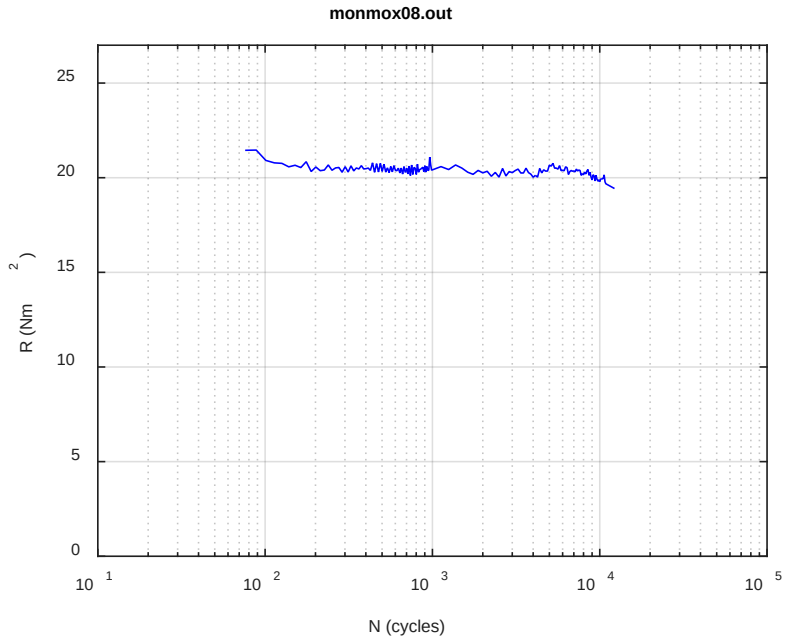
monmox08.out
25
20
15
10
5
0
R (Nm 2)
10 1
10 2
10 3
10 4
10 5
N (cycles)

(c)

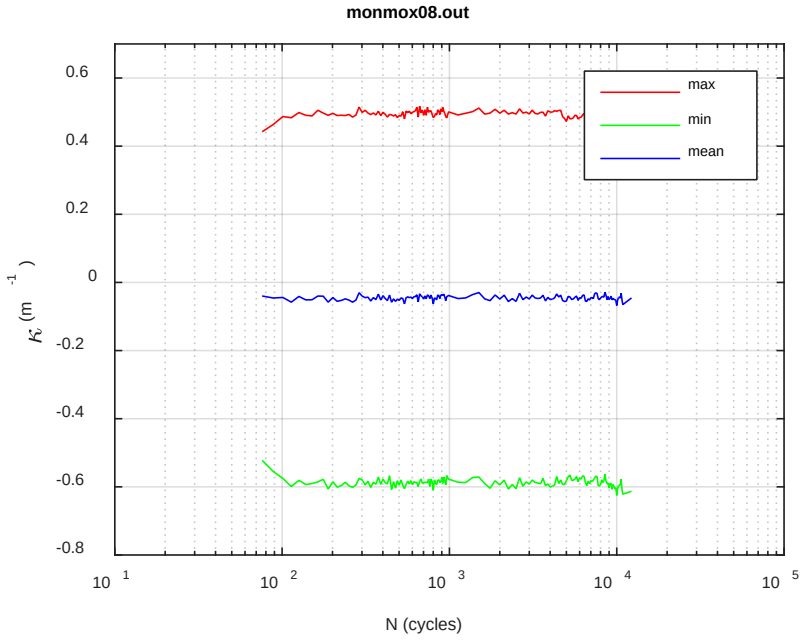
monmox08.out
max
min
mean
0.6
0.4
0.2
0
-0.2
-0.4
-0.6
-0.8
κ (m -1)
10 1
10 2
10 3
10 4
10 5
N (cycles)

(d)

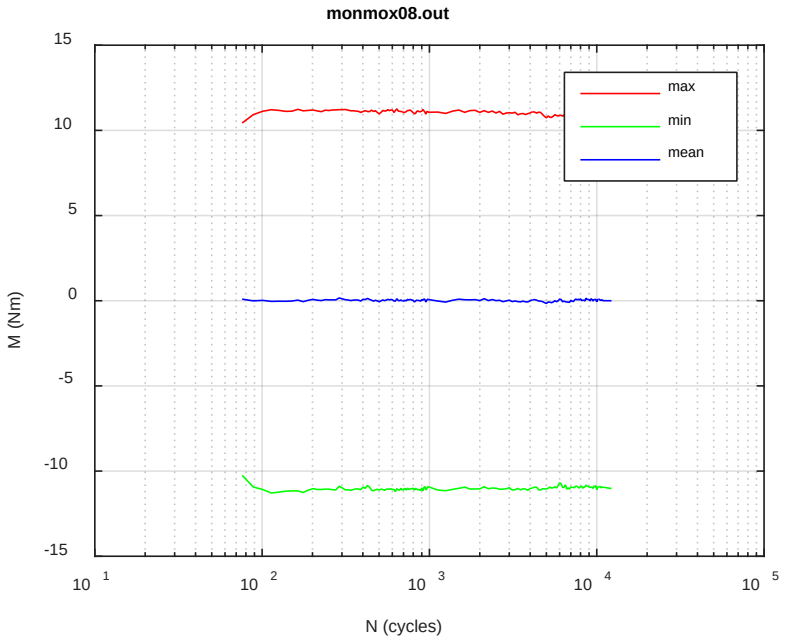

(e)

Fig. C.23. Monitoring-based responses: (a) curvature range, (b) moment range, (c) rigidity, (d) curvature peak/valley, (e) moment peak/valley, MOX08, 12.70 Nm, Nf = 1.29E+04 cycles.

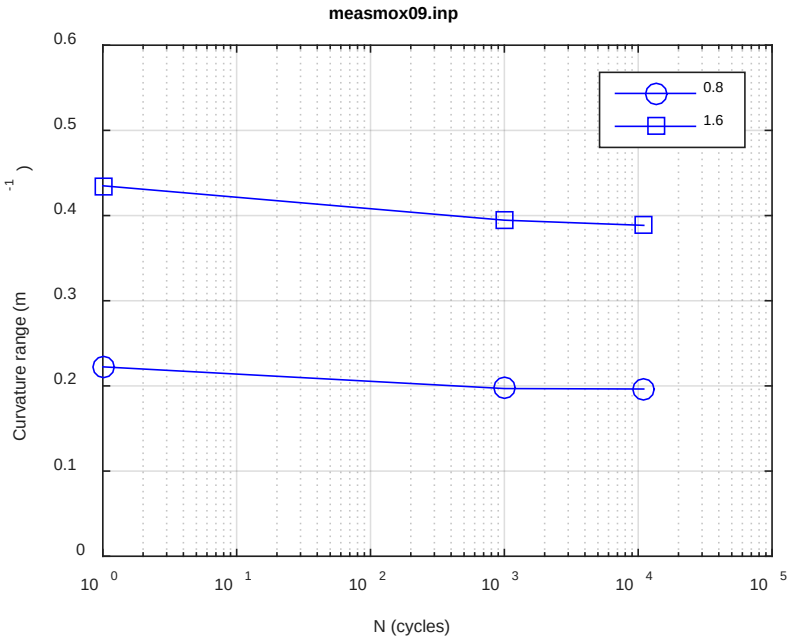
measmox09.inp
Curvature range (m -1)
N (cycles)
0.8
1.6
0
0.1
0.2
0.3
0.4
0.5
0.6
10 0
10 1
10 2
10 3
10 4
10 5

(a)

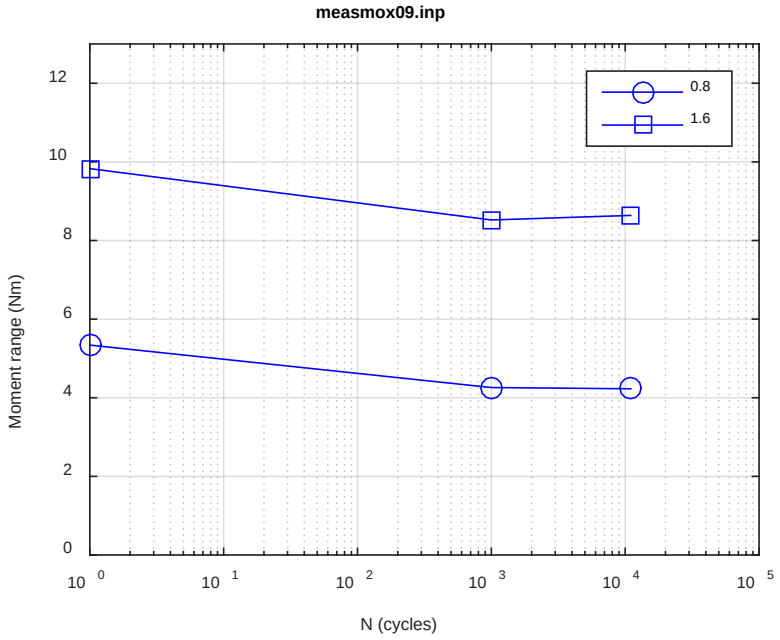
measmox09.inp
Moment range (Nm)
N (cycles)
0.8
1.6
0
2
4
6
8
10
12
10 0
10 1
10 2
10 3
10 4
10 5

(b)

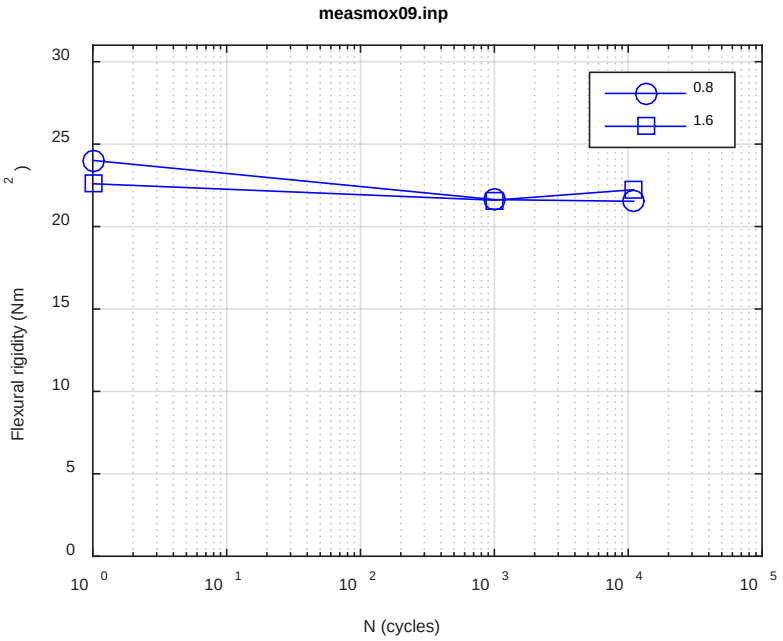
measmox09.inp
0.8
1.6
Flexural rigidity (Nm 2)
N (cycles)
30
25
20
15
10
5
0
10 0
10 1
10 2
10 3
10 4
10 5

(c)

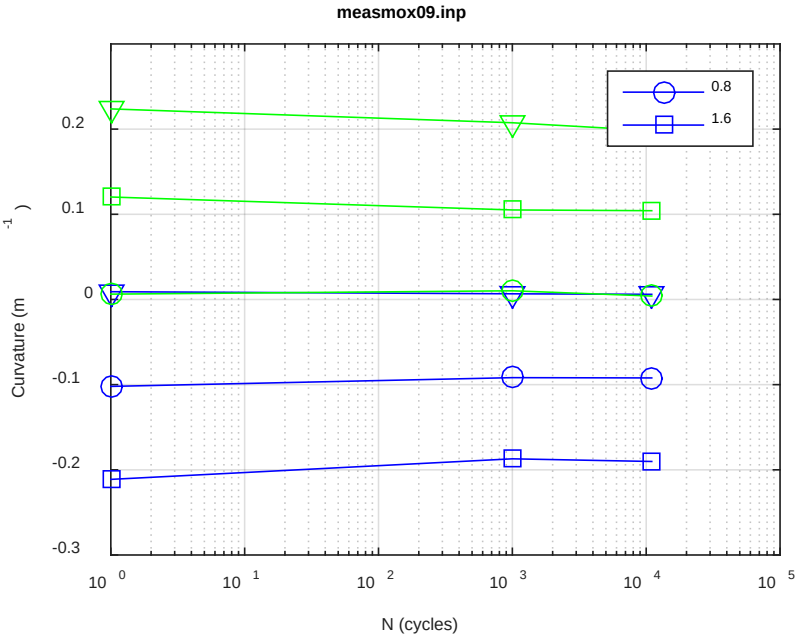
measmox09.inp
0.8
1.6
Curvature (m -1)
N (cycles)
0.2
0.1
0
-0.1
-0.2
-0.3
10 0
10 1
10 2
10 3
10 4
10 5

(d)

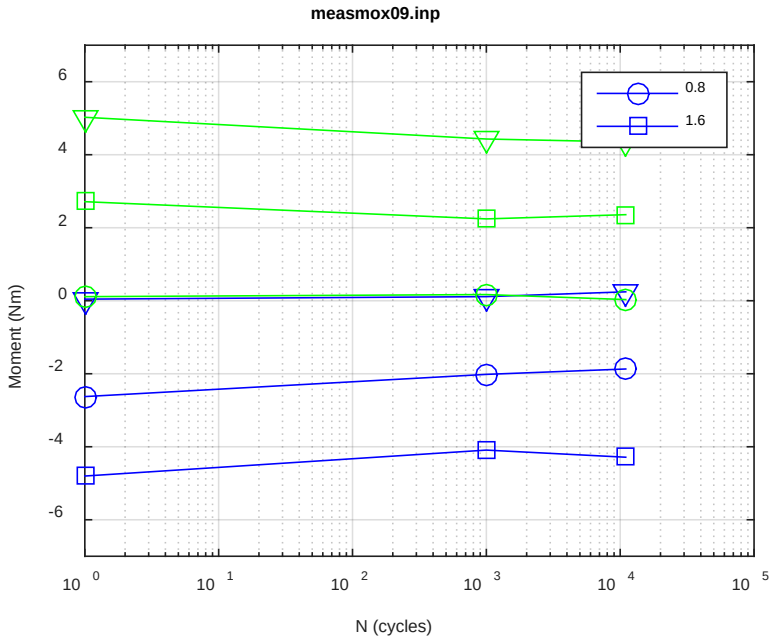

(e)

Fig. C.24. Measurement-based responses: (a) curvature range, (b) moment range, (c) rigidity, (d) curvature peak/valley, (e) moment peak/valley, MOX09, 7.62 Nm.

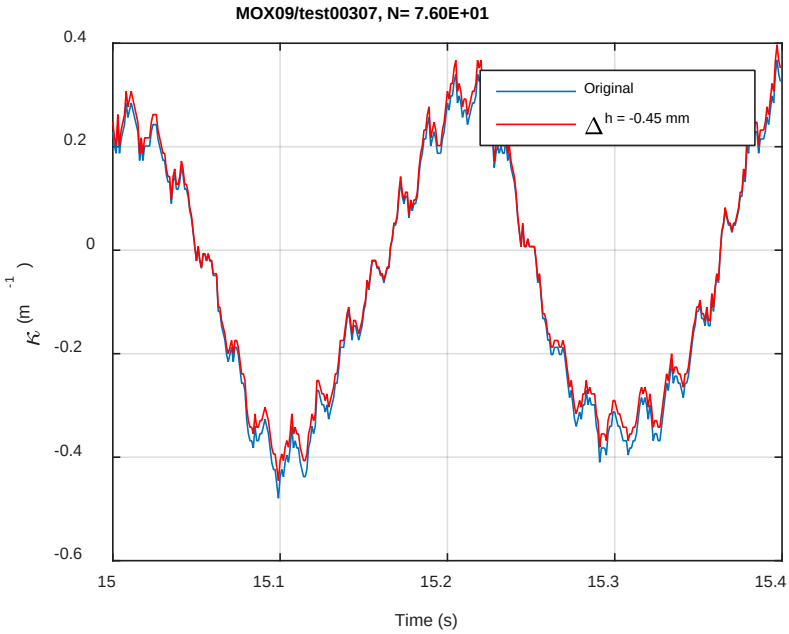
MOX09/test00307, N= 7.60E+01
Original
Δh = -0.45 mm
κ (m-1)
Time (s)

(a)

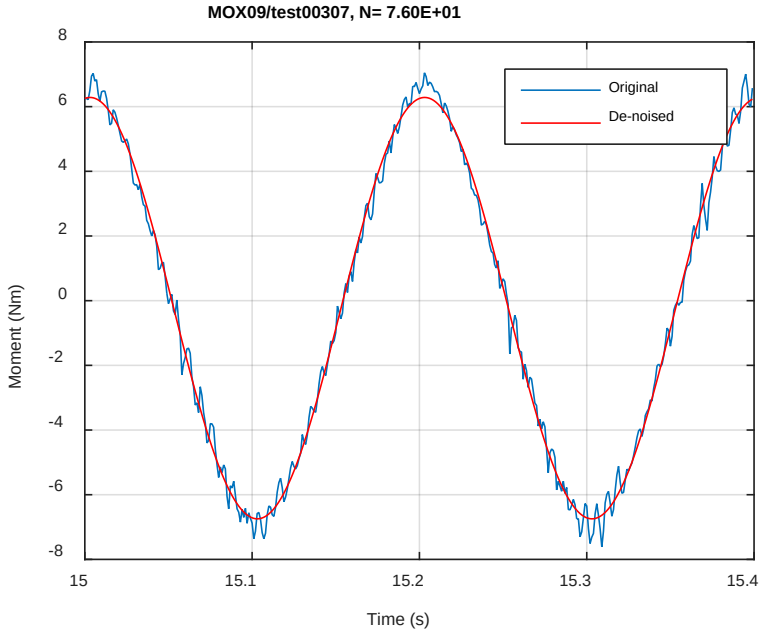
MOX09/test00307, N= 7.60E+01
Original
De-noised
Moment (Nm)
Time (s)

(b)

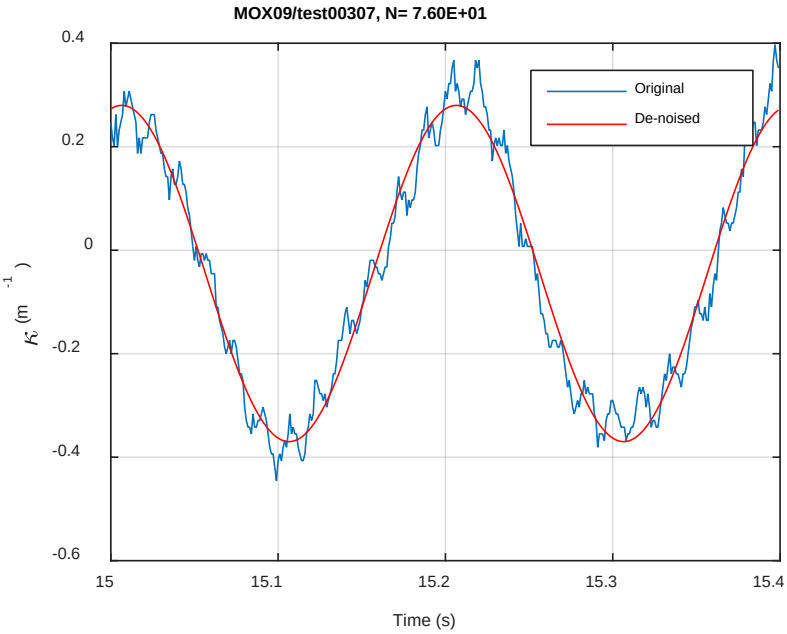

(c)

Fig. C.25. Monitoring-based responses: (a) curvature, (b) moment, (c) curvature, MOX09, 7.62 Nm, Ns = 7.60E+01 cycles.

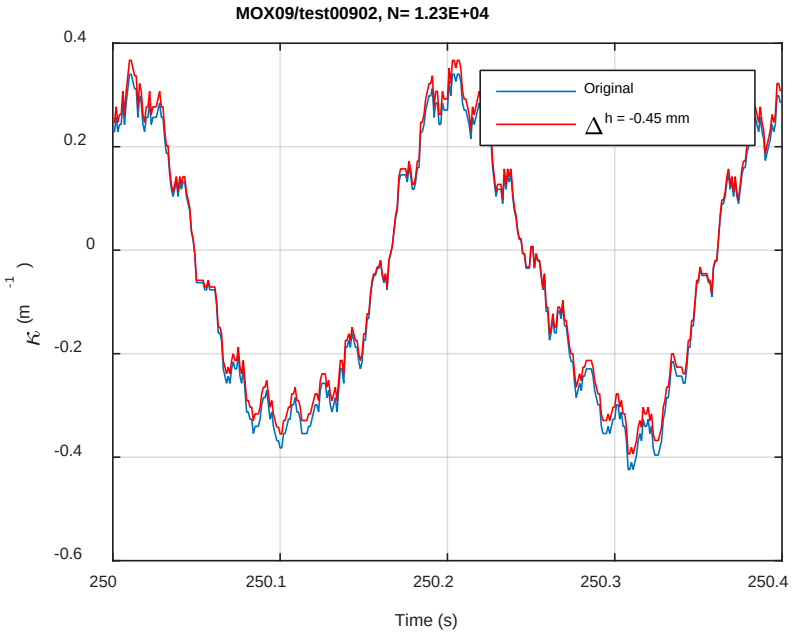
MOX09/test00902, N= 1.23E+04
Original
Δh = -0.45 mm
κ (m-1)
Time (s)
0.4
0.2
0
-0.2
-0.4
-0.6
250
250.1
250.2
250.3
250.4

(a)

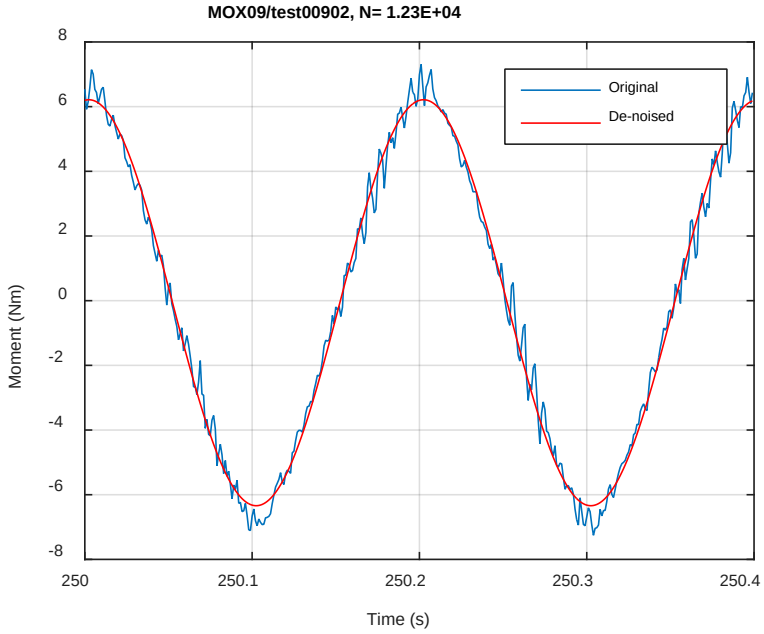
MOX09/test00902, N= 1.23E+04
Original
De-noised
Moment (Nm)
Time (s)
8
6
4
2
0
-2
-4
-6
-8
250
250.1
250.2
250.3
250.4

(b)

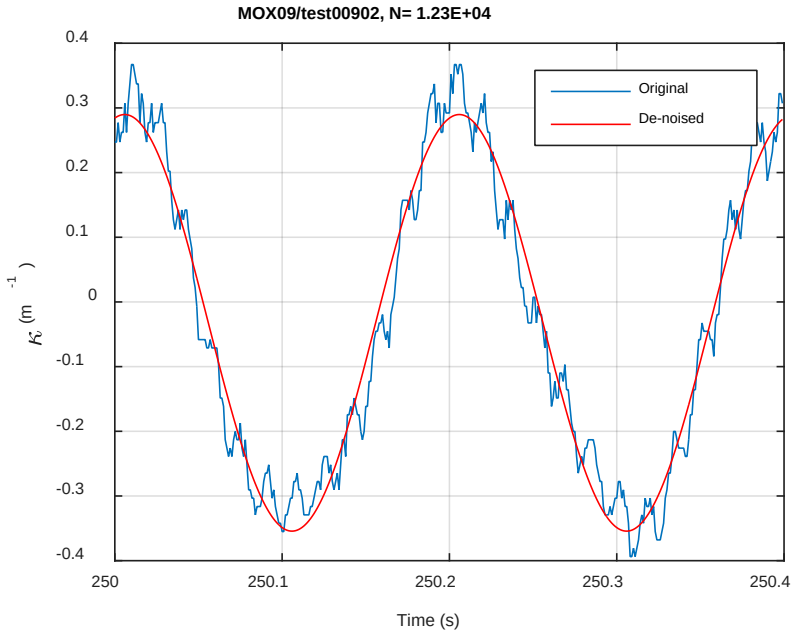

(c)

Fig. C.26. Monitoring-based responses: (a) curvature, (b) moment, (c) curvature, MOX09, 7.62 Nm, Ns = 1.23E+04 cycles.

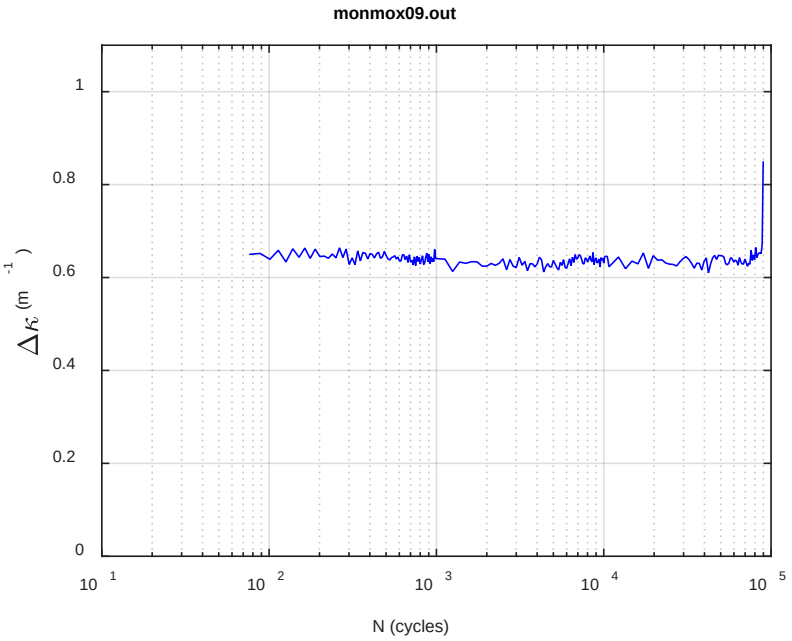
monmox09.out
1
0.8
0.6
0.4
0.2
0
Δκ (m -1)
10 1
10 2
10 3
10 4
10 5
N (cycles)

(a)

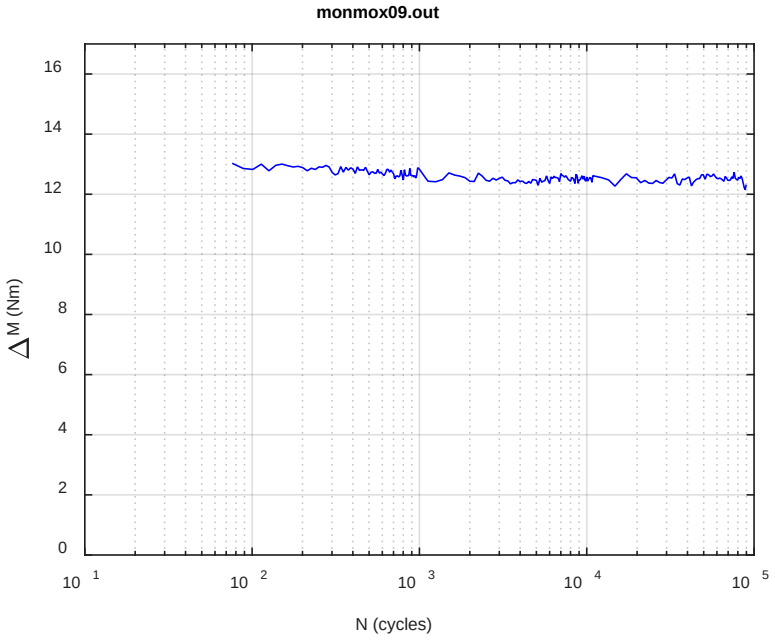
monmox09.out
16
14
12
10
8
6
4
2
0
Δ M (Nm)
10 1
10 2
10 3
10 4
10 5
N (cycles)

(b)

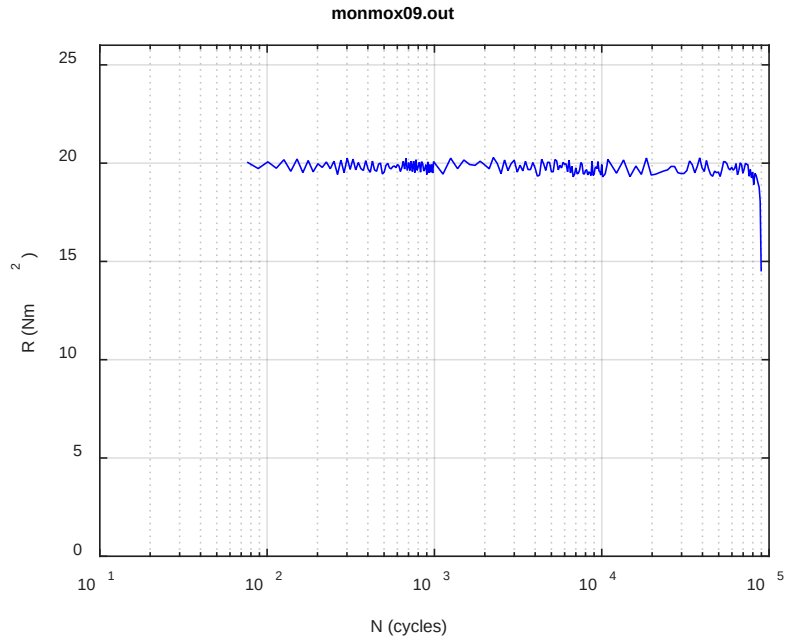
monmox09.out
25
20
15
10
5
0
R (Nm 2)
10 1
10 2
10 3
10 4
10 5
N (cycles)

(c)

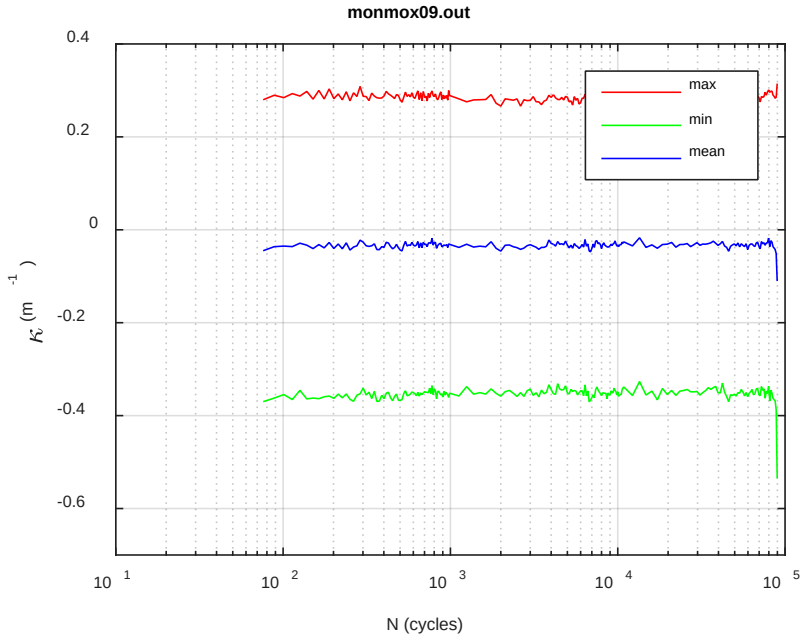
monmox09.out
0.4
0.2
0
-0.2
-0.4
-0.6
κ (m -1)
max
min
mean
10 1
10 2
10 3
10 4
10 5
N (cycles)

(d)

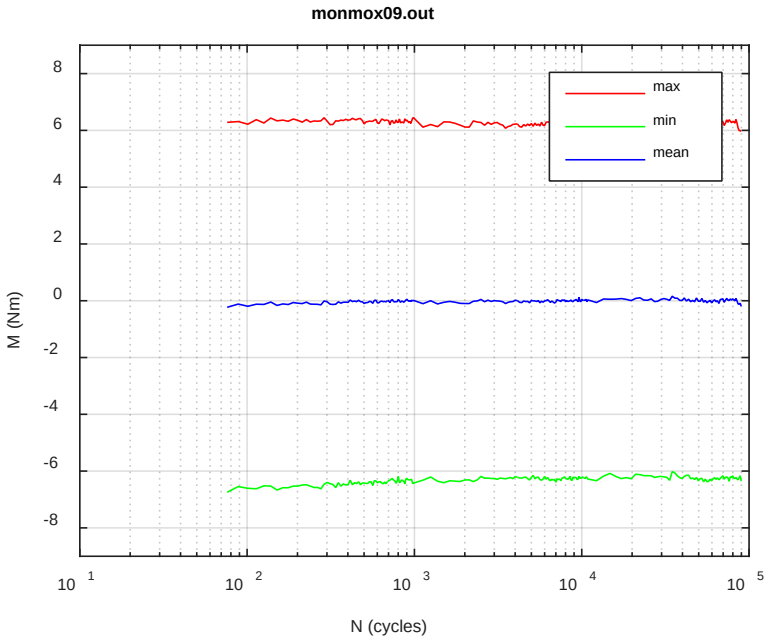

(e)

Fig. C.27. Monitoring-based responses: (a) curvature range, (b) moment range, (c) rigidity, (d) curvature peak/valley, (e) moment peak/valley, MOX09, 7.62 Nm, Nf = 8.98E+04 cycles.

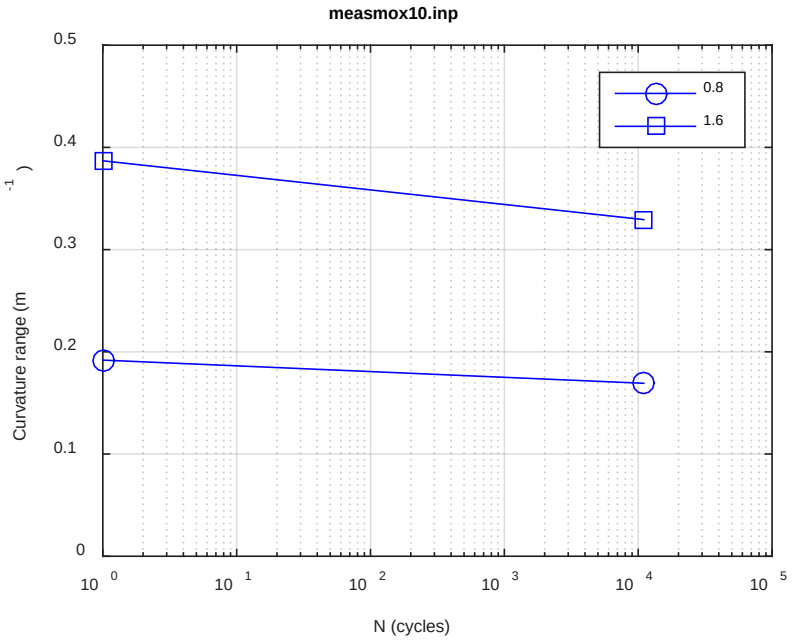
measmox10.inp
0.8
1.6
Curvature range (m-1)
N (cycles)
0
0.1
0.2
0.3
0.4
0.5
10 0
10 1
10 2
10 3
10 4
10 5

(a)

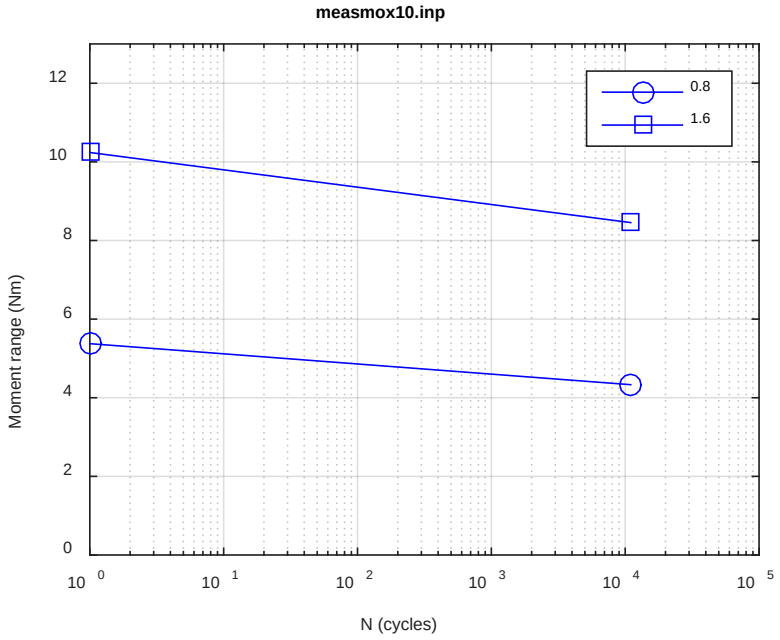
measmox10.inp
0.8
1.6
Moment range (Nm)
N (cycles)
0
2
4
6
8
10
12
10 0
10 1
10 2
10 3
10 4
10 5

(b)

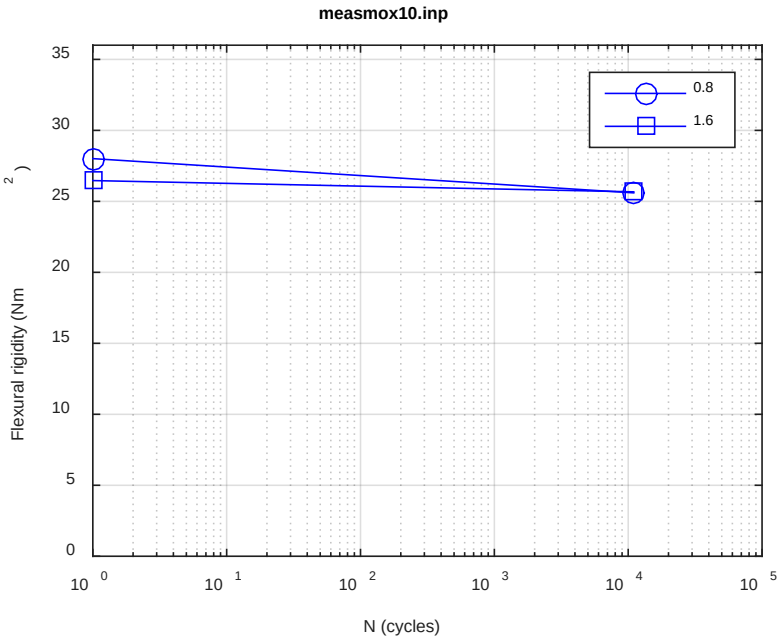
measmox10.inp
Flexural rigidity (Nm 2)
N (cycles)
0.8
1.6
35
30
25
20
15
10
5
0
10 0
10 1
10 2
10 3
10 4
10 5

(c)

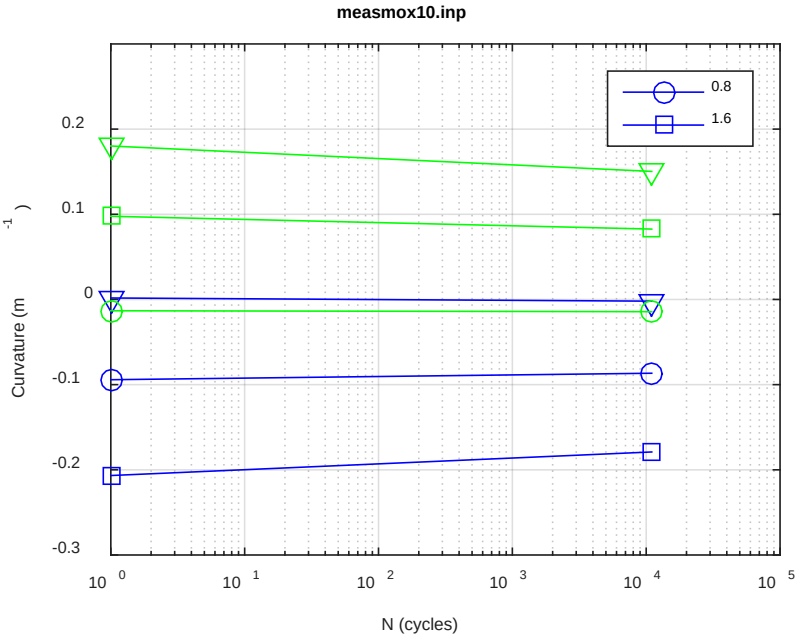
measmox10.inp
Curvature (m -1)
N (cycles)
0.8
1.6
0.2
0.1
0
-0.1
-0.2
-0.3
10 0
10 1
10 2
10 3
10 4
10 5

(d)

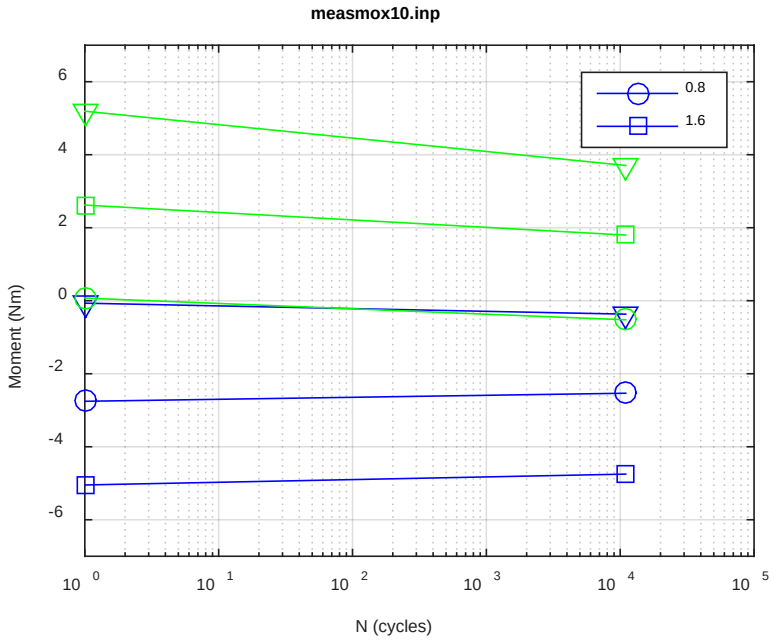

(e)

Fig. C.28. Measurement-based responses: (a) curvature range, (b) moment range, (c) rigidity, (d) curvature peak/valley, (e) moment peak/valley, MOX10, 10.16 Nm.

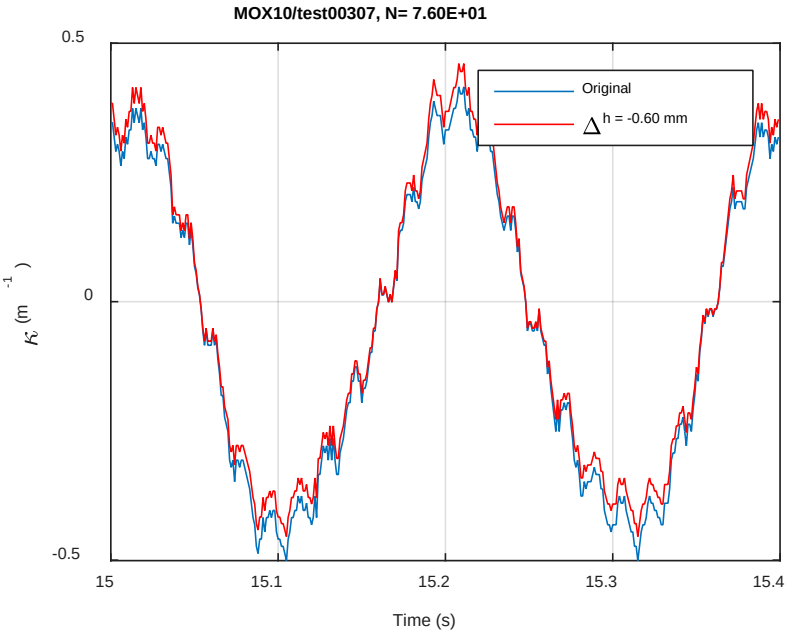
MOX10/test00307, N= 7.60E+01
Original
Δh = -0.60 mm
κ (m-1)
0.5
0
-0.5
15
15.1
15.2
15.3
15.4
Time (s)

(a)

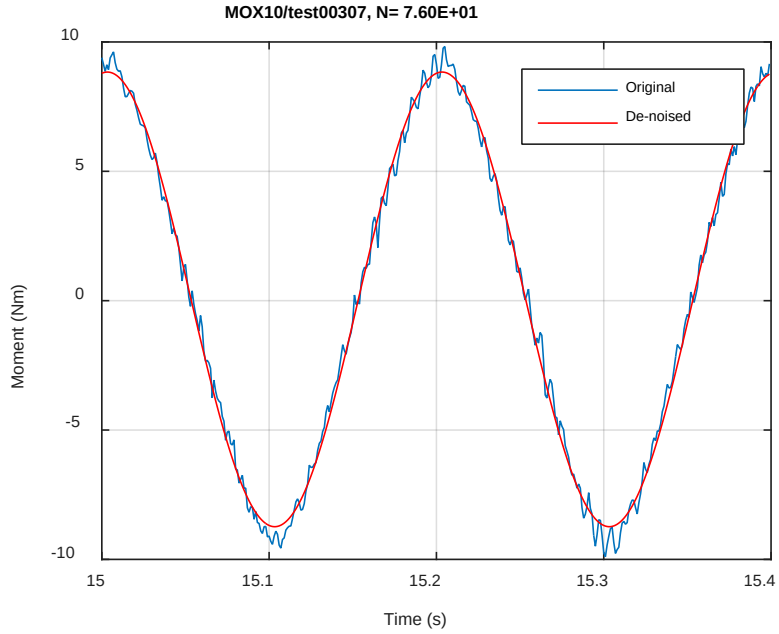
MOX10/test00307, N= 7.60E+01
Original
De-noised
Moment (Nm)
10
5
0
-5
-10
15
15.1
15.2
15.3
15.4
Time (s)

(b)

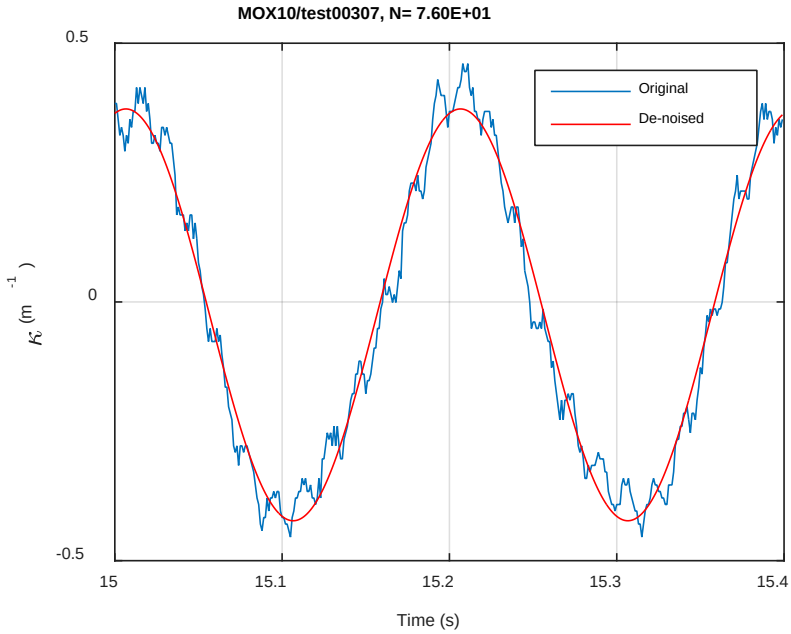

(c)

Fig. C.29. Monitoring-based responses: (a) curvature, (b) moment, (c) curvature, MOX10, 10.16 Nm, Ns = 7.60E+01 cycles.

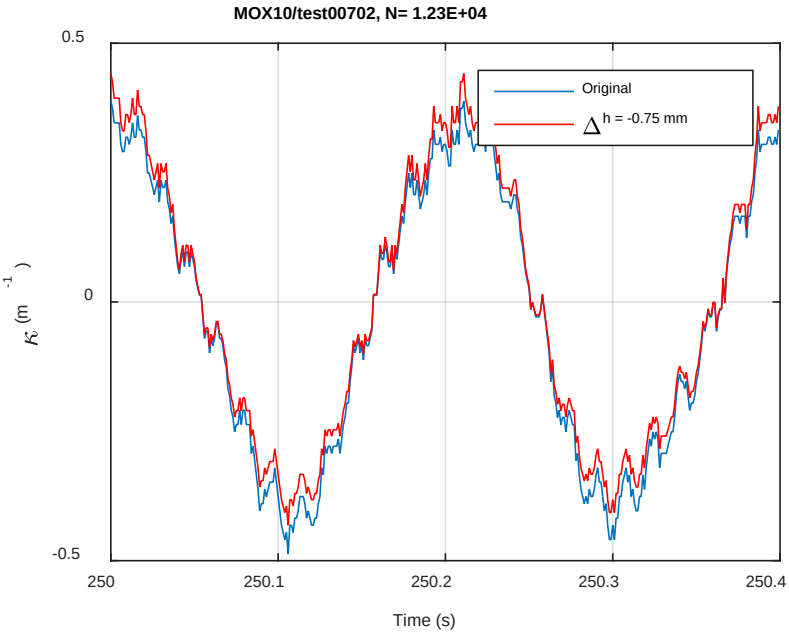
MOX10/test00702, N= 1.23E+04
0.5
0
-0.5
250
250.1
250.2
250.3
250.4
Time (s)
κ (m-1)
Original
Δh = -0.75 mm

(a)

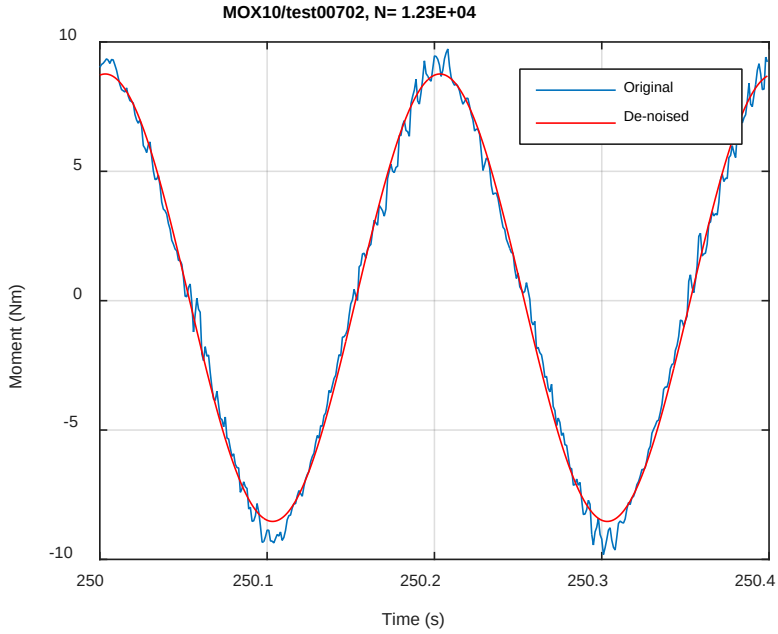
MOX10/test00702, N= 1.23E+04
10
5
0
-5
-10
250
250.1
250.2
250.3
250.4
Time (s)
Moment (Nm)
Original
De-noised

(b)

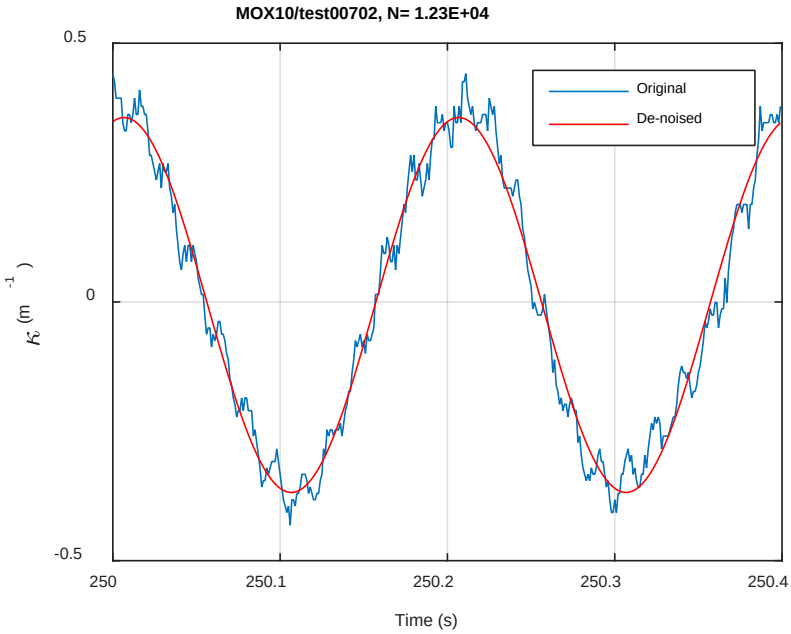

(c)

Fig. C.30. Monitoring-based responses: (a) curvature, (b) moment, (c) curvature, MOX10, 10.16 Nm, Ns = 1.23E+04 cycles.

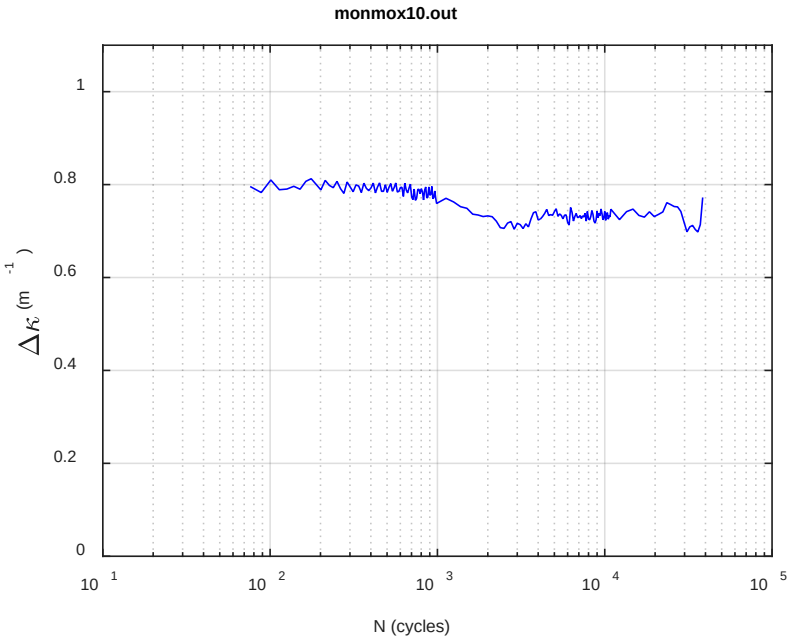
monmox10.out
1
0.8
0.6
0.4
0.2
0
$\Delta\kappa$ (m^{-1})
10^1
10^2
10^3
10^4
10^5
N (cycles)

(a)

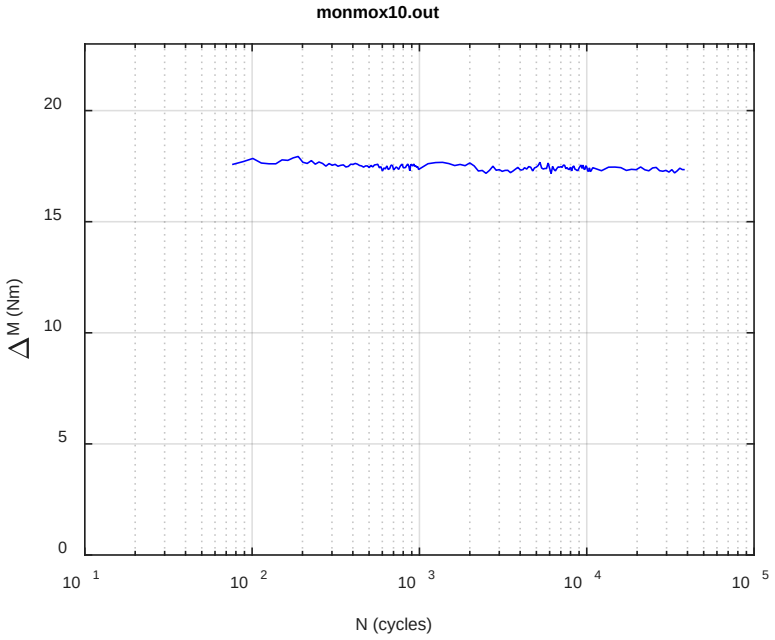
monmox10.out
20
15
10
5
0
Δ M (Nm)
10^1
10^2
10^3
10^4
10^5
N (cycles)

(b)

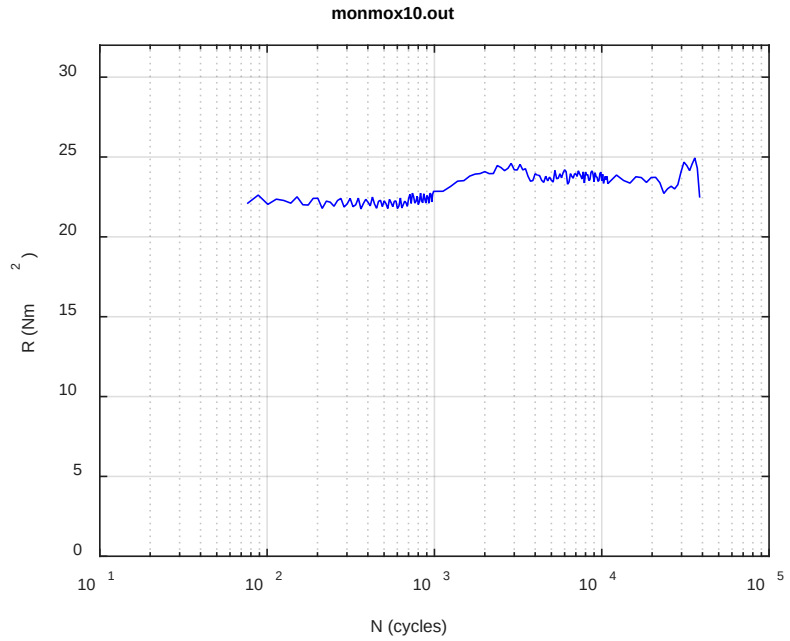
monmox10.out
R (Nm 2)
N (cycles)

(c)

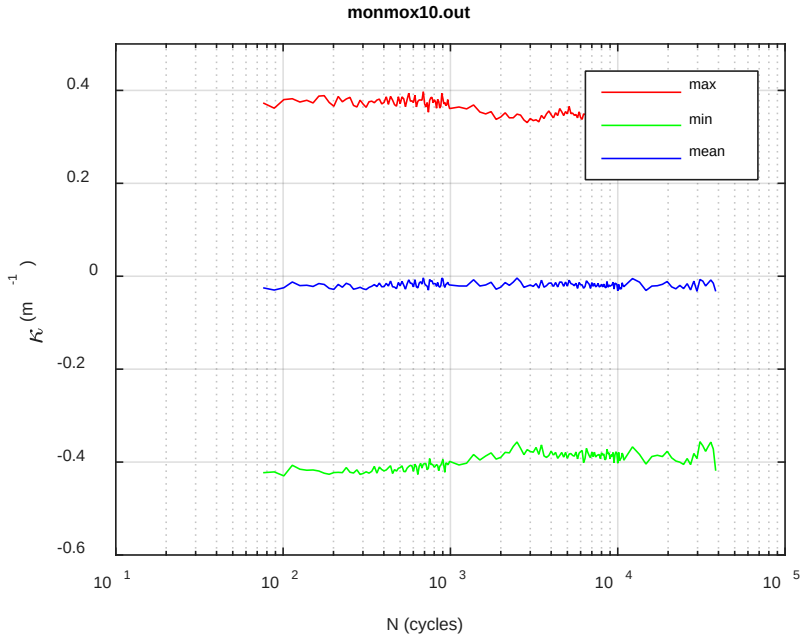
monmox10.out
max
min
mean
κ (m -1)
N (cycles)

(d)

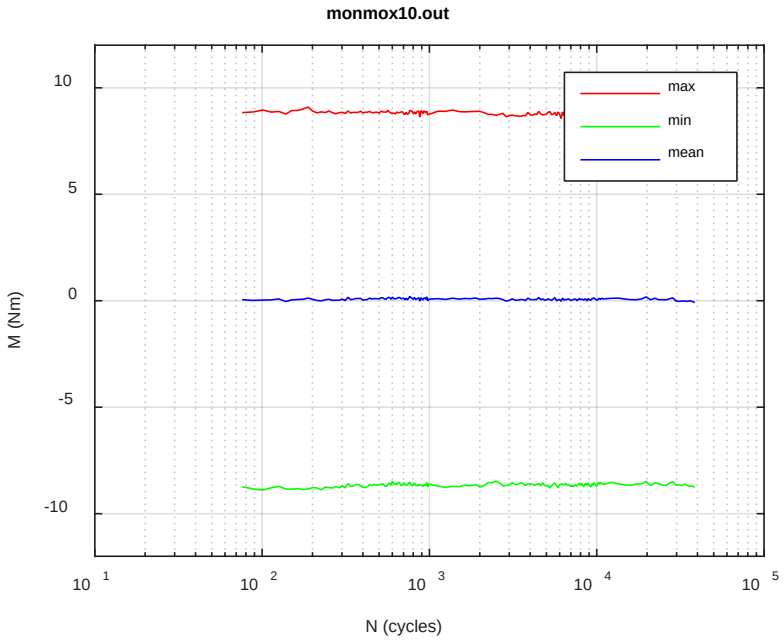

(e)

Fig. C.31. Monitoring-based responses: (a) curvature range, (b) moment range, (c) rigidity, (d) curvature peak/valley, (e) moment peak/valley, MOX10, 10.16 Nm, Nf = 3.85E+04 cycles.

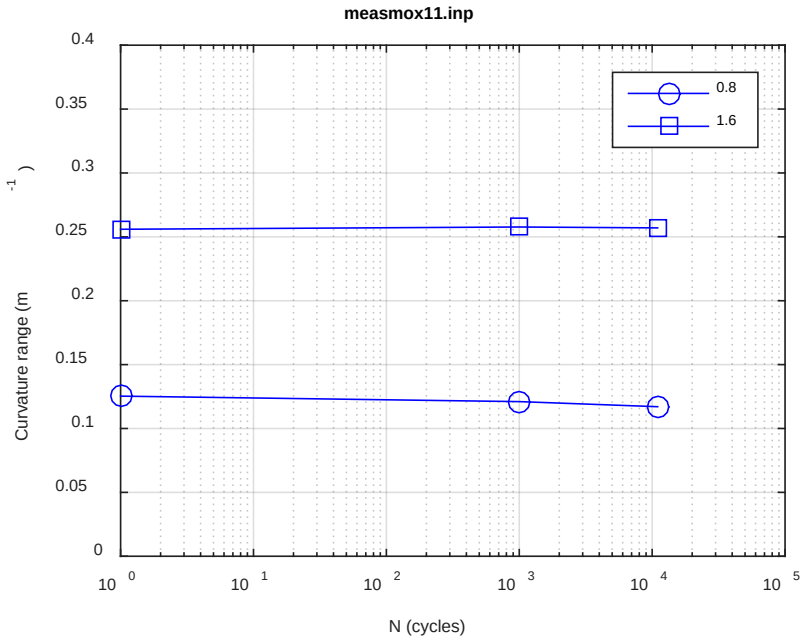
measmox11.inp
Curvature range (m-1)
N (cycles)
0.8
1.6
0
0.05
0.1
0.15
0.2
0.25
0.3
0.35
0.4
10 0
10 1
10 2
10 3
10 4
10 5

(a)

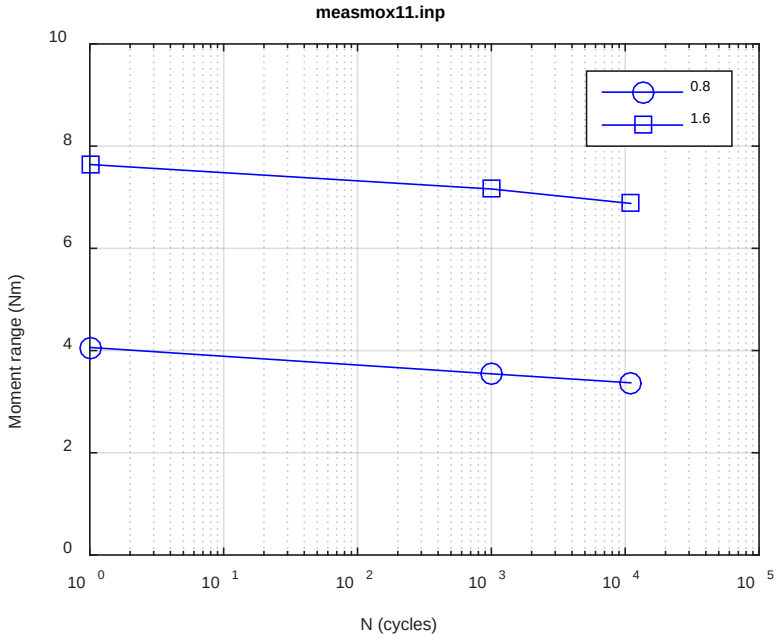
measmox11.inp
Moment range (Nm)
N (cycles)
0.8
1.6
0
2
4
6
8
10
10 0
10 1
10 2
10 3
10 4
10 5

(b)

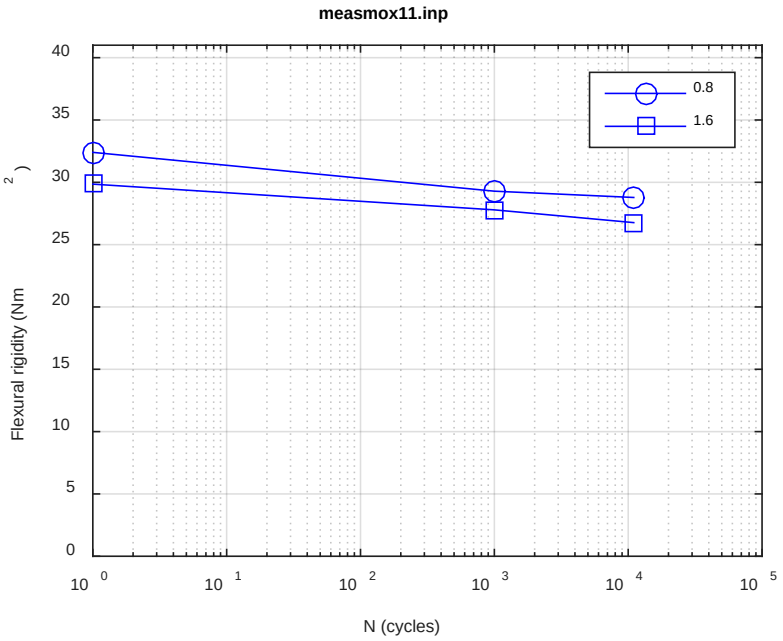
measmox11.inp
Flexural rigidity (Nm 2)
N (cycles)
0.8
1.6
0
5
10
15
20
25
30
35
40
10 0
10 1
10 2
10 3
10 4
10 5

(c)

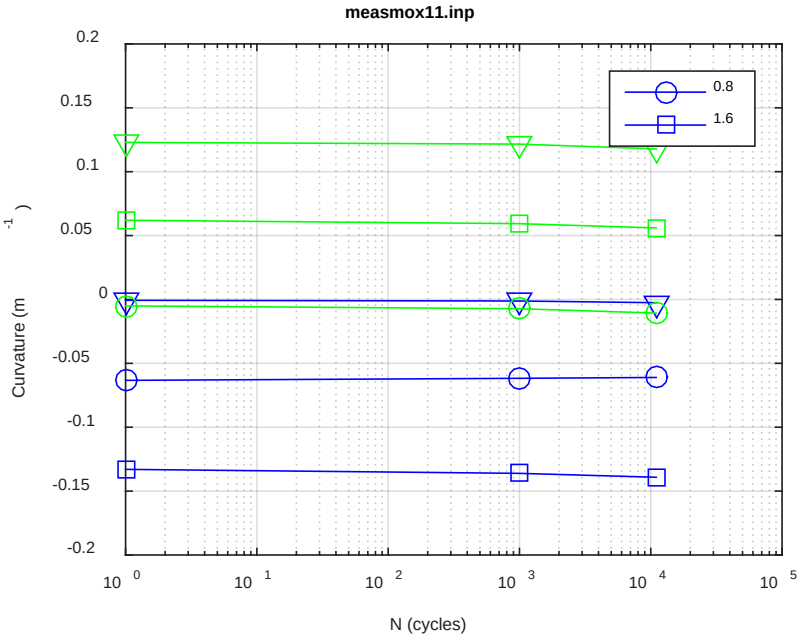
measmox11.inp
Curvature (m -1)
N (cycles)
0.8
1.6
0.2
0.15
0.1
0.05
0
-0.05
-0.1
-0.15
-0.2
10 0
10 1
10 2
10 3
10 4
10 5

(d)

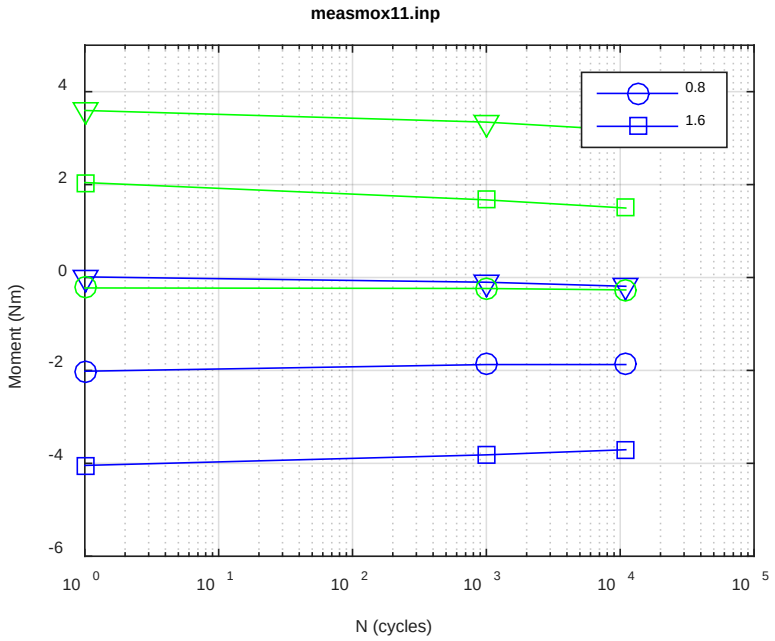

(e)

Fig. C.32. Measurement-based responses: (a) curvature range, (b) moment range, (c) rigidity, (d) curvature peak/valley, (e) moment peak/valley, MOX11, 10.16 Nm.

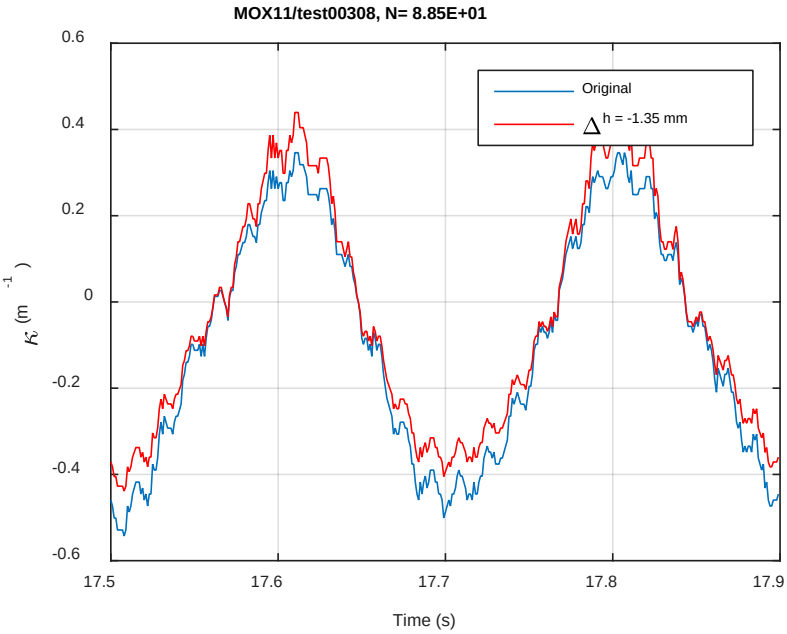
MOX11/test00308, N= 8.85E+01
Original
Δh = -1.35 mm
κ (m-1)
Time (s)
0.6
0.4
0.2
0
-0.2
-0.4
-0.6
17.5
17.6
17.7
17.8
17.9

(a)

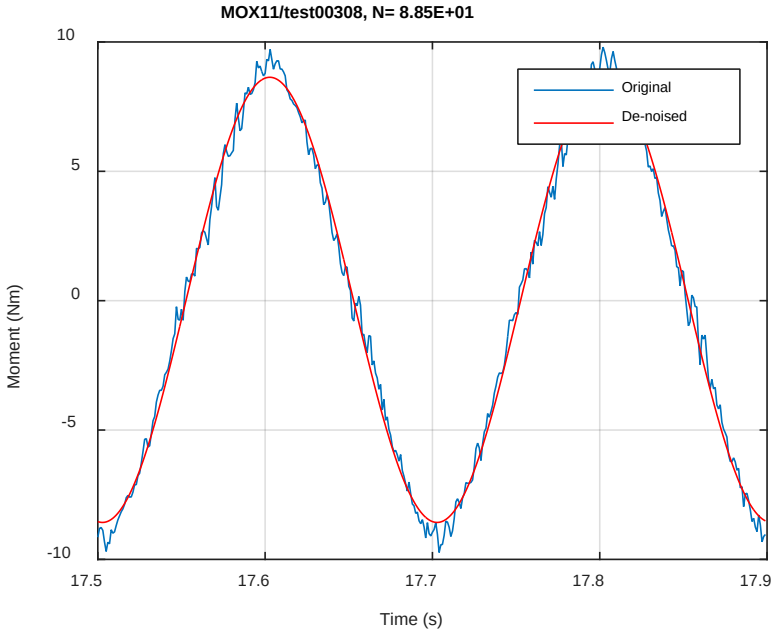
MOX11/test00308, N= 8.85E+01
Original
De-noised
Moment (Nm)
Time (s)
10
5
0
-5
-10
17.5
17.6
17.7
17.8
17.9

(b)

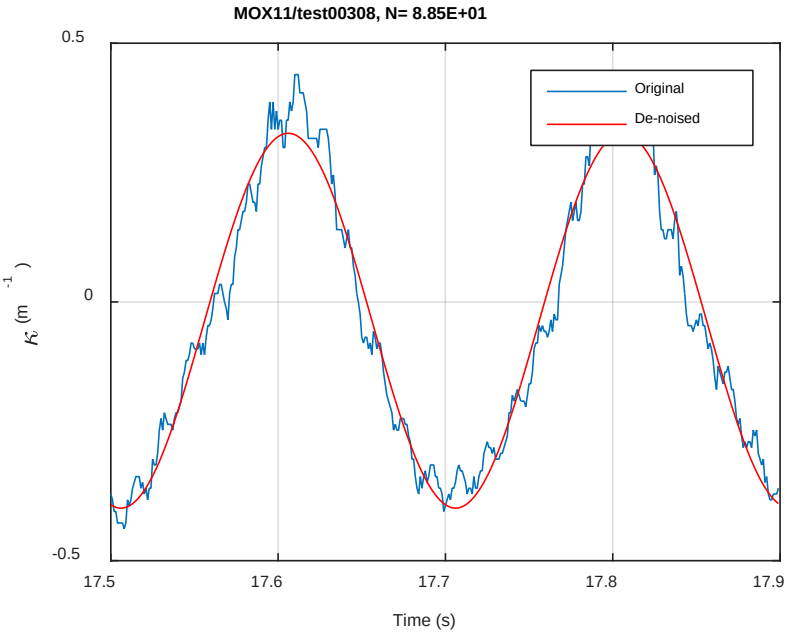

(c)

Fig. C.33. Monitoring-based responses: (a) curvature, (b) moment, (c) curvature, MOX11, 10.16 Nm, Ns = 8.85E+01 cycles.

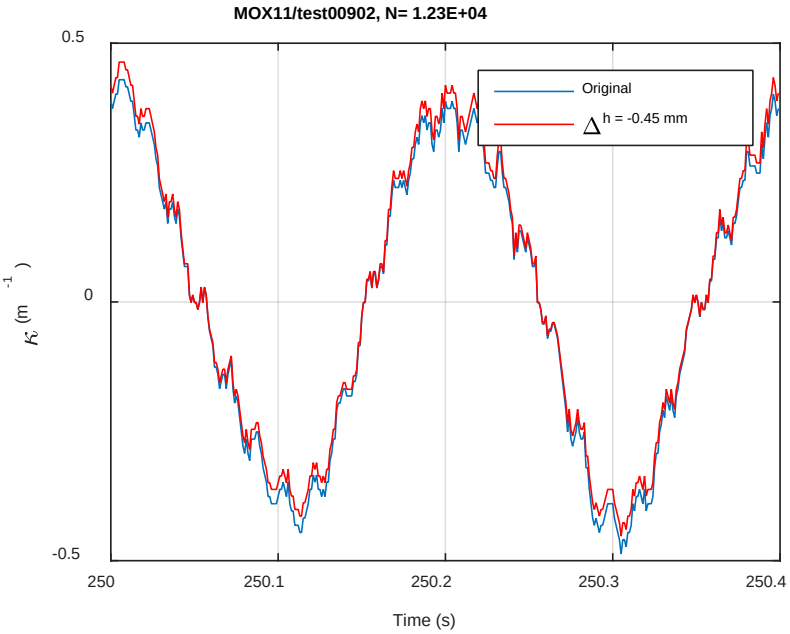
MOX11/test00902, N= 1.23E+04
Original
Δh = -0.45 mm
κ (m-1)
Time (s)
0.5
0
-0.5
250
250.1
250.2
250.3
250.4

(a)

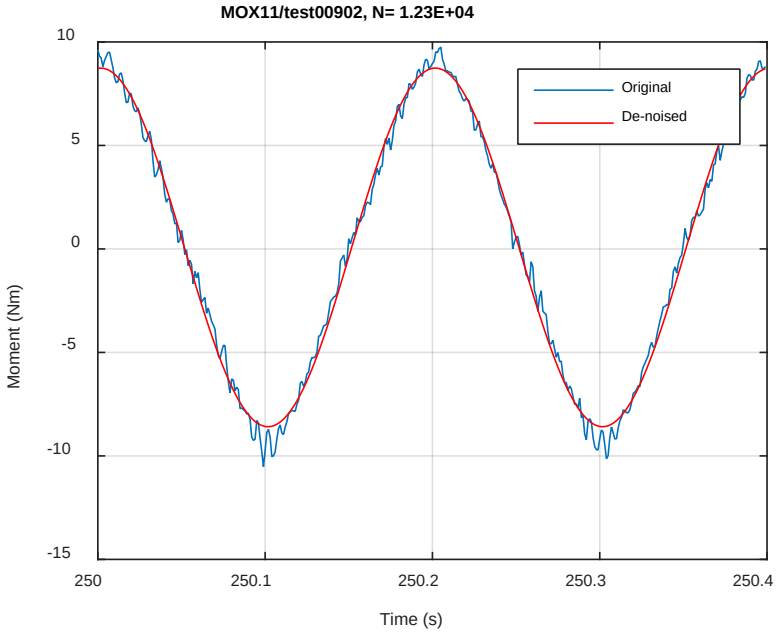
MOX11/test00902, N= 1.23E+04
Original
De-noised
Moment (Nm)
Time (s)
10
5
0
-5
-10
-15
250
250.1
250.2
250.3
250.4

(b)

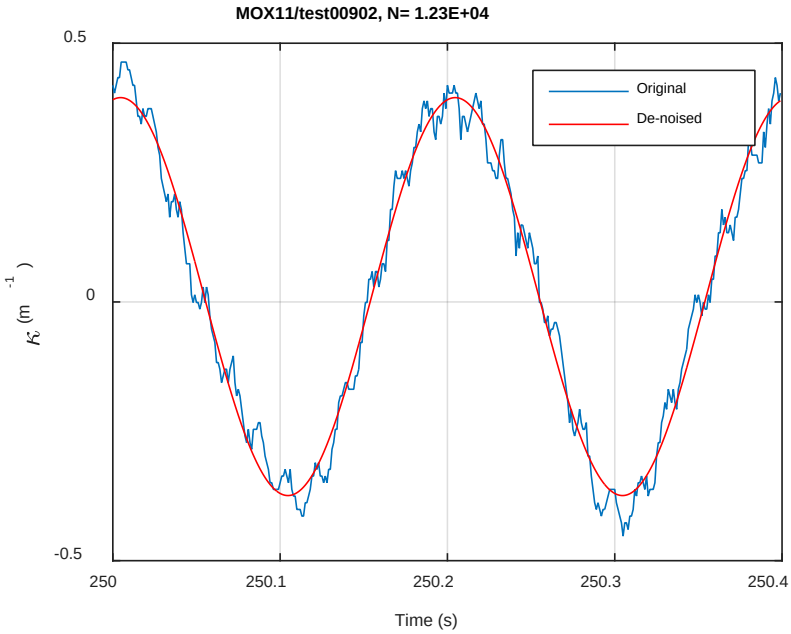

(c)

Fig. C.34. Monitoring-based responses: (a) curvature, (b) moment, (c) curvature, MOX11, 10.16 Nm, Ns = 1.23E+04 cycles.

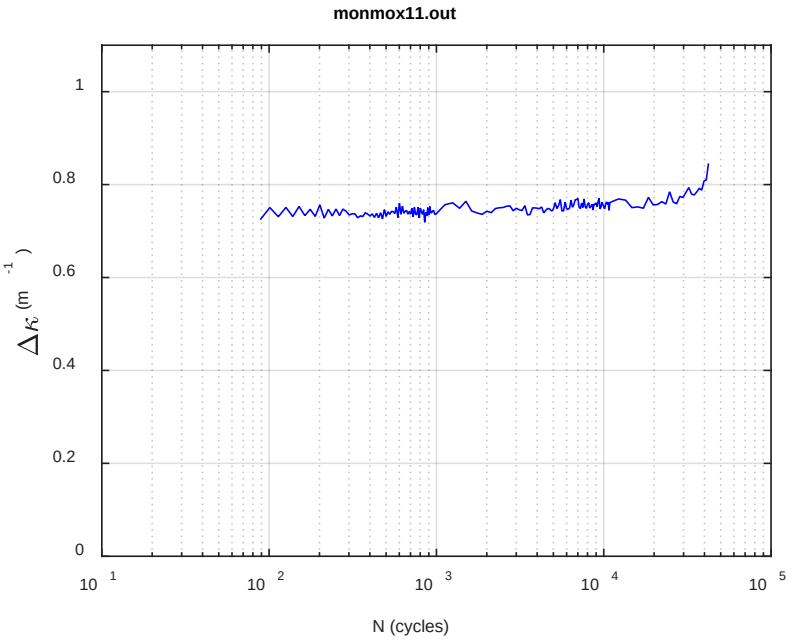
monmox11.out
1
0.8
0.6
0.4
0.2
0
Δκ (m-1)
10 1
10 2
10 3
10 4
10 5
N (cycles)

(a)

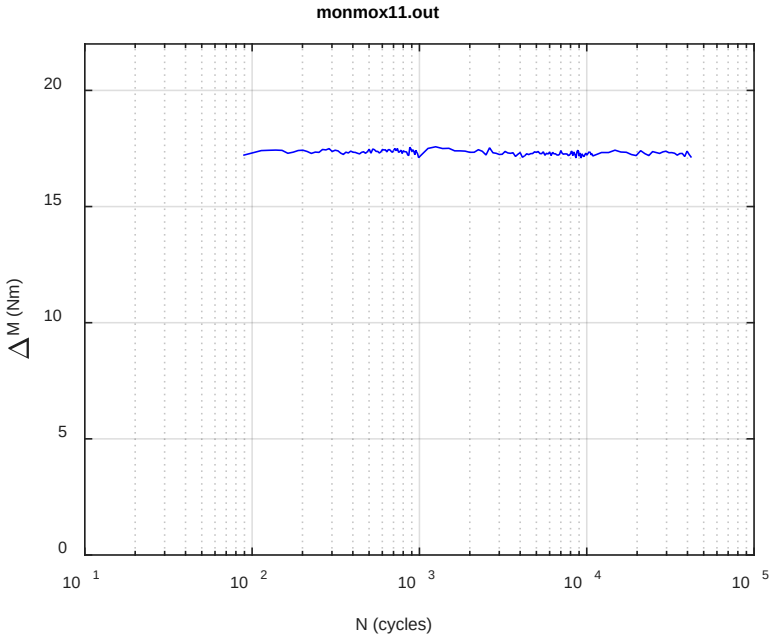
monmox11.out
20
15
10
5
0
Δ M (Nm)
10 1
10 2
10 3
10 4
10 5
N (cycles)

(b)

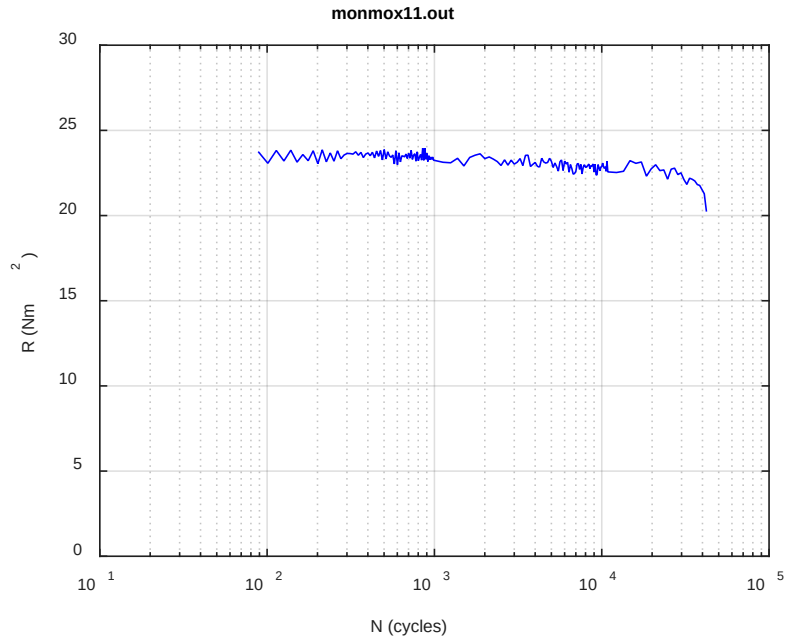
monmox11.out
30
25
20
15
10
5
0
R (Nm 2)
10 1
10 2
10 3
10 4
10 5
N (cycles)

(c)

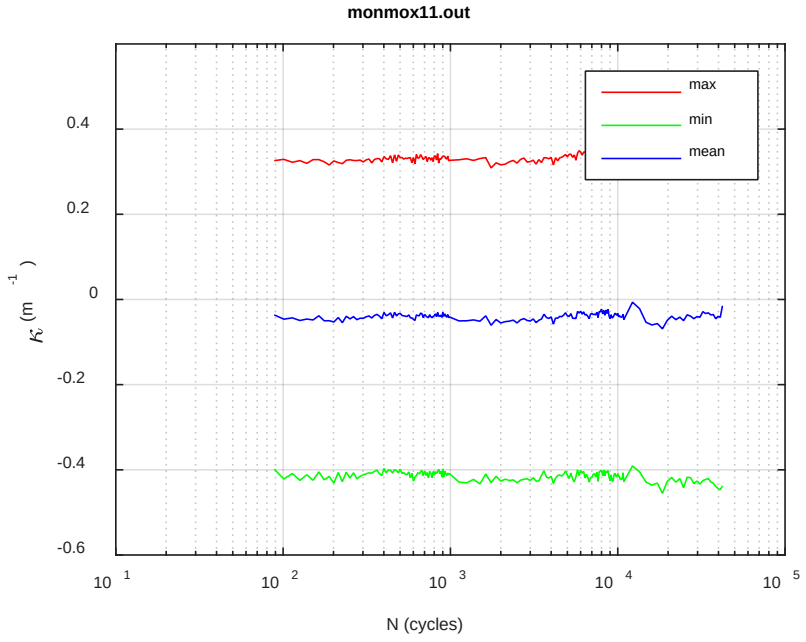
monmox11.out
max
min
mean
0.4
0.2
0
-0.2
-0.4
-0.6
κ (m -1)
10 1
10 2
10 3
10 4
10 5
N (cycles)

(d)

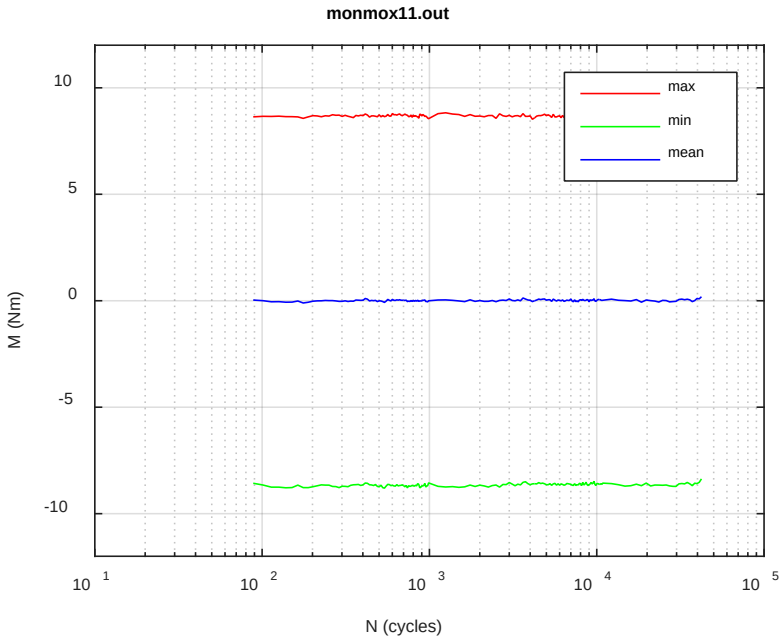

(e)

Fig. C.35. Monitoring-based responses: (a) curvature range, (b) moment range, (c) rigidity, (d) curvature peak/valley, (e) moment peak/valley, MOX11, 10.16 Nm, Nf = 4.23E+04 cycles.

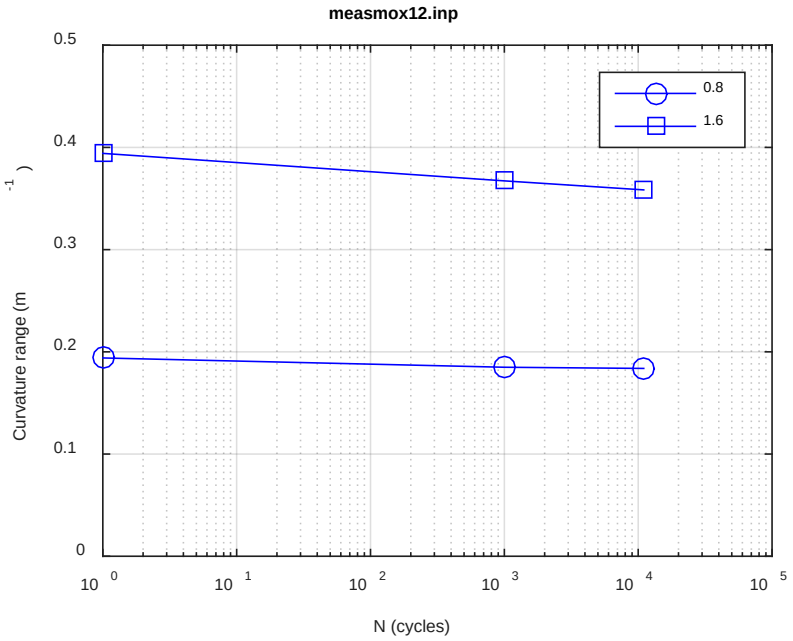
measmox12.inp
0.5
0.4
0.3
0.2
0.1
0
Curvature range (m -1)
0.8
1.6
10 0
10 1
10 2
10 3
10 4
10 5
N (cycles)

(a)

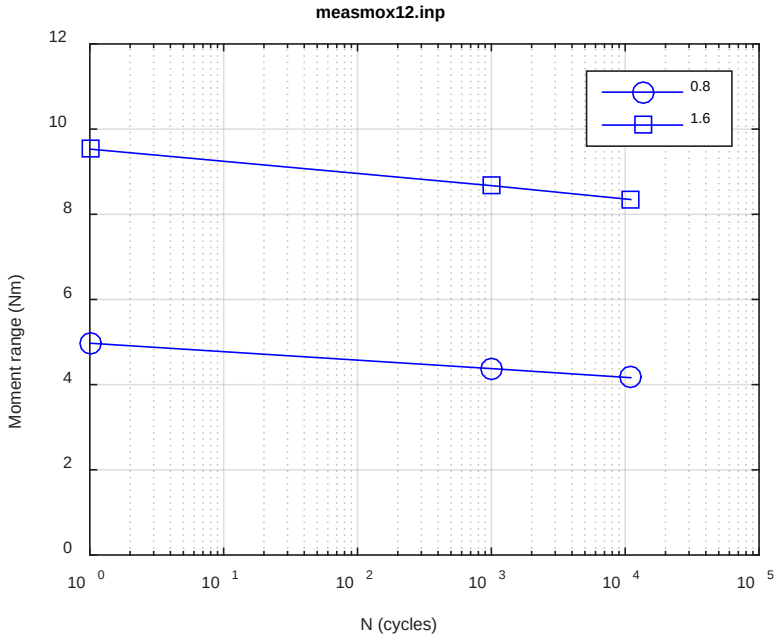
measmox12.inp
12
10
8
6
4
2
0
Moment range (Nm)
0.8
1.6
10 0
10 1
10 2
10 3
10 4
10 5
N (cycles)

(b)

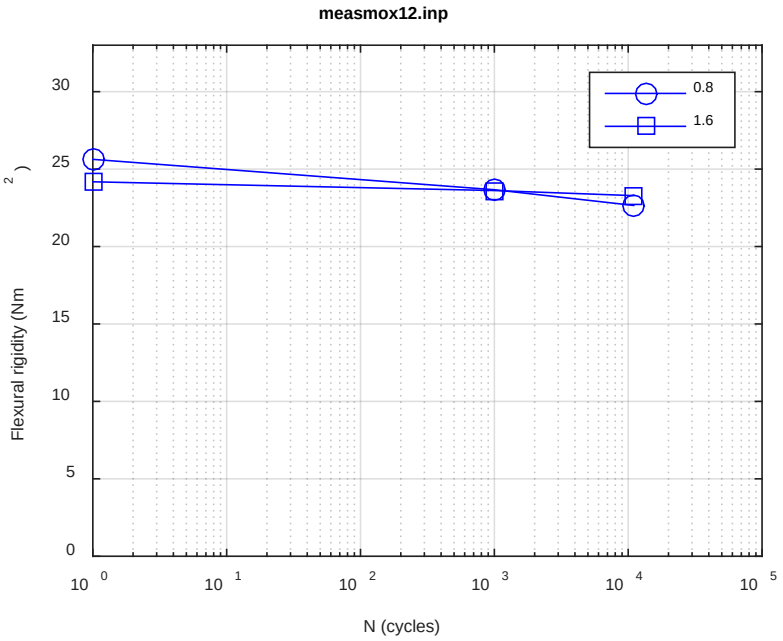
measmox12.inp
0.8
1.6
Flexural rigidity (Nm 2)
N (cycles)
0
5
10
15
20
25
30
10 0
10 1
10 2
10 3
10 4
10 5

(c)

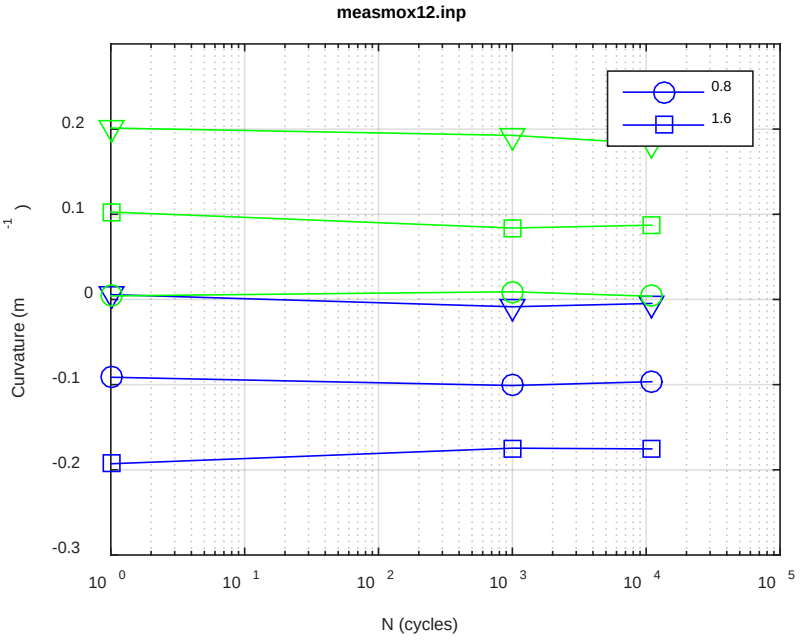
measmox12.inp
0.8
1.6
Curvature (m -1)
N (cycles)
0.2
0.1
0
-0.1
-0.2
-0.3
10 0
10 1
10 2
10 3
10 4
10 5

(d)

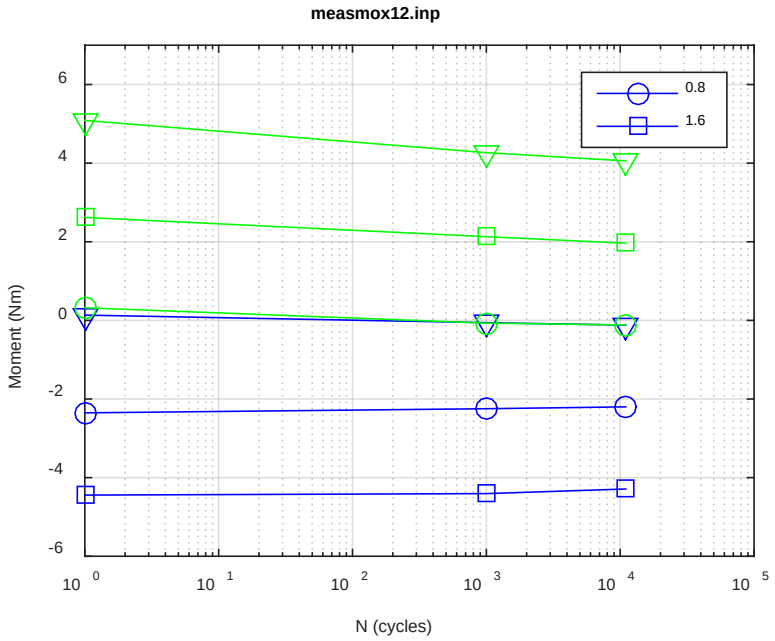

(e)

Fig. C.36. Measurement-based responses: (a) curvature range, (b) moment range, (c) rigidity, (d) curvature peak/valley, (e) moment peak/valley, MOX12, 10.16 Nm.

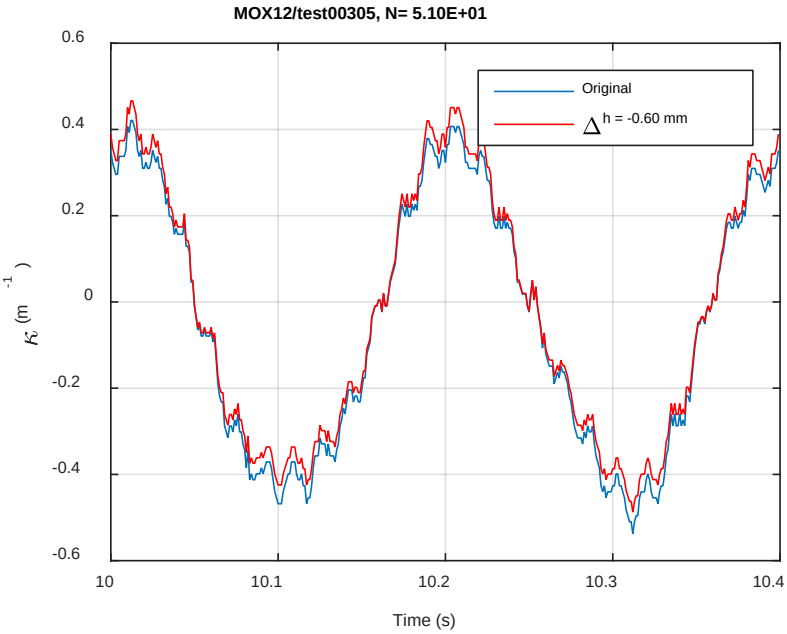
MOX12/test00305, N= 5.10E+01
Original
Δh = -0.60 mm
κ (m-1)
Time (s)
0.6
0.4
0.2
0
-0.2
-0.4
-0.6
10
10.1
10.2
10.3
10.4

(a)

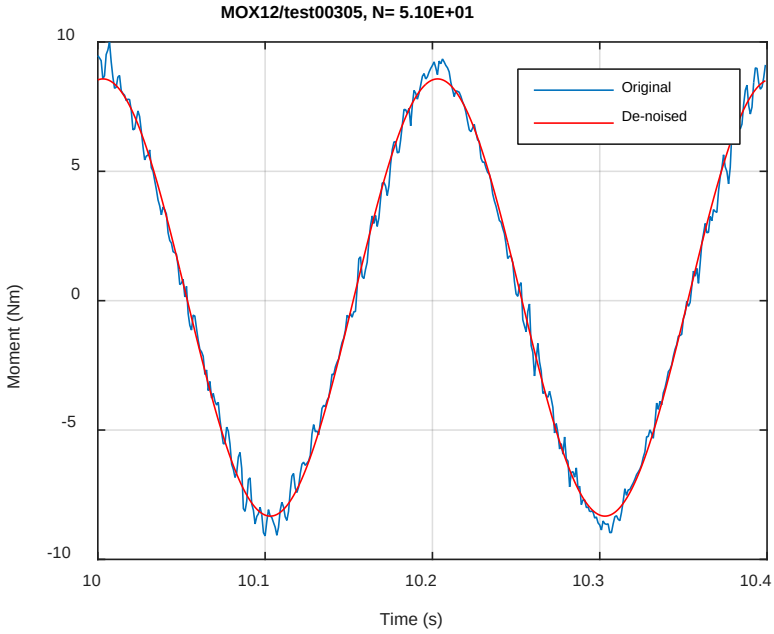
MOX12/test00305, N= 5.10E+01
Original
De-noised
Moment (Nm)
Time (s)
10
5
0
-5
-10
10
10.1
10.2
10.3
10.4

(b)

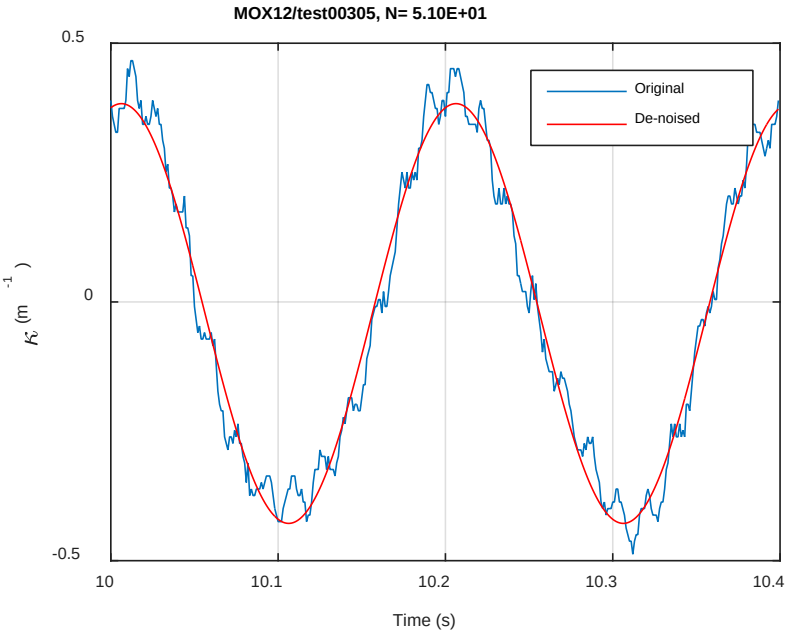

(c)

Fig. C.37. Monitoring-based responses: (a) curvature, (b) moment, (c) curvature, MOX12, 10.16 Nm, Ns = 5.10E+01 cycles.

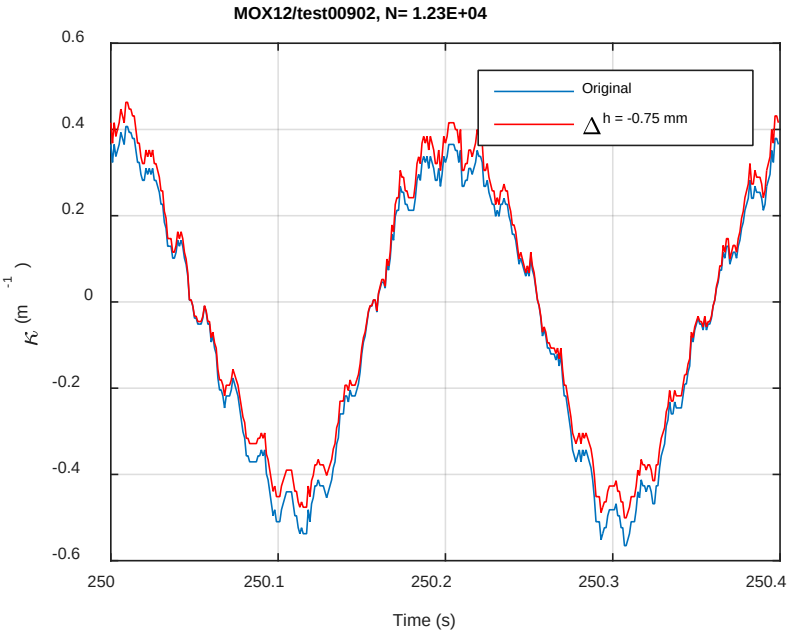
MOX12/test00902, N= 1.23E+04
Original
Δh = -0.75 mm
κ (m-1)
Time (s)
0.6
0.4
0.2
0
-0.2
-0.4
-0.6
250
250.1
250.2
250.3
250.4

(a)

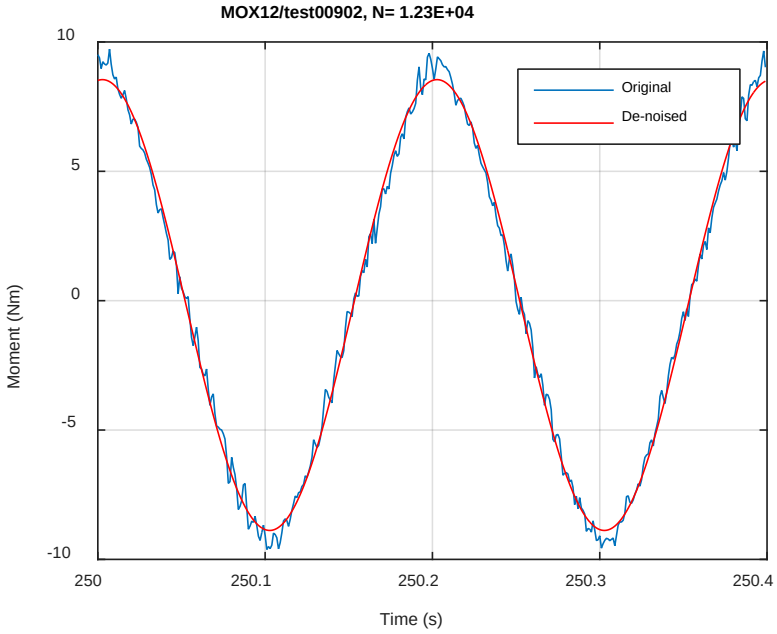
MOX12/test00902, N= 1.23E+04
Original
De-noised
Moment (Nm)
Time (s)
10
5
0
-5
-10
250
250.1
250.2
250.3
250.4

(b)

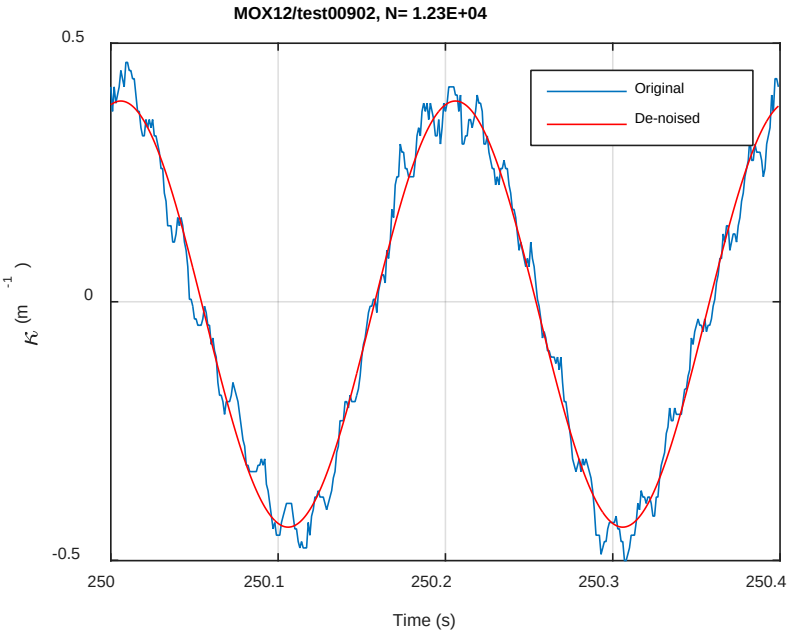

(c)

Fig. C.38. Monitoring-based responses: (a) curvature, (b) moment, (c) curvature, MOX12, 10.16 Nm, Ns = 1.23E+04 cycles.

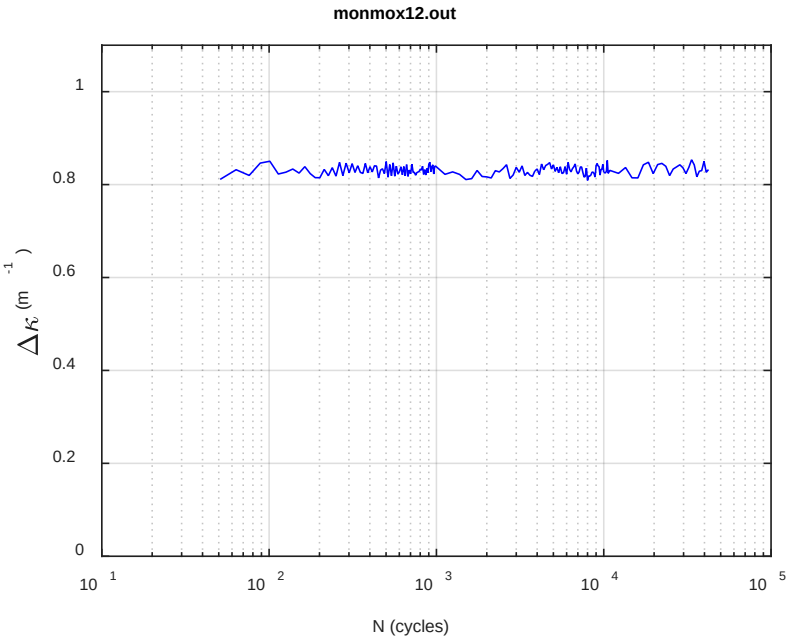
monmox12.out
1
0.8
0.6
0.4
0.2
0
$\Delta\kappa$ (m^{-1})
10 1
10 2
10 3
10 4
10 5
N (cycles)

(a)

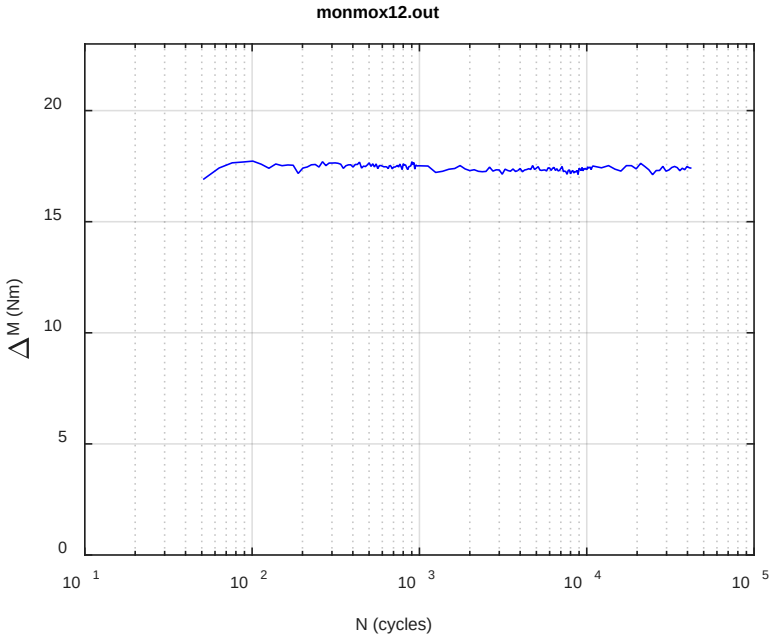
monmox12.out
20
15
10
5
0
Δ M (Nm)
10 1
10 2
10 3
10 4
10 5
N (cycles)

(b)

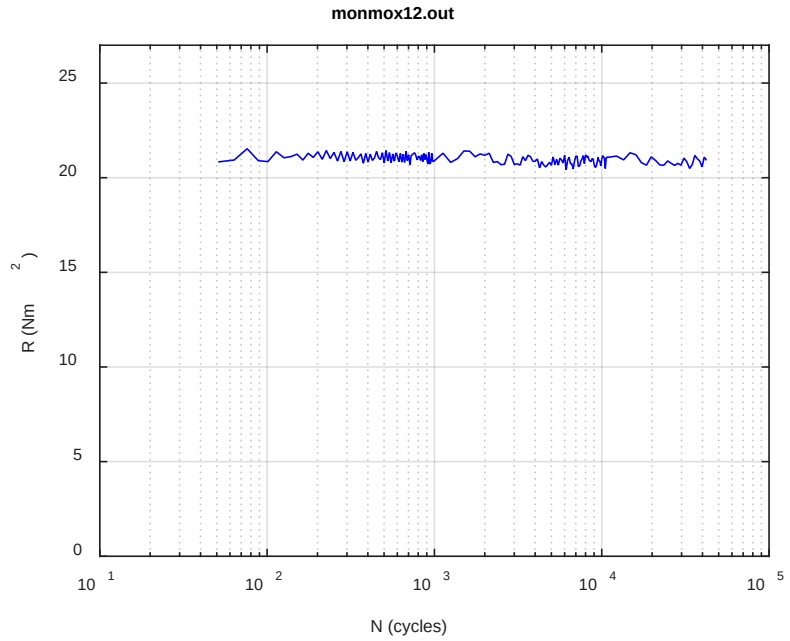
monmox12.out
25
20
15
10
5
0
R (Nm 2)
10 1
10 2
10 3
10 4
10 5
N (cycles)

(c)

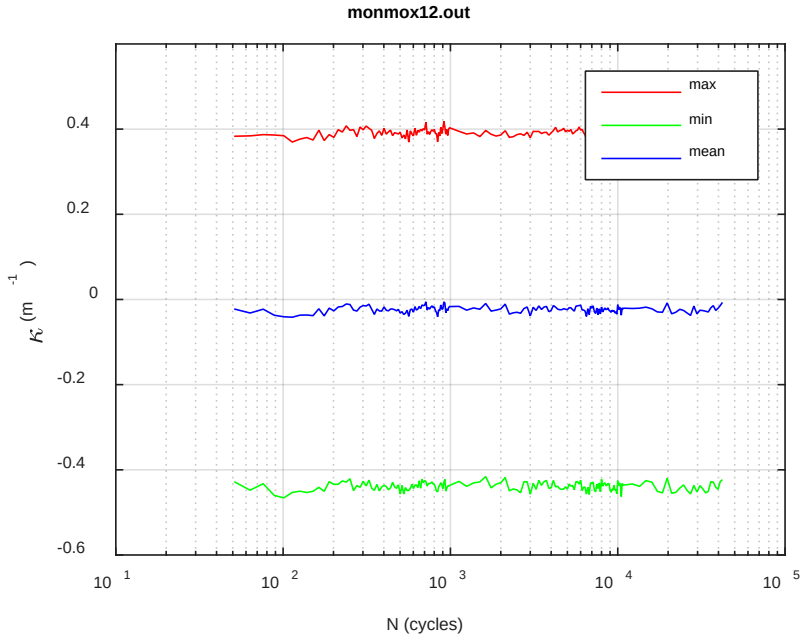
monmox12.out
max
min
mean
0.4
0.2
0
-0.2
-0.4
-0.6
κ (m -1)
10 1
10 2
10 3
10 4
10 5
N (cycles)

(d)

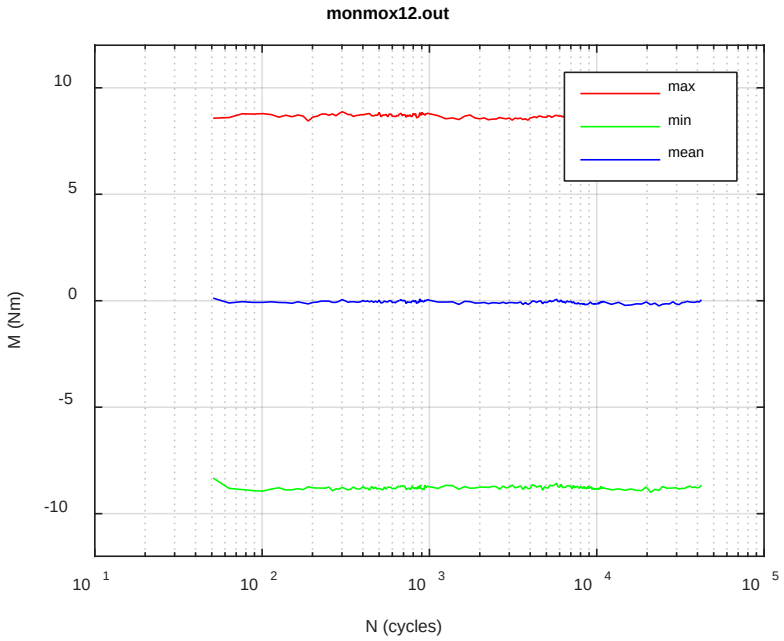

(e)

Fig. C.39. Monitoring-based responses: (a) curvature range, (b) moment range, (c) rigidity, (d) curvature peak/valley, (e) moment peak/valley, MOX12, 10.16 Nm, Nf = 4.23E+04 cycles.

APPENDIX D
CIRFT TESTING RESULTS OF LMK SNF – PART II

TABLE OF CONTENTS

Measurement and monitoring rigidity curves for LMK BWR SNF

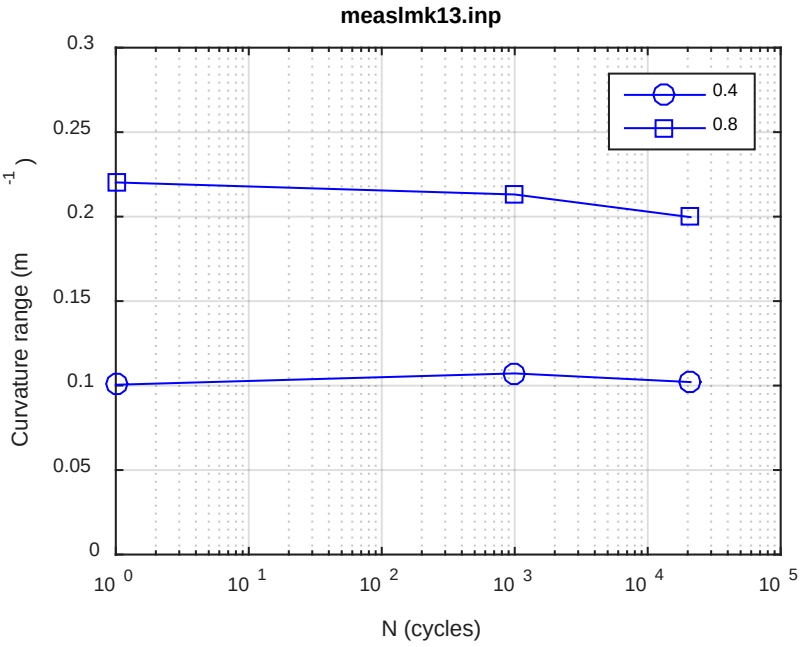
measlmk13.inp
0.3
0.25
0.2
0.15
0.1
0.05
0
Curvature range (m -1)
0.4
0.8
10 0
10 1
10 2
10 3
10 4
10 5
N (cycles)

(a)

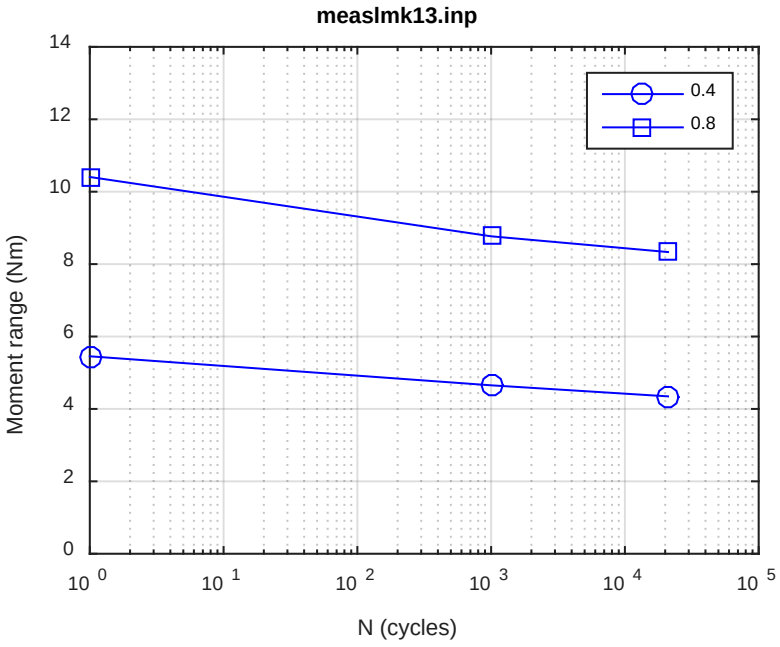
measlmk13.inp
14
12
10
8
6
4
2
0
Moment range (Nm)
0.4
0.8
10 0
10 1
10 2
10 3
10 4
10 5
N (cycles)

(b)

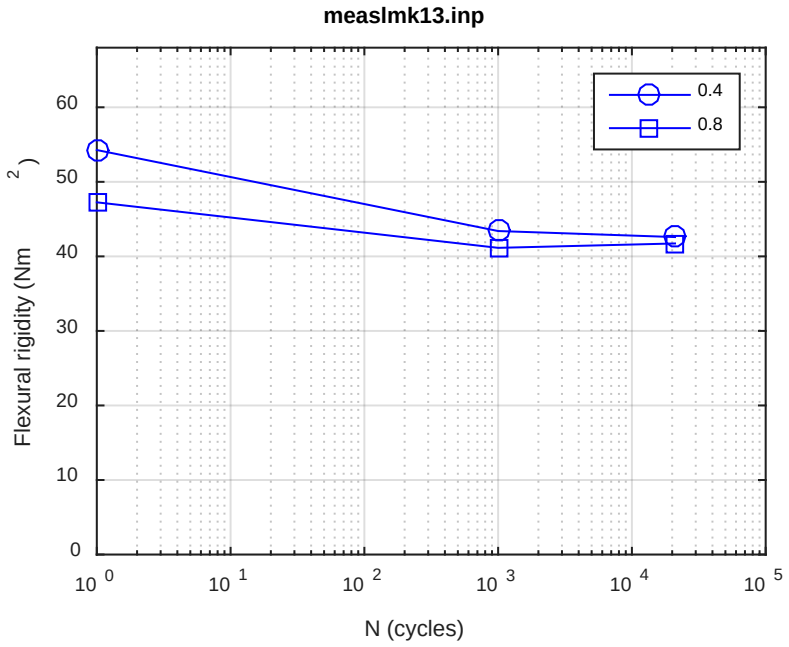
measlmk13.inp
0.4
0.8
Flexural rigidity (Nm 2)
N (cycles)

(c)

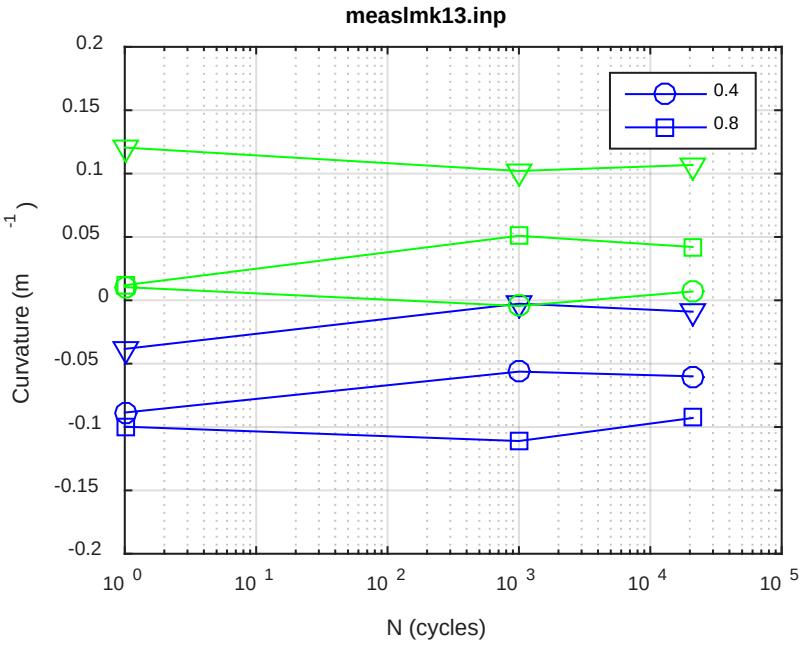
measlmk13.inp
0.4
0.8
Curvature (m -1)
N (cycles)

(d)

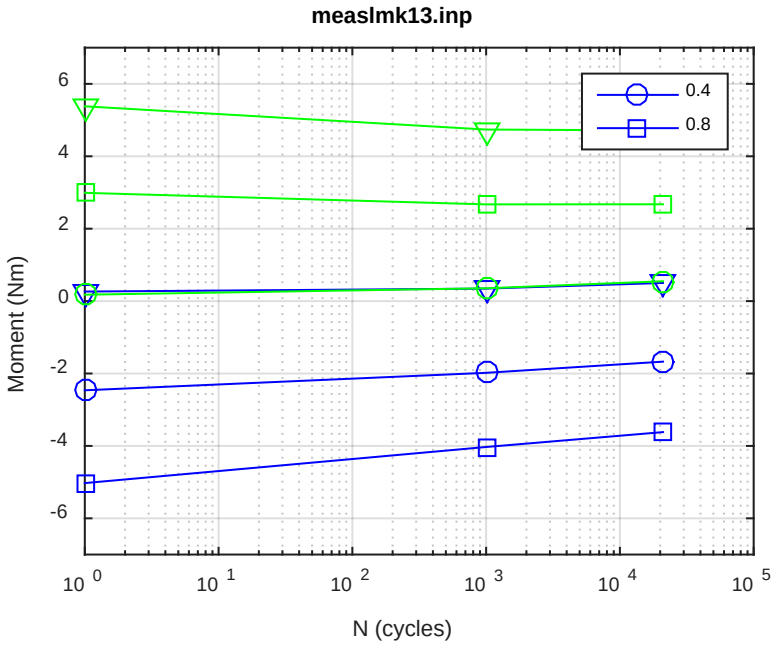

(e)

Fig. D.1 Measurement-based responses: (a) curvature range, (b) moment range, (c) rigidity, (d) curvature peak/valley, (e) moment peak/valley, LMK13, 25.40 Nm.

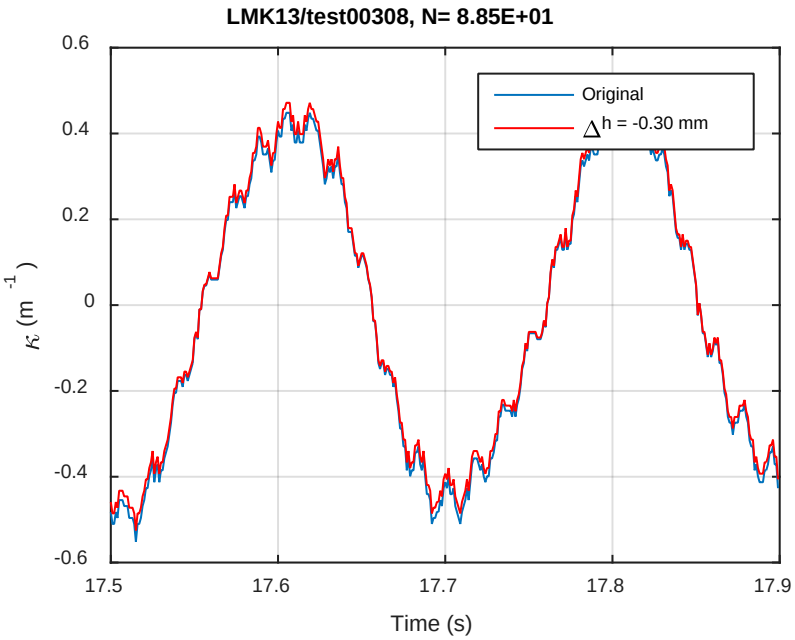
LMK13/test00308, N= 8.85E+01
Original
Δh = -0.30 mm
κ (m-1)
Time (s)
0.6
0.4
0.2
0
-0.2
-0.4
-0.6
17.5
17.6
17.7
17.8
17.9

(a)

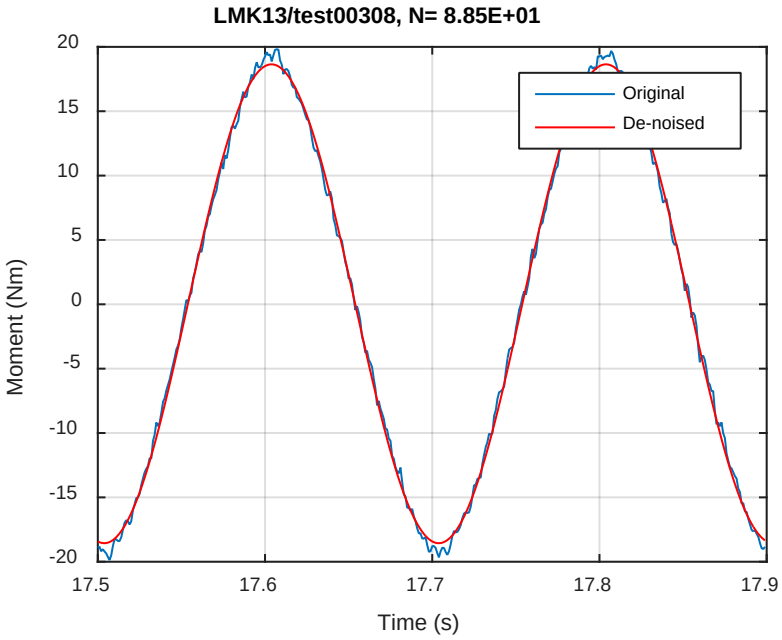
LMK13/test00308, N= 8.85E+01
Original
De-noised
Moment (Nm)
Time (s)
20
15
10
5
0
-5
-10
-15
-20
17.5
17.6
17.7
17.8
17.9

(b)

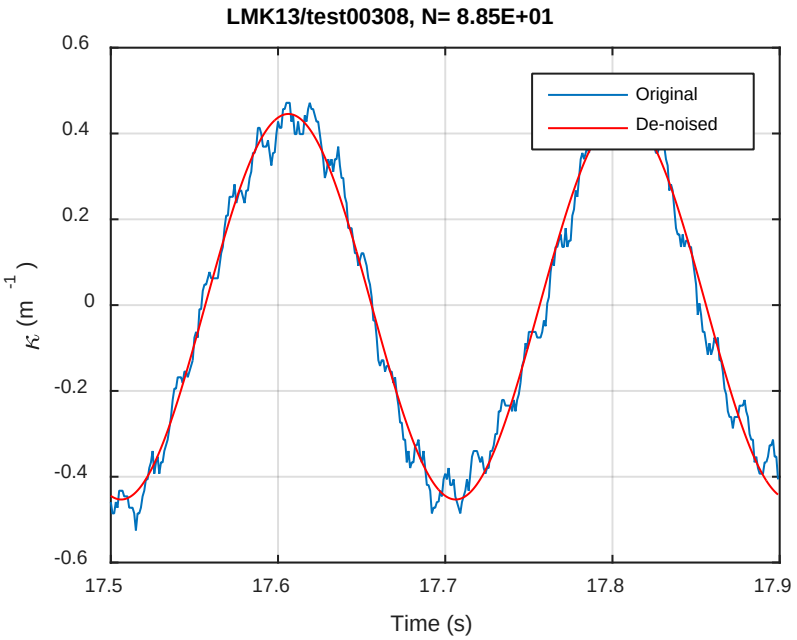

(c)

Fig. D.2 Monitoring-based responses: (a) curvature, (b) moment, (c) curvature, LMK13, 25.40 Nm, Ns = 8.85E+01 cycles.

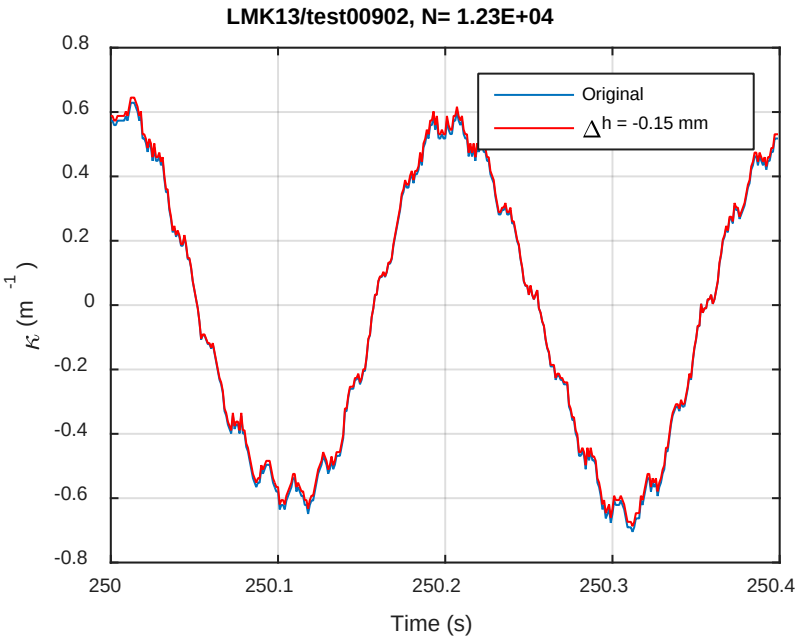
LMK13/test00902, N= 1.23E+04
Original
Δh = -0.15 mm
κ (m-1)
Time (s)
0.8
0.6
0.4
0.2
0
-0.2
-0.4
-0.6
-0.8
250
250.1
250.2
250.3
250.4

(a)

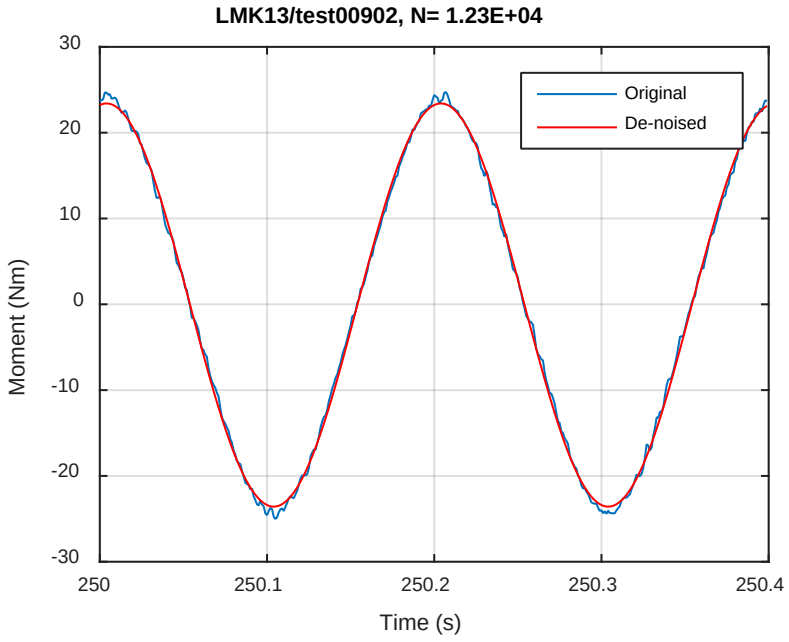
LMK13/test00902, N= 1.23E+04
Original
De-noised
Moment (Nm)
Time (s)
30
20
10
0
-10
-20
-30
250
250.1
250.2
250.3
250.4

(b)

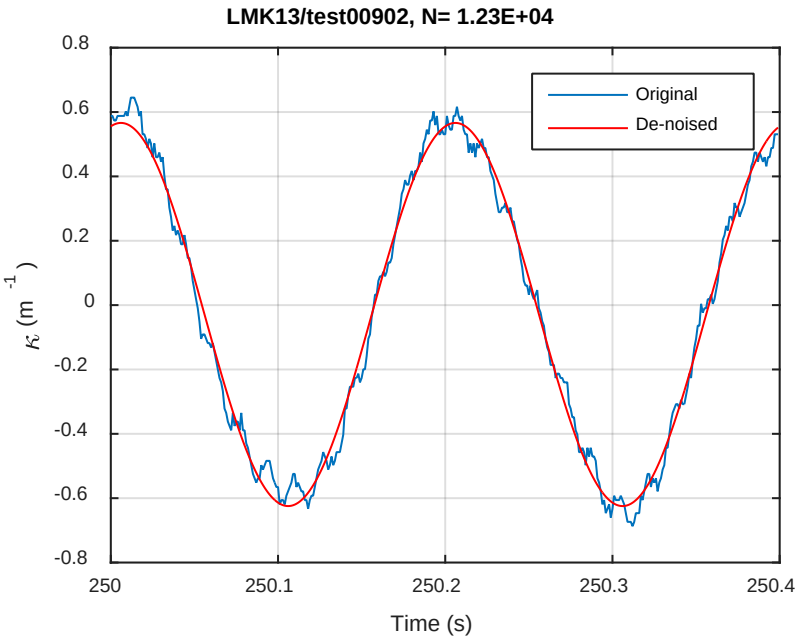

(c)

Fig. D.3 Monitoring-based responses: (a) curvature, (b) moment, (c) curvature, LMK13, 25.40 Nm, Ns = 1.23E+04 cycles.

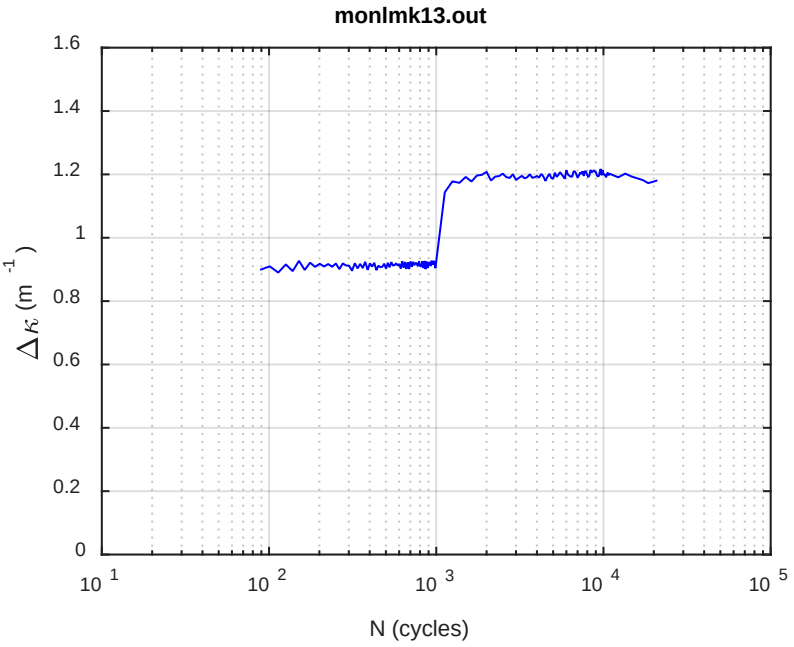
monlmk13.out
1.6
1.4
1.2
1
0.8
0.6
0.4
0.2
0
Δκ (m -1)
10 1
10 2
10 3
10 4
10 5
N (cycles)

(a)

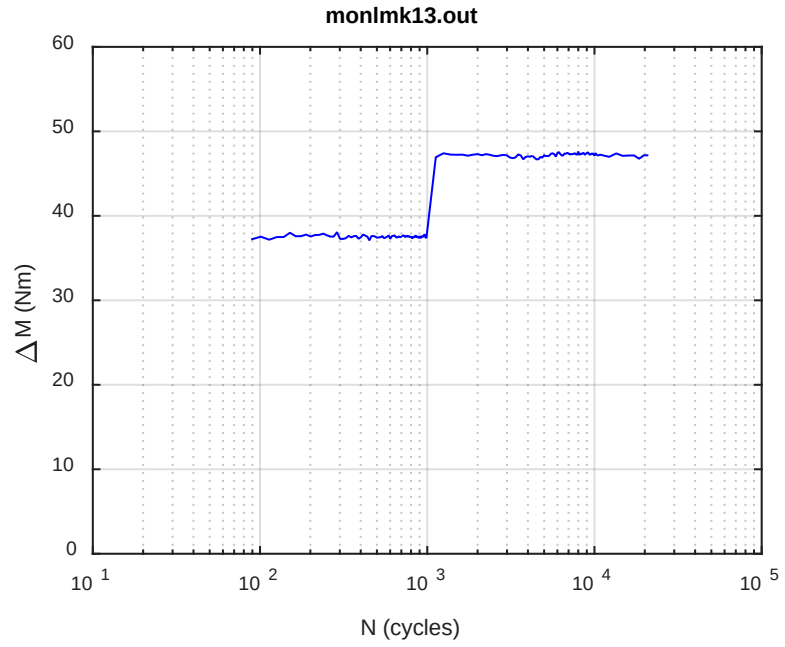
monlmk13.out
60
50
40
30
20
10
0
ΔM (Nm)
10 1
10 2
10 3
10 4
10 5
N (cycles)

(b)

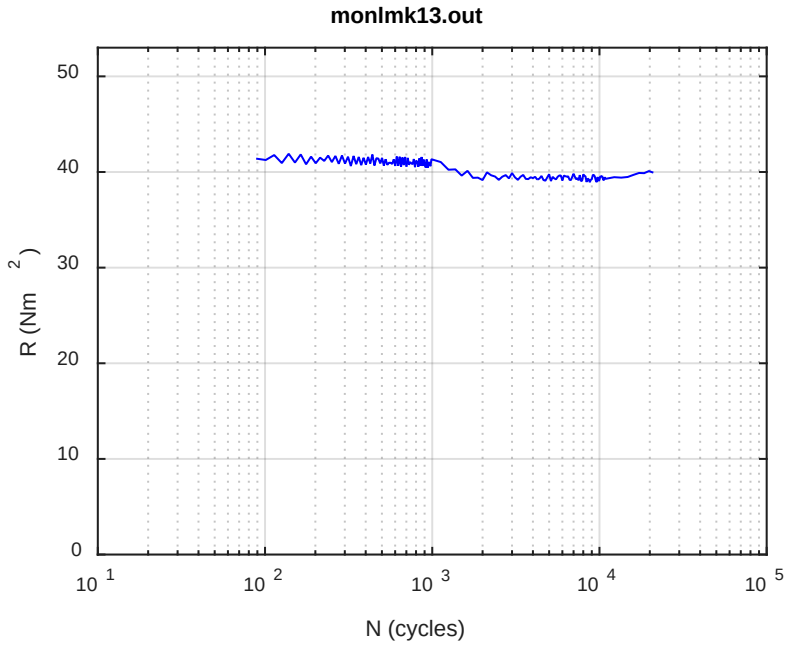
monlmk13.out
R (Nm 2)
N (cycles)

(c)

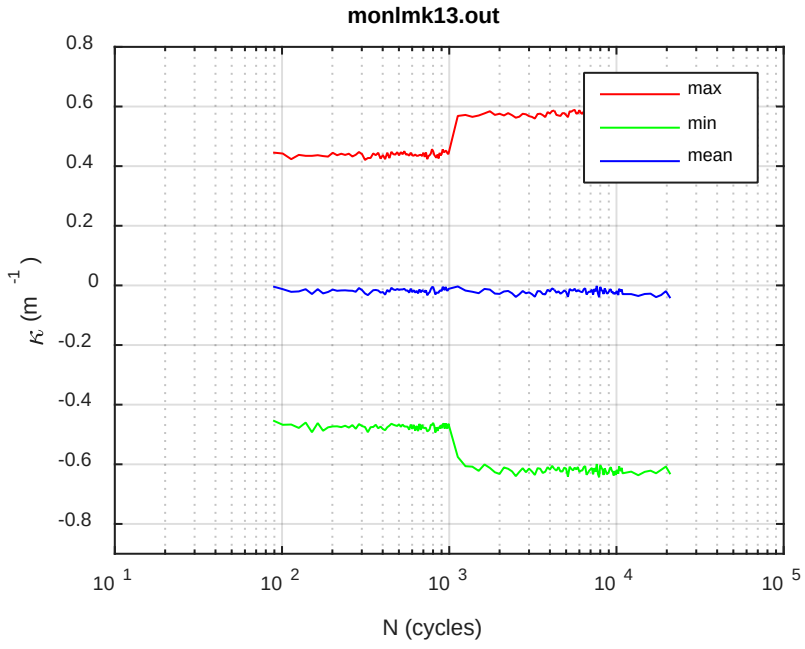
monlmk13.out
max
min
mean
κ (m -1)
N (cycles)

(d)

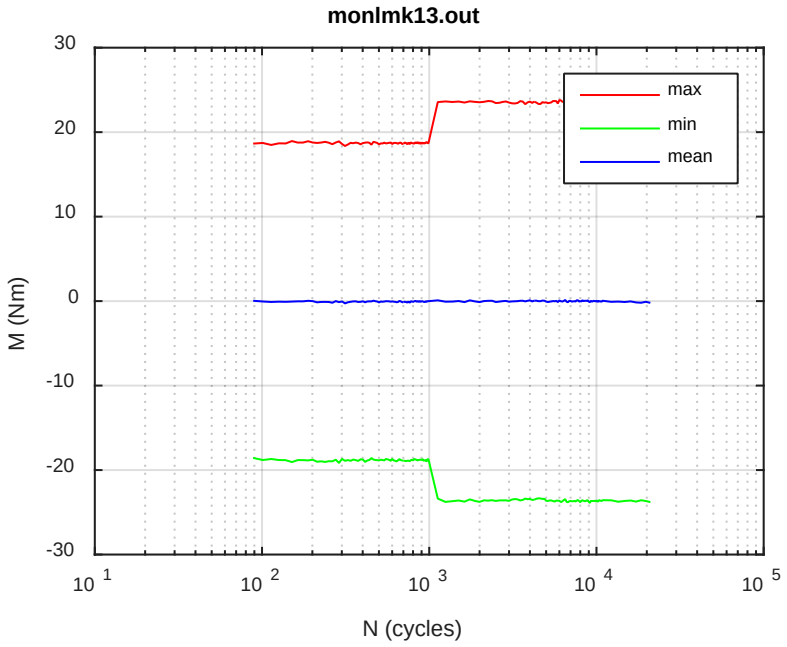

(e)

Fig. D.4 Monitoring-based responses: (a) curvature range, (b) moment range, (c) rigidity, (d) curvature peak/valley, (e) moment peak/valley, LMK13, 25.40 Nm, Nf = 2.10E+04 cycles.

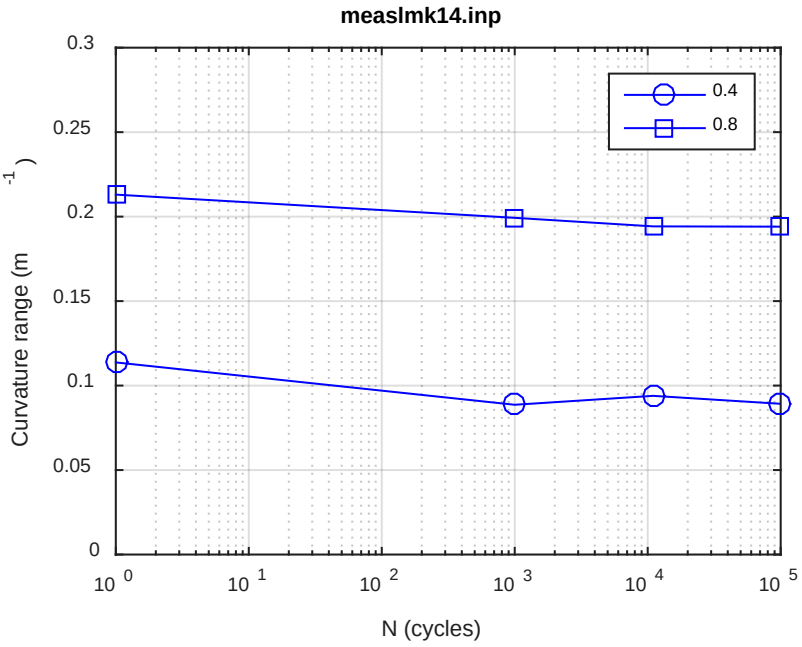
measlmk14.inp
0.4
0.8
Curvature range (m -1)
N (cycles)
0.3
0.25
0.2
0.15
0.1
0.05
0
10 0
10 1
10 2
10 3
10 4
10 5

(a)

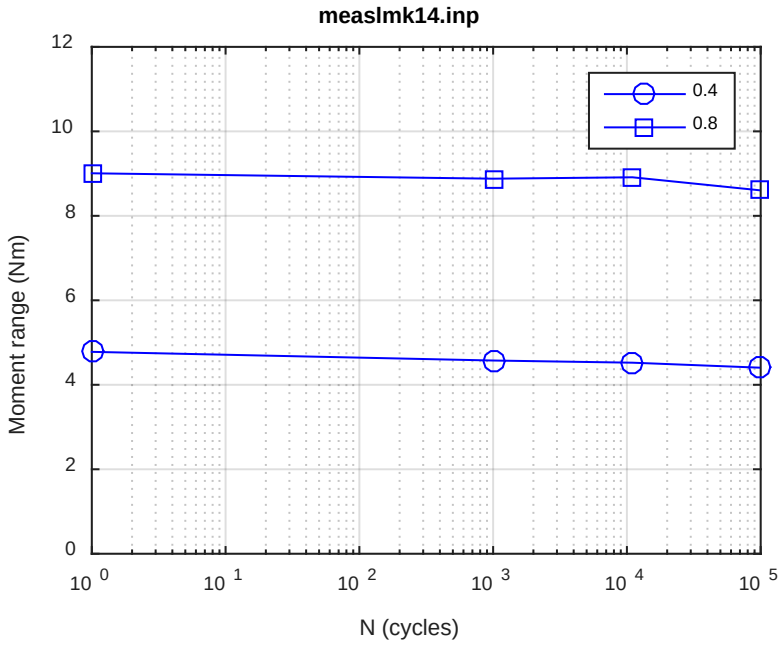
measlmk14.inp
0.4
0.8
Moment range (Nm)
N (cycles)
12
10
8
6
4
2
0
10 0
10 1
10 2
10 3
10 4
10 5

(b)

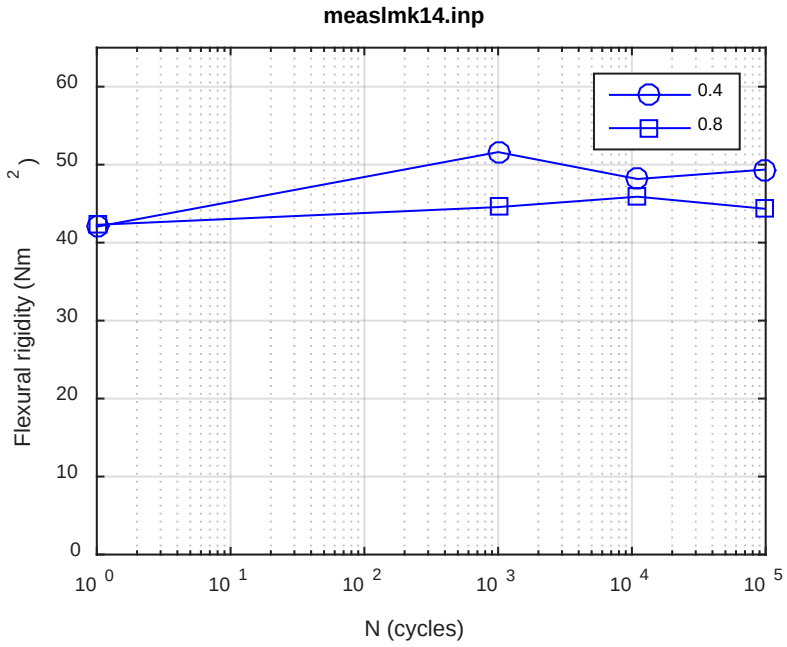
measlmk14.inp
0.4
0.8
Flexural rigidity (Nm 2)
N (cycles)
0
10
20
30
40
50
60
10 0
10 1
10 2
10 3
10 4
10 5

(c)

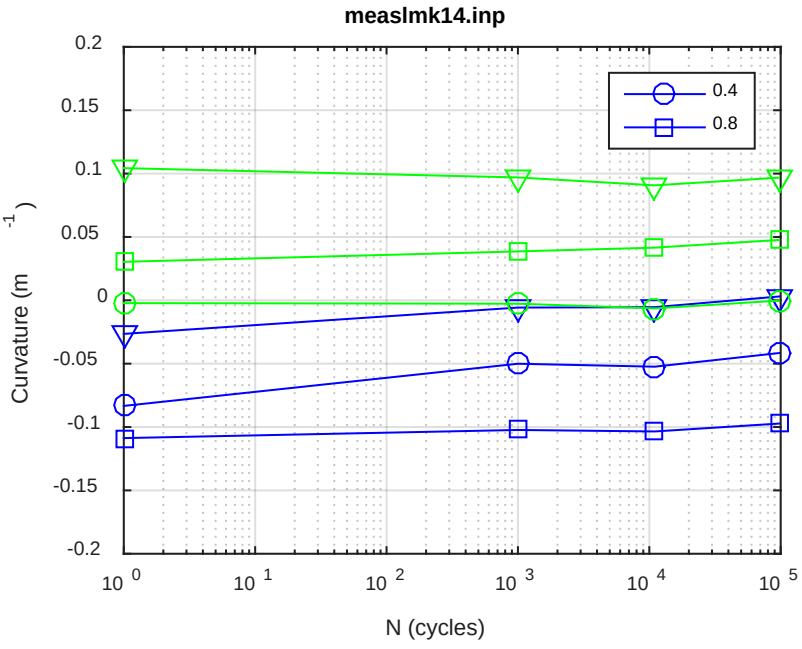
measlmk14.inp
0.4
0.8
Curvature (m -1)
N (cycles)
0.2
0.15
0.1
0.05
0
-0.05
-0.1
-0.15
-0.2
10 0
10 1
10 2
10 3
10 4
10 5

(d)

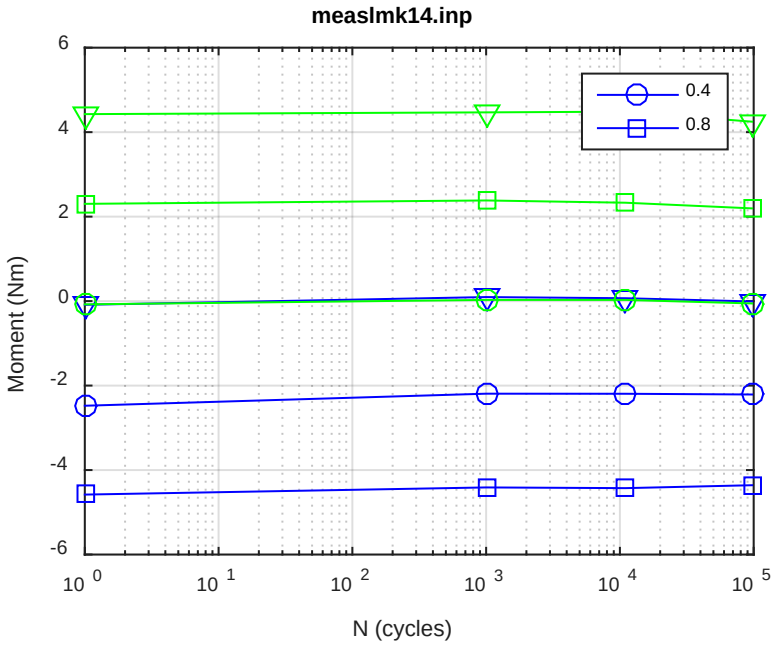

(e)

Fig. D.5 Measurement-based responses: (a) curvature range, (b) moment range, (c) rigidity, (d) curvature peak/valley, (e) moment peak/valley, LMK14, 10.16 Nm.

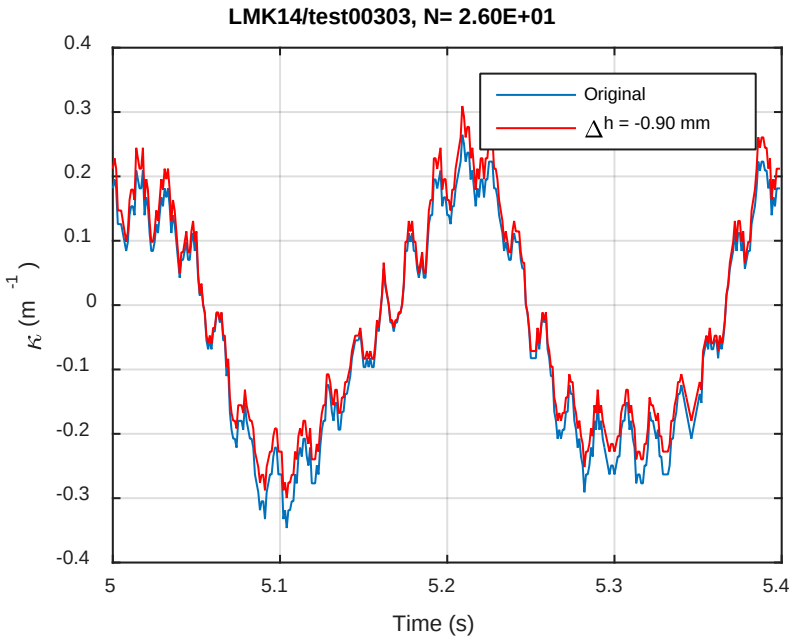
LMK14/test00303, N= 2.60E+01
Original
Δh = -0.90 mm
κ (m-1)
Time (s)
0.4
0.3
0.2
0.1
0
-0.1
-0.2
-0.3
-0.4
5
5.1
5.2
5.3
5.4

(a)

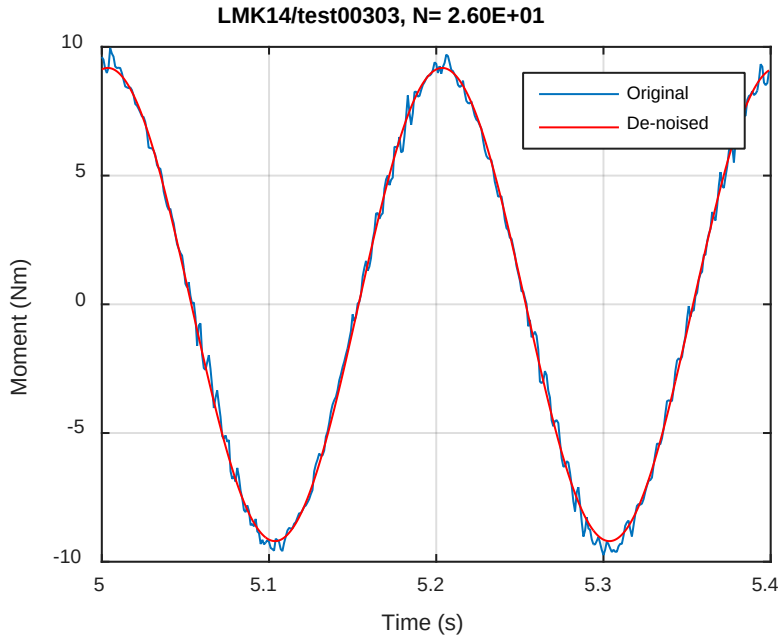
LMK14/test00303, N= 2.60E+01
Original
De-noised
Moment (Nm)
Time (s)
10
5
0
-5
-10
5
5.1
5.2
5.3
5.4

(b)

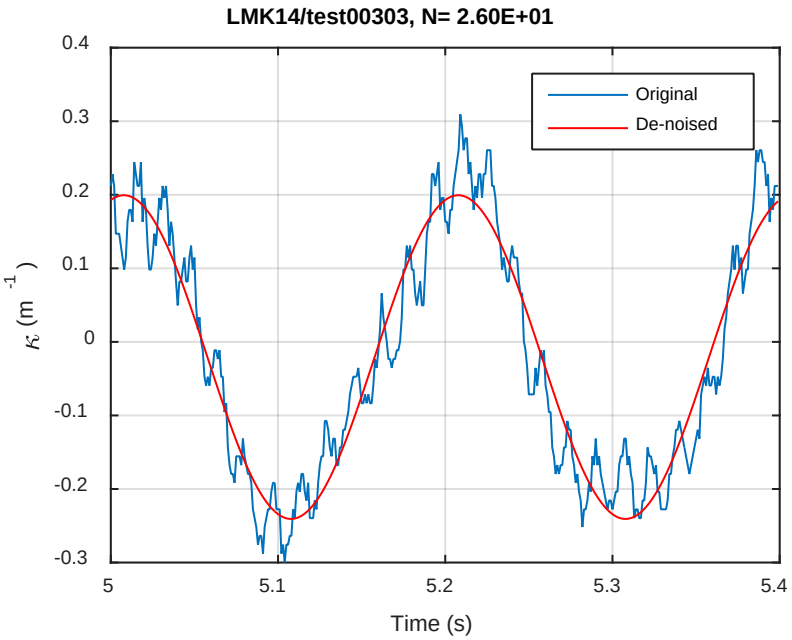

(c)

Fig. D.6 Monitoring-based responses: (a) curvature, (b) moment, (c) curvature, LMK14, 10.16 Nm, Ns = 2.60E+01 cycles.

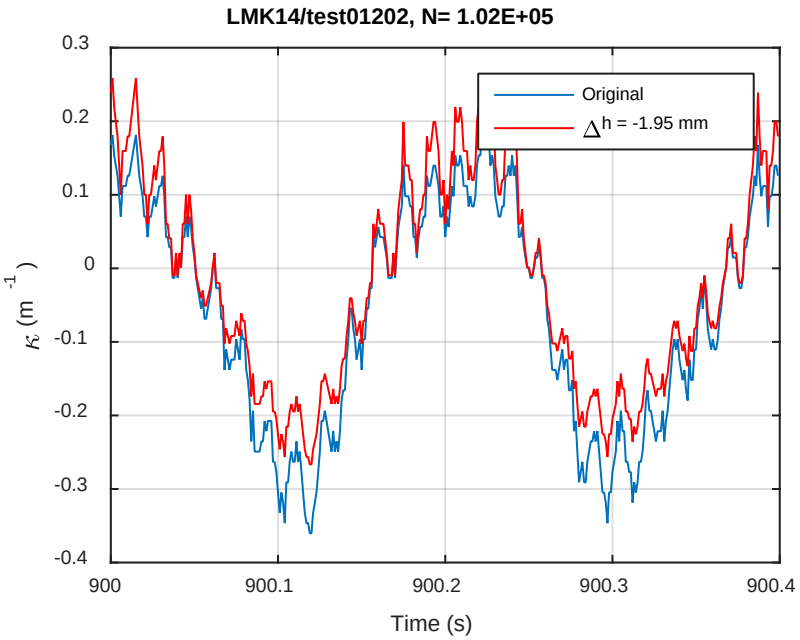
LMK14/test01202, N= 1.02E+05
Original
Δh = -1.95 mm
κ (m-1)
Time (s)
0.3
0.2
0.1
0
-0.1
-0.2
-0.3
-0.4
900
900.1
900.2
900.3
900.4

(a)

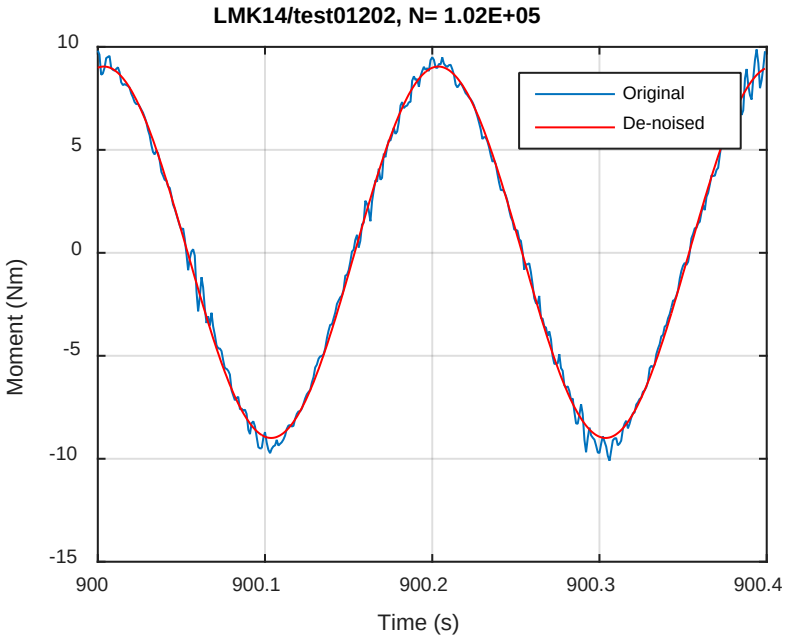
LMK14/test01202, N= 1.02E+05
Original
De-noised
Moment (Nm)
Time (s)
10
5
0
-5
-10
-15
900
900.1
900.2
900.3
900.4

(b)

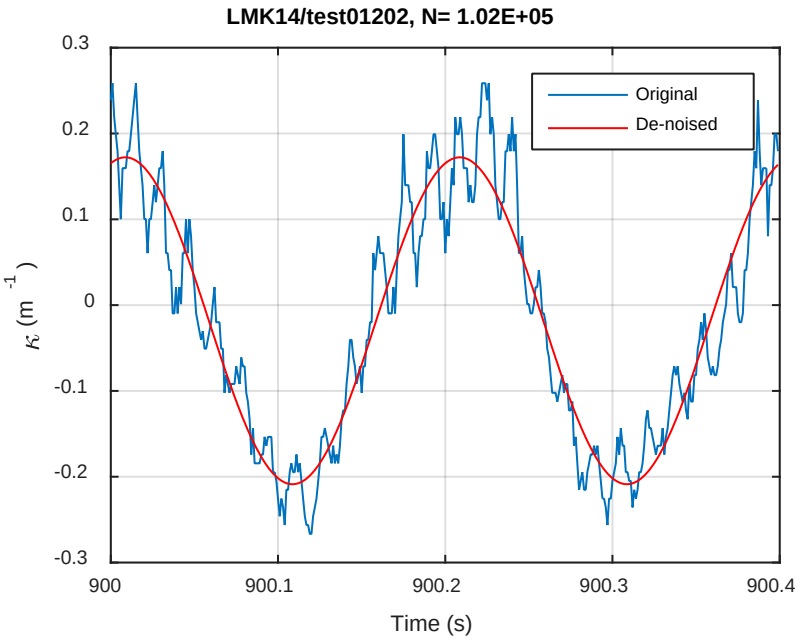

(c)

Fig. D.7 Monitoring-based responses: (a) curvature, (b) moment, (c) curvature, LMK14, 10.16 Nm, Ns = 1.02E+05 cycles.

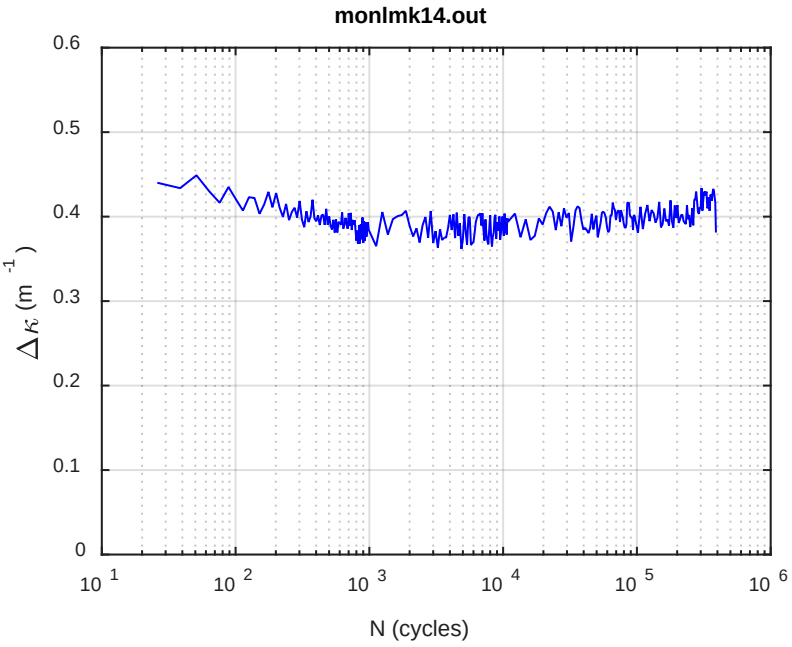
monlmk14.out
0.6
0.5
0.4
0.3
0.2
0.1
0
Δκ (m -1)
10 1
10 2
10 3
10 4
10 5
10 6
N (cycles)

(a)

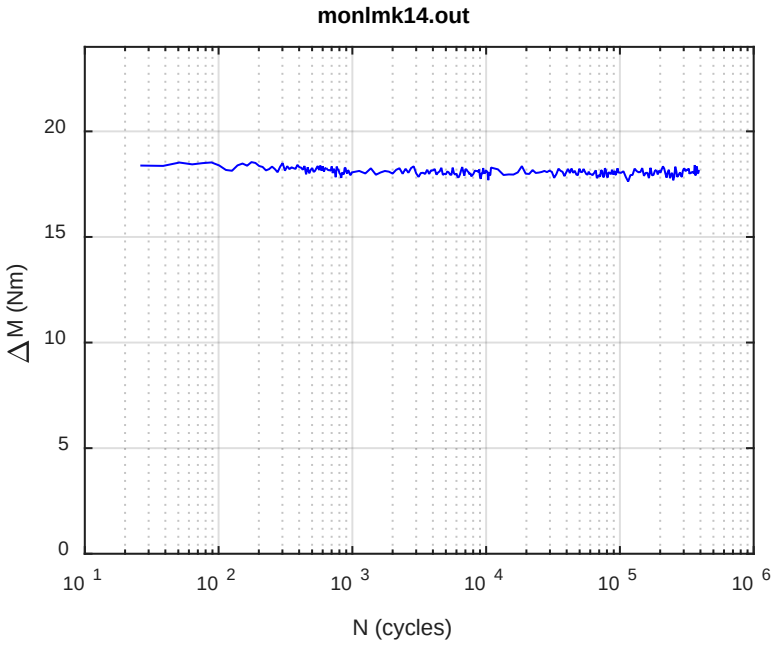
monlmk14.out
20
15
10
5
0
ΔM (Nm)
10 1
10 2
10 3
10 4
10 5
10 6
N (cycles)

(b)

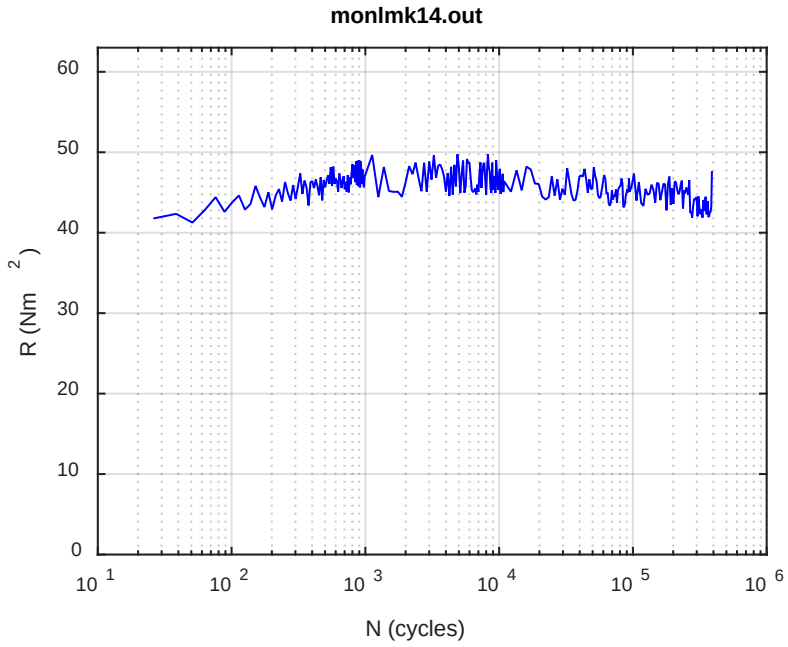
monlmk14.out
R (Nm 2)
N (cycles)

(c)

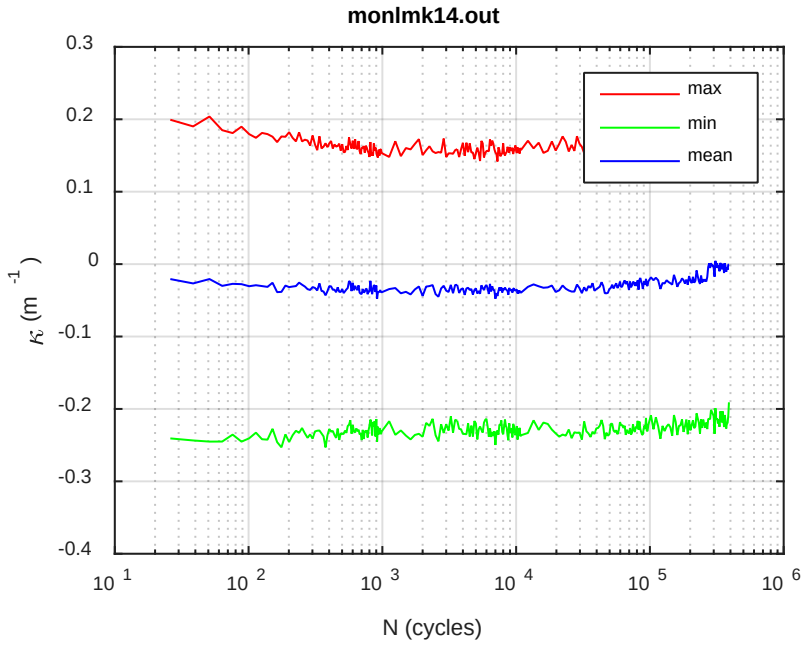
monlmk14.out
max
min
mean
κ (m -1)
N (cycles)

(d)

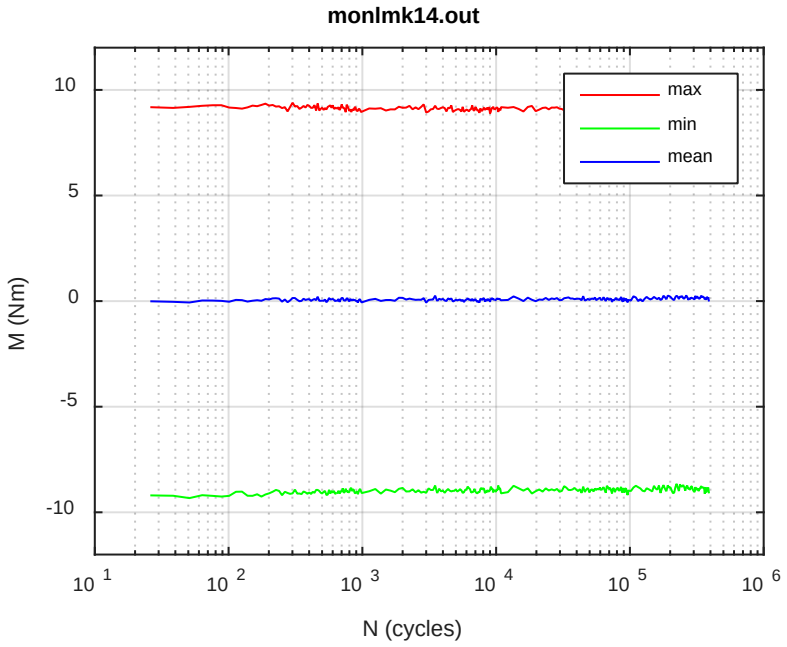

(e)

Fig. D.8 Monitoring-based responses: (a) curvature range, (b) moment range, (c) rigidity, (d) curvature peak/valley, (e) moment peak/valley, LMK14, 10.16 Nm, Nf = 3.90E+05 cycles.

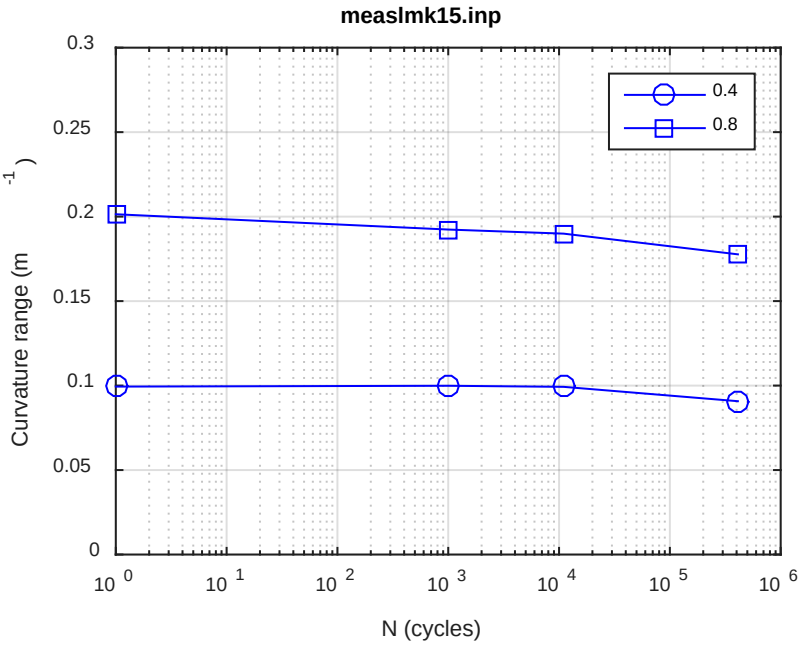
measlmk15.inp
0.3
0.25
0.2
0.15
0.1
0.05
0
Curvature range (m -1)
0.4
0.8
10 0
10 1
10 2
10 3
10 4
10 5
10 6
N (cycles)

(a)

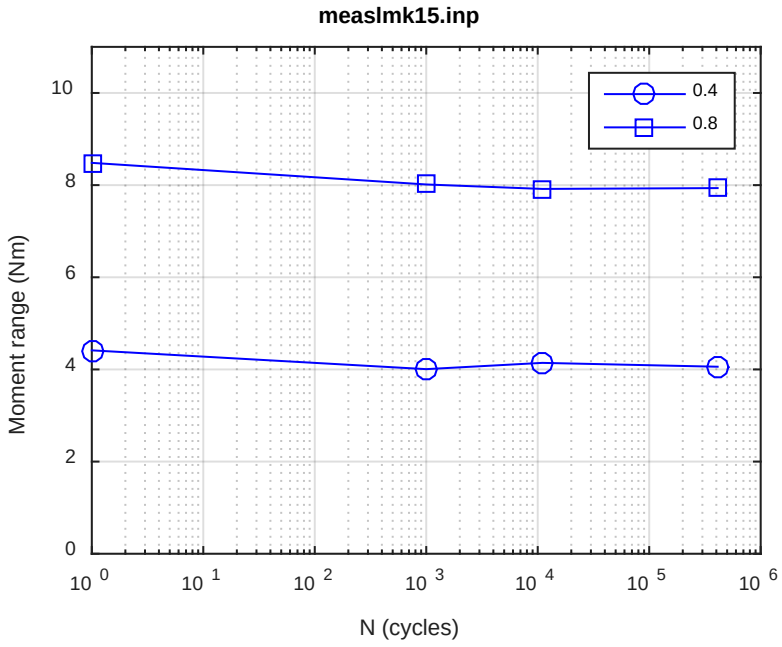
measlmk15.inp
10
8
6
4
2
0
Moment range (Nm)
0.4
0.8
10 0
10 1
10 2
10 3
10 4
10 5
10 6
N (cycles)

(b)

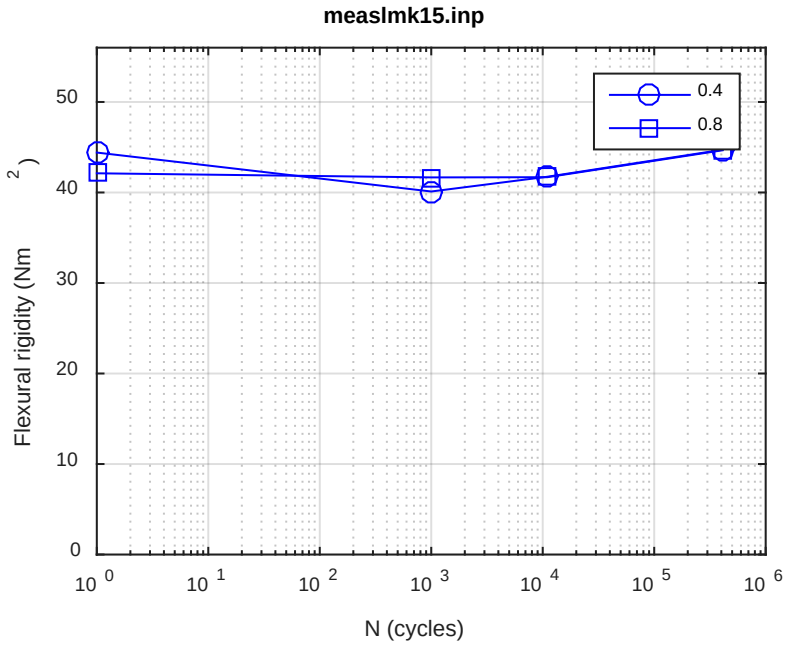
measlmk15.inp
0.4
0.8
Flexural rigidity (Nm 2)
N (cycles)

(c)

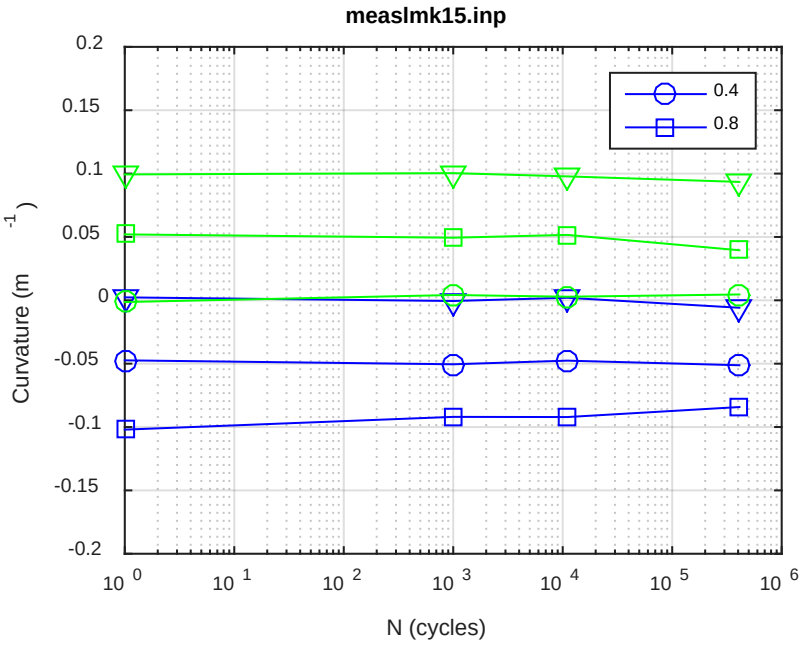
measlmk15.inp
0.4
0.8
Curvature (m -1)
N (cycles)

(d)

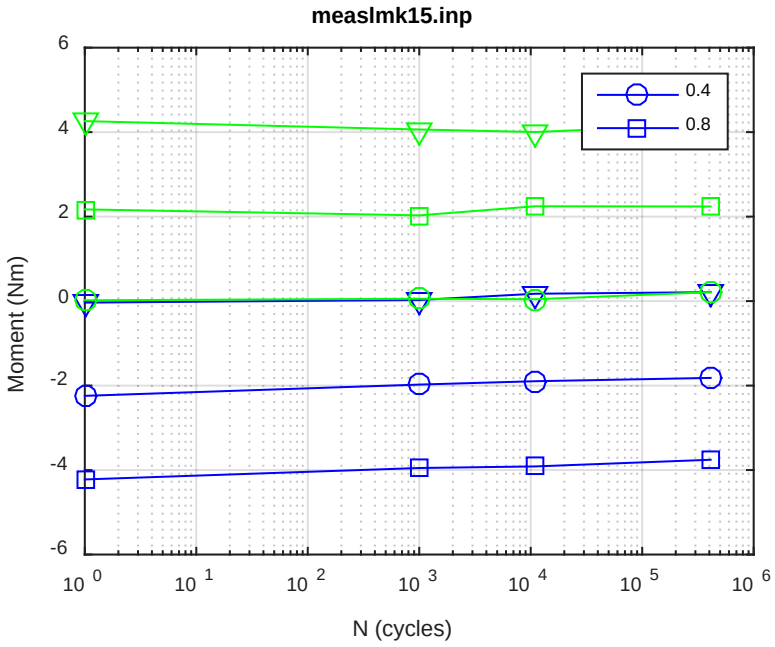

(e)

Fig. D.9 Measurement-based responses: (a) curvature range, (b) moment range, (c) rigidity, (d) curvature peak/valley, (e) moment peak/valley, LMK15, 10.16 Nm.

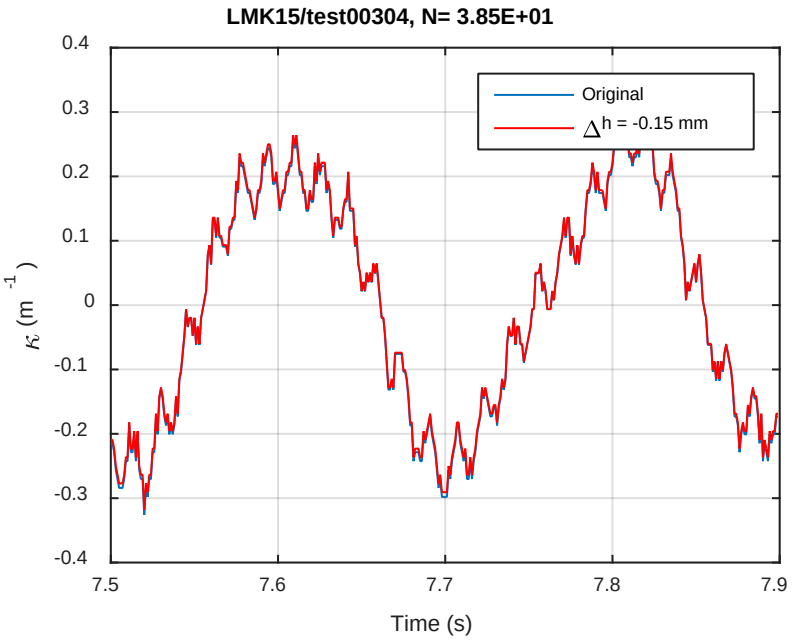
LMK15/test00304, N= 3.85E+01
Original
Δh = -0.15 mm
κ (m-1)
Time (s)
0.4
0.3
0.2
0.1
0
-0.1
-0.2
-0.3
-0.4
7.5
7.6
7.7
7.8
7.9

(a)

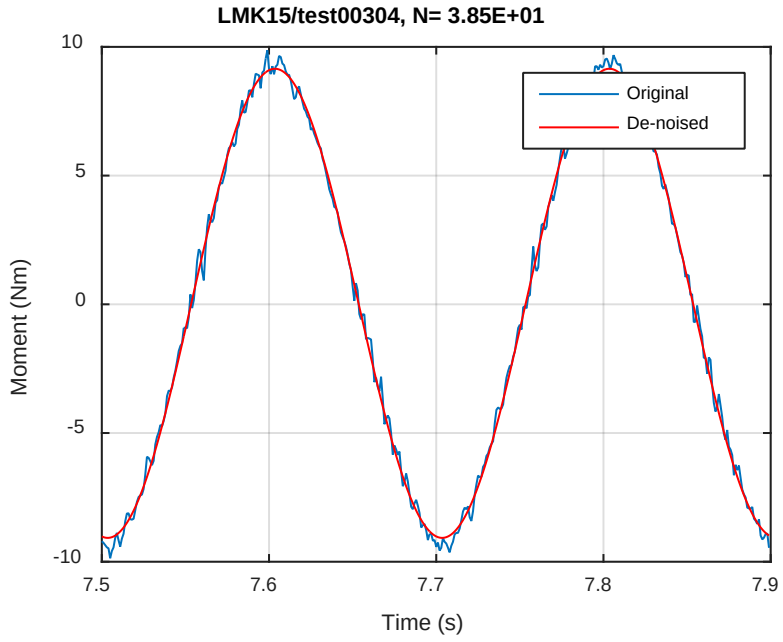
LMK15/test00304, N= 3.85E+01
Original
De-noised
Moment (Nm)
Time (s)
10
5
0
-5
-10
7.5
7.6
7.7
7.8
7.9

(b)

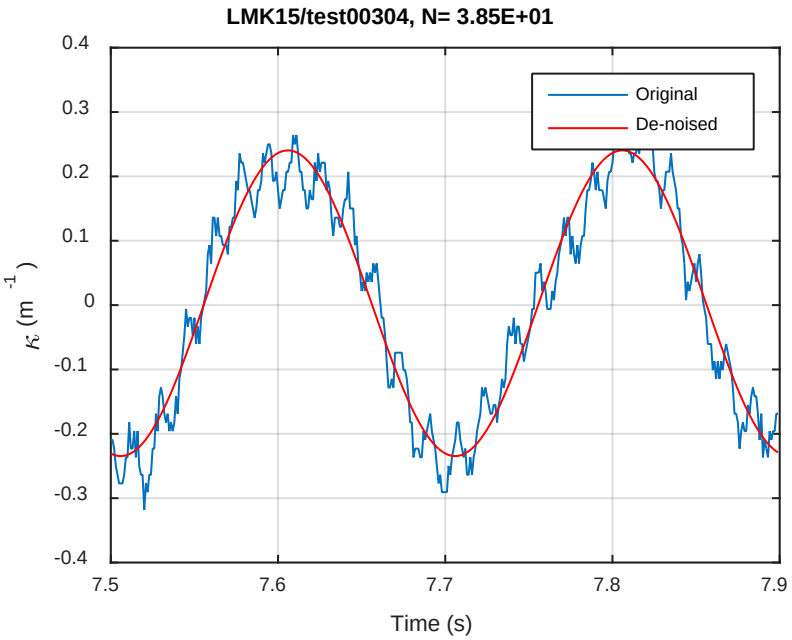

(c)

Fig. D.10 Monitoring-based responses: (a) curvature, (b) moment, (c) curvature, LMK15, 10.16 Nm, Ns = 3.85E+01 cycles.

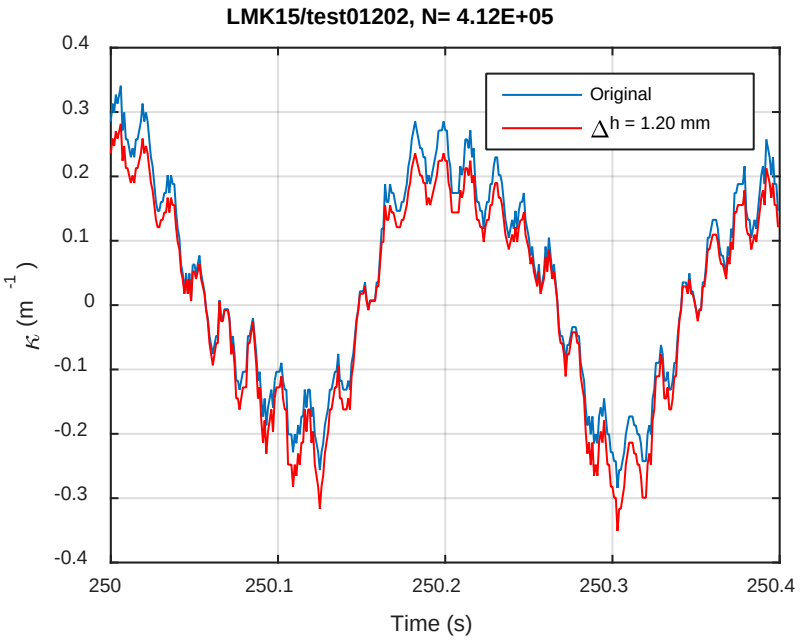
LMK15/test01202, N= 4.12E+05
Original
Δh = 1.20 mm
κ (m-1)
Time (s)
0.4
0.3
0.2
0.1
0
-0.1
-0.2
-0.3
-0.4
250
250.1
250.2
250.3
250.4

(a)

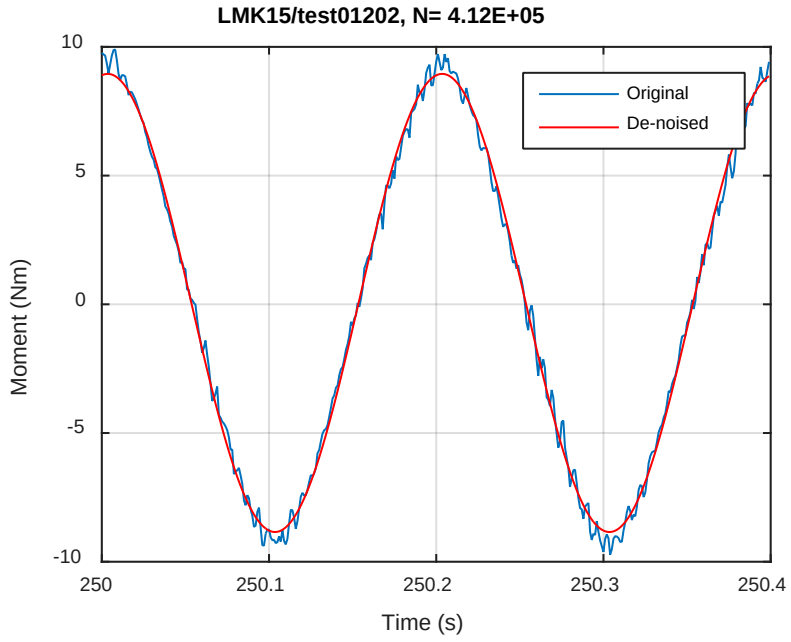
LMK15/test01202, N= 4.12E+05
Original
De-noised
Moment (Nm)
Time (s)
10
5
0
-5
-10
250
250.1
250.2
250.3
250.4

(b)

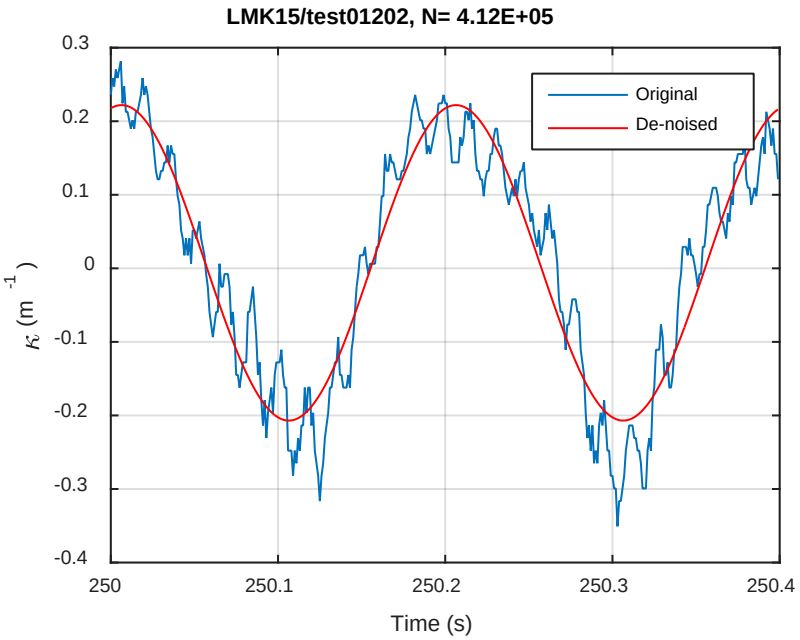

(c)

Fig. D.11 Monitoring-based responses: (a) curvature, (b) moment, (c) curvature, LMK15, 10.16 Nm, Ns = 4.12E+05 cycles.

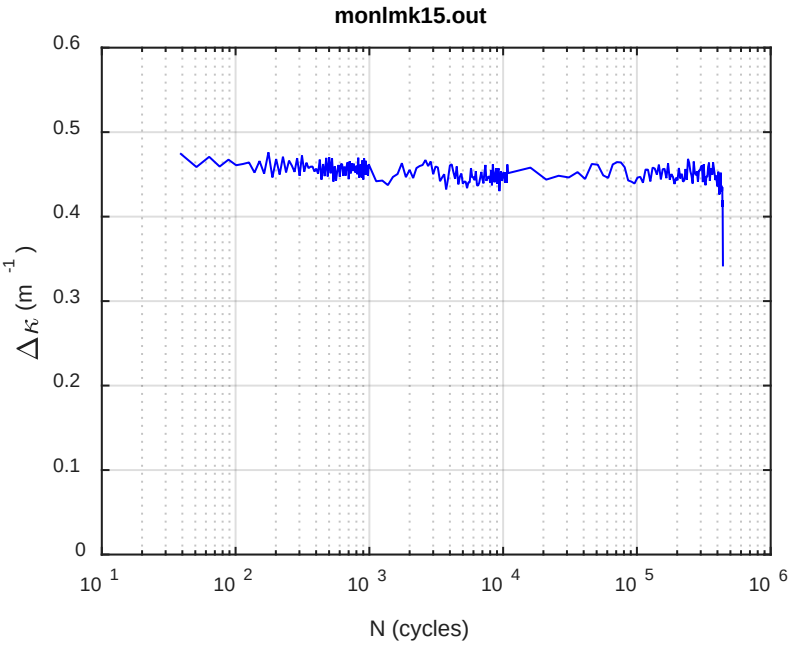
monlmk15.out
0.6
0.5
0.4
0.3
0.2
0.1
0
Δκ (m -1)
10 1
10 2
10 3
10 4
10 5
10 6
N (cycles)

(a)

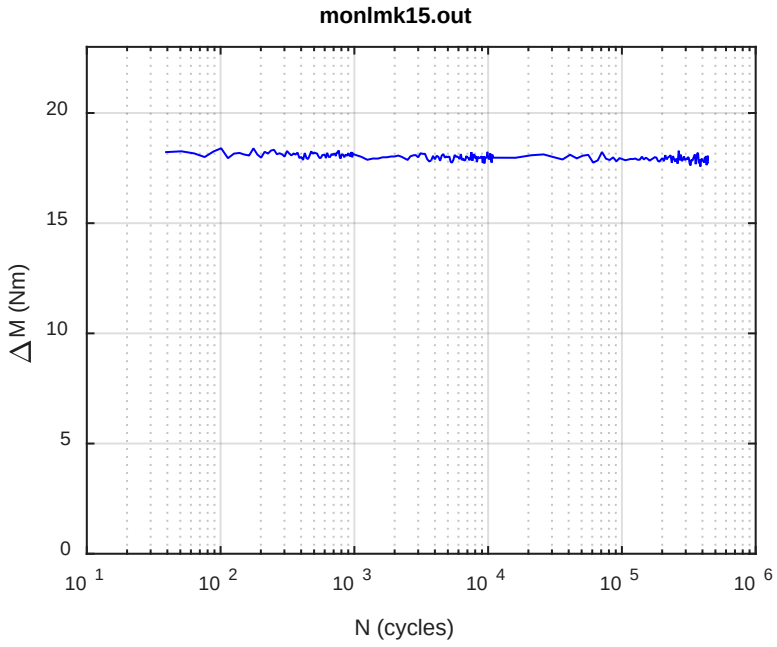
monlmk15.out
20
15
10
5
0
ΔM (Nm)
10 1
10 2
10 3
10 4
10 5
10 6
N (cycles)

(b)

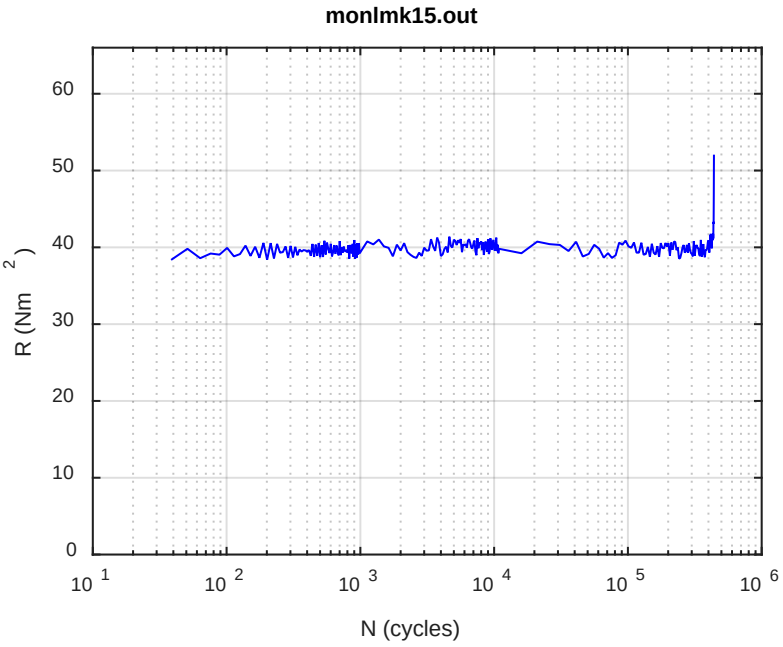
monlmk15.out
R (Nm 2)
N (cycles)

(c)

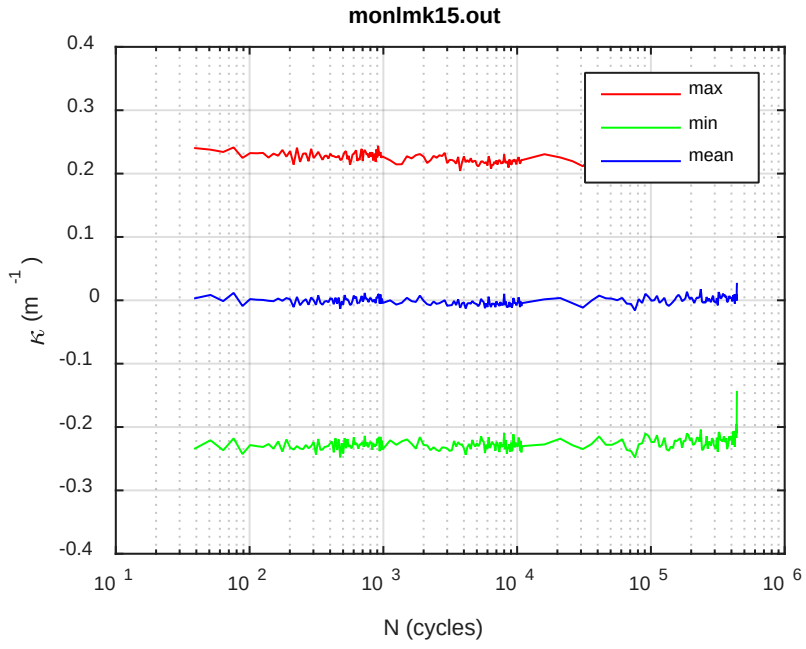
monlmk15.out
max
min
mean
κ (m -1)
N (cycles)

(d)

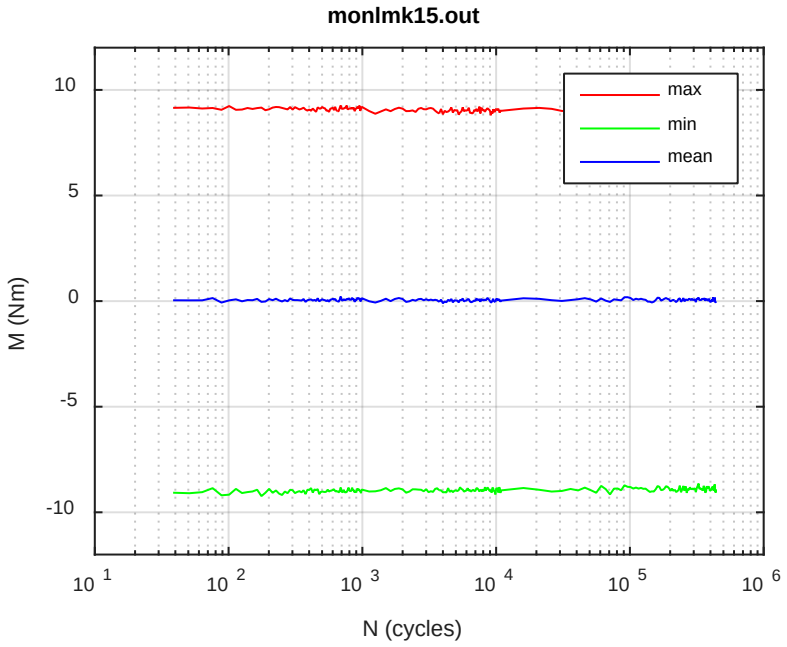

(e)

Fig. D.12 Monitoring-based responses: (a) curvature range, (b) moment range, (c) rigidity, (d) curvature peak/valley, (e) moment peak/valley, LMK15, 10.16 Nm, Nf = 4.41E+05 cycles.

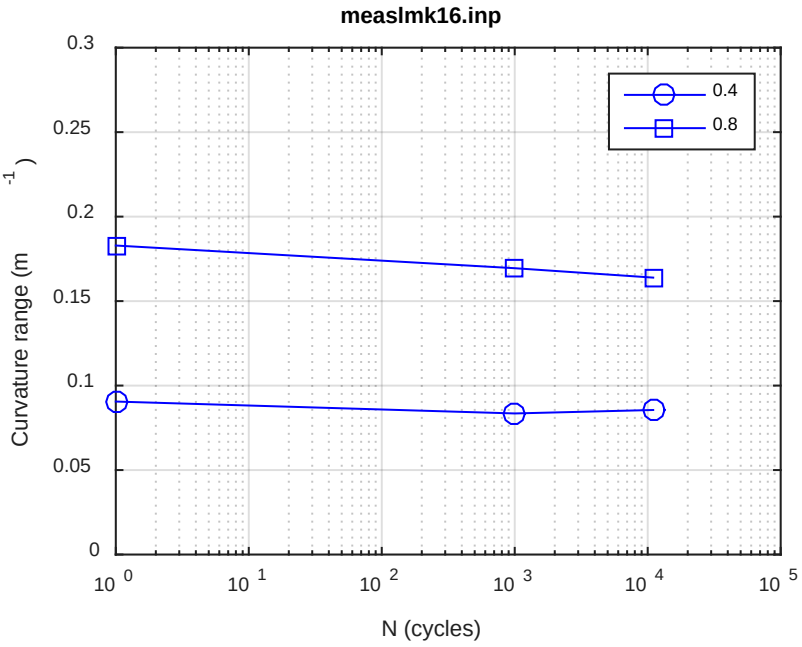
measlmk16.inp
0.3
0.25
0.2
0.15
0.1
0.05
0
Curvature range (m -1)
0.4
0.8
10 0
10 1
10 2
10 3
10 4
10 5
N (cycles)

(a)

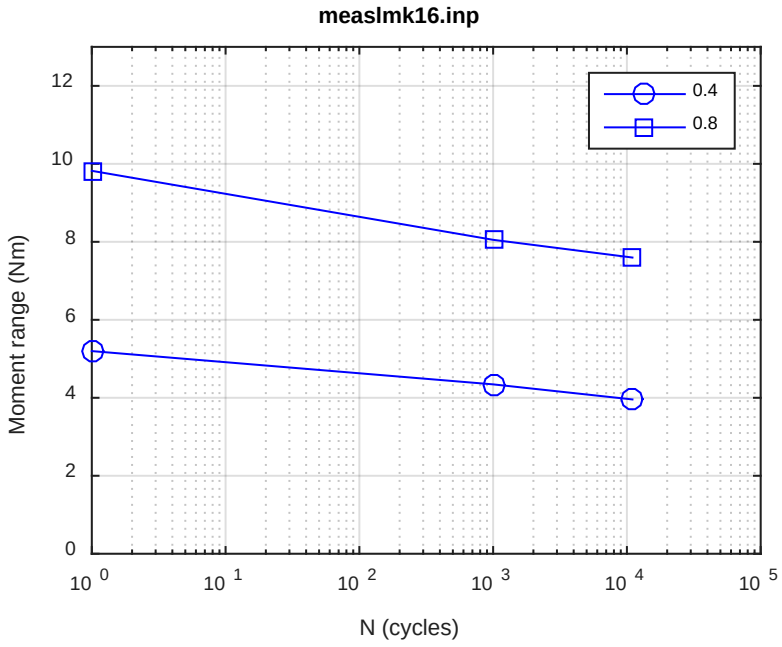
measlmk16.inp
12
10
8
6
4
2
0
Moment range (Nm)
0.4
0.8
10 0
10 1
10 2
10 3
10 4
10 5
N (cycles)

(b)

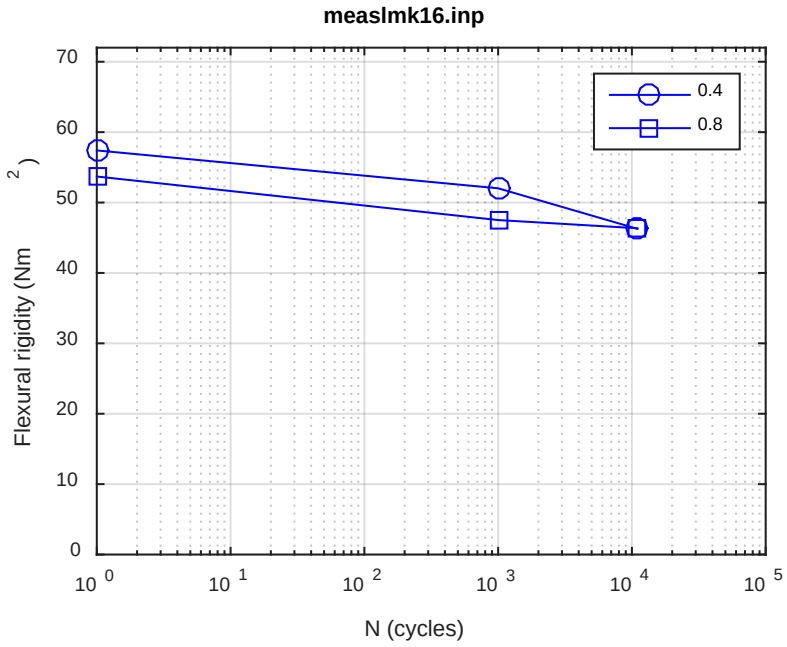
measlmk16.inp
Flexural rigidity (Nm 2)
N (cycles)
0.4
0.8
70
60
50
40
30
20
10
0
10 0
10 1
10 2
10 3
10 4
10 5

(c)

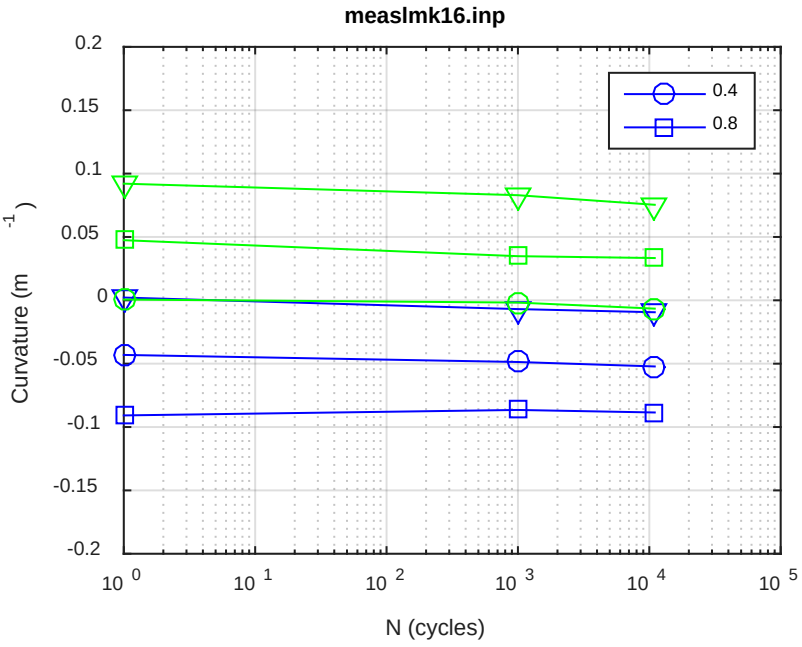
measlmk16.inp
Curvature (m -1)
N (cycles)
0.4
0.8
0.2
0.15
0.1
0.05
0
-0.05
-0.1
-0.15
-0.2
10 0
10 1
10 2
10 3
10 4
10 5

(d)

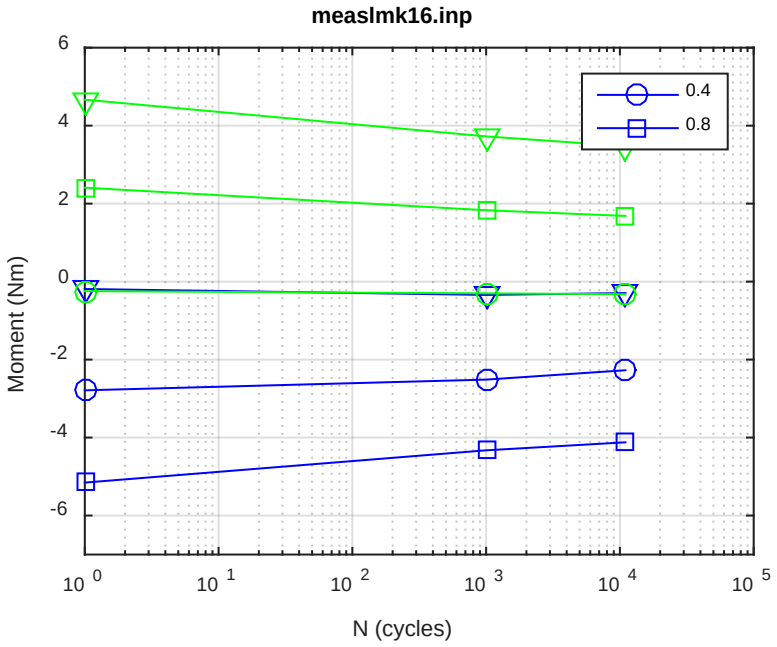

(e)

Fig. D.13 Measurement-based responses: (a) curvature range, (b) moment range, (c) rigidity, (d) curvature peak/valley, (e) moment peak/valley, LMK16, 30.48 Nm.

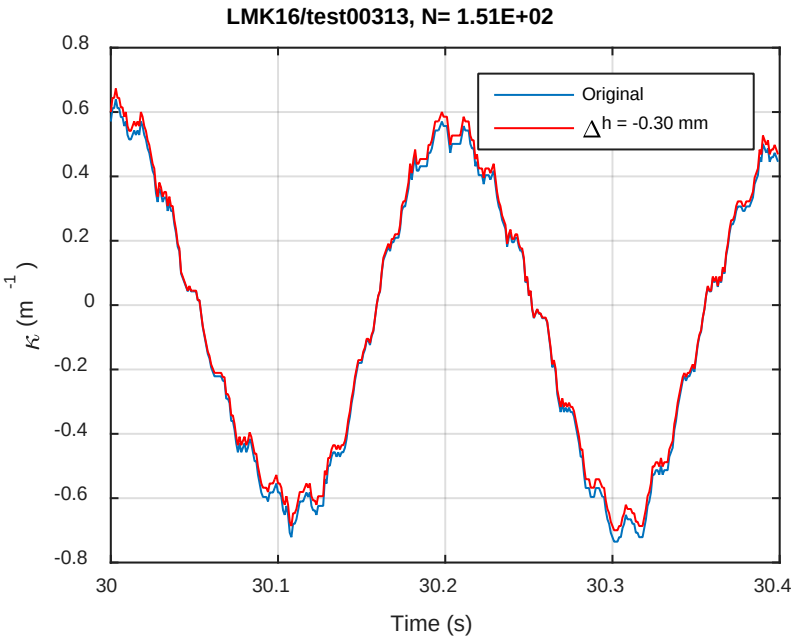
LMK16/test00313, N= 1.51E+02
Original
Δh = -0.30 mm
κ (m-1)
Time (s)
0.8
0.6
0.4
0.2
0
-0.2
-0.4
-0.6
-0.8
30
30.1
30.2
30.3
30.4

(a)

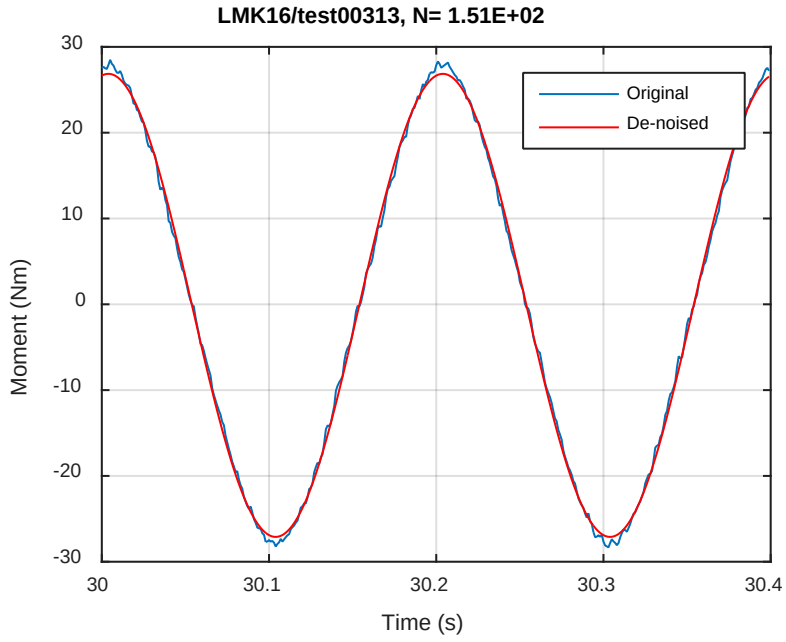
LMK16/test00313, N= 1.51E+02
Original
De-noised
Moment (Nm)
Time (s)
30
20
10
0
-10
-20
-30
30
30.1
30.2
30.3
30.4

(b)

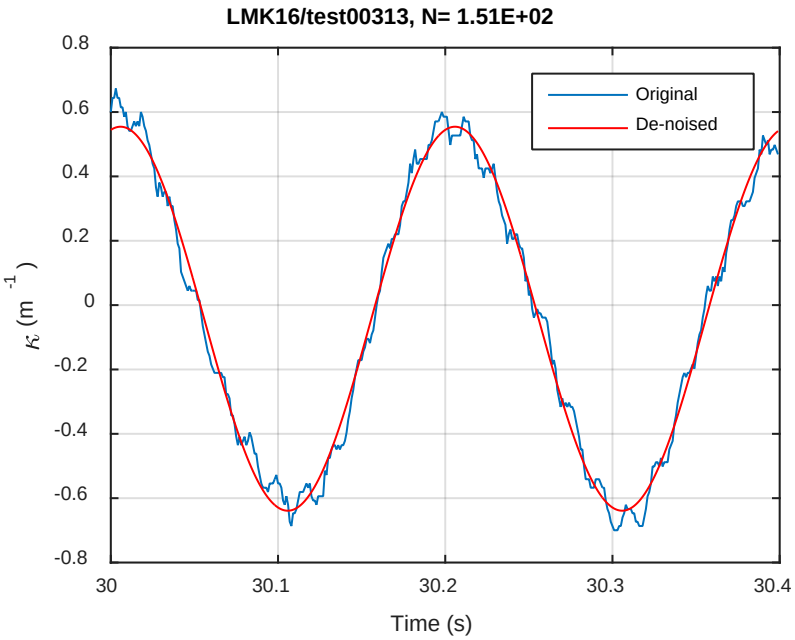

(c)

Fig. D.14 Monitoring-based responses: (a) curvature, (b) moment, (c) curvature, LMK16, 30.48 Nm, Ns = 1.51E+02 cycles.

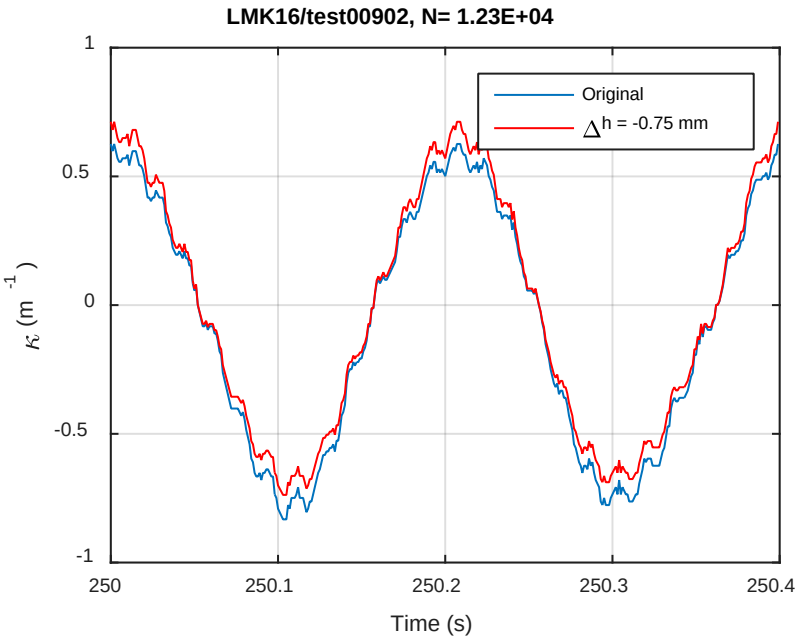
LMK16/test00902, N= 1.23E+04
Original
Δh = -0.75 mm
κ (m-1)
Time (s)
1
0.5
0
-0.5
-1
250
250.1
250.2
250.3
250.4

(a)

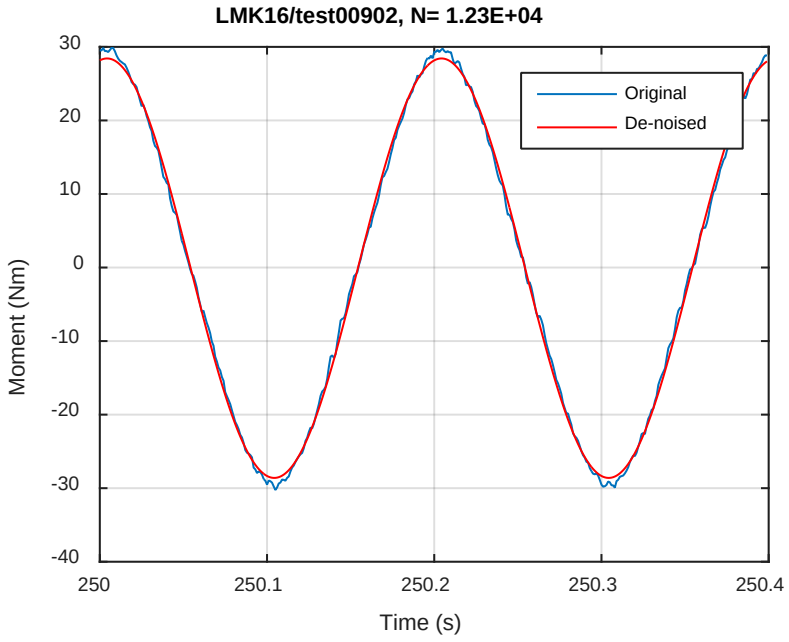
LMK16/test00902, N= 1.23E+04
Original
De-noised
Moment (Nm)
Time (s)
30
20
10
0
-10
-20
-30
-40
250
250.1
250.2
250.3
250.4

(b)

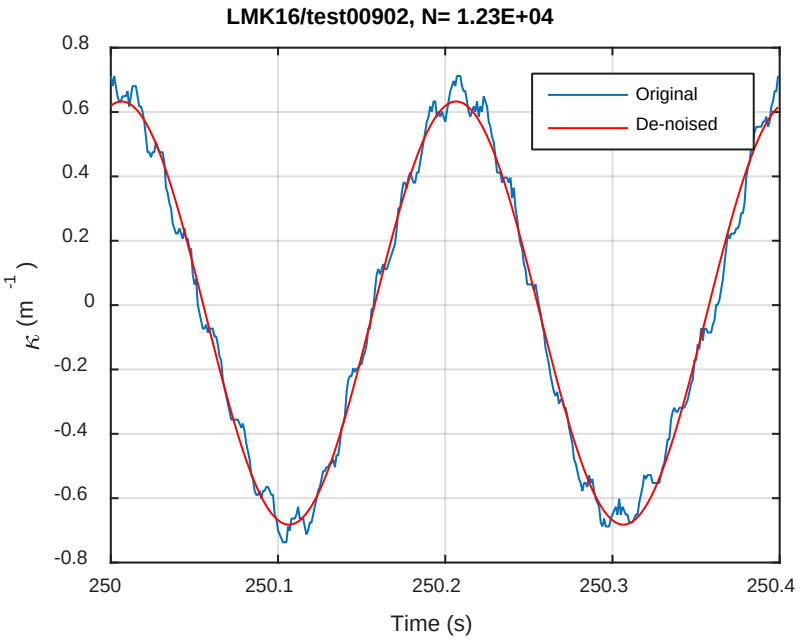

(c)

Fig. D.15 Monitoring-based responses: (a) curvature, (b) moment, (c) curvature, LMK16, 30.48 Nm, Ns = 1.23E+04 cycles.

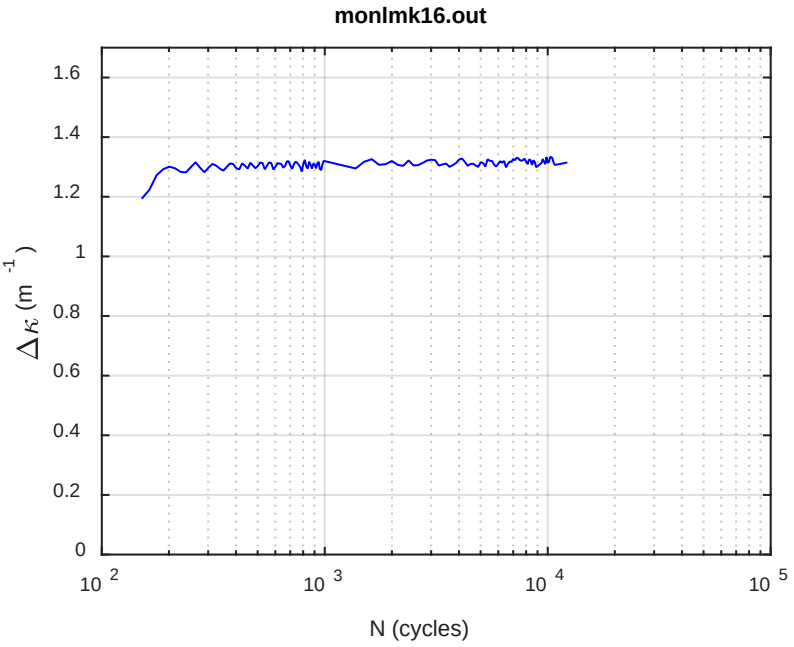
monlmk16.out
1.6
1.4
1.2
1
0.8
0.6
0.4
0.2
0
Δκ (m -1)
10 2
10 3
10 4
10 5
N (cycles)

(a)

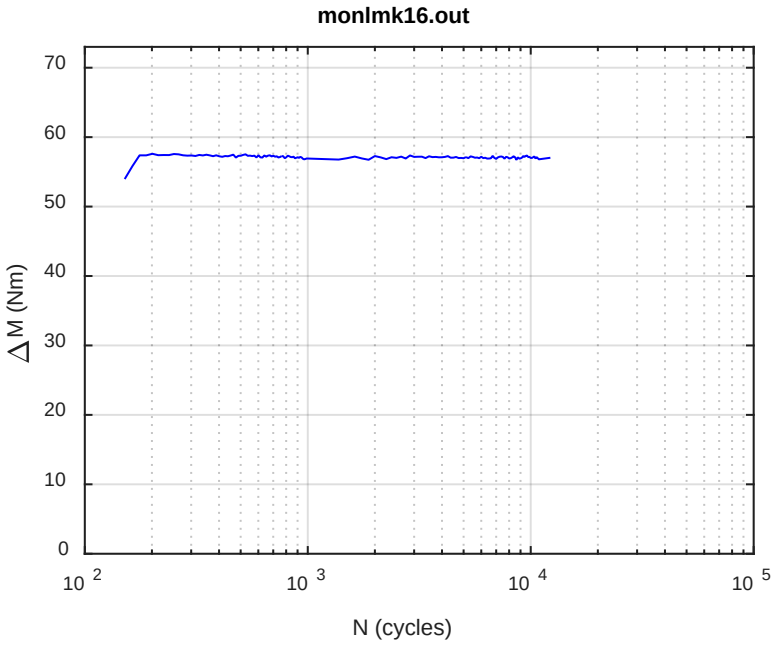
monlmk16.out
70
60
50
40
30
20
10
0
ΔM (Nm)
10 2
10 3
10 4
10 5
N (cycles)

(b)

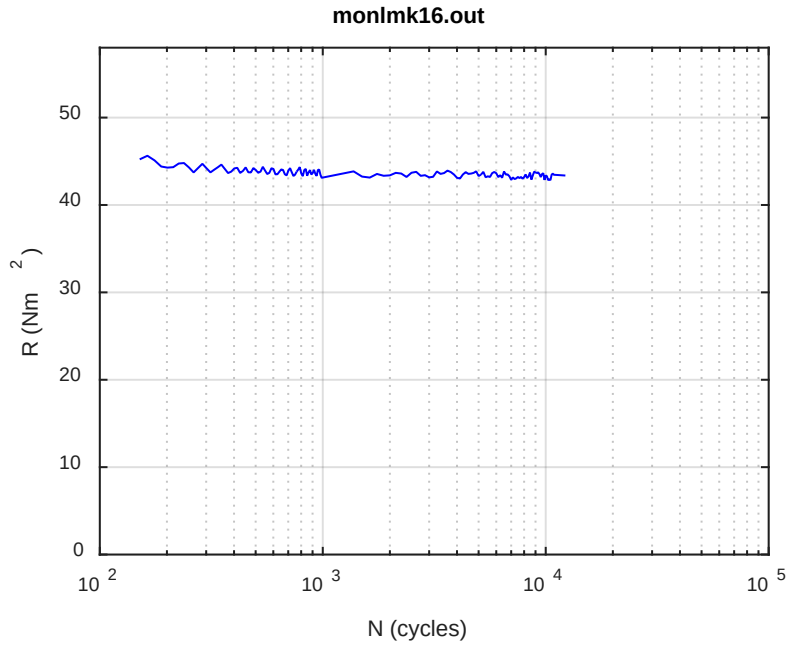
monlmk16.out
R (Nm 2)
N (cycles)

(c)

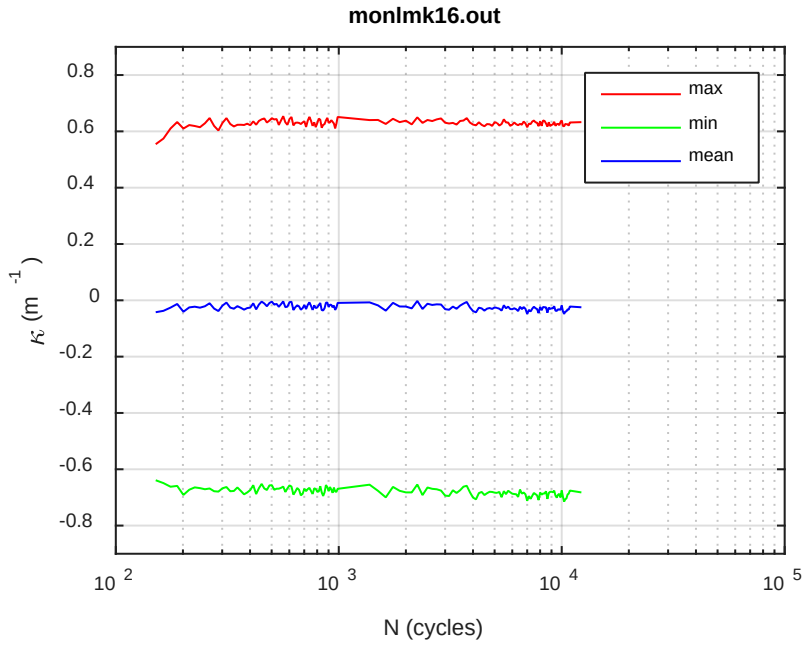
monlmk16.out
max
min
mean
κ (m -1)
N (cycles)

(d)

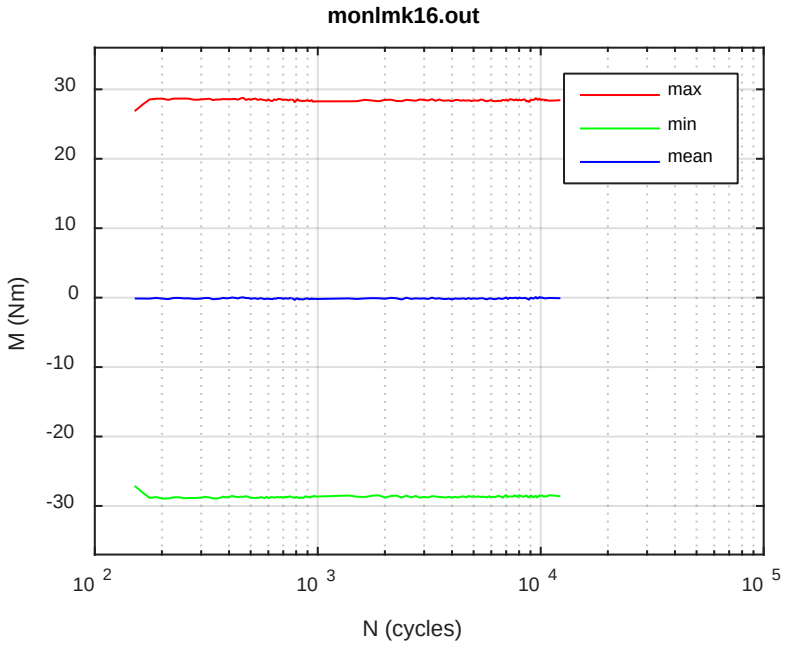

(e)

Fig. D.16 Monitoring-based responses: (a) curvature range, (b) moment range, (c) rigidity, (d) curvature peak/valley, (e) moment peak/valley, LMK16, 30.48 Nm, Nf = 1.36E+04 cycles.

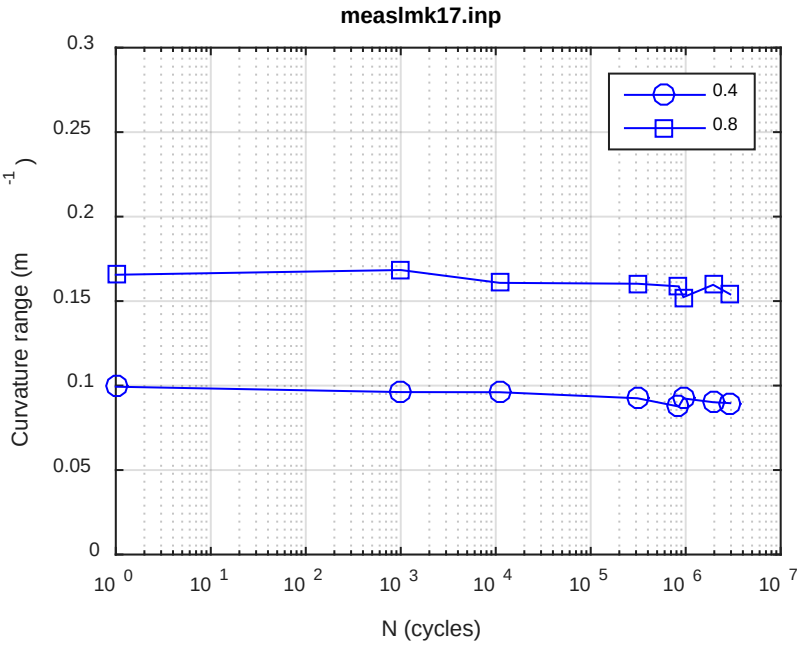
measlmk17.inp
0.4
0.8
Curvature range (m -1)
N (cycles)

(a)

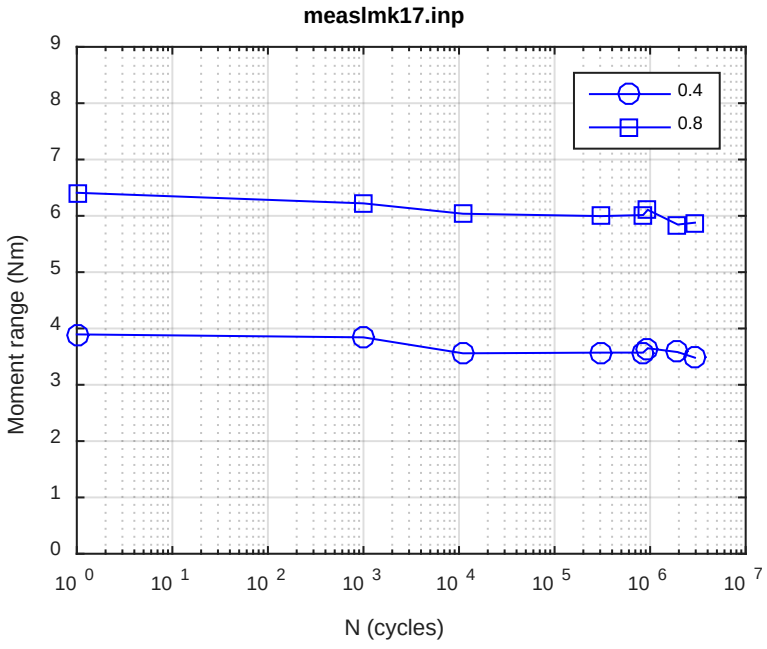
measlmk17.inp
0.4
0.8
Moment range (Nm)
N (cycles)

(b)

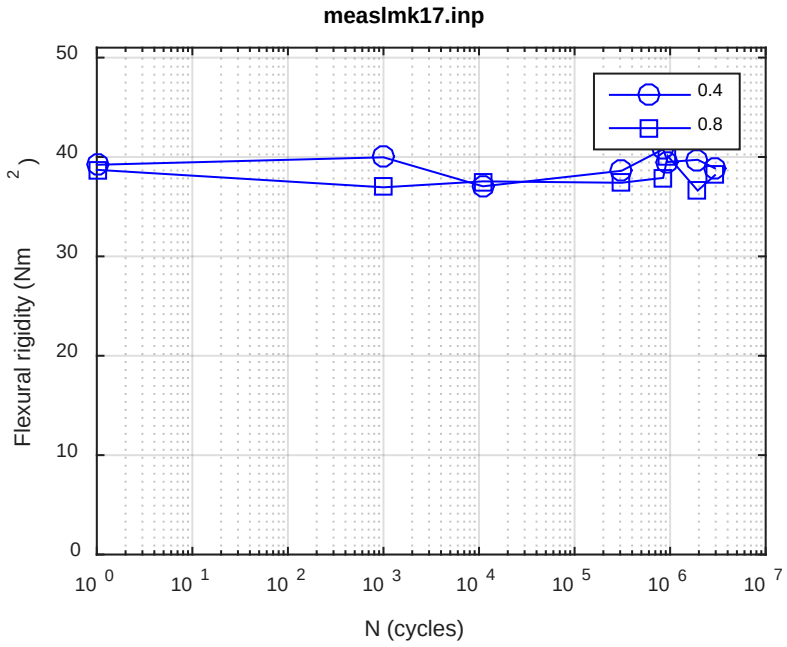
measlmk17.inp
Flexural rigidity (Nm 2)
N (cycles)
0.4
0.8
50
40
30
20
10
0
10 0
10 1
10 2
10 3
10 4
10 5
10 6
10 7

(c)

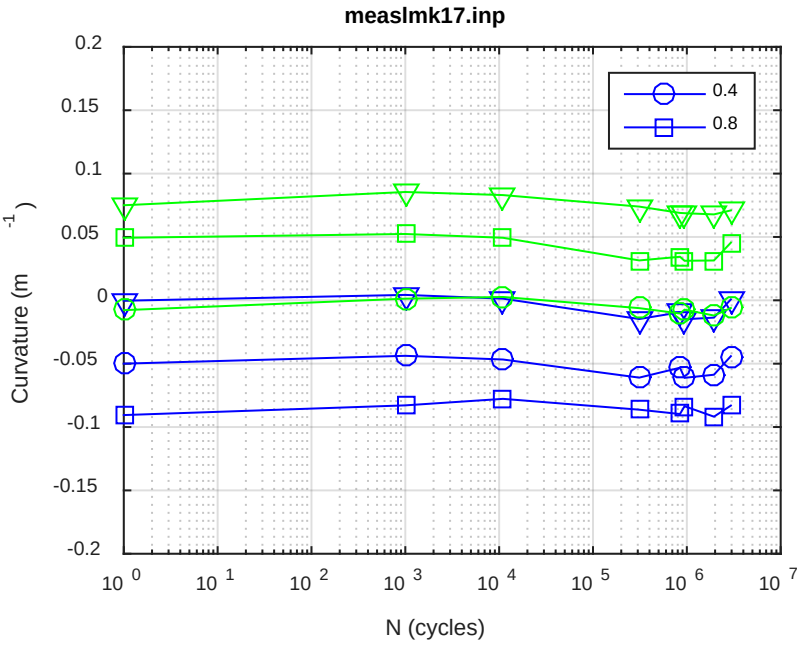
measlmk17.inp
Curvature (m -1)
N (cycles)
0.4
0.8
0.2
0.15
0.1
0.05
0
-0.05
-0.1
-0.15
-0.2
10 0
10 1
10 2
10 3
10 4
10 5
10 6
10 7

(d)

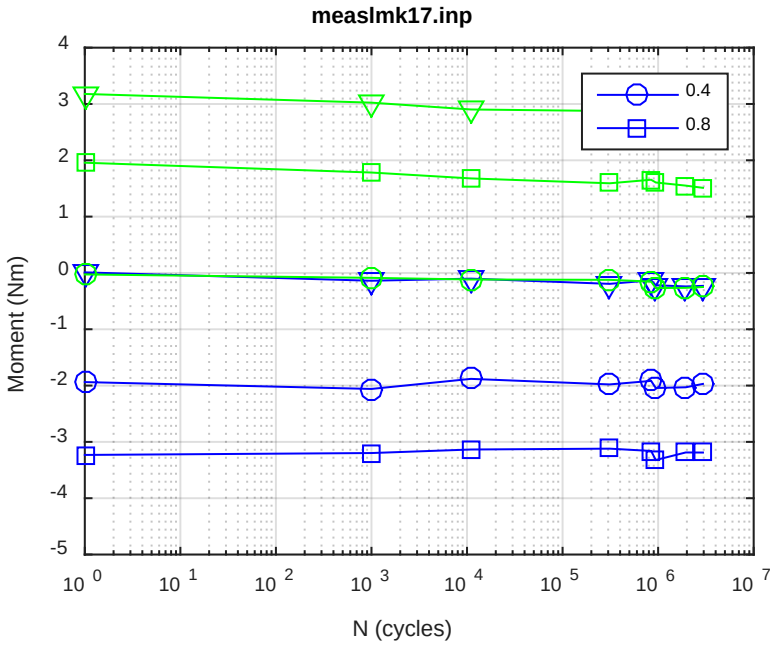

(e)

Fig. D.17 Measurement-based responses: (a) curvature range, (b) moment range, (c) rigidity, (d) curvature peak/valley, (e) moment peak/valley, LMK17, 8.64 Nm.

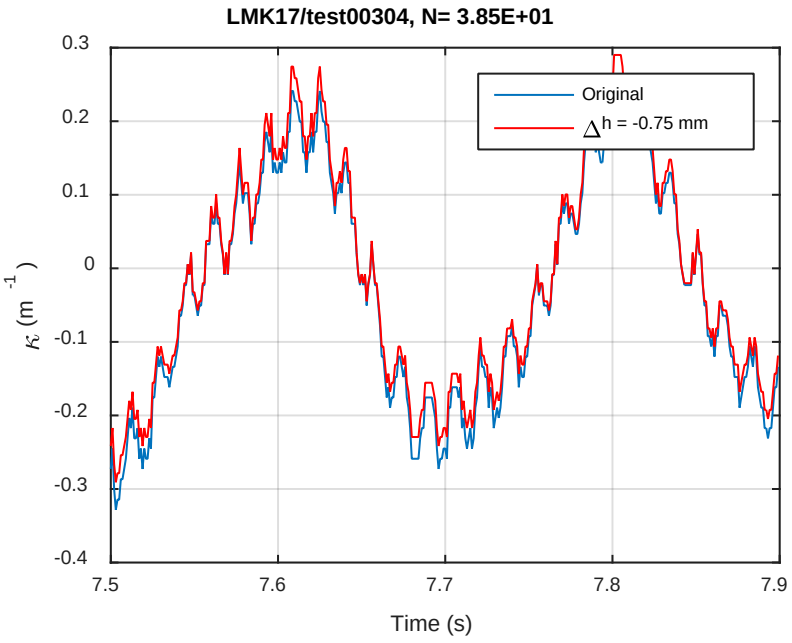
LMK17/test00304, N= 3.85E+01
Original
Δh = -0.75 mm
κ (m-1)
Time (s)
0.3
0.2
0.1
0
-0.1
-0.2
-0.3
-0.4
7.5
7.6
7.7
7.8
7.9

(a)

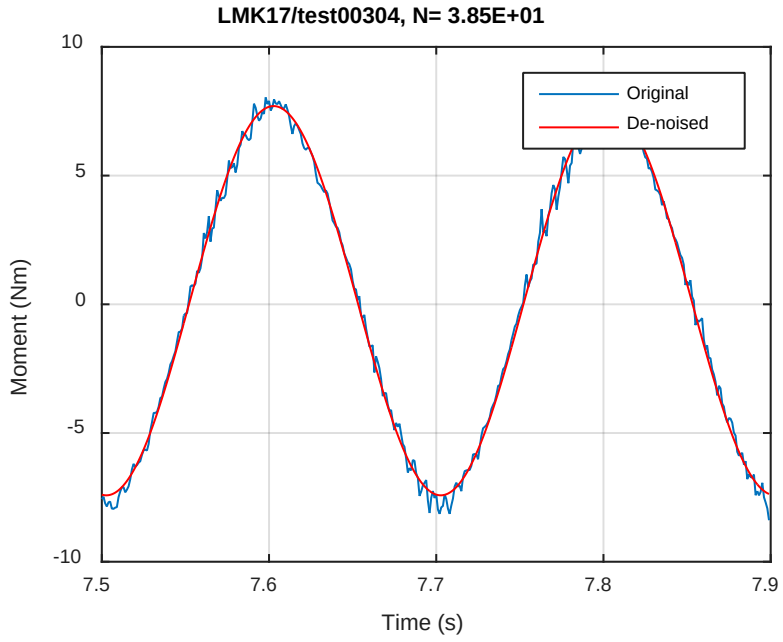
LMK17/test00304, N= 3.85E+01
Original
De-noised
Moment (Nm)
Time (s)
10
5
0
-5
-10
7.5
7.6
7.7
7.8
7.9

(b)

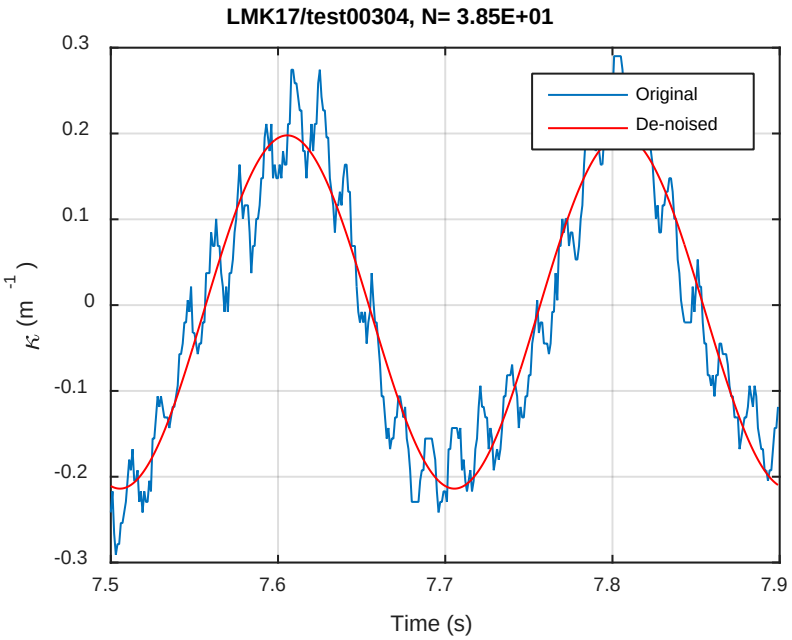

(c)

Fig. D.18 Monitoring-based responses: (a) curvature, (b) moment, (c) curvature, LMK17, 8.64 Nm, Ns = 3.85E+01 cycles.

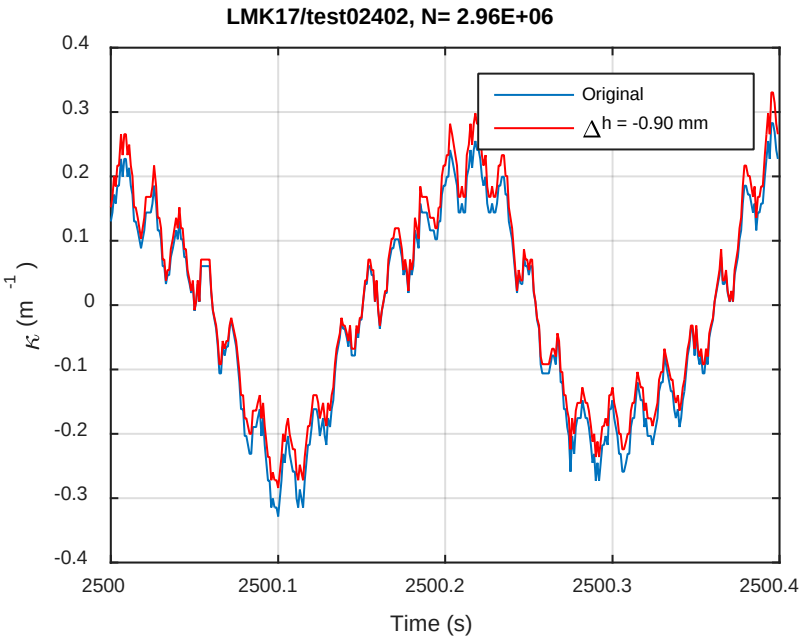
LMK17/test02402, N= 2.96E+06
Original
Δh = -0.90 mm
κ (m-1)
Time (s)
0.4
0.3
0.2
0.1
0
-0.1
-0.2
-0.3
-0.4
2500
2500.1
2500.2
2500.3
2500.4

(a)

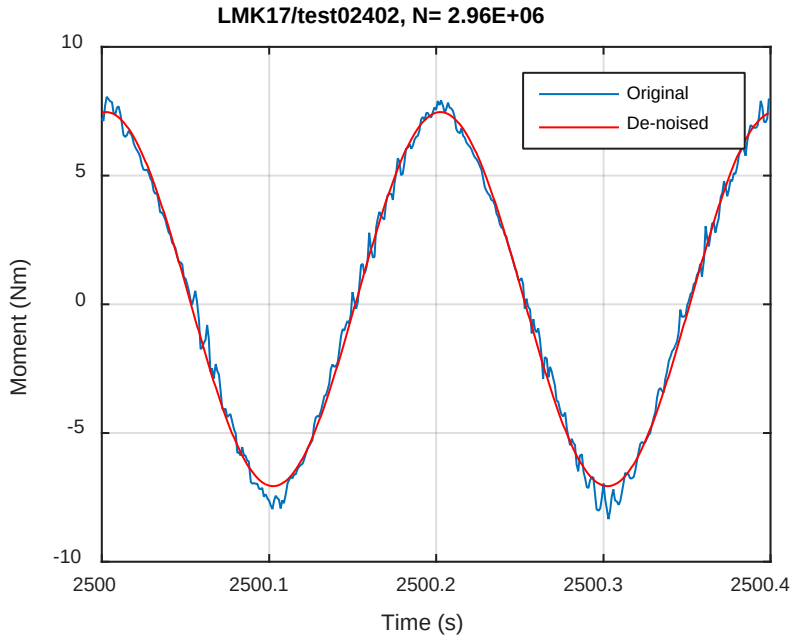
LMK17/test02402, N= 2.96E+06
Original
De-noised
Moment (Nm)
Time (s)
10
5
0
-5
-10
2500
2500.1
2500.2
2500.3
2500.4

(b)

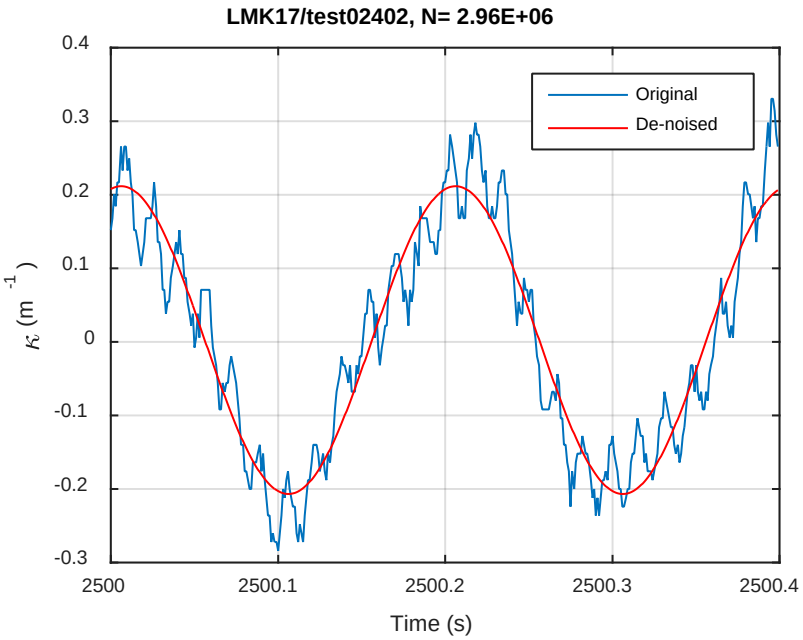

(c)

Fig. D.19 Monitoring-based responses: (a) curvature, (b) moment, (c) curvature, LMK17, 8.64 Nm, Ns = 2.96E+06 cycles.

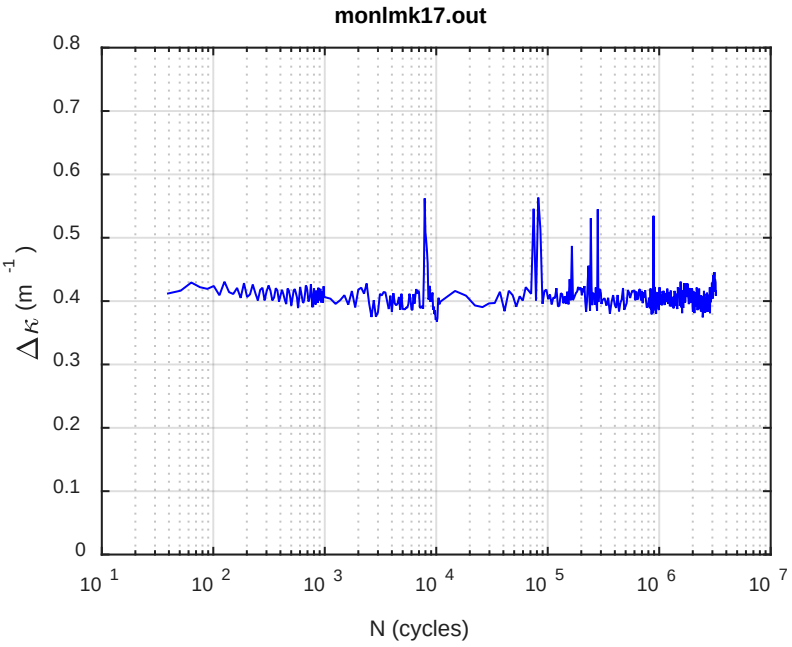
monlmk17.out
0.8
0.7
0.6
0.5
0.4
0.3
0.2
0.1
0
Δκ (m -1)
10 1
10 2
10 3
10 4
10 5
10 6
10 7
N (cycles)

(a)

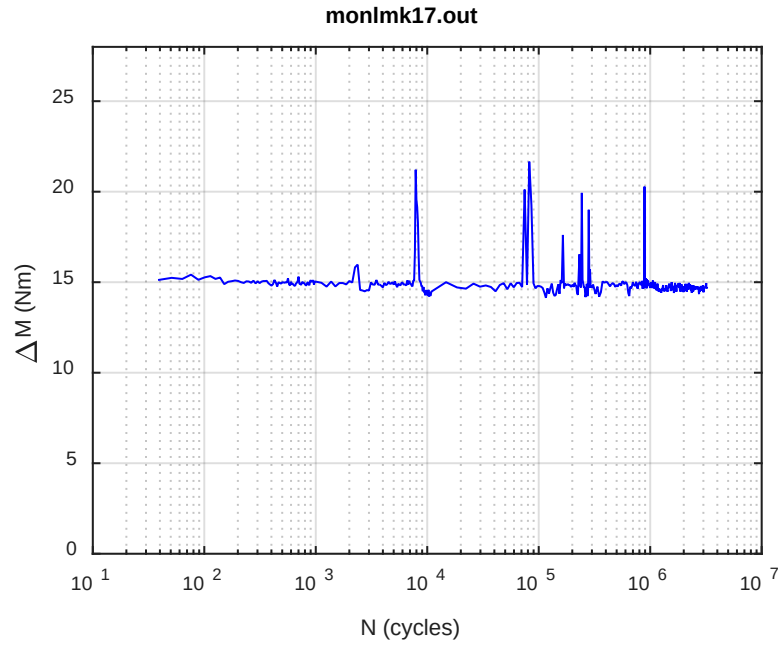
monlmk17.out
25
20
15
10
5
0
ΔM (Nm)
10 1
10 2
10 3
10 4
10 5
10 6
10 7
N (cycles)

(b)

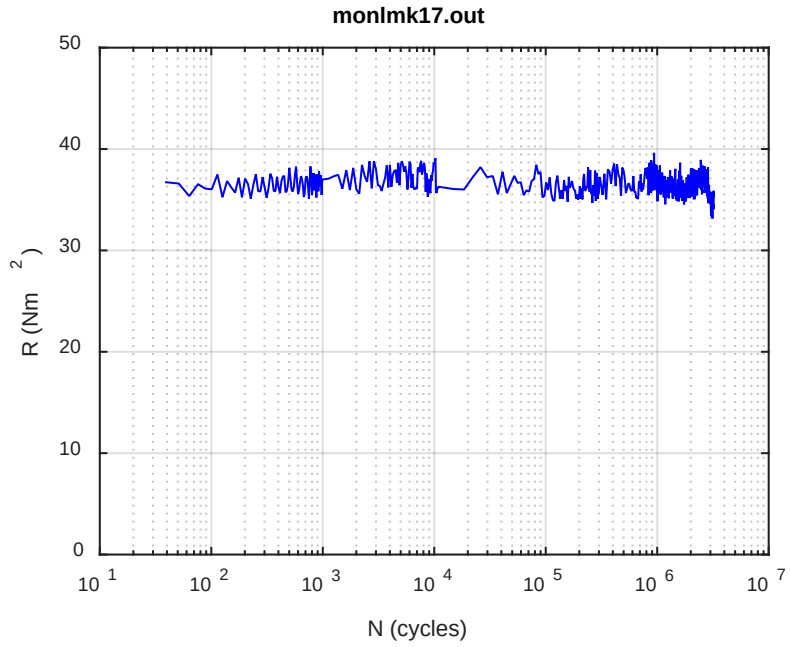
monlmk17.out
R (Nm 2)
N (cycles)

(c)

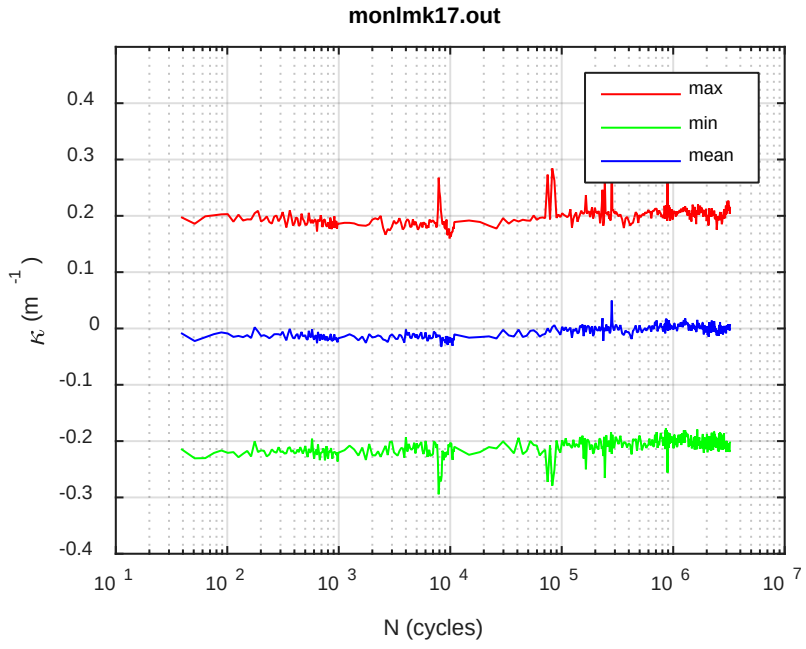
monlmk17.out
max
min
mean
κ (m -1)
N (cycles)

(d)

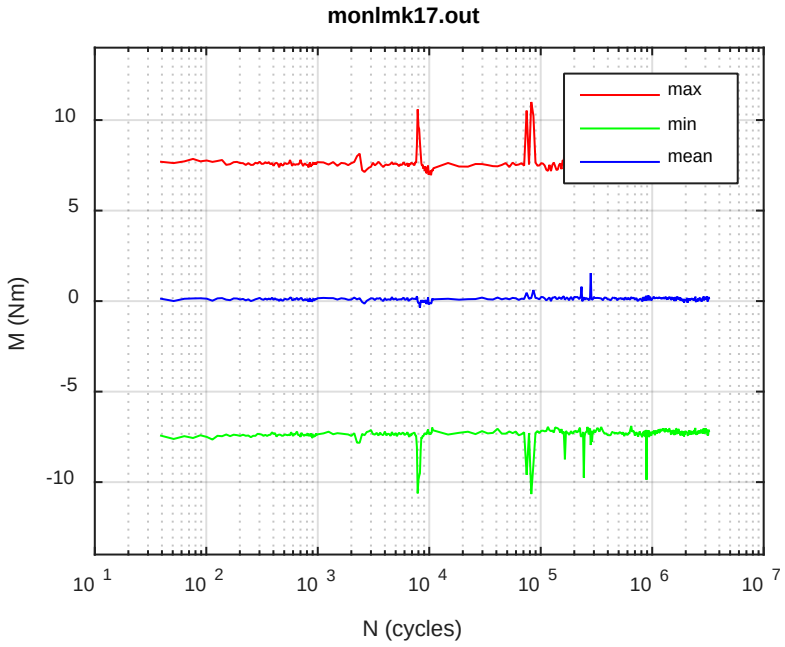

(e)

Fig. D.20 Monitoring-based responses: (a) curvature range, (b) moment range, (c) rigidity, (d) curvature peak/valley, (e) moment peak/valley, LMK17, 8.64 Nm, Nf = 3.37E+06 cycles.

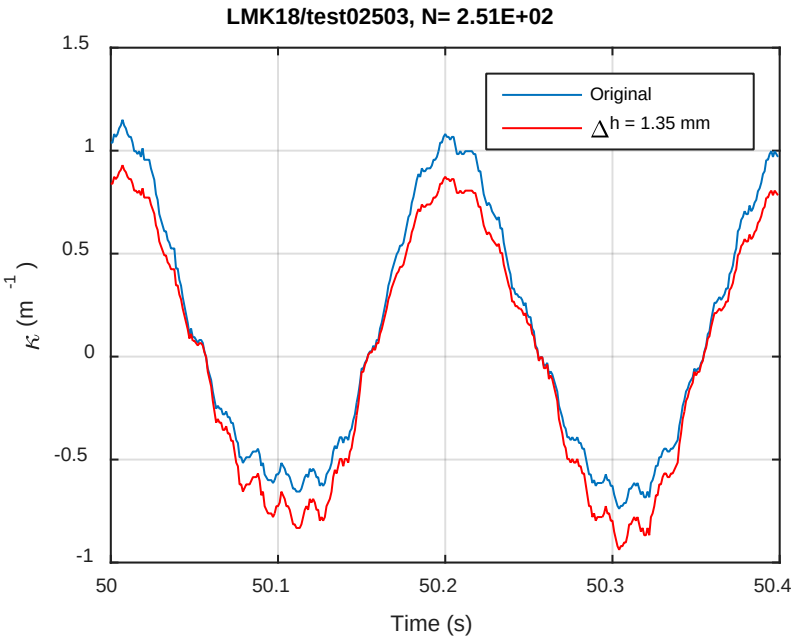
LMK18/test02503, N= 2.51E+02
Original
Δh = 1.35 mm
κ (m -1)
Time (s)
1.5
1
0.5
0
-0.5
-1
50
50.1
50.2
50.3
50.4

(a)

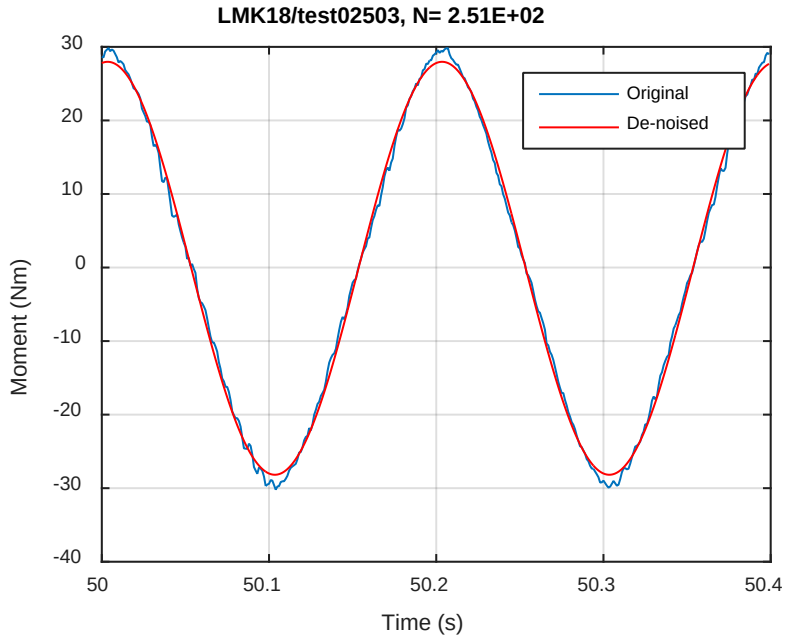
LMK18/test02503, N= 2.51E+02
Original
De-noised
Moment (Nm)
Time (s)
30
20
10
0
-10
-20
-30
-40
50
50.1
50.2
50.3
50.4

(b)

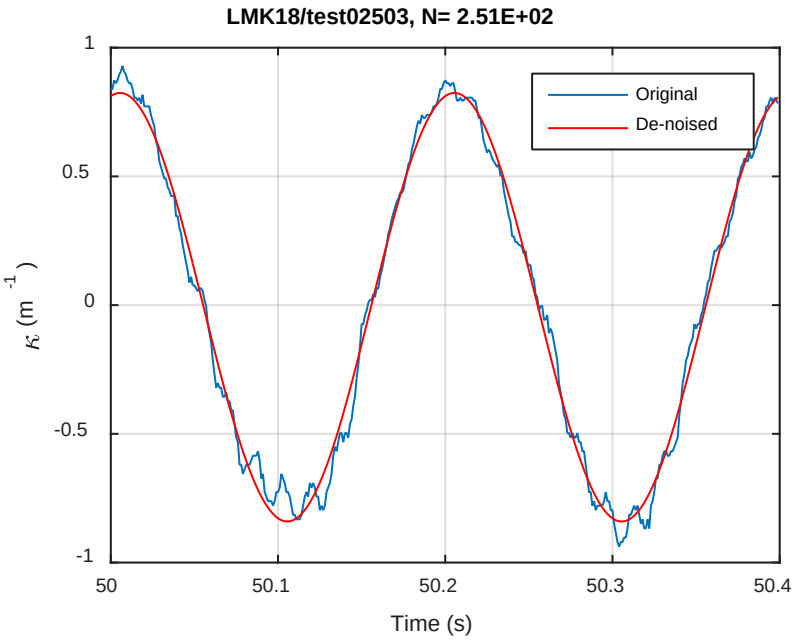

(c)

Fig. D.21 Monitoring-based responses: (a) curvature, (b) moment, (c) curvature, LMK18, 30.48 Nm, Ns = 2.51E+02 cycles.

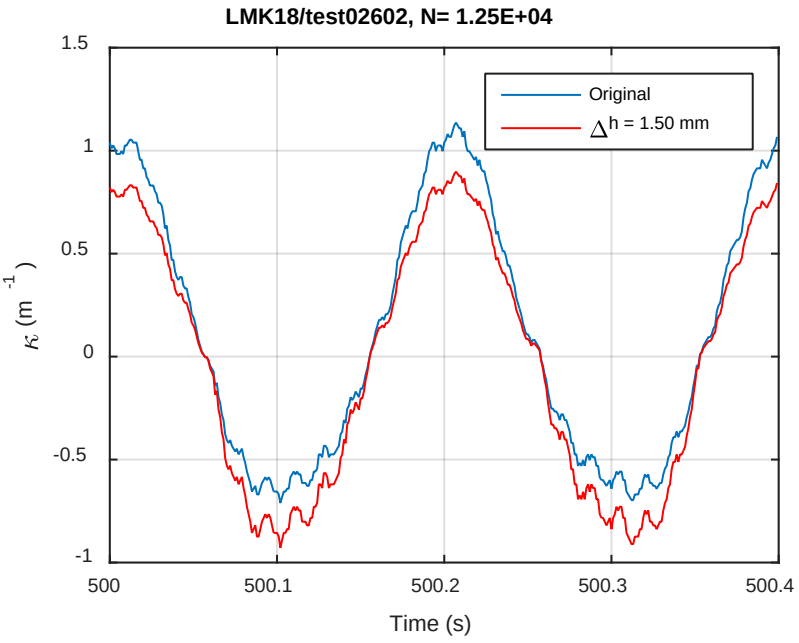
LMK18/test02602, N= 1.25E+04
Original
Δh = 1.50 mm
κ (m -1)
Time (s)
1.5
1
0.5
0
-0.5
-1
500
500.1
500.2
500.3
500.4

(a)

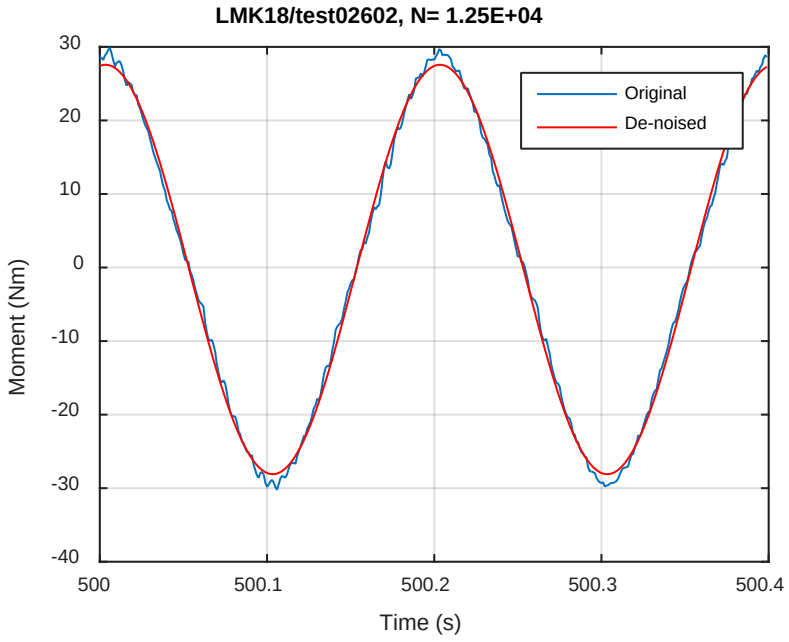
LMK18/test02602, N= 1.25E+04
Original
De-noised
Moment (Nm)
Time (s)
30
20
10
0
-10
-20
-30
-40
500
500.1
500.2
500.3
500.4

(b)

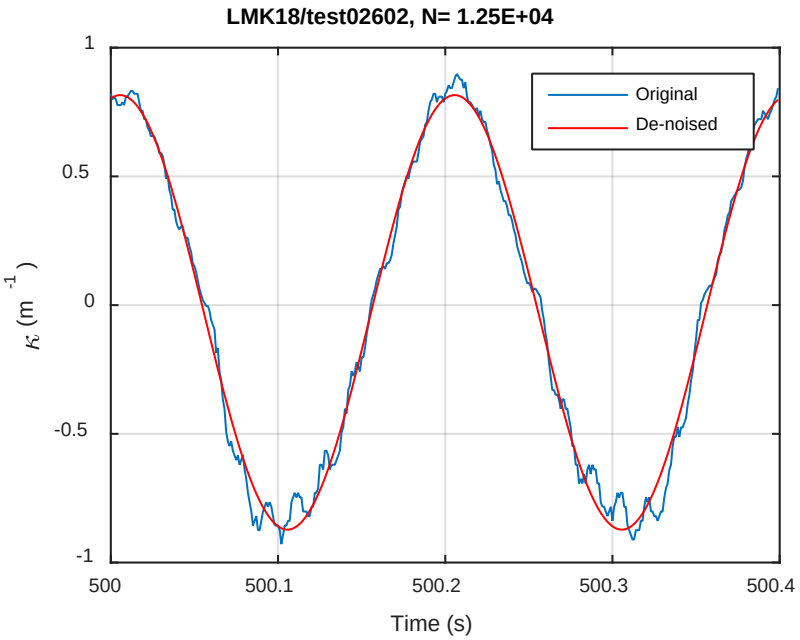

(c)

Fig. D.22 Monitoring-based responses: (a) curvature, (b) moment, (c) curvature, LMK18, 30.48 Nm, Ns = 1.25E+04 cycles.

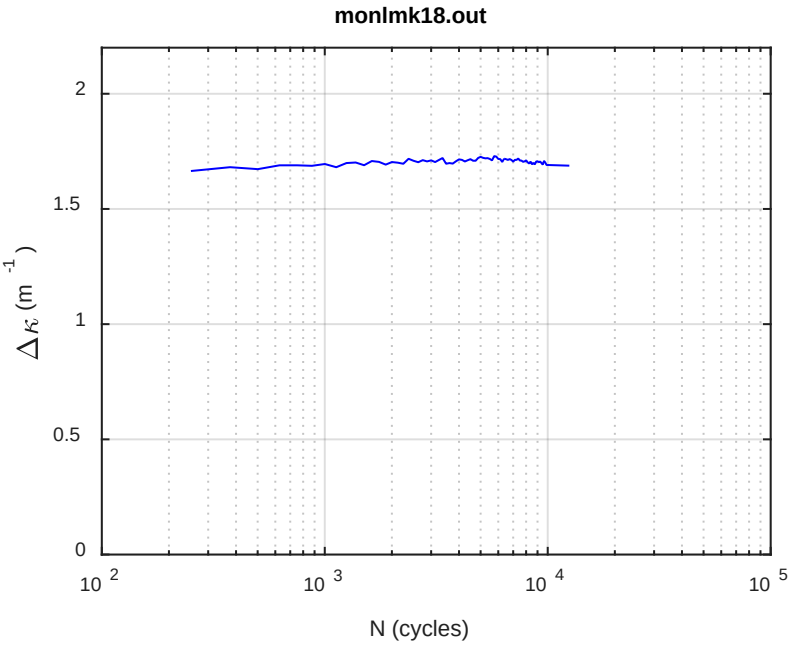
monlmk18.out
2
1.5
1
0.5
0
Δκ (m -1)
10 2
10 3
10 4
10 5
N (cycles)

(a)

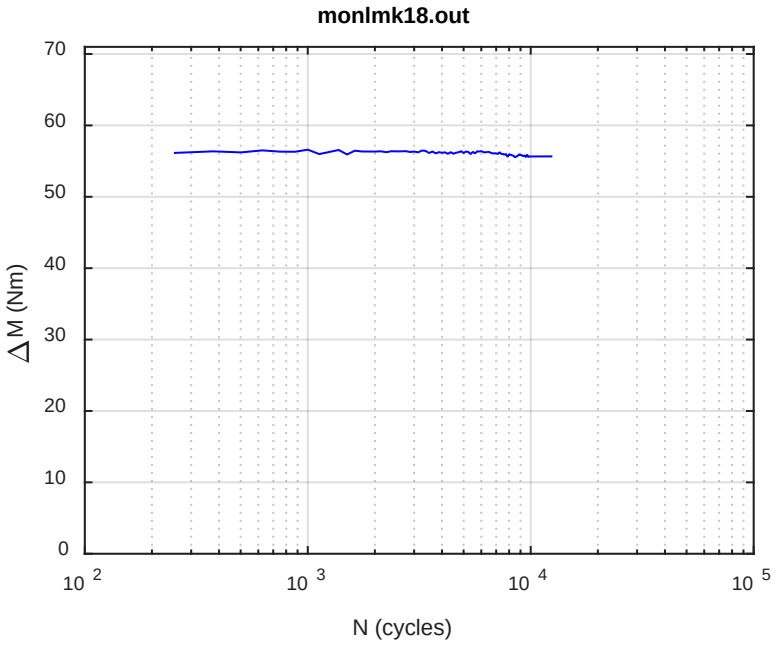
monlmk18.out
70
60
50
40
30
20
10
0
ΔM (Nm)
10 2
10 3
10 4
10 5
N (cycles)

(b)

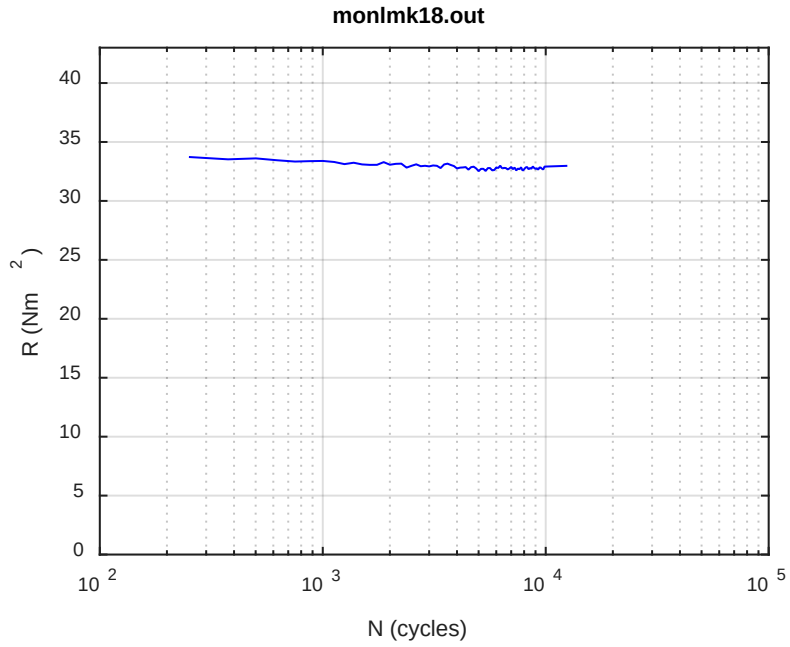
monlmk18.out
R (Nm 2)
N (cycles)

(c)

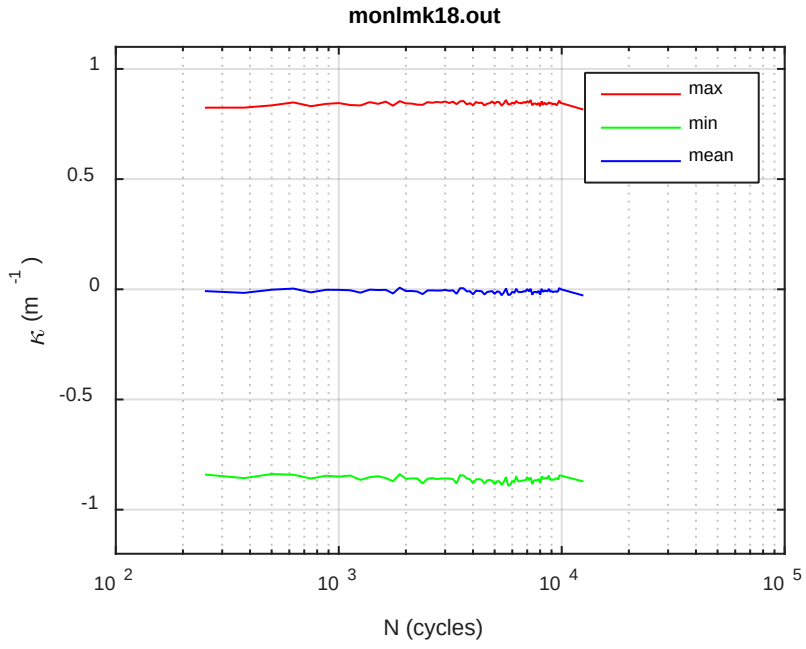
monlmk18.out
max
min
mean
κ (m -1)
N (cycles)

(d)

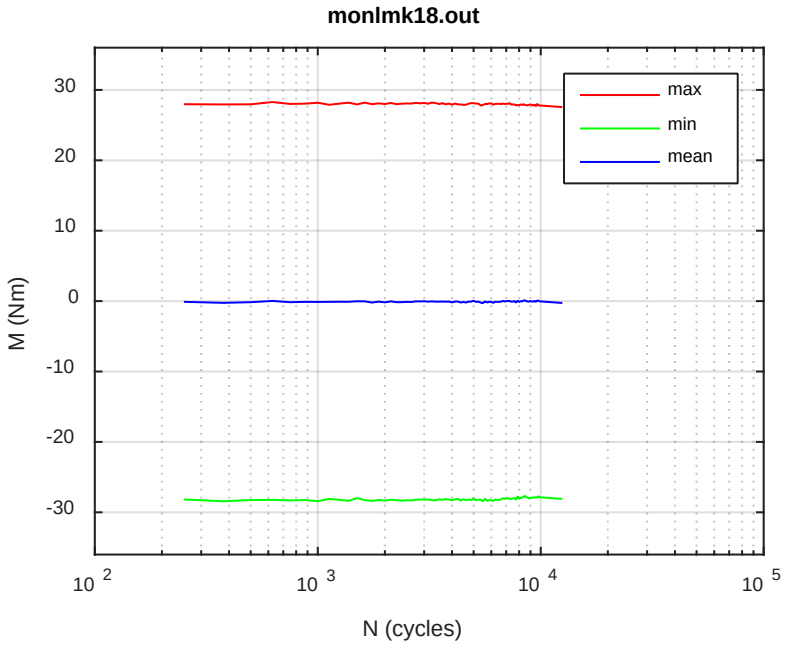

(e)

Fig. D.23 Monitoring-based responses: (a) curvature range, (b) moment range, (c) rigidity, (d) curvature peak/valley, (e) moment peak/valley, LMK18, 30.48 Nm, Nf = 1.31E+04 cycles.

APPENDIX E
CIRFT TESTING RESULTS OF MOX – PART II

TABLE OF CONTENTS

Measurement and monitoring rigidity curves of MOX

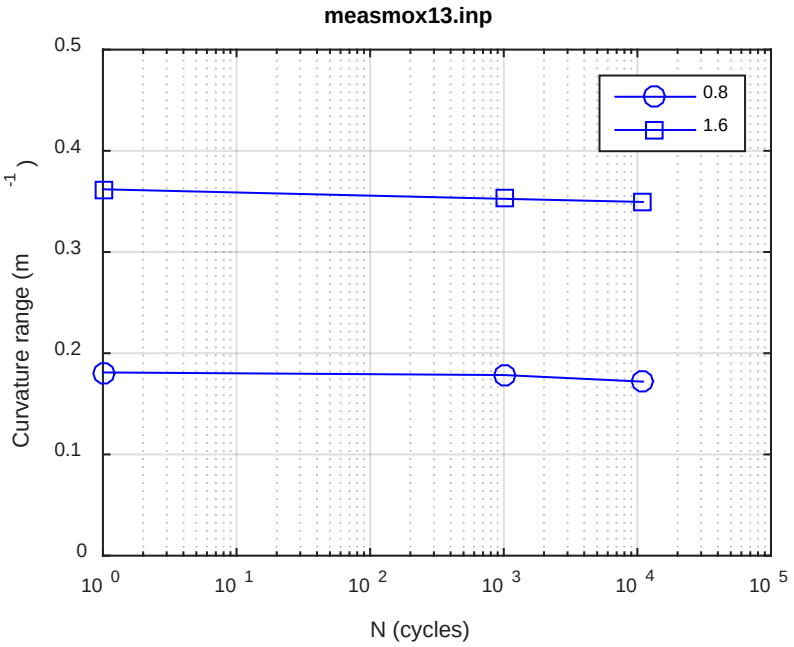
measmox13.inp
0.5
0.4
0.3
0.2
0.1
0
Curvature range (m -1)
0.8
1.6
10 0
10 1
10 2
10 3
10 4
10 5
N (cycles)

(a)

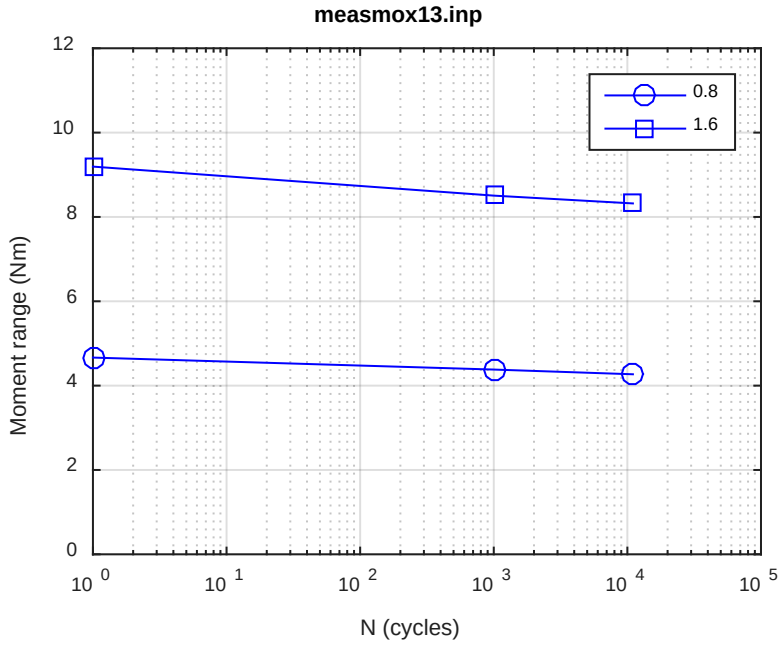
measmox13.inp
12
10
8
6
4
2
0
Moment range (Nm)
0.8
1.6
10 0
10 1
10 2
10 3
10 4
10 5
N (cycles)

(b)

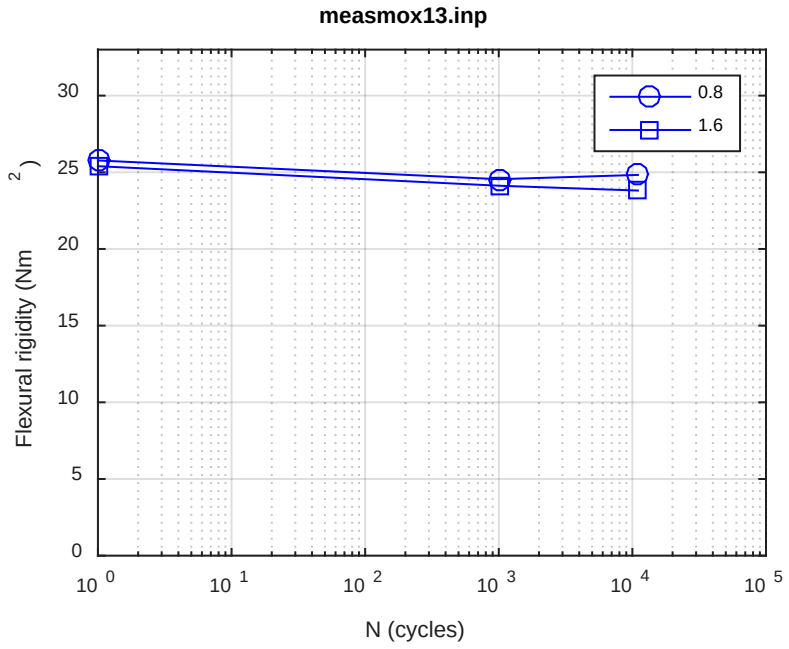
measmox13.inp
0.8
1.6
Flexural rigidity (Nm 2)
N (cycles)

(c)

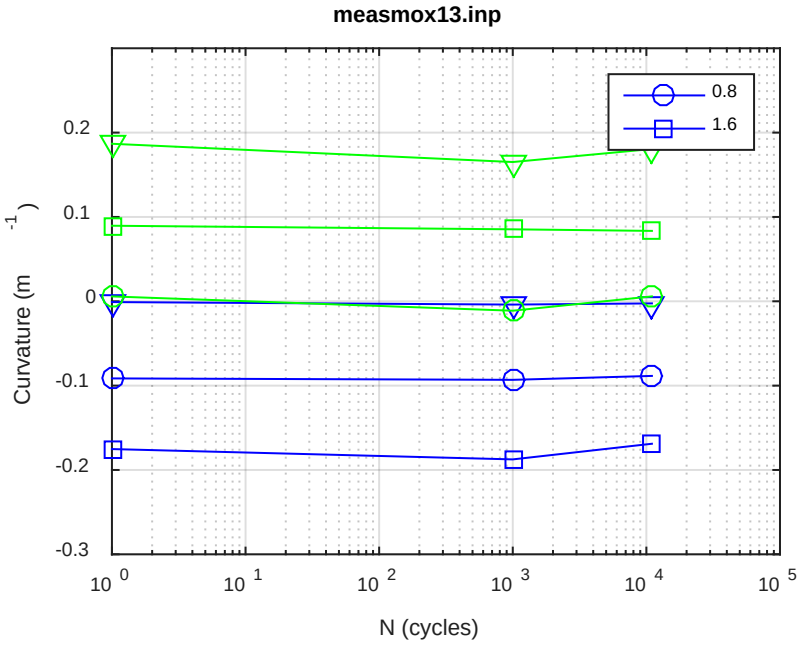
measmox13.inp
0.8
1.6
Curvature (m -1)
N (cycles)

(d)

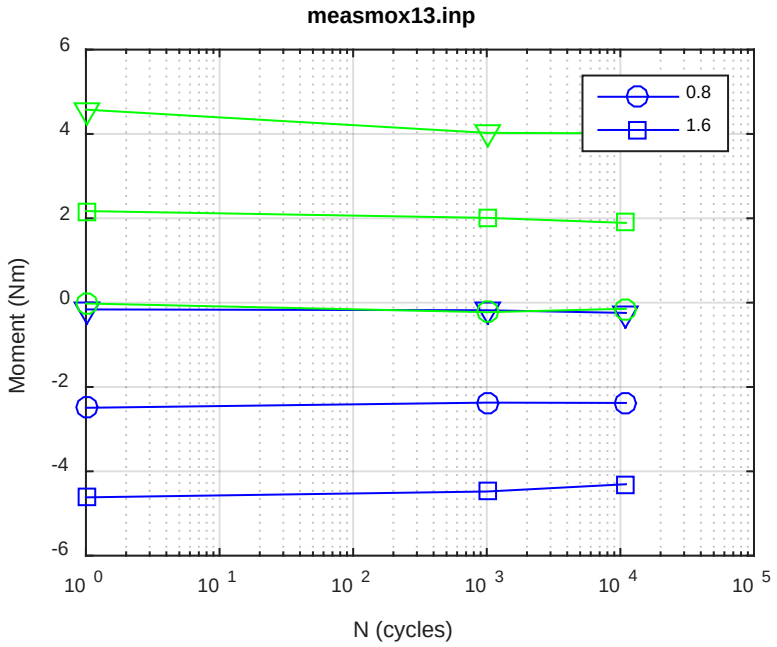

(e)

Fig. E.1 Measurement-based responses: (a) curvature range, (b) moment range, (c) rigidity, (d) curvature peak/valley, (e) moment peak/valley, MOX13, 10.16 Nm.

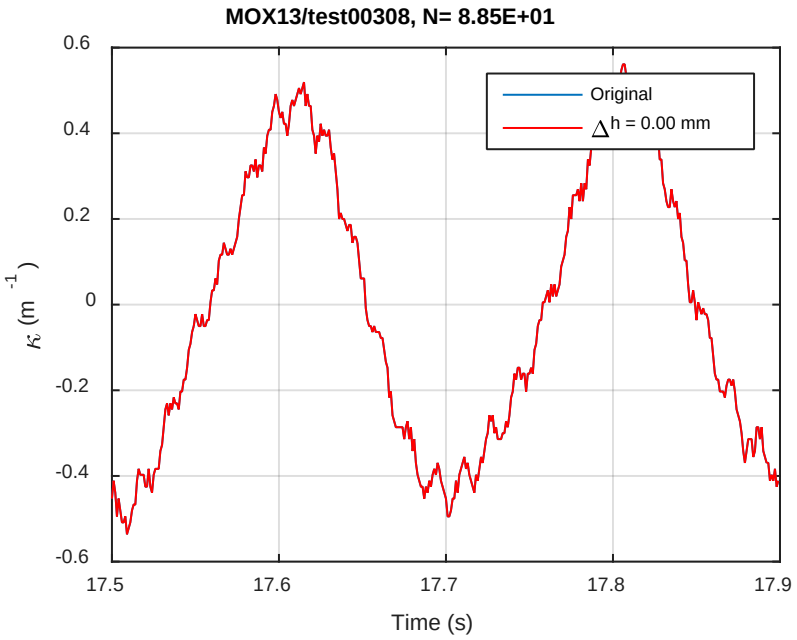
MOX13/test00308, N= 8.85E+01
Original
Δh = 0.00 mm
κ (m-1)
Time (s)
0.6
0.4
0.2
0
-0.2
-0.4
-0.6
17.5
17.6
17.7
17.8
17.9

(a)

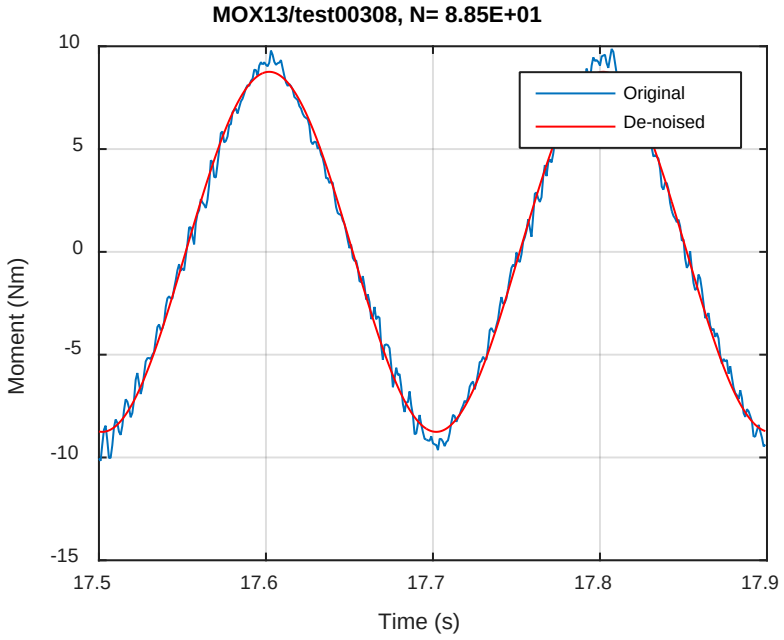
MOX13/test00308, N= 8.85E+01
Original
De-noised
Moment (Nm)
Time (s)
10
5
0
-5
-10
-15
17.5
17.6
17.7
17.8
17.9

(b)

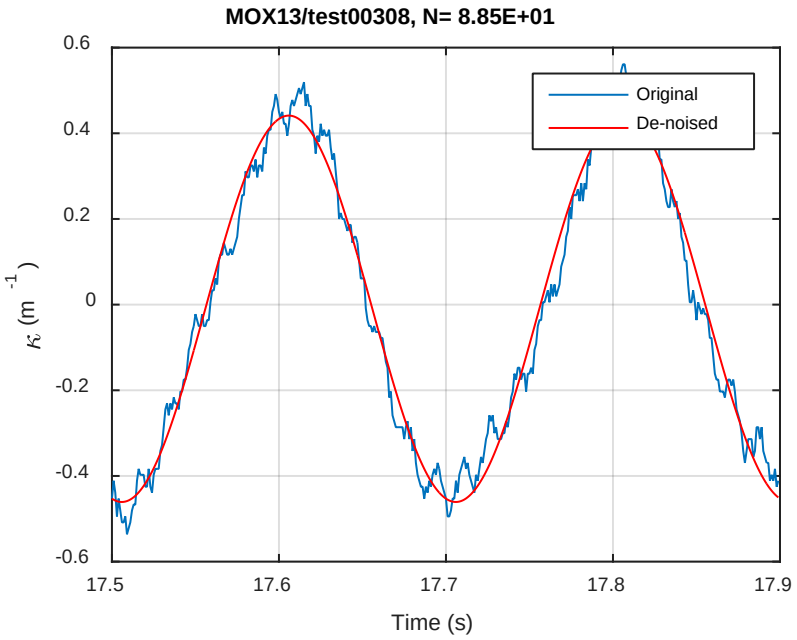

(c)

Fig. E.2 Monitoring-based responses: (a) curvature, (b) moment, (c) curvature, MOX13, 10.16 Nm, Ns = 8.85E+01 cycles.

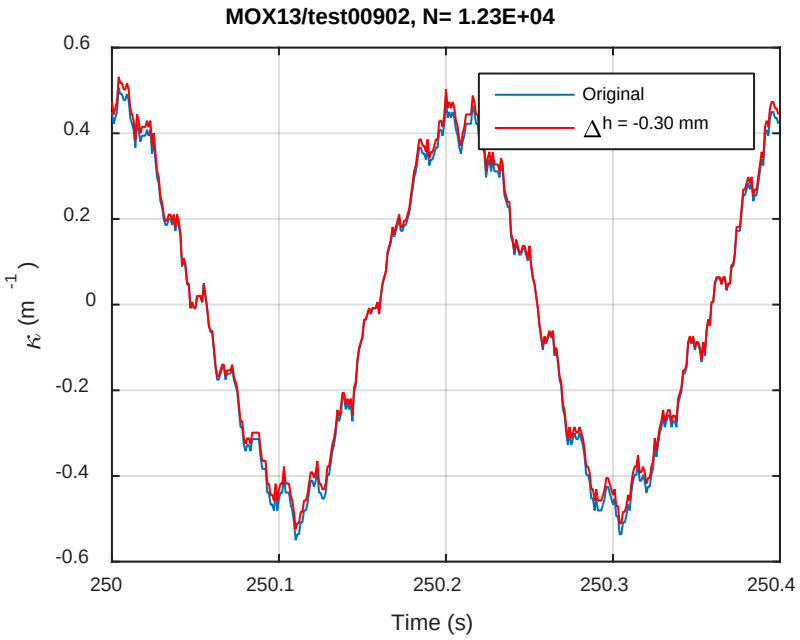
MOX13/test00902, N= 1.23E+04
Original
Δh = -0.30 mm
κ (m-1)
Time (s)
0.6
0.4
0.2
0
-0.2
-0.4
-0.6
250
250.1
250.2
250.3
250.4

(a)

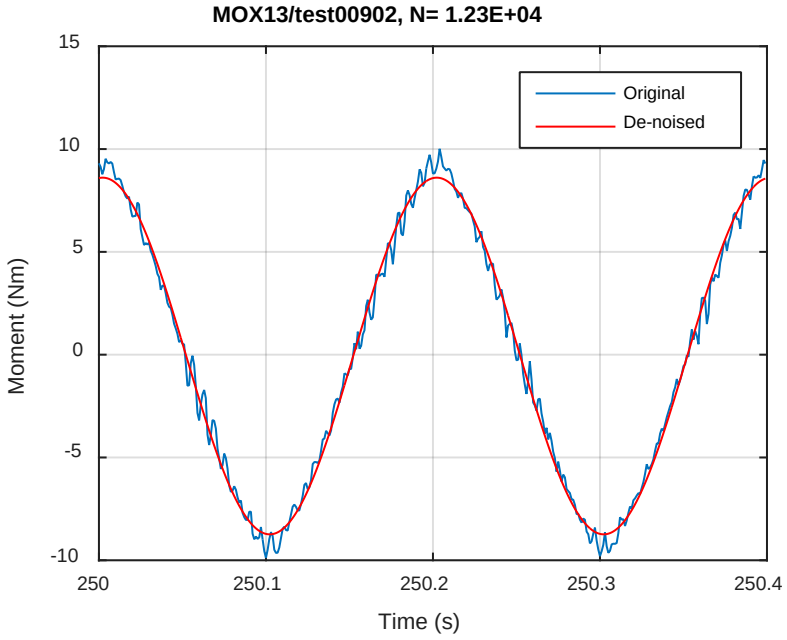
MOX13/test00902, N= 1.23E+04
Original
De-noised
Moment (Nm)
Time (s)
15
10
5
0
-5
-10
250
250.1
250.2
250.3
250.4

(b)

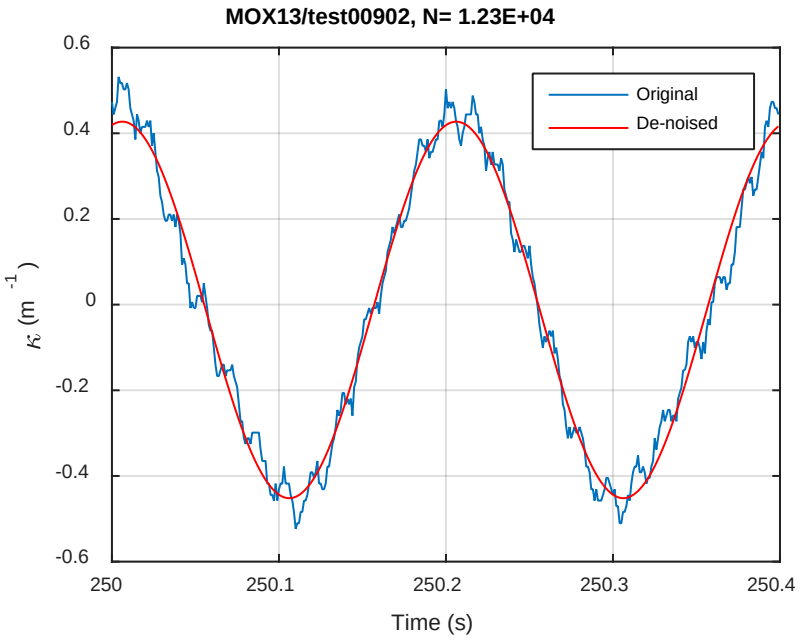

(c)

Fig. E.3 Monitoring-based responses: (a) curvature, (b) moment, (c) curvature, MOX13, 10.16 Nm, Ns = 1.23E+04 cycles.

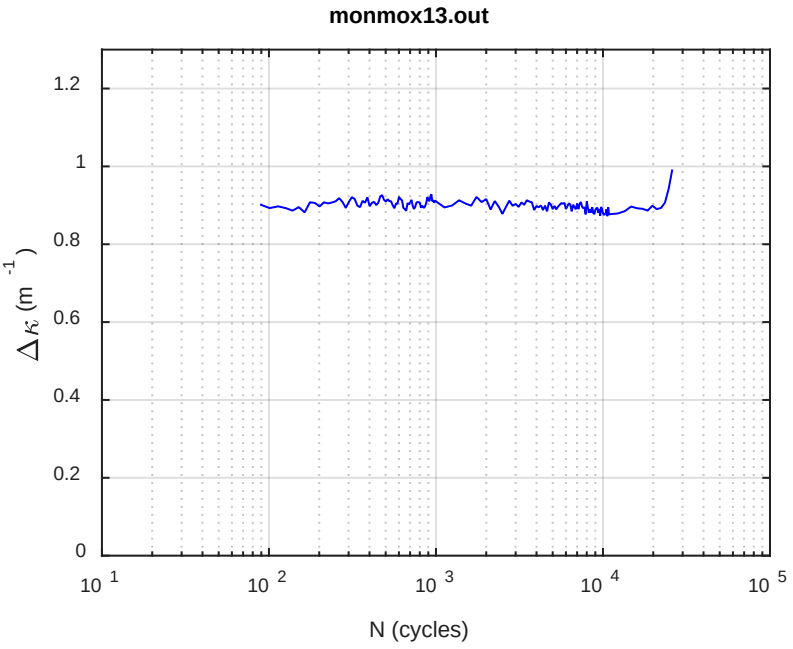
monmox13.out
1.2
1
0.8
0.6
0.4
0.2
0
Δκ (m -1)
10 1
10 2
10 3
10 4
10 5
N (cycles)

(a)

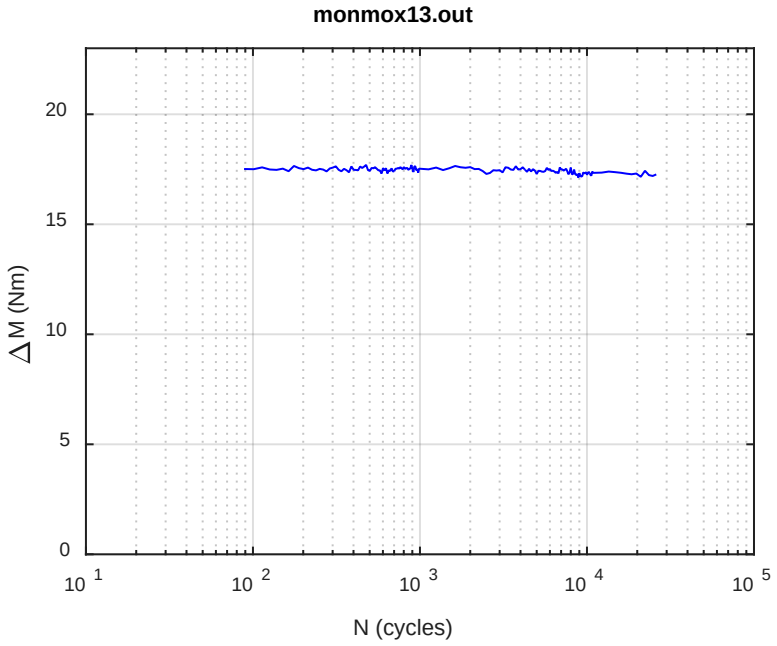
monmox13.out
20
15
10
5
0
ΔM (Nm)
10 1
10 2
10 3
10 4
10 5
N (cycles)

(b)

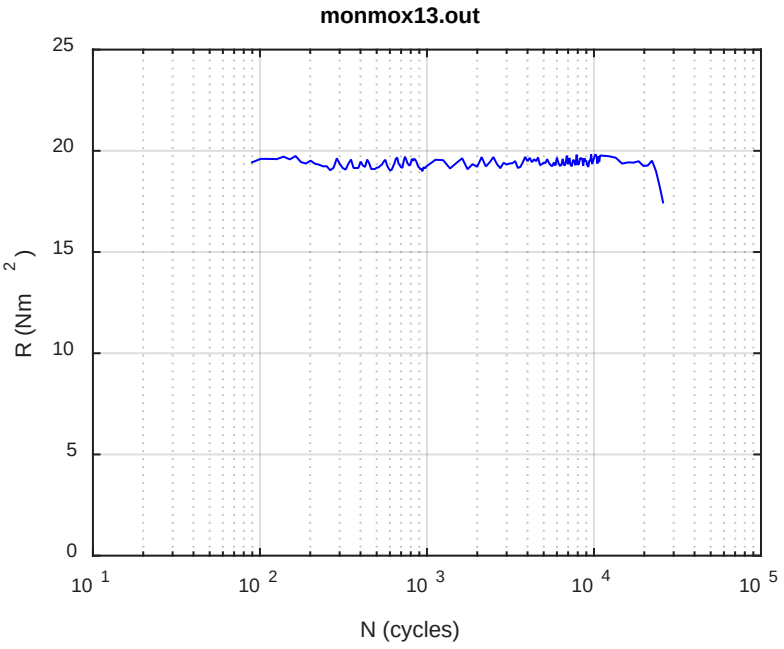
monmox13.out
R (Nm 2)
N (cycles)

(c)

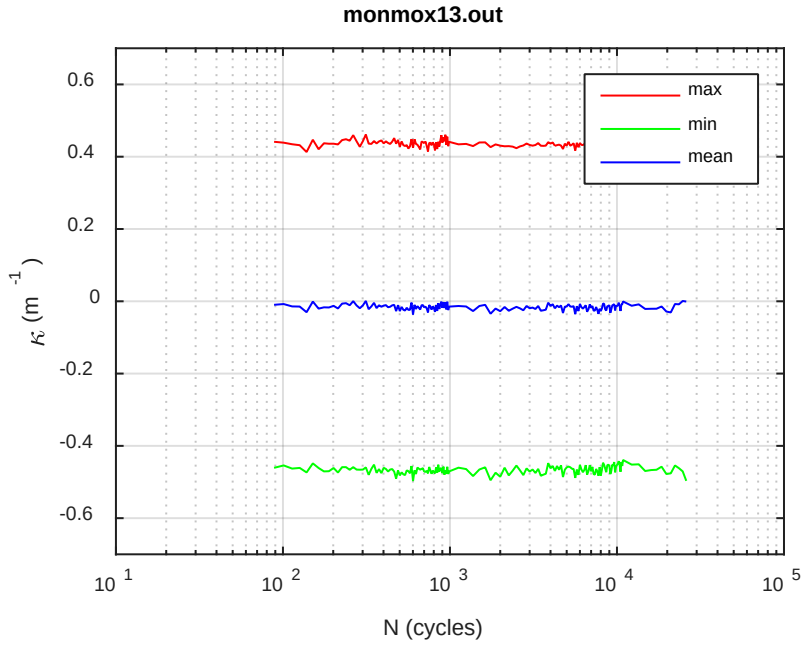
monmox13.out
max
min
mean
κ (m -1)
N (cycles)

(d)

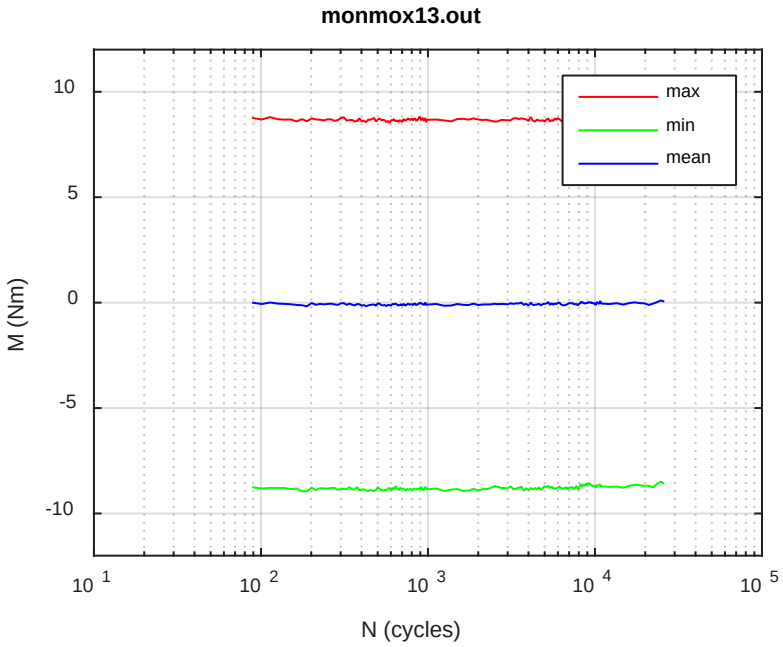

(e)

Fig. E.4 Monitoring-based responses: (a) curvature range, (b) moment range, (c) rigidity, (d) curvature peak/valley, (e) moment peak/valley, MOX13, 10.16 Nm, Nf = 2.70E+04 cycles.

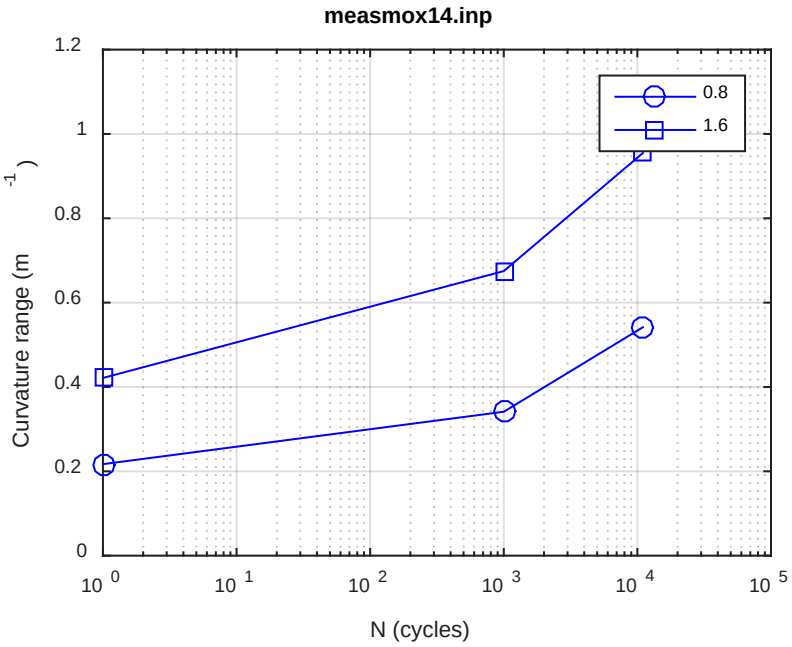
measmox14.inp
Curvature range (m-1)
N (cycles)
0.8
1.6
0
0.2
0.4
0.6
0.8
1
1.2
10 0
10 1
10 2
10 3
10 4
10 5

(a)

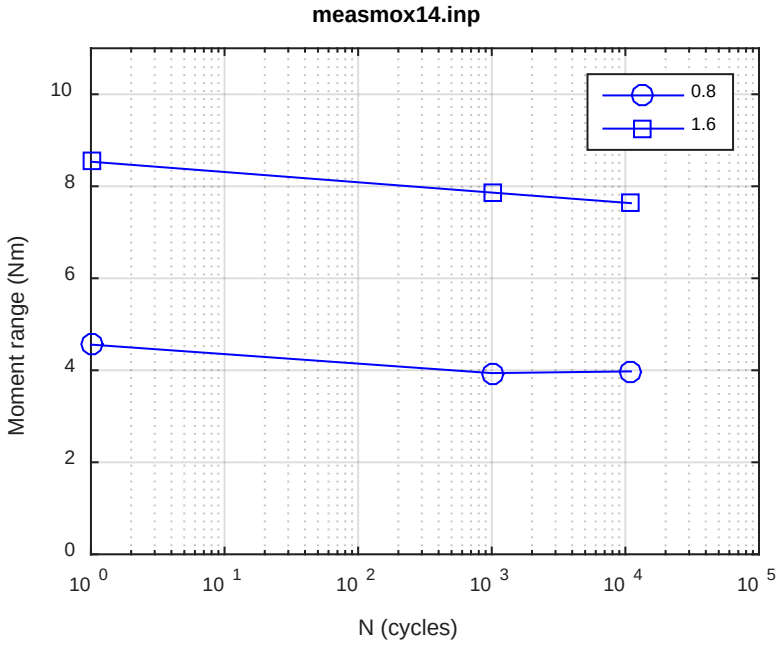
measmox14.inp
Moment range (Nm)
N (cycles)
0.8
1.6
0
2
4
6
8
10
10 0
10 1
10 2
10 3
10 4
10 5

(b)

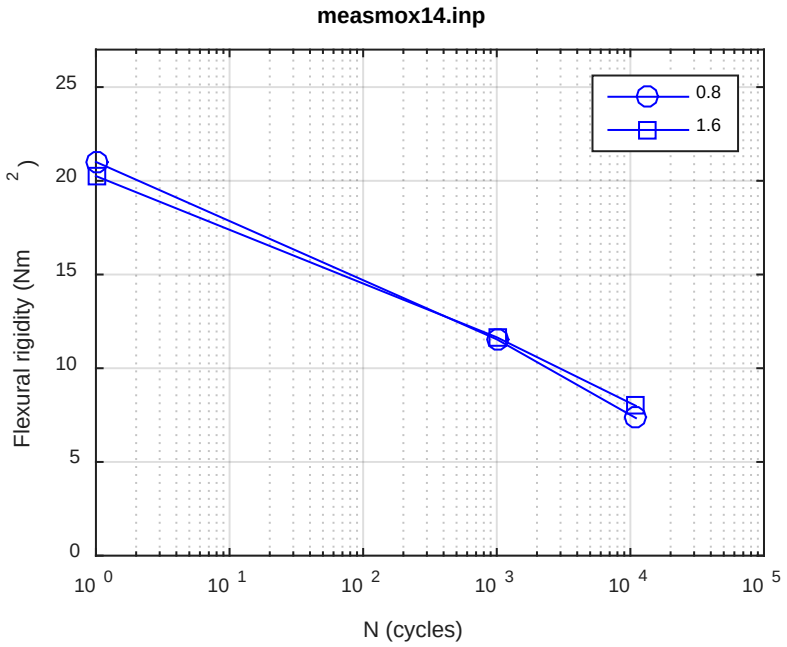
measmox14.inp
Flexural rigidity (Nm 2)
N (cycles)
0.8
1.6
0
5
10
15
20
25
10 0
10 1
10 2
10 3
10 4
10 5

(c)

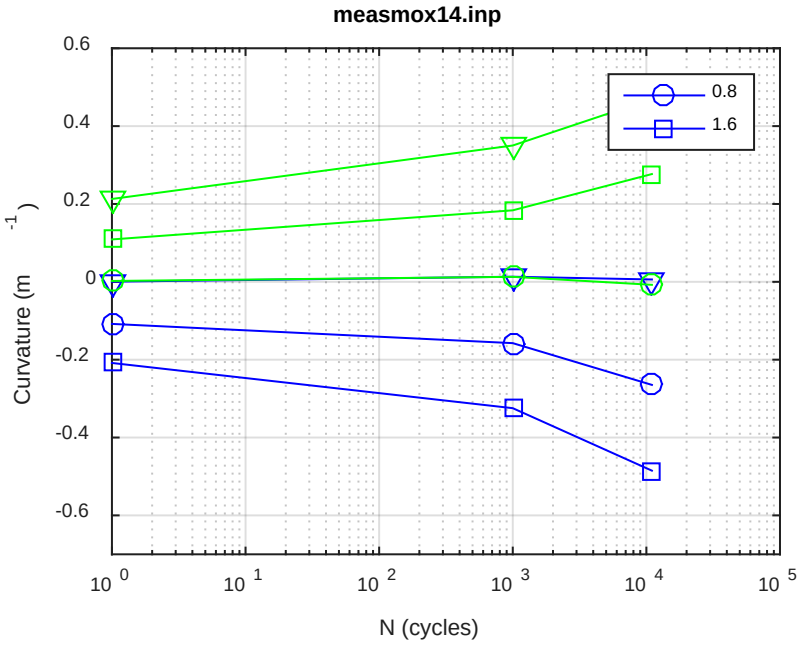
measmox14.inp
Curvature (m -1)
N (cycles)
0.8
1.6
0.6
0.4
0.2
0
-0.2
-0.4
-0.6
10 0
10 1
10 2
10 3
10 4
10 5

(d)

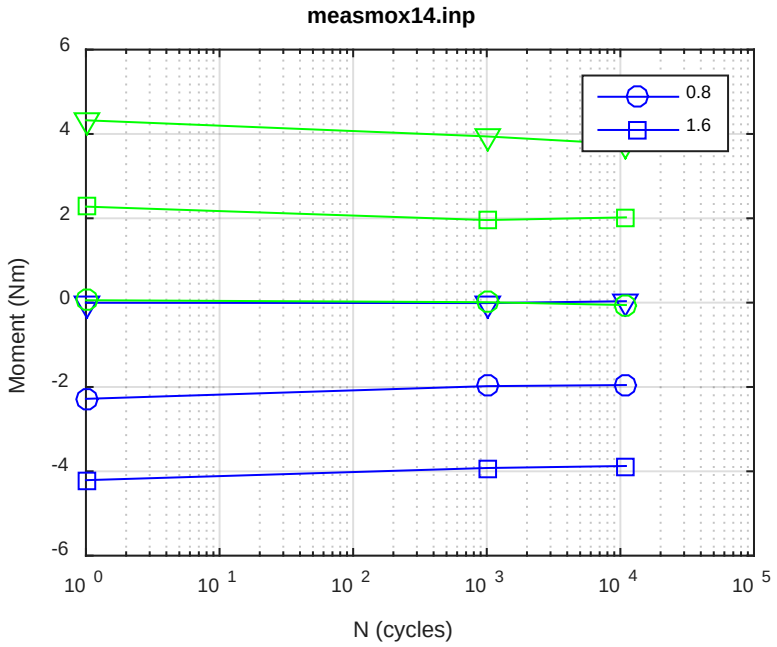

(e)

Fig. E.5 Measurement-based responses: (a) curvature range, (b) moment range, (c) rigidity, (d) curvature peak/valley, (e) moment peak/valley, MOX14, 7.62 Nm.

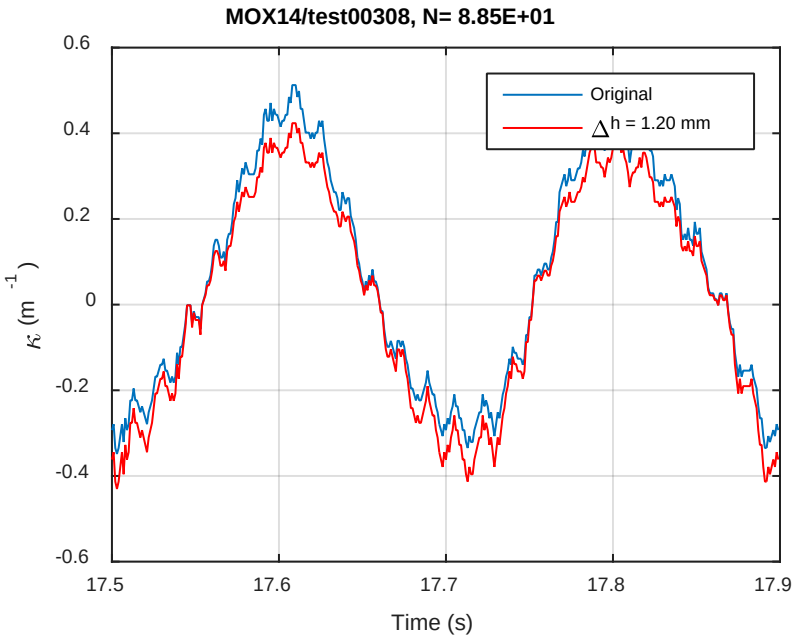
MOX14/test00308, N= 8.85E+01
Original
Δh = 1.20 mm
κ (m-1)
Time (s)
0.6
0.4
0.2
0
-0.2
-0.4
-0.6
17.5
17.6
17.7
17.8
17.9

(a)

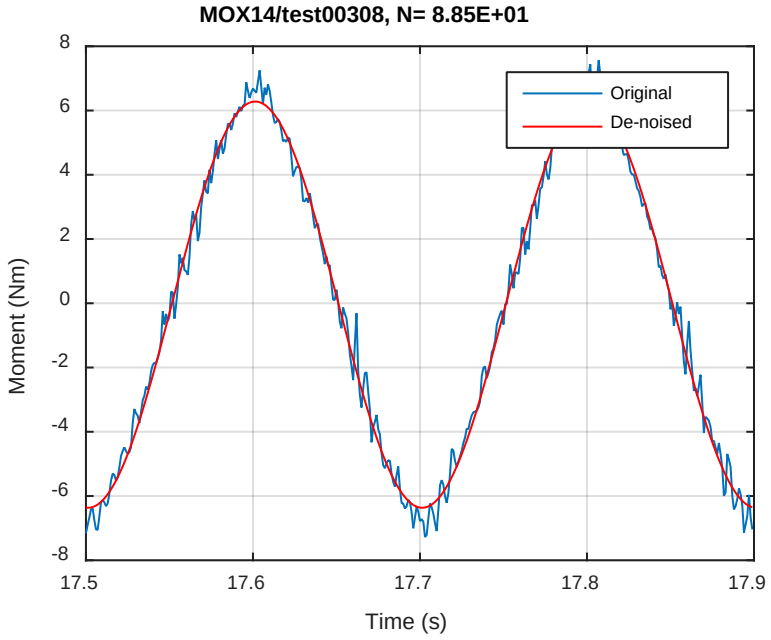
MOX14/test00308, N= 8.85E+01
Original
De-noised
Moment (Nm)
Time (s)
8
6
4
2
0
-2
-4
-6
-8
17.5
17.6
17.7
17.8
17.9

(b)

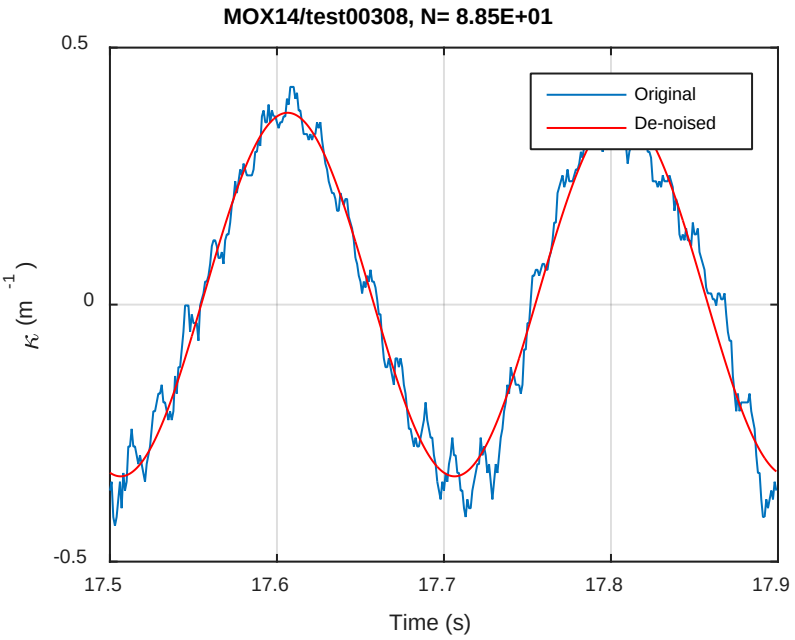

(c)

Fig. E.6 Monitoring-based responses: (a) curvature, (b) moment, (c) curvature, MOX14, 7.62 Nm, Ns = 8.85E+01 cycles.

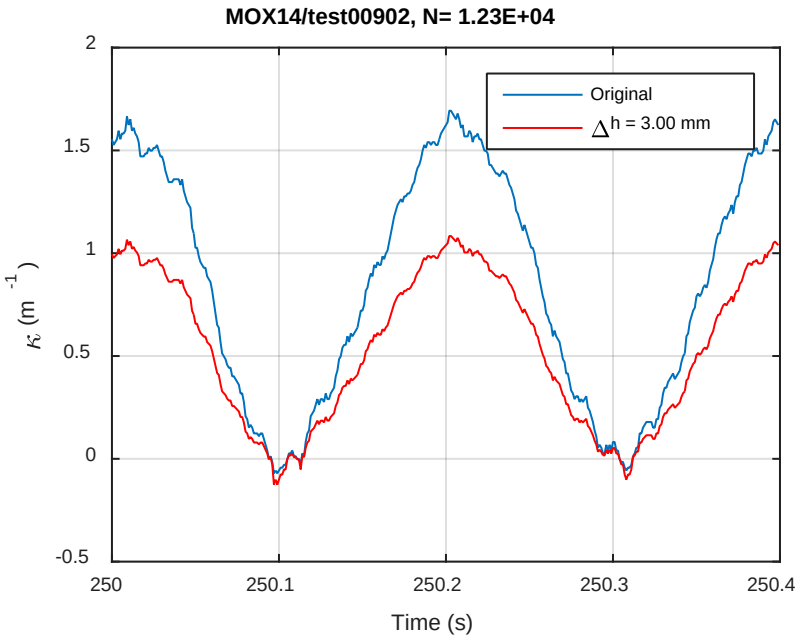
MOX14/test00902, N= 1.23E+04
Original
Δh = 3.00 mm
κ (m-1)
Time (s)
2
1.5
1
0.5
0
-0.5
250
250.1
250.2
250.3
250.4

(a)

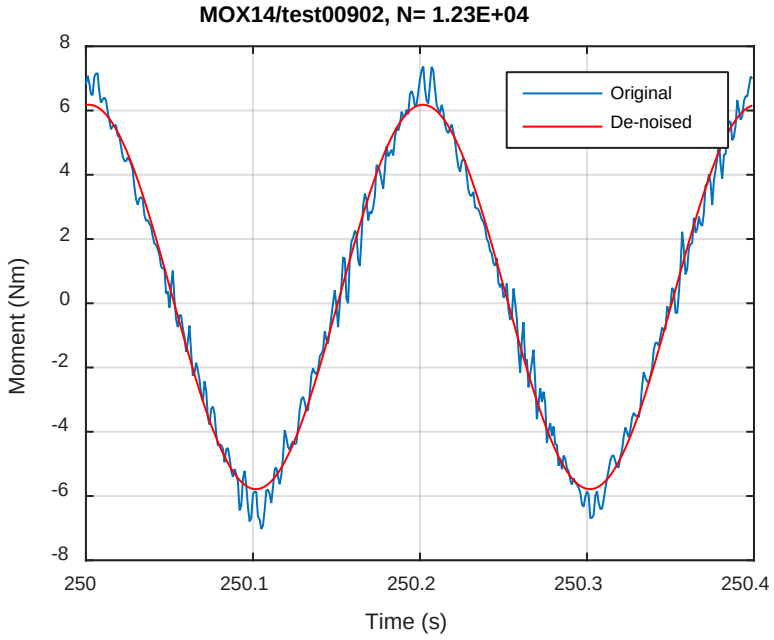
MOX14/test00902, N= 1.23E+04
Original
De-noised
Moment (Nm)
Time (s)
8
6
4
2
0
-2
-4
-6
-8
250
250.1
250.2
250.3
250.4

(b)

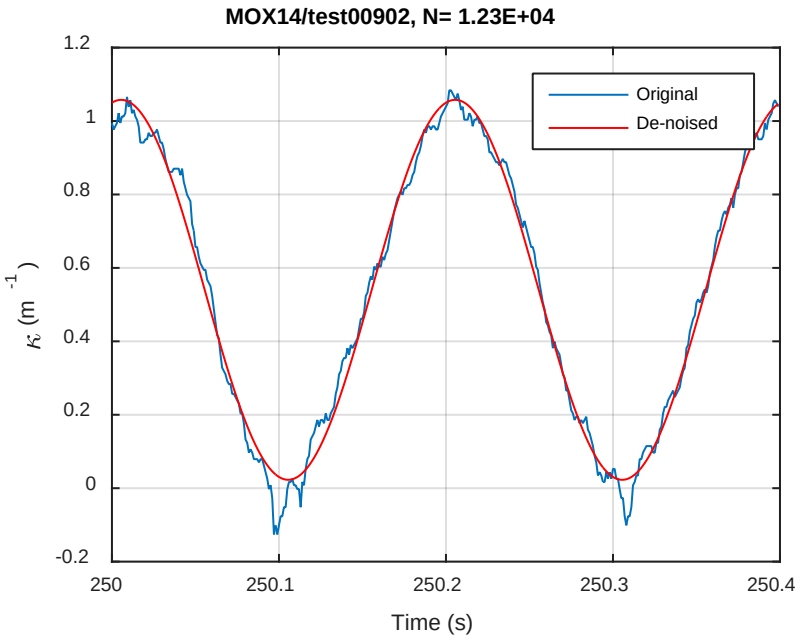

(c)

Fig. E.7 Monitoring-based responses: (a) curvature, (b) moment, (c) curvature, MOX14, 7.62 Nm, Ns = 1.23E+04 cycles.

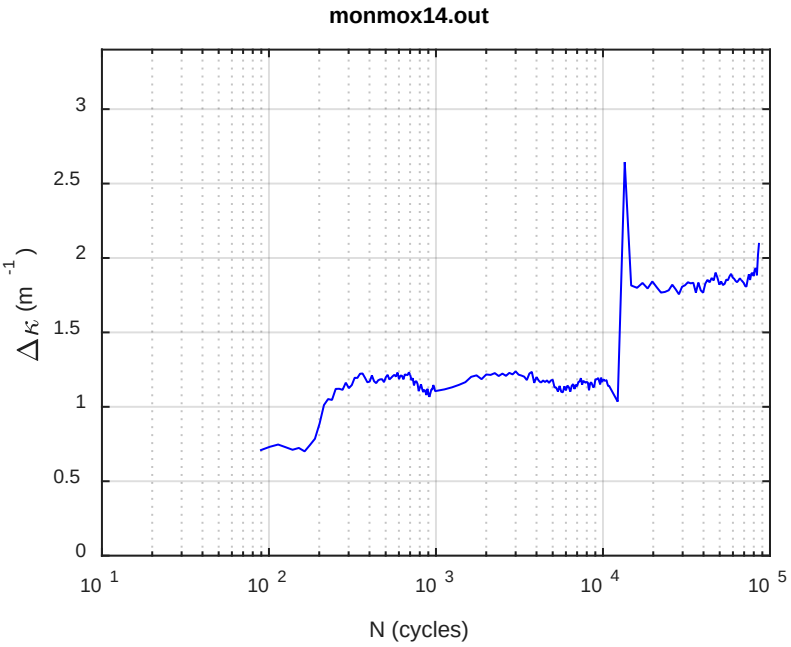
monmox14.out
Δκ (m -1)
N (cycles)
0
0.5
1
1.5
2
2.5
3
10 1
10 2
10 3
10 4
10 5

(a)

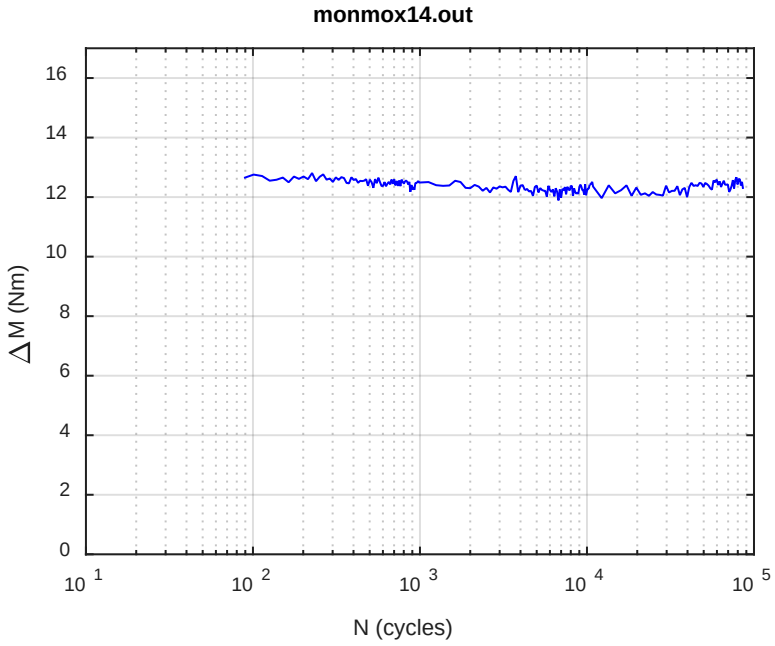
monmox14.out
ΔM (Nm)
N (cycles)
0
2
4
6
8
10
12
14
16
10 1
10 2
10 3
10 4
10 5

(b)

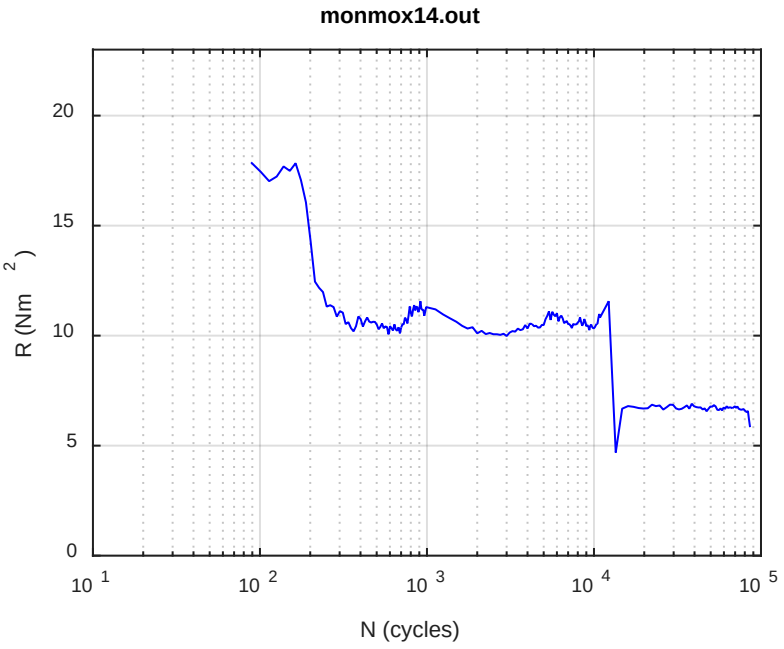
monmox14.out
R (Nm 2)
N (cycles)

(c)

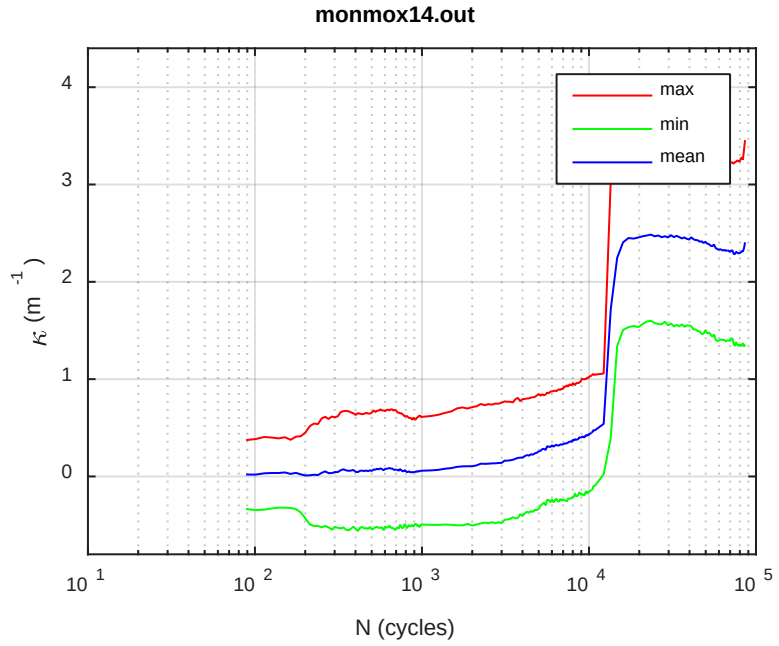
monmox14.out
max
min
mean
κ (m -1)
N (cycles)

(d)

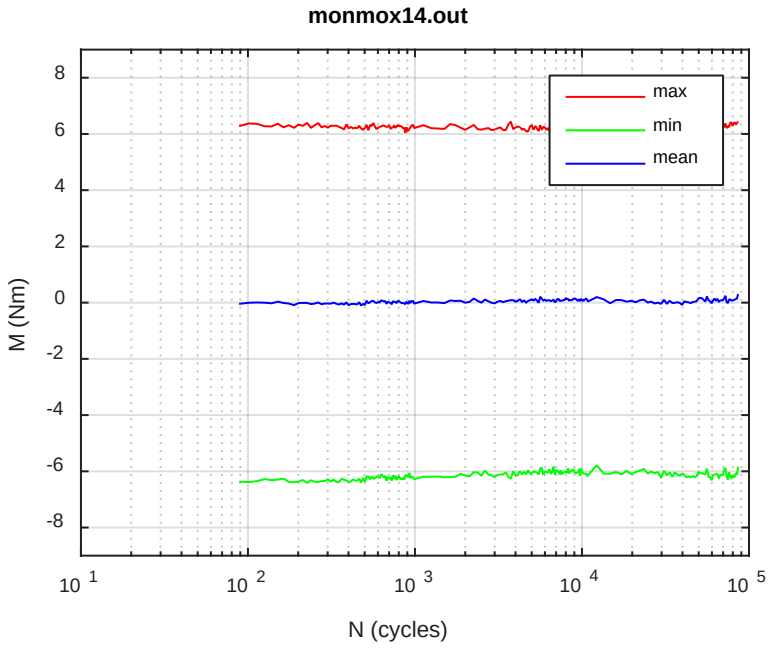

(e)

Fig. E.8 Monitoring-based responses: (a) curvature range, (b) moment range, (c) rigidity, (d) curvature peak/valley, (e) moment peak/valley, MOX14, 7.62 Nm, Nf = 8.72E+04 cycles.

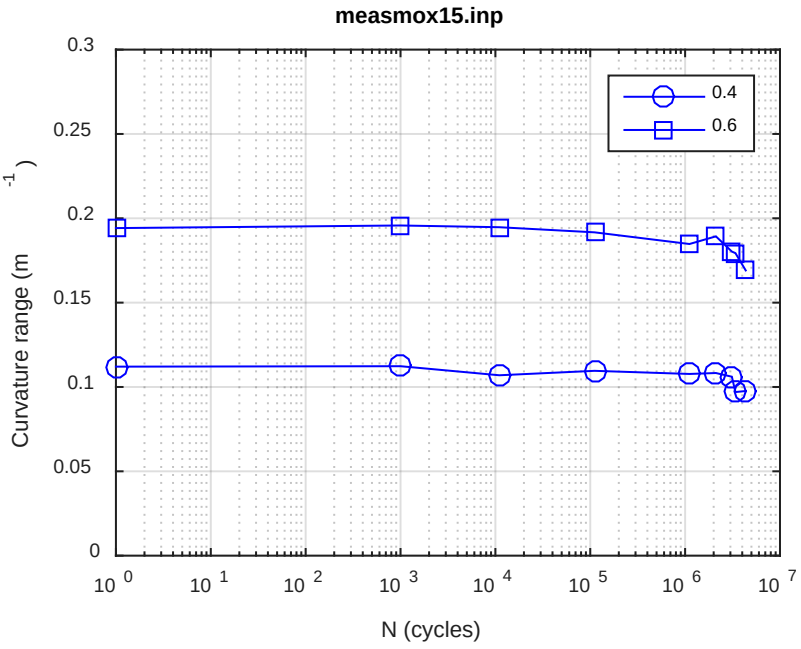
measmox15.inp
Curvature range (m -1)
N (cycles)
0.4
0.6
0
0.05
0.1
0.15
0.2
0.25
0.3
10 0
10 1
10 2
10 3
10 4
10 5
10 6
10 7

(a)

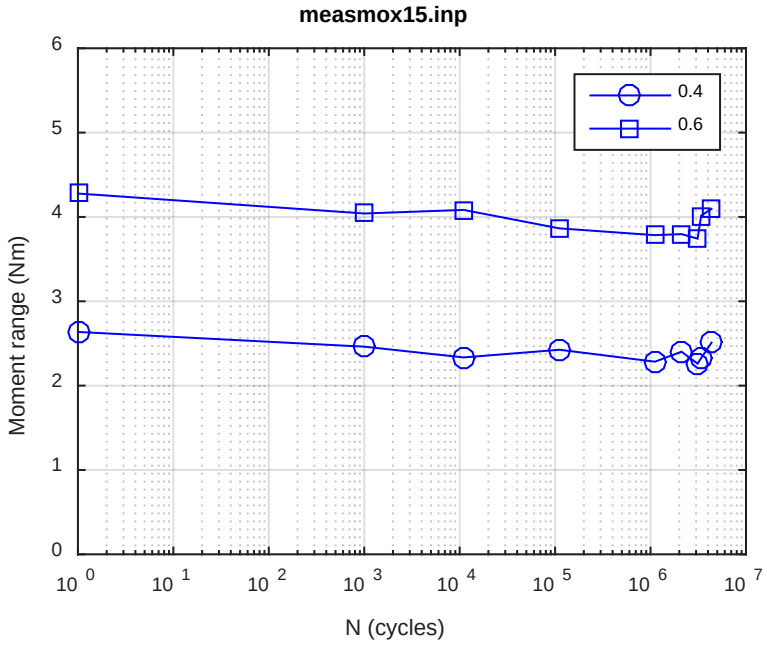
measmox15.inp
Moment range (Nm)
N (cycles)
0.4
0.6
0
1
2
3
4
5
6
10 0
10 1
10 2
10 3
10 4
10 5
10 6
10 7

(b)

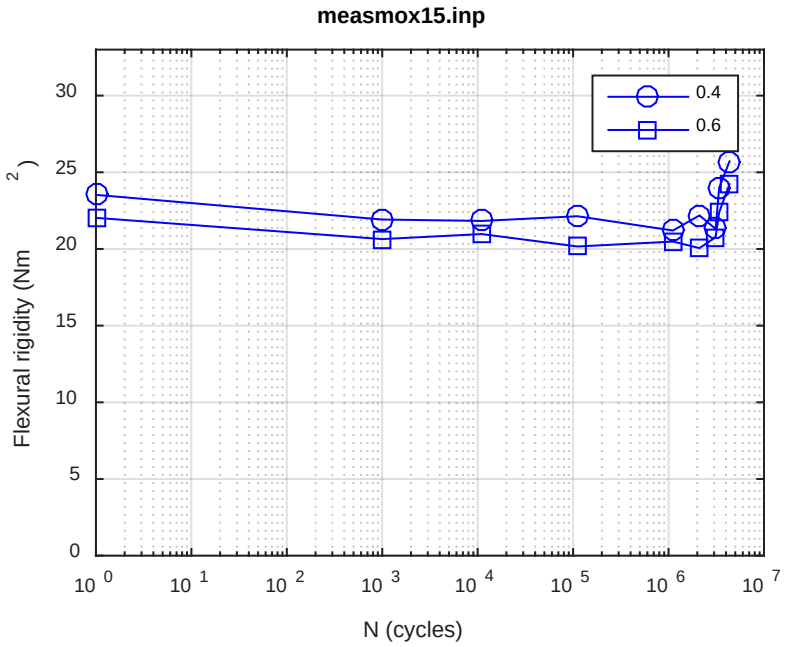
measmox15.inp
0.4
0.6
Flexural rigidity (Nm 2)
N (cycles)
0
5
10
15
20
25
30
10 0
10 1
10 2
10 3
10 4
10 5
10 6
10 7

(c)

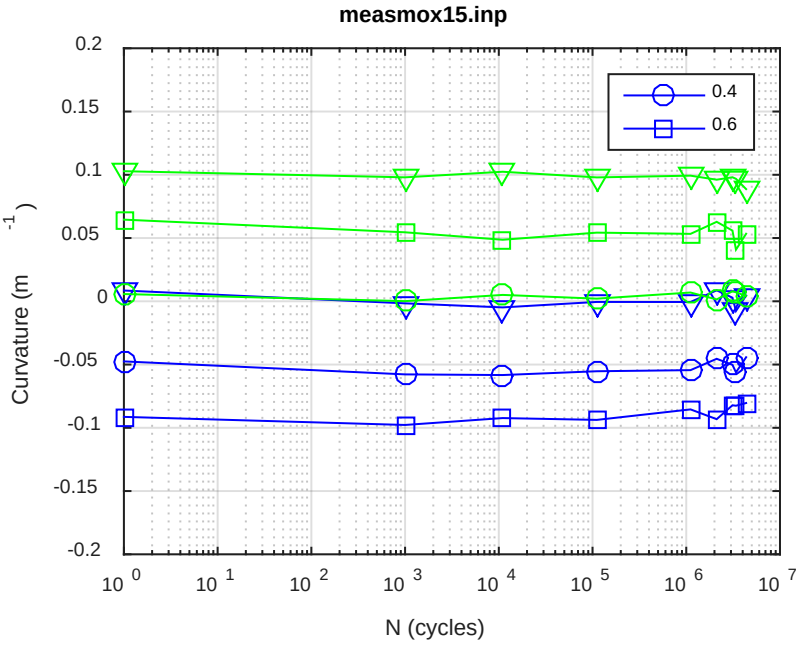
measmox15.inp
0.4
0.6
Curvature (m -1)
N (cycles)
0.2
0.15
0.1
0.05
0
-0.05
-0.1
-0.15
-0.2
10 0
10 1
10 2
10 3
10 4
10 5
10 6
10 7

(d)

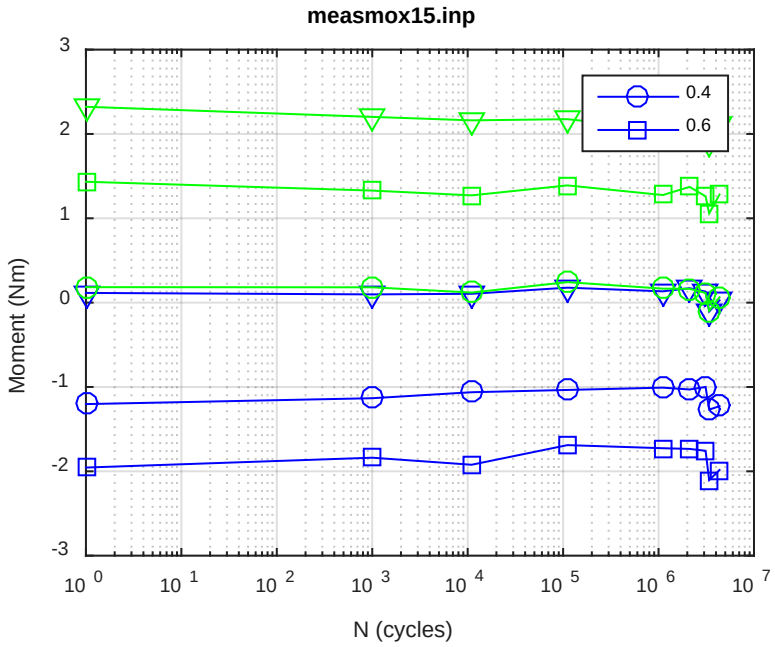

(e)

Fig. E.9 Measurement-based responses: (a) curvature range, (b) moment range, (c) rigidity, (d) curvature peak/valley, (e) moment peak/valley, MOX15, 5.08 Nm.

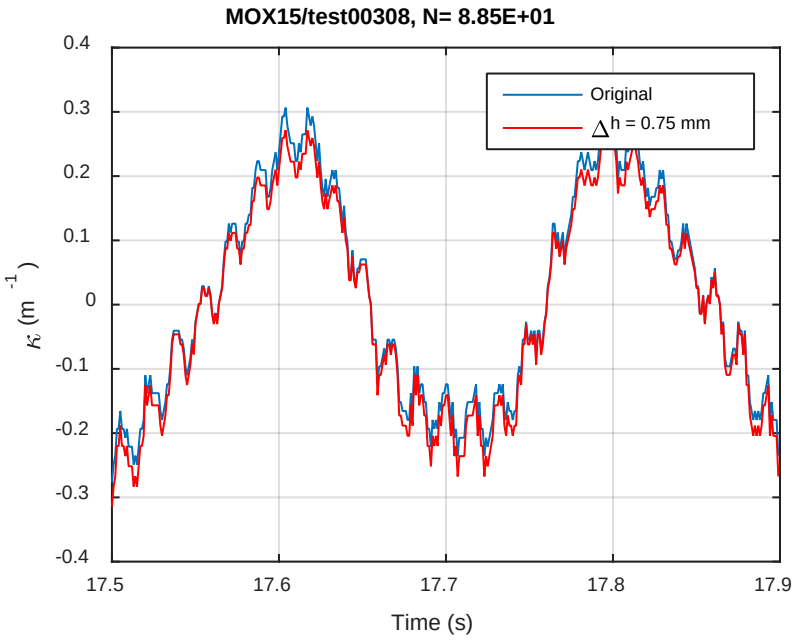
MOX15/test00308, N= 8.85E+01
Original
Δh = 0.75 mm
κ (m-1)
Time (s)
0.4
0.3
0.2
0.1
0
-0.1
-0.2
-0.3
-0.4
17.5
17.6
17.7
17.8
17.9

(a)

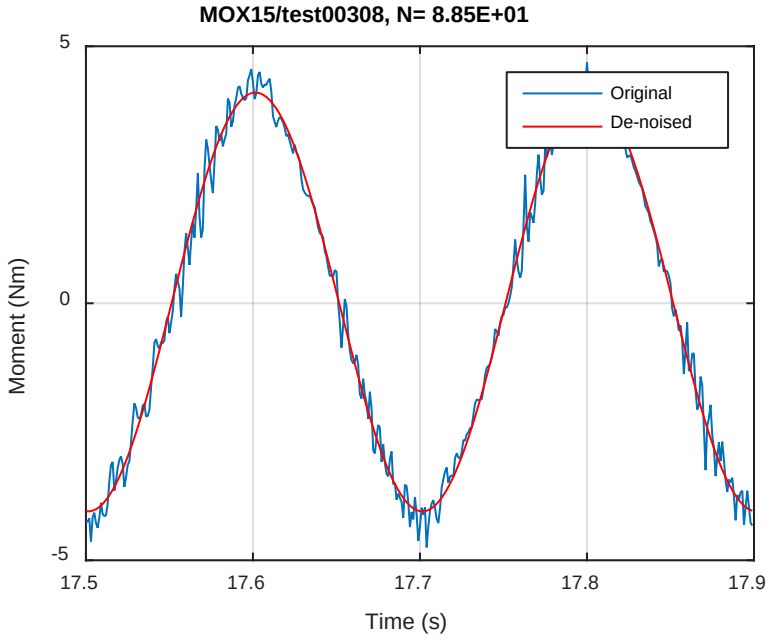
MOX15/test00308, N= 8.85E+01
Original
De-noised
Moment (Nm)
Time (s)
5
0
-5
17.5
17.6
17.7
17.8
17.9

(b)

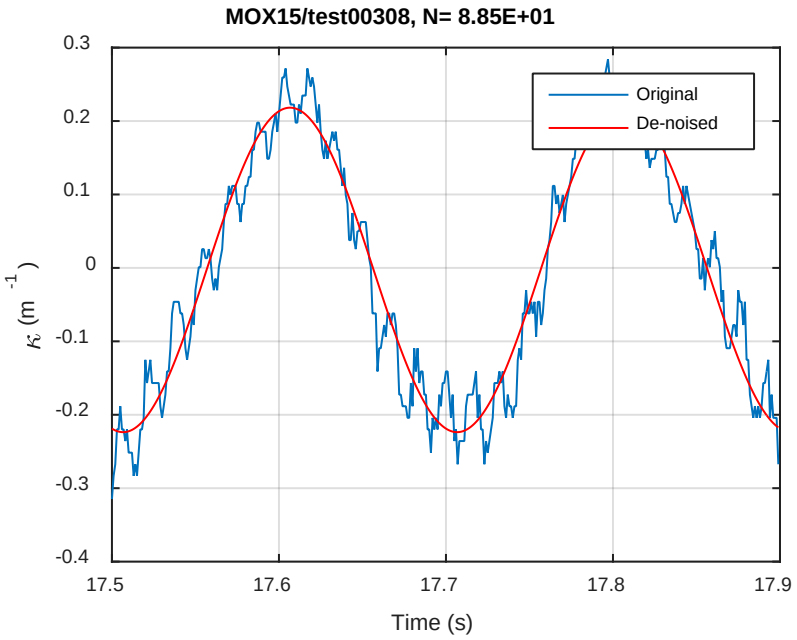

(c)

Fig. E.10 Monitoring-based responses: (a) curvature, (b) moment, (c) curvature, MOX15, 5.08 Nm, Ns = 8.85E+01 cycles.

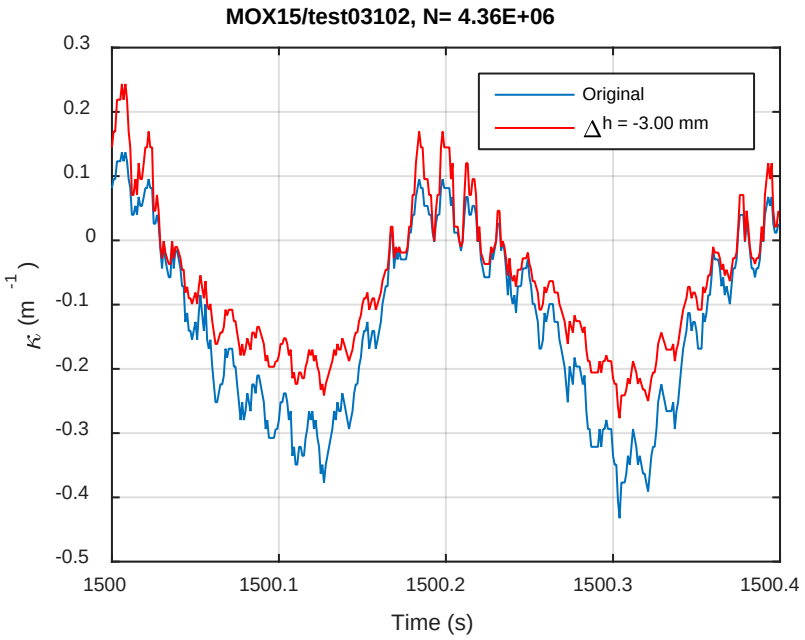
MOX15/test03102, N= 4.36E+06
Original
Δh = -3.00 mm
κ (m-1)
Time (s)
0.3
0.2
0.1
0
-0.1
-0.2
-0.3
-0.4
-0.5
1500
1500.1
1500.2
1500.3
1500.4

(a)

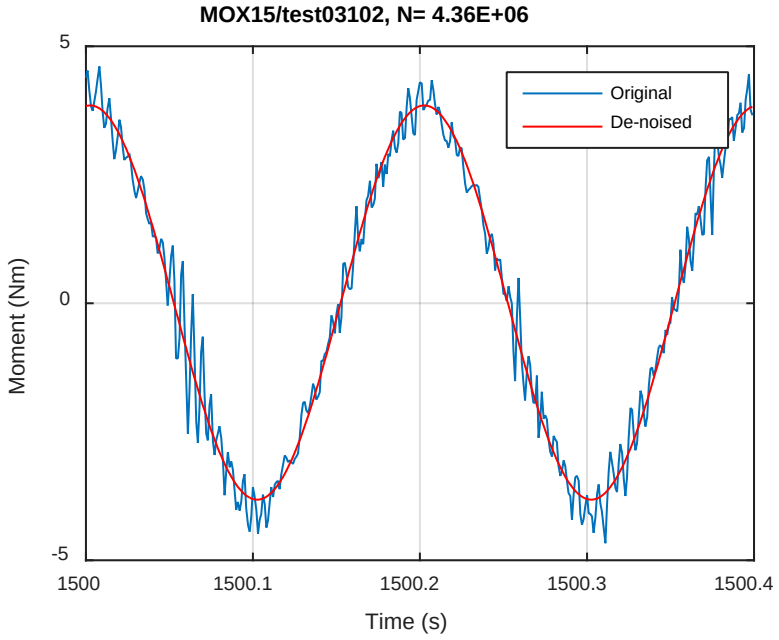
MOX15/test03102, N= 4.36E+06
Original
De-noised
Moment (Nm)
Time (s)
5
0
-5
1500
1500.1
1500.2
1500.3
1500.4

(b)

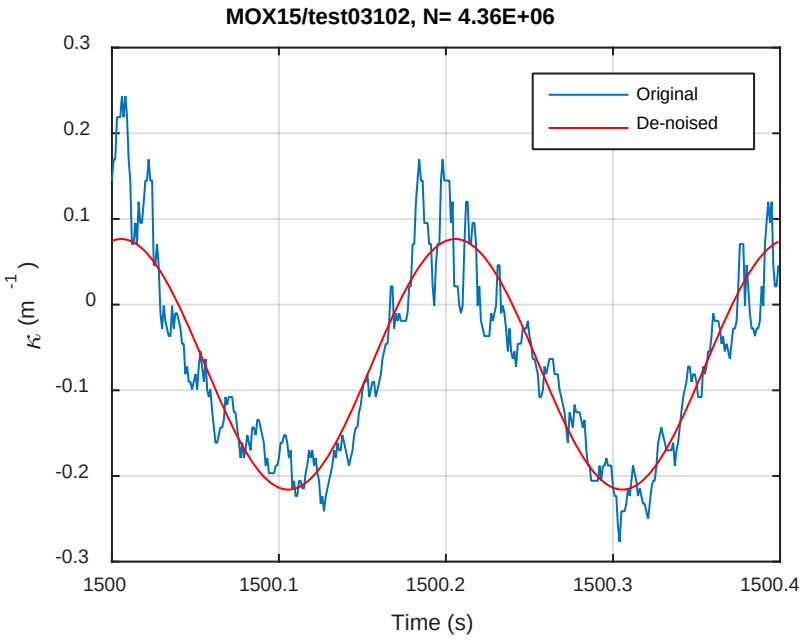

(c)

Fig. E.11 Monitoring-based responses: (a) curvature, (b) moment, (c) curvature, MOX15, 5.08 Nm, Ns = 4.36E+06 cycles.

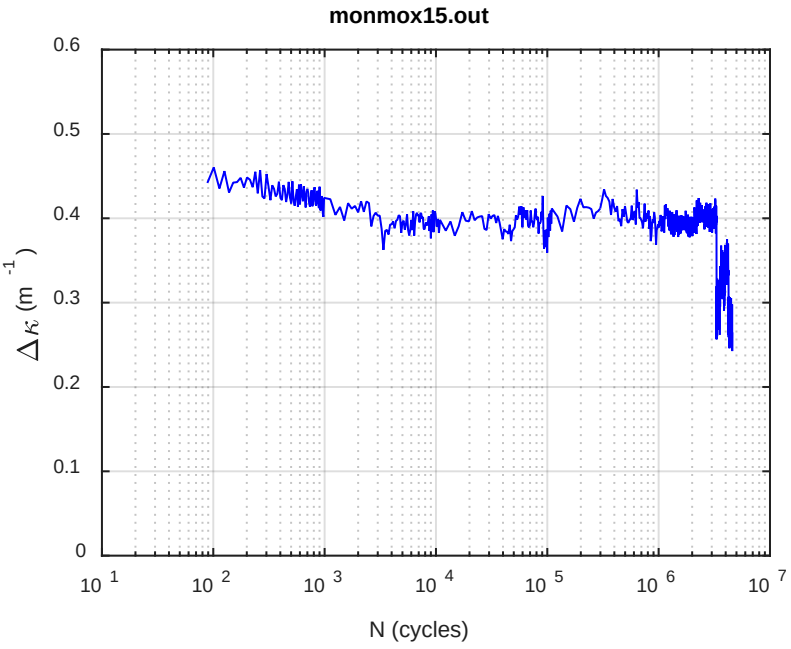
monmox15.out
0.6
0.5
0.4
0.3
0.2
0.1
0
Δκ (m -1)
10 1
10 2
10 3
10 4
10 5
10 6
10 7
N (cycles)

(a)

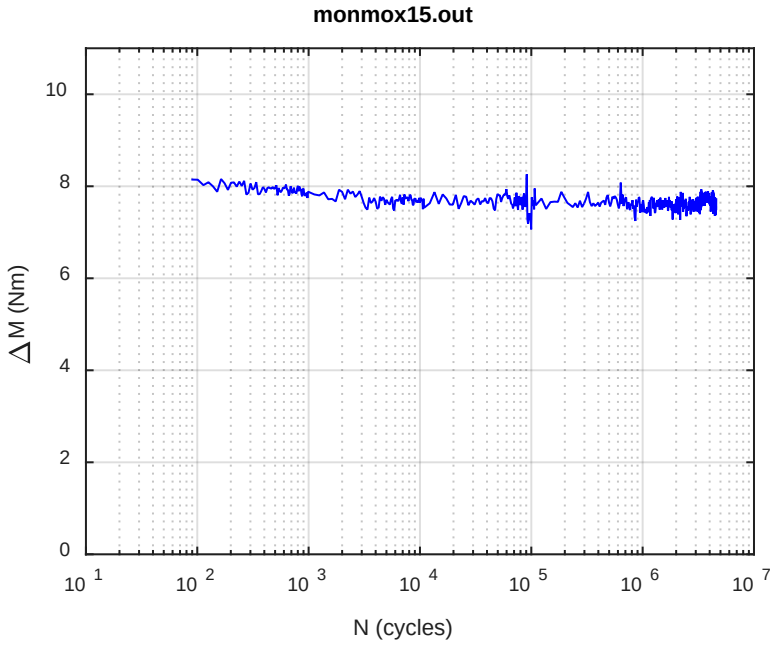
monmox15.out
10
8
6
4
2
0
ΔM (Nm)
10 1
10 2
10 3
10 4
10 5
10 6
10 7
N (cycles)

(b)

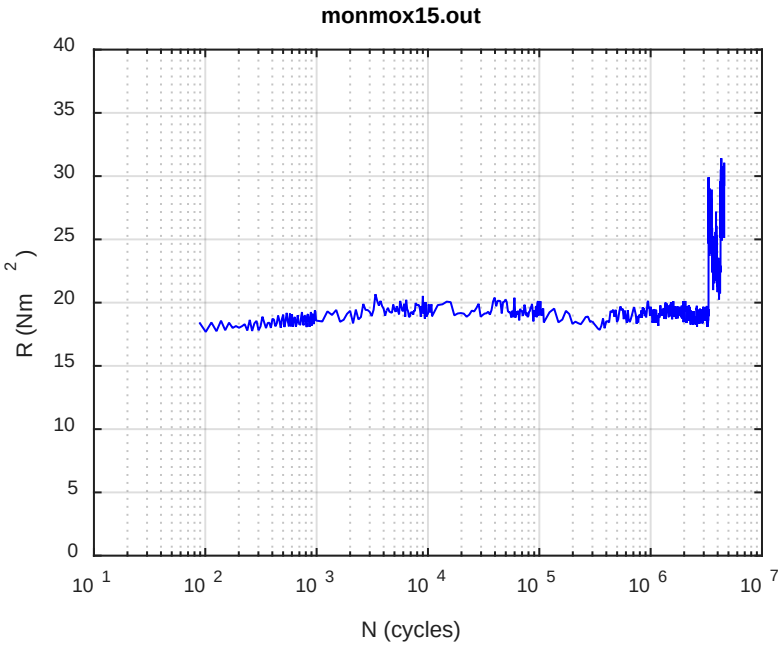
monmox15.out
R (Nm 2)
N (cycles)

(c)

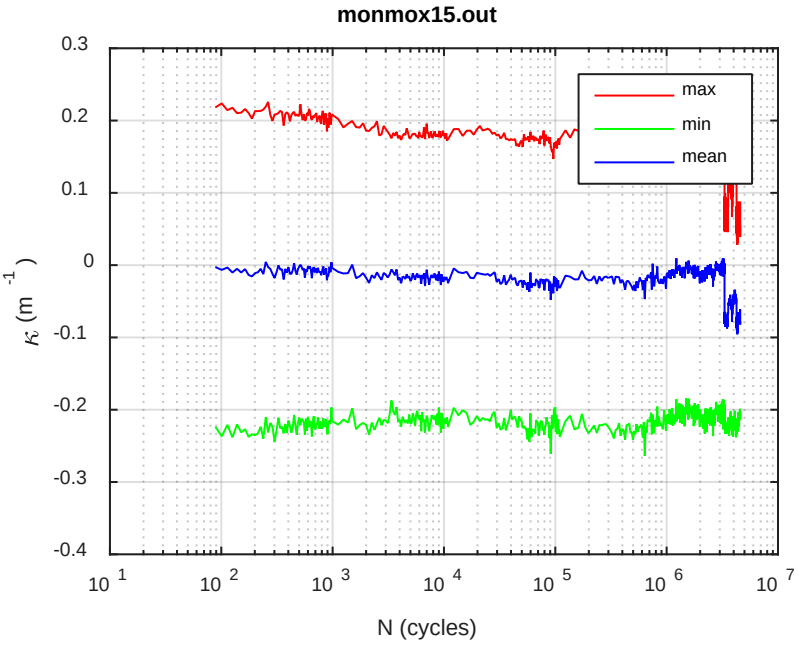
monmox15.out
max
min
mean
κ (m -1)
N (cycles)

(d)

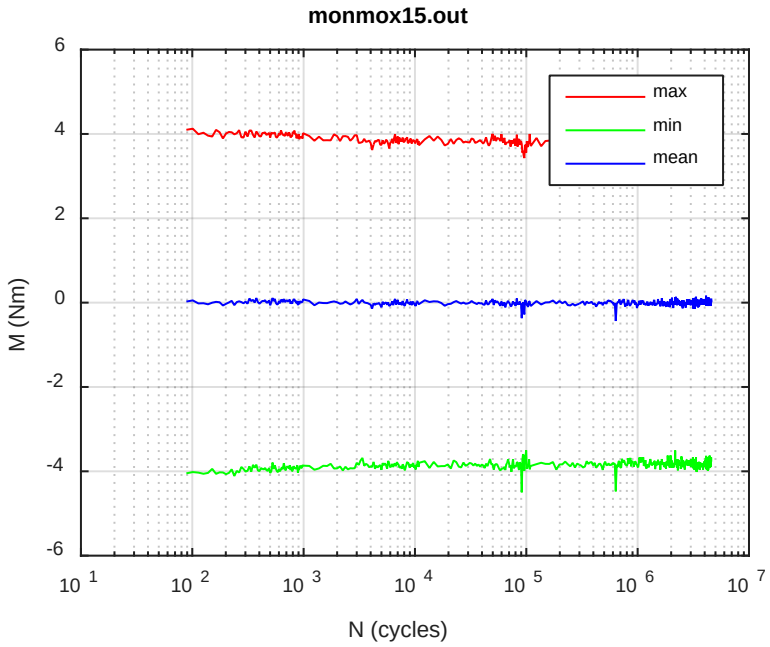

(e)

Fig. E.12 Monitoring-based responses: (a) curvature range, (b) moment range, (c) rigidity, (d) curvature peak/valley, (e) moment peak/valley, MOX15, 5.08 Nm, Nf = 4.65E+06 cycles.

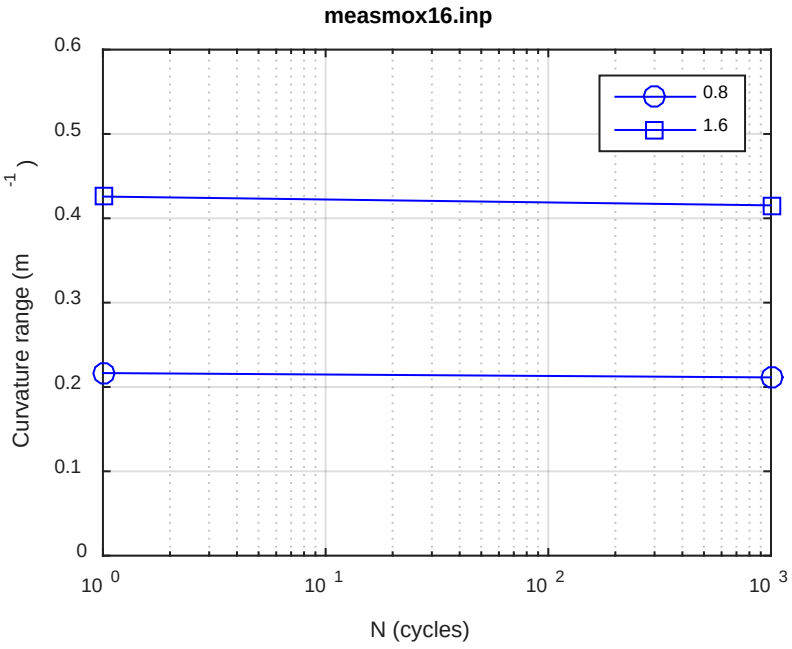
measmox16.inp
0.8
1.6
Curvature range (m -1)
N (cycles)
0
0.1
0.2
0.3
0.4
0.5
0.6
10 0
10 1
10 2
10 3

(a)

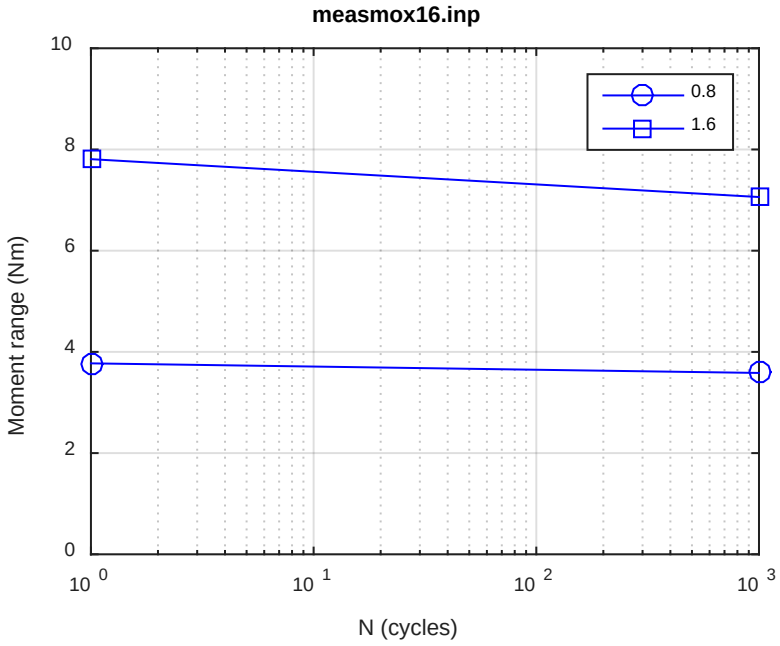
measmox16.inp
0.8
1.6
Moment range (Nm)
N (cycles)
0
2
4
6
8
10
10 0
10 1
10 2
10 3

(b)

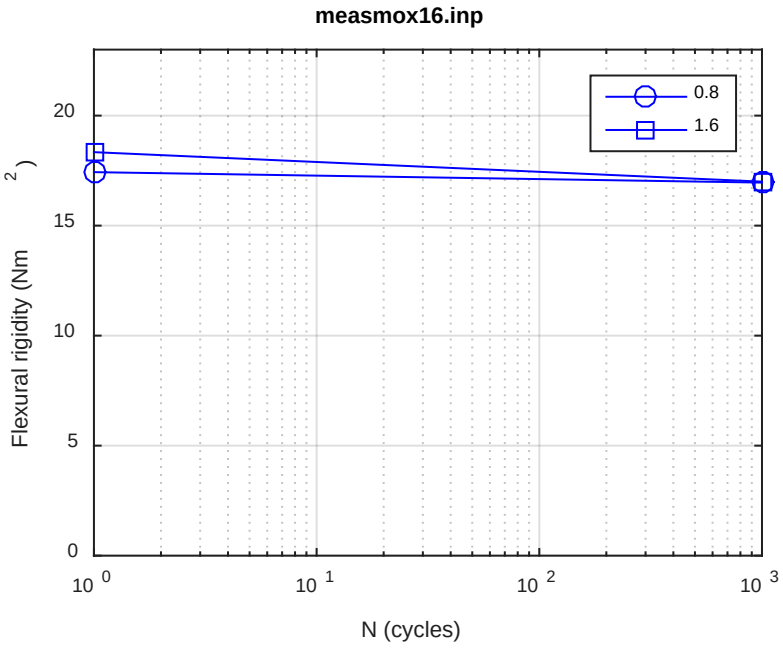
measmox16.inp
0.8
1.6
Flexural rigidity (Nm 2)
20
15
10
5
0
10 0
10 1
10 2
10 3
N (cycles)

(c)

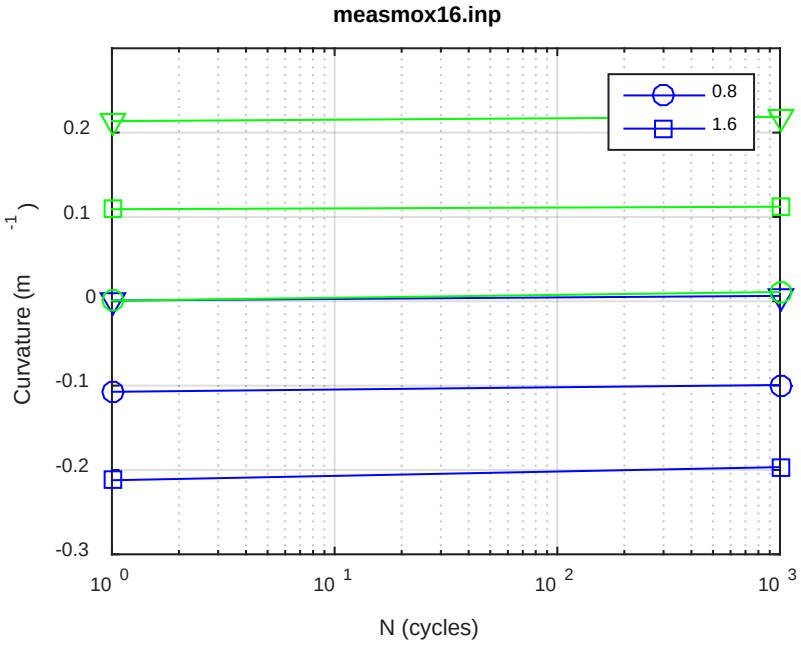
measmox16.inp
0.8
1.6
Curvature (m -1)
0.2
0.1
0
-0.1
-0.2
-0.3
10 0
10 1
10 2
10 3
N (cycles)

(d)

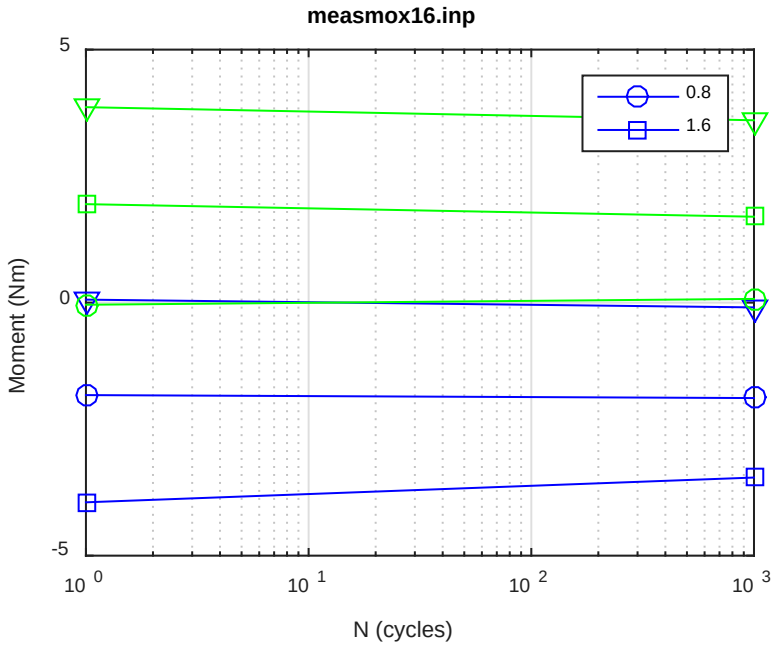

(e)

Fig. E.13 Measurement-based responses: (a) curvature range, (b) moment range, (c) rigidity, (d) curvature peak/valley, (e) moment peak/valley, MOX16, 15.24 Nm.

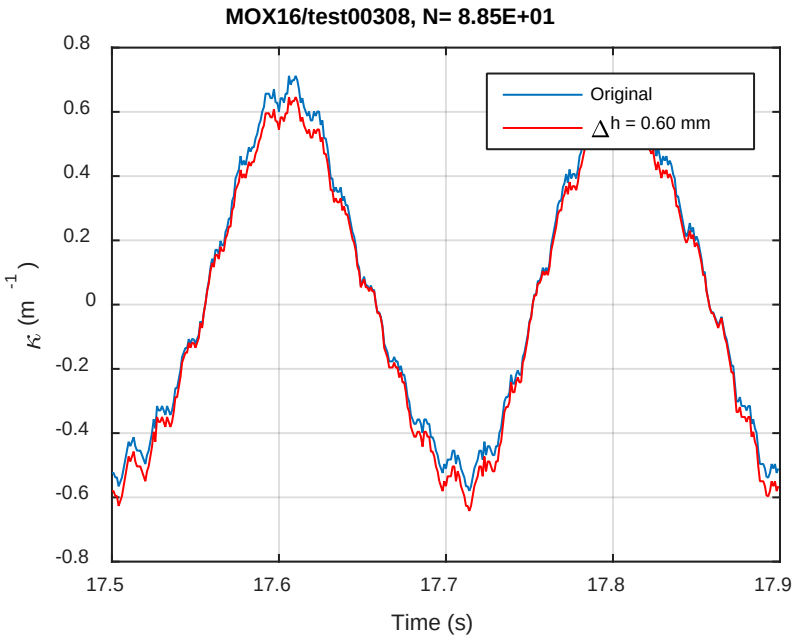
MOX16/test00308, N= 8.85E+01
Original
Δh = 0.60 mm
κ (m-1)
Time (s)
0.8
0.6
0.4
0.2
0
-0.2
-0.4
-0.6
-0.8
17.5
17.6
17.7
17.8
17.9

(a)

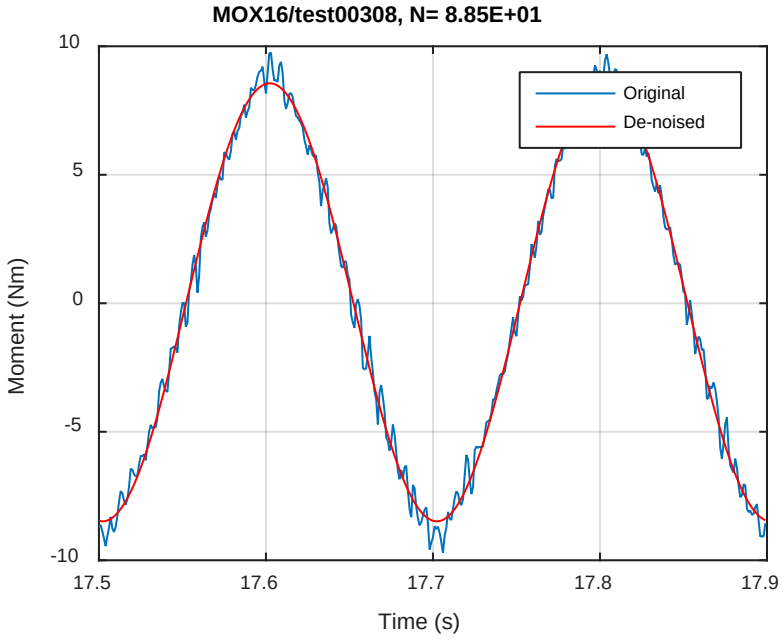
MOX16/test00308, N= 8.85E+01
Original
De-noised
Moment (Nm)
Time (s)
10
5
0
-5
-10
17.5
17.6
17.7
17.8
17.9

(b)

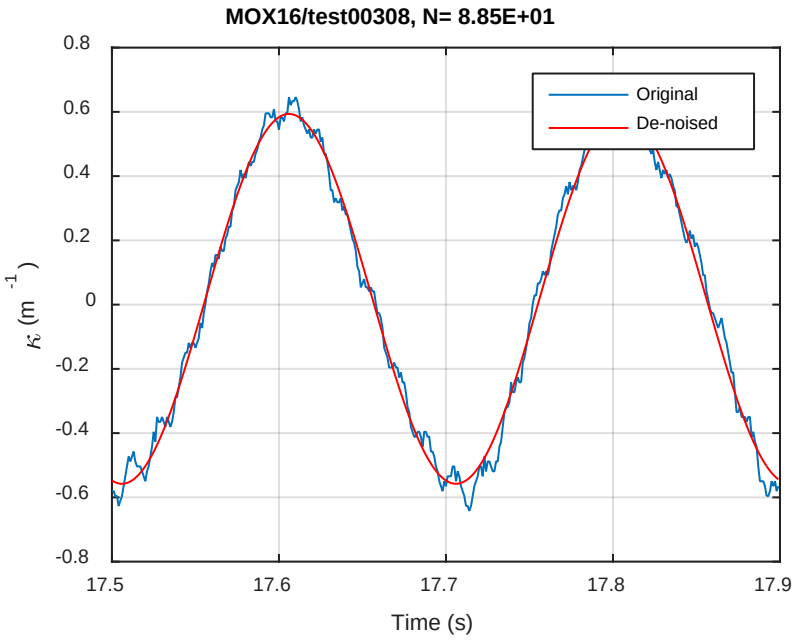

(c)

Fig. E.14 Monitoring-based responses: (a) curvature, (b) moment, (c) curvature, MOX16, 15.24 Nm, Ns = 8.85E+01 cycles.

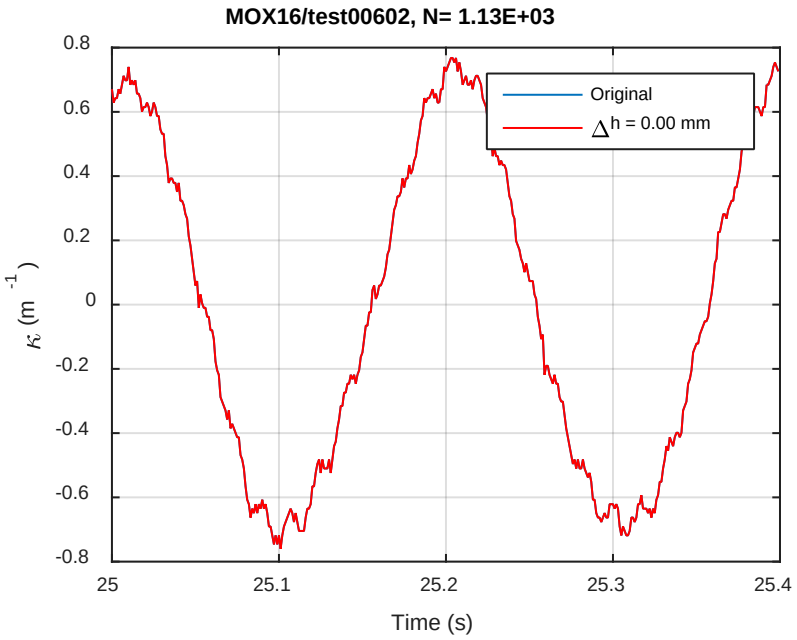
MOX16/test00602, N= 1.13E+03
Original
Δh = 0.00 mm
κ (m-1)
Time (s)

(a)

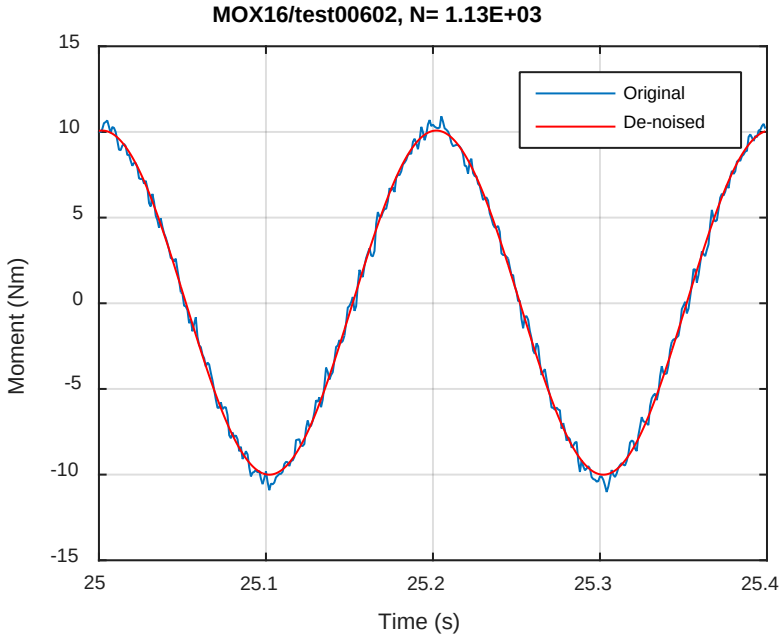
MOX16/test00602, N= 1.13E+03
Original
De-noised
Moment (Nm)
Time (s)

(b)

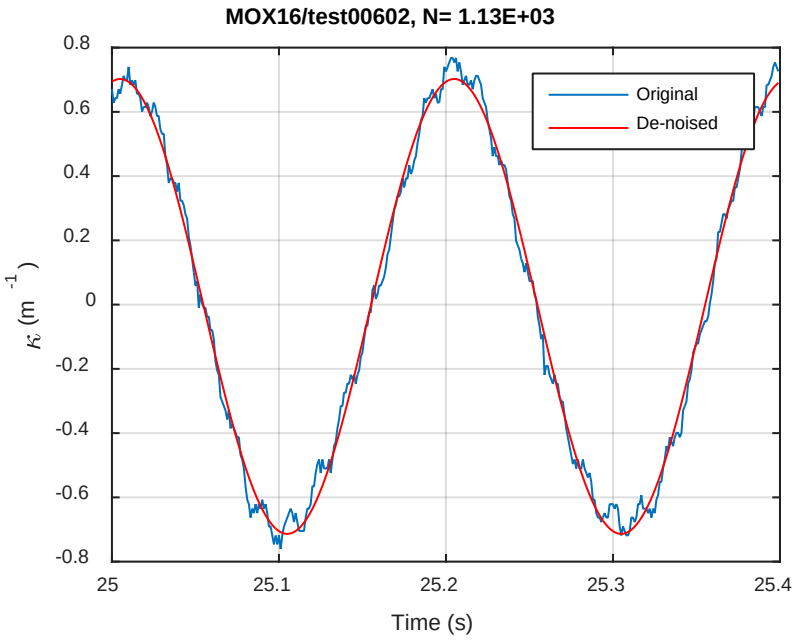

(c)

Fig. E.15 Monitoring-based responses: (a) curvature, (b) moment, (c) curvature, MOX16, 15.24 Nm, Ns = 1.13E+03 cycles.

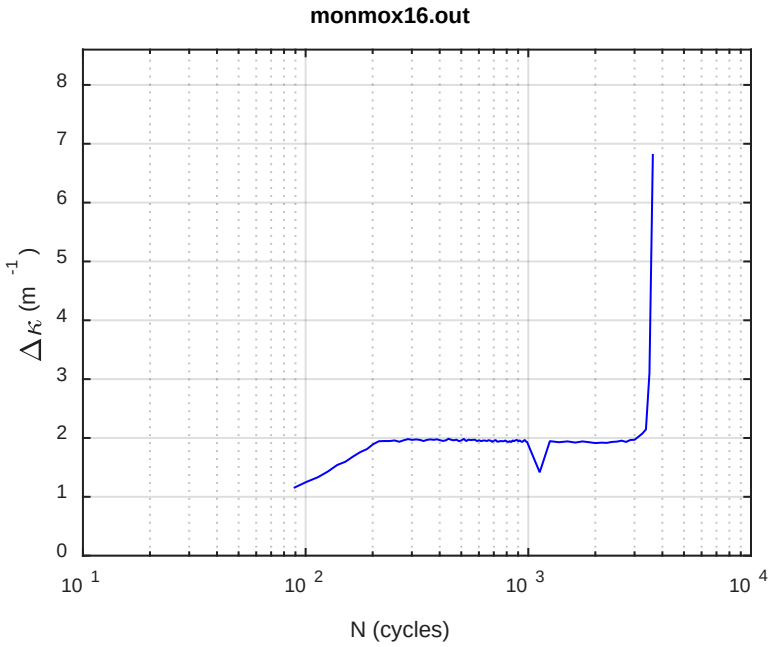
monmox16.out
8
7
6
5
4
3
2
1
0
Δκ (m -1)
10 1
10 2
10 3
10 4
N (cycles)

(a)


monmox16.out
35
30
25
20
15
10
5
0
ΔM (Nm)
10 1
10 2
10 3
10 4
N (cycles)

(b)

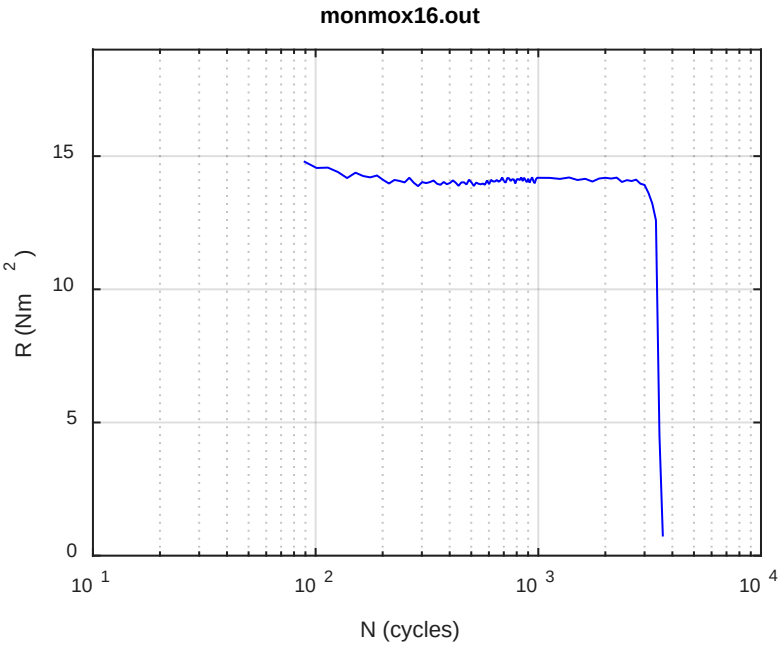
monmox16.out
R (Nm 2)
15
10
5
0
10 1
10 2
10 3
10 4
N (cycles)

(c)

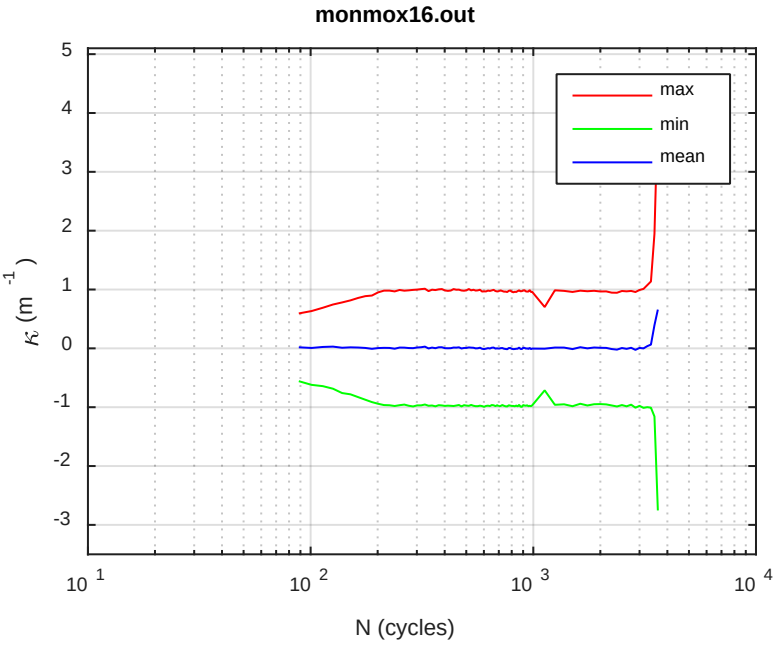
monmox16.out
κ (m -1)
5
4
3
2
1
0
-1
-2
-3
max
min
mean
10 1
10 2
10 3
10 4
N (cycles)

(d)

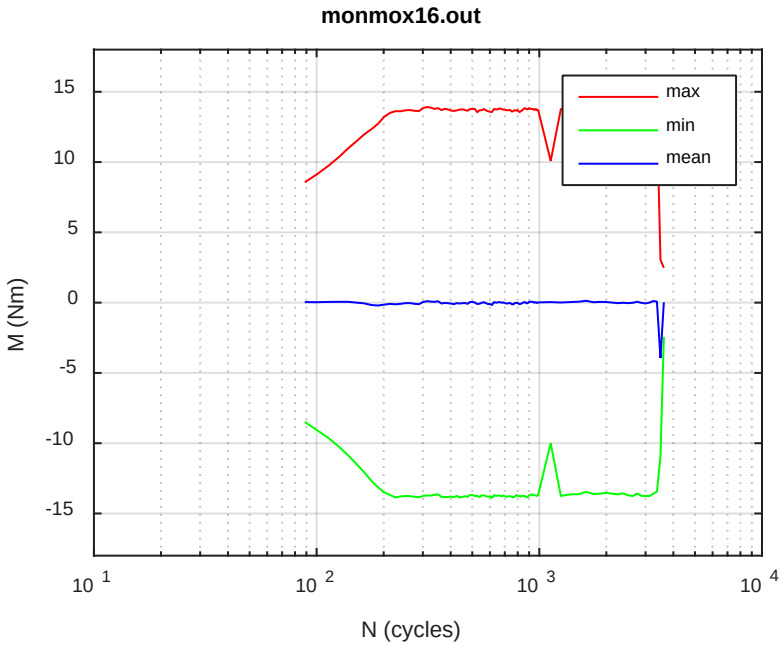

(e)

Fig. E.16 Monitoring-based responses: (a) curvature range, (b) moment range, (c) rigidity, (d) curvature peak/valley, (e) moment peak/valley, MOX16, 15.24 Nm, Nf = 3.66E+03 cycles.

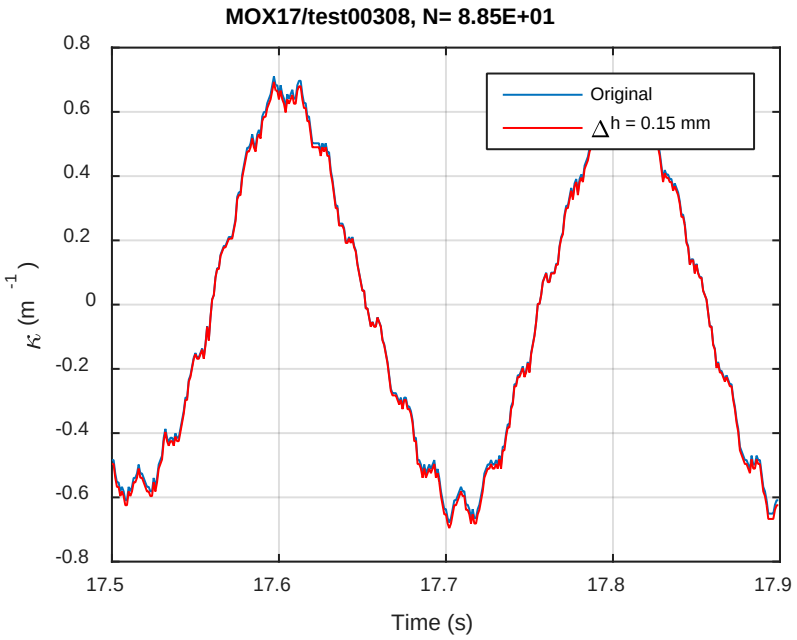
MOX17/test00308, N= 8.85E+01
Original
Δh = 0.15 mm
κ (m -1)
Time (s)
0.8
0.6
0.4
0.2
0
-0.2
-0.4
-0.6
-0.8
17.5
17.6
17.7
17.8
17.9

(a)

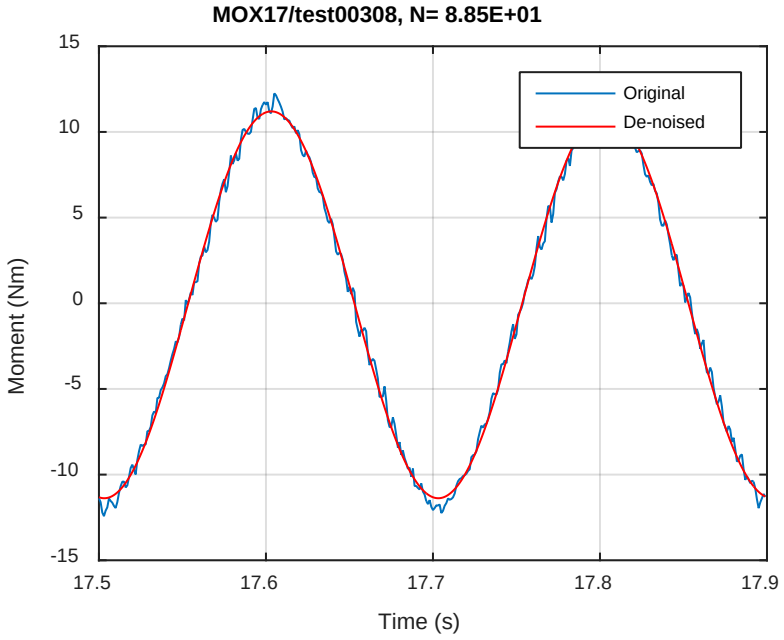
MOX17/test00308, N= 8.85E+01
Original
De-noised
Moment (Nm)
Time (s)
15
10
5
0
-5
-10
-15
17.5
17.6
17.7
17.8
17.9

(b)

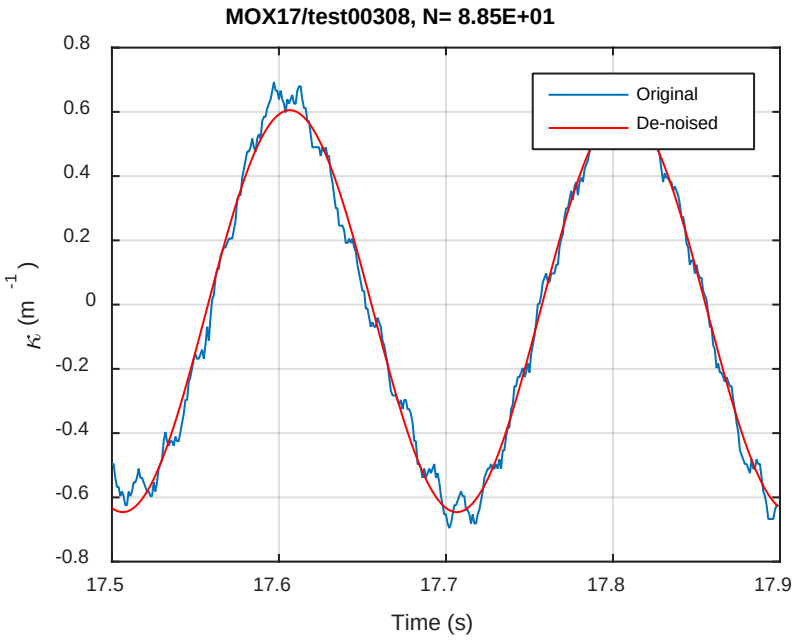

(c)

Fig. E.17 Monitoring-based responses: (a) curvature, (b) moment, (c) curvature, MOX17, 12.70 Nm, Ns = 8.85E+01 cycles.

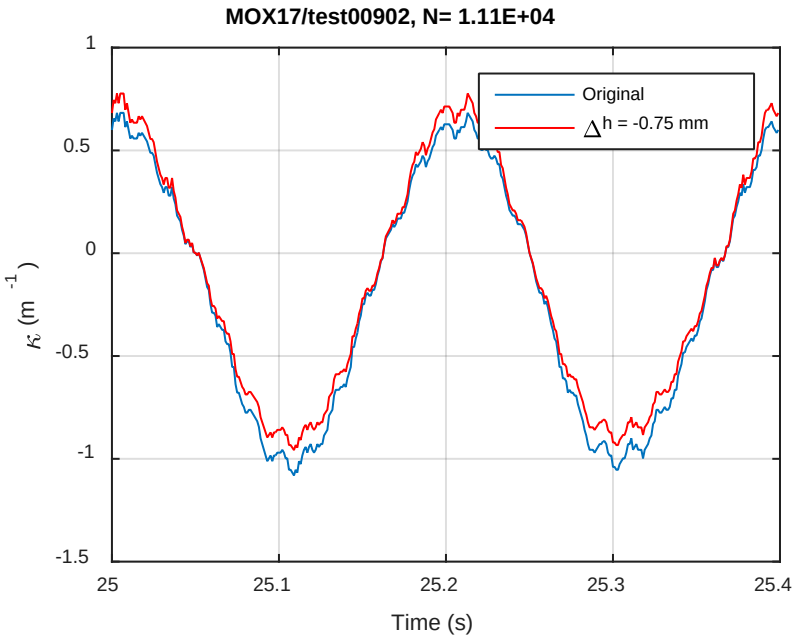
MOX17/test00902, N= 1.11E+04
Original
Δh = -0.75 mm
κ (m-1)
Time (s)
1
0.5
0
-0.5
-1
-1.5
25
25.1
25.2
25.3
25.4

(a)

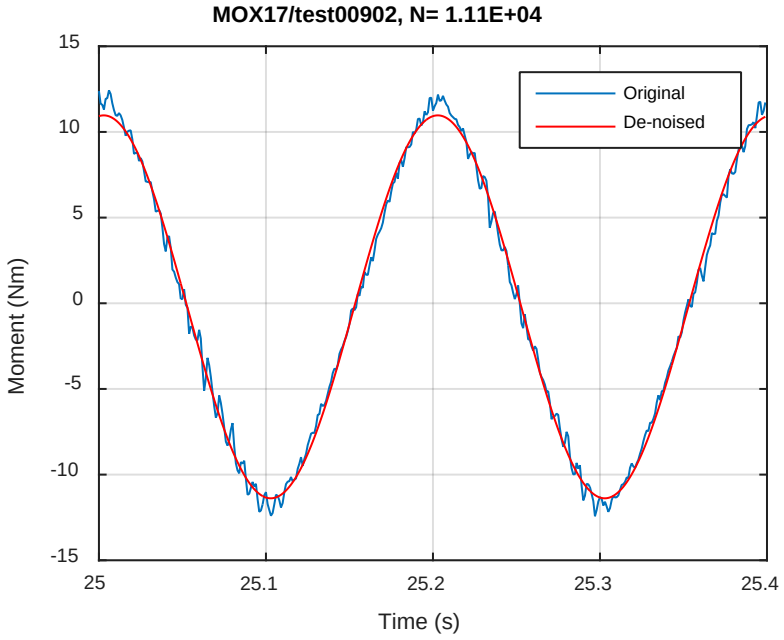
MOX17/test00902, N= 1.11E+04
Original
De-noised
Moment (Nm)
Time (s)
15
10
5
0
-5
-10
-15
25
25.1
25.2
25.3
25.4

(b)

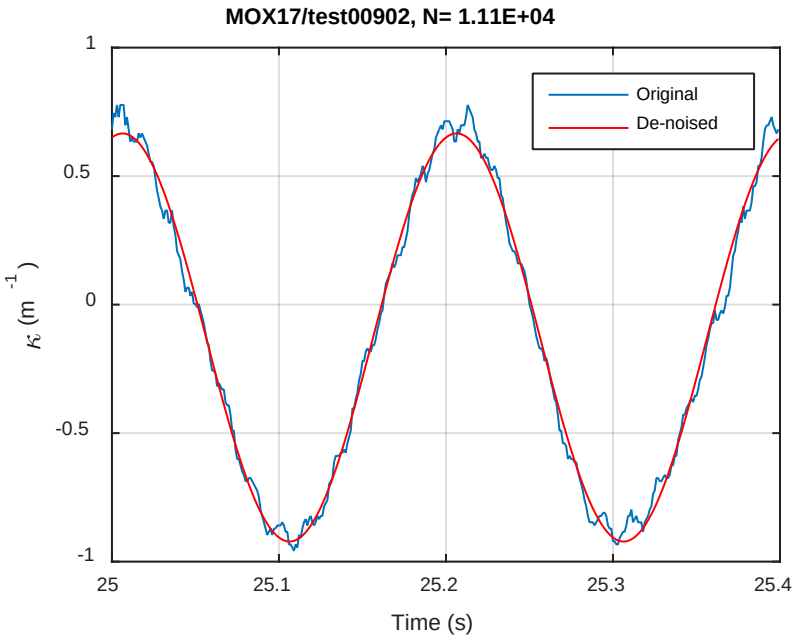

(c)

Fig. E.18 Monitoring-based responses: (a) curvature, (b) moment, (c) curvature, MOX17, 12.70 Nm, Ns = 1.11E+04 cycles.

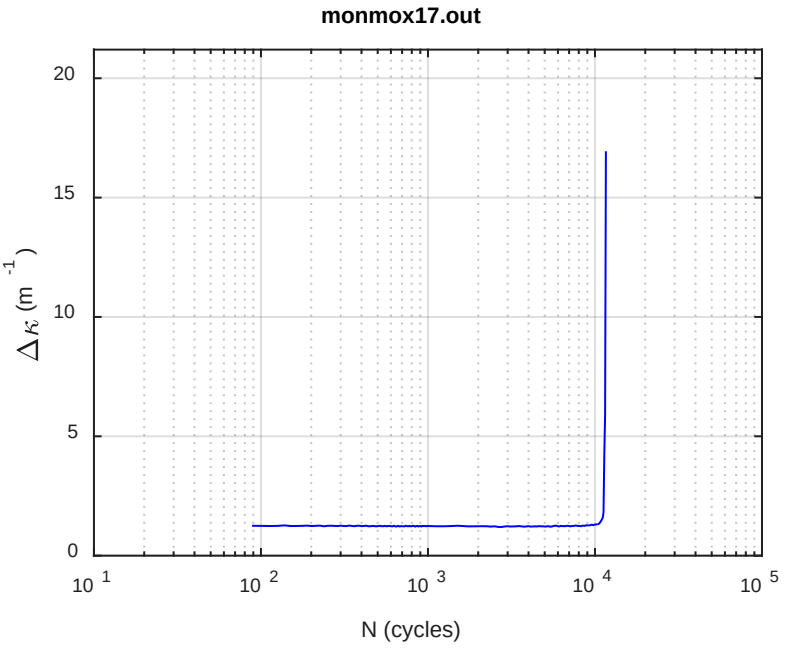
monmox17.out
20
15
10
5
0
$\Delta\kappa$ (m $^{-1}$)
10^{1}
10^{2}
10^{3}
10^{4}
10^{5}
N (cycles)

(a)

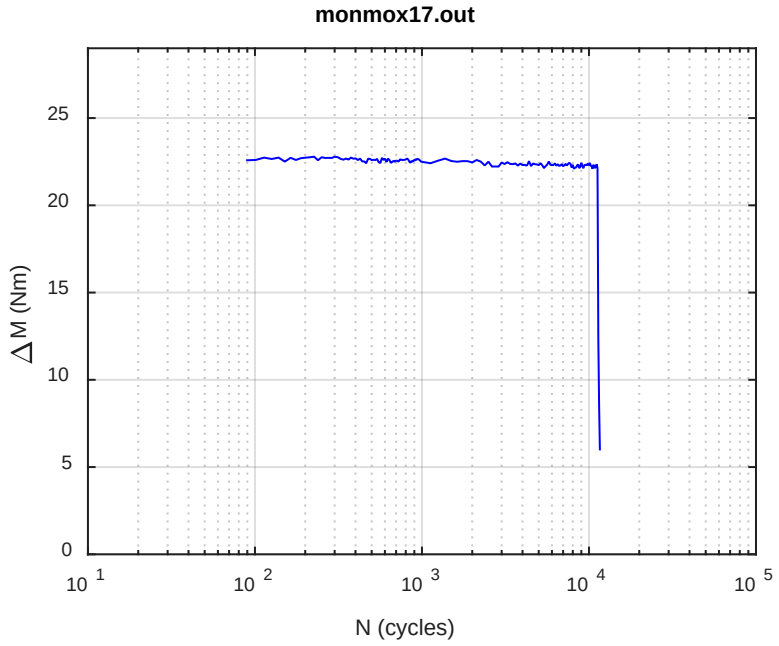
monmox17.out
25
20
15
10
5
0
ΔM (Nm)
10^{1}
10^{2}
10^{3}
10^{4}
10^{5}
N (cycles)

(b)

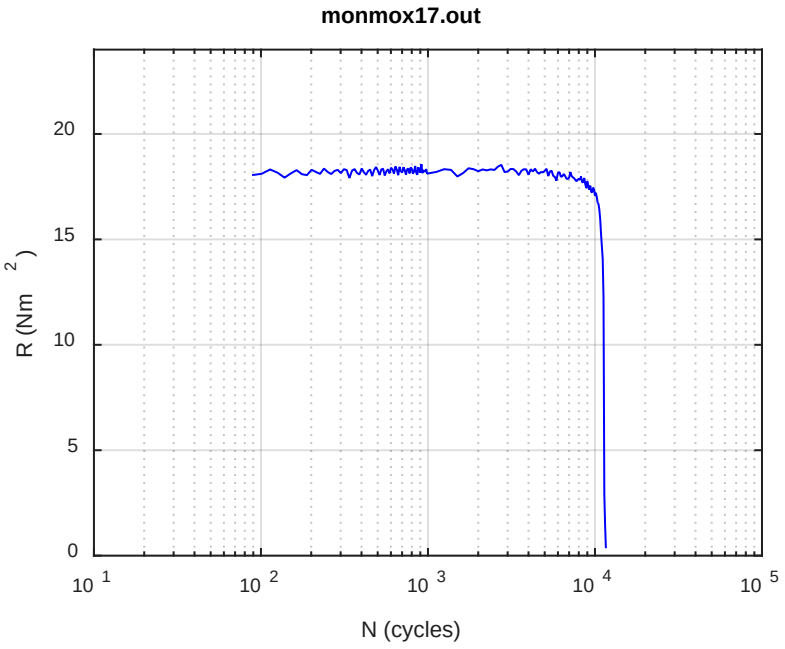
monmox17.out
R (Nm 2)
20
15
10
5
0
10 1
10 2
10 3
10 4
10 5
N (cycles)

(c)

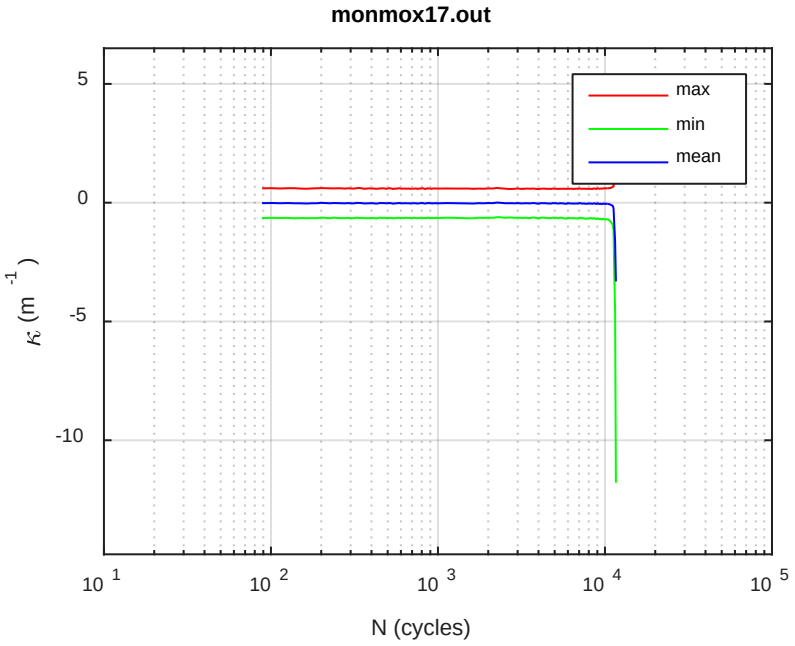
monmox17.out
max
min
mean
κ (m -1)
5
0
-5
-10
10 1
10 2
10 3
10 4
10 5
N (cycles)

(d)

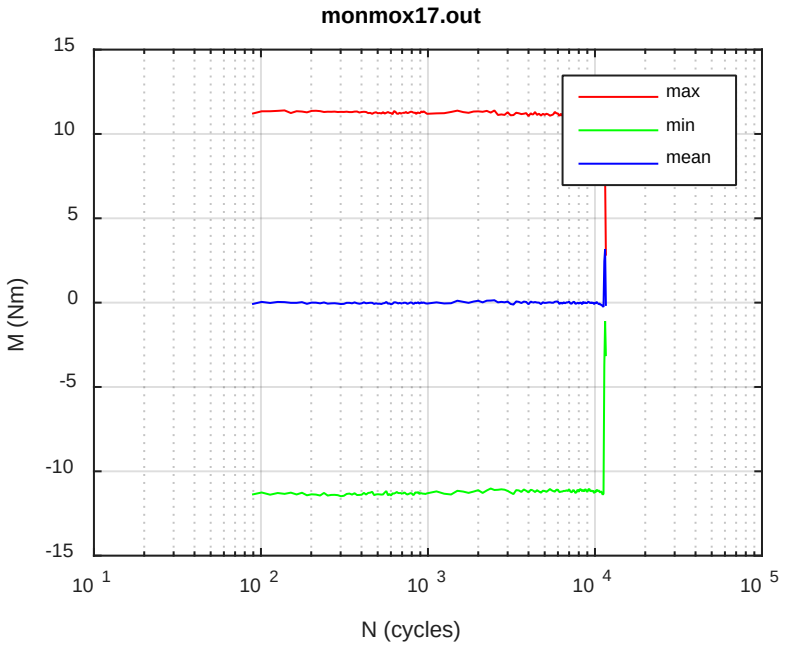

(e)

Fig. E.19 Monitoring-based responses: (a) curvature range, (b) moment range, (c) rigidity, (d) curvature peak/valley, (e) moment peak/valley, MOX17, 12.70 Nm, Nf = 1.16E+04 cycles.

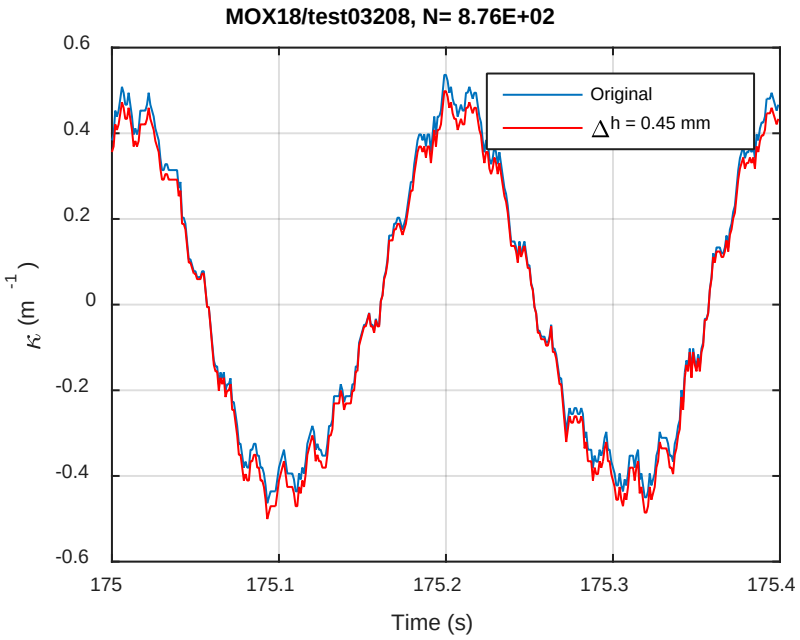
MOX18/test03208, N= 8.76E+02
Original
Δh = 0.45 mm
κ (m -1)
Time (s)
0.6
0.4
0.2
0
-0.2
-0.4
-0.6
175
175.1
175.2
175.3
175.4

(a)

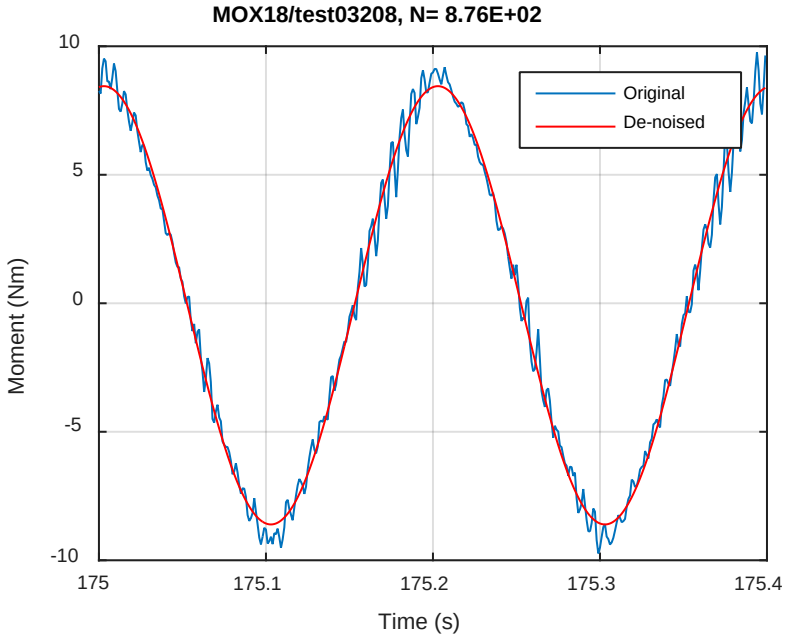
MOX18/test03208, N= 8.76E+02
Original
De-noised
Moment (Nm)
Time (s)
10
5
0
-5
-10
175
175.1
175.2
175.3
175.4

(b)

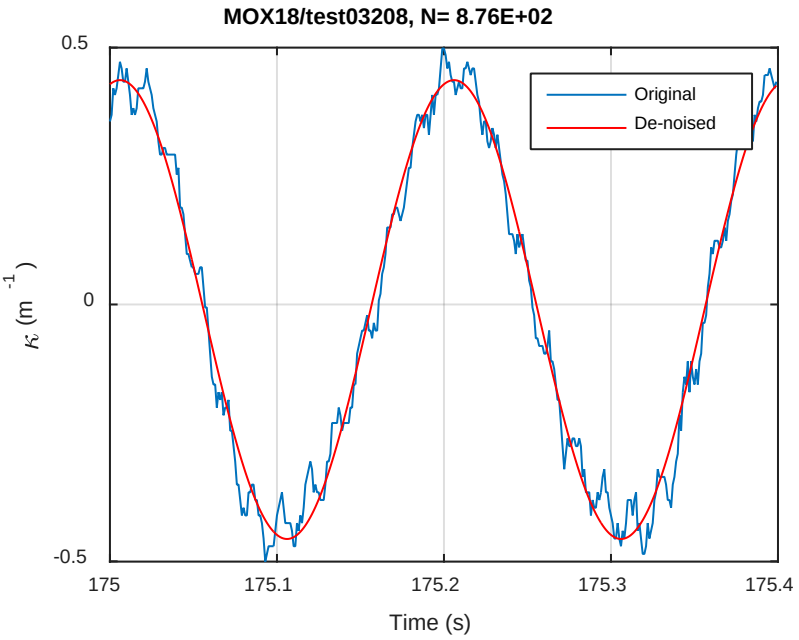

(c)

Fig. E.20 Monitoring-based responses: (a) curvature, (b) moment, (c) curvature, MOX18, 10.16 Nm, Ns = 8.76E+02 cycles.

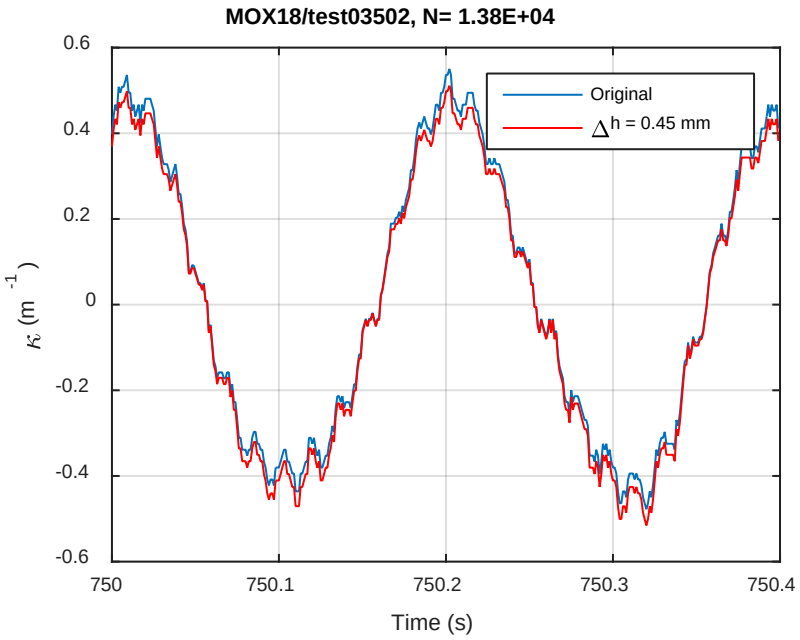
MOX18/test03502, N= 1.38E+04
Original
Δh = 0.45 mm
κ (m-1)
Time (s)
0.6
0.4
0.2
0
-0.2
-0.4
-0.6
750
750.1
750.2
750.3
750.4

(a)

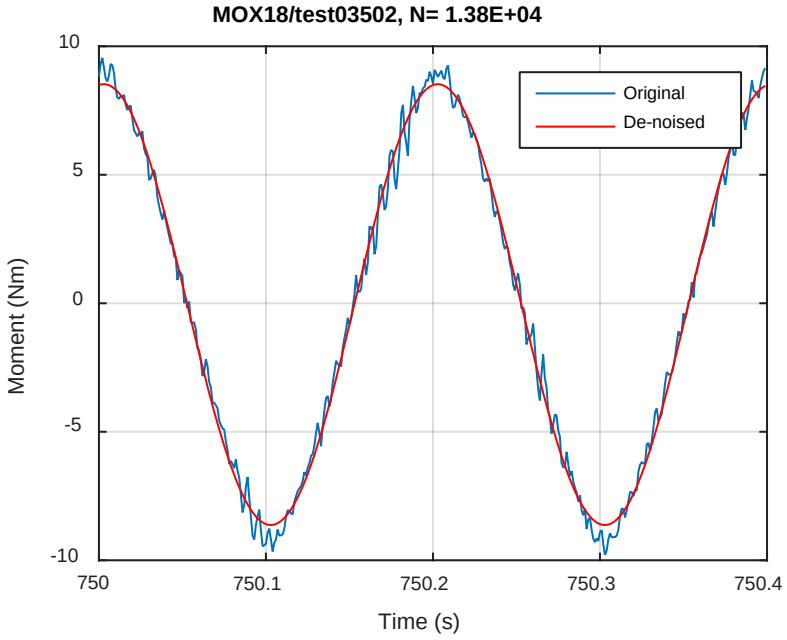
MOX18/test03502, N= 1.38E+04
Original
De-noised
Moment (Nm)
Time (s)
10
5
0
-5
-10
750
750.1
750.2
750.3
750.4

(b)

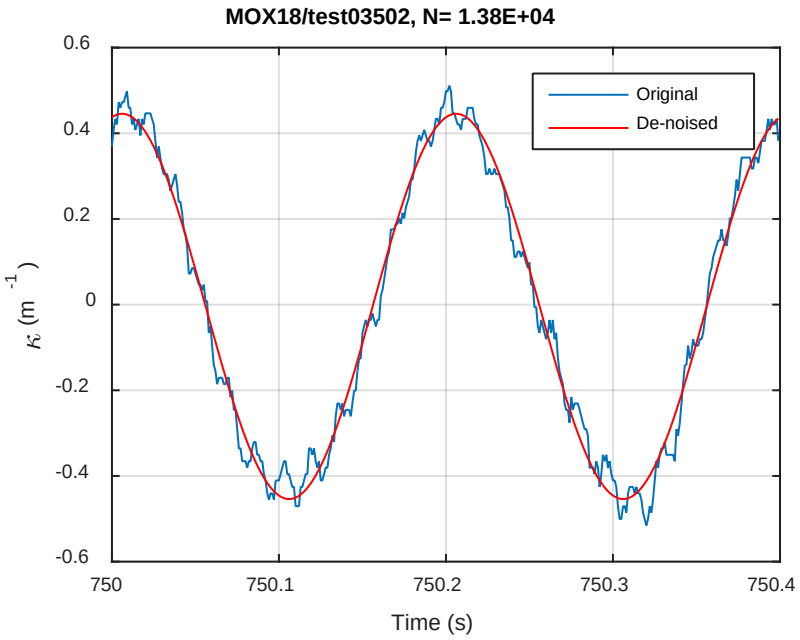

(c)

Fig. E.21 Monitoring-based responses: (a) curvature, (b) moment, (c) curvature, MOX18, 10.16 Nm, Ns = 1.38E+04 cycles.

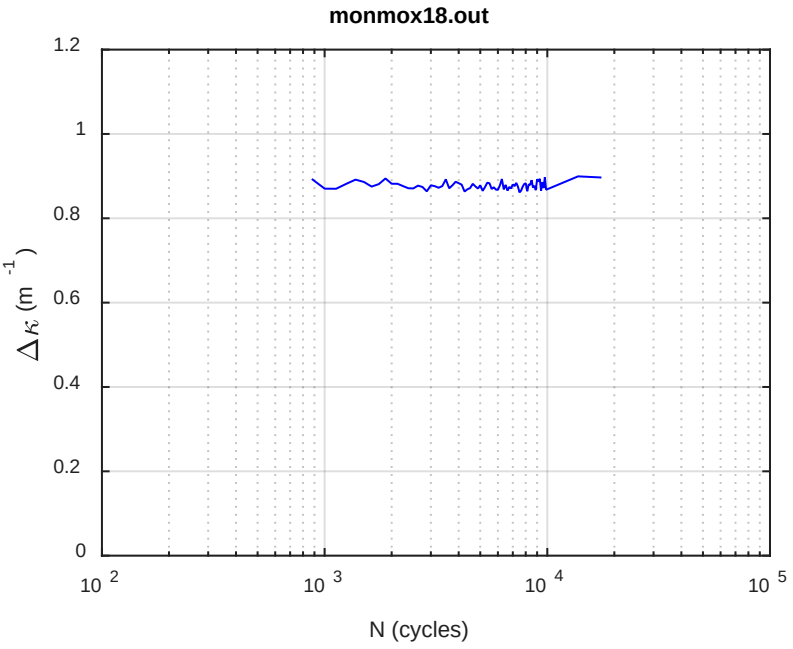
monmox18.out
1.2
1
0.8
0.6
0.4
0.2
0
Δκ (m -1)
10 2
10 3
10 4
10 5
N (cycles)

(a)

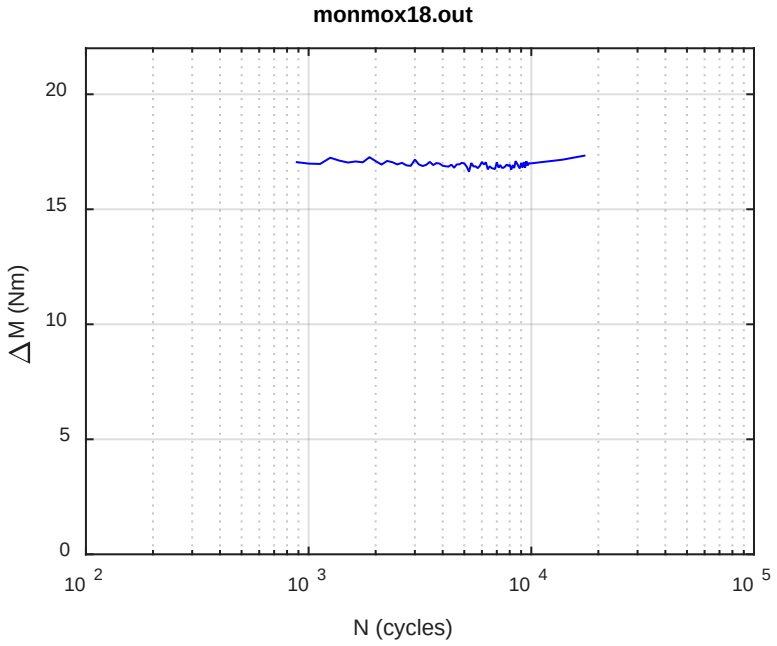
monmox18.out
20
15
10
5
0
ΔM (Nm)
10 2
10 3
10 4
10 5
N (cycles)

(b)

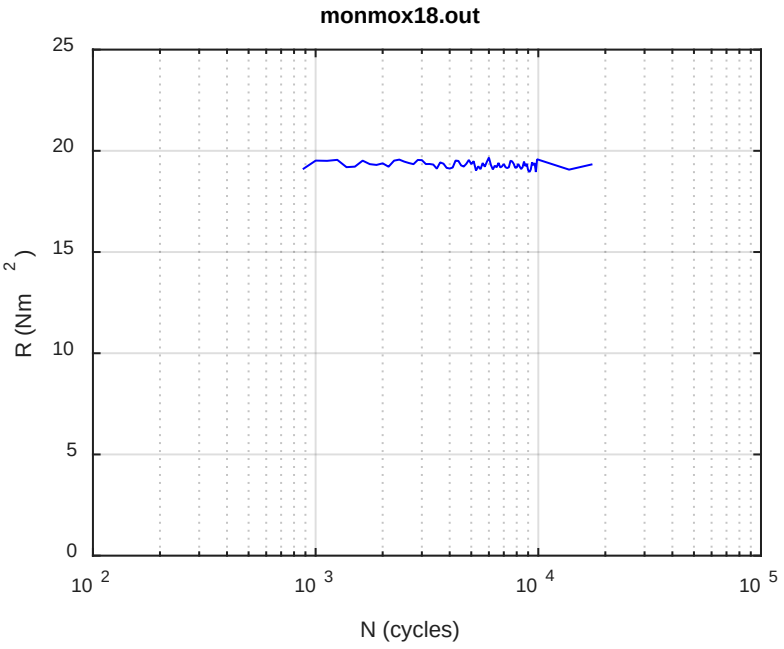
monmox18.out
25
20
15
10
5
0
R (Nm 2)
10 2
10 3
10 4
10 5
N (cycles)

(c)

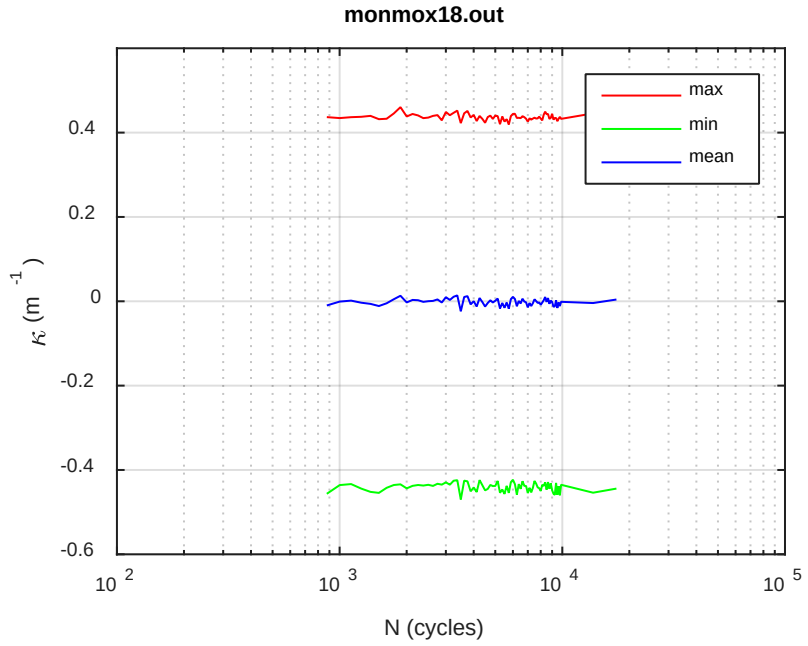
monmox18.out
max
min
mean
0.4
0.2
0
-0.2
-0.4
-0.6
κ (m -1)
10 2
10 3
10 4
10 5
N (cycles)

(d)

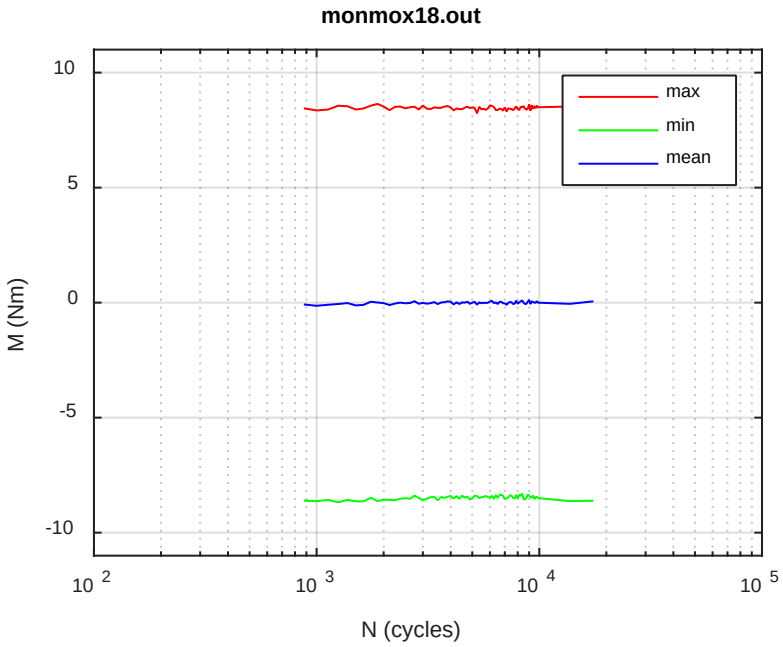

(e)

Fig. E.22 Monitoring-based responses: (a) curvature range, (b) moment range, (c) rigidity, (d) curvature peak/valley, (e) moment peak/valley, MOX18, 10.16 Nm, Nf = 1.95E+04 cycles.

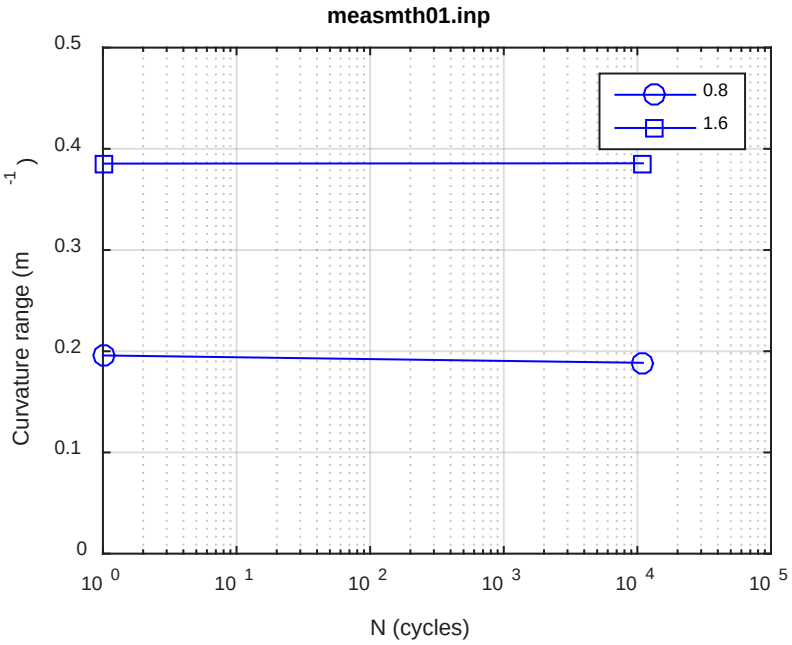
measmth01.inp
0.5
0.4
0.3
0.2
0.1
0
Curvature range (m -1)
0.8
1.6
10 0
10 1
10 2
10 3
10 4
10 5
N (cycles)

(a)

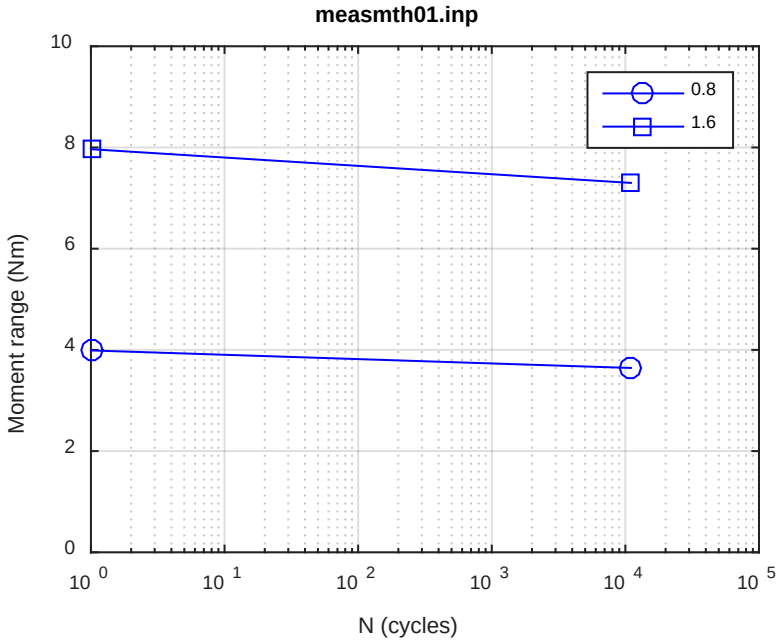
measmth01.inp
10
8
6
4
2
0
Moment range (Nm)
0.8
1.6
10 0
10 1
10 2
10 3
10 4
10 5
N (cycles)

(b)

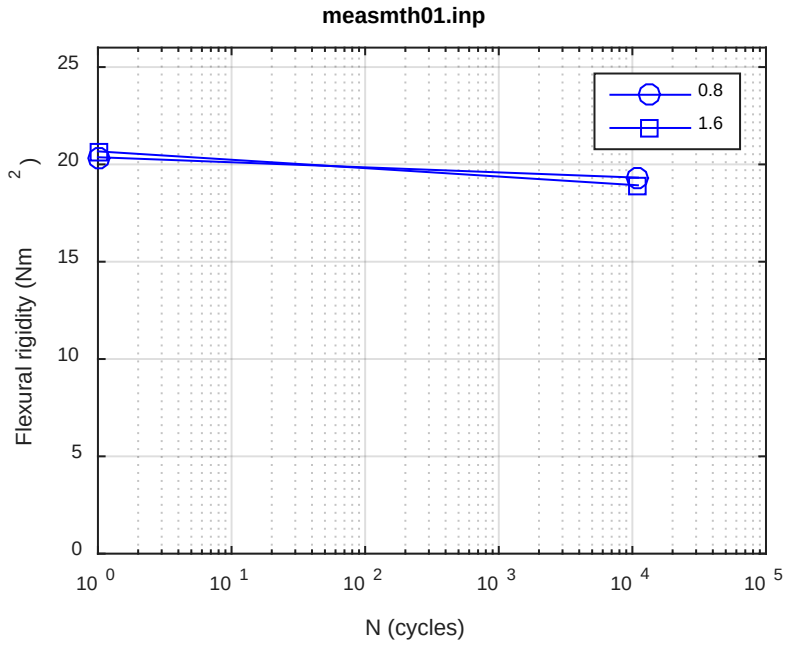
measmth01.inp
0.8
1.6
Flexural rigidity (Nm 2)
N (cycles)
25
20
15
10
5
0
10 0
10 1
10 2
10 3
10 4
10 5

(c)

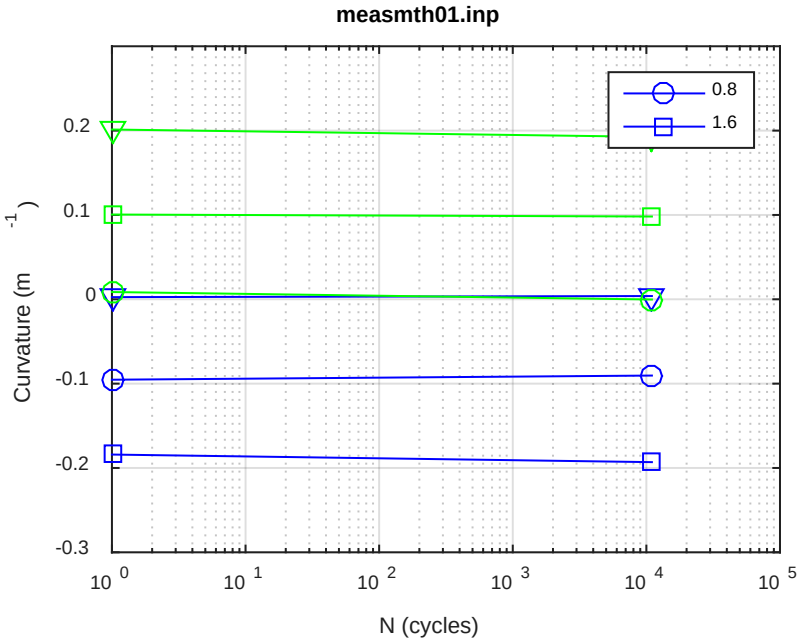
measmth01.inp
0.8
1.6
Curvature (m -1)
N (cycles)
0.2
0.1
0
-0.1
-0.2
-0.3
10 0
10 1
10 2
10 3
10 4
10 5

(d)

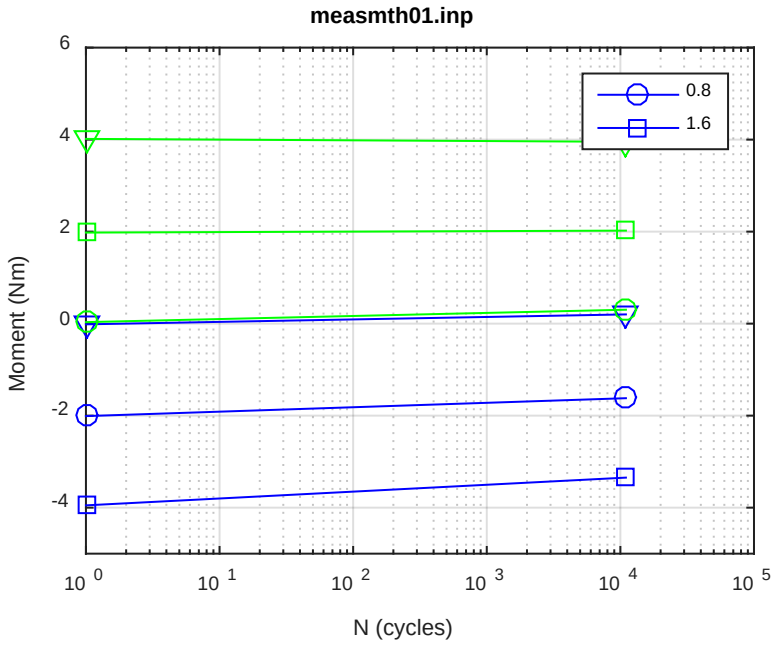

(e)

Fig. E.23 Measurement-based responses: (a) curvature range, (b) moment range, (c) rigidity, (d) curvature peak/valley, (e) moment peak/valley, MTH01, 10.16 Nm.

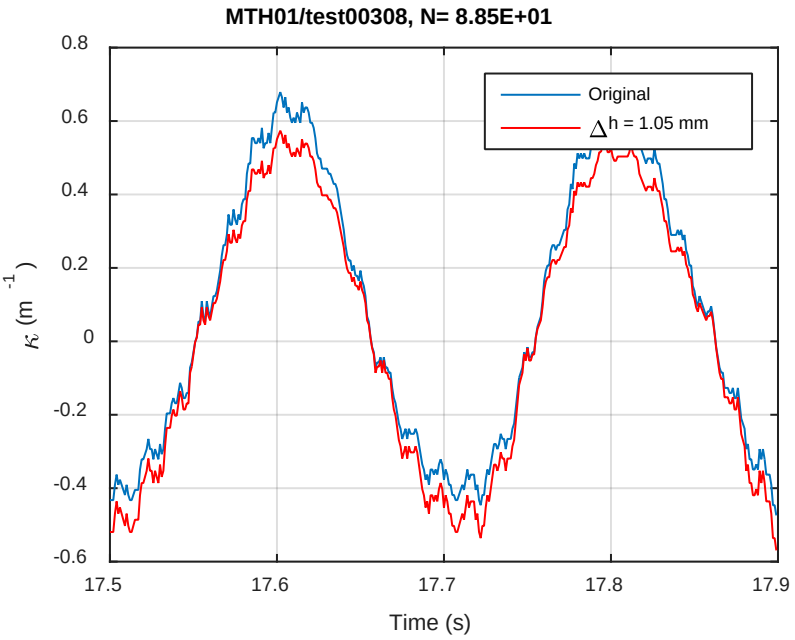
MTH01/test00308, N= 8.85E+01
Original
Δh = 1.05 mm
κ (m -1)
Time (s)
0.8
0.6
0.4
0.2
0
-0.2
-0.4
-0.6
17.5
17.6
17.7
17.8
17.9

(a)

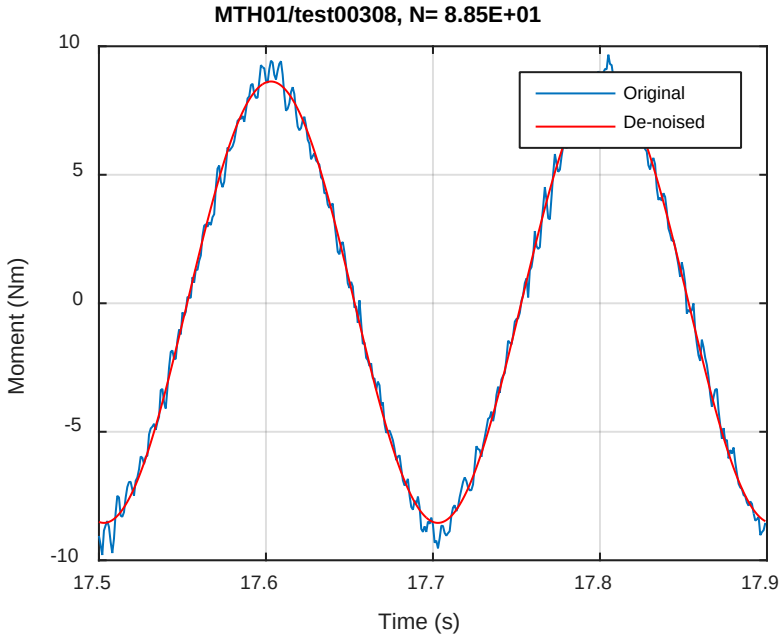
MTH01/test00308, N= 8.85E+01
Original
De-noised
Moment (Nm)
Time (s)
10
5
0
-5
-10
17.5
17.6
17.7
17.8
17.9

(b)

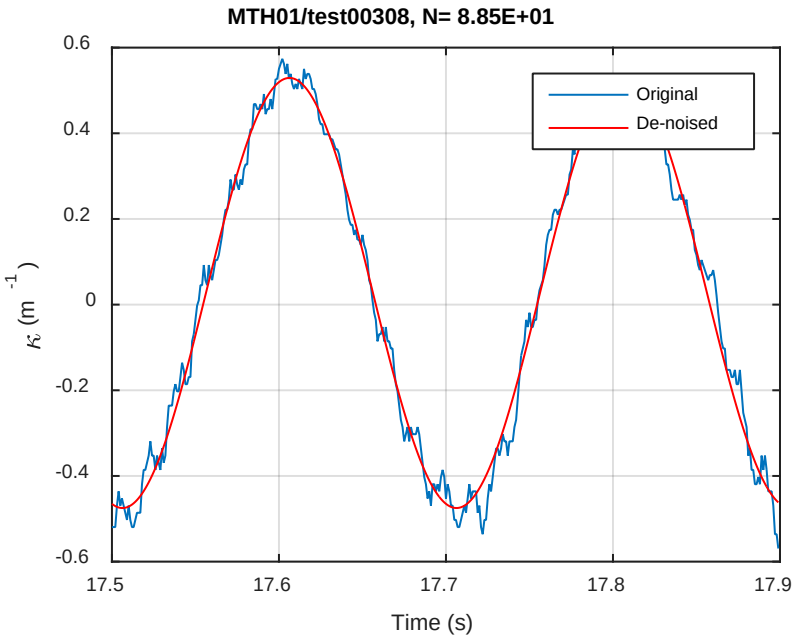

(c)

Fig. E.24 Monitoring-based responses: (a) curvature, (b) moment, (c) curvature, MTH01, 10.16 Nm, Ns = 8.85E+01 cycles.

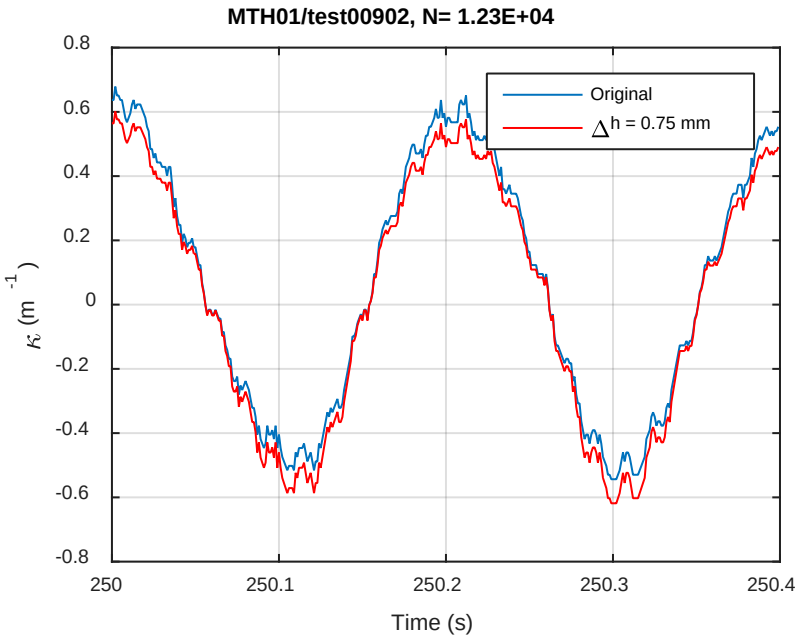
MTH01/test00902, N= 1.23E+04
Original
Δh = 0.75 mm
κ (m-1)
Time (s)
0.8
0.6
0.4
0.2
0
-0.2
-0.4
-0.6
-0.8
250
250.1
250.2
250.3
250.4

(a)

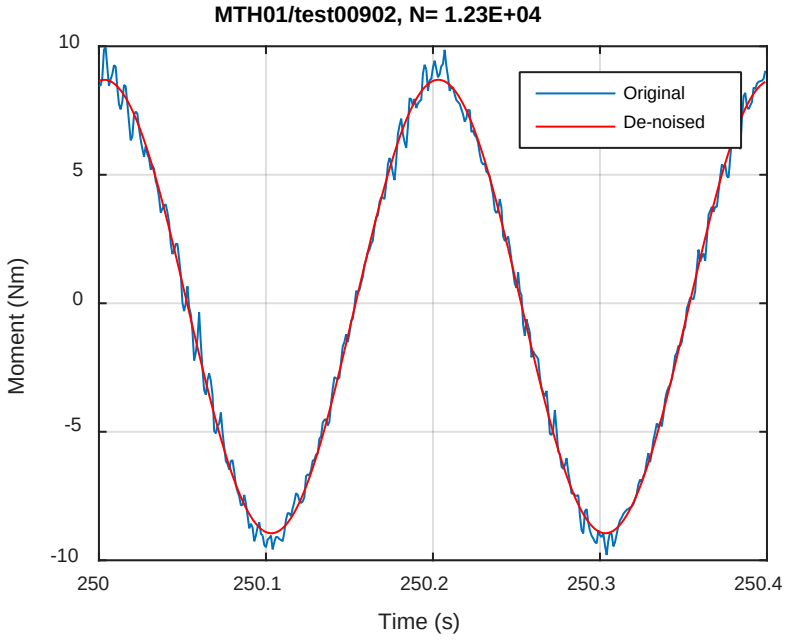
MTH01/test00902, N= 1.23E+04
Original
De-noised
Moment (Nm)
Time (s)
10
5
0
-5
-10
250
250.1
250.2
250.3
250.4

(b)

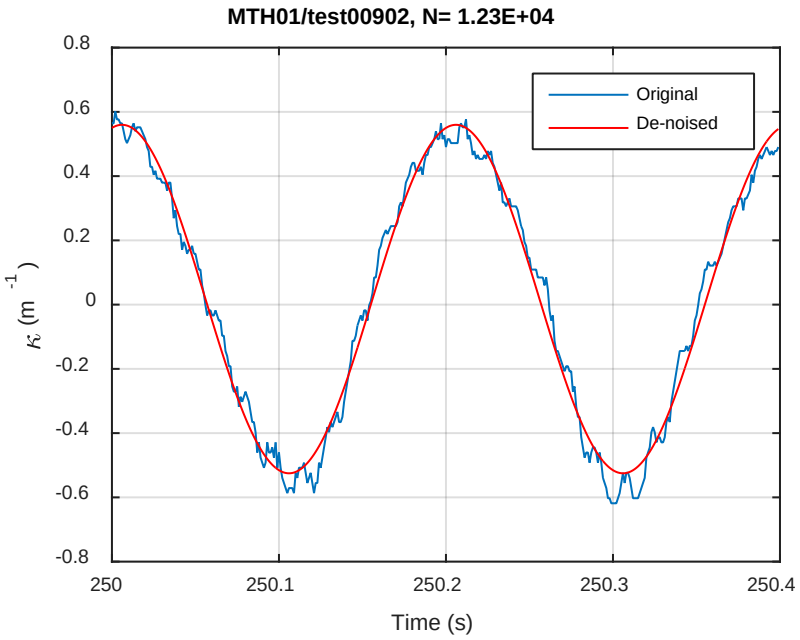

(c)

Fig. E.25 Monitoring-based responses: (a) curvature, (b) moment, (c) curvature, MTH01, 10.16 Nm, Ns = 1.23E+04 cycles.

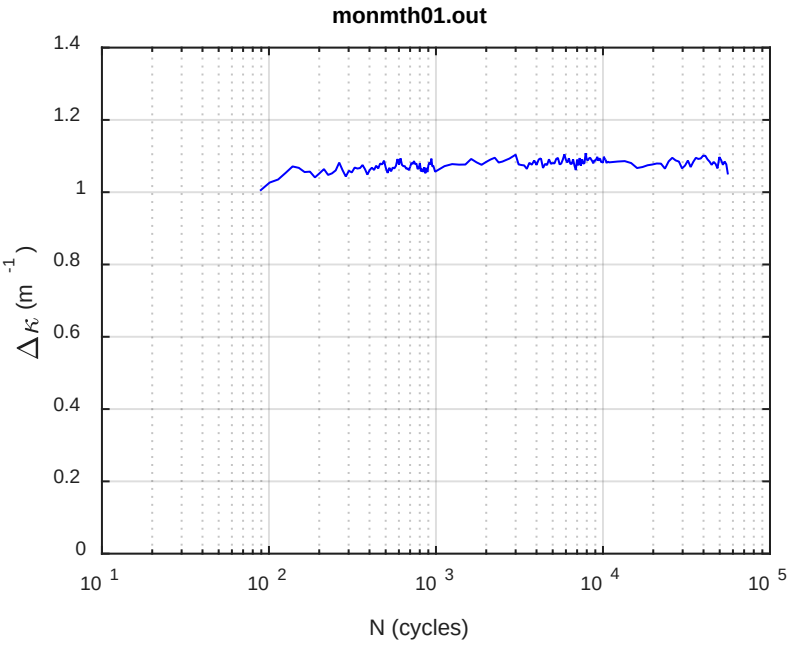
monmth01.out
1.4
1.2
1
0.8
0.6
0.4
0.2
0
Δκ (m -1)
10 1
10 2
10 3
10 4
10 5
N (cycles)

(a)

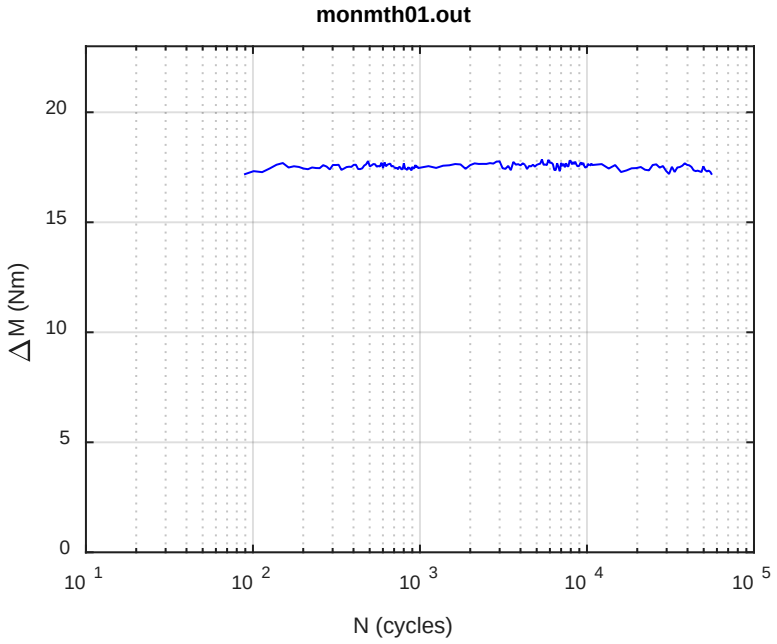
monmth01.out
20
15
10
5
0
ΔM (Nm)
10 1
10 2
10 3
10 4
10 5
N (cycles)

(b)

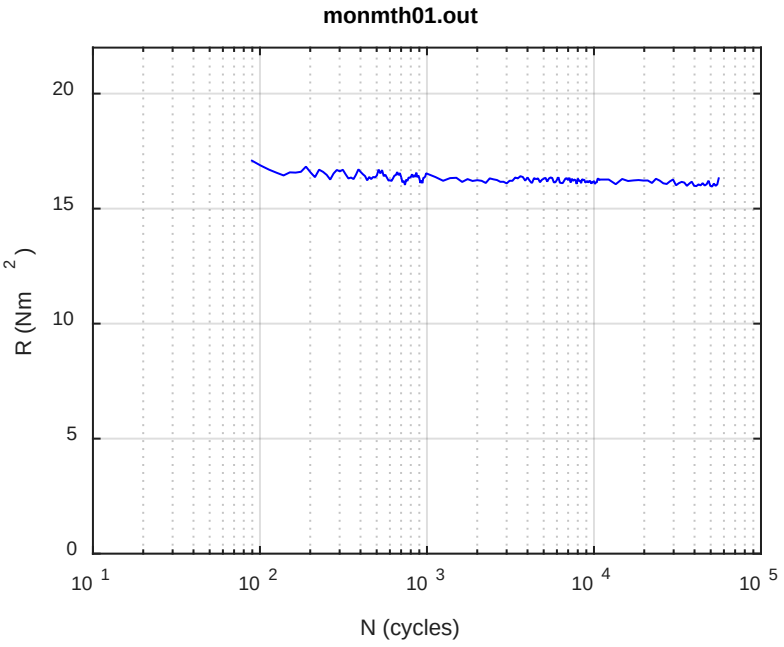
monmth01.out
R (Nm 2)
N (cycles)

(c)

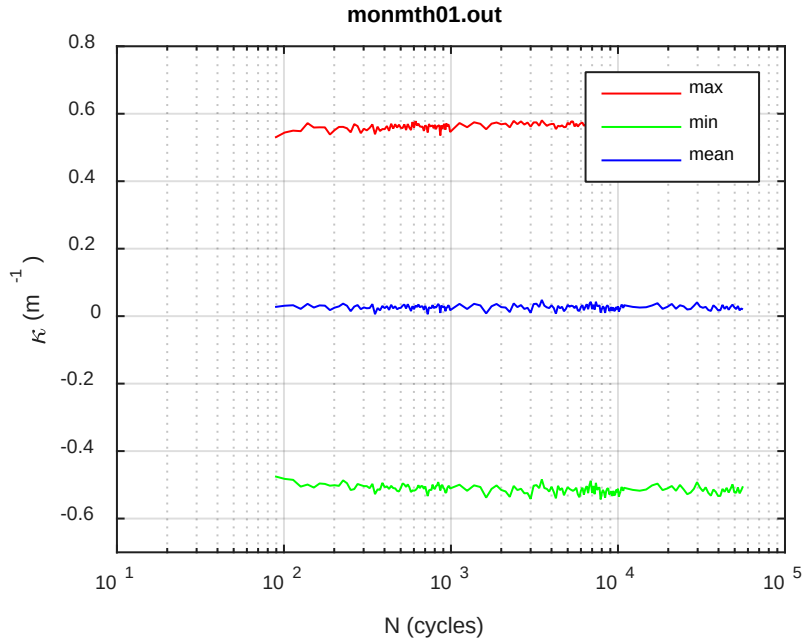
monmth01.out
max
min
mean
κ (m -1)
N (cycles)

(d)

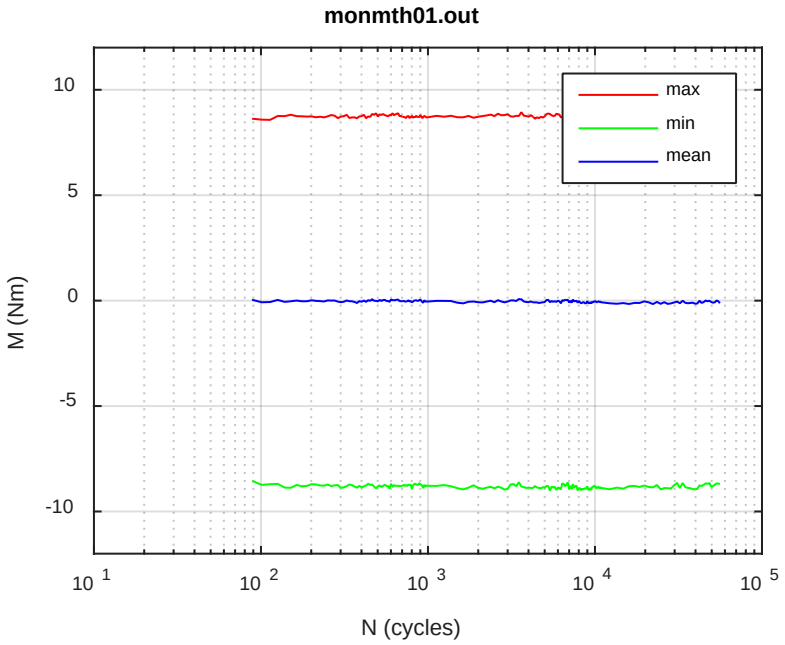

(e)

Fig. E.26 Monitoring-based responses: (a) curvature range, (b) moment range, (c) rigidity, (d) curvature peak/valley, (e) moment peak/valley, MTH01, 10.16 Nm, Nf = 5.70E+04 cycles.

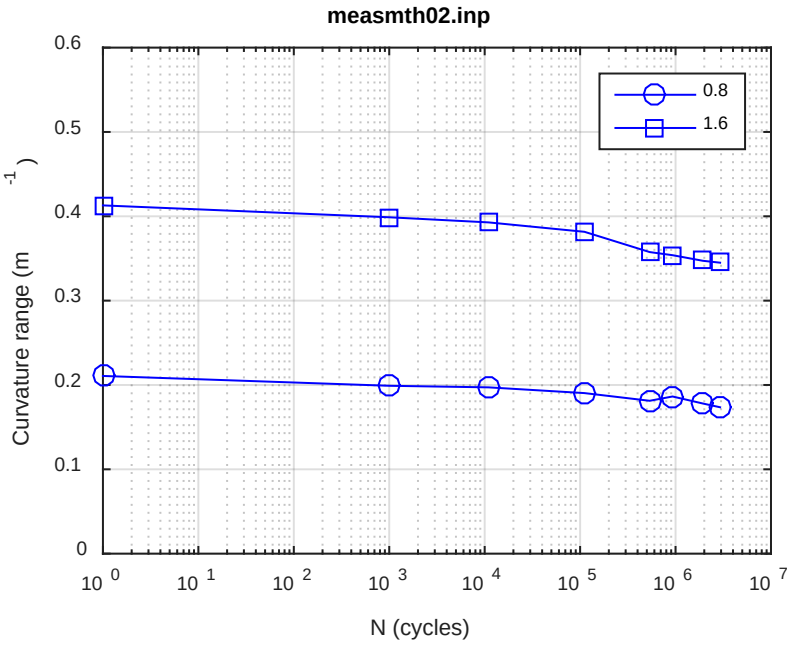
measmth02.inp
Curvature range (m -1)
N (cycles)
0.8
1.6
0
0.1
0.2
0.3
0.4
0.5
0.6
10 0
10 1
10 2
10 3
10 4
10 5
10 6
10 7

(a)

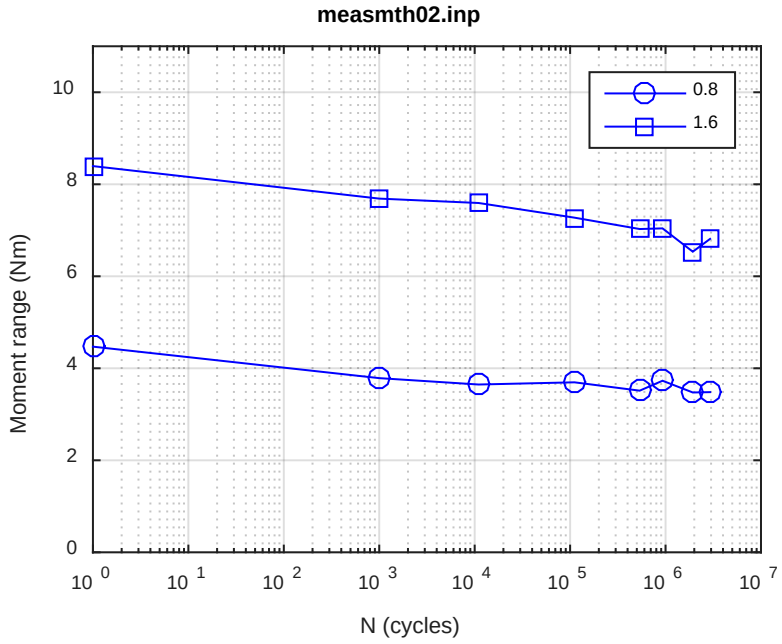
measmth02.inp
Moment range (Nm)
N (cycles)
0.8
1.6
0
2
4
6
8
10
10 0
10 1
10 2
10 3
10 4
10 5
10 6
10 7

(b)

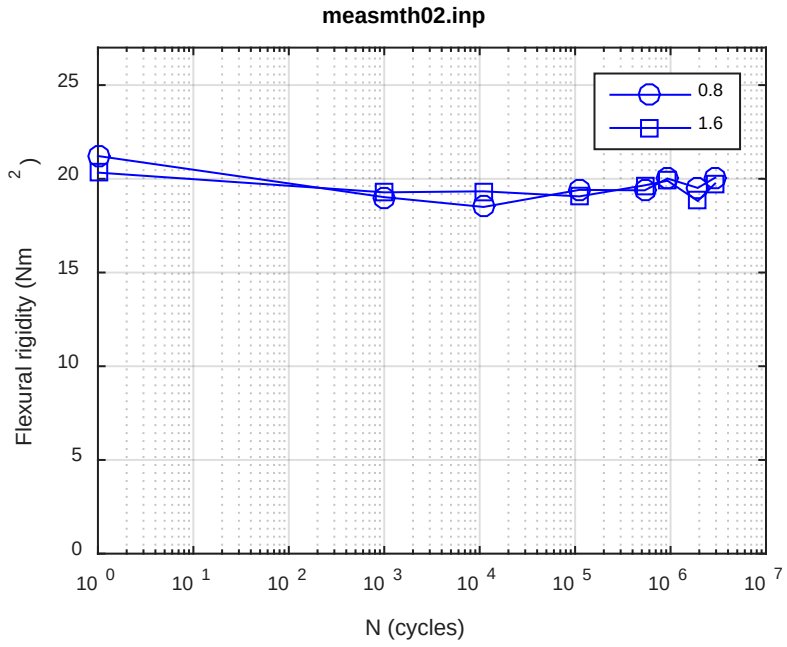
measmth02.inp
0.8
1.6
Flexural rigidity (Nm 2)
25
20
15
10
5
0
10 0
10 1
10 2
10 3
10 4
10 5
10 6
10 7
N (cycles)

(c)

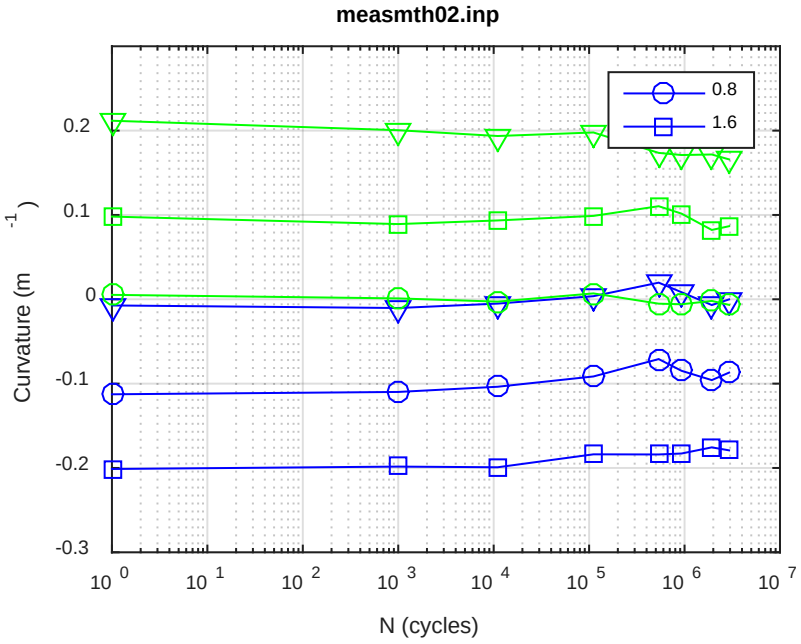
measmth02.inp
0.8
1.6
Curvature (m -1)
0.2
0.1
0
-0.1
-0.2
-0.3
10 0
10 1
10 2
10 3
10 4
10 5
10 6
10 7
N (cycles)

(d)

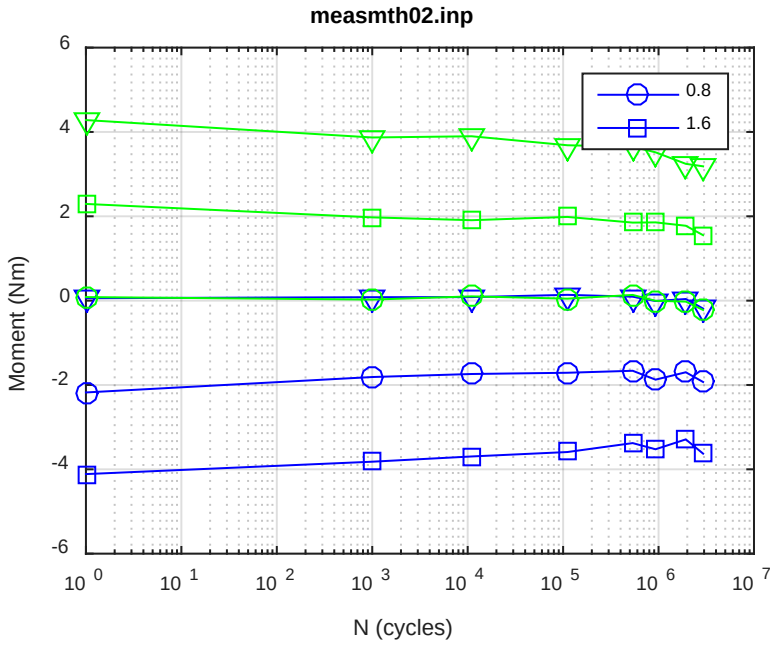

(e)

Fig. E.27 Measurement-based responses: (a) curvature range, (b) moment range, (c) rigidity, (d) curvature peak/valley, (e) moment peak/valley, MTH02, 7.62 Nm.

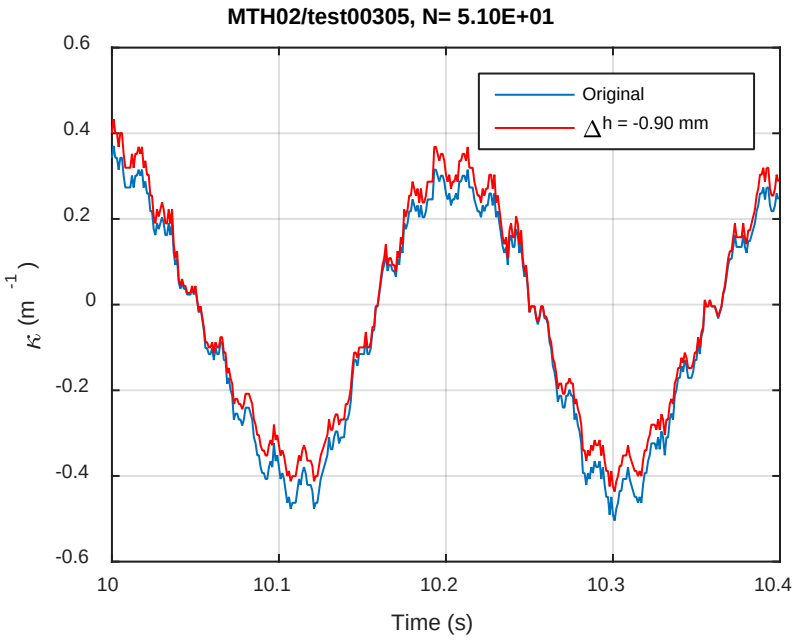
MTH02/test00305, N= 5.10E+01
Original
Δh = -0.90 mm
κ (m-1)
Time (s)
0.6
0.4
0.2
0
-0.2
-0.4
-0.6
10
10.1
10.2
10.3
10.4

(a)

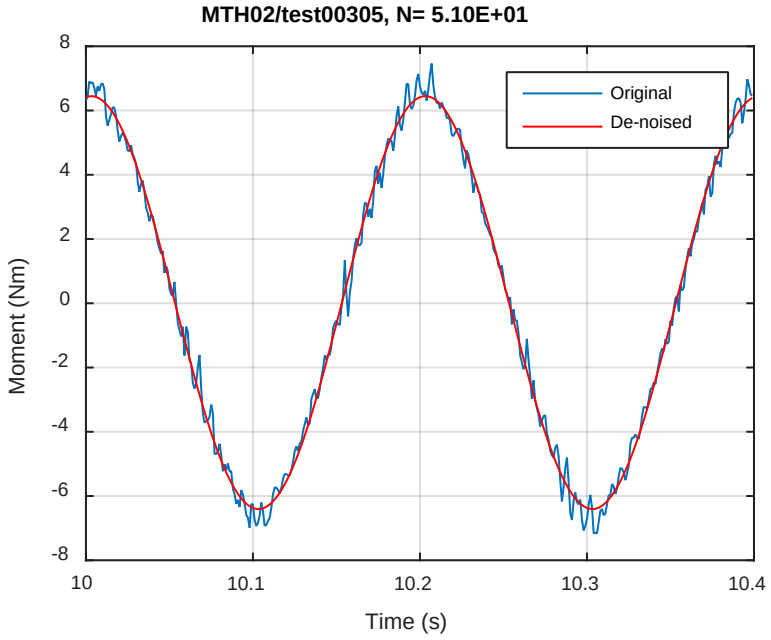
MTH02/test00305, N= 5.10E+01
Original
De-noised
Moment (Nm)
Time (s)
8
6
4
2
0
-2
-4
-6
-8
10
10.1
10.2
10.3
10.4

(b)

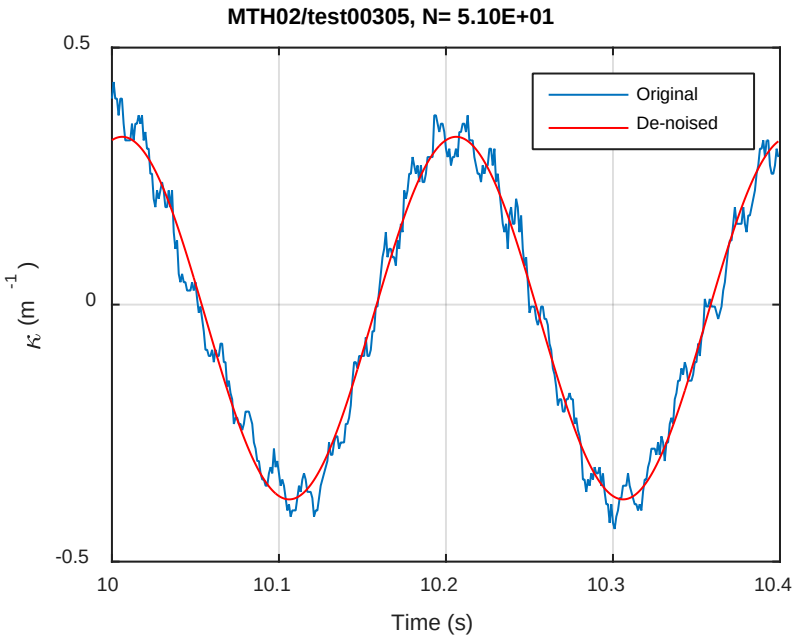

(c)

Fig. E.28 Monitoring-based responses: (a) curvature, (b) moment, (c) curvature, MTH02, 7.62 Nm, Ns = 5.10E+01 cycles.

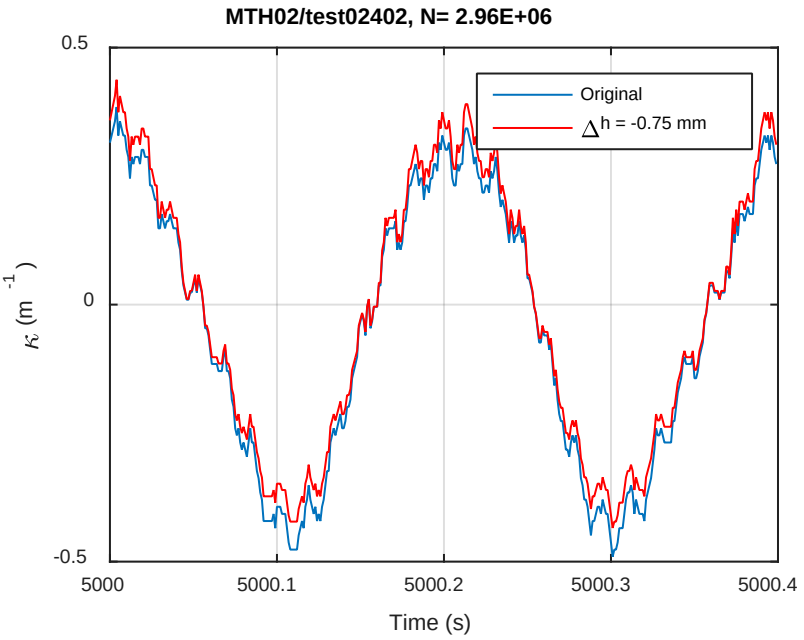
MTH02/test02402, N= 2.96E+06
Original
Δh = -0.75 mm
κ (m-1)
0.5
0
-0.5
5000
5000.1
5000.2
5000.3
5000.4
Time (s)

(a)

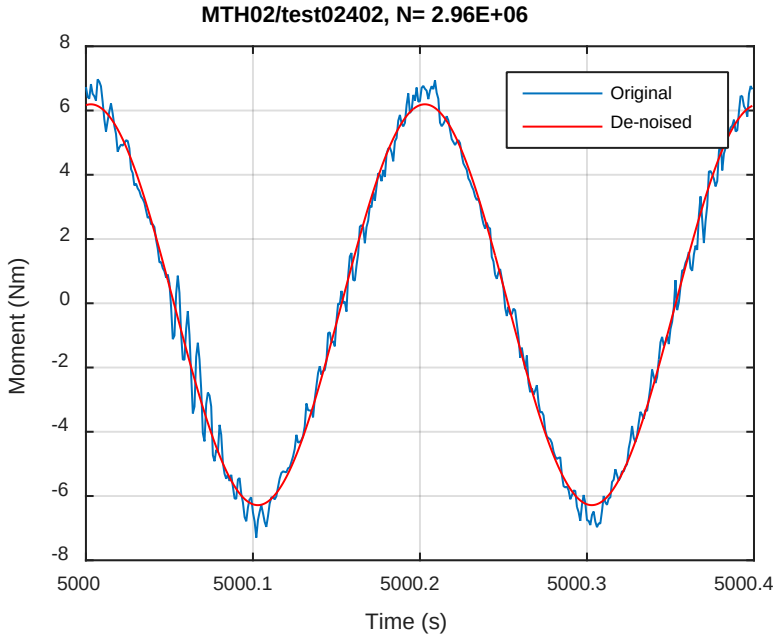
MTH02/test02402, N= 2.96E+06
Original
De-noised
Moment (Nm)
8
6
4
2
0
-2
-4
-6
-8
5000
5000.1
5000.2
5000.3
5000.4
Time (s)

(b)

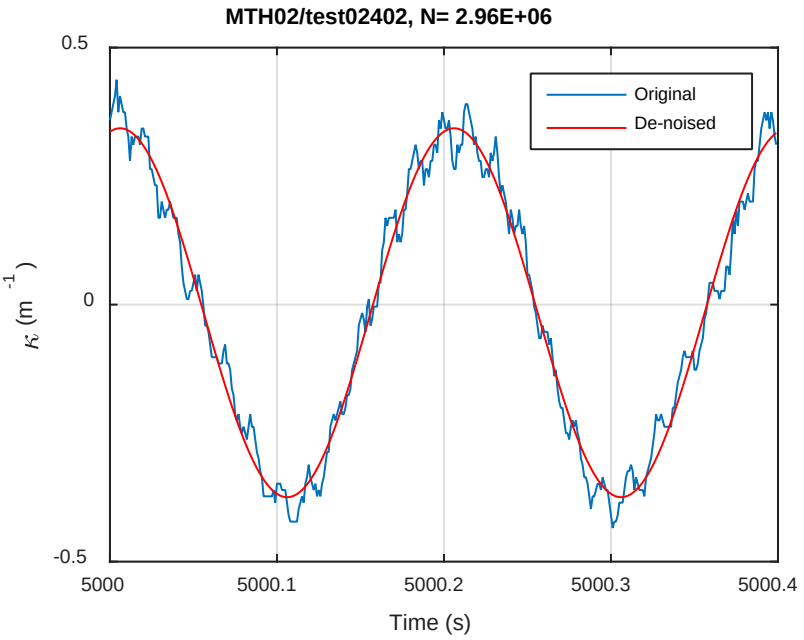

(c)

Fig. E.29 Monitoring-based responses: (a) curvature, (b) moment, (c) curvature, MTH02, 7.62 Nm, Ns = 2.96E+06 cycles.

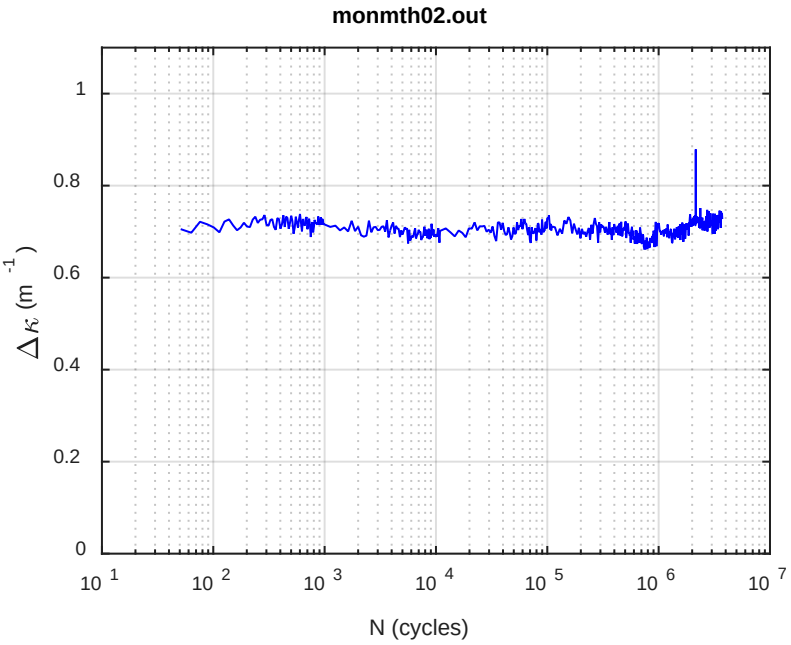
monmth02.out
1
0.8
0.6
0.4
0.2
0
Δκ (m -1)
10 1
10 2
10 3
10 4
10 5
10 6
10 7
N (cycles)

(a)

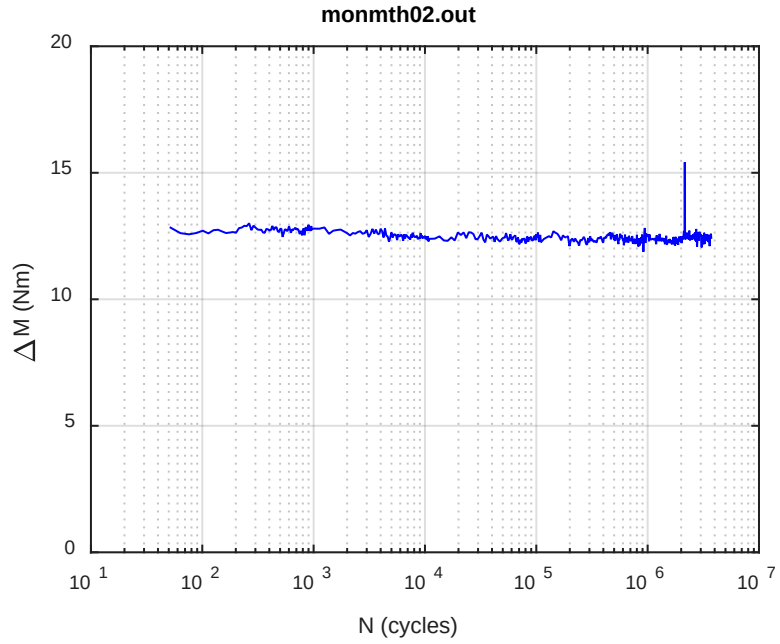
monmth02.out
20
15
10
5
0
ΔM (Nm)
10 1
10 2
10 3
10 4
10 5
10 6
10 7
N (cycles)

(b)

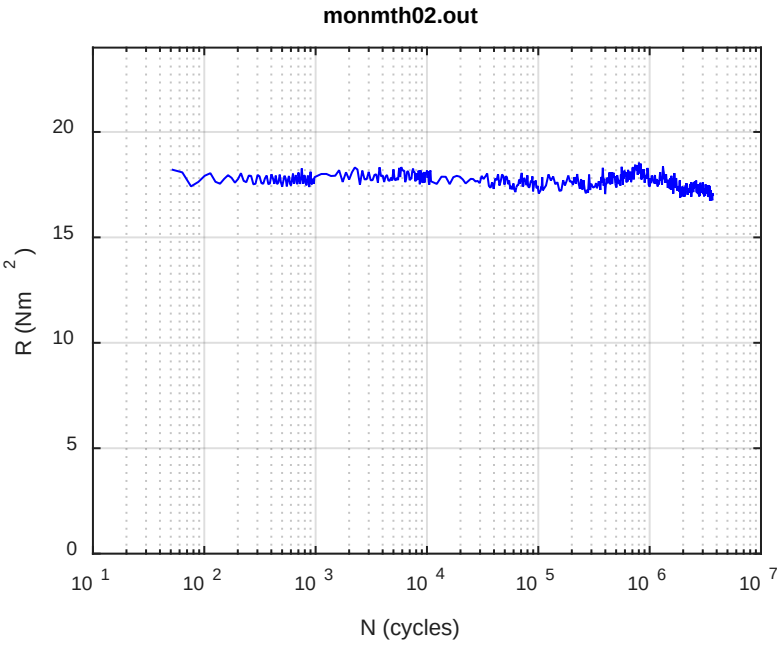
monmth02.out
R (Nm 2)
N (cycles)

(c)

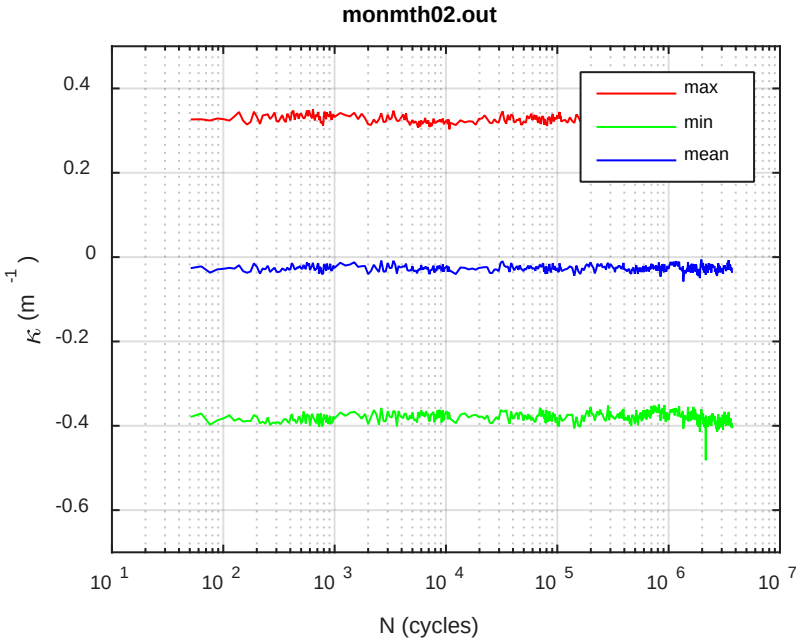
monmth02.out
max
min
mean
κ (m -1)
N (cycles)

(d)

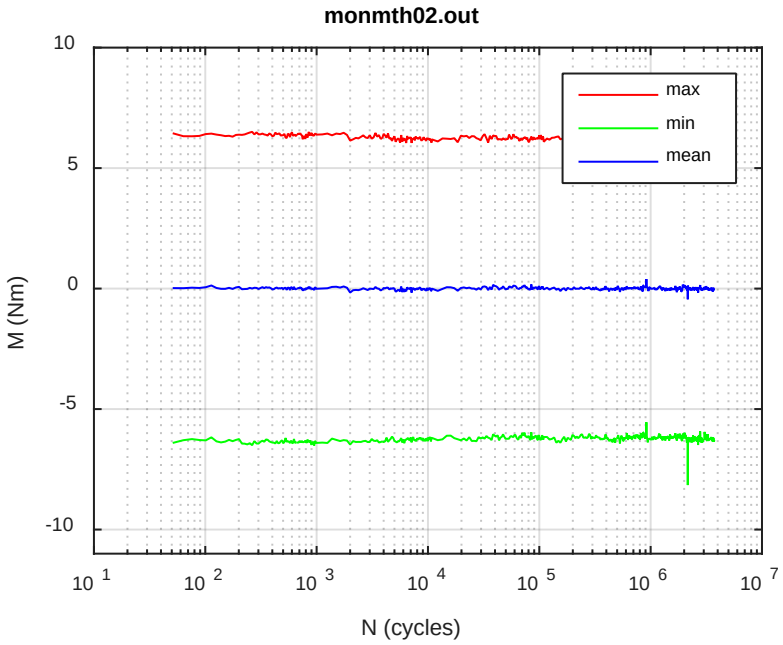

(e)

Fig. E.30 Monitoring-based responses: (a) curvature range, (b) moment range, (c) rigidity, (d) curvature peak/valley, (e) moment peak/valley, MTH02, 7.62 Nm, Nf = 3.75E+06 cycles.

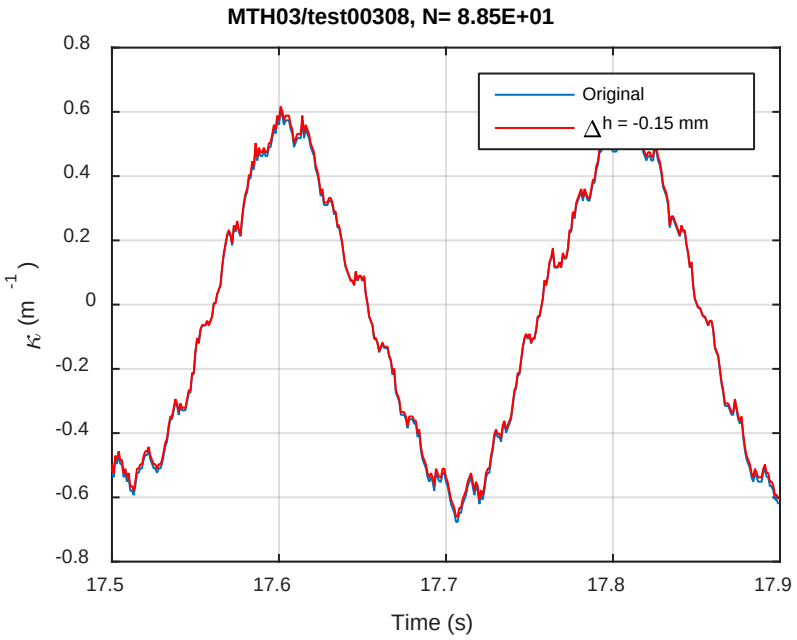
MTH03/test00308, N= 8.85E+01
Original
Δh = -0.15 mm
κ (m -1)
Time (s)
0.8
0.6
0.4
0.2
0
-0.2
-0.4
-0.6
-0.8
17.5
17.6
17.7
17.8
17.9

(a)

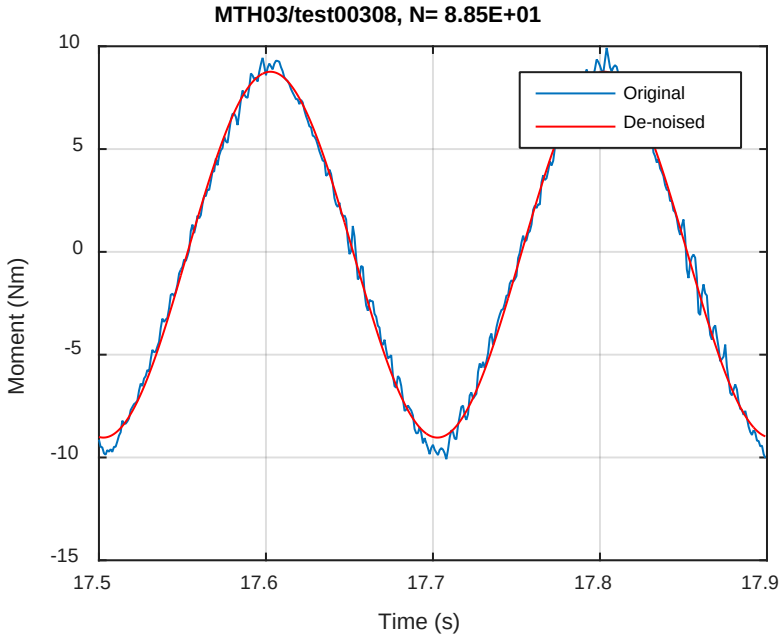
MTH03/test00308, N= 8.85E+01
Original
De-noised
Moment (Nm)
Time (s)
10
5
0
-5
-10
-15
17.5
17.6
17.7
17.8
17.9

(b)

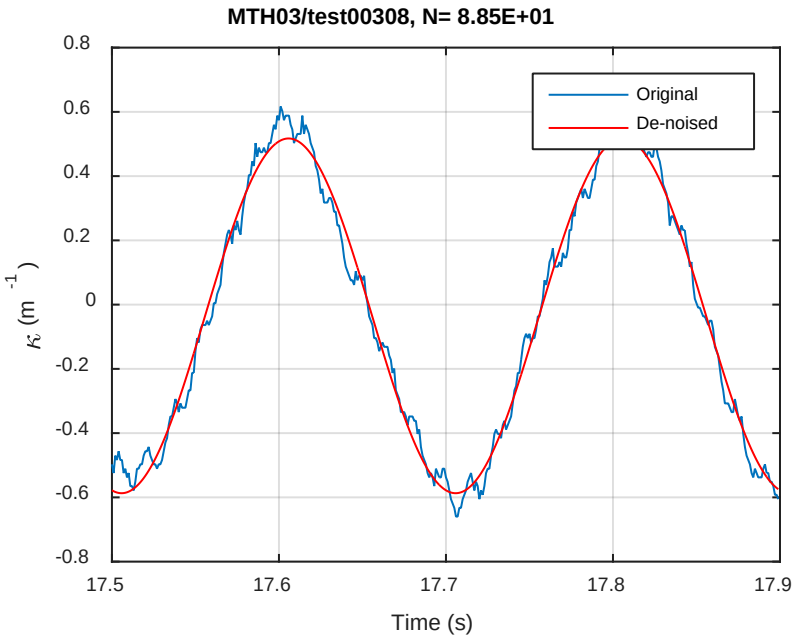

(c)

Fig. E.31 Monitoring-based responses: (a) curvature, (b) moment, (c) curvature, MTH03, 12.70 Nm, Ns = 8.85E+01 cycles.

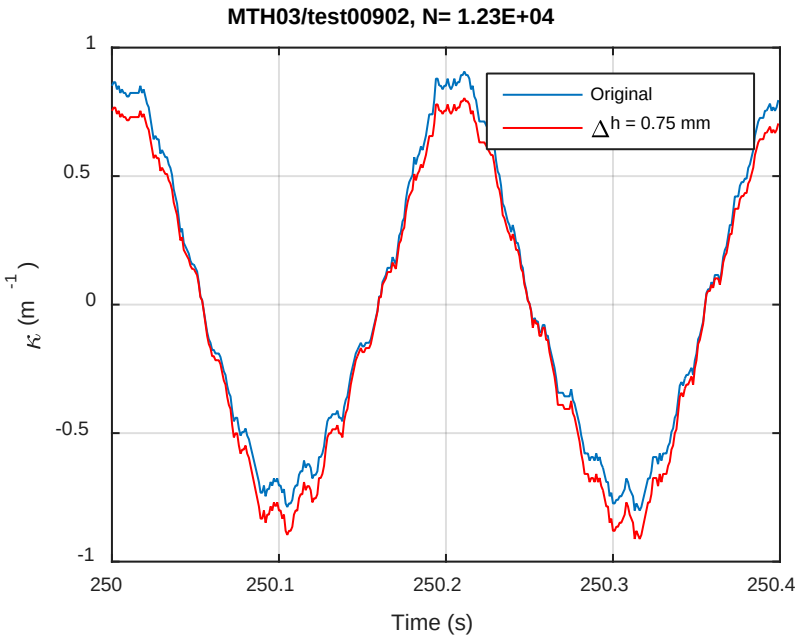
MTH03/test00902, N= 1.23E+04
Original
Δh = 0.75 mm
κ (m-1)
Time (s)
1
0.5
0
-0.5
-1
250
250.1
250.2
250.3
250.4

(a)

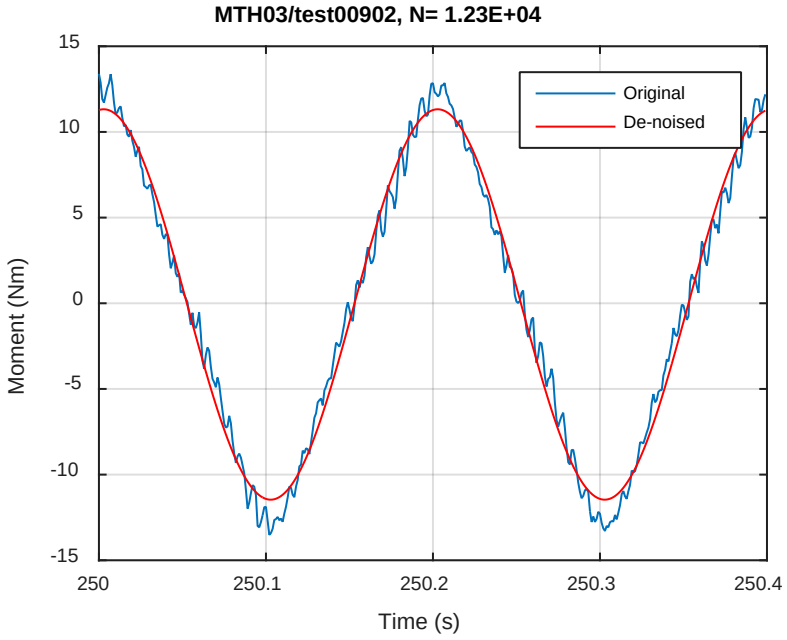
MTH03/test00902, N= 1.23E+04
Original
De-noised
Moment (Nm)
Time (s)
15
10
5
0
-5
-10
-15
250
250.1
250.2
250.3
250.4

(b)

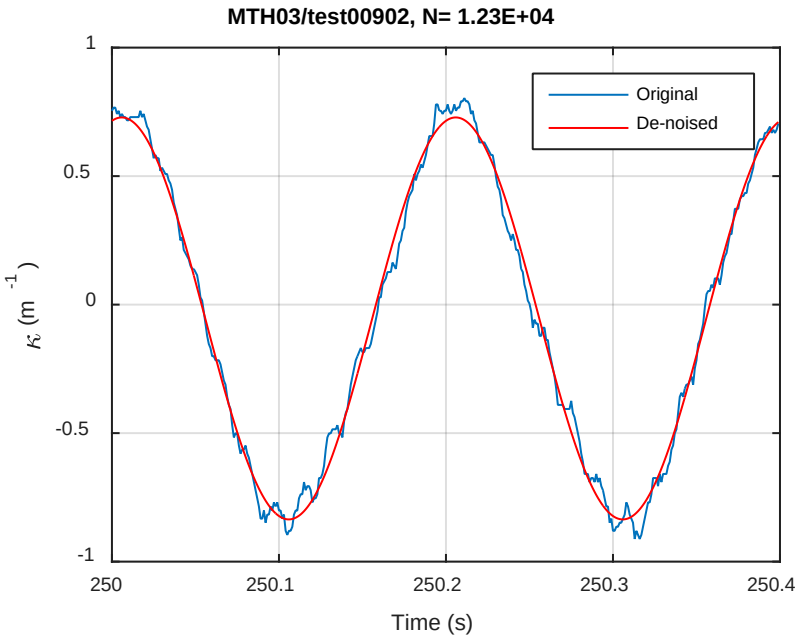

(c)

Fig. E.32 Monitoring-based responses: (a) curvature, (b) moment, (c) curvature, MTH03, 12.70 Nm, Ns = 1.23E+04 cycles.

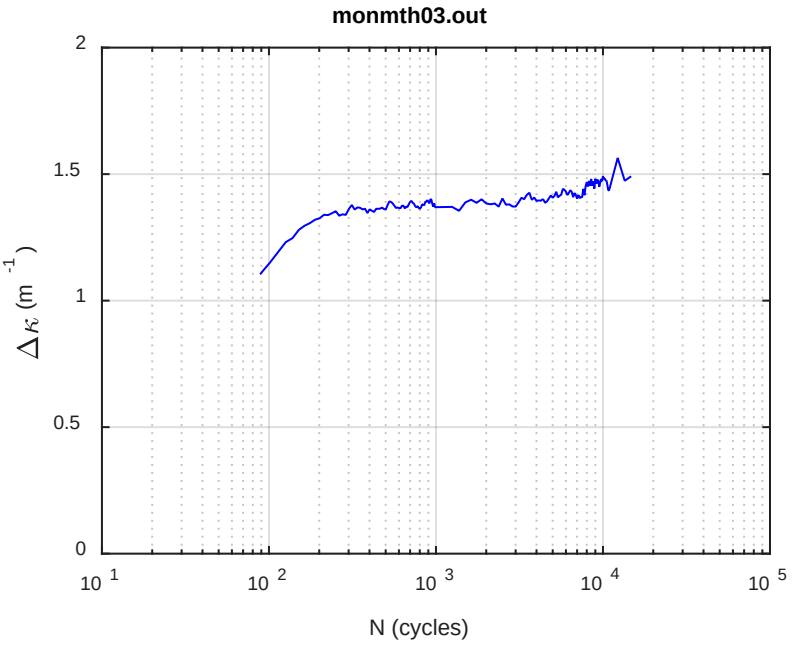
monmth03.out
2
1.5
1
0.5
0
Δκ (m -1)
10 1
10 2
10 3
10 4
10 5
N (cycles)

(a)

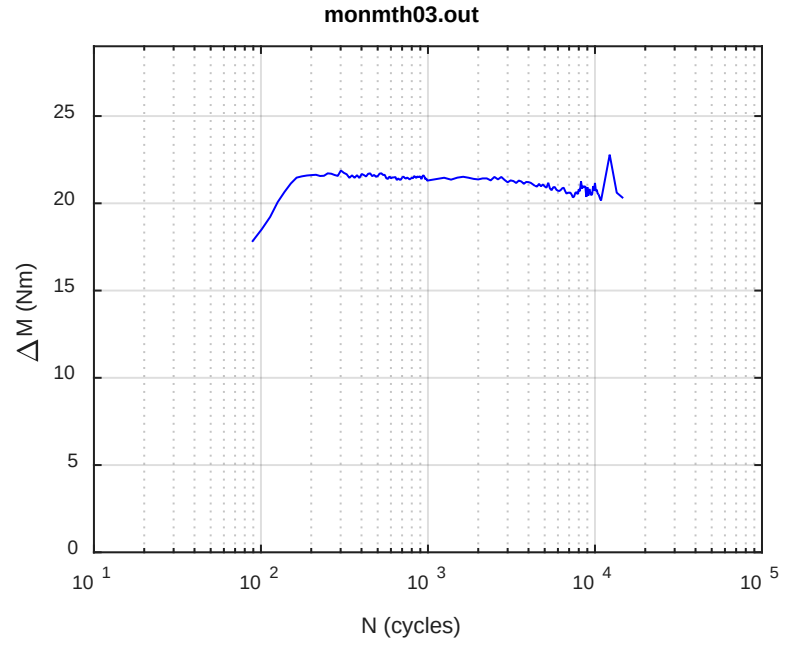
monmth03.out
25
20
15
10
5
0
ΔM (Nm)
10 1
10 2
10 3
10 4
10 5
N (cycles)

(b)

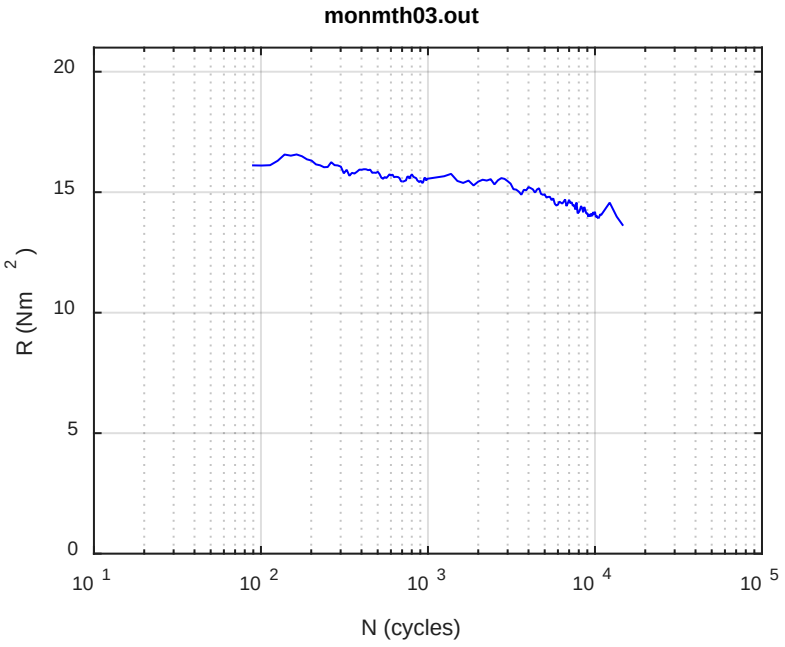
monmth03.out
20
15
10
5
0
R (Nm 2)
10 1
10 2
10 3
10 4
10 5
N (cycles)

(c)

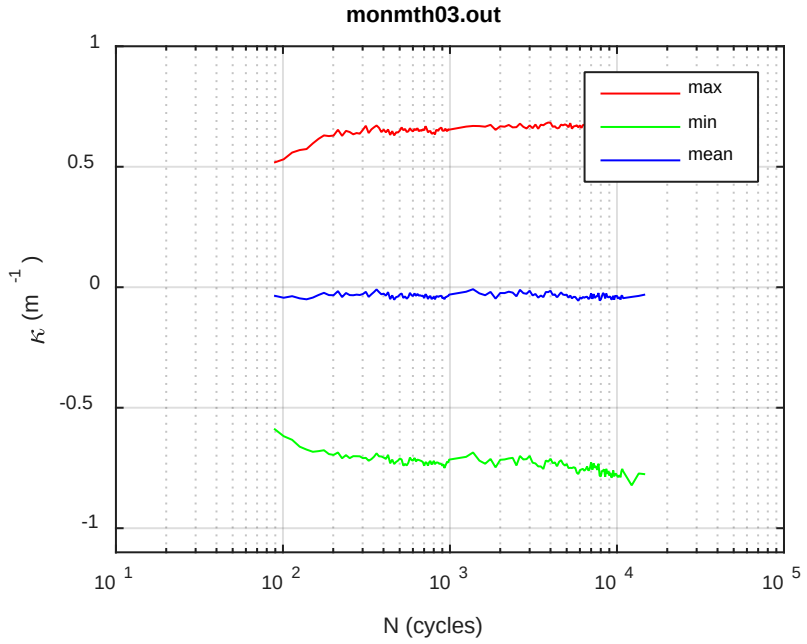
monmth03.out
1
0.5
0
-0.5
-1
κ (m -1)
max
min
mean
10 1
10 2
10 3
10 4
10 5
N (cycles)

(d)

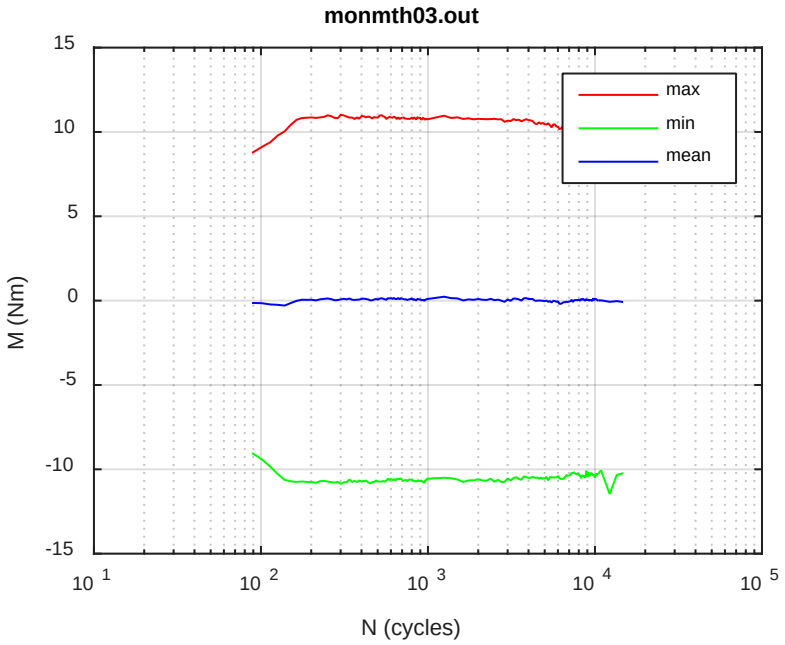

(e)

Fig. E.33 Monitoring-based responses: (a) curvature range, (b) moment range, (c) rigidity, (d) curvature peak/valley, (e) moment peak/valley, MTH03, 12.70 Nm, Nf = 1.51E+04 cycles.

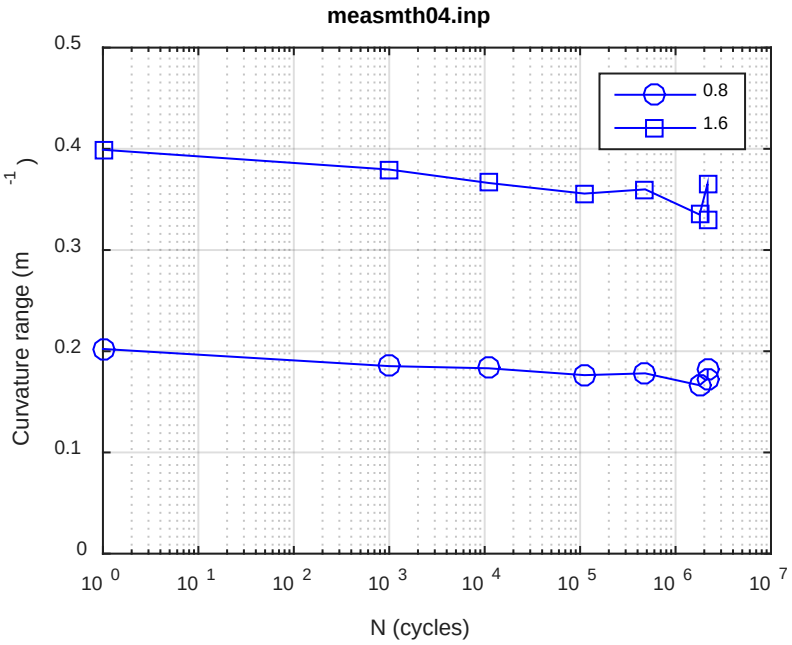
measmth04.inp
0.8
1.6
Curvature range (m -1)
N (cycles)
0
0.1
0.2
0.3
0.4
0.5
10 0
10 1
10 2
10 3
10 4
10 5
10 6
10 7

(a)

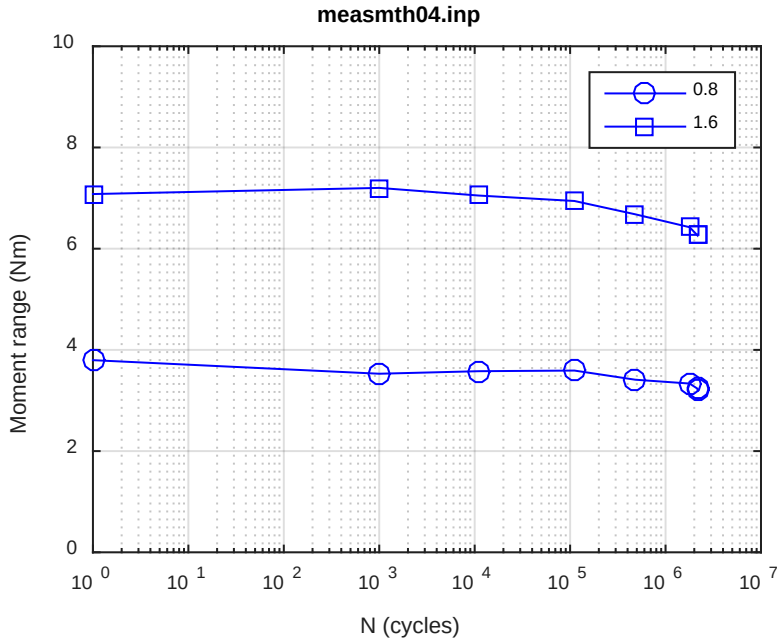
measmth04.inp
0.8
1.6
Moment range (Nm)
N (cycles)
0
2
4
6
8
10
10 0
10 1
10 2
10 3
10 4
10 5
10 6
10 7

(b)

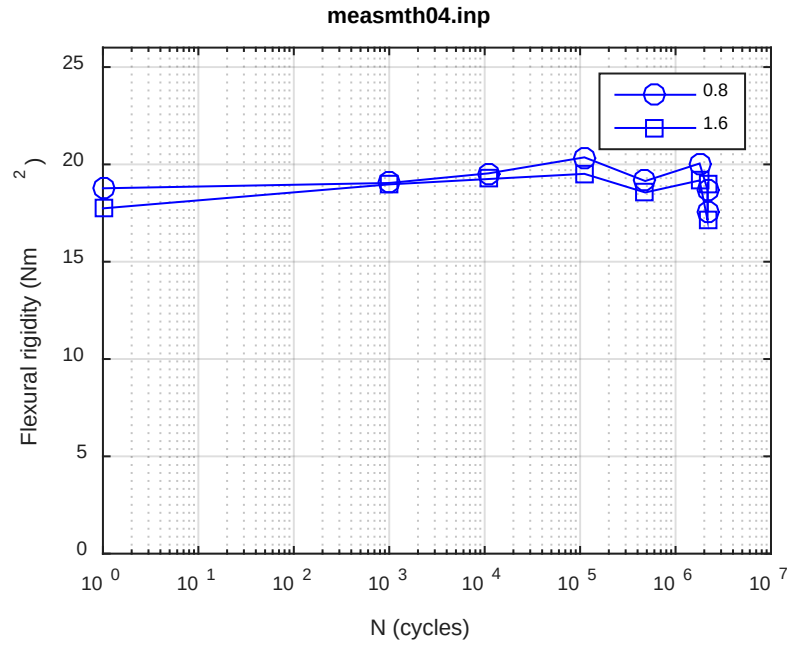
measmth04.inp
Flexural rigidity (Nm 2)
N (cycles)
0.8
1.6
25
20
15
10
5
0
10 0
10 1
10 2
10 3
10 4
10 5
10 6
10 7

(c)

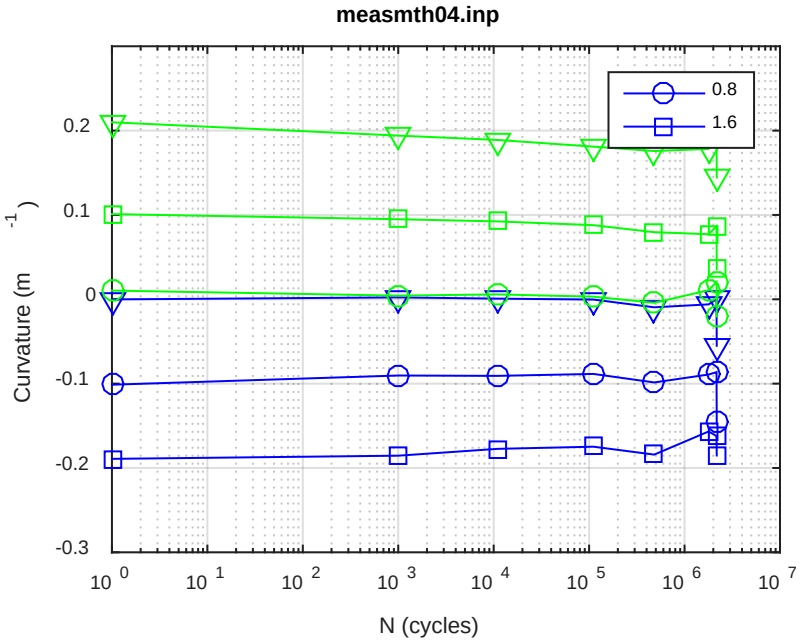
measmth04.inp
Curvature (m -1)
N (cycles)
0.8
1.6
0.2
0.1
0
-0.1
-0.2
-0.3
10 0
10 1
10 2
10 3
10 4
10 5
10 6
10 7

(d)

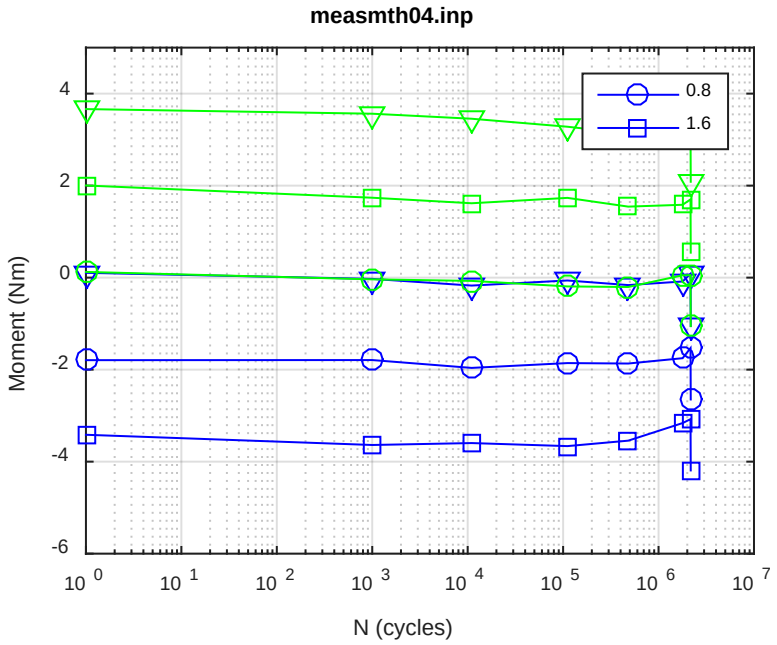

(e)

Fig. E.34 Measurement-based responses: (a) curvature range, (b) moment range, (c) rigidity, (d) curvature peak/valley, (e) moment peak/valley, MTH04, 7.62 Nm.

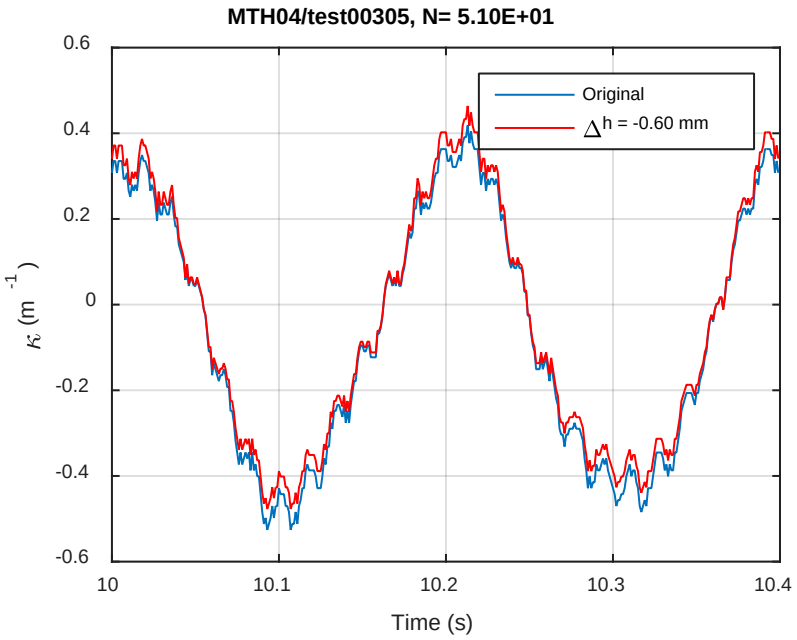
MTH04/test00305, N= 5.10E+01
Original
Δh = -0.60 mm
κ (m-1)
Time (s)
0.6
0.4
0.2
0
-0.2
-0.4
-0.6
10
10.1
10.2
10.3
10.4

(a)

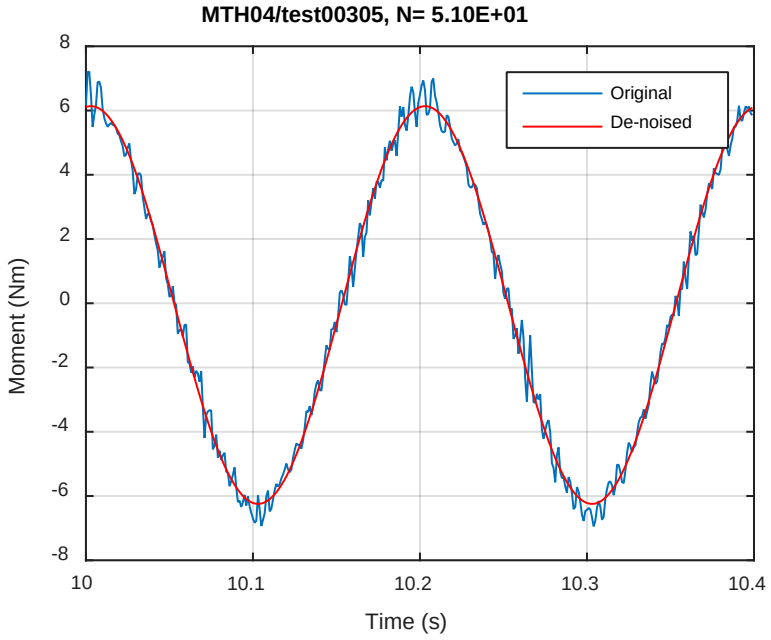
MTH04/test00305, N= 5.10E+01
Original
De-noised
Moment (Nm)
Time (s)
8
6
4
2
0
-2
-4
-6
-8
10
10.1
10.2
10.3
10.4

(b)

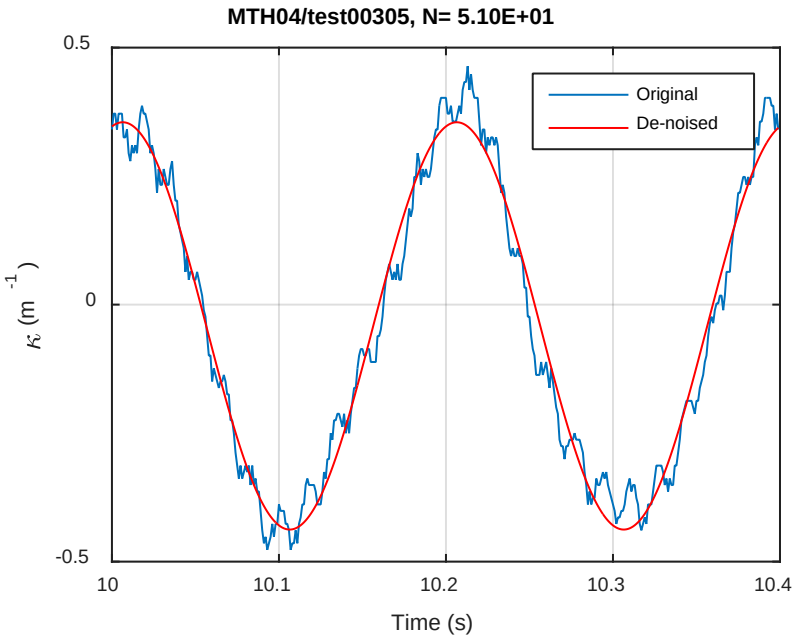

(c)

Fig. E.35 Monitoring-based responses: (a) curvature, (b) moment, (c) curvature, MTH04, 7.62 Nm, Ns = 5.10E+01 cycles.

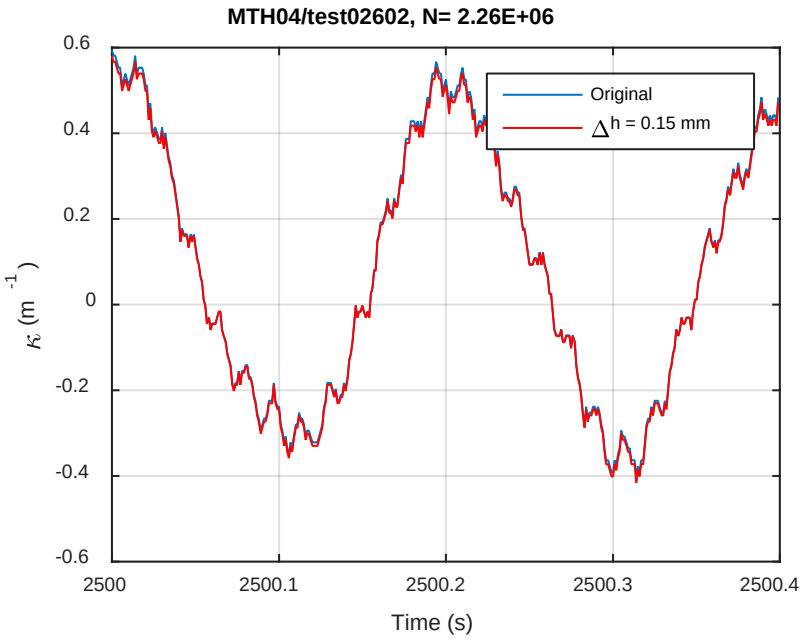
MTH04/test02602, N= 2.26E+06
Original
Δh = 0.15 mm
κ (m-1)
Time (s)
0.6
0.4
0.2
0
-0.2
-0.4
-0.6
2500
2500.1
2500.2
2500.3
2500.4

(a)

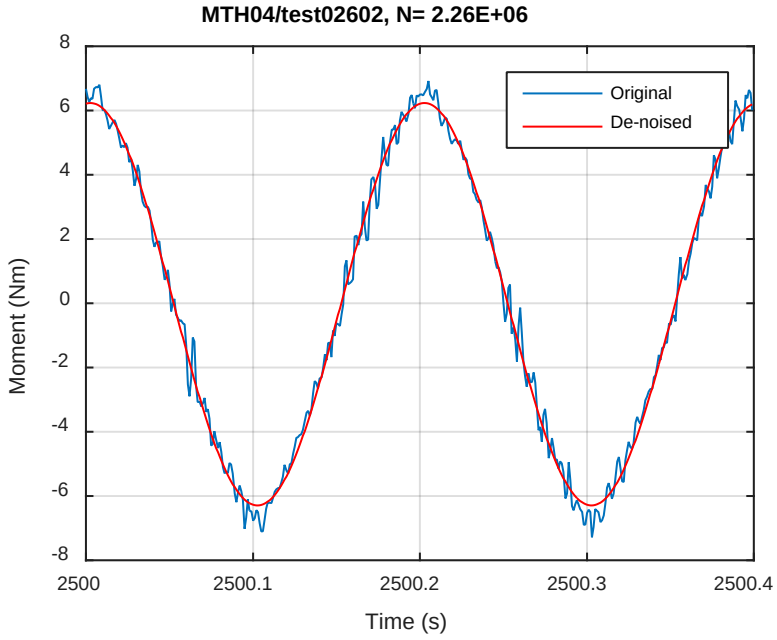
MTH04/test02602, N= 2.26E+06
Original
De-noised
Moment (Nm)
Time (s)
8
6
4
2
0
-2
-4
-6
-8
2500
2500.1
2500.2
2500.3
2500.4

(b)

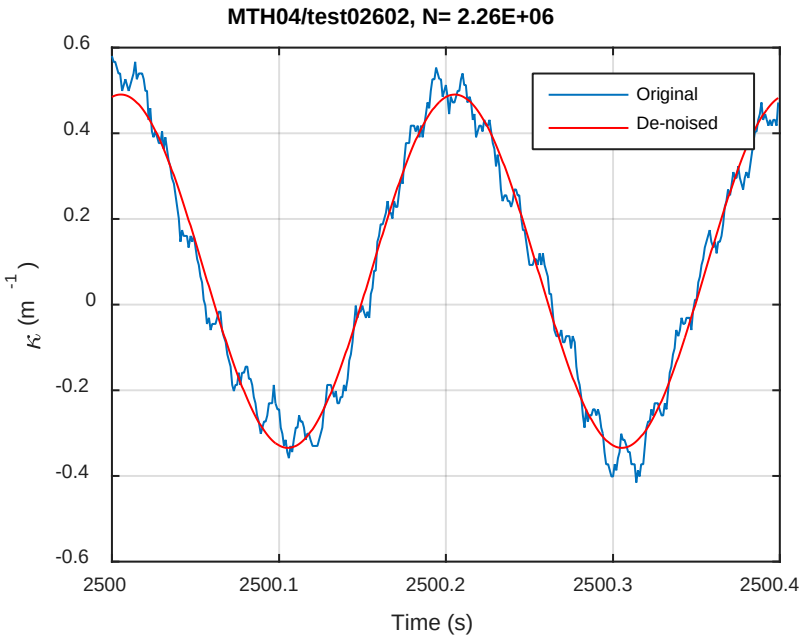

(c)

Fig. E.36 Monitoring-based responses: (a) curvature, (b) moment, (c) curvature, MTH04, 7.62 Nm, Ns = 2.26E+06 cycles.

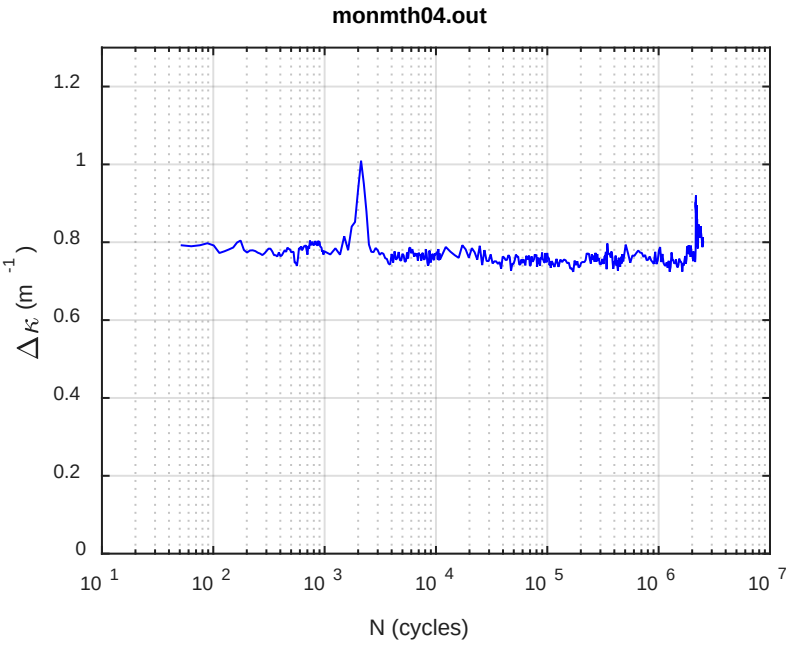
monmth04.out
1.2
1
0.8
0.6
0.4
0.2
0
Δκ (m -1)
10 1
10 2
10 3
10 4
10 5
10 6
10 7
N (cycles)

(a)

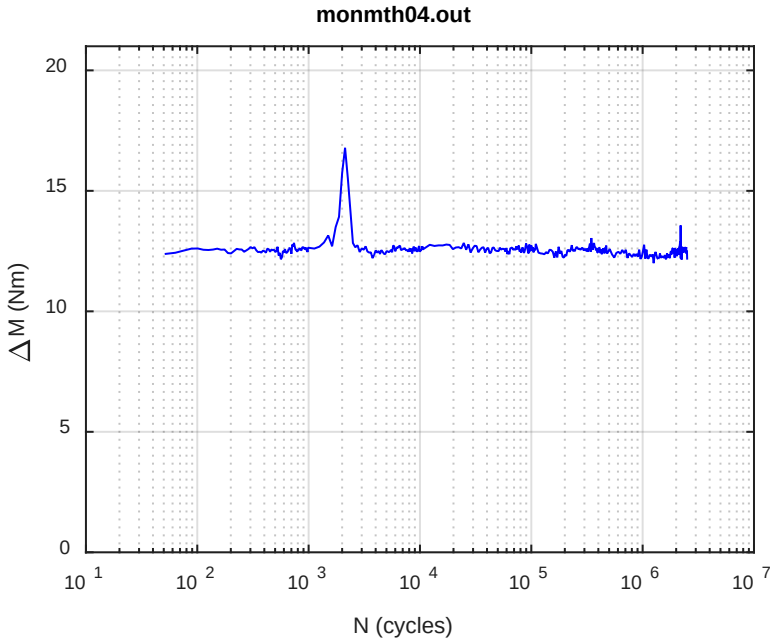
monmth04.out
20
15
10
5
0
ΔM (Nm)
10 1
10 2
10 3
10 4
10 5
10 6
10 7
N (cycles)

(b)

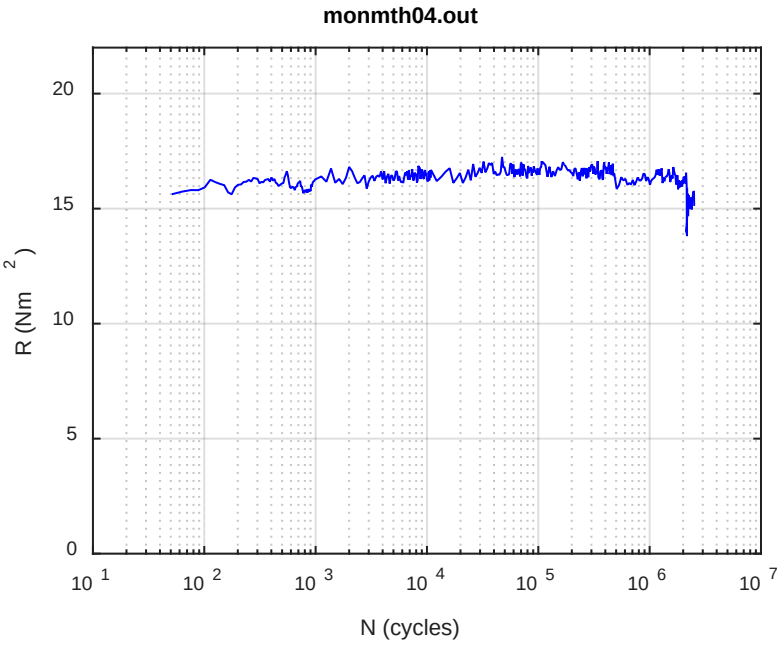
monmth04.out
R (Nm 2)
N (cycles)

(c)

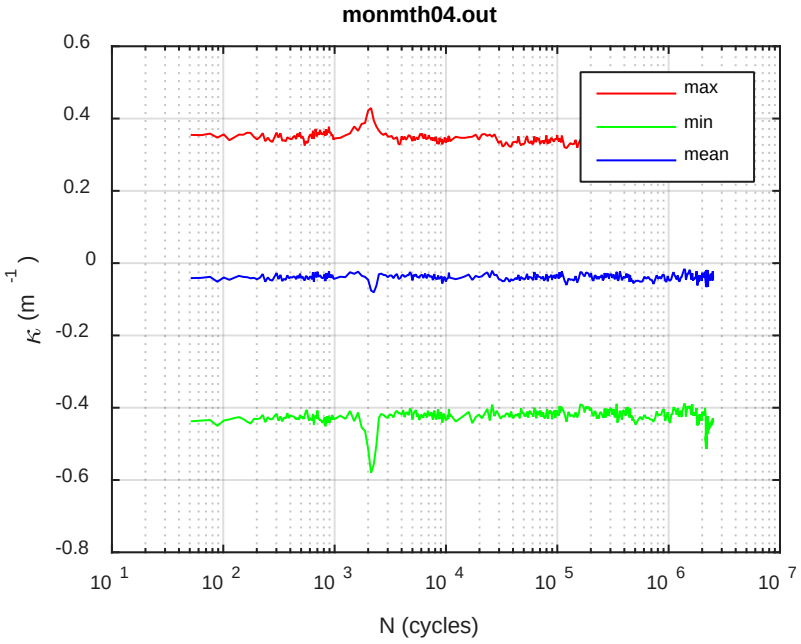
monmth04.out
max
min
mean
κ (m -1)
N (cycles)

(d)

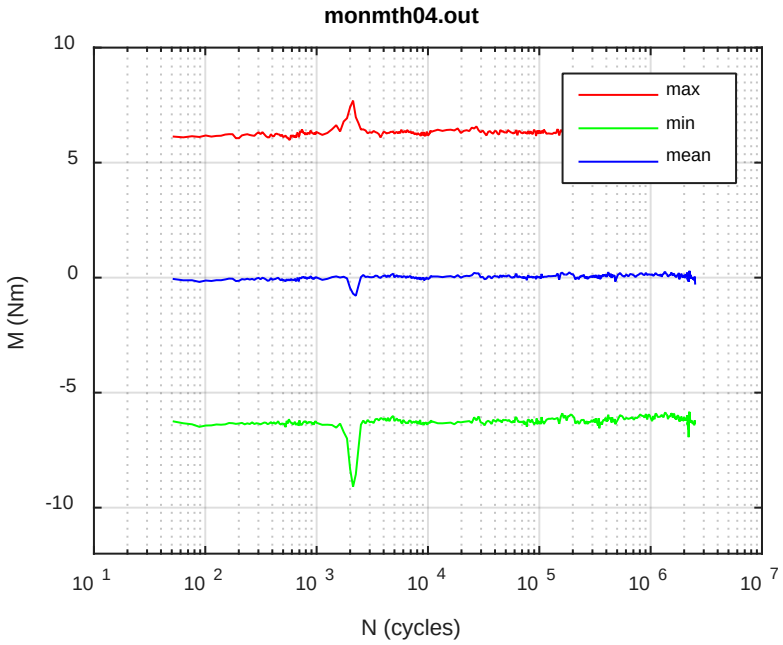

(e)

Fig. E.37 Monitoring-based responses: (a) curvature range, (b) moment range, (c) rigidity, (d) curvature peak/valley, (e) moment peak/valley, MTH04, 7.62 Nm, Nf = 2.51E+06 cycles.

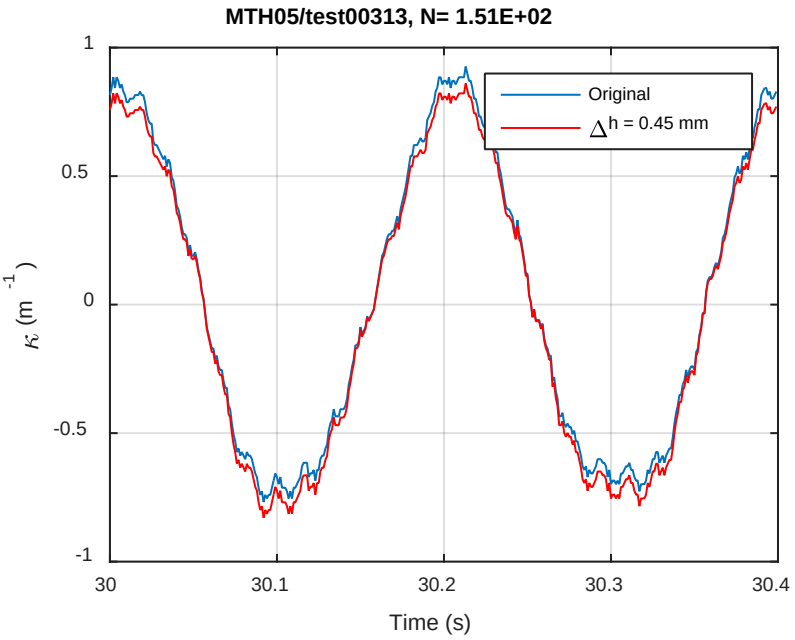
MTH05/test00313, N= 1.51E+02
Original
Δh = 0.45 mm
κ (m -1)
Time (s)
1
0.5
0
-0.5
-1
30
30.1
30.2
30.3
30.4

(a)

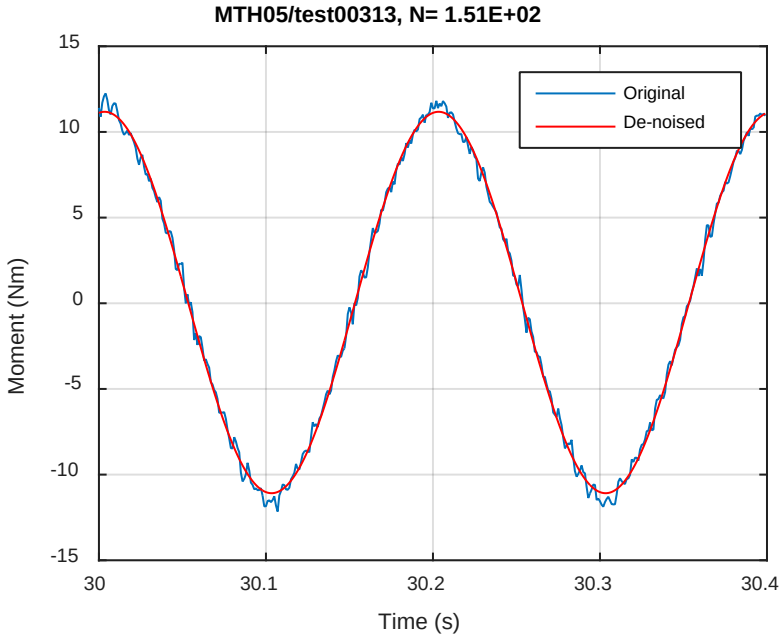
MTH05/test00313, N= 1.51E+02
Original
De-noised
Moment (Nm)
Time (s)
15
10
5
0
-5
-10
-15
30
30.1
30.2
30.3
30.4

(b)

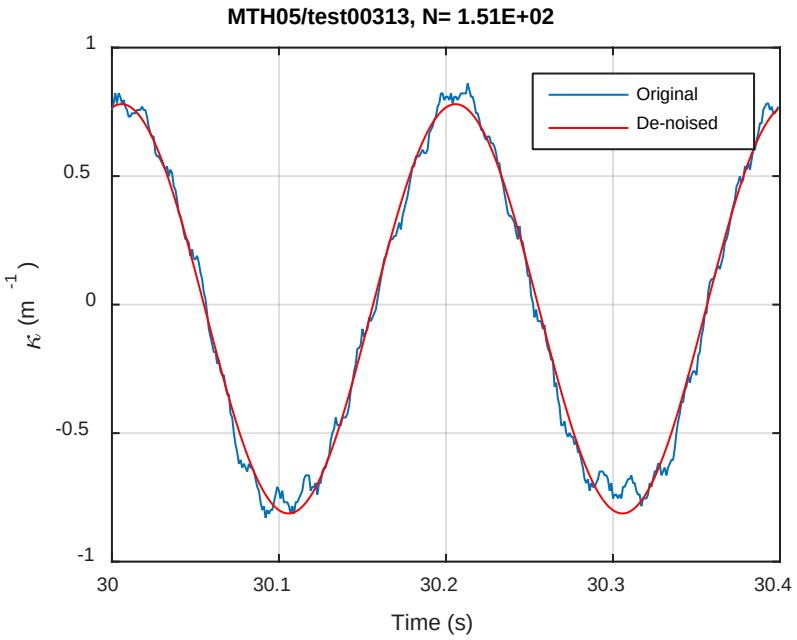

(c)

Fig. E.38 Monitoring-based responses: (a) curvature, (b) moment, (c) curvature, MTH05, 12.70 Nm, Ns = 1.51E+02 cycles.

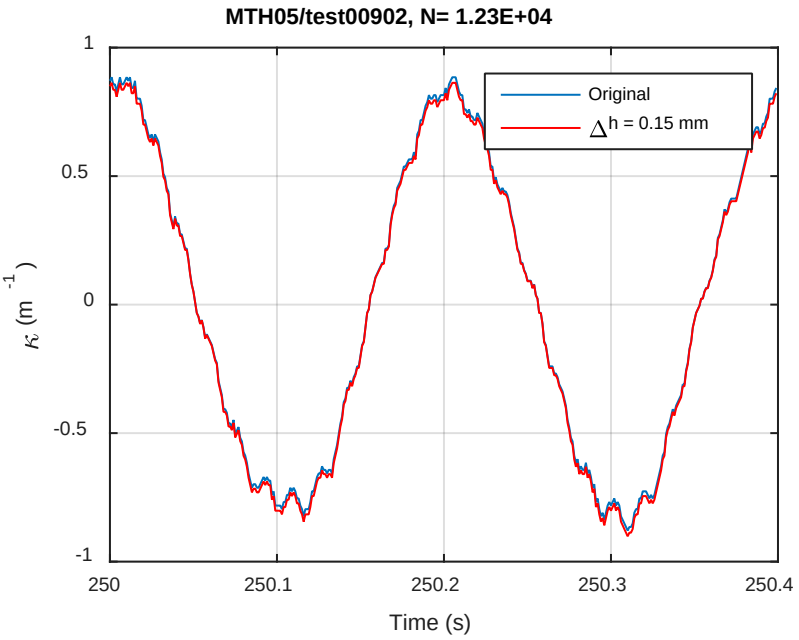
MTH05/test00902, N= 1.23E+04
Original
Δh = 0.15 mm
κ (m-1)
Time (s)
1
0.5
0
-0.5
-1
250
250.1
250.2
250.3
250.4

(a)

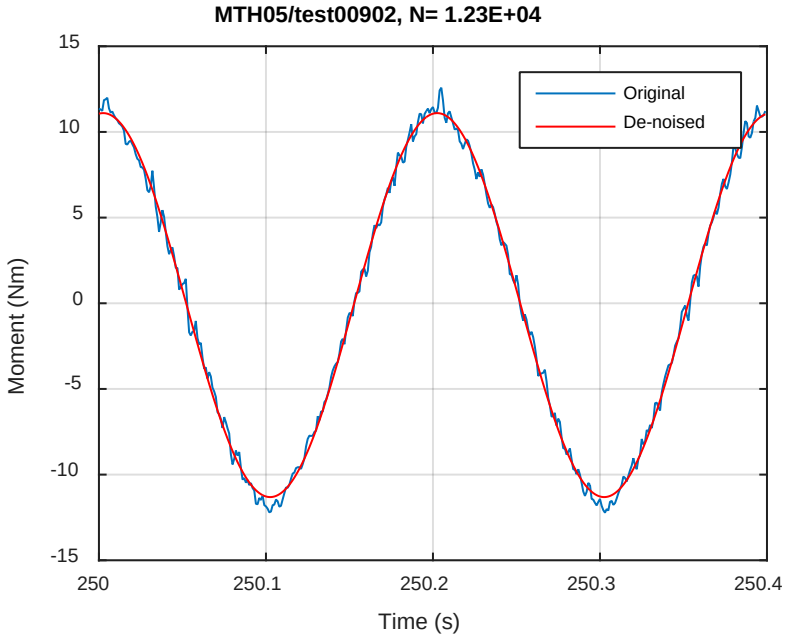
MTH05/test00902, N= 1.23E+04
Original
De-noised
Moment (Nm)
Time (s)
15
10
5
0
-5
-10
-15
250
250.1
250.2
250.3
250.4

(b)

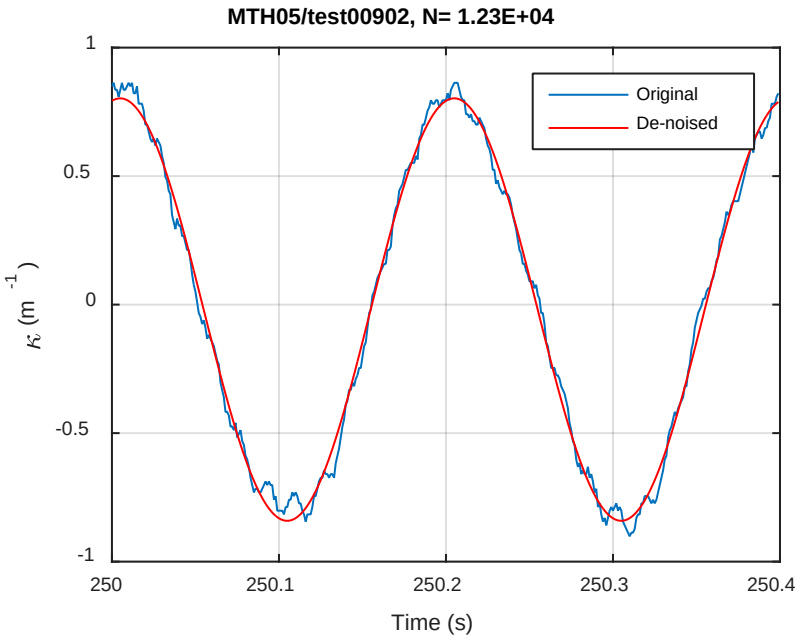

(c)

Fig. E.39 Monitoring-based responses: (a) curvature, (b) moment, (c) curvature, MTH05, 12.70 Nm, Ns = 1.23E+04 cycles.

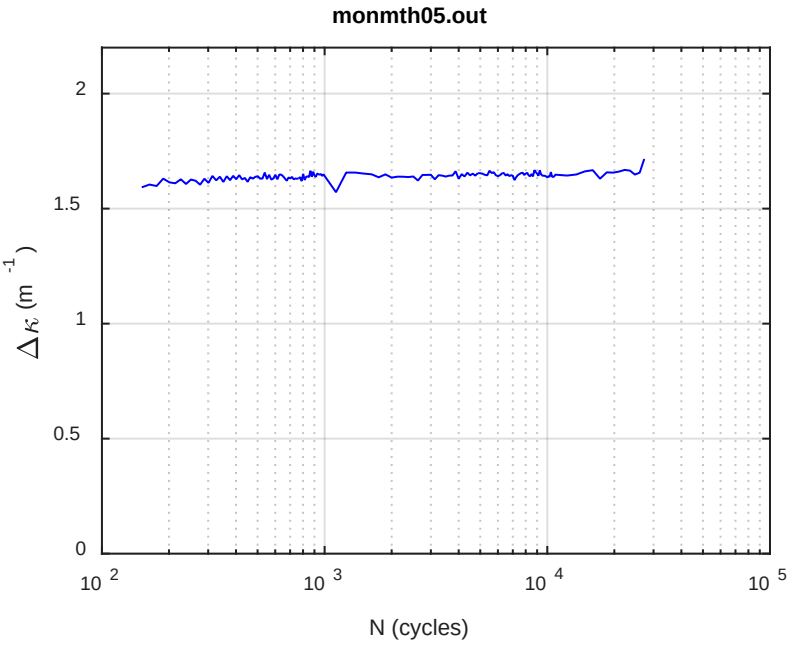
monmth05.out
2
1.5
1
0.5
0
Δκ (m -1)
10 2
10 3
10 4
10 5
N (cycles)

(a)

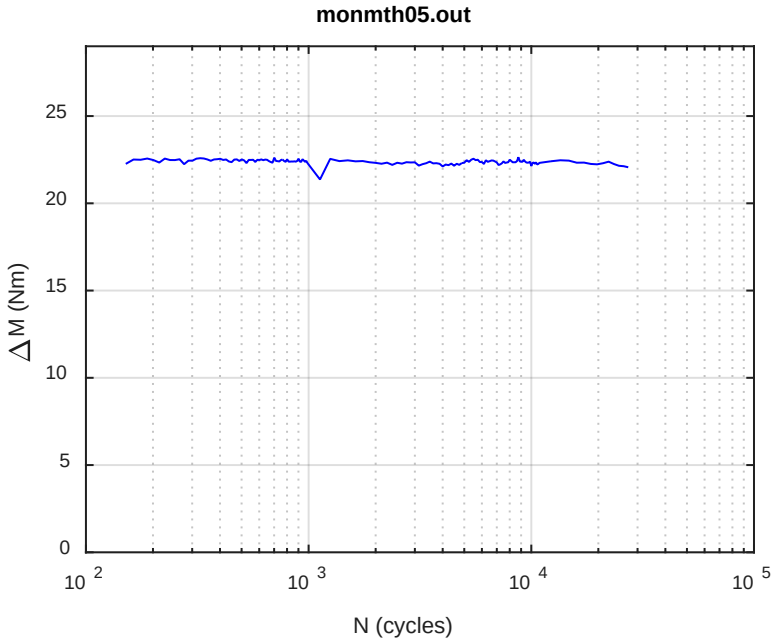
monmth05.out
25
20
15
10
5
0
ΔM (Nm)
10 2
10 3
10 4
10 5
N (cycles)

(b)

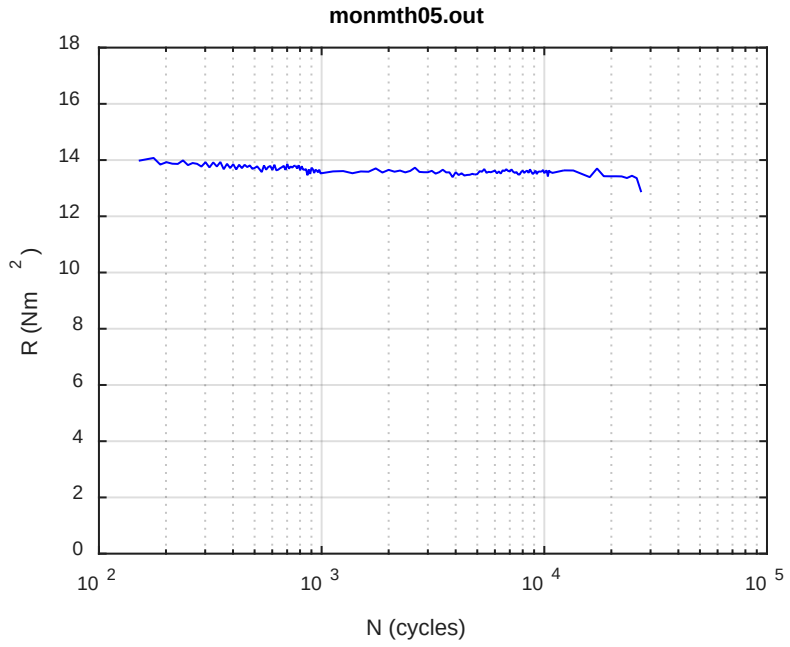
monmth05.out
R (Nm 2)
N (cycles)
18
16
14
12
10
8
6
4
2
0
10 2
10 3
10 4
10 5

(c)

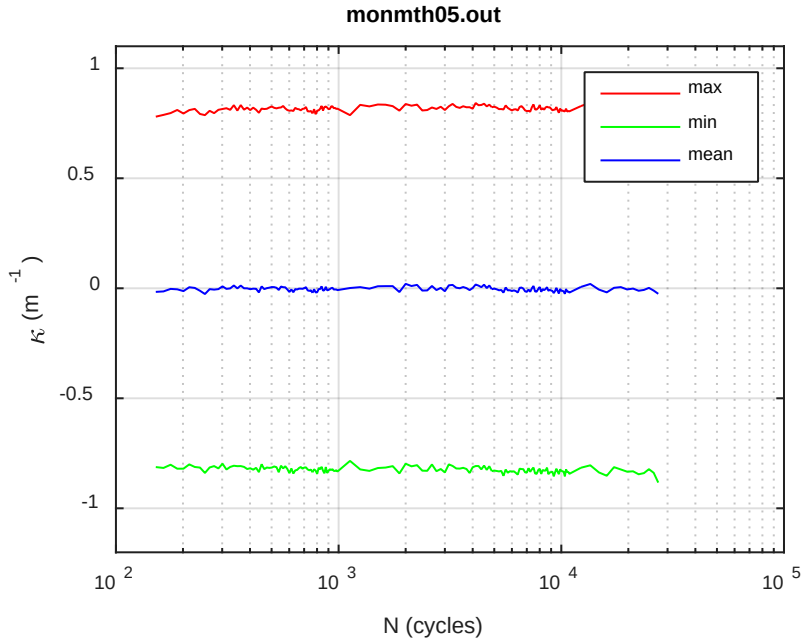
monmth05.out
κ (m -1)
N (cycles)
max
min
mean
1
0.5
0
-0.5
-1
10 2
10 3
10 4
10 5

(d)

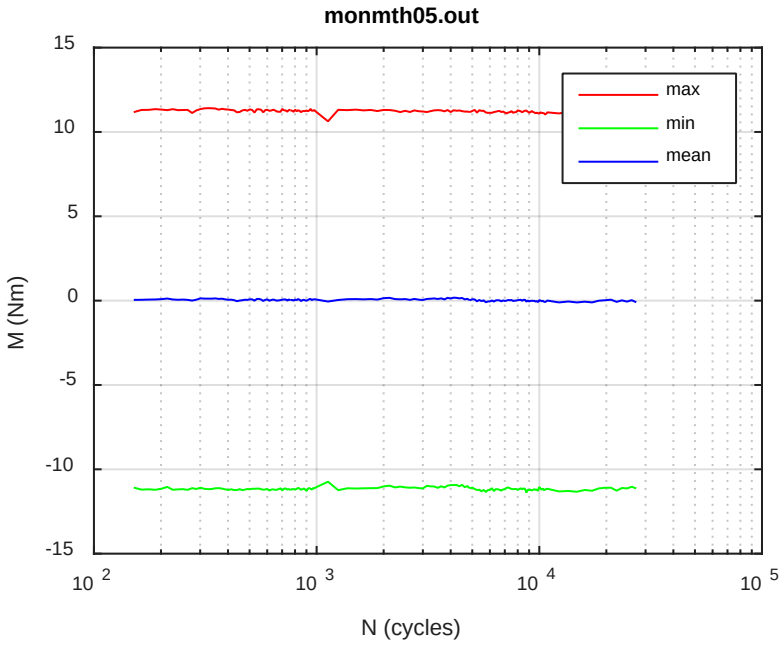

(e)

Fig. E.40 Monitoring-based responses: (a) curvature range, (b) moment range, (c) rigidity, (d) curvature peak/valley, (e) moment peak/valley, MTH05, 12.70 Nm, Nf = 2.76E+04 cycles.

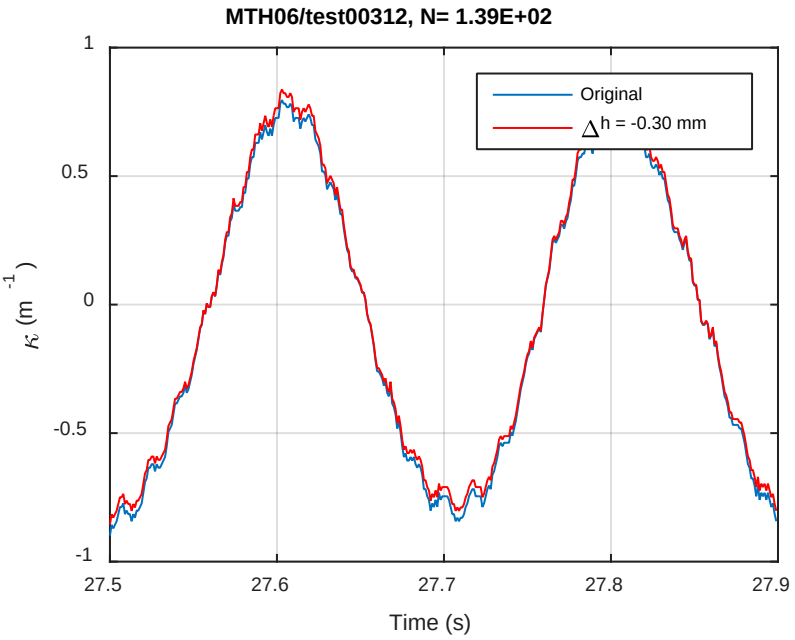
MTH06/test00312, N= 1.39E+02
Original
Δh = -0.30 mm
κ (m -1)
Time (s)
1
0.5
0
-0.5
-1
27.5
27.6
27.7
27.8
27.9

(a)

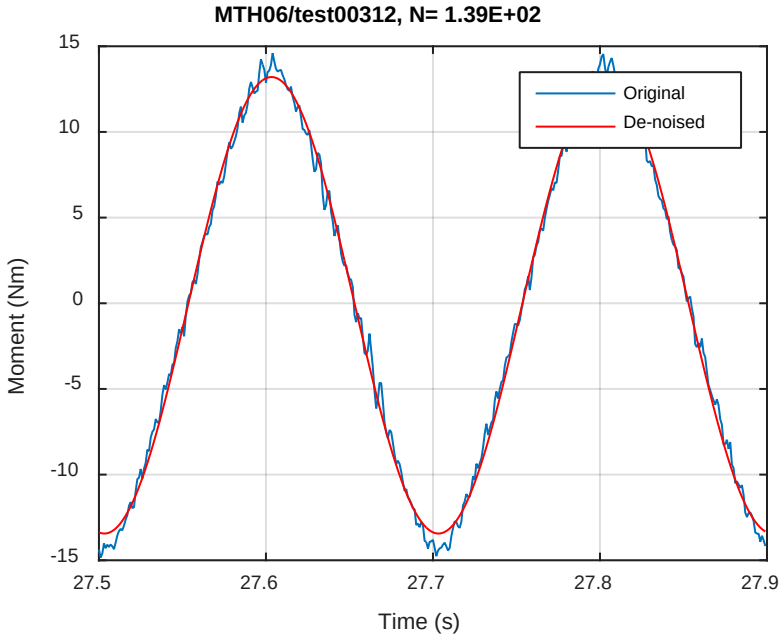
MTH06/test00312, N= 1.39E+02
Original
De-noised
Moment (Nm)
Time (s)
15
10
5
0
-5
-10
-15
27.5
27.6
27.7
27.8
27.9

(b)

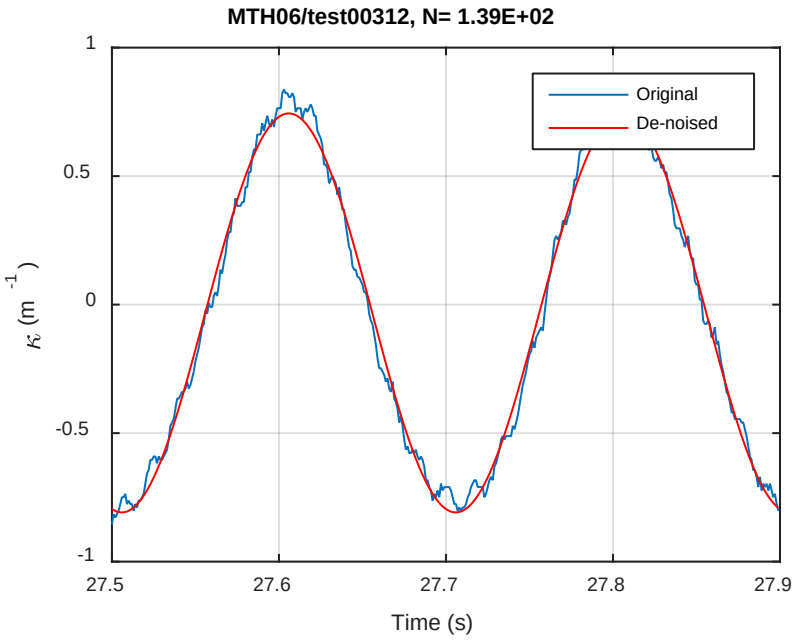

(c)

Fig. E.41 Monitoring-based responses: (a) curvature, (b) moment, (c) curvature, MTH06, 15.24 Nm, Ns = 1.39E+02 cycles.

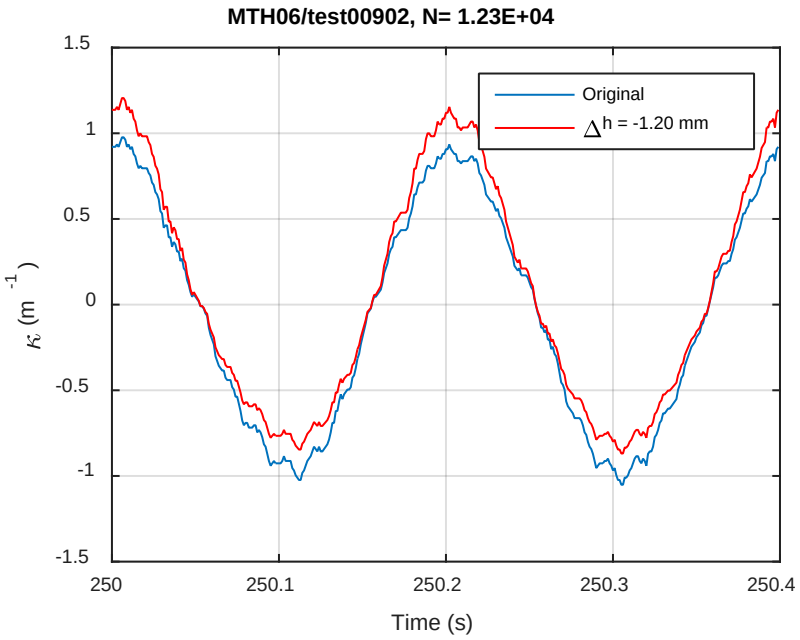
MTH06/test00902, N= 1.23E+04
Original
Δh = -1.20 mm
κ (m-1)
Time (s)
1.5
1
0.5
0
-0.5
-1
-1.5
250
250.1
250.2
250.3
250.4

(a)

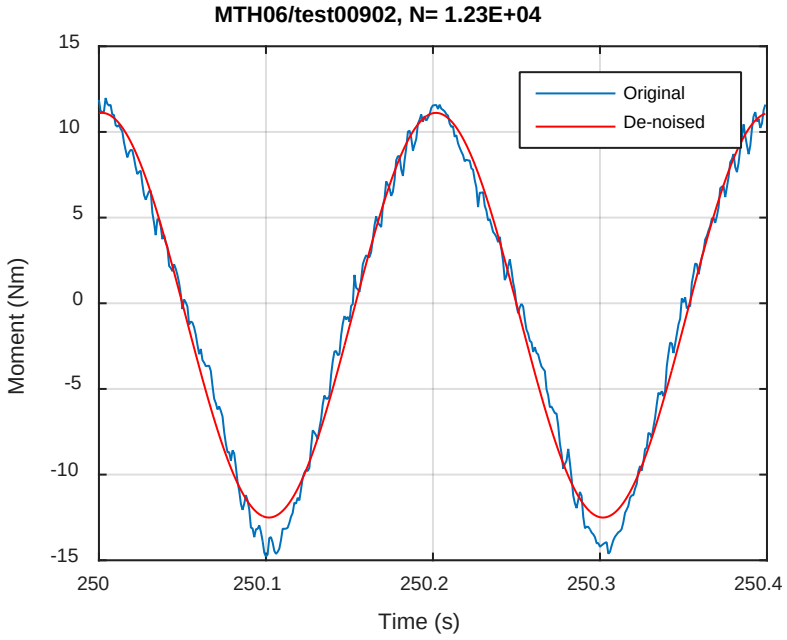
MTH06/test00902, N= 1.23E+04
Original
De-noised
Moment (Nm)
Time (s)
15
10
5
0
-5
-10
-15
250
250.1
250.2
250.3
250.4

(b)

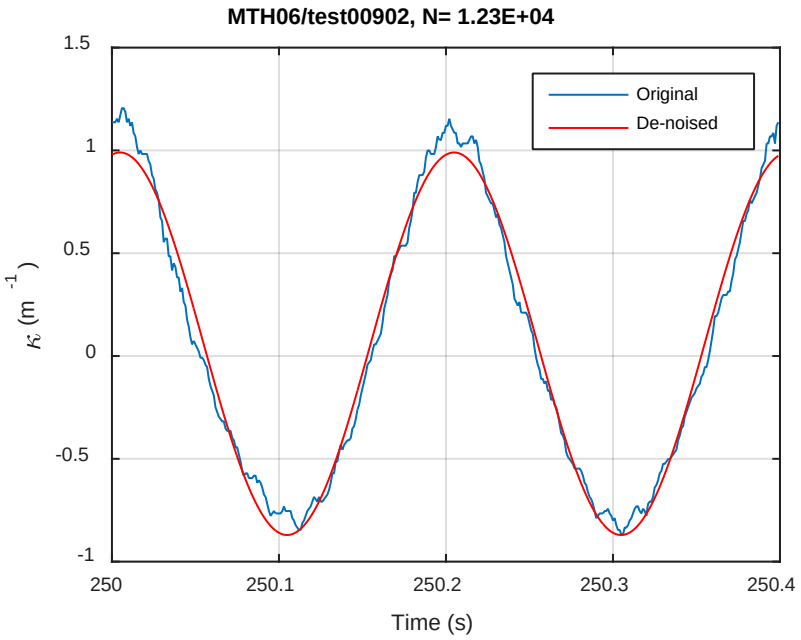

(c)

Fig. E.42 Monitoring-based responses: (a) curvature, (b) moment, (c) curvature, MTH06, 15.24 Nm, Ns = 1.23E+04 cycles.

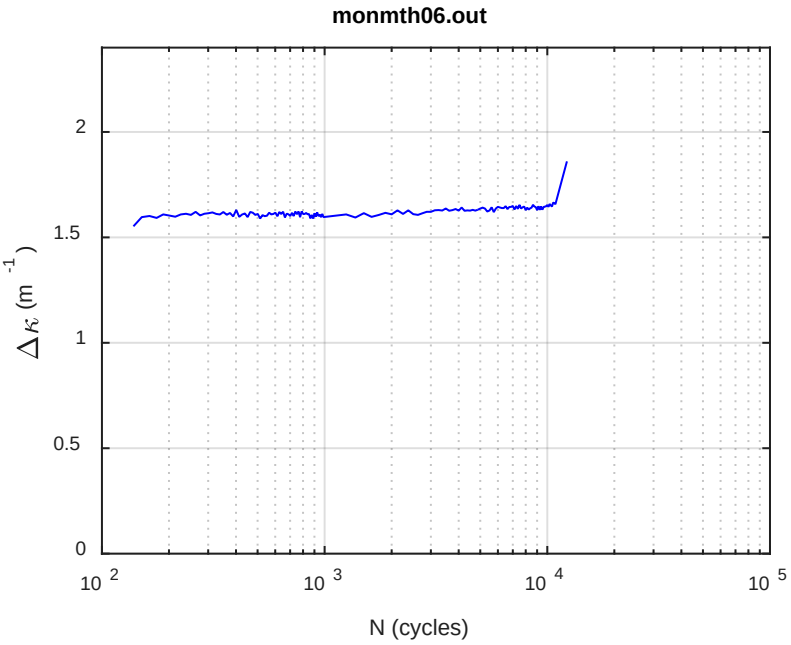
monmth06.out
2
1.5
1
0.5
0
Δκ (m -1)
10 2
10 3
10 4
10 5
N (cycles)

(a)

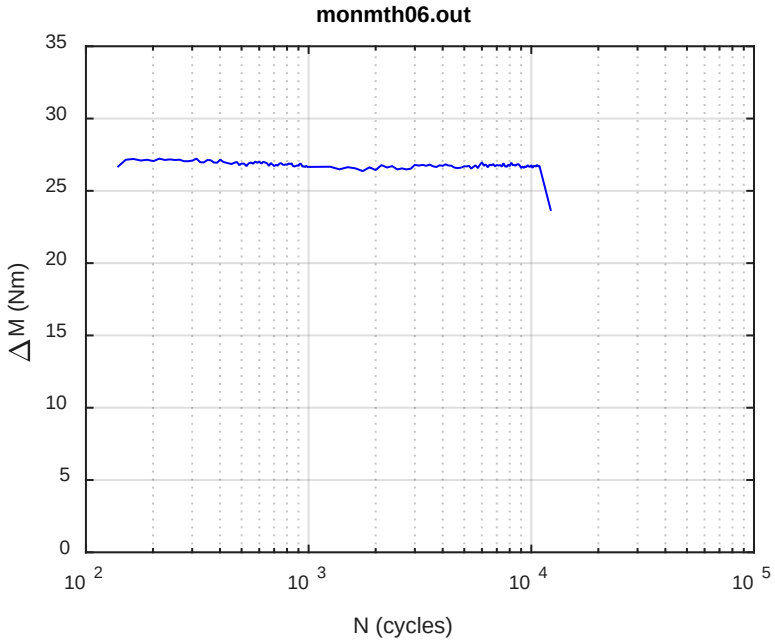
monmth06.out
35
30
25
20
15
10
5
0
ΔM (Nm)
10 2
10 3
10 4
10 5
N (cycles)

(b)

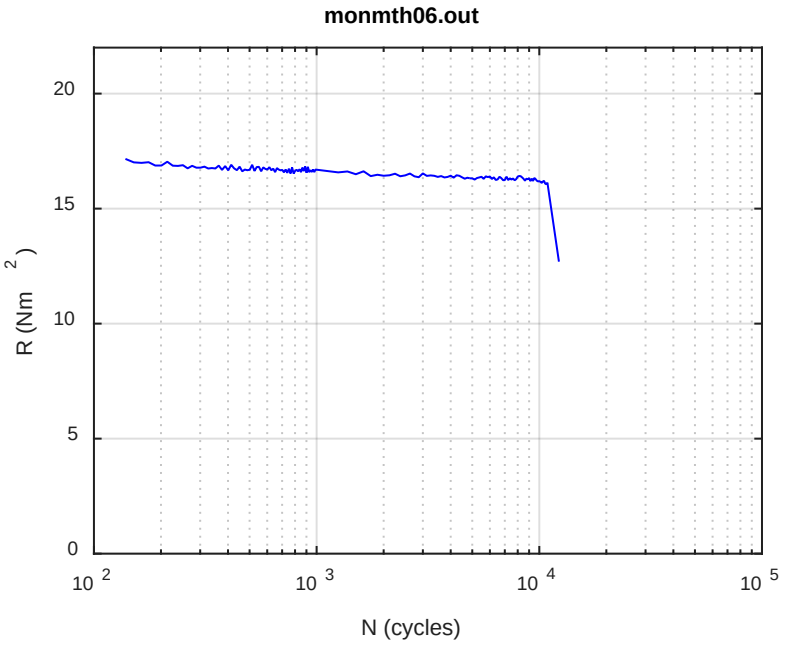
monmth06.out
20
15
10
5
0
R (Nm 2)
10 2
10 3
10 4
10 5
N (cycles)

(c)

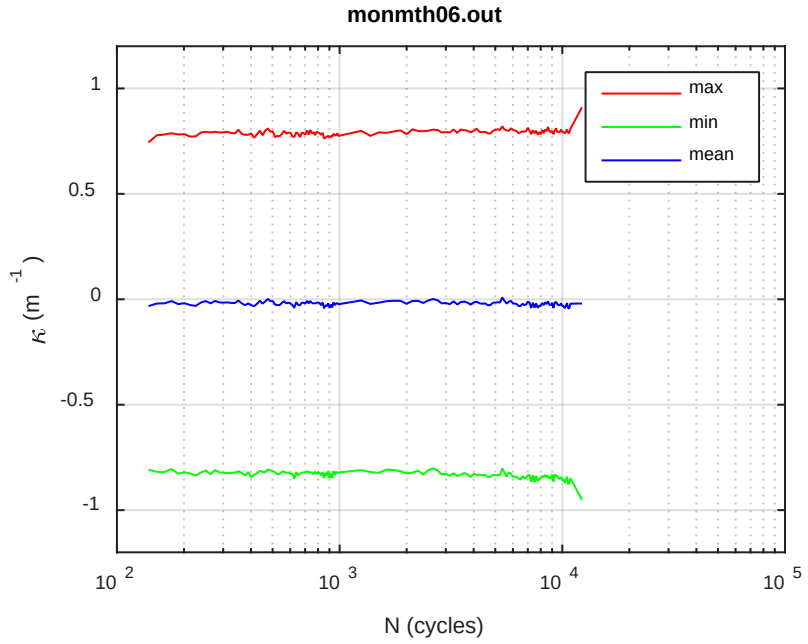
monmth06.out
max
min
mean
1
0.5
0
-0.5
-1
κ (m -1)
10 2
10 3
10 4
10 5
N (cycles)

(d)

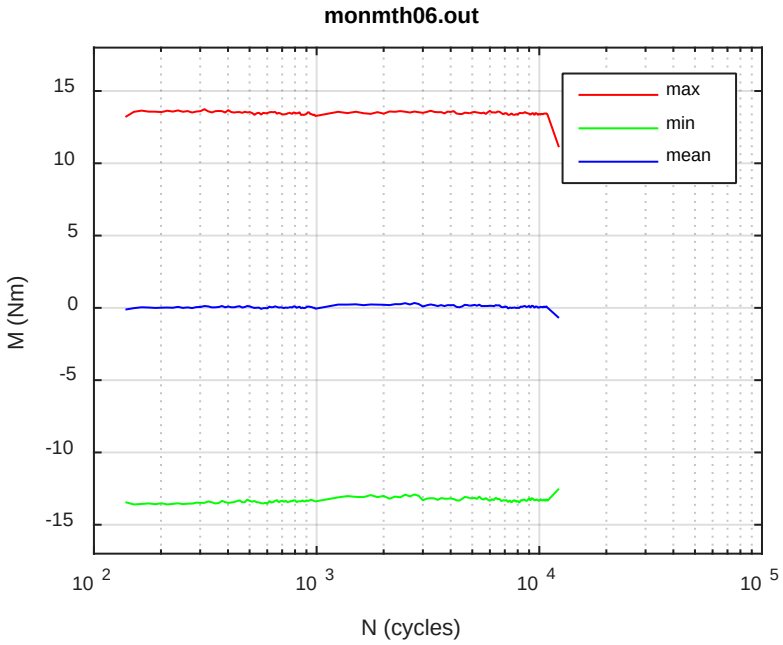

(e)

Fig. E.43 Monitoring-based responses: (a) curvature range, (b) moment range, (c) rigidity, (d) curvature peak/valley, (e) moment peak/valley, MTH06, 15.24 Nm, Nf = 1.25E+04 cycles.

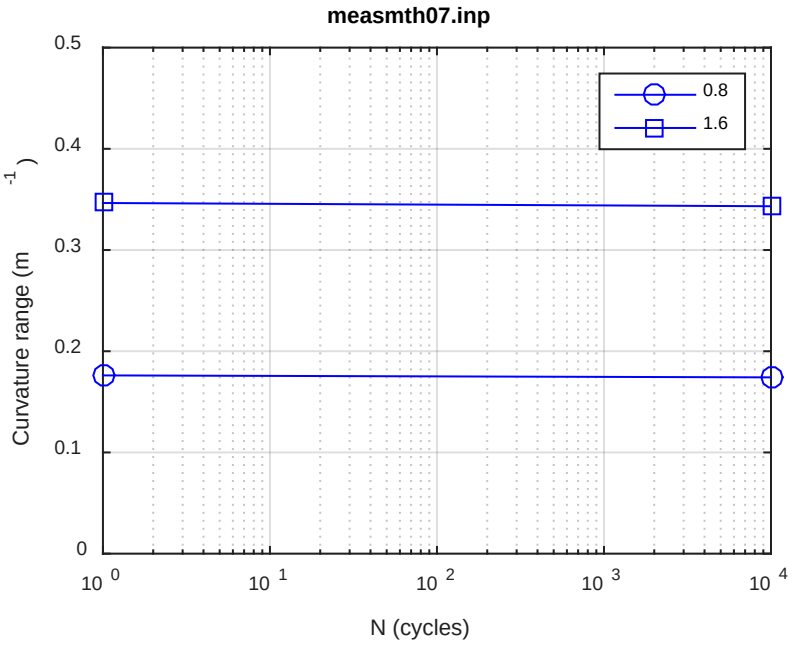
measmth07.inp
0.8
1.6
Curvature range (m -1)
N (cycles)
0
0.1
0.2
0.3
0.4
0.5
10 0
10 1
10 2
10 3
10 4

(a)

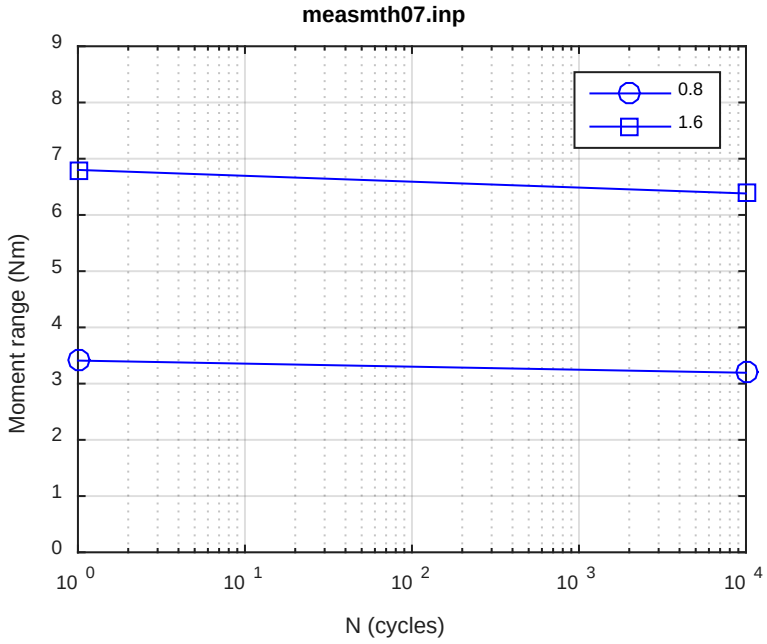
measmth07.inp
0.8
1.6
Moment range (Nm)
N (cycles)
0
1
2
3
4
5
6
7
8
9
10 0
10 1
10 2
10 3
10 4

(b)

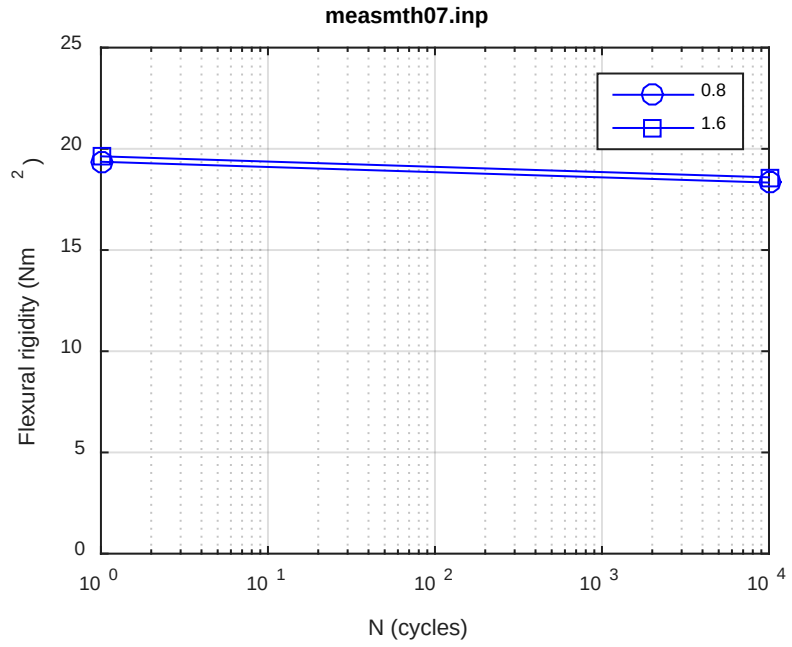
measmth07.inp
0.8
1.6
Flexural rigidity (Nm 2)
N (cycles)
25
20
15
10
5
0
10 0
10 1
10 2
10 3
10 4

(c)

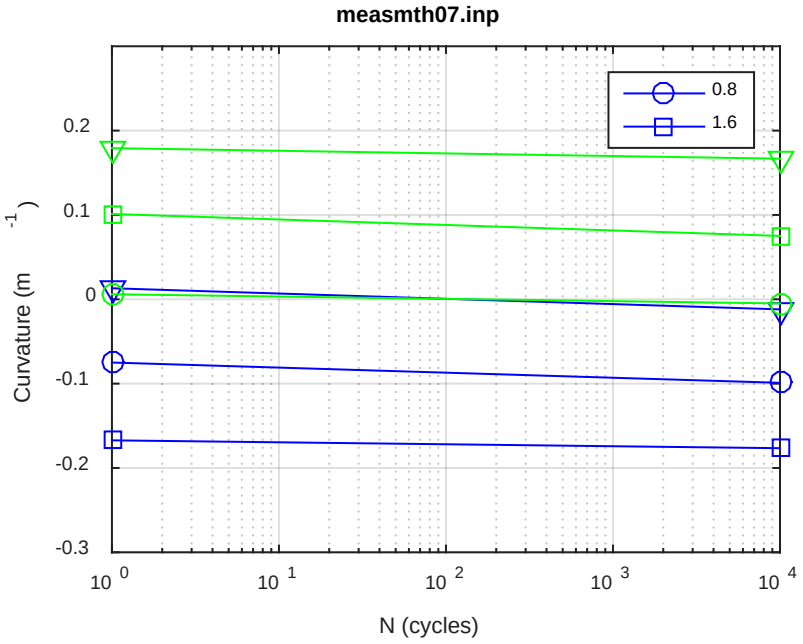
measmth07.inp
0.8
1.6
Curvature (m -1)
N (cycles)
0.2
0.1
0
-0.1
-0.2
-0.3
10 0
10 1
10 2
10 3
10 4

(d)

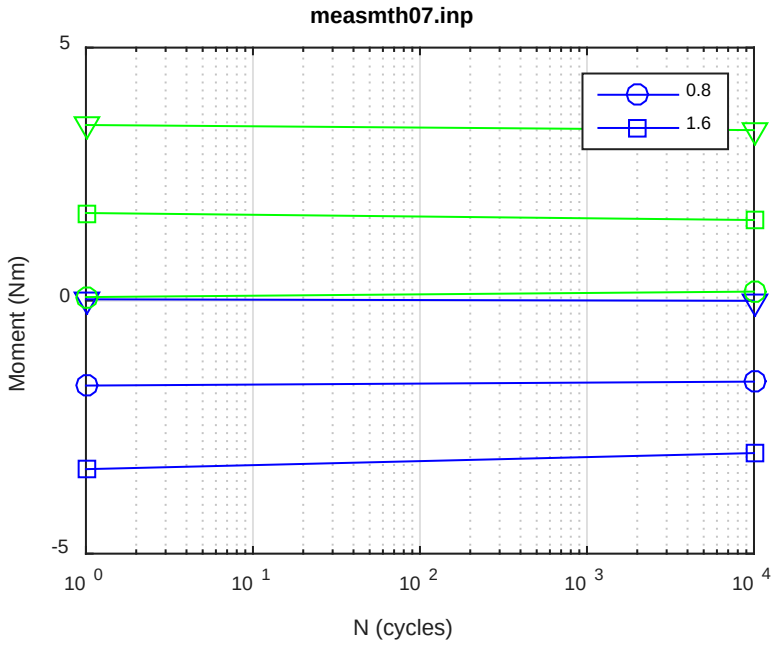

(e)

Fig. E.44 Measurement-based responses: (a) curvature range, (b) moment range, (c) rigidity, (d) curvature peak/valley, (e) moment peak/valley, MTH07, 12.70 Nm.

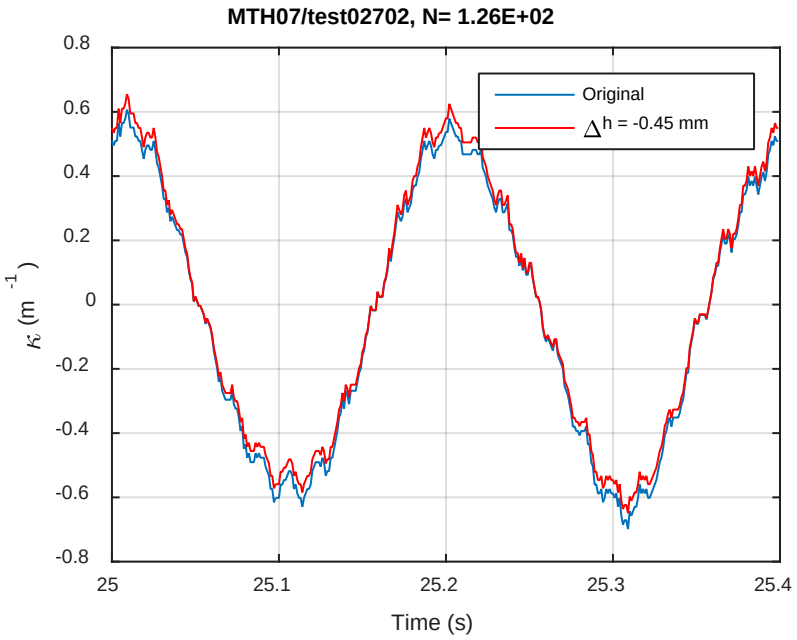
MTH07/test02702, N= 1.26E+02
Original
Δh = -0.45 mm
κ (m -1)
Time (s)
0.8
0.6
0.4
0.2
0
-0.2
-0.4
-0.6
-0.8
25
25.1
25.2
25.3
25.4

(a)

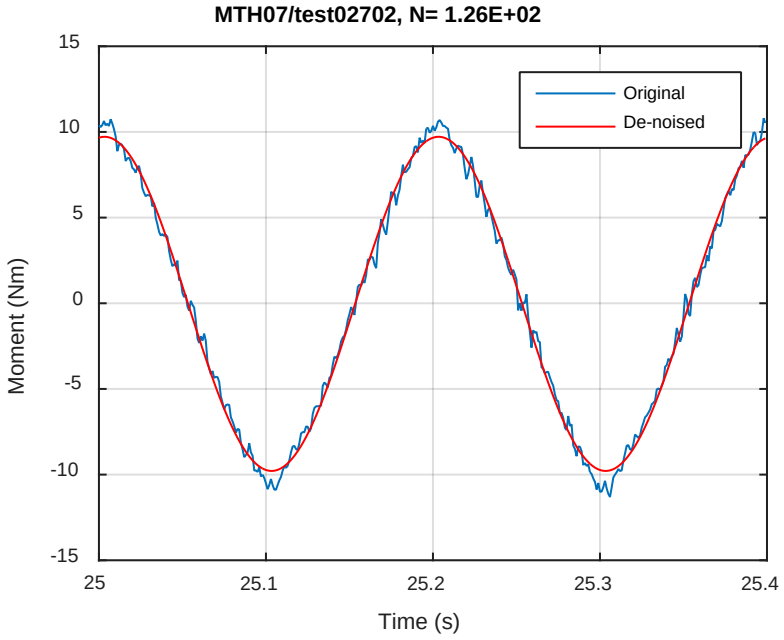
MTH07/test02702, N= 1.26E+02
Original
De-noised
Moment (Nm)
Time (s)
15
10
5
0
-5
-10
-15
25
25.1
25.2
25.3
25.4

(b)

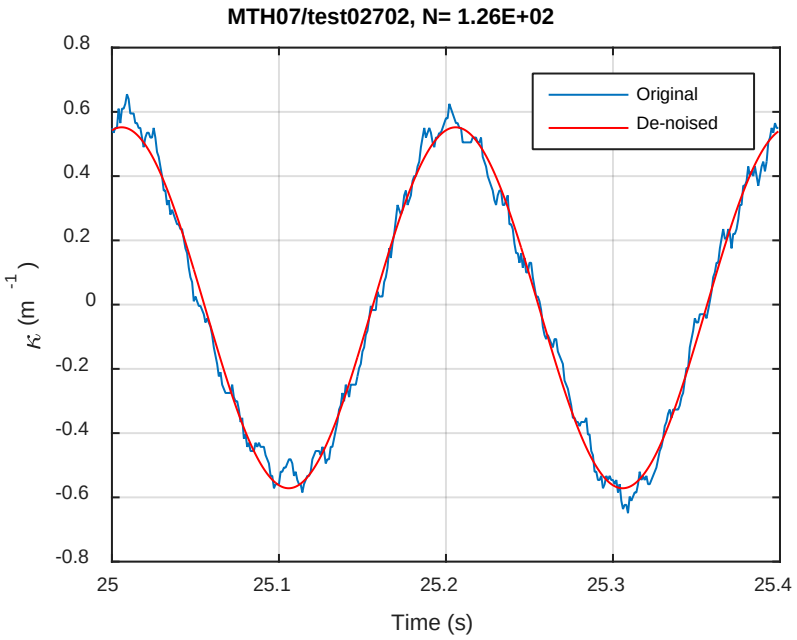

(c)

Fig. E.45 Monitoring-based responses: (a) curvature, (b) moment, (c) curvature, MTH07, 12.70 Nm, Ns = 1.26E+02 cycles.

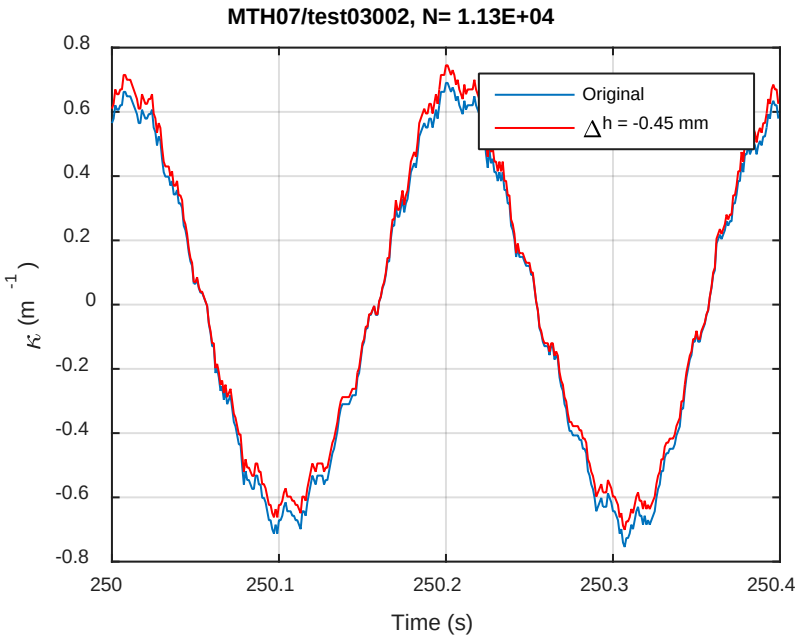
MTH07/test03002, N= 1.13E+04
Original
Δh = -0.45 mm
κ (m-1)
Time (s)
0.8
0.6
0.4
0.2
0
-0.2
-0.4
-0.6
-0.8
250
250.1
250.2
250.3
250.4

(a)

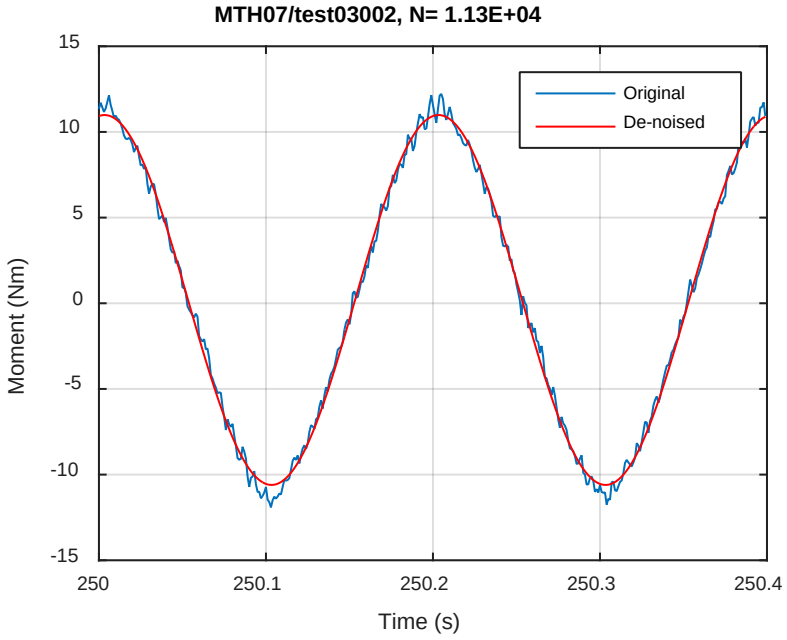
MTH07/test03002, N= 1.13E+04
Original
De-noised
Moment (Nm)
Time (s)
15
10
5
0
-5
-10
-15
250
250.1
250.2
250.3
250.4

(b)

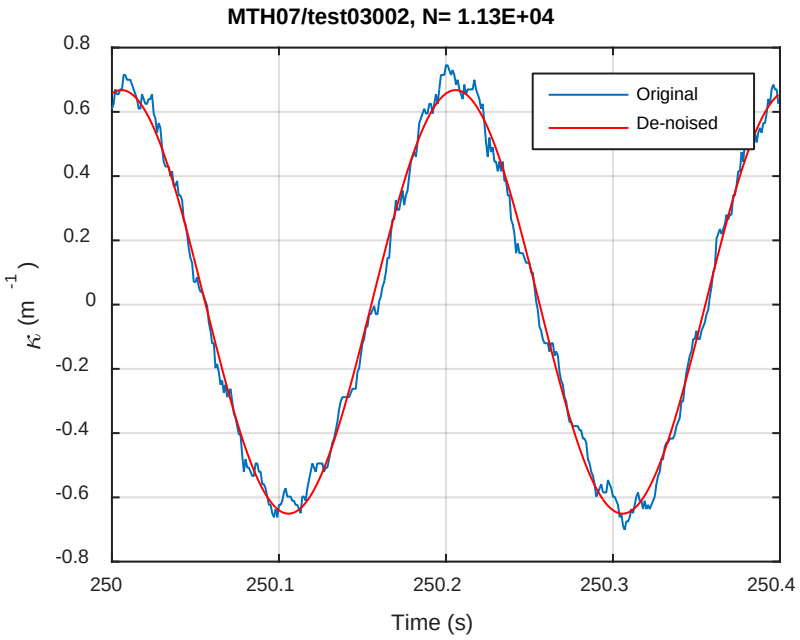

(c)

Fig. E.46 Monitoring-based responses: (a) curvature, (b) moment, (c) curvature, MTH07, 12.70 Nm, Ns = 1.13E+04 cycles.

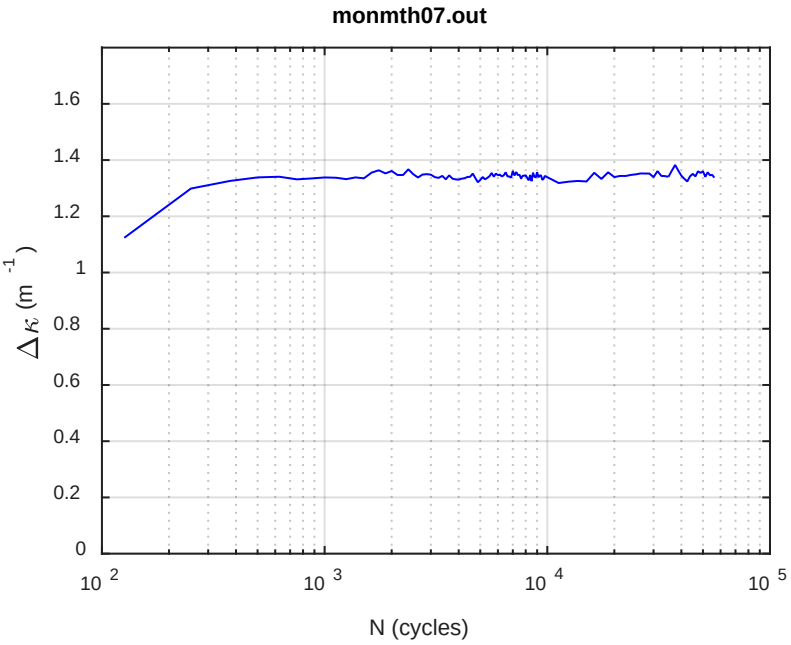
monmth07.out
1.6
1.4
1.2
1
0.8
0.6
0.4
0.2
0
Δκ (m -1)
10 2
10 3
10 4
10 5
N (cycles)

(a)

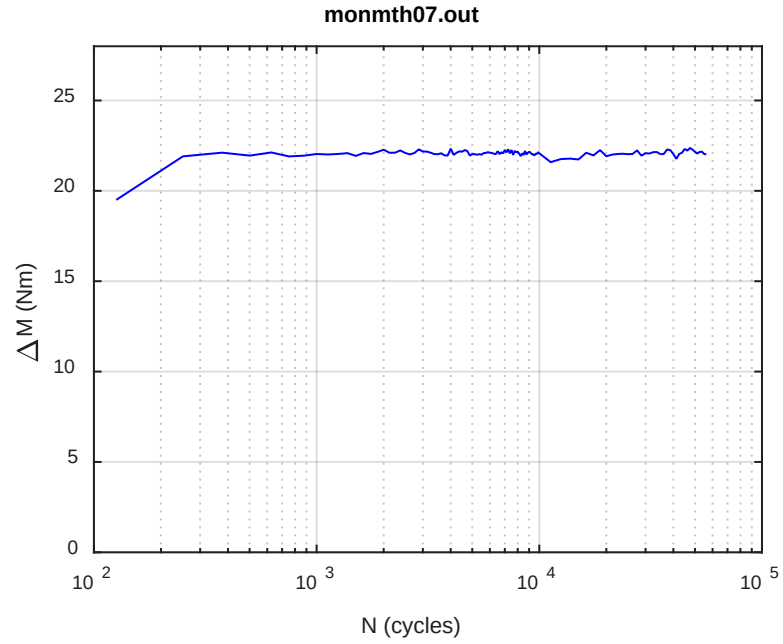
monmth07.out
25
20
15
10
5
0
ΔM (Nm)
10 2
10 3
10 4
10 5
N (cycles)

(b)

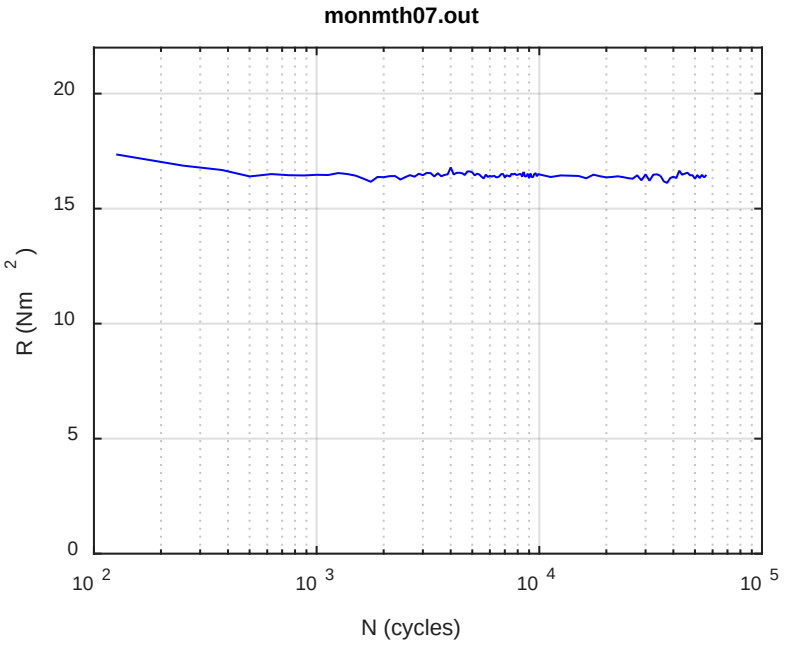
monmth07.out
20
15
10
5
0
R (Nm 2)
10 2
10 3
10 4
10 5
N (cycles)

(c)

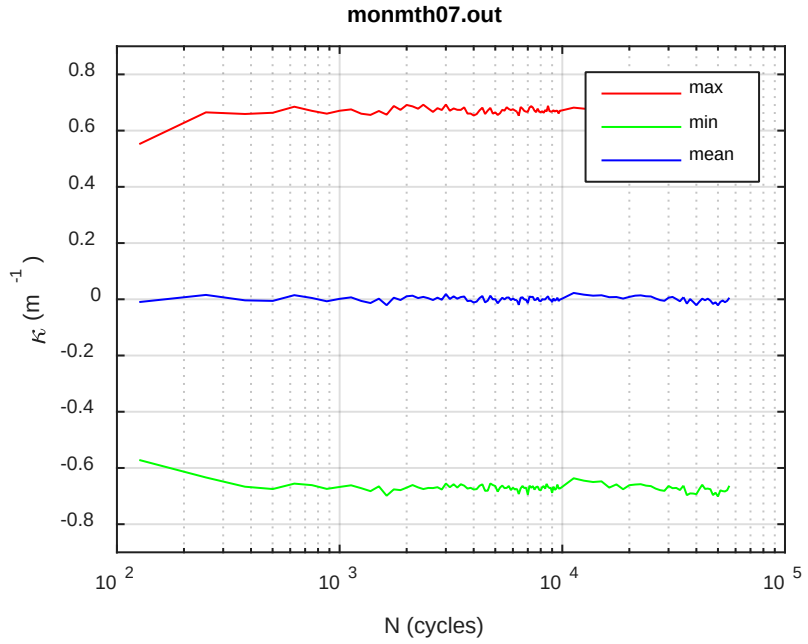
monmth07.out
max
min
mean
0.8
0.6
0.4
0.2
0
-0.2
-0.4
-0.6
-0.8
κ (m -1)
10 2
10 3
10 4
10 5
N (cycles)

(d)

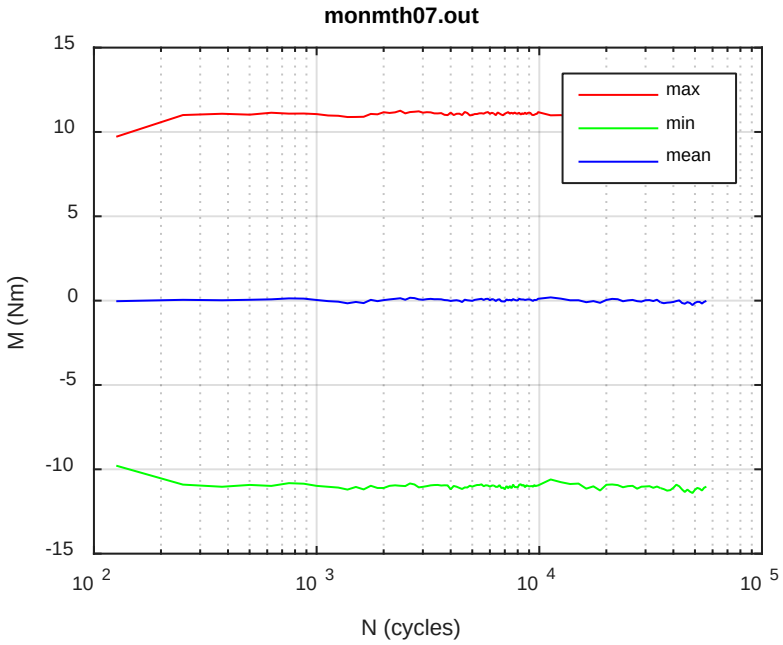

(e)

Fig. E.47 Monitoring-based responses: (a) curvature range, (b) moment range, (c) rigidity, (d) curvature peak/valley, (e) moment peak/valley, MTH07, 12.70 Nm, Nf = 5.73E+04 cycles.

APPENDIX F
CIRFT TESTING RESULTS OF HBR SNF– PART II

Table of Contents

Measurement and monitoring rigidity curves of HBR HR data

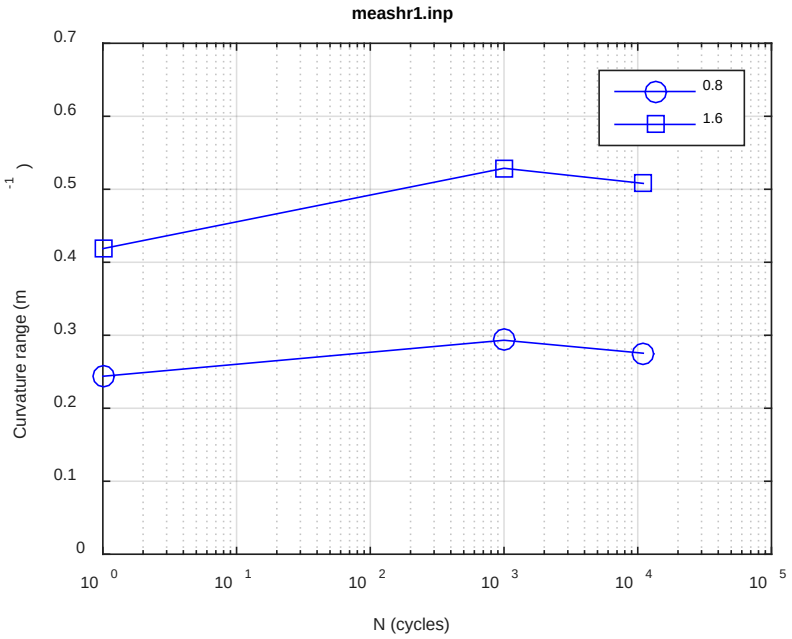
meashr1.inp
0.8
1.6
Curvature range (m -1)
N (cycles)
0
0.1
0.2
0.3
0.4
0.5
0.6
0.7
10 0
10 1
10 2
10 3
10 4
10 5

(a)

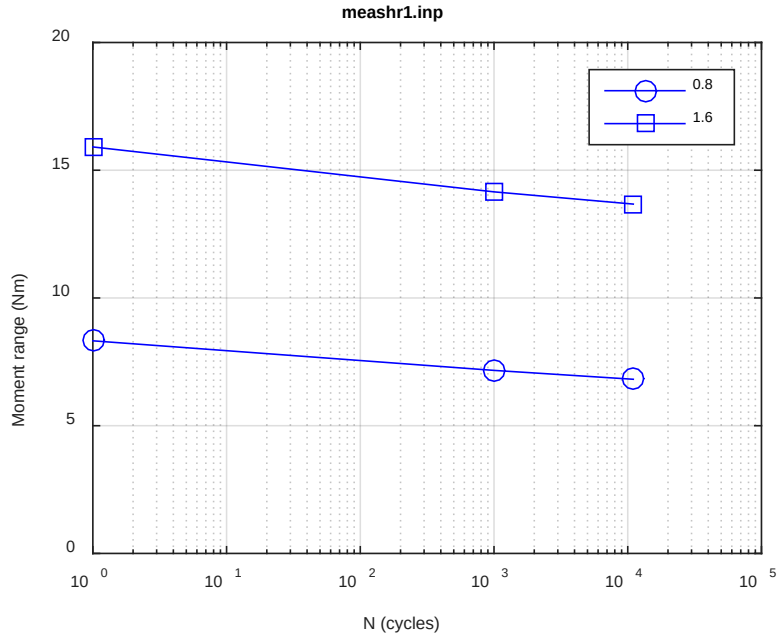
meashr1.inp
0.8
1.6
Moment range (Nm)
N (cycles)
0
5
10
15
20
10 0
10 1
10 2
10 3
10 4
10 5

(b)

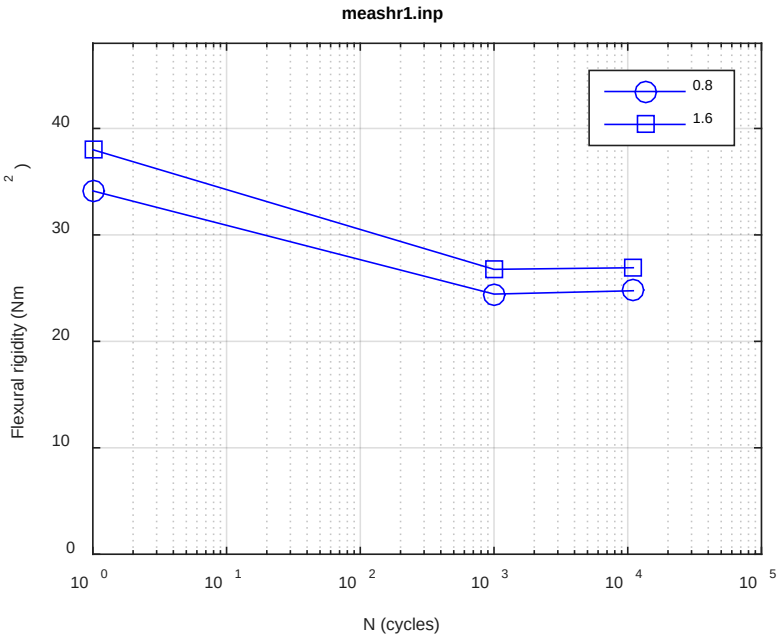
meashr1.inp
0.8
1.6
Flexural rigidity (Nm 2)
0
10
20
30
40
10 0
10 1
10 2
10 3
10 4
10 5
N (cycles)

(c)

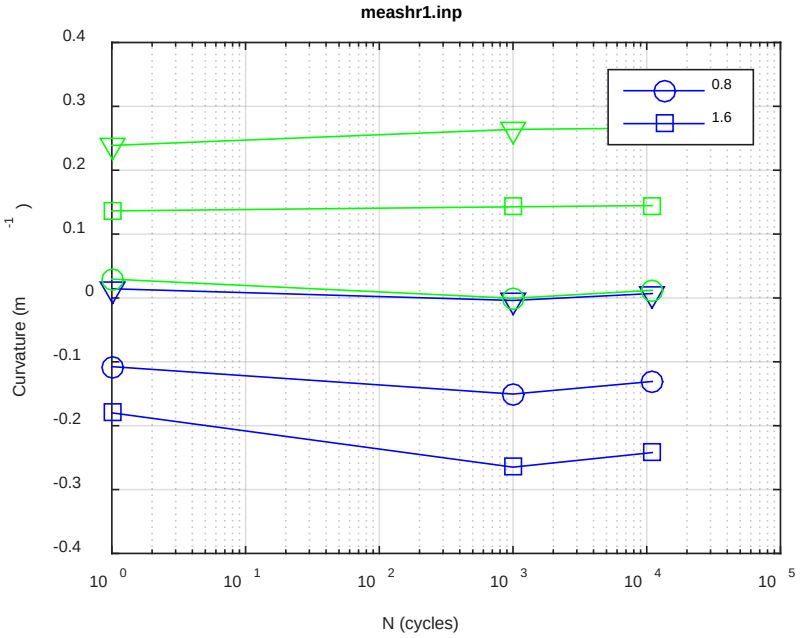
meashr1.inp
0.8
1.6
Curvature (m -1)
0.4
0.3
0.2
0.1
0
-0.1
-0.2
-0.3
-0.4
10 0
10 1
10 2
10 3
10 4
10 5
N (cycles)

(d)

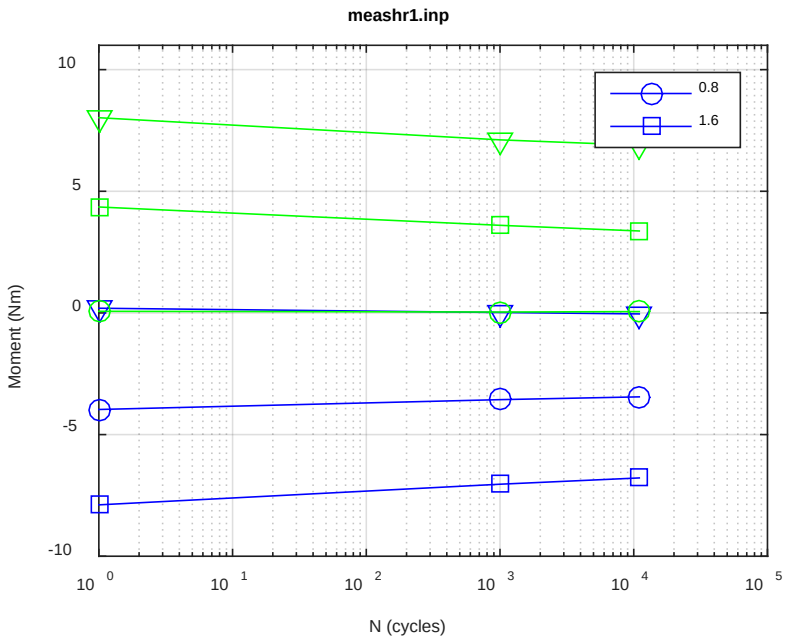

(e)

Fig. F.1 Measurement-based responses: (a) curvature range, (b) moment range, (c) rigidity, (d) curvature peak/valley, (e) moment peak/valley, HR1, 15.24 Nm.

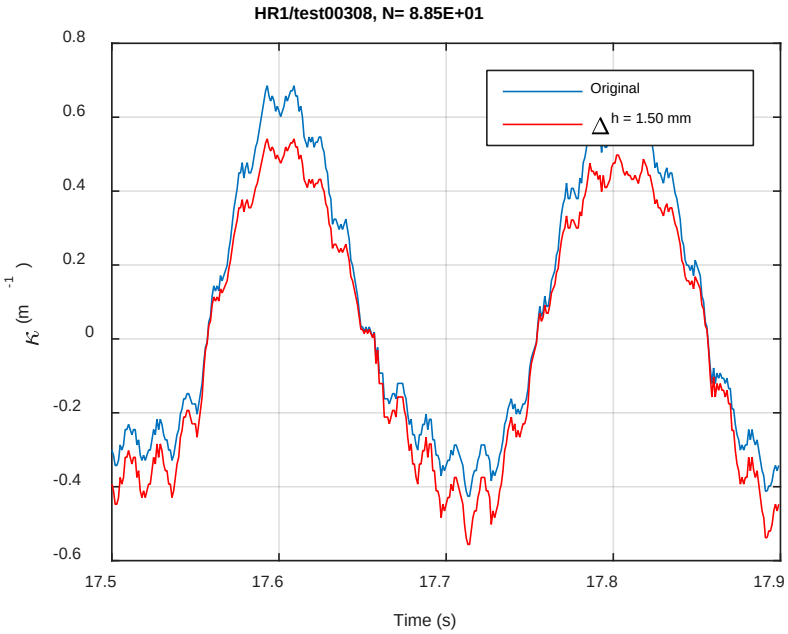
HR1/test00308, N= 8.85E+01
Original
Δh = 1.50 mm
κ (m-1)
Time (s)
0.8
0.6
0.4
0.2
0
-0.2
-0.4
-0.6
17.5
17.6
17.7
17.8
17.9

(a)

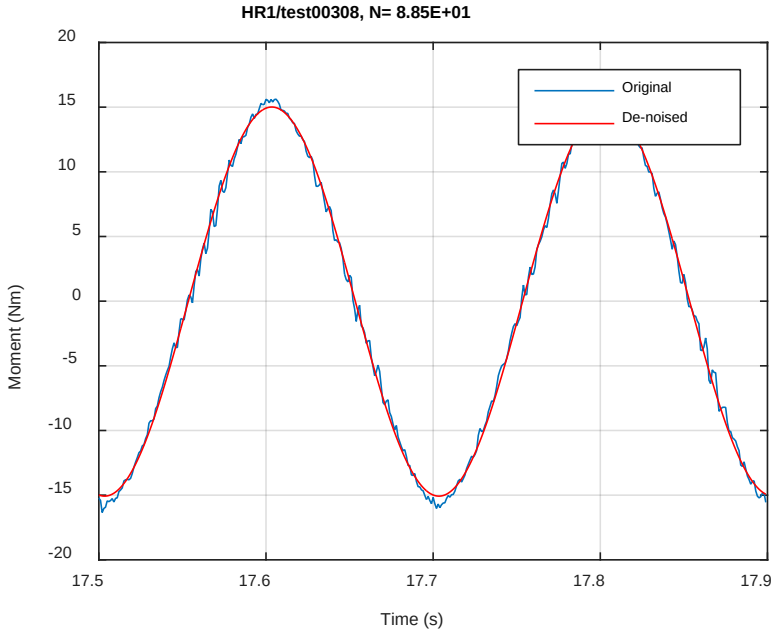
HR1/test00308, N= 8.85E+01
Original
De-noised
Moment (Nm)
Time (s)
20
15
10
5
0
-5
-10
-15
-20
17.5
17.6
17.7
17.8
17.9

(b)

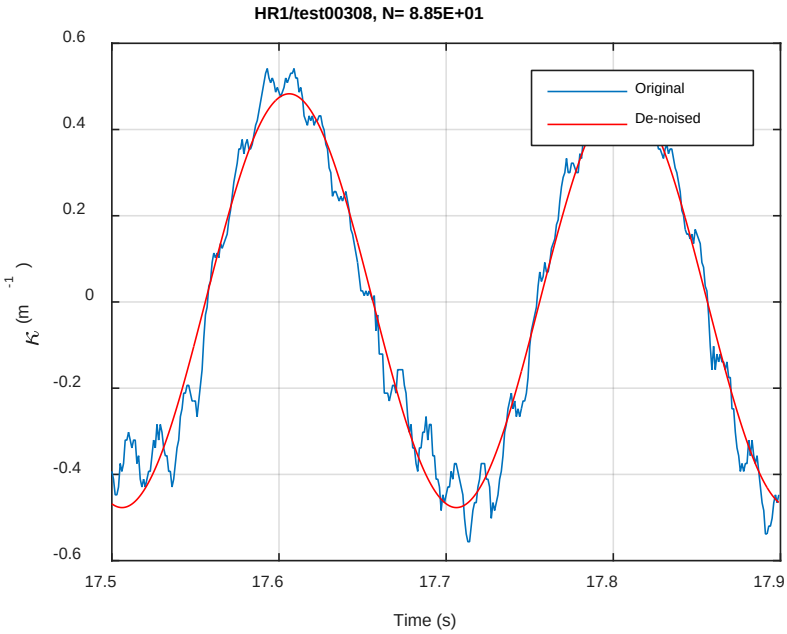

(c)

Fig. F.2 Monitoring-based responses: (a) curvature, (b) moment, (c) curvature, HR1, 15.24 Nm, Ns = 8.85E+01 cycles.

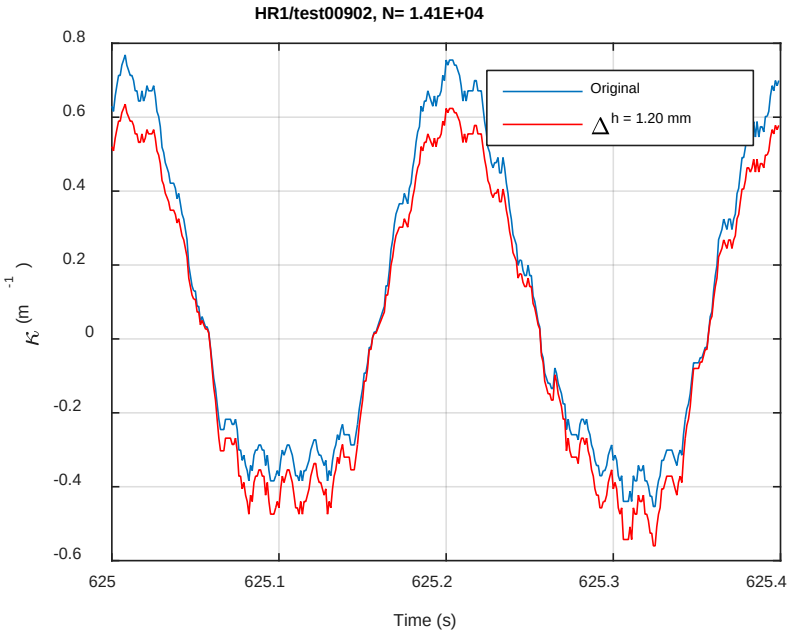
HR1/test00902, N= 1.41E+04
Original
Δh = 1.20 mm
κ (m-1)
Time (s)
0.8
0.6
0.4
0.2
0
-0.2
-0.4
-0.6
625
625.1
625.2
625.3
625.4

(a)

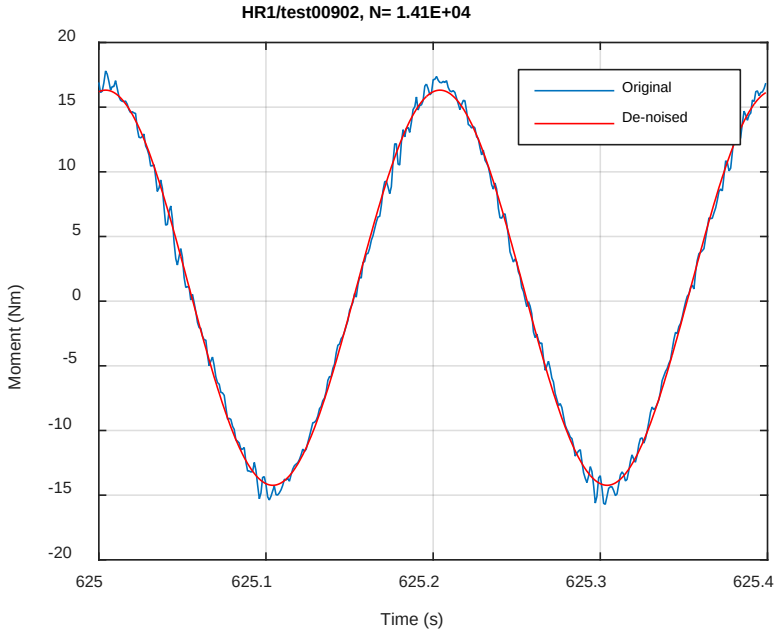
HR1/test00902, N= 1.41E+04
Original
De-noised
Moment (Nm)
Time (s)
20
15
10
5
0
-5
-10
-15
-20
625
625.1
625.2
625.3
625.4

(b)

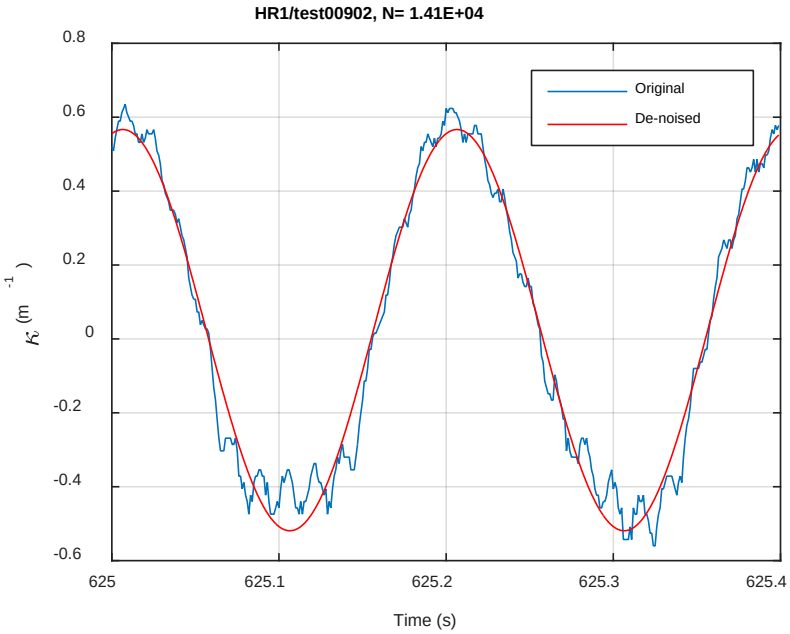

(c)

Fig. F.3 Monitoring-based responses: (a) curvature, (b) moment, (c) curvature, HR1, 15.24 Nm, Ns = 1.41E+04 cycles.

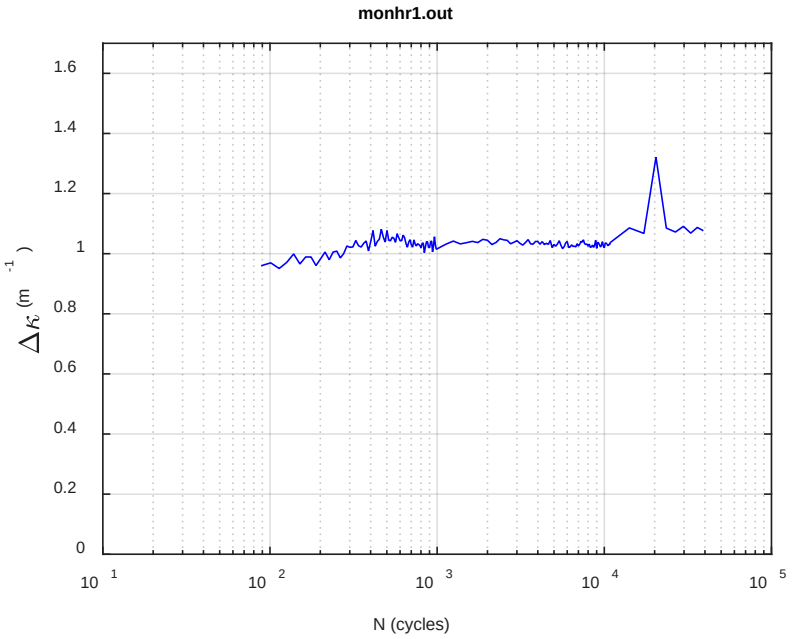
monhr1.out
1.6
1.4
1.2
1
0.8
0.6
0.4
0.2
0
Δκ (m -1)
10 1
10 2
10 3
10 4
10 5
N (cycles)

(a)

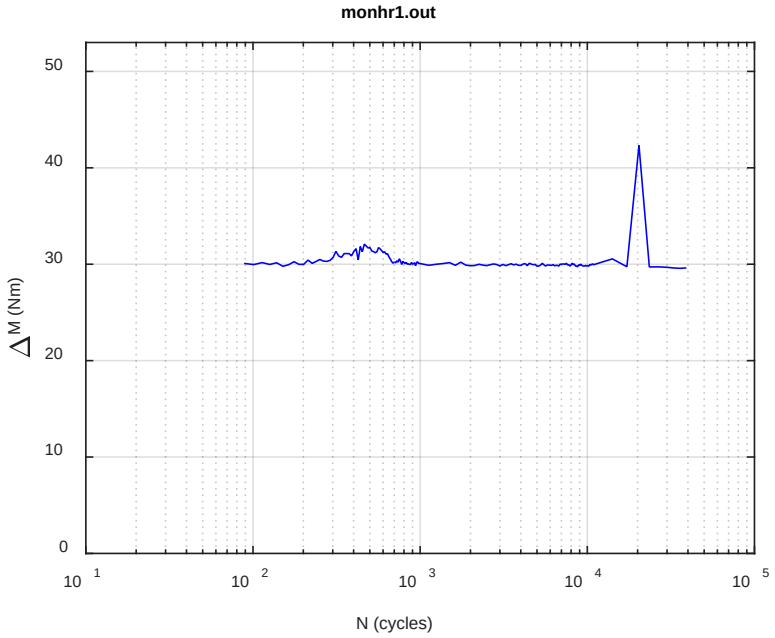
monhr1.out
50
40
30
20
10
0
ΔM (Nm)
10 1
10 2
10 3
10 4
10 5
N (cycles)

(b)

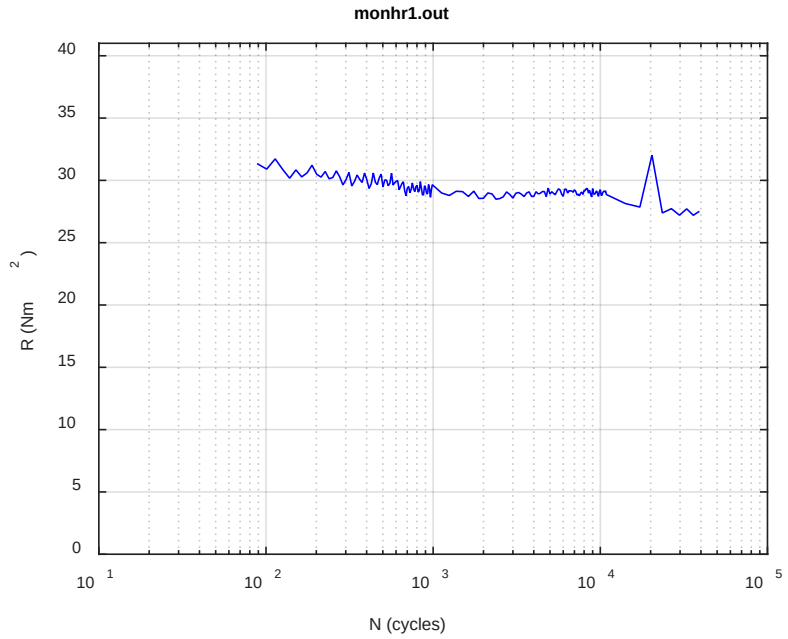

(c)

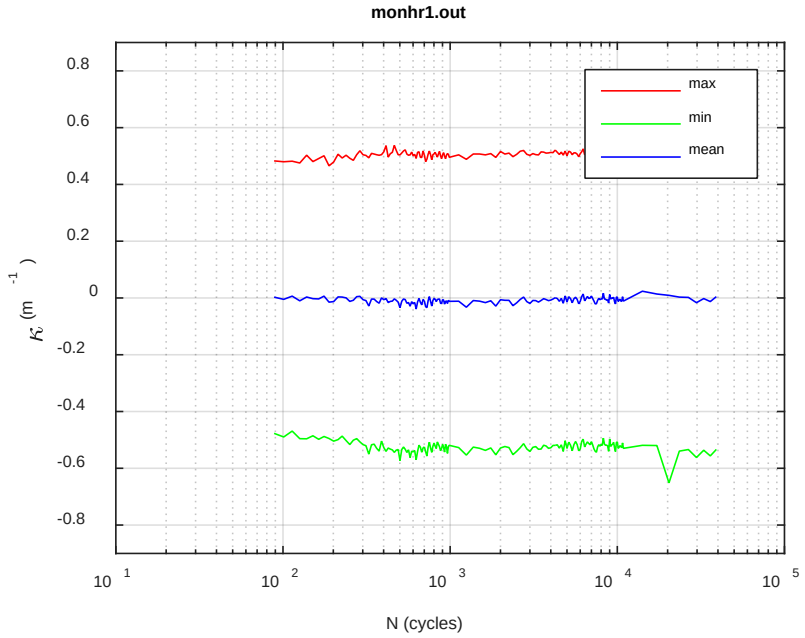

(d)

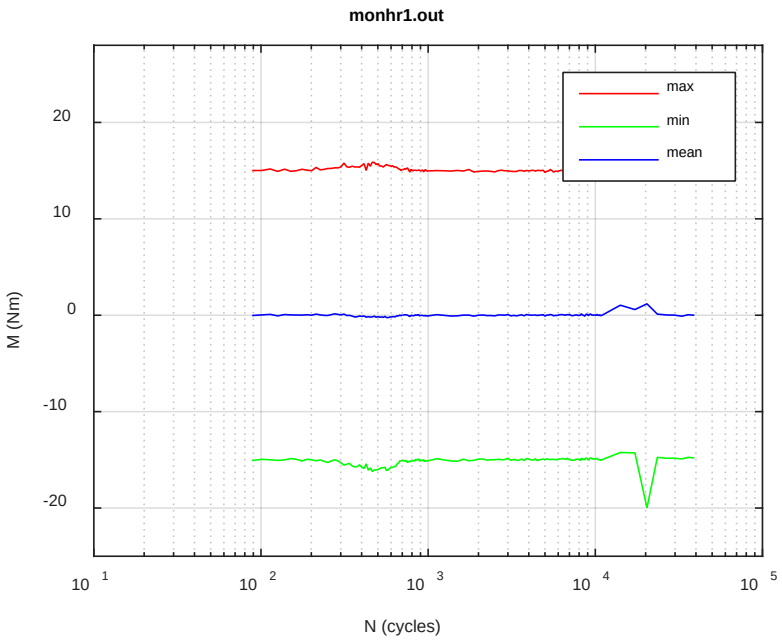

(e)

Fig. F.4 Monitoring-based responses: (a) curvature range, (b) moment range, (c) rigidity, (d) curvature peak/valley, (e) moment peak/valley, HR1, 15.24 Nm, Nf = 4.19E+04 cycles.

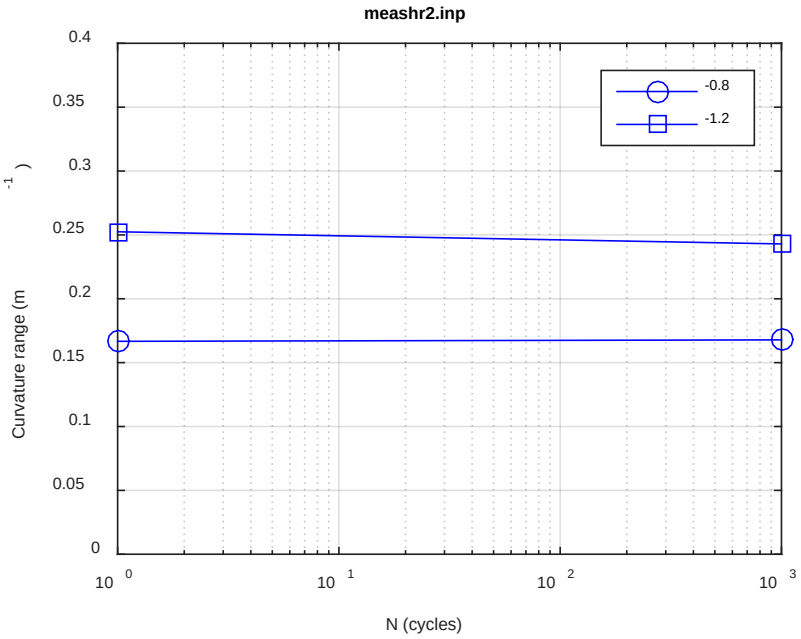
meashr2.inp
-0.8
-1.2
Curvature range (m-1)
N (cycles)
0.4
0.35
0.3
0.25
0.2
0.15
0.1
0.05
0
10 0
10 1
10 2
10 3

(a)

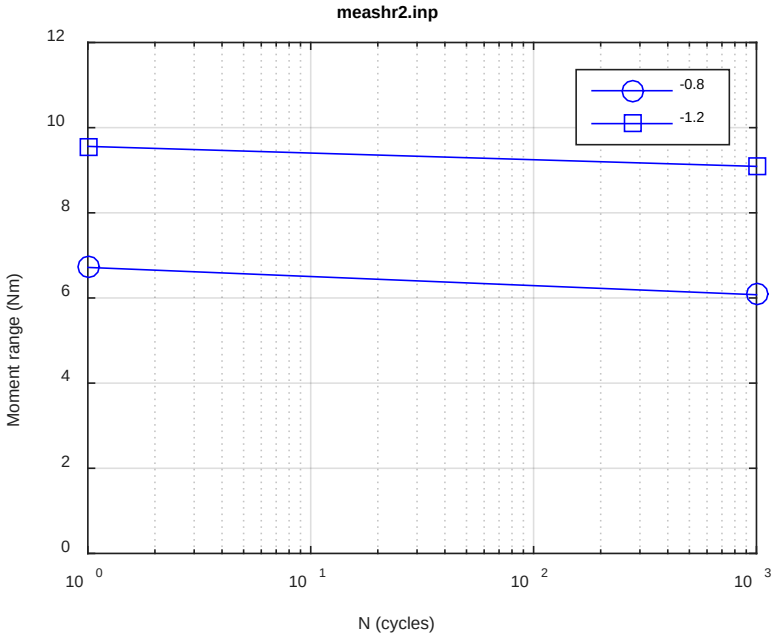
meashr2.inp
-0.8
-1.2
Moment range (Nm)
N (cycles)
12
10
8
6
4
2
0
10 0
10 1
10 2
10 3

(b)

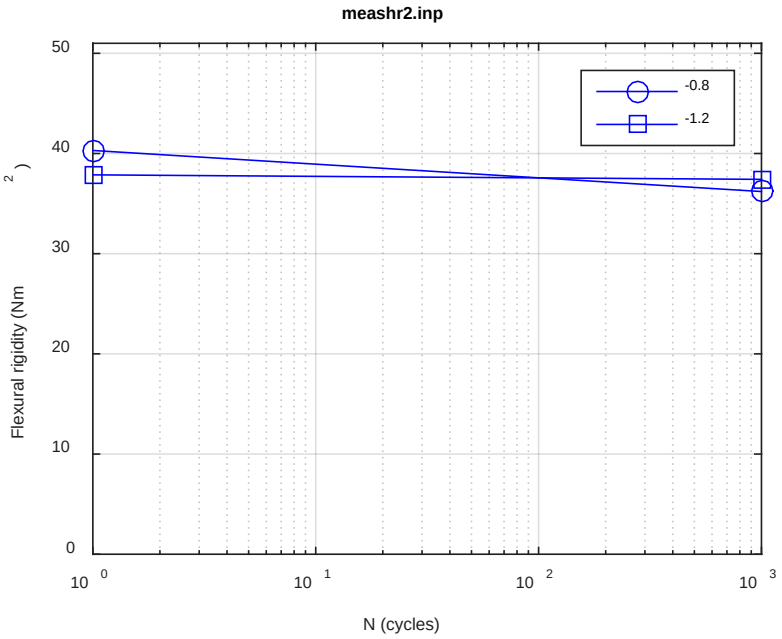
meashr2.inp
-0.8
-1.2
Flexural rigidity (Nm 2)
N (cycles)
50
40
30
20
10
0
10 0
10 1
10 2
10 3

(c)

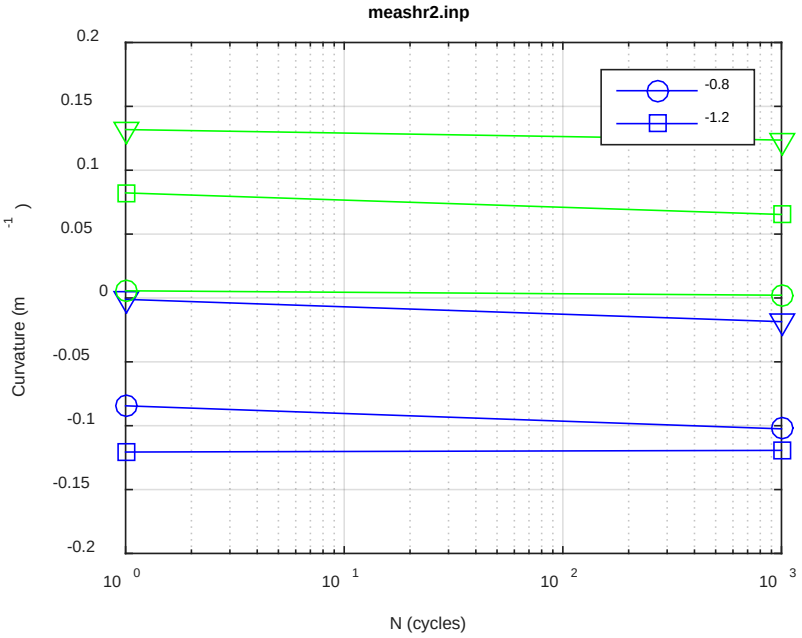
meashr2.inp
-0.8
-1.2
Curvature (m -1)
N (cycles)
0.2
0.15
0.1
0.05
0
-0.05
-0.1
-0.15
-0.2
10 0
10 1
10 2
10 3

(d)

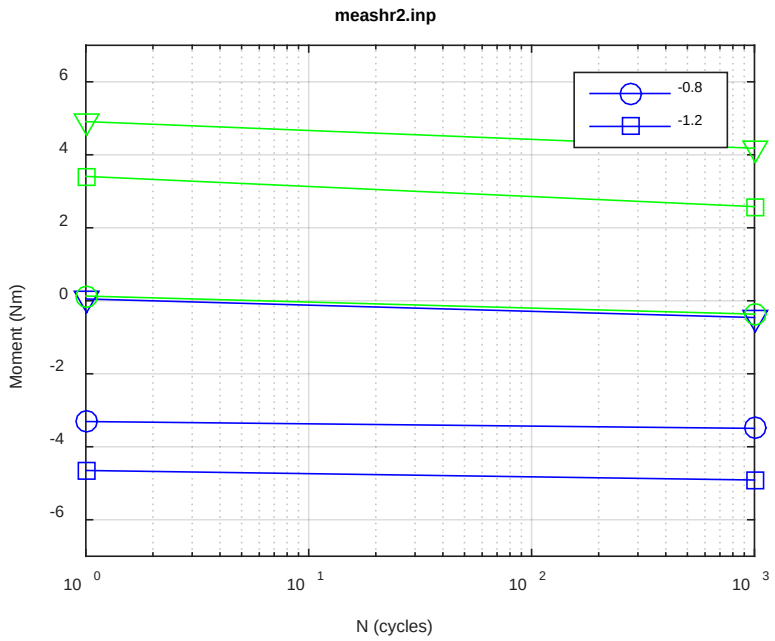

(e)

Fig. F.5 Measurement-based responses: (a) curvature range, (b) moment range, (c) rigidity, (d) curvature peak/valley, (e) moment peak/valley, HR2, 16.26 Nm.

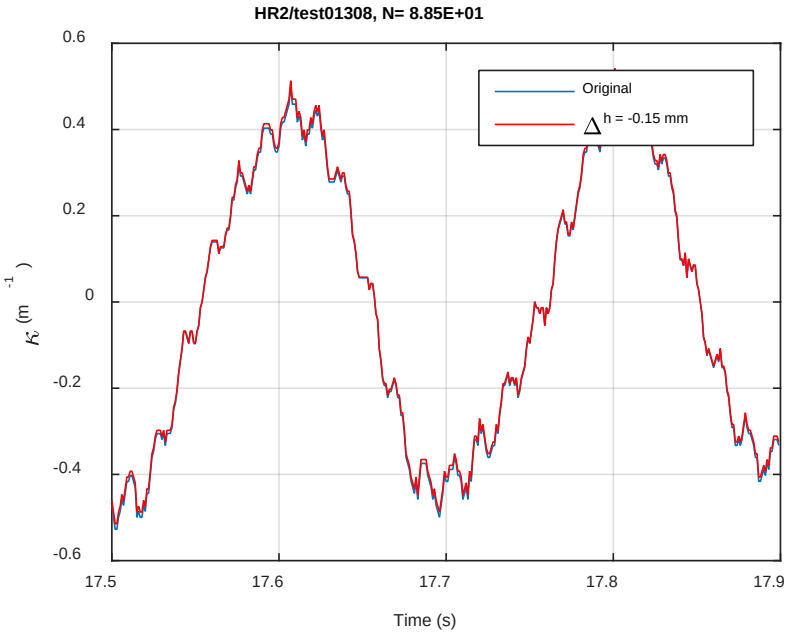
HR2/test01308, N= 8.85E+01
Original
Δh = -0.15 mm
κ (m-1)
Time (s)

(a)

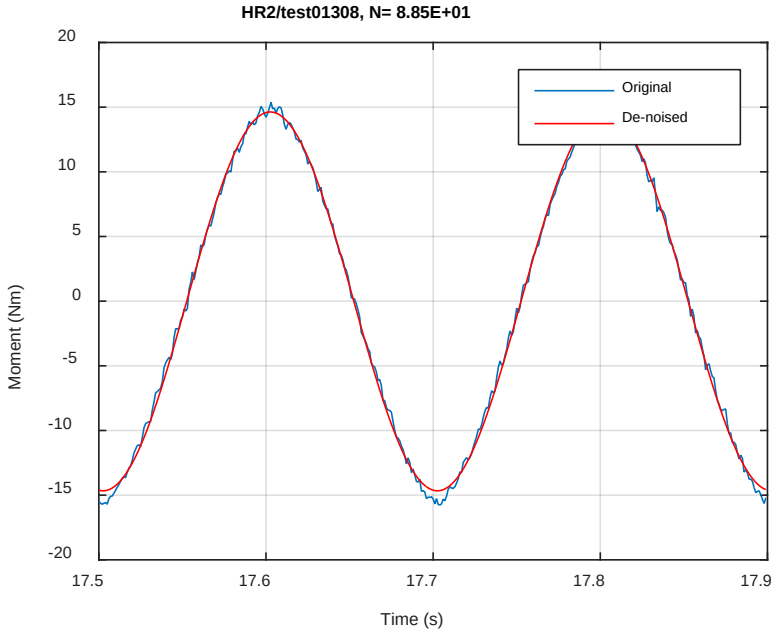
HR2/test01308, N= 8.85E+01
Original
De-noised
Moment (Nm)
Time (s)

(b)

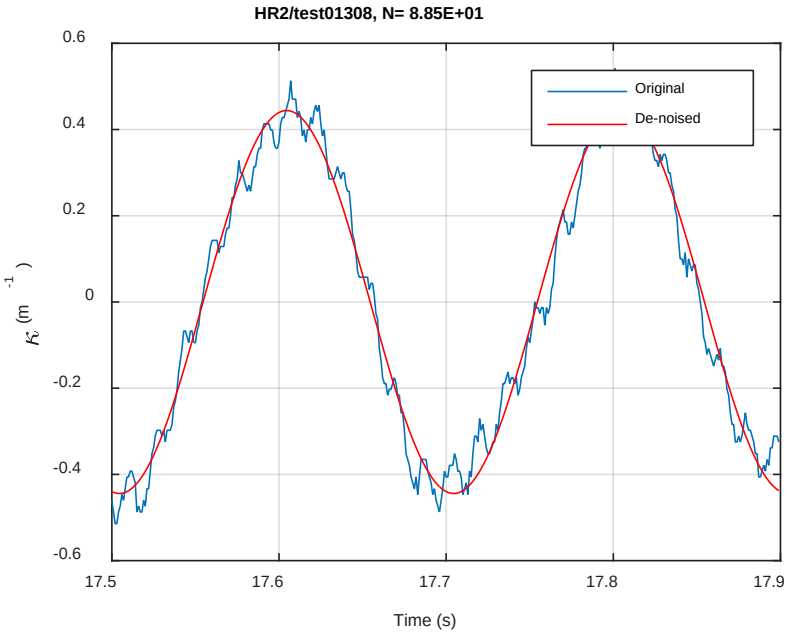

(c)

Fig. F.6 Monitoring-based responses: (a) curvature, (b) moment, (c) curvature, HR2, 16.26 Nm, Ns = 8.85E+01 cycles.

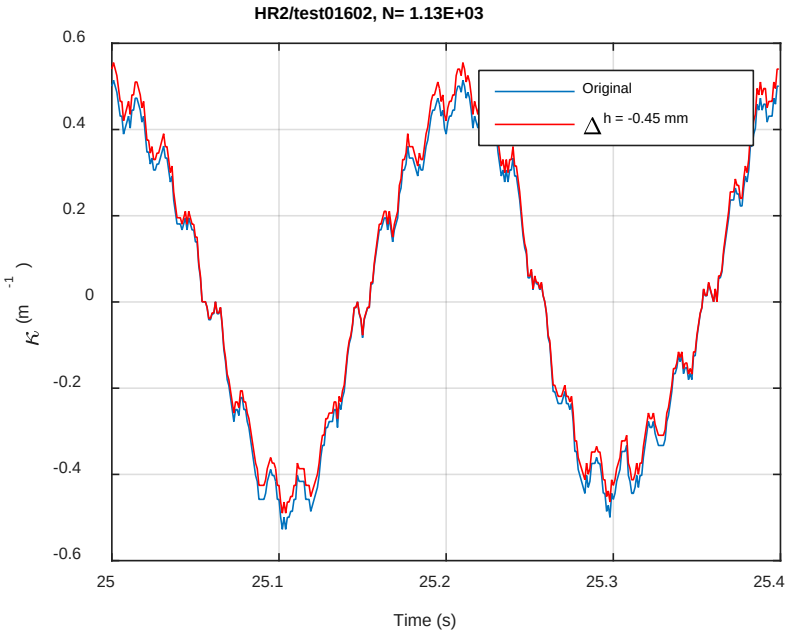
HR2/test01602, N= 1.13E+03
Original
Δh = -0.45 mm
κ (m-1)
Time (s)

(a)

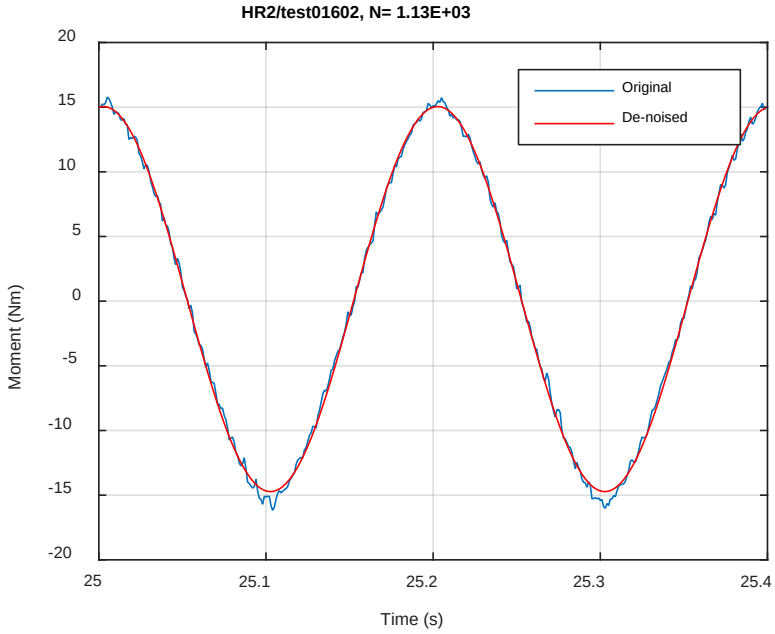
HR2/test01602, N= 1.13E+03
Original
De-noised
Moment (Nm)
Time (s)

(b)

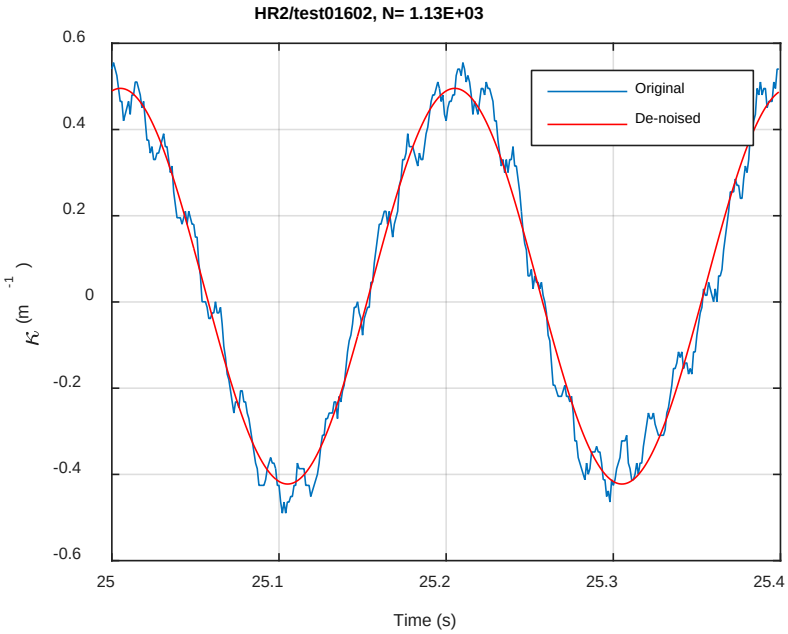

(c)

Fig. F.7 Monitoring-based responses: (a) curvature, (b) moment, (c) curvature, HR2, 16.26 Nm, Ns = 1.13E+03 cycles.

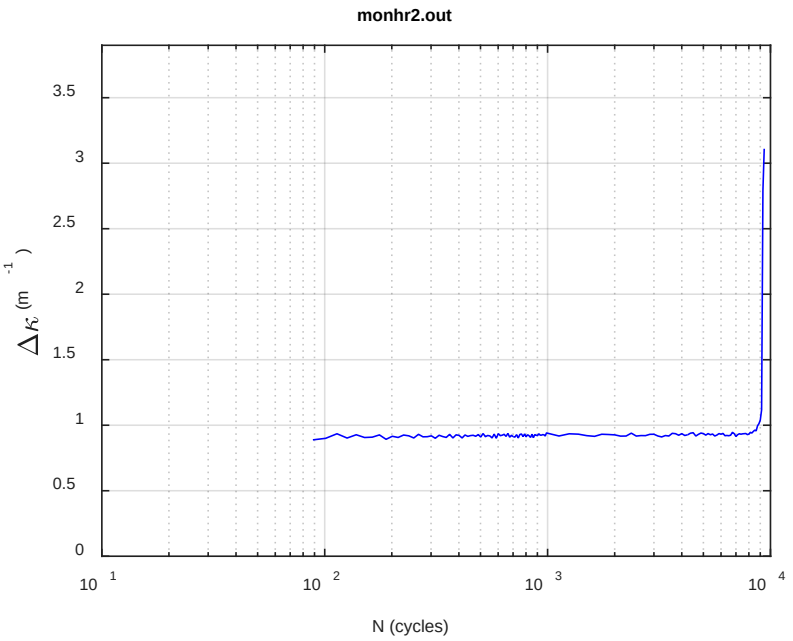
monhr2.out
3.5
3
2.5
2
1.5
1
0.5
0
$\Delta\kappa$ (m^{-1})
10 1
10 2
10 3
10 4
N (cycles)

(a)

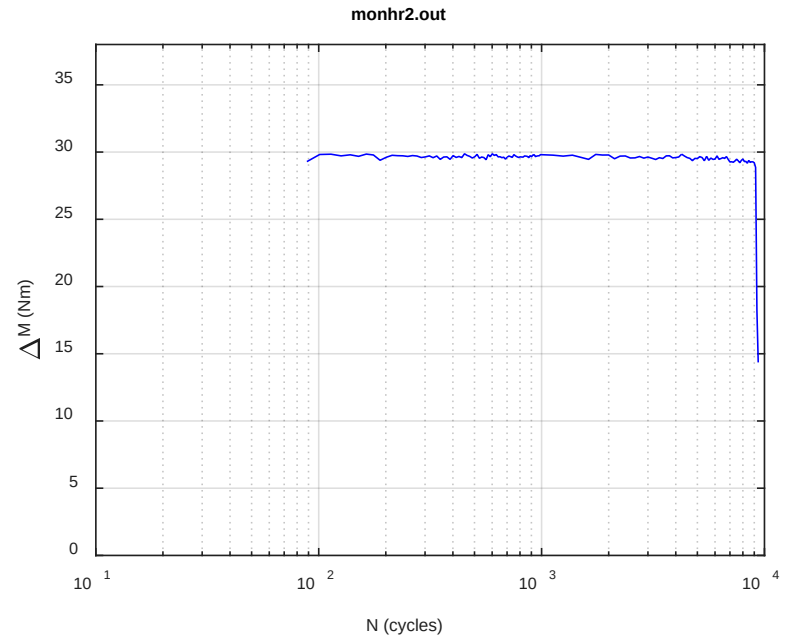
monhr2.out
35
30
25
20
15
10
5
0
Δ M (Nm)
10 1
10 2
10 3
10 4
N (cycles)

(b)

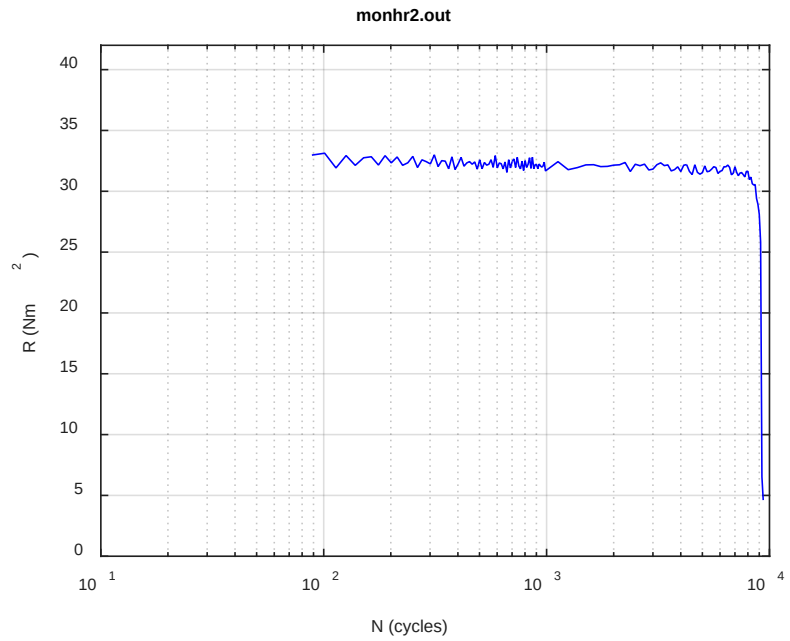

(c)

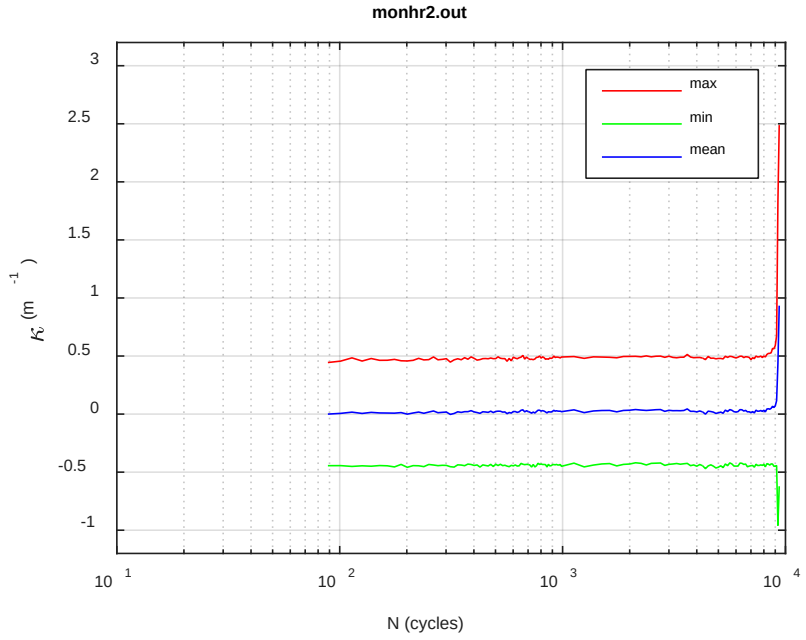

(d)

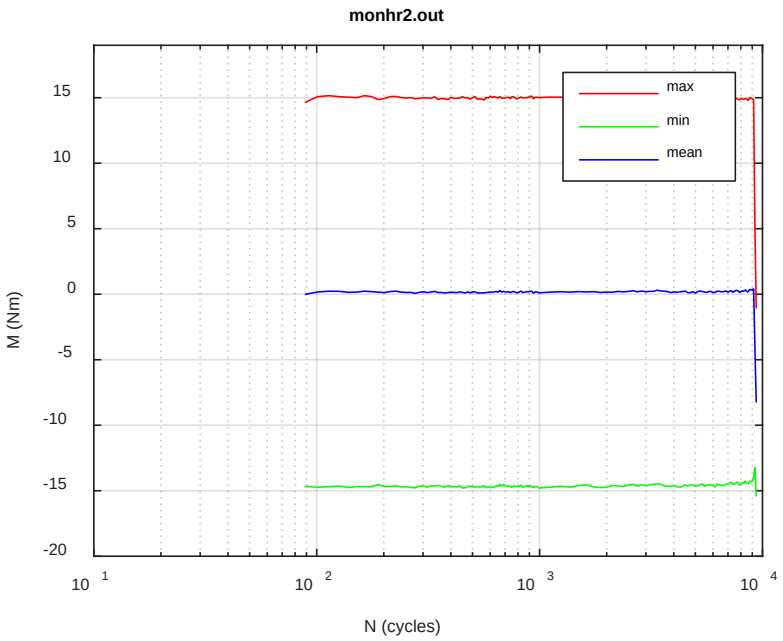

(e)

Fig. F.8 Monitoring-based responses: (a) curvature range, (b) moment range, (c) rigidity, (d) curvature peak/valley, (e) moment peak/valley, HR2, 16.26 Nm, Nf = 9.47E+03 cycles.

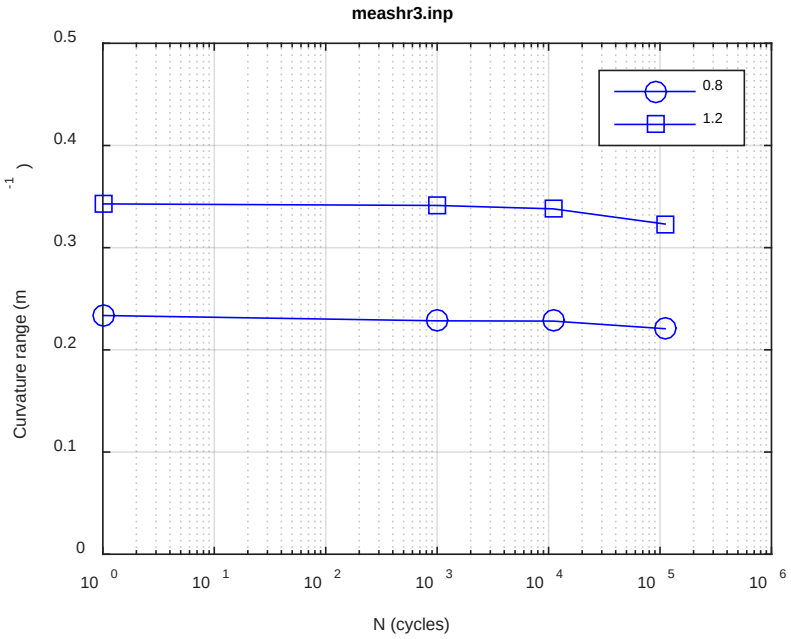
meashr3.inp
0.8
1.2
Curvature range (m -1)
N (cycles)
0
0.1
0.2
0.3
0.4
0.5
10 0
10 1
10 2
10 3
10 4
10 5
10 6

(a)

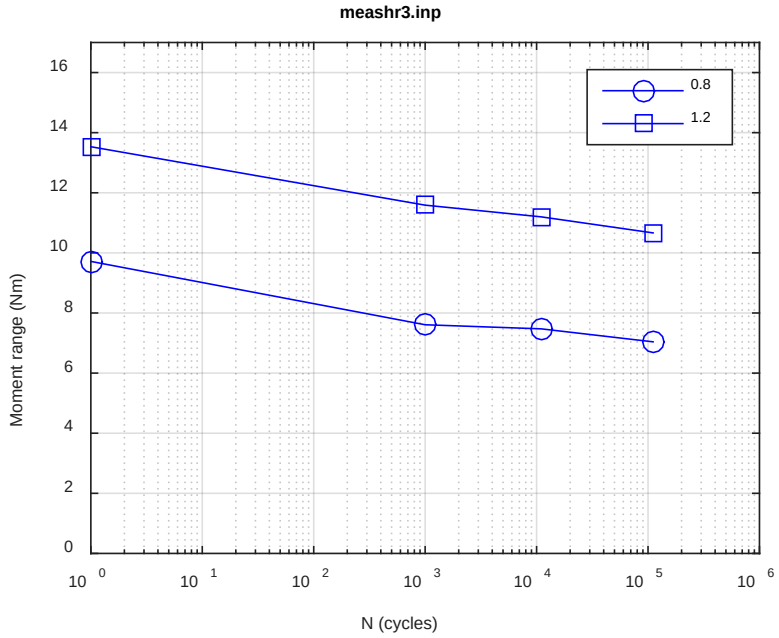
meashr3.inp
0.8
1.2
Moment range (Nm)
N (cycles)
0
2
4
6
8
10
12
14
16
10 0
10 1
10 2
10 3
10 4
10 5
10 6

(b)

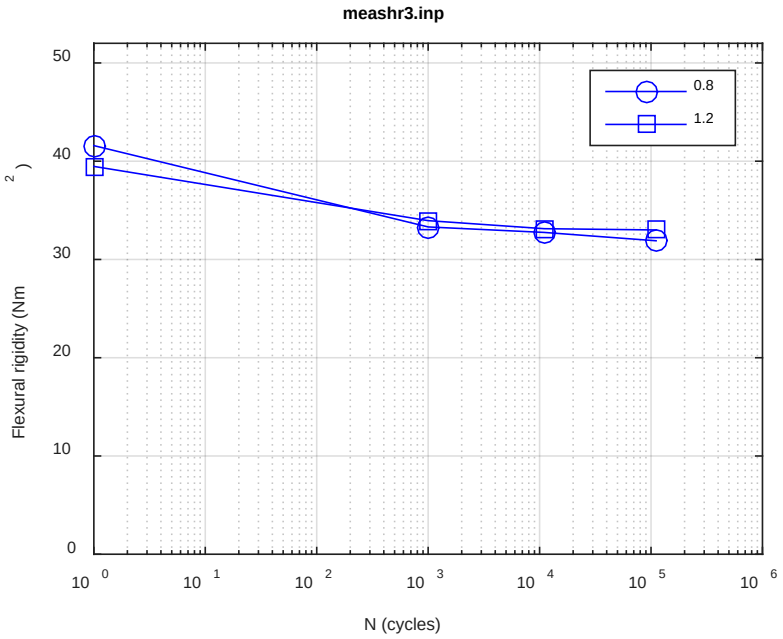
meashr3.inp
0.8
1.2
Flexural rigidity (Nm 2)
N (cycles)

(c)

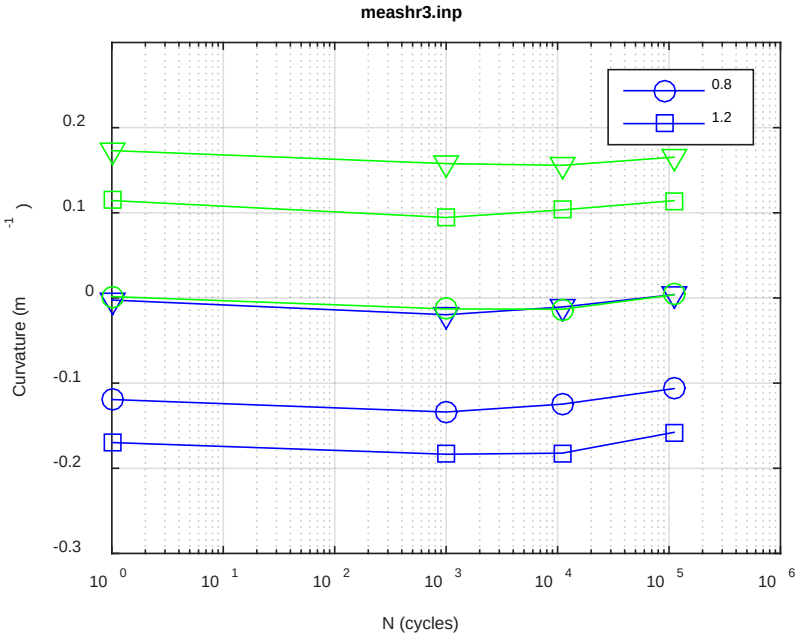
meashr3.inp
0.8
1.2
Curvature (m -1)
N (cycles)

(d)

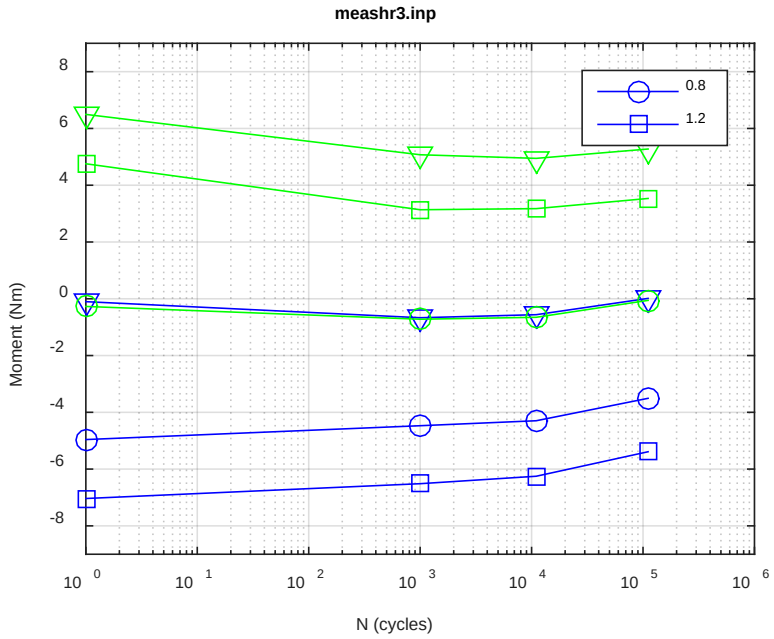

(e)

Fig. F.9 Measurement-based responses: (a) curvature range, (b) moment range, (c) rigidity, (d) curvature peak/valley, (e) moment peak/valley, HR3, 10.16 Nm.

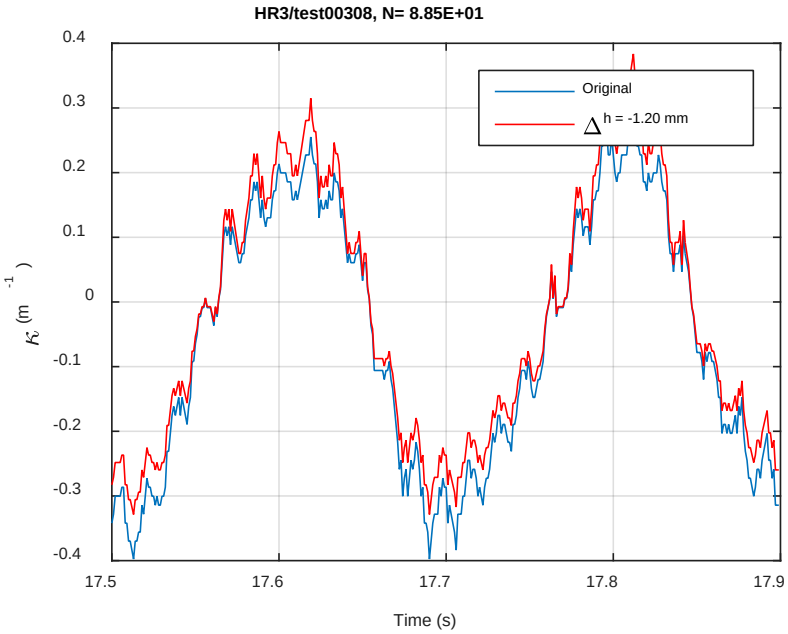
HR3/test00308, N= 8.85E+01
Original
Δh = -1.20 mm
κ (m-1)
Time (s)

(a)

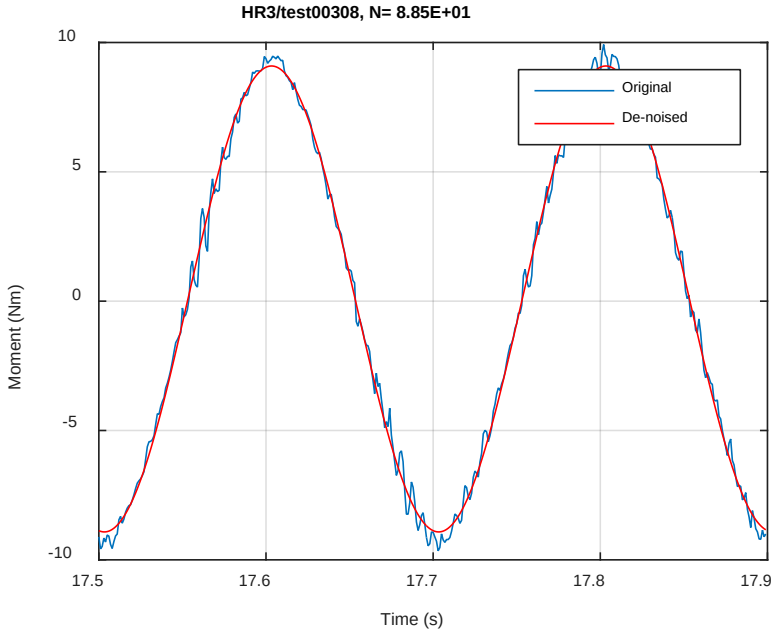
HR3/test00308, N= 8.85E+01
Original
De-noised
Moment (Nm)
Time (s)

(b)

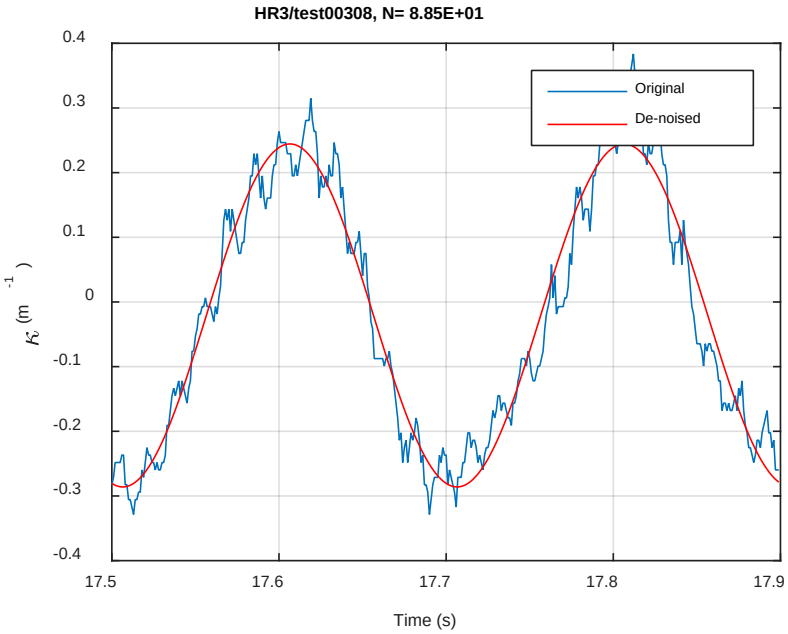

(c)

Fig. F.10 Monitoring-based responses: (a) curvature, (b) moment, (c) curvature, HR3, 10.16 Nm, Ns = 8.85E+01 cycles.

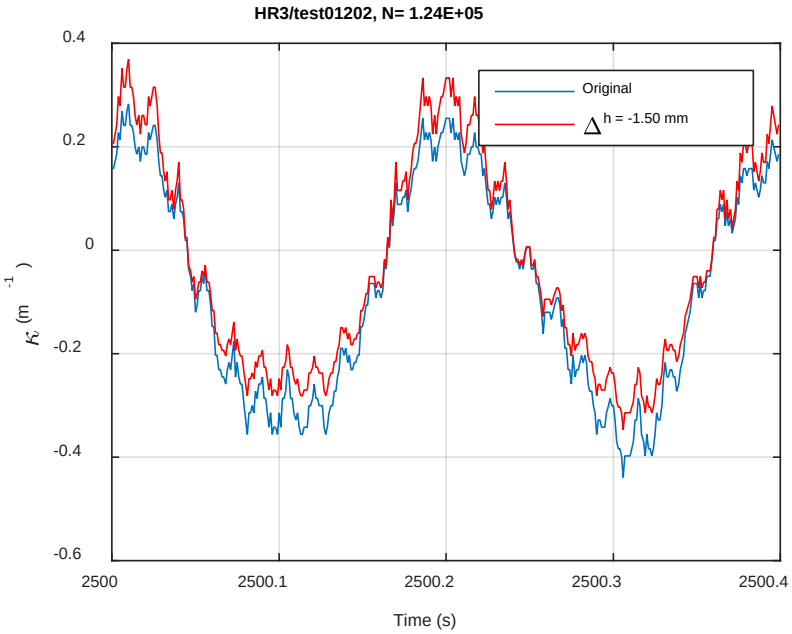
HR3/test01202, N= 1.24E+05
Original
Δh = -1.50 mm
κ (m-1)
Time (s)
0.4
0.2
0
-0.2
-0.4
-0.6
2500
2500.1
2500.2
2500.3
2500.4

(a)

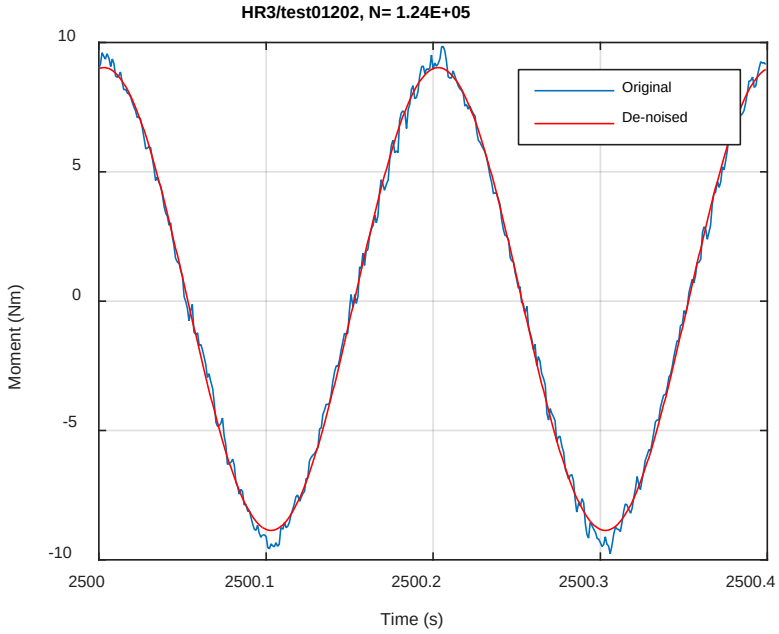
HR3/test01202, N= 1.24E+05
Original
De-noised
Moment (Nm)
Time (s)
10
5
0
-5
-10
2500
2500.1
2500.2
2500.3
2500.4

(b)

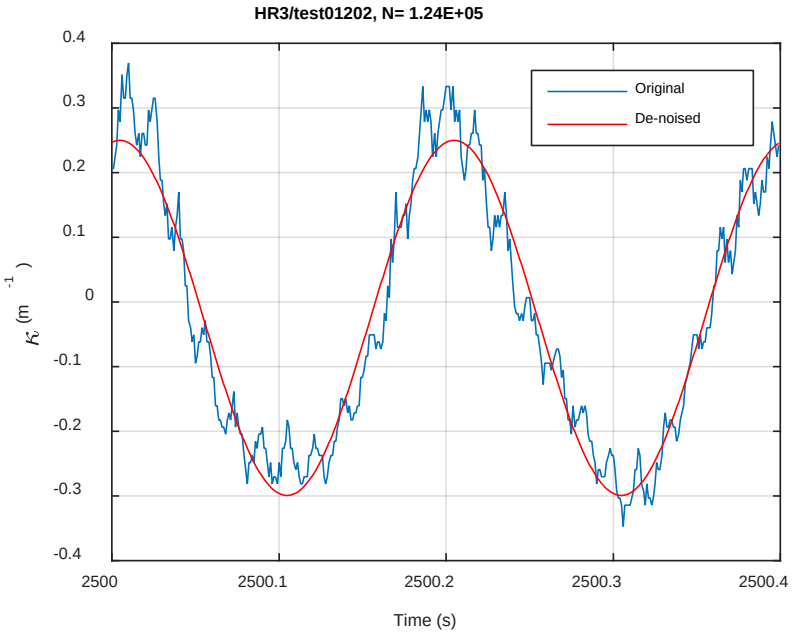

(c)

Fig. F.11 Monitoring-based responses: (a) curvature, (b) moment, (c) curvature, HR3, 10.16 Nm, Ns = 1.24E+05 cycles.

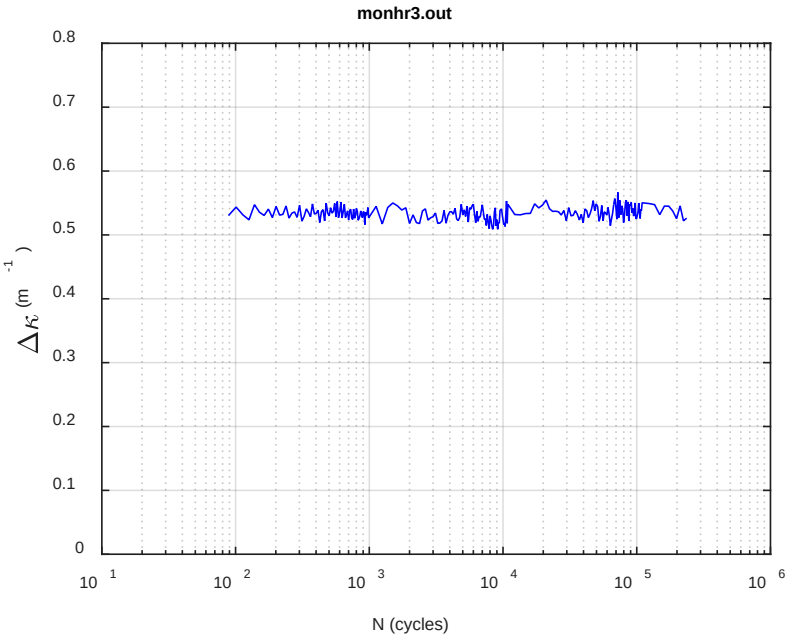
monhr3.out
0.8
0.7
0.6
0.5
0.4
0.3
0.2
0.1
0
Δκ (m -1)
10 1
10 2
10 3
10 4
10 5
10 6
N (cycles)

(a)

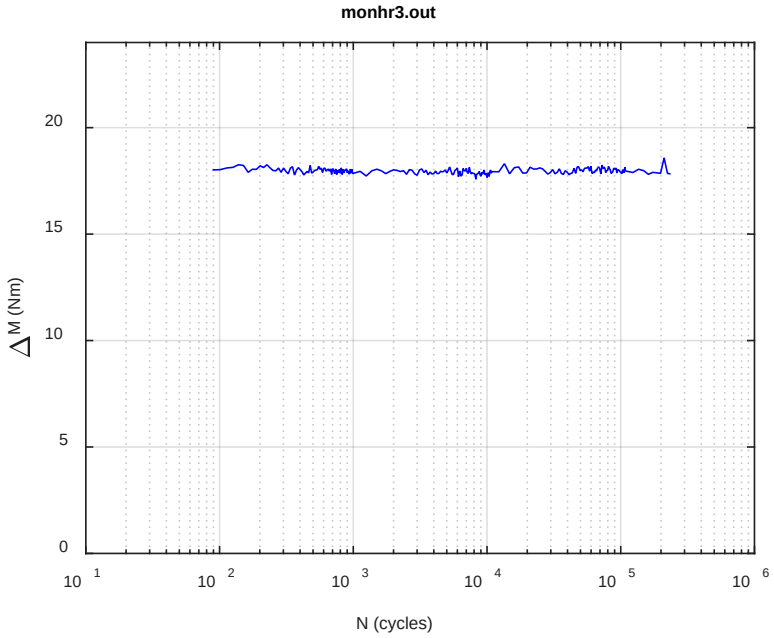
monhr3.out
20
15
10
5
0
ΔM (Nm)
10 1
10 2
10 3
10 4
10 5
10 6
N (cycles)

(b)

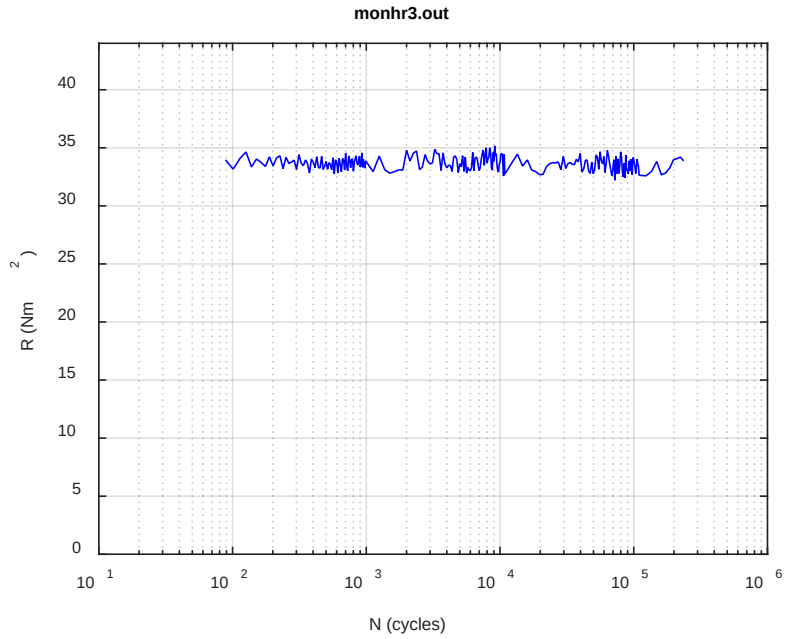

(c)

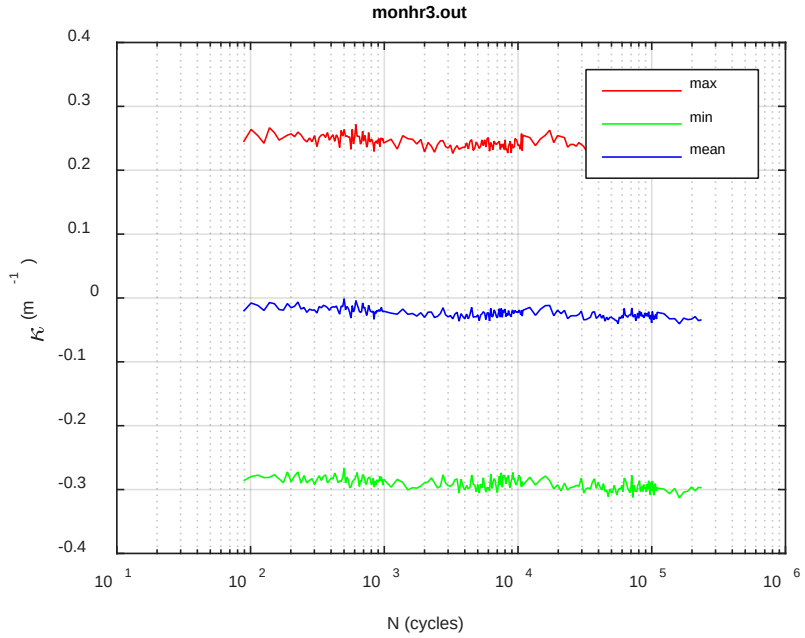

(d)

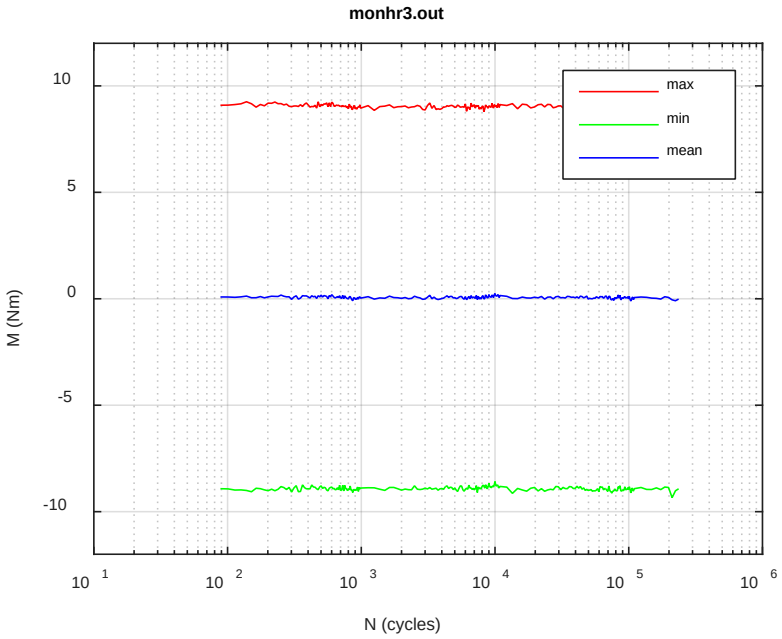

(e)

Fig. F.12 Monitoring-based responses: (a) curvature range, (b) moment range, (c) rigidity, (d) curvature peak/valley, (e) moment peak/valley, HR3, 10.16 Nm, Nf = 2.44E+05 cycles.

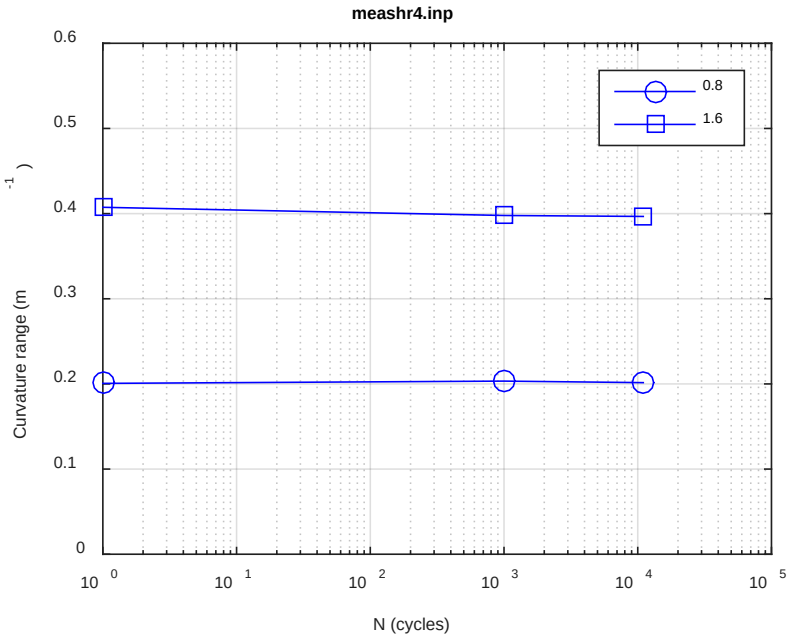
meashr4.inp
0.8
1.6
Curvature range (m -1)
N (cycles)
0
0.1
0.2
0.3
0.4
0.5
0.6
10 0
10 1
10 2
10 3
10 4
10 5

(a)

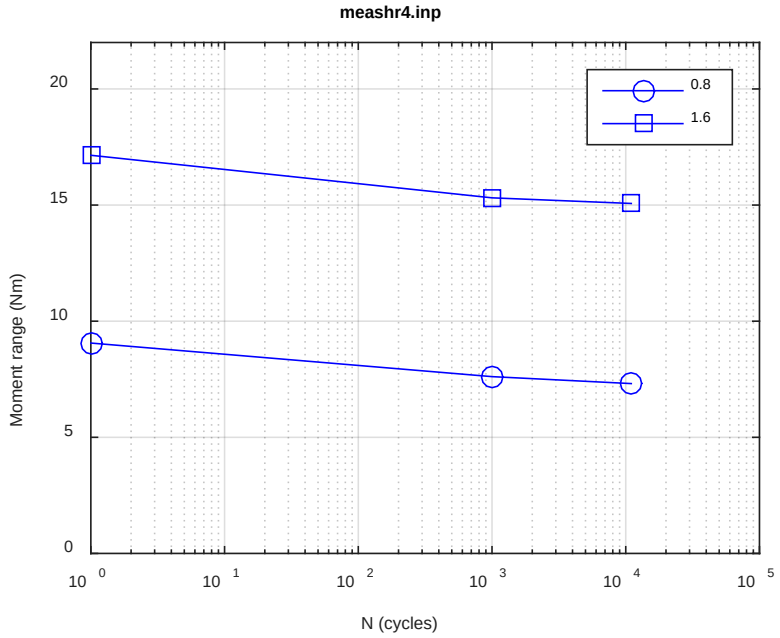
meashr4.inp
0.8
1.6
Moment range (Nm)
N (cycles)
0
5
10
15
20
10 0
10 1
10 2
10 3
10 4
10 5

(b)

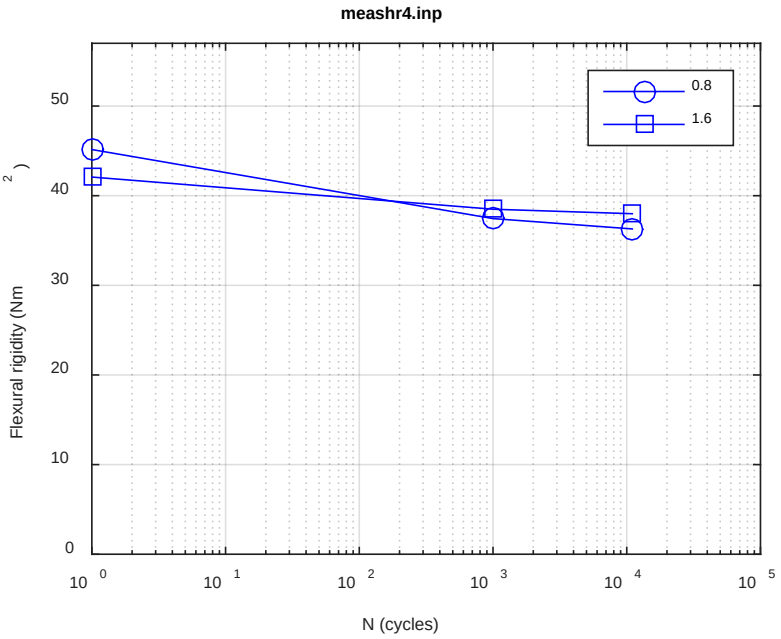
meashr4.inp
0.8
1.6
Flexural rigidity (Nm 2)
N (cycles)
0
10
20
30
40
50
10 0
10 1
10 2
10 3
10 4
10 5

(c)

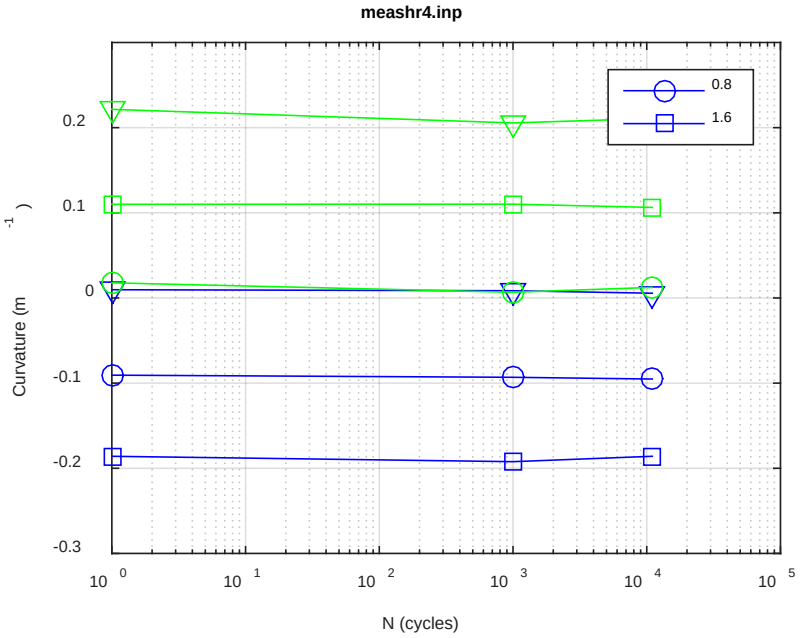
meashr4.inp
0.8
1.6
Curvature (m -1)
N (cycles)
0.2
0.1
0
-0.1
-0.2
-0.3
10 0
10 1
10 2
10 3
10 4
10 5

(d)

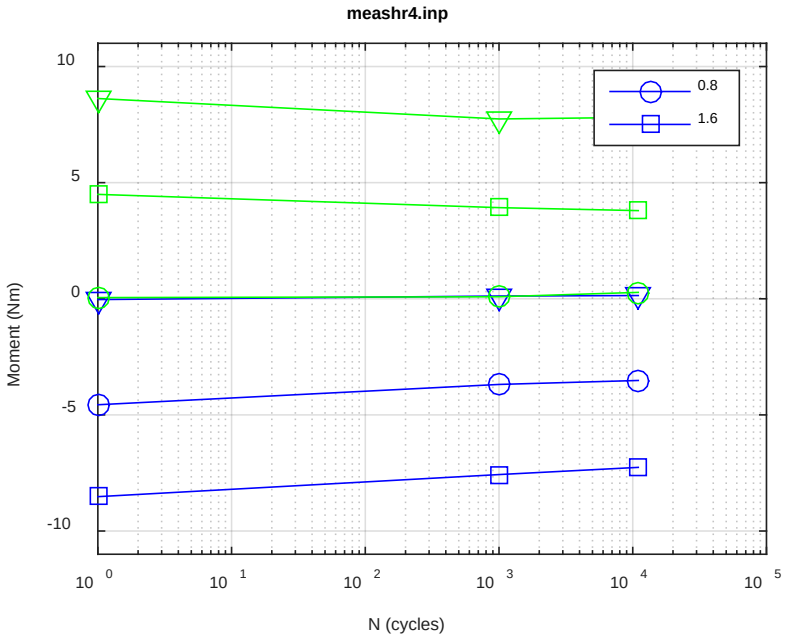

(e)

Fig. F.13 Measurement-based responses: (a) curvature range, (b) moment range, (c) rigidity, (d) curvature peak/valley, (e) moment peak/valley, HR4, 16.26 Nm.

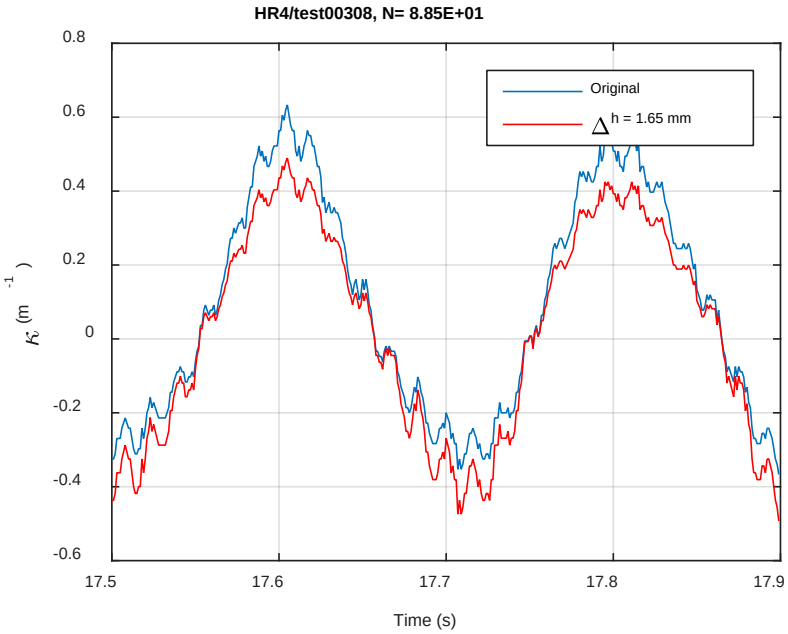
HR4/test00308, N= 8.85E+01
Original
Δh = 1.65 mm
κ (m-1)
Time (s)

(a)

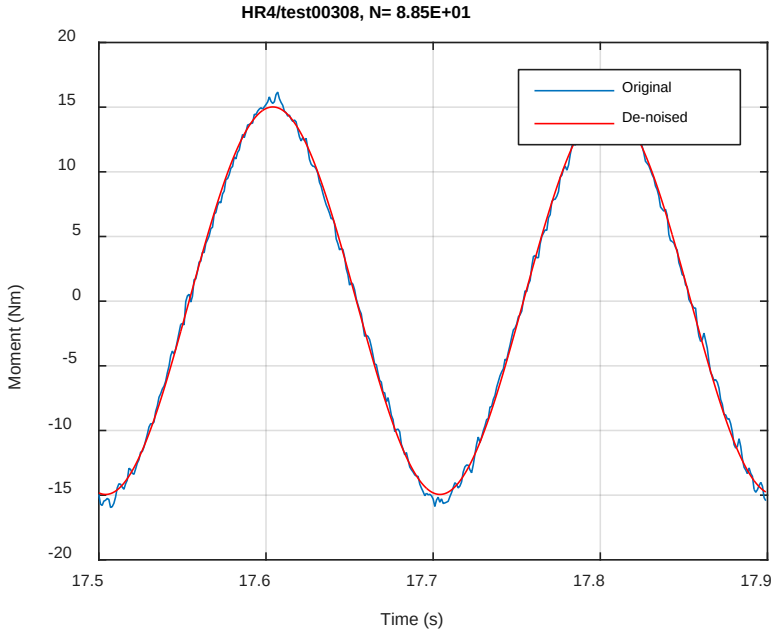
HR4/test00308, N= 8.85E+01
Original
De-noised
Moment (Nm)
Time (s)

(b)

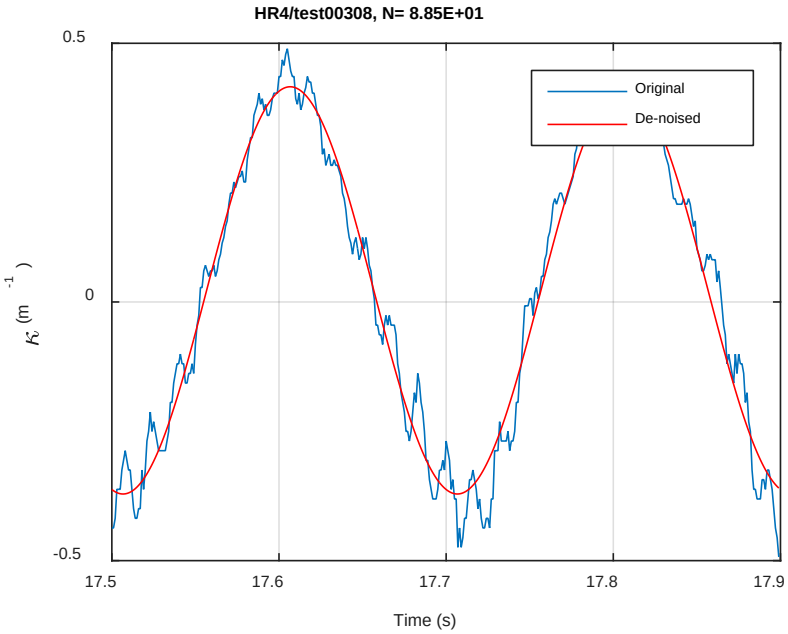

(c)

Fig. F.14 Monitoring-based responses: (a) curvature, (b) moment, (c) curvature, HR4, 16.26 Nm, Ns = 8.85E+01 cycles.

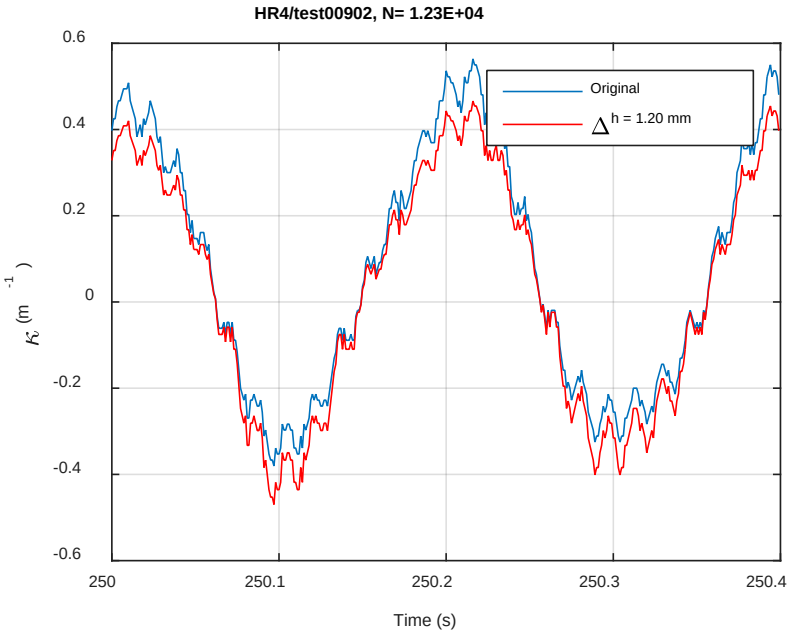
HR4/test00902, N= 1.23E+04
Original
Δh = 1.20 mm
κ (m-1)
Time (s)
0.6
0.4
0.2
0
-0.2
-0.4
-0.6
250
250.1
250.2
250.3
250.4

(a)

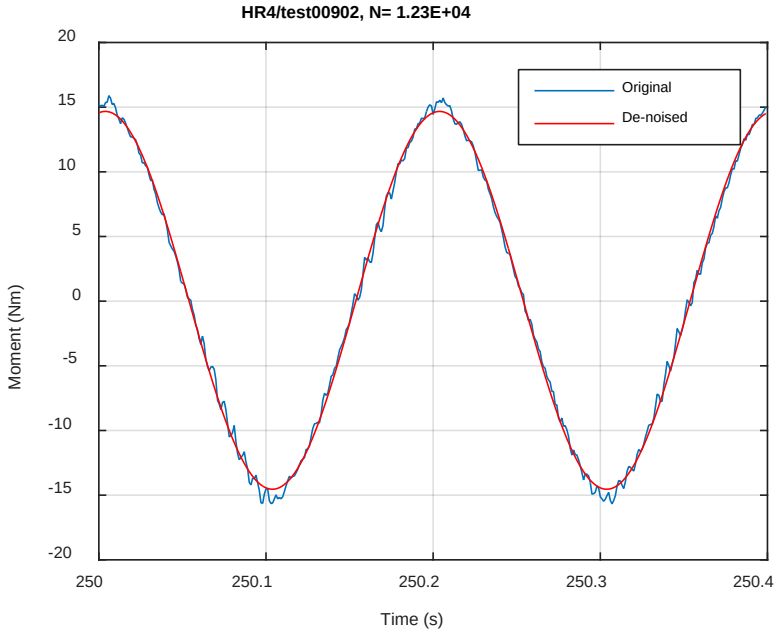
HR4/test00902, N= 1.23E+04
Original
De-noised
Moment (Nm)
Time (s)
20
15
10
5
0
-5
-10
-15
-20
250
250.1
250.2
250.3
250.4

(b)

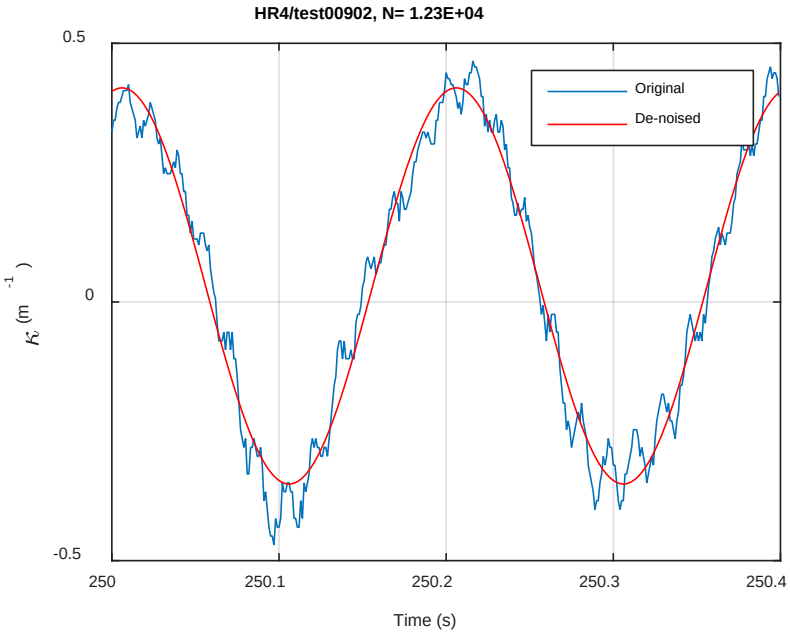

(c)

Fig. F.15 Monitoring-based responses: (a) curvature, (b) moment, (c) curvature, HR4, 16.26 Nm, Ns = 1.23E+04 cycles.

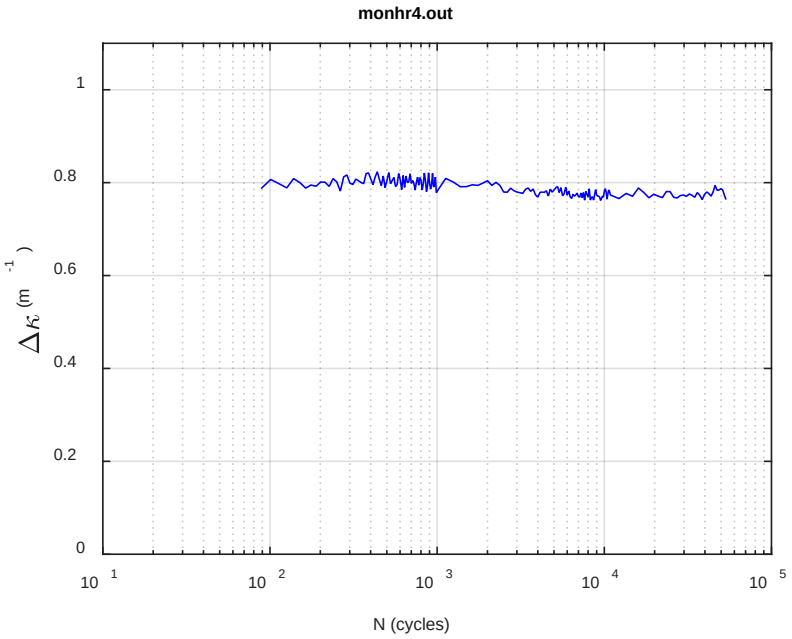
monhr4.out
1
0.8
0.6
0.4
0.2
0
Δκ (m -1)
10 1
10 2
10 3
10 4
10 5
N (cycles)

(a)

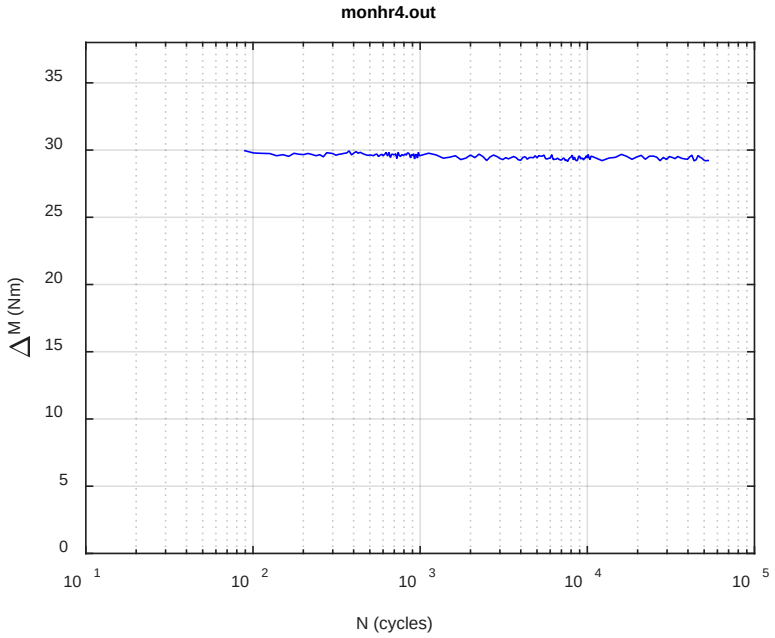
monhr4.out
35
30
25
20
15
10
5
0
Δ M (Nm)
10 1
10 2
10 3
10 4
10 5
N (cycles)

(b)

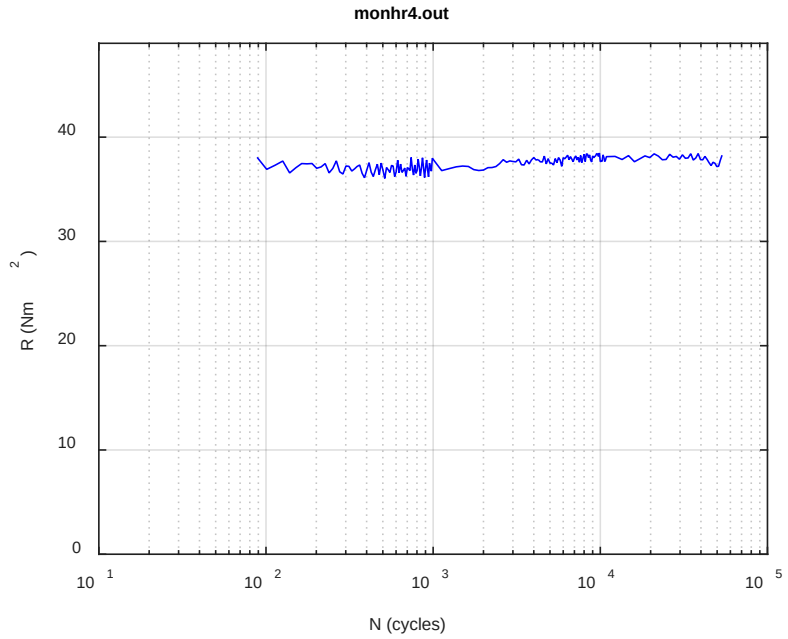
monhr4.out
R (Nm 2)
40
30
20
10
0
10 1
10 2
10 3
10 4
10 5
N (cycles)

(c)

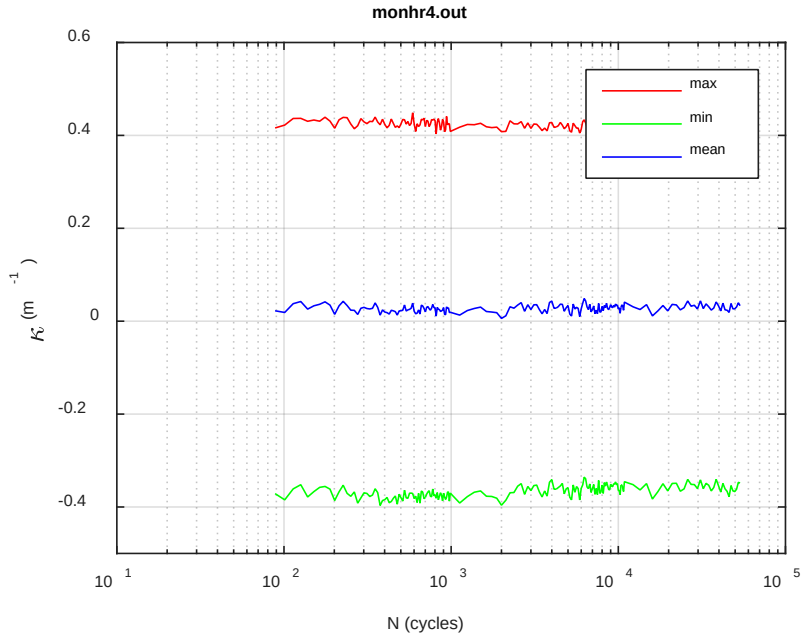
monhr4.out
κ (m -1)
0.6
0.4
0.2
0
-0.2
-0.4
max
min
mean
10 1
10 2
10 3
10 4
10 5
N (cycles)

(d)

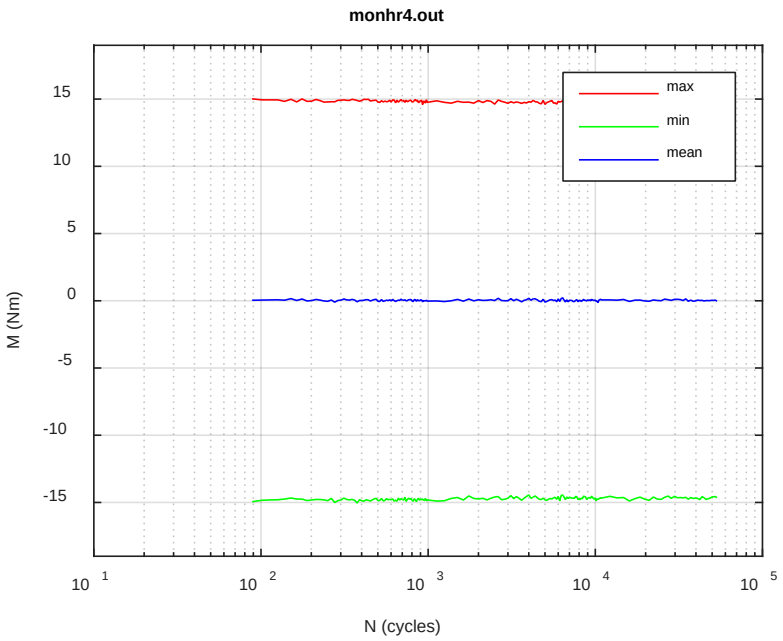

(e)

Fig. F.16 Monitoring-based responses: (a) curvature range, (b) moment range, (c) rigidity, (d) curvature peak/valley, (e) moment peak/valley, HR4, 16.26 Nm, Nf = 5.47E+04 cycles.

This page intentionally left blank.